

Polymers and Polymeric Composites: A Reference Series

Federico Carpi *Editor*

Electromechanically Active Polymers

A Concise Reference

 **cost**
EUROPEAN COOPERATION
IN SCIENCE AND TECHNOLOGY

 **Springer** Reference

Polymers and Polymeric Composites: A Reference Series

Series Editor

Sanjay Palsule

Indian Institute of Technology-Roorkee

Saharanpur, India

This series provides a comprehensive collection of reference handbooks on all aspects around polymers and polymeric composites. Polymeric materials of all sorts have been emerging as key materials for many applications and for meeting the challenges of the 21st century. From commodity applications to engineering and high tech applications, even including aerospace subsystems, these materials have an important role to play. The study of polymeric and polymeric composite materials is one of the most important and of the most vibrant focus areas in chemical and material scientific research. "Polymers and Polymeric Composites: A Reference Series" compiles the most comprehensive reference handbooks on these materials under one roof. Readers will find all they need to know in well-organized and thoroughly structured reference works covering various topics, such as the structures and properties of polymers, polymeric materials and composites (e.g. structures of amorphous and of crystalline polymers, viscoelastic properties, mechanical and thermal properties, and many more); methods and methodology (including polymer characterization, polymerization reaction engineering, polymer processing, and many more); or different compound classes (from polymer additives, polymer blends, and fiber reinforced composites, to liquid crystalline polymers, nano-polymers and nano-polymeric composites, and even bio-polymeric materials). While each volume is dedicated to a selected topic, concisely structured and thoroughly edited by experts, with contributions written by leading scientists, the complete collection provides the most comprehensive and most complete overview over the entire field of polymers and polymeric composites. Volumes in this series serve as reference compilation for every scientist working with or on polymers, polymeric materials and composites, whether at universities or in industry, from graduate student level to practitioners and lead scientists alike.

More information about this series at <http://www.springer.com/series/15068>

Federico Carpi
Editor

Electromechanically Active Polymers

A Concise Reference

With 433 figures and 24 Tables



Editor

Federico Carpi
School of Engineering and Materials Science
Queen Mary University of London
London, UK

ISBN 978-3-319-31528-7 ISBN 978-3-319-31530-0 (eBook)
ISBN 978-3-319-31529-4 (print and electronic bundle)
DOI 10.1007/978-3-319-31530-0

Library of Congress Control Number: 2016946176

© Springer International Publishing Switzerland 2016

This work is subject to copyright. All rights are reserved by the Publisher, whether the whole or part of the material is concerned, specifically the rights of translation, reprinting, reuse of illustrations, recitation, broadcasting, reproduction on microfilms or in any other physical way, and transmission or information storage and retrieval, electronic adaptation, computer software, or by similar or dissimilar methodology now known or hereafter developed.

The use of general descriptive names, registered names, trademarks, service marks, etc. in this publication does not imply, even in the absence of a specific statement, that such names are exempt from the relevant protective laws and regulations and therefore free for general use.

The publisher, the authors and the editors are safe to assume that the advice and information in this book are believed to be true and accurate at the date of publication. Neither the publisher nor the authors or the editors give a warranty, express or implied, with respect to the material contained herein or for any errors or omissions that may have been made.

Printed on acid-free paper

This Springer imprint is published by Springer Nature
The registered company is Springer International Publishing AG Switzerland
The registered company address is: Gewerbestrasse 11, 6330 Cham, Switzerland

Preface

Electromechanically active polymers (EAPs) consist of “intelligent” or “smart” soft materials that are inherently able to change dimensions and/or shape in response to electrical stimuli. As such, they transduce electrical energy into mechanical work, serving as actuators. They can also operate in reverse mode, transducing mechanical work into electrical energy, enabling their use as mechano-electrical sensors or mechanical energy harvesters to generate electricity. These functionalities come with unique properties, such as electrically-controllable strains and stresses, high mechanical flexibility, and often stretchability, low mass density, structural simplicity, ease of processing, scalability, no acoustic noise and, in most cases, low costs. Owing to the unique combination of these functional and structural properties, EAP transducers are often referred to also as “artificial muscles.” They are studied for applications in a diversity of fields, including haptics, optics, acoustics, fluidics, automotive, robotics, orthotics, medical tools, artificial organs, and energy harvesting.

A few years ago, the rapid expansion of the EAP technologies stimulated in Europe the creation of the “European Scientific Network for Artificial Muscles” (ESNAM), gathering the most active research institutes, industrial developers, and end users in the EAP field. That initiative had in Europe its ideal environment. Indeed, over the past four decades the Old Continent has been concentrating a growing number of research institutes with recognized expertise in key areas of what was progressively emerging as a new field of science and technology. Aimed at addressing the widely perceived need for cooperation in that expanding field, from the year 2007 a small group of qualified and motivated partners informally established ESNAM, which then steadily grew up until the year 2010, when it was awarded with a European COST (Cooperation in Science and Technology) grant (COST Action MP1003), until 2014. By that time, ESNAM had become the first example of a structured network in the EAP field, gathering 74 member organizations from 26 European countries, able to strengthen the impact of the EAP science and technology. In 2014, the network has evolved into a nonprofit international association called EuroEAP Society (European Society for Electromechanically Active Polymer Transducers and Artificial Muscles). The society is at present actively pursuing its mission to promote and contribute to the scientific and technological advancement of EAPs.

This book represents one of the scientific legacies of ESNAM. It is not just another book on EAPs. It is meant to serve as a concise reference for the entire EAP field, filling a critical gap within the related scientific literature: the lack of a comprehensive and organized introduction at a tutorial level. Indeed, the purpose of this book is not to describe the latest findings and innovations, but, rather, present basic concepts and established knowledge in a simple form, especially conceived for those who are entering the field for the first time. Nevertheless, while the book is primarily designed for new comers, especially students, it also aims at serving as a unique reference, useful even to researchers and practitioners.

Chapters on fundamentals, materials, device configurations, models, applications, as well as operative guidelines on how to start experimenting cover all the EAP categories, which are divided in seven sections. The first four sections deal with ionic EAPs, i.e., those materials that are activated by an electrically-induced transport of ions and/or molecules: gels, ionic polymer-metal composites, conducting polymers, and electroresponsive carbon based materials. The last three sections deal with electronic EAPs, i.e., those materials that are activated by electrostatic forces: piezoelectric and electrostrictive polymers, polymer electrets and ferroelectrets, and dielectric elastomers. Within each EAP family (ionic and electronic), the sequential order of presentation of the materials belonging to the family roughly corresponds to the chronological order of their discovery/invention. This is aimed at providing the reader with an idea about the development that the EAP field has undergone on the global scale substantially from the 1950s onwards.

The creation of this book has been made possible by a combined effort at different levels and from different actors: the section Editors, who have greatly helped in conceiving the focus of the chapters, selecting the authors, and revising the contributions; the authors, who have offered outstanding competence and significant dedication to prepare highly valuable content; and the European COST programme, which has financially supported the ESNAM network and the publication of this book. I have full faith that the combination of all these efforts has made this book a useful reference for a diversity of readers interested in the exciting EAP field.

Federico Carpi
Queen Mary University of London, UK
December 2015

Acknowledgment

Financial support for the publication of this book from COST (European Cooperation in Science and Technology), via the COST Action “European Scientific Network for Artificial Muscles” – ESNAM (MP1003), is gratefully acknowledged.

COST is a pan-European intergovernmental framework. Its mission is to enable breakthrough scientific and technological developments leading to new concepts and products and thereby contribute to strengthening Europe’s research and innovation capacities.

It allows researchers, engineers, and scholars to jointly develop their own ideas and take new initiatives across all fields of science and technology, while promoting multi- and interdisciplinary approaches. COST aims at fostering a better integration of less research intensive countries to the knowledge hubs of the European Research Area. The COST Association, an International not-for-profit Association under Belgian Law, integrates all management, governing, and administrative functions necessary for the operation of the framework. The COST Association has currently 36 Member Countries. www.cost.eu

December 2015



COST is supported by
the EU Framework Programme
Horizon 2020

Contents

Section I Polymer Gels	1
1 Polymer Gels as EAPs: Fundamentals	3
Andreas Voigt and Andreas Richter	
2 Polymer Gels as EAPs: Materials	27
Garima Agrawal and Andrij Pich	
3 Polymer Gels as EAPs: Models	53
Thomas Wallmersperger and Peter Leichsenring	
4 Polymer Gels as EAPs: Applications	83
Martin Elstner and Andreas Richter	
5 Polymer Gels as EAPs: How to Start Experimenting with Them	101
Bernhard Ferse, Luis Pedrero, Marcus Tietze, and Andreas Richter	
Section II Ionic Polymer–Metal Composites	129
6 IPMCs as EAPs: Fundamentals	131
Kinji Asaka, Kwang Kim, Keisuke Oguro, and Mohsen Shahinpoor	
7 IPMCs as EAPs: Materials	151
Kwang Kim, Viljar Palmre, Jin-Han Jeon, and Il-Kwon Oh	
8 IPMCs as EAPs: Models	171
Kwang Kim, Viljar Palmre, David Pugal, Tyler Stalbaum, Zheng Chen, Xiaobo Tan, and Masaki Yamakita	
9 IPMCs as EAPs: Applications	191
Kinji Asaka, Kentaro Takagi, Norihiro Kamamichi, Youngsu Cha, and Maurizio Porfiri	
10 IPMCs as EAPs: How to Start Experimenting with Them	215
Kinji Asaka, Karl Kruusamäe, Kwang Kim, Viljar Palmre, and Kam K. Leang	

Section III	Conducting Polymers	235
11	Conducting Polymers as EAPs: Fundamentals and Materials	237
	Toribio F. Otero and José G. Martínez	
12	Conducting Polymers as EAPs: Device Configurations	257
	Gursel Alici, Rahim Mutlu, Daniel Melling, Edwin W. H. Jager, and Keiichi Kaneto	
13	Conducting Polymers as EAPs: Microfabrication	293
	Edwin W. H. Jager, Ali Maziz, and Alexandre Khaldi	
14	Conducting Polymers as EAPs: Characterization Methods and Metrics	319
	Daniel Melling and Edwin W. H. Jager	
15	Conducting Polymers as EAPs: Physical Description and Simulation	353
	Meisam Farajollahi, Gursel Alici, Mirza Saquib Sarwar, and John D. W. Madden	
16	Conducting Polymers as EAPs: Applications	385
	Keiichi Kaneto, Edwin W. H. Jager, Gursel Alici, and Hidenori Okuzaki	
17	Conducting Polymers as EAPs: How to Start Experimenting with Them	413
	José G. Martinez, Cedric Plesse, Frederic Vidal, and Wen Zheng	
Section IV	Electroresponsive Carbon-Based Materials	437
18	Electrochemically Driven Carbon-Based Materials as EAPs: Fundamentals and Device Configurations	439
	Janno Torop, Anna-Liisa Peikolainen, Alvo Aabloo, Mihkel Koel, Kinji Asaka, and Ray H. Baughman	
19	Electrothermally Driven Carbon-Based Materials as EAPs: Fundamentals and Device Configurations	455
	Javad Foroughi, Geoffrey M. Spinks, John D. W. Madden, Ray H. Baughman, and Seon Jeong Kim	
20	Electrochemically and Electrothermally Driven Carbon-Based Materials as EAPs: How to Start Experimenting with Them	471
	Indrek Must, Geoffrey M. Spinks, and Alvo Aabloo	

Section V Piezoelectric and Electrostrictive Polymers	487
21 Piezoelectricity and Electrostriction	489
Reimund Gerhard	
22 Piezoelectric and Electrostrictive Polymers as EAPs: Materials	509
Ji Su and Yoshiro Tajitsu	
23 Piezoelectric and Electrostrictive Polymers as EAPs: Devices and Applications	533
Siegfried Bauer and Simona Bauer-Gogonea	
Section VI Polymer Electrets and Ferroelectrets	549
24 Polymer Electrets and Ferroelectrets as EAPs: Fundamentals	551
Ingrid Graz and Axel Mellinger	
25 Polymer Electrets and Ferroelectrets as EAPs: Materials	561
Xunlin Qiu	
26 Polymer Electrets and Ferroelectrets as EAPs: Characterization	591
Michael Wübbenhorst, Xiaoqing Zhang, and Tristan Putzeys	
27 Polymer Electrets and Ferroelectrets as EAPs: Devices and Applications	625
Yuji Suzuki and Yoshinobu Yasuno	
28 Polymer Electrets and Ferroelectrets as EAPs: Models	645
Dmitry Rychkov and Ruy Alberto Pisani Altafim	
29 Polymer Electrets and Ferroelectrets as EAPs: How to Start Experimenting with Them	661
Simona Bauer-Gogonea, Siegfried Bauer, Richard Baumgartner, Alexander Kogler, Markus Krause, and Reinhard Schwödäuer	
Section VII Dielectric Elastomers	669
30 Dielectric Elastomers as Electroactive Polymers (EAPs): Fundamentals	671
Ron Pelrine and Roy Kornbluh	
31 Dielectric Elastomers (DEs) as EAPs: Materials	687
Anne L. Skov, Qibing Pei, Dorina Opris, Richard J. Spontak, Giuseppe Gallone, Herbert Shea, and Mohammed Y. Benslimane	

32 Dielectric Elastomers as EAPs: Models	715
Helmut F. Schlaak, Massimiliano Gei, Eliana Bortot, Henry Haus, and Holger Mößinger	
33 Dielectric Elastomers as EAPs: Applications	739
Qibing Pei, Wei Hu, David McCoul, Silmon James Biggs, David Stadler, and Federico Carpi	
34 Dielectric Elastomers as EAPs: How to Start Experimenting with Them	767
Herbert Shea, Soo Jin Adrian Koh, Ingrid Graz, and Jun Shintake	
Index	789

Section Editors

Section I: Polymer Gels

Yoshihito Osada Riken Advanced Science Institute, Wako, Saitama, Japan

Andreas Richter Technical University of Dresden, Dresden, Germany

Section II: Ionic Polymer-Metal Composites

Kinji Asaka National Institute of Advanced Industrial Science and Technology, Tokyo, Japan

Kwang Kim University of Nevada, Las Vegas, USA

Keisuke Oguro National Institute of Advanced Industrial Science and Technology, Tokyo, Japan

Section III: Conducting Polymers

Edwin Jager Linköping University, Linköping, Sweden

John Madden University of British Columbia, Vancouver, BC, Canada

Toribio Otero University of Cartagena, Cartagena, Spain

Frédéric Vidal University of Cergy-Pontoise, Cergy-Pontoise, France

Section IV: Electroresponsive Carbon-Based Materials

Alvo Aabloo University of Tartu, Cergy-Pontoise, Estonia

Ray H. Baughman University of Texas, Dallas, USA

Geoffrey Spinks University of Wollongong, Wollongong, NSW, Australia

Section V: Piezoelectric and Electrostrictive Polymers

Siegfried Bauer Johannes Kepler University, Linz, Austria

Zhongyang Cheng Auburn University, Zhongyang, AL, USA

Eiichi Fukada Kobayasi Institute of Physical Research, Tokyo, Japan

Qiming Zhang Pennsylvania State University, State College, PA, USA

Section VI: Polymer Electrets and Ferroelectrets

Reimund Gerhard University of Potsdam, Reimund, Germany

Gerhard Sessler Darmstadt University of Technology, Darmstadt, Germany

Section VII: Dielectric Elastomers

Roy Kornbluh SRI International, Menlo Park, CA, USA

Anne Ladegaard Skov Technical University of Denmark, Lyngby, Denmark

Qibing Pei University of California, Los Angeles, USA

Ron Pelrine SRI International, Menlo Park, CA, USA

Contributors

Alvo Aabloo Intelligent Materials and Systems Lab, Institute of Technology, University of Tartu, Tartu, Estonia

Garima Agrawal DWI-Leibniz Institute for Interactive Materials, Institute of Technical and Macromolecular Chemistry, RWTH Aachen University, Aachen, Germany

Gursel Alici School of Mechanical, Materials, and Mechatronic Engineering, ARC Centre of Excellence for Electromaterials Science, University of Wollongong, Wollongong, NSW, Australia

Ruy Alberto Pisani Altafim Departamento de Sistemas de Computação, Federal University of Paraíba, João Pessoa, PB, Brazil

Kinji Asaka Inorganic Functional Material Research Institute, National Institute of Advanced Industrial Science and Technology (AIST), Ikeda, Osaka, Japan

Siegfried Bauer Soft Matter Physics, Johannes Kepler University Linz, Linz, Austria

Simona Bauer-Gogonea Soft Matter Physics, Johannes Kepler University Linz, Linz, Austria

Ray H. Baughman The Alan G. MacDiarmid NanoTech Institute, University of Texas at Dallas, Richardson, TX, USA

Richard Baumgartner Soft Matter Physics, Johannes Kepler University Linz, Linz, Austria

Mohammed Y. Benslimane Danfoss PolyPower A/S, Nordborg, Denmark

Silmon James Biggs Parker Hannifin Inc., Sunnyvale, CA, USA

Eliana Bortot Faculty of Mechanical Engineering, Technion - Israel Institute of Technology, Haifa, Israel

Federico Carpi School of Engineering and Materials Science, Queen Mary University of London, London, UK

Youngsu Cha Center for Robotics Research, Korea Institute of Science and Technology, Seoul, Republic of Korea

Zheng Chen Department of Electrical Engineering and Computer Science, Wichita State University, Wichita, KS, USA

Martin Elstner TU Dresden, Center for Advancing Electronics Dresden (cfaed), Dresden, Germany

Meisam Farajollahi Mechanical Engineering, Advanced Materials and Process Engineering Lab, University of British Columbia, Vancouver, BC, Canada

Bernhard Ferse Faculty of Electrical and Computer Engineering, Institute of Semiconductors and Microsystems, Technische Universität Dresden, Dresden, Germany

Javad Foroughi ARC Centre of Excellence for Electromaterials Science, Intelligent Polymer Research Institute, University of Wollongong, North Wollongong, NSW, Australia

Giuseppe Gallone Department of Civil and Industrial Engineering, University of Pisa, Pisa, Italy

Massimiliano Gei School of Engineering, Cardiff University, Cardiff, UK

Reimund Gerhard Applied Condensed-Matter Physics, Institute of Physics and Astronomy, Faculty of Science, University of Potsdam, Potsdam-Golm, Germany

Ingrid Graz Soft Matter Physics, Johannes Kepler University Linz, Linz, Austria

Henry Haus Institute of Electromechanical Design, Technische Universität Darmstadt, Darmstadt, Germany

Wei Hu Henry Samueli School of Engineering and Applied Science, University of California – Los Angeles, Los Angeles, CA, USA

Edwin W. H. Jager Department of Physics, Chemistry and Biology (IFM), Linköping University, Linköping, Sweden

Biosensors and Bioelectronics, Linköping University, Linköping, Sweden

Jin-Han Jeon School of Mechanical, Aerospace and Systems Engineering, Korea Advanced Institute of Science and Technology (KAIST), Daejeon, Republic of Korea

Norihiro Kamamichi Department of Robotics and Mechatronics, Tokyo Denki University, Tokyo, Japan

Keiichi Kaneto Kyushu Institute of Technology, Eamex Co. Ltd, Chuoku, Fukuoka, Japan

Osaka Institute of Technology, Eamex Co. Ltd., Osaka, Japan

Alexandre Khaldi Department of Physics, Chemistry and Biology (IFM), Linköping University, Linköping, Sweden

Kwang Kim Department of Mechanical Engineering, University of Nevada, Las Vegas, NV, USA

Seon Jeong Kim Center for Self-Powered Actuation and Department of Biomedical Engineering, Hanyang University, Seoul, South Korea

Mihkel Koel Department of Chemistry, Tallinn University of Technology, Tallinn, Estonia

Alexander Kogler Soft Matter Physics, Johannes Kepler University Linz, Linz, Austria

Soo Jin Adrian Koh Department of Mechanical Engineering, National University of Singapore, Singapore, Singapore

Roy Kornbluh SRI International, Menlo Park, CA, USA

Markus Krause Soft Matter Physics, Johannes Kepler University Linz, Linz, Austria

Karl Kruusamäe Department of Mechanical Engineering, University of Texas at Austin, Austin, USA

Kam K. Leang Department of Mechanical Engineering, University of Utah, Salt Lake City, UT, USA

Peter Leichsenring Institut für Festkörpermechanik, TU Dresden, Dresden, Germany

Holger Mößinger Institute of Electromechanical Design, Technische Universität Darmstadt, Darmstadt, Germany

John D. W. Madden Electrical and Computer Engineering, Advanced Materials and Process Engineering Lab, University of British Columbia, Vancouver, BC, Canada

José G. Martínez Center for Electrochemistry and Intelligent Materials (CEMI), Universidad Politécnica de Cartagena, Cartagena, Spain

Ali Maziz Department of Physics, Chemistry and Biology (IFM), Linköping University, Linköping, Sweden

David McCoul Henry Samueli School of Engineering and Applied Science, University of California – Los Angeles, Los Angeles, CA, USA

Daniel Melling Institute for Medical Science and Technology, University of Dundee, Dundee, UK

Axel Mellinger Department of Physics, Central Michigan University, Mount Pleasant, MI, USA

Indrek Must IMS lab, Institute of Technology, University of Tartu, Tartu, Estonia

Rahim Mutlu School of Mechanical, Materials, and Mechatronic Engineering, ARC Centre of Excellence for Electromaterials Science, University of Wollongong, Wollongong, NSW, Australia

Keisuke Oguro National Institute of Advanced Industrial Science and Technology (AIST), Ikeda, Osaka, Japan

Il-Kwon Oh School of Mechanical, Aerospace and Systems Engineering, Korea Advanced Institute of Science and Technology (KAIST), Daejeon, Republic of Korea

Hidenori Okuzaki Interdisciplinary Graduate School of Medicine and Engineering, University of Yamanashi, Kofu, Yamanashi, Japan

Dorina Opris Functional Polymers Laboratory, EMPA, Swiss Federal Laboratories for Materials Science and Technology, Dübendorf, Switzerland

Toribio F. Otero Electrochemistry, Intelligent Materials and Devices, Universidad Politécnica de Cartagena, Cartagena, Spain

Viljar Palmre Department of Mechanical Engineering, University of Nevada, Las Vegas, NV, USA

Luis Pedrero Faculty of Electrical and Computer Engineering, Institute of Semiconductors and Microsystems, Technische Universität Dresden, Dresden, Germany

Qibing Pei Henry Samueli School of Engineering and Applied Science, University of California – Los Angeles, Los Angeles, CA, USA

Anna-Liisa Peikolainen Intelligent Materials and Systems Lab, Institute of Technology, University of Tartu, Tartu, Estonia

Ron Pelrine SRI International, Menlo Park, CA, USA

Andrij Pich DWI-Leibniz Institute for Interactive Materials, Institute of Technical and Macromolecular Chemistry, RWTH Aachen University, Aachen, Germany

Cedric Plesse Université de Cergy-Pontoise, Cergy-Pontoise cedex, France

Maurizio Porfiri Department of Mechanical and Aerospace Engineering, Tandon School of Engineering, New York University, Brooklyn, NY, USA

David Pugal University of Nevada, Reno, NV, USA

Tristan Putzeys Department of Physics and Astronomy, Soft Matter and Biophysics Section, KU Leuven, Leuven, Belgium

Xunlin Qiu Department of Physics and Astronomy, University of Potsdam, Potsdam-Golm, Germany

Andreas Richter Institute of Semiconductors and Microsystems, Faculty of Electrical and Computer Engineering, Dresden University of Technology and Center for Advancing Electronics Dresden, Dresden, Germany

Dmitry Rychkov Institute of Physics and Astronomy, University of Potsdam, Potsdam, Germany

Mirza Saquib Sarwar Electrical and Computer Engineering, Advanced Materials and Process Engineering Lab, University of British Columbia, Vancouver, BC, Canada

Helmut F. Schlaak Institute of Electromechanical Design, Technische Universität Darmstadt, Darmstadt, Germany

Reinhard Schwödiauer Soft Matter Physics, Johannes Kepler University Linz, Linz, Austria

Mohsen Shahinpoor Biomedical Engineering/Advanced Robotics (BEAR) Laboratories, Department of Mechanical Engineering, Graduate School of Biomedical Science and Engineering, University of Maine, Orono, ME, USA

Herbert Shea LMTS: Microsystems For Space Technologies Lab, EPFL, Neuchâtel, Switzerland

Jun Shintake LIS: Laboratory of Intelligent Systems, EPFL, Lausanne, Switzerland

Anne L. Skov Technical University of Denmark (DTU), Lyngby, Denmark

Geoffrey M. Spinks ARC Centre of Excellence for Electromaterials Science, Intelligent Polymer Research Institute, University of Wollongong, North Wollongong, NSW, Australia

Richard J. Spontak Department of Chemical and Biomolecular Engineering, North Carolina State University, Raleigh, NC, USA

David Stadler Optotune AG, Dietikon, Switzerland

Tyler Stalbaum Department of Mechanical Engineering, University of Nevada, Las Vegas, NV, USA

Ji Su Advanced Materials and Processing Branch, NASA Langley Research Center, Hampton, VA, USA

Yuji Suzuki The University of Tokyo, Tokyo, Japan

Yoshiro Tajitsu Faculty of Engineering Science, Kansai University, Osaka, Japan

Kentaro Takagi Department of Mechanical Science and Engineering, Nagoya University, Nagoya, Japan

Xiaobo Tan Department of Electrical and Computer Engineering; Department of Mechanical Engineering, Michigan State University, East Lansing, MI, USA

Marcus Tietze Faculty of Electrical and Computer Engineering, Institute of Semiconductors and Microsystems, Technische Universität Dresden, Dresden, Germany

Janno Torop Intelligent Materials and Systems Lab, Institute of Technology, University of Tartu, Tartu, Estonia

Frederic Vidal Université de Cergy-Pontoise, Cergy-Pontoise cedex, France

Andreas Voigt Institute of Semiconductors and Microsystems, Faculty of Electrical and Computer Engineering, Dresden University of Technology and Center for Advancing Electronics Dresden, Dresden, Germany

Michael Wübbenhorst Department of Physics and Astronomy, Soft Matter and Biophysics Section, KU Leuven, Leuven, Belgium

Thomas Wallmersperger Institut für Festkörpermechanik, TU Dresden, Dresden, Germany

Masaki Yamakita Department of Mechanical and Control Engineering, Tokyo Institute of Technology, Tokyo, Japan

Yoshinobu Yasuno Kobayashi Institute of Physical Research, Tokyo, Japan

Xiaoqing Zhang School of Physics Science and Engineering, Tongji University, Shanghai, China

Wen Zheng School of Mechanical Engineering, Shanghai Jiao Tong University, Shanghai, China

Section I
Polymer Gels

Andreas Voigt and Andreas Richter

Contents

1	Introduction	4
2	Thermodynamics	6
2.1	Neutral Temperature-Responsive Hydrogels	6
3	Swelling Kinetics	14
3.1	The Tanaka-Fillmore Swelling Theory	14
3.2	Swelling Theory by Doi	17
3.3	Influences on Swelling Kinetics	19
4	Sensitivities	20
5	Challenges	21
	References	23

Abstract

Smart hydrogels are soft polymer particles that swell and deswell by taking up water according to external stimuli. After a general introduction, we extensively discuss the thermodynamics that governs the swelling equilibrium of neutral and polyelectrolyte gels. The kinetics of gel swelling is then presented in two models: The Tanaka-Fillmore model that is based on pure mechanics and the more advanced model by Doi which includes thermodynamic processes as the reason for swelling and deswelling. In the following section, the possible sensitivities with which smart hydrogels have been equipped are discussed. Finally we outline the current challenges of fabricating hydrogels with improved mechanical properties.

A. Voigt (✉) • A. Richter

Institute of Semiconductors and Microsystems, Faculty of Electrical and Computer Engineering,
Dresden University of Technology and Center for Advancing Electronics Dresden, Dresden,
Germany

e-mail: Andreas.Voigt@tu-dresden.de; andreas.richter7@tu-dresden.de

Keywords

Stimuli-sensitive hydrogel • Stimuli-responsive hydrogel • Temperature-responsive hydrogel • PNIPAAm • Polyelectrolyte hydrogel • Hydrogel swelling • Hydrogel deswelling • Swelling kinetics • Flory-Rehner theory • Tanaka-Fillmore theory

1 Introduction

Smart hydrogels are based on long polymer chains that are cross-linked with each other to form a network. When the network comes into contact with water, water diffuses in, which leads to the formation of the gel. The size of the gel can be a multiple of the size of the network in the dry state. Conventional hydrogels swell once when they come into contact with water and remain in the swollen state. In contrast, for smart hydrogels the equilibrium swelling degree depends strongly on a specific thermodynamic variable or environmental parameter.

The most common groups of stimuli-sensitive hydrogels are temperature-sensitive hydrogels, based on neutral polymers such as cross-linked poly(*n*-isopropylacrylamide) (PNIPAAm) (Schild 1992), and pH-sensitive hydrogels, based on polymers such as sodium poly(acrylate) (Kuhn et al. 2010). However, there are also gels which show a sensitivity toward specific chemicals in the solvent, light intensity, electric fields, or biomolecules. Since the swelling degree shows a very sudden change when passing a critical value of the thermodynamic variable, this behavior is described as a volume phase transition. Figure 1a, b shows a PNIPAAm gel in the deswollen and swollen state.

The swelling process involves a significant transport of matter into the gel. In general, it can be considered as a two-step process: The first step is the fast change of the thermodynamic variable. In the case of a temperature change, heat must be transported into or out of the gel. This process is characterized by the heat diffusion constant which is typically in the order of $D_T = 10^{-3} \text{ cm}^2/\text{s}$. In the case of a pH value

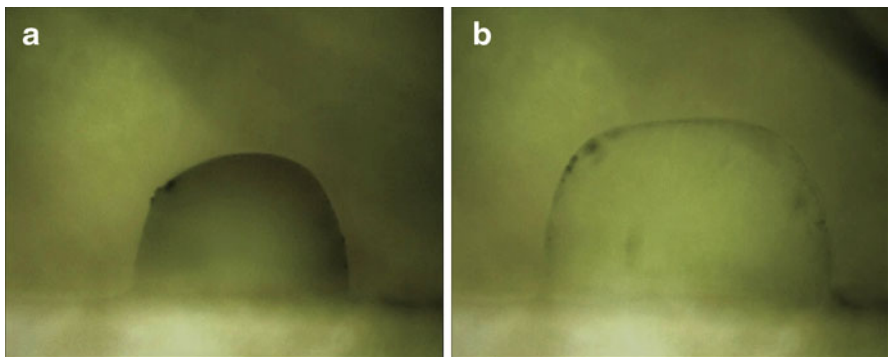


Fig. 1 Microscope image of a deswollen and a swollen PNIPAAm hydrogel. Here swelling and deswelling is stimulated by a change of temperature

change, ions must diffuse into or out of the solvent in the gel. The characteristic particle diffusion coefficient is typically in the order of $D_S = 10^{-5} \text{ cm}^2/\text{s}$. After this initial process, the gel is in a nonequilibrium. The swelling and deswelling happens on a slower timescale and is characterized by a cooperative diffusion coefficient $D_{coop} = 10^{-6} \dots 10^{-7} \text{ cm}^2/\text{s}$, where the term “cooperative” refers to the fact that a movement of solvent particles is accompanied by a corresponding deformation of the polymer network. Swelling/deswelling proceeds until the swelling degree reaches its equilibrium value which is at the minimum of the free energy.

Hydrogels can be used in sensors, actuators, or combined sensors/actuators. In sensors the sensitivity of the gel is used to trigger a volume change which is then measured and transformed into an electric signal (Richter et al. 2008). In actuators the thermodynamic variable is controlled externally (e.g., by heating a temperature-sensitive hydrogel) to achieve a volume change that effects in an actuator function (Richter 2009). In a combined sensor/actuator setup, an internal thermodynamic variable is sensed and the resulting volume change directly affects the system performance. An example is the use of hydrogels as smart valves, where the fluidic resistance depends directly on the chemical constituents of the liquid (Richter et al. 2007). Hydrogel actuators have two distinct features: (1) While forces are relatively low, the relative volume change is the highest possible of all known actuator materials. The energy density (work a hydrogel actuator can perform per unit volume) is in the upper range of all actuators (Greiner et al. 2012). (2) Hydrogels are soft-wet materials and need a solvent supply for swelling. These two characteristics define the application field of smart hydrogels and the special approaches that have to be taken for fabrication and operation.

Hydrogels have been used to build artificial-muscle-type demonstrators such as “gel fishes” (Kurauchi et al. 1991; Osada and Gong 1998), the “artificial elbow” (Suzuki 1991), the “gel hand” (Kurauchi et al. 1991), and the “gel motor” (Mitsumata et al. 1998, 2000). Hydrogel-based membranes were used to achieve chemically responsive (Osada and Takeuchi 1981, 1983) and temperature-sensitive (Peters et al. 1997) liquid separation. Macrovalves based on hydrogel particles were demonstrated to be usable for temperature-dependent, pH-dependent, and solvent-dependent flow control (Arndt et al. 2000). Microvalves that are sensitive toward pH value (Beebe et al. 2000) and toward glucose content (Baldi et al. 2003) or that can be controlled electronically (Richter et al. 2003) are an important step toward integrated smart micro-total analysis systems. Hydrogel-based microsensors for pH measurement have been built based on optically detected cantilever deflection (Bashir et al. 2002), based on optical Bragg gratings (Marshall et al. 2003) and based on microgravimetry (Richter et al. 2004). Furthermore, hydrogel microsensors were built for salt content detection (Liu et al. 2003) and glucose detection (Han et al. 2002). One of only a handful examples where a high integration for MEMS technology has been demonstrated is the construction of a high-resolution tactile display with hydrogels (Richter and Paschew 2009). In microfluidics hydrogels are on the threshold for applications in microfluidic integrated circuits (Greiner et al. 2012).

In the following we present a description of the fundamental physical properties of hydrogels.

2 Thermodynamics

2.1 Neutral Temperature-Responsive Hydrogels

Here we describe neutral temperature-sensitive hydrogels that consist of polymers that show a lower critical solution temperature (LCST) behavior in their uncross-linked state. The LCST is the temperature above which hydrophobic forces dominate over hydrophilic forces, which leads to a separation of the mixed polymer-solvent phase into two phases, one polymer rich and the other solvent rich. By the same mechanism of hydrophilicity and hydrophobicity, a cross-linked gel of this type will start swelling below the LCST. PNIPAAm gels are one famous example of neutral temperature-sensitive hydrogels and are considered for the model described in the following sections. The model is based on the theories of Flory, Huggins, and Rehner developed in the 1940s and 1950s (Huggins 1941, 1943; Flory 1942, 1944, 1953; Flory and Rehner 1943a, b).

Figure 2 shows the hydrogel in the solvent bath at pressure p . The system is closed in the thermodynamic sense: There is no exchange of solvent or polymer particles with the surroundings. The system temperature T can be regulated by a heater/cooler. In the dry state, the gel volume is equal to the volume V_p of the polymer including the cross-linker. In the swollen state, the gel has taken up a volume V_s of the solvent leading to a total gel volume of $V_{gel} = V_p + V_s$. The swelling state is often characterized by two quantities, the volume swelling degree $Q = V_{gel}/V_p$ or the polymer volume fraction $\varphi = V_p/V_{gel} = Q^{-1}$. We assume that the total volume of polymer and solvent in the bath remains constant during the swelling or deswelling process, i.e., the molar volume \bar{V}_s of the solvent is constant, independent of the volume fraction of the polymer in the gel. For water $\bar{V}_s = 18$ ml/mol. We describe the system by the Helmholtz free energy $F(T, V_s)$, where T is the temperature of the system.¹ Note that we have omitted the polymer volume V_p and the total solvent volume in the independent variables of F , since these values are considered constant. Since V_p is constant, we could also describe the free energy as a function of T and Q or as a function of T and φ . V_s is a macroscopic order parameter of the system. In equilibrium it takes the value that minimizes F . We take $F_0(T) = F(T, V_s = 0)$ as the free energy that the system would have for a completely dry hydrogel separate from the solvent. It is practical to work with the difference $\Delta F(T, V_s) = F(T, V_s) - F_0(T)$ which is the free energy gained from hydrogel swelling. We consider only 3D swelling without mechanical constraints. Two phenomena contribute to the value of ΔF : The mixing of the polymer chains with the solvent molecules and the elasticity of the polymer network:

$$\Delta F = \Delta F_{mix} + \Delta F_{elast}. \quad (1)$$

¹Some authors use the Gibbs free energy G which results in a completely equivalent description, since both external pressure and total volume of the system are considered constant.

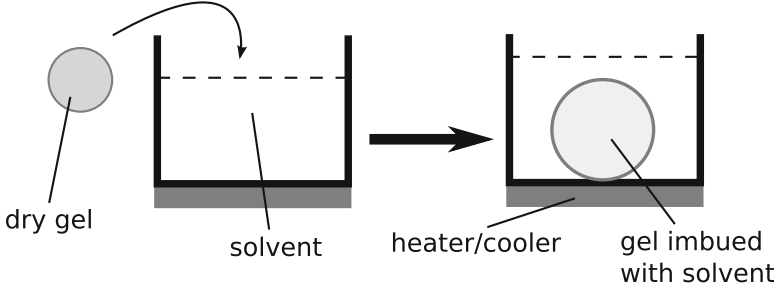


Fig. 2 The dry hydrogel is put into a bath with a solvent. The gel takes up solvent until it reaches an equilibrium state. The temperature of the bath-hydrogel system can be set by a heater/cooler. The equilibrium swelling degree of the gel depends on the set temperature. The system is thermodynamically closed since there is no exchange of particles with the surroundings. The volume of the system is assumed to be constant during swelling or deswelling of the hydrogel

The contribution by mixing can be separated in an entropic part and an interaction part:

$$\Delta F_{mix} = \Delta F_{entr} + \Delta F_{inter}. \quad (2)$$

The entropic contribution arises from the number of arrangements that the polymer chains and solvent molecules can adopt for a given V_p and V_s . This expression is similar to the well-known expression for an ideal solution (Kittel and Kroemer 1980). The difference arises from the fact that the size of the solvent molecules and the solute molecules is largely different (Flory 1942; Hirotsu 1991):

$$\Delta F_{entr} = RTn_s \ln(1 - \varphi) = RT \frac{V_p}{V_s} (\varphi^{-1} - 1) \ln(1 - \varphi), \quad (3)$$

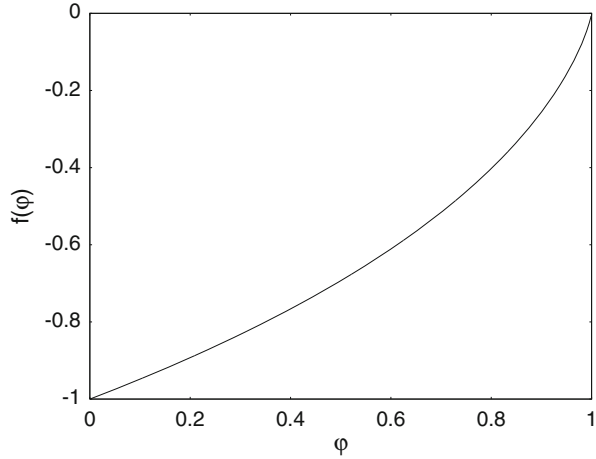
where $R = 8.3144621 \text{ J/(K mol)}$ is the universal gas constant, and n_s is the amount of solvent in the gel (in mol). The function $(\varphi^{-1} - 1) \ln(1 - \varphi)$ is plotted in Fig. 3. The function is monotonously decreasing from high values of φ to low values of φ , i.e., in nonequilibrium the entropic part of ΔF will push the system toward higher swelling degrees.

The contribution by the interaction is given by

$$\Delta F_{inter} = RTn_s \chi \varphi = RT \frac{V_p}{V_s} (\varphi^{-1} - 1) \chi \varphi, \quad (4)$$

where χ is the Flory polymer-solvent interaction parameter. In the original theory of Flory, it was defined as $\chi = 3(2u_{ps} - u_{pp} - u_{ss})/kT$, where $k = 1.3806488 \text{ J/K}$ is the Boltzmann constant. The u_{ps} , u_{pp} , and u_{ss} are pairwise polymer-solvent, polymer-polymer, and solvent-solvent interaction energies which are assumed to be constant. Real systems show deviations from the ideal assumptions of the Flory-Huggins model (Rubinstein and Colby 2003). The shortcomings of the Flory theory are

Fig. 3 The free energy of mixing is proportional to the function $f(\varphi) = (\varphi^{-1} - 1)\ln(1 - \varphi)$. Mixing itself always tends to increase gel volume



compensated by modifying the expression for χ . Empiric values of χ are often given in the form $\chi = A(\varphi) + B(\varphi)/T$, where A is called the “entropic part” and B/T the “enthalpic part.” Following Hirotsu (1991), we approximate A to be of the shape $A = A_1 + A_2\varphi$ and B to be independent of φ ,

$$\chi = A_1 + \frac{B}{T} + A_2\varphi, \quad (5)$$

with the following values for PNIPAAm²:

$$\begin{aligned} A_1 &= 3.677, \\ A_2 &= 0.259, \\ B &= -903.12 K. \end{aligned} \quad (6)$$

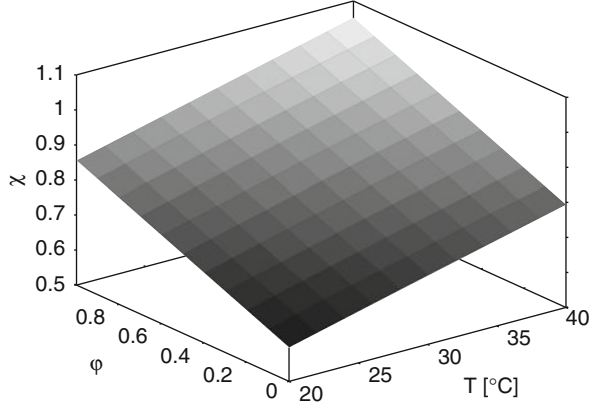
Figure 4 shows the dependence of χ on polymer volume fraction and temperature in the region of the volume phase transition.

The elastic contribution arises from the polymer chains that are elongated during swelling. Like in rubber elasticity, this change of free energy is based on entropy elasticity. Here we consider the approximation of swelling in the affine limit (Wall 1942, 1943; Hermans 1947; Wall and Flory 1951). The swelling is assumed to be isotropic in all three spatial dimensions. This leads to an elastic contribution to the free energy of

$$\begin{aligned} \Delta F_{elast} &= \frac{3}{2}RTn_c(\alpha^2 - 1 - \ln\alpha) \\ &= \frac{3}{2}RTV_p\bar{V}_s r \left(\varphi^{-\frac{2}{3}} - 1 + \frac{1}{3}\ln\varphi \right). \end{aligned} \quad (7)$$

²These values are calculated from the values given in Hirotsu’s paper, who states them in a different shape based on the chemical potential.

Fig. 4 The Flory-Rehner parameter χ characterizes the interaction between the polymer and the solvent. High values of χ indicate that separation of polymer and solvent is energetically favorable while low values indicate that mixing is favorable. Shown here is the temperature and polymer volume fraction dependence of χ for PNIPAAm and water



Here n_c is the amount of polymer chains in the gel (in mol), $\alpha = \varphi^{-1/3}$ is the length extension ratio relative to the dry state, and $r = \bar{V}_s/\bar{V}_c$ is the ratio of the molar volumes of the solvent and the polymer chains.

Using Eqs. 1, 2, 3, 4, 5, 6, and 7, we can calculate ΔF . Figure 5 shows ΔF as a function of temperature T and swelling degree Q for a PNIPAAm gel with a molar chain weight of $m_c = 10,000$ g/mol. Note that from m_c , the ratio r can be calculated by

$$r = \frac{\bar{V}_s}{\bar{V}_c} = \frac{m_s/\rho_s}{m_c/\rho_c}, \quad (8)$$

where m_s is the molar weight of the solvent and ρ_s and ρ_c are the densities of the solvent and the polymer (mass per volume). For high temperatures the free energy shows a sharp minimum around $Q = 2$; i.e., in the deswollen equilibrium state, the PNIPAAm hydrogel will have a volume twice as large as in the dry state. Below the transition temperature, the volume phase transition takes place: The equilibrium value of Q (i.e., the position of the minimum of ΔF) abruptly increases.

Like the free energy, the osmotic pressure π acting on the gel has a contribution from mixing and elasticity:

$$\pi = -\frac{\partial \Delta F}{\partial V_{gel}} = -\frac{\partial \Delta F_{mix}}{\partial V_{gel}} - \frac{\partial \Delta F_{elast}}{\partial V_{gel}} = \pi_{mix} + \pi_{elast}. \quad (9)$$

Note that $\frac{\partial}{\partial V_{gel}} = \frac{\partial}{\partial V_s}$, since $V_{gel} = V_p + V_s$ and V_p is constant. For the gel the solvent and the polymer themselves are considered incompressible. A volume change of the gel is always due to solvent moving out of or into the gel. For a gel in equilibrium, the total osmotic pressure is zero.

The chemical potential $\Delta\mu$ denotes the change in free energy that occurs when transferring solvent from the outside of the gel into the gel (unit, J/mol). It can be calculated from the osmotic pressure using

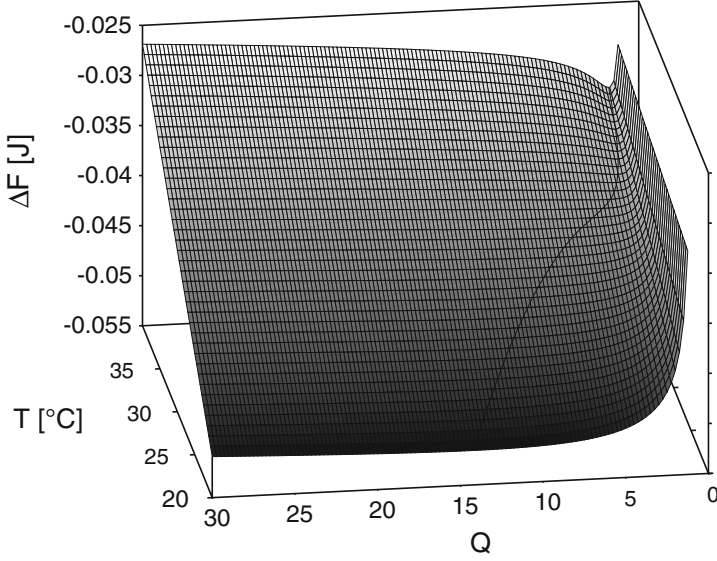


Fig. 5 Free energy ΔF as a function of temperature T and swelling degree Q for a PNIPAAm gel with a volume of 1 mm^3 in the dry state. For a given temperature, the equilibrium swelling degree Q_{eq} will be at the minimum position of ΔF , indicated by the plotted curve

$$\Delta\mu = \frac{\partial\Delta F}{\partial n_s} = \frac{\partial V_{gel}}{\partial n_s} \frac{\partial\Delta F}{\partial V_{gel}} = -\bar{V}_s \pi. \quad (10)$$

To calculate $\Delta\mu$ from the φ -dependent expression for ΔF derived before, we use the following relation:

$$\Delta\mu = \frac{\partial\Delta F}{\partial n_s} = \frac{\partial V_s}{\partial n_s} \frac{\partial\varphi}{\partial V_s} \frac{\partial\Delta F}{\partial\varphi} = -\bar{V}_s \frac{\varphi^2}{V_p} \frac{\partial\Delta F}{\partial\varphi}. \quad (11)$$

Using Eqs. 1, 2, 3, 4, 5, 6, 7, and 11, we obtain:

$$\Delta\mu = RT \left[\ln(1 - \varphi) + \varphi + (A_1 - A_2 + B/T) \varphi^2 + 2A_2 \varphi^3 + r \left(\varphi^{\frac{1}{3}} - \frac{1}{2} \varphi \right) \right]. \quad (12)$$

In equilibrium $\Delta\mu$ is zero. The equation obtained by setting Eq. 12 to zero is called the Flory-Rehner equation. It gives an implicit definition of the equilibrium function $\varphi_{eq}(T, r)$. Equivalently we can consider $Q_{eq}(T, m_c)$. Figure 6 shows this function for a temperature range between $20 \text{ }^\circ\text{C}$ and $40 \text{ }^\circ\text{C}$ and molar chain weights between 2000 g/mol and $50,000 \text{ g/mol}$. As expected, weaker cross-linking (corresponding to higher values of m_c) leads to a higher volume in the swollen state. Weaker cross-linking also leads to a sharper transition, since gels with weak cross-linking are closer to the behavior of polymer solutions. The onset of the swelling is independent

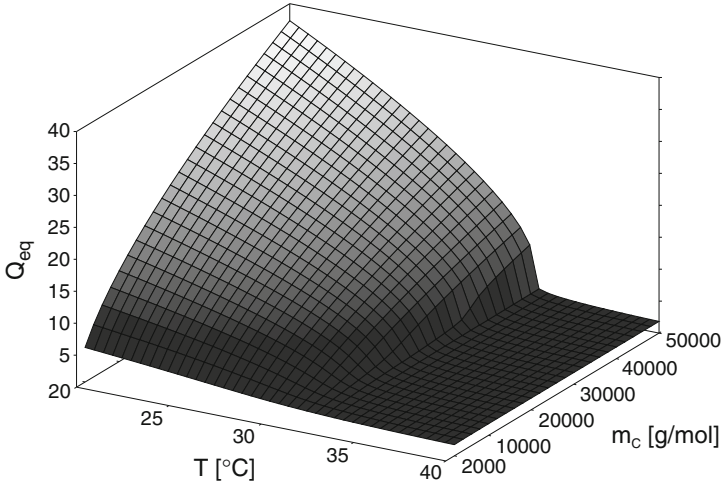


Fig. 6 Equilibrium swelling degree as a function of temperature T and molar netchain mass m_c . At values below the transition temperature $T \approx 33.8^\circ\text{C}$, the gel is in a swollen state. Strong cross-linking (low values of m_c) leads to lower values of the equilibrium swelling degree

of the cross-linking and corresponds to the LCST of the polymer solution. The volume in the deswollen state is roughly independent of the cross-linking ($Q_{eq} \approx 2$). For the swollen state, Q_{eq} is proportional to $m_c^{3/5}$ (Doi 2009). Note that the inverse function $T(\varphi_{eq}, r)$ can be obtained analytically from Eq. 12:

$$T(\varphi_{eq}, r) = \frac{-B\varphi_{eq}^2}{\ln(1 - \varphi_{eq}) + r\varphi_{eq}^{1/3} + (1 - r/2)\varphi_{eq} + (A_1 - A_2)\varphi_{eq}^2 + 2A_2\varphi_{eq}^3}. \quad (13)$$

Imagine we want to use the hydrogel as a mechanical actuator. The actuator can be switched from the contracted to the expanded state by switching the temperature between an initial temperature T_{init} above the critical value of the phase transition and a final temperature T_{final} below the critical value. The function ΔF can be used to estimate the work that the hydrogel actuator can perform. We assume $T_{init} = 40\text{K}$ since it is well above the value of the LCST. If the free energy is completely converted to work, then the work can be calculated by

$$W(T_{init}, T_{final}, m_c) = \Delta F(T_{final}, Q_{eq}(T_{init}, m_c)) - \Delta F(T_{final}, Q_{eq}(T_{final}, m_c)). \quad (14)$$

Note that in applications the realizable value of the work will be lower since energy will be lost to polymer-solvent friction during swelling. Dividing the obtained work by the volume of the actuator in the swollen state, we obtain the energy density w of the actuator (see Fig. 7). As can be seen, driving the actuator with a large temperature difference $\Delta T = T_{init} - T_{final}$ not only leads to a larger stroke but also to an increased energy density. Stronger cross-linking increases the energy

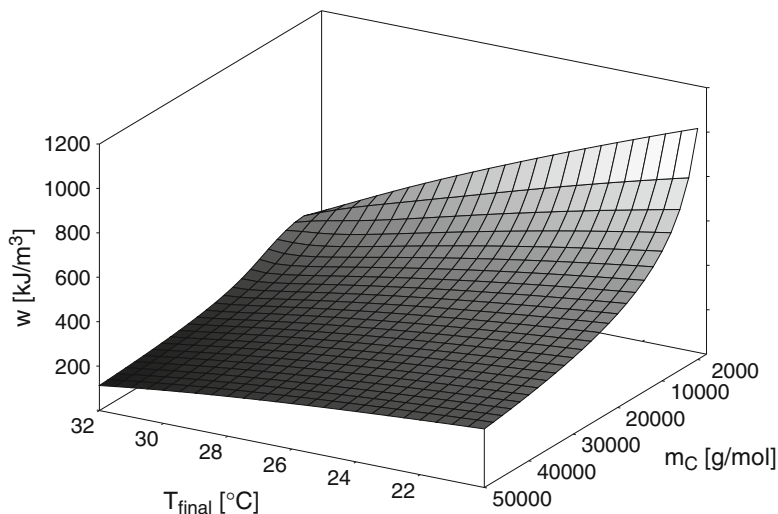


Fig. 7 Energy density of a hydrogel actuator. The hydrogel actuator is driven by changing the temperature between an initial value of $T_{\text{init}} = 40^{\circ}\text{C}$ and a final temperature T_{final} . The energy density is defined as the maximum work obtained from the volume change, divided by the gel volume in the swollen state at T_{final} . Stronger cross-linking (lower values of the netchain molar weight m_C) leads to higher work densities. However, it also leads to a smaller stroke (see Fig. 6). A large temperature difference $\Delta T = T_{\text{init}} - T_{\text{final}}$ increases both stroke and energy density

density but leads to a decreased stroke. The estimation shows that hydrogels can be used as actuators with relatively low force, extremely high stroke, and high overall energy density.

2.1.1 Polyelectrolyte Hydrogels

Like neutral hydrogels, polyelectrolyte hydrogels are built of cross-linked polymers. However, the monomers contain ionizable groups that get dissociated or protonated in water, leaving a charged monomer in the network and the corresponding counterions in water. Anionic polyelectrolytes release positively charged ions. Examples are sodium poly(acrylate) which releases sodium ions (Na^+) and poly(methacrylic acid) which releases hydrogen ions (H^+). The network of cationic polyelectrolyte gels in solutions is charged positively. Examples are poly([3-(methacryloylamino)propyl]trimethylammonium chloride) which releases chloride ions (Cl^-) and poly(2-vinylpyridine) which gets protonated. Anionic/acidic gels are in the deswollen state for low pH values and in the swollen state for high pH values, while cationic/basic gels are in the swollen state for low pH values and in the deswollen state for high pH values.

Consider a polyelectrolyte gel in a bath without ions. The polymer network is charged and the solvent in the hydrogel contains freely moving counterions. The hydrogel as a whole is neutral, as is the bath. In addition to the mixing and the elastic contribution, there is a contribution to the free energy of the system stemming from

the counterions (English et al. 2000). This contribution consists of an entropic part and an energetic part. The entropic part is calculated as the entropy of mixing the ions with the solvent (Kittel and Kroemer 1980). The energetic part results from the constant electric potential γ in the hydrogel. This potential is different from the bath potential (which we set to zero) due to the fact that there is an electric double layer at the boundary of the hydrogel:

$$\Delta F_{ion} = RT \sum_{i=1}^{\sigma} n_i \left[\ln \frac{n_i \bar{V}_s}{V_s} - 1 \right] + \sum_{i=1}^{\sigma} z_i e n_i N_A \gamma. \quad (15)$$

Here σ denotes the number of ion species, the index i denotes the ion species, n_i denotes the amount (in moles) of ion species i , N_A denotes the Avogadro constant, z_i denotes the i th ion valence, and e denotes the unit of electrostatic charge.

When we calculate the osmotic pressure from this expression, we see that it has an additional contribution:

$$\pi = \pi_{mix} + \pi_{elast} + \pi_{ion} \quad (16)$$

with

$$\pi_{ion} = RT \sum_{i=1}^{\sigma} c_i, \quad (17)$$

where c_i denotes the concentration of ion species i (unit: mol/m³).

When the polyelectrolyte gel is placed into a bath containing ions, we have to add the contribution of these freely moving ions to the free energy:

$$\Delta F_{bath} = RT \sum_{i=1}^{\sigma} n_i^B \left[\ln \frac{n_i^B \bar{V}_S}{V^B} - 1 \right] + \sum_{i=1}^{\sigma} z_i e n_i^B N_A \gamma^B, \quad (18)$$

where n_i^B indicates the amount of ions of type i in the bath, V^B is the bath volume, and γ^B is the electrostatic potential in the bath. This results in an osmotic pressure of

$$\pi = \pi_{mix} + \pi_{elast} + \pi_{ion} + \pi_{bath}, \quad (19)$$

with

$$\pi_{bath} = -RT \sum_{i=1}^{\sigma} c_i^B, \quad (20)$$

where c_i^B is the concentration of ions of type i in the bath.

In this section we have described the basics of the thermodynamics of polyelectrolyte gels. Note that these models contain some rough approximations. For more accurate models, we refer the reader to Chu et al. (1995), De et al. (2002), Hong

et al. (2010) and Arndt and Sadowski (2014). We conclude this section by stating two important facts about polyelectrolyte hydrogels: Typically the volume swelling degree of polyelectrolyte gels is higher than that of neutral gels, and swelling is faster. Also polyelectrolyte gels usually show a strong hysteresis in the curves describing the swelling degree as a function of pH value due to charge screening phenomena, while the hysteresis of neutral hydrogels in the curve describing the swelling degree as a function of temperature is very small or nonexistent.

3 Swelling Kinetics

The swelling or deswelling of a smart gel is triggered by the change of an environmental variable. The permeation of this initial stimulus into the gel happens quickly. Typically thermal diffusion coefficients are in the order of $10^{-3} \text{ cm}^2/\text{s}$ and particle diffusion coefficients are in the order of $10^{-5} \text{ cm}^2/\text{s}$ (Richter 2009).

The change of the environmental variable brings the system into nonequilibrium. Swelling kinetics describes the time-dependent process of the gel changing its size until the new equilibrium state is reached. In swelling the network expands and solvent is taken up by the gel. For the use of hydrogels as actuators and sensors in engineering, it is important to know their response kinetics depending on their composition and environmental influences. The swelling process happens much slower than the spreading of the initial stimulus. Here we consider that the initial process has happened instantaneously and only describe the slow second process. In the first section, we present the classical theory by Tanaka and Fillmore from the 1970s. In the second section, we describe the current thermodynamic-based multi-field theory. Note that some authors have proposed sharp-interface theories which will not be presented here (Tomari and Doi 1994; Dolbow et al. 2004).

3.1 The Tanaka-Fillmore Swelling Theory

The Tanaka-Fillmore theory (Tanaka et al. 1973; Tanaka and Fillmore 1979) is a purely mechanical theory based on the theory of elasticity (Lifshitz et al. 1986). The gel network is described by a displacement vector field $\mathbf{u}(\mathbf{r})$. This field describes how every point in a certain state is shifted compared to the equilibrium reference state. A point that is at \mathbf{r} in the reference state is shifted to $\mathbf{r}'(\mathbf{r}) = \mathbf{r} + \mathbf{u}(\mathbf{r})$ in the deformed state. In the reference state, $\mathbf{u}(\mathbf{r})$ is zero for all \mathbf{r} . Expansion and contraction of the network corresponds to solvent flowing into or out of the gel.

Initially the gel is in a deformed state. Deformation leads to inner stresses described by the stress tensor (Lifshitz et al. 1986):

$$\sigma_{ik} = K(\nabla \cdot \mathbf{u})\delta_{ik} + 2G \left(u_{ik} - \frac{1}{3}(\nabla \cdot \mathbf{u})\delta_{ik} \right), \quad (21)$$

where

$$u_{ik} = \frac{1}{2} \left(\frac{\partial u_k}{\partial r_i} + \frac{\partial u_i}{\partial r_k} \right). \quad (22)$$

Here ∇ is the Nabla operator, K is the bulk modulus, and G the shear modulus. The first term in Eq. 21 describes the stress resulting from volume compression and the second term the stress resulting from deformations by shearing. The force (per volume) resulting from inner stresses can be calculated by

$$\mathbf{f}_{stress} = \nabla \cdot \boldsymbol{\sigma}. \quad (23)$$

The relative movement between solvent and gel network leads to a friction force (per volume) of

$$\mathbf{f}_{friction} = -\zeta \frac{\partial \mathbf{u}}{\partial t}, \quad (24)$$

where ζ is the coefficient of friction between polymer and solvent.

Newton's equation of motion for the gel is then

$$\rho \frac{\partial^2 \mathbf{u}}{\partial t^2} = \mathbf{f}_{stress} + \mathbf{f}_{friction} = \nabla \cdot \boldsymbol{\sigma} - \zeta \frac{\partial \mathbf{u}}{\partial t}, \quad (25)$$

where ρ denotes the mass density. Due to the high polymer-solvent friction, the inertia term is considered to be negligible, leading to the final equation of motion:

$$\frac{\partial \mathbf{u}}{\partial t} = \frac{\nabla \cdot \boldsymbol{\sigma}}{\zeta}. \quad (26)$$

Using Eq. 21 we obtain the partial differential equation:

$$\frac{\partial \mathbf{u}}{\partial t} = \frac{K + \frac{G}{3}}{\zeta} \nabla (\nabla \cdot \mathbf{u}) + \left(\frac{G}{\zeta} \right) \Delta \mathbf{u}, \quad (27)$$

where Δ denotes the Laplace operator.

In the case of a spherical gel and spherical symmetry, the vectors of the displacement field only point in the radial direction, and the field can be described by a scalar function u of the scalar radius variable r :

$$\mathbf{u}(\mathbf{r}) = u(r) \frac{\mathbf{r}}{r} \quad (28)$$

Then Eq. 27 reduces to

$$\frac{\partial u}{\partial t} = D_{coop} \frac{\partial}{\partial r} \left\{ \frac{1}{r^2} \left[\frac{\partial}{\partial r} (ru) \right] \right\}, \quad (29)$$

with

$$D_{coop} = \frac{K + \frac{4}{3}G}{\zeta}. \quad (30)$$

D_{coop} is called the cooperative diffusion coefficient. Note, though Eq. 29 mathematically is exactly the radial term of the diffusion equation in spherical coordinates, this equation was physically not derived from diffusion theory. Typical values of D_{coop} for neutral hydrogels are 10^{-7} cm²/s (Gehrke 1993), and typical values for polyelectrolyte hydrogels are $(5 \cdot 10^{-7} \dots 10^{-5})$ cm²/s (Skouri et al. 1995; Milimouk et al. 2001).

The solution of Eq. 29 can be written as a superposition of eigenfunctions $F_n(r)$:

$$u(r, t) = \sum_n F_n(r) \exp\left(-n^2 \frac{D_{coop} \pi^2}{r_0^2} t\right). \quad (31)$$

The amplitudes of the eigenfunctions decay with higher orders. In addition, higher-order functions have a faster decay in time. In a very rough approximation, we can neglect the higher-order terms:

$$r(t) = r_0 + u(r_0, t) = r_0 - (r_0 - r_i) \exp\left(-\frac{t}{\tau}\right), \quad (32)$$

where r_0 is the equilibrium radius of the gel and r_i is the initial radius of the gel. The characteristic time τ can be calculated from the cooperative diffusion coefficient by

$$\tau = \frac{r_0^2}{\pi^2 D_{coop}}. \quad (33)$$

Note that Eq. 32 can be used both for swelling and deswelling of hydrogels. In the first case, $(r_0 - r_i) > 0$ and in the second case $(r_0 - r_i) < 0$. The characteristic Eq. 33 can be extended to estimate the swelling times of gels with other geometries, where r_0 has to be substituted by a characteristic size (see Fig. 8).

The Tanaka-Fillmore model was the first model that described the temporal behavior of swelling/deswelling. It is still widely used to estimate the swelling/deswelling times from the geometry and the cooperative diffusion coefficient, which can also be measured by dynamic light scattering (Shibayama 1998, 2006; Shibayama and Norisuye 2002). However, it has several serious limitations:

- It is a purely mechanical model not linked to the thermodynamic diffusion processes taking place during swelling.
- It only describes the movement of the polymer network and does not consider the solvent flow.

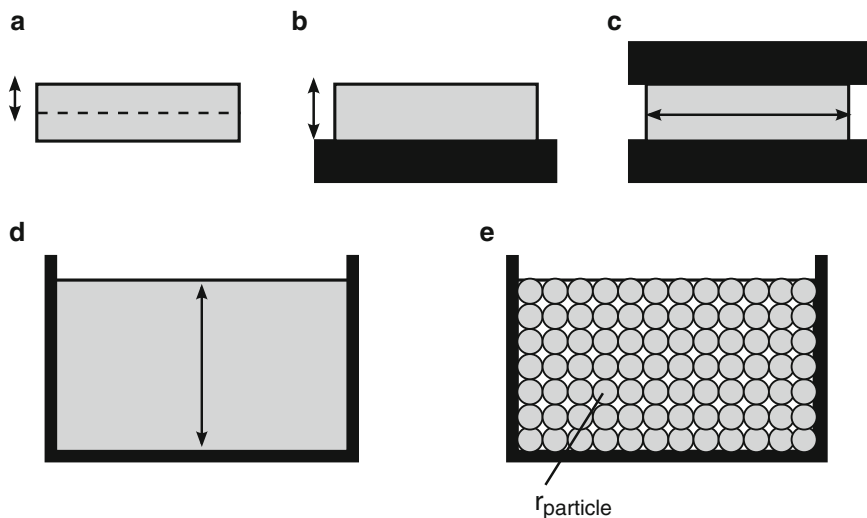


Fig. 8 Characteristic gel dimension for different geometries. The characteristic length dimension is indicated by the double arrows. **(a)** Gel sheet surrounded by solvent. **(b)** Gel sheet attached to a surface. **(c)** Gel sheet between two plates. **(d)** Gel in a vessel. **(e)** Gel particles in a vessel: here the characteristic length scale is given by the radius of the particles and the swelling times are therefore considerably lower than in **(d)**

- Neither the mechanical moduli nor the equilibrium state are derived from more fundamental principles.
- It does not describe the observed different times for swelling and deswelling of hydrogels.

Therefore advanced models have been presented in the twenty-first century that reconcile the Flory-Rehner thermodynamic theory with the mechanical approach of the Tanaka-Fillmore theory.

3.2 Swelling Theory by Doi

In the swelling theory by Doi (2009), like in the Tanaka-Fillmore theory, the hydrogel is treated as a continuous mechanical object described by a deformation field \mathbf{r}' and according inner tensions described by the stress tensor field σ_{ij} . However, instead of calculating σ_{ij} from values of the bulk modulus and the shear modulus that are assumed to be given, it is derived from the free energy density A :

$$A(F_{ij}, T) = A_{mix}(F_{ij}, T) + A_{elast}(F_{ij}, T). \quad (34)$$

Here $F_{ij} = \partial r'_i / \partial r_j$ is the deformation gradient that describes how a local volume element is strained/compressed, sheared, and rotated in the deformation of the hydrogel.

From Eq. 34 the stress tensor can be calculated as

$$\sigma_{ij}(\mathbf{r}') = \frac{\partial A}{\partial F_{ik}} F_{jk}(\mathbf{r}'). \quad (35)$$

In addition to the polymer deformation and the corresponding velocity field $\mathbf{v}_p = \partial \mathbf{r}' / \partial t$, the solvent pressure field p and the solvent flow velocity field \mathbf{v}_s are considered. The dynamic models are based on the following assumptions:

1. Validity of the assumption of a quasi-infinitesimally slow permeation process:

$$\nabla \cdot (\boldsymbol{\sigma} - p\mathbf{I}) = 0. \quad (36)$$

2. Validity of Darcy's law of porous media (Whitaker 1986):

$$\mathbf{v}_s - \mathbf{v}_p = -\kappa_0(\varphi)\nabla p, \quad (37)$$

where κ_0 is the polymer permeability.

3. The law of mass conservation:

$$\frac{\partial \varphi}{\partial t} = -\nabla \cdot (\varphi \mathbf{v}_p). \quad (38)$$

4. The incompressibility condition:

$$\nabla [\varphi \mathbf{v}_p + (1 - \varphi) \mathbf{v}_s] = 0. \quad (39)$$

Equations 34, 35, 36, 37, 38, and 39 are a set of nonlinear partial differential equations that describe the time-dependent behavior of the deformation field \mathbf{r}' , the solvent flow field \mathbf{v}_s , and the solvent pressure field p . The equations can be linearized around an equilibrium value φ_0 to describe gel dynamics for small deformation. Equation 36 is transformed to

$$\left(K + \frac{G}{3}\right) \nabla \nabla \cdot \mathbf{u} + G \nabla^2 \mathbf{u} = \nabla p, \quad (40)$$

where

$$K = \varphi_0^2 \left(\frac{\partial^2}{\partial \varphi^2} \left(\frac{A(\varphi)}{\varphi} \right) \right)_{\varphi_0} \quad (41)$$

is the osmotic modulus and

$$G = \frac{\partial^2}{\partial \varepsilon^2} A \left(\lambda_1 = \lambda_{eq}(1 + \varepsilon), \lambda_2 = \lambda_3 = \lambda_{eq} \left(1 - \frac{\varepsilon}{2} \right) \right) \quad (42)$$

is the shear modulus, where $\lambda_{eq} = \varphi_0^{-1/3}$. Note that the polymer and solvent are incompressible. Compression of the gel can only be achieved in the sense that solvent is squeezed out of the gel.

Darcy's law Eq. 37 and the incompressibility law Eq. 39 are transformed to

$$\nabla \dot{\mathbf{u}} = (1 - \varphi_0) \kappa_0 \nabla^2 \mathbf{p}. \quad (43)$$

In the linearized form, Eqs. 41 and 43 describe the time dependence of the displacement field \mathbf{u} and the pressure field p . The Tanaka-Fillmore Eq. 27 can be obtained from these equations under the assumption of the special case that the polymer deformation velocity field and the solvent velocity field are in exactly opposite directions for every point in the whole space. The cooperative diffusion coefficient then has the form

$$D = \left(K + \frac{4}{3} G \right) (1 - \varphi_0) \kappa_0. \quad (44)$$

The Doi theory is much more general than the Tanaka-Fillmore theory. It is nonlinear and derived from gel thermodynamics. In its linearized version, we obtain thermodynamic-based values for K and G . In addition it describes the observed shorter values for deswelling than swelling correctly since the characteristic times depend on the sharpness of the minimum of the free energy function (see Fig. 5). The disadvantage of the theory is an increased complexity which, especially in its nonlinear form, makes intuitive and analytical handling of the equations much more difficult than in the Tanaka-Fillmore theory. Many contemporary theories follow the Doi theory with small variations (Wang 2007; Larobina and Greco 2012; Wang and Hong 2012; Bouklas and Huang 2012).

3.3 Influences on Swelling Kinetics

For certain applications it is necessary to have short swelling/deswelling times. This can be achieved by three measures: (a) small hydrogel sizes, (b) high osmotic pressure, and (c) low polymer-solvent friction.

The swelling/deswelling times scale roughly quadratic with the size of the hydrogel (see Eq. 33). The osmotic pressure depends on its three contributions, namely, the energetic, the mixing, and the elastic part. For polyelectrolyte gels the osmotic pressure can be increased by a high concentration of ionized groups and by a high concentration of ions in the buffer (see Eqs. 17 and 20). This can be achieved by a high density of active groups, high ionic strengths, and high buffer diffusivity and concentration (Richter 2006). For smart neutral hydrogels, a strong temperature dependence of the interaction parameter leads to higher osmotic pressures. The

osmotic pressure stemming from elastic contributions can be increased by a higher cross-linking density (see Eq. 7). Note that the measures mentioned here correspond to maximizing the osmotic modulus in the equilibrium state (see Eq. 41). Low polymer-solvent friction corresponds to a low value of the permeability or a low viscosity. This can be achieved by choice of an adequate solvent.

Other factors that have an influence on the swelling/deswelling times are the limitation of the swelling agent (e.g., by a mesh) or the application of an external force (Richter 2006).

4 Sensitivities

Hydrogels can exhibit sensitivity toward a large number of physical quantities and chemical and biochemical substances. Therefore they are promising candidates for the application as sensors, actuators, and sensors-actuators, especially in fluidic systems. However they have not yet found widespread application. This can be attributed to the following facts:

1. Some hydrogels show a limited selectivity toward one environmental parameter. An example is PNIPAAm which shows both a sensitivity toward temperature and alcohol concentration.
2. Some hydrogels swell irreversibly, limiting their usage to a single time.
3. Some hydrogels show a hysteresis in their behavior.
4. Some sensitivities are weak, making the sensors usable as actuators but not as sensors.
5. It is challenging, cumbersome, and expensive to synthesize hydrogels with sensitivity tailored toward very specific chemicals.

Nonetheless especially the potential of temperature-, pH-, and solvent-sensitive hydrogels has been shown in various publications (Kuckling et al. 2000; Luo et al. 2003; Arndt et al. 1999, 2000, 2001a, b; Boyko et al. 2003; Beebe et al. 2000; Tanaka 1978). In the following we shortly discuss hydrogels with a sensitivity to various physical and (bio-)chemical quantities:

Temperature-sensitive hydrogels can come in two varieties: Hydrogels with a lower critical solution temperature (LCST) characteristic are in the deswollen state for high temperatures, e.g., PNIPAAm where the critical temperature is around 33.8 °C (Hirotsu 1991). Hydrogels with an upper critical solution temperature (UCST) characteristic are in the deswollen state for low temperatures, e.g., the copolymer acetoacetoxyethyl methacrylate and 2-hydroxyethyl methacrylate in an ethanol-water mixture with an UCST around 40 °C (Boyko et al. 2003). UCST gels are much rarer than LCST gels and have not been found to exist in pure water solution. Temperature-sensitive hydrogels have also been shown to be affected by ultrasonic waves, since these can induce a heating of the gel.

Solvent-sensitive hydrogels show a dependence of the swelling degree on the composition of the solvent. The swelling/deswelling processes are usually too

complex to predict the phase transition from the first principles. Therefore the solubility parameter (unit: $(\text{J}/\text{cm}^3)^{0.5}$) was introduced to characterize polymers and solvents. If the solubility parameter of the polymer is close to that of the solvent, the gel will be in the swollen state, as has been shown for poly(acetoacetoxyethyl methacrylate) for different solutions (Boyko et al. 2003). The swelling of PNIPAAm gels in aqueous alcohol solutions shows an interesting behavior: For pure water and low concentrations of alcohol, the gel will be in the swollen state. Above a critical alcohol concentration value $c_{crit,low}$, the gel is in the deswollen state, up to a higher value $c_{crit,high}$ where the gel swells again (Richter et al. 2007).

pH sensitive hydrogels can come in two groups: Acidic gels (Arndt et al. 1999; Beebe et al. 2000; Kuckling et al. 2000) swell for high pH values, while basic gels (Beebe et al. 2000) swell for low pH values. An example of an acidic gel is the copolymer poly(vinyl alcohol)/poly(acrylic acid) PVA/PAA. The sensitivity comes from the acidic component PAA. Below the pH corresponding to the pK_a value of PAA, the acid groups are protonated and therefore neutral: The gel is in the deswollen state. When the pH value of the solution increases, the acidic groups get deprotonated. The ionized groups repel each other which leads to the swelling of the gel. Gels sensitive to pH value usually show a strong hysteresis in their behavior. This is attributed to a screening effect, where ions from the solution (e.g., Na^+) can take the place of hydrogen atoms after deprotonation (Suzuki and Suzuki 1995).

Hydrogels with a *sensitivity toward specific species of ions*, e.g., CrO_4^{2-} , Na^+ , K^+ (Irie et al. 1993), Pb^{2+} (Tanaka et al. 1995), Cu^{2+} , and Cd^{2+} (Li et al. 2002) have been synthesized. Compared to pH-sensitive gels, they usually show only moderate reversibility.

Hydrogels sensitive to *electric fields* have been demonstrated in the literature (Kurauchi et al. 1991; Tanaka et al. 1982; Filipcsei et al. 2000). However, the fields have to be quite strong, such that an operation as a sensor is not feasible.

Hydrogels with a sensitivity toward *light* (Suzuki and Tanaka 1990) have a potential to work both as sensors and actuators.

Magnetic particles have been incorporated into hydrogels to build hydrogels sensitive toward *magnetic fields* (Zrínyi and Szabó 2001). However, only a change of shape, but no volume change, can be effected. Again the effect is weak, so the gel can only be used as an actuator, not as a sensor.

Hydrogels with a *sensitivity toward biochemicals* such as glucose (Kataoka et al. 1998; Brahim et al. 2002; Baldi et al. 2003), antigens (Miyata et al. 1999), and other biochemical agents (Peppas and Huang 2002) have been manufactured. They have potential to play a role in microfluidic platforms for biomedical analysis and synthesis.

5 Challenges

Ideal gels are perfectly homogeneous in their structure: The network has evenly distributed cross-links, constant mesh size, no defects, no loose ends or loops in the mesh, and a constant mobility of the cross-links. However, real hydrogels show a

strong deviation from this perfect state. This imperfection affects the swelling degree, swelling kinetics, mechanical properties, and optical properties of the gel. Reducing the imperfections is therefore an important endeavor of scientific polymer research. In general, the inhomogeneities increase with increasing cross-linker density and decrease with increasing degree of ionization for polyelectrolyte gels (Okay 2009).

The reason for the inhomogeneities is the limited control that can be exercised on the polymerization and cross-linking reactions (Shibayama and Norisuye 2002). This leads to side reactions and incomplete cross-linking. According to Shibayama and Norisuye, the resulting inhomogeneities can be classified in the following four categories:

1. Spatial inhomogeneities resulting from nonrandom spatial variations of cross-link density. They result in anomalous scattering.
2. Topological irregularities (network defects), such as dangling chains, loops, and chain entrapment. They affect the dynamics and swelling behavior of gels.
3. Connectivity inhomogeneities depending on cluster size, distribution, and architecture of polymer chains. These inhomogeneities govern the dynamics of the system.
4. Mobility inhomogeneities which are variations of the local degree of mobility due to cross-links. They are responsible for scattering speckles in gels.

Knowing the relation between gel structure and gel properties helps to design gels that are superior in their mechanical and swelling behavior (Shibayama 2012). Special “tough gels” have been developed that overcome the limitations of “conventional” gels by reducing the amount of inhomogeneities or introducing other stability-enhancing mechanisms. Four types of gels are especially worth mentioning:

1. Slide ring gels (Okumura and Ito 2001): Here the cross-linking is achieved by cyclodextrin rings that are threaded by the polymer chains of poly(ethylene glycol).
2. Nanocomposite gels (Haraguchi and Takehisa 2002): The cross-linking is achieved by physical interaction of the polymer chains with clay platelets with a typical width of 30 nm and a height of 1 nm.
3. Double-network gels (Gong et al. 2003): These are interpenetrating structures of two polymer networks that are not cross-linked with each other.
4. Tetra-PEG gels (Sakai et al. 2008) are made by cross-end coupling of two kinds of tetra-PEG macromers with complementary functional groups.

All these approaches promise to lead to more homogeneous, stable, and durable gels. However, there is no general-purpose hydrogel that is adequate for all thinkable applications. Instead, the chosen polymer, the chosen cross-linker, and the used cross-linking condition must always be fit to the needed sensitivity, swelling behavior, and mechanical properties.

Acknowledgments We thank Bernhard Ferse for fruitful discussions about the thermodynamics of hydrogels and inhomogeneous networks. This work was supported by the German Research Foundation (DFG) within the cluster of excellence “Center for Advancing Electronics Dresden” and by the European Social Fund.

References

- Arndt MC, Sadowski G (2014) Thermodynamic model for polyelectrolyte hydrogels. *J Phys Chem B* 118:10534–10542. doi:10.1021/jp501798x
- Arndt K-F, Richter A, Ludwig S et al (1999) Poly(vinyl alcohol)/poly(acrylic acid) hydrogels: FT-IR spectroscopic characterization of crosslinking reaction and work at transition point. *Acta Polym* 50:383–390. doi:10.1002/(SICI)1521-4044(19991201)50:11/12<383::AID-APOL383>3.0.CO;2-Z
- Arndt K-F, Kuckling D, Richter A (2000) Application of sensitive hydrogels in flow control. *Polym Adv Technol* 11:496–505. doi:10.1002/1099-1581(200008/12)11:8/12<496::AID-PAT996>3.0.CO;2-7
- Arndt K-F, Schmidt T, Menge H (2001a) Poly(vinyl methyl ether) hydrogel formed by high energy irradiation. *Macromol Symp* 164:313–322. doi:10.1002/1521-3900(200102)164:1<313::AID-MASY313>3.0.CO;2-D
- Arndt K-F, Schmidt T, Reichelt R (2001b) Thermo-sensitive poly(methyl vinyl ether) micro-gel formed by high energy radiation. *Polymer* 42:6785–6791. doi:10.1016/S0032-3861(01)00164-1
- Baldi A, Gu Y, Loftness PE et al (2003) A hydrogel-actuated environmentally sensitive microvalve for active flow control. *J Microelectromech Syst* 12:613–621. doi:10.1109/JMEMS.2003.818070
- Bashir R, Hilt JZ, Elibol O et al (2002) Micromechanical cantilever as an ultrasensitive pH microsensor. *Appl Phys Lett* 81:3091–3093. doi:10.1063/1.1514825
- Beebe DJ, Moore JS, Bauer JM et al (2000) Functional hydrogel structures for autonomous flow control inside microfluidic channels. *Nature* 404:588–590. doi:10.1038/35007047
- Bouklas N, Huang R (2012) Swelling kinetics of polymer gels: comparison of linear and nonlinear theories. *Soft Matter* 8:8194–8203. doi:10.1039/C2SM25467K
- Boyko V, Lu Y, Richter A, Pich A (2003) Preparation and characterization of acetoacetoxyethyl methacrylate-based gels. *Macromol Chem Phys* 204:2031–2039. doi:10.1002/macp.200350058
- Brahim S, Narinesingh D, Guiseppi-Elie A (2002) Bio-smart hydrogels: co-joined molecular recognition and signal transduction in biosensor fabrication and drug delivery. *Biosens Bioelectron* 17:973–981. doi:10.1016/S0956-5663(02)00089-1
- Chu Y, Varanasi PP, McGlade MJ, Varanasi S (1995) pH-induced swelling kinetics of polyelectrolyte hydrogels. *J Appl Polym Sci* 58:2161–2176. doi:10.1002/app.1995.070581203
- De SK, Aluru NR, Johnson B et al (2002) Equilibrium swelling and kinetics of pH-responsive hydrogels: models, experiments, and simulations. *J Microelectromechanical Syst* 11:544–555. doi:10.1109/JMEMS.2002.803281
- Doi M (2009) Gel dynamics. *J Phys Soc Jpn* 78:052001. doi:10.1143/JPSJ.78.052001
- Dolbow J, Fried E, Ji H (2004) Chemically induced swelling of hydrogels. *J Mech Phys Solids* 52:51–84. doi:10.1016/S0022-5096(03)00091-7
- English AE, Edelman ER, Tanaka T (2000) Polymer hydrogel phase transitions, Chapter 6. In: Tanaka T (ed) *Experimental methods in polymer science*. Academic, Boston, pp 547–589
- Filipcei G, Fehér J, Zrinyi M (2000) Electric field sensitive neutral polymer gels. *J Mol Struct* 554:109–117. doi:10.1016/S0022-2860(00)00564-0
- Flory PJ (1942) Thermodynamics of high polymer solutions. *J Chem Phys* 10:51–61. doi:10.1063/1.1723621
- Flory PJ (1944) Network structure and the elastic properties of vulcanized rubber. *Chem Rev* 35:51–75. doi:10.1021/cr60110a002

- Flory PJ (1953) Principles of polymer chemistry. Cornell University Press, Ithaca
- Flory PJ, Rehner J (1943a) Statistical mechanics of cross-linked polymer networks I. Rubberlike elasticity. *J Chem Phys* 11:512–520. doi:10.1063/1.1723791
- Flory PJ, Rehner J (1943b) Statistical mechanics of cross-linked polymer networks II. Swelling. *J Chem Phys* 11:521–526. doi:10.1063/1.1723792
- Gehrke SH (1993) Synthesis, equilibrium swelling, kinetics, permeability and applications of environmentally responsive gels. In: Dušek PK (ed) *Responsive gels: volume transitions II*. Springer, Berlin/Heidelberg, pp 81–144
- Gong JP, Katsuyama Y, Kurokawa T, Osada Y (2003) Double-network hydrogels with extremely high mechanical strength. *Adv Mater* 15:1155–1158. doi:10.1002/adma.200304907
- Greiner R, Allerdissen M, Voigt A, Richter A (2012) Fluidic microchemomechanical integrated circuits processing chemical information. *Lab Chip* 12:5034–5044. doi:10.1039/C2LC40617A
- Han IS, Han M-H, Kim J et al (2002) Constant-volume hydrogel osmometer: a new device concept for miniature biosensors. *Biomacromolecules* 3:1271–1275. doi:10.1021/bm0255894
- Haraguchi K, Takehisa T (2002) Nanocomposite hydrogels: a unique organic–inorganic network structure with extraordinary mechanical, optical, and swelling/de-swelling properties. *Adv Mater* 14:1120–1124. doi:10.1002/1521-4095(20020816)14:16<1120::AID-ADMA1120>3.0.CO;2-9
- Hermans JJ (1947) Deformation and swelling of polymer networks containing comparatively long chains. *Trans Faraday Soc* 43:591–600. doi:10.1039/TF9474300591
- Hirotsu S (1991) Softening of bulk modulus and negative Poisson's ratio near the volume phase transition of polymer gels. *J Chem Phys* 94:3949–3957. doi:10.1063/1.460672
- Hong W, Zhao X, Suo Z (2010) Large deformation and electrochemistry of polyelectrolyte gels. *J Mech Phys Solids* 58:558–577. doi:10.1016/j.jmps.2010.01.005
- Huggins ML (1941) Solutions of long chain compounds. *J Chem Phys* 9:440. doi:10.1063/1.1750930
- Huggins ML (1943) Thermodynamic properties of solutions of high polymers: the empirical constant in the activity equation. *Ann N Y Acad Sci* 44:431–443. doi:10.1111/j.1749-6632.1943.tb52763.x
- Irie M, Misumi Y, Tanaka T (1993) Stimuli-responsive polymers: chemical induced reversible phase separation of an aqueous solution of poly(*N*-isopropylacrylamide) with pendent crown ether groups. *Polymer* 34:4531–4535. doi:10.1016/0032-3861(93)90160-C
- Kataoka K, Miyazaki H, Bunya M et al (1998) Totally synthetic polymer gels responding to external glucose concentration: their preparation and application to on–off regulation of insulin release. *J Am Chem Soc* 120:12694–12695. doi:10.1021/ja982975d
- Kittel CH, Kroemer H (1980) *Thermal physics*, 2nd edn. W. H. Freeman, New York
- Kuckling D, Adler H-JP, Arndt K-F et al (2000) Temperature and pH dependent solubility of novel poly(*N*-isopropylacrylamide)-copolymers. *Macromol Chem Phys* 201:273–280. doi:10.1002/(SICI)1521-3935(20000201)201:2<273::AID-MACP273>3.0.CO;2-E
- Kuhn W, Kunzle O, Katchalsky A (2010) Dénouement de molécules en chaînes polyvalentes par des charges électriques en solution. *Bull Soc Chim Belg* 57:421–431. doi:10.1002/bscb.19480571002
- Kurauchi T, Shiga T, Hirose Y, Okada A (1991) Deformation behaviors of polymer gels in electric field. In: DeRossi D, Kajiwara K, Osada Y, Yamauchi A (eds) *Polymer gels*. Plenum Press, New York, pp 237–246
- Larobina D, Greco F (2012) Prediction of the effects of constitutive viscoelasticity on stress-diffusion coupling in gels. *J Chem Phys* 136:134904. doi:10.1063/1.3699978
- Li W, Zhao H, Teasdale PR et al (2002) Synthesis and characterisation of a polyacrylamide–polyacrylic acid copolymer hydrogel for environmental analysis of Cu and Cd. *React Funct Polym* 52:31–41. doi:10.1016/S1381-5148(02)00055-X
- Lifshitz EM, Kosevich AM, Pitaevskii LP (1986) Fundamental equations, Chapter I. In: Lifshitz EM, Kosevich AM, Pitaevskii LP (eds) *Theory of elasticity*, 3rd edn. Butterworth-Heinemann, Oxford, pp 1–37

- Liu X, Zhang X, Cong J et al (2003) Demonstration of etched cladding fiber Bragg grating-based sensors with hydrogel coating. *Sens Actuators B* 96:468–472. doi:10.1016/S0925-4005(03)00605-1
- Luo Q, Mutlu S, Gianchandani YB et al (2003) Monolithic valves for microfluidic chips based on thermoresponsive polymer gels. *ELECTROPHORESIS* 24:3694–3702. doi:10.1002/elps.200305577
- Marshall AJ, Blyth J, Davidson CAB, Lowe CR (2003) pH-sensitive holographic sensors. *Anal Chem* 75:4423–4431
- Milimouk I, Hecht AM, Beysens D, Geissler E (2001) Swelling of neutralized polyelectrolyte gels. *Polymer* 42:487–494. doi:10.1016/S0032-3861(00)00360-8
- Mitsumata T, Ikeda K, Gong JP, Osada Y (1998) Solvent-driven chemical motor. *Appl Phys Lett* 73:2366–2368. doi:10.1063/1.122505
- Mitsumata T, Ikeda K, Gong JP, Osada Y (2000) Controlled motion of solvent-driven gel motor and its application as a generator. *Langmuir* 16:307–312. doi:10.1021/la990483o
- Miyata T, Asami N, Uragami T (1999) A reversibly antigen-responsive hydrogel. *Nature* 399:766–769. doi:10.1038/21619
- Okay O (2009) General properties of hydrogels. In: Gerlach G, Arndt K-F (eds) *Hydrogel sensors and actuators*. Springer, Berlin/Heidelberg, pp 1–14
- Okumura Y, Ito K (2001) The polyrotaxane gel: a topological gel by figure-of-eight cross-links. *Adv Mater* 13:485–487. doi:10.1002/1521-4095(200104)13:7<485::AID-ADMA485>3.0.CO;2-T
- Osada Y, Gong J-P (1998) Soft and wet materials: polymer gels. *Adv Mater* 10:827–837. doi:10.1002/(SICI)1521-4095(199808)10:11<827::AID-ADMA827>3.0.CO;2-L
- Osada Y, Takeuchi Y (1981) Water and protein permeation through polymeric membrane having mechanochemically expanding and contracting pores. Function of chemical valve. I. *J Polym Sci Polym Lett Ed* 19:303–308. doi:10.1002/pol.1981.130190605
- Osada Y, Takeuchi Y (1983) Protein and sugar separation by mechanochemical membrane having “chemical valve” function. *Polym J* 15:279–284. doi:10.1295/polymj.15.279
- Peppas NA, Huang Y (2002) Polymers and gels as molecular recognition agents. *Pharm Res* 19:578–587. doi:10.1023/A:1015389609344
- Peters EC, Svec F, Fréchet JMJ (1997) Thermally responsive rigid polymer monoliths. *Adv Mater* 9:630–633. doi:10.1002/adma.19970090807
- Richter A (2006) Hydrogel-based μ TAS. In: Leondes CT (ed) *MEMS/NEMS*. Springer US, New York, pp 473–503
- Richter A (2009) Hydrogels for actuators. In: Gerlach G, Arndt K-F (eds) *Hydrogel sensors and actuators*. Springer, Berlin/Heidelberg, pp 221–248
- Richter A, Paschew G (2009) Optoelectrothermic control of highly integrated polymer-based MEMS applied in an artificial skin. *Adv Mater* 21:979–983. doi:10.1002/adma.200802737
- Richter A, Kuckling D, Howitz S et al (2003) Electronically controllable microvalves based on smart hydrogels: magnitudes and potential applications. *J Microelectromech Syst* 12:748–753. doi:10.1109/JMEMS.2003.817898
- Richter A, Bund A, Keller M, Arndt K-F (2004) Characterization of a microgravimetric sensor based on pH sensitive hydrogels. *Sens Actuators B* 99:579–585. doi:10.1016/j.snb.2004.01.011
- Richter A, Wenzel J, Kretschmer K (2007) Mechanically adjustable chemostats based on stimuli-responsive polymers. *Sens Actuators B* 125:569–573. doi:10.1016/j.snb.2007.03.002
- Richter A, Paschew G, Klatt S et al (2008) Review on hydrogel-based pH sensors and microsensors. *Sensors* 8:561–581. doi:10.3390/s8010561
- Rubinstein M, Colby RH (2003) *Polymer physics*. Oxford University Press, Oxford
- Sakai T, Matsunaga T, Yamamoto Y et al (2008) Design and fabrication of a high-strength hydrogel with ideally homogeneous network structure from tetrahedron-like macromonomers. *Macromolecules* 41:5379–5384. doi:10.1021/ma800476x
- Schild HG (1992) Poly(*N*-isopropylacrylamide): experiment, theory and application. *Prog Polym Sci* 17:163–249. doi:10.1016/0079-6700(92)90023-R

- Shibayama M (1998) Spatial inhomogeneity and dynamic fluctuations of polymer gels. *Macromol Chem Phys* 199:1–30. doi:10.1002/(SICI)1521-3935(19980101)199:1<1::AID-MACP1>3.0.CO;2-M
- Shibayama M (2006) Universality and specificity of polymer gels viewed by scattering methods. *Bull Chem Soc Jpn* 79:1799–1819. doi:10.1246/bcsj.79.1799
- Shibayama M (2012) Structure–mechanical property relationship of tough hydrogels. *Soft Matter* 8:8030–8038. doi:10.1039/C2SM25325A
- Shibayama M, Norisuye T (2002) Gel formation analyses by dynamic light scattering. *Bull Chem Soc Jpn* 75:641–659. doi:10.1246/bcsj.75.641
- Skouri R, Schosseler F, Munch JP, Candau SJ (1995) Swelling and elastic properties of polyelectrolyte gels. *Macromolecules* 28:197–210. doi:10.1021/ma00105a026
- Suzuki M (1991) Amphoteric polyvinyl alcohol hydrogel and electrohydrodynamic control method for artificial muscles. In: DeRossi D, Kajiwara K, Osada Y, Yamauchi A (eds) *Polymer gels*. Plenum Press, New York, pp 221–236
- Suzuki A, Suzuki H (1995) Hysteretic behavior and irreversibility of polymer gels by pH change. *J Chem Phys* 103:4706–4710. doi:10.1063/1.470608
- Suzuki A, Tanaka T (1990) Phase transition in polymer gels induced by visible light. *Nature* 346:345–347. doi:10.1038/346345a0
- Tanaka T (1978) Collapse of gels and the critical endpoint. *Phys Rev Lett* 40:820–823. doi:10.1103/PhysRevLett.40.820
- Tanaka T, Fillmore DJ (1979) Kinetics of swelling of gels. *J Chem Phys* 70:1214–1218. doi:10.1063/1.437602
- Tanaka T, Hocker LO, Benedek GB (1973) Spectrum of light scattered from a viscoelastic gel. *J Chem Phys* 59:5151–5159. doi:10.1063/1.1680734
- Tanaka T, Nishio I, Sun S-T, Ueno-Nishio S (1982) Collapse of gels in an electric field. *Science* 218:467–469. doi:10.1126/science.218.4571.467
- Tanaka T, Wang C, Pande V et al (1995) Polymer gels that can recognize and recover molecules. *Faraday Discuss* 101:201–206. doi:10.1039/FD9950100201
- Tomari T, Doi M (1994) Swelling dynamics of a gel undergoing volume transition. *J Phys Soc Jpn* 63:2093–2101. doi:10.1143/JPSJ.63.2093
- Wall FT (1942) Statistical thermodynamics of rubber. *J Chem Phys* 10:132–134. doi:10.1063/1.1723668
- Wall FT (1943) Statistical thermodynamics of rubber. III. *J Chem Phys* 11:527–530. doi:10.1063/1.1723793
- Wall FT, Flory PJ (1951) Statistical thermodynamics of rubber elasticity. *J Chem Phys* 19:1435–1439. doi:10.1063/1.1748098
- Wang X (2007) Modeling the nonlinear large deformation kinetics of volume phase transition for the neutral thermosensitive hydrogels. *J Chem Phys* 127:174705. doi:10.1063/1.2779029
- Wang X, Hong W (2012) A visco-poroelastic theory for polymeric gels. *Proc R Soc Lond Math Phys Eng Sci* 468:3824–3841. doi:10.1098/rspa.2012.0385
- Whitaker S (1986) Flow in porous media I: a theoretical derivation of Darcy's law. *Transp Porous Media* 1:3–25. doi:10.1007/BF01036523
- Zrínyi M, Szabó D (2001) Muscular contraction mimicked by magnetic gels. *Int J Mod Phys B* 15:557–563. doi:10.1142/S0217979201005015

Garima Agrawal and Andrij Pich

Contents

1	Introduction	28
2	Hydrogel Synthesis	29
2.1	Physical Cross-Linking	29
2.2	Chemical Cross-Linking	31
2.3	Irradiation Cross-Linking	35
3	Smart Hydrogels	36
3.1	Temperature-Responsive Hydrogels	36
3.2	pH-Responsive Hydrogels	38
3.3	Light-Responsive Hydrogels	39
3.4	Electro-Responsive Hydrogels	41
4	Conclusions	44
	References	44

Abstract

Smart hydrogels, exhibiting response to various stimuli such as temperature, pH, light, electric field, etc., have been extensively explored due to their high potential in different areas ranging from actuators to biomedical applications. A number of synthetic pathways have been developed to synthesize hydrogels with desired chemical structure and to tune the mechanical properties and the swelling degree of these switchable materials. These synthetic approaches also provide the possibility of incorporating various functionalities inside hydrogel network and thus in turn controlling their response. The available methods for the fabrication of various types of functional hydrogels and their characteristic properties will be reviewed in this chapter.

G. Agrawal • A. Pich (✉)

DWI-Leibniz Institute for Interactive Materials, Institute of Technical and Macromolecular Chemistry, RWTH Aachen University, Aachen, Germany

e-mail: garima.agrawal@ugent.be; pich@dwi.rwth-aachen.de

Keywords

Smart hydrogels • Actuators • Swelling • Response

1 Introduction

In recent years, hydrogels have received dramatically increasing interest indicating their potential for research and practical applications (Ahmed 2013; Kopecek 2009; Wichterle and Lim 1960). Hydrogels are generally defined as three-dimensional cross-linked polymer networks, which contain large amounts of water and can be synthesized by different physical or chemical methods. Based on the selected synthetic procedure, hydrogels can not only be fabricated in different physical forms such as micro-/nanoparticles, coatings, and films, but also their chemical properties like chemical composition, presence of functional groups, and cross-link density can be tuned (Doring et al. 2013; Samchenko et al. 2011). As a result, hydrogels are extensively used for a wide range of applications including tissue engineering and regenerative medicine (Lee and Mooney 2001); diagnostics (van der Linden et al. 2003); drug and protein delivery (Hoare and Kohane 2008; Plunkett and Moore 2004; Vashist and Ahmad 2013); biomedical implants (Corkhill et al. 1989; Gadelha et al. 2012); biosensors and actuators (Shin et al. 2012; Vilozny et al. 2011); cell encapsulation (Phelps et al. 2012); protein separation (Gunavadhhi et al. 2012), as a material for contact lenses (Hennink and van Nostrum 2012); and so on. The preparation, physicochemical properties, and applications of hydrogels have been described in various excellent books and reviews. These articles give an overview over the various aspects of hydrogel area including the fundamental understanding of their synthesis and characterization (Ahmed 2013; Kopecek 2009; Gulrez et al. 2011; Samal et al. 2014).

To be suitable for various present and future applications, it is important to control the properties of hydrogels which can be achieved by using a number of synthetic approaches including physical or chemical cross-linking (Ahmed 2013; Burkert et al. 2007). Physical gels are generally prepared by taking advantage of various physical interactions such as hydrogen bonding, ionic interaction, van der Waals interactions, and molecular entanglement between the polymer chains (Hennink and van Nostrum 2012). On the other hand, strong gels are prepared by chemical cross-linking of multifunctional monomers simultaneously during polymerization or subsequent cross-linking after the polymer formation (Ahmed 2013).

Since a dynamic response toward external stimuli is of extreme importance for various applications, extensive research has been done for the development of stimuli-sensitive (smart or switchable or intelligent) hydrogels in recent years (Stuart et al. 2010; Garg et al. 2013). This is generally achieved by the incorporation of stimuli-responsive monomer either directly into the backbone or as side groups (Samal et al. 2014). These hydrogels show either the change in volume phase transition or sol-gel transition when triggered by the change in environmental conditions. Various physical (temperature, pressure, light, magnetic, electric,

sound, or mechanical), chemical (pH, ionic strength, solvent, electrochemical), and biological stimuli (specific molecular recognition) can be applied to control different properties of switchable hydrogels such as permeability, degradability, swelling, hydrophobicity, and mechanical strength (Samchenko et al. 2011; Peppas et al. 2006). Multifunctional hydrogels have also been reported which show a change in equilibrium behavior upon exposure to the combination of different stimuli (Zhang et al. 2011; Hendrickson et al. 2010).

2 Hydrogel Synthesis

Several polymerization techniques have been used over the past years for the preparation of hydrogels with desired properties. It is of interest to fabricate hydrogels with various additional aspects like chemical functionality for binding the guest molecules, degradability, controlled porosity, and mechanical strength. This can be achieved by using different preparation methods which will be discussed in this chapter. In general, various synthetic approaches adopted in the literature so far can be mainly categorized into three groups: (1) physical cross-linking, (2) chemical cross-linking, and (3) irradiation cross-linking.

2.1 Physical Cross-Linking

Physically cross-linked gels have recently obtained a great deal of attention, especially in biomedical applications, due to the absence of potential toxicity caused by the unreacted chemical cross-linker and the relative ease of preparation. This improves the compatibility of produced hydrogels with encapsulated natural substances, and also the extra step for free cross-linker removal can be avoided. Several methods reported in the literature in this area have been described below.

2.1.1 Ionic Interactions

Physical gels can be synthesized by the addition of multivalent counterions in the polyelectrolyte solution. One of the most common examples in this area is alginate hydrogel complexed by Ca^{2+} ions (Berger et al. 2004). Tong et al. reported the formation of alginate/porous CaCO_3 microparticle hybrid hydrogels by in situ release of Ca^{2+} ions. It was shown that the mechanical properties of these hydrogels can be tuned by changing alginate/ CaCO_3 weight ratio, and these hydrogels can be used for drug loading and sustained release (Wang et al. 2008). Hybrid alginate/chitosan (*N,O*-carboxymethyl chitosan, NOCC) hydrogels were synthesized by Sung et al. using Ca^{2+} ion solution for oral protein delivery (Lin et al. 2005). Similarly, chitosan/polylysine, chitosan/glycerol phosphate, and chitosan/dextran hydrogels have also been reported in the literature (Hennink and van Nostrum 2012; Bajpai et al. 2008; Zhao et al. 2009a).

When polycationic and polyanionic polymers are mixed, then they stick together due to ionic interactions between them and form soluble or insoluble complexes.

This approach is known as complex coacervation, and it has also been used for the development of physically cross-linked hydrogels (Farris et al. 2009). Some of the examples in this area are complexes of positively and negatively charged triblock copolymers based on poly(allyl glycidyl ether)-*block*-ethylene glycol-*block*-allyl glycidyl ether) (Hunt et al. 2011), polycationic chitosan and polyanionic xanthan (Chellat et al. 2000), protein, and hydrocolloids (Magnin et al. 2004).

2.1.2 Hydrogen Bonding

Several examples of physically cross-linked hydrogels have been reported in literature by taking advantage of H bonding between the components. Poly(ethyleneglycol) prepolymer with bifunctional 2-ureido-4[1H]-pyrimidinone (UPy) acted as hydrogelator in water, and self-healing hydrogels were prepared based on H-bonding interactions (van Gemert et al. 2012). These hydrogels exhibited excellent self-healing properties based on dynamic assembly and disassembly of UPy unit in response to any in situ damage. Copolymers of 2-(dimethylamino)-ethyl methacrylate (DMAEMA) and 2-(3-(6-methyl-4-oxo-1,4-dihydropyrimidin-2-yl)ureido) ethyl methacrylate (SCMHBMA) formed supramolecular hydrogels in water under basic conditions (Cui and Campo 2012). Carboxymethyl cellulose (CMC) hydrogels prepared under acidic conditions were reported by Takigami et al. based on H bonding between carboxylic groups (Takigami et al. 2007). Similarly, carboxymethylated chitosan hydrogels, poly[(ethylene oxide)/acrylic acid] hydrogels, and poly[(ethylene oxide)/methacrylic acid] hydrogels were also fabricated by H bonding-generated cross-linking under acidic conditions (Gulrez et al. 2011; Hoffman 2002). The hydrogel formation in these cases occurs only in acidic medium when the carboxylic groups are protonated suggesting that the swelling behavior of these hydrogels is highly pH dependent.

A variety of hydrogels such as poly(vinyl alcohol) (PVA)/carboxymethyl cellulose (CMC) have been prepared by repeated freeze–thaw cycles which led to the microcrystal formation in the structure supported by hydrogen bonding (Xiao and Gao 2008; Zhang et al. 2013). Hydrogels prepared by using this method have sufficient mechanical strength. Some examples in this category are the hydrogels of polysaccharides like hyaluronan, CMC, xanthan, β -glucan, locust bean gum, starch, maltodextrins, and agarose (Zhang et al. 2013; Giannouli and Morris 2003). Hydrogels of hemicellulose, PVA, and chitin nanowhiskers were prepared using this method with high mechanical strength, swelling degree, and thermal stability (Guan et al. 2014). PVA/water-soluble chitosan hydrogels prepared by combination of freeze–thaw and γ -irradiation have also been reported in literature for wound dressing (Yang et al. 2008).

Biodegradable injectable chitosan hydrogels have been prepared by using glycerophosphate as gelling agent (Chenite et al. 2000, 2001; Khodaverdi et al. 2013). However, this method results in the presence of negative charge moieties and turbidity which are undesirable. Other phosphate-free gelling agents such as 1,3-propanediol, 1,2-propanediol, glycerol, mannitol, or polyoses (e.g., trehalose) have also been used in order to reduce the toxicity (Schuetz et al. 2008; Singh et al. 2010). It is postulated that the gelation occurs due to secondary

hydrophobic or hydrogen-bonding interactions between the polysaccharide chains. It was shown by Gekko et al. that water-structuring molecules like polyols indeed favor the hydrophobic interactions (Gekko and Ito 1990).

2.1.3 Multiple Interactions

Protein engineering, a relatively new branch of materials chemistry, is being extensively explored for the design of new proteins by understanding the protein folding and recognition process. The physical and chemical properties of such proteins can be controlled by variation of the amino acid sequences. As a result these proteins have been used for the preparation of hydrogels with desired properties. Self-assembling proteins consisting of silk and elastin-like amino acid sequences, also known as ProLastins, undergo irreversible solution to gel transformation under physiological conditions. The time-dependent gelation phenomena can be further controlled by variation of temperature, solution conditions, and additives. The gel properties and drug release rate can also be tuned by changing the amino acid sequence of ProLastins (Cappello et al. 1998). Shear thinning, injectable, and self-healing hydrogels were synthesized by using two component materials, having modular protein domain which is also known as WW domain and proline-rich peptide domains, based on protein–protein interactions for cell encapsulation applications (Wong Po Foo et al. 2009). Poly(*N*-(2-hydroxypropyl)methacrylamide) (PHPMA) hydrogels were developed by using natural and engineered proteins exhibiting coiled-coil interactions (Wang et al. 1999; Tang et al. 2001). The combination of protein and polymer was achieved based on metal complex formation between the histidine groups of proteins and metal chelating ligands on polymer (Wang et al. 1999).

Agar-agar, carrageenan, gelatin, and gellan gum are some of the naturally occurring polysaccharides which have been widely explored for physically cross-linked gel formation (Gulrez et al. 2011; Funami et al. 2007; Noda et al. 2008). Carrageenan, an extensively used thickening agent in food industry, has one sulfate group per disaccharide and forms firm gels. When the hot solution of carrageenan is cooled below the gel point, i.e., between 30 °C and 70 °C, random coils convert into double helices (Wu and Imai 2012). If Na⁺, K⁺, or Ca²⁺ ions are present in the system, they counter the charge generated by sulfate groups without hindering the double helix formation and close packing which results into further aggregation of double helices forming three-dimensional gel network (Mangione et al. 2005; Bixler et al. 2001; Ikeda et al. 2001; Morris et al. 1980). Gels with desired strengths have also been prepared by using pullulan in combination with carrageenan or xanthan gum for food packaging applications (Wu and Imai 2012; Trinetta et al. 2011). PVA hydrogels with carrageenan and agar were prepared by Varshney et al. with improved mechanical properties for wound dressing (Varshney 2007).

2.2 Chemical Cross-Linking

Chemically cross-linked hydrogels are prepared by connecting the polymer chains via covalent bonds, and their degradability is limited depending on their chemical

structure. The available methods for the fabrication of such hydrogels will be summarized here.

2.2.1 Cross-Linking by Radical Polymerization

Radical polymerization is one of the most extensively used techniques to prepare chemically cross-linked hydrogels. Poly(2-hydroxyethyl methacrylate) (PHEMA) hydrogels, first described by Wichterle and Lim in 1954 (Wichterle and Lim 1960), are a frequently researched hydrogel system and generally prepared by radical polymerization of HEMA using a cross-linker such as ethylene glycol dimethacrylate (EGDMA) and peroxide initiator (Hennink and van Nostrum 2012; Seidel and Malmonge 2000). Furthermore, by incorporating desired amounts of methacrylic acid (MAA), pH-sensitive poly(HEMA-MAA) hydrogel particles were fabricated using ammonium persulfate/tetramethylethylenediamine (APS/TEMED) as free radical initiator for oral delivery of insulin (Tyagi et al. 2011). Similarly, thermo-responsive poly(*N*-isopropylacrylamide/acrylamide/HEMA) (NIPAM/AAm/HEMA) hydrogels and temperature/pH dual-responsive poly(L-glutamic acid)/NIPAM/HEMA hydrogels were also reported in the literature (Yildiz et al. 2002; Zhao et al. 2009b). Hydrogel preparation using this method relies on the incorporation of vinyl groups as pendant moieties or end groups. Several polymers such as dextran (Cassano et al. 2009; Carvalho et al. 2007), albumin (Park 1988), hydroxyethyl starch (Sturesson and Degling Wikingsson 2000), polyaspartamide (Sun et al. 2009), PVA (Artyukhov et al. 2011), and hyaluronic acid (HA) (Ifkovits and Burdick 2007) have been functionalized with acrylate groups in order to develop their respective hydrogels either by using a redox initiator pair or a photoinitiator triggered by light for various applications. Similarly, gelatin-poly(ethylene glycol) (PEG) hydrogels and 3,4-dihydroxyphenylalanine (DOPA)-modified PEG hydrogels were reported by Hutson et al. and Lee et al., respectively (Hutson et al. 2011; Lee et al. 2002).

Atom transfer radical polymerization (ATRP) is an effective method for the design of multifunctional, nanostructured materials for a variety of applications due to precise control obtained over macromolecular structure and functionality. ATRP can be performed in a variety of different solvents and is tolerant to most of the functional groups. Thermoresponsive hydrogels based on 2-(2-methoxyethoxy) ethyl methacrylate (MEO₂MA) were synthesized by Matyjaszewski et al. via ATRP (Yoon et al. 2010). Furthermore, MEO₂MA-oligo(ethylene oxide) methyl ether methacrylate (OEOMA)-HEMA hydrogels were formed by ATRP (Yoon et al. 2011). Hydroxy groups of these hydrogels were further converted to ATRP initiating sites to grow dangling chains by “graft from” ATRP. This method provided the possibility of introducing required functionality without synthesizing additional macromonomers. Since hydrogel properties depend on the chemical structure of the building blocks, ATRP has been used for the synthesis of very well-defined functional polymers, which have been further used for hydrogel fabrication. P(DMAEMA-co-HEMA)-b-P(NIPAM)-b-P(DMAEMA-co-HEMA)-based hydrogels were prepared by combination of ATRP and glutaraldehyde-based cross-linking (Xu et al. 2006). Nanostructured hybrid hydrogels based on POEOMA prepared

by a combination of ATRP and free radical polymerization were also reported by Matyjaszewski et al. (Bencherif et al. 2009).

Recently, Reversible addition–fragmentation chain transfer (RAFT) technique is gaining increased attention due to the possibility of generating highly controlled molecular weight polymers with low polydispersity providing a versatile platform for precise synthesis of hydrogels with complex architectures. OEOMA-diethylene glycol methyl ether methacrylate (DEG)-2-(methacryloyloxy)ethyl trimethylammonium chloride (TMA) block copolymers developed by RAFT were used as temperature- and salt-responsive reversible hydrogels (Hemp et al. 2014). PNIPAM hydrogels were synthesized by RAFT using *N,N*-methylenebisacrylamide (BIS) as a cross-linker and 4-cyanopentanoic acid dithiobenzoate as chain transfer reagent. It was found that RAFT hydrogels showed accelerated shrinking kinetics and higher swelling ratio as compared to conventional hydrogels (Liu et al. 2006). Thermoreversible HA/PNIPAM hydrogels were fabricated by Mortisen et al. via combination of click chemistry and RAFT polymerization for cell and drug therapy (Mortisen et al. 2010).

2.2.2 Cross-Linking by Addition Reactions

Hydrogels can be synthesized by cross-linking of the polymer chains using bi-, tri-, or multifunctional cross-linking agents, which react with the functional group of the polymer via addition reaction. Due to the presence of chemical cross-linking agents and their toxicity issue, such hydrogels should be extensively cleaned after their preparation to remove the traces of unreacted cross-linker, monomers, and oligomers. In general these gels can be loaded with guest materials either during or after gel preparation. However, especially in the case of biomedical applications for controlled drug and protein release, these gels are mostly loaded afterward in order to avoid the denaturation of biomaterials. Since these hydrogels are composed of chemically cross-linked networks, their degradation is rather limited.

Several examples of polysaccharide hydrogels prepared by cross-linking with 1,6-hexamethylenediisocyanate (Chen et al. 2013; Hovgaard and Brøndsted 1995), divinylsulfone (Ibrahim et al. 2010; Gehrke et al. 1998), 1,6-hexanedibromide (Coviello et al. 1999) etc. have been reported in the literature. Injectable, biodegradable thiolated glycol chitosan-based hydrogels were synthesized by cross-linking with water-soluble oligo(acryloyl carbonate)-*b*-poly(ethylene glycol)-*b*-oligo(acryloyl carbonate) triblock copolymers based on Michael-type addition reaction (Yu et al. 2011). Thiol-modified HA and gelatin-based hydrogels with controlled mechanical properties and biodegradation rate have been fabricated by using poly(ethylene glycol) diacrylate (PEGDA) as cross-linker (Burdick and Prestwich 2011). Thiolated HA hydrogels cross-linked with PEGDA (Young and Engler 2011) and degradable hydrogels prepared by reaction of PEG dithiol and PEGDA (Elbert et al. 2001) are some other examples of this cross-linking method.

2.2.3 Cross-Linking by Condensation Reactions

Water-soluble polymers functionalized with various groups such as $-\text{NH}_2$, $-\text{OH}$, $-\text{COOH}$, etc. can be used for the cross-linking reaction through reaction with their complementary groups via condensation mechanism to fabricate hydrogels. Water-

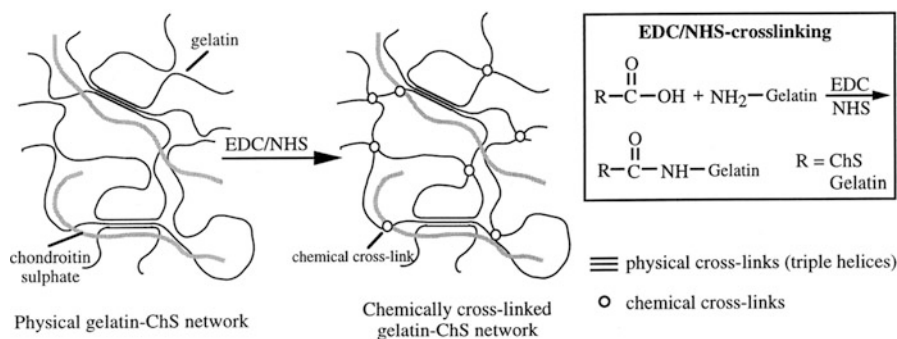


Fig. 1 Schematic representation of a physical and a chemical gelatin – ChS network. A physical gelatin network contains triple-helix junctions (*dotted gray color lines*). By chemical cross-linking of this physical network with EDC and NHS, chemical junctions are introduced (○) (Reproduced from Kuijpers et al. 2000b)

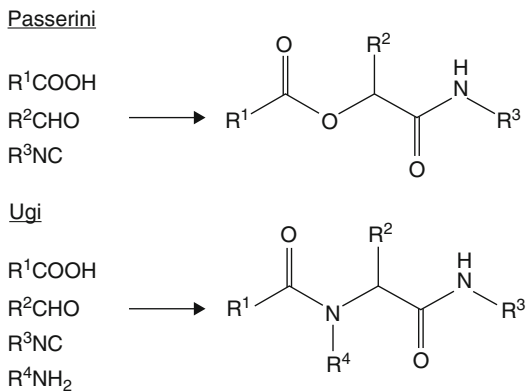
soluble carbodiimide (EDC) and *N*-hydroxysuccinimide (NHS) coupling reaction has been efficiently used for the synthesis of gelatin (Kuijpers et al. 2000a), collagen (Omobono et al. 2014), alginate/PEG-diamines (Eiselt et al. 1999), and gelatin/chondroitin sulfate (ChS) (Kuijpers et al. 2000b)-based hydrogels (Fig. 1). EDC cross-linked recombinant human collagen (RHC) hydrogels were synthesized by Fagerholm et al. as a substitute for corneal implant (Fagerholm et al. 2010). These implants were successfully tested in phase 1 clinical study to address the current donor cornea shortage. Later on, a bifunctional epoxy-based cross-linker, 1,4-butanediol diglycidyl ether (BDDGE), was also used for developing collagen hydrogel-based corneal substitutes (Koh et al. 2013).

Isocyanide multicomponent reactions such as Passerini and Ugi condensation are another efficiently used method for the fabrication of naturally occurring and chemically modified polysaccharide-based hydrogels (Rudick 2013). In case of Passerini reaction, carboxylic groups of the polymer chains are reacted with dialdehyde cross-linker yielding α -(acryloxy)amide, whereas Ugi condensation involves the reaction with diamine generating α -(acylamino)amide linkage (Fig. 2; Rudick 2013; de Nooy et al. 1999, 2000; Crescenzi et al. 2003; Bu et al. 2004; Di Meo et al. 2006). Due to the differences in the chemical structure of the products, the hydrogels prepared via Ugi reaction are more stable in comparison to the ones prepared with Passerini reaction, which degrade at ambient temperature under basic conditions (de Nooy et al. 2000).

2.2.4 Cross-Linking by Click Chemistry

Recently, click chemistry has emerged as a versatile and viable platform for the development of hydrogels due to its high reactivity, bioorthogonality, high specificity, and high yield. Various hydrogels based on PVA (Ossipov and Hilborn 2006), PEG (van Dijk et al. 2010), PNIPAM/HEMA (Xu et al. 2008), PNIPAM/ β -cyclodextrin (β -CD) (Xu et al. 2009), HA (Crescenzi et al. 2007), etc. were fabricated

Fig. 2 Chemical structures of the products formed by Passerini and Ugi reactions (Reproduced from (de Nooy et al. 1999))



using copper-catalyzed azide–alkyne click reaction (CuAAC). HA hydrogels prepared by CuAAC have been used as drug reservoirs and cell scaffolds (Crescenzi et al. 2007). Similarly, bisphosphonate-functionalized dextran hydrogel particles were developed by CuAAC in order to address bone disease (Heller et al. 2013). Lin et al. synthesized hydrogels with tunable mechanical and biochemical properties by reacting norbornene-functionalized four-arm PEG with dithiol peptide or dithiothreitol via thiol-ene click chemistry (Shih and Lin 2012, 2013). Diels–Alder reaction has also been employed for the development of various hydrogels with desired properties. Hydrogels synthesized by reaction of maleimide- and furan-modified HA, poly(*N,N*-dimethylacrylamide-co-furfuryl methacrylate), and dimaleimide-PEG via Diels–Alder reaction are some of the examples in this category (Wei et al. 2009; Tan et al. 2011). Readers are referred to several excellent reviews published in the literature describing the fundamental aspects of hydrogel prepared by click chemistry and their applications (Nimmo and Shoichet 2011; Lallana et al. 2012; Uliniuc et al. 2012; Jiang et al. 2014).

2.3 Irradiation Cross-Linking

High-energy radiation, especially electron beam (EB) and gamma (γ) irradiation, has been frequently used as a cross-linking method for the preparation of various hydrogels. When polymers are irradiated with γ or EB, radicals are formed on the polymer chain, which can recombine with different polymer chains forming covalent bonds and thus result into the formation of a cross-linked hydrogel network. The advantages of using these methods are the absence of toxic chemical cross-linkers and the simultaneous sterilization of the product especially if biomedical applications are concerned.

PNIPAM hydrogels were developed by Panda et al. by simultaneous polymerization and cross-linking via EB. Microstructure of the prepared hydrogels and their swelling behavior was tuned based on the irradiation dose, dose rate, and temperature while irradiation (Panda et al. 2000). PVA/polyaniline composite hydrogels

fabricated by EB treatment showed no cytotoxicity in MTT assays exhibiting their potential for biosensing and smart drug delivery (Dispenza et al. 2012). Vinyl end-group-functionalized poloxamer was used to prepare hydrogels with EB. These hydrogels were loaded with triamcinolone acetonide for the topical treatment of buccal mucosa and wounded skin in rats (Choi et al. 2013). Superabsorbent carboxymethylcellulose/clay hydrogels were fabricated by Salmawi et al. via EB irradiation (El Salmawi and Ibrahim 2011). These hydrogels were tested for their water retention capacity and also for simulated urine to analyze their potential in personal care product industry.

A straightforward synthetic strategy for the preparation of a uniform PNIPAM/Au hybrid hydrogel was reported by Zhu et al. (2012). In this approach, the PNIPAM hydrogels and the Au nanoparticles (NPs) were formed simultaneously via γ -irradiation. The developed hydrogels were further used for tunable conversion of *o*-nitroaniline to 1,2-benzenediamine. Similarly, antimicrobial 2-acrylamido-2-methylpropane sulfonic acid/AgNP hybrid hydrogels were prepared in a single step by using γ -irradiation (Boonkaew et al. 2014). HA/ChS/PVA (Zhao et al. 2014), PAA/Zn NPs (Park et al. 2013), PVA/chitosan (Tahtat et al. 2011), poly(vinyl pyrrolidone) (PVP)/AgNPs (Khampieng et al. 2014), and cationic starch/AAM (Song et al. 2014) are some other examples reported in the literature.

3 Smart Hydrogels

Hydrogels showing significant response to environmental stimuli such as temperature, pH, light, solvent, and electric and magnetic fields are known as smart hydrogels. Due to the extreme importance of these stimuli-sensitive hydrogels in various fields, an overview of various types of smart hydrogels and their characteristic properties has been given here.

3.1 Temperature-Responsive Hydrogels

Temperature-responsive hydrogels are one of the most extensively studied classes of smart hydrogels, which has been proved a potential candidate for various biomedical applications. Based on their response toward the temperature of the surrounding medium, these hydrogels can be classified in two categories (Laftah et al. 2011). The first group includes hydrogels where polymer chains exhibit lower critical solution temperature (LCST), which means that hydrogels are swollen below LCST and shrink as the temperature increases above LCST. In general, LCST polymers have a combination of hydrophilic and hydrophobic segments in the polymer chain. At temperature below LCST, hydrophilic interactions with water dominate, and the hydrogels are swollen. On the other hand, as the temperature increases above LCST, the hydrogen bonds with water are broken, and hydrophobic interactions between the polymer chains dominate resulting into the deswelling of hydrogels due to the expulsion of water from the hydrogel network. The critical temperature at which the

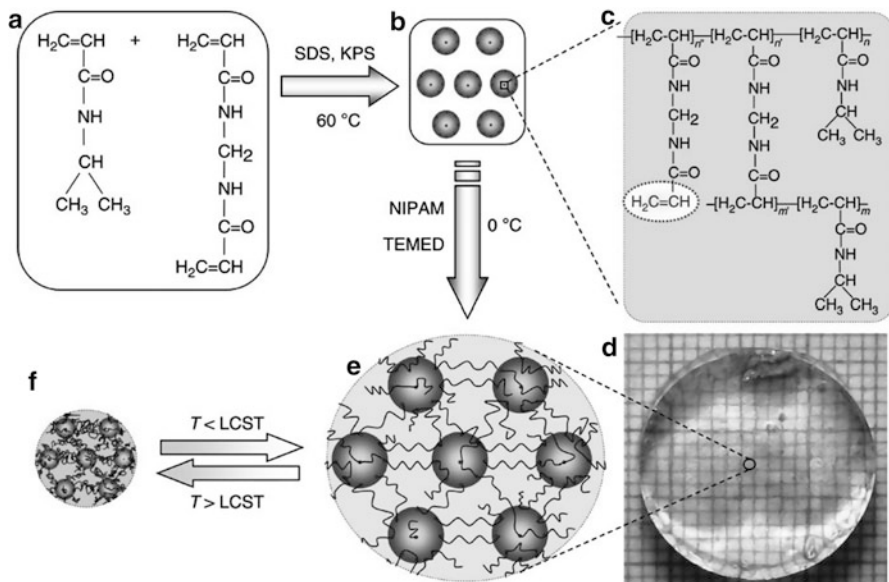


Fig. 3 (a) Chemical structure of NIPAM and MBA. (b) ANGs bearing unsaturated double bonds fabricated by precipitation polymerization of NIPAM and MBA, which is initiated by KPS in the presence of amphiphilic SDS. (c) Chemical structure of the ANG showing the unsaturated double bonds from the unreacted parts of the ANGs and the NIPAM units. (d) Optical image showing the NSG, which is fabricated from the ANGs and NIPAM with TEMED as an accelerator at 0 °C, is transparent at temperature below the LCST. (e, f) Internal structure of the nanostructured NSG hydrogel in the swollen state at temperature below the LCST (e) and in the shrunken state at temperature above the LCST (f) (Reproduced from (Xia et al. 2013))

hydrogels start to shrink can be tuned by different ways. For example, addition of small amounts of hydrophilic or ionic comonomers shifts LCST to higher temperature, while hydrophobic comonomers shift it to lower temperature (Ankareddi and Brazel 2011; Pena-Francesch et al. 2014). LCST of these hydrogels can also be tuned by changing the solvent composition and the ratio of hydrophilic to hydrophobic polymer content in the hydrogel (Yu et al. 2012).

PNIPAM and poly(*N*-vinylcaprolactam) (PVCL)-based hydrogels are the most common examples of LCST-type hydrogels which show on/off drug release at low and high temperatures, respectively (Wang et al. 2011; Deen et al. 2012; Liang et al. 2012; Agrawal et al. 2013a). Due to the abovementioned properties, these hydrogels are being extensively explored for controlled drug delivery applications. Nanostructured smart PNIPAM hydrogels were developed by Xia et al. using controllable active nanogels as nanocross-linkers (Fig. 3). These hydrogels show very fast response to environmental stimuli and possess very high elastic properties (Xia et al. 2013).

Another group of hydrogels are designed from polymers that possess upper critical solution temperature (UCST), which means that these hydrogels show deswelling behavior below UCST, while they are swollen above UCST. At lower

temperature than UCST, complex structures are formed due to strong hydrogen bonding, and the hydrogel is in the shrunken state. At higher temperature above UCST, hydrogen bonds are broken, and the hydrogels are able to swell to their full capacity. Polyacrylamide (PAAm) and polyacrylic acid (PAA) are some of the most investigated examples of UCST-type hydrogels (Ning et al. 2013; Shirakura et al. 2014; Seuring and Agarwal 2012). Cisplatin-loaded PAAm/PAA hydrogel nanoparticles were reported for controlled drug release based on UCST behavior (Shirakura et al. 2014). Various sol–gel reversible thermosensitive hydrogels have also been developed based on poly(ethylene oxide)-*b*-poly(propylene oxide)-*b*-poly(ethylene oxide). Pluronics, Tetronics, and poloxamer are the most commonly used thermo-reversible gels in this category which exist as a free-flowing solution at ambient temperature and gel at body temperature (Laftah et al. 2011).

Poly(*N,N*-diethylacrylamide) (PDEAAm) (Geever et al. 2011), hemicellulose, and PNIPAM (Yang et al. 2011)-based LCST-type temperature-sensitive hydrogels with pulsatile swelling behavior were developed by Geever et al. and Yang et al., respectively, using UV irradiation technique. Temperature-responsive hydrogels based on three-arm star copolymer having β -CD as a core were developed by Zhang et al. (2012). PNIPAM and poly(*N,N*-dimethylacrylamide) (PDMA) copolymer chains were grown on β -CD core using RAFT method. It was found that the special star-shaped topology and collapsed PNIPAM chains resulted into gel formation.

Due to their tunable phase transition temperature and fast response toward the change in the surrounding environment, LCST-type gels have been the most promising candidates for actuators. In this context, highly integrated PNIPAM hydrogel-based microelectromechanical systems with excellent actuator properties and time behavior have been developed by Richter et al. to fabricate artificial skin (Richter and Paschew 2009).

3.2 pH-Responsive Hydrogels

pH-responsive hydrogels are prepared by polymerizing the pH-sensitive monomers having ionizable functional groups or by cross-linking of polyelectrolytes which show swelling or deswelling in response to the change in pH of the surrounding medium (Agrawal et al. 2012, 2013b). The dramatic variation in the properties of hydrogels above and below a critical pH occurs due to the change in hydrophilic/hydrophobic balance of polymer chains resulting from electrostatic interactions. Based on the nature of ionizable pendant group, these hydrogels can be classified into anionic or cationic hydrogels. In general, the anionic hydrogels comprise of monomers containing carboxylic (mainly PAA, PMAA), sulfonic, or phosphate as pendant groups. Anionic hydrogels show maximum swelling when pKa of ionizable groups is higher than the pH of the surrounding medium due to the maximum charge density causing electrostatic repulsion. Cationic hydrogels consist mainly of amine group containing monomers such as poly(ethylene amine) (PEI), poly(diethylaminoethyl methacrylate) (PDMAEMA), etc. In contrast to anionic hydrogels, cationic hydrogels show maximum swelling when pH of the surrounding medium is

lower than pK_b of ionizable groups. Due to the changes occurring in the physiological properties of hydrogels upon varying the pH, these responsive hydrogels have been explored in various fields including biomedical applications.

pH-responsive poly(2-vinylpyridine-co-divinylbenzene) hydrogels loaded with magnetic iron oxide, fluorescent CdSe/ZnS quantum dots (QDs), and metallic gold were developed by Riedinger et al. for drug delivery and sensor applications (Riedinger et al. 2011). Methacrylic acid-grafted poly(ethylene glycol) P(MAA-g-EG) hydrogels loaded with hydrophobic poly(methyl methacrylate) (PMMA) nanoparticles were synthesized via UV irradiation method. These hydrogels showed successful release of fluorescein, used as hydrophobic model therapeutic agent, upon changing the pH from 2.0 to 7.0 and thus exhibiting their potential for release while passing from the stomach (low pH) to upper small intestine (neutral pH) (Schoener et al. 2012). Inspired by blue mussel adhesive proteins, self-healing multi-pH-responsive hydrogels were developed using DOPA-functionalized poly(allylamine). Based on pH-dependent DOPA/iron coordination chemistry, self-healing and high-strength hydrogels were obtained when pH is changed from acid toward basic value (Krogsgaard et al. 2013). Biodegradable, pH-responsive PMAA hydrogels were developed by Peppas et al. using polycaprolactone diacrylate as cross-linker (VanBlarcom and Peppas 2011). These hydrogels were further incorporated as sensing components in silicon-based microsensors.

pH-responsive, self-healing hydrogels were reported by He et al. using 1,3-benzenediboric acid (BDDBA) and four-arm PEG catechol (cPEG). BDDBA forms borate esters with catechol groups under basic conditions resulting into 3D gel network formation (He et al. 2011).

pH-sensitive poly(2-(diisopropylamino)ethyl methacrylate) (PDPA) and biocompatible poly(2-(methacryloyloxy)-ethyl phosphorylcholine) (PMPC)-based responsive hydrogels were reported by Yoshikawa et al. (2011). PDPA/PMPC hydrogels show tunable elastic properties based on pH of the surrounding medium. These hydrogels were used as substrates for myoblast cell adhesion, and it was found that hydrogel elasticity greatly influences the cell behavior (Fig. 4).

3.3 Light-Responsive Hydrogels

Increasing attention has been paid for the development of light-responsive hydrogels as light stimulus can be controlled both spatially and temporally with high accuracy and great convenience. Therefore, such hydrogels are very important for various cutting-edge applications such as optical switches, display units, ophthalmic drug delivery, tissue culture, etc. (Tomatsu et al. 2011). Photoresponsive hydrogels are mainly composed of polymeric network and photoreactive moiety. At first the optical signal is captured by photoreactive moiety and converted to chemical signal (via isomerization, cleavage, or dimerization) which is transferred to the rest of the hydrogel network resulting into the change in its physiological/chemical properties such as elasticity, viscosity, shape, degree of swelling, and so on. Irradiation requirements for these changes to happen depend on the type of photoresponsive moiety

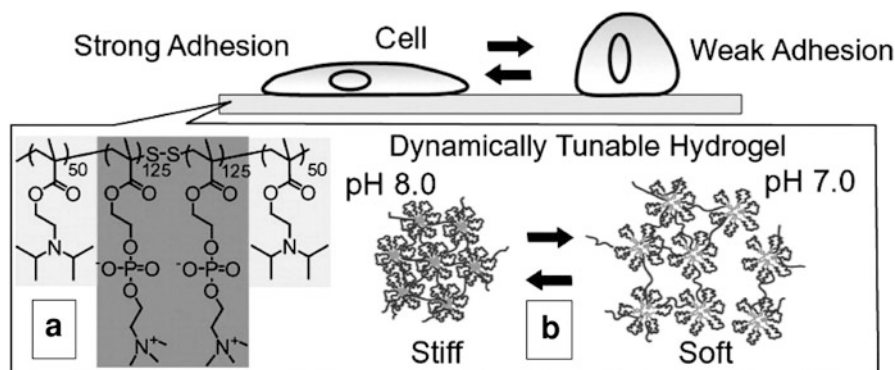


Fig. 4 Chemical structure of the pH-sensitive PDPA50-PMPC250-PDPA50 triblock copolymer (a); schematic representation of the structural changes that occur within the micellar gel network on adjusting the gel pH by the addition of either acid or base (b) (Reproduced from (Yoshikawa et al. 2011))

present in the hydrogel network. The most commonly used photoactive groups to develop photoresponsive hydrogels are azobenzene (Sakai et al. 2007), spiropyran (Kamenjicki Maurer et al. 2005), *o*-nitrobenzylester (Kloxin et al. 2009), triphenylmethane (Kurihara et al. 1998), coumarin (Jin et al. 2010) etc. The most common methods to develop photoresponsive hydrogels are (a) chemical modification of hydrogels with photoresponsive groups (Kloxin et al. 2009; Jin et al. 2010; Shi et al. 2009; Yan et al. 2012), (b) polymers cross-linked by photoresponsive supramolecular assembly (Yamaguchi et al. 2012; Zhou et al. 2013; Peng et al. 2010; Tamesue et al. 2010; Liao et al. 2010; Zhao and Stoddart 2009), and (c) supramolecular hydrogel formation of photoresponsive low molecular weight gelators (Qiu et al. 2009; Li et al. 2010; Matsumoto et al. 2008).

Photoresponsive PAAm/PEG-based hydrogels loaded with upconversion nanoparticles were developed by Yan et al. (2012). The developed hydrogels show gel-sol transition upon exposure to continuous-wave near-infrared (NIR) light (980 nm), and the entrapped large, inactive biomacromolecules (protein and enzyme) can be released on demand (Fig. 5).

Dextran-based biocompatible and photoresponsive hydrogels for light-controlled protein release applications have been reported by Peng et al. based on inclusion complex of *trans* azobenzene and cyclodextrin as a photo-switchable cross-linker (Peng et al. 2010).

Photodegradable ortho-nitrobenzyl (*o*-NB) groups containing hydrogels were synthesized by Griffin et al. via redox polymerization for successful human mesenchymal stem cell (hMSC) encapsulation (90 % viability post-encapsulation) and their controlled release (Griffin and Kasko 2012). The degradation of hydrogel was tuned by changing the number of aryl ether groups on *o*-NB. Balancing the degradation constant of these hydrogels resulted into light-induced biased delivery of multiple cell types with great precision (Fig. 6).

Light stimulus provides high spatial and temporal accuracy with great convenience, which makes light-responsive hydrogels very attractive. However, these

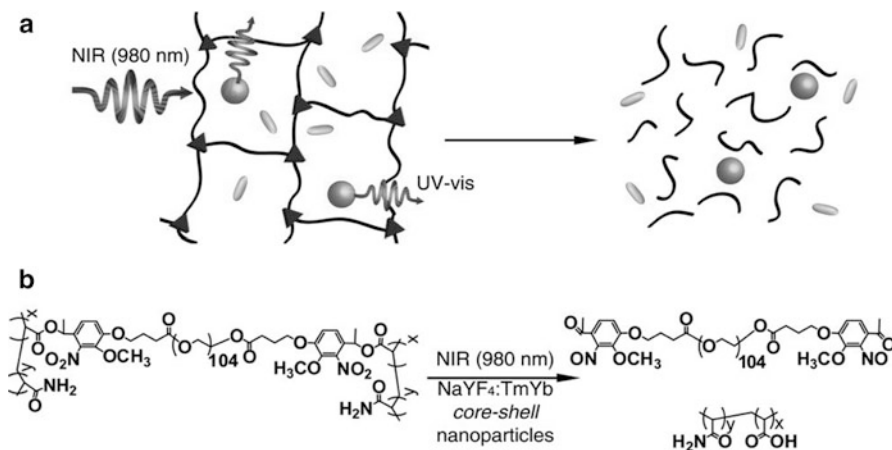


Fig. 5 (a) Schematic illustration of the NIR light-triggered degradation of a photosensitive hydrogel using the UV light generated by encapsulated UCNPs. The polymeric components are depicted as black lines, the photocleavable cross-links as red triangles, the UCNPs as green spheres, and the trapped biomacromolecules as yellow rods. (b) The NIR light-induced photoreaction of the hydrogel via UV light emitted by loaded NaYF₄:TmYb core-shell UCNPs (Reproduced from (Yan et al. 2012))

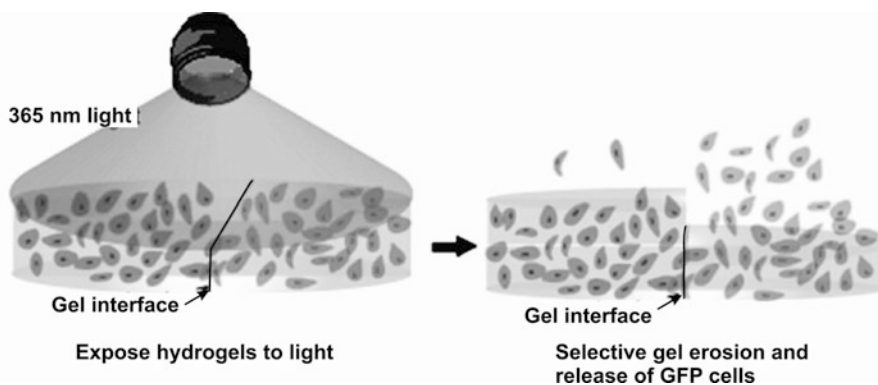


Fig. 6 Light-induced release of encapsulated RFG or GFP-expressing hMSCs (Reproduced from Griffin and Kasko 2012)

hydrogels show slow response and limited reversibility. Additionally, if the chromophores are not chemically attached to the gels, they can also be leached out rendering the gel unresponsive for further use (Priya James et al. 2014).

3.4 Electro-Responsive Hydrogels

In the last two decades, booming research has been done on electro-responsive hydrogels for various applications such as actuators and drug delivery (Qiu and

Park 2001; Murdan 2003). Using electric field as an external stimulus gives the opportunity to precisely control the hydrogel response by varying the current magnitude, current duration, and interval between the current pulses (Samal et al. 2014). When an electrical field is applied, such hydrogels undergo various physiological changes like expansion, contraction, elongation, and bending, thereby performing mechanical work. The type and extent of physiological change depends on the hydrogel shape and its position relative to electric field source (Messing and Schmidt 2011). Upon applying electric field, the response of hydrogel which is in contact with electrodes might be different from the one which is placed in water without touching the electrodes (Qiu and Park 2001). Swelling/deswelling of hydrogel in response to electric current has been employed for drug release applications, whereas elongation and bending have been investigated for valves and actuators, molecular machines, switches and artificial muscles, etc.

Muscular contractions and flagellar and ciliary movement shown by living organisms are results of isothermal conversion of chemical energy into mechanical work. A synthetic polymer gel system able to perform this chemomechanical transformation can serve as an actuator or artificial muscle. Poly(2-acrylamido-2-methylpropane-sulfonic acid) (PAMPS) hydrogels were fabricated by Osada et al. via radical polymerization using BIS cross-linker as a model of electrically driven muscle (Osada et al. 1992). Formation of a complex between positively charged surfactant and negatively charged gel under electric field causes bending of hydrogel. This hydrogel performs worm-like motion upon repeated on/off application of current.

Electro-responsive hydrogels are generally prepared by polymers having plenty of ionizable groups. Therefore, these hydrogels show response to both pH and electric field. Sodium acrylate-based hydrogels were synthesized by Kaetsu et al. via photopolymerization and γ -irradiation (Kaetsu et al. 1992). These hydrogels were used for pulsating release of methylene blue caused by electrophoretic movement of polymeric ions leading to squeezing effect. PAAm-g-xanthan gum hydrogels for transdermal intermittent release of ketoprofen on demand were reported by Kulkarni et al. Here, hydrolysis of CONH₂ groups on PAAm to COOH groups was performed in order to generate electro-responsive hydrogels. Chitosan gels were prepared by acetylation of chitosan and subsequently hydration for the release of neutral (hydrocortisone), anionic (benzoic acid), and cationic (lidocaine hydrochloride) drug molecules in response to electric field (Ramanathan and Block 2001). Electro-sensitive PAA/fibrin hydrogels were synthesized by free radical polymerization and cross-linking of acrylic acid in the presence of fibrin, using APS/ TEMED as redox initiator and BIS as a cross-linking agent (Rahimi et al. 2012). These hydrogels work as a mechanical pump under electric field, which can direct the alignment of porcine smooth muscle cells and facilitate their infiltration and distribution throughout the hydrogel structure (Fig. 7; Rahimi et al. 2012).

Organic conducting polymers have also been used for the formulation of electro-responsive hydrogels. PVP/polyaniline NPs or PVA/polyaniline NP hydrogels were prepared by γ -irradiation using PVP or PVA as a steric stabilizer resulting into the cross-linking of PVP or PVA component (Dispenza et al. 2007). The conducting

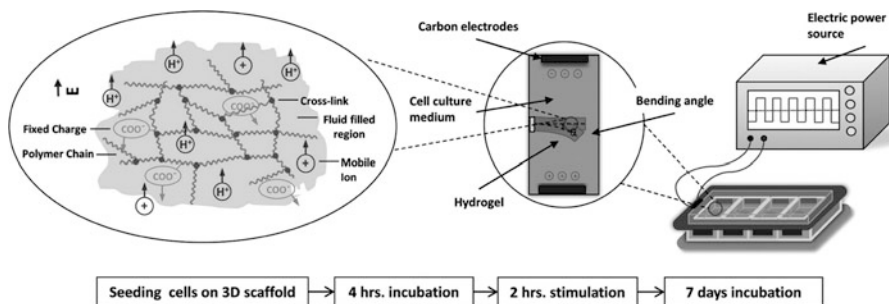


Fig. 7 Schematic representation of polyelectrolyte hydrogel bending under electrical stimuli. The gel shrinks at its anode side and swells at the cathode side when exposed to electrical field (polarization of voltage changes every 60s) (Reproduced from (Rahimi et al. 2012))

poly(methylmethacrylate-co-pyrrolylmethylstyrene)-g-polypyrrole (PMMAPMS/g-PPy) was prepared by Park et al. via electrochemical reaction with PMMAPMS and pyrrole in the electrolyte solution containing lithium perchlorate and a mixture solvent of acetonitrile and dichloromethane (Park and Park 2002). Voltage-switchable artificial muscle materials based on polypyrrole/carbon black doped PAAm/PAA actuating at near neutral pH were prepared by Moschou et al. via radical polymerization. Electric actuation of the developed hydrogels can be tuned by changing the polymerization temperature and the use of BIS cross-linking agent (Moschou et al. 2006).

PVCL-based microgels synthesized by precipitation polymerisation were loaded with Poly(3,4-ethylenedioxythiophene) (PEDOT) nanorods (Hain et al. 2008a, b). It was shown that PEDOT nanorods' loading as well as their morphology can be controlled by adjusting the monomer concentration and alcohol concentration in aqueous phase during the synthesis. The TEM images show that PEDOT nanorods are predominantly located in the microgel shell and are more densely packed if the nanorod amount increases (Fig. 8a–c). The obtained microgels show responsiveness toward temperature and oxidation/reduction of the conjugated polymer by changing pH (Fig. 8d, e). These hybrid microgels were further used to prepare thick homogeneous films, and their electrical properties were tuned by varying PEDOT content inside the microgels.

Additionally, the mechanical and actuator properties of hydrogels can be further improved by the incorporation of additional components inside the gel-like supra-molecular cross-links, induced by clay nanoparticles or polyrotaxanes (Naficy et al. 2011). The fabrication of PNIPAM/clay hybrid gels using inorganic clay as a multifunctional cross-linker in place of an organic cross-linker bisacrylamide has been reported by Fan et al. (Haraguchi et al. 2002). It was shown that the hybrid gels exhibit extraordinary mechanical toughness, tensile moduli, and tensile strengths, while bisacrylamide cross-linked gels are weak and brittle in nature. On the other hand, PNIPAM/PAA-based hydrogels have been synthesized by Imran et al. using slide-ring polyrotaxane cross-linkers. The resulting hydrogels are surprisingly

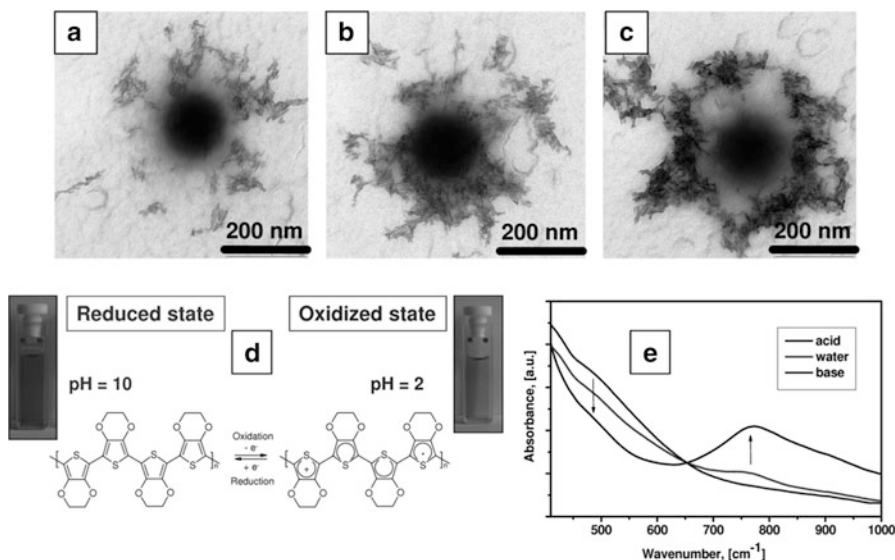


Fig. 8 TEM images of microgels with different PEDOT loading: (a) 4.6 wt.%, (b) 6.3 wt.%, (c) 12.6 wt.%; (d) schematic representation for reduced and oxidized PEDOT; (e) UV-vis spectra of the PEDOT-modified microgel (arrows point out the change of the spectra upon acid addition) (Reproduced from Hain et al. 2008a)

stretchable and tough because the cross-linked α -cyclodextrin molecules can move along the polyethylene glycol chains (Bin Imran et al. 2014).

4 Conclusions

The recent developments in the synthesis of functional hydrogels are reviewed herein. A wide range of available synthetic methods allows incorporating various functional groups inside the hydrogel network, controlling mechanical properties and swelling degree resulting in smart hydrogels, which can respond to various stimuli such as temperature, pH, light, electric field, etc. Due to their stimuli-sensitive properties, these smart hydrogels are being extensively explored for various applications such as cell encapsulation, controlled drug delivery, artificial muscles, etc.

References

- Agrawal G, Schürings M, Zhu X, Pich A (2012) Microgel/SiO₂ hybrid colloids prepared using a water soluble silica precursor. *Polymer* 53:1189
- Agrawal G, Wang J, Brüster B, Zhu X, Möller M, Pich A (2013a) Degradable microgels synthesized using reactive polyvinylalkoxysiloxanes as crosslinkers. *Soft Matter* 9:5380

- Agrawal G, Schürings MP, van Rijn P, Pich A (2013b) Formation of catalytically active gold-polymer microgel hybrids via a controlled in situ reductive process. *J Mater Chem A* 1:13244
- Ahmed EM (2013) Hydrogel: Preparation, characterization, and applications. *J Adv Res*. doi:10.1016/j.jare.2013.07.006
- Ankareddi I, Brazel CS (2011) Development of a thermosensitive grafted drug delivery system—synthesis and characterization of NIPAAm-based grafts and hydrogel structure. *J Appl Polym Sci* 120:1597
- Artyukhov A, Shtilman M, Kuskov A, Fomina A, Lisovyy D, Golunova A, Tsatsakis A (2011) Macroporous polymeric hydrogels formed from acrylate modified polyvinyl alcohol macromers. *J Polym Res* 18:667
- Bajpai AK, Shukla SK, Bhanu S, Kankane S (2008) Responsive polymers in controlled drug delivery. *Prog Polym Sci* 33:1088
- Bencherif SA, Siegwart DJ, Srinivasan A, Horkay F, Hollinger JO, Washburn NR, Matyjaszewski K (2009) Nanostructured hybrid hydrogels prepared by a combination of atom transfer radical polymerization and free radical polymerization. *Biomaterials* 30:5270
- Berger J, Reist M, Mayer JM, Felt O, Gurny R (2004) Structure and interactions in chitosan hydrogels formed by complexation or aggregation for biomedical applications. *Eur J Pharm Biopharm* 57:35
- Bin Imran A, Esaki K, Gotoh H, Seki T, Ito K, Sakai Y, Takeoka Y (2014) Article number: 5124 Extremely stretchable thermosensitive hydrogels by introducing slide-ring polyrotaxane cross-linkers and ionic groups into the polymer network. *Nat Commun* 5:1 doi:10.1038/ncomms6124.
- Bixler HJ, Johndro K, Falshaw R (2001) Kappa-2 carrageenan: structure and performance of commercial extracts: II. Performance in two simulated dairy applications. *Food Hydrocolloids* 15:619
- Boonkaew B, Barber PM, Rengpipat S, Supaphol P, Kempf M, He J, John VT, Cuttle L (2014) Development and characterization of a novel, antimicrobial, sterile hydrogel dressing for burn wounds: single-step production with gamma irradiation creates silver nanoparticles and radical polymerization. *J Pharm Sci* 103:3244
- Bu H, Kjøniksen A-L, Knudsen KD, Nyström B (2004) Rheological and structural properties of aqueous alginate during gelation via the Ugi multicomponent condensation reaction. *Biomacromolecules* 5:1470
- Burdick JA, Prestwich GD (2011) Hyaluronic acid hydrogels for biomedical applications. *Adv Mater* 23:H41
- Burkert S, Schmidt T, Gohs U, Dorschner H, Arndt K-F (2007) Cross-linking of poly(N-vinyl pyrrolidone) films by electron beam irradiation. *Radiat Phys Chem* 76:1324
- Cappello J, Crissman JW, Crissman M, Ferrari FA, Textor G, Wallis O, Whitley JR, Zhou X, Burman D, Aukerman L, Stedronsky ER (1998) In-situ self-assembling protein polymer gel systems for administration, delivery, and release of drugs. *J Control Release* 53:105
- Carvalho J, Gonçalves C, Gil AM, Gama FM (2007) Production and characterization of a new dextrin based hydrogel. *Eur Polym J* 43:3050
- Cassano R, Trombino S, Muzzalupo R, Tavano L, Picci N (2009) A novel dextran hydrogel linking trans-ferulic acid for the stabilization and transdermal delivery of vitamin E. *Eur J Pharm Biopharm* 72:232
- Chellat F, Tabrizian M, Dumitriu S, Chornet E, Magny P, Rivard C-H, Yahia LH (2000) In vitro and in vivo biocompatibility of chitosan-xanthan polyionic complex. *J Biomed Mater Res* 51:107
- Chen Y-Y, Wu H-C, Sun J-S, Dong G-C, Wang T-W (2013) Injectable and thermoresponsive self-assembled nanocomposite hydrogel for long-term anticancer drug delivery. *Langmuir* 29:3721
- Chenite A, Chaput C, Wang D, Combes C, Buschmann MD, Hoemann CD, Leroux JC, Atkinson BL, Binette F, Selmani A (2000) Novel injectable neutral solutions of chitosan form biodegradable gels in situ. *Biomaterials* 21:2155
- Chenite A, Buschmann M, Wang D, Chaput C, Kandani N (2001) Rheological characterisation of thermogelling chitosan/glycerol-phosphate solutions. *Carbohydr Polym* 46:39

- Choi SG, Baek EJ, Davaa E, Nho Y-C, Lim Y-M, Park J-S, Gwon H-J, Huh KM, Park J-S (2013) Topical treatment of the buccal mucosa and wounded skin in rats with a triamcinolone acetamide-loaded hydrogel prepared using an electron beam. *Int J Pharm* 447:102
- Corkhill PH, Hamilton CJ, Tighe B (1989) Synthetic hydrogels. VI. Hydrogel composites as wound dressings and implant materials. *J Biomater* 10:3
- Coviello T, Grassi M, Rambone G, Santucci E, Carafa M, Murtas E, Riccieri FM, Alhaique F (1999) Novel hydrogel system from scleroglucan: synthesis and characterization. *J Control Release* 60:367
- Crescenzi V, Francescangeli A, Capitani D, Mannina L, Renier D, Bellini D (2003) Hyaluronan networking via Ugi's condensation using lysine as cross-linker diamine. *Carbohydr Polym* 53:311
- Crescenzi V, Cornelio L, Di Meo C, Nardecchia S, Lamanna R (2007) Novel hydrogels via click chemistry: synthesis and potential biomedical applications. *Biomacromolecules* 8:1844
- Cui J, Campo AD (2012) Multivalent H-bonds for self-healing hydrogels. *Chem Commun* 48:9302
- de Nooy AEJ, Masci G, Crescenzi V (1999) Versatile synthesis of polysaccharide hydrogels using the passerini and Ugi multicomponent condensations. *Macromolecules* 32:1318
- de Nooy AEJ, Capitani D, Masci G, Crescenzi V (2000) Ionic polysaccharide hydrogels via the Passerini and Ugi multicomponent condensations: Synthesis, behavior and solid-state NMR characterization. *Biomacromolecules* 1:259
- Deen GR, Lim EK, Mah CH, Heng KM (2012) New cationic linear copolymers and hydrogels of N-vinyl caprolactam and N-acryloyl-N'-ethyl piperazine: Synthesis, reactivity, influence of external stimuli on the LCST and swelling properties. *Ind Eng Chem Res* 51:13354
- Di Meo C, Capitani D, Mannina L, Brancaleoni E, Galesso D, De Luca G, Crescenzi V (2006) Synthesis and NMR characterization of new hyaluronan-based NO donors. *Biomacromolecules* 7:1253
- Dispenza C, Fiandaca G, Lo Presti C, Piazza S, Spadaro G (2007) Electrical properties of γ -crosslinked hydrogels incorporating organic conducting polymers. *Radiat Phys Chem* 76:1371
- Dispenza C, Sabatino MA, Niconov A, Chmielewska D, Spadaro G (2012) E-beam crosslinked, biocompatible functional hydrogels incorporating polyaniline nanoparticles. *Radiat Phys Chem* 81:1456
- Doring A, Birnbaum W, Kuckling D (2013) Responsive hydrogels—structurally and dimensionally optimized smart frameworks for applications in catalysis, micro-system technology and material science. *Chem Soc Rev* 42:7391
- Eiselt P, Lee KY, Mooney D (1999) Rigidity of two-component hydrogels prepared from alginate and poly(ethylene glycol)-diamines. *J Macromol* 32:5561
- El Salmawi K, Ibrahim S (2011) Characterization of superabsorbent carboxymethylcellulose/clay hydrogel prepared by electron beam irradiation. *Macromol Res* 19:1029
- Elbert DL, Pratt AB, Lutolf MP, Halstenberg S, Hubbell JA (2001) Protein delivery from materials formed by self-selective conjugate addition reactions. *J Control Release* 76:11
- Fagerholm P, Lagali NS, Merrett K, Jackson WB, Munger R, Liu Y, Polarek JW, Söderqvist M, Griffith M (2010) A biosynthetic alternative to human donor tissue for inducing corneal regeneration: 24-month follow-up of a phase I clinical study. *Sci Transl Med* 2:46ra61
- Farris S, Schaich KM, Liu L, Piergiovanni L, Yam KL (2009) Development of polyion-complex hydrogels as an alternative approach for the production of bio-based polymers for food packaging applications: a review. *Trends Food Sci Technol* 20:316
- Funami T, Hiroe M, Noda S, Asai I, Ikeda S, Nishinari K (2007) Influence of molecular structure imaged with atomic force microscopy on the rheological behavior of carrageenan aqueous systems in the presence or absence of cations. *Food Hydrocolloids* 21:617
- Gadelha M, Chieffo C, Bai S, Hu X, Frohman L (2012) A subcutaneous octreotide hydrogel implant for the treatment of acromegaly. *Endocr Pract* 18:870
- Garg T, Singh S, Goyal AK (2013) Stimuli-sensitive hydrogels: An excellent carrier for drug and cell delivery. *Crit Rev Ther Drug Carrier Syst* 30:369
- Geever L, Lyons J, Higginbotham C (2011) Photopolymerisation and characterisation of negative temperature sensitive hydrogels based on *N,N*-diethylacrylamide *J Mater Sci* 46:509

- Gehrke SH, Uhden LH, McBride JF (1998) Enhanced loading and activity retention of bioactive proteins in hydrogel delivery systems. *J Control Release* 55:21
- Gekko K, Ito H (1990) Competing solvent effects of polyols and guanidine hydrochloride on protein stability. *J Biochem* 107:572
- Giannouli P, Morris ER (2003) Cryogelation of xanthan. *Food Hydrocolloids* 17:495
- Griffin DR, Kasko AM (2012) Photodegradable macromers and hydrogels for live cell encapsulation and release. *J Am Chem Soc* 134:13103
- Guan Y, Bian J, Peng F, Zhang X-M, Sun R-C (2014) High strength of hemicelluloses based hydrogels by freeze/thaw technique. *Carbohydr Polym* 101:272
- Gulrez SKH, Al-Assaf S, Phillips GO (2011) Hydrogels: Methods of preparation, characterisation and applications. In: Carpi A (ed) *Progress in molecular and environmental bioengineering – from analysis and modeling to technology applications*. InTech, Rijeka
- Gunavadhi M, Maria LAA, Chamundeswari VN, Parthasarathy M (2012) Nanotube-grafted polyacrylamide hydrogels for electrophoretic protein separation. *Electrophoresis* 33:1271
- Hain J, Eckert F, Pich A, Adler H-J (2008a) Multi-sensitive microgels filled with conducting poly(3,4-ethylenedioxythiophene) nanorods. *Macromol Rapid Commun* 29:472
- Hain J, Schrinner M, Lu Y, Pich A (2008b) Design of multicomponent microgels by selective deposition of nanomaterials. *Small* 4:2016
- Haraguchi K, Takehisa T, Fan S (2002) Effects of clay content on the properties of nanocomposite hydrogels composed of poly(Nisopropylacrylamide) and clay. *Macromolecules* 35:10162
- He L, Fullenkamp DE, Rivera JG, Messersmith PB (2011) pH responsive self-healing hydrogels formed by boronate-catechol complexation. *Chem Commun* 47:7497
- Heller DA, Levi Y, Pelet JM, Doloff JC, Wallas J, Pratt GW, Jiang S, Sahay G, Schroeder A, Schroeder JE, Chyan Y, Zurenko C, Querbes W, Manzano M, Kohane DS, Langer R, Anderson DG (2013) Modular ‘Click-in-Emulsion’ bone-targeted nanogels. *Adv Mater* 25:1449
- Hemp ST, Smith AE, Bunyard WC, Rubinstein MH, Long TE (2014) RAFT polymerization of temperature- and salt-responsive block copolymers as reversible hydrogels. *Polymer* 55:2325
- Hendrickson GR, Smith MH, South AB, Lyon LA (2010) Design of multiresponsive hydrogel particles and assemblies. *Adv Funct Mater* 20:1697
- Hennink WE, van Nostrum CF (2012) Novel crosslinking methods to design hydrogels. *Adv Drug Deliv Rev* 64(Suppl):223
- Hoare TR, Kohane DS (2008) Hydrogels in drug delivery: Progress and challenges. *Polymer* 49:1993
- Hoffman AS (2002) Hydrogels for biomedical applications. *Adv Drug Deliv Rev* 54:3
- Hovgaard L, Brøndsted H (1995) Dextran hydrogels for colon-specific drug delivery. *J Control Release* 36:159
- Hunt JN, Feldman KE, Lynd NA, Deek J, Campos LM, Spruell JM, Hernandez BM, Kramer EJ, Hawker C (2011) Tunable, high modulus hydrogels driven by ionic coacervation. *J Adv Mater* 23:2327
- Hutson CB, Nichol JW, Aubin H, Bae H, Yamanlar S, Al-Haque S, Koshy ST, Khademhosseini A (2011) Synthesis and characterization of tunable poly(ethylene glycol): gelatin methacrylate composite hydrogels. *Tissue Eng Part A* 17:1713
- Ibrahim S, Kang QK, Ramamurthi A (2010) The impact of hyaluronic acid oligomer content on physical, mechanical, and biologic properties of divinyl sulfone-crosslinked hyaluronic acid hydrogels. *J Biomed Mater Res A* 94A:355
- Ifkovits JL, Burdick JA (2007) Review: photopolymerizable and degradable biomaterials for tissue engineering applications. *Tissue Eng* 13:2369
- Ikeda S, Morris VJ, Nishinari K (2001) Microstructure of aggregated and nonaggregated κ -carrageenan helices visualized by atomic force microscopy. *Biomacromolecules* 2:1331
- Jiang Y, Chen J, Deng C, Suuronen EJ, Zhong Z (2014) Click hydrogels, microgels and nanogels: Emerging platforms for drug delivery and tissue engineering. *Biomaterials* 35:4969
- Jin Q, Liu X, Liu G, Ji J (2010) Fabrication of core or shell reversibly photo cross-linked micelles and nanogels from double responsive water-soluble block copolymers. *Polymer* 51:1311

- Kaetsu I, Uchida K, Morita Y, Okubo M (1992) Synthesis of electro-responsive hydrogels by radiation polymerization of sodium acrylate. *Int J Radiat Appl Instrum Part C Radiat Phy Chem* 40:157
- Kamenjicki Maurer M, Lednev IK, Asher SA (2005) Photoswitchable spirobenzopyran- based photochemically cControlled photonic crystals. *Adv Funct Mater* 15:1401
- Khampiang T, Brikshavana P, Supaphol P (2014) Silver nanoparticle-embedded poly(vinyl pyrrolidone) hydrogel dressing: gamma-ray synthesis and biological evaluation. *J Biomater Sci Polym Ed* 25:826
- Khodaverdi E, Ganji F, Tafaghodi M, Sadoogh M (2013) Effects of formulation properties on sol-gel behavior of chitosan/glycerolphosphate hydrogel. *Iran Polym J* 22:785
- Kloxin AM, Kasko AM, Salinas CN, Anseth KS (2009) Photodegradable hydrogels for dynamic tuning of physical and chemical properties. *Science* 324:59
- Koh LB, Islam MM, Mitra D, Noel CW, Merrett K, Odorcic S, Fagerholm P, Jackson WB, Liedberg B, Phopase J, Griffith M (2013) Epoxy cross-linked collagen and collagen-laminin peptide hydrogels as corneal substitutes. *J Funct Biomater* 4:162
- Kopecek J (2009) Hydrogels: From soft contact lenses and implants to self-assembled nanomaterials. *J Polym Sci Part A Polym Chem* 47:5929
- Krogsgaard M, Behrens MA, Pedersen JS, Birkedal H (2013) Self-healing mussel-inspired multi-pH-responsive hydrogels. *Biomacromolecules* 14:297
- Kuijpers AJ, van Wachem PB, van Luyn MJA, Engbers GHM, Krijgsveld J, Zaat SAJ, Dankert J, Feijen J (2000a) In vivo and in vitro release of lysozyme from cross-linked gelatin hydrogels: a model system for the delivery of antibacterial proteins from prosthetic heart valves. *J Control Release* 67:323
- Kuijpers AJ, Engbers GHM, Meyvis TKL, de Smedt SSC, Demeester J, Krijgsveld J, Zaat SAJ, Dankert J, Feijen J (2000b) Combined gelatin-chondroitin sulfate hydrogels for controlled release of cationic antibacterial proteins. *Macromolecules* 33:3705
- Kurihara S, Ueno Y, Nonaka T (1998) Preparation of poly(vinyl alcohol)-graft-N-isopropylacrylamide copolymer membranes with triphenylmethane leucocyanide and permeation of solutes through the membranes. *J Appl Polym Sci* 67:1931
- Lafiah WA, Hashim S, Ibrahim AN (2011) Polymer hydrogels: A review *Polym-Plast Technol Eng* 50:1475
- Lallana E, Fernandez-Trillo F, Sousa-Herves A, Riguera R, Fernandez-Megia E (2012) Click chemistry with polymers, dendrimers, and hydrogels for drug delivery. *Pharm Res* 29:902
- Lee KY, Mooney DJ (2001) Hydrogels for tissue engineering. *Chem Rev* 101:1869
- Lee BP, Dalsin JL, Messersmith PB (2002) Synthesis and gelation of DOPA-modified poly(ethylene glycol) hydrogels. *Biomacromolecules* 3:1038
- Li X, Gao Y, Kuang Y, Xu B (2010) Enzymatic formation of a photoresponsive supramolecular hydrogel. *Chem Commun* 46:5364
- Liang X, Kozlovskaya V, Chen Y, Zavgorodnya O, Kharlampieva E (2012) Thermosensitive multilayer hydrogels of poly(N-vinylcaprolactam) as nanothin films and shaped capsules. *Chem Mater* 24:3707
- Liao X, Chen G, Liu X, Chen W, Chen F, Jiang M (2010) Photoresponsive pseudopolyrotaxane hydrogels based on competition of host-guest interactions. *Angewandte Chemie* 122:4511
- Lin Y-H, Liang H-F, Chung C-K, Chen M-C, Sung H-W (2005) Physically crosslinked alginate/N, O-carboxymethyl chitosan hydrogels with calcium for oral delivery of protein drugs. *Biomaterials* 26:2105
- Liu Q, Zhang P, Qing A, Lan Y, Lu M (2006) Poly(N-isopropylacrylamide) hydrogels with improved shrinking kinetics by RAFT polymerization. *Polymer* 47:2330
- Magnin D, Lefebvre J, Chornet E, Dumitriu S (2004) Physicochemical and structural characterization of a polyionic matrix of interest in biotechnology, in the pharmaceutical and biomedical fields. *Carbohydr Polym* 55:437
- Mangione MR, Giacomazza D, Bulone D, Martorana V, Cavallaro G, San Biagio PL (2005) K⁺ and Na⁺ effects on the gelation properties of κ-Carrageenan. *Biophys Chem* 113:129

- Matsumoto S, Yamaguchi S, Ueno S, Komatsu H, Ikeda M, Ishizuka K, Iko Y, Tabata KV, Aoki H, Ito S, Noji H, Hamachi I (2008) Photo gel–sol/sol–gel transition and its patterning of a supramolecular hydrogel as stimuli-responsive biomaterials. *Chem Eur J* 14:3977
- Messing R, Schmidt AM (2011) Perspectives for the mechanical manipulation of hybrid hydrogels. *Polym Chem* 2:18
- Morris ER, Rees DA, Robinson G (1980) Cation-specific aggregation of carrageenan helices: Domain model of polymer gel structure. *J Mol Biol* 138:349
- Mortisen D, Peroglio M, Alini M, Eglin D (2010) Tailoring thermoreversible hyaluronan hydrogels by “Click” chemistry and RAFT polymerization for cell and drug therapy. *Biomacromolecules* 11:1261
- Moschou EA, Madou MJ, Bachas LG, Daunert S (2006) Voltage-switchable artificial muscles actuating at near neutral pH. *Sens Actuators B* 115:379
- Murdan S (2003) Electro-responsive drug delivery from hydrogels. *J Control Release* 92:1
- Naficy S, Brown HR, Razal JM, Spinks GM, Whitten PG (2011) Progress toward robust polymer hydrogels. *Aust J Chem* 64:1007
- Nimmo CM, Shoichet MS (2011) Regenerative biomaterials that “Click”: Simple, aqueous-based protocols for hydrogel synthesis, surface immobilization, and 3D patterning. *Bioconjug Chem* 22:2199
- Ning J, Kubota K, Li G, Haraguchi K (2013) Characteristics of zwitterionic sulfobetaine acrylamide polymer and the hydrogels prepared by free-radical polymerization and effects of physical and chemical crosslinks on the UCST. *React Funct Polym* 73:969
- Noda S, Funami T, Nakauma M, Asai I, Takahashi R, Al-Assaf S, Ikeda S, Nishinari K, Phillips GO (2008) Molecular structures of gellan gum imaged with atomic force microscopy in relation to the rheological behavior in aqueous systems. 1. Gellan gum with various acyl contents in the presence and absence of potassium. *Food Hydrocolloids* 22:1148
- Omobono MA, Zhao X, Furlong MA, Kwon C-H, Gill TJ, Randolph MA, Redmond RW (2014) Enhancing the stiffness of collagen hydrogels for delivery of encapsulated chondrocytes to articular lesions for cartilage regeneration. *J Biomed Mater Res A*. doi:10.1002/jbm.a.35266
- Osada Y, Okuzaki H, Hori H (1992) A polymer gel with electrically driven motility. *Nature* 355:242
- Ossipov DA, Hilborn J (2006) Poly(vinyl alcohol)-based hydrogels formed by “Click Chemistry”. *Macromolecules* 39:1709
- Panda A, Manohar SB, Sabharwal S, Bhardwaj YK, Majali AB (2000) Synthesis and swelling characteristics of poly (N-isopropylacrylamide) temperature sensitive hydrogels crosslinked by electron beam irradiation. *Radiat Phys Chem* 58:101
- Park K (1988) Enzyme-digestible swelling hydrogels as platforms for long-term oral drug delivery: synthesis and characterization. *Biomaterials* 9:435
- Park YH, Park SB (2002) Preparation and electroactivity of poly(methylmethacrylate-co-pyrrolyl-methylstyrene)-g-polypyrrole. *Synth Met* 128:229
- Park J-S, Kuang J, Gwon H-J, Lim Y-M, Jeong S-I, Shin Y-M, Seob Khil M, Nho Y-C (2013) Synthesis and characterization of zinc chloride containing poly(acrylic acid) hydrogel by gamma irradiation. *Radiat Phys Chem* 88:60
- Pena-Francesch A, Montero L, Borrós S (2014) Tailoring the LCST of thermosensitive hydrogel thin films deposited by iCVD. *Langmuir* 30:7162
- Peng K, Tomatsu I, Kros A (2010) Light controlled protein release from a supramolecular hydrogel. *Chem Commun* 46:4094
- Peppas NA, Hilt JZ, Khademhosseini A, Langer R (2006) Hydrogels in biology and medicine: From molecular principles to bionanotechnology. *Adv Mater* 18:1345
- Phelps EA, Enemchukwu NO, Fiore VF, Sy JC, Murthy N, Sulchek TA, Barker TH, Garcia A (2012) Maleimide cross-linked bioactive PEG hydrogel exhibits improved reaction kinetics and cross-linking for cell encapsulation and in situ delivery. *J Adv Mater* 24:64
- Plunkett KN, Moore JS (2004) Patterned dual pH-responsive core-shell hydrogels with controllable swelling kinetics and volumes. *Langmuir* 20:6535

- Priya James H, John R, Alex A, Anoop KR (2014) Smart polymers for the controlled delivery of drugs – a concise overview. *Acta Pharm Sin B* 4:120
- Qiu Y, Park K (2001) Environment-sensitive hydrogels for drug delivery. *Adv Drug Deliv Rev* 53:321
- Qiu Z, Yu H, Li J, Wang Y, Zhang Y (2009) Spiropyran-linked dipeptide forms supramolecular hydrogel with dual responses to light and to ligand-receptor interaction. *Chem Commun* 23:3342
- Rahimi N, Molin DG, Cleij TJ, van Zandvoort MA, Post M (2012) Electrosensitive polyacrylic acid/fibrin hydrogel facilitates cell seeding and alignment. *J Biomater Sci Polym Ed* 13:1448
- Ramanathan S, Block LH (2001) The use of chitosan gels as matrices for electrically-modulated drug delivery. *J Control Release* 70:109
- Richter A, Paschew G (2009) Optoelectrothermic control of highly integrated polymer-based MEMS applied in an artificial skin. *Adv Mater* 21:979
- Riedinger A, Pernia Leal M, Deka SR, George C, Franchini IR, Falqui A, Cingolani R, Pellegrino T (2011) “Nanohybrids” based on pH-responsive hydrogels and inorganic nanoparticles for drug delivery and sensor applications. *Nano Lett* 11:3136
- Rudick JG (2013) Innovative macromolecular syntheses via isocyanide multicomponent reactions. *J Polym Sci Part A Polym Chem* 51:3985
- Sakai T, Murayama H, Nagano S, Takeoka Y, Kidowaki M, Ito K, Seki T (2007) Photoresponsive slide-ring gel. *Adv Mater* 19:2023
- Samal SK, Dash M, Dubrue P, Van Vlierberghe S (2014) In: Aguilar MR, Román JS (eds) *Smart polymer hydrogels: properties, synthesis and applications*. Woodhead, Cambridge, UK
- Samchenko Y, Ulberg Z, Korotych O (2011) *Adv Colloid Interface Sci* 168:247
- Schoener CA, Hutson HN, Peppas NA (2012) pH-responsive hydrogels with dispersed hydrophobic nanoparticles for the delivery of hydrophobic therapeutic agents. *Polym Int* 61:874
- Schuetz YB, Gurny R, Jordan O (2008) A novel thermoresponsive hydrogel based on chitosan. *Eur J Pharm Biopharm* 68:19
- Seidel JM, Malmonge SM (2000) Synthesis of polyHEMA hydrogels for using as biomaterials. Bulk and solution radical-initiated polymerization techniques. *Mater Res* 3:79
- Seuring J, Agarwal S (2012) Polymers with upper critical solution temperature in aqueous solution. *Macromol Rapid Commun* 33:1898
- Shi D, Matsusaki M, Akashi M (2009) Photo-cross-linking induces size change and stealth properties of water-dispersible cinnamic acid derivative nanoparticles. *Bioconjug Chem* 20:1917
- Shih H, Lin C-C (2012) Cross-linking and degradation of step-growth hydrogels formed by thiol-ene photoclick chemistry. *Biomacromolecules* 13:2003
- Shih H, Lin C-C (2013) Visible-light-mediated thiol-ene hydrogelation using eosin-Y as the only photoinitiator. *Macromol Rapid Commun* 34:269
- Shin J, Han SG, Lee W (2012) Dually tunable inverse opal hydrogel colorimetric sensor with fast and reversible color changes. *Sens Actuators B* 168:20
- Shirakura T, Kelson TJ, Ray A, Malyarenko AE, Kopelman R (2014) Hydrogel nanoparticles with thermally controlled drug release. *ACS Macro Lett* 3:602
- Singh A, Sharma PK, Garg VK, Garg G (2010) Hydrogels: A review *Int J Pharm Sci Rev Res* 4:97
- Song W, Guo Z, Yao Y, Zheng H, Zhao Z (2014) Cross-link copolymerization of cationic starch by gamma irradiation and its swelling-shrinking and flocculating behaviors. *Starch-Stärke* 66:345
- Stuart MAC, Huck WTS, Genzer J, Muller M, Ober C, Stamm M, Sukhorukov GB, Szleifer I, Tsukruk VV, Urban M, Winnik F, Zauscher S, Luzinov I, Minko S (2010) Emerging applications of stimuli-responsive polymer materials. *Nat Mater* 9:101
- Sturesson C, Degling Wikingson L (2000) Comparison of poly(acryl starch) and poly(lactide-co-glycolide) microspheres as drug delivery system for a rotavirus vaccine. *J Control Release* 68:441
- Sun S, Cao H, Su H, Tan T (2009) Preparation and characterization of a novel injectable in situ cross-linked hydrogel. *Polym Bull* 62:699
- Tahtat D, Mahlous M, Benamer S, Nacer Khodja A, Larbi Youcef S, Hadjarab N, Mezaache W (2011) Influence of some factors affecting antibacterial activity of PVA/Chitosan based hydrogels synthesized by gamma irradiation. *J Mater Sci Mater Med* 22:2505

- Takigami M, Amada H, Nagasawa N, Yagi T, Kasahara T, Takigami S, Tamada M (2007) Preparation and properties of CMC gel. *Trans Mater Res Soc Jpn* 32:713
- Tamesue S, Takashima Y, Yamaguchi H, Shinkai S, Harada A (2010) Photoswitchable supramolecular hydrogels formed by cyclodextrins and azobenzene polymers. *Angew Chem* 122:7623
- Tan H, Rubin JP, Marra KG (2011) Direct synthesis of biodegradable polysaccharide derivative hydrogels through aqueous diels-alder chemistry. *Macromol Rapid Commun* 32:905
- Tang A, Wang C, Stewart RJ, Kopeček J (2001) The coiled coils in the design of protein-based constructs: hybrid hydrogels and epitope displays. *J Control Release* 72:57
- Tomatsu I, Peng K, Kros A (2011) Photoresponsive hydrogels for biomedical applications. *Adv Drug Deliv Rev* 63:1257
- Trinetta V, Cutter CN, Floros JD (2011) Effects of ingredient composition on optical and mechanical properties of pullulan film for foodpackaging applications. *LWT Food Sci Technol* 44:2296
- Tyagi P, Kumar A, Kumar Y, Lahiri SS (2011) Synthesis and characterization of poly(HEMA-MAA) hydrogel carrier for oral delivery of insulin. *J Appl Polym Sci* 122:2004
- Uliniuc A, Popa M, Hamaide T, Dobromir M (2012) New approaches in hydrogel synthesis e click chemistry: a review. *Cellul Chem Technol* 46:1
- van der Linden HJ, Herber S, Olthuis W, Bergveld P (2003) Stimulus-sensitive hydrogels and their applications in chemical (micro)analysis. *Analyst* 128:325
- van Dijk M, van Nostrum CF, Hennink WE, Rijkers DTS, Liskamp RM (2010) Synthesis and characterization of enzymatically biodegradable PEG and peptide-based hydrogels prepared by click chemistry. *J Biomacromol* 11:1608
- van Gemert GML, Peeters JW, Söntjens SHM, Janssen HM, Bosman AW (2012) Self-healing supramolecular polymers in action. *Macromol Chem Phys* 213:234
- VanBlarcom D, Peppas N (2011) Microcantilever sensing arrays from biodegradable, pH-responsive hydrogels. *Biomed Microdevices* 13:829
- Varshney L (2007) Role of natural polysaccharides in radiation formation of PVA-hydrogel wound dressing. *Nucl Instrum Methods Phys Res Sect B* 255:343
- Vashist A, Ahmad S (2013) Hydrogels: smart materials for drug delivery. *Orient J Chem* 29:861
- Vilozny B, Schiller A, Wessling RA, Singaram B (2011) Multiwell plates loaded with fluorescent hydrogel sensors for measuring pH and glucose concentration. *J Mater Chem* 21:7589
- Wang C, Stewart RJ, Kopeček J (1999) Hybrid hydrogels assembled from synthetic polymers and coiled-coil protein domains. *Nature* 397:417
- Wang C, Liu H, Gao Q, Liu X, Tong Z (2008) Alginate-calcium carbonate porous microparticle hybrid hydrogels with versatile drug loading capabilities and variable mechanical strengths. *Carbohydr Polym* 71:476
- Wang J, Sutti A, Wang X, Lin T (2011) Fast responsive and morphologically robust thermo-responsive hydrogel nanofibres from poly(*N*-isopropylacrylamide) and POSS crosslinker. *Soft Matter* 7:4364
- Wei H-L, Yang Z, Zheng L-M, Shen Y-M (2009) Thermosensitive hydrogels synthesized by fast Diels-Alder reaction in water. *Polymer* 50:2836
- Wichterle O, Lim D (1960) Hydrophilic Gels for Biological Use *Nature* 185:117
- Wong Po Foo CTS, Lee JS, Mulyasmita W, Parisi-Amon A, Heilshorn SC (2009) Two-component protein-engineered physical hydrogels for cell encapsulation. *Proc Natl Acad Sci* 106:22067
- Wu P, Imai M (2012) Novel Biopolymer Composite Membrane Involved with Selective Mass Transfer and Excellent Water Permeability In: Ning RY (ed) *Advancing desalination*. InTech, Rijeka
- Xia L-W, Xie R, Ju X-J, Wang W, Chen Q, Chu L-Y (2013) Nano-structured smart hydrogels with rapid response and high elasticity. *Nat Commun* 4:1 2226. doi:10.1038/792ncomms3226
- Xiao C, Gao Y (2008) Preparation and properties of physically crosslinked sodium carboxymethylcellulose/poly(vinyl alcohol) complex hydrogels. *J Appl Polym Sci* 107:1568
- Xu F-J, Kang E-T, Neoh K-G (2006) pH- and temperature-responsive hydrogels from crosslinked triblock copolymers prepared via consecutive atom transfer radical polymerizations. *Biomaterials* 27:2787

- Xu X-D, Chen C-S, Wang Z-C, Wang G-R, Cheng S-X, Zhang X-Z, Zhuo R-X (2008) "Click" chemistry for in situ formation of thermoresponsive P(NIPAAm-co-HEMA)-based hydrogels. *J Polym Sci Part A Polym Chem* 46:5263
- Xu X-D, Chen C-S, Lu B, Wang Z-C, Cheng S-X, Zhang X-Z, Zhuo R-X (2009) Modular synthesis of thermosensitive P(NIPAAm-co-HEMA)/ β -CD based hydrogels via click chemistry. *Macromol Rapid Commun* 30:157
- Yamaguchi H, Kobayashi Y, Kobayashi R, Takashima Y, Hashidzume A, Harada A (2012) Photoswitchable gel assembly based on molecular recognition. *Nat Commun* 3:603
- Yan B, Boyer J-C, Habault D, Branda NR, Zhao Y (2012) Near infrared light triggered release of biomacromolecules from hydrogels loaded with upconversion nanoparticles. *J Am Chem Soc* 134:16558
- Yang X, Liu Q, Chen X, Yu F, Zhu Z (2008) Investigation of PVA/ws-chitosan hydrogels prepared by combined γ -irradiation and freeze-thawing. *Carbohydr Polym* 73:401
- Yang JY, Zhou XS, Fang J (2011) Synthesis and characterization of temperature sensitive hemicellulose-based hydrogels. *Carbohydr Polym* 86:1113
- Yildiz B, İşik B, Kış M (2002) Thermoresponsive poly(N-isopropylacrylamide-co-acrylamide-co-2-hydroxyethyl methacrylate) hydrogels. *React Funct Polym* 52:3
- Yoon JA, Gayathri C, Gil RR, Kowalewski T, Matyjaszewski K (2010) Comparison of the thermoresponsive deswelling kinetics of poly(2-(2-methoxyethoxy)ethyl methacrylate) hydrogels prepared by ATRP and FRP. *Macromolecules* 43:4791
- Yoon JA, Kowalewski T, Matyjaszewski K (2011) Comparison of thermoresponsive deswelling kinetics of poly(oligo(ethylene oxide) methacrylate)-based thermoresponsive hydrogels prepared by "Graft-from" ATRP. *Macromolecules* 44:2261
- Yoshikawa HY, Rossetti FF, Kaufmann S, Kaindl T, Madsen J, Engel U, Lewis AL, Armes SP, Tanaka M (2011) Quantitative evaluation of mechanosensing of cells on dynamically tunable hydrogels. *J Am Chem Soc* 133:1367
- Young JL, Engler A (2011) Hydrogels with time-dependent material properties enhance cardiomyocyte differentiation in vitro. *J Biomater* 32:1002
- Yu Y, Deng C, Meng F, Shi Q, Feijen J, Zhong Z (2011) Novel injectable biodegradable glycol chitosan-based hydrogels crosslinked by Michael-type addition reaction with oligo(acryloyl carbonate)-b-poly(ethylene glycol)-b-oligo(acryloyl carbonate) copolymers. *J Biomed Mater Res A* 99A:316
- Yu Y, Liu Y, Kong Y, Zhang E, Jia F, Li S (2012) Synthesis and characterization of temperature-sensitive poly(N-isopropylacrylamide) hydrogel with comonomer and semi-IPN material. *Polym-Plast Technol Eng* 51:854
- Zhang Y, Tao L, Li S, Wei Y (2011) Synthesis of multiresponsive and dynamic chitosan-based hydrogels for controlled release of bioactive molecules. *Biomacromolecules* 12:2894
- Zhang H, Yan Q, Kang Y, Zhou L, Zhou H, Yuan J, Wu S (2012) Fabrication of thermo-responsive hydrogels from star-shaped copolymer with a biocompatible β -cyclodextrin core. *Polymer* 53:3719
- Zhang H, Zhang F, Wu J (2013) Physically crosslinked hydrogels from polysaccharides prepared by freeze-thaw technique. *React Funct Polym* 73:923
- Zhao Y-L, Stoddart JF (2009) Azobenzene-based light-responsive hydrogel system. *Langmuir* 25:8442
- Zhao QS, Ji QX, Xing K, Li XY, Liu CS, Chen XG (2009a) Preparation and characteristics of novel porous hydrogel films based on chitosan and glycerophosphate. *Carbohydr Polym* 76:410
- Zhao C, Zhuang X, He P, Xiao C, He C, Sun J, Chen X, Jing X (2009b) Synthesis of biodegradable thermo- and pH-responsive hydrogels for controlled drug release. *Polymer* 50:4308
- Zhao L, Gwon H-J, Lim Y-M, Nho Y-C, Kim SY (2014) Hyaluronic acid/chondroitin sulfate-based hydrogel prepared by gamma irradiation technique. *Carbohydr Polym* 102:598
- Zhou L, Li J, Luo Q, Zhu J, Zou H, Gao Y, Wang L, Xu J, Dong Z, Liu J (2013) Dual stimuli-responsive supramolecular pseudo-polyrotaxane hydrogels. *Soft Matter* 9:4635
- Zhu C-H, Hai Z-B, Cui C-H, Li H-H, Chen J-F, Yu S-H (2012) In situ controlled synthesis of thermosensitive poly(N-isopropylacrylamide)/Au nanocomposite hydrogels by gamma radiation for catalytic application. *Small* 8:930

Thomas Wallmersperger and Peter Leichsenring

Contents

1	List of Symbols	54
1.1	Greek Symbols	54
1.2	Latin Symbols	55
1.3	Constants	57
1.4	Subscripts and Superscripts	57
1.5	Other Symbols and Operators	57
2	Introduction	58
3	Literature Review	59
4	Modeling on Different Scales	61
5	Macroscopic Models	62
5.1	Statistical Theory	62
6	Mesosopic Models	65
6.1	Chemo-Electro-Mechanical Transport Model	65
6.2	Theory Based on Porous Media	71
7	Comparison	77
8	Conclusion and Outlook	78
	References	78

Abstract

Polyelectrolyte gels, often referred as ionic polymer gels are quite attractive intelligent materials. They consist of a solid phase, i.e., a polymer network with fixed charges, and a liquid phase with mobile ions. Typically these gels are immersed in a solution bath. An application of different kinds of stimuli – e.g., chemical (change of salt concentration or pH), thermal, magnetical, or electrical – leads to a new equilibrium between the different forces, such as osmotic pressure

T. Wallmersperger (✉) • P. Leichsenring
Institut für Festkörpermechanik, TU Dresden, Dresden, Germany
e-mail: Thomas.Wallmersperger@tu-dresden.de; Peter.Leichsenring@tu-dresden.de

forces, electrostatic forces, and (visco-)elastic forces. This occurs in cooperation with absorption or delivery of the solvent resulting in a (local) change of volume.

In the present chapter, an overview over different modeling alternatives for chemically and electrically stimulated polyelectrolyte gels, placed in a solution bath, are given.

First, the statistical theory – a theory in which only the global swelling is of interest – is reviewed. By refining the scale, two different mesoscopic models are presented: first, the chemo-electro-mechanical transport model and second, a continuum model based on porous media. These models are capable of describing the changes of the local variables: concentrations, electric field, and displacement. So, e. g., by the application of an electric field, a bending movement of the polymer gel can be realized which is in excellent correlation with experimental investigations.

Concluding, the statistical theory is an efficient method to easily model the chemical stimulation of polyelectrolyte gels and the two continuum-based formulations are capable of simulating both chemically and electrically induced swelling or bending. So, they are an excellent technique to model hydrogel bending actuators or grippers.

Keywords

Ionic polymer gels • Polyelectrolyte gels • Modeling • Numerical simulation • Statistical theory • Transport model • Continuum model • Coupled multi-field formulation

1 List of Symbols

1.1 Greek Symbols

Symbol	Description	Unit
$\boldsymbol{\varepsilon}, \varepsilon_{kl}$	Mechanical strain	–
\hat{c}	Energy production density	J s m^{-3}
$\boldsymbol{\varepsilon}^c, \varepsilon_{kl}^c$	Elastic strain	–
$\boldsymbol{\varepsilon}^\pi, \varepsilon_{kl}^\pi$	Swelling strain	–
ε_r	Relative permittivity	–
η	Dilatation factor	–
η^α	Entropy density of the constituent α	J kg K^{-1}
$\hat{\eta}^\alpha$	Total enthalpy production density of the constituent α	$\text{J m}^3 \text{s K}^{-1}$
λ_i	Swelling in i -direction	–
λ_s	Mean swelling	–
μ	Chemical potential	J mol^{-1}
μ^0	Chemical zero potential	J mol^{-1}
$\mu^\beta = \frac{F}{RT} D^\beta$	Ion mobility of the species β	$\text{m}^2 \text{s}^{-1} \text{V}^{-1}$

(continued)

Symbol	Description	Unit
μ_α^*	Electrochemical potential of the species α	J mol^{-1}
ν	Poisson ratio	—
ν_e	Effective number of moles per polymer chain	mol
ν^*	Number of elastically effective network chains	mol
$\dot{\zeta}^\alpha$	Entropy production density of the constituent α	$\text{J m}^3\text{s K}^{-1}$
$\Delta\pi$	Osmotic pressure difference	N m^{-2}
ρ	Mass density	kg m^{-3}
\hat{Q}	Production density of mass	$\text{kg m}^{-3}\text{s}^{-1}$
ρ^α	Partial (mass) density of the constituent α	kg m^{-3}
$\rho^{\alpha R}$	Real (mass) density of the constituent α	kg m^{-3}
ρ_e	Electric charge	C m^{-3}
σ, σ_{kl}	Cauchy stress tensor	N m^{-2}
ζ^α	External entropy supply density	$\text{J m}^3\text{s K}^{-1}$
\mathbf{v}, v_k	Velocity	m s^{-1}
ϕ^α, ϕ_k	Entropy efflux density	$\text{J m}^2\text{s K}^{-1}$
ϕ_p	Polymer volume fraction	—
χ	Flory-Huggins gel-solution interaction parameter	—
χ, χ_k	Motion function	m
χ_1^*	Mole fraction of the solvent	—
χ_e	Electric susceptibility	—
φ^α	Volume fraction of the constituent α	—
Ψ	Electric potential	V
ψ, ψ_i	Arbitrary field function	—

1.2 Latin Symbols

Symbol	Description	Unit
a_α	Activity of the species α	mol m^{-3}
\bar{a}_α	Normalized activity of the species α	—
\mathbf{a}, a_k	Acceleration	m s^{-2}
A	Structural factor	—
\mathbf{b}, b_k	Body forces	N kg^{-1}
\mathbf{B}, B_k	Magnetic field	V s m^{-2}
c	Molar concentration	mol m^{-3}
\bar{c}	Normalized molar concentration	—
c_0	Initial molar concentration	mol m^{-3}
\mathbf{C}, C_{klmn}	Elasticity tensor	N m^{-2}

(continued)

Symbol	Description	Unit
D^α	Diffusion coefficient of the species α	$\text{m}^2 \text{s}^{-1}$
\mathbf{D}, D_i	Dielectric displacement	A s m^{-2}
\mathbf{e}_i	Unit vectors in x_i -direction	–
E	Young's modulus	N m^{-2}
\mathbf{E}, E_k	Electric field	V m^{-1}
f_α	Activity coefficient of the species α	–
F	Gibbs free energy	J
g	Osmotic coefficient	–
g	Swelling coefficient	$\text{m}^2 \text{N}^{-1}$
$\tilde{\mathbf{g}} = \tilde{g}_{kl} = g\delta_{kl}$	Swelling tensor	$\text{m}^2 \text{N}^{-1}$
\mathcal{G}	Gel domain	–
$\partial\mathcal{G}$	Gel surface	–
$\hat{\mathbf{h}}, \hat{h}_k$	Total production density of angular momentum	N m^{-2}
\mathbf{H}, H_k	Magnetizing field	A m^{-1}
\mathbf{J}, J_k	Electric current density	A m^{-2}
m^α	Mass of a species or constituent α	kg
$\hat{\mathbf{m}}, \hat{m}_k$	Production density of angular momentum	N m^{-2}
n	Number of static segments per chain	–
n	Molar number	mol
N_b	Number of bound species	–
N_f	Number of mobile species	–
$\hat{\mathbf{p}}, \hat{p}_k$	Production density of momentum	N m^{-3}
\mathbf{P}, P_k	Electric polarization	A s m^{-2}
\mathcal{P}	Complete domain	–
$q = \phi_p^{-1}$	Swelling ratio	–
q_0	Initial swelling	–
q_r	Relative swelling	–
\mathbf{q}, q_k	Heat flux due to close-range effects	J s m^{-2}
r^α	Heat flux due to long-range effects	J s kg^{-1}
$\hat{\mathbf{s}}, \hat{s}_k$	Total production density of momentum	N m^{-3}
\mathcal{S}	Solution domain	–
$\partial\mathcal{S}$	Solution surface	–
t	Time	s
T	Temperature	K
\hat{u}	Total energy production density	J s m^{-3}
u^α	Internal energy density of the constituent α	J kg^{-1}
\mathbf{u}, u_k	Displacement vector	m
v	Volume in the current configuration	m^3
v_1	Molar volume of the solvent	$\text{m}^3 \text{mol}^{-1}$
V	Volume in the swollen state	m^3

(continued)

Symbol	Description	Unit
V_0	Initial volume in the dry state	m^3
$\mathbf{x}, x_i, \mathbf{X}, X_i$	Position in the current and the reference state, respectively	m
z	Valence of the ions	–

1.3 Constants

Constant	Description	Value
c	Speed of light in vacuum	$c = 299792458 \frac{\text{m}}{\text{s}}$
ε_0	Vacuum permittivity for the electric field	$\varepsilon_0 = 8.854157 \times 10^{-12} \frac{\text{A s}}{\text{V m}}$
F	Faraday constant	$F = 96485.3365 \frac{\text{C}}{\text{mol}}$
R	Universal gas constant	$R = 8.3144621 \frac{\text{J}}{\text{mol K}}$

1.4 Subscripts and Superscripts

Index	Description
0	Initial
1	Solvent
α	Denoting species in Sect. 6.1 and constituents in Sect. 6.2
(g)	Gel
(s)	Solution
el	Elastic
ion	Ion
M	Mixing
ref	Reference

1.5 Other Symbols and Operators

Operator	Description
$\frac{\partial(\cdot)}{\partial t}$	Partial time derivative
$\frac{D(\cdot)}{Dt} = (\cdot)$	Material time derivative
$\frac{\partial(\cdot)}{\partial x_k} = (\cdot)_{,k}$	Derivative in space
δ_{kl}	Kronecker delta
$\Delta(\cdot)$	Difference
ϵ_{klm}	Permutation tensor
\mathcal{L}	Langevin function

2 Introduction

Polyelectrolyte gels, often referred as polymer gels, consist of a solid phase, i.e., a polymer network with fixed charges, and a liquid phase with mobile ions, see Fig. 1. Typically, these gels are immersed in a solution bath.

The polymer gels can be seen as a mixture of different constituents: The gel (g) comprises:

- Polymer (network) or solid phase (P)
- Fixed charges (A^-) or (K^+) bound to the polymer network
- Pore fluid or solvent (F)
- Mobile anions ($-$) and cations ($+$)

The solution (s) contains:

- Fluid or solvent (F)
- Mobile anions ($-$) and cations ($+$)

Polyelectrolyte gels show large volume changes by inducing small variations in their external conditions. For example, by changing the chemical milieu (i.e., change of salt concentrations or pH in the solution) or by changing the temperature, a phase transformation resulting in a swelling or deswelling of the polymer gel is obtained.

By the application of an electric field between the electrodes in the solution bath, a local swelling or deswelling – resulting in a bending of the polymer – is obtained.

Also magnetic gels – by the application of magnetic fields – show phase changes resulting in small local geometrical deformations. Please note that these kinds of gels will not be discussed in the present chapter.

An overview of deformations of a hydrogel probe under different kinds of stimulation is shown in Fig. 2.

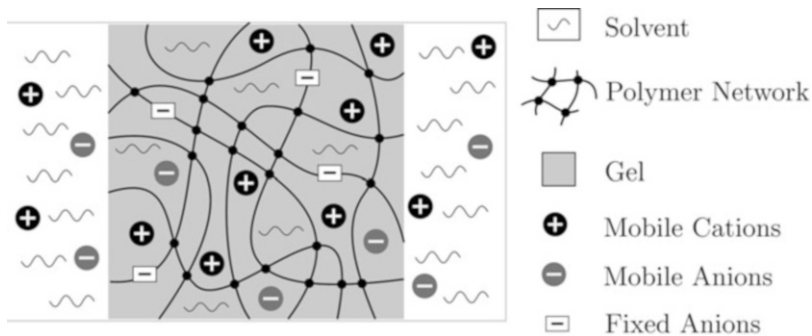


Fig. 1 Polymer gel in a solution bath

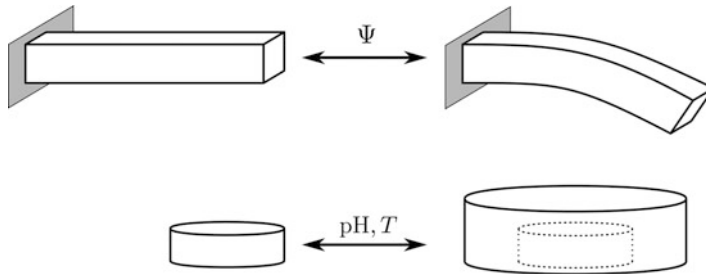


Fig. 2 Deformation of a polyelectrolyte gel probe under electrical (*top*), chemical, or thermal stimulation (*bottom*)

3 Literature Review

A brief review is given on modeling approaches for ionic EAPs. Specifically, numerical models considering chemical, electrical, and mechanical stimuli are subject of matter. The literature review is given in a chronological order.

In the 1940s, Flory and Rehner (1943a, b) formulated the swelling behavior of polymer networks based on a thermodynamic approach. This theory can be applied to EAPs by adapting the respective contributions to the Gibbs free energy with statistically identified relations. From the equilibrium condition, the swelling behavior can be derived. Based on the equation of motion, Tanaka and Fillmore (1979) described the swelling kinetics. These two fundamental theories have been developed further to investigate the polymer swelling behavior on a macroscopic scale.

Various experimental investigations have been carried to comprise them with statistical models. For chemically induced swelling, the works of Ohmine and Tanaka (1982), Umemoto et al. (1991), and English et al. (1996) shall be mentioned.

For electrically induced gel swelling, experimental data have been published by Hamlen et al. (1965), Tanaka et al. (1982), Shiga and Kurauchi (1990), and Hirai et al. (1995).

Experimental investigations and analytical equilibrium swelling investigations of hydrogels in aqueous solutions based on thermodynamics have been published by Orlov et al. (2006, 2007) and Ermatchkov et al. (2010).

The recent work of Hong et al. (2009) applies the statistical theory in the regime of Finite Elements to investigate swelling-induced deformation, contact, and bifurcation of gels. This approach was extended by Lucantonio et al. (2013) determining the transient behavior in a continuum mechanical approach.

The macroscopic theory is not directly applicable to electrical stimulation. An approach to incorporate this type of stimulation is given by Rička and Tanaka (1984) and Gülch et al. (2000) describing the swelling of a weakly charged ionic gel as a function of the ionic composition of the solvent. Further theoretical works have been published by Shiga and Kurauchi (1990), Doi et al. (1992), and Shahinpoor (1994). Brock et al. (1994) presented a dynamic model of a linear hydrogel actuator.

To achieve a more precise understanding of the swelling behavior of EAPs, multiple models incorporating microscale properties have been developed by many authors. These so-called mesoscale models are based on the principles of modern continuum mechanics. In the present review, modeling approaches based on porous media, mass transport, as well as an interfacial model are considered.

The continuum mechanical framework by Gurtin and Voorhees (1993) is based on the assumption of a volume phase transition triggered by the motion of evolving interfaces. This sharp interface is separating the swollen and collapsed phases of the underlying polymer network and its dynamics are driven by mass transport and mechanical stress. A numerical strategy to obtain approximate solutions to the stated nonlinear evolution equations is published for chemical sensitive hydrogels by Dolbow et al. (2005) and in a subsequent article for temperature sensitive hydrogels by Dolbow et al. (2006).

Another approach considering the interaction of an EAP in a surrounding solution is a formulation based on accounting several superposing fields.

Grimshaw et al. (1990) have presented a coupled formulation for chemically and electrically induced swelling in polyelectrolyte gels and de Gennes et al. (2000) described the mechanoelectric effects in ionic gels. Tamagawa and Taya (2000) and Li et al. (2007) investigated the ion distribution and the ion transport by applying a chemoelectric model. De and Aluru (2004) proposed a chemo-electro-mechanical model for the simulation of pH-sensitive hydrogel while using a multiphysical modeling approach. Li and Lai (2011) simulated ionic-strength-sensitive hydrogels by a multi-effect coupling model. Wallmersperger et al. (2004, 2008) as well as Ballhause and Wallmersperger (2008) have published electrochemical and chemo-electro-mechanical formulations for ionic gels under chemical and electrical stimulation. Temperature-sensitive polyelectrolyte gels have been investigated by Keller et al. (2011). A fully coupled chemo-electro-mechanical multifield formulation was published by Wallmersperger et al. (2013).

By treating the constituents of EAPs separately, their interactions can be considered and hence a numerical model on a smaller scale is derivable. Based on the Theory of Mixtures which was first described by Bowen (1976) and the concept of volume fractions, the Theory of Porous Media can be derived. Like other continuum mechanical models, the porous media theory requires constitutive relations; particularly the interactions of the constituents have to be considered. The Theory of Porous Media was essentially enhanced by Bowen (1980), by Mow et al. (1980), in which theoretical and experimental results can be found, and by de Boer (2000). Frijns et al. (1997), Sun et al. (1999), and van Loon et al. (2003) presented a triphasic and quadriphasic mixture theory for the simulation of hydrated tissues. For ionic gels, a modeling approach was presented by Ehlers (2002) and by Acartürk (2009). A more general approach for a multiple-component, multiple-phase, polarizable, swelling porous medium with charged particles is given by Bennethum and Cushman (2002a). An examination of the electric potential inside charged, soft, hydrated tissues was given by Lai et al. (2000).

A special themed issue on responsive gels was edited by Sadowski (2011).

On the atomistic scale, the conformation change of hydrogels in water has been studied by Walter et al. (2010). An overview over modeling on different scales has been given in Wallmersperger et al. (2008b). Deformation mechanisms as well as tracer diffusion in hydrogels by molecular dynamic simulations were published by Tabatabaei et al. (2011) and Weeber et al. (2012). Nonlinear effects in hydrogel-based chemical sensors were investigated by Guenther et al. (2009).

In 2011, a review article on gel-swelling theories was published by Quesada-Perez et al. (2011).

4 Modeling on Different Scales

For the modeling of polymer gels it is important to distinguish: (i) if only the macroscopic swelling or bending is of interest, (ii) if the mesoscopic transport phenomena will be investigated, or (iii) if the microscopic ion-ion or ion-polymer interaction should be considered, see Fig. 3.

Generally, the computational effort increases when going from the macroscale over the mesoscale up to the microscale. If real sensor or actuator applications are of interest, in most cases mesoscopic or macroscopic modeling is predestined. In order to understand the physicochemical mechanisms underlying the conversion, i.e., the mechanical deformation, the theoretical and experimental facts behind the swelling process have to be investigated.

By presenting models on different scales, we want to shed more light on the local and global swelling behavior of polymer gels under various kinds of stimulation. Therefore, the present chapter is structured as follows:

In Sect. 5, the statistical theory, a macroscopic model, is explained. In Sect. 6 two different mesoscopic models are presented: first, the chemo-electro-mechanical transport model (Sect. 6.1), then a continuum model based on porous media (Sect. 6.2) are described in detail.

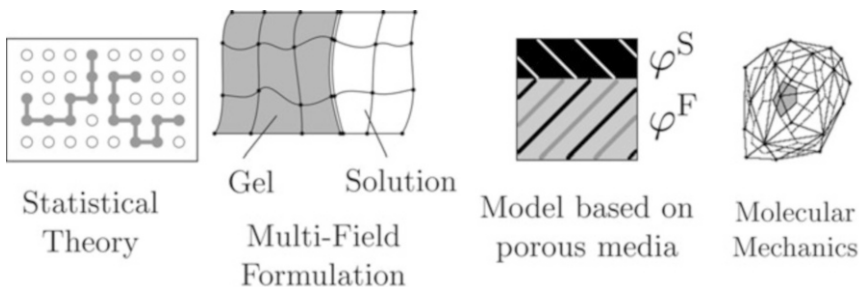


Fig. 3 Modeling on different scales

Microscopic models such as the discrete element theory or investigations by molecular dynamics are not further discussed in the present chapter.

5 Macroscopic Models

5.1 Statistical Theory

In the 1940s, Flory and Rehner (Flory and Rehner 1943a, b; Flory 1953) were the first to formulate a theory of “swelling of network structures.” Within this theory, the change of ambient conditions (i.e., change in the solution surrounding the gel) can be represented by a change of the Gibb’s free energy ΔF . Please note that this theory is just an equilibrium theory and does not give any time behavior leading from one state to another.

The total energy F in the respective domain (gel or solution) is the sum of the:

- Free energy of mixing ΔF_M
- Free energy of elastic deformation ΔF_{el}
- Free energy depending on ion concentrations ΔF_{ion} (see, e.g., Rička and Tanaka (1984), Schröder and Oppermann (1996))

The equilibrium state is characterized by a minimum of the total free energy. This means that the chemical potentials μ_1 of the solvent in the gel phase (g) and in the surrounding solution phase (s) are identical:

$$\Delta\mu_1 = \mu_1^{(g)} - \mu_1^{(s)} = 0 \quad (1)$$

$$\begin{aligned} \Delta\mu_1 &= \left(\frac{\partial \Delta F_M}{\partial n_1} \right)_{p,T} + \left(\frac{\partial \Delta F_{el}}{\partial n_1} \right)_{p,T} + \left(\frac{\partial \Delta F_{ion}}{\partial n_1} \right)_{p,T} \\ &= \underbrace{\Delta\mu_{1,M}}_{\text{mixture potential}} + \underbrace{\Delta\mu_{1,el}}_{\text{elastic potential}} + \underbrace{\Delta\mu_{1,ion}}_{\text{ion potential}} = 0 \end{aligned} \quad (2)$$

where n_1 is the molar number of the solvent.

In the dry state of the polymer gel, polymer matrix and solvent are completely separated.

In the swollen state, the solvent has diffused into the gel phase, i.e., the gel phase now consists of both polymer and solvent.

5.1.1 Mixture Potential

The mixture potential $\Delta\mu_{1,M}$ reads (Flory 1953)

$$\Delta\mu_{1,M} = RT \left(\ln(1 - \phi_p) + \phi_p + \chi\phi_p^2 \right) \quad (3)$$

where ϕ_p is the volume fraction of the polymer in the gel phase, χ is the Flory-Huggins gel-solution interaction parameter, $R = 8.3143 \text{ J (mol K)}^{-1}$ is the universal gas constant, and T the temperature. The total swelling ratio $q = \frac{V}{V_0} = \frac{1}{\phi_p}$ is given by the product of the initial q_0 and the relative swelling q_r according to the reference state. V is the actual volume and V_0 the initial volume in dry state.

5.1.2 Elastic Potential

The elastic deformation of the polymer network consists of two successive processes: (i) expansion due to free swelling then (ii) deformation under constant volume while keeping the enthalpy of the system constant.

The free energy resulting from the elastic deformation can be given as (Flory 1943b)

$$\Delta F_{\text{el}} = \frac{1}{2} RT v_e \left[\lambda_x^2 + \lambda_y^2 + \lambda_z^2 - 3 - \ln(\lambda_x \lambda_y \lambda_z) \right] \quad (4)$$

where v_e is the effective number of moles of polymer chains in the gel and $\lambda_i = 1 + \varepsilon_i$ is the swelling (stretch) in i -direction. For isotropic swelling, i.e., $\lambda_s = \lambda_x = \lambda_y = \lambda_z$ with $\lambda_s^3 = q = \frac{V}{V_0} = \frac{1}{\phi_p}$, we obtain

$$\Delta F_{\text{el}} = \frac{1}{2} RT v_e \left[3 \lambda_s^2 - 3 - \ln(\lambda_s^3) \right]. \quad (5)$$

By inserting Eq. 5 in the second term of Eq. 2, the elastic potential may be given as

$$\Delta \mu_{1,\text{el}} = v_1 RT \frac{v_e}{V_0} \left(\phi_p^{\frac{1}{3}} - \frac{1}{2} \phi_p \right) \quad (6)$$

where v_1 is the molar volume of the solvent.

A similar expression for the Gaussian elastic potential was given by Schröder (1994):

$$\Delta \mu_{1,\text{el}} = \nu^* RT v_1 \eta A q_0^{-1} q_r^{-\frac{1}{3}} \quad (7)$$

where ν^* is the number in (mole) of elastically effective network chains per unit dry volume, A the structural factor, and η the dilatation factor (Schröder 1994, Schröder and Oppermann 1996).

The chemical potential related to elastic deformation according to the non-Gaussian theory can be given as (Schröder 1994)

$$\Delta \mu_{1,\text{el}} = \nu^* RT v_1 \eta A q_0^{-1} q_r^{-2/3} n^{1/2} \mathcal{L}^{-1} \left(\frac{q_r^{1/3}}{n^{1/2}} \right) \quad (8)$$

where \mathcal{L} is the Langevin function and n is the number of static segments per chain. For more details refer, e.g., to Treloar (1958).

For the investigation of a directional swelling, assuming identical elongations in y - and z -direction, Lee (1996) has derived a formulation for the free energy.

5.1.3 Mobile Ion Potential

The mobile ion potential results from the differences in the charge density between (solvent in the) gel and ambient solution. An increase of the mobile concentrations in the solution bath leads to a reduction of the concentration differences between gel and solution and thus to a decrease of the swelling.

The chemical potential μ_α of a species α is formulated by

$$\Delta\mu_\alpha = \mu_\alpha^0 + RT \ln(\bar{a}_\alpha) = \mu_\alpha^0 + RT \ln(\bar{c}_\alpha) + RT \ln(f_\alpha) \quad (9)$$

where μ_α^0 is the reference potential or zero-potential, a_α is the activity, and c_α the concentration of the species. The activity of the species α is defined by $a_\alpha = f_\alpha c_\alpha$ where f_α is the activity coefficient of the species α . Please note that the activities and the concentrations in Eq. 9 are given in a dimensionless form: $\bar{a}_\alpha = \frac{a_\alpha}{1 \text{ mol m}^{-3}}$ and $\bar{c}_\alpha = \frac{c_\alpha}{1 \text{ mol m}^{-3}}$. The activity coefficient is always equal to or lower than one. For diluted solutions, the activity coefficient is nearly one (as in ideal solutions); thus in the following, the activity coefficient will be set to $f_\alpha = 1$ for all species α . From this, the chemical potential is obtained to

$$\Delta\mu_\alpha = \mu_\alpha^0 + RT \ln(\bar{c}_\alpha). \quad (10)$$

Another formulation of the chemical (mobile ion) potential is given in Flory (1953) by

$$\Delta\mu_1 = \mu_1^0 + g RT \ln(\chi_1^*) \quad (11)$$

where g is the osmotic coefficient and χ_1^* is the mole fraction of the solvent in the solution or gel phase.

For diluted solution we obtain

$$\mu_1^{(g)} = \mu_1^0 - RTv_1 \sum_\alpha c_\alpha^{(g)} \quad (\text{gel phase}) \quad (12a)$$

$$\mu_1^{(s)} = \mu_1^0 - RTv_1 \sum_\alpha c_\alpha^{(s)} \quad (\text{solution phase}) \quad (12b)$$

for the chemical potential in the gel phase $\mu_1^{(g)}$ and in the solution phase $\mu_1^{(s)}$. The chemical potential due to differences of the charge density in both phases reads

$$\Delta\mu_{1,\text{ion}} = \mu_1^{(g)} - \mu_1^{(s)} = -RTv_1 \sum_\alpha (c_\alpha^{(g)} - c_\alpha^{(s)}) \quad (13)$$

Additionally, the distribution of the ions of the different species has to fulfill the electroneutrality condition in both phases (gel and solution):

$$\sum_{\alpha}^{N_f+N_b} (c_{\alpha}^{(g)} - c_{\alpha}^{(s)}) = 0 \quad (14)$$

where N_f is the number of mobile species and N_b the number of bound species.

5.1.4 Electrochemical Potential

The electrochemical potential μ_{α}^* for one species α consisting of the chemical potential and the electrical potential reads

$$\mu_{\alpha}^* = \underbrace{\mu_{\alpha}}_{\text{chemical potential}} + \underbrace{z_{\alpha} F \Psi}_{\text{electrical potential}} = \mu_{\alpha}^0 + RT \ln(\bar{a}_{\alpha}) + z_{\alpha} F \Psi \quad (15)$$

where z_{α} is the valence of the species α , Ψ is the electric potential, and F the Faraday constant. If we consider the condition of identical electrochemical potential in the whole domain, i.e., in the gel and the solution (Hamann and Vielstich 1998), we obtain

$$\mu_{\alpha}^{(g)} + z_{\alpha} F \Psi^{(g)} = \mu_{\alpha}^{(s)} + z_{\alpha} F \Psi^{(s)} \quad (16a)$$

$$RT \ln\left(\frac{\bar{c}_{\alpha}^{(g)}}{\bar{c}_{\alpha}^{(s)}}\right) + z_{\alpha} F \Psi^{(g)} = RT \ln\left(\frac{\bar{c}_{\alpha}^{(s)}}{\bar{c}_{\alpha}^{(s)}}\right) + z_{\alpha} F \Psi^{(s)} \quad (16b)$$

for all species α . Assuming identical activity coefficients, we obtain the Donnan equation

$$\frac{c_{\alpha}^{(g)}}{c_{\alpha}^{(s)}} = \exp\left(-z_{\alpha} \frac{F}{RT} (\Psi^{(g)} - \Psi^{(s)})\right) \quad (17)$$

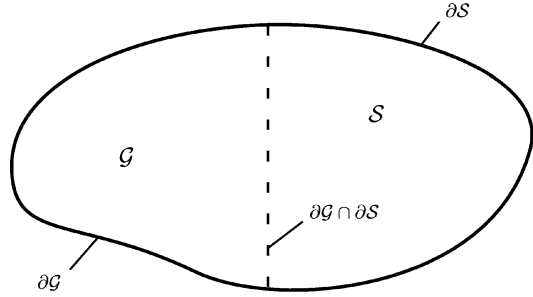
in which the ratio of the ion concentrations inside and outside the gel (at the gel-solution interface) is given.

6 Mesoscopic Models

6.1 Chemo-Electro-Mechanical Transport Model

For modeling the transport within both the gel and the surrounding solution, in this section, a continuum chemo-electro-mechanical formulation is presented. For this formulation, (i) the balance laws of the different constituents, i.e., polymer, solution, mobile, and bound charges; (ii) the kinematics; as well as (iii) the materials laws have to be considered.

Fig. 4 Decomposition of the whole domain \mathcal{P} into the hydrogel \mathcal{G} and the solution domain \mathcal{S}



6.1.1 General Definitions

A hydrogel placed in a solution bath is considered. The whole gel-solution domain \mathcal{P} is decomposed into a hydrogel domain \mathcal{G} and a solution domain \mathcal{S} . The hydrogel domain \mathcal{G} is enclosed by a surface $\partial\mathcal{G}$ and the solution domain \mathcal{S} is enclosed by a surface $\partial\mathcal{S}$, see Fig. 4.

In the present research, the problem is formulated in a Cartesian coordinate system. For this, the index notation is used. The Einstein summation convention, i.e., the summation over identical indices within a term is performed. The spatial derivative $u_{i,j}$ of the displacement vector \mathbf{u} –

$$\mathbf{u} = \sum_i (u_i \mathbf{e}_i) = u_i \mathbf{e}_i \quad (18)$$

where \mathbf{e}_i are the unit vectors in x_i -direction and u_i are the coordinates in x_i -direction – is given as follows:

$$u_{i,j} = \frac{\partial u_i}{\partial x_j}; \quad i = 1, 2, 3 \quad \text{and} \quad j = 1, 2, 3. \quad (19)$$

In Sect. 6.1, the following definitions are made:

- The species α comprise mobile anions, mobile cations, and bound charges (anions (A⁻) and cations (K⁺)).
- The species β only comprise the mobile charges: anions (–) and cations (+).
- The species γ only comprise the bound charges.

6.1.2 Kinematics

It is necessary to specify the configuration of the polymer gel in the domain at each instance of time. In general, the initial or reference configuration at $t = 0$ is – in many cases – different to the other configurations at $t > 0$ which are called the current or deformed configurations.

Since the formulation given in the present chapter is based on the assumption of infinitesimal displacements, the distinction between the current and the initial

configurations can be neglected. Thus, the deformation gradients are quite small and the strain $\boldsymbol{\varepsilon}$ of the polymer gel may be given by

$$\varepsilon_{ij} = \frac{1}{2} (u_{i,j} + u_{j,i}). \quad (20)$$

6.1.3 Balance Laws

In this section, the balance laws for the different involved fields are given:

Electrical Field

The electrical field is described by the Maxwell equations of electrostatics in both the gel domain \mathcal{G} and the solution domain \mathcal{S} , i.e., in the complete domain \mathcal{P} by

$$D_{i,i} = \rho_e \quad \text{in } \mathcal{P} \quad \text{and} \quad (21a)$$

$$\epsilon_{ijk} E_k, \quad j = 0 \quad \text{in } \mathcal{P} \quad (21b)$$

where \mathbf{D} is the dielectric displacement vector, \mathbf{E} the electric field vector, and ϵ the permutation tensor. ρ_e is the charge density given by

$$\rho_e = F \sum_{\alpha}^{N_f + N_b} (z^{\alpha} c^{\alpha}) \quad \text{in } \mathcal{P} \quad (22)$$

where F is the Faraday constant, z^{α} the valence of the α -th ionic species, c^{α} the concentration of the α -th species, N_f the number of mobile species, and N_b the number of bound species; for more details, please refer to Wallmersperger et al. (2013).

The electric potential Ψ is related to the electric field vector \mathbf{E} by

$$E_i = -\Psi,_{i} \quad \text{in } \mathcal{P} \quad (23)$$

Chemo-Physical Field

The governing equations for the chemophysical field may be obtained by formulating the local balance relation of mass for each species α .

The governing equation for the mobile ions β may be given by

$$\frac{\partial c^{\beta}}{\partial t} = \left(D^{\beta} c^{\beta},_i + z^{\beta} c^{\beta} \mu^{\beta} \Psi_i \right),_i + c^{\beta} v_{i,i} \quad \text{in } \mathcal{P} \quad (24)$$

where c^{β} is the concentration of the β -th mobile species, D^{β} is the diffusion coefficient of the β -th species, and $\mu^{\beta} = \frac{F}{RT} D^{\beta}$ is their mobility. R is the universal gas constant, T the temperature, and \mathbf{v} the velocity of the fluid containing the species β .

The governing equation for the bound charges results from the conservation of bound charges (in the gel)

$$c^\gamma = c_0^\gamma(1 - \varepsilon_{ii}) \quad \text{in } \mathcal{G} \quad (25)$$

where c^γ is the concentration of the γ -th bound species and c_0^γ is the initial concentration of the γ -th species.

Additionally to the mobile and bound concentrations, also equations for the reference concentrations for each mobile species have to be given in order to capture not only chemical but also electrical stimulation. The governing equations for the reference concentrations $c^{\beta\text{ref}}$ may be given by

$$\left(D^{\beta\text{ref}} c_{,i}^{\beta\text{ref}} \right)_{,i} = 0 \quad \text{in } \mathcal{G}. \quad (26)$$

As can be seen, this equation results from Eq. 24 by setting the convection and migration terms as well as the time derivative of the concentration equal to zero.

Mechanical Field

After considering the balance of mass, the balance of momentum

$$\rho \dot{v}_i - \sigma_{ji,j} = \rho b_i \quad \text{in } \mathcal{G} \quad (27)$$

with the material time derivative of the velocity \mathbf{v} defined by

$$\dot{v}_j = \frac{Dv_j}{Dt} = \frac{\partial v_j}{\partial t} + \frac{\partial v_j}{\partial x_k} \frac{\partial x_k}{\partial t} = \frac{\partial v_j}{\partial t} + v_{j,k} v_k \quad (28)$$

for the whole gel also has to be fulfilled.

The variable \mathbf{b} is the vector of body forces, ρ is the mass density, and $\boldsymbol{\sigma}$ is the stress tensor acting on \mathcal{G} .

In absence of body forces and by neglecting the inertial terms, the balance of momentum can be simplified to

$$\sigma_{ji,j} = 0 \quad \text{in } \mathcal{G} \quad (29)$$

The balance of angular momentum (by neglecting any distributed moment loads) results in the symmetry of the stress tensor, i.e.,

$$\sigma_{ji} = \sigma_{ij} \quad \text{in } \mathcal{G}. \quad (30)$$

Osmotic Pressure

The osmotic pressure difference $\Delta\pi$ between gel and solution resulting from the concentrations of the mobile ions in the different regions may be calculated by (Wallmersperger and Ballhause 2008; Wallmersperger et al. 2013)

$$\Delta\pi = -RT \sum_{\beta=1}^{N_r} (\Delta c^\beta - \Delta c_0^\beta) \quad (\text{in } \mathcal{G}) \quad (31)$$

where $\Delta c^\beta = (c^\beta - c^{\beta\text{ref}})$ and $\Delta c_0^\beta = (c_0^\beta - c_0^{\beta\text{ref}})$. Please note that the initial concentrations are marked by the index “0.” The distribution of the reference concentrations in space $c^{\beta\text{ref}}$ of the mobile species β can be obtained from Eq. 26.

6.1.4 Constitutive Laws

By incorporating the constitutive laws into the balance equations, a complete set of governing equations is derived.

For the electric field, a constitutive equation – assuming a linear relation between the electric field \mathbf{E} and the dielectric displacement \mathbf{D} – may be given by

$$D_i = \varepsilon_0 \varepsilon_r E_i \quad (32)$$

where ε_0 is the vacuum permittivity and ε_r the relative permittivity. Combining Eqs. 21a, 22, 23, and 32 results in

$$\Psi_{,ii} = -\frac{F}{\varepsilon_0 \varepsilon_r} \sum_{\alpha=1}^{N_r+N_b} (z^\alpha c^\alpha) \quad \text{in } \mathcal{P} \quad (33)$$

Please keep in mind that for the chemical field, the constitutive relations between the electrochemical potential and the fluxes already have been incorporated in the balance equation in order to obtain Eq. 24.

For the mechanical constitutive law, a linear elastic behavior of the gel is assumed – which is true for small deformations as it normally occurs, e.g., under electrical stimulation. In this case, the relationship is expressed by the generalized Hooke’s law

$$\sigma_{ij} = C_{ijkl} \varepsilon_{kl}^e \quad (34)$$

where \mathbf{C} is the elasticity tensor and $\boldsymbol{\varepsilon}^e$ is the elastic strain.

The total strain $\boldsymbol{\varepsilon}$ is the sum of the elastic strain $\boldsymbol{\varepsilon}^e$ and the swelling strain $\boldsymbol{\varepsilon}^\pi$:

$$\varepsilon_{kl} = \varepsilon_{kl}^e + \varepsilon_{kl}^\pi \quad (35)$$

By defining the swelling strain $\boldsymbol{\varepsilon}^\pi$ by

$$\varepsilon_{kl}^\pi = \Delta\pi \tilde{g}_{kl} = \Delta\pi g \delta_{kl} \quad (36)$$

where \tilde{g} is the tensor of the swelling coefficients, g is a general swelling coefficient, and $\boldsymbol{\delta}$ is the Kronecker delta, Eq. 34 results in

$$\sigma_{ij} = C_{ijkl} \varepsilon_{kl}^e = C_{ijkl} (\varepsilon_{kl} - \varepsilon_{kl}^\pi) = C_{ijkl} (\varepsilon_{kl} - \Delta\pi g \delta_{kl}). \quad (37)$$

In the case of an isotropic material behavior, the elasticity tensor is given by (Hahn 1985)

$$C_{ijkl} = \frac{E}{2(1+\nu)} \left[\delta_{ik} \delta_{jl} + \delta_{il} \delta_{jk} + \frac{2\nu}{1-2\nu} \delta_{ij} \delta_{kl} \right] \quad (38)$$

where E is the Young's modulus and ν the Poisson ratio.

6.1.5 Boundary Conditions, Initial Conditions, and Transition Conditions

Additionally to the governing equations, also boundary conditions, initial conditions, and transition conditions for the different fields have to be incorporated.

For the chemical field,

- Boundary conditions for the normal fluxes, for the concentrations, and for the electrochemical potential
- Initial conditions for the mobile and bound charges as well as
- Transition conditions for the normal fluxes and the electrochemical potential at the gel-solution interface have to be given.

For the electrical field,

- Boundary conditions for the electric potential and the normal component of the dielectric displacement as well as
- Transition conditions for the same variables have to be given.

For the mechanical field,

- Boundary conditions for the displacements and the stresses have to be given.

6.1.6 Discretization

The resulting initial-boundary value problem is a fully coupled chemo-electro-mechanical formulation. This problem may be solved by a numerical method, e.g., by the Finite Element Method, the Finite Difference Method, or a combined method. For more details, see, e.g., Wallmersperger and Ballhause (2008).

6.1.7 Numerical Example

In the present section, the behavior of a hydrogel strip in a solution bath with applied electric field is investigated. As discussed in Sect. 2, the application of an electric field results in local variations of the concentrations at the gel-solution interface in both gel and solution phase. Due to the higher conductivity corresponding to the larger number of mobile ions in the gel than in the solution, the increase of the electric potential – from the cathode to the anode side – in the gel is smaller than in the solution. The smaller increase of the electric potential in the gel is compensated

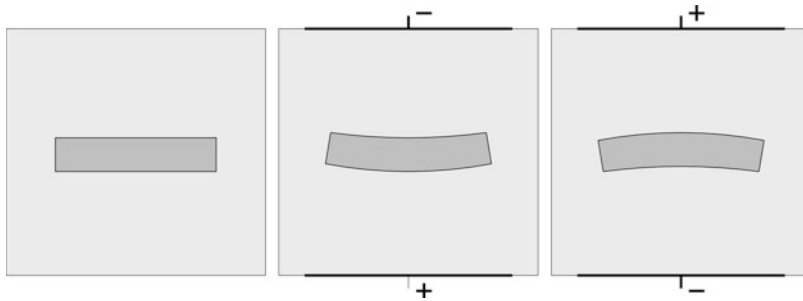


Fig. 5 Schematic bending of an anionic hydrogel under the influence of an electric field

by a smaller “jump” at the cathode side and a larger one at the anode side of the gel. This corresponds to a smaller osmotic pressure difference at the cathode side and a larger one at the anode side of the gel.

The larger differences of the electric potential (hyperpolarization) and the larger osmotic pressure difference at the anode side as well as the depolarization at the cathode side of the gel are responsible for locally different swelling ratios: an additional swelling on the anode-side and a slight deswelling on the cathode side for anionic gels, leading to the bending of the gel strip in an external electric field, see Fig. 5.

6.2 Theory Based on Porous Media

6.2.1 Introduction

The Theory of Porous Media (TPM) is a concept based on the fundamentals of classical continuum mechanics and thermodynamics. It is used in numerous fields of research to model the behavior of saturated porous solid materials. The fluid-structure interaction within the material is incorporated by a statistical homogenization of a representative elementary volume. Hence, no knowledge of the geometry and the structure of the interfering components is required; the investigated domain has to be rather large and it has to comprise a sufficiently homogenous substructure.

6.2.2 Theory of Mixtures

The constituents exhibit differing material properties. Superimposing the constituents and considering the mechanical interaction of internal interfaces is known as the theory of mixtures. The mixture is quantified by the local volume fraction φ^α of each constituent α . In the deformed configuration it is defined by

$$\varphi^\alpha = \frac{dv^\alpha}{dv} \quad (39)$$

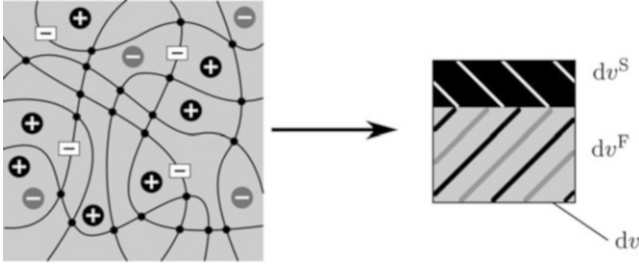


Fig. 6 Constituents incorporated in the polymer gel. The solid phase is denoted by “S” and the fluid phase by “F”

where dv^α denotes the partial volume of the constituent in the substantial volume element dv . As shown in Fig. 6, the considered constituents of the solid phase (S) are the polymer network and fixed charges; the fluid phase (F) incorporates the liquid (L) and the mobile anions and cations.

The incorporated constituents are denoted by α as follows:

$$\alpha = \{S, \underbrace{L, \gamma}_{\text{fluid F}}\}, \quad \text{where } \gamma = \{+, -\}.$$

The volume of the mixture is then defined as

$$v = \sum_{\alpha} v^{\alpha} = \sum_{\alpha} \int_{\Omega} dv^{\alpha}. \quad (40)$$

If the mixture is fully saturated, the saturation condition

$$\sum_{\alpha} \varphi^{\alpha} = 1 \quad (41)$$

can be incorporated. Having defined the partial volume of each constituent, several measures for the density can be defined. The real density $\varrho^{\alpha R}$ of the constituent is given by

$$\varrho^{\alpha R} = \frac{dm^{\alpha}}{dv^{\alpha}} \quad (42)$$

whereas the partial density ϱ^{α} is defined by

$$\varrho^{\alpha} = \frac{dm^{\alpha}}{dv} \quad (43)$$

where m^{α} is the mass of the constituent α .

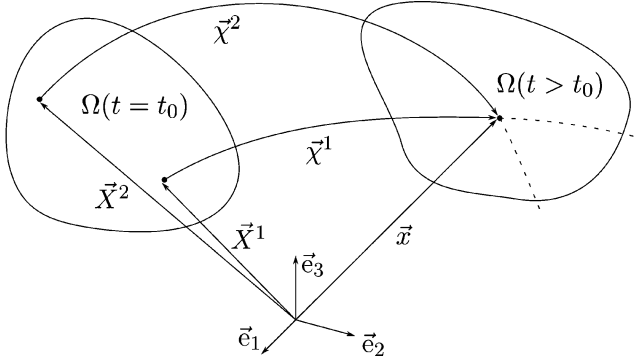


Fig. 7 Kinematics for a multiphasic continuum

6.2.3 Kinematics

Observing the continuum in the deformed state, one can find that the constituents defining the current configuration originate from differing positions in the reference configuration. Therefore

$$x_i = \chi_i^\alpha(X_i^\alpha, t) \quad (44)$$

holds as shown in Fig. 7, where χ^α is the motion function of the constituent α .

Naturally the time derivative of the motion can be found with respect to the considered constituent. For the velocity, one can find in Lagrangian form

$$v_i^\alpha = \frac{\partial}{\partial t} \chi_i^\alpha(X_i^\alpha, t) \quad (45)$$

and subsequently the acceleration can be obtained by

$$a_i^\alpha = \frac{\partial^2}{\partial t^2} \chi_i^\alpha(X_i^\alpha, t). \quad (46)$$

For a vector field function ψ , the material time derivative is defined by

$$(\dot{\psi}_i)^\alpha = \frac{D}{Dt} \psi_i = \frac{\partial}{\partial t} \psi_i + \psi_{i,k} v_k^\alpha. \quad (47)$$

A similar expression applies for a scalar valued function.

6.2.4 Balance Equations

Following the principles of continuum mechanics, the balance relations of mechanics and electrodynamics are presented. They follow general principles or the laws of nature. Based on the principles by Truesdell and Noll (2003), the balance equations

are given separately for each constituent. The mechanical interactions of the inner interfaces have to be considered in the production terms.

For the mechanical field, the balance equations balance of mass, balance of momentum, and balance of angular momentum are given in the differential form for a fixed reference system.

The balance of mass is given by

$$(\hat{\rho}^\alpha)^\alpha + \varrho^\alpha v_{k,k}^\alpha = \hat{\varrho}^\alpha \quad (48)$$

and the balance of momentum and balance of angular momentum are given by

$$\sigma_{kl,k}^\alpha + \varrho^\alpha (b_l^\alpha - a_l^\alpha) = -\hat{p}_l^\alpha \quad (49)$$

$$\epsilon_{kmn} \sigma_{mn}^\alpha = \hat{m}_k^\alpha. \quad (50)$$

The direct production densities for the mass, momentum, and angular momentum are denoted by $\hat{\varrho}^\alpha$, \hat{p}^α , and \hat{m}^α , respectively. The Cauchy stress tensor is given by σ^α and body forces are considered by b^α .

To investigate the thermo-mechanical interactions, the laws of thermodynamics are applied. The first law of thermodynamics can be considered as a balance equation with the internal energy density u^α and the heat fluxes q^α and r^α due to close-range and long-range effects, respectively. Considering the direct energy production density \hat{e}^α , one can obtain

$$\varrho^\alpha (u^\alpha)^\alpha - \sigma_{kl}^\alpha v_{l,k}^\alpha + q_{k,k}^\alpha - \varrho^\alpha r^\alpha = \hat{e}^\alpha. \quad (51)$$

Considering the second law of thermodynamics, restrictions of the constitutive equations can be derived in the framework of allowable thermodynamic processes. The second law of thermodynamics

$$\varrho^\alpha (\eta^\alpha)^\alpha - \phi_{k,k}^\alpha - \zeta^\alpha = \hat{\xi}^\alpha \quad (52)$$

is given by considering the entropy density η^α , the entropy flux density ϕ^α , the external entropy supply density ζ^α , and the entropy production density $\hat{\xi}^\alpha$.

The direct production densities in Eqs. 48, 49, 50, 51, and 52 can be split into a total and into an indirect part. In detail, for the direct production densities, one can obtain

$$\hat{p}_l^\alpha = \hat{s}_l^\alpha - \hat{\varrho}^\alpha v_l^\alpha \quad (53a)$$

$$\hat{m}_k^\alpha = \hat{h}_k^\alpha - \epsilon_{klm} \chi_l^0 s_m^\alpha \quad (53b)$$

$$\hat{e}^\alpha = \hat{u}^\alpha - \hat{p}_l^\alpha v_l^\alpha - \hat{\varrho}^\alpha \left(u^\alpha + \frac{1}{2} v_l^\alpha v_l^\alpha \right) \quad (53c)$$

$$\hat{\xi}^\alpha = \hat{\eta}^\alpha - \hat{\varrho}^\alpha \eta^\alpha, \quad (53d)$$

where \hat{s}^α , \hat{h}^α , \hat{u}^α , and $\hat{\eta}^\alpha$ are the total production densities of the respective balance equations.

For the mixture, one can obtain the balance equations by summing up over every constituent. Then the well-known forms of the classic one-phasic continuum mechanics can be obtained and consequently the total production density terms have to vanish. Therefore

$$\sum_{\alpha} \hat{q}^\alpha = 0, \quad \sum_{\alpha} \hat{s}_l^\alpha = 0, \quad \sum_{\alpha} \hat{h}_k^\alpha = 0, \quad \sum_{\alpha} \hat{u}^\alpha = 0 \quad (54)$$

holds. For the mixture, the second law of thermodynamics leads to the inequality

$$\sum_{\alpha} \hat{\eta}^\alpha \geq 0 \quad (55)$$

which states that the entropy production of the whole structure has to be zero or positive at any time.

The four Maxwell equations describe the electro-magneto-dynamical behavior. They are given for a fixed reference system as follows (Eringen and Maugin 1990):

$$\text{Gau\ss}'\text{s law} \quad D_{k,k} = \rho_e \quad (56)$$

$$\text{Gau\ss}'\text{s law for magnetism} \quad B_{k,k} = 0 \quad (57)$$

$$\text{Faraday's law} \quad \epsilon_{klm} E_{m,l} = -\frac{1}{c} \frac{\partial B_k}{\partial t} \quad (58)$$

$$\text{Amp\`ere's law} \quad \epsilon_{klm} H_{m,l} = \frac{1}{c} J_k + \frac{1}{c} \frac{\partial D_k}{\partial t} \quad (59)$$

The electric and magnetic fields are denoted by \mathbf{E} and \mathbf{B} , and the dielectric displacement and the magnetizing field are denoted by \mathbf{D} and \mathbf{H} , respectively. The electric charge density is given by ρ_e . The electric current density is denoted by \mathbf{J} and the speed of light by c .

The macroscopic material behavior for the electric field is generally defined by

$$D_k = \epsilon_0 E_k + P_k \quad (60)$$

where \mathbf{P} is the electric polarization vector of the material and ϵ_0 the vacuum permittivity of the electric field. An explanation for deviating polarizations of the constituents based on statistical assumptions is given in Bennethum and Cushman (2002b). However, it is assumed that the same (homogenized) electro-magnetic field applies to all of the constituents and therefore only the balance equations of the mixture have to be considered. The electric polarization is then given by

$$P_k = \varepsilon_0 \chi_e E_k \quad (61)$$

with the material dependent electric susceptibility χ_e . Then the constitutive relation between the electric field and the dielectric displacement can be obtained by

$$\begin{aligned} D_k &= \varepsilon_0(1 + \chi_e)E_k \\ &= \varepsilon_0 \varepsilon_r E_k \end{aligned} \quad (62)$$

where ε_r is the relative permittivity.

Investigating the chemo-electro-mechanical behavior of EAPs, one can consider that due to the diffusion dominated processes the time derivatives in Eqs. 52 and 53a can be set to zero. In the absence of an externally applied magnetic field, the Maxwell equations simplify to a set of equations for the electrostatic case and

$$\varepsilon_0 \varepsilon_r E_{k,k} = \rho_e \quad (63)$$

$$\epsilon_{klm} E_{m,l} = 0 \quad (64)$$

applies.

6.2.5 Remarks

The presented framework gives a general overview for a continuum-based modeling concept. It does not contain constitutive relations representing the chemo-electro-mechanical behavior. Therefore, the production densities are yet unknown and the coupling mechanisms of the constituents have not been derived. Several approaches to incorporate constitutive relations can be found in the literature. For the swelling behavior of charged hydrated tissues, one can find approaches in Gu et al. (1999), Bennethum and Cushman (2002a, b), and Acartürk (2009).

Lai et al. (2000) present an investigation of the electric potential of soft tissues under varying external stimuli. In most cases, a local electroneutrality condition is assumed

$$\sum_{\alpha} \rho_e^{\alpha} = F \sum_{\alpha} z^{\alpha} c^{\alpha} \varphi^F = 0 \quad (65)$$

where the Faraday law is applied to calculate the charge density based on the ion concentration. The valence of the ions is denoted by z^{α} ; F is the Faraday constant and φ^F is the volume fraction of the fluid. The electroneutrality condition might be used for coupling the electrical field described by Eqs. 54 and 55 with the thermomechanical balance equations.

In the presented theory, only the gel phase is modeled and interactions with the surrounding fluid are not considered. Therefore the jump boundary conditions have to be applied based on laws of physics.

7 Comparison

The modeling approaches introduced in Sects. 5 and 6 are compared based on their characteristics to simulate the behavior of EAPs under various external stimulations and based on their modeling scale.

The presented modeling approaches are based on deviating assumptions. The macroscopic theory which is based on the Flory and Rehner (1943a, b) swelling theory is a potential formulation where the free Gibbs energy is formulated for the incorporated effects. It depends on statistically determined parameters.

A continuum-based approach is given by the model based on the transport phenomena. The field equations describing the behavior of the respective species are superimposed. They are formulated for the mechanical, electrical, and chemical field.

The theory based on porous media is also a continuum-based approach. Unlike the theory based on transport phenomena, each constituent is incorporated separately following the principles of classical continuum mechanics.

Both continuum-based approaches are formulated with respect to the transient behavior. They are therefore suitable for investigating the time-dependent swelling behavior whereas the classical statistical theory is suitable for determining the steady-state swelling behavior. By incorporating this theory in the framework of classical continuum mechanics, the statistical theory would also be accessible for transient analyses. Multiple approaches based on the statistical theory have been published to investigate the swelling behavior under chemical, mechanical, and thermal stimuli. For analyzing the swelling behavior of polyelectrolyte gels under an electrical stimulus, it is not applicable in general. The continuum-based theories, however, consider external electrical, chemical, and mechanical loads. By modeling the gel and solution phase separately, the transport theory is especially applicable for investigating the swelling behavior under electrical stimuli and varying chemical stimuli due to perturbation within the solution as interfacial interactions are respected in the modeling approach. The theory based on porous media is particularly suitable for investigating the diffusive and convective behavior of each constituent within the gel phase separately. As no interfacial interactions of the gel and solution are considered, the jump boundary conditions have to be formulated by laws of physics.

The computational costs vary. Naturally, the transient models are computationally more expensive than models representing the steady-state swelling behavior. For the Theory of Porous Media, the balance equations – following the concept of classical continuum mechanics – are incorporated for each constituent. Thus, for considering more constituents, the computational costs increase. However, even for a simple case, incorporating the solid phase – skeleton with fixed charges – and the fluid phase with one mobile ionic species, the computational costs are higher compared to the model based on the transport phenomena. A reason could be the more complex coupling between the field equations.

A comparison of the different models is given in Table 1.

Table 1 Comparison of the modeling approaches

Statistical model	Transport model	Model based on porous media
Approach based on the equilibrium of the Gibbs free energy	Continuum-based approach	Continuum-based approach
Gel domain only	Gel and solution domain considered	Gel domain only
Steady-state swelling behavior representable	Transient behavior representable	Transient behavior representable
Mechanical, thermal, and chemical stimuli applicable, extendable to consider electrical stimuli	Mechanical, thermal, chemical, and electrical stimuli directly applicable	Mechanical and thermal stimuli applicable, chemical and electrical stimuli can be respected as boundary conditions based on physical laws
Low computational costs	Higher computational costs; depending on number of species	Higher computational costs; depending on number of constituents

8 Conclusion and Outlook

In the present chapter, an overview over different modeling alternatives for chemically and electrically stimulated polyelectrolyte gels, placed in a solution bath, were given.

First, the statistical theory – a global theory in which only the global swelling is of interest – was reviewed. Second, two different models on the mesoscale were presented: (i) the chemo-electro-mechanical transport model and (ii) a continuum model based on porous media. As was shown, these models are capable of describing the changes of the local variables: concentrations, electric field, and displacement. So, e.g., by the application of an electric field, a bending movement of the polymer gel can be realized which is in excellent correlation with experimental investigations.

As was shown, the statistical theory is an efficient method to model the chemical stimulation of polyelectrolyte gels and the two continuum-based formulations are capable of simulating both chemically and electrically induced swelling or bending. So, the second ones are excellent techniques to model hydrogel bending actuators or gel grippers.

References

- Acartürk, AY (2009) Simulation of charged hydrated porous materials, PhD thesis, Universität Stuttgart
- Ballhause D, Wallmersperger T (2008) Coupled chemo-electro-mechanical finite element simulation of hydrogels: I. Chemical stimulation. *Smart Mater Struct* 17(4):045011

- Bennethum LS, Cushman JH (2002a) Multicomponent, multiphase thermodynamics of swelling porous media with electroquasistatics: I. Macroscale field equations. *Transport Porous Media* 47:309–336
- Bennethum LS, Cushman JH (2002b) Multicomponent, multiphase thermodynamics of swelling porous media with electroquasistatics: II. Constitutive theory. *Transport Porous Media* 47:337–362
- Bowen RM (1976) Theory of mixtures, Part I. In: Eringen AC (ed) *Continuum physics III*. Academic, New York
- Bowen RM (1980) Incompressible porous media models by use of the theory of mixtures. *Int J Eng Sci* 18:1129–1148
- Brock D, Lee W, Segalman D, Witkowski W (1994) A dynamic model of a linear actuator based on polymer hydrogel. *J Int Mater Syst Struct* 5:764–771
- de Boer R (2000) *Theory of porous media*. Springer, Berlin
- de Gennes PJ, Okumura K, Shahinpoor M, Kim KJ (2000) Mechanoelectric effects in ionic gels. *Europhys Lett* 50(4):513–518
- De SK, Aluru NR (2004) A chemo-electro-mechanical mathematical model for simulation of pH sensitive hydrogels. *Mech Mater* 36(5–6):395–410
- Doi M, Matsumoto M, Hirose Y (1992) Deformation of ionic polymer gels by electric fields. *Macromolecules* 25:5504–5511
- Dolbow J, Fried E, Ji H (2005) A numerical strategy for investigating the kinetic response of stimulus-responsive hydrogels. *Comput Meth Appl Mech Eng* 194:4447–4480
- Dolbow J et al (2006) Kinetics of thermally induced swelling of hydrogels. *Int J Solid Struct* 43 (2006):1878–1907
- Ehlers W (2002) Foundations of multiphase and porous materials. In: Ehlers W, Blum J (eds) *Porous media: theory, experiments and numerical applications*. Springer, Heidelberg/Berlin
- English AE, Mafé S, Manzanares JA, Yu X, Grosberg AY, Tanaka T (1996) Equilibrium swelling properties of polyampholytic hydrogels. *J Chem Phys* 104(21):8713–8720
- Eringen AC, Maugin GA (1990) *Electrodynamics of continua I*. Springer, New York
- Ermatchkov V, Ninni L, Maurer G (2010) Thermodynamics of phase equilibrium for systems containing n-isopropyl acrylamide hydrogels. *Fluid Phase Equilibria* 296:140–148
- Flory PJ (1953) *Principles of polymer chemistry*. Cornell University Press, Ithaca
- Flory PJ, Rehner J Jr (1943a) Statistical mechanics of cross-linked polymer networks I. Rubberlike elasticity. *J Chem Phys* 11:512–520
- Flory PJ, Rehner J Jr (1943b) Statistical mechanics of cross-linked polymer networks II. Swelling. *J Chem Phys* 11:521–526
- Frijns AJH, Huyghe JM, Janssen JD (1997) A validation of the quadriphasic mixture theory for intervertebral disc tissue. *Int J Eng Sci* 35(15):1419–1429
- Grimshaw PE, Nussbaum JH, Grodzinsky AJ, Yarmush ML (1990) Kinetics of electrically and chemically induced swelling in polyelectrolyte gels. *J Chem Phys* 93(6):4462–4472
- Gu WY, Lai WM, Mow VC (1999) Transport of multi-electrolytes in charged hydrated biological soft tissues. *Transp Porous Media* 34:143–157
- Guenther G, Gerlach G, Wallmersperger T (2009) Non-linear effects in hydrogel-based chemical sensors: experiment and modeling. *J Int Mater Syst Struct* 20(8):949–961
- Gülch RW, Holdenried J, Weible A, Wallmersperger T, Kröplin B (2000) Polyelectrolyte gels in electric fields: a theoretical and experimental approach. In: Bar-Cohen Y (ed) *Proceeding of the 7th international symposium on smart structures and materials: electroactive polymer actuators and devices*, vol 3987–3927. SPIE, Bellingham, Washington, pp 193–202
- Gurtin ME, Voorhees PW (1993) The continuum mechanics of coherent two-phase elastic solids with mass transport. *Proc R Soc A* 440(1909):323–343
- Hahn HG (1985) *Elastizitätstheorie*. B. G. Teubner, Stuttgart
- Hamann CH, Vielstich W (1998) *Elektrochemie*, 3rd edn. Wiley-VCH, Weinheim
- Hamlen RP, Kent CE, Shafer SN (1965) Electrolytically activated contractile polymer. *Nature* 206:1149–1150

- Hirai M, Hirai T, Sukumoda A, Nemoto H, Amemiya Y, Kobayashi K, Ueki T (1995) Electrically induced reversible structural change of a highly swollen polymer gel network. *J Chem Soc Faraday Trans* 91(3):473–477
- Hong W, Liu Z, Suo Z (2009) Inhomogeneous swelling of a gel in equilibrium with a solvent and mechanical load. *Int J Solid Struct* 46(17):3282–3289
- Keller K, Wallmersperger T, Kröplin B, Günther M, Gerlach G (2011) Modelling of temperature-sensitive polyelectrolyte gels by the use of the coupled chemo-electromechanical formulation. *Mech Mater* 18(7):511–523
- Lai WM, Mow VC, Sun DD, Ateshian GA (2000) On the electric potentials inside a charged soft hydrated biological tissue: streaming potential versus diffusion potential. *J Biomech Eng* 122(4):336–346
- Lee W (1996) Polymer gel based actuator: dynamic model of gel for real time control. PhD thesis, MIT, Boston
- Li H, Lai F (2011) Transient analysis of the effect of the initial fixed charge density on the kinetic characteristics of the ionic-strength-sensitive hydrogel by a multi-effect-coupling model. *Anal Bioanal Chem* 399(3):1233–1243
- Li H, Luo R, Lam KY (2007) Modeling of ionic transport in electric-stimulus-responsive hydrogels. *J Membr Sci* 289(1–2):284–296
- Lucantonio A, Nardinocchi P, Teresi L (2013) Transient analysis of swelling-induced large deformations in polymer gels. *J Mech Phys Solid* 61:205–218
- Mow VC, Kuei SC, Lai WM, Armstrong CG (1980) Biphasic creep and relaxation of articular cartilage in compression: theory and experiments. *ASME J Biomed Eng* 102:73–84
- Ohmine I, Tanaka T (1982) Salt effects on the phase transition of ionic gels. *J Chem Phys* 77(11):5725–5729
- Orlov Y, Xu X, Maurer G (2006) Equilibrium swelling of n-isopropylacrylamide based ionic hydrogels in aqueous solutions of organic solvents: comparison of experiment with theory. *Fluid Phase Equilib* 249(1–2):6–16
- Orlov Y, Xu X, Maurer G (2007) An experimental and theoretical investigation on the swelling of n-isopropyl acrylamide based ionic hydrogels in aqueous solutions of (sodiumchloride or di-sodium hydrogen phosphate). *Fluid Phase Equilib* 254(1–2):1–10
- Quesada-Perez M, Maroto-Centeno J, Forcada J, Hidalgo-Alvarez R (2011) Gel swelling theories: the classical formalism and recent approaches. *Soft Matter* 7:10536
- Rička J, Tanaka T (1984) Swelling of ionic gels: quantitative performance of the donnan theory. *Macromolecules* 17(12):2916–2921
- Sadowski G (2011) Special themed issue on ‘responsive gels’. *Colloid Polym Sci* 289:453
- Schröder UP (1994) Experimentelle und theoretische Untersuchungen an hochgequollenen hydrogelen. PhD thesis, Institut für Textil und Faserchemie der Universität Stuttgart
- Schröder UP, Oppermann W (1996) Properties of polyelectrolyte gels. In: Cohen Addad JP, de Gennes P-J (eds) *Physical properties of polymeric gels*. Wiley, Chichester, pp 19–38
- Shahinpoor M (1994) Continuum electromechanics of ionic polymer gels as artificial muscles for robotic applications. *Smart Mater Struct* 3:367–372
- Shiga T, Kurauchi T (1990) Deformation of polyelectrolyte gels under the influence of electric field. *J Appl Polym Sci* 39:2305–2320
- Sun DN, Gu WY, Guo XE, Lai WM, Mow VC (1999) A mixed finite element formulation of triphasic mechano-electrochemical theory for charged, hydrated biological soft tissues. *Int J Num Meth Eng* 45(10):1375–1402
- Tabatabaei F, Lenz O, Holm C (2011) Simulational study of anomalous tracer diffusion in hydrogels. *Colloid Polym Sci* 289(5–6):523–534
- Tamagawa H, Taya M (2000) A theoretical prediction of the ions distribution in an amphoteric polymer gel. *Mater Sci Eng A* 285(1–2):314–325
- Tanaka T, Fillmore DJ (1979) Kinetics of swelling of gels. *J Chem Phys* 70(3):1214–1218
- Tanaka T, Nishio I, Sun S-T, Ueno-Nishio S (1982) Collapse of gels in an electric field. *Science* 218:467–469

- Treloar LRG (1958) *The physics of rubber elasticity*. Oxford University Press, Oxford
- Truesdell C, Noll W (2003) *The non-linear field theories of mechanics*. Springer, Berlin
- Umamoto S, Okui N, Sakai T (1991) Contraction behavior of poly(acrylonitrile) gel fibers. In: Rossi DD, Kajiwara K, Osada Y, Yamauchi A (eds) *Polymer gels – fundamentals and biomedical applications*. Plenum Press, New York/London, pp 257–270
- van Loon R, Huyghe JM, Wijlaars MW, Baaijens FPT (2003) 3D FE implementation of an incompressible quadriphasic mixture model. *Int J Num Meth Eng* 57(9):1243–1258
- Wallmersperger T, Ballhause D (2008) Coupled chemo-electro-mechanical finite element simulation of hydrogels: II. Electrical stimulation. *Smart Mater Struct* 17(4):045012
- Wallmersperger T, Kröplin B, Gülch RW (2004) Coupled chemo-electro-mechanical formulation for ionic polymer gels – numerical and experimental investigations. *Mech Mater* 36(5–6): 411–420
- Wallmersperger T, Wittel FK, D’Ottavio M, Kröplin B (2008) Multiscale modeling of polymer gels – chemo-electric model versus discrete element model. *Mech Adv Mater Struct* 15(3–4): 228–234
- Wallmersperger T, Attaran A, Keller K, Brummund J, Guenther M, Gerlach G (2013) Modeling and simulation of hydrogels for the application as bending actuators. In: Gabriele S, Walter R (eds) *Progress in colloid and polymer science*, vol 140. Springer, Berlin, pp 189–204
- Walter J, Ermatchkov V, Vrabec J, Hasse H (2010) Molecular dynamics and experimental study of conformation change of poly(n-isopropylacrylamide) hydrogels in water. *Fluid Phase Equilib* 296:164–172
- Weeber R, Kantorovich S, Holm C (2012) Deformation mechanisms in 2D magnetic gels studied by computer simulations. *Soft Matter* 8:9923–9932

Martin Elstner and Andreas Richter

Contents

1	Introduction	84
2	Control Principles	85
3	Fabrication Techniques	86
4	Conducting Materials	86
5	Actuator Devices and Artificial Muscles	89
6	Optical Devices	89
7	Medical Devices	90
8	Thermostats and Chemostats	90
9	Microfluidics and Labs-on-a-Chip	92
9.1	State of the Art	92
9.2	Integrated Microchemomechanical Systems	93
9.3	Hydrogel-Based Materials as Actuators in Microfluidics	93
9.4	Integrated Circuits for Chemical Information Processing	95
10	Conclusions	96
	References	97

Abstract

Stimuli-responsive hydrogels display a variety of interesting features that make them ideal candidates for technological applications. The applicable stimuli range from temperature, pH, and (bio)chemical species to electric fields and light; some materials can even be controlled by multiple stimuli. Hydrogel materials can be

M. Elstner (✉)

TU Dresden, Center for Advancing Electronics Dresden (cfaed), Dresden, Germany
e-mail: martin.elstner@tu-dresden.de

A. Richter

Institute of Semiconductors and Microsystems, Faculty of Electrical and Computer Engineering,
Dresden University of Technology and Center for Advancing Electronics Dresden, Dresden,
Germany
e-mail: andreas.richter7@tu-dresden.de

synthesized by a single-step free-radical polymerization, and various methods to introduce them into a final system are discussed. This chapter covers applications of smart hydrogels in various (micro-)systems starting from transparent conductors over stimuli-sensitive optical components and drug delivery devices for medical applications. Intensively discussed are microfluidic applications starting from single components as thermostats, chemostats, and valves toward complex integrated systems. Finally, we outline the implications of autonomous microfluidic devices to the field of chemical information processing.

Keywords

Hydrogels • Microsystems • Microfluidics • System integration • Fabrication techniques

1 Introduction

Microsystems technology lacks a diverse material with a comparable significance as silicon in microelectronics. Our strong conviction is that hydrogels could take this place. They can act as actuators or combined sensor-actuators in a broad variety of microsystems (Richter 2009).

Our research in this field focuses on chemical microsystems such as micropumps (Richter et al. 2009), chemostats (a device that keeps the concentration of a chemical species constant in a solution) (Richter et al. 2007), and fluidic microprocessors for chemical information processing (Greiner et al. 2012).

Current microsystem architectures are dominated by the basic principle of microelectromechanical systems (MEMS) (Au et al. 2011), which means that they are nothing more than complex computer-controlled systems. A computer must control each component or compartment. Increasing the functionality by increasing the address space requires an adequate scaling of the computer software, the electromechanical transducers, and the control electrodes, which leads to a fast reaching of the efficiency limit (Unger et al. 2000).

Besides the dominating MEMS principles mentioned above, there is a strong interest to utilize active material as solid-state actuators. As known from microelectronics, this integrated circuit (IC) approach provides fundamental advantages in component design, chip architecture, and fabrication technology. Beyond “traditional” solid-state actuators like shape memory alloys (Benard et al. 1998) and piezoelectric components (Yang et al. 2004), which are too expensive for a large-scale production technology, stimuli-responsive polymers are promising materials. Well-known examples are shape memory (Lendlein and Kelch 2002; Lendlein et al. 2005) and electrically conductive polymers (Smela et al. 1995; Jager et al. 2000; Smela 2003), but probably the best features are displayed by the stimuli-responsive hydrogels. These materials display reversible first-order volume phase transition behavior and response to small changes of environmental parameters, e.g., $\Delta T = 6$ K, with drastic changes of the volume from completely swollen to completely shrunken and vice versa.

Compared to other solid-state actuators, these hydrogels provide one of the highest energy densities and also the highest change of volume known from solid-state actuators (Eddington and Beebe 2004; Ziaie et al. 2004). The cooperative diffusion coefficient D_{Coop} is in the order of 10^{-7} to $10^{-5} \text{ cm}^2\text{s}^{-1}$. Hence, they are significantly faster than shape memory polymers $\{D_{\text{Coop}} \approx (10^{-7} \text{ to } 10^{-8}) \text{ cm}^2\text{s}^{-1}\}$ or conducting polymers ($D_{\text{Coop}} \approx 10^{-9} \text{ cm}^2\text{s}^{-1}$) (Richter 2009). It is remarkable that D_{Coop} of the hydrogels are in the same order of magnitude as the self-diffusion coefficients D_{Self} of molecules important in microfluidics and living organisms $\{D_{\text{Self}}(\text{Na}) = 1.3 \cdot 10^{-5} \text{ cm}^2\text{s}^{-1}, D_{\text{Self}}(\text{H}_2\text{O}) = 2.27 \cdot 10^{-5} \text{ cm}^2\text{s}^{-1}\}$. This ensures that active hydrogel-based components can operate on the same timescale as the processes driven by self-diffusion. The characteristic time constant of hydrogels depends on the square of the characteristic size; thus, hydrogels become significantly faster by decreasing the characteristic size. The response time of hydrogel actuators of the size of 1 mm is in the order of several seconds, by 250 μm characteristic size in the range of 300 ms; in the range of 1 μm , the response time is in the order of 10 ms. In conclusion, in the range of technology nodes $\leq 250 \mu\text{m}$, hydrogel-based components fulfill the time requirements of microfluidics, which has typically flow velocities in the order of mm s^{-1} (Greiner et al. 2012).

2 Control Principles

A multitude of different stimuli can act on responsive polymer gels and influence their behavior. The materials can be responsive to a single stimulus or to a broader range of stimuli. An application-dependent challenge for the material designer is the tuning of these control parameters. The most common control parameter is temperature, since the temperature sensitivity of smart hydrogels is intensively studied (Richter et al. 2009). The lower critical transition temperature (LCST) behavior of poly(*N*-isopropylacrylamide) (PNIPAAm) allows to switch at a near physiological temperature of 32 °C which points to medical and biological applications. A comprehensive overview of thermal responsive polymers can be found in reference (Roy et al. 2013).

Thermal control is also relatively easy to link with an electronic control, such that an electronic heating element or Peltier element influences the temperature, following the swelling characteristics of the hydrogel (Richter et al. 2007). A thermocouple can be used to measure the temperature near or even inside the hydrogel. Additional, chemical stimuli such as pH value or alcohol and salt concentrations can act as control variables (Richter et al. 2007; Richter 2009). These input variables can change the amount of water available to the polymer network or the hydrophilicity of the polymer chain. In thermoresponsive hydrogels, the chemical stimuli influence also the phase-changing temperature and vice versa. The direct electronic control of polymeric gels allows the construction of transparent loudspeakers (Keplinger et al. 2013) or artificial muscles (Nawroth et al. 2012).

Also the direct influence of an electric field can be used to control the properties of hydrogels. In ionic gels, the applied electric field fosters ion exchange and the expulsion of charged guest molecules (Kikuchi and Okano 2002).

The tight interlink of a variety of stimuli within the polymeric gel material allows to convert different signal levels into each other. Especially signal transformation from and into the electronic domain is of great importance for signal handling with established computer-based methods.

3 Fabrication Techniques

Hydrogels can be prepared by a multitude of synthetic techniques (Mathur et al. 1996). For stimuli-responsive hydrogels, free-radical polymerization is the method of choice. Thereby, a monomer solution that contains also a multifunctional cross-linking agent is polymerized under the influence of an initiator. This initiator can work via a photochemical (Greiner et al. 2012) or a thermal (Richter et al. 2007) trigger. The polymerization process should be conducted in the absence of oxygen, since the formed radicals would interact with oxygen molecules, which reduces the product quality or oppresses the product formation completely (Greiner et al. 2012).

The fixation of a hydrogel material can be a challenging part of the manufacturing process due to their soft occurrence. In microfluidic applications, narrowing or cage-like structures can hold hydrogels in place, especially if a certain movement of the active component is tolerable or desirable.

Adhesive films can help to hold the active element in place, but a large adhesive area can also influence the actuating performance (Kim et al. 2004). Also a direct surface attachment during the hydrogel synthesis is possible, for instance, with a surface modification that fits to the polymerization process (Plueddemann 2013). A charged surface is a more flexible approach of surface adhesion and allows to keep oppositely charged hydrogels in place (Kim et al. 2004). This bonding technique is reversible and can be switched on and off by environmental conditions such as the pH value.

Joined structures are also possible if the polymeric gel is directly polymerized inside the final cavity or channel (see Fig. 1). The material can be held in place by appropriate structures, and temporary support can be given by meltable plugs (Lin et al. 2014).

4 Conducting Materials

Beside the outlined applications in microsystems technologies, polymer gels are suitable for more classical electronic applications.

Many strategies are proposed that could form electronically conducting hydrogels, such as micro-patterning of conducting polymers (Sekine et al. 2010), the incorporation of graphene (Xu et al. 2013), or polyaniline dual networks

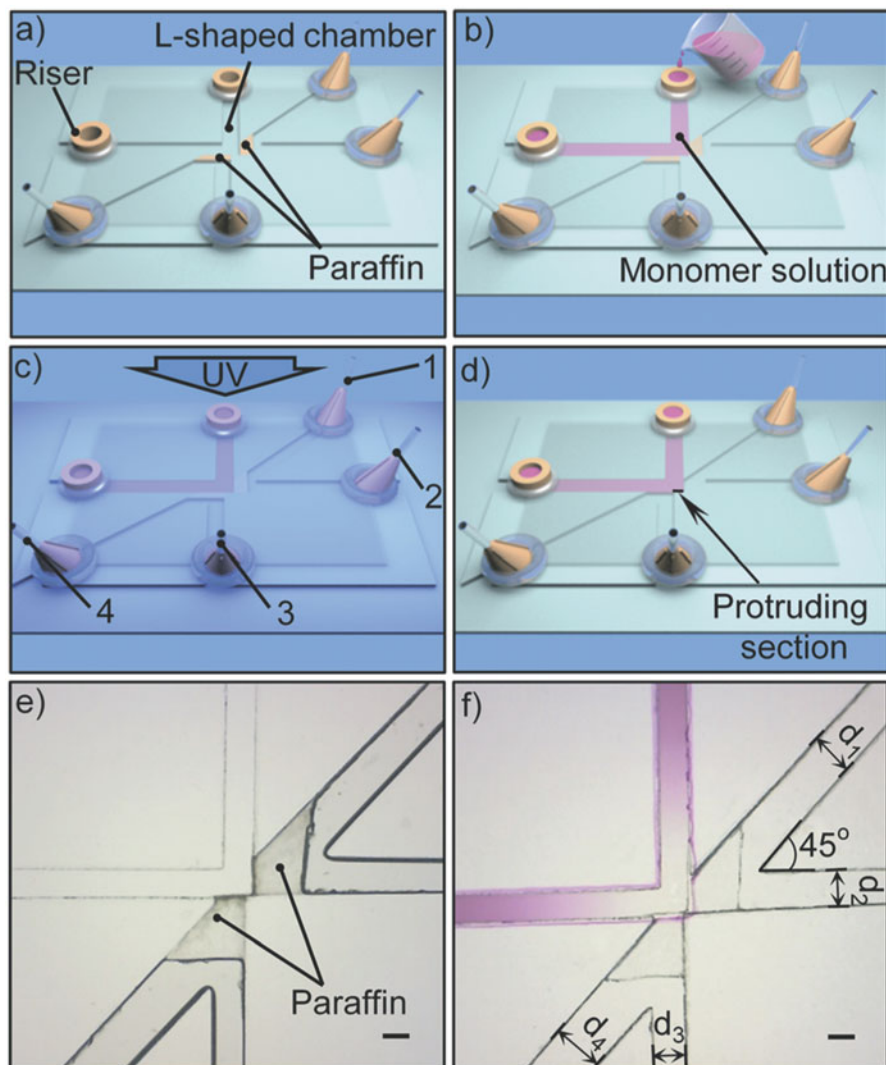


Fig. 1 Thermal switchable microfluidic chip. (a) Paraffin plugs define a L-shaped chamber, which can be filled with the monomer solution (b) and polymerized by UV exposure (c). (d) Thermal treatment removes the paraffin plugs after the polymerization. (e) Detailed view on the paraffin plugged channel structure. (f) Final channel structure with a swollen hydrogel valve (Image adopted from Lin et al. (2014) with permission)

(Ding et al. 2014). However, beside such elaborated synthetic approaches, a very simple, versatile, and direct strategy can be used. To obtain a conducting material, hydrogels can be prepared from saline solutions instead of pure water. Depending on the intended use, the gel has to be prevented from leaking by encapsulation.

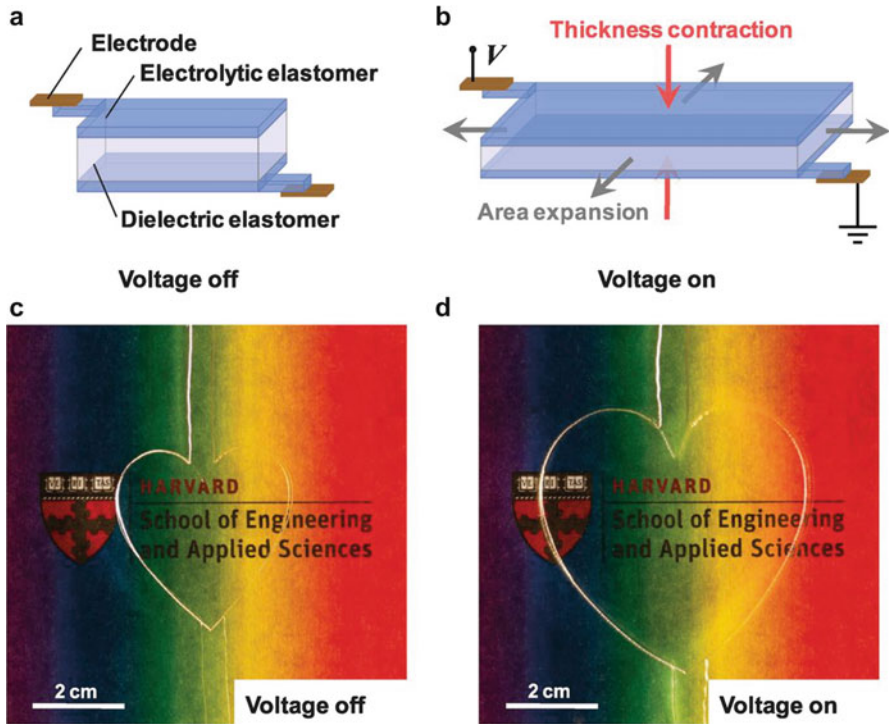


Fig. 2 Fast, transparent voltage-induced actuator. The dielectric elastomer (1 mm thick 3 M VHB 4910 tape) is sandwiched between two layers of electrolytic elastomer (100 μm thick polyacrylamide hydrogel with NaCl as electrolyte). Applying a voltage reduces the sandwich thickness and concurrently increases the area. This switching is reversible, but the area expansion reduces with increasing the driving frequency and vanishes around 1 kHz (Image adopted from Keplinger et al. (2013) with permission)

Also the potential of electrochemical reactions should be minded, which can limit the area of applications.

The stretchable, optical transparent ionic conductor presented by Whitesides and Sun et al. can act as actuator or loudspeaker without electrochemical reactions (Keplinger et al. 2013). The ionic conductors display a higher resistivity than many electronic conductors, but the overall sheet resistance in stretchable and transparent devices is lower than in all existing electronic (namely, ITO, AgNWs, SWNTs, graphene) conductors.

The excellent transparency (see Fig. 2) of the material allows to mount loudspeakers directly on top of displays. Such a setup is also very favorable for noise-canceling windows. The transparent actuator is also suited for tactile feedback to the users of touch displays (Rogers 2013).

5 Actuator Devices and Artificial Muscles

Another actuating principle is used by the artificial muscle approach. Popular in robotics are pneumatically operated muscles of the McKibben type (Zhang and Philen 2011). They consist of a tube-like shell of interwoven fibers. The basic operation principle is that a lateral expansion of this membrane yields an axial contraction caused by the woven structure (Bar-Cohen 2002).

Stimuli-responsive hydrogel materials with their swelling and shrinking properties are an interesting material class for artificial muscle. They allow to translate a chemical stimulus into a mechanical force. With this property, responsive gel material-based artificial muscles come close to their biological antetype and can be controlled by biocompatible stimuli.

An actuator setup based on pH-responsive hydrogel beads has demonstrated to handle loads up to the kilogram range (Tondou et al. 2010). The active component is formed of ion-exchange resin beads that employ a carboxylic acid ($-\text{COOH}$) functionality. Depending on the pH value of the surrounding medium, this functional group can be either protonated or deprotonated, resulting in different charges of the polymer chains. At low pH levels (acidic solution, high concentration of H^+ -ions), the carboxylic acid group will stay protonated, and the polymer chain is uncharged. At high pH levels (basic solution, high concentration of OH^- -ions), the carboxylic acid functional group gets deprotonated (to the corresponding base $-\text{COO}^-$), and as a consequence, the polymer chain becomes charged. In consequence, the ion-exchange resin swells during the transition from low to high pH and shrinks by altering the pH from high to low.

The artificial muscle membrane is filled with such resin beads, and by pumping HCl (acid, low pH) or NaOH (base, high pH) solutions through this membrane, the swelling and shrinking of the resin beads changes the lateral expansion of the muscle (Tondou et al. 2009). A precise tuning of the chemical stimuli by a selection of buffer solutions allows to switch such a muscle architecture by slight changes of the pH (Tondou et al. 2010).

In a complete biomimetic approach, Dabiri and Parker et al. demonstrated the construction of an artificial jellyfish (Nawroth et al. 2012). The device is formed by an elastomeric membrane coated with the active hydrogel. By applying a pulsed electric field (1 Hz, 2.5 V cm^{-1} , 10 ms pulse duration), a bending of the laminated structure is induced. This folds the dislike structure to a bowel and expels water which acts as a driving force for the movement. Overall, the mechanic behavior of this device is in excellent agreement with the natural antetype.

6 Optical Devices

The stimuli responsiveness and transparency to visible light makes hydrogel materials to interesting candidates for adaptive optical materials. This is demonstrated by the transparent loudspeaker (see Fig. 2), which can be directly placed in front of a

display (Keplinger et al. 2013). More challenging than transparent films are imaging components like lenses. The use of stimuli-responsive hydrogel droplets as tunable microlenses was demonstrated using their temperature and pH switching abilities (Kim et al. 2004). The swelling and shrinking allows to adjust the focal length of the lens according to the environmental conditions.

Bio-responsive hydrogel lenses can be prepared from functional modified polymer gels. Antigen-antibody binding to a microlens was achieved by biotin functionalization. The optical system responds in an analogue manner to input concentrations and could enable the construction of label-free optical biosensors (Kim et al. 2007).

7 Medical Devices

One of the key driving forces in the development of active hydrogel materials is their prospective application as drug delivery systems (Lee et al. 2013). Possible carrier systems range from small vials capped with a stimuli-responsive polymer that shrinks or dissolves under certain conditions (Nuxoll 2013) over hydrogel-based micropumps (Nuxoll 2013) to loaded hydrogel beads (Jung et al. 2013) and smart vesicles (Mura et al. 2013). This field of research is dominated by synthetic chemistry and material science, and a lot of carefully designed materials are presented in the literature. We want to point the interested reader to this comprehensive review articles: (Qiu and Park 2012) and (Hoffman 2012).

Analytical devices play also a major role in the field of medical research and therapy. Their miniaturization, enhancement, and cost reduction are one of the main goals of the lab-on-a-chip approach, which will be discussed in Sect. 9.

8 Thermostats and Chemostats

The thermoresponsive properties of many smart hydrogels make them the ideal candidates for thermostats. If their environment temperature increases above a threshold value, they shrink, and this actuation can be used to regulate the temperature. A thermostatable valve as displayed in Fig. 1 could enable a flow of liquids in case of elevated temperature (Lin et al. 2014). At low temperatures, the swollen hydrogel blocks the channel interconnection between the channel pairs 1–2 and 3–4. At an elevated temperature, the hydrogel shrinks, and the channel interconnection is opened. This enables a flow of liquids from the channel pair 1–2 to channel pair 3–4. A thermostatic behavior is achieved, if such a functionality is used to switch a cooling medium flow. This results in a flow of a cold liquid in case of a temperature above the threshold value.

A thermal adaptive microfluidic structure (TAMS) with a high-level control system was proposed in 2012. To reduce the energy consumption of cooling systems, e.g., in electronic computers, it is favorable to reduce the amount of the cooling medium to a minimum. This is achieved by dividing the whole device in smaller substructures (see Fig. 3), each of these substructures can switch the medium

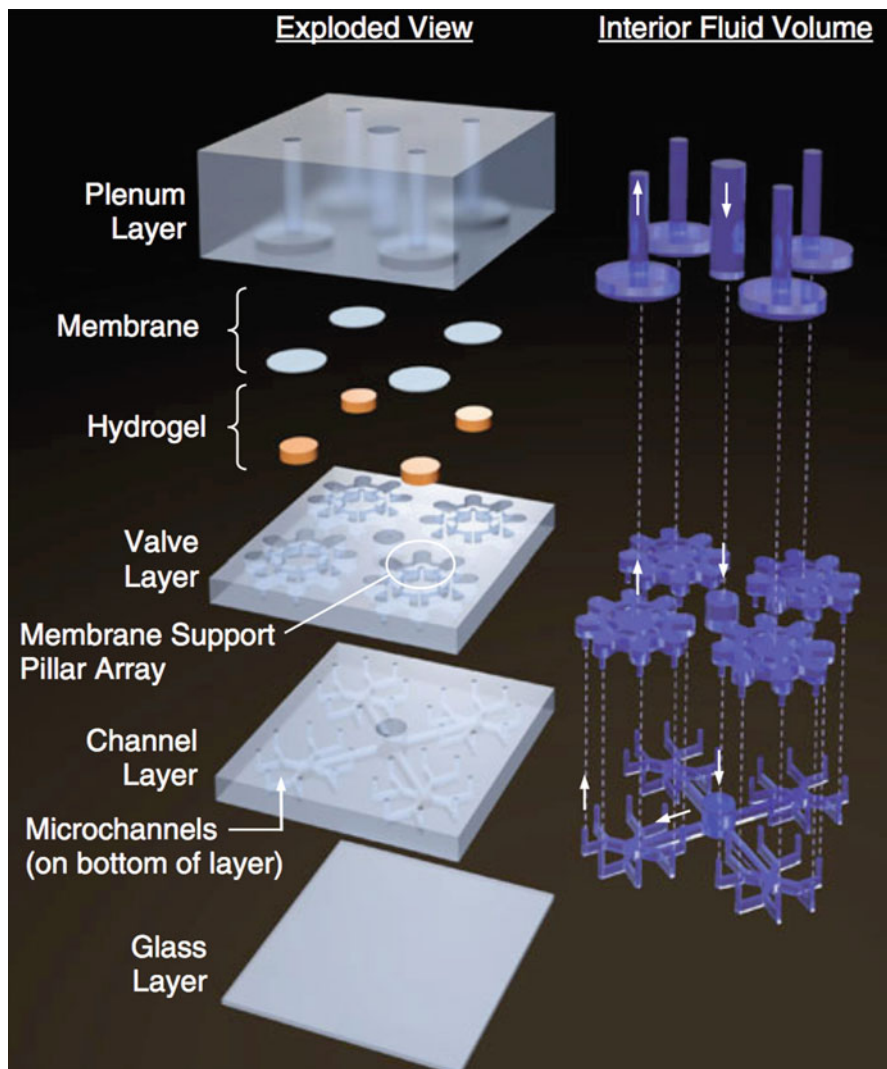


Fig. 3 Exploded view of the thermally adaptive microfluidic structure (TAMS, *left hand*) and the fluid-filled parts with indicated flow directions (*right hand view*) (Image adopted from reference (Hart and Silva 2012) with permission)

flow independently and autonomously. Due to the abandonment of external control devices, the concept is ideally suited for downscaling and system integration (Hart and Silva 2012).

Tightly related to the concept of thermostats is the idea of chemostats. Instead of the thermal switching behavior of the active hydrogel element, their concentration-dependent volume change can be used to control a fluid stream (Richter et al. 2007).

In a possible usage scenario, the device would monitor the production of alcohol, and if a threshold concentration is reached, the reaction mixture is diluted by fresh medium from the outside.

In a combined usage of both stimuli (chemical and thermal), the concentration threshold of the device can be controlled by adjusting the device temperature (Richter et al. 2007).

9 Microfluidics and Labs-on-a-Chip

9.1 State of the Art

Over the last 25 years, besides electronic ICs, another IC concept has been established, the microfluidic ICs or “lab-on-a-chip” (LoC). In contrast to microelectronics, its basic idea is the automation and functional scaling of liquid processing at microscale with a huge potential impact on life sciences. The significance of the LoC technology can be illustrated by nucleotide analysis, a fast-growing field providing completely new opportunities in diagnostics, agriculture, and general life science (Niemz et al. 2011; Zhang and Guo 2011; Park et al. 2011; Craw and Balachandran 2012; Donatin and Drancourt 2012; Thompson et al. 2014). Besides the development of new chemicals and protocols, however, a further key factor of success has to be addressed: the ability for automation and technical optimization of the liquid processing at the microscale. With the growing complexity of the methods, manual performance becomes less efficient, as the timescale becomes larger and the probability of errors and contaminations increases, especially for such sensitive analytes as nucleic acids, proteins, or single cells.

For relevant analyses, outside special laboratories, e.g., in medical practices, critical care units or resource-limited environments, pipetting robots, and comparable systems, cannot be used. Here, integrated microfluidic circuits, the so-called lab-on-a-chip, provide – in principle – an ideal approach for automation (Whitesides 2006; Linder 2007; Sia and Kricka 2008; Chin et al. 2012). Following the original idea to utilize the irresistible power of integrated and highly integrated circuits for fluid manipulation, protocols of any complexity could be automated in extremely efficient manner. Especially in point-of-care diagnostics, several small-scale and medium-scale integrated LoC are already commercialized (Chin et al. 2012).

In contrast, the field of highly functional LoC is quite problematic. This field is commercially most attractive; as a result of scaling, a drastic increase of efficiency and functionality as well as the development of new revolutionary methods can be expected. However, only few commercial applications in special fields of high-throughput screening are available. Most of them are limited to applications with small address space to control valves and valve compartments. It is significant that the industry that relays on chemical big data, e.g., “next-generation” PCR and sequencing, mainly favors pipetting robots instead of LoC.

9.2 Integrated Microchemomechanical Systems

In contrast, a microelectronic IC is not a computer-controlled device, but, in form of the microprocessor, it is the heart of a computer, because of the fundamental different functional principle. The electronic IC consists of thousands or even millions of basic circuits, which autonomously process electronic information. That is the functional base of the huge performance of microelectronic IC technology. Additionally, the ICs have a layer-by-layer chip architecture with solid-state components made from lithographically patterned layers of intrinsically active materials. The smaller the lithographic structures, the larger the integration density of components per chip area. This is the foundation of technological scaling of electronic ICs.

In our research, we investigated the question, whether, and if yes, how a transfer of the functional concept of microelectronics to microfluidic IC technology could be possible. Indeed, we discovered a suitable approach (Greiner et al. 2012; Allerdißen et al. 2013; Voigt et al. 2014). Our concept of microchemomechanical (μ CHEM) LoC is based on circuitries processing chemical signals with components made from intrinsically active polymers able to respond to thermodynamic control conditions, especially to chemical control parameters.

Our concept brings drastic consequences for nearly each aspect of the LoC technology. The processing of chemical information (concentrations of certain chemicals) by circuitries with active material components leads to four features: (a) The system architecture of LoC systems is extremely simplified. Organized similar to an electronic microprocessor, the control unit, the execution unit, and the instructions are on a single chip. Consequently, the IC does not need any computer control; it is an autonomous and self-sufficient liquid-handling system. (b) The event-controlled (feedback, feed forward) circuit-based processing of chemical information will drastically expand the possibilities of LoC technology and has the potential to form the foundation of new kinds of methods in chemistry, material science, and life science. (c) It significantly simplifies the chip architecture. The introduction of solid-state material-based components and circuitries allows simplest and compact IC architectures organized as different, overlapping layers. (d) The μ CHEM IC concept is scalable. The circuit-based concept provides functional scalability, whereas the lithographically patterned layer-by-layer architecture enables technological scaling.

In conclusion, in case of success, it can be expected that our concept will change the rules of lab-on-a-chip technology.

9.3 Hydrogel-Based Materials as Actuators in Microfluidics

The outlined properties make stimuli-responsive hydrogels interesting for actuator materials in microfluidics. In principle, these gels can be controlled directly by electric fields (Tanaka et al. 1982) or light (Suzuki and Tanaka 1990). But in reality, these control principles are too slow and display no or weak reversibility.

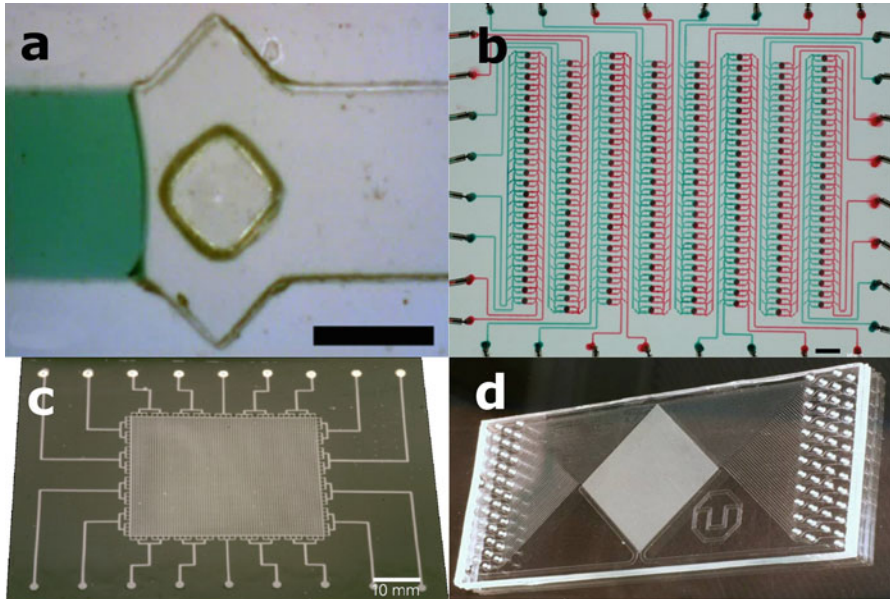


Fig. 4 Circuits with intrinsically active polymers. (a) Closing valve with a colored fluid approaching from the *left* as used in chips like in **b** and **d**. (b) Chemomechanical IC for long time monitoring of bioreactors with 2.096 active elements (Greiner et al. 2012). (c) Multimodal MEMS display with 4.320 actuator pixels (Paschew et al. 2013). (d) 48×48 -matrix-IC for high-integrated combinatorial analysis in the life sciences with 7.012 active elements (Adopted from reference (Greiner et al. 2012))

By introduction of an electrothermic interface (Richter et al. 2003), the base to control temperature-sensitive hydrogel actuators on chip level is laid (Gerlach and Arndt 2009). To fabricate and integrate gel actuators into microsystems, two photopatterning approaches are established (Hoffmann et al. 1999; Kuckling et al. 1999; Beebe et al. 2000). In microfluidics, two key components are developed: (a) well-working microvalves are already commercialized and investigated by many other groups (Zhang et al. 2012; Benito-Lopez et al. 2014) and (b) several types of micropumps exist (Richter et al. 2009; Bae et al. 2014).

A significant step toward was the development of a large-scale integration (LSI) technology for hydrogel-based MEMS (Richter and Paschew 2009) (see Fig. 4c). This research comprised the solution of two major challenges: (a) a technology suitable for LSI of hydrogel-based devices at large-area substrates and (b) a control method able to individually address thousands of hydrogel actuators placed on the IC substrate. In our initial work, we presented an intermodal display device (Fig. 1) that consists of more than 4.300 actuator pixels (modulators) with a density of around 300 actuator pixels per cm^2 (now the address space of our IC controller is in the VLSI range). This device has unique characteristics and displays

(a) monochrome visual as well as (b) tactile properties such as softness, contours, profiles, and textures of a virtual surface with high spatial resolution. In our actual research, we transfer this concept to (i) large-scale integrated and (ii) free programmable MEMS-LoC.

9.4 Integrated Circuits for Chemical Information Processing

Stimuli-responsive hydrogels are smart materials providing properties, which go far beyond the features of common actuator materials. The unique property of stimuli-responsive hydrogels is to respond to small changes of concentrations of a chemical species with a large change of volume (Li et al. 2002). The components introduced in this chapter (valves, pumps, chemostats) open the door to a new field of application with possibly ground-breaking potential: integrated circuits that process chemical information by chemically responsive components. We developed approaches for both, analogue and discrete paradigms of information processing, which are quite different from each other.

9.4.1 Discrete Circuits

Discrete circuits are mainly intended to automate and parallelize complex protocols of analytics, diagnostics, etc., which have fixed programs. Since diagnostic devices are often used only once (due to contamination), another class of intrinsically active materials can be utilized: phase change polymers providing an irreversible onetime sensor-actuator effect (Greiner et al. 2012). The signal processing concept of these circuits is as follows. We use (1) discrete control signals (e.g., the binary concentration of water) and (2) the multidimensionality of chemical information. All information is part of the process medium, and the data signals in the form of, e.g., the interesting molecules and the detection reagents and also the control signal. In more simple words, when the process liquid is pumped in an air-filled channel network and the liquid front is reaching a component, then, due to the sensitive properties of the active material of the component, it carries out a specific fluidic operation predefined in time and functions by design and material properties. Connected to circuitries, these components, e.g., switches, realize in sequential or parallel manner well-defined programs – without any computer control (see Fig. 4a and b).

The concept of our components differs significantly from elements of MEMS especially regarding the time behavior. MEMS components need a fast response to the electronic control signal. If our components would close the channel immediately after activation, then the liquid flow including all signals would stop also immediately. Subsequent structures, e.g., components or cascades, could not be activated. Hence, the time behavior of the components defines the time schedule of the IC program and has to be adapted to the time necessary to activate the next functional group. Therefore, there is a need for components, whose response time can be adjusted in a wide range between immediately and several minutes. It should be noted that we successfully realized components closing immediately, which

means, they close so fast that no liquid can pass the valve seat. However, we found only one application: a venting valve.

We successfully realized several ICs for long-term monitoring of bioreactors. We found several basic questions on material, component, architecture, signaling, and circuitry level, which have to be answered in future research. Exemplified by different ICs with an address space in the LSI range (see Fig. 4b), a functional scaling is already demonstrated. However, the ICs are handmade and not yet based on a scalable technology (Greiner et al. 2012). A pointer to combinatorial chemical research can be given by our 48×48 cross-analyzing chip. This chip acts also completely autonomously and can mix 48 reagents with 48 samples. The closing of the reaction chambers and the mixing of sample and reagent are controlled by hydrogel materials.

9.4.2 Analogue Circuits

This approach, which requires reversible stimuli-responsive polymers, allows us to investigate the possibilities beyond current LoC as foundation of new classes of methods. Together with others, we are researching the basics of multidimensional chemical information theory, system architecture of μ CHEMS-ICs, and signal processing of multidimensional information. Additionally, we developed a general concept of analogue chemical transistors including modeling, simulation, and experimental characterization. Together with collaborators, we are investigating the foundation of a computer-aided IC design flow. On the level of basic circuits, we successfully realized the first component-based chemical oscillators in the form of a delay line oscillator with chemical feedback toward alcohol concentrations in water. In the future, we want to augment this technology with enhanced chemical selectivity and sensitivity. This should enable the automatic processing of more complex chemical species and their subsequent usage for information processing (Elstner et al. 2014).

10 Conclusions

Stimuli-responsive hydrogels are an interesting class of materials with a broad range of applications in electronics, medicine, optics, microfluidics, and micro-engineering in general. The past decades were dominated by a steady flow of new concept proposals from the application-oriented researchers. Combined with the broadened library of active hydrogel materials that is supplied by the chemistry and material science community, these concepts can now be tested on a lot of relevant problems. The coming years will indicate which concepts can keep the promised gains. In our belief, the multi-stimuli-responsive materials are of great importance since they can translate signals from one domain to another domain. We expect that autonomously operating lab-on-a-chip architectures will change the rules in life sciences and analytical chemistry.

References

- Allerdißen M, Greiner R, Richter A (2013) Microfluidic microchemomechanical systems. In: Vincenzini P, Lorenzelli L (eds) *Advances in science and technology*. Trans Tech, Pfaffikon, Switzerland, pp 84–89
- Au AK, Lai H, Utela BR, Folch A (2011) Microvalves and micropumps for bioMEMS. *Micromachines* 2:179–220
- Bae YM, Lee K-H, Yang J et al (2014) Hydrogel-based capillary flow pumping in a hydrophobic microfluidic channel. *Jpn J Appl Phys* 53:067201
- Bar-Cohen Y (2002) Electroactive polymers as artificial muscles: a review. *J Spacecr Rockets* 39:822–827
- Beebe DJ, Moore JS, Bauer JM et al (2000) Functional hydrogel structures for autonomous flow control inside microfluidic channels. *Nature* 404:588–590
- Benard WL, Kahn H, Heuer AH, Huff MA (1998) Thin-film shape-memory alloy actuated micropumps. *J Microelectromech Syst* 7:245–251
- Benito-Lopez F, Antoñana-Díez M, Curto VF et al (2014) Modular microfluidic valve structures based on reversible thermoresponsive ionogel actuators. *Lab Chip* 14:3530–3538
- Chin CD, Linder V, Sia SK (2012) Commercialization of microfluidic point-of-care diagnostic devices. *Lab Chip* 12:2118–2134
- Craw P, Balachandran W (2012) Isothermal nucleic acid amplification technologies for point-of-care diagnostics: a critical review. *Lab Chip* 12:2469–2486
- Ding H, Zhong M, Kim YJ et al (2014) Biologically derived soft conducting hydrogels using heparin-doped polymer networks. *ACS Nano* 8:4348–4357
- Donatin E, Drancourt M (2012) DNA microarrays for the diagnosis of infectious diseases. *Méd Mal Infect* 42:453–459
- Eddington DT, Beebe DJ (2004) Flow control with hydrogels. *Adv Drug Deliv Rev* 56:199–210
- Elstner M, Axthelm J, Schiller A (2014) Sugar-based molecular computing by material implication. *Angew Chem Int Ed* 53:7339–7343
- Gerlach G, Arndt K-F (2009) *Hydrogel sensors and actuators: engineering and technology*. Springer-Verlag, Berlin Heidelberg
- Greiner R, Allerdisen M, Voigt A, Richter A (2012) Fluidic microchemomechanical integrated circuits processing chemical information. *Lab Chip* 12:5034–5044
- Hart RA, da Silva AK (2012) Self-optimizing, thermally adaptive microfluidic flow structures. *Microfluid Nanofluid* 14:121–132
- Hoffman AS (2012) Hydrogels for biomedical applications. *Adv Drug Deliv Rev* 64(Suppl):18–23
- Hoffmann J, Plötner M, Kuckling D, Fischer W-J (1999) Photopatterning of thermally sensitive hydrogels useful for microactuators. *Sens Actuators Phys* 77:139–144
- Jager EWH, Smela E, Inganäs O (2000) Microfabricating conjugated polymer actuators. *Science* 290:1540–1545
- Jung J, Arnold RD, Wicker L (2013) Pectin and charge modified pectin hydrogel beads as a colon-targeted drug delivery carrier. *Colloids Surf B Biointerfaces* 104:116–121
- Keplinger C, Sun J-Y, Foo CC et al (2013) Stretchable, transparent, ionic conductors. *Science* 341:984–987
- Kikuchi A, Okano T (2002) Pulsatile drug release control using hydrogels. *Adv Drug Deliv Rev* 54:53–77
- Kim J, Serpe MJ, Lyon LA (2004) Hydrogel microparticles as dynamically tunable microlenses. *J Am Chem Soc* 126:9512–9513
- Kim J, Singh N, Lyon LA (2007) Displacement-induced switching rates of bioresponsive hydrogel microlenses. *Chem Mater* 19:2527–2532
- Kuckling D, Adler H-JP, Arndt K-F et al (1999) Photocrosslinking of thin films of temperature-sensitive polymers. *Polym Adv Technol* 10:345–352
- Lee SC, Kwon IK, Park K (2013) Hydrogels for delivery of bioactive agents: a historical perspective. *Adv Drug Deliv Rev* 65:17–20

- Lendlein A, Kelch S (2002) Shape-memory polymers. *Angew Chem Int Ed* 41:2034–2057
- Lendlein A, Jiang H, Jünger O, Langer R (2005) Light-induced shape-memory polymers. *Nature* 434:879–882
- Li W, Zhao H, Teasdale PR et al (2002) Synthesis and characterisation of a polyacrylamide–polyacrylic acid copolymer hydrogel for environmental analysis of Cu and Cd. *React Funct Polym* 52:31–41
- Lin S, Wang W, Ju X-J et al (2014) A simple strategy for in situ fabrication of a smart hydrogel microvalve within microchannels for thermostatic control. *Lab Chip* 14:2626–2634
- Linder V (2007) Microfluidics at the crossroad with point-of-care diagnostics. *Analyst* 132:1186–1192
- Mathur AM, Moorjani SK, Scranton AB (1996) Methods for synthesis of hydrogel networks: a review. *J Macromol Sci Part C* 36:405–430
- Mura S, Nicolas J, Couvreur P (2013) Stimuli-responsive nanocarriers for drug delivery. *Nat Mater* 12:991–1003
- Nawroth JC, Lee H, Feinberg AW et al (2012) A tissue-engineered jellyfish with biomimetic propulsion. *Nat Biotechnol* 30:792–797
- Niemz A, Ferguson TM, Boyle DS (2011) Point-of-care nucleic acid testing for infectious diseases. *Trends Biotechnol* 29:240–250
- Nuxoll E (2013) BioMEMS in drug delivery. *Adv Drug Deliv Rev* 65:1611–1625
- Park S, Zhang Y, Lin S et al (2011) Advances in microfluidic PCR for point-of-care infectious disease diagnostics. *Biotechnol Adv* 29:830–839
- Paschew G, Körbitz R, Richter A (2013) Multimodal, high-resolution imaging system based on stimuli-responsive polymers. *Advances in Science and Technology*, In, pp 44–49
- Plueddemann EP (2013) Silane coupling agents. Springer Science & Business Media, New York
- Qiu Y, Park K (2012) Environment-sensitive hydrogels for drug delivery. *Adv Drug Deliv Rev* 64 (Suppl):49–60
- Richter A (2009) Hydrogels for Actuators. In: Gerlach G, Arndt K-F (eds) *Hydrogel sensors and actuators*. Springer, Berlin/Heidelberg, pp 221–248
- Richter A, Paschew G (2009) Optoelectrothermic control of highly integrated polymer-based MEMS applied in an artificial skin. *Adv Mater* 21:979–983
- Richter A, Kuckling D, Howitz S et al (2003) Electronically controllable microvalves based on smart hydrogels: magnitudes and potential applications. *J Microelectromech Syst* 12:748–753
- Richter A, Türke A, Pich A (2007) Controlled double-sensitivity of microgels applied to electronically adjustable chemostats. *Adv Mater* 19:1109–1112
- Richter A, Klatt S, Paschew G, Klenke C (2009) Micropumps operated by swelling and shrinking of temperature-sensitive hydrogels. *Lab Chip* 9:613–618
- Rogers JA (2013) A clear advance in soft actuators. *Science* 341:968–969
- Roy D, Brooks WLA, Sumerlin BS (2013) New directions in thermoresponsive polymers. *Chem Soc Rev* 42:7214–7243
- Sekine S, Ido Y, Miyake T et al (2010) Conducting polymer electrodes printed on hydrogel. *J Am Chem Soc* 132:13174–13175
- Sia SK, Kricka LJ (2008) Microfluidics and point-of-care testing. *Lab Chip* 8:1982–1983
- Smela E (2003) Conjugated polymer actuators for biomedical applications. *Adv Mater* 15:481–494
- Smela E, Inganäs O, Lundström I (1995) Controlled folding of micrometer-size structures. *Science* 268:1735–1738
- Suzuki A, Tanaka T (1990) Phase transition in polymer gels induced by visible light. *Nature* 346:345–347
- Tanaka T, Nishio I, Sun S-T, Ueno-Nishio S (1982) Collapse of gels in an electric field. *Science* 218:467–469
- Thompson AM, Paguirigan AL, Kreutz JE et al (2014) Microfluidics for single-cell genetic analysis. *Lab Chip* 14:3135–3142
- Tondu B, Emirkhanian R, Mathé S, Ricard A (2009) A pH-activated artificial muscle using the McKibben-type braided structure. *Sens Actuators Phys* 150:124–130

- Tondu B, Mathé S, Emirkhanian R (2010) Low pH-range control of McKibben polymeric artificial muscles. *Sens Actuators Phys* 159:73–78
- Unger MA, Chou H-P, Thorsen T et al (2000) Monolithic microfabricated valves and pumps by multilayer soft lithography. *Science* 288:113–116
- Voigt A, Greiner R, Allerdifen M et al (2014) Towards computation with microchemomechanical systems. *Int J Found Comput Sci* 25:507–523
- Whitesides GM (2006) The origins and the future of microfluidics. *Nature* 442:368–373
- Xu Y, Lin Z, Huang X et al (2013) Flexible solid-state supercapacitors based on three-dimensional graphene hydrogel films. *ACS Nano* 7:4042–4049
- Yang E-H, Lee C, Mueller J, George T (2004) Leak-tight piezoelectric microvalve for high-pressure gas micropropulsion. *J Microelectromech Syst* 13:799–807
- Zhang D, Guo J (2011) The development and standardization of testing methods for genetically modified organisms and their derived products. *J Integr Plant Biol* 53:539–551
- Zhang Z, Philen M (2011) Review: pressurized artificial muscles. *J Intell Mater Syst Struct* 53:539–551, 1045389X11420592
- Zhang Y, Liu Z, Swaddiwudhipong S et al (2012) pH-sensitive hydrogel for micro-fluidic valve. *J Funct Biomater* 3:464–479
- Ziaie B, Baldi A, Lei M et al (2004) Hard and soft micromachining for BioMEMS: review of techniques and examples of applications in microfluidics and drug delivery. *Adv Drug Deliv Rev* 56:145–172

Polymer Gels as EAPs: How to Start Experimenting with Them

5

Bernhard Ferse, Luis Pedrero, Marcus Tietze, and Andreas Richter

Contents

1	What Are Hydrogels?	103
2	Preparation of Hydrogels	104
2.1	Presynthesis	105
2.2	Synthesis	105
2.3	Postsynthesis	106
3	Basic Material Characterization	107
3.1	Degree of Swelling	107
3.2	Sol–Gel Content	108
3.3	The Phase Transition	109
3.4	Sol–Gel Transition	110
3.5	Swelling Kinetics	114
4	Patterning of Hydrogels	115
4.1	Patterning of Hydrogel Thin Films	116
4.2	Printing Techniques	118
5	Designing Simple Devices	119
5.1	How to Build a Valve Using a Hydrogel	119
5.2	Design Parameters	120
6	Conclusion	122
	References	122

In Memoriam of Prof. Dr. rer. nat. habil. Karl-Friedrich Arndt, Chair of Physical Chemistry of Polymers, TU Dresden

B. Ferse (✉) • L. Pedrero • M. Tietze

Faculty of Electrical and Computer Engineering, Institute of Semiconductors and Microsystems, Technische Universität Dresden, Dresden, Germany

e-mail: Bernhard.Ferse@tu-dresden.de; luis.pedrero@tu-dresden.de; marcus.tietze@tu-dresden.de

A. Richter

Institute of Semiconductors and Microsystems, Faculty of Electrical and Computer Engineering, Dresden University of Technology and Center for Advancing Electronics Dresden, Dresden, Germany

e-mail: andreas.richter7@tu-dresden.de

Abstract

Electromechanically active polymers (EAP) show great potential for many actuator applications. In this context, hydrogels which are also considered as active polymers have shown also actuator and sensor applications due to their volume phase transition. Nevertheless, in the general term of electromechanically active polymers there is not an exact definition about what is an active polymer. Hydrogels can be considered as active polymer materials not only because of their volume phase transition but also due to their electrical and dielectric properties depending on their internal or chemical modification. The most spread definition of hydrogels is that they are soft and wet materials which show very intriguing properties regarding their volume phase transition. Applications of hydrogels are tightly restricted due to their relative mechanical weakness. In the past 10 years a lot of research has been done in the field of modifying the mechanical properties of hydrogels in order to adapt these materials to daily life requirements. They have been used as sensors and actuators in many fields of science and engineering including microfluidics and biomedicine. In this chapter, we briefly present the main properties of hydrogels, some of the methods used to characterize them as well as the principal applications from an engineering and general point of view. This chapter could be used as a general introduction to the topic of hydrogels, more specifically thermal responsive ones, and also represents an opportunity for all those who want to enter to the field of hydrogels.

Keywords

Gel • Polymer • Experiment • Hydrogel • Characterization

Abbreviations

AIBN	Azobisisobutyronitrile
BIS	<i>N,N'</i> -Methylenebisacrylamide
BPO	Benzoyl peroxide
DMIAAm	<i>N, N</i> -Dimethylmaleinimidethylacrylamide
EBL	Electron beam lithography
LCST	Lower critical solution temperature
mTM	Microtransfer molding
NIPAAm	<i>N</i> -Isopropyl acrylamide
PAAm	Poly(acrylic acid)
PEG	Poly(ethylene glycol)
PNIPAAm	Poly(<i>N</i> -isopropyl acrylamide)
PVA	Poly(vinyl alcohol)
PVME	Poly(vinyl methyl ether)
RET	Rubber elasticity theory
UCST	Upper critical solution temperature
UV	Ultraviolet
VPT	Volume phase transition
μCP	μ-Contact printing

Symbols

A	Structure factor (RET)
B	Volume factor (RET)
c	Concentration
d	Diameter of a gel cylinder
D	Diffusion coefficient
D_{coop}	Cooperative diffusion coefficient
F	Helmholtz free energy
G	Gibbs free energy
G'	Storage modulus
G''	Loss modulus
$g^{(1)}(t)$	Electric field correlation function
$g^{(2)}(t)$	Intensity correlation function
m	Mass
n	Number of moles
M	Molecular weight
M_w	Weight average molecular weight
p	Pressure
Q	Degree of swelling
Q_m	Mass degree of swelling
Q_v	Volume degree of swelling
R	Gas constant ($8.314 \text{ J K}^{-1} \text{ mol}^{-1}$)
r	Radius
R_h	Hydrodynamic radius
T	Temperature
t	Decay time
\bar{V}_i	Partial molar volume of component i
V_i	Molar volume of component i
$\langle \rangle$	Time average
$\langle I \rangle_{t,P}$	Total time-averaged scattering intensity at a const. position
Δ	Total change
λ	Wavelength
μ_i	Chemical potential of component i
ρ	Density
τ	Time constant
ν_c	Cross-linking density (mol network chains/volume)
χ	Huggins interaction parameter

1 What Are Hydrogels?

The word gel originate from the Latin *gelo* (to freeze something) or *gelida* (cold water) resulting in the derived word *gelatum* (frozen). A hydrogel absorbs water within its polymer network and consequently it swells. During the swelling process,

Table 1 Classification of gels (Flory 1974)

Flory type gel	Definition
I	Ordered lamellar structures of mesophases
II	Disordered covalent polymer networks
III	Formed gels through physical aggregation, disordered polymer networks containing ordered regions
IV	Particulate, disordered structures

it seems that the stored water “freezes.” In the swollen state, more than 99 % of the gel can consist of the swelling agent, nevertheless it can still elastically keep its predestined shape and geometry.

In 1974, Flory classified the gels in his introduction to the “Faraday discussion on gels and gelation” in four categories, which can in principle be classified into two different classes, namely: covalently cross-linked materials (chemical gels, Flory type II) and gels with noncovalent interactions (physical gels, Flory type I, III, IV) (Flory 1974). In Table 1, a description of the definition of every type of gel is given.

In covalent cross-linked networks, permanent network junctions are formed via chemical bonds. Gels in which chemical bonds exist cannot be dissolved, therefore they are also called irreversible gels. Two methods exist to synthesize polymer networks based on covalent bonds. The cross-linking process can take place immediately during the polymerization (mainly accessible by a free radical polymerization) (Stenekes and Hennink 2000; Singh et al. 2006; Norrish 1937), or after the polymerization the cross-linking follows in a second step, e.g., click chemistry or cycloaddition (Zweifel 1983; Berger and Zweifel 1983; Finter et al. 1984, 1985; Coqueret 1999; Coqueret et al. 1991; Coleman et al. 1998; Chapiro 1962; Charlesby and Alexander 1955; Gaylord and Adler 1963). In contrast, physical gels are formed by physical interactions like hydrogen bonds, ionic interaction, local crystallization, and helix formation (e.g., gelatin) and belong to type III of Flory’s classification (Nijenhuis 2007). The properties of these gels depend on temperature, pH, and solvent changes, so the gelling is a reversible process.

2 Preparation of Hydrogels

In the next section, the synthesis of two types of pH-sensitive hydrogels is discussed in detail. One example is the cross-linking of copolymer of sodium acrylate and *N,N*-methylenebisacrylamide (cross-linking comonomer (BIS)) and the other example, a condensation product of linear poly(acrylic acid) (PAA) and a linear poly(vinyl alcohol) (PVA).

In general, the preparation of hydrogels can be divided into three parts: presynthesis, synthesis, and postsynthesis.

2.1 Presynthesis

The polymerization of monomers offers a huge potential to design gels in different dimensions and geometries. It is possible to obtain thin films, membranes, or patterns via surface coatings and lithography in sizes between some $10 \mu\text{m}^3$ and several 100cm^3 . For later applications, predestined gels can be easily adapted for sensor and actuator technology components.

The required equipment to synthesize them includes precision laboratory balances, standard laboratory equipment, and equipment for working under shielding gas. During the preparation and handling of the polymerization solutions, the use of a glove box is recommended, since the reaction mechanism is strongly influenced by the presence of oxygen.

A precise control technology for the initiation of the polymerization is needed. This is provided by a photoinitiation, which requires the presence of a suitable wavelength light source. Typically, can be used UV short-arc lamps with a power between 300 and 1000 W.

Furthermore, with this method it is possible to pattern hydrogels (Richter and Paschew 2009), which is a prerequisite in microfluidic applications. Therefore, the photopolymerization in the last 20 years has become an increasingly investigated and developed method (Kuckling et al. 2003; Nakayama and Matsuda 1992).

In contrast, the preparation of hydrogels from prepolymers via cross-linking condensation reaction offers a simple method for the preparation of films/membranes and coated surfaces. Here, in addition to the aforementioned laboratory equipment, a spin coater is necessary as well as a cabinet for drying and curing. The use of inert gas techniques is not required, since the underlying reaction is not affected by oxygen.

2.2 Synthesis

Poly(Acrylic Acid)/Poly (Vinyl Alcohol) Gel: The condensing cross-linking of PAA and PVA offers a rapid method for the preparation of pH-sensitive layers of hydrogels for many applications like sensorics (Richter et al. 2004b).

For the preparation of this material, a solution with 15.0 wt% PVA and 7.5 wt% PAA is prepared by dissolving the corresponding quantities in distilled water at $80 \text{ }^\circ\text{C}$ under stirring. The resulting solutions are mixed to a ratio of PVA/PAA 4:1 and are further stirred for 1 h at $60 \text{ }^\circ\text{C}$. Then the solution is diluted for a better processability to 5 wt% of the total dissolved polymer mass. This solution can be directly processed after filtration, e.g., with a spin coater. The produced coatings are dried at $45 \text{ }^\circ\text{C}$ for 1 h and are subsequently cured at $130 \text{ }^\circ\text{C}$ for 30 min. Finally, an extraction step for removal of non-cross-linked polymer components from the gel should be done. Longer cure times result in hard gels with low degrees of swelling. Depending on the molecular weights of the used prepolymers, the cure time can vary. Reheating the extracted gel layers to temperatures above $100 \text{ }^\circ\text{C}$ leads to a further cross-linking.

Photoinitiated Free Radical Polymerization of Sodium Acrylate: This manufacturing process provides a huge variation of the produced gel geometries. Besides the production of films, the preparation of patterned gel particles is also possible. The preparation starts from a monomer solution with a concentration of 1.25 mol/l sodium acrylate. To the solution were added 1–1.5 mol% of the photoinitiator (Irgacure[®] 2959), based on the molar amount of the monomer. To prepare homogeneous gels with reproducible properties, the exclusion of oxygen is essential, since oxygen is able to act on the polymerization reaction and trigger premature polymerization, leading to the termination of the polymerization.

In addition to the previous process, in a round-bottom flask an accurately weighed quantity of the cross-linking agent (BIS) is filled and diluted in the appropriate volume of distilled water. The solution is degassed for 30 min with argon to remove oxygen. Subsequently, the exact weighed mass of photoinitiator is transferred in the flask in absence of oxygen. For this purpose the synthesis is carried out in an argon glove box. The present solution is sensitive to light; therefore the flask should be covered with aluminum foil. To dissolve the photoinitiator, the solution must be stirred again for about 10 min. Now, this solution can be exposed to an appropriate source of light. Again, special attention must be paid to the absence of oxygen in order to obtain reproducible results. The negative influence of oxygen on the reaction increases with increasing miniaturization of the hydrogel (reduction of the reaction volume).

Previous experiments on a 1000 W UV-lamp (50 mW/cm² at 365 nm) (Greiner et al. 2012) have shown that the cooling of the polymerization reaction by an ice bath has a beneficial effect. Typically, polymerization of 2–7 min is required depending on the size structure of the photomask. In general, the smaller the feature size the longer the structure that needs to be exposed.

To finish the polymerization process, an extraction step needs to be done in order to remove the unreacted monomer, cross-linker, and photoinitiator from the system. This is necessary; otherwise the photoinitiator could still react for a certain amount of time and so lead to unwanted material properties.

2.3 Postsynthesis

Finally, the prepared gels need to be conditioned in order to extract the hydrogels from low molecular and unreacted substances. For this purpose, the hydrogel will be subjected to multiple swell/deswell cycles. Ideally, a Soxhlet extraction is useful. After conditioning the gels possess a higher degree of swelling, than in the preparation state due to the orientation of the network chains. Gels which respond to pH values are alternately submerged in solutions having a pH below 3 and above 9. Now to end the process, the gels can be extracted, leaved in distilled water, and then stored wet or dried again.

3 Basic Material Characterization

Before using the synthesized hydrogels, some basic characterization of the hydrogels is necessary. The precise information about the swelling behavior (swelling degree, phase transition, swelling kinetics) as well as the sol–gel transition (gelation threshold, gel point) gives evidences to the mechanical properties and performance of hydrogels. The structure-properties relationship is an important key factor to design hydrogels with defined properties for later applications.

3.1 Degree of Swelling

The degree of swelling is one of the characteristic parameters of hydrogels. It depends on cross-linking density, charge density, and polymer concentration after the gel preparation. The driving force for water absorption during the swelling is the difference between the chemical potentials of the solvent in the inner and outer polymeric phase. The chemical potential μ_i of a component i under a constant temperature T , pressure p , and a constant mole number n_j is defined as follows:

$$d\mu_i = \left(\frac{\partial G}{\partial n_i} \right)_{T, p, n_{j \neq i}} \quad (1)$$

where the Gibbs free energy G of a two-component system is given by (Thiel et al. 1995; Quesada-Perez et al. 2011)

$$G = f(T, p, n_1, n_2). \quad (2)$$

The indices 1 and 2 denote the solvent and polymer, respectively.

The volume expansion as a result of the swelling is restricted by the deformation of the network chains. The swelling of a gel is then characterized by two opposing effects: (i) the absorption of the swelling agent into the polymer network due to solvent-polymer interactions (mixing term) (Huggins 1941, 1943) and (ii) the reduction of the entropy (entropy elasticity) of the network chains resulting from the expansion of the network due to the swelling (elastic deformation term) (Flory 1944; Flory and Rehner 1943a, b). The whole change of the chemical potential of the solvent during the swelling process is characterized as a function of polymer concentration and is well described by the Flory-Rehner equation (Flory 1953).

$$\Delta\mu_1 = RT \left[\underbrace{\ln(1 - \phi_2) + \phi_2 + \chi\phi_2^2}_{\text{mixing term } (\Delta\mu_{mix})} + \underbrace{v_c V_1 (A\eta\phi_2^{\frac{1}{3}} - B\phi_2)}_{\text{elastic term } (\Delta\mu_{el})} \right] \quad (3)$$

where ϕ_2 is the volume fraction of the polymer, χ the Huggins interaction parameter, A the structure factor, B the volume factor, η the memory term, V_1 the partial molar volume of the solvent, and ν_c the cross-linking density. The factors of A , B , and η are available from the phantom network model (Arndt et al. 2009).

At the equilibrated degree of swelling we have $\Delta\mu_1 = 0$. With increasing cross-linking density ν_c the degree of swelling $Q_V = 1/\phi_2$ decreases. The increase in polymer concentration leads also to a decrease in the degree of swelling.

Hooper et al. (1990) have shown on the basis of polyacrylamide hydrogels that with increasing the cross-linker concentration or increasing monomer concentration, the degree of swelling of hydrogels decreases due to the increasing density of the cross-linking junctions and the associated increase in the rigidity of the polymer network. Furthermore, with increasing hydrophilicity of the monomers, the tendency to absorb water into the network also increases (Thiel et al. 1995), due to a change of polymer-solvent interactions represented by the χ -parameter.

By microscopic measurements of the degree of swelling (Flory-Rehner theory) or rather by compression measurements (rubber elasticity theory (RET)) the network parameters, such as cross-linking density or the molecular weight of network chains M_c can also be determined ($\nu_c = \rho_2/M_c$) (Flory et al. 1976; James and Guth 1943; Wall 1942, 1943, 1951; Hermans 1947).

The degree of swelling can be expressed as volume Q_V or mass degree of swelling Q_m . Hence, Q_m is defined by the total mass of the swelling agent related to the mass of the dried gel (Eckert 2003).

$$Q_m = \frac{(m_s - m_d)}{m_d} \quad (4)$$

For a cylindrical thin gel, the degree of swelling (V/V_0) can be described by the ratio between the diameters of the cylinder in the swollen d to the deswollen state d_0 .

$$Q_V = \frac{V}{V_0} = \left(\frac{d}{d_0}\right)^3 \quad (5)$$

Both degrees of swelling can be converted into each other by the next relation, using the density ρ of polymer and solvent.

$$Q_V = 1 + (Q_m - 1) \frac{\rho_0}{\rho_{\text{solvent}}} \quad (6)$$

3.2 Sol-Gel Content

Cross-linked polymers usually contain a quantity of monomer molecules (or polymer molecules) that are not connected to the network. These molecules are soluble and represent the soluble fraction of the network. The sol fraction provides information in how far the gelation has progressed. The more the sol fraction is

present the smaller the cross-linking, and this directly influence the mechanical properties of the gels.

Furthermore, the sol fraction must be completely removed for a precise characterization of the network parameters of the gels. Otherwise the estimation of the parameters could be not accurately estimated. The sol fraction can be calculated as follows (Eckert 2008):

$$s[\%] = \left(1 - \frac{m_{\text{extracted}}}{m_{\text{non-extracted}}} \right) \cdot 100 \quad (7)$$

3.3 The Phase Transition

Since the first observation and investigation of phase transitions of swollen hydrogels by Tanaka in 1978 (Tanaka 1978), a large number of such systems have been analyzed and interpreted, especially regarding their physicochemical interrelations.

Studies of the swelling behavior of hydrogels must take into account many parameters. A differentiated view of ionic and nonionic hydrogels as well as of the swelling behavior of hydrogels in pure water or in aqueous solutions is important.

Some hydrogels exhibit a phase transition induced by external stimuli. Dušek and Patterson predicted this phase transition after evaluating the Flory-Rehner theory (Dušek and Patterson 1968). However, it was not until another 10 years had passed, before T. Tanaka (1978) added a critical amount of an organic solvent to a water-swollen polyacrylamide gel inducing a collapse of the gel, which was observed for the first time. That is what we know today as an externally induced volume phase transition.

In temperature-sensitive hydrogels, an increase of temperature results in a discontinuous change of volume. In this case, the swelling agent is released from the hydrogel to form a separate phase. This property is called “thermo-responsive.” Based on poly(*N*-isopropyl acrylamide) (PNIPAAm) hydrogels in pure water, Hirokawa and Tanaka (1984) showed that a phase transition occurs at about 33 °C. In this process, a contraction in volume of 80 % of the gel is observed. With further increase of the temperature, no another strong volume changes are detectable. When comparing the collapse of the gel induced by a temperature change with the phase separation of simple chain polymers, a direct correlation can be immediately deduced. Thus, PNIPAAm solutions have a lower critical solution temperature (LCST) of approximately 31 °C (Schild 1992). The end-to-end distance of the macromolecules in an infinitely dilute solution decreases dramatically at this temperature (Beltran et al. 1990). At this point, a separation between the polymer and the solution occurs.

For a large number of polymers, the conditions for a LCST behavior are given. This includes polymers containing ether groups, such as poly(vinyl methyl ether), polymers with alcohol groups, like hydroxypropyl cellulose, and polymers

containing substituted amide groups as poly(*N*-isopropylacrylamide). Also known are polymers which show a separation into two different phases when falling below a critical temperature. This UCST behavior (upper critical solution temperature) was observed, for example, in poly[3-(*N*-(3-methacrylamidopropyl)-*N,N'*-dimethyl ammonium propane sulfonate)] (Kretschmer 2005; Chen and Hoffman 1995).

The phase separation in thermoresponsive polymers in aqueous solution is caused by a delicate balance between the hydrophilic and hydrophobic groups in the polymer (Salgado-Rodríguez et al. 2004). This process of phase separation (LCST behavior) is driven by entropy. By heating the system, the largest share (exchange) of the free energy of mixing is spent (used) for the destruction of hydrogen bonds between solvent and polymer. These hydrogen bonds are formed between the solvent molecules and the “moderately hydrophilic” side groups of the polymer. Increasing the temperature leads to increasing interactions, which partially destroy the structuring of water and thus cause a destabilization of the hydrophobic side chains in the aqueous solution (Kretschmer 2005).

The phase transition point for temperature-responsive or pH-responsive hydrogels or in general for polymers exhibiting a volume phase transition is one of the basic variables in the network characterization. The volume phase transition (VPT) of temperature-responsive hydrogels may vary depending on the nature of the cross-linker or the addition of comonomers, as they both change the balance between polymer and solvent (which is a function of the Flory-Huggins χ -parameters). Qualitatively, the higher the hydrophobicity of the polymer the lower the LCST (Kuckling et al. 2012).

Adding organic solvents into hydrogels can also change the LCST. For example, in PNIPAAm gels the temperature of the phase transition is reduced dramatically below room temperature by a water-ethanol ratio of approx. 50:50. Hence, at room temperature the hydrogels are in an unswollen state (Kuckling et al. 2009).

The VPT of gels can be determined by measuring degree of swelling as a function of the external stimulus (e.g., *T*, pH). The inflection point of the curve (shrinking process vs. stimulus) is considered as transition point.

Furthermore, assuming a first-order phase transition, the VPT can be detected by caloric methods. With a differential scanning calorimetry (DSC) measurement, the heat change, which provides information about the internal free energy or latent heat, can be determined (Otake et al. 1990; Hirotsu 1993, 1994). Figure 1 shows two curves of the DSC method for PNIPAAm with different cross-linking concentrations. The cross-linker used for this case was layered silicates (Haraguchi et al. 2002; Ferse 2007).

3.4 Sol–Gel Transition

The sol–gel transition is one of the critical phenomena of polymers (Winter and Mours 1997; Stauffer 1998; Stauffer et al. 1982; Adam and Lairez 1996; Adam et al. 1987; Dastidar et al. 2005; Hecht and Geißler 1987; Munch et al. 1983). In order to observe the progress of the reaction during gelation, it is of great importance to

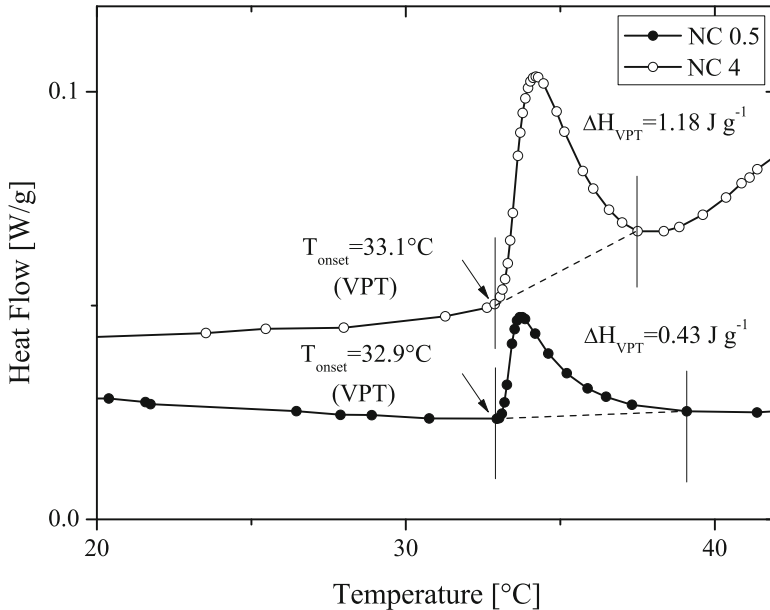


Fig. 1 Specific heat measurements of PNIPAAm gels with two different cross-linking concentrations ratios (Ferse 2007). The temperature of the VPT was recorded at the onset of the peak. The results are from PNIPAAm-nanocomposite hydrogels consisting of 0.5 mol% (NC0.5) and 4.0 mol% (NC4) clay (Laponite), respectively

identify the gel point (Ferse et al. 2008). The control of mechanical properties depends on the knowledge of this point. At the gel point, an infinitely large molecule is formed. The resulting gel at the gel point is a self-similar distribution of fractal areas of all sizes, from a monomer to a first infinitely large cluster.

The cross-linking of macromolecules is associated with a change in the mobility of the network chains. This can be observed by the *dynamic light scattering* (DLS) technique, which is a nondestructive method to monitor the formation of network structures. Current research focuses on the study of the gelation of polymers in order to understand the mechanisms during cross-linking (Shibayama 2012). When the gelation process is characterized applying DLS, the gel point is particularly important. At this point, the weight average molecular weight (M_w) diverges and can be taken as $M_w \rightarrow \infty$ (see Fig. 4). The investigation of the polymer solution until reaching the gel point leads to a better understanding of the network structure, e.g., cluster formation, secondary reactions. Especially secondary reactions cause network defects which influence the mechanical properties of the gels.

The appearing of spatial inhomogeneities in the network structure plays an important role for investigations of the gelation process by DLS. Shibayama and Norisuye (2002) showed that four types of network spatial inhomogeneities exist in the gel (Fig. 2). The largest contribution of the “heterodyne scattering” (total scattering displacement of the network obtained from DLS measurements) derives

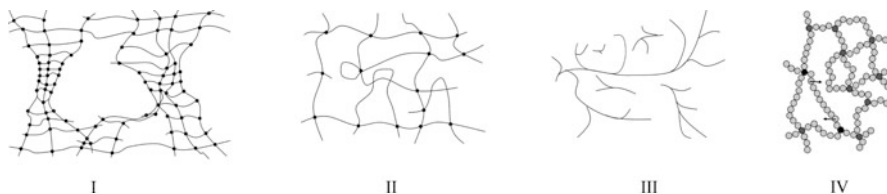


Fig. 2 Schematic representation of the spatial inhomogeneities, (I) spatial inhomogeneities, (II) topological inhomogeneities, (III) connectivity inhomogeneities, and (IV) mobility inhomogeneities. (Adapted with permission from Shibayama and Norisuye 2002)

from the network defects, which describe the spatial differences in network density. The topological inhomogeneities directly result from the defects in the network, such as entanglements or loose chain ends. They also influence the swelling behavior of the gels. At the gel point, irregular linkages play an important factor in the polymer architecture. They are related to the size of the cluster distribution just prior to gelation point. They influence the movements inside the gel and finally lead to local differences of the polymer movement due to the formation of cross-linking points, also referred to as mobility heterogeneities. They are also the reason for the occurrence of strong fluctuations in scattering intensity, the so-called speckle patterns.

When the gel point is reached, the slow modes dominate and a power law of the autocorrelation function is obtained:

$$g^{(2)}(t) - 1 = \frac{\langle I(0)I(t) \rangle}{I^2} \propto t^{-\mu}, \quad (8)$$

where $0.9 \leq \mu \leq 0.19$. (Geissler 1993; Boyko and Richter 2004; Ferse et al. 2007). Here $\langle I(t) \rangle$ is the scattering intensity at a time t with respect to $t = 0$ and $\langle \dots \rangle$ denotes a time average. When approaching the gel point, the slow modes become dominant and a power-law function appears (Norisuye et al. 1998). The power-law behavior, which has no characteristic relaxation time, is self-similar. The incipient gel is a self-similar (fractal) distribution of fractal clusters of all sizes, from monomer to the infinite cluster. For many gelling systems, a clear power-law behavior in the time-intensity correlation function at the gelation threshold has been reported (Geissler 1993; Boyko and Richter 2004; Ferse et al. 2007).

Previous publications (Shibayama and Norisuye 2002; Shibayama 2006) have shown that four methods of dynamic light scattering (DLS) are applicable for the determination of the gelation threshold: (i) the change in the scattered intensity (occurrence of speckle patterns), (ii) the power-law behavior in the time-intensity correlation function (TCF), (iii) a characteristic broadening of the decay time distribution function, and (iv) the suppression of the initial amplitude of the TCF. Each of these methods is a phenomenon based on the characteristic features of gels, i.e., (i) inhomogeneity, (ii, iii) connectivity divergence, and (iv) nonergodicity. In DLS at the gelation threshold a “power-law behavior” for the TCF is revealed (Ngai et al. 2004; Richter 2007).

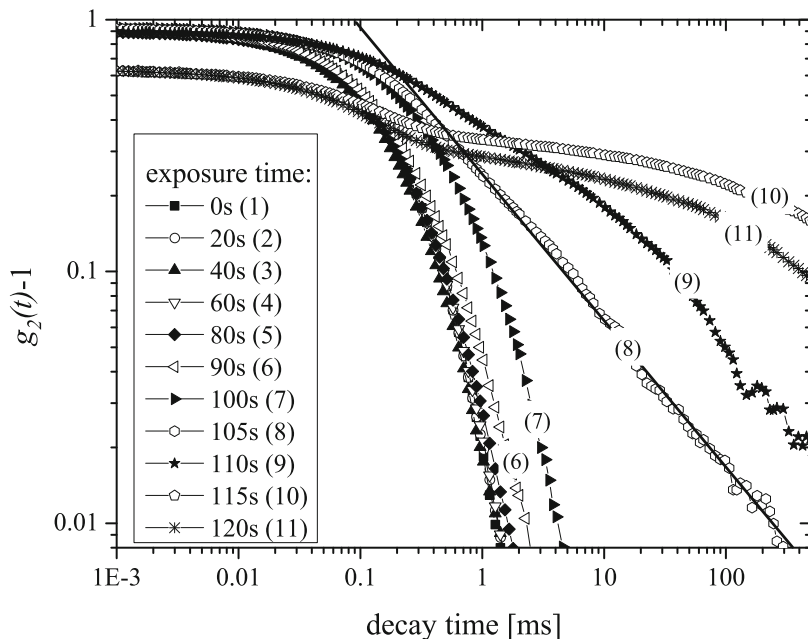


Fig. 3 TCFs of the photopolymerizing nanocomposite system obtained at different exposure times with a power density of 5 mW/cm^2 . At an exposure time of 105 s the gel point can be observed with a characteristic power law (Reprinted with permission from Ferse et al. 2008. Copyright 2015 American Chemical Society)

The results in Fig. 3 (Ferse et al. 2008) show time correlation functions of a photo initiated polymerization of NIPAAm using layered silicates as cross-linkers. A typical sol–gel transition can be seen in the TCFs. The gelation threshold (the gel point) is observed at an exposure time of 105 s. A linear fit of the correlation function can be obtained in the range between 0.3 ms and 100 ms, with an exponent (from Eq. 8) of the power law $\mu = 0.5 \text{ ms}$. At higher exposure times a relaxation (typically for normal gels) at $t = 0.5 \text{ ms}$ is observed; this is due to movements in the internal network.

By simple sol–gel analysis, it was possible to detect the gel point macroscopically. The results in Fig. 4 show a perfect match with the values determined by dynamic light scattering. The gel point is again found at an exposure time of approximately 105 s. At this point the viscosity increases dramatically and the sol content w_{sol} decreases continuously. After almost 110 s exposure time, a mechanically stable gel is completely obtained. The average molecular weight M_w (determined by static light scattering) becomes infinite at the gel point (see previous section and ► Chap. 4, “Polymer Gels as EAPs: Applications,” Elstner M, Richter A).

By performing rheology experiments at the gel point, important observations also can be made. Here, similar results to those produced with DLS can be obtained.

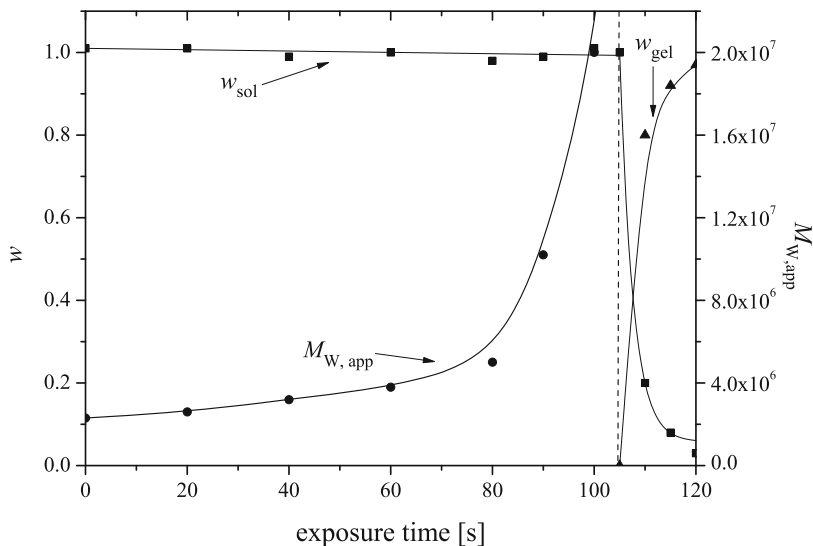


Fig. 4 Sol–gel analysis of a photopolymerized nanocomposite hydrogel. The gel point is observed at an exposure time of 105 s (Reprinted with permission from Ferse et al. 2008. Copyright 2015 America Chemical Society)

For this reason, in some cases the dynamic light scattering is also referred to micro-rheology experiment.

In 1997, Winter and Mours (1997) were the first ones to discover a behavior according to the power law at the gel point for the storage modulus G' and the loss modulus G'' over a wide frequency spectrum. This behavior can be calculated with the following equation:

$$G'(\omega) \propto G''(\omega) \propto \omega^n \text{ with } 0 < n < 1 \quad (9)$$

$$\frac{G''(\omega)}{G'(\omega)} = \tan \delta = \tan \left(\frac{n\pi}{2} \right) \quad (10)$$

3.5 Swelling Kinetics

One of the main and most usable properties of the polymeric networks is the ability to absorb and swell solvents (Shibayama and Norisuye 2002). Many applications of hydrogels as sensors or actuators are based on the change in their degree of swelling. Therefore, it is important to know the characteristic times that hydrogels need in order to respond to changes on the environmental conditions. This time can be identified from the diffusion coefficient of the solvent.

The swelling process can be described as a diffusion of different species. By swelling, a solvent has to diffuse into the polymer network while the polymer chains expand.

To obtain characteristic factors of swelling and deswelling process there are a huge number of techniques. For simplicity usually the determination of the degree of swelling is done as a function of a physical quantity like time or temperature. In this way, it is possible to measure the dimension of a defined gel by optical methods or by weighing the mass during the swelling (Tanaka et al. 1973; Tanaka and Fillmore 1979; Li and Tanaka 1990; Peters and Candau 1986).

Due to the cooperative properties of the network chains, the swelling process of gels is very different from the diffusion process of gases and liquids. In 1973, Tanaka, Hocker, and Benedek formulated the general equation of motion for polymer networks (THB theory) (Tanaka et al. 1973). They realized that the polymer chains are connected by chemical bonds and a gel has to be treated as a continuum. In addition, the network behaves as an assembly of springs due to their entropy elasticity.

With this theory the cooperative diffusion coefficient D_{coop} of the hydrogel can be estimated, which is an important parameter to define the swell kinetics. This parameter is extensively explained by Arndt et al. (2009). In ► [Chap. 4, “Polymer Gels as EAPs: Applications,”](#) a more detailed introduction to this topic is presented (See ► [Chap. 1, “Polymer Gels as EAPs: Fundamentals,”](#) Voigt A).

4 Patterning of Hydrogels

The most used patterning techniques can be in general divided into at least four categories, such as photolithography, direct writing techniques, printing techniques, and particle beam lithography. Usually the technique is associated directly with the degree of complexity of the pattern, as well as the dimensions of the required pattern. Another factor is the functionalization of the pattern. But sometimes the requirement to reduce the pattern size down to the nano- and micrometer scale is what defines the technique to use. This is obviously directly related to the used material and substrate.

The patterning of hydrogels is not a new concept and has been applied over the last 10 years to volumetric as well as thin films, the last one being the most important since many applications in sensors and actuators are based on this form. For many applications, in situ photopolymerization and photo cross-linking using UV light in the liquid phase are the most used. An alternative approach is to cross-link a prefabricated dry film of the sensitive polymer.

A variety of techniques allows the patterning of polymers, see [Table 2](#). Particularly interesting phenomena in the nanometer regime, including electronic processes like the “quantum size effect,” the Coulomb blockade, and the tunneling of single electrons, have grown the interest in the nanostructuring of polymers. Also another feature is that the response times of hydrogels can be reduced to seconds or less by reducing their dimensions. This allows for using them in many different applications, like sensors and MEMS. It is known that micro- and nanosized smart

Table 2 Selection of the most used patterning techniques

Patterning technique	Applications	Definition/ resolution
Ink-jet printing (Barry et al. 2009; de Gans et al. 2004)	Sensors, actuators, and electronic devices	10 μm
Photo cross-linking (Ebara et al. 2003; Bae and Okano 1990; Feil et al. 1993)	Diverse applications	10 nm
Imprinting lithographic techniques (Gale 1997)	Electronics and microfluidics devices	25 nm
Microcontact printing (Kaneko et al. 1998) (μCP) (Xia and Whitesides 1998)	Surface functionalization in preparation for printing, sensorics	35–5000 nm
Electron beam lithography (Lercel et al. 1993)	Electronics, microfluidics	1–75 nm
Dip-pen nanolithography (Tsuda et al. 2005; Wouters and Schubert 2003, 2004)	Automatic fluidic valves	10 nm

hydrogels have been produced in order to build such devices (Richter 2006). This is usually done by means of patterning hydrogel thin films or layers.

4.1 Patterning of Hydrogel Thin Films

To structure thin films or layers of different sensitive polymer hydrogels we have several options to choose. Well-known methods are electron beam lithography or the photo cross-linking irradiation through masks. Here, masks, which contain the information of the desired structure, are laid on the polymer layer. The covered areas of the layer are not irradiated and therefore cannot form networks and adhere to the substrate. These areas can be easily removed with a suitable solvent after irradiation. On the substrate, the negative image of the mask remains as a cross-linked polymeric layer. The use of masks is particularly important for structures in the millimeter and micron regime, see Fig. 5 (Paschew 2006; Guenther et al. 2008). For patterning on the nanometer scale, the electron beam lithography is mostly used (Schmidt et al. 2006). With this technique a direct writing in the polymeric layer is possible due to a cross-linking of the irradiated polymers.

To get an insight into the production methods, the application, and the magnitude of the generated structures, we will describe in the following sections the most important techniques to pattern hydrogels and polymer gels in general. Table 2 shows the main patterning techniques on used hydrogels.

In the field of hydrogels, several works have been published in the last years (Ward et al. 2001; Singh et al. 2006; Ito 1999; Suzuki et al. 2000; Chen et al. 1998a, b; Bhatia et al. 1997; Mönch et al. 2011) in which several types of irradiation have been used. Among them two important radiation sources are the most used: the UV-photolithography and the electron beam lithography.

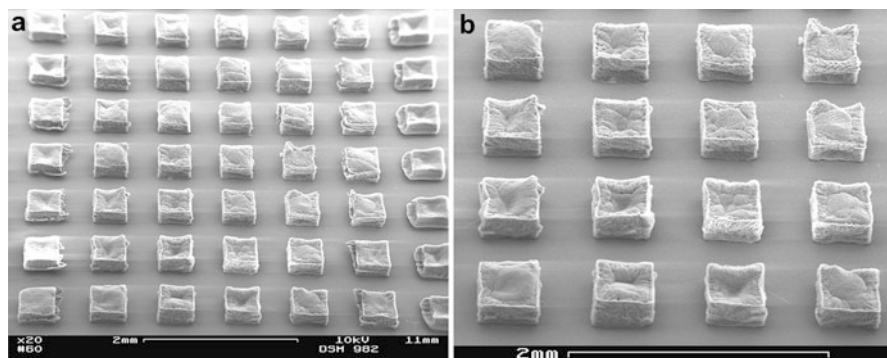


Fig. 5 Hydrogel patterns produced (dry state) by UV photopolymerization (50 mW/cm^2) (Paschew 2006). The right-hand picture is an enlarged image of the original one (*left side*)

Photolithography: Photolithography consists of transferring geometric shapes on a mask to a light sensitive surface. Since 1959, this is the most important fabrication technique in the semiconductor industry to produce integrated circuits (Lang 1996; Nuzzo 2001; Suzuki et al. 2000). The photolithographic techniques are based on a projector system, wherein the image of a mask is reduced by a system of optical lenses and projected onto the surface. In this technique, light sensitive materials are used as resist materials, which have the property to disintegrate or cross-link. The not irradiated material is usually removed and in this case we speak about a negative resist. If the irradiated material is disintegrated, we speak about a positive resist-based lithography.

Lithography is the most studied method since the microelectronic industry fabricates silicon-based transistors. This can be achieved with several types of light sources, including UV–vis light and X-ray (electron and ion beam). These sources with the appropriated photomask can generate patterns with a resolution varying from micrometers to 100 nm (see Fig. 5) (Paschew 2006). Photolithography offers many advantages, but the cost of the equipment and infrastructure despite recent developments is still relatively high. Therefore new approach and techniques are needed in order to produce high quality nanostructures. Very recently Li et al. (2014) have developed a new method of lithography which, using the proximity effect and using synthetic nanomotors and Janus particles, was able to produce nanopatterns. They use the well-defined nanomotors trajectories (metallic nanowires motors) over the surface features as mobile nanomasks and Janus sphere motors as near-field nanolenses to manipulate light beams for generating a myriad of nanoscale features through modular nanomotor design. This new approach is obviously not suitable for large-area photolithography, nevertheless could be used to produce structures in the subnanometric regime.

Electron beam lithography: This technique was developed soon after the development of scanning electron microscopy in 1955 and offers an attractive alternative to the X-ray and UV-lithography (Schmidt et al. 2006; Guillen et al. 1994). Electron beam lithography (EBL) offers higher patterning resolution since the

electron beam can be readily focused to a diameter of approximately 1 nm. Electron beam lithography is intensively used in both resist-based and chemical approaches.

4.2 Printing Techniques

Printing techniques are also very popular and are also considered as a novel process to patterning hydrogels. We can distinguish between different approaches such as micromolding in capillaries (MIMIC) (Kim et al. 1995), microtransfer molding (mTM) (Zhao et al. 1996), and microcontact printing (μ CP) (Perl et al. 2009). The last two ones are considered as stamping methods which involve the direct patterning or the deposition of the ink molecule on the substrate using elastomeric material. Due to its simplicity and cost-effective, microcontact printing is nowadays the most used and efficient method for the generation of patterns in hydrogels; with this technique we can achieve structures with dimension above 100 nm (Huck 2007).

4.2.1 Microcontact Printing

One of the principal advantages of the microcontact printing technique is that you can pattern large-area surfaces (planar and curved) in an efficient way. The second great advantage of this technique is that a large variety of “ink molecules” can be deposited. The operation principle of the technique is quite simple and very similar to printing ink on paper with a rubber stamp. Usually the poly(dimethylsiloxane) (PDMS) is used as a stamp, this material, which is considered to be the conventional stamp material in soft lithography, has shown great performance in micrometer-scale processes (Kelby and Huck 2010). This is impregnated with a solution of “ink molecules,” after which it is placed in contact with the substrate. The μ CP approach requires a stamp that can make direct molecular contact with the metal and an ink that can bind sufficiently strongly to the metal (Huang et al. 2012). To produce topographically-patterned surfaces, μ CP can be used to directly print the initiator or print a noninitiating derivative and then backfill with initiator precursors.

4.2.2 Ink-Jet Printing

Ink-jet has shown a great potential in the last years as one of the most versatile and attractive deposition techniques for patterning polymers and inorganic particles. It has become the most used technique for many industrial and scientific applications, like chemical and gas sensors among others (Chang et al. 2004, 2005; de Gans et al. 2004; Pierik et al. 2008; Barry et al. 2009; Chang et al. 2010; Fujie et al. 2012). The method is the same as ink-jet-type printers on paper, as it delivers the exact amount of the materials on demand in a form of droplets of fluids on the desired surfaces. Nowadays ink-jet-type polymer printers can deliver between 2,000 up to 13,000 in. droplets in a second. They use capillary nozzles, which can be controlled by piezoelectric mechanisms.

5 Designing Simple Devices

The macroscopic properties of hydrogels (elasticity, volume in swollen state) can be used to design sensors and other smart devices like actuators. In the past section we learned a few of the principal techniques to synthesize smart gels and also different techniques to pattern and functionalize hydrogels in a broad range of dimensions. These macroscopic properties can be seen as the key feature to design devices. In the next section we will design a simple valve taking into account some of the properties of hydrogels.

5.1 How to Build a Valve Using a Hydrogel

There are many ways to design a valve with hydrogels, and in principle this can be done with or without extra elements. Usually the hydrogel or active sensor material is placed inside a chamber, which is entrapped in a cage. We can therefore divide our design process into two different categories: (a) in which the active material is part of the closing process and (b) in which the force produced by the swelling of the hydrogels is used to activate an extra mechanism. For the first case, the process medium flow surrounds the hydrogel. The cage or chamber encloses the hydrogel, and an increase of the hydrogel volume in the xy -plane will result in the occlusion of the channel. This approach is more suitable for chemosensors, where the hydrogel is surrounded by the element. For case (b) usually the use of a membrane is very convenient since the separation between control flow and the signal flow allows the use of other external stimuli. Nevertheless, for temperature-sensitive hydrogels both approaches are convenient. For the latter case, the deflection of the thin elastic membrane push another mechanism (like a piston or a metallic valve) which will produce an occlusion of the channel and the close condition is fulfilled. For both cases, the valve type needs to be designed according to its application (pH sensitive valve, or temperature sensitive valve).

The above Fig. 6 (Allerdissen et al. 2012; Greiner et al. 2012; Klatt et al. 2012) represent a simple design for the case (a). In this case, the hydrogel is surrounded by

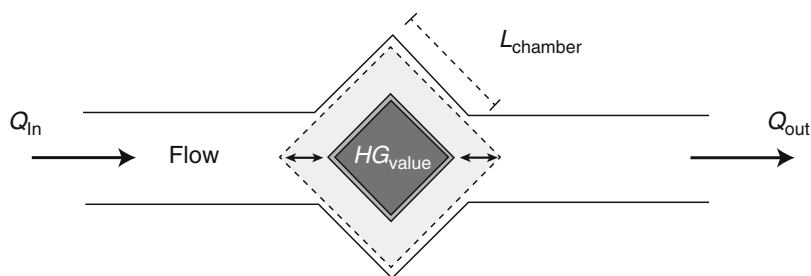


Fig. 6 Schematic design of an automatic hydrogel-based valve. The hydrogel is located on the actuator chamber. The hydrogel will swell and consequently fill the inner chamber closing the liquid flow (normally open condition)

the medium in which the temperature of the flow medium or the chemical diluted in the flow is the control signal (solvent). When the hydrogels start to swell, the volume in the chamber is occupied and the flow is limited. This valve type works as a normally closed valve, since we use the LCST phase transition of the hydrogel. Other more complex designs use a bypass, in such a way that the hydrogel works as an actuator in an automatic mode and the bypass to the source of the process medium is established. In the open state, the process medium is passing the actuator chamber, in the closed state; the solvent can flow back to the inlet using the bypass. This design guarantees a continuous and local stimulus at the hydrogel actuator.

An important parameter to consider is the actuation of the hydrogel on the valve seat as well as the size of the hydrogel components, including the decision whether we use bulk or small hydrogels microparticles enclosed in a chamber. This factor plays an important role in the performance of the device and will be briefly explored in the next section.

5.2 Design Parameters

The focus is the hydrogel component, which has to be optimized in its functional and time behavior. In principle the higher the component the larger the change of swelling and thus the larger its “sensitivity.” In reality, a compromise between design, fabrication, and function have to be found. The swelling behavior of the hydrogel should be carefully analyzed and the actuation design limited to the linear response regime of the hydrogel OP_1 and not where the hydrogel swelling is already in saturation OP_2 ; this can be better understood in Fig. 7.

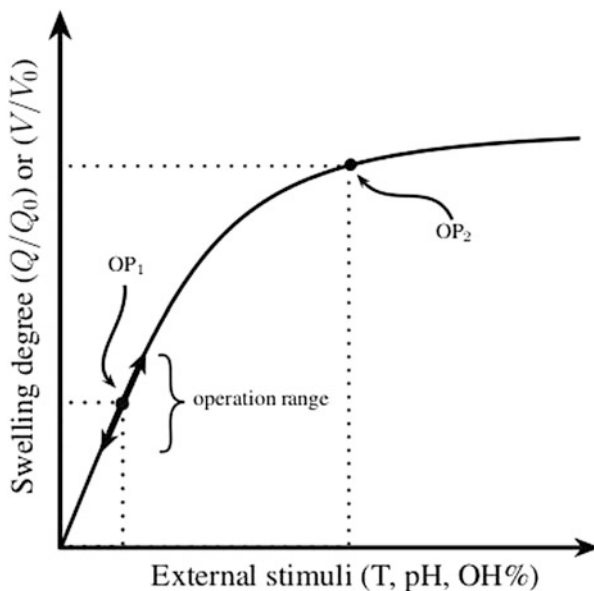
In this way, we ensure a rapid response of the valve. The characteristic dimension of the hydrogel element has strong influence on the time behavior of the sensor. As expressed in Sect. 3.5 the time constant of the swelling process considering a cylindrical hydrogel structure can be expressed in terms of the internal microscopic constant of the hydrogels as (Tanaka and Fillmore 1979):

$$t \sim d^2 / D_{coop} \quad (11)$$

which depends on the square of d , which is the radius of a cylindrical hydrogel structure and D_{coop} which is the cooperative diffusion coefficient. It is also possible for the case (b) to use small particles of hydrogels. They have the property to swell faster than hydrogels in bulk state. The diameter of the particles in the dry state can vary between $(400 \pm 100) \mu\text{m}$. In that case, the effective d corresponds to the radii of the particles (Richter 2009; Richter et al. 2003, 2004b, 2007a, 2009). Indeed the response time of the ethanol sensor is in the range of 20–30 min. This should be fast enough for most applications, since change in concentration is a low dynamic process.

For the case in which valves or sensors use a thin membrane, it is important to consider as a parameter the counterpressure of the elastic detectable membrane. This pressure depends on the thickness of the membrane and on its Young modulus (Y).

Fig. 7 Schematic description of the swelling process of a hydrogel versus an arbitrary external parameter



Compared to the Young modulus of the swollen hydrogel of 10 kPa, this is relatively small and therefore does not affect significantly by the hydrogel swelling. However, small differences between the swelling and shrinking times can be found, and these usually are attributed to the microscopic parameters (elasticity, D_{coop} , Young's modulus) and cannot be addressed to the membrane effect. Generally, a compromise must be found between the robustness of the sensor, which increases with a more robust membrane, and the increasing counterpressure, which can decrease the amplitude of swelling and thus decrease the sensitivity of the hydrogel component.

In principle, in order to design functional hydrogel valves not only the material parameters have to be considered but also the design and the operational parameter. This will play an important role on the fabrication and working of the valve. In the next section, we will only comment the most important points on these three parameters.

The main characteristic of the valve will be strongly influenced by the properties of the actuator material, which will directly influence the switching performance of hydrogel-based valves. These material parameters are intrinsic of the hydrogels, and the swelling behavior is strongly dependent on them. The swelling process is a controlled diffusion process, therefore the switching time is mainly determined by the characteristic size of the actuator. For the case of thermal sensitive hydrogels like PNIPAAm, the thickness of the hydrogel film and in case of particles its diameter will determine how easily the thermal flow will actuate on the hydrogel, driven near thermal phase transition. Nevertheless, the phase transition can be also modified by the concentration of certain reactive groups inside the hydrogel. This, as seen in the beginning of the chapter, will affect significantly the swelling kinetics. The filling

degree of actuator chamber (vol-%) or packing factor also plays a major role on the switching performance of the valve. This parameter is usually considered as a design parameter since it is part of the valve chamber design. Usually this factor is measured in the dry state of the hydrogel and expressed in vol%. The filling degree or packing factor will modify the closing time and of course the opening time of the valve. That has been observed and investigated in several works (Au et al. 2011; Klatt et al. 2012; Richter et al. 2009; Richter et al. 2003, 2007b). Of course there is a compromise between the filling factor and the opening/closing process. Depending on the priority of opening and shut-off time this parameter has to be optimized. Another important design parameter is the size of the actuator or actuator chamber. The bigger the actuator chamber the longer the switching time of the valve (see Fig. 6). For electronically driven microvalves, which are controlled via a thermal electronic interface, the temperature gradient across the valve chamber is an important operational parameter. The opening time depends strongly on the applied heating power. Above a certain power value, which depends on the heat capacity of valve body, a further increase of heating power results only in a slight decrease of the opening time. For a better understanding of these parameters, the reader can be referred to the above cited literature.

6 Conclusion

This chapter described some fundamentals aspects on hydrogels, with the aim of providing a brief guide on how to start working with them. Hydrogels are synthesized for applications in sensing and microfluidics using the actuation work by swelling. Three dimensional polymer networks exhibit inhomogeneities that can influence the mechanical properties as well as the reliability of applications, due to insufficient control of the chemical reaction. Actually, the complete mechanism of cross-linking is not fully understood yet in order to avoid such network inhomogeneities. Therefore a detailed network characterization is necessary for better understanding of gels, as described in this chapter.

Acknowledgment The authors thank M. Dzieniencki (TU Dresden) for DSC measurements.

References

- Adam M, Lairez D (1996) Sol–gel transition. In: Cohen Addad JP (ed) Physical properties of polymeric gels. Wiley, Chichester
- Adam M, Delsanti M, Munch JP, Durand D (1987) Size and mass determination of clusters obtained by polycondensation near the gelation threshold. *J Physique* 48(10):1809–1819
- Allerdissen M, Greiner R, Richter A (2012) Microfluidic microchemomechanical systems. *Adv Sci Technol* 81:84–89
- Aoyagi T, Ebara M (2000) Novel bifunctional polymer with reactivity and temperature sensitivity. *J Biomater Sci Polym Edn* 11(1):101–110

- Arndt K-F, Krahl F, Richter S, Steiner G (2009) Swelling-related processes in hydrogels. In: Gerlach G, Arndt K-F (eds) Hydrogel sensors and actuators. Springer, Berlin/Heidelberg
- Au AK, Lai H, Utela BR, Folch A (2011) Microvalves and micropumps for BioMEMS. *Micromachines* 2(2):179–220
- Bae YH, Okano T (1990) Temperature dependence of swelling of crosslinked poly (*N*, *N*-alkyl substituted acrylamides) in water. *J Polym Sci Part B Polym Phys* 28(6):923–936
- Barry RA III, Shepherd RF, Hanson JN, Nuzzo RG, Wiltzius P, Lewis JA (2009) Direct-write assembly of 3D hydrogel scaffolds for guided cell growth. *Adv Mater* 21(23):2407–2410
- Beltran S, Hooper HH, Blanch HW, Prausnitz JM (1990) Swelling equilibria for ionized temperature-sensitive gels in water and in aqueous salt solutions. *J Chem Phys* 92(3):2061–2066
- Berger J, Zweifel H (1983) Neue photoreaktive Polymere mit seitenständigen Dimethylmaleinimid-Gruppen. I. Radikalische homo-und copolymerisation von *N*-(5-methyl-3-oxa-4-oxo-hexen-5-yl)-dimethylmaleinimid. *Angew Makromol Chem* 115(1):163–181
- Bhatia SN, Yarmush ML, Toner M (1997) Controlling cell interactions by micropatterning in co-cultures: hepatocytes and 3T3 fibroblasts. *J Biomed Mater Res* 34(2):189–199
- Boyko V, Richter S (2004) Monitoring of the gelation process on a radical chain cross-linking reaction based on *N*-vinylcaprolactam by using dynamic light scattering. *Macromol Chem Phys* 205(6):724–730
- Chang CJ, Wu FM, Chang SJ, Hsu MW (2004) Influence of UV-curable compositions and rib properties on ink-jet-type color filter performance. *Jpn J Appl Phys* 43:6280–6285
- Chang CJ, Chang SJ, Shih KC, Pan FL (2005) Improving mechanical properties and chemical resistance of ink-jet printer color filter by using diblock polymeric dispersants. *J Polym Sci Polym Phys* 43(22):3337–3353
- Chang CJ, Hung ST, Lin CK, Chen CY, Kuo EH (2010) Selective growth of ZnO nanorods for gas sensors using ink-jet printing and hydrothermal processes. *Thin Solid Films* 519(5):1693–1698
- Chapiro A (ed) (1962) Radiation chemistry of polymeric systems. Interscience, New York
- Charlesby A, Alexander P (1955) Reticulation of polymers in aqueous solution by γ -rays. *J Chim Phys Phys Chim Biol* 552:699–709
- Chen G, Hoffman AS (1995) Graft copolymers that exhibit temperature-induced phase transitions over a wide range of pH. *Nature* 373(6509):49–52
- Chen G, Imanishi Y, Ito Y (1998a) Photolithographic synthesis of hydrogels. *Macromolecules* 31(13):4379–4381
- Chen G, Imanishi Y, Ito Y (1998b) pH-sensitive thin hydrogel microfabricated by photolithography. *Langmuir* 14(22):6610–6612
- Coleman MM, Hu Y, Sobkowiak M, Painter PC (1998) Infrared characterization of poly(vinyl cinnamate) and its blends with poly(4-vinyl phenol) before and after UV exposure. *J Polym Sci Part B: Polym Phys* 36(9):1579–1590
- Coqueret X (1999) Photoreactivity of polymers with dimerizable side-groups: kinetic analysis for probing morphology and molecular organization. *Macromol Chem Phys* 200(7):1567–1579
- Coqueret X, El Achari A, Hajaiej A, Lablache-Combiere A, Loucheux C, Randrianarisoa L (1991) Some aspects of the reactivity of photo-dimerizable esters grafted onto silicone main chain polymers. *Makromol Chem* 192(7):1517–1534
- Dastidar P, Okabe S, Nakano K, Iida K, Miyata M, Tohnai N, Shiyama M (2005) Facile syntheses of a class of supramolecular gelator following a combinatorial library approach: dynamic light scattering and small-angle neutron scattering studies. *Chem Mater* 17(4):741–748
- de Gans BJ, Duineveld PC, Schubert US (2004) Inkjet printing of polymers: state of the art and future developments. *Adv Mater* 16(3):203–213
- Dušek K, Patterson D (1968) Transition in swollen polymer networks induced by intramolecular condensation. *J Polym Sci A-2* 6(7):1209–1216
- Ebara M, Yamato M, Hirose M, Aoyagi T, Kikuchi A, Sakai K, Okano T (2003) Copolymerization of 2-carboxyisopropylacrylamide with *N*-isopropylacrylamide accelerates cell detachment from grafted surfaces by reducing temperature. *Biomacromolecules* 4(2):344–349

- Eckert F (2003) Bestimmung der kooperativen Diffusionskoeffizienten von Poly(acrylsäure)-Netzwerken. Diploma thesis, TU Dresden
- Eckert F (2008) Netzwerkheterogenität und kooperative Bewegung: Untersuchung von Netzwerken unterschiedlicher Vernetzungsmechanismen mit dynamischer Lichtstreuung. PhD-Thesis, TU Dresden
- Feil H, Bae YH, Feijen J, Kim SW (1993) Effect of comonomer hydrophilicity and ionization on the lower critical solution temperature of *N*-isopropylacrylamide copolymers. *Macromolecules* 26(10):2496–2500
- Ferse B (2007) Smarte Nano-Komposit-Hydrogele. Diploma thesis, TU Dresden
- Ferse B, Richter S, Arndt K-F, Richter A (2007) Investigation of gelling aqueous clay dispersions with dynamic light scattering. *Macromol Symp* 254(1):378–385
- Ferse B, Richter S, Eckert F, Kulkarni A, Papadakis CM, Arndt K-F (2008) Gelation mechanism of poly(*N*-isopropylacrylamide)–clay nanocomposite hydrogels synthesized by photopolymerization. *Langmuir* 24(21):12627–12635
- Finter J, Widmer E, Zweifel H (1984) A new class of photopolymers with pendent dimethylmaleimide groups. II. Photocrosslinking of homo- and copolymers of *N*-(5-methyl-3-oxa-4-oxohexen-5-yl)-dimethylmaleimide. *Angew Makromol Chem* 128(1):71–97
- Finter J, Haniotis Z, Lohse F, Meier K, Zweifel H (1985) A new class of photopolymers with pendent dimethylmaleimide groups III. Comparative study of different photopolymers with pendent olefinic structures including dimethylmaleimide groups. *Angew Makromol Chem* 133(1):147–170
- Flory PJ (1944) Network structure and the elastic properties of vulcanized rubber. *Chem Rev* 35(1):51–75
- Flory PJ (1953) Principles of polymer chemistry. Cornell University Press, Ithaca
- Flory PJ (1974) Introductory lecture. *Disc Farad Soc* 57(1):7–18
- Flory PJ, Rehner J Jr (1943a) Statistical mechanics of cross-linked polymer networks. I. Rubberlike elasticity. *J Chem Phys* 11(11):512–520
- Flory PJ, Rehner J Jr (1943b) Statistical mechanics of cross-linked polymer networks. II. Swelling. *J Chem Phys* 11(11):521–526
- Flory PJ, Gordon M, McCrum NG (1976) Statistical thermodynamics of random networks. *Proc R Soc Lond A* 351:351–380
- Fujie T, Desii A, Ventrelli L, Mazzolai B, Mattoli V (2012) Inkjet printing of protein microarrays on freestanding polymeric nanofilms for spatio-selective cell culture environment. *Biomed Microdevices* 14(6):1069–76
- Gale MT (1997) Replication techniques for diffractive optical elements. *Microelectron Eng* 34:321–339
- Gaylord NG, Adler G (1963) Book reviews. In: Chapiro A (ed) Radiation chemistry of polymeric systems high polymers. Interscience, New York
- Geissler E (1993) Dynamic light scattering from polymer gels. In: Brown W (ed) Dynamic light scattering. Clarendon, Oxford
- Greiner R, Allerdisen M, Voigt A, Richter A (2012) Fluidic microchemomechanical integrated circuits processing chemical information. *Lab Chip* 12(23):5034–5044
- Guenther M, Gerlach G, Corten C, Kuckling D, Sorber J, Arndt K-F (2008) Hydrogel-based sensor for a rheochemical characterization of solutions. *Sens Actuators B* 132(2):471
- Guillen G, Wight S, Bennett J, Tarlov MJ (1994) Patterning of self assembled alkanethiol monolayers on silver by microfocus ion and electron beam bombardment. *Appl Phys Lett* 65(5):534–536
- Haraguchi K, Takehisa T, Fan S (2002) Effects of clay content on the properties of nanocomposite hydrogels composed of poly(*N*-isopropylacrylamide) and clay. *Macromolecules* 35(27):10162–10171
- Hecht AM, Geissler E (1987) Kinetic observations by SAXS and centrifugation of a gelating system. *Macromolecules* 20(10):2485–2490
- Hermans JJ (1947) Deformation and swelling of polymer networks containing comparatively long chains. *Trans Faraday Soc* 43(1):591–600

- Hirokawa Y, Tanaka T (1984) Volume phase transition in a nonionic gel. *J Chem Phys* 81(12): 6379–6380
- Hirotsu S (1993) Coexistence of phases and the nature of first-order phase transition in poly-*N*-isopropylacrylamide gels. *Adv Polym Sci* 110:1–26
- Hirotsu S (1994) Static and time-dependent properties of polymer gels around the volume phase transition. *Phase Trans* 47(3–4):183–240
- Hooper HH, Baker JP, Blanch HW, Prausnitz JM (1990) Swelling equilibria for positively ionized polyacrylamide hydrogels. *Macromolecules* 23(4):1096–1104
- Huang HL, Chen JK, Hough MP (2012) Using soft lithography to fabricate gold nanoparticle patterns for bottom-gate field effect transistors. *Thin Solid Films* 524:304–308
- Huck WTS (2007) Self-assembly meets nanofabrication: recent developments in microcontact printing and dip-pen nanolithography. *Angew Chem Int Ed* 46(16):2754–2757
- Huggins ML (1941) Solutions of long-chain compounds. *J Chem Phys* 9(5):440–440
- Huggins ML (1943) Thermodynamic properties of solutions of high polymers. The empirical constant in the activity equation. *Ann NY Acad Sci* 44:431–443
- Ito Y (1999) Photolithographic synthesis of intelligent microgels. *J Intell Mater Syst Struct* 10(7): 541–547
- James HM, Guth E (1943) Theory of the elastic properties of rubber. *J Chem Phys* 11(10):455–481
- Kabiri K, Omidian H, Hashemi SA, Zohuriaan-Mehr MJ (2003) Synthesis of fast-swelling superabsorbent hydrogels: effect of crosslinker type and concentration on porosity and absorption rate. *Eur Polym J* 39(7):1341–1348
- Kaneko Y, Nakamura S, Sakai K, Aoyagi T, Kikuchi A, Sakurai Y, Okano T (1998) Rapid deswelling response of poly(*N*-isopropylacrylamide) hydrogels by the formation of water release channels using poly(ethylene oxide) graft chains. *Macromolecules* 31(18): 6099–6105
- Kelby TS, Huck WTS (2010) Controlled bending of microscale aulpolyelectrolyte brush bilayers. *Macromolecules* 43(12):5382–5386
- Kim E, Xia Y, Whitesides GM (1995) Polymer microstructures formed by moulding in capillaries. *Nature* 376:581–584
- Klatt S, Allerdissen M, Körbitz R, Voit B, Arndt K-F, Richter A (2012) Hydrogel-based microfluidic systems. *Adv Sci Technol* 81:90–95
- Kretschmer K (2005) Dünne, multi-sensitive Hydrogelschichten aus photovernetzbaaren Blockcopolymeren. PhD thesis, TU Dresden
- Kuckling D, Hoffman J, Plötner M, Ferse D, Kretschmer K, Adler HJP, Arndt KF, Reichelt R (2003) Photo cross-linkable PNIPAAm copolymers 3: microfabricated temperature responsive hydrogels. *Polymer* 44:4455–4462
- Kuckling D, Arndt K-F, Richter S (2009) Synthesis of hydrogels. In: Gerlach G, Arndt K-F (eds) *Hydrogel sensors and actuators*. Springer, Berlin/Heidelberg
- Kuckling D, Doering A, Krahl F, Arndt K-F (2012) Stimuli responsive polymer systems. In: Matyjaszewski K, Möller M (eds) *Polymer science: a comprehensive reference*, vol 8. Elsevier BV, Amsterdam, pp 377–413
- Lang W (1996) Silicon microstructuring technology. *Mater Sci Eng R17*(1):1–55
- Lercel M, Tiberio RC, Chapman PF, Craighead HG, Sheen CW, Parikh AN, Allara DL (1993) Self-assembled monolayer electron-beam resists on GaAs and SiO₂. *J Vac Sci Technol B* 11(6): 2823–2828
- Li Y, Tanaka T (1990) Kinetics of swelling and shrinking of gels. *J Chem Phys* 92(2):1365–1371
- Li J, Gao W, Dong R, Pei A, Sattayasamitsathit S, Wang J (2014) Nanomotor lithography. *Nat Commun* 5:5026
- Nakayama Y, Matsuda T (1992) Preparation and characteristics of photocrosslinkable hydrophilic polymer having cinnamate moiety. *J Polym Sci A, Polym Chem* 30:2451–2457
- Mönch I, Makarov D, Koseva R, Baraban L, Karnaushenko D, Kaiser C, Arndt K-F, Schmidt OG (2011) Rolled-up magnetic sensor: nanomembrane architecture for in-flow detection of magnetic objects. *ACS Nano* 5(9):7436–7442

- Munch JP, Ankrim M, Hild G, Candau S (1983) Dynamic light scattering study of the radical copolymerization of styrene-meta divinylbenzene. *J Phys Lett* 44(2):73–78
- Ngai T, Wu C, Chen Y (2004) Origins of the speckles and slow dynamics of polymer gels. *J Phys Chem B* 108(18):5532–5540
- Nijenhuis K (2007) On the nature of crosslinks in thermoreversible gels. *Polym Bull* 58(1):27–42
- Norisuye T, Takeda M, Shibayama M (1998) Cluster-size distribution of cross-linked polymer chains across the gelation threshold. *Macromolecules* 31(16):5316–5322
- Norrish RGW (1937) On the principle of primary recombination in relation to the velocity of thermal reactions in solution. *Trans Faraday Soc* 33:1521–1528
- Nuzzo RG (2001) The future of electronics manufacturing is revealed in the fine print. *Proc Natl Acad Sci* 98(9):4827–4829
- Otake K, Inomata H, Konno M, Saito S (1990) Thermal analysis of the volume phase transition with *N*-isopropylacrylamide gels. *Macromolecules* 23(1):283–289
- Paschew G (2006) Entwicklung eines hoch aufgelösten taktile Displays. Diploma thesis, TU Dresden
- Perl A, Reinhoudt DN, Huskens J (2009) Microcontact printing: limitations and achievements. *Adv Mater* 21(22):2257–2268
- Peters A, Candau SJ (1986) Kinetics of swelling of polyacrylamide gels. *Macromolecules* 19(7):1952–1955
- Peters A, Candau SJ (1988) Kinetics of swelling of spherical and cylindrical gels. *Macromolecules* 21(7):2278–2282
- Pierik A, Dijkstra M, Raaijmakers A, Wismans T, Stapert H (2008) Quality control of inkjet technology for DNA microarray fabrication. *Biotechnol J* 3(12):1581–1590
- Quesada-Perez M, Maroto-Centeno JA, Forcada J, Hidalgo-Alvarez R (2011) Gel swelling theories: the classical formalism and recent approaches. *Soft Matter* 7(22):10536–10547
- Richter S (2006) Contributions to the dynamical behavior of cross-linked and cross-linking systems: stimulus-sensitive microgels and hydrogels, reversible and irreversible gelation processes. Habilitationsschrift, TU Dresden
- Richter S (2007) Recent gelation studies on irreversible and reversible systems with dynamic light scattering and rheology. A concise summary. *Macromol Chem Phys* 208(14):1495–1502
- Richter A (2009) Hydrogels for actuators. In: Gerlach G, Arndt K-F (eds) *Hydrogel sensors and actuators*, Springer Series on chemical sensors and biosensors. Springer, Berlin/Heidelberg, pp 221–248
- Richter A, Paschew G (2009) Optoelectrothermic control of highly integrated polymer-based MEMS applied in an artificial skin. *Adv Mater* 21(9):979–983
- Richter A, Kuckling D, Howitz S, Gehring T, Arndt K-F (2003) Electronically controllable microvalves based on smart hydrogels: magnitudes and potential applications. *J Microelectromech Syst* 12(5):748–753
- Richter A, Bund A, Keller M, Arndt K-F (2004a) Characterization of a microgravimetric sensor based on pH sensitive hydrogels. *Sens Actuators B Chem* 99(2–3):579–585
- Richter A, Klenke C, Arndt K-F (2004b) Adjustable low dynamic pumps based on hydrogels. *Macromol Symp* 210(1):377–384
- Richter A, Türke A, Pich A (2007a) Controlled double-sensitivity of microgels applied to electronically adjustable chemostats. *Adv Mater* 19(8):1109–1112
- Richter A, Wenzel J, Kretschmer K (2007b) Mechanically adjustable chemostats based on stimuli-responsive polymers. *Sens Actuators B Chem* 125(2):569–573
- Richter A, Paschew G, Klatt S, Lienig J, Arndt K-F, Adler H-J (2008) Review on hydrogel-based pH sensors and microsensors. *Sensors* 8(1):561–581
- Richter A, Klatt S, Paschew G, Klenke C (2009) Micropumps operated by swelling and shrinking of temperature-sensitive hydrogels. *Lab Chip* 9(4):613–618
- Salgado-Rodríguez R, Licea-Claverie A, Arndt K-F (2004) Smart pH/temperature sensitive hydrogels with tailored transition temperature. *J Mex Chem Soc* 57(2):118–126

- Schild HG (1992) Poly(*N*-isopropylacrylamide)-experiment, theory and application. *Progr Polym Sci* 17(2):163–249
- Schmidt T, Mönch JI, Arndt K-F (2006) Temperature-sensitive hydrogel pattern by electron-beam lithography. *Macromol Mater Eng* 291(7):755–761
- Shibayama M (2006) Universality and specificity of polymer gels viewed by scattering methods. *Bull Chem Soc Jpn* 79(12):1799–1819
- Shibayama M (2012) Structure–mechanical property relationship of tough hydrogels. *Soft Matter* 8(31):8030–8038
- Shibayama M, Norisuye T (2002) Gel formation analyses by dynamic light scattering. *Bull Chem Soc Jpn* 75(4):641–659
- Singh D, Kuckling D, Choudhary V, Adler HJ, Koul V (2006) Synthesis and characterization of poly(*N*-isopropylacrylamide) films by photopolymerisation. *Polym Adv Technol* 17(3):186–192
- Stauffer D (1998) Gelierungstheorie: Versäumte Zusammenarbeit von Physik und Chemie. *Ber Bunsen Ges Phys Chem* 102(11):1672–1678
- Stauffer D, Coniglio A, Adam M (1982) Gelation and critical phenomena. *Adv Polym Sci* 44:103–158
- Stenekes RJH, Hennink WE (2000) Polymerization kinetics of dextran-bound methacrylate in an aqueous two phase system. *Polymer* 41(15):5563–5569
- Suzuki K, Matsui S, Ochiai Y (eds) (2000) Sub-half-micron lithography for ULSIs. Cambridge University Press, Cambridge/New York
- Tanaka T (1978) Collapse of gels and the critical endpoint. *Phys Rev Lett* 40(12):820–823
- Tanaka T, Fillmore DJ (1979) Kinetics of swelling of gels. *J Chem Phys* 70(3):1214–1218
- Tanaka T, Hocker LO, Benedek GB (1973) Spectrum of light scattered from a viscoelastic gel. *J Chem Phys* 59(9):5151–5159
- Thiel J, Maurer G, Prausnitz JM (1995) Hydrogele: Verwendungsmöglichkeiten und thermodynamische Eigenschaften. *Chem Ing Tech* 67(12):1567–1583
- Tsuda Y, Kikuchi A, Yamato M, Sakurai Y, Umezu M, Okano T (2004) Control of cell adhesion and detachment using temperature and thermoresponsive copolymer grafted culture surfaces. *J Biomed Mater Res* 69A(1):70–78
- Tsuda Y, Kikuchi A, Yamato M, Nakao A, Sakurai Y, Umezu M, Okano T (2005) The use of patterned dual thermoresponsive surfaces for collective recovery as co-cultured cell sheets. *Biomaterials* 26(14):1885–1893
- Wall FT (1942) Statistical thermodynamics of rubber. *J Chem Phys* 10(2):132–134
- Wall FT (1943) Statistical thermodynamics of rubber. III. *J Chem Phys* 11(11):527–530
- Wall FT (1951) Statistical thermodynamics of rubber elasticity. *J Chem Phys* 19(12):1435–1439
- Ward JH, Bashir R, Peppas NA (2001) Micropatterning of biomedical polymer surfaces by novel UV polymerization techniques. *J Biomed Mater Res* 56(3):351–360
- Winter HH, Mours M (1997) Rheology of polymers near liquid–solid transitions. *Adv Polym Sci* 134:165–234
- Wouters D, Schubert US (2003) Nanolithography and nanochemistry: probe-related patterning techniques and chemical modification for nanometer-sized devices. *Angew Chem Int Ed* 43:2480–2495
- Wouters D, Schubert US (2004) Nanolithography and nanochemistry: probe-related patterning techniques and chemical modification for nanometer-sized devices. *Angew Chem Int Ed* 43(19):2480–2495
- Xia Y, Whitesides GM (1998) Soft lithography. *Angew Chem Inter Ed* 37(5):550–575
- Zhao X, Xia Y, Whitesides GM (1996) Fabrication of three-dimensional micro-structures: microtransfer molding. *Adv Mater* 8(10):837–840
- Zweifel H (1983) Polymers with pendent dimethylmaleimide groups as highly sensitive photocrosslinkable systems. *Photogr Sci Eng* 27(3):114–118

Section II

Ionic Polymer–Metal Composites

Kinji Asaka, Kwang Kim, Keisuke Oguro, and Mohsen Shahinpoor

Contents

1	General Introduction and Historical Review	132
2	Device Configuration	134
3	Characterization of IPMC Actuators	136
4	Electromechanical Modeling of IPMCs	138
5	Electrochemistry of IPMCs	143
6	Mechanical Properties of IPMCs	144
7	Conclusions	146
	References	147

Abstract

This chapter reviews the fundamentals of ionic polymer–metal composites (IPMCs), which are used for sensors and actuators. First, the basic structure of IPMCs is described, and a brief review of their development is provided. Then,

K. Asaka (✉)

Inorganic Functional Material Research Institute, National Institute of Advanced Industrial Science and Technology (AIST), Ikeda, Osaka, Japan
e-mail: asaka-kinji@aist.go.jp

K. Kim

Department of Mechanical Engineering, University of Nevada, Las Vegas, Las Vegas, NV, USA
e-mail: kwang.kim@unlv.edu

K. Oguro

National Institute of Advanced Industrial Science and Technology (AIST), Ikeda, Osaka, Japan
e-mail: oguro-keisuke@aist.go.jp

M. Shahinpoor

Biomedical Engineering/Advanced Robotics (BEAR) Laboratories, Department of Mechanical Engineering, Graduate School of Biomedical Science and Engineering, University of Maine, Orono, ME, USA
e-mail: shah@maine.edu

the configurations of various devices based on them, including those of the electrode materials and ionic polymers, are described. Then, the basic techniques used to characterize IPMCs are described. In the next section, electromechanical models and, in particular, a physics-based model of an IPMC actuator are discussed. Finally, electrochemical models, including an Alternating Current impedance equivalent circuit model and an electrode reaction model, and a mechanical model are discussed.

Keywords

Ionic Polymer-Metal Composite (IPMC) • Ionic Polymer • Electrodes • Characterization • Electromechanical model • Nernst-Planck equation • Onsager relation • Electrochemical model • Impedance • Cyclic voltammetry • Mechanical model

1 General Introduction and Historical Review

Ionic polymer–metal composites (IPMCs), which are composed of an ionic polymer (IP) and metal electrodes, are one of the most promising electroactive polymer (EAP) materials for soft actuators and sensors. Known as bending actuators, IPMCs exhibit soft and extremely large bending motions in the presence of large ionic currents (Fig. 1).

Moreover, IPMCs are capable of large bending actuations when subjected to low voltages. When the voltage is applied, the counter cations move toward the cathode side with dragging water, resulting in a pressure gradient in the ionic gel polymer (Fig. 2).

In addition to their bending properties, IPMC actuators have a number of advantages that make them attractive for use in various biomedical and human affinity applications:

1. Low driving voltage (1–3 V)
2. Relatively high-frequency response (up to several hundred hertz)
3. Large displacement
4. Soft
5. Can be formed into any shape
6. Miniaturizable
7. Activatable in water or wet conditions as well as dry conditions

In addition to their actuation capabilities, IPMCs exhibit remarkable sensing properties. In particular, an electric current is generated in IPMCs in response to bending moments imposed on them; the generated voltage can be as high as tens of millivolts for large bending displacements. This property makes them suitable for use in soft mechanical sensors and energy harvesting systems.

Hamlen et al. were the first to report the direct transformation of electrical energy into mechanical work using an IP gel (Hamlen et al. 1965). Since 1965, many pioneering researchers have investigated the electric response of ionic gels (DeRossi

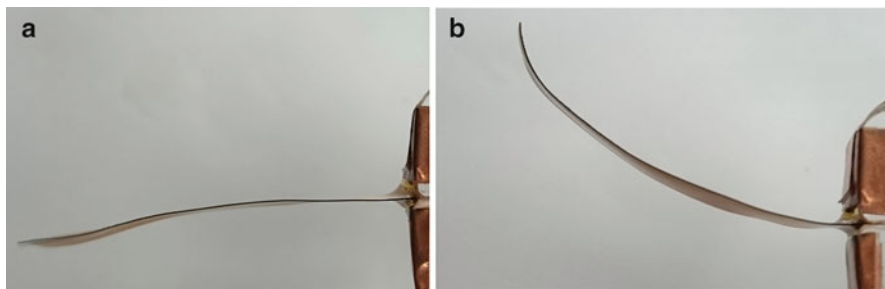
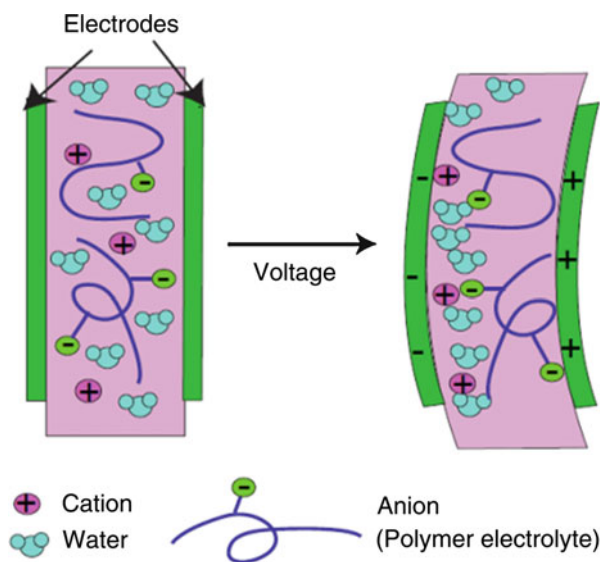


Fig. 1 Photograph showing the bending motion of a typical IPMC actuator. (a) Before applying voltage. (b) After applying voltage

Fig. 2 Schematic view of the bending response mechanism of an IPMC actuator



et al. 1991). Oguro et al. were the first to report the bending response of a perfluor-sulfonic acid membrane (Nafion 117) plated with platinum electrodes and activated by low voltages (~ 1 V) (Oguro et al. 1992). A similar concept was also reported by Shahinpoor (1992). Electromechanical actuators and mechano-electrical sensors based on IPs were introduced as IPMCs by Shahinpoor et al. (1998). Moreover, in 1999, Fujiwara et al. developed Nafion/gold IPMCs (Fujiwara et al. 1999). The first comprehensive reviews of IPMCs (Shahinpoor and Kim 2001, 2004, 2005; Kim and Shahinpoor 2003) suggested that they are more durable and exhibit higher responses than any other electric response of polymer gels. Hence, many researchers have investigated IPMC actuators and sensors for use in various applications. Recently, several articles on EAPs, including reviews, as well as a review article on IPMCs have been published (Kim and Tadokoro 2007; Shahinpoor et al. 2007; Carpi and Smela 2009; Jo et al. 2013; Asaka and Okuzaki 2014).

In the following sections, configurations of IPMC devices, including the electrode materials and IPs used, the basic techniques employed for characterizing IPMCs, the electromechanical and mechanical modeling of IPMCs, and their electrochemistry, will be described.

2 Device Configuration

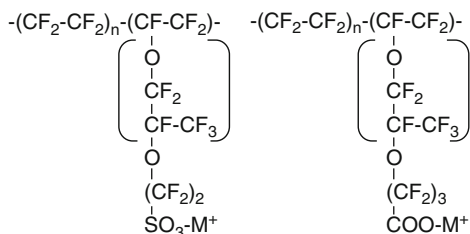
The basic configuration of an IPMC device is shown in Fig. 2. The composite is composed of an IP plated between two metal electrodes. Electrodes play a significant role in the electromechanical coupling of IPMCs. The physical properties of the electrodes, such as their electric conductivity, mechanical durability, and surface morphology, have a significant effect on the actuation performance and reliability of IPMCs. The ideal electrodes for IPMCs should be highly electrically conductive, mechanically compliant, and durable against cyclic deformations and must remain electrochemically inert in corrosive environments (e.g., water) in the presence of an electric potential (~ 4 V). These design requirements limit the choice of available electrode materials considerably. A variety of electrically conductive materials have been investigated for use as IPMC electrodes, including metals (Pt (Kim and Shahinpoor 2003), Au (Fujiwara et al. 1999), Ag (Chung et al. 2006), Cu–Pt (Johanson et al. 2008), Pd–Pt (Kim and Kim 2008), and Pd (Aoyagi and Omiya 2013)), transition metal oxides (Akle et al. 2006; Kim et al. 2009), conducting polymers (Pasquale et al. 2014), and various carbon derivatives such as carbon nanotubes (Levitsky et al. 2004), graphene (Lu et al. 2013), and nanoporous activated and carbide-derived carbons (Palmre et al. 2011; Vunder et al. 2014).

There are two main methods for plating the electrodes for IPMCs. The most widely investigated IPMC electrode materials are Pt (Kim and Shahinpoor 2003) and Au (Fujiwara et al. 1999). The electrodes can be plated by a chemical plating method, which is a chemical process consisting of three steps: (1) roughening of the surface of the IP by sandblasting or other methods, (2) ensuring the adsorption of the metal complex by immersing the IP in an aqueous solution of the metal complex, and (3) fabricating the metal electrodes on the surface of the IP by reducing the adsorbed metal complex. Another method is the so-called “direct assembly” method, which is a physical loading method (Akle et al. 2006). In this method, first, a dispersing solution consisting of the electrode material and the IP in a suitable solvent is prepared. This solution is then directly coated or sprayed on the surface of the IP surface.

IP membranes also play an important role in determining the actuator performance. In particular, the electrochemomechanical properties of IP membranes, such as their ion-transport properties (ion-exchange capacity, liquid electrolyte uptake, and ionic conductivity) and mechanical properties (tensile modulus, strength, and elongation), must be evaluated carefully, if one wishes to enhance actuator performance.

Perfluorinated polymers, such as Nafion and Flemion, which contain ionic sulfonate and carboxylate groups, respectively, are the most widely investigated IP

Fig. 3 Chemical structure of fluorinated polymers



materials used in IPMC actuators (Fig. 3) (Asaka and Oguro 2009a). However, these perfluorinated ionomer membranes suffer from a few drawbacks, such as a low actuation bandwidth; low blocking force; low durability; environmental unfriendliness, given that they are fluorinated polymers; and high cost of fabrication, which limit their practical application.

To overcome these problems, a number of synthetic IPs have been proposed. Among these alternative IPs, sulfonated hydrocarbon polymers have received significant attention, owing to their cost effectiveness, ease of fabrication, tunable stiffness, and good ion-transport properties, which result from their controllable monomer composition, especially via the manipulation of the block copolymers. Naturally abundant functional biopolymers such as cellulose derivatives and chitosan have been considered for their high ionic conductivity, environmental friendliness, low cost, and ability to form uniform films. Another solution is to embed functional nanoparticles in a polymer matrix to fabricate a high-performance nanocomposite membrane (Jo et al. 2013).

The counterions and solvents of IPs play an important role in determining the actuator performance. The differences in the properties of the hydrophilic and hydrophobic cations in the perfluorosulfonic acid polymer determine the bending speed and amplitude of the IPMC actuator (Nemat-Nasser and Wu 2003; Asaka and Oguro 2009a). Water is the most widely investigated solvent for IPMC actuators, since the ionic conductivity of IPs in an aqueous environment is usually higher than that in other solvents. In order to develop an IPMC actuator operable in air, an organic solvent and an ionic liquid to be used as a solvent and electrolyte have been developed (Bennett and Leo 2004; Akle et al. 2006; Nemat-Nasser and Zamani 2006; Lee and Yoo 2009; Kikuchi and Tsuchitani 2009; Kikuchi et al. 2011; Lin et al. 2011).

One of the advantages of IPMCs as actuator materials is that they can be readily formed into various shapes, their properties can be engineered, and they can potentially be integrated with microelectromechanical systems-based sensors as control devices to produce smart systems. An IP such as Nafion can be synthesized readily by casting the dispersing solution and evaporating the solvent or by hot molding the thermoplastic resin. The electrodes can also be patterned readily using a PC-controlled mechanical or optical (laser) cutting machine. Therefore, there have many reports on IPMC devices of different shapes and various electrode configurations (Asaka and Oguro 2009b).

3 Characterization of IPMC Actuators

In order to characterize an IPMC actuator, it is necessary to electromechanically characterize it on the basis of actuation and force measurements. These methods are described in ► Chap. 10, “IPMCs as EAPs: How to Start Experimenting with Them” of this book. Here, the techniques used to characterize an IP and its plated electrodes are described (Rajagopalan et al. 2010; Wang et al. 2010; Panwar et al. 2012; Wang et al. 2014). These are also important for developing new actuator materials.

Characterizing an IP for an IPMC actuator involves determining its water content, ion-exchange capacity, ionic conductivity, and mechanical properties, as described below.

The water content of an IP is determined by determining the difference in the weights of fully water-equilibrated and vacuum-dried IP samples. One example method is described below:

The surface of the water-equilibrated IP is wiped quickly with absorbent paper, in order to remove any excess water, and the fully hydrated IP is weighed immediately (W_h). The IP is then dried overnight in a vacuum at 80 °C, and the weight of the dried IP (W_d) is then measured. The water content (W_C) of the IP is given by Eq. 1:

$$w_c = \frac{(w_h - w_d)}{w_d}. \quad (1)$$

The ion-exchange capacity of the IP is evaluated using a chemical titration method. One example method is as follows:

First, the IP is immersed in a saturated solution of an electrolyte containing the appropriate counterions overnight, in order to exchange the protons with the counterions. Then, the protons in the solution are titrated against a 0.1 N NaOH solution using phenolphthalein as the indicator.

The ionic conductivity is evaluated through AC impedance measurements. The IP film is sandwiched between two stainless steel electrodes, to which an AC perturbation of low magnitude (e.g., 10 mV_{rms}) with frequencies of 1 Hz to 100 kHz is applied using a complex impedance analyzer. The IP is immersed in deionized water for 24 h before its ionic conductivity is measured. The ionic conductivity, κ , is evaluated using Eq. 2:

$$\kappa = \frac{h}{RS}, \quad (2)$$

where R is the resistance at a limiting high frequency, h is the thickness of the IP film, and the S is the area of the IP film.

The mechanical properties of an IP are determined by evaluating its tensile strength and modulus. Stress/strain measurements are performed on a film of the IP with a cross-sectional area S and length L , and the tensile modulus of the IP is calculated from its initial slope; the tensile strength of the IP is obtained from the strain value at which the IP film breaks.

Dynamical mechanical analysis is also employed to determine the mechanical properties of IPs. The dynamic mechanical properties (storage modulus and loss factor) of an IP are measured using a dynamic mechanical analyzer in the tensile mode. An IP film (rectangular) is used for measuring the dynamic mechanical properties. Frequency sweeps are performed at a small strain or stress at different temperatures. The IPMC sample can also be used to measure the dynamic mechanical properties.

In the case of new IP materials, standard chemical analysis techniques, such as infrared spectroscopy, nuclear magnetic resonance, X-ray photoelectron spectroscopy, and X-ray diffraction analysis, and thermogravimetric analysis and/or standard structural analysis methods, such as scanning electron microscopy (SEM), transmission electron microscopy (TEM), and atomic force microscopy (AFM), are used.

In order to characterize the plated electrodes, their electrical capacitance, conductivity, and mechanical properties must be determined. The electrical capacitance, C_E , of the plated electrodes of an IPMC is estimated using Eq. 3 on the basis of the peak-to-peak charging current, i_d , which is determined from the cyclic voltammogram:

$$C_E = \frac{i_d}{V_o}, \quad (3)$$

where V_o is the sweep rate of the applied triangular voltage. Here, it is assumed that the electrical capacitances of the two electrodes are the same.

Cyclic voltammetry (CV) is performed on the IPMC, which is sandwiched by the two electrodes, by applying a triangular voltage.

The electrical conductivity of the plated electrodes is estimated from their sheet resistances, which are measured using a low-resistivity meter with a four-pin probe (measurement range of 10^{-2} to $10^6 \Omega$).

The tensile strength and stress of the IPMC are measured in the same manner as those of the IP. The bending stiffness of a fully hydrated IPMC sample is estimated using the free oscillation attenuation method. By bending the sample to the appropriate initial displacement, the free vibration response can be recorded. The natural frequency of the cantilever, f_n , is obtained from the fast Fourier transform of the free vibration response curve. The stiffness of the IPMC, E_{eq} , is determined using Eq. 4, which is based on the thin cantilever beam theory of material mechanics:

$$E_{eq} = \left(\frac{2\pi}{3.515} \right)^2 f_n^2 \frac{l}{L} m l^3 \frac{12}{h^3 t}, \quad (4)$$

where the parameters h , t , m , l , and L represent the thickness, width, weight, and the free and total lengths of the IPMC strip, respectively.

It is also essential to observe the morphologies of the plated electrodes using SEM, TEM, or AFM. Figure 4 shows a SEM image of a cross section of a Pt-plated Nafion 117 membrane. As can be seen from the figure, the morphology of the plated electrodes determines the electrochemical and mechanical properties of the IPMC and thus its electromechanical actuation performance.

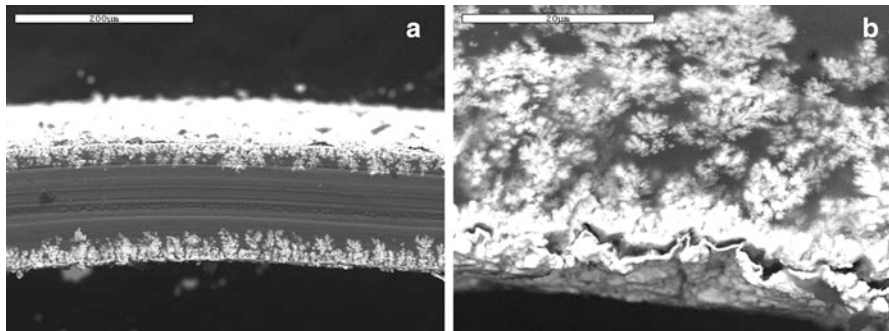


Fig. 4 (a) SEM image of a cross section of a typical IPMC thin strip and (b) SEM image showing the penetration of the plated metal electrodes in a fractal-like manner around nanoclusters within the material

4 Electromechanical Modeling of IPMCs

The primary objective of modeling IPMCs is to facilitate IPMC fabrication and performance prediction, to understand the underlying principles of IPMC actuation and sensing, and to develop functional real-time control systems for IPMC devices. Subsequent chapters of this book will provide detailed overviews of IPMC modeling with a specific emphasis on physics-based models and control models. The underlying governing equations as well as the methods employed for solving these equations will be discussed. Basically, two types of IPMC actuators models are used: physics-based models and control models. Physics-based models, or white-box models, provide a thorough understanding of the IPMC electromechanical phenomena; however, these models are more complex and often numerical in nature.

This section focuses on physics-based models of IPMCs and compares the contributions made by various research groups. In IPMCs, the underlying causes of electromechanical (actuator) transduction need the study on the transport of ion and water molecule in IPMCs. The electromechanical coupling effect of IPMCs is dependent on the transport of the inner ions and water molecules. First, while focusing on the process of the transport of ions and water in IPMCs, the main aspects of physics-based model are reviewed. Then, the recent developments in static models based on the ion clusters in perfluorinated acid membranes are introduced.

A fundamental physics-based model of IPMCs is shown below; in this model, the phenomena of electromechanical and mechanoelectrical transduction are induced in the IPMC by an ionic current. This results in a nonzero spatial charge in the vicinity of the electrodes. For both cases, the ionic current in the polymer can be described using the Nernst–Planck equation (Pugal et al. 2011, 2013):

$$\frac{\partial C}{\partial t} + \nabla \cdot (-D\nabla C - z\mu FC\nabla\phi - \mu C\Delta V\nabla P) = 0, \quad (5)$$

where C is the cation concentration; μ is the mobility of the cations; D is the diffusion coefficient; F is the Faraday constant; z is the charge number; ΔV is the molar volume, which determines the cation hydrophilicity; P is the solvent pressure; and ϕ is the electric potential in the polymer.

The gradient of the electric potential can be described using Poisson's equation (Pugal et al. 2011, 2013):

$$-\nabla^2 \phi = \frac{F\rho}{\varepsilon}, \quad (6)$$

where ε is the absolute dielectric permittivity and ρ is the charge density and is defined as follows:

$$\rho = C - C_a, \quad (7)$$

where C_a is the local anion concentration.

These basic equations form the so-called Poisson–Nernst–Planck (PNP) model for IPMCs and describe the fundamental physics within the polymer membrane. A number of authors have developed electromechanical (actuator) and mechanoelectrical (sensor) models based on the PNP model as well as modified PNP models (Nemat-Nasser 2002; Nemat-Nasser and Zamani 2006; Wallmersperger et al. 2007; Zhang and Yang 2007; Porfiri 2008; Chen and Tan 2008; Aureli et al. 2009). This model will be described further in subsequent chapters of this book.

The underlying causes of transduction in solvent fluxes and ion currents have been discussed previously by several authors. Asaka and Oguro (2000) proposed an IPMC model in which the bending response is attributed to the electroosmosis flow in the ionic gel film by taking into account only the water flow in the membrane. Tadokoro et al. (2000) developed a frictional model, in which the cations together with the hydrated water migrate from the anode to the cathode, owing to the electrostatic force. The electrostatic force is balanced by the frictional force and the diffusion force induced by the concentration gradients. On the other hand, for the free water molecules, the frictional force is solely balanced by the diffusion force. The water flow causes the cathode side to swell, which results in the bending motion of the IPMC. The governing equation is as follows:

$$eE = \eta_I v_I + kT \nabla \ln C_I + n_{aW} kT \nabla \ln C_W, \quad (8)$$

$$kT \nabla \ln C_W = \eta_W v_W, \quad (9)$$

where e is the element charge, k is the Boltzmann constant, v_i is the velocity, and η_i is the viscous resistance coefficient of the i th component.

In the same year, de Gennes et al. (2000) proposed a more comprehensive theory using the standard Onsager relations for the electric current, j_e , and water flux, j_s , based on irreversible thermodynamics:

$$j_e = -\sigma_e \nabla \psi - \lambda \nabla p, \quad (10)$$

$$j_s = -\kappa \nabla p - \gamma \nabla \psi, \quad (11)$$

where σ_e is the conductance, κ is Darcy's permeability, and λ is Onsager's coupling constant. They qualitatively discussed the actuation and sensor properties; however, a quantitative analysis was not performed using these equations.

Yamaue et al. (2005) developed the electrostress diffusion coupling model for describing the deformation dynamics of ion gels under an electric field. This model is a straightforward extension of the stress diffusion coupling model, which was proposed by Doi (2009). By taking into account the coupling of the network stress with the solvent permeation of the gel network and by adding a kinetics equation for the ion flux and electric potential, Yamaue and coworkers could derive a complete set of equations for gel deformation. In this model, the Onsager coefficients, given by Eqs. 10 and 11, are represented by the following microscopic material parameters:

$$\sigma_e = \frac{C_p q_p^2}{\zeta_p} + \sum_i \frac{C_i q_i^2}{\zeta_i}, \quad (12)$$

$$\lambda = -\frac{q_p}{\zeta_p} (1 - \Phi_p) + \sum_i \frac{c_i q_i w_i}{\zeta_i}, \quad (13)$$

$$\kappa = \frac{(1 - \Phi_p)^2}{c_p \zeta_p} + \sum_i \frac{c_i w_i^2}{\zeta_i}, \quad (14)$$

where the suffixes p , s , and i denote the polymer, solvent, and ions, respectively, and c , q , ζ , and w represent the concentration (number of molecules per unit volume), charge, friction constant related to the solvent, and specific volume, respectively.

Then, the friction constant for the free ions is given by the Stokes–Einstein law:

$$\zeta_i = 6\pi\eta a_i, \quad (15)$$

where η is the viscosity of the solvent and a_i is the ionic radius. Then, the friction constant of the polymer gel, ζ_p , is given by

$$\zeta_p = \frac{6\pi\eta}{\xi_b^2 c_p}, \quad (16)$$

where ξ_b is the diameter of the microhydrophilic channel.

Using Eqs. 15 and 16, the Onsager coefficients can be written as

$$\sigma_e = \frac{c_p q_p^2}{6\pi\eta \xi_b} \left\{ c_p \xi_b^3 + \frac{\xi_b}{a_i} \right\}, \quad (17)$$

$$\lambda = \frac{c_p q_p \xi_b^2}{6\pi\eta} \left\{ -(1 - \Phi_p) - \frac{4\pi}{3} \left(\frac{a_i}{\xi_b} \right)^2 \right\}, \quad (18)$$

$$\kappa = \frac{(1 - \varnothing_p)^2 \xi_b^2}{6\pi\eta} \left\{ 1 + \left(\frac{4\pi}{3(1 - \varnothing_p)} \right)^2 c_p \xi_b^3 \left(\frac{a_i}{\xi_b} \right)^3 \right\}. \quad (19)$$

Equations 17 and 18 show that the conductivity decreases and the rate of electroosmosis increases as the ion size increases with respect to the channel size. These results have been shown to qualitatively agree with those of displacement experiments (Yamaue et al. 2005). The initial peak curvature, CUR , is given by the following equation:

$$CUR = \frac{4}{h^2} \frac{\lambda}{\sigma_e} Q. \quad (20)$$

This suggests that the initial curvature is driven by the pressure gradient caused in the ion gel by the electroosmosis flow. Hence, the initial curvature is a function of the ionic charge, Q , and the water transference coefficient, λ/σ_e , which describes the number of water molecules transferred per counter cation transferred. The experimentally determined initial curvature of an IPMC actuator (Nafion 117/Au) having various ionic forms could be reproduced with fidelity using the theoretical curves described by Eqs. 17, 18, and 20 (Yamaue et al. 2005).

Recently, Zhu et al. (2013a, b) developed a physics-based IPMC model using the extended Nernst–Planck equation, which takes into the coupling effects, as follows:

$$J_i = -d_{II} \left(\nabla c_i + \frac{z_i F c_i}{RT} \nabla \varnothing + \frac{\bar{V}_{Ic_i}}{RT} \nabla p \right) - n_{dI} d_{wW} \left(\nabla c_w + \frac{\bar{V}_{wc_w}}{RT} \nabla p \right) - c_i K \nabla p, \quad (21)$$

$$J_w = -d_{wW} \left(\nabla c_w + \frac{\bar{V}_{wc_w}}{RT} \nabla p \right) - n_{dW} d_{II} \left(\nabla c_i + \frac{z_i F c_i}{RT} \nabla \varnothing + \frac{\bar{V}_{Ic_i}}{RT} \nabla p \right) - c_w K \nabla p. \quad (22)$$

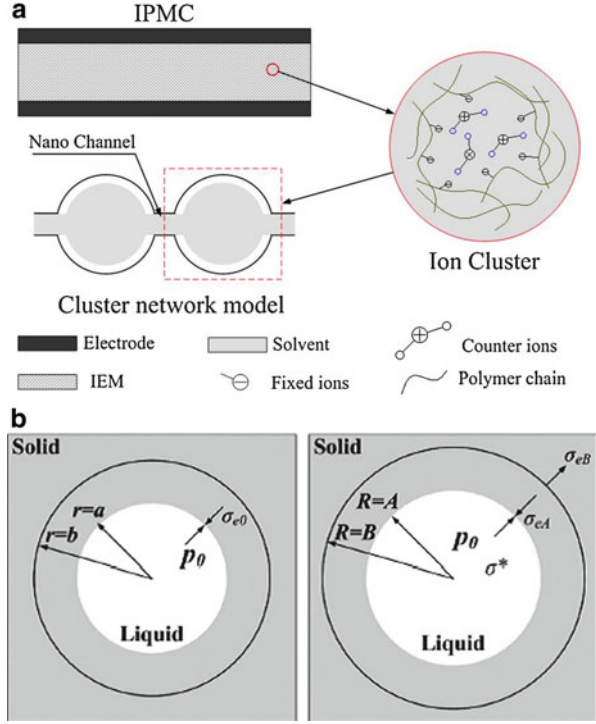
By solving Eqs. 21 and 22 and by coupling them with the Poisson equation (Eq. 6) and the continuity equation (Eq. 23) using a computational method, the redistribution of the cations and water in response to the applied voltage could be calculated:

$$\frac{\partial c_i}{\partial t} + \nabla J_i = 0 \quad (i = I, W). \quad (23)$$

Based on the ion-cluster model of the perfluorosulfonic acid polymer, shown in Fig. 5, the change in the concentration of the cations and water transfer into those which are calculated by Eqs. 21, 22, and 23 results in the pressure state in the cluster by using the following relations:

$$\sigma_{eB} - \sigma_{eA} = \frac{E_{dry}}{3} \left(\left(\frac{1 + w_v}{1 + w_{vo}} \right)^{-\frac{4}{3}} - \left(\frac{w_v}{w_{vo}} \right)^{-\frac{4}{3}} \right), \quad (24)$$

Fig. 5 Ion-cluster model of a perfluorosulfonic acid-based IPMC. (a) Ion-cluster network mode and (b) schematic view of the stress valance in the ion cluster (Reproduced from Zhu et al. 2013a)



where σ_{eB} and σ_{eA} are the external and internal stresses of the ion cluster, respectively (Fig. 5b); E_{dry} is the elastic modulus of the dry polymer; and w_v and w_{v0} are the volume fraction and initial volume fraction of the water in the ionic polymer, respectively (Zhu et al. 2013a, b).

The hydrostatic pressure of the ion cluster is given by

$$p_h = -\sigma_{eA}. \tag{25}$$

By adding the osmotic pressure, Π , the electrostatic stress, p_e , and the capillary pressure, Π_σ (eigenstresses), in the ion cluster, which are induced by the redistribution of the ions and water, the total internal pressure, p , of the ion cluster can be calculated (Zhu et al. 2013a, b):

$$p = p_h + \Pi_\sigma - \Pi - p_e. \tag{26}$$

By establishing the above model, Zhu et al. could successfully describe the complicated deformation behaviors of the IPMC under various conditions (Zhu et al. 2013a, b).

5 Electrochemistry of IPMCs

The standard AC impedance technique is a powerful tool for exploring the electrochemical properties of IPMCs, as it can be used to determine their equivalent electric circuits.

It is assumed that the IPMC is composed of an IP film sandwiched between two perfectly conductive metal electrodes. The linearized PNP model is used to describe the dynamics of the electric potential and the concentration of the mobile counterions within the polymer. In the case of the flat electrodes, by solving the partial differential equation based on the PNP model, the equivalent circuit, which is composed of the following lumped capacitances – the double-layer capacitance, C_d , the bulk capacitance C_b , and the bulk conductance, S_b (see Fig. 6a) – can be obtained (Aureli and Porfiri 2012).

The chemical (electroless) plating process for plating the metal electrodes, which has been described previously, is typically repeated several times, in order to increase the thickness and hence the electric conductivity of the electrode layers. The sequential plating steps result in a dendrite-like structure in the electrode layer; this structure penetrates into the ionic polymer, as shown in Fig. 4. In such a case, the interface between the IP and the electrode is rough. Further, the equivalent circuit of the IPMC is a distributed circuit composed of a capacitance, $C(r)$, and a conductance, $S(r)$, as shown in Fig. 6b (Aureli and Porfiri 2012).

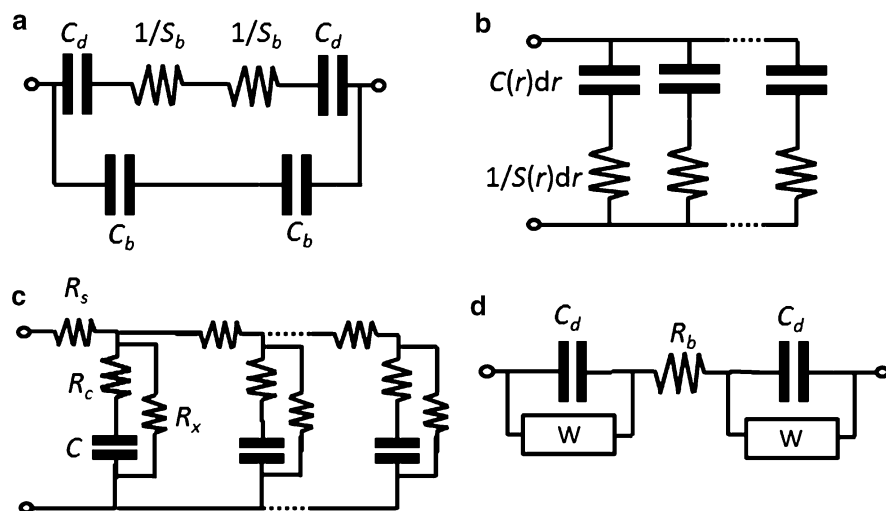


Fig. 6 Equivalent circuits of the IPMC. (a) Lumped capacitance and resistance model. (b) Distributed circuit model that takes into account the roughness of the plated electrodes. (c) A possible distributed circuit model that takes into account the surface resistance of the plated electrodes. (d) A possible circuit model that takes into account the ion transport in the porous electrodes

The above discussion assumes that the plated electrodes are perfectly conductive. However, the actual resistance of the plated electrodes is not negligible. When considering the surface resistance of the plated electrodes, several authors have proposed the distributed equivalent circuit shown in Fig. 6c (Shahinpoor and Kim 2000; Paquette et al. 2003; Punning et al. 2007; Chen and Tan 2008). In this figure, C is the distributed element of the double-layer capacitance, R_e is that of the electrolyte resistance, R_s is that of the surface resistance of the electrode, and R_x is the shunt resistance.

The electrode layers formed using the physical loading method are usually relatively thicker (more than 10 μm in thickness), and the composite layers are composed of nanoparticles of the electrode material and the ionic polymer. These layers are both electronically and ionically conductive. The impedance for such electrodes is assumed to be similar to that of porous electrodes. Levie (1963, 1964) was the first to develop a transmission line circuit (TLC) model of the porous electrode consisting of the electrolyte resistance and the double-layer capacitance. Subsequently, a number of authors proposed modified TLC models for the impedance of porous electrodes on the basis of Levie's model. Bisquert (2000) reviewed the various impedance models for porous electrodes. The composite electrode layers prepared by the physical loading method could be successfully represented by the impedance model for porous electrodes, as shown in Fig. 6d; this model is composed of the double-layer capacitance, C_d ; the Warburg diffusion capacitance, W ; and the electrolyte resistance, R_b (Liu et al. 2012; Cha and Porfiri 2013).

Another important tool for electrochemical analysis is CV, which is used for estimating the double-layer capacitance of the electrode layer, as described in Sect. 3. CV is the standard electrochemical technique for studying the electrode reactions (Bard and Falkner 2001). The redox reactions involving the Pt, Au, and Pd electrodes used in IPMCs have been studied using CV, and the obtained results have been discussed with respect to the displacement behavior (Asaka and Oguro 2000; Kim et al. 2011; Aoyagi and Omiya 2013). Figure 7 shows the results of CV and displacement measurements for a Pt-IPMC in an H_2SO_4 solution. It can be seen clearly that the displacement direction is regulated by the redox reaction of the Pt electrodes. When coupled with the phenomena occurring in IPs (see Sect. 5), the dependence of the displacement behavior of the IPMC on the various parameters, such as the amplitude of the applied voltage, the IP species, the electrode materials, the counterion species, the pH level, and the water content, becomes complex.

6 Mechanical Properties of IPMCs

As has been described previously, IPMCs bend toward the cathode or anode (depending on whether a cation- or anion-exchange polymer is used) under the influence of an applied voltage, owing to the migration of the counterions with solvent molecules. This results in a pressure gradient and difference in the bending

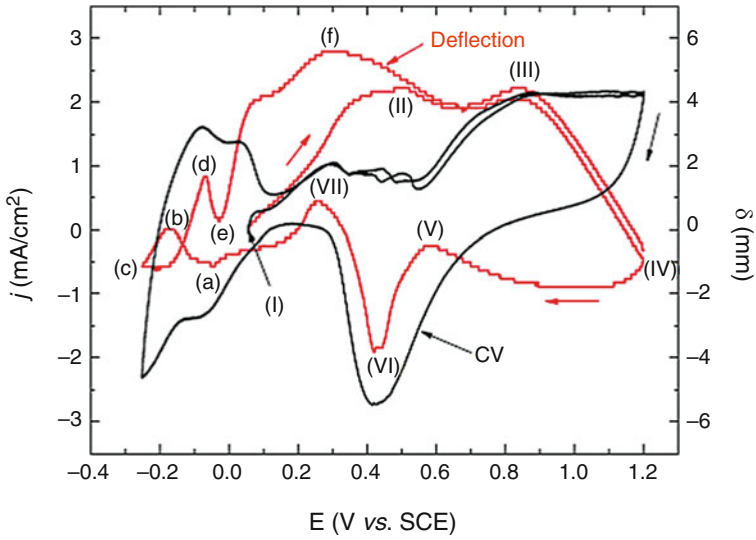


Fig. 7 Results of cyclic voltammetry (CV) and displacement measurements (deflection) performed on the Pt electrode of an IPMC actuator in H_2SO_4 solution (Reproduced from Kim et al. 2011)

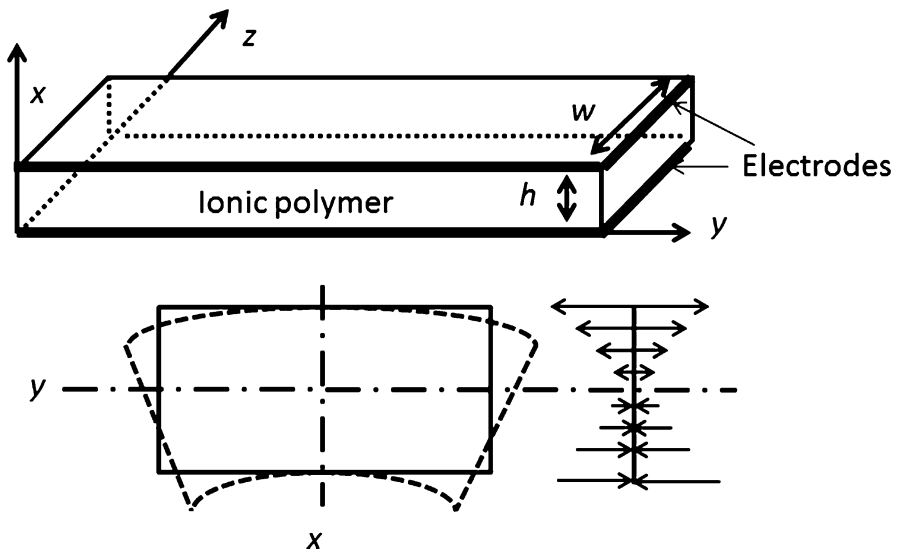


Fig. 8 Stress distribution in an IPMC along the thickness direction

stress between the two sides of the membrane. The situation is similar to that related to the stress distribution caused by the moment, as shown in Fig. 8 (He et al. 2011).

In this case, the bending moment, M , along the z -axis is given by the following equation:

$$M = \int_0^h \sigma(x, t) w x dx, \quad (27)$$

where w is the width of the IPMC and $\sigma(x, t)$ is the stress distribution along the thickness direction.

According to the Euler–Bernoulli law, the curvature of the IPMC actuator, CUR , at zero load while assuming that the actuator is perfectly homogeneous along the z -axis is given by

$$CUR = \frac{M}{EI}, \quad (28)$$

where E is the Young modulus of the IPMC actuator and $I (=2/3 Wh^3)$ is the second moment of inertia of the IPMC.

Further, the blocking force of the IPMC, F , is given by

$$F = \frac{M}{L}, \quad (29)$$

where L is the distance of the IPMC actuator.

Therefore, the curvature of the IPMC at load F is given by the following equation:

$$CUR = \frac{M - FL}{EI}, \quad (30)$$

The displacement, δ , can be related to the curvature by the following equation:

$$CUR = \frac{2\delta}{L^2 + \delta^2} \cong \frac{2\delta}{L^2}, \quad (31)$$

The bending moment, M , is a function of the time, t , and the applied voltage, V , and can be derived from electromechanical and electrochemical models described in Sects. 6 and 7. The mechanical model described here is most basic one and assumes that the IPMC is homogeneous. More rigorous models are described in subsequent chapters of this book.

7 Conclusions

Since the initial reports on IPMCs, significant advances have been made in the development of IPMC actuators and sensors. Electrodes play a significant role in determining the degree of electromechanical coupling in IPMCs. A variety of electrically conductive materials have been investigated for use for IPMC electrodes, including metals, transition metal oxides, conducting polymers, and various carbon derivatives. IP membranes also play an important role in determining the actuator

performance. Perfluorinated polymers, such as Nafion and Flemion, which contain ionic sulfonate and carboxylate groups, respectively, are the most widely investigated IP materials used in IPMC actuators. However, these perfluorinated ionomer membranes suffer from a few drawbacks, such as a low actuation bandwidth; low blocking force; low durability; environmental unfriendliness, given that they are fluorinated polymers; and high cost of fabrication, which limit their use in practical applications. To overcome these problems, a number of synthetic IPs have been proposed.

The various techniques used to characterize IPs and plated electrodes were described, as these are also important for developing new actuator materials.

This chapter focused on physics-based models of IPMCs and compared the contributions made by various research groups. In IPMCs, the underlying causes of electromechanical (actuator) transduction need the study on the transport of ion and water molecule in IPMCs. The electromechanical coupling effect of IPMCs is dependent on the transport of the inner ions and water molecules. In this chapter, while focusing on the transport process of ions and water in IPMCs, physics-based models of IPMCs were reviewed. Further, the recent developments in static models based on the ion-cluster structure of perfluorinated acid membranes were introduced.

In the last two sections of this chapter, the basics of the electrochemistry of IPMCs and their mechanical modeling were discussed.

Given the recent developments in the materials used for IPMCs and owing to the elucidation of the working principles of IPMC actuators and sensor, IPMCs are increasingly being used in various biomedical applications, including in biomimetic robotics and sensor/actuator integration, and for energy harvesting.

References

- Akle BJ, Bennett MD, Leo DJ (2006) High-strain ionomeric-ionic liquid electroactive actuators. *Sens Actuators A* 126:173–181
- Aoyagi W, Omiya M (2013) Mechanical and electrochemical properties of an IPMC actuator with palladium electrodes in acid and alkaline solutions. *Smart Mater Struct* 22:055028 (10 pp)
- Asaka K, Oguro K (2000) Bending of Polyelectrolyte Membrane-platinum composites by electric stimuli. Part II. Response kinetics. *J Electroanal Chem* 480:186–198
- Asaka K, Oguro K (2009a) IPMC actuators: fundamentals. In: Carpi F, Smela E (eds) *Biomedical applications of electroactive polymer actuators*. Wiley, Chichester, pp 103–119
- Asaka K, Oguro K (2009b) Active microcatheter and biomedical soft devices based on IPMC actuators. In: Carpi F, Smela E (eds) *Biomedical applications of electroactive polymer actuators*. Wiley, Chichester, pp 103–119
- Asaka K, Okuzaki H (eds) (2014) *Soft actuators – material, modeling, applications and future perspectives*. Springer, Tokyo
- Aureli M, Porfiri M (2012) Effect of electrode surface roughness on the electrical impedance of ionic polymer–metal composites. *Smart Mater Struct* 21:105030
- Aureli M, Lin W, Porfiri M (2009) On the capacitance-boost of ionic polymer metal composites due to electroless plating: theory and experiments. *J Appl Phys* 105:104911
- Bard AJ, Faulkner LF (2001) *Electrochemical methods: fundamentals and applications*, 2nd edn. Wiley, New York

- Bennett MD, Leo DJ (2004) Ionic liquids as stable solvents for ionic polymer transducers. *Sens Actuators A-Phys* 115:79–90
- Bisquert J (2000) Influence of the boundaries in the impedance of porous film electrodes. *Phys Chem Chem Phys* 2:4185–4192
- Carpi F, Smela E (eds) (2009) *Biomedical applications of electroactive polymer actuators*. Wiley, Chichester
- Cha Y, Porfiri M (2013) Bias-dependent model of the electrical impedance of ionic polymer-metal composites. *Phys Rev E* 87:022403
- Chen Z, Tan X (2008) A control-oriented and physics-based model for ionic polymer-metal composite actuators. *IEEE/ASME Trans Mechatron* 13(5):519–529
- Chung CK, Fung PK, Hong YZ et al (2006) A novel fabrication of ionic polymer-metal composites (IPMC) actuator with silver nano-powders. *Sens Actuators B* 117:367–375
- de Gennes PG, Okumura K, Shahinpoor M, Kim KJ (2000) Mechanoelectric effects in ionic gels. *Europhys Lett* 50:513–518
- de Levie R (1963) On porous electrodes in electrolyte solutions: I. Capacitance effects. *Electrochim Acta* 8:751–780
- de Levie R (1964) On porous electrodes in electrolyte solutions—IV. *Electrochim Acta* 9:1231–1245
- DeRossi D, Kajiwaru K, Osada Y, Yamauchi A (eds) (1991) *Polymer gels – fundamentals and biomedical applications*. Plenum Press, New York
- Doi M (2009) Gel dynamics. *J Phys Soc Jpn* 78(5): 052001
- Fujiwara N, Asaka K, Nishimura Y et al (1999) Preparation of gold-solid electrolyte composites as electric stimuli responsive materials. *Chem Mater* 12:1750–1754
- Hamlen RP, Kent CE, Shafer SN (1965) Electrolytically activated contractile polymer. *Nature* 206:1149–1150
- He Q, Yu M, Song L et al (2011) Experimental study and model analysis of the performance of IPMC membranes with various thickness. *J Bionic Eng* 8:77–85
- Jo CH, Pugal D, Oh IK et al (2013) Recent advances in ionic polymer-metal composite actuators and their modeling and applications. *Prog Polym Sci* 38(7):1037–1066
- Johanson U, Maeorg U, Sammelseg V et al (2008) Electrode reactions in Cu-Pt coated ionic polymer actuators. *Sens Actuators B* 31:340–346
- Kikuchi K, Tsuchitani S (2009) Nafion based polymer actuators with ionic liquids as solvent incorporated at room temperature. *J Appl Phys* 106:053519
- Kikuchi K, Sakamoto T, Tsuchitani S et al (2011) Comparative study of bending characteristics of ionic polymer actuators containing ionic liquids for modeling actuation. *J Appl Phys* 109:073505
- Kim SM, Kim KJ (2008) Palladium buffer-layered high performance ionic polymer-metal composites. *Smart Mater Struct* 17:035011
- Kim KJ, Shahinpoor M (2003) Ionic polymer-metal composites – II. Manufacturing techniques. *Smart Mater Struct* 12:65–79
- Kim KJ, Tadokoro S (eds) (2007) *Electroactive polymers for robotics applications*. Springer, London
- Kim SM, Tiwari R, Kim KJ (2009) A novel ionic polymer-metal composites incorporating ZnO thin film. *Smart Mater Struct Electroactive Polym Actuators Devices* 7287:72870W-1-7
- Kim D, Kim KJ, Nam JD et al (2011) Electro-chemical operation of ionic polymer-metal composites. *Sens Actuators B* 155(2011):106–113
- Lee JW, Yoo YT (2009) Anion effects in imidazolium ionic liquids on the performance of IPMCs. *Sens Actuators B* 137:539–546
- Levitsky IA, Kanelos P, Euler WB (2004) Electromechanical actuation of composite material from carbon nanotubes and ionomeric polymer. *J Chem Phys* 121:1058–1165
- Lin J, Liu Y, Zhang QM (2011) Charge dynamics and bending actuation in Aquivion membrane swelled with ionic liquids. *Polymer* 52:540–546
- Liu Y, Zhao R, Ghaffari M et al (2012) Equivalent circuit modeling of ionomer and ionic polymer conductive network composite actuators containing ionic liquids. *Sens Actuators A* 181:70–76

- Lu L, Liu J, Zhang Y et al (2013) Graphene-stabilized silver nanoparticle electrochemical electrode for actuator design. *Adv Mater* 25:1270–1274
- Nemat-Nasser S (2002) Micromechanics of actuation of ionic polymer-metal composites. *J Appl Phys* 92:2899–2915
- Nemat-Nasser S, Wu Y (2003) Comparative experimental study of ionic polymer-metal composites with different backbone ionomers and in various cation forms. *J Appl Phys* 93:5255–5267
- Nemat-Nasser S, Zamani S (2006) Modeling of electrochemomechanical response of ionic polymer-metal composites with various solvents. *J Appl Phys* 100:064310
- Oguro K, Kawami Y, Takenaka H (1992) Bending of an ion-conducting polymer film-electrode composite by an electric stimulus at low voltage. *J Micromach Soc* 5:27–30
- Palmre V, Lust E, Janes A et al (2011) Electroactive polymer actuators with carbon aerogel electrodes. *J Mater Chem* 21:2577–2583
- Panwar V, Lee C, Ko SY et al (2012) Dynamic mechanical, electrical, and actuation properties of ionic polymer metal composites using PVDF/PVP/PSSA blend membranes. *Mater Chem Phys* 135:928–937
- Paquette JW, Kim KJ, Nam JD et al (2003) An equivalent circuit model for ionic polymer-metal composites and their performance improvement by a clay-based polymer nano-composite technique. *J Intell Mater Syst Struct* 14:633–642
- Pasquale GD, Graziani S, Messina FG et al (2014) An investigation of the structure–property relationships in ionic polymer polymer composites (IP2Cs) manufactured by polymerization in situ of PEDOT/PSS on Nafion R 117. *Smart Mater Struct* 23:035018 (12pp)
- Porfiri M (2008) Charge dynamics in ionic polymer metal composites. *J Appl Phys* 104:104915
- Pugal D, Kim KJ, Aabloo A (2011) An explicit physics-based model of ionic polymer-metal composite actuators. *J Appl Phys* 110(8):084904
- Pugal D, Solin P, Aabloo A, Kim KJ (2013) IPMC mechanoelectric transduction: its scalability and optimization. *Smart Mater Struct* 22(12):125029
- Punning A, Kruusmaa M, Aabloo A (2007) Surface resistance experiments with IPMC sensors and actuators. *Sens Actuators A* 133:200–209
- Rajagopalan M, Jeon JH, Oh IK (2010) Electric-stimuli-responsive bending actuator based on sulfonated polyetherimide. *Sens Actuators B* 151:198–204
- Shahinpoor M (1992) Conceptual design, kinematics and dynamics of swimming robotic structures using ionic polymeric gel muscles. *Smart Mater Struct* 1:91–94
- Shahinpoor M, Kim KJ (2000) The effect of surface-electrode resistance on the performance of ionic polymer-metal composite (IPMC) artificial muscles. *Smart Mater Struct* 9:543–551
- Shahinpoor M, Kim KJ (2001) Ionic polymer-metal composites – I. Fundamentals. *Smart Mater Struct* 10:819–833
- Shahinpoor M, Kim KJ (2004) Ionic polymer-metal composites – III. Modeling and simulation as biomimetic sensors, actuators, transducers and artificial muscles. *Smart Mater Struct* 13:1362–1388
- Shahinpoor M, Kim KJ (2005) Ionic polymer-metal composites – IV. Industrial and mechanical applications. *Smart Mater Struct* 14:197–214
- Shahinpoor M, Bar-Cohen Y, Simpson JO, Smith J (1998) Ionic polymer-metal composites (IPMCs) as biomimetic sensors, actuators and artificial muscles—a review. *Smart Mater Struct* 7:R15–R30
- Shahinpoor M, Kim KJ, Mojarrad M (2007) Artificial muscles – applications of advanced polymeric nanocomposites. CRC Press, New York/London
- Tadokoro S, Yamagami S, Takamori T et al (2000) Modeling of nafion-Pt composite actuators (ICPF) by ionic motion. *Smart Mater Struct Electroactive Polym Actuators Devices* 3987:92–102
- Vunder V, Itik M, Poldsalu I et al (2014) Inversion based control of ionic polymer–metal composite actuators with nanoporous carbon based electrodes. *Smart Mater Struct* 23:025010
- Wallmersperger T, Leo DJ, Kothera CS (2007) Transport modeling in ionomeric polymer transducers and its relationship to electromechanical coupling. *J Appl Phys* 101:024912

- Wang XL, Oh IK, Lee S (2010) Electroactive artificial muscle based on crosslinked PVA/SPTES. *Sens Actuators B* 150:57–64
- Wang Y, Zhu Z, Chen H et al (2014) Effects of preparation steps on the physical parameters and electromechanical properties of IPMC actuators. *Smart Mater Struct* 23:125015
- Yamaue T, Mukai H, Asaka K, Doi M (2005) Electrostress diffusion coupling model for polyelectrolyte gels. *Macromolecules* 38:1349–1356
- Zhang L, Yang Y (2007) Modeling of an ionic polymer–metal composite beam on human tissue. *Smart Mater Struct* 16:S197–S206
- Zhu Z, Asaka K, Chang L et al (2013a) Multiphysics of ionic polymer-metal composite actuator. *J Appl Phys* 114:084902
- Zhu Z, Asaka K, Chang L et al (2013b) Physical interpretation of deformation evolvement with water content of ionic polymer-metal composite actuator. *J Appl Phys* 114:184902

Kwang Kim, Viljar Palmre, Jin-Han Jeon, and Il-Kwon Oh

Contents

1	Electrode Materials	152
1.1	Metallic Electrode Materials	153
1.2	Nonmetallic Electrode Materials	156
2	Ionic Polymer Membranes	158
2.1	Sulfonated Hydrocarbon Backbone Membranes	159
2.2	Sulfonated Block Copolymer Membrane Materials	159
2.3	Biopolymer Membrane Materials	162
2.4	Nanocarbon-Composite Membrane Materials	164
3	Conclusions	167
	References	168

Abstract

This chapter provides an overview of the materials used for manufacturing IPMC actuators and sensors. Recently, considerable effort has been put into investigating various electrode materials and ionic polymer membranes to increase the actuation performance of IPMC and overcome some of the shortcomings to improve their reliability and stability. Various metallic and nonmetallic electrode materials with notable electrochemical and electromechanical properties have

K. Kim (✉) • V. Palmre

Department of Mechanical Engineering, University of Nevada, Las Vegas, Las Vegas, NV, USA
e-mail: kwang.kim@unlv.edu; viljar.palmre@gmail.com

J.-H. Jeon • I.-K. Oh

School of Mechanical, Aerospace and Systems Engineering, Korea Advanced Institute of Science and Technology (KAIST), Daejeon, Republic of Korea
e-mail: jhjeon2010@kaist.ac.kr; ikoh@kaist.ac.kr

been considered for IPMC electrodes. Herein, some of the more commonly used noble metal-based electrodes and recently introduced nonmetallic conductive material (such as transition metal oxide and various carbon derivatives)-based electrode designs along with specific manufacturing approaches are introduced, highlighting their key aspects and design challenges. Also, several representative ionic polymer membranes used for IPMC fabrication such as sulfonated aromatic hydrocarbon, block copolymers, biopolymers, and nanocomposites capable of providing higher electro-chemo-mechanical properties have been investigated. Herein, more recently developed membrane materials including self-assembled sulfonated polyimide block copolymers, functional cellulose-based biopolymers, and graphene-reinforced nanocomposites are introduced, considering their main advantages, facile synthesis process (such as freeze drying method, all-solution process, and electrospinning technique) and actuation performance.

Keywords

Carbide-derived carbons (CDCs) • Degree-of-sulfonation (DOS) • Direct assembly method • Electrode materials • Metallic electrode materials • Nonmetallic electrode materials • Freeze-dried bacterial cellulose (FDBC) • Graphene-Nafion polymer actuator • Impregnation-reduction method • Ionic polymer-metal composites (IPMCs) • Biopolymer membrane materials • Electromechanical properties of • Metallic electrode materials • Nanocarbon-composite membrane materials • Nonmetallic electrode materials • Sulfonated block copolymer membrane materials • Sulfonated hydrocarbon backbone membranes • Pendent sulfonated chitosan (PSC) • Polyaniline (PANI) • Sulfonated poly(amic acid) (SPAA) • Sulfonated poly(styrene-ran-ethylene) (SPSE) • Sulfonated polyimide (SPI)

1 Electrode Materials

Electrodes have a significant role in the electromechanical coupling of IPMC. Their physical properties such as electric conductivity, mechanical durability, and surface morphology can strongly affect the actuation performance and reliability of IPMC material. Proper electrodes for IPMC should be highly electrically conductive, mechanically compliant, durable against cyclic deformations, and electrochemically inert for operation in corrosive environment (e.g., water) in the presence of electric potential (~ 4 V). These design requirements limit considerably the choice of available materials. Various types of electrically conductive materials have been investigated for use in IPMC electrodes, including metals (primarily noble metals), transition metal oxides, and various carbon derivatives such as nanotubes, graphene, and nanoporous-activated and carbide-derived carbons. This chapter intends to provide an overview of these developments and current challenges.

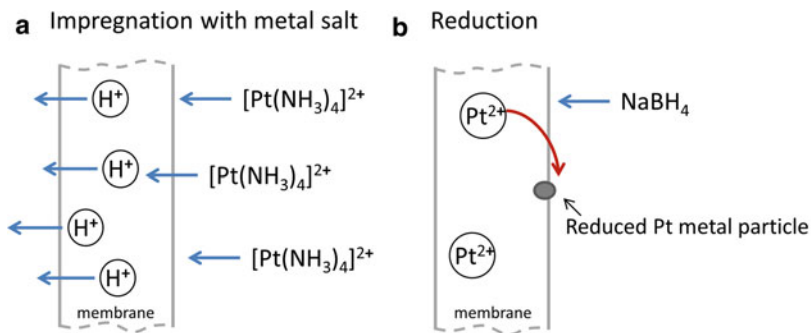
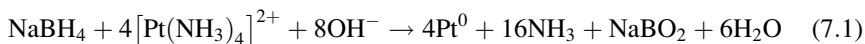


Fig. 1 Impregnation and reduction steps in the electroless plating process

1.1 Metallic Electrode Materials

Since the introduction of IPMC materials, the platinum and gold have been most widely used electrode materials for IPMC fabrication due to their high electrochemical stability and excellent electrical conductivity. These materials are fabricated into electrodes using chemical deposition method, also known as impregnation-reduction method or electroless plating (Shahinpoor and Kim 2001; Fujiwara et al. 2000). This method can be used with a wide range of ionic polymer membranes that have ability to selectively exchange cations or anions. The state-of-the-art manufacturing process of IPMC via electroless plating consists of three main steps. First, the ionic polymer membrane is impregnated with desired metal salt by soaking it in respective metal complex solution, such as tetraammineplatinum(II) chloride hydrate ($\text{Pt}(\text{NH}_3)_4\text{Cl}_2 \cdot \text{H}_2\text{O}$). The metal complex cations diffuse into the polymer through ion-exchange process as illustrated in Fig. 1. Secondly, the platinum complex cations in the polymer are reduced to metallic form at the membrane surface by a chemical reduction process in a solution containing sodium borohydride (NaBH_4). The reduction process occurs according the following reaction:



The described impregnation-reduction steps are typically repeated 1–3 times in order to increase the thickness and electric conductivity of the electrodes. The third step is the secondary plating (or surface electroding) process to deposit additional Pt at the outer surface of the electrode to further increase the electrode surface conductivity. The composite is immersed in the Pt complex solution, and by using reducing agents such as hydroxylamine hydrochloride and hydrazine monohydrate, the platinum is deposited on the top of the initial Pt electrode layer. A detailed description of the fabrication process can be found in (Kim and Shahinpoor 2003).

As can be seen in Fig. 2, the metallic platinum particles concentrate predominantly near the interface boundaries, typically within 5–20 μm range from the

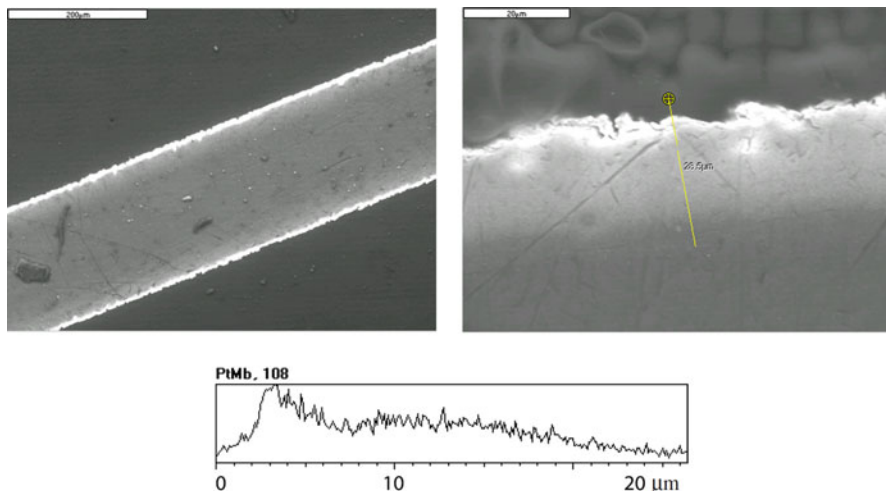


Fig. 2 Two SEM images (*top*) showing the cross section (*left*) and close-up (*right*) of a typical IPMC. The *bottom* graph shows an X-ray line scan of Pt. As can be seen, Pt is dense at the surface (Shahinpoor and Kim 2001. © IOP Publishing. Reproduced by permission of IOP Publishing. All rights reserved.)

surface. The plating conditions such as soaking time, concentrations, and temperatures are critical to the plating process and determine the penetration depth and conductivity of electrodes that affect the performance of IPMC (Kim and Shahinpoor 2003; Nemat-Nasser 2002). One of the concerns associated with Pt electrodes are developing microcracks under prolonged cyclic operation, leading to decrease in the electrode surface conductivity (Punning et al. 2007). Gold electrodes are more elastic and offer better mechanical stability and higher electrical conductivity, but on the other hand, their fabrication involves more complex processing (Fujiwara et al. 2000).

Several alternative materials and their combinations have been researched for IPMC electrodes. Using palladium as a supporting layer underneath the platinum layer has shown improved mechanical stability and higher transduction performance compared to the conventional platinum electrodes (Kim and Kim 2008; Palmre et al. 2014). In this electrode configuration, the Pd is deposited at the inner surface of the ionomer membrane prior to Pt surface layer using electroless plating method. With appropriate control of the plating conditions, highly dispersed Pd particles can be created not only at the ionomer surface, but deep in the polymer membrane (Fig. 3), thereby increasing notably the specific surface area of the electrodes (Palmre et al. 2014). This highly capacitive Pd electrode interface provides significant increase in the blocking force (Fig. 4) and mechano-electrical output of IPMC. However, the actuation response is slower compared to regular Pt electrodes.

IPMC electrodes composed of copper and platinum have been reported (Johanson et al. 2008), in which the reversible electrochemical processes – Cu dissolution and

Fig. 3 SEM micrograph of the cross sections of 1 mm thick Pd-Pt IPMC (*top*), and corresponding EDS line scan profile for elements of Pt and Pd (*bottom*) (Reproduced from Palmre et al. 2014)

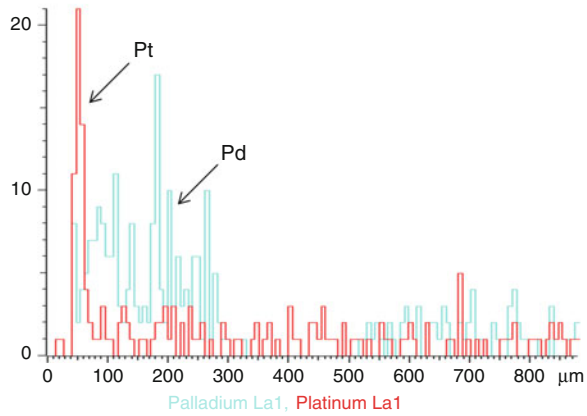
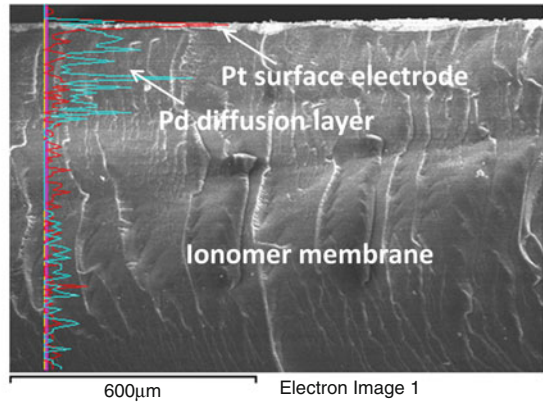
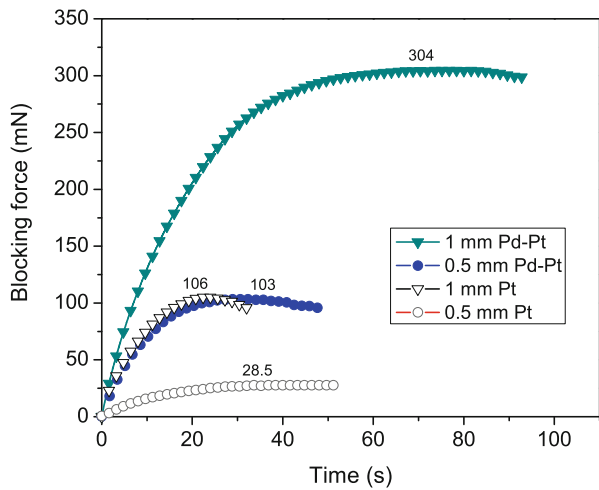


Fig. 4 Blocking force response in time for IPMCs with Pt and Pd-Pt electrodes at 4 V DC input (Reproduced from Palmre et al. 2014)



subsequent reduction of Cu^{2+} ions at the cathode upon actuation can maintain electrical conductivity between the platinum particles during the deformation. The drawbacks of this electrode configuration are the copper layer oxidation and growth of copper dendrites at the electrodes. Also, silver nanopowder and nickel have been used as cost-effective electrode materials (Chung et al. 2006; Siripong et al. 2006). However, the low electrochemical stability of these materials can limit the cycle life of IPMC.

From the aforementioned materials, the noble metals (Pt, Au, or Pd) are usually a preferred choice for IPMC electrodes due to their high electrical conductivity and electrochemical stability and availability in cation complex form that can be effectively used with electroless plating method.

1.2 Nonmetallic Electrode Materials

Recently, various nonmetallic conductive materials have gained interest as electrode materials for IPMCs. For instance, transition metal oxide powders (such as RuO_2) (Akle et al. 2007b), carbon nanotubes (Akle and Leo 2008; Lee et al. 2007), graphene (Kim et al. 2014b), highly porous-activated and carbide-derived carbons (Palmre et al. 2009), and carbon aerogels (Palmre et al. 2011) have been investigated for IPMC electrodes. The powder materials can be assembled into electrodes by physical heat-pressing using direct assembly method (Akle et al. 2007a) or casting technique (Fukushima et al. 2005). The direct assembly method consists of first mixing the conductive powder in Nafion-alcohol dispersion and then applying the conductor/ionomer mixture directly by painting on the surface of ionic polymer membrane (Fig. 5). Finally, the obtained composite is laminated between two gold foil layers by heat-pressing to conjugate the electrodes layers with the membrane (Fig. 6). Alternatively, the casting technique is based on casting the conductive powder/polymer mixture into individual electrode films and assembling them together by heat-pressing. Compared to the noble metals, the conductive powders are less expensive and have a large specific surface area, which is desired for creating high charge density at polymer-electrode interface. For instance, the specific surface area of carbon nanotubes can be up to $1000 \text{ m}^2/\text{g}$, while the highly porous carbide-derived carbons (CDCs) typically range from 1000 to $2000 \text{ m}^2/\text{g}$. CDCs are produced by extraction of metal ions from carbide precursor by chlorination at elevated temperatures (Presser et al. 2011). CDCs are also unique for their precisely controllable synthesis process that allows fine-tuning the pore dimensions according to electrolyte properties (Gogotsi et al. 2003). However, the mentioned powder materials have generally insufficient electric conductivity. Therefore, the electrode surface is covered additionally with a conductive gold foil layer (Akle et al. 2007a; Palmre et al. 2009). The added metallic layer makes the manufacturing process often more complicated and can cause problems due to the delamination under cyclic deformation (Akle et al. 2007b). The porous carbon materials, particularly activated carbons and carbide-derived carbons prepared at low chlorination temperatures, also tend to have poor electrical conductivity within the electrode cross section

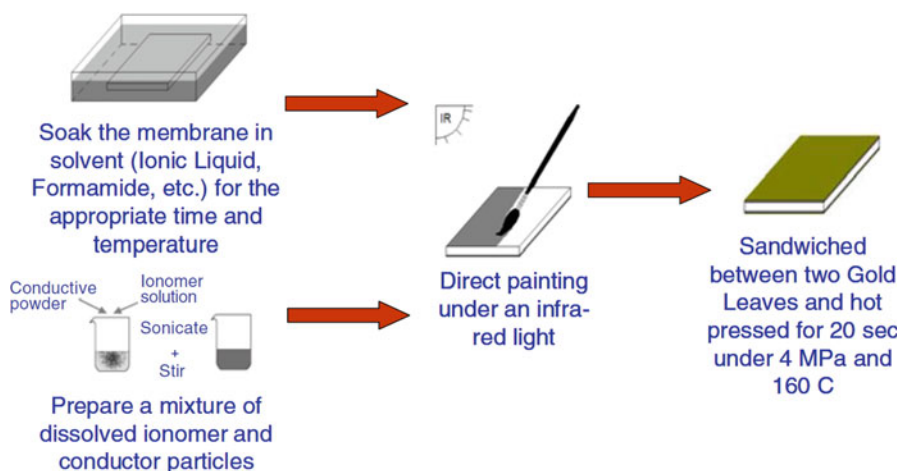


Fig. 5 Schematic showing the four steps of the direct assembly process for building IPMC materials (Reproduced from Akle et al. 2007a, with kind permission from Springer Science and Business Media.)

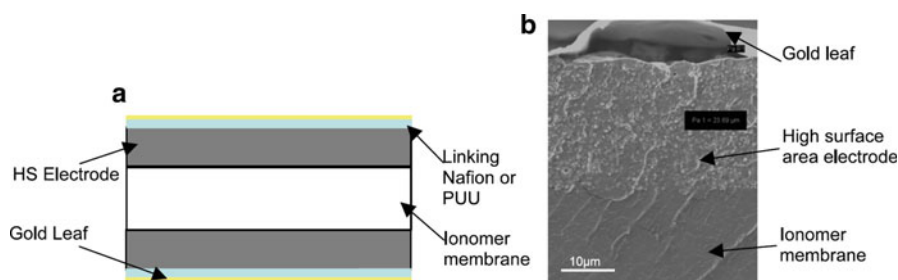


Fig. 6 (a) Schematic of IPMC assembled using direct assembly process. (b) SEM image of the upper high surface area RuO₂ electrode (Akle et al. 2007b. © IOP Publishing. Reproduced by permission of IOP Publishing. All rights reserved)

(Palmre et al. 2012). This results in a slow electrical double-layer charging and a slow electromechanical response of an actuator. Also, it has been noted that activated carbons, despite having a large specific surface area, exhibit a limited capacitance due to their low mesoporosity and resulting poor electrolyte accessibility (Lu et al. 2011). Therefore, conductive additives such as nanotubes, carbon black, and polyaniline (PANI) have been added in the carbon electrodes to increase the mesoporosity as well as electric conductivity, thereby improving considerably the performance of the electrodes (Lu et al. 2011; Sugino et al. 2011).

Several studies have indicated that the accumulation of electrolyte charges in the vicinity of electrodes is the key to producing a high strain and force output of IPMC (Akle et al. 2006; Wallmersperger et al. 2008; Pugal et al. 2011).

Table 1 Electromechanical properties of IPMCs with different conductive electrode materials (Palmre et al. 2009)

Electrode material	Maximum peak-to-peak stain (mε)	Maximum strain rate (me s ⁻¹)	Blocking force (mN)
Carbide-derived carbon	20.4	2.3	3.6
Coconut shell-based activated carbon	10.3	1.6	3.1
RuO ₂ (anhydrous)	9.4	0.93	3.3
RuO ₂ (hydrous)	6.9	1.7	3.5

Therefore, designing the electrodes with high specific surface area is gaining momentum in the development of IPMC materials (Torop et al. 2011; Palmre et al. 2011, 2014; Sugino et al. 2011). Promising electrode materials for this purpose are the mentioned highly porous carbons and carbon nanotubes. The CDC-based IPMC electrodes have shown one of the best performances among nonmetallic electrodes, exceeding the peak strain and strain rate of RuO₂ electrodes more than twice (Table 1) (Palmre et al. 2009). However, there are still challenges to overcome such as insufficient electric conductivity and limited electrolyte diffusion in the carbon electrode structure. Also, it is important to note that the nonmetallic powder materials require physical assembly by heat-pressing and therefore are mainly suited for fabricating “dry-type” actuators based on nonvolatile electrolytes such as ionic liquids (Akle et al. 2007b). One of the challenges with using the ionic liquids as electrolytes is the lower response speed compared to the water-solvated membranes (Bennett and Leo 2004). Therefore, water-based IPMCs manufactured by electroless plating of noble metals that offer one of the fastest strain responses and ability to be operated in aqueous environment are more suited for underwater robotic applications.

2 Ionic Polymer Membranes

Ionic polymer membranes play an important role in determining actuator performances. Especially, their electro-chemo-mechanical properties, such as ion transport properties (ionic-exchange capacity (IEC), liquid electrolyte uptake and ionic conductivity, etc.) and the mechanical properties (tensile modulus, strength, and elongation, etc.), must be evaluated carefully to enhance the actuator performances. As the most popular materials used for IPMC membranes, perfluorinated polymers, such as Nafion and Flemion with ionic sulfonate or carboxylate groups, respectively, are widely investigated. Nafion is a perfluorinated sulfonic acid ionomer membrane consisting of a Teflon-like backbone and short side chains terminated by hydrophilic sulfonic acid groups. However, these perfluorinated ionomer membranes suffer from significant drawbacks, such as low actuation bandwidth, low blocking force and durability, environmentally unfriendliness of fluorinated polymer, and high cost of fabrication, which curtail their practical applications. To overcome these problems, many synthetic ionic polymers have been proposed as leading candidates. As one of

alternative ionic polymers, sulfonated hydrocarbon polymers have received significant amount of attention due to their cost-effectiveness, easy fabrication, tunable stiffness, and high ion transport properties, resulting from their controllable monomer composition, especially via manipulation of block copolymers. Another solution is to utilize naturally abundant functional biopolymers, such as cellulose-derivatives and chitosan with high ionic conductivity, environmental friendliness, low cost, and uniform film formation. Yet another solution is to reinforce functional nanoparticles in a polymer matrix, resulting in a high-performance nanocomposite membrane. This section intends to provide an overview of the recent research developments in ionic polymer membranes.

2.1 Sulfonated Hydrocarbon Backbone Membranes

A great deal of effort has been invested in the development of sulfonated aromatic or aliphatic hydrocarbon backbone polymers by adopting the post sulfonation process, blending method, and cross-linking procedure to control hydrophilic-hydrophobic morphology and electro-chemo-mechanical properties. For instance, sulfonated poly(styrene-ran-ethylene) (SPSE, Wang et al. 2010a) with aliphatic hydrocarbon backbone, cross-linked SPSE (XSPSE, Wang et al. 2010c) with better microphase-separated morphology by UV irradiation, and sulfonated aromatic PEI (polyetherimide) (SPEI, Rajagopalan et al. 2010) with controllable stiffness have been investigated as alternative IPMC membranes. Also, several ionic networking membranes have been developed through blending and cross-linking methods. Poly(styrene-alt-maleimide) (PSMI)-incorporated poly(vinylidene fluoride) (PVDF) (PSMI/PVDF, Lu et al. 2008a, b) exhibited several times larger bending performance than the Nafion counterpart due to unique hydrophilic nanochannels. Sulfonated poly(ether ether ketone)-incorporated PVDF (SPEEK/PVDF, Jeon et al. 2009) showed excellent electromechanical responses due to the tailored stiffness and nanochannels inside the ionic networking matrix. Cross-linked PVA/SPTES (Wang et al. 2010b) was developed by physical cross-linking between SPTES (sulfonated poly(arylenethioethersulfone)) copolymer and PVA (polyvinyl alcohol), resulting in an absence of back-relaxation and a dramatic increase in bending deformation. Different types of hydrocarbon backbone membranes have also been presented and compared (Jo et al. 2013). However, these hydrocarbon series still have limitations that do not satisfy the desired electro-chemo-mechanical properties and fail to deliver better actuation performances beyond those of Nafion (Fig. 7).

2.2 Sulfonated Block Copolymer Membrane Materials

Several sulfonated block copolymers such as SSEBS (sulfonated poly(styrene-*b*-ethylene-co-butylene-*b*-styrene)) block copolymer (Wang et al. 2007), ABA-Triblock copolymer (Imaizumi et al. 2012), sulfonated pentablock ABCBA copolymers (Gao et al. 2012), and sulfonated pentablock ionomer (PBI)-based

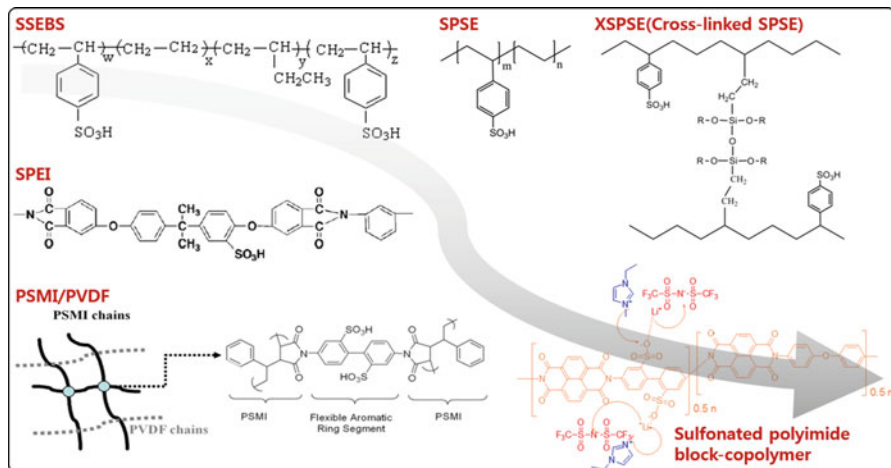


Fig. 7 Several hydrocarbon backbone membranes for preparing IPMC membrane materials (SSEBS, Wang et al. 2007. © 2007 Elsevier Ltd. Reproduced by permission of Elsevier BV.; SPSE, Wang et al. 2010a. © 2010 Society of Chemical Industry. Reproduced by permission of John Wiley & Sons, Inc.; SSPSE, Wang et al. 2010c. © 2010 Elsevier Ltd. Reproduced by permission of Elsevier BV.; SPEI, Rajagopalan et al. 2010. © 2010 Elsevier Ltd. Reproduced by permission of Elsevier BV.; PSMI/PVDF, Lu et al. 2008a. © 2008 WILEY-VCH Verlag GmbH & Co. Reproduced by permission of John Wiley & Sons, Inc.; SPI, Cheedarala et al. 2014. © 2014 WILEY-VCH Verlag GmbH & Co. Reproduced by permission of John Wiley & Sons, Inc. All rights reserved.)

copolymers (Vargantwar et al. 2012), which contain hydrophilic nanochannels and well-organized nanostructure networks with micro-/nanomorphology, have been investigated to enhance actuator performance. Unfortunately, these sulfonated block copolymer membranes have difficulties in fabrication, which include a complex synthesis procedure and low mass production, and deficiencies in their electrochemo-mechanical properties. Therefore, an alternative synthetic approach is needed to develop novel and simple block copolymers with intriguing nanostructures in a polymer matrix. As one of promising block copolymers, sulfonated polyimide (SPI) block copolymers contain alternate hydrophobic and hydrophilic multiblocks having aliphatic and aromatic segments and display high thermal stability, high ionic conductivity, reliable mechanical properties, and low price. Recently SPI-based actuator with well-defined silver electrodes was developed via an in situ self-metallization (Song et al. 2011). The total fabrication procedure involves the synthesis of a sulfonated poly(amic acid) (SPAA) membrane precursor for SPI derived from BTDA, ODA, and lithium-containing BDSA as a dianhydride and diamine, respectively. After the ionic-exchange process with the Ag salt, the SPAA-Ag⁺ membrane was subjected to thermal treatment, resulting in imidization of SPAA and simultaneous reduction of silver cations to silver metal layer on both sides of the membrane as shown in Fig. 8a, b.

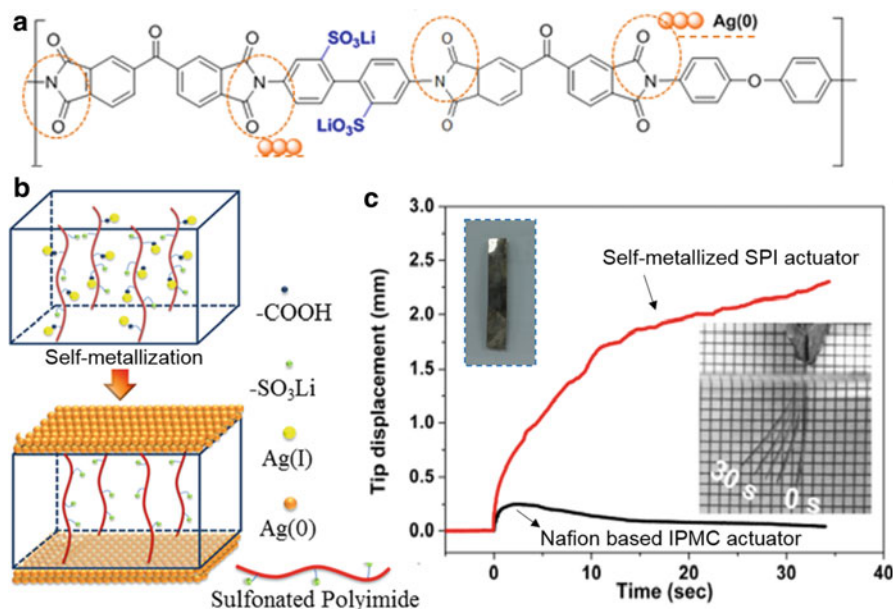


Fig. 8 (a) Chemical structure of SPI with self-metallized silver electrodes, (b) schematic illustration of self-metallization process, (c) step responses of self-metallized SPI actuator and Nafion-based IPMC actuator under 0.5 V DC voltage (Song et al. 2011. © 2011 WILEY-VCH Verlag GmbH & Co. Reproduced by permission of John Wiley & Sons, Inc. All rights reserved.)

Compared with a Nafion-based actuator, the self-metallized SPI actuator with highly conductive silver electrodes showed a much larger tip displacement without the back-relaxation phenomenon under low 0.5 V DC voltage (Fig. 8c). But further investigation for high-performance actuator is needed due to its moderate electroactive performance and poor durability, resulting from the oxidation of silver layers under higher voltage stimulation. Furthermore, SPI-based actuators from a combination of ionic liquid, polyimide, and carbon electrode materials were reported (Imaizumi et al. 2013). But, until now, SPI-based polymer actuators, which have relatively high mechanical properties, low actuation performance, and inferior durability due to densely packed polymer matrix and low compatibility with metallic electrodes fabricated by electroless plating, have not been improved.

Very recently a self-assembled 3D ionic networked SPI polymer actuator with π - π stacked layers and alternate hydrophilic nanochannels have been investigated by introducing simple and strong atom-level regio-specific interaction of hydrophilic and hydrophobic SPI coblocks with anions and cations in the ionic liquid (EMI. Tf_2N) (Cheedarala et al. 2014). Moreover, facile and ultrafast all-solution process involving solvent blending, dry casting, and drop casting was developed to make all-organic soft actuators with highly conductive and flexible PEDOT:PSS electrodes (Fig. 9a). This higher bending performance of the newly developed Ntda-SPI- SO_3Li -EMI. Tf_2N is induced by the high ionic conductivity and tuned

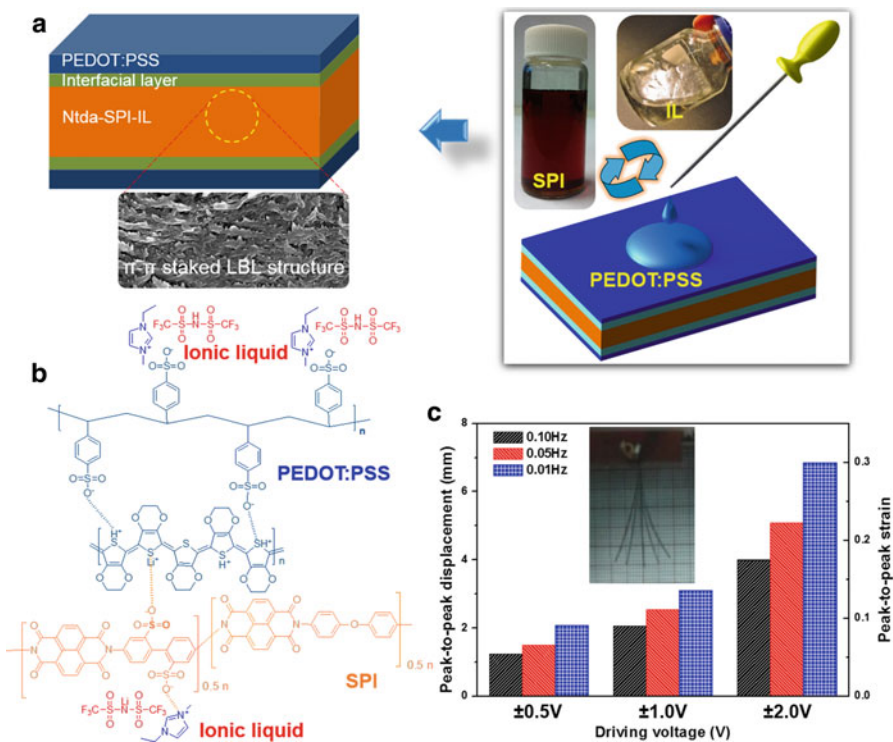


Fig. 9 (a) Schematic illustration of SPI actuator based on a π - π stacked 3D ionic network membrane and ultrafast solution processing, (b) chemical interaction among SPI, ionic liquid, and PEDOT:PSS, (c) peak-to-peak strains at different voltages and frequencies (Cheedarala et al. 2014). © 2014 WILEY-VCH Verlag GmbH & Co. Reproduced by permission of John Wiley & Sons, Inc. All rights reserved.)

mechanical properties, resulting from strong ionic interactions among the SO_3Li , ionic liquid and PEDOT:PSS, and π - π stacked 3D-networked polymer matrix with continuous and interconnected ion transport nanochannels (Fig. 9b). Therefore, large peak-to-peak strains of over 0.05 were acquired in all frequency ranges over ± 0.5 V as shown in (Fig. 9c).

2.3 Biopolymer Membrane Materials

Development of high-performance biopolymer membranes has been attempted to solve the problems of conventional synthetic ionic polymers. As one of efforts, well-defined and regular electrospun PANI/CA biopolymer actuators with a good dispersion of chopped PANI (polyaniline) nanoparticles inside the CA (cellulose acetate) nanofibers were reported (Hong et al. 2013). Only a small amount of chopped PANI nanoparticles (0.1 % and 0.5wt%), inducing well-dispersed nanoporous structures

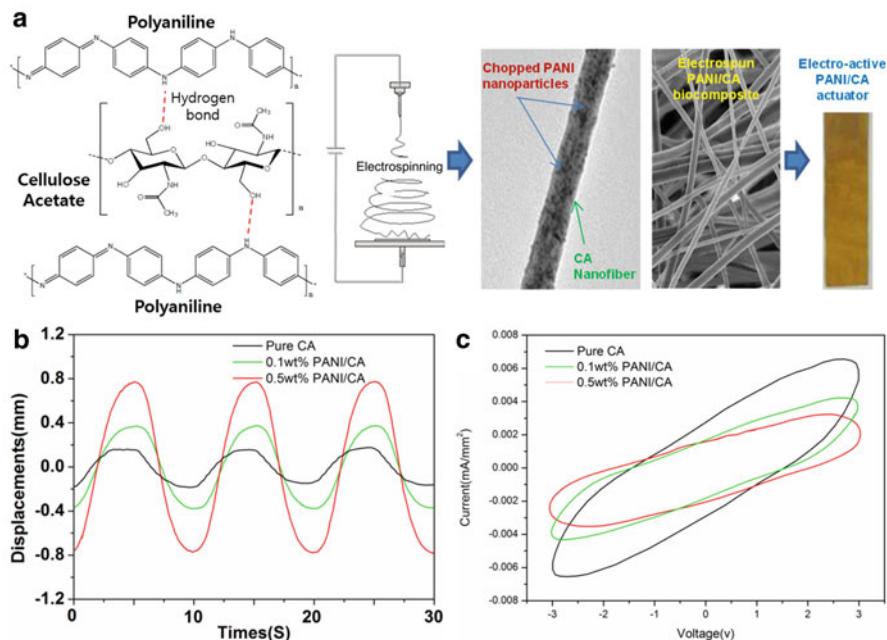


Fig. 10 (a) Schematic diagram of fabrication process for electrospun PANI/CA actuators, (b) harmonic responses, (c) hysteresis responses of electrospun actuators under sinusoidal electrical inputs with peak voltage of 3 V and excitation frequency of 0.1 Hz (Hong et al. 2013). © 2013 Elsevier Ltd. Reproduced by permission of Elsevier BV. All rights reserved.)

(Fig. 10a), can improve the actuation performance of cellulose-based actuators due to the enhanced material properties as presented in Fig. 10b. Moreover, the consumed power of 0.5wt% PANI/CA actuator is lower than that of others because of the effect of highly conductive PANI nanoparticles and their good dispersion in CA matrix (Fig. 10c). Therefore, this investigation suggests that the electrospinning is an extremely practical and effective technique for constructing a series of well-dispersed nanoporous membranes with controllable and repeatable products, unlike conventional casting method.

To make high-performance air-working actuators, ionic liquids as mobile salts should be embedded in the cellulose membrane. But pure cellulose is not familiar with absorbing much ionic liquid because of its packed structure and high crystallinity. Therefore, freeze-dried bacterial cellulose (FDBC) with sponge-like porous network structure through a simple freeze-dry method at -50°C for 24 h can be used to solve these problems. Because FDBC with high porosity and large surface area can absorb a large quantity of ionic liquid and exhibit enhanced electrochemical properties. A novel high-performance electro-active biopolymer actuator with a tri-layered sandwich structure that consists of FDBC and poly(3,4-ethylenedioxythiophene) poly(styrenesulfonate) (PEDOT:PSS) face sheet layers was developed as presented in Fig. 11a (Kim et al. 2013). The actuation

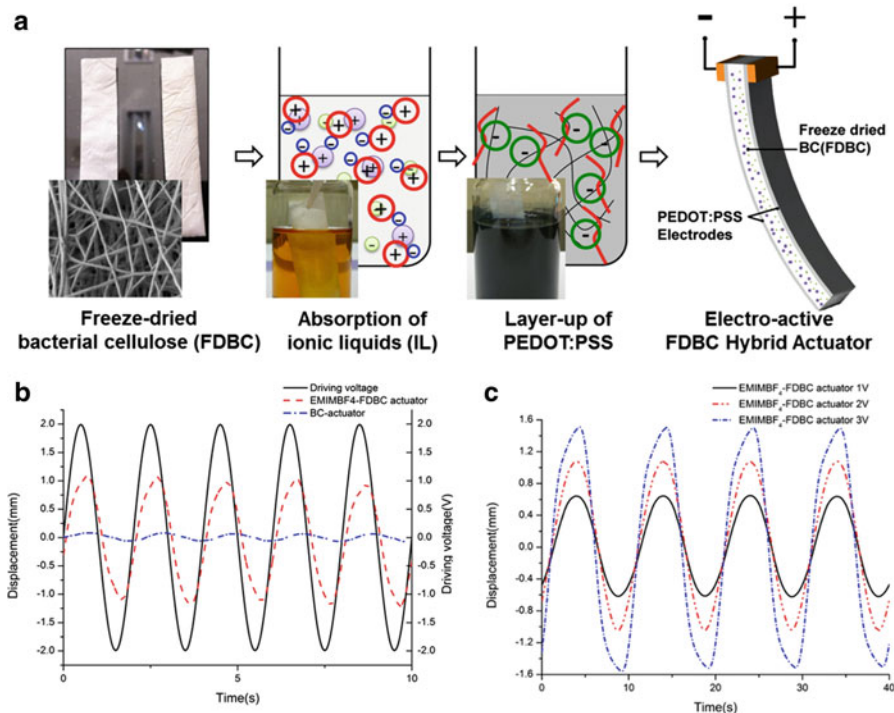


Fig. 11 (a) Fabrication steps of the FDBC actuator, (b) actuation performance of a FDBC actuator compared with a pure BC actuator, (c) harmonic response of FDBC actuators using EMIM-BF₄ (Kim et al. 2013. © 2013 IOP Publishing Ltd. Reproduced by permission of IOP Publishing. All rights reserved.)

performance of the developed actuator was significantly improved through the synergistic effects of the electrochemical doping processes of PEDOT:PSS electrode layers and sufficient ion migration of the dissociated ionic liquids inside the FDBC with a sponge form. So the FDBC actuator exhibited a much larger bending deformation than pure bacterial cellulose actuator as shown in Fig. 11b. Also, under sinusoidal excitation with an excitation frequency of 0.1 Hz and peak voltage of 3 V, the EMIM-BF₄ absorbed FDBC actuator, inducing much larger bending deformations, reached a peak tip displacement of ± 1.511 mm (Fig. 11c).

2.4 Nanocarbon-Composite Membrane Materials

Reinforcement by the incorporation of electrically conductive 0D/1D/2D/3D carbon nanoparticles into polymer matrix is a promising approach to achieve improved electro-chemo-mechanical properties including enhanced ionic transport properties and tunable mechanical stiffness over pristine polymers. Therefore, conductive

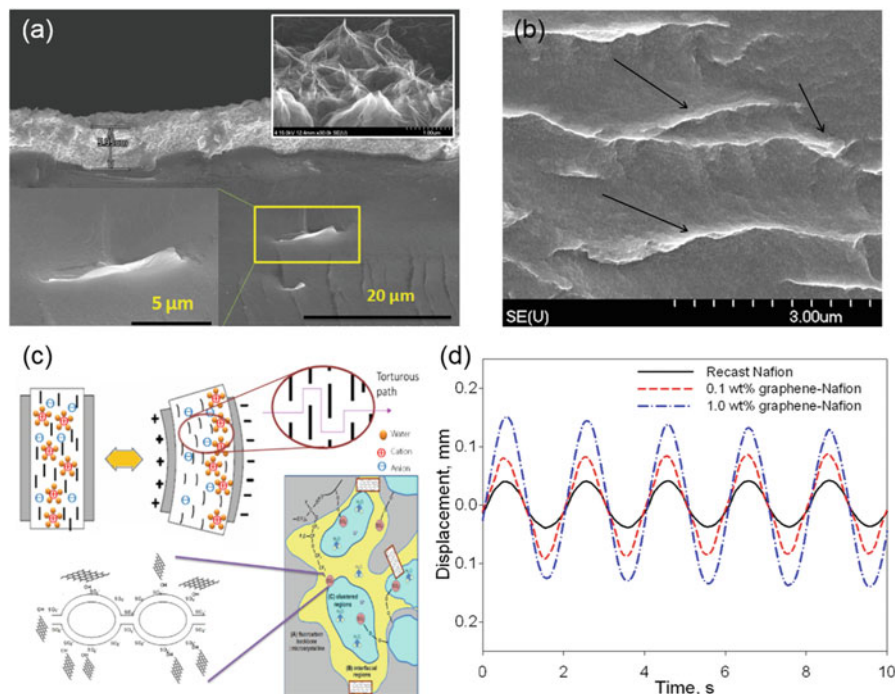


Fig. 12 Graphene-Nafion polymer actuator; (a) cross-sectional SEM image, (b) magnified SEM image, (c) schematic representation of ionic conductivity in hydrated graphene-Nafion composites, (d) harmonic response (Jung et al. 2011). © 2010 Elsevier Ltd. Reproduced by permission of Elsevier BV. All rights reserved.)

carbon nanoparticles such as 0D (fullerene, polyhydroxylated fullerene (PHF)), 1D (SWNT, MWNT, CNF), 2D (Graphene), and 3D (hierarchical G-CNT-Fe/G-CNT-Pd carbon nanostructure) have been reinforced into ionic polymer membranes to enhance their physicochemical properties and actuation performance. Several nanocomposite actuators have been investigated, i.e., (i) 0D carbon nanostructures: C₆₀-reinforced Nafion (Jung et al. 2010; Oh et al. 2010), fullerenol-cellulose (Li et al. 2011), and fullerenol-SPEI (Rajagopalan and Oh 2011), (ii) 1D carbon nanostructures : CNF-reinforced SSEBS (Wang et al. 2009), (iii) 2D carbon nanostructures : Graphene-Nafion (Jung et al. 2011), Graphene oxide-chitosan (Jeon et al. 2013), and Ionic polymer-graphene composite (IPGC, Kim et al. 2014b), (iv) 3D carbon nanostructures : 3D G-Fe-reinforced polyurethane (Lee et al. 2014), and 3D G-Pd-reinforced conducting polymer (Kim et al. 2014a).

Especially graphene is an intriguing 2D flat material of monolayer carbon atoms whose distinct properties make it very promising in actuator applications. Recently, a graphene-reinforced Nafion nanocomposite actuator was developed as shown in Fig. 12a (Jung et al. 2011). The layered structure of graphene in the graphene-Nafion composites showed that graphene layers are aligned parallel to the surface of

membrane and can provide tortuous pathway for ion transport (Fig. 12b, c). Although higher graphene concentration showed a decrease in water adsorption caused by the reduction of degree of ion clustering due to a decrease in the cluster size and the exchange sites per cluster, a marginal increase in IEC with increasing graphene was observed, thereby leading to enhanced actuation performance. The tip displacement of the 1.0 wt% graphene-reinforced actuator is almost two times that of the recast Nafion-based IPMC actuator (Fig. 12d). These results demonstrate that the electro-chemo-mechanical properties and actuation performances were significantly improved due to a minute loading of graphene, resulting from the great interaction between graphene and Nafion.

In order to develop an economically viable, highly durable, and bio-friendly ionic polymer actuator with superior electro-chemo-mechanical properties, a simple route for a high-performance ionic bio-nanocomposite based on pendent sulfonated chitosan (PSC) and functionalized graphene oxide (GO) have been investigated (Jeon et al. 2013). The amine groups in the chitosan were actively used to tune the degree of sulfonation (DOS) of PSC by controlled reaction with 1,3-propyl sultone and with GO. Thus, PSC can act as a higher ionic-exchangeable membrane due to the availability of propyl sulfonic acid groups that can strongly binding with free amines and with ionic liquid. Furthermore, electro-chemo-mechanical activities of PSC can be maximized by simply reinforcing with GO, resulting in improving in-plane mechanical stiffness and electro-chemo-mechanical properties through strong ionic interactions and bonding with free amines and sulfonic acid groups (Fig. 13a). Minute loading of graphene oxide (1.0 wt%) to PSC greatly improves step responses without the back-relaxation phenomenon (Fig. 13b, c). This improvement can be attributed to relatively higher ionic conductivity and large capacitance, and effective delay of ionic liquid migration in the reduced ionic pores homogeneously distributed in GO(1.0 wt%)-PSC-IL matrix.

Recent attention to the correlation of morphological structure (microphase-separated morphology, well-dispersed porous structures and self-assembled nanostructures, etc.) with ion migration mechanisms to enable more efficient ion transport has led to new ways to make high-performance IPMC actuators. There are several research approaches to easily controlling hydrophobic and hydrophilic composition, size of ionic nanochannels, and their stiffness of ionic polymer membranes as well as modulating significant factors such as their ionic-exchange capacity, degree of sulfonation, capacitance, ionic conductivity, liquid electrolyte uptake, and mechanical properties. As one of the recent advances in ionic polymer membranes, herein we briefly introduced promising alternative ionic polymer membranes such as self-assembled sulfonated polyimide block copolymers, functional cellulose-based biopolymers, and graphene-reinforced nanocomposites, and technical considerations including freeze drying method, all-solution process, electrospinning technique, and reinforcement of conductive nanoparticles. Especially, the sulfonated 3D-networked porous structure membranes based on sulfonated polyimide block copolymer and pendent sulfonated chitosan biopolymers can be promising candidates for high-performance ionic polymer membrane materials. Furthermore, electrically conductive and hierarchical nanoparticle additives like 3D carbon

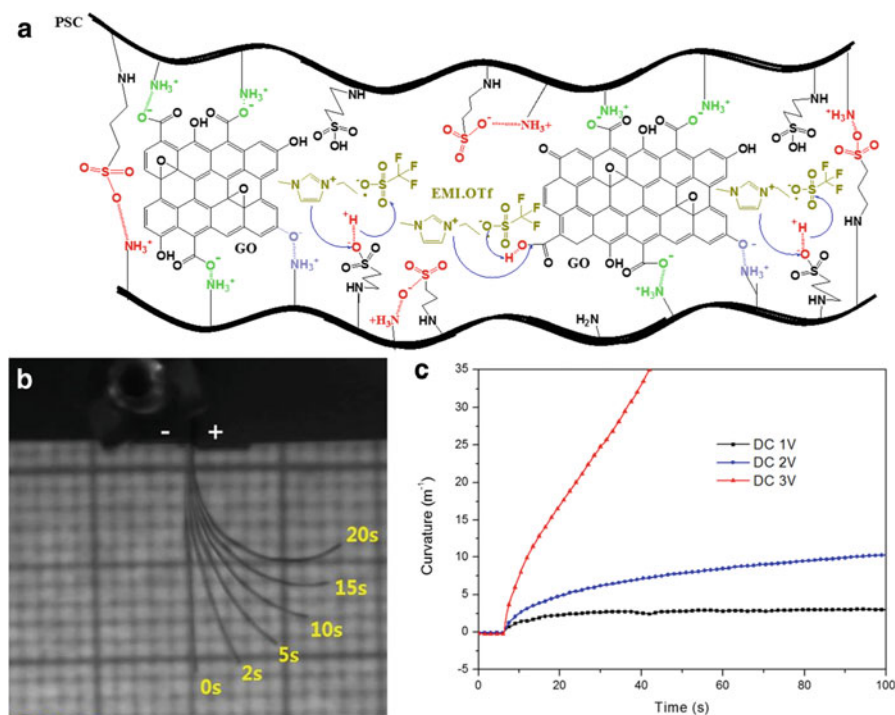


Fig. 13 (a) Synthesis of GO-PSC-IL bio-nanocomposite membrane, (b) electro-mechanically deformed shapes of GO(1.0 wt%)-PSC-IL actuator under a step input, (c) step responses of GO (1.0 wt%)-PSC-IL actuator according to driving voltages (Jeon et al. 2013. © 2013 WILEY-VCH Verlag GmbH & Co. Reproduced by permission of John Wiley & Sons, Inc. All rights reserved.)

nanostructures can greatly increase the output tip displacement, generated blocking force and energy efficiency even more. However, there is still need for more challenges and research studies to realize full potential of the ionic polymer-based high-performance IPMCs and overcome their insufficient controllable structure, material properties, and low repeatability and robustness of the actuation performance.

3 Conclusions

In this chapter, recent developments in electrode materials and ionic polymer membranes used for manufacturing IPMCs were reviewed. Although noble metals such as platinum and gold are commonly used for electrodes in water-based systems and applications for their excellent electrochemical properties, also various nonmetallic conductive carbon derivatives are considered as promising alternatives for fabricating “dry-type” IPMC actuators. These carbon derivatives include nanotubes and nanoporous-activated and carbide-derived carbons. While their electric conductivity

is generally less than that of noble metals, the mentioned carbon materials offer some important qualities such as high specific surface area and lower cost.

In spite of wide popularity of Nafion membranes, other less expensive and better-performing ionomers have been explored for IPMCs. One of the alternatives is sulfonated hydrocarbon polymers that offer cost-effectiveness, easy fabrication, tunable stiffness, and high ion transport properties, resulting from their controllable monomer composition. Also, naturally abundant functional biopolymers, such as cellulose-derivatives and chitosan with high ionic conductivity, environmental friendliness, and low cost, have been used for IPMC membrane. A promising approach is also reinforcement by incorporating functional carbon nanoparticles, such as fullerenes, nanotubes, and graphene, in a polymer matrix, resulting in a high-performance nanocomposite membrane.

Acknowledgments KJK acknowledges the financial support from various agencies who supported IPMC research including the US Office of Naval Research (ONR), US National Science Foundation (NSF), and National Aeronautics and Space Administration (NASA).

References

- Akle BJ, Leo DJ (2008) Single-walled carbon nanotubes – ionic polymer electroactive hybrid transducers. *J Intell Mater Syst Struct* 19:905–915
- Akle BJ, Bennett MD, Leo DJ (2006) High-strain ionomeric-ionic liquid electroactive actuators. *Sensors Actuators A Phys* 126(1):173–181
- Akle BJ, Bennett MD, Leo DJ et al (2007a) Direct assembly process: a novel fabrication technique for large strain ionic polymer transducers. *J Mater Sci* 42(16):7031–7041
- Akle B, Nawshin S, Leo D (2007b) Reliability of high strain ionomeric polymer transducers fabricated using the direct assembly process. *Smart Mater Struct* 16(2):S256–S261
- Bennett MD, Leo DJ (2004) Ionic liquids as stable solvents for ionic polymer transducers. *Sensors Actuators A Phys* 115:79–90
- Cheedarala RV, Jeon JH, Kee CD et al (2014) Bio-inspired all-organic soft actuator based on π - π stacked 3D ionic network membrane and Ultra-Fast Solution Processing. *Adv Funct Mater* (In press)
- Chung CK, Fung PK, Hong YZ, Ju MS, Lin CCK, Wu TC (2006) A novel fabrication of ionic polymer-metal composites (IPMC) actuator with silver nano-powders. *Sensors Actuators B Chem* 117(2):357–375
- Fujiwara N, Asaka K, Nishimura Y et al (2000) Preparation of gold – solid polymer electrolyte composites as electric stimuli-responsive materials. *Chem Mater* 12(6):1750–1754
- Fukushima T, Asaka K, Kosaka A et al (2005) Fully plastic actuator through layer-by-layer casting with ionic-liquid-based bucky gel. *Angew Chem Int Ed* 44:2410–2413
- Gao R, Wang D, Heflin JR et al (2012) Imidazolium sulfonate-containing pentablock copolymer–ionic liquid membranes for electroactive actuators. *J Mater Chem* 22:13473–13476
- Gogotsi Y, Nikitin A, Ye H et al (2003) Nanoporous carbide-derived carbon with tunable pore size. *Nat Mater* 2(9):591–594
- Hong CH, Ki SJ, Jeon JH et al (2013) Electroactive bio-composite actuators based on cellulose acetate nanofibers with specially chopped polyaniline nanoparticles through electrospinning. *Compos Sci Technol* 87:135–141
- Imazumi S, Kokubo H, Watanabe M (2012) Polymer actuators using ion-gel electrolytes prepared by self-assembly of ABA-triblock copolymers. *Macromolecules* 45(1):401–409

- Imaizumi S, Ohtsuki Y, Yasuda T et al (2013) Printable polymer actuators from ionic liquid, soluble polyimide, and ubiquitous carbon materials. *ACS Appl Mater Inter* 5(13):6307–6315
- Jeon JH, Kang SP, Oh IK (2009) Novel biomimetic actuator based on SPEEK and PVDF. *Sensor Actuators B* 143(1):357–364
- Jeon JH, Kumar R, Kee CD et al (2013) Dry-type artificial muscles based on pendent sulfonated chitosan and functionalized graphene oxide for greatly enhanced ionic interactions and mechanical stiffness. *Adv Funct Mater* 23(48):6007–6018
- Johanson U, Mäeorg U, Sammelseg V, Brandell D, Punning A, Kruusmaa M, Aabloo A (2008) Electrode reactions in Cu-Pt coated ionic polymer actuators. *Sensor Actuators B* 31:340–346
- Jo CH, Pugal D, Oh IK et al (2013) Recent advances in ionic polymer-metal composite actuators and their modeling and applications. *Prog Polym Sci* 38(7):1037–1066
- Jung JH, Vadahanambi S, Oh IK (2010) Electro-active nano-composite actuator based on fullerene-reinforced Nafion. *Compos Sci Technol* 70(4):584–592
- Jung JH, Jeon JH, Sridhar V et al (2011) Electro-active graphene–Nafion actuators. *Carbon* 49(4):1279–1289
- Kim SM, Kim KJ (2008) Palladium buffer-layered high performance ionic polymer-metal composites. *Smart Mater Struct* 17(3):035011
- Kim KJ, Shahinpoor M (2003) Ionic polymer-metal composites: II. Manufacturing techniques. *Smart Mater Struct* 12(1):65–79
- Kim SS, Jeon JH, Kee CD et al (2013) Electro-active hybrid actuators based on freeze-dried bacterial cellulose and PEDOT:PSS. *Smart Mater Struct* 22(8):085026
- Kim HJ, Randriamahazaka H, Oh IK (2014a) Highly conductive, capacitive, flexible and soft electrodes based on 3D graphene-nanotube-palladium hybrid and conducting polymer. *Small* 10(24):5023–5029
- Kim J, Jeon JH, Kim HJ et al (2014b) Durable and water-floatable ionic polymer actuator with hydrophobic and asymmetrically laser-scribed reduced graphene oxide paper electrodes. *ACS Nano* 8(3):2986–2997
- Lee DY, Park IS, Lee MH et al (2007) Ionic polymer–metal composite bending actuator loaded with multi-walled carbon nanotubes. *Sensors Actuators A Phys* 133(1):117–127
- Lee SH, Jung JH, Oh IK (2014) 3D networked graphene-ferromagnetic hybrids for fast shape memory polymers with enhanced mechanical stiffness and thermal conductivity. *Small* 10(19):3880–3886
- Li J, Vadahanambi S, Kee CD et al (2011) Electrospun fullerene-cellulose biocompatible actuators. *Biomacromolecules* 12(6):2048–2054
- Lu J, Kim SG, Lee S et al (2008a) A biomimetic actuator based on an ionic networking membrane of poly(styrene-alt-maleimide)-incorporated poly(vinylidene fluoride). *Adv Funct Mater* 18(8):1290–1298
- Lu J, Kim SG, Lee S et al (2008b) Fabrication and actuation of electro-active polymer actuator based on PSMI-incorporated PVDF. *Smart Mater Struct* 17(4):045002
- Lu W, Hartman R, Qu L et al (2011) Nanocomposite electrodes for high-performance supercapacitors. *J Phys Chem Lett* 2(6):655–660
- Nemat-Nasser S (2002) Micromechanics of actuation of ionic polymer-metal composites. *J Appl Phys* 92:2899–2915
- Oh IK, Jung JH, Jeon JH et al (2010) Electro-chemo-mechanical characteristics of fullerene-reinforced ionic polymer-metal composite transducers. *Smart Mater Struct* 19(7):075009
- Palmre V, Brandell D, Maeorg U et al (2009) Nanoporous carbon-based electrodes for high strain ionomeric bending actuators. *Smart Mater Struct* 18(9):095028
- Palmre V, Lust E, Jänes A et al (2011) Electroactive polymer actuators with carbon aerogel electrodes. *J Mater* 21:2577–2583
- Palmre V, Torop J, Arulepp M et al (2012) Impact of carbon nanotube additives on carbide-derived carbon-based electroactive polymer actuators. *Carbon* 50(12):4351–4358
- Palmre V, Kim SJ, Pugal D, Kim K (2014) Improving electromechanical output of IPMC by high surface area Pd-Pt electrodes and tailored ionomer membrane thickness. *Int J Smart Nano Mater* 5(2):99–113

- Presser V, Heon M, Gogotsi Y (2011) Carbide-derived carbons – from porous networks to nanotubes and graphene. *Adv Funct Mater* 21:810–833
- Pugal D, Kim KJ, Aabloo A (2011) An explicit physics-based model of ionic polymer-metal composite actuators. *J Appl Phys* 110:084904–084909
- Punning A, Kruusmaa A, Aabloo A (2007) Surface resistance experiments with IPMC sensors and actuators. *Sensors Actuators A Phys* 133(1):200–209
- Rajagopalan M, Oh IK (2011) Fullerenol-based electroactive artificial muscles utilizing biocompatible polyetherimide. *ACS Nano* 5(3):2248–2256
- Rajagopalan M, Jeon JH, Oh IK (2010) Electric-stimuli-responsive bending actuator based on sulfonated polyetherimide. *Sensor Actuators B* 151(1):57–64
- Shahinpoor M, Kim KJ (2001) Ionic polymer-metal composites: I. Fundamentals. *Smart Mater Struct* 10(4):819–833
- Siripong M, Fredholm S, Nguyen QA, Shih B, Itescu J, Stolk J (2006) Symposium W – electroresponsive polymers and their applications, MRS proceedings. *Mater Res Soc* 889.
- Song J, Jeon JH, Oh IK et al (2011) Electro-active polymer actuator based on sulfonated polyimide with highly conductive silver electrodes via self-metallization. *Macromol Rapid Commun* 32(19):1583–1587
- Sugino T, Kiyohara K, Takeuchi I et al (2011) Improving the actuating response of carbon nanotube/ionic liquid composites by the addition of conductive nanoparticles. *Carbon* 49:3560–3570
- Torop J, Palmre V, Arulepp M, Sugio T, Asaka K, Aabloo A (2011) Flexible supercapacitor-like actuator with carbide-derived carbon electrodes. *Carbon* 49:3113–3119
- Vargantwar PH, Roskov KE, Ghosh TK et al (2012) Enhanced biomimetic performance of ionic polymer-metal composite actuators prepared with nanostructured block ionomers. *Macromol Rapid Commun* 33(1):61–68
- Wallmersperger T, Akle BJ, Leo DJ et al (2008) Electrochemical response in ionic polymer transducers: an experimental and theoretical study. *Compos Sci Technol* 68:1173–1180
- Wang XL, Oh IK, Lu J et al (2007) Biomimetic electro-active polymer based on sulfonated poly(styrene-*b*-ethylene-co-butylene-*b*-styrene). *Mater Lett* 61(29):5117–5120
- Wang XL, Oh IK, Kim JB (2009) Enhanced electromechanical performance of carbon nano-fiber reinforced sulfonated poly(styrene-*b*-[ethylene/butylene]-*b*-styrene) actuator. *Compos Sci Technol* 69(13):2098–2101
- Wang XL, Oh IK, Chen TH (2010a) Electro-active polymer actuators employing sulfonated poly(styrene-*ran*-ethylene) as ionic membranes. *Polym Int* 59(3):305–312
- Wang XL, Oh IK, Lee S (2010b) Electroactive artificial muscle based on crosslinked PVA/SPTES. *Sensor Actuators B* 150(1):57–64
- Wang XL, Oh IK, Xu L (2010c) Electro-active artificial muscle based on irradiation-crosslinked sulfonated poly(styrene-*ran*-ethylene). *Sensor Actuators B* 145(2):635–642

Kwang Kim, Viljar Palmre, David Pugal, Tyler Stalbaum,
Zheng Chen, Xiaobo Tan, and Masaki Yamakita

Contents

1	Physics-Based Model	172
1.1	Ionic Current in the Polymer Membrane	172
1.2	Solid Mechanics Physics	175
1.3	Simplified Model	176
2	Control Models	177
2.1	Physics-Based and Control-Oriented Model for IPMC Actuators	177
2.2	Empirical Model for Mechanical Simulations	184
2.3	Actuator Model	188
2.4	Mechanical Model	188
3	Conclusions	189
	References	189

K. Kim (✉) • V. Palmre • T. Stalbaum
Department of Mechanical Engineering, University of Nevada, Las Vegas, NV, USA
e-mail: kwang.kim@unlv.edu; viljar.palmre@gmail.com; tyler.stalbaum@unlv.edu

D. Pugal
University of Nevada, Reno, NV, USA
e-mail: david.pugal@gmail.com

Z. Chen
Department of Electrical Engineering and Computer Science, Wichita State University, Wichita,
KS, USA
e-mail: zheng.chen@wichita.edu

X. Tan
Department of Electrical and Computer Engineering; Department of Mechanical Engineering,
Michigan State University, East Lansing, MI, USA
e-mail: xbtan@egr.msu.edu

M. Yamakita
Department of Mechanical and Control Engineering, Tokyo Institute of Technology, Tokyo, Japan
e-mail: yamakita@ac.ctrl.titech.ac.jp

Abstract

The primary objectives of modeling IPMCs are to facilitate researchers with IPMC fabrication and performance prediction, to better understand the underlying principles of IPMC actuation and sensing, and to develop functional real-time control systems for IPMC devices. This chapter provides an overview of IPMC modeling with specific emphasis on physics-based models and control models. The underlying governing equations are presented and methods of solving are discussed.

Keywords

IPMC • Modeling • Controls

1 Physics-Based Model

Effective application of IPMCs in robotic devices relies on the ability to predict performance and achieve real-time control of IPMC actuators. Several studies have focused on this by developing models for IPMCs. Purely empirical models, or black-box models, have been developed to describe the bending response for a given voltage input of an IPMC actuator. Although these models can predict performance for a calibrated IPMC sample, they provide no insight into the underlying physics of IPMC electromechanical transduction. Semi-empirical models, or gray-box models, have been presented which incorporate some IPMC physics while using experimental data to accommodate model shortcomings. Physics-based models, or white-box models, provide a thorough understanding of IPMC electromechanical phenomena; however, these models are more complex and often limited to numerical solving methods. This section focuses on physics-based models of IPMCs and presents the governing partial differential equations which are most commonly employed. Contributions from various research groups are discussed.

The fundamental theory of IPMC electromechanical transduction (actuation) and mechano-electrical transduction (sensing) will be presented using the same governing equations. Differences between actuation and sensing phenomena will be highlighted throughout.

1.1 Ionic Current in the Polymer Membrane

The polymer membrane of an IPMC consists of anions fixed to the polymer backbone and freely positioned positive ions, or cations. In a hydrated state, micro-channels in the polymer expand to allow free transport of cations and attracted water molecules through the membrane. When a voltage is applied to IPMC electrodes, the cations migrate away from the anode, dragging attracted water molecules. This causes osmotic pressure change with localized swelling near the cathode interface and contraction near the anode, which results in an overall

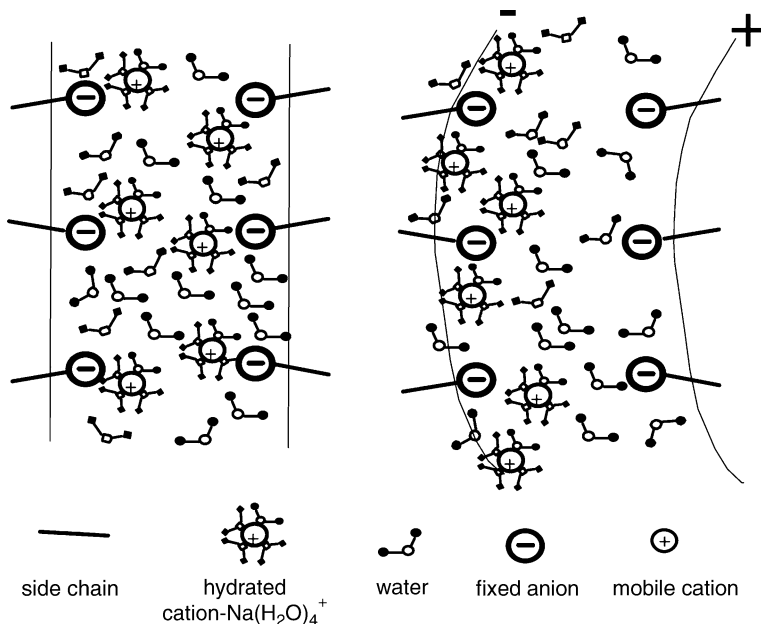


Fig. 1 Schematic of the migration of hydrated cations within the polymer network (Shahinpoor and Kim 2004. © IOP Publishing. Reproduced by permission of IOP Publishing. All rights reserved)

deformation of the IPMC. A basic schematic of an IPMC polymer structure and transduction phenomenon is shown in Fig. 1.

In the case of sensing, a given deformation causes ionic rearrangement, which in turn results in a measurable voltage at the electrodes. This phenomenon is understood to be roughly the reverse transduction of an IPMC actuator. At the same time, there are various ways in which the physics behind mechano-electrical transduction of IPMCs is understood. Physics-based models have been proposed based on ionic motion (Tadokoro et al. 2000). Other authors have explained the underlying causes of the transduction with solvent fluxes and pressure gradients based on the standard Onsager relations (Gennes et al. 2000). In such systems, the induced electric field is proportional to the applied bending torque, which causes a pressure gradient in the polymer. A different approach to describe the mechano-electrical transduction is to consider the electrostatic interaction within the polymer (Nemat-Nasser and Li 2000). While the charge sensing in this model is connected to ionic dipoles that are induced in the polymer clusters, it has been proposed that the charge density on the surface of the polymer is proportional to the induced stress (Farinholt and Leo 2004). Using the same governing equations, the model was later expanded to add the effects of electrode resistance (Chen et al. 2007). This resulted in a compact, transfer-function representation of the physics-based model which will be further discussed in Sect. 8.2.

The governing equations presented herein comprise a fundamental physics-based model of IPMCs. The underlying cause of the phenomenon of IPMC electromechanical and mechano-electrical transduction is induced ionic current and resulting nonzero spatial charge in the vicinity of the electrodes. Ionic current in the polymer for both cases can be described by the Nernst–Planck equation (Pugal et al. 2013):

$$\frac{\partial C}{\partial t} + \nabla \cdot (-D\nabla C - z\mu FC\nabla\phi - \mu C\Delta V\nabla P) = 0 \quad (1)$$

where C is cation concentration, μ is the mobility of the cations, D is the diffusion coefficient, F is the Faraday constant, z the is charge number, ΔV is the molar volume which quantifies the cation hydrophilicity, P is the solvent pressure, and ϕ is the electric potential in the polymer.

An important difference between IPMC electromechanical and mechano-electrical transduction is the magnitude, direction, and significance of individual terms in Eq. 1. Besides the concentration time derivative, the terms of Eq. 1 consist of three flux terms governed by the field gradients of electric potential, concentration, and solvent pressure. In case of actuation, the electric potential gradient term is significantly more prevalent than the solvent pressure flux, that is, $zF\nabla\phi \gg \Delta V\nabla P$; therefore, the pressure flux term is often neglected in actuation model implementation. However, in case of sensing, these terms are of similar significance and neither should be neglected. It is also interesting to note the direction of the electric potential gradient is opposite for sensing as compared to actuation because the ionic current is governed by an induced pressure gradient rather than an applied voltage. Conceptual models of IPMC actuation and sensing are shown in Fig. 2. Field gradient directions are indicated.

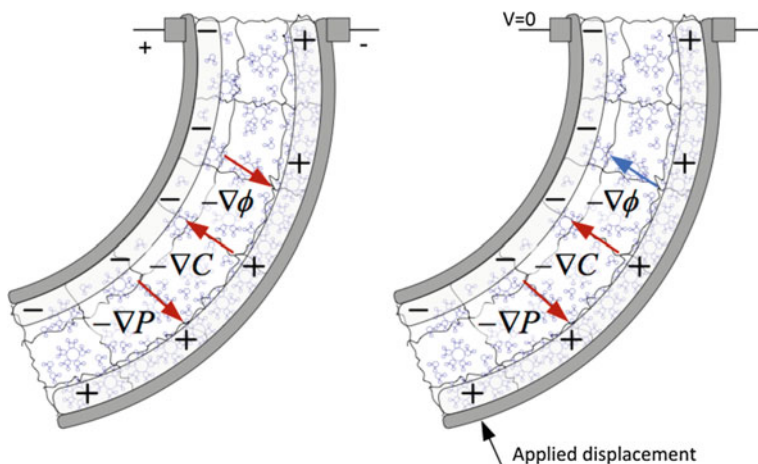


Fig. 2 Conceptual models of IPMC electromechanical (*left*) and mechano-electrical (*right*) transduction with the formed field gradients (Pugal et al. 2013. © IOP Publishing. Reproduced by permission of IOP Publishing. All rights reserved)

The electric potential gradient term can be described by Poisson's equation (Pugal et al. 2013):

$$-\nabla^2 \phi = \frac{F\rho}{\varepsilon} \quad (2)$$

where ε is the absolute dielectric permittivity and ρ is charge density defined as:

$$\rho = C - C_a \quad (3)$$

where C_a is local anion concentration. While the cation concentration C is governed by the Nernst–Planck Eq. 1, the anion concentration is related to local volumetric strain. The volume changes in the polymer matrix affect the local anion concentration as anions are fixed to the polymer backbone. Hence, the anion concentration C_a is expressed:

$$C_a = C_0 \left[1 - \left(\frac{\partial u_1}{\partial x} + \frac{\partial u_2}{\partial y} + \frac{\partial u_3}{\partial z} \right) \right] \quad (4)$$

where u_1 , u_2 , and u_3 are local displacements in the x , y , and z directions respectfully, and C_0 is the initial ion concentration.

Equations 1 and 2 make up what is commonly called the Poisson–Nernst–Planck (PNP) model for IPMCs and describes the fundamental physics within the polymer membrane.

1.2 Solid Mechanics Physics

The linear elastic material model can be used to describe the deformation of IPMCs. The constitutive relation of Hooke's Law can be used to relate stress and strain in the polymer as:

$$\begin{bmatrix} \sigma_{11} \\ \sigma_{22} \\ \sigma_{33} \\ \sigma_{12} \\ \sigma_{23} \\ \sigma_{13} \end{bmatrix} = \begin{bmatrix} 2\mu + \lambda & \lambda & \lambda & 0 & 0 & 0 \\ \lambda & 2\mu + \lambda & \lambda & 0 & 0 & 0 \\ \lambda & \lambda & 2\mu + \lambda & 0 & 0 & 0 \\ 0 & 0 & 0 & \mu & 0 & 0 \\ 0 & 0 & 0 & 0 & \mu & 0 \\ 0 & 0 & 0 & 0 & 0 & \mu \end{bmatrix} \begin{bmatrix} \varepsilon_{11} \\ \varepsilon_{22} \\ \varepsilon_{33} \\ 2\varepsilon_{12} \\ 2\varepsilon_{23} \\ 2\varepsilon_{13} \end{bmatrix} \quad (5)$$

where ε_{ij} is the normal strain in the i -direction for $i = j$ and a shear strain for $i \neq j$. Stress terms σ_{ij} are defined similarly. The constants μ and λ are Lamé's constants, defined as

$$\mu = \frac{E}{2(1 + \nu)}, \quad \lambda = \frac{\nu E}{(1 + \nu)(1 - 2\nu)} \quad (6)$$

where E is Young's modulus and ν is Poisson's ratio.

The system is in equilibrium if Navier's displacement equations are satisfied, given by the relation:

$$-\nabla \cdot \sigma = \mathbf{F} \quad (7)$$

where \mathbf{F} is the body force vector per unit volume.

Newton's second law is used to describe time-dependent deformation:

$$\rho_p \frac{\partial^2 \mathbf{u}}{\partial t^2} - \nabla \cdot \sigma = \mathbf{F} \quad (8)$$

where \mathbf{u} is the local displacement vector and ρ_p is the polymer density.

In 2D Cartesian coordinates, the Navier's displacement equations take the form:

$$(\lambda + \mu) \left(\frac{\partial^2 u_1}{\partial x^2} + \frac{\partial^2 u_2}{\partial y \partial x} \right) + \mu \left(\frac{\partial^2 u_1}{\partial x^2} + \frac{\partial^2 u_1}{\partial y^2} \right) + F_1 = 0 \quad (9)$$

$$(\lambda + \mu) \left(\frac{\partial^2 u_1}{\partial x \partial y} + \frac{\partial^2 u_2}{\partial y^2} \right) + \mu \left(\frac{\partial^2 u_2}{\partial x^2} + \frac{\partial^2 u_2}{\partial y^2} \right) + F_2 = 0 \quad (10)$$

In the case of IPMC electromechanical transduction, $F_2 = 0$ and F_1 can be expressed as a function of cation concentration, $F_1 = A(C - C_a)$, where A is a constant (Pugal et al. 2011). For mechano-electrical transduction, the body force can be neglected and the bending is governed by appropriate boundary conditions.

1.3 Simplified Model

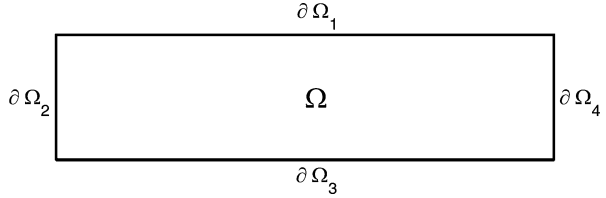
Although the provided equations described both transduction types of IPMCs, some terms are more prevalent than others for different transductions. For instance, it is reasonable to neglect the third flux term in Eq. 1 in the case of electromechanical transduction as it is very small compared to the second term. Also, while the local anion concentration can be expressed as a constant in the case of electromechanical transduction, it plays an important role in mechano-electrical transduction where field gradients are significantly smaller.

In the following example, coupling of the Navier equations and the Nernst–Planck equation is presented based on a simplified model where $C_a = C_0$ is a constant and $\Delta V \Delta P \approx 0$. This simplification is generally assumed acceptable in the case of electromechanical transduction.

IPMC material is modeled via a multi-physics coupled problem, consisting of the PNP system of equations coupled to the Navier equation. Finite element methods of solving are typically utilized in simulating the solution.

For modeling an IPMC strip, a rectangular 2D domain $\Omega \subset \mathbb{R}^2$ with boundaries $\partial\Omega_{1..4} \subset \partial\Omega$ as shown in Fig. 3 can be considered.

Fig. 3 The calculation domain $\Omega \subset \mathbb{R}^2$ with boundaries $\partial\Omega_1 \dots 4 \subset \partial\Omega$ (Pugal et al. 2013. © IOP Publishing. Reproduced by permission of IOP Publishing. All rights reserved)



The Nernst–Planck equation with simplifications as detailed above has the form

$$\frac{\partial C}{\partial t} + \nabla \cdot (-D\nabla C - z\mu FC\nabla\phi) = 0 \quad (11)$$

As there is no flow through the domain's boundary, Eq. 11 is equipped with a Neumann boundary condition:

$$-D \frac{\partial C}{\partial n} - \mu FC \frac{\partial \phi}{\partial n} = 0 \quad (12)$$

For normal actuation of the IPMC, a positive voltage V_{pos} boundary condition is prescribed on $\partial\Omega_1$ and a zero voltage boundary condition on $\partial\Omega_3$:

$$\phi_{\partial\Omega_1} = V_{\text{pos}}, \quad \phi_{\partial\Omega_3} = 0 \quad (13)$$

On the rest of the boundary, ϕ has zero normal derivatives, and it is thus equipped with Neumann boundary conditions:

$$\frac{\partial \phi_{\partial\Omega_2}}{\partial n} = \frac{\partial \phi_{\partial\Omega_4}}{\partial n} = 0 \quad (14)$$

For the Navier equations 9 and 10, the following Dirichlet boundary conditions can be applied:

$$u_{1_{\partial\Omega_2}} = u_{2_{\partial\Omega_2}} = 0 \quad (15)$$

If no external forces are considered, zero Neumann boundary conditions can be applied on $\partial\Omega$ for the Navier equations.

2 Control Models

2.1 Physics-Based and Control-Oriented Model for IPMC Actuators

In this section, a physics-based and control-oriented actuation model for IPMC actuators is presented. The model combines the seemingly incompatible advantages of both the white-box models (capturing key physics) and the black-box models

(amenable to control design). The proposed modeling approach provides an interpretation of the sophisticated physical processes involved in IPMC actuation from a systems perspective. The model development starts from the governing PDE (Nemat-Nasser and Li 2000; Farinholt 2005) that describes the charge redistribution dynamics under external electrical field, electrostatic interactions, ionic diffusion, and ionic migration along the thickness direction. The model incorporates the effect of distributed surface resistance, which is known to influence the actuation behavior of IPMCs (Shahinpoor and Kim 2000). Moreover, by converting the original PDE into the Laplace domain, an exact solution is obtained, leading to a compact, analytical model in the form of infinite-dimensional transfer function. The model can be further reduced to low-order models, which again carry physical interpretations and are geometrically scalable. Most of the modeling work was published in Chen and Tan (2008).

2.1.1 Governing Equation

Let D , E , φ , and ρ denote the electric displacement, the electric field, the electric potential, and the charge density, respectively. The following equations hold:

$$\nabla \cdot D = \rho = F(C^+ - C^-) \quad (16)$$

$$E = -\nabla\varphi = \frac{D}{\kappa_e} \quad (17)$$

where κ_e is the effective dielectric constant of the polymer, F is Faraday's constant, and C^+ and C^- are the cation and anion concentrations, respectively. The ion transportation can be captured by a second-order linear PDE in terms of charge density (Nemat-Nasser and Li 2000; Farinholt 2005):

$$\frac{\partial\rho}{\partial t} - d\Delta^2\rho + \frac{F^2 dC^-}{k_e RT} (1 - C^- \Delta V)\rho = 0. \quad (18)$$

Nemat-Nasser and Li assumed that the induced stress is proportional to the charge density (Nemat-Nasser and Li 2000):

$$\sigma = \alpha_0 \rho \quad (19)$$

where α_0 is the coupling constant. To ease the equation,

$$K \triangleq \frac{F^2 dC^-}{k_e RT} (1 - C^- \Delta V). \quad (20)$$

Farinholt investigated the current response of a cantilevered IPMC beam when the base is subject to step and harmonic actuation voltages (Farinholt 2005). A key assumption is that the ion flux at the polymer/metal interface is zero, which serves as a boundary condition for Eq. 18, leading to

$$\frac{\partial^3 \varphi(x, s)}{\partial x^3} - \frac{K}{d} \frac{\partial \varphi}{\partial x} \Big|_{x=\pm h} = 0. \tag{21}$$

2.1.2 Electrical Impedance Model

From Eq. 19, the stress induced by the actuation input is directly related to the charge density distribution ρ . Therefore, as a first step in developing the actuation model, we will derive the electrical impedance model in this section. While the latter is of interest in its own right, one also obtains the explicit expression for ρ as a by-product of the derivation. Consider Fig. 4, where the beam is clamped at one end $z = 0$ and is subject to an actuation voltage producing the tip displacement $w(t)$ at the other end $z = L$. The neutral axis of the beam is denoted by $x = 0$, and the upper and lower surfaces are denoted by $x = h$ and $x = -h$, respectively.

Performing Laplace transform for the time variable of $\rho(x, z, t)$ (noting the independence of ρ from the y coordinate), one converts Eq. 18 into the Laplace domain:

$$s\rho(x, z, s) - d \frac{\partial^2 \rho(x, z, s)}{\partial x^2} + K\rho(x, z, s) = 0 \tag{22}$$

where s is the Laplace variable. Define $\beta(s)$ such that $\beta(s) = (s + K)/d$. The generic solution for Eq. 22 can be obtained as

$$\rho(x, z, s) = 2c_2(z, s)\sinh(\beta(s)x). \tag{23}$$

The z -dependent transfer function $c_2(z, s)$ depends on the boundary condition of the PDE Eq. 21. Using Eq. 23 and the field Eqs. 16 and 17, one can derive the expressions for the electric field E and then for the electric potential φ in the Laplace domain:

$$E(x, z, s) = 2c_2(z, s) \frac{\cosh(\beta(s)x)}{\kappa_e \beta(s)} + a_1(z, s) \tag{24}$$

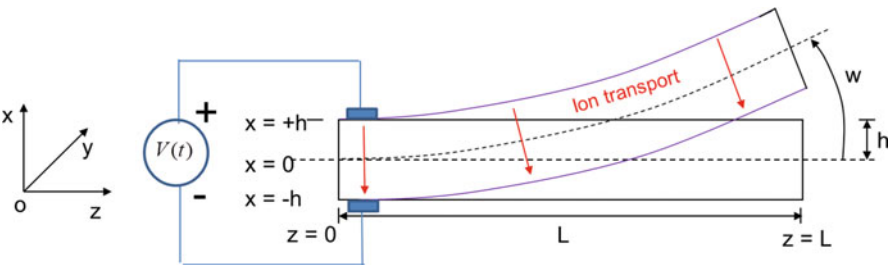


Fig. 4 Geometric definitions of an IPMC cantilever beam

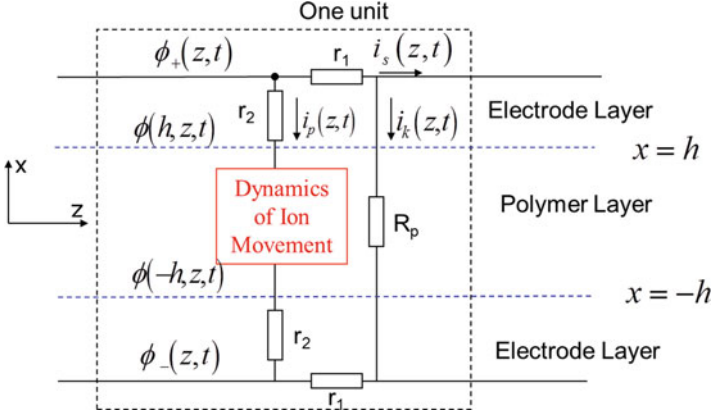


Fig. 5 Illustration of the IPMC impedance model with surface resistance (© 2008 IEEE. Reprinted with permission from Chen and Tan 2008)

$$\varphi(x, z, s) = 2c_2(z, s) \frac{\sinh(\beta(s)x)}{\kappa_e \beta^2(s)} - a_1(z, s)x + a_2(z, s) \quad (25)$$

where $a_1(z, s)$ and $a_2(z, s)$ are appropriate functions to be determined based on the boundary conditions on φ , which are affected by the distributed surface resistance on the electrodes.

The surface electrode of an IPMC typically consists of aggregated nanoparticles formed during chemical reduction of noble metal salt (such as platinum salt) (Kim and Shahinpoor 2003). The surface resistance is thus non-negligible and has an influence on the sensing and actuation behavior of an IPMC (Shahinpoor and Kim 2000). In this modeling work, the effect of distributed surface resistance is incorporated into the impedance model, as illustrated in Fig. 5.

Let the electrode resistance per unit length be r_1 in z direction and r_2 in x direction. One can further define these quantities in terms of fundamental physical parameters: $r'_1 = r_1/W$, $r'_2 = r_2/W$, with r_1 and r_2 representing the surface resistance per {unit length \cdot unit width} in z and x directions, respectively. In Fig. 5, $i_p(z, s)$ is the distributed current per unit length going through the polymer due to the ion movement, $i_k(z, s)$ represents the leaking current per unit length, and $i_s(z, s)$ is the surface current on the electrodes. R_p denotes the through-polymer resistance per unit length, which can be written as $R'_p = R_p/W$, with R'_p being the polymer resistance per {unit length \cdot unit width}. Note that by the continuity of current, the current $i_s(z, s)$ on the top surface equals that on the bottom surface but with an opposite direction. The surface current $i_s(0, s)$ at $z = 0$ is the total actuation current $I(s)$.

The following equations capture the relationships between $i_s(z, s)$, $i_p(z, s)$, $i_k(z, s)$, $\varphi_{\pm}(z, s)$:

$$\frac{\partial \varphi_{\pm}(z, s)}{\partial z} = \mp \frac{r'_1}{W} i_s(z, s) \quad (26)$$

$$\frac{\partial i_s(z, s)}{\partial z} = -(i_p(z, s) + i_k(z, s)). \quad (27)$$

From the potential condition at $z = 0$, i.e., $\varphi_{\pm}(0, s) = \pm V(s)/2$, the boundary conditions for Eq. 25 are derived as

$$\phi(\pm h, z, s) = \phi_{\pm}(z, s) \mp i_p(z, s)r'_2/W. \quad (28)$$

With Eqs. 26 and 28, one gets

$$\phi(\pm h, z, s) = \frac{\pm V(s)}{2} \mp \int_0^z \frac{r'_1}{W} i_s(\tau, s) d\tau - \frac{r'_2}{W} i_p(z, s). \quad (29)$$

Combining Eq. 29 with Eq. 25, one can solve for the functions $a_1(z, s)$ and $a_2(z, s)$ in the generic expression for $\varphi(x, z, s)$. With consideration of the boundary condition Eq. 21, one can solve for $c_2(z, s)$. With $a_1(z, s)$, $a_2(z, s)$, and $c_2(z, s)$, one obtains $E(h, z, s)$ from Eq. 24

$$E(h, z, s) = -\frac{\phi(h, z, s)}{h} \frac{\gamma(s)(s + K)}{\gamma(s)s + K \tanh(\gamma(s))} \quad (30)$$

where $\gamma(s) \triangleq h\beta(s)$. Define the actuation current along the negative x -axis direction to be positive. The current i_p due to the ion movement can be obtained as

$$i_p(z, s) = -sWD(h, z, s) = -sWk_e E(h, z, s). \quad (31)$$

The leaking current i_k can be obtained as

$$i_k(z, s) = \frac{\phi_+(z, s) - \phi_-(z, s)}{R'_p/W}. \quad (32)$$

With Eqs. 30, 31, and 32, one can solve the PDE Eq. 27 for the surface current $i_s(z, s)$ with the boundary condition $i_s(L, s) = 0$. The total actuation current $I(s) = i_s(0, s)$ can be obtained, from which the transfer function for the impedance can be shown to be

$$Z(s) = \frac{V(s)}{I(s)} = \frac{2\sqrt{B(s)}}{A(s)\tanh(\sqrt{B(s)}L)} \quad (33)$$

where

$$A(s) \triangleq \frac{\theta(s)}{1 + r'_2\theta(s)/W} + \frac{2W}{R'_p}, \quad B(s) \triangleq \frac{r'_1}{W}A(s), \quad (34)$$

$$\theta(s) \triangleq \frac{sW\kappa_e\gamma(s)(s+K)}{h(s\gamma(s)+K\tanh(\gamma(s)))}. \quad (35)$$

(See Chen and Tan (2008) for the detailed derivation.)

2.1.3 Actuation Model

First, we derive the transfer function $H(s)$ relating the free-tip displacement of an IPMC beam, $w(L, s)$, to the actuation voltage $V(s)$, when the beam dynamics (inertia, damping, etc.) is ignored. From Eqs. 19 and 23, one obtains the generic expression for the stress $\sigma(x, z, s)$ generated due to actuation

$$\sigma(x, z, s) = 2\alpha_0 c_2(z, s) \sinh(\beta(s)x). \quad (36)$$

Note that $c_2(z, s)$ is available from the derivation of the impedance model. When considering the surface resistance, the bending moment $M(z, s)$ is obtained as

$$\begin{aligned} M(z, s) &= \int_{-h}^h x\sigma(x, z, s)Wdx \\ &= \frac{2\alpha_0 K W k_e (\gamma(s) - \tanh(\gamma(s))) \phi(h, z, s)}{(s\gamma(s) + K \tanh(\gamma(s)))}. \end{aligned} \quad (37)$$

From the linear beam theory (Gere and Timoshenko 1997)

$$\frac{\partial^2 w(z, s)}{\partial z^2} = \frac{M(z, s)}{YI} \quad (38)$$

where Y is the effective Young modulus of the IPMC and $I = 2/3Wh^3$ is the moment of inertia of the IPMC. Solving Eq. 38 with boundary conditions $w(0, s) = 0$ and $w'(0, s) = 0$, one can get

$$w(L, s) = \frac{f(s)}{L^2} \cdot \frac{V(s)L^2 - 4 \int_0^L \int_0^z \int_0^{z'} r'_1 / W i_s(\tau, s) d\tau dz' dz}{1 + r'_2 \theta(s) / W} \quad (39)$$

where

$$f(s) \triangleq - \frac{\alpha_0 W L^2 K k_e (\gamma(s) - \tanh(\gamma(s)))}{YI (\gamma(s)s + K \tanh(\gamma(s)))}. \quad (40)$$

After doing three times integration of $i_s(\tau, s)$ in Eq. 39, one thus obtains the transfer function:

$$H(s) = \frac{w(L, s)}{V(s)} = f(s) \cdot g(s) \cdot X(s) \quad (41)$$

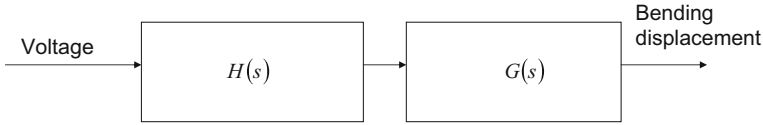


Fig. 6 Actuation model structure (© 2008 IEEE. Reprinted with permission from Chen and Tan 2008)

where

$$g(s) \triangleq \frac{2}{1 + r'_2 \theta(s)/W} \quad (42)$$

$$X(z, s) \triangleq \frac{1 - \sec h(\sqrt{B(s)}L) - \tanh(\sqrt{B(s)}L) \sqrt{B(s)}L}{B(s)}. \quad (43)$$

Note that the blocking force output $F(s)$ at the tip can be derived via $F(s) = w(L, s) K_0$, where $K_0 = 3YI/L^3$ denotes the spring constant of the beam.

Back to the free bending case, in order to accommodate the vibration dynamics of the beam, we cascade $G(s)$ to $H(s)$, as illustrated in Fig. 6. As the output of $G(s)$ represents the bending displacement (as that of $H(s)$ does), $G(s)$ will have a dc gain of 1. Since the actuation bandwidth of an IPMC actuator is relatively low (under 10 Hz), it often suffices to capture the mechanical dynamics $G(s)$ with a second-order system (first vibration mode):

$$G(s) = \frac{\omega_n^2}{s^2 + 2\xi\omega_n s + \omega_n^2} \quad (44)$$

where ω_n is the natural frequency of the IPMC beam and ξ is the damping ratio. The natural frequency ω_n can be further expressed in terms of the beam dimensions and mechanical properties (Voltera and Zachmanoglou 1965).

2.1.4 Model Reduction

An important motivation for deriving a transfer function-type actuation model is its potential use for real-time feedback control. For practical implementation of feedback control design, the model needs to be finite-dimensional, i.e., being a finite-order, rational function of s . However, in the actuation model derived earlier, $H(s)$ is infinite dimensional since it involves nonrational functions including $\sinh(\cdot)$, $\cosh(\cdot)$, $\sqrt{\cdot}$, etc. A systematic approach to model reduction is Padé approximation (Baker and Graves-Morris 1996), where one can approximate $H(s)$ with a rational function of specified order. However, the computation involved is lengthy and the resulting coefficients for the reduced model can be complex. Therefore, in this chapter, a much simpler, alternative approach is proposed for model reduction by exploiting the knowledge of physical parameters and specific properties of hyperbolic functions.

Based on the physical parameters (see Chen and Tan 2008), $|\gamma(s)| \gg 10$, and $K \gg 10^6$, which allows one to make the approximation in the low-frequency range (<100 Hz): $\tanh(\gamma(s)) \approx 1$ and $\gamma(s) \approx h\sqrt{K/d} =: \gamma$. With the above approximations, one can simplify $f(s)$, $\theta(s)$, and $g(s)$ as

$$f(s) \approx -\frac{L^2\alpha_0W}{2YI} \frac{Kk_e(\gamma-1)}{(\gamma s+K)} \quad (45)$$

$$\theta(s) \approx \frac{sWk_e\gamma(s+K)}{h(\gamma s+K)} \quad (46)$$

$$g(s) \approx \frac{2h(\gamma s+K)}{r_2^2\gamma k_e s(s+K) + h(\gamma s+K)}. \quad (47)$$

The Taylor series expansions of $\sinh(a)$ and $\cosh(a)$ will be used for approximation $X(s)$:

$$X(s) \approx \frac{1 + \sum_{n=0}^m (a^{2n+2}/(2n+1)! - a^{2n}/(2n)!)}{\sum_{n=0}^m a^{2n+2}/(2n)!}. \quad (48)$$

with $a = \sqrt{B(s)}L$, for some finite integer m . When $|s|$ is small (low-frequency range) and $2r_1'/R_p'$ is small (which is indeed the case, see Chen and Tan 2008), $|\sqrt{B(s)}L|$ is small and Eq. 34 approximates $X(s)$ well with a small integer m . Note that only even-degree terms appear in Eq. 48, and hence Eq. 48 is a function of $B(s)L^2$ instead of $\sqrt{B(s)}L$. Finally, since $B(s)$ is a rational function of $\theta(s)$ and $\theta(s)$ is approximated by a rational function Eq. 46, one can obtain an approximation to $X(s)$ by a rational function of s .

Combining Eqs. 45 and 47 and the approximation to $X(s)$, one gets a rational approximation to $H(s)$. Since the mechanical dynamics $G(s)$ is already rational, one obtains a finite-dimensional of actuation model. Note that a reduced model is still a physical model. In particular, it is described in terms of fundamental physical parameters and is, thus, geometrically scalable. This represents a key difference from other low-order, black-box models, in which case the parameters have no physical meanings and one would have to reidentify the parameters empirically for every actuator.

2.2 Empirical Model for Mechanical Simulations

If we consider an element of linear type actuator and an integrated artificial muscle actuator as shown in Fig. 7, physical model using partial differential equations is too complicated for numerical simulation of mechanical systems with such actuator.

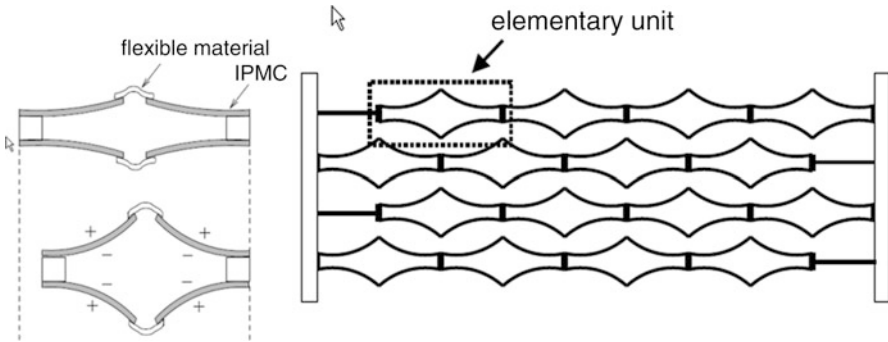


Fig. 7 Concept of integrated linear actuators (Reproduced from Development of an artificial muscle linear actuator using ionic polymer–metal composites. Yamakita M, Kamamichi N, Kaneda Y, Asaka K, Luo ZW, *Advanced Robotics*, 2004, Taylor & Francis Ltd, reprinted by permission of the publisher Taylor & Francis Ltd, www.tandfonline.com)

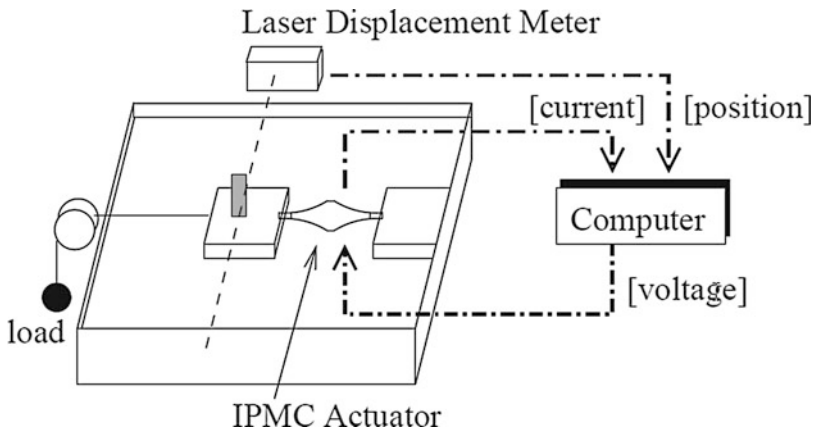


Fig. 8 Experimental setup for system identification (Reproduced from Development of an artificial muscle linear actuator using ionic polymer–metal composites. Yamakita M, Kamamichi N, Kaneda Y, Asaka K, Luo ZW, *Advanced Robotics*, 2004, Taylor & Francis Ltd, reprinted by permission of the publisher Taylor & Francis Ltd, www.tandfonline.com)

Also, properties of the constructed model can be different from an actual one (Yamakita et al. 2004, 2008; Kamamichi et al. 2007; Nishida et al. 2012). In those cases, empirical model of the system is useful for numerical simulations. However, it should be noted that the empirical model should give relationships both between control voltage and displacement and between applied force and displacement.

In order to identify both properties, one can construct an experimental system as illustrated in Fig. 8.

We assume the structure of a transfer function shown in Fig. 9, consisting of two subsystems $P_1(s)$ and $P_2(s)$ that are connected in series.

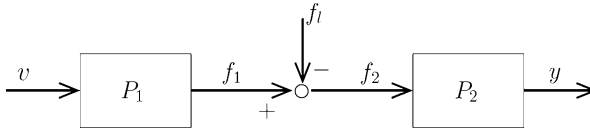


Fig. 9 Structure of the actuator model. Reproduced from Development of an artificial muscle linear actuator using ionic polymer–metal composites. Yamakita M, Kamamichi N, Kaneda Y, Asaka K, Luo ZW, *Advanced Robotics*, 2004, Taylor & Francis Ltd, reprinted by permission of the publisher (Taylor & Francis Ltd, www.tandfonline.com)

The transfer functions are identified as in the following steps:

1. Identification of $P(s)$:

Measure a response from input voltage v to displacement y , then compute the system $P(s) = P_2(s)P_1(s)$ from input–output data using a subspace identification algorithm.

2. Identification of $P_2(s)$:

Measure a response from load f_j to displacement y , then compute the system $P_2(s)$ from input–output data using a subspace identification algorithm.

3. Computation of $P_1(s)$:

Compute the system $P_1(s)$ as $P_2(s)^{-1}P(s)$.

The identification of the system `curvefit()` or `n4sid()` in Matlab system can be used. If a force sensor is available, $P_1(s)$ can be identified independently.

One example of the identified transfer functions are given as

$$P_1(s) = -\frac{1.50 \times 10^{-3}s^2 + 1.09 \times 10^{-2}s + 3.98 \times 10^{-2}}{s^3 + 6.13s^2 + 3.23 \times 10s + 7.12 \times 10}, \quad (49)$$

$$P_2(s) = -\frac{3.49 \times 10^3s^2 + 1.23 \times 10^6s + 3.81 \times 10^6}{s^4 + 7.19s^3 + 6.49 \times 10^4s^2 + 4.14 \times 10^5s + 1.33 \times 10^6}. \quad (50)$$

The fitting result of the identified model is shown in Fig. 10, indicating rather large deviation from the experimental result.

It is reasonable to assume that the actuator has many nonlinear characteristics and one of the most influential factors is the dynamics of load since the bending characteristics of the film highly depend on the load. In order to include the effect, static nonlinear block can be inserted in front of the linear dynamics of $P_2(s)$, i.e., Hammerstein model for $P_2(s)$ (see Fig. 11).

For the static nonlinearity, any nonlinear function can be used. One of the examples is RBF (radial basis function) as

$$N_1 = \sum_{i=0}^{n_1} \alpha_i \phi_i^1, \quad N_2 = \sum_{i=0}^{n_2} \beta_i \phi_i^2 \quad (51)$$

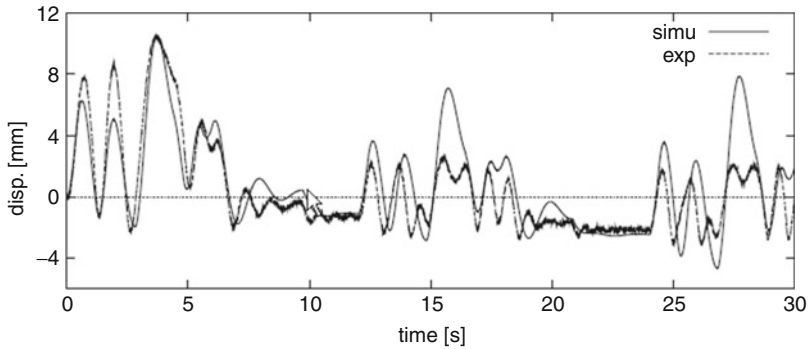


Fig. 10 Experimental versus simulated displacement in time using linear time invariant (LTI) model (Reproduced from Development of an artificial muscle linear actuator using ionic polymer–metal composites. Yamakita M, Kamamichi N, Kaneda Y, Asaka K, Luo ZW, *Advanced Robotics*, 2004, Taylor & Francis Ltd, reprinted by permission of the publisher Taylor & Francis Ltd, www.tandfonline.com)

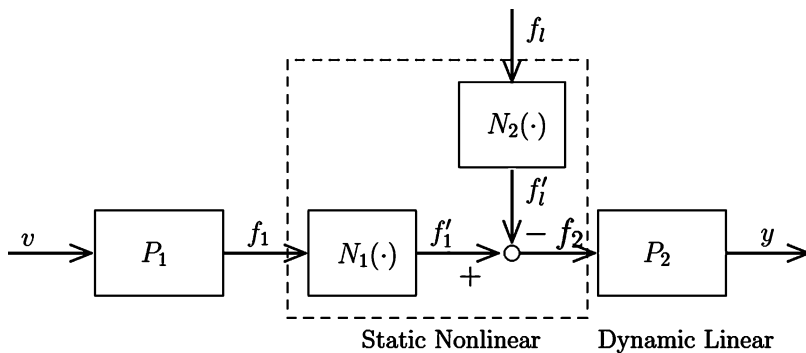


Fig. 11 Structure of the actuator model using Hammerstein model (Reproduced from Development of an artificial muscle linear actuator using ionic polymer–metal composites. Yamakita M, Kamamichi N, Kaneda Y, Asaka K, Luo ZW, *Advanced Robotics*, 2004, Taylor & Francis Ltd, reprinted by permission of the publisher Taylor & Francis Ltd, www.tandfonline.com)

$$\phi_i^1 = \exp\left(-\frac{(f_l - \bar{f}_i)^2}{2\sigma^2}\right) f_1, \quad i = 0 - 2, \tag{52}$$

$$\phi_i^2 = f_l^i, \quad i = 0 - 2, \tag{53}$$

$$\bar{f}_0 = 0.0, \bar{f}_1 = 1.16 \times 10^{-3}, \bar{f}_2 = 2.37 \times 10^{-3}, \sigma = \frac{(\bar{f}_1 + \bar{f}_2)}{2} \tag{54}$$

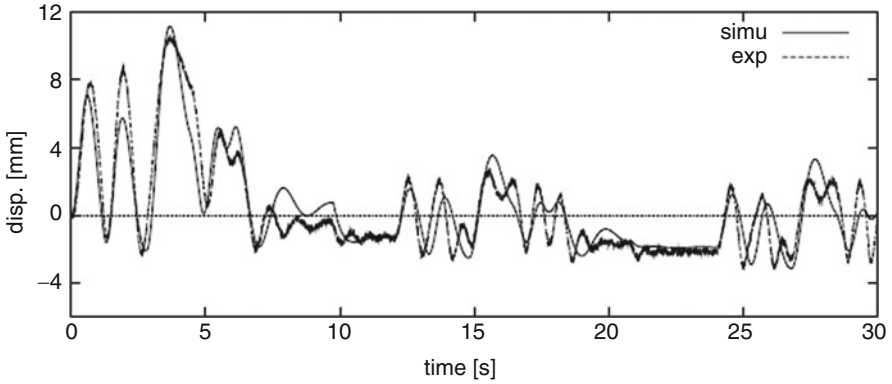


Fig. 12 Experimental displacement response versus simulated result from the improved model (Reproduced from Development of an artificial muscle linear actuator using ionic polymer–metal composites. Yamakita M, Kamamichi N, Kaneda Y, Asaka K, Luo ZW, *Advanced Robotics*, 2004, Taylor & Francis Ltd, reprinted by permission of the publisher (Taylor & Francis Ltd, www.tandfonline.com))

If we use the nonlinear structure, the response of the model is improved (see Fig. 12).

When the LTI model of the actuator applies a force vector f to a mechanical system where state space representations of the actuator and the mechanical system are represented as follows:

2.3 Actuator Model

$$\begin{cases} \dot{x}_a = A_a + b_v v - b_f f \\ y_a = C_a x_a \end{cases} \quad (55)$$

2.4 Mechanical Model

$$\begin{cases} \dot{x}_m = f_m(x_m) + g_m(x_m)f \\ y_m = h_m(x_m) \end{cases} \quad (56)$$

where f is an interaction force vector, then f can be solved by a velocity constraint:

$$\dot{y}_a = \dot{y}_m \quad (57)$$

as

$$C_a \dot{x}_a = \frac{\partial h_m}{\partial x_m} \dot{x}_m \rightarrow C_a (A_a x_a + b_v v - b_f f) = \frac{\partial h_m}{\partial x_m} (f_m(x_m) + g_m(x_m) f) \quad (58)$$

$$f = \left(\frac{\partial h_m}{\partial x_m} g_m(x_m) + C_a b_f \right)^{-1} \left(C_a (A_a x_a + b_v v) - \frac{\partial h_m}{\partial x_m} f_m(x_m) \right).$$

If the actuator model contains input nonlinearity, f should be solved numerically to satisfy the velocity constraint in general.

3 Conclusions

In this chapter, latest physics-based models and control models of IPMC were reviewed. Physics-based models provide thorough understanding of the underlying physics of IPMC transduction phenomena. However, these models are more complex and often limited to numerical solving methods. The fundamental theory of IPMC electromechanical and mechanoelectrical transduction were presented using the same governing equations. Differences between actuation and sensing phenomena were explicitly explained.

Physics-based and control-oriented actuation model was presented that combines the seemingly incompatible advantages of both the white-box models (capturing key physics) and the black-box models (amenable to control design). This modeling approach provides an interpretation of the sophisticated physical processes involved in IPMC actuation from a systems perspective. Also, an empirical model for mechanical simulations was described that can be implemented for complex mechanical systems when physical model using partial differential equations is too complicated for numerical simulation.

Acknowledgments KJK acknowledges the financial support from various agencies who supported IPMC research including the US Office of Naval Research (ONR), US National Science Foundation (NSF), and National Aeronautics and Space Administration (NASA).

References

- Baker G, Graves-Morris P (1996) Padé approximants. Cambridge University Press, New York
- Chen Z, Tan X (2008) A control-oriented and physics-based model for ionic polymer-metal composite actuators. *IEEE/ASME Trans Mechatron* 13(5):519–529
- Chen Z, Tan X, Will A, Ziel C (2007) A dynamic model for ionic-polymer metal composite sensors. *Smart Mater Struct* 16(4):1477
- Farinholt K (2005) Modeling and characterization of ionic polymer transducers for sensing and actuation. PhD dissertation, Virginia Polytechnic, Inst. State Univ., Blacksburg
- Farinholt K, Leo DJ (2004) Modeling of electromechanical charge sensing in ionic polymer transducers. *Mech Mater* 36(5):421–433
- Gennes PGD, Okumura K, Shahinpoor M, Kim KJ (2000) Mechanoelectric effects in ionic gels. *Europhys Lett* 50(4):513

- Gere J, Timoshenko S (1997) *Mechanics of materials*, 4th edn. PWS-Kent, Boston
- Kamamichi N, Yamakita M, Kozuki T et al (2007) Doping effects to robotic systems with ionic polymer-metal composite actuators. *Adv Robotics* 21(1):65–85
- Kim KJ, Shahinpoor M (2003) Ionic polymer-metal composites. Part II. Manufacturing techniques. *Smart Mater Struct* 12:65–79
- Nemat-Nasser S, Li JY (2000) Electromechanical response of ionic polymer-metal composites. *J Appl Phys* 87(7):3321–3331
- Nishida G, Sugiura M, Yamakita M et al (2012) Multi-input multi-output integrated ionic polymer-metal composite for energy controls. *Micromachines* 3(1):126–136
- Pugal D, Kim KJ, Aabloo A (2011) An explicit physics-based model of ionic polymer-metal composite actuators. *J Appl Phys* 110(8):084904
- Pugal D, Solin P, Aabloo A, Kim KJ (2013) IPMC mechano-electrical transduction: its scalability and optimization. *Smart Mater Struct* 22(12):125029
- Shahinpoor M, Kim K (2000) The effect of surface-electrode resistance on the performance of ionic polymer-metal composite (IPMC) artificial muscles. *Smart Mater Struct* 9:543–551
- Shahinpoor M, Kim KJ (2004) Ionic polymer-metal composites: III. Modeling and simulation as biomimetic sensors, actuators, transducers, and artificial muscles. *Smart Mater Struct* 13(6):1362
- Tadokoro S, Yamagami S, Takamori T, Oguro K (2000) Modeling of nafion-Pt composite actuators (ICPF) by ionic motion. In: *Proc. SPIE 3987, Smart Structures and Materials 2000: Electroactive Polymer Actuators and Devices (EAPAD)*, 92. Smart materials and structures: electroactive polymer actuators and devices, vol 3987. pp 92–102
- Voltera E, Zachmanoglou E (1965) *Dynamics of vibrations*. Charles E. Merrill Books, Indianapolis
- Yamakita M, Kamamichi N, Kaneda Y et al (2004) Development of artificial muscle linear actuator using ionic polymer-metal composites. *Adv Robotics* 18(4):383–399
- Yamakita M, Sera A, Kamamichi N, Asaka K (2008) Integrated design of an ionic polymer-metal composite actuator/sensor. *Adv Robotics* 22(9):913–928

Kinji Asaka, Kentaro Takagi, Norihiro Kamamichi, Youngsu Cha,
and Maurizio Porfiri

Contents

1	Biomedical Applications	192
1.1	Active Micro-catheter	192
1.2	Micro-pump	194
1.3	Human Affinity Tactile Devices	195
2	Biomimetic Robots	196
2.1	Introduction	197
2.2	Brief Review on Fishlike Robots	197
2.3	Phenomenon of Growing Wave of a Swimming Snake Robot: Do Living Fishes Utilize Their Elastic Bodies for Efficient Swimming?	198
2.4	Brief Review on Walking Robots and Others	200
2.5	Conclusions on Biomimetic Robots	201

K. Asaka (✉)

Inorganic Functional Material Research Institute, National Institute of Advanced Industrial Science
and Technology (AIST), Ikeda, Osaka, Japan

e-mail: asaka-kinji@aist.go.jp

K. Takagi

Department of Mechanical Science and Engineering, Nagoya University, Nagoya, Japan

e-mail: takagi@nuem.nagoya-u.ac.jp

N. Kamamichi

Department of Robotics and Mechatronics, Tokyo Denki University, Tokyo, Japan

e-mail: nkama@fr.dendai.ac.jp

Y. Cha

Center for Robotics Research, Korea Institute of Science and Technology, Seoul, Republic of Korea

e-mail: givemong@kist.re.kr

M. Porfiri

Department of Mechanical and Aerospace Engineering, Tandon School of Engineering, New York
University, Brooklyn, NY, USA

e-mail: mporfiri@nyu.edu

3	Sensor/Actuator Integrated (Feedback) Systems	202
3.1	Sensor Function of IPMCs	202
3.2	Sensor Systems and Application to Feedback Control	203
4	Energy Harvesting	206
4.1	Energy Harvesting from the Undulations of a Biomimetic Fish Tail	207
4.2	Energy Harvesting from Torsional Vibrations	208
4.3	Energy Harvesting from Wedge Slamming Impacts	208
5	Conclusions	210
	References	210

Abstract

IPMC actuators have number of advantages for the applications such as low drive voltage (less than 3 V), relatively high response (100 Hz), large displacement, soft material, capability of activation in water or in wet condition, possibility to work in dry condition, durability, and easy to miniaturize. In recent years, a great number of applications based on the IPMCs have been carried out by many workers. In this chapter, IPMC research on biomedical applications, biomimetic robotics, sensor/actuator integration, and energy harvesting is reviewed.

Keywords

Ionic Polymer-Metal Composite • IPMC • Biomedical Applications • Biomimetic Robot • Sensor/Actuator Integration • Energy Harvesting

1 Biomedical Applications

IPMC actuators are soft, flexible, and low drive voltage. Hence, they are very safe for humans. In addition, they are easy to deform in any shape and to miniaturize. Thanks to these advantages, many researchers have tried to apply them to many biomedical applications. In this section, applications of IPMC actuators to biomedical applications such as micro-catheter, micro-pump, and human-affinity tactile devices such as Braille displays are reviewed.

1.1 Active Micro-catheter

Micro-catheter-based diagnosis and therapy for intravascular treatment have become increasingly popular. By using conventional micro-catheters that are only soft polymer-based tubes and are not capable of moving actively, it needs certain skill for surgeons to control the tip of the catheter by using guide wires for the operations. Hence, actively controllable micro-catheter and guide wires from outside of the human body – “active micro-catheter” are very useful for catheter-based diagnosis and therapy. In order to develop micro-active catheters, a micro-actuator for controlling the tip of the catheter is a key technology. From the viewpoint of the previously mentioned advantages of IPMC actuators, such as soft, low drive voltage and easy to miniaturize, the IPMC actuator was applied to the active micro-catheter for aneurysm surgery on the brain.

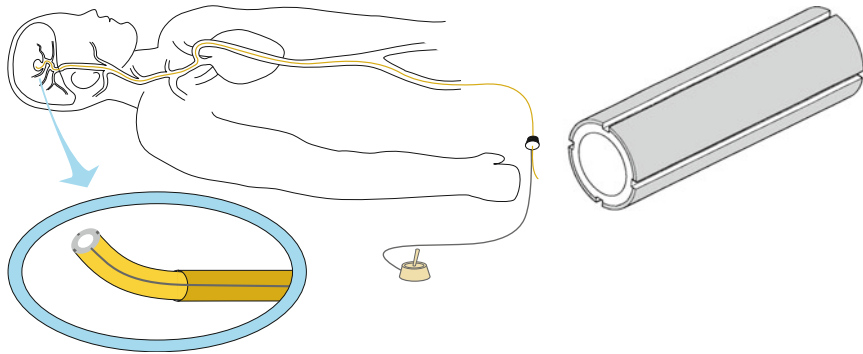


Fig. 1 Schematic view of a micro-active catheter for aneurysm surgery (*left*) on the brain based on a tubular IPMC actuator (*right*) (Reproduced from Oguro et al. 1999)

Guo et al. firstly developed the active guide wire for the micro-catheter based on the IPMC actuator (Guo et al. 1995). They proposed a prototype model of micro-catheter with active guide wire using IPMC actuator (Pt-plated Nafion film) which has two bending degrees of freedom. By using this prototype, they carried out “in vitro” experiments based on blood vessel simulator system composed of a glass blood vessel simulator, a pump for circulating physiological saline, an instrument for measurement, and a heater. They confirmed the inserting motion of the prototype into aneurysm under various experimental conditions such as temperatures, flow rates of circulating saline, diameters of blood vessel simulator, etc. Therefore, they concluded that the proposed catheter system with guide wire works properly and that it can improve the effectiveness of conventional procedure for intravascular operations.

Oguro et al. developed micro-active catheter system without guide wire based on a tubular IPMC actuator with four electrodes around the tube that can drive tubular ionic polymer to bend to multiple directions (Fig. 1) (Oguro et al. 1999). The tubular IPMC actuator of 0.8 mm in outer diameter for the active catheter was successfully developed by applying the sequential plating of gold electrodes around the Flemion (perfluorocarboxylic acid polymer) tube; fabricating four electrodes around the tube by laser ablation cutting after plating. In order to bend the tubular actuator of 0.8 mm in outer diameter for more than 90°, Flemion, which is softer than Nafion, was used as an ionic polymer.

The motion of the tube to all directions can be controlled with combined signals applied to four electrodes around the tube. For the practical usage of the tip of the micro-active catheter for intravascular neurosurgery as shown in Fig. 1, the tubular actuator of external diameter of 0.8 mm in the swollen state was attached to the end of catheter. The actuator is 2 cm and the total length of the catheter is 1.5 m. The tip of the active catheter can be controlled from outside of the human body with a small joystick bent more than 90° within 10 s in physiological saline without gas evolution. Intravascular in vivo tests of the micro-catheter with an animal were also carried out.

Fang et al. proposed the sensing/actuating IPMC for active guide wire in checking the bifurcation of blood vessels without integrating a bulky sensor or adjusting the curvature of IPMC-based active guide wire (Fang and Lin 2010). They developed a prototype of micro-catheter with active guide wire using a gold-plating Nafion IPMC that has a sensing and actuating function. The sensing is based on an amplitude modulation–demodulation technique to obtain deformation-sensing signal converted from the variation of the electric resistances in the IPMC electrodes.

1.2 Micro-pump

In microfluidic systems or lab-on-a-chip technology, the micro-pump is an essential element. Among many types of micro-pumps proposed, they fall into two categories: mechanical micro-pumps and nonmechanical micro-pumps. In order to generate stroke volumes of mechanical micro-pumps, diaphragms are widely used. Previously, piezoelectric, thermopneumatic, electrostatic, and electromagnetic actuators have been used for the diaphragms for micro-pumps. The IPMC is a new promising actuator used for this application since it has an ability to generate a larger bending deformation (more than 1 %) under a low voltage (less than 1 V) and to operate not only in liquid, but also in air, as compared to previously used actuators.

Guo et al. developed the micro-pump using the IPMC actuator, which has a size of 10 mm in diameter and 20 mm in length (Guo et al. 1997). They successfully obtained the flow 4.5 ml/min ~ 37.8 ml/min of the micro-pump by changing the frequency of the applied voltage (Fig. 2). The micro-pump using the IPMC actuator is able to make a micro-flow and silent for driving, which is suitable for the

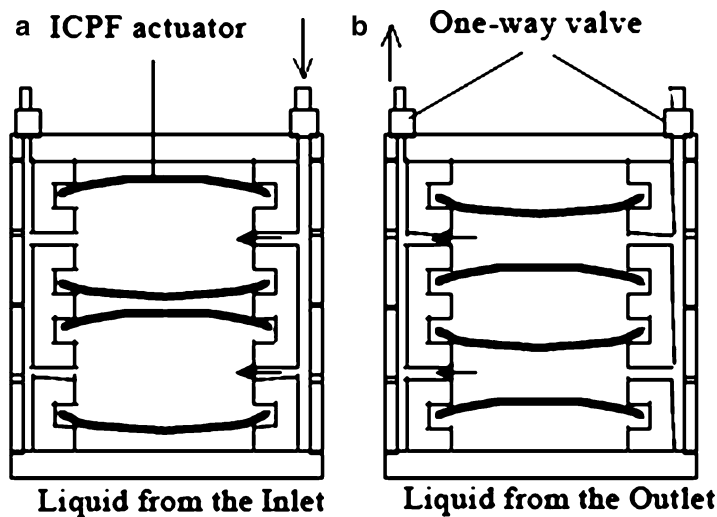


Fig. 2 Micro-pump using the IPMC (ICPF) actuators as diaphragms (Reproduced from Guo et al. 1997)

biomedical uses. Nguyen et al. also developed micro-pump using the IPMC actuator as the diaphragm (Nguyen et al. 2008). By using Nafion/silica-nanocomposite-based IPMC actuator, they developed a prototype of a micro-pump composed of the IPMC diaphragm with a flexible structure fabricated from polydimethylsiloxane (PDMS) material, which has a size of 20×20 mm (area) \times 5 mm (height). A maximum flow rate of 0.76 ml/min and a maximum back pressure of 1.5 kPa were recorded at an applied voltage of 3 V and a driving frequency of 3 Hz. Lee and Kim studied the design of IPMC actuator-driven micro-pump (Lee and Kim 2006). In order to design an effective IPMC diaphragm for a valveless micro-pump, they studied the optimum electrode shape of the IPMC diaphragm and the estimation of its stroke volume by using a finite element analysis (FEA). Based on the analysis, they concluded that the mean output flow rate of the IPMC actuator-driven valveless micro-pump was estimated at a low Reynolds number of about 50.

1.3 Human Affinity Tactile Devices

The IPMC actuator is soft and flexible and has a low drive voltage. Hence, it is very safe for human. If the IPMC film can be successfully patterned and integrated, and each micro-actuator strip can be controlled separately, human-affinity tactile information communication system can be developed.

A flexible and light page-type Braille display of which the effective size is 4×4 cm² and consists of 144 dots and 24 Braille letters as shown in Fig. 3 has been developed by Kato et al., by integrating the IPMC actuator array with organic transistors developed by them (Kato et al. 2007). The IPMC actuator array composed of 12×12 rectangular actuators whose size is 1×4 mm² was mechanically processed using a NC cutting machine from one IPMC actuator film. Each Braille dot is controlled by the up/down motion of a small semisphere that is attached to the tip of each rectangular IPMC actuator under the rubberlike surface of the display. The total thickness and the weight of the entire devices are 1 mm and 5.3 g, respectively. The readability of the sheet-like Braille display using the IPMC actuator was tested by the reading tests in which four visually impaired persons participated. All persons that attended were able to recognize the Braille format which this Braille display showed. This result shows that the generating force and the displacement of this device are sufficient to facilitate reading by the visually impaired persons.

The issue that remains to be addressed is the stability of the device. The IPMC actuator used was water-swollen gold-plating Nafion, which is usually operated in wet condition. On the contrary, organic transistors degrade easily in moisture and/or oxygen. In order to solve this issue, based on ionic-liquid-based bucky-gel actuator with organic transistor, ultra-thin and light Braille display that is operable in air for long time has been developed (Fukuda et al. 2011).

Konyo et al. developed the tactile display using the IPMC actuator (Konyo et al. 2007). The IPMC actuator has many advantages including high spatial resolution, wide frequency range, an ability of generate stimuli in multiple directions, wearability, and safety, as compared to the conventional actuators used for the

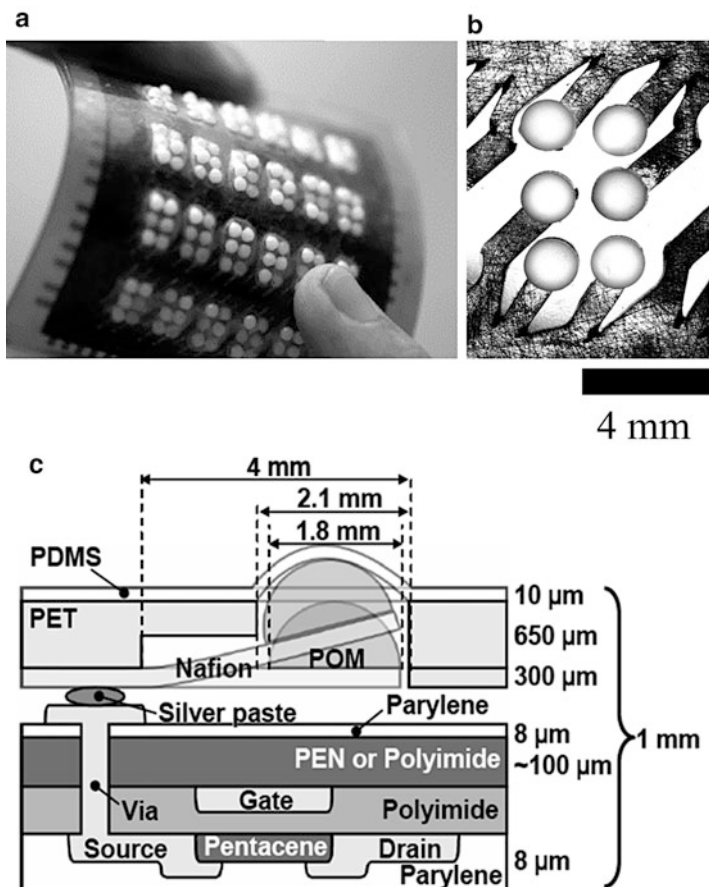


Fig. 3 Sheet-type Braille display based on the IPMC actuators: (a) photograph of the Braille display, (b) photograph of one Braille cell composed of six dots attached with IPMC actuator films, (c) a cross-sectional illustration of one Braille dot. The IPMC actuator is driven by an organic transistor. (Reproduced from Kato et al. 2007)

tactile display such as magnetic oscillators, piezoelectric actuators, shape memory alloy actuators, pneumatic devices, etc. They successfully produced total textural feeling related to the physical properties of materials by focusing on the following three sensations: roughness, softness, and friction.

2 Biomimetic Robots

The second section in this chapter briefly reviews biomimetic robots using IPMC actuators. Fishlike robots are reviewed firstly. In the experiment of a snake robot, the wave motion grows from the head to the tail even without feedback control. This interesting phenomenon may support a hypothesis that living animals utilize the

elasticity of their bodies or muscles when they swim. Walking robots and other types of robots using IPMCs are also reviewed briefly in the latter part of the second section.

2.1 Introduction

Biomimetics is the development of novel technologies through the distillation of principles from the study of biological systems (Lepora et al. 2013). Because ionic polymer–metal composites (IPMCs) can be driven by low voltage and usually require water for work (Shahinpoor et al. 1998), it is an attractive idea to use IPMCs for biomimetic robots (Bar-Cohen and Breazael 2003; Roper et al. 2011; Chu et al. 2012; Kim et al. 2013).

In this section, biomimetic robots using IPMCs are briefly reviewed. Firstly, some fishlike robots are introduced. Especially for a snake robot, it was found that the wave motion increased from the head toward the tail even without feedback control (Takagi et al. 2006a). A mathematical model can predict the phenomenon of growing wave of the robot. Interestingly, similar phenomena can be observed in the swimming of living snakes and slender fishes (Azuma 1992). A brief discussion is presented for the phenomena observed in both the robot and the living animals. In the latter part of this section, walking robots and other types of robots are briefly reviewed.

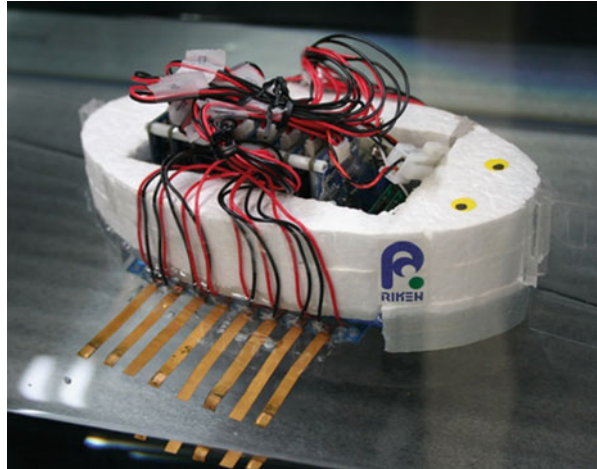
2.2 Brief Review on Fishlike Robots

Many researches on fishlike robots using IPMC actuators have been conducted. In the early stage of the researches on IPMCs, Mojarrad and Shahinpoor developed a biomimetic underwater robot (Mojarrad and Shahinpoor 1997a). The first commercial product using IPMCs in the world was a goldfish-like robot developed by EAMEX company in Japan (Bar-Cohen 2003). The fish robot of EAMEX could swim in a water tank by wireless power supply. The methods of wireless powering of IPMCs have been also discussed by some researchers (Lee et al. 2012; Abdelnour et al. 2012).

Guo et al. developed a fishlike robot (Guo et al. 2003). They measured the swimming speed and the propulsive force of the robot. Aiming at autonomous robots, some researchers have developed battery-powered robots without tethers, e.g., a tadpole robot (Kim et al. 2005) and fish robots with a caudal fin (Chen et al. 2010; Aureli et al. 2010a).

Another direction of the research is increasing the degrees of freedom of the fin(s) of a biomimetic robot. Nakabo et al. developed a snake robot from an IPMC strip by segmenting the electrodes into some parts (Nakabo et al. 2007). The snake robot swims by applying the appropriate distributed voltages. Takagi et al. discovered that the amplitude of the traveling wave on the flexible snake robot grew from the head to the tail (Takagi et al. 2006a). This interesting phenomenon will be briefly discussed in

Fig. 4 Autonomous raylike robot (Takagi et al. 2006b)



the next subsection. Kamamichi and Yamakita developed a three-link snake robot (Yamakita et al. 2007). They also proposed a self-excitation control method to generate oscillating motion (Kamamichi et al. 2006).

Robots with more complex shapes have been also reported. Punning et al. proposed a raylike robot using IPMCs (Punning et al. 2004). Takagi et al. developed an autonomous raylike robot (Takagi et al. 2006b) shown in Fig. 4. The robot consisted of a plastic body, 16 IPMCs, a microcontroller, amplifiers, and a battery. Chen et al. also developed a manta ray robot (Chen et al. 2012). Palmre et al. discussed the design of a fin (Palmre et al. 2013). They set some IPMC actuators into a soft boot material to create an active control surface. As other unique fishlike robots, jellyfish robots have been proposed (Yeom and Oh 2009; Najem et al. 2012).

2.3 Phenomenon of Growing Wave of a Swimming Snake Robot: Do Living Fishes Utilize Their Elastic Bodies for Efficient Swimming?

Figure 5 shows the snake robot developed by Nakabo et al. The electrodes of the IPMC are segmented into seven parts. Therefore distributed voltages can be applied to the IPMC. The snake robot can swim by applying traveling-wave voltages of the appropriate frequency and wavelength. In the experiment of the snake robot, the amplitude of the wave motion increases from the head toward the tail even though the amplitudes of the applied voltages are constants.

Figure 6 shows the captured swimming motion of the snakelike robot in the experiment. The solid lines are the obtained shapes by image processing. The dotted lines are the envelope of the traveling wave. Clearly the amplitude of the tail side is

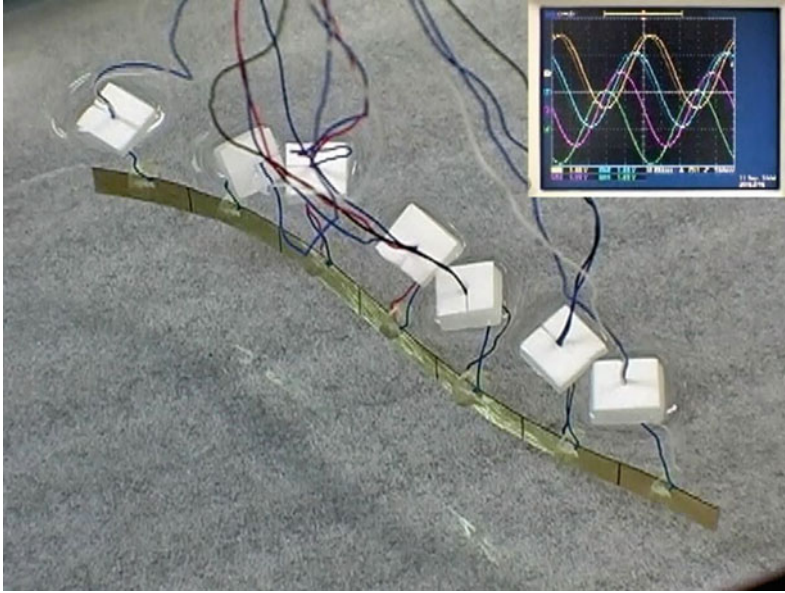


Fig. 5 Snake-like robot (Reproduced from Takagi et al. 2006a)

greater than that of the head side. Note that this shape of the envelope is generated by itself and without control. Although the input voltage is uniformly applied to the robot, the resultant deflection is not uniform and growing from the head to the tail, as shown in Fig. 7. It should be noted that the similar growing wave can be observed in the swimming of living snakes and slender fishes (Azuma 1992). The growing wave on the body of a fish is known to increase the efficiency of the swimming (Lighthill 1960). The phenomenon observed in the robot may indicate that the living aquatic animals utilize the elasticity of their bodies and muscles when they swim.

The envelope can be predicted by a simple mathematical model based on Euler–Bernoulli beam (Takagi et al. 2006a). Conversely, as a relation between the forward dynamics and the inverse dynamics, Cheng et al. estimated muscle force of a living fish using a simple beam model (Cheng et al. 1998). According to the reference (Takagi et al. 2006a), the envelope function denoted by $A(x)$ is given by

$$A(x) = \sqrt{\sum_{m=1}^{\infty} \sum_{n=1}^{\infty} A_m A_n \phi_m(x) \phi_n(x) \cos(\theta_m - \theta_n)}$$

where A_i and θ_i are parameters depending on the material constants, the boundary condition, the frequency ω , and the wavelength λ . $\phi_i(x)$ is the eigenfunction (mode shape function) of bending deflection of a beam with free–free ends. We can show the function $A(x)$ becomes an increasing function by the parameter estimation of the experimental data. See the reference (Takagi et al. 2006a) for the details.

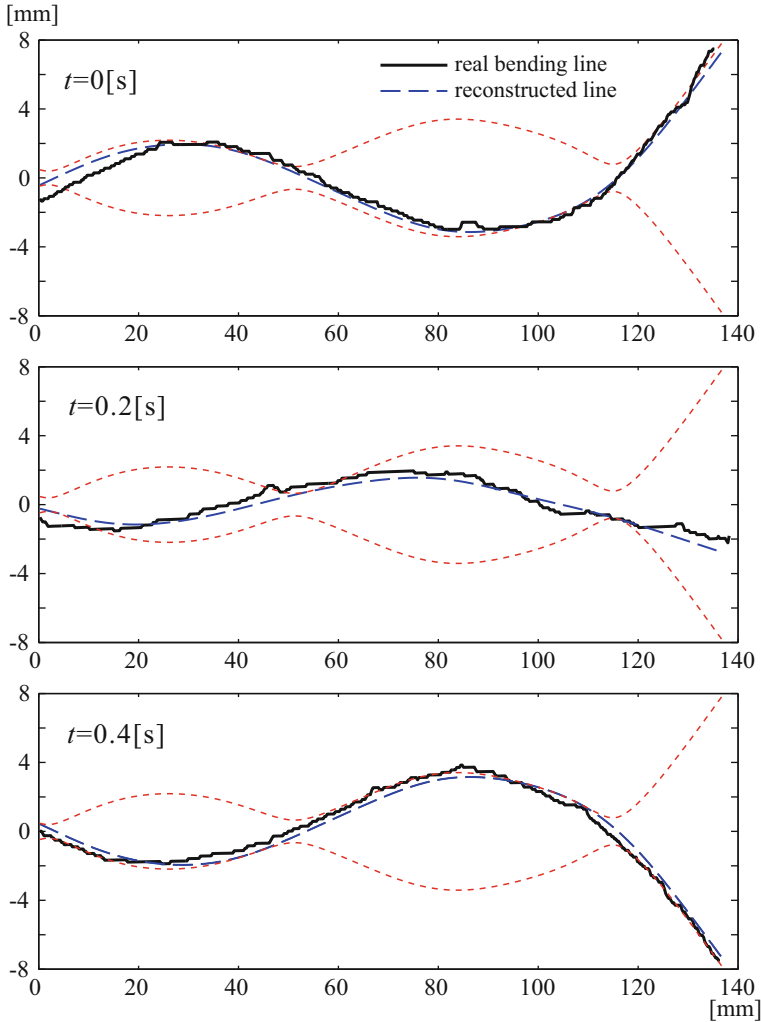


Fig. 6 Captured motion of the snakelike robot in the experiment (Reproduced from Takagi et al. 2006a). The head of the robot is located in the left hand side. *Dashed lines* show the fitted shapes, and *dotted lines* show the envelopes

2.4 Brief Review on Walking Robots and Others

Compared with the fishlike robots, other types of biomimetic robots are not so much reported. Some walking robots are studied, such as biped, quadruped, and multi-legged robots.

Yamakita and Kamamichi developed a biped robot (Yamakita et al. 2004). They also proposed a mechanism to convert the bending motion into the linear motion.

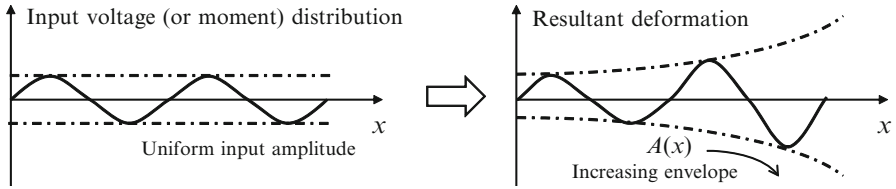
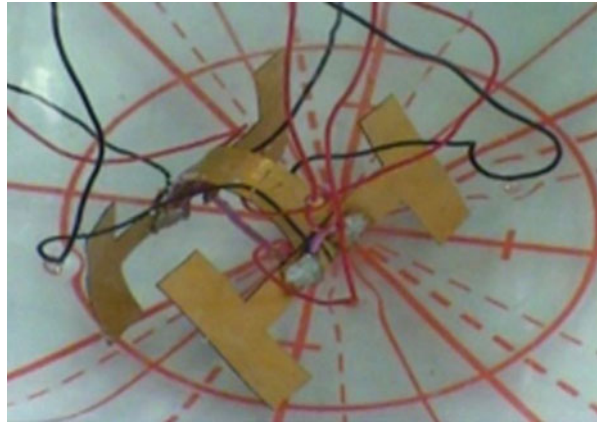


Fig. 7 Schematic illustration of the uniform input (*left*) and the resultant deformation with the increasing envelope (*right*)

Fig. 8 Quadruped underwater robot with fully IPMC body (Reproduced from Tomita et al. 2011)



There also exists another mechanism to convert the bending motion into the rotational motion (Takagi et al. 2005).

Guo et al. proposed a multi-legged robot (Guo et al. 2012). Chang and Kim also developed a multi-legged robot (Chang and Kim 2013). Tomita et al. proposed a quadruped robot directly made from an IPMC sheet shown in Fig. 8 (Tomita et al. 2011). Takagi et al. discovered that copper electrodes can enhance the deformation of IPMCs by unintended ion exchange (Takagi et al. 2014) in the experiment of the quadruped robot.

Shahinpoor et al. showed an idea of flapping flying machine (Shahinpoor et al. 1998). Arena et al. proposed a wormlike robot (Arena et al. 2006). As a robot similar to the snake robots, however, much smaller, Sareh et al. proposed artificial cilia (Sareh et al. 2012).

2.5 Conclusions on Biomimetic Robots

IPMCs are attractive actuators for biomimetic robots due to its softness and usability in water. Some researches on biomimetic robot have been briefly reviewed in this section, such as fishlike robots, walking robots, and other types of robots.

This section also introduced a notable phenomenon of growing wave of a snake robot. The living animals may utilize the elasticity of their bodies and muscles, as the phenomenon observed in the robot. As well as mimicking functions of living animals, the future direction of the researches on biomimetic robot are expected to reveal the energy-efficient motions of living animals.

3 Sensor/Actuator Integrated (Feedback) Systems

Some of the EAP materials can be used as a sensor and an actuator in same devices. IPMC is a typical example of such materials. In this section, the sensor function of the IPMC and its application to the sensor/actuator feedback systems are explained.

3.1 Sensor Function of IPMCs

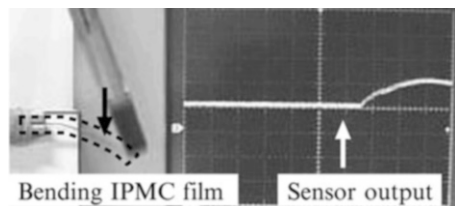
It is known that IPMC can be used as a sensor, as the IPMC generates electromotive force when it is deformed (Mojarrad and Shahinpoor 1997b; Shahinpoor et al. 1998). Figure 9 shows the sensor response of IPMC, where the strip of the IPMC was deformed and the output voltage was observed by an oscilloscope. Depending on the size or the composition of the strips, the electromotive force of several millivolts can be observed, and IPMC can be used as sensors sufficiently.

In order to realize the control and soft actuation of IPMC actuators, a “soft” and “light” sensing device is needed. The most effective device is the IPMC itself. IPMC has important advantages for utilization as a sensing device:

- It is highly sensitive and outputs voltage of millivolt order.
- It is usable over a wide range of deformation.
- It is flexible and can be integrated into a soft actuator system.

Figure 10 shows the verification result of the sensor function. The strip of the IPMC was fixed as a cantilever and was deformed manually. Its deformation was measured by a laser displacement meter, and the output voltage was pre-amplified and measured. The size of the strip used in the experiment was 20×2 mm and 0.2 mm of thickness. From the result, the output signals arise through the deformation of the strip, and the magnitude of the output signals is related to that of the

Fig. 9 Output response of IPMC sensors



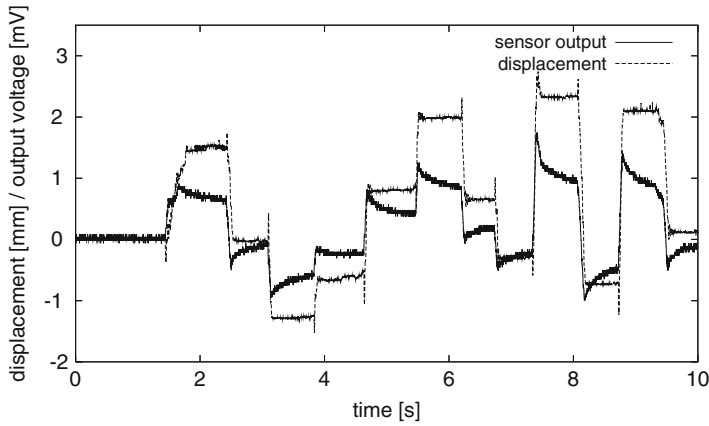


Fig. 10 Experimental result of the IPMC sensor response

deformation. It is also confirmed that the sensor characteristics are dynamical as the slow decay of the output signal exists in a constant deformation.

For system applications of soft materials, it is important to analyze and model the responses. Some models of the sensor function of IPMCs were studied from the viewpoint of the black/gray box modeling (Newbury and Leo 2003; Bonomo et al. 2006) and the white box (physical and chemical) modeling (Farinholt and Leo 2004).

3.2 Sensor Systems and Application to Feedback Control

Since the characteristics of the sensor output are dynamical, we should compensate the dynamics to estimate the deformation of IPMC from the sensor signals. In this section, an estimation method and an example of feedback controls based on the estimation results of the sensor systems are described (Yamakita et al. 2008).

3.2.1 Estimation Method

To estimate the deformation from the sensor output, we identify the dynamics using input–output data as a linear time-invariant (LTI) system and construct a sensor system using an observer based on the linear system control theory.

The model of the sensor is assumed to be represented by a LTI model as

$$\begin{cases} \dot{x} = Ax + Bu \\ y = Cx + Du \end{cases} \quad (1)$$

where y is an output of the system which is the output voltage, u is an input of the system which is the deformation of the IPMC, and x is a state variable of the system.

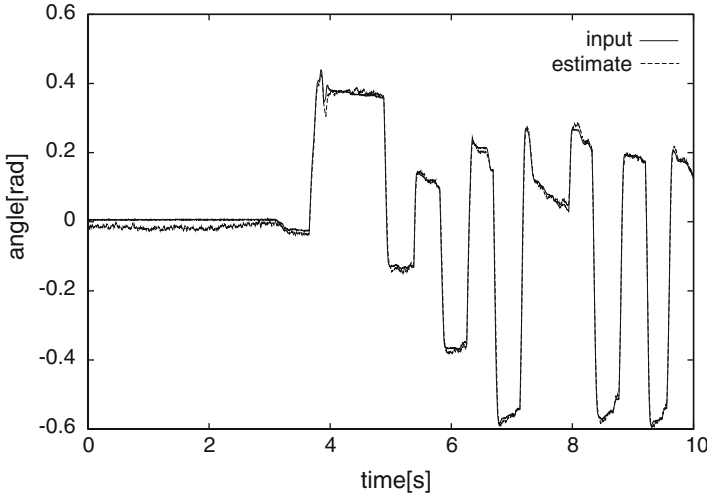


Fig. 11 Estimation result of the sensor system

Assume that the variation of the input is not fast, i.e., $\dot{u} \approx 0$, then the augmented system can be defined as

$$\begin{cases} \dot{\bar{x}} = \bar{A}\bar{x} \\ y = \bar{C}\bar{x} \end{cases} \quad (2)$$

where \bar{x} is the state of the augmented system, and

$$\bar{x} = \begin{bmatrix} x \\ u \end{bmatrix}, \quad \bar{A} = \begin{bmatrix} A & B \\ 0 & 0 \end{bmatrix}, \quad \bar{C} = [C \quad D].$$

If the system of Eq. 2 is observable, the input u can be estimated by the observer, which is a part of the state of the augmented system. The observer system based on the stationary Kalman filter is represented as

$$\dot{\hat{x}} = (\bar{A} - K\bar{C})\hat{x} + Ky, \quad (3)$$

where K is a gain matrix of the optimal observer.

Figure 11 shows the estimation result of the sensor system based on the observer as above procedure. By utilizing the identified linear model and the observer, the deformation of the film can be measured with high accuracy.

3.2.2 Feedback Control Based on the Sensor Signal

In order to confirm the validity of the sensor system, we demonstrate an experiment of feedback control using IPMC sensor/actuator. In the experiments, a pair of IPMC strips is connected in parallel. One of the IPMC strips is used as an actuator, and

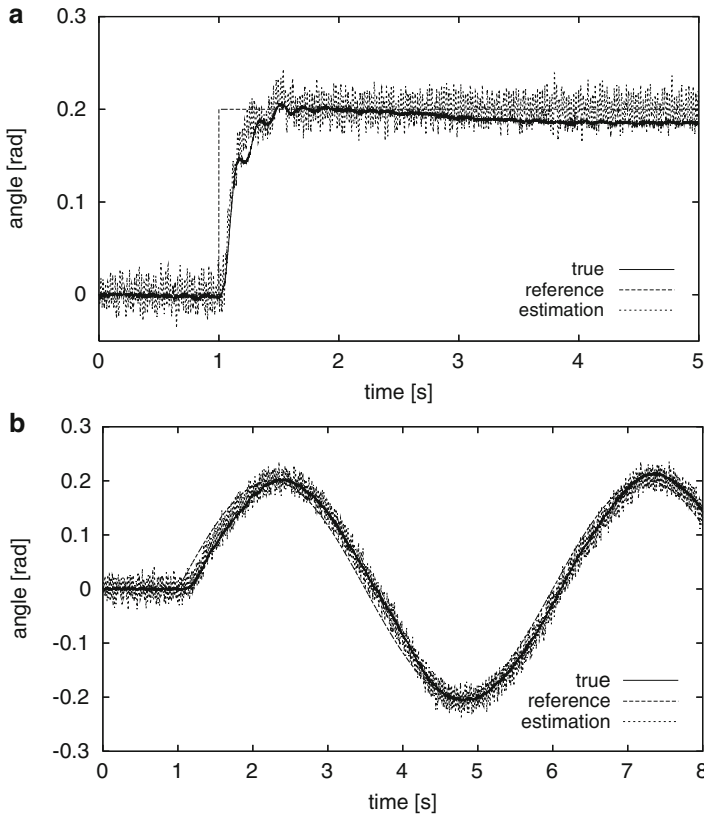


Fig. 12 Experimental results of feedback control based on the sensor signal. (a) Feedback control to the fixed value. (b) Feedback control to the sinusoidal wave

another is used as a sensor. Then the deformation of the strips is controlled using the estimated value by the sensor system.

Figure 12 shows the experimental results of feedback control by using the signals of the IPMC sensor system. We applied PID controller based on the estimated deformation. The figures plot the reference, estimated, and real deformation over time, and the reference trajectories were step and sinusoidal signals, respectively. The estimation of the deformation and the feedback control were realized sufficiently with only some errors of the estimation.

Several researchers have also attempted to realize self-sensing actuations of IPMCs. The term “self-sensing” means the realization of sensing without attaching the sensing device. One of the methods is construction of the sensor/actuator integrated device with patterned electrodes, which separates the actuating and sensing parts on one strip of IPMCs (Nakadoi et al. 2007). The patterned device can be constructed by removing electrodes with a laser ablation or a mechanical

cutting and also constructed by partial electrode formation with chemical treatment. Another method is an estimation approach based on measurements of electrodes resistance (Kruusamae et al. 2011; Punning et al. 2007; Nam and Ahn 2014) and impedance (Cha et al. 2013c; Cha and Porfiri 2014). The electrode resistance of both surfaces changes according to the deformation. The deformation can be estimated by measuring the voltage signals related to the resistance variations. Although the improvements in the performance are needed for practical use, IPMCs have a great potential in applications of soft robots and controlled devices.

4 Energy Harvesting

Recent breakthroughs in lightweight electroactive materials have promoted major scientific and technological advancements in the area of energy harvesting for powering miniature electronic devices (Erturk and Inman 2011). In the context of underwater energy harvesting, IPMCs are receiving considerable attentions for several advantageous attributes, including their inherent ability to work in wet environments, their large electrical capacitance, and their small stiffness (Shahinpoor and Kim 2001; Jo et al. 2013). Considerable efforts have thus been placed in design and modeling of IPMC-based energy harvesting devices (Brufau-Penella et al. 2008; Tiwari et al. 2008; Aureli et al. 2010b; Anand et al. 2010; Giacomello and Porfiri 2011; Peterson and Porfiri 2012; Cellini et al. 2014a, b; Hu et al. 2014).

In particular, energy harvesting from underwater flexural vibrations of an IPMC strip excited at its base has been explored in Aureli et al. (2010b). A similar scenario has been studied in Brufau-Penella et al. (2008) to investigate IPMC-based energy harvesting for air vibrations. Energy harvesting from flexural vibrations has also been addressed in Anand et al. (2010), where a detailed analysis of the role of the electrodes' composition can be found. Flexural vibrations have been leveraged in the design of fluttering heavy flags in Giacomello and Porfiri (2011) for energy scavenging from a steady water flow as well as in Cellini et al. (2014a) to investigate IPMC-based energy harvesting from fluid-induced buckling. Underwater energy harvesting of a parallel array of IPMCs with a common base excitation has been considered in Cellini et al. (2014b). Experimental evidence of the feasibility of IPMC-based energy harvesting from different deformation modes is presented in Tiwari et al. (2008), where experimental data on cyclic bending, tension, and shear in air can be found. Moreover, IPMC-based energy harvesting from the impact of self-propagating vortex rings has been tackled in Peterson and Porfiri (2012) and Hu et al. (2014). Notably, a concise summary of some of these efforts can be found in Porfiri and Peterson (2013).

Here, we summarize some of our recent work on the integration of IPMCs in relatively unconventional underwater energy harvesting devices. Specifically, we assess the feasibility of IPMCs for energy harvesting from the undulations of a

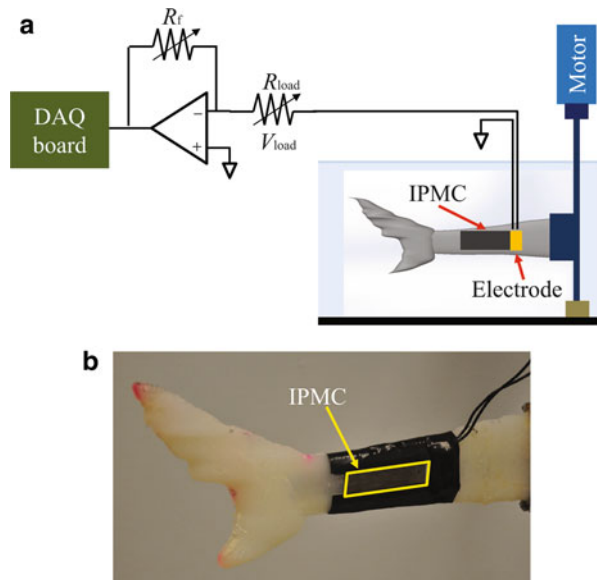
biomimetic fish tail (Cha et al. 2013a), underwater torsional vibrations (Cha et al. 2013b), and hull slamming (Cha et al. 2012).

4.1 Energy Harvesting from the Undulations of a Biomimetic Fish Tail

First, we report on energy harvesting from the bending vibrations of a biomimetic tail in a quiescent fluid (Cha et al. 2013a). This research is motivated by the evidence that fish locomotion is associated with a number of energy sources that could be tapped through IPMCs (Dabiri 2007). Figure 13 shows an IPMC attached on one side of a biomimetic tail, designed based on shark morphometric data in Kohler et al. (1995). The tail is fabricated through injection molding of silicone, and a slender stainless steel beam is inserted in the mold to increase the overall stiffness of the biomimetic fish tail. The undulations of the biomimetic tail are modeled by studying the nonlinear underwater vibrations of an equivalent beam with varying rectangular cross section, through the hydrodynamic function proposed in Phan et al. (2013). The electrical behavior of the IPMC is simply described via a lumped circuit model consisting of a resistor, a capacitor, and a voltage source connected in series and controlled by the deformation of the tail.

The harvested power from the IPMC is obtained by connecting it to a shunting resistor. We find that the power output is maximized when the shunting resistance matches IPMC internal impedance, the test structure is excited at its resonance frequency, and the IPMC is placed in the vicinity of the clamped side of the tail. The optimal harvested power is on the order of 10–100 pW per unit base angle.

Fig. 13 (a) Schematic of the experimental setup for energy harvesting characterization and (b) detailed view of the biomimetic tail hosting the IPMC (Reproduced from Cha et al. 2013a)



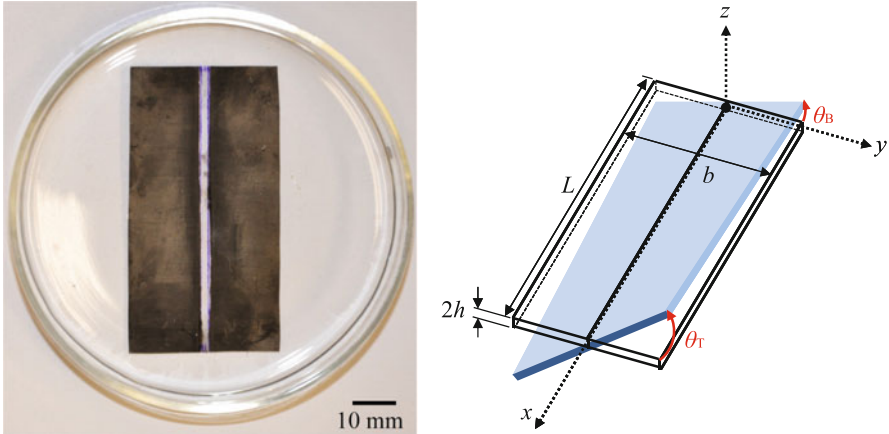


Fig. 14 (Left) A patterned IPMC and (right) schematic of the IPMC undergoing torsional vibration (Reproduced from Cha et al. 2013b)

4.2 Energy Harvesting from Torsional Vibrations

Second, we consider energy harvesting from underwater torsional vibrations of a cantilevered IPMC strip subject to harmonic base excitation (Cha et al. 2013b). The IPMC is split into two separate parts through patterned electrodes, as shown in Fig. 14, to enhance the sensitivity to torsional deformations. Ideally, the IPMC response would be zero without patterned electrodes, since the charges generated on each electrode would vanish due to the skew symmetry of the deformation with respect to the beam axis. The IPMC pattern is obtained by masking specific areas of the polymer with tape during plating (Jeon et al. 2008). The IPMC is modeled as a thin beam undergoing torsional vibrations, and the effect of the encompassing fluid is described using the hydrodynamic function developed in Aureli et al. (2012). The IPMC electrical response is described via a lumped circuit model, where the voltage source is controlled by the total twist angle.

Experimental results show that energy harvesting is optimized when the shunting resistance matches the overall IPMC impedance and the optimal harvested power is on the order of 10–100 pW.

4.3 Energy Harvesting from Wedge Slamming Impacts

Finally, we briefly describe the mechanics of energy transfer from the impact of an IPMC-based wedge on the free surface of a quiescent liquid (Cha et al. 2012). This wedge is composed of a rigid aluminum structure to which two IPMCs are clamped on both sides and connected to the bottom of a T-shaped mount that slides freely within the rails. During experiments, the wedge is raised to a selected drop height from 2 to 8 cm and then released to freely fall on the water. The two IPMCs are

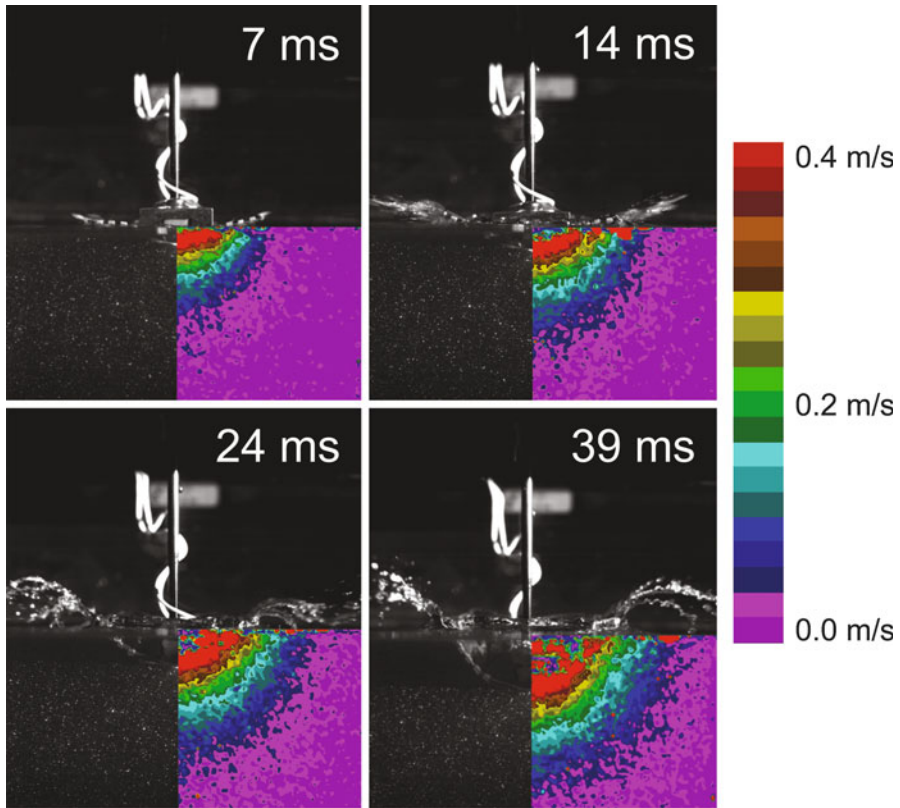


Fig. 15 Snapshots of the wedge impacting the free surface with superimposed PIV data for the *right* hand side of the wedge at the drop height 2 cm (Reproduced from Cha et al. 2012)

connected in parallel through the common aluminum clamps. The motions of the fluid and the IPMC-based wedge are recorded through a time-resolved particle image velocimetry (PIV) system. Figure 15 shows four snapshots of the IPMC-based wedge impacting the water surface, along with the corresponding velocity intensity computed for the right half of the wedge. The energy transfer during slamming can be obtained by computing the peak strain energy from the IPMC deformation. The peak energy is found at the onset of the IPMC deformation.

The energy transfer rate from the input potential energy to the strain energy during a slamming impact is on the order of 1.4–3.8 %. The output electrical energy in the IPMC can be partitioned into the contribution stored in the capacitor and the energy dissipated in the resistor. We find that the electrical energy stored in the capacitor varies from 5 to 20 pJ as the drop height varies between 2 and 8 cm, while the energy dissipated in the resistor is one order of magnitude larger. The conversion rate of strain energy to electrical energy is on the order of 0.000003–0.000036 %.

5 Conclusions

In this chapter we reviewed the latest research on the applications of IPMC actuators, including biomedical applications, biomimetic robotics, sensor/actuator integration, and energy harvesting. Since the IPMC actuators have many advantages for human-affinity biomedical applications such as soft, flexible, low-voltage drive, easy to deform in any shape and to miniaturize, many researchers have tried to apply them to many biomedical applications. The applications of the IPMC actuators to micro-catheter, micro-pump, and human-affinity tactile devices such as Braille displays have been demonstrated.

IPMCs are attractive actuators for biomimetic robots due to the softness and the ability to use in water. Fish robots, snake robots, and walking robots based on the IPMC actuators have been demonstrated. As well as mimicking functions of living animals, the future direction of the researches on biomimetic robot are expected to reveal the energy-efficient motions of living animals.

The IPMCs can be used as a sensor and an actuator in the same device. The sensor function of the IPMC and its application to the sensor/actuator feedback systems have been explored. Energy-harvesting-based IPMCs have also been explored. In the context of underwater energy harvesting, IPMCs are receiving considerable attentions for several advantageous attributes, including their inherent ability to work in wet environments, their large electrical capacitance, and their small stiffness. Energy harvesting based on the IPMCs from the undulations of a biomimetic fish tail, underwater torsional vibrations, and hull slamming has been demonstrated.

In conclusion, on the basis of the established research of materials and mathematical modeling of IPMCs described in the preceding chapters, the proposed applications of the IPMCs in this chapter are promising. In the near future, various commercial products are expected to be realized from the proposed applications in this chapter.

Acknowledgments Part of this research was supported by the National Science Foundation under grant numbers CMMI-0745753 and CMMI-0926791 and by the Office of Naval Research under grant number N00014-10-1-0988. The authors would also like to thank Dr. Catherine N. Phan, Mr. Linfeng Shen, Dr. Matteo Verotti, and Dr. Horace Walcott who have contributed to the research efforts summarized in this chapter and Dr. Sean D. Peterson who has been a critically important collaborator in our research on energy harvesting through IPMCs.

References

- Abdelnour K, Stinchcombe A, Porfiri M, Zhang J, Childress S (2012) Wireless powering of ionic polymer metal composites toward hovering microswimmers. *IEEE/ASME Trans Mech* 17 (5):924–935
- Anand SV, Arvind K, Bharath P, Mahapatra DR (2010) Energy harvesting using ionic electro-active polymer thin films with Ag-based electrodes. *Smart Mater Struct* 19(4):045026
- Arena P, Bonomo C, Fortuna L, Frasca M, Graziani S (2006) Design and control of an IPMC wormlike robot. *IEEE Trans Syst Man Cybern B Cybern* 36(5):1044–1052

- Aureli M, Kopman V, Porfiri M (2010a) Free-locomotion of underwater vehicles actuated by ionic polymer metal composites. *IEEE/ASME Trans Mech* 15(4):603–614
- Aureli M, Prince C, Porfiri M, Peterson SD (2010b) Energy harvesting from base excitation of ionic polymer metal composites in fluid environments. *Smart Mater Struct* 19(1):015003
- Aureli M, Pagano C, Porfiri M (2012) Nonlinear finite amplitude torsional vibrations of cantilevers in viscous fluids. *J Appl Phys* 111(12):124915
- Azuma A (1992) *The biokinetics of flying and swimming*. Springer, Tokyo
- Bar-Cohen Y (2003) From the editor. In: *World wide electro active polymers newsletter*. 5(1). http://ndea.jpl.nasa.gov/nasa-nde/newsltr/WW-EAP_Newsletter5-1.pdf. Accessed 21 June 2014
- Bar-Cohen Y, Breazeal C (eds) (2003) *Biologically inspired intelligent robots*. SPIE Press, Washington, DC
- Bonomo C, Fortuna L, Giannone P, Graziani S, Strazzeri S (2006) A model for ionic polymer metal composites as sensors. *Smart Mater Struct* 15:749–758
- Brufau-Penella J, Puig-Vidal M, Giannone P, Graziani S, Strazzeri S (2008) Characterization of the harvesting capabilities of an ionic polymer-metal composite device. *Smart Mater Struct* 17(1):015009
- Cellini F, Cha Y, Porfiri M (2014a) Energy harvesting from fluid-induced buckling of ionic polymer metal composites. *J Int Mater Syst Struct* 25(12):1496–1510
- Cellini F, Intartaglia C, Soria L, Porfiri M (2014b) Effect of hydrodynamic interaction on energy harvesting in arrays of ionic polymer metal composites vibrating in a viscous fluid. *Smart Mater Struct* 23(4):045015
- Cha Y, Phan CN, Porfiri M (2012) Energy exchange during slamming impact of an ionic polymer metal composite. *Appl Phys Lett* 101(9):094103
- Cha Y, Verotti M, Walcott H, Peterson SD, Porfiri M (2013a) Energy harvesting from the tail beating of a carangiform swimmer using ionic polymer-metal composites. *Bioinspir Biomim* 8(3):036003
- Cha Y, Shen L, Porfiri M (2013b) Energy harvesting from underwater torsional vibrations of a patterned ionic polymer metal composite. *Smart Mater Struct* 22(5):055027
- Cha Y, Cellini F, Porfiri M (2013c) Electrical impedance controls mechanical sensing in ionic polymer metal composites. *Phys Rev E* 88(6):062603
- Chang Y, Kim W (2013) Aquatic ionic-polymer-metal-composite insectile robot with multi-DOF legs. *IEEE/ASME Trans Mech* 18(2):547–555
- Cha Y, Porfiri M (2014) Mechanics and electrochemistry of ionic polymer metal composites. *J Mech Phys Solids* 71:156–178.
- Chen Z, Shataru S, Tan X (2010) Modeling of biomimetic robotic fish propelled by an ionic polymer-metal composite caudal fin. *IEEE/ASME Trans Mech* 15(3):448–459
- Chen Z, Uma T, Bart-Smith H (2012) Bio-inspired robotic manta ray powered by ionic polymer-metal composite artificial muscles. *Int J Smart Nano Mater* 3(4):296–308
- Cheng J, Pedley T, Altringham J (1998) A continuous dynamic beam model for swimming fish. *Phil Trans R Soc B* 353(1371):981–997
- Chu W, Lee K, Song S, Han M, Lee J, Kim H, Kim M, Park Y, Cho K, Ahn S (2012) Review of biomimetic underwater robots using smart actuators. *Int J Precis Eng Manufact* 13(7):1281–1292
- Dabiri JO (2007) Renewable fluid dynamic energy derived from aquatic animal locomotion. *Bioinspir Biomim* 2(3):L1
- Erturk A, Inman DJ (2011) *Piezoelectric energy harvesting*. Wiley, Chichester
- Fang B-K, Lin C-CK JM-S (2010) Development of sensing/actuating ionic polymer-metal composite (IPMC) for active guide-wire system. *Sens Actuators A* 158:1–9
- Farinholt K, Leo D-J (2004) Modeling of electromechanical charge sensing in ionic polymer transducers. *Mech Mater* 36:421–433
- Fukuda K, Sekitani T, Zschieschang U et al (2011) A 4 V operation, flexible Braille display using organic transistors, carbon nanotube actuators, and static random-access memory. *Adv Funct Mater* 21:4019–4027

- Giacomello A, Porfiri M (2011) Underwater energy harvesting from a heavy flag hosting ionic polymer metal composites. *J Appl Phys* 109(8):084903
- Guo S, Fukuda T et al (1995) Micro active guide wire catheter using ICPF actuator. In: *Proceeding of 1995 IEEE/RSJ international conference on intelligent robots and systems (IROS 95)*, vol 2, Pittsburgh. pp 172–177
- Guo S, Fukuda T et al (1997) Development of the micro pump using ICPF actuator. In: *Proceeding of 1997 I.E. international conference on robotics and automation, Albuquerque*, pp 266–271
- Guo S, Fukuda T, Asaka K (2003) A new type of fish-like underwater microrobot. *IEEE/ASME Trans Mech* 8(1):136–141
- Guo S, Shi L, Xiao N, Asaka K (2012) A biomimetic underwater microrobot with multifunctional locomotion. *Robot Autonom Syst* 60:1472–1483
- Hu J, Cha Y, Porfiri M, Peterson SD (2014) Energy harvesting from a vortex ring impinging on an annular ionic polymer metal composite. *Smart Mater Struct* 23(7):074014
- Jeon JH, Yeom SW, Oh IK (2008) Fabrication and actuation of ionic polymer metal composites patterned by combining electroplating with electroless plating. *Compos A* 39(4):588–596
- Jo C, Pugal D, Oh IK, Kim KJ, Asaka K (2013) Recent advances in ionic polymer-metal composite actuators and their modeling and applications. *Prog Polym Sci* 38(7):1037–1066
- Kamamichi N, Yamakita M, Asaka K, Luo Z (2006) A snake-like swimming robot using IPMC actuator/sensor. In: *Proceedings 2006 I.E. international conference robotics and automation, ICRA 2006*. Orland, Florida, pp 1812–1817
- Kato Y, Sekitani T, Takamiya M et al (2007) Sheet-type Braille displays by integrating organic field-effect transistors and polymeric actuators. *IEEE Trans Electron Devices* 54:202–209
- Kim B, Kim D, Jung J, Park J (2005) A biomimetic undulatory tadpole robot using ionic polymer-metal composite actuators. *Smart Mater Struct* 14:1579–1585
- Kim K, Tan X, Choi H, Pugal D (2013) *Biomimetic robotic artificial muscles*. World Scientific Publishing, Singapore
- Kohler NE, Casey JG, Turner PA (1995) Length-weight relationships for 13 species of sharks from the western North Atlantic. *Fish Bull* 93(2):412–418
- Konyo M, Tadokoro S, Asaka K (2007) Applications of ionic polymer-metal composites: multiple-dof devices using soft actuators and sensor. In: Kim KJ, Tadokoro S (eds) *Electroactive polymers for robotic applications: artificial muscles and sensors*. Springer, London, pp 227–262
- Kruusamae K, Brunetto P, Punning A, Kodu M, Jaaniso R, Graziani S, Fortuna L, Aabloo A (2011) Electromechanical model for a self-sensing ionic polymer-metal composite actuating device with patterned surface electrodes. *Smart Mater Struct* 20:124001
- Lee S, Kim KJ (2006) Design of IPMC actuator-driven valve-less micropump and its flow rate estimation at low Reynolds numbers. *Smart Mater Struct* 15:1103–1109
- Lee J, Yim W, Bae C, Kim K (2012) Wireless actuation and control of ionic polymer-metal composite actuator using a microwave link. *Int J Smart Nano Mater* 3(4):244–262
- Lepora N, Verschure P, Prescott T (2013) The state of the art in biomimetics. *Bioinspir Biomim* 8:013001
- Lighthill M (1960) Note on the swimming of slender fish. *J Fluid Mechanics* 9:305–317
- Mojarrad M, Shahinpoor M (1997a) Biomimetic robotic propulsion using polymeric artificial muscles. In: *Proceedings of the 1997 I.E. international conference on robotics and automation, ICRA 1997*. Albuquerque, New Mexico, pp 2152–2157
- Mojarrad M, Shahinpoor M (1997b) Ion-exchange-metal composite sensor films. In: *Proceedings of SPIE, Smart structures and materials, smart sensing, processing, and instrumentation*, 3042. San Diego, California, pp 52–60
- Najem J, Sarles S, Akle B, Leo D (2012) Biomimetic jellyfish-inspired underwater vehicle actuated by ionic polymer metal composite actuators. *Smart Mater Struct* 21:094026
- Nakabo Y, Mukai T, Asaka K (2007) Biomimetic soft robots using IPMC. In: Kim K, Tadokoro S (eds) *Electroactive polymers for robotics applications*. Springer, London, pp 165–198

- Nakadoi H, Sera A, Yamakita M, Asaka K, Luo Z-W, Ito K (2007) Integrated actuator-sensor system on patterned IPMC film: consideration of electronic interference. In: Proceedings of IEEE international conference on mechatronics. Kumamoto, Japan
- Nam D-N-C, Ahn K-K (2014) Modeling and control of a self-sensing polymer metal composite actuator. *Smart Mater Struct* 23:025025
- Newbury K-M, Leo D-J (2003) Linear electromechanical model of ionic polymer transducers – part I: model development. *J Intell Mater Syst Struct* 14:333–342
- Nguyen TT, Goo NS, Nguyen VK, Yoo Y, Park S (2008) Design, fabrication, and experimental characterization of a flap valve IPMC micropump with a flexibly supported diaphragm. *Sens Actuators A* 141:640–648
- Oguro K, Fujiwara N, Asaka K, et al. (1999) Polymer electrolyte actuator with gold electrodes. In: Bar-Cohen Y (ed) *Proceeding of the SPIE 6th annual international symposium on smart structures and materials*, Newport Beach, pp 64–71
- Palmre V, Hubbard J, Fleming M, Pugal D, Kim S, Kim K, Leang K (2013) An IPMC-enabled bio-inspired bending/twisting fin for underwater applications. *Smart Mater Struct* 22:014003
- Peterson SD, Porfiri M (2012) Energy exchange between a vortex ring and an ionic polymer metal composite. *Appl Phys Lett* 100(11):114102
- Phan CN, Aureli M, Porfiri M (2013) Finite amplitude vibrations of cantilevers of rectangular cross sections in viscous fluids. *J Fluid Struct* 40:52–69
- Porfiri M, Peterson SD (2013) Energy harvesting from fluids using ionic polymer metal composites. In: Elvin N, Erturk A (eds) *Advances in energy harvesting methods*. Springer, New York, pp 221–240
- Punning A, Anton M, Kruusmaa M, Aabloo A (2004) A biologically inspired ray-like underwater robot with electroactive polymer pectoral fins. In: Proceedings of the international IEEE conference mechatronics and robotics. Aachen, pp 241–245
- Punning A, Kruusmaa M, Aabloo A (2007) A self-sensing ion conducting polymer metal composite (IPMC) actuator. *Sens Actuators A* 136:656–664
- Roper D, Sharma S, Sutton R, Culverhouse P (2011) A review of developments towards biologically inspired propulsion systems for autonomous underwater vehicles. In: Proceedings of institution of mechanical engineers, Part M: J. Engineering for the Maritime Environment, vol 225, pp 77–96. doi:10.1177/1475090210397438
- Sareh S, Rossiter J, Conn A, Drescher K, Goldstein RE (2012) Swimming like algae: biomimetic soft artificial cilia. *J R Soc Interface* 10:20120666
- Shahinpoor M, Bar-Cohen Y, Simpson J, Smith J (1998) Ionic polymer-metal composites (IPMCs) as biomimetic sensors, actuators and artificial muscles - A review. *Smart Mater Struct* 7: R15–R30
- Shahinpoor M, Kim KJ (2001) Ionic polymer-metal composites: I. Fundamentals. *Smart Mater Struct* 10(4):819–833
- Takagi K, Luo Z, Asaka K, Tahara K (2005) Limited-angle motor using ionic polymer-metal composite. In: Proceedings of SPIE 5759, smart structures and materials 2005: electroactive polymer actuators and devices (EAPAD). San Diego, California, p 487
- Takagi K, Nakabo Y, Luo Z, Mukai T, Yamamura M, Hayakawa Y (2006a) An analysis of the increase of bending response in IPMC dynamics given uniform input. In: Proceedings of SPIE 6168, smart structures and materials 2006: electroactive polymer actuators and devices (EAPAD). San Diego, California, p 616814
- Takagi K, Yamamura M, Luo Z, Onishi M, Hirano S, Asaka K, Hayakawa Y (2006b) Development of a rajiform swimming robot using ionic polymer artificial muscles. In: 2006 IEEE/RSJ international conference on intelligent robots and systems. Beijing, pp 1861–1866
- Takagi K, Tomita N, Asaka K (2014) A simple method for obtaining large deformation of IPMC actuators utilizing copper tape. *Adv Robot* 28(7):513–521
- Tiwari R, Kim KJ, Kim SM (2008) Ionic polymer-metal composite as energy harvesters. *Smart Struct Syst* 4(5):549–563

- Tomita N, Takagi K, Asaka K (2011) Development of a quadruped soft robot with fully IPMC body. In: 2011 Proceedings of SICE annual conference. Tokyo, pp 1687–1690
- Yamakita M, Kamamichi N, Kaneda Y, Asaka K, Luo Z (2004) Development of an artificial muscle linear actuator using ionic polymer-metal composites. *Adv Robot* 18(4):383–399
- Yamakita M, Kamamichi N, Luo Z, Asaka K (2007) Robotic application of IPMC actuators with redoping capability. In: Kim K, Tadokoro S (eds) *Electroactive polymers for robotics applications*. Springer, London, pp 199–226
- Yamakita M, Sera A, Kamamichi N, Asaka K (2008) Integrated design of an ionic polymer–metal composite actuator/sensor. *Adv Robot* 22:913–928
- Yeom S, Oh I (2009) A biomimetic jellyfish robot based on ionic polymer metal composite actuators. *Smart Mater Struct* 18:085002

IPMCs as EAPs: How to Start Experimenting with Them

10

Kinji Asaka, Karl Kruusamäe, Kwang Kim, Viljar Palmre, and
Kam K. Leang

Contents

1	Introduction	216
2	Fabrication of IPMC	216
2.1	Ionic Polymer	216
2.2	Electrode Plating	218
2.3	Fabrication of Actuator Devices	218
3	Electromechanical Characterization of IPMCs	219
3.1	Considerations for the Experimental Setup	220
3.2	Representing Experimental Results	222
3.3	Reporting the Electromechanical Response	224
4	Implementation and Control of IPMCs	225
4.1	IPMC Actuators for Creating Complex Deformations	225
4.2	Feedforward and Feedback Control for Mitigating IPMC Back Relaxation	227
5	Conclusion	231
	References	232

K. Asaka (✉)

Inorganic Functional Material Research Institute, National Institute of Advanced Industrial Science and Technology (AIST), Ikeda, Osaka, Japan

e-mail: asaka-kinji@aist.go.jp

K. Kruusamäe

Department of Mechanical Engineering, University of Texas at Austin, Austin, USA

e-mail: karl.kruusamae@utexas.edu

K. Kim • V. Palmre

Department of Mechanical Engineering, University of Nevada, Las Vegas, NV, USA

e-mail: kwang.kim@unlv.edu; viljar.palmre@gmail.com

K.K. Leang

Department of Mechanical Engineering, University of Utah, Salt Lake City, UT, USA

e-mail: kam.k.leang@utah.edu

Abstract

This chapter describes how to start experiments with ionic polymer–metal composite (IPMC) actuators. In the first part, a fabrication of IPMC actuator element is summarized. In the next part, how to setup a measurement system of IPMC actuator and test the actuator performance is described. In the last part, a control method of IPMC actuator is discussed. From the information in this chapter, experiments with IPMC actuators can be started.

Keywords

Ionic polymer-metal composite (IPMC) • Ionic polymer • Electroplating • Electromechanical characterization • Control method

1 Introduction

In this chapter, how to start experiments with IPMC actuators in order to apply them to various applications as shown in the previous chapters are described. In order for that, how to fabricate IPMC actuator elements, how to set up a measurement system of IPMC actuator and test the actuator performance, and a control method of IPMC actuator are described in this chapter.

2 Fabrication of IPMC

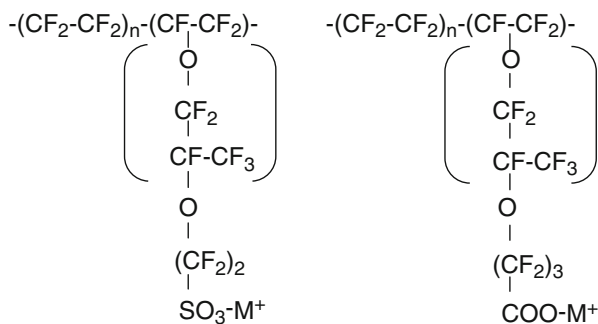
As shown in the previous chapters, an ionic polymer–metal composite (IPMC) is composed of an ionic polymer plated with metal electrodes. By deforming the ionic polymer and patterning the plated electrodes, soft actuator devices that are capable of moving in multiple degrees of freedom can be fabricated.

In the first part of this section of starting experiments with IPMC actuator, basics of ionic polymer used for IPMC, electroplating method, and fabrication of IPMC device including deforming ionic polymer and patterning electrode are described. Since details of ionic polymers and plating methods are described in the preceding chapters, this part describes only a summary of them.

2.1 Ionic Polymer

For IPMCs, their performances critically depend on ionic polymer used. Ionic polymers usually used for the IPMC are perfluorosulfonic acid or perfluoro-carboxylic acid polymers, of which the typical chemical structures are shown in Fig. 1. One can obtain various types of thin films made from perfluorosulfonic acid from E. I. du Pont de Nemours and Company as commercial products (Nafion).

Fig. 1 Chemical structures of perfluorosulfonic acid (*left*) and perfluorocarboxylic acid polymers (*right*)



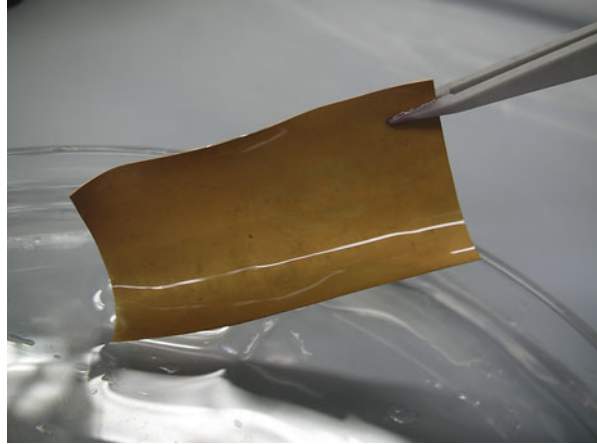
Other several companies supply similar compounds. Asahi Glass Co., Ltd. produces perfluorocarboxylic acid type polymer films (Flemion).

Hydration of the perfluorinated ionic polymers (PIPs) depends on the ionic form and ion-exchange capacity (Asaka et al. 2001). In the case of the Nafion membrane, the water content decreases with the increase in the hydrophobicity of the counter cation. The ionic conductivity also depends on the ionic size, the hydration, the charge density of the ionic polymer, etc. For instance, the alkali cation-form and alkaline earth cation-form PIPs have larger conductivity than alkyl ammonium cation-form PIPs. Increasing the size of the alkyl ammonium cation decreases the conductivity. These results are closely related on the ion-cluster structure of the PIP.

It is well-known that the PIP swelled with water has a hydrophilic channel-linked ion-cluster structure surrounding with hydrophobic perfluoro-backbone polymer network (Yeo and Yeager 1985). Counterions and water transfer through hydrophilic narrow channel-linked ion cluster. If hydrophilic small cations such as Li^+ , Na^+ , K^+ , etc. transfer through the channel, large mobility (high ionic conductivity) and little water drag take place, which result in higher response and smaller displacement of the actuation of the IPMC. The opposite is true in the case of hydrophobic large cations such as TEA^+ and TBA^+ (Onishi et al. 2001a). In other words, the actuation performance of the IPMC can be controlled by changing counter cation species in the PIP, which can be easily changed by immersing the IPMC in electrolyte solution for more than one night. The details of the behavior of the IPMC actuation response of various ionic forms can be described by recent improvement in multi-physical modeling (Yamaue et al. 2005; Zhu et al. 2013a, b) of IPMC actuation based on ion-cluster structure of ionic polymer.

The perfluorinated ionic polymers are still the best ionic polymers for the IPMC. However, these polymers have some limitations, especially their high cost for applications. Therefore, recently, various hydrocarbon-based ionic polymers for the IPMC have been developed (Jo et al. 2013).

Fig. 2 Photograph of a gold-plated Nafion IPMC



2.2 Electrode Plating

An established method of the electroplating on the ionic polymers is a chemical plating method using platinum or gold electrodes. Details are described in the preceding chapters.

After roughening the surface of the ionic polymer by dry blasting or emery paper, the ionic polymer is immersed in the aqueous solution of a metal complex salt. Then, the metal complex adsorbed in the ionic polymer is reduced by the reducing agent. The sequential plating technique has been developed for optimizing the electrode structure, which has large electrochemical area and soft mechanical property (Onihsi et al. 2001b). Figure 2 shows the photograph of the gold-plated IPMC.

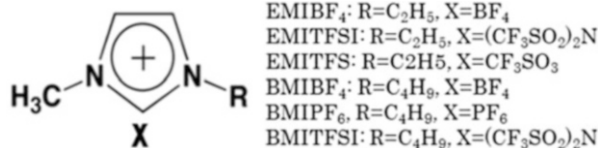
Recently, the electroplating methods of nanoparticles of other metals, metal oxides, or carbons including several physical technologies such as their printing or pressing were developed (Akle et al. 2006; Palmre et al. 2009).

2.3 Fabrication of Actuator Devices

In order to fabricate the IPMC actuator device, forming the ionic polymer and patterning the plating electrodes are often needed. Forming the fluorinated ion-exchange polymer can be easily done by casting the dispersing solution and evaporating the solvent or hot molding the thermoplastic resin and activating the ionic polymer by hydrolysis. Preparing the ionic polymer of various shapes and connecting with other materials can also be done by the same method (Asaka and Oguro 2009).

In order to make an IPMC device that can move in multiple degrees of freedom, the plating electrodes need to be patterned. In the laboratory, the plating electrode

Fig. 3 Chemical structure of ionic liquids used for IPMCs



can be patterned by cutting the plating electrode by PC-controlled mechanical or optical (laser) cutting machine (Asaka and Oguro 2009). The details on the fabrication of IPMC actuator devices including forming and patterning electrodes for complex motions will be described in the Sect. 10.3.

As mentioned previously, the actuation performances such as response speed, displacement amplitude, back relaxation, etc. can be controlled by changing counter cations. In order for this to happen, an IPMC element is immersed in the concentrated electrolyte solution (more than 0.1 mol/l) of the desired dopant cation.

The solvent in Nafion and Flemion for giving the optimum performances of the IPMC actuators is water. However, water-swollen IPMCs are difficult to be operated in the air for long time, since water is evaporated. In order to solve this issue, ionic liquids (ILs) have been used as solvents and ions for the IPMC actuator. Ionic liquids (ILs) are known to be nonvolatile and show high ionic conductivities and wide potential windows. ILs used for the IPMCs are shown in Fig. 3. In order to change the solvent in the IPMC to ILs, the IPMC is immersed in IL-containing solution after completely removing the water from the IPMC (Kikuchi and Tsuchitani 2009). Another method is that dehydrated Nafion is immersed in ILs, and then, the electrode layers are assembled on the surface of the Nafion by coating conducting nanoparticles with ILs (Akle et al. 2006).

3 Electromechanical Characterization of IPMCs

In this part of the chapter, we will demonstrate how to measure and represent the electromechanical performance of a bending IPMC actuator. In literature one can find that in order to truly understand the workings of an IPMC, a wide range of electrical, mechanical, electrochemical, and other measurements need to be carried out. Nevertheless, after obtaining a new IPMC, the most interesting question to most of the engineers and researchers is: Will it work and how well does it perform? The common way to characterize IPMC actuators is by measuring their maximum stroke and blocking force. As the overall electromechanical response is dependent on a range of factors, including the amplitude, frequency, and the shape of the driving signal, it is a good idea to construct an experimental setup where some of these parameters can be easily altered. A basic measurement system allows determining the stroke and the blocking force of an IPMC under a variety of driving signals.

3.1 Considerations for the Experimental Setup

The experimental setup for measuring electromechanical performance of an IPMC actuator consists of a clamp to mount the IPMC sample, a data recording device (e.g., digital oscilloscope or computer equipped for data acquisition), a function generator, a current amplifier, a force sensor, and a laser displacement sensor or a video camera (Figs. 4 and 5). The process diagram of electromechanical characterization is given in Fig. 6.

The role of the mounting clamp is to position the actuator in a cantilever configuration while also acting as an outlet for driving voltage. Because IPMCs contain solvent such as water or ionic liquid that may leak out, it is better to use noble metal (such as gold) for electric contacts to avoid oxidation or any other kind of deterioration of conductivity. The pressure of clamping has been reported to influence the performance of IPMC (Moeinkhah et al. 2013); thus, it is recommended to have some control over it. Moreover, for minimizing the influence of gravitational

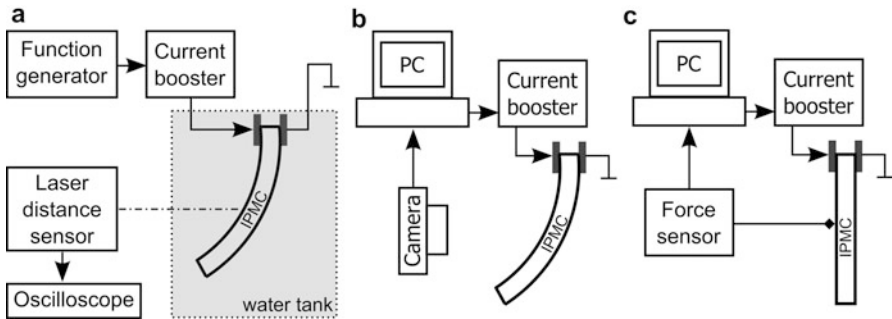


Fig. 4 Example of experimental setups for electromechanical characterization of bending IPMC

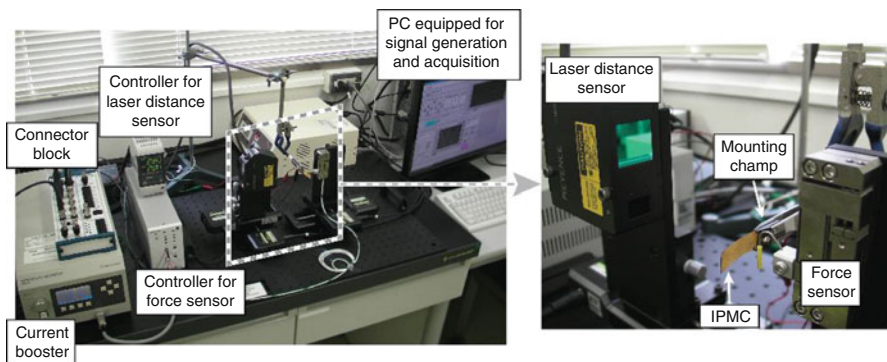


Fig. 5 Photographs of an experimental setup for measuring stroke and force of a bending IPMC in ambient environment

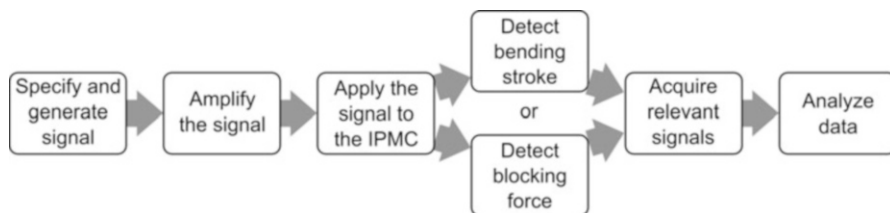


Fig. 6 Flowchart for electromechanical characterization of IPMC actuator

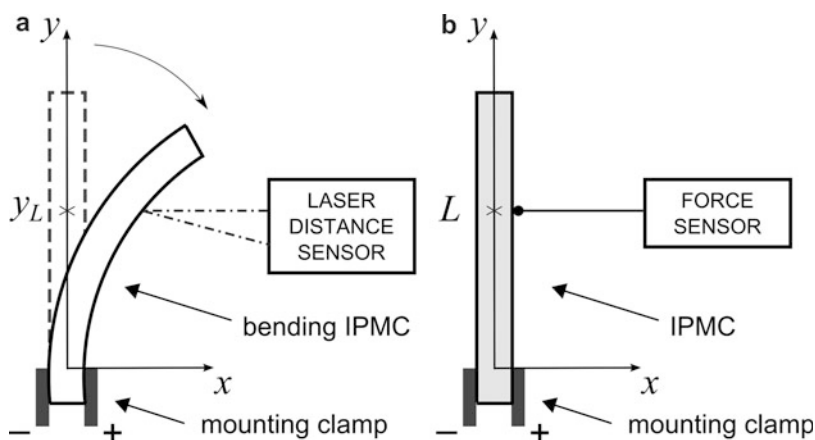


Fig. 7 Positioning of IPMC and (a) laser displacement sensor or (b) force sensor

force on the performance of the actuator, it is practical to position the IPMC so that the bending occurs in the horizontal plane (e.g., Fig. 5).

The most widely used method for measuring the stroke of an IPMC actuator is by means of a laser distance sensor (Fig. 7a). In addition to fast response and good precision, laser displacement sensors are quite easy to operate. Once the laser beam is pointed to the actuator, it detects movement in the direction of x -axis at a fixed distance y_L (Fig. 7a). The analog output of laser displacement sensors is often linearly related to the measured distance. The main drawback of using this kind of sensing is that relatively large portion of bending data is discarded – for instance, the displacement at a single point cannot always be used to unequivocally describe the whole shape of the IPMC actuator.

Video cameras can also be implemented to measure the bending amplitude of an IPMC (Fig. 4b). The biggest advantage of using a video camera is the possibility to record the mechanical response of the whole shape of the actuator. However, extracting relevant data from the video can be rather complicated, especially in comparison with laser displacement sensor. However, the state of the art of video imaging systems and their built-in functionality are rapidly

evolving, so that the technology is continuously becoming more reliable and user-friendly.

Since many IPMCs operate best in water, it may be necessary to submerge the IPMC sample in a tank of deionized water during the electromechanical measurements (Fig. 4a). As cameras and displacement sensors remain outside the tank, parallelepiped water tank is recommended to minimize uncertainty due to optical distortions.

Blocking force of an IPMC can be determined by using a load cell with suitable operating range. As the measured forces are typically in the range of millinewtons, even the slightest vibrations can affect the experimental results.

The driving signals are usually specified and created by using a dedicated function generator or a PC with appropriate software and hardware (e.g., National Instruments LabVIEW with a suitable interface device). For amplifying the driving signal, a potentiostat or a custom-made conditioning circuit can be used. The peak current consumption of an IPMC is dependent on the material properties as well as the dimensions of the actuator sample. For instance, a water-based IPMC with Na^+ cations and dimensions of $50 \times 10 \times 0.2$ mm can show peak current consumption over 1 A under rectangular input signal with amplitude of 2 V (Anton et al. 2008). There is no convention about which type of driving signal to prefer when characterizing IPMC actuators, but rectangular and sinusoidal are used most often.

The input voltage must take into account the electrochemical window of the solvent used in a particular IPMC. Typically 1–2 V is sufficient to observe noteworthy actuation response without any decomposition. Even though threshold voltage for water electrolysis is about 1.23 V, higher input voltages can be applied to a water-based IPMC as the potential between the electrode layers of an IPMC remains below that level. It is quite challenging to precisely determine the upper limits for input voltage but closely observing the behavior of current can help to identify the presence of undesired electrochemical processes. For experiments carried out inside a water tank, the use of too high input voltage can result in the production of oxyhydrogen which in turn can lead to a catastrophic failure of the system.

3.2 Representing Experimental Results

Figure 8 depicts an example of signals acquired when characterizing an IPMC actuator.

In Fig. 8 the stroke of a cantilever actuator is given in terms of the displacement x at a constant distance y_L (Fig. 7a). Whereas this kind of time domain plots is highly informative, in order to manage large quantities of data, one might select a single number, such as the maximum displacement value (x_{\max}), to describe the performance of the actuator under a particular input signal. However, in addition to the

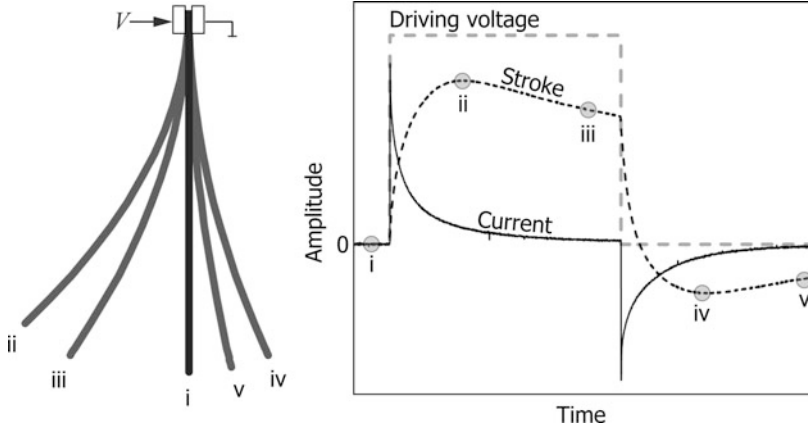


Fig. 8 Example of IPMC's bending behavior and corresponding signals

properties of the actuator and parameters of the input signal, the (maximum) displacement value is dependent on the geometry of the experimental setup, especially on the distance y_L .

One way to overcome the dependency to geometry is to assume uniform (i.e., circular) curvature of the actuator during its work cycle. In this case, the actuation is expressed as the curvature κ or bend radius $r = \kappa^{-1}$ of the sample. If the curvature is obtained using a video camera or a laser profilometer, it can provide an accurate description for the overall shape of the actuator. However, if the curvature is calculated from the displacement x using the well-known geometrical relations given in Eq. 1, the results may be biased. Since an IPMC can be regarded to behave like a transmission line, its curvature is often larger at smaller values of y_L (Punning et al. 2009; Vunder et al. 2012; Kruusamäe et al. 2014):

$$\kappa = \frac{2x}{y_L^2 + x^2} \stackrel{x \ll r}{\Rightarrow} \kappa \approx \frac{2x}{y_L^2} \tag{1}$$

In the cases of actuator exhibiting a complex behavior of bending or its initial shape cannot be accurately described by a circular curve, a more general approach that divides the length of an actuator into vectors of equal length has been proposed (Punning et al. 2009; Vunder et al. 2012). Each vector is described by its angle relative to the previous vector (Fig. 9), thus allowing representations of a large variety of shapes. The accuracy of such representation is determined by the number of vectors used to describe the IPMC.

Due to the wide range of IPMC actuators produced all over the world, there is a pressing need for an objective method to compare their electromechanical performance. The most common way of comparing bending actuators is based on estimating the difference of strains in the electrodes of the IPMC. As a result of the

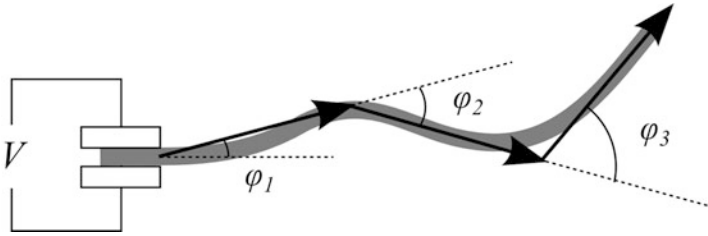


Fig. 9 Vector-based representation of a bending actuator

widespread use of laser displacement sensors, maximum strain difference ε is typically calculated as given in Eq. 2 (Kruusamäe et al. 2014):

$$\varepsilon = \frac{2tx_{\max}}{y_L^2 + x_{\max}^2} \quad (2)$$

This estimation of maximum strain difference is being extensively implemented to compare the electromechanical performance of actuators of different length and thickness t . However, since Eq. 2 is directly based on Eq. 1, the results may be skewed in the similar fashion as discussed above for uniform curvature.

The blocking force of a bending IPMC actuator is also dependent on the position of force sensor head as well as the dimensions of the actuator (Anton et al. 2008). For the purpose of physical modeling, it is useful to convert the blocking force F into bending moment M :

$$M = FL \quad (3)$$

where L is the distance between the mounting clamp and force sensor head (Fig. 7b).

3.3 Reporting the Electromechanical Response

As discussed above, the way the experimental setup is constructed can influence the interpretation of IPMC's performance. Given that to date there is no standard of carrying out the electromechanical measurements of IPMCs nor a universal characteristic to objectively compare the stroke or the force of different bending actuators, it is best to accompany the results with detailed description of the geometry of the experimental setup and parameters of the driving signals.

Furthermore, it is very important to report the ambient humidity and temperature during the electromechanical measurements as the performance of both water- and ionic liquid-based IPMCs has been reported to be influenced by these parameters (Brunetto et al. 2010; Must et al. 2014).

In order to interpret the electromechanical results, the performance of IPMCs is often reported alongside of a variety of characteristics such as the capacitance of the actuator, current during the operation cycle, charge accumulated by the time of maximum displacement/blocking force, conductivity of the electrodes, viscoelasticity of the materials, etc. Finding out how all these parameters relate to the electromechanical response of IPMCs is a subject of ongoing research in the field of electroactive polymers.

4 Implementation and Control of IPMCs

While the previous sections of this chapter concern the experimental testing and characterization of IPMCs, the following section describes how to implement and control the IPMC actuators in specific robotic designs and applications. IPMCs are highly regarded for biomimetic underwater systems, such as autonomous ocean mapping and surveillance robots that move through their environment by imitating the swimming motion of aquatic animals. However, in order to emulate the behavior of even the simplest of these organisms, the robotic control surfaces must enable multiple degrees of freedom motion. This section describes how to utilize and control the IPMC actuators to create complex deformations such as bending, twisting, flapping, and other bioinspired motion for robotic applications. The approaches discussed include patterning the surface electrodes and selectively activating the specific sectors or, alternatively, incorporating IPMC actuators into a soft boot material for creating a control surface. In addition, the feedforward and feedback control method for mitigating the back relaxation of IPMC by controlled activation of sectored electrodes is presented.

4.1 IPMC Actuators for Creating Complex Deformations

IPMC strip actuators are conventionally used in the cantilever configuration to generate a bending motion for propulsion of underwater robotic systems. However, this approach creates a simple 1D bending motion and performance is rather limited. To enable more complex multiple degrees of freedom motion, such as twisting, IPMCs with patterned (sectored) electrodes have been designed (Hubbard et al. 2014). Patterning of IPMC electrodes can be done after plating process using a computer-controlled milling machine equipped with a microsurface routing end mill (Kim et al. 2011). The end mill, rotating ~ 3000 rev/min, is programmed to follow a predefined trajectory that defines the electrode pattern. The end mill removes the necessary metal down to a membrane surface, creating a monolithic IPMC with isolated electrodes, as shown in Fig. 10. Figure 10a shows the typical experimental setup with two laser displacement sensors to measure the bending and twisting motion of patterned IPMC.

For the monolithic IPMC with four isolated electrode pads (Fig. 10), the twisting motion is produced by phase shifting the input signal between the left and right

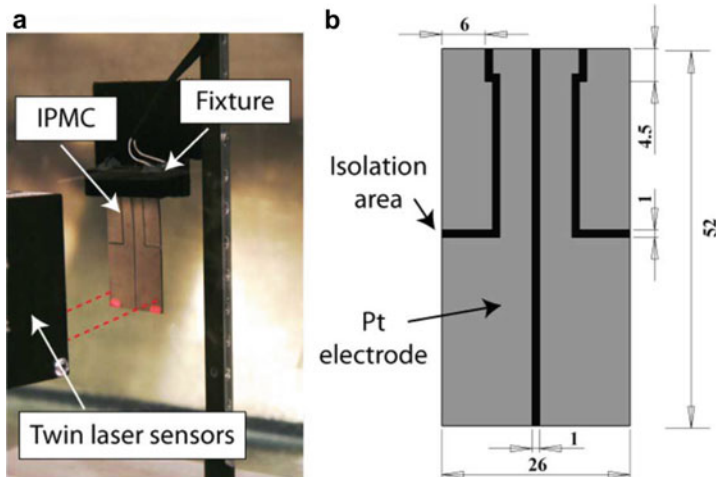


Fig. 10 (a) Experimental setup for measuring bending/twisting response for (b) an example patterned IPMC (units in mm) (© 2014 IEEE. Reprinted, with permission, from Hubbard et al. (2014) Monolithic IPMC fins for propulsion and maneuvering in bioinspired underwater robotics. *IEEE J Ocean Eng* 39(3):540–551)

sectors. In the case of 180° phase shifting, the patterned IPMC can achieve the maximum twist angle of 8.46° at 4 V DC input. The twist angle increases significantly with increasing input voltage as well as decreasing actuation frequency (sinusoidal input). These trends are shown in Fig. 11, demonstrating the ability of monolithic IPMC to generate practical twisting motion.

An alternative approach for producing complex bioinspired motion involves integrating IPMC actuators into a soft silicone material to create an active control surface, called a “fin” (see Fig. 12) (Palmre et al. 2013). The fin can be used to achieve complex deformation depending on the placement and orientation of the actuator strips. In contrast to the monolithic IPMCs with patterned electrodes described earlier, this design approach does not require (1) the expensive process of electroless plating platinum all throughout the actuator surface and (2) specially machining (patterning) the electrodes. Therefore, conventional IPMC actuators such as those with rectangular shapes can be used. The unique advantage of this structural design is that custom shaped fins and control surfaces can be easily fabricated without special materials processing. The molding process of silicone rubber is relatively inexpensive and does not require functionalizing or “activating” the boot material as in case of preparing IPMCs.

Figure 13 shows three IPMC actuator strips embedded in a soft silicone structure. The twisting motion is produced by phase shifting the same input signal by 180° between the outer two IPMCs. The center IPMC is not actuated in order to not obstruct the movement of either adjacent IPMCs. A square-wave signal of 4 V at 50 mHz was applied to drive the boot-IPMC. As shown in Fig. 13, the maximum twist angle measured at this input is approximately 12° . Photographs indicate that

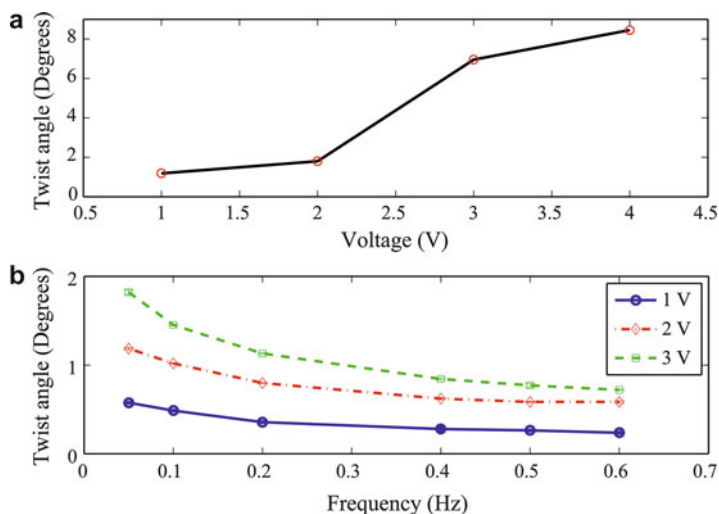


Fig. 11 (a) Twist angle of IPMC versus amplitude of DC input voltage and (b) twist angle versus input signal frequency (sinusoidal input) (© 2014 IEEE. Reprinted, with permission, from Hubbard et al. (2014) Monolithic IPMC fins for propulsion and maneuvering in bioinspired underwater robotics. IEEE J Ocean Eng 39(3):540–551)

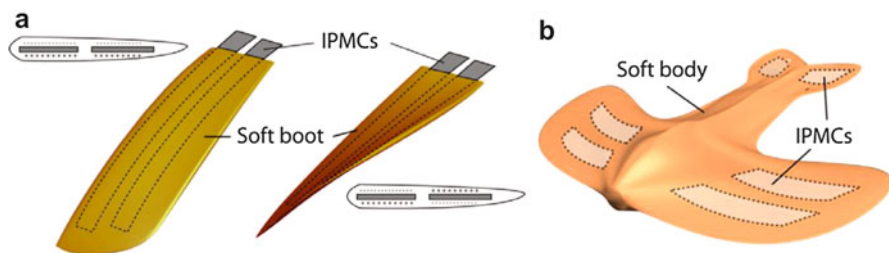


Fig. 12 (a) IPMCs integrated into soft boot structure illustrating bending and twisting motion by selectively activating electrodes and (b) example soft bioinspired robotic platform with embedded IPMC actuators (Palmre et al. 2013) (© IOP Publishing. Reproduced with permission from IOP Publishing. All rights reserved)

due to the flexible boot structure, a complex shape is produced so that the angle varies both along the length and height of the control surface.

4.2 Feedforward and Feedback Control for Mitigating IPMC Back Relaxation

In some applications, the attractive qualities of IPMC actuators can be overshadowed by undesired dynamic effects and nonlinearities, the most obvious of which is “back

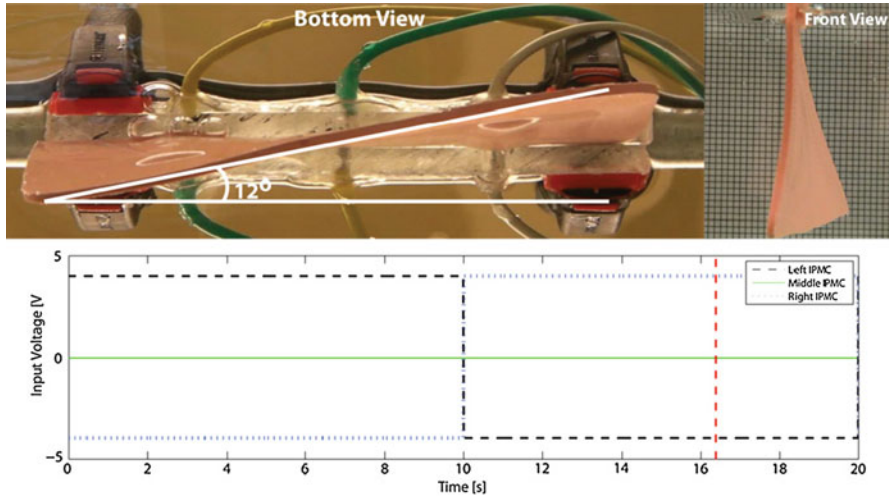


Fig. 13 Two views showing the maximum twist angle achieved at 4 V square-wave input. Bottom: the input voltage and the time of maximum deflection noted by the red dotted line (Palmre et al. 2013) (© IOP Publishing. Reproduced with permission from IOP Publishing. All rights reserved)

relaxation” that can lead to significant positioning error (Fleming et al. 2012). When subjected to a DC voltage, a Nafion-based IPMC in the traditional cantilever configuration undergoes a relatively fast deflection toward the anode, followed by a slow relaxation in the opposite direction, i.e., toward the cathode (Nemat-Nasser 2002). It is commonly accepted that the so-called back relaxation effect is due to diffusion forces acting on the solvent within the ionomer membrane. This effect can cause significant positioning error and compromise the use of IPMCs in static and low-frequency applications.

Fleming et al. developed a control method to mitigate back relaxation, utilizing sectored IPMCs (Fleming et al. 2012). This method involves driving different sectors of the IPMC in opposing directions, thereby canceling out the back relaxation. The basic concept is illustrated in Fig. 14, showing the relaxation experienced by each sector when activated by opposing inputs (u_1 and u_2) and the net cancelling effect.

In this configuration, the outer portions of IPMC serve as one sector (Sector 1) and are driven by input $u_1(t)$, while the middle portion serves as a second sector (Sector 2) and is driven by input $u_2(t)$. Thus, the IPMC comprises two controllable sectors. To control the performance of the sectored IPMC, the feedforward architecture in Fig. 15 can be used. In this diagram, $C_1(s)$ and $C_2(s)$ are the controllers and $G_1(s)$ and $G_2(s)$ are their respective transfer functions associated with Sector 1 and Sector 2, respectively. $Y_d(s)$ is the desired trajectory. This structure represents an open loop version of the master–slave control system. The advantage of the open

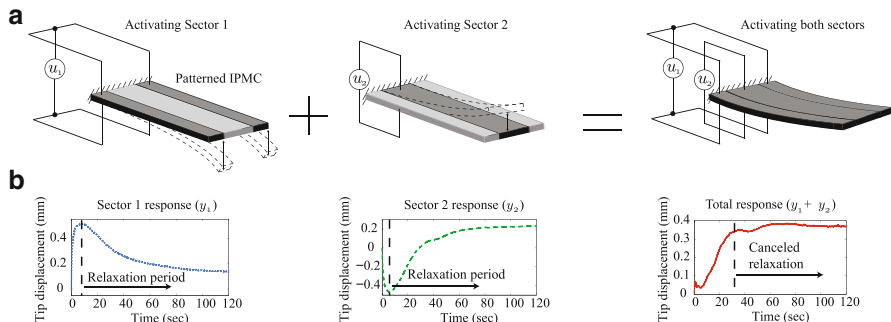
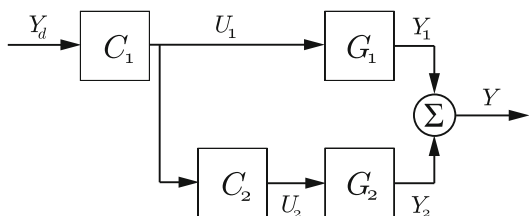


Fig. 14 Concept: (a) independently controlling each sector to produce a net cancelling effect and (b) corresponding experimental step responses (Fleming et al. 2012) (© IOP Publishing. Reproduced with permission from IOP Publishing. All rights reserved)

Fig. 15 Feedforward control scheme for sectored IPMC (Fleming et al. 2012) (© IOP Publishing. Reproduced with permission from IOP Publishing. All rights reserved)



loop feedforward control method is that the sensor feedback is not required, thereby simplifying the implementation. However, feedback control can be integrated to further improve performance, where feedback can come from laser sensors or strain-based sensors (Leang et al. 2012). In this configuration, the input generated by $C_1(s)$ (the master controller) is fed into $C_2(s)$ (the slave controller).

The slave controller, $C_2(s)$, serves to counteract the back relaxation of Sector 1 by inducing back relaxation in the reverse direction for Sector 2. With the inputs accordingly weighted, the back relaxation of each sector roughly cancels out. Then, $C_2(s)$ is responsible for setting $U_2(s)$ in appropriate proportion to $U_1(s)$, such that the IPMC sectors relax the same amount.

To account for nonlinearity, disturbances, and other undesirable effects not captured in the model, a feedback controller ($C_0(s)$) can be integrated with the feedforward controller. As shown in Fig. 16, the feedback loop is arranged such that the feedforward and feedback inputs ($U_{ff}(s)$ and $U_{fb}(s)$, respectively) are added to produce $U_1(s)$.

Figure 17 illustrates the experimental implementation of the feedforward/feedback control system. A custom-made voltage/current amplifier is employed to drive the IPMC (Leang et al. 2012). A clamp mount with the six contacts is used to connect the three sectors of IPMC with the source terminals. The outer two sectors

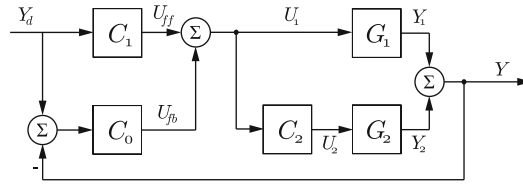


Fig. 16 Integrated feedforward/feedback control scheme for sectored IPMC (Fleming et al. 2012) (© IOP Publishing. Reproduced with permission from IOP Publishing. All rights reserved)

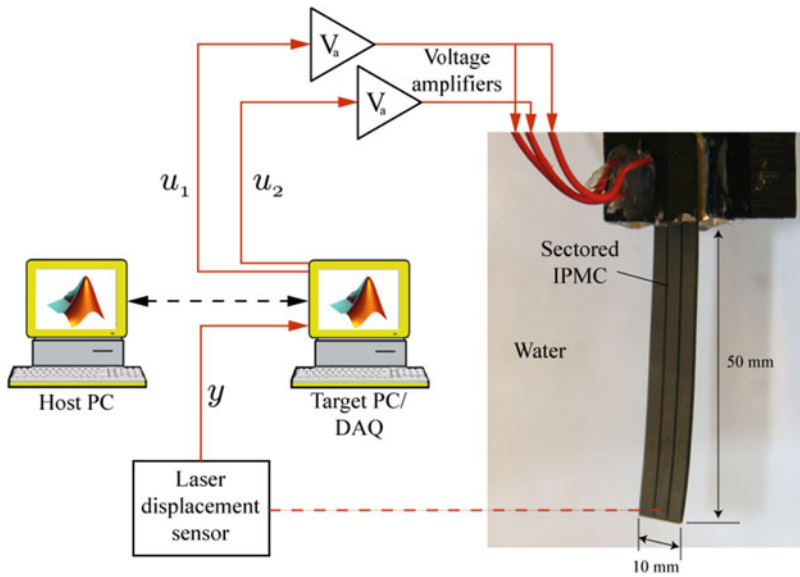
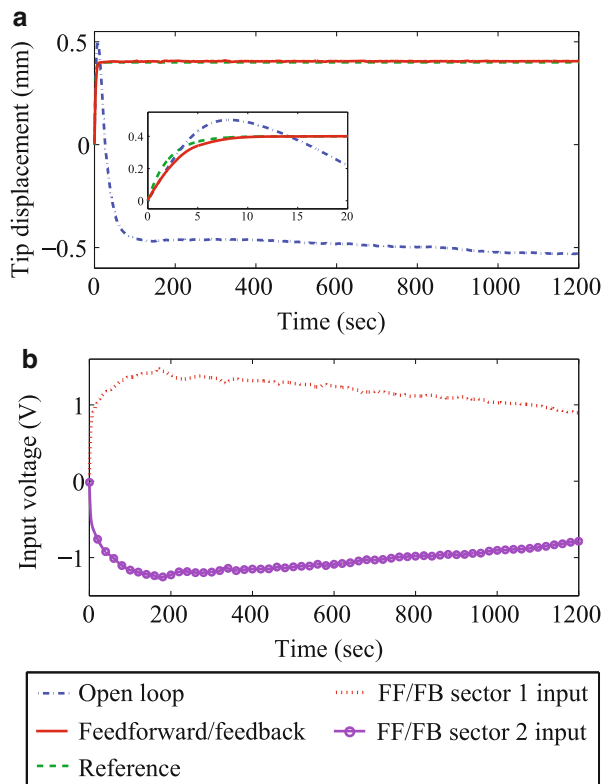


Fig. 17 Experimental setup for controlling the IPMC with two effective sectors (Fleming et al. 2012) (© IOP Publishing. Reproduced with permission from IOP Publishing. All rights reserved)

are driven in unison, making them function as one sector. MATLAB, in conjunction with Simulink and xPC target, is used to operate a 12-bit data acquisition card, which serves to output the voltage signals and also record the IPMC tip displacement using a laser displacement sensor.

Figure 18 shows the displacement response of IPMC subjected to the exponential reference under feedforward/feedback control for 20 min (1200 s). It can be seen that with this control method, the IPMC is able to maintain a steady position for the entire period. As seen in Fig. 18, under open loop condition, the IPMC begins to relax after approximately 10 s. In case of feedforward/feedback control, there was no indication of back relaxation for a period 120 times longer.

Fig. 18 Sected IPMC with a 20-min exponential reference: (a) displacement response and (b) input voltage (Fleming et al. 2012) © IOP Publishing. Reproduced with permission from IOP Publishing. All rights reserved



5 Conclusion

In this chapter, how to start experiments with IPMC actuators including a fabrication of IPMC actuator element, how to setup a measurement system of IPMC actuator and test the actuator performance, and a control method of IPMC actuator were described.

In the first part, basics of ionic polymer used for the IPMC, electroplating method, and fabrication of IPMC device including deforming ionic polymer and patterning electrode were briefly summarized.

In the second part, how to measure and represent the electromechanical performance of a bending IPMC actuator was described. The common way to characterize IPMC actuators is by measuring their maximum stroke and blocking force. A basic measurement system which allows determining the stroke and the blocking force of an IPMC under a variety of driving signals was discussed. How to represent the electromechanical experimental results was also explained.

The last part describes how to implement and control the IPMC actuators in specific robotic designs and applications. In order to use the IPMC actuators for various robotic systems, the IPMC actuators need to create complex deformations such as bending, twisting, flapping, and other bioinspired motion. The approaches including patterning the surface electrodes and selectively activating the specific sectors or, alternatively, incorporating IPMC actuators into a soft boot material for creating a control surface have been shown. In addition, the feedforward and feedback control method for mitigating the back relaxation of IPMC by controlled activation of sectored electrodes has been presented.

Overall, we hope that this chapter provides useful indications on how to start experiments with IPMC actuators. Interested readers can start the research of IPMC actuators by referring to the state-of-the-art research of IPMC, which are described more in detail in the preceding chapters.

References

- Akle BJ, Bennett MD, Leo DJ (2006) High-strain ionomeric-ionic liquid electroactive actuators. *Sens Actuators A126*:173–181
- Anton M, Aabloo A, Punning A, Kruusmaa M (2008) A mechanical model of a non-uniform ionomeric polymer metal composite actuator. *Smart Mater Struct* 17(2):25001–25004
- Asaka K, Oguro K (2009) Active microcatheter and biomedical soft devices based on IPMC actuators. In: Carpi F, Smela E (eds) *Biomedical applications of electroactive polymer actuators*. Wiley, Chichester, pp 121–136
- Asaka K, Fujiwara N, Oguro K et al (2001) State of water and ionic conductivity of solid polymer electrolyte membranes in relation to polymer actuators. *J Electroanal Chem* 505:24–32
- Brunetto P, Fortuna L, Giannone P et al (2010) Static and dynamic characterization of the temperature and humidity influence on IPMC actuators. *IEEE Trans Instr Meas* 59(4):893–908
- Fleming MJ, Kim KJ, Leang KK (2012) Mitigating IPMC back relaxation through feedforward and feedback control of patterned electrodes. *Smart Mater Struct* 21, 085002
- Hubbard JJ, Fleming M, Palmre V et al (2014) Monolithic IPMC fins for propulsion and maneuvering in bioinspired underwater robotics. *IEEE J Ocean Eng* 39(3):540–551
- Jo C, Pugal D, Oh I-K et al (2013) Recent advances in ionic polymer–metal composite actuators and their modeling and applications. *Prog Polym Sci* 38:1037–1066
- Kikuchi K, Tsuchitani S (2009) Nafion[®]-based polymer actuators with ionic liquids as solvent incorporated at room temperature. *J Appl Phys* 106, 053519
- Kim KJ, Pugal D, Leang KK (2011) A twistable ionic polymer–metal composite artificial muscle for marine applications. *Mar Technol Soc J* 45:83–98
- Kruusamäe K, Mukai K, Sugino T, Asaka K (2014) Mechanical behaviour of bending bucky-gel actuators and its representation. *Smart Mater Struct* 23(2), 025031
- Leang KK, Shan Y, Song S, Kim KJ (2012) Integrated sensing for IPMC actuators using strain gages for underwater applications. *IEEE/ASME Trans Mechatronics* 17:345–355
- Moeinkhah H, Jung J-Y, Jeon J-H et al (2013) How does clamping pressure influence actuation performance of soft ionic polymer–metal composites? *Smart Mater Struct* 22(2), 025014
- Must I, Vunder V, Kaasik F et al (2014) Ionic liquid-based actuators working in air: the effect of ambient humidity. *Sens Actuators B Chem* 202:114–122
- Nemat-Nasser S (2002) Micromechanics of actuation of ionic polymer–metal composites. *J Appl Phys* 92:2899–2915
- Onishi K, Sewa S, Asaka K et al (2001a) The effects of counter ions on characterization and performance of a solid polymer electrolyte actuator. *Electrochim Acta* 46:1233–1241

- Onishi K, Sewa S, Asaka K et al (2001b) Morphology of electrodes and bending response of the polymer electrolyte actuator. *Electrochim Acta* 46:737–743
- Palmre V, Brandell D, Maeorg U et al (2009) Nanoporous carbon-based electrodes for high strain ionomeric bending actuators. *Smart Mater Struct* 18, 095028
- Palmre V, Hubbard JJ, Fleming M et al (2013) An IPMC-enabled bio-inspired bending/twisting fin for underwater applications. *Smart Mater Struct* 22, 014003
- Punning A, Johanson U, Anton M et al (2009) A distributed model of ionomeric polymer metal composite. *J Intell Mater Syst Struct* 20(14):1711–1724
- Vunder V, Punning A, Aabloo A (2012) Mechanical interpretation of back-relaxation of ionic electroactive polymer actuators. *Smart Mater Struct* 21(11):115023
- Yamaue T, Mukai H, Asaka K, Doi M (2005) Electrostress diffusion coupling model for polyelectrolyte gels. *Macromolecules* 38:1349–1356
- Yeo RS, Yeager HL (1985) Structural and transport properties of perfluorinated ion-exchange membranes. *Modern Aspect of Electrochem* 16:437–505
- Zhu Z, Asaka K, Chang L et al (2013a) Multiphysics of ionic polymer–metal composite actuator. *J Appl Phys* 114, 084902
- Zhu Z, Asaka K, Chang L et al (2013b) Physical interpretation of deformation evolvement with water content of ionic polymer-metal composite actuator. *J Appl Phys* 114:184902

Section III
Conducting Polymers

Toribio F. Otero and José G. Martínez

Contents

1	Introduction	238
1.1	Materials	239
1.2	Actuators Based on Conducting Polymers: Operation Principle	239
2	Reactions Driving the Actuation	240
2.1	Oxidation (p-Doping) with Exchange of Anions	240
2.2	Oxidation (p-Doping) with Exchange of Cations	241
2.3	Reduction (n-Doping) with Exchange of Cations	241
3	Configurations of the Actuators	241
3.1	Bending Artificial Muscles	242
3.2	Linear Artificial Muscles	243
4	Theoretical Models	243
4.1	Mechanical and Mathematical Models	244
4.2	Electrochemical Model	245
5	Controversial Technical Aspects	246
6	Simultaneous Multifunctionality and Multi-tool Device	246
6.1	Sensing Motors	247
7	Summary	248
	References	250

T.F. Otero (✉)

Electrochemistry, Intelligent Materials and Devices, Universidad Politécnica de Cartagena, Cartagena, Spain

e-mail: toribio.fotero@upct.es

J.G. Martínez

Center for Electrochemistry and Intelligent Materials (CEMI), Universidad Politécnica de Cartagena, Cartagena, Spain

e-mail: josean.martinez@upct.es

Abstract

Films of conducting polymers (CPs) follow reversible volume variations by electrochemical oxidation/reduction in liquid electrolytes: the actuation principles are presented. Actuators, or artificial muscles, transducing those volume variations into large macroscopic movements are presented here. The same reaction gives exchange of anions, or cations, and opposed film volume variations (here described) from different families of CPs. Transduction from the small local volume changes to macroscopic movements has required different designs and structures. A good control of the movement requires a good theoretical description. Two different approaches, as mechanical-based devices or as electrochemical devices, are presented. Moreover the electrochemical reaction driving the muscles movement also senses any physical or chemical variable acting on the reaction energy. The sensing principle is presented giving dual sensing-actuators: an actuator, a mechanical sensor, a chemical sensor, a thermal sensor, and an electrical sensor work simultaneously, driven by the same reaction, in a physically uniform device. Only haptic muscles from mammals are dual actuating-sensor originating proprioception: the mammal brain is aware of position, movement rate and direction, trailed weight, muscle fatigue state, or working temperature during movements. The artificial proprioceptive equations, attained from electrochemical, mechanical, and polymeric principles, allow an easy description and control of the multi-tool device.

Keywords

Chemical creeping • Conducting polymers (CPs) • Bending artificial muscles • Creeping effects • Electrochemical model • Electrochemomechanical characterization • Exchange of cations • Reduction (n-doping) • Hysteresis • Asymmetry • Osmotic and electroosmotic effects • Irreversible parallel reactions • Linear artificial muscles • Materials • Mechanical and mathematical models • Movement • Reproducibility • Operation principle • Oxidation • Sensing motors • Faraday's laws • Mechanical creeping • Oxidation (p-doping) • Exchange of anions • van't Hoff factor

1 Introduction

At the end of the 1970s from the last century, Professors MacDiarmid, Heeger, and Shirakawa (Chiang et al. 1977; Shirakawa et al. 1977) realized that a polyacetylene film could change its electronic conductivity by over seven orders of magnitude (from insulator to 10^3 S cm^{-1}) under doping/de-doping, according with the physical terminology, or under reversible oxidation/reduction following the chemical terminology. The discovery was acknowledged with the Nobel Prize in Chemistry 2000. This was the beginning of the explosion of a new field of research, even if some of the components had been discovered years before (Letheby 1862; Dallolio et al. 1968; Breitenb and Heckner 1973; Ito et al. 1974; Messina et al. 1976). From then an exponential increase of the number of papers exists originating numerous reviews, books, and handbooks (Skotheim and Reynolds 2006; Müllen et al. 2013).

1.1 Materials

Despite the bibliographic explosion, few efforts have been done to attempt a classification of this material's forest. Up to eight different material families of conducting polymers have been proposed (Otero 1999, 2013): basic polymers, substituted, self-doped, copolymers, blends with organic macroions, hybrids with inorganic macroions, composites, and salts of the different conducting polymers. Each family is constituted by hundreds of different materials, in which only a low percentage (<10 %) have been synthesized at present.

1.2 Actuators Based on Conducting Polymers: Operation Principle

Actuation is originated by reversible volume variation of the conducting polymer film to lodge, or expel, ions and solvent driven by oxidation/reduction (doping/de-doping) reactions (Fig. 1). The driving electrochemical reactions must follow the Faraday's laws: the consumed charge (Q) determines the number of ions (n) exchanged between the CP film and the electrolyte;

$$n = Q/e \quad (1)$$

where e ($1,602 \cdot 10^{-19}$ C) is the electron charge. Thus the charge also controls the specific concentration (moles of ions per unit of polymer weight) variation of ions inside a conducting polymer film in which weight is w :

$$\Delta c = \Delta Q/wzF \quad (2)$$

With the ion crystallographic radius, the volume occupied by one mole of ions, V_a , is attained. The film volume variation required (ΔV) to lodge those ions is:

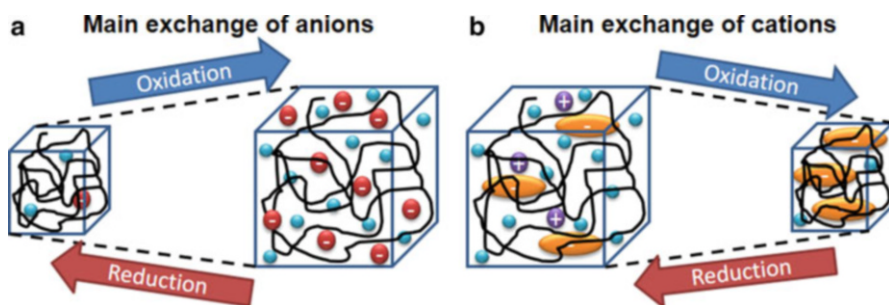


Fig. 1 Volume variations during redox reactions: (a) For conducting polymer exchanging anions: swelling during oxidation and shrinking during reduction; (b) for conducting polymer exchanging cations: shrinking during oxidation and swelling during reduction

$$\frac{\Delta V}{w} = \frac{nV_a}{w} \quad (3)$$

where w represents the mass of the neutral polymer film reacting during actuation.

The number of solvent molecules exchanged during the reaction is due to the variation of the concentration of ions inside the polymer, being quantified by the osmotic pressure (Π), which follows the van't Hoff equation:

$$\Pi = icRT \quad (4)$$

where i is the dimensionless van't Hoff factor, c is the actual concentration of counterions inside the polymer film, $R = 0.082 \text{ L atm K}^{-1} \text{ mol}^{-1}$ is the gas constant, and T is the absolute temperature. From Eq. 2 the ionic concentration in the conducting polymer film (c) is a function of the charge: the osmotic pressure and the solvent concentration must be under control of the charge. And the film volume variation during reactions is a result of the two exchanged components: ions and solvent (water):

$$\frac{\Delta V}{w} = \frac{nV_a + mV_w}{w} = \Delta c_a V_a + \Delta c_{aq} V_{aq} \quad (5)$$

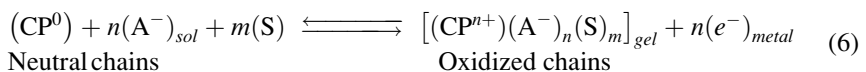
Being V_a the molar volume of the anion and V_{aq} the water molar volume, Δc_a is the ionic specific concentration variation per unit of polymer weight, and Δc_{aq} is the variation of the specific concentration of water molecules in the reacting (dense gel) film. Being Δc_a (Eq. 2) and Δc_w (from Eq. 4) a linear function of the charge consumed during the reaction-driven actuation, the film volume variation must be under linear control of the charge consumed by the film reaction. Thus the charge is expected to control both the film volume variation and the actuation magnitudes.

2 Reactions Driving the Actuation

Summarizing the previous paragraph key point for a good characterization of those actuators based on conducting polymers, or any other reaction-based actuator, is to identify the reaction, or reactions, driving the device actuation.

2.1 Oxidation (p-Doping) with Exchange of Anions

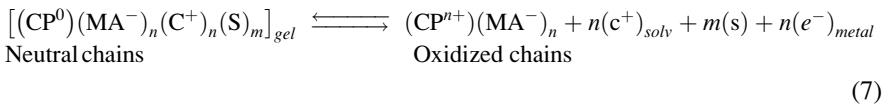
During oxidation electrons are extracted from the polymer chains generating positive charges. The reaction only occurs if, simultaneously, negative charges (anions, A^-) penetrate from the solution inside the film to keep the film charge balanced:



The presence of anions in the film forces the entrance of solvent (S) to keep the film's osmotic balance, forming a dense gel, indicated by the subindex gel. The film swells during oxidation to lodge counterions and solvent and shrinks during reduction to expel them.

2.2 Oxidation (p-Doping) with Exchange of Cations

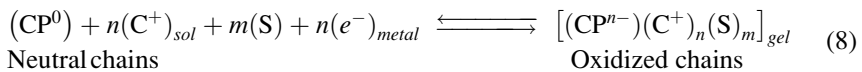
Macroanions are present in blends of conducting polymers. The macroanion remains trapped in the material during oxidation/reduction forcing the exchange of cations (C^+) for charge balance and solvent for osmotic balance. The actuation-driven reaction can be summarized as



The film shrinks during oxidation and swells during reduction.

2.3 Reduction (n-Doping) with Exchange of Cations

Some conducting polymers, as thiophene and thiophene derivatives, can be reduced from the neutral state of the chains (Arias-Pardilla et al. 2010): electrons are injected to the chains generating negative charges (n-doping) that must be compensated by entrance of cations from the solution forcing the osmotic entrance of solvent for osmotic balance. The reaction can be summarized as



The CP film expands during reduction by entrance of cations and water from the solution and shrinks during oxidation.

3 Configurations of the Actuators

A free-standing conducting polymer film or fiber is the simplest actuator (DellaSanta et al. 1997). Electrochemical reactions (6, 7, and 8) promote volume variations following equations (1, 2, 3, 4, and 5), and this can be used to build linear actuators.

Usually dimensional variations in these are very low, not useful to produce macroscopic movements.

3.1 Bending Artificial Muscles

One of the simplest ways to transduce small volume variations of the conducting polymer film during reactions (6, 7, and 8) into macroscopic movement is through bilayer or multilayer bending structures. The simplest is the bilayer structure (Fig. 2a): an active layer (conducting polymer) changing its volume during reaction and a passive layer keeping its volume constant (Pei and Inganas 1992a; Otero et al. 1992, 1994; Smela et al. 1993; Baughman 1996; Jager et al. 2000a, b; Higgins et al. 2003; Deshpande et al. 2005a, b; Alici et al. 2011) or two different active layers (asymmetric bilayers) in which the volume changes in opposite directions during the same reaction (Shakuda et al. 1993; Takashima et al. 1997, 2003; Onoda et al. 1999a, b, 2005; Okamoto et al. 2000, 2001; Nakano and Okamoto 2001; Wang et al. 2002; Okuzaki and Hattori 2003; Sansinena et al. 2003; Onoda and Tada 2004; Han and Shi 2006; Otero et al. 2014; Fuchiwaki and Otero 2014; Fuchiwaki et al. 2015). Thus, microscopic variations of the mechanical stress gradient generated across the bilayer interface by swelling/shrinking processes during reaction promote a bending macroscopic movement of the device.

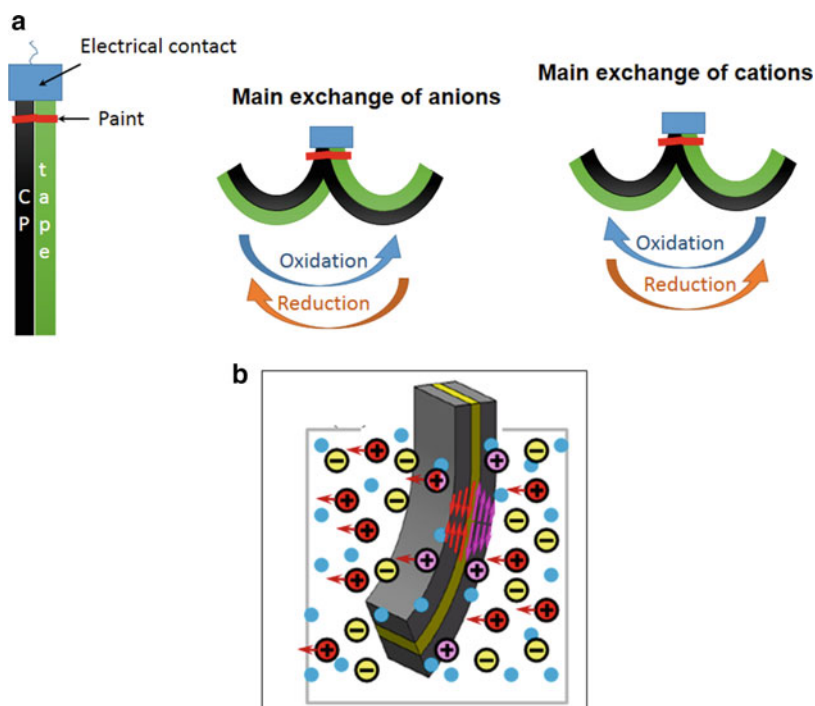


Fig. 2 (a) Bilayer device scheme in solution formed by a conducting polymer film and a nonconductive film. (b) Bending movements of a triple layer: conducting polymer/tape/conducting polymer (Reproduced from García-Córdova et al. (2011), with permission of the Royal Society of Chemistry)

The bilayer device requires a counter-electrode to allow the current flow, expending there most of the consumed electrical energy. Trilayer actuators (Fig. 2b) use two CP films, electrode and counter-electrode, with cooperative actuation due to opposed volume variations during current flow, increasing the efficiency of the actuator (Han and Shi 2004; Alici and Huynh 2006; John et al. 2008; Yao et al. 2008; Zainudeen et al. 2008; García-Córdova et al. 2011).

3.2 Linear Artificial Muscles

As mentioned above any free-standing conducting polymer films constitutes the simplest linear actuator based on conducting polymers. However, its effective movement is usually very low, not applicable to real macroscopic devices.

Moreover linear actuators constituted by any single film above mentioned, other structures provide more effective linear movements. Fibers of different materials can be coated with conducting polymers by chemical polymerization in order to get linear actuators: fibers obtained by extrusion (Mazzoldi et al. 1998), fibers obtained by electrospinning (Ismail et al. 2011) (Fig. 3a), or hollow fibers of solid polymer electrolyte (Plesse et al. 2010) getting two concentric CP films separated by the electrolytic medium, allowing its movement in air (Plesse et al. 2009; Doebbelin et al. 2010; Vidal et al. 2010). Microrods (Cho et al. 2011) and nanorods (Park et al. 2009; Vlad et al. 2012) of conducting polymers and bundles of films or fibers were investigated to produce vertical displacements of objects (Lu et al. 2002). Cylinders of conducting polymer were generated using springs and helical metallic wires (Spinks et al. 2003; Ding et al. 2003; Hara et al. 2003, 2005) or zigzag metal wires (Hara et al. 2004; Morita et al. 2010) as substrates, looking for uniform potential and current distributions inside the film and uniform linear movements. Origami structures with polypyrrole-coated paper have also been used (Okuzaki et al. 2008) (Fig. 3b) to produce linear movements.

Linear displacement can be attained also by combination of different bending structures as bilayers (Otero and Broschart 2006; Fuchiwaki et al. 2009; Naka et al. 2010) or trilayers (Otero et al. 2007) (Fig. 3c), bending in opposite directions.

4 Theoretical Models

Most of the inorganic and polymeric actuators present in current technological world are based on volume variations produced by electric fields. Engineers and physicists are familiar with those physical and mathematical models developed during the past century to describe piezoelectric, electrostrictive, ferroelectric, coulombic, or electroosmotic actuators. Some of those models have been translated to try to describe actuators based on conducting polymers, driven by charge, not by fields.

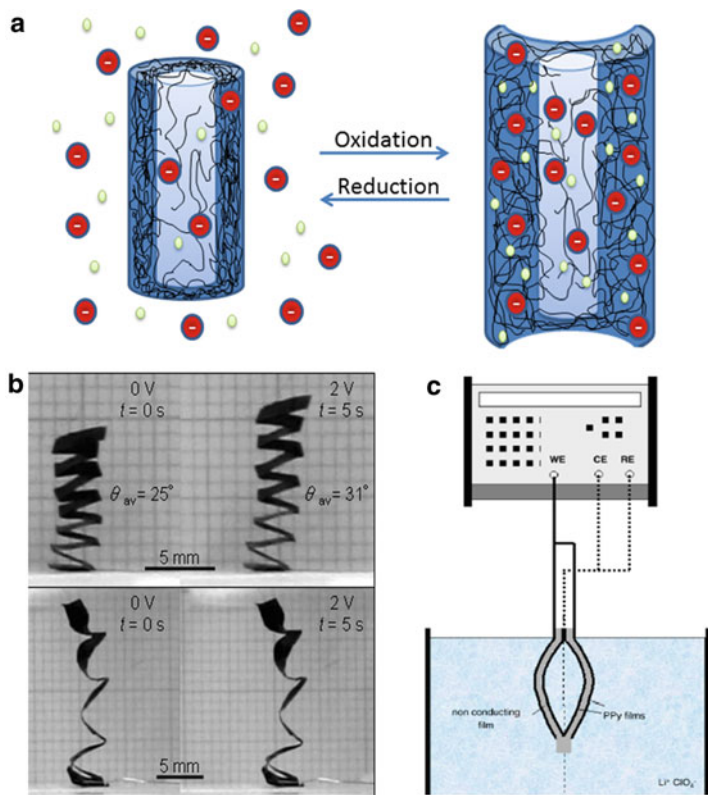


Fig. 3 (a) Linear actuation of a conducting polymer-coated fiber (Reproduced from Ismail et al. (2011), with permission from Elsevier). (b) Origami shapes with polypyrrole-coated paper (Reproduced from Okuzaki et al. (2008), with permission from the Institute of Physics). (c) Linear actuator from two bending triple layer actuator (Reproduced from Otero et al. (2007), with permission from Elsevier)

4.1 Mechanical and Mathematical Models

For bending actuators, the bending beam (Timoshenko 1925; Gere and Goodno 2012) is the most used mechanical method. It assumes that (I) the thickness of the beam is small compared with the minimum radius of curvature, which constitutes a limitation from most actuators based on CP describing very large linear amplitudes (over 180°), and (II) a linear relationship exists between the material stress and strain and (III) the Young's modulus, Y , and the actuation expansion coefficient of the conducting polymer, α , keeps constant – it does not depend on the location inside each layer. Considering such assumptions, the curvature radius (being R_∞ the radius at the equilibrium and R_0 the initial radius) is a function of h , the thickness of the conducting and nonconductive films, indicated by subscripts C and NC , respectively,

and $\alpha(t)$, the volume changes locally produced at the interfaces between both films (Pei and Ingnas 1992b, 1993a, b):

$$\frac{1}{R_\infty} - \frac{1}{R_0} = \frac{6\alpha(t)}{\frac{(Y_C h_C^2 - Y_{NC} h_{NC}^2)^2}{Y_C Y_{NC} h_C h_{NC}} + 4(h_C + h_{NC})} \quad (9)$$

This model has been improved by different authors to fit theoretical and experimental strain and modulus variations along the polymer films (Christophersen et al. 2006), actuator's position, rate, and force generated by the actuator (Alici et al. 2006; Alici and Huynh 2006) or to be used in multilayer systems (Du et al. 2010).

In order to solve the system of equations describing the different physical and chemical processes involved during actuation, well-known engineering methodologies, as the finite element method (Metz et al. 2006; Shapiro and Smela 2007; Gutta et al. 2011; Wang et al. 2014; Xiang et al. 2014) and the equivalent transmission line model (Albery and Mount 1993; Ren and Pickup 1995; Paasch 2000; Bisquert et al. 2000; Yim et al. 2007; Fang et al. 2008a, b; Shoa et al. 2010, 2011; Nguyen et al. 2014), have been used.

4.2 Electrochemical Model

Another option to describe movement rates and position is from the electrochemical nature of the film reactions (Eqs. 6, 7, and 8) driven by the film volume variation (Eqs. 1, 2, 3, 4, and 5).

Empirical results from bending bilayer or trilayer actuators corroborate that the described angle (angle) is under linear control of the charge (Q) consumed by the conducting polymer film reaction (Otero and Sansiñena 1997; Otero and Cortes 2004; Conzuelo et al. 2010; Valero et al. 2011):

$$\text{angle}(t) = \text{angle}_0 + kQ(t) \quad (10)$$

where angle_0 describes the initial position of the actuator and $\text{angle}(t)$ the position at any time t of current flow, being k the coulo-dynamic constant of every actuator system: actuator constitutive materials, solvent, and salt.

By differentiating the previous expression:

$$\omega(t) = \frac{d(\text{angle}(t))}{dt} = k \frac{dQ(t)}{dt} = kI(t) \quad (11)$$

where $\omega(t)$ is the angular rate of the bending moment (bending actuators) and I the current flowing through the actuator at any time (t). Equations 10 and 11 describe the Faradic control of the movement: the muscle position and the angular rate of its movement are linear functions of the consumed charge and the applied current, respectively.

Results from actuators based on different conducting polymers exchanging anions (Otero and Sansiñena 1997; Otero and Cortes 2004) or cations (Valero et al. 2011) and moving in different electrolytes (Otero and Martínez 2012; Otero et al. 2013; Valero et al. 2014) have corroborated the Faradic nature (Eqs. 10 and 11).

5 Controversial Technical Aspects

Reproducibility of the movement: Engineers and physicists consider that any mechanical actuator is subjected to great dispersions on consecutive movements. Electrochemists, supported by Eqs. 5 and 10 and experimental results, advocate the almost total reproducibility of the movement consuming a constant charge.

Irreversible parallel reactions: The use of back metals (sputtered, spring, or helical wires) can promote some water electrolysis during actuation (Otero et al. 2014): the reproducibility of the actuating charge decreases, and the progressive degradation originates rising actuating potentials on consecutive cycles. But still the same charge gives the same angular displacement.

Creeping effects: Chemical creeping – when the CP layer is a polymeric blend with organic macroions, the same charge produces the same bending angle, but the initial angle is not recovered originating a creeping effect (Valero et al. 2015). By deep oxidation of the CP, the creeping displacement is almost fully recovered.

Mechanical creeping: Under mechanical stress the CP film experiences a viscoelastic irreversible deformation on each cycle. How to recover this deformation is a pending point.

Electrochemomechanical characterization: By simultaneous recording of electrochemical responses and displacements (video recording), a good characterization of the actuators is attained: voltammetric (i - e), chronoamperometric (i - t), or chronopotentiometric (E - t) responses when the actuator is submitted to potential sweeps, constant potentials, or constant currents, respectively, and dynamopotentiometric (α - E), dynamo-coulometric (α - Q), or dynamo-amperometric (α - i) responses in order to prove Eqs. 5, 10, and 11.

Hysteresis, asymmetry, and osmotic and electroosmotic effects: The entrance of solvent is a physical (osmotic) effect following the electrochemical (Sect. 2) entrance of ions. The solvent is expelled by electroosmosis when the shrinking film approaches to the closing potential (Fuchiwaki et al. 2015). Those two physical effects induce some hysteresis and loop shapes of the coulodynamic responses, generating some minor problems for the control of the actuator movement.

6 Simultaneous Multifunctionality and Multi-tool Device

One reaction (6, 7, or 8) changes, simultaneously, the value of several properties (multifunctionality) of the material (composition-dependent properties), each of them mimicking a biological function. Engineers and robot designers are dreaming with haptic motors, motors sensing by themselves any working variable. Those

reactions change simultaneously the film volume (actuator) and the film potential (sensor) envisaging the development of sensing-actuators where both, the actuator and the sensor, are driven, simultaneously, by the same reaction (6, 7, or 8): two tools working simultaneously in one device.

Nowadays technologies do not offer any parallel multi-tool device; only haptic muscles originating proprioception, awareness, and consciousness can inspire such simultaneous multifunctionality.

6.1 Sensing Motors

Sensing principle for reacting systems (reacting materials or reaction-driven devices) when subjected to energetic perturbations (thermal, chemical, mechanical, or electrical here) responds by adapting the reaction energy to the new energetic conditions (Otero and Martinez 2015).

For any actuator based on electrochemical reactions, the electrical energy (U) consumed by the driving reaction is

$$U = I(A)E(V) = \frac{Q(C)}{t(s)}E(V) \quad (12)$$

where (I) represents the current flowing through the actuator, $Q(C)$ is the consumed charge, and $E(V)$ is the material potential at any time $t(s)$.

Thus,

1. For electrochemical actuators driven by flow of a constant current (I), any change of the working energetic (U) conditions (mechanical, thermal, chemical, electrical) will be sensed by the instantaneous adaptation of the device potential (E) evolution, during actuation, to the new working energetic conditions: potentiometric sensors.
2. For electrochemical devices driven by a potential step (working under constant potential), any energetic (U) perturbation (mechanical, thermal, chemical, electrical) will be detected by the instantaneous adaptation of the current (I) flowing through the device to the new working energetic conditions: galvanometric sensors.

The quantitative expression for the different sensors comes from the adaptation of the Butler-Volmer basic equation of any electrochemical reaction (Otero et al. 2012; Martinez and Otero 2012, 2014):

$$i_a = FV k_{a0} [A^-]^d [POI^*]^e \exp\left(\frac{(1-\alpha)nF(E-E_0)}{RT}\right) \exp\left(\frac{\Delta(PV)}{RT}\right) \quad (13)$$

This equation links actuating and sensing magnitudes: the current flowing through the actuator (i_a), the actuator potential (E), the working temperature (T), the working

chemical conditions $[A^-]$ (electrolyte concentration here), and the working mechanical conditions, $\Delta(PV)$. When the actuator is driven by flow of a constant current, the potential (E) evolution from this equation is a function of (senses) the chemical, thermal, or mechanical working conditions.

Experimental results from different conducting polymers in different electrolytes corroborate the theoretical description. Figure 4a presents empirical (full lines) and theoretical (dashed lines) evolutions of the muscle potential during the same angular displacement every time (same initial and final position) driven by a constant current in a different concentration of electrolyte every time: the muscle responds to rising concentrations (rising chemical potential or rising ambient chemical energy) by consuming lower electrical energy (the actuator potential evolves at lower values during current flow). Working in higher thermal (at higher temperatures) or in higher chemical (electrolyte concentration) energetic ambient requires the consumption of lower electrical energy during actuation and the potential evolves at lower values during actuation. Trailing rising masses or meeting and obstacle requires the production of rising amounts of energy by the actuators and the concomitant shift (Eq. 13) to higher muscle potentials during actuation.

Figure 4b, b' show the calibration lines (muscle potential and consumed energy, respectively) for muscles sensing the working electrolyte concentration after three different times of current flow. Figure 4c, c' show the calibration lines for the muscle thermal sensor and Fig. 4d, d' for the muscle current sensor from similar results to those shown by Fig. 4a attained now at different temperatures or under flow of different constant currents. Theoretical and experimental results as thermal, mechanical, chemical and electrical sensors for different conducting polymers and electrolytes have been reviewed recently (Otero and Martínez 2015).

As conclusion actuators based on conducting polymers are electrical polymeric motors sensing by themselves the working conditions. One actuator, a mechanical sensor, a thermal sensor, a chemical sensor and an electrical sensor work simultaneously driven by the same electrochemical reaction in a physically uniform device. Actuating (current and charge) and sensing (potential) signals are present, simultaneously and at any working time, in the two connecting wires. This ensemble mimics haptic muscles allowing the construction of the concomitant artificial proprioceptive devices and tools.

7 Summary

Getting improved actuators based on electroactive conducting polymers requires a good knowledge and control of both, the conducting polymer synthesis mechanism and the reactions driving its volume variation during the device actuation.

During actuation identifying the driving reaction is a key point to determine the exchanged ion and the amount of exchanged solvent per ion. Bilayer actuators are some of the best tools to identify the ionic exchanges during the driving reaction. Counterions and solvent must be managed in order to get the highest volume variation per unit of polymer weight and per unit of consumed charge. Working with dry actuators by using dry electrolyte films (following the pressure of nowadays

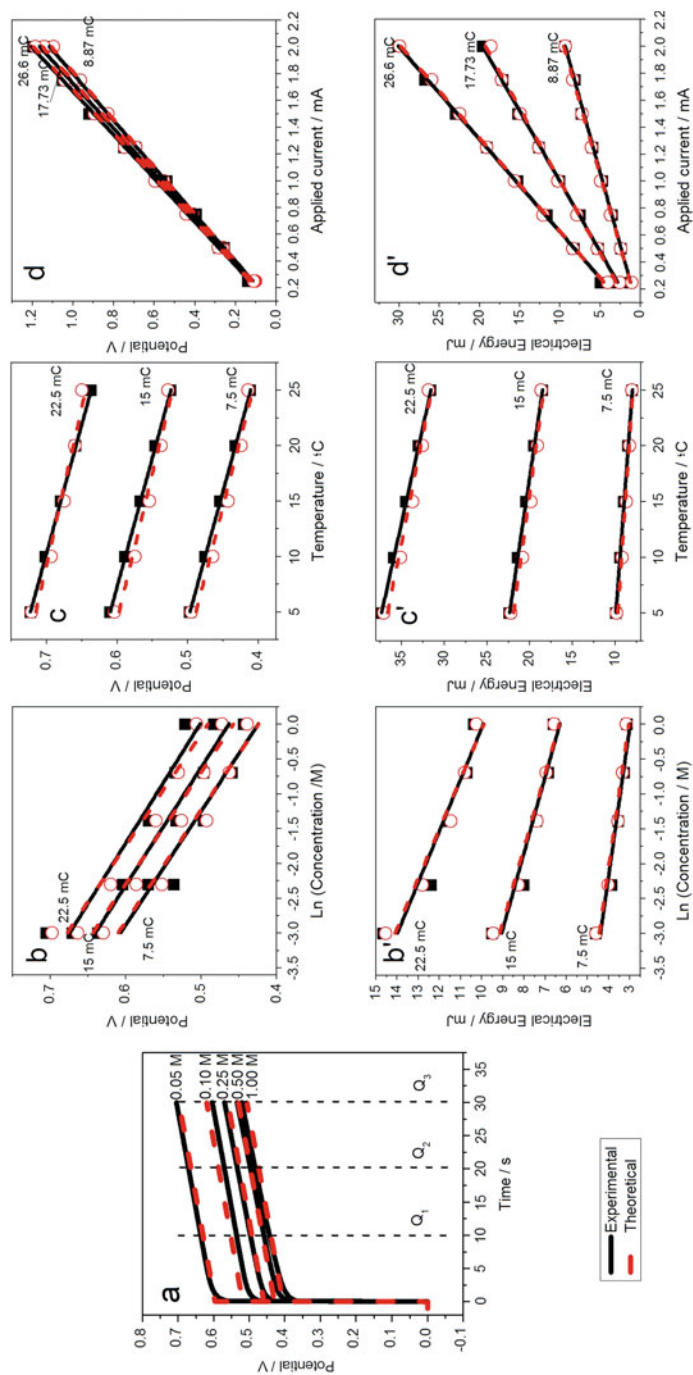


Fig. 4 Anodic experimental (*full lines*) and theoretical (*dotted lines*) chronopotentiograms (evolution of the muscle potential) obtained by flow of ± 0.75 mA through a polypyrrole/tape bilayer muscles including 1.6 mg of active pPy describing every time a movement of $\pi/2$ radians in a different concentration of LiClO_4 aqueous solution. **(b)** Experimental and theoretical (Eqs. 8 and 9) muscle potentials after flow of three (always the same) intermediate charges when the muscles go through the same intermediate angles, in different electrolyte concentrations, **(c)** at different temperatures, and **(d)** under different driving currents; **(b')** evolution of the experimental and theoretical consumed electrical energies after the same times of current flow as a function of the electrolyte concentration **(c')** at different temperatures and **(d')** under different applied currents (Reproduced from Otero et al. (2012), Martínez and Otero (2012) with permission of the ACS)

technologies) the actuation is unpaired by two reasons: first the extra volume variation due to the solvent exchange and second the plasticizer nature of the solvent is lost increasing the resistance during the movement. Two different theoretical models are being developed: based on mechanical principles and adding the Faradic exchange of ions as one of the involved equations or based on electrochemical principles. Those models have different approaches to those controversial technical aspects presented in Sect. 5.

The electrochemical model allows, through the basic equation of the electrochemical kinetics (Eq. 13), the construction and quantitative description of one actuator and several sensors working simultaneously in a physically uniform device. Such sensing polymeric motors do not exist in current human technologies; only haptic muscles provide some parallel dual system. Human proprioception is based on haptic muscles, and artificial proprioceptive equations were attained from Eq. 13 (Otero and Martínez 2015).

Acknowledgments Authors acknowledge the financial support from Spanish Government (MCI) Projects MAT2008-06702 and ESNAM, the European Scientific Network for Artificial Muscles. J. G. Martínez acknowledges Spanish Education Ministry for the FPU grant (AP2010-3460).

References

- Albery W, Mount A (1993) Application of a transmission-line model to impedance studies on a poly(vinylferrocene)-modified electrode. *J Chem Soc Faraday Trans* 89:327–331. doi:10.1039/ft9938900327
- Alici G, Huynh NN (2006) Predicting force output of trilayer polymer actuators. *Sensors Actuators Phys* 132:616–625. doi:10.1016/j.sna.2006.02.046
- Alici G, Mui B, Cook C (2006) Bending modeling and its experimental verification for conducting polymer actuators dedicated to manipulation applications. *Sensors Actuators Phys* 126:396–404. doi:10.1016/j.sna.2005.10.020
- Alici G, Punning A, Shea HR (2011) Enhancement of actuation ability of ionic-type conducting polymer actuators using metal ion implantation. *Sensors Actuators B Chem* 157:72–84. doi:10.1016/j.snb.2011.03.028
- Arias-Pardilla J, Walker W, Wudl F, Otero TF (2010) Reduction and oxidation doping kinetics of an electropolymerized donor–acceptor low-bandgap conjugated copolymer. *J Phys Chem B* 114(40):12777–12784
- Baughman RH (1996) Conducting polymer artificial muscles. *Synth Met* 78:339–353. doi:10.1016/0379-6779(96)80158-5
- Bisquert J, Belmonte GG, Santiago FF et al (2000) Application of a distributed impedance model in the analysis of conducting polymer films. *Electrochem Commun* 2:601–605. doi:10.1016/S1388-2481(00)00089-8
- Breitenb M, Heckner K (1973) Electrochemical studies on formation and properties of polyaniline films. *J Electroanal Chem* 43:267–286. doi:10.1016/S0022-0728(73)80497-8
- Chiang C, Fincher C, Park Y et al (1977) Electrical-conductivity in doped polyacetylene. *Phys Rev Lett* 39:1098–1101. doi:10.1103/PhysRevLett.39.1098
- Cho MS, Choi JJ, Kim TS, Lee Y (2011) In situ three-dimensional analysis of the linear actuation of polypyrrole micro-rod actuators using optical microscopy. *Sensors Actuators B Chem* 156:218–221. doi:10.1016/j.snb.2011.04.021

- Christophersen M, Shapiro B, Smela E (2006) Characterization and modeling of PPy bilayer microactuators – part I. Curvature. *Sensors Actuators B Chem* 115:596–609. doi:10.1016/j.snb.2005.10.023
- Conzuelo LV, Arias-Pardilla J, Cauch-Rodríguez JV et al (2010) Sensing and tactile artificial muscles from reactive materials. *Sensors* 10:2638–2674. doi:10.3390/s100402638
- Dallolio A, Dascola G, Varacca V, Bocchi V (1968) Electronic paramagnetic resonance and conductivity of a black electrolytic oxypyrrrole. *C R Seances Acad Sci Ser C* 267:433–435
- DellaSanta A, DeRossi D, Mazzoldi A (1997) Performance and work capacity of a polypyrrole conducting polymer linear actuator. *Synth Met* 90:93–100
- Deshpande SD, Kim J, Yun SR (2005a) New electro-active paper actuator using conducting polypyrrole: actuation behaviour in LiClO₄ acetonitrile solution. *Synth Met* 149:53–58. doi:10.1016/j.synthmet.2004.11.001
- Deshpande SD, Kim J, Yun SR (2005b) Studies on conducting polymer electroactive paper actuators: effect of humidity and electrode thickness. *Smart Mater Struct* 14:876–880. doi:10.1088/0964-1726/14/4/048
- Ding J, Liu L, Spinks GM et al (2003) High performance conducting polymer actuators utilising a tubular geometry and helical wire interconnects. *Synth Met* 138:391–398. doi:10.1016/S0379-6779(02)00453-8
- Doebbelin M, Marcilla R, Pozo-Gonzalo C, Mecerreyes D (2010) Innovative materials and applications based on poly(3,4-ethylenedioxythiophene) and ionic liquids. *J Mater Chem* 20:7613–7622. doi:10.1039/c0jm00114g
- Du P, Lin X, Zhang X (2010) A multilayer bending model for conducting polymer actuators. *Sensors Actuators Phys* 163:240–246. doi:10.1016/j.sna.2010.06.002
- Fang Y, Tan X, Alici G (2008a) Robust adaptive control of conjugated polymer actuators. *IEEE Trans Control Syst Technol* 16:600–612. doi:10.1109/TCST.2007.912112
- Fang Y, Tan X, Shen Y et al (2008b) A scalable model for trilayer conjugated polymer actuators and its experimental validation. *Mater Sci Eng C Biomim Supramol Syst* 28:421–428. doi:10.1016/j.msec.2007.04.024
- Fuchiwaki M, Otero TF (2014) Polypyrrole–para-phenolsulfonic acid/tape artificial muscle as a tool to clarify biomimetic driven reactions and ionic exchanges. *J Mater Chem B* 2:1954–1965. doi:10.1039/C3TB21653E
- Fuchiwaki M, Tanaka K, Kaneto K (2009) Planate conducting polymer actuator based on polypyrrole and its application. *Sensors Actuators Phys* 150:272–276. doi:10.1016/j.sna.2009.01.011
- Fuchiwaki M, Martinez JG, Otero TF (2015) Polypyrrole asymmetric bilayer artificial muscle: driven reactions, cooperative actuation, and osmotic effects. *Adv Funct Mater* 25:1535–1541. doi:10.1002/adfm.201404061
- García-Córdova F, Valero L, Ismail YA, Otero TF (2011) Biomimetic polypyrrole based all three-in-one triple layer sensing actuators exchanging cations. *J Mater Chem* 21:17265–17272. doi:10.1039/C1JM13374H
- Gere JM, Goodno BJ (2012) *Mechanics of materials*, Edición: revised. Cengage Learning, Stamford
- Gutta S, Realmuto J, Yim W, Kim KJ (2011) Dynamic model of a cylindrical ionic polymer-metal composite actuator. In: 2011 8th international conference on ubiquitous robots and ambient intelligence (URAI). Songdo Conventia, Incheon, pp 326–330
- Han GY, Shi GQ (2004) High-response tri-layer electrochemical actuators based on conducting polymer films. *J Electroanal Chem* 569:169–174. doi:10.1016/j.jelechem.2004.02.025
- Han GY, Shi GQ (2006) Electrochemical actuator based on single-layer polypyrrole film. *Sensors Actuators B Chem* 113:259–264. doi:10.1016/j.snb.2005.02.055
- Hara S, Zama T, Sewa S et al (2003) Polypyrrole-metal coil composites as fibrous artificial muscles. *Chem Lett* 32:800–801
- Hara S, Zama T, Ametani A et al (2004) Enhancement in electrochemical strain of a polypyrrole-metal composite film actuator. *J Mater Chem* 14:2724–2725. doi:10.1039/b409169h

- Hara S, Zama T, Tanaka N et al (2005) Artificial fibular muscles with 20% strain based on polypyrrole-metal coil composites. *Chem Lett* 34:784–785. doi:10.1246/cl.2005.784
- Higgins SJ, Lovell KV, Rajapakse RMG, Walsby NM (2003) Grafting and electrochemical characterisation of poly-(3,4-ethylenedioxythiophene) films, on Nafion and on radiation-grafted polystyrenesulfonate-polyvinylidene fluoride composite surfaces. *J Mater Chem* 13:2485–2489. doi:10.1039/b303424k
- Ismail YA, Martínez JG, Al Harrasi AS et al (2011) Sensing characteristics of a conducting polymer/hydrogel hybrid microfiber artificial muscle. *Sensors Actuators B Chem* 160:1180–1190. doi:10.1016/j.snb.2011.09.044
- Ito T, Shirakawa H, Ikeda S (1974) Simultaneous polymerization and formation of polyacetylene film on surface of concentrated soluble Ziegler-type catalyst solution. *J Polym Sci Part Polym Chem* 12:11–20. doi:10.1002/pol.1974.170120102
- Jager EWH, Inganas O, Lundström I (2000a) Microrobots for micrometer-size objects in aqueous media: potential tools for single-cell manipulation. *Science* 288:2335–2338. doi:10.1126/science.288.5475.2335
- Jager EWH, Smela E, Inganas O (2000b) Microfabricating conjugated polymer actuators. *Science* 290:1540–1545. doi:10.1126/science.290.5496.1540
- John S, Alici G, Cook C (2008) Frequency response of polypyrrole trilayer actuator displacement. In: Bar-Cohen Y (ed) *Electroactive polymer actuators and devices (EAPAD)*. Spie-Int Soc Optical Engineering, Bellingham
- Letheby H (1862) XXIX. On the production of a blue substance by the electrolysis of sulphate of aniline. *J Chem Soc* 15:161–163. doi:10.1039/JS8621500161
- Lu W, Fadeev A, Qi B et al (2002) Use of ionic liquids for pi-conjugated polymer electrochemical devices. *Science* 297:983–987. doi:10.1126/science.1072651
- Martínez JG, Otero TF (2012) Biomimetic dual sensing-actuators: theoretical description. Sensing electrolyte concentration and driving current. *J Phys Chem B* 116:9223–9230. doi:10.1021/jp302931k
- Martínez JG, Otero TF (2014) Mechanical awareness from sensing artificial muscles: experiments and modeling. *Sensors Actuators B Chem* 195:365–372. doi:10.1016/j.snb.2013.12.099
- Mazzoldi A, Degl'Innocenti C, Michelucci M, De Rossi D (1998) Actuating properties of polyaniline fibers under electrochemical stimulation. *Mater Sci Eng C Biomim Mater Sens Syst* 6:65–72. doi:10.1016/S0928-4931(98)00036-8
- Messina R, Sarazin C, Yu L, Buvet R (1976) Semi-conducting polymer membranes with redox exchange properties – polyaniline and polypyrrole. *J Chim Phys Phys Chim Biol* 73:919–921
- Metz P, Alici G, SpinkS GM (2006) A finite element model for bending behaviour of conducting polymer electromechanical actuators. *Sensors Actuators Phys* 130:1–11. doi:10.1016/j.sna.2005.12.010
- Morita T, Chida Y, Hoshino D et al (2010) Fabrication and characterization of a polypyrrole soft actuator having corrugated structures. *Mol Cryst Liq Cryst* 519:121–127. doi:10.1080/15421401003609681
- Müllen K, Reynolds JR, Masuda T (eds) (2013) *Conjugated polymers: a practical guide to synthesis*. Royal Society of Chemistry, Cambridge
- Naka Y, Fuchiwaki M, Tanaka K (2010) A micropump driven by a polypyrrole-based conducting polymer soft actuator. *Polym Int* 59:352–356. doi:10.1002/pi.2762
- Nakano T, Okamoto Y (2001) Synthetic helical polymers: conformation and function. *Chem Rev* 101:4013–4038. doi:10.1021/cr0000978
- Nguyen CH, Alici G, Wallace G (2014) An advanced mathematical model and its experimental verification for trilayer conjugated polymer actuators. *IEEE Asme Trans Mechatron* 19:1279–1288. doi:10.1109/TMECH.2013.2280012
- Okamoto T, Tada K, Onoda M (2000) Bending machine using anisotropic polypyrrole films. *Jpn J Appl Phys Part 1* 39:2854–2858. doi:10.1143/JJAP.39.2854

- Okamoto T, Kato Y, Tada K, Onoda M (2001) Actuator based on doping/undoping-induced volume change in anisotropic polypyrrole film. *Thin Solid Films* 393:383–387. doi:10.1016/S0040-6090(01)01124-5
- Okuzaki H, Hattori T (2003) Electrically induced anisotropic contraction of polypyrrole films. *Synth Met* 135:45–46. doi:10.1016/S0379-6779(02)00653-7
- Okuzaki H, Saito T, Suzuki H et al (2008) A biomorphic origami actuator fabricated by folding a conducting paper. *J Phys Conf Ser* 127:012001. doi:10.1088/1742-6596/127/1/012001
- Onoda M, Tada K (2004) Anisotropic bending machine using conducting polypyrrole. *IEICE Trans Electron* E87C:128–135
- Onoda M, Okamoto T, Tada K, Nakayama H (1999a) Polypyrrole films with anisotropy for artificial muscles and examination of bending behavior. *Jpn J Appl Phys Part 2* 38:L1070–L1072. doi:10.1143/JJAP.38.L1070
- Onoda M, Tada K, Nakayama H (1999b) Polypyrrole films with anisotropy. *Synth Met* 102:1321–1322. doi:10.1016/S0379-6779(98)01031-5
- Onoda M, Shonaka H, Tada K (2005) A self-organized bending-beam electrochemical actuator. *Curr Appl Phys* 5:194–201. doi:10.1016/j.cap.2004.06.013
- Otero TF (1999) Conducting polymers, electrochemistry, and biomimicking processes. In: White RE, Bockris JO, Conway BE (eds) *Modern aspects of electrochemistry*. Springer US, New York, pp 307–434
- Otero TF (2013) Biomimetic conducting polymers: synthesis, materials, properties, functions, and devices. *Polym Rev* 53:311–351. doi:10.1080/15583724.2013.805772
- Otero TF, Rodríguez J, Santamaría C Músculos artificiales formados por multicapas: polímeros conductores-polímeros no conductores. 11
- Otero TF, Broschart M (2006) Polypyrrole artificial muscles: a new rhombic element. Construction and electrochemomechanical characterization. *J Appl Electrochem* 36:205–214. doi:10.1007/s10800-005-9048-0
- Otero TF, Cortes MT (2004) Artificial muscle: movement and position control. *Chem Commun* 284–285. doi:10.1039/b313132g
- Otero TF, Martínez JG (2012) Artificial muscles: A tool to quantify exchanged solvent during biomimetic reactions. *Chem Mater* 24:4093–4099. doi:10.1021/cm302847r
- Otero TF, Martínez JG (2015) Physical and chemical awareness from sensing polymeric artificial muscles. Experiments and modeling. *Prog Polym Sci* 44:62–78. doi:10.1016/j.progpolymsci.2014.09.002
- Otero TF, Sansiñena JM (1997) Bilayer dimensions and movement in artificial muscles. *Bioelectrochem Bioenerg* 42:117–122. doi:10.1016/S0302-4598(96)05112-4
- Otero TF, Angulo E, Rodríguez J, Santamaría C (1992) Electrochemomechanical properties from a bilayer: polypyrrole/non-conducting and flexible material – artificial muscle. *J Electroanal Chem* 341:369–375. doi:10.1016/0022-0728(92)80495-P
- Otero TF, Angulo E, Rodríguez F, Santamaría C (1994) Dispositivos laminares que emplean polímeros conductores capaces de provocar movimientos mecánicos
- Otero T, Cortes M, Arenas G (2007) Linear movements from two bending triple-layers. *Electrochim Acta* 53:1252–1258. doi:10.1016/j.electacta.2007.01.081
- Otero TF, Sanchez JJ, Martínez JG (2012) Biomimetic dual sensing-actuators based on conducting polymers. Galvanostatic theoretical model for actuators sensing temperature. *J Phys Chem B* 116:5279–5290. doi:10.1021/jp300290s
- Otero TF, Martínez JG, Zaifoglu B (2013) Using reactive artificial muscles to determine water exchange during reactions. *Smart Mater Struct* 22:104019. doi:10.1088/0964-1726/22/10/104019
- Otero TF, Martínez JG, Fuchiwaki M, Valero L (2014) Structural electrochemistry from freestanding polypyrrole films: full hydrogen inhibition from aqueous solutions. *Adv Funct Mater* 24:1265–1274. doi:10.1002/adfm.201302469
- Paasch G (2000) The transmission line equivalent circuit model in solid-state electrochemistry. *Electrochem Commun* 2:371–375. doi:10.1016/S1388-2481(00)00040-0

- Park SJ, Cho MS, Nam JD et al (2009) The linear stretching actuation behavior of polypyrrole nanorod in AAO template. *Sensors Actuators B Chem* 135:592–596. doi:10.1016/j.snb.2008.09.040
- Pei Q, Ingnas O (1992a) Conjugated polymers and the bending cantilever method – electrical muscles and smart devices. *Adv Mater* 4:277–278. doi:10.1002/adma.19920040406
- Pei Q, Ingnas O (1992b) Electrochemical applications of the bending beam method 1. Mass-transport and volume changes in polypyrrole during redox. *J Phys Chem* 96:10507–10514. doi:10.1021/j100204a071
- Pei Q, Ingnas O (1993a) Electrochemical applications of the bending beam method, a novel way to study ion-transport in electroactive polymers. *Solid State Ion* 60:161–166. doi:10.1016/0167-2738(93)90291-A
- Pei Q, Ingnas O (1993b) Electrochemical applications of the bending beam method 2. Electroshrinking and slow relaxation in polypyrrole. *J Phys Chem* 97:6034–6041. doi:10.1021/j100124a041
- Plesse C, Vidal F, Teyssie D, Chevrot C (2009) Conducting IPN fibers: a new design for linear actuation in open air. In: Vincenzini P, BarCohen Y, Carpi F (eds) *Artificial muscle actuators using electroactive polymers*. Trans Tech Publications Ltd, Stafa-Zurich, pp 53–58
- Plesse C, Vidal F, Teyssie D, Chevrot C (2010) Conducting polymer artificial muscle fibres: toward an open air linear actuation. *Chem Commun* 46:2910–2912. doi:10.1039/c001289k
- Ren X, Pickup P (1995) Impedance measurements of ionic-conductivity as a probe of structure in electrochemically deposited polypyrrole films. *J Electroanal Chem* 396:359–364. doi:10.1016/0022-0728(95)04064-U
- Sansinena JM, Gao JB, Wang HL (2003) High-performance, monolithic polyaniline electrochemical actuators. *Adv Funct Mater* 13:703–709. doi:10.1002/adfm.200304347
- Shakuda S, Morita S, Kawai T, Yoshino K (1993) Dynamic characteristics of bimorph with conducting polymer gel. *Jpn J Appl Phys Part 1* 32:5143–5146. doi:10.1143/JJAP.32.5143
- Shapiro B, Smela E (2007) Bending actuators with maximum curvature and force and zero interfacial stress. *J Intell Mater Syst Struct* 18:181–186. doi:10.1177/1045389X06063801
- Shirakawa H, Louis E, Macdiarmid A et al (1977) Synthesis of electrically conducting organic polymers – halogen derivatives of polyacetylene, (CH)_x. *J Chem Soc Chem Commun* 578–580. doi:10.1039/c39770000578
- Shoa T, Madden JDW, Munce NR, Yang V (2010) Analytical modeling of a conducting polymer-driven catheter. *Polym Int* 59:343–351. doi:10.1002/pi.2783
- Shoa T, Yoo DS, Walus K, Madden JDW (2011) A dynamic electromechanical model for electrochemically driven conducting polymer actuators. *IEEE/ASME Trans Mechatron* 16:42–49. doi:10.1109/TMECH.2010.2090166
- Skotheim TA, Reynolds J (eds) (2006) *Handbook of conducting polymers*, 3rd edn. CRC Press, New York
- Smela E, Ingnas O, Pei Q, Lundstrom I (1993) Electrochemical muscles – micromachining fingers and corkscrews. *Adv Mater* 5:630–632. doi:10.1002/adma.19930050905
- Spinks GM, Zhou DZ, Liu L, Wallace GG (2003) The amounts per cycle of polypyrrole electro-mechanical actuators. *Smart Mater Struct* 12:468–472. doi:10.1088/0964-1726/12/3/318
- Takashima W, Uesugi T, Fukui M et al (1997) Mechanochemical effect of polyaniline film. *Synth Met* 85:1395–1396. doi:10.1016/S0379-6779(97)80289-5
- Takashima W, Pandey SS, Kaneto K (2003) Bi-ionic actuator by polypyrrole films. *Synth Met* 135:61–62. doi:10.1016/S0379-6779(02)00680-X
- Timoshenko S (1925) Analysis of bi-metal thermostats. *J Opt Soc Am Rev Sci Instrum* 11:233–255. doi:10.1364/JOSA.11.000233
- Valero L, Arias-Pardilla J, Cauch-Rodríguez J et al (2011) Characterization of the movement of polypyrrole–dodecylbenzenesulfonate–perchlorate/tape artificial muscles. Faradaic control of reactive artificial molecular motors and muscles. *Electrochim Acta* 56:3721–3726. doi:10.1016/j.electacta.2010.11.058

- Valero L, Otero TF, Martínez JG (2014) Exchanged cations and water during reactions in polypyrrole macroions from artificial muscles. *ChemPhysChem* 15:293–301. doi:10.1002/cphc.201300878
- Valero L, Martínez JG, Otero TF (2015) Creeping and structural effects in Faradaic artificial muscles. *J Solid St Electrochem* 19:2683–2689. doi:10.1007/s10008-015-2775-1
- Vidal F, Plesse C, Aubert P-H et al (2010) Poly(3,4-ethylenedioxythiophene)-containing semi-interpenetrating polymer networks: a versatile concept for the design of optical or mechanical electroactive devices. *Polym Int* 59:313–320. doi:10.1002/pi.2772
- Vlad A, Dutu CA, Jedrasik P et al (2012) Vertical single nanowire devices based on conducting polymers. *Nanotechnology* 23:025302. doi:10.1088/0957-4484/23/2/025302
- Wang HL, Gao JB, Sansinena JM, McCarthy P (2002) Fabrication and characterization of polyaniline monolithic actuators based on a novel configuration: integrally skinned asymmetric membrane. *Chem Mater* 14:2546–2552. doi:10.1021/cm010933+
- Wang X, Alici G, Tan X (2014) Modeling and inverse feedforward control for conducting polymer actuators with hysteresis. *Smart Mater Struct* 23:025015. doi:10.1088/0964-1726/23/2/025015
- Xiang X, Alici G, Mutlu R, Li W (2014) How the type of input function affects the dynamic response of conducting polymer actuators. *Smart Mater Struct* 23:105008. doi:10.1088/0964-1726/23/10/105008
- Yao Q, Alici G, Spinks GA (2008) Feedback control of tri-layer polymer actuators to improve their positioning ability and speed of response. *Sensors Actuators Phys* 144:176–184. doi:10.1016/j.sna.2008.01.005
- Yim W, Lee J, Kim KJ (2007) An artificial muscle actuator for biomimetic underwater propulsors. *Bioinspir Biomim* 2:S31. doi:10.1088/1748-3182/2/2/S04
- Zainudeen UL, Careem MA, Skaarup S (2008) PEDOT and PPy conducting polymer bilayer and trilayer actuators. *Sensors Actuators B Chem* 134:467–470. doi:10.1016/j.snb.2008.05.027

Gursel Alici, Rahim Mutlu, Daniel Melling, Edwin W. H. Jager, and Keiichi Kaneto

Contents

1	Introduction	258
2	EAPs as Actuators	259
2.1	Device Examples Based on Bilayer Configuration	262
2.2	Devices Based on a Tri-layer Configuration	268
3	EAPs as Sensors	275
4	Device Configurations Based on PEDOT/PSS	281
5	Critical Research Issues and Outlook	283
	References	286

Abstract

This chapter focuses on device configurations based on conjugated polymer transducers. After the actuation and sensing configurations in the literature are presented, some successful device configurations are reviewed, and a detailed account of their operation principles is described. The chapter is concluded with

G. Alici (✉) • R. Mutlu

School of Mechanical, Materials, and Mechatronic Engineering, ARC Centre of Excellence for Electromaterials Science, University of Wollongong, Wollongong, NSW, Australia
e-mail: gursel@uow.edu.au; rmutlu@uow.edu.au

D. Melling

Institute for Medical Science and Technology, University of Dundee, Dundee, UK
e-mail: d.melling@dundee.ac.uk

E.W.H. Jager

Department of Physics, Chemistry and Biology (IFM), Linköping University, Linköping, Sweden
Biosensors and Bioelectronics, Linköping University, Linköping, Sweden
e-mail: edwin.jager@liu.se

K. Kaneto

Kyushu Institute of Technology, Eamex Co. Ltd, Chuoku, Fukuoka, Japan
e-mail: Kaneto@life.kyutech.ac.jp

critical research issues. With reference to the significant progress made in the field of EAP transducers in the last two decades, there is an increasing need to change our approach to the establishment of new device configurations, novel device concepts, and cutting-edge applications. To this aim, we should start from the performance specifications and end up with the material synthesis conditions and properties which will meet the performance specifications (top-to-down approach). The question should be “what electroactive material or materials can be used for a specific purpose or application,” rather than looking for an application or a device concept suitable to the unique properties of the EAPs and transducers already made of these materials. The field is mature enough to undertake this paradigm change.

Keywords

4D printing • Active flexure • Actuators • Bilayer configuration • Freestanding polymer • Linear stroke polymer • Polypyrrole (PPy)–metal coil composite • Tri-layer configuration • Bending principle • Deflecting/bending tubes • Dimethyl sulfoxide (DMSO) • EAP transducers • Actuators (*see* actuators) • As sensors • Electrodeposition • Freestanding polymer actuator • Ionic liquid/polyurethane (IL/PU) gels • Joule heating • Lamina emergent mechanism • Linear stroke polymer actuator • Mechanochemoelectrical behavior • Micro linear positioner • Microactuators • NEMO • Parallel five-bar mechanism • Peristaltic motion • Petal-shaped diaphragm • Poly(3,4-ethylenedioxythiophene)/poly(styrene sulfonate) (PEDOT/PSS) • PPy–zigzag metal composite actuator • Solid-state actuators • Stiffening spring system • Strain rates • Tube-in-tube actuator node (TITAN) • WANDA • Young’s modulus

1 Introduction

The field of electroactive transducers has reached a certain maturity that they can be used in establishing functional devices. The object of this chapter is to review configurations for functional devices articulated with EAP actuators, or combination of actuators and sensors, which can be considered as the devices. It is our understanding that a device is an invention or a means such as a mechanical, electrical, or a combination of both, for a particular purpose. A transducer is a device which converts one form of energy into another, e.g., electrical into mechanical and vice versa. This follows that EAP transducers refer to the actuators, sensors, and energy harvesters made of electroactive polymers.

Ideally, the configuration of a device should be formulated in the light of the design or performance requirements. Unfortunately, the progress in the EAP transducers in the last two decades has not allowed us to follow such a top-to-down approach yet; design the device configuration in the light of the performance or design requirements, and then synthesize the material and its processing techniques. The EAP technology has been based on using the material processed with a specific

technique and then establishing the device configuration to demonstrate the capabilities of these materials in various applications.

The scope of this chapter is limited to the macro-sized device configurations. For micro-sized or overly miniaturized configurations, a special care should be paid to the scaling laws and their implications for the device operation and meeting the design requirements. We cannot simply scale down configurations of a macro-device and expect them to deliver basic performance requirements. For the device configurations based on micro-sized polymer transducers, the readers are referred to relevant chapters of this book. Polypyrrole (PPy), PEDOT/PSS, and polyaniline (PANI) are the most commonly used conjugated polymers to establish transducers. Their elastic moduli are within the range of 200 MPa to 7 GPa in reinforced fibers. The discussion in this chapter centers around the device concepts or configurations based on PPy and PEDOT/PSS polymer transducers.

2 EAPs as Actuators

In this section, we present various device configurations articulated with conjugated polymer actuators.

Initially, conjugated polymer actuators were prepared in their most basic form, which was a freestanding film. They were tested as thin films operating in an electrolyte to understand their fundamental performance metrics such as strain, strain rate, stress, force, work capacity, and modulus of elasticity and how the mechanical properties change with the operating and synthesis conditions. In this basic configuration, they were in the form of linear actuators – converting electrical energy into mechanical energy. As shown in Fig. 1, as well reported in the literature, the mechanical output (strain) is generated due to the mass transport of the electrolyte ions in and out of the polymer film (Della Santa et al. 1997; Baughman 1996; Hara et al. 2003a, 2005a; Kaneko et al. 1997; Bay et al. 2003; Chiarelli et al. 1994; Otero et al. 2014). The electrochemical cell consisting of the reference (Ag/AgCl),

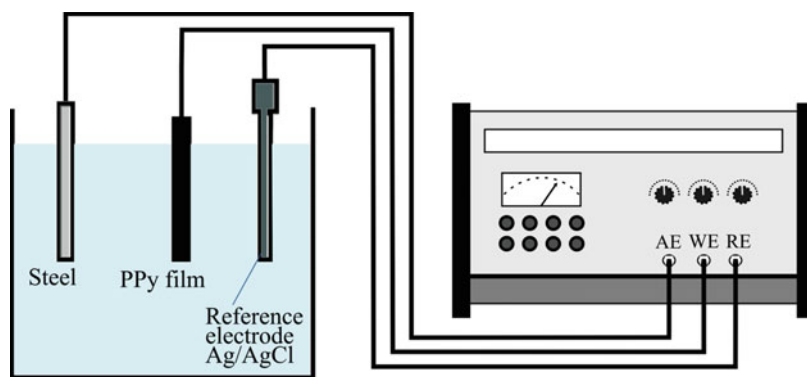


Fig. 1 Configuration of a freestanding polymer actuator

auxiliary (stainless steel or platinum mesh), and working (PPy film) electrodes immersed in an electrolyte is electrically stimulated by applying a potential difference or passing current between the electrodes via the contacts. The PPy film contracts or expands depending on its electrochemical state (oxidation or reduction) and the size of the anion. When a large anion (e.g., DBS^-) is used, it shrinks upon oxidation. On the other hand, when a small anion (TFSI^-) is used, it expands upon oxidation (positive potential applied). The reverse of these two cases happens when the PPy sample is reduced under a negative potential applied. For some salts, a mixture of both processes can occur which reduces the mechanical work output. This configuration, which is known as the freestanding polymer actuator, is not quite practical due to requiring two extra electrodes and an aqueous medium consisting of ions, a limited choice of counterions, and more importantly generating an insufficient mechanical output (Hutchison et al. 2000; Gandhi et al. 1995; Hara et al. 2005a). If it is made with a cross-sectional area of 30 mm^2 , it can lift a load of up to 30 kg. Obviously, it is not possible to scale this configuration to such a large cross section. Therefore, no noticeable devices purely based on the freestanding actuators have been reported in the literature.

The electrochemically generated strain in conducting polymers was commonly less than 5 % before Hara et al. (2003b, 2004a, b) found an innovative synthetic method of PPy in 2003. They found that the PPy films, which were electrochemically generated from methyl benzoate solution of tetra-*n*-butylammonium (TBA) tetrafluoroborate (BF_4), exhibited the electrochemical strain and stress of 12.4 % and 22 MPa, respectively. In 2004, they improved the method to attain the extremely large strain of approximately 40 % by using the methyl benzoate solutions of $\text{Li}(\text{C}_n\text{F}_{2n+1}\text{SO}_2)_2\text{N}$ ($n = 4$) (Hara et al. 2004c, e, 2005a, b). The chemicals were used as commercial grades purchased from Sigma-Aldrich, Inc., Tokyo, Kasei Kogyo Co. Ltd., Wako Pure Chemical Ltd., and Lancaster Synthesis Inc. for their materials supplied. Two types of PPy films were prepared by electrodeposition, namely, high-density compact films and porous spongy films. Methyl benzoate was the key solvent for both types of films. The electrolytes of group (a) TBABF_4 , TBAPF_6 , and $\text{TBACF}_3\text{SO}_3$ (Hara et al. 2003a, 2004a, b, d, 2005a) and group (b) TBATFSI (TFSI, bis(trifluoromethanesulfonyl)imide), LiTFSI , and/or $\text{Li}(\text{C}_n\text{F}_{2n+1}\text{SO}_2)_2\text{N}$ ($n = 1, 2, 3, 4$) (Hara et al. 2004c, 2005a, b, c, d) were found to generate the high-density film and the porous film, respectively.

PPy films were electrochemically deposited on an electrode plate of Pt, Ti, or indium tin oxide (ITO) glass, in an electrolyte solution of methyl benzoate, PPy (0.25 mol/dm^3), and electrolytes of (a) or (b) group. Electrodeposition of PPy was carried out typically by using a potentiogalvanostat at constant current of 0.2 A/cm^2 for 4 h at room temperature or lower temperatures. When the electrolyte of group (a) TBABF_4 (0.25 mol/dm^3) was employed, the surface morphology was smooth (Hara et al. 2004a) at the electrode side. The thickness and conductivity of films were ca. 0.02 mm and 80–120 S/cm, respectively. On the other hand, the use of electrolyte group (b) resulted in porous surface morphology (Hara et al. 2004c) as shown in Fig. 2 and the thickness of 0.03 mm and conductivity of 30–120 S/cm.

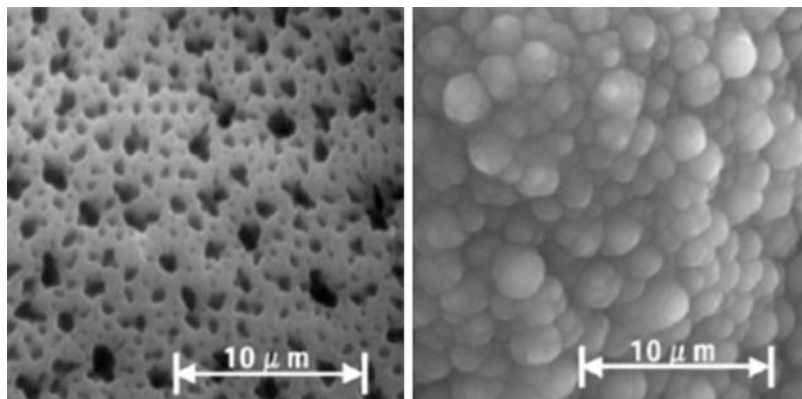


Fig. 2 SEM photographs of TFSA-doped PPy film prepared on Pt electrode: electrode side (*left*) and solution side (*right*) (Reproduced with permission from the Royal Society of Chemistry (Hara et al. 2004c))

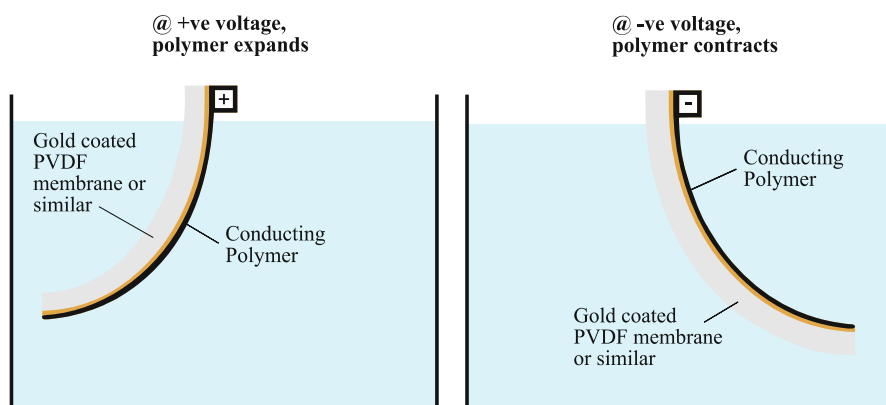


Fig. 3 Configuration of a bilayer polymer actuator

Compared to freestanding conjugated polymer actuators, a bilayer configuration is more practical and can be used in establishing devices. A typical bilayer configuration consists of a non-extensible metal layer (e.g., platinum, gold, and similar nonreactive noble metal) or a similar conductor (Otero et al. 1992) and the conjugated film, as shown in Fig. 3. The function of the metal layer is to constrain the strain of the conjugated film so that the whole structure can generate a bending motion, like a bimetal or a cantilever beam, if its one end, where the electrical input is applied, is fixed and serves as an electrode to activate the conjugated film. This configuration can be analogous to a single link, or a crank with a limited rotation, connected to the ground with a revolute joint, more accurately like a flexure-jointed robotic arm. Depending on the size (especially length), the actuators with a bilayer configuration can generate large bending angles and bend into complex shapes such

as spirals. The shape and layout of this configuration have been used to demonstrate various devices and applications. It is up to the designer to tailor this configuration to establish new functional devices. In fact, this bilayer configuration has been widely used in microactuators to demonstrate various biotechnological and medical applications (Carpi and Smela, 2009; Jager et al. 1999, 2000, 2013; Smela et al. 1999; Gaihre et al. 2012; Otero et al. 1992).

Another bilayer configuration is to have two conducting polymer layers with different strains, in order to generate a bending displacement proportional to the strain difference of the polymer layers.

To minimize the constraining effect of the metal layer, a thin layer of gold or platinum can be coated on a polymer substrate such as poly(vinylidene fluoride) (PVDF) or Kapton or any flexible material to establish a bilayer configuration (Gaihre et al. 2013). For the modeling, analysis, and characterization of this actuator configuration, the readers are referred to the wide literature on the topic (Christophersen et al. 2006; Pei and Inganlås 1992, 1993; Grande and Otero 1999; Wang et al. 1990, 2004; Smela and Gadegaard 2001; Pyo et al. 2003; Otero et al. 1997; Gandhi et al. 1995).

2.1 Device Examples Based on Bilayer Configuration

One of the interesting applications of the bilayer configuration is realized by Madden et al. (2004) to establish a variable camber propeller for the trailing edge of an aquatic foil. The propeller was made of a bilayer polymer actuator with the dimensions of 150 mm × 30 mm × 30 μm. The aim was to replace the gearing mechanism in large vessels with smart actuators. A 3.5 μm thin polyethylene film was used to encapsulate the actuator so that the propeller could be tested in water. The propeller was able to generate 0.7 N (five times less than the required force of 3.5 N) and a bending angle of >30° in 4 s. They concluded that although the work density of the actuator was enough to produce the desired bending angle, the force output and speed of the actuation had to be improved in order to articulate the variable camber foils with polymer actuators.

Although bilayer configuration is more practical than the freestanding configuration, it has some disadvantages, primarily the need to operate in a certain aqueous medium, i.e., electrolytic solution, and delamination. As presented in the next subsection, the tri-layer configuration has been developed to eliminate these disadvantages and hence widen the application areas of the conjugated polymer transducers.

It must be noted that an actuator with a linear displacement output can be used in more applications. To meet this demand, there have been some attempts to establish actuator configurations with a linear displacement output, in fact rectilinear, along a single direction (Lu et al. 2004; Hara et al. 2004d). One of the earliest attempts was realized by Mazzoldi et al. (1998). They placed a polyaniline (PANI) fiber doped in HClO₄ onto a solid polymer electrolyte and rolled them into a cylindrical structure, where the PANI is in the middle. A copper wire was then helically wrapped around the cylinder to make the linear dry actuator.

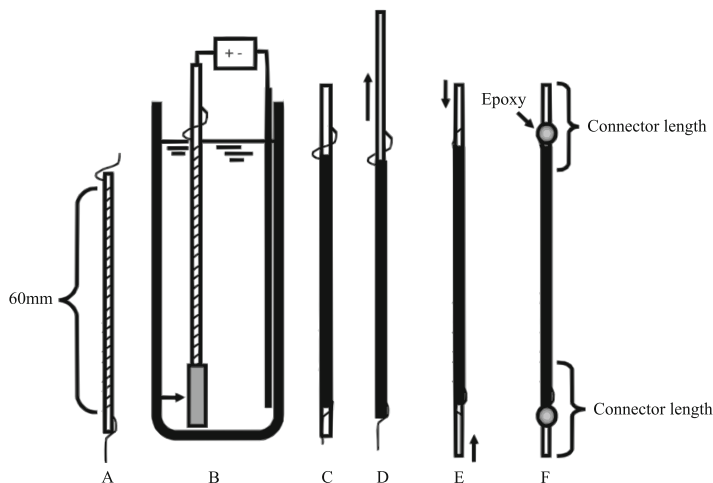


Fig. 4 Preparation steps for the linear stroke polymer actuator (Ding et al. 2003). *A.* 25 μm platinum wire is spirally wrapped around 125 μm wire; *B.* Electropolymerization of PPy layer; *C.* 125 μm center wire is withdrawn; *D.* Insertion of two short 125 μm connectors into each end; *E.* 25 μm wire is pulled tight around ends to ensure good electrical connection and epoxy glued in place (Reprinted with permission from Ding et al. 2003. Copyright (2003) Elsevier Limited)

Madden et al. proposed a linear bilayer actuator operating in air (Madden et al. 1999). It is obtained by coating both sides of a PPy film with a gel electrolyte around which the counter-electrode strips are wrapped to finish the actuator.

Another linear stroke polymer actuator has been proposed by Ding et al. (2003). It is based on hollow PPy fibers with a helical wire interconnect. Its preparation is shown in Fig. 4. This actuator configuration, which provides up to 5 % axial strain, usable strains ($>1\%$) to at least 8 MPa and peak strain rates of up to 13 % per second, can be used in the applications typified by a Braille display, which is described in the chapter of this book on the applications of conducting polymer actuators. A two-electrode arrangement was used to quantify the performance of the actuator under various inputs.

The response time of the actuation configurations based on the PPy thin layer has been improved by using metal coils (Hara et al. 2003b, 2004a) as the core of fibular actuators and metal plating (Hara et al. 2004a; Eamex HP) on which PPy layers are deposited. One striking example is a linear actuator fabricated in a thin tube with a length of 20 mm and diameter of 1 mm. This actuator can lift 25 g with the speed of 1 mm/s under 2.0 V. This thin tube PPy actuator developed by Eamex Company Ltd. is shown Fig. 5. The actuator was constructed with two pieces of electrodes, namely, a PPy tube of active working electrode and a PPy counter electrode. The surface of the PPy counter electrode was treated with an aqueous hydrogen peroxide solution, resulting in the insulating layer at the surface and acting as a separator. The PPy counter electrode was put in the PPy tube with an appropriate electrolyte.

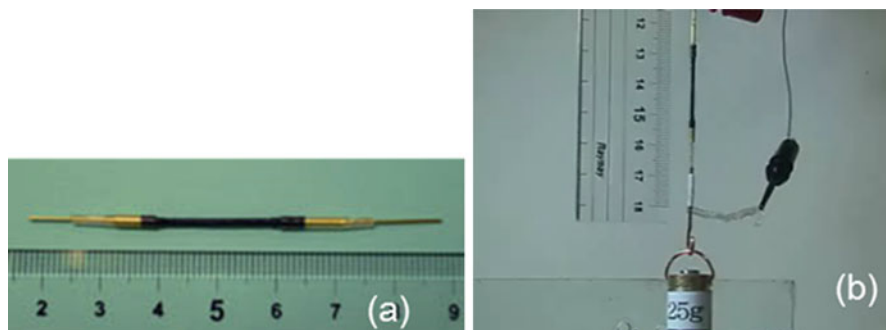


Fig. 5 (a) PPy tube actuator with an effective length of 20 mm and a diameter of 1.0 mm and (b) a photograph of the actuator (Reproduced from Eamex HP (<http://eamex.co.jp/>))

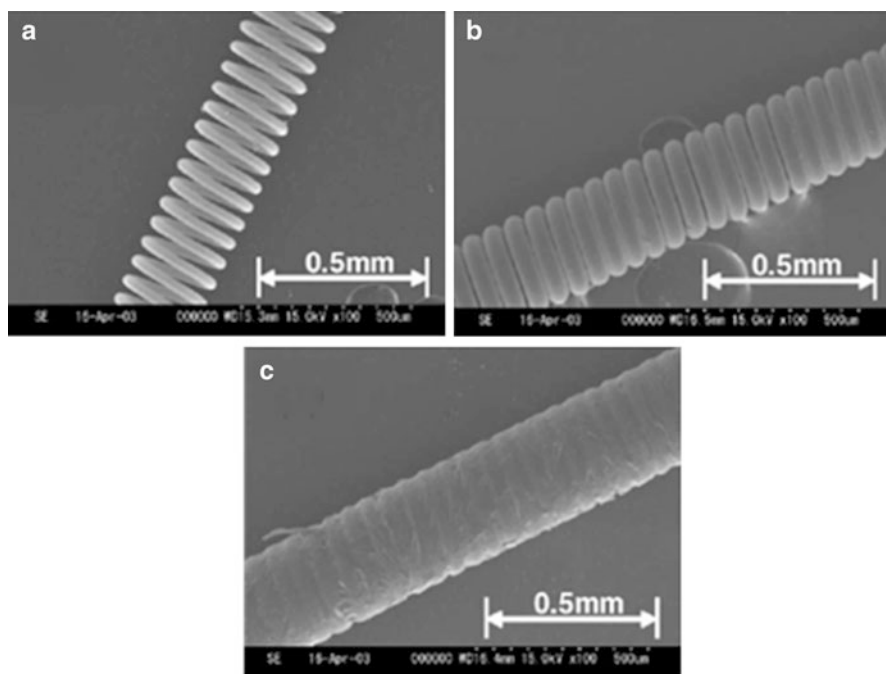


Fig. 6 SEM photographs of (a) bare W (tungsten) wire, (b) PPy electrochemically deposited at 0.125 mA/cm^2 for 8 h and (c) 16 h in methyl benzoate solution of TBABF₄ (0.5 mol/dm^3) (Reproduced from Hara et al. 2004d)

Another PPy–metal coil composite actuator configuration was established by electrochemically depositing PPy layer on metal coils (Hara et al. 2004d, 2005c). Figure 6 shows the scanning electron micrographs (SEMs) (Hara et al. 2004d) of the electrochemically deposited PPy on W (tungsten) coil with a diameter of 0.25 mm, pitch of 0.06 mm, and wire diameter of 0.03 mm. The PPy deposited coils were

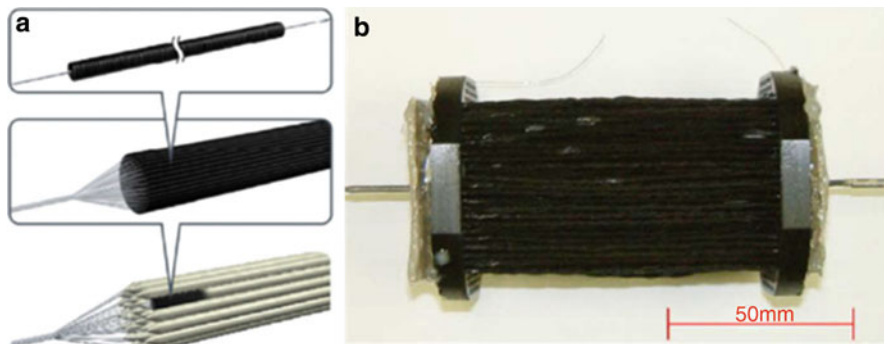


Fig. 7 (a) Schematic drawing of bundles assembled with PPy deposited coils and (b) photograph of a prototype bundle of 1600 piece PPy coils (Reproduced from Hara et al. 2004d)

assembled as bundles of the coils as shown in Fig. 7a. A piece of PPy deposited on the W coil showed the electrochemical strain of 8.5 % and a contraction force of 0.2 N, which were the typical maximum values. The contraction force of the composite bundle was increased in proportion to the number of the coils assembled while keeping the same strain.

The prototype shown in Fig. 7 is a soft actuator assembled with bundles of PPy deposited on nickel-plated stainless steel coils. This actuator configuration lifted 22 kg. Arrangement of the counter electrode, which was a challenging issue, was solved by assigning a counter electrode to each bundle to reduce the diffusion time of the ions.

As an extension of the PPy–metal composite actuator configuration, a high-performance PPy was electrochemically deposited on a zigzag metal substrate (Hara et al. 2004a), which was obtained by sputtering Ti or Au on polyethylene terephthalate (PET) film as shown in Fig. 8a. This configuration is known as “PPy–zigzag metal composite actuator.” The electrochemical deposition was performed in methyl benzoate solution of TBACF₃SO₃ (0.2 mol/dm³) at a constant current mode of 0.2 mA/cm² at room temperature for 4 h on the zigzag metal/PET film substrate. During the electrochemical deposition of PPy film on a metal substrate, the growing front of PPy film extended beyond the edge of the metal substrate. Namely, even though the pattern of the electrode substrate on PET was zigzag as in Fig. 8a, the PPy film spread over the gap of the metal electrode uniformly as shown in Fig. 8b. After the electrochemical deposition of PPy film, the PET substrate was peeled off from the PPy–zigzag metal. The PPy film on the zigzag metal was again immersed in the pyrrole electrolyte solution, and the PPy was electrochemically deposited to obtain both sides covered with PPy–zigzag metal composites.

The electrochemical actuation of the PPy–zigzag metal composite was performed in aqueous solution of NaPF₆ (1.0 mol/dm³), with voltage cycle between -0.9 and $+0.7$ V vs. Ag/Ag⁺ at 2 mV/s. The maximum electrochemical strain was 21.4 %, which was much larger than that of the freestanding PPy film (12.8 %) operating in the same electrolyte solution (TBACF₃SO₃). The enhancement of electrochemical strain in the PPy–zigzag metal composite has been explained as follows: The

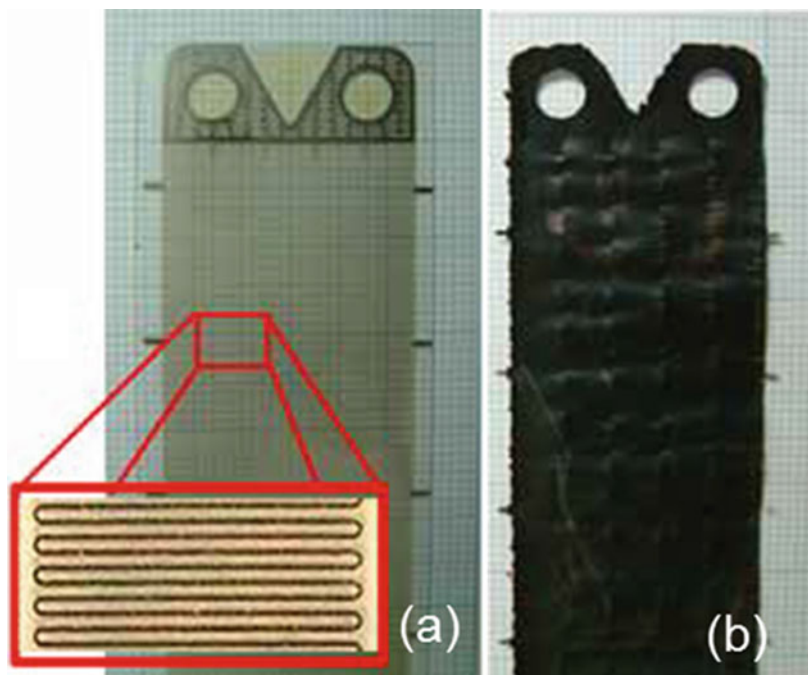


Fig. 8 Photographs of (a) zigzag metal sputtered on PET substrate with the width of 26 mm and length of 90 mm and (b) PPy film electrochemically deposited on the zigzag metal-PET film (Reproduced with permission from the Royal Society of Chemistry (Hara et al. 2004a))

expansion and contraction of PPy film usually occur three-dimensionally; however, in the PPy-zigzag electrode structure, while the expansion and contraction are constrained in the width direction, they are allowed in the longitudinal direction. This increases the strain in the longitudinal direction. The PPy-zigzag metal composite can be piled up to generate a larger contraction force. An actuator assembled with 20 units of PPy-zigzag metal composites lifted 13 kg (Hara et al. 2004a).

The next generation of the conjugated polymer actuator is the tri-layer layer actuator (Alici and Higgins 2009). Figure 9 illustrates this configuration and outlines the operation principle for these full solid-state actuators. The laminated structure generates a simple bending motion, like a cantilevered beam. In contrast to a single polymer layer with uniform strain (i.e., no bending), the inclusion of a middle PVDF layer separating two polymer layers results in a differential strain at each layer causing bending, as shown in Fig. 9. The synthesis of this tri-layer configuration starts with the sputter coating of gold particles (thickness ranging between 10 and 100 Å) on both sides of a PVDF sheet (Millipore), which is like a filter membrane with a pore size of 0.45 μm and nominal thickness of 110 μm. The coated layers of gold serve to increase the conductivity of the polymer electrodes to be grown. Propylene carbonate (PC, Aldrich) and lithium bis(trifluoromethanesulfonyl)imide

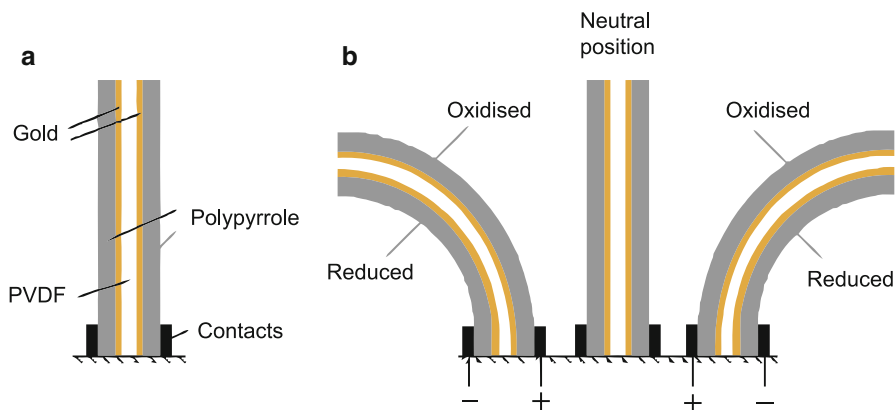


Fig. 9 (a) Schematic structure of a tri-layer conducting polymer actuator and (b) schematic representation of the bending principle. This actuator is anion driven; the anions in the salt move into the positively charged electrode to cause a volume expansion. If it is cation driven, the cations in the salt move into the negatively charged electrode to cause volume expansion; hence, the bending direction will be from the negative electrode to the positive electrode – the opposite of what is shown (Alici 2009)

(Li^+TFSI^- , 3 M) were used as received. Pyrrole (Merck) was distilled and stored under nitrogen at $-20\text{ }^\circ\text{C}$ before use (Wu et al. 2006; John et al. 2008).

Using a potentiostat/galvanostat, the polypyrrole (PPy) layers were grown galvanostatically on the gold-coated PVDF for 12 h from the growth solution. With this growth time, the thickness of each polymer layer was approximately $30\text{ }\mu\text{m}$. The deposition temperature was $-33\text{ }^\circ\text{C}$ and the synthesized bulk sheet was doped with TFSI^- ions.

The structure of the actuator with electrolyte stored in the PVDF membrane functions as an electrochemical cell and is electrically stimulated by applying a potential difference or passing current between the polymer electrodes via the contacts. During oxidation (positive potential applied), the negatively charged TFSI^- anions move toward the inside of the positively charged polymer electrode to maintain charge neutrality and hence cause a volume expansion in the polymer electrode. At the opposing negatively charged polymer electrode, the ejection of the TFSI^- anions during reduction causes a volume contraction. This differential volume change between the two polymer electrode layers results in the bending toward the negative electrode/cathode, as depicted in Fig. 9b. Thus, volume changes in the polymer occur due to movement of charge-balancing anions in and out of the polymer layers. The incorporation of associated solvent molecules due to osmotic effects may also contribute to the volume changes, in addition to the bending electrostatic forces between the displaced ions and the polymer backbone that are also believed to contribute to the bending (Velmurugu and Skaarup 2005; Otero and Martinez 2012; Otero et al. 2013; Valero et al. 2014). The actuation speed and overall volume change also depend on many electro-chemo-mechanical parameters, including the thickness of the polymer layers, the ion type and sizes, charge injected (potential applied), the ionic

concentration, the solvent, and the width of the actuator (Wu et al. 2006; Spinks et al. 2009; Conzuelo et al. 2010; Otero and Cortes 2004; Otero et al. 2007, 2012a; Valero et al. 2011; Martínez and Otero 2014; Han and Shi 2004a, b).

The tri-layer configuration has been the most practical configuration for applications in wet and dry environments. However, one issue associated with them is the evaporation of the solvent if a conventional electrolyte is used and the actuator is not properly encapsulated. Of course, if an ionic liquid electrolyte is used, no need of encapsulation, no solvent will be used with a trade-off of a decrease in the speed of response and strain.

2.2 Devices Based on a Tri-layer Configuration

A significant number of prototype devices have been built using tri-layer actuators – thanks to their multilayer structure, which allows the two electrodes and the ionic source to be readily incorporated. The most noticeable ones are reported in references (Fay et al. 2010; McGovern et al. 2009; Alici et al. 2007; Alici and Huynh 2007; Mutlu and Alici 2010b; Mutlu et al. 2011, 2014; Fang and Tan 2010; Sansinena et al. 1997) and briefly summarized below.

2.2.1 Extended Deflections

Large motion/deflection can be achieved by designing petal-shaped diaphragms made of a tri-layer polymer substrate, as shown in Fig. 10. This petal-shaped diaphragm was fabricated using PDMS-based microelectromechanical system (MEMS) processes to establish a pump, which is described in the chapter of this book on the applications of conducting polymer actuators (Fang and Tan 2010). The petal-shaped tri-layer actuator was adhered to a low-stiffness passive payer, which deforms together with the active tri-layer to generate enough pressure variation in the pump reservoir. The lower is the modulus of elasticity of the passive layer, the lower is the voltage input needed to stretch the passive layer, therefore operating the whole assembly.

2.2.2 Peristaltic Motion

Peristaltic motion is a commonly used principle to propel liquids. To this aim, Wu et al. (2005) synthesized a tri-layer polypyrrole actuator, which was in a confined cylindrical configuration, to induce fluid movement through an inner channel in a single unit. A number of these units are connected in series to provide a peristaltic action for a novel microfluidic pump which is described in the chapter of this book on the applications of conducting polymer actuators. The schematic diagram explaining the assembly of this actuation configuration called “the tube-in-tube actuator node (TITAN)” is shown in Fig. 11. This peristaltic motion concept was tested using a symmetrical pulsed potential waveform over a 60 s cycle. First, a positive pulse of 1 V was applied and kept constant at +1 V for 30 s to expand the inner chamber of the working electrode, and then a negative pulse, which was gradually changed from 0 to -1 V, was applied to contract the inner chamber of the working electrode and kept at -1 V for 30 s to optimize the operating potential for the peristaltic motion.

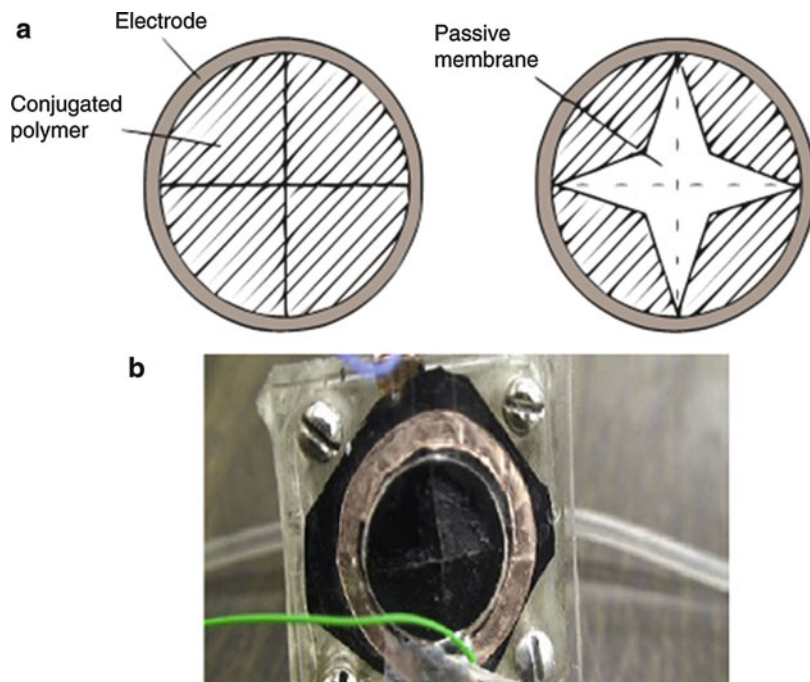


Fig. 10 (a) Schematic representation of a petal-shaped diaphragm before actuation and upon actuation and (b) a view of the petal-shaped diaphragm made of a tri-layer polymer substrate (Reprinted with permission from Fang and Tan 2010. Copyright (2010) Elsevier Limited)

2.2.3 Bending Tubes and Controlled Curvature Change

There exist a variety of applications where tubular structures have to bend or change curvature, for example, in steerable catheters and guide wires. The design concepts for deflecting/bending tubes which have been proposed by Baughman et al. and Della Santa are illustrated in Fig. 12 (Santa et al. 1996; Della Santa and De-Rossi 1996; Mazzoldi and De Rossi 2000; Baughman et al. 1991). These configurations are based on employing one or two pairs of antagonistic actuators on two or four sides of the tubular structure (Baughman et al. 1991). This concept which has been employed in a catheter investigated by Shao and others (Mazzoldi and De Rossi 2000; Shoa et al. 2009) consists of a four-electrode conducting polymer actuator fabricated directly on a commercial catheter tip with external and internal diameters of 0.5 and 0.28 mm, respectively. Shao et al. employed laser micromachining to pattern the PPy electrodes into the polymer coating. The complete assembly, shown in Fig. 13, is encapsulated inside a structure containing an ionic electrolyte. This concept has been applied to a steerable catheter which is described in the chapter of this book on the applications of conducting polymer actuators.

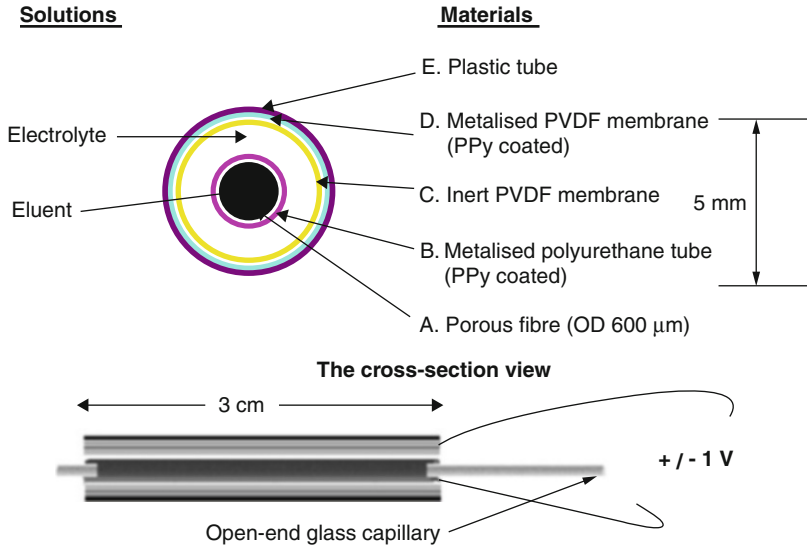


Fig. 11 Configuration and assembly of the tube-in-tube actuation concept (TITAN). *A*: a porous PVDF fiber to provide support for the metallized polyurethane tube (OD 1050 μm , ID 950 μm). *B*: as a working electrode, a metallized polyurethane tube wrapped with $\phi 50$ μm platinum wire coated with polypyrrole. *C*: a PVDF membrane used for the electrolyte storage. *D*: as the auxiliary electrode, a metallized PVDF membrane coated with polypyrrole connected via stainless steel mesh. *E*: a plastic tube with a length of 3 cm (OD 5 mm, ID 4 mm) used to pack the entire assembly (Reprinted with permission from Wu et al. 2005. Copyright (2005) Institute of Physics)

Micromuscle AB took an alternative design path to achieve a much simpler operation while taking into account standard surgical practices during angioplasty procedures. Surgeons using standard fixed curvature guide wires and guide catheters already can achieve a full 360° circular motion of the tip by simply rotating the guide wire. Since only an active curvature change is needed and not a full 3D motion, PPy was applied only on one side of the coil that forms the tip of commercial guide wires (Krogh and Jager 2007; Wilson et al. 2007). In this design, only one electrode needs to be addressed, and blood is used as the external electrolyte, making both the fabrication and operation extremely simple. When a potential is applied, the PPy volume increases or decreases resulting in an increased or decreased curvature of the tip of a catheter-like medical device, as shown in Fig. 14.

The need to electronically change the curvature exists in a variety of devices. Another example is guiding a cochlear implant into the inner ear. The aim is to guide a multichannel array of pre-curved electrodes into the cochlea to electrically stimulate the hearing nerves in order to restore hearing in deaf people. Insertion of an array of electrodes into the cochlea is a challenging task requiring soft and accurately controllable actuators. Similar to the guide wire mentioned above, active control of the curvature of the cochlear implant during implantation is achieved by adding a PPy actuator to one side of an existing medical device. However, in order not to disturb the confined environment of cochlea, Zhou et al. (2003) have proposed to use

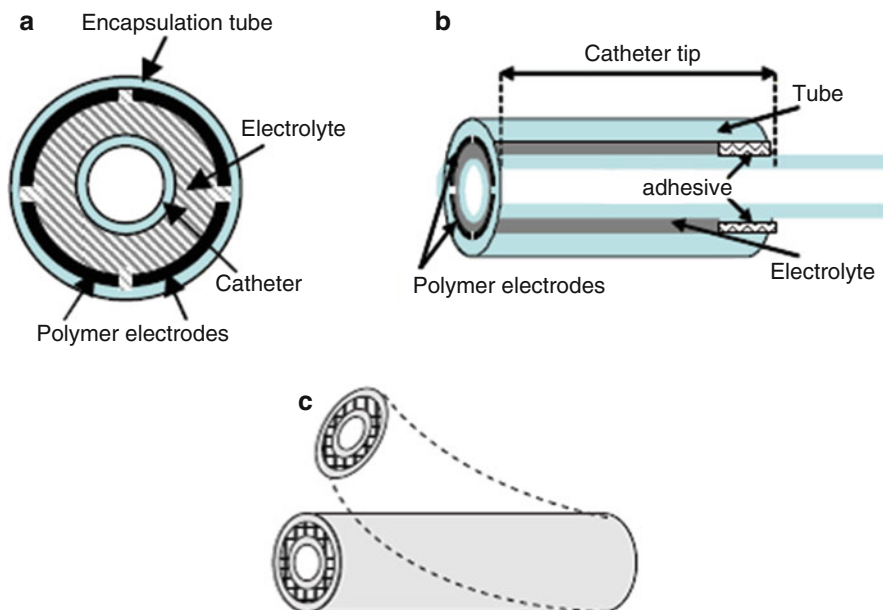


Fig. 12 A view of the bending tube concept based on the dry-type polymer actuators, proposed for a steerable catheter (Reprinted with permission from Shoa et al. 2009. Copyright (2009) John Wiley and Sons)

a tri-layer polymer actuator. The electrodes shown in Fig. 15a have a length ranging between 22 and 30 mm and bend into a curve with a total bending angle $>400^\circ$. When a tri-layer polymer actuator is long enough (20 mm) under 1 V, it can bend more than 180° , as shown in Fig. 15b.

2.2.4 Controlled Deflection Change for Propulsion

The tri-layer configuration which generates a large deflection has been employed to propel swimming devices. The first of such devices (Alici et al. 2007) shown in Fig. 16 has eight fins (i.e., tri-layer polymer actuators) installed along both sides of a rigid body to move the device in a direction perpendicular to the longitudinal axis of the body. The rigid body is made of prepregged carbon fiber strips of 0.3 mm thickness and hardened with resin. The device mimics the motion of a boxfish having a rigid body with side or paired fins running through the rigid body, like a fish having pectoral fins (Sfakiotakis et al. 1999). The fins or polymer benders behave as individually controlled flexible membranes. Each fin is activated with sinusoidal inputs such that there is a phase lag between the movements of the successive fins, and the frequency and amplitude of the input can be changed to create enough thrust force for propulsion. Based on the large deflection of the tri-layer configuration, two more devices, called NEMO (McGovern et al. 2009)

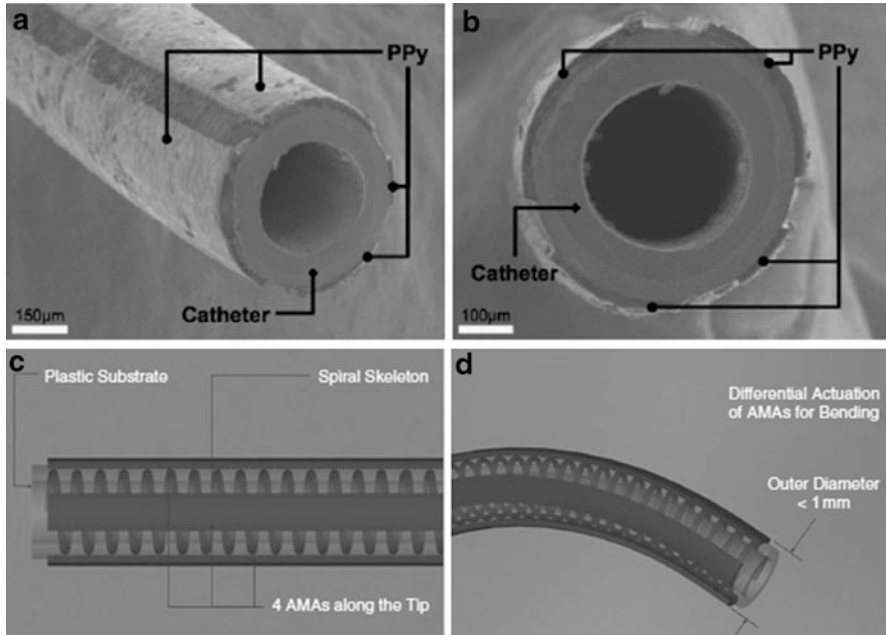


Fig. 13 Views of the design and prototypes of four-segment conjugated polymer electrodes while bending a steerable catheter-like tube (Reprinted with permission from Shoa et al. 2009. Copyright (2009) John Wiley and Sons)

and WANDA (Fay et al. 2010), have been established. The tri-layer configuration has been used as the caudal fins to propel the fish, as illustrated in Figs. 17 and 18.

James et al. (2007) attempted to mimic the movement of a sunfish pectoral fin. To this aim, they used a combination tri-layer (fabricated using a procedure slightly different than the seamless fabrication process described above) and linear polymer actuators to actively control the shape or webbing of a fin. This all conducting polymer fin, which is illustrated in Fig. 19, can generate the cupping motion of the sunfish pectoral fin. However, the speed of the polymer actuators is not sufficient to create surfaces with varying 3D geometry.

2.2.5 Controlled Deflection Change for Manipulation

The tri-layer actuator configuration has been used as the active flexural joints of a two-finger gripper, as depicted in Fig. 20 (Alici and Huynh 2007). The conducting polymer part of the finger works as an actuator and a flexure joint called *active flexure (acti-flex)* joint, while the carbon fiber attached to the end of the polymer serves as a rigid link for the finger. The gripper, which is described in detail in the chapter of this book on the applications of conducting polymer actuators, can lift and handle as much as 50 times of its total mass under 1.5 V.

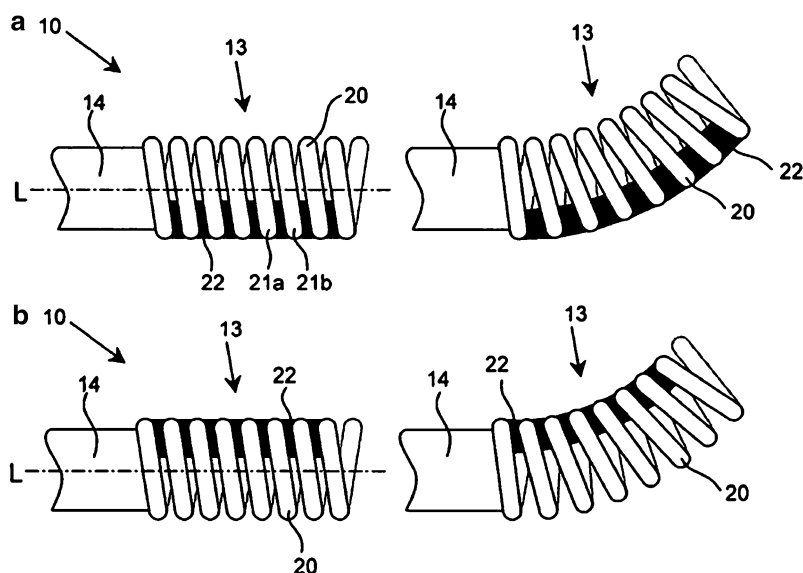


Fig. 14 By expansion and contraction in (a) and (b), respectively, a PPY-based actuator controls the curvature of the controllable segment of a catheter-like medical device (Reproduced from Krogh and Jager 2007)

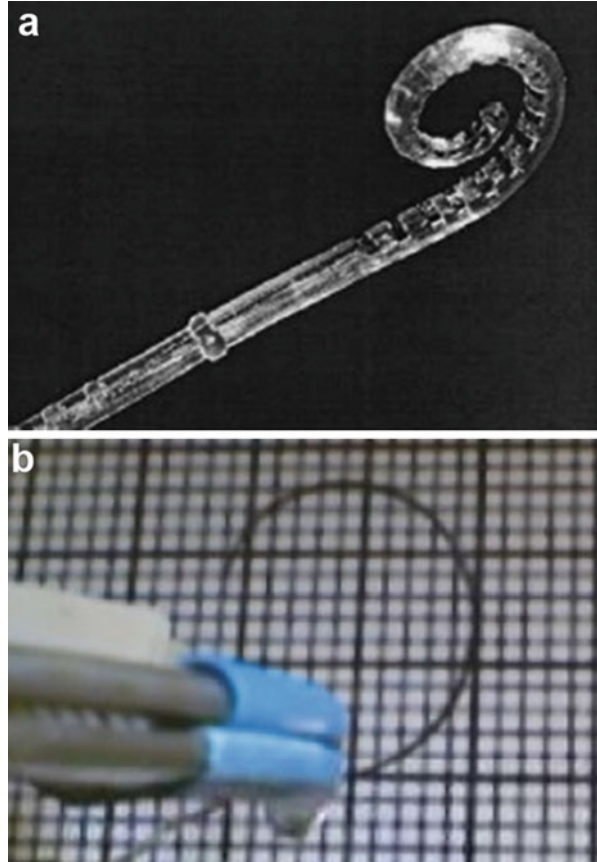
2.2.6 Seamless Integration of Tri-layer Configuration in Engineering Mechanisms

By taking the advantage of the active flexure joint concept, the tri-layer configuration has been used to build a parallel five-bar mechanism, converting the bending motion of the tri-layer configuration into a rectilinear output, as illustrated in Fig. 21 (Burriss et al. 2011). This soft mechanism can be used as the soft limbs of Stewart platform-based parallel manipulators (Gallardo-Alvarado et al. 2012). This paves the way toward establishing soft manipulation devices.

Mutlu and Alici (2010a) have employed the concept of a suitably designed contact surface to constrain the bending of the tri-layer configuration in order to virtually change or tune the stiffness of the tri-layer configuration, as illustrated in Fig. 22. They have demonstrated that the effective stiffness can be tailored in a nonlinear fashion to meet the stiffness requirement of an application although the stiffness of the artificial muscles is constant for a given geometric size and electrical and chemical operation conditions.

As well reported in the literature, the mechanical output of the conjugated polymer actuators is limited. One effective method is to transform the mechanical output into a desired output in a stable and scalable way through some engineering mechanisms, as shown in Fig. 23 (Mutlu and Alici 2010b). The force output and stability of this mechanism are linearly proportional to the number of polymer actuators in the form of the tri-layer configuration. The proposed mechanism converts the bending displacement of a polymer actuator into a rectilinear movement of

Fig. 15 (a) A view of Nucleus 24 contour – the most commonly used electrode arrays for cochlear implants – and (b) a tri-layer actuator is proposed to steer and guide the electrodes into the inner ear (Zhou et al. 2003)

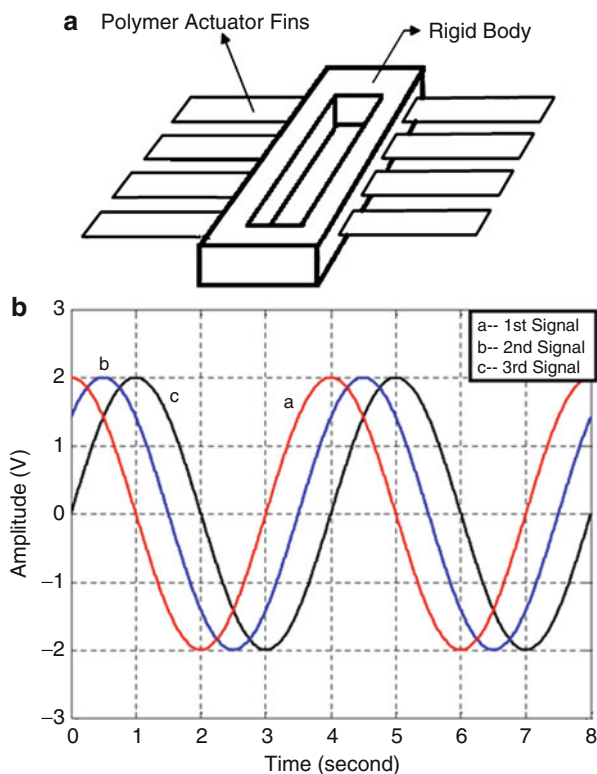


an output point. This device concept can be used as a programmable switch, a pump in microelectromechanical systems (MEMSs), or a multistable linear actuation mechanism by adjusting the input voltage and scaling down the mechanism further.

Another interesting and novel mechanism established is a lamina emergent mechanism, which is initially in a 2D configuration, and upon activation, it generates a motion perpendicular to its initial 2D plane. To this aim, Mutlu et al. (2011) patterned a planar substrate of the tri-layer configuration into a spiral configuration, which transformed itself into a 3D conical helix shape under an electrical input, as illustrated in Fig. 24. This configuration can be used as the artificial flagellum of bacteria robots. The objects built as 2D or 3D objects, but upon activation add another dimension (e.g., from 2D to 3D), are recently called 4D printing. In fact, the concept of 4D printing has been for the first time applied to this class of actuators in 2011 (Mutlu et al. 2011).

As an extension of this novel concept, Mutlu et al. (2014) proposed a micro linear positioner, shown in Fig. 25. Multiple spirals aligned properly stabilize the mechanism while it operates. This active-compliant mechanism can be used as a micro

Fig. 16 (a) Configuration of the prototype swimming device articulated with tri-layer polymer actuator and (b) the input voltage applied to each fin consecutively with a delay (Alici et al. 2007)



stage as well as an optical zoom mechanism for mobile phone cameras and similar devices, which is described in the chapter of this book on the applications of conducting polymer actuators. Compared to similar efforts to build an autofocus lens mechanism (liquid membrane lens) based on DEA elastomer actuators (Carpí et al. 2011a), this consumes a very small electric energy, not creating a safety risk with a small footprint. This is a very good example of thinking beyond the boundaries of a research field, on the contrary following a cross-disciplinary approach to bring novel ideas and concepts.

3 EAPs as Sensors

Of the transducer configurations presented above, the tri-layer is the most suitable for mechanical sensing. Conjugated polymer sensors, which are still in their infancy, have not been tested for a realistic application yet. Significant research efforts have been dedicated to their use as mechanical sensors, their performance quantification, understanding the sensing principle, geometry optimization, and coupling between sensing and actuation (Wu et al. 2007; Alici et al. 2008; John et al. 2009; Shoa et al. 2010; Andrews et al. 2004; Wallace et al. 1999; Otero et al. 2012b; Martínez

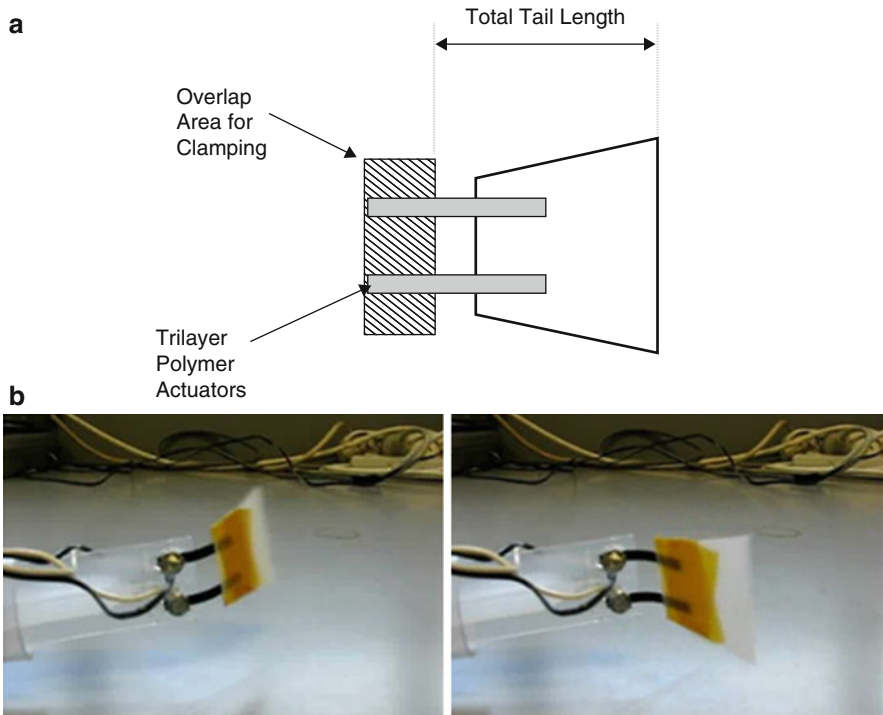


Fig. 17 (a) The caudal fin arrangement of NEMO the fish articulated with tri-layer actuators and (b) two extreme configurations of the fin during propulsion

and Otero 2012; Otero and Martinez 2015). The similarity between actuation and sensing principles of conducting polymer transducers is illustrated in Fig. 26. Wu et al. (2007) reported that a tri-layer configuration used as a sensor can generate a voltage output in the mV range. The polarity and magnitude of the voltage generated under a mechanical input depend on the size of dopant ions. A small mobile dopant, such as ClO_4^- , and the large immobile DBS^- dopant have produced negative (out-of-phase) and positive (in-phase) voltages, respectively. Furthermore, the potentiostatic mode (current output) is more sensitive than the galvanostatic mode (voltage output) to employ the polymer as a displacement sensor. This is in agreement with the fact that while conducting polymers are excellent charge generators, they produce low voltages, as opposed to piezoelectric materials/generators. Takashima et al. (1997) reported on the mechanically induced current observed in polyaniline films under a tensile load, without considering the effect of dopant ions. The mechanism behind this “mechanochemoelectrical” behavior is said to be the stretching of the film that changes the polymer density and, hence, induces a redox current. The induced charge is proportional to the axial stress applied to the film.

Otero and his associates (Otero and Cortés 2003a, b) reported on touch sensing, suggesting that any device based on conducting polymers will sense every variable

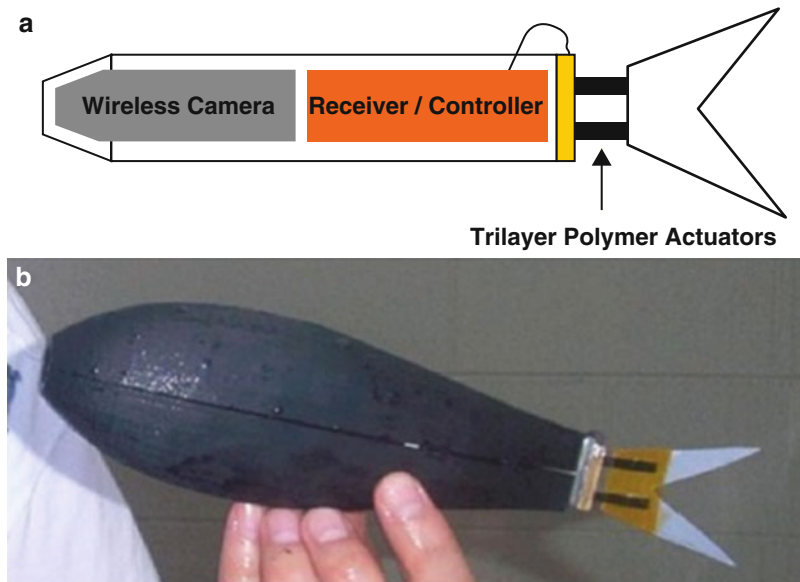


Fig. 18 (a) An overview of WANDA the fish articulated with $2\times$ tri-layer actuators and its optimized caudal fin arrangement (Fay et al. 2010; Carpi et al. 2011b) and (b) a photo of WANDA with its optimized body and caudal fin to minimize the drag force and increase its swimming efficiency, compared to NEMO

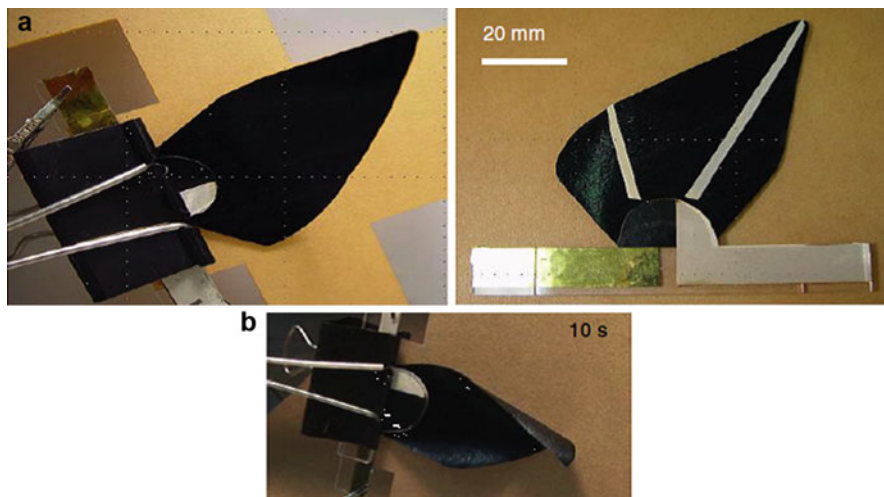


Fig. 19 (a) Views of the fin design using the tri-layer substrate as the fin's webbing and (b) when it generates a large cupping motion in 10 s (Reprinted with permission from James et al. 2007. Copyright (2007) Institute of Physics)

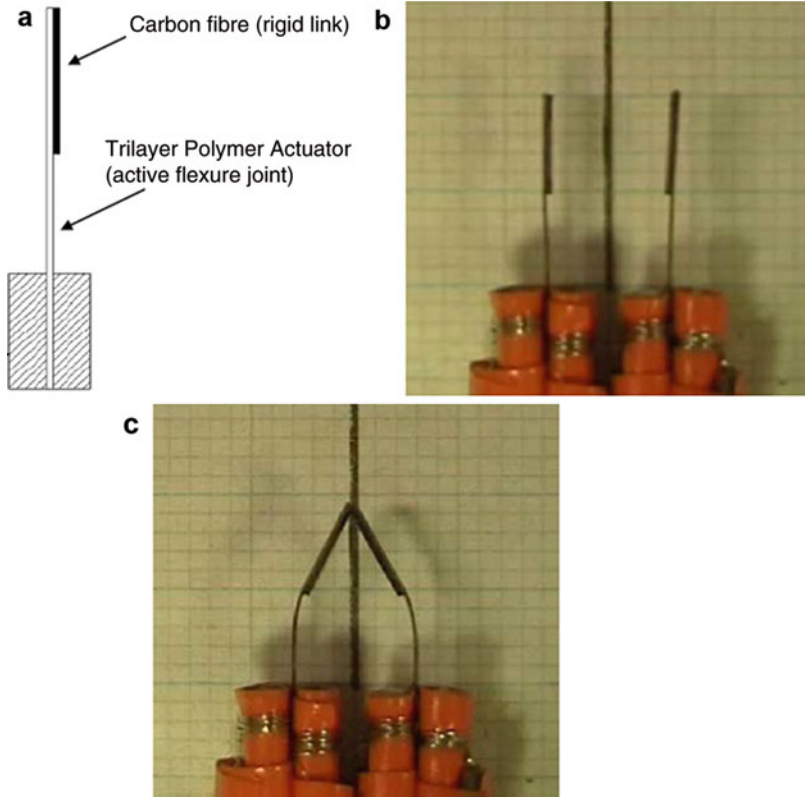


Fig. 20 (a) A schematic of the robotic finger, (b) and (c) views of a two-finger gripper articulated with tri-layer polymer actuators before activation and upon activation, respectively (Alici and Huynh 2007)

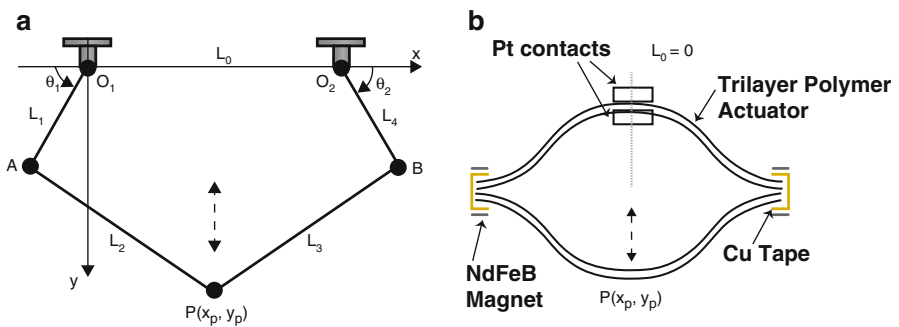


Fig. 21 (a) Linear actuation module based on a parallel five-bar mechanism and (b) the one articulated with the tri-layer actuators as the cranks and $L_0 = 0$ (Burriss et al. 2011)

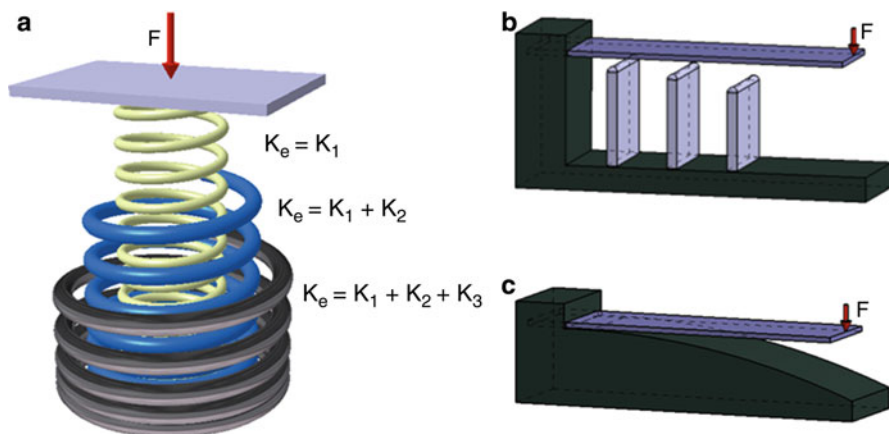


Fig. 22 (a) Discrete stiffening spring system, which has inspired to propose two ways, (a) and (b), of enhancing the effective stiffness of the tri-layer actuator configuration (Mutlu and Alici 2010a)

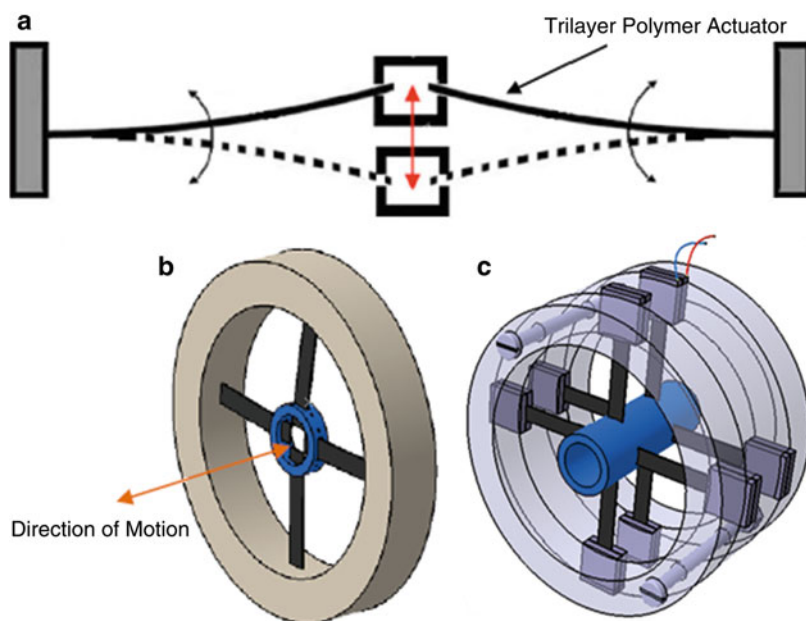


Fig. 23 (a) The concept of a multistable mechanism, and (b), (c) its application to propelling a shuttle with four and eight tri-layer actuators (Mutlu and Alici 2010b)

affecting the electrochemical reaction rate. The sensing concept is based on the fact that when a conjugated polymer actuator is driven by a constant current and comes across an obstacle in front of its trajectory, this will result in a potential difference, which indicates the presence of an obstacle. This actuation and sensing capability of

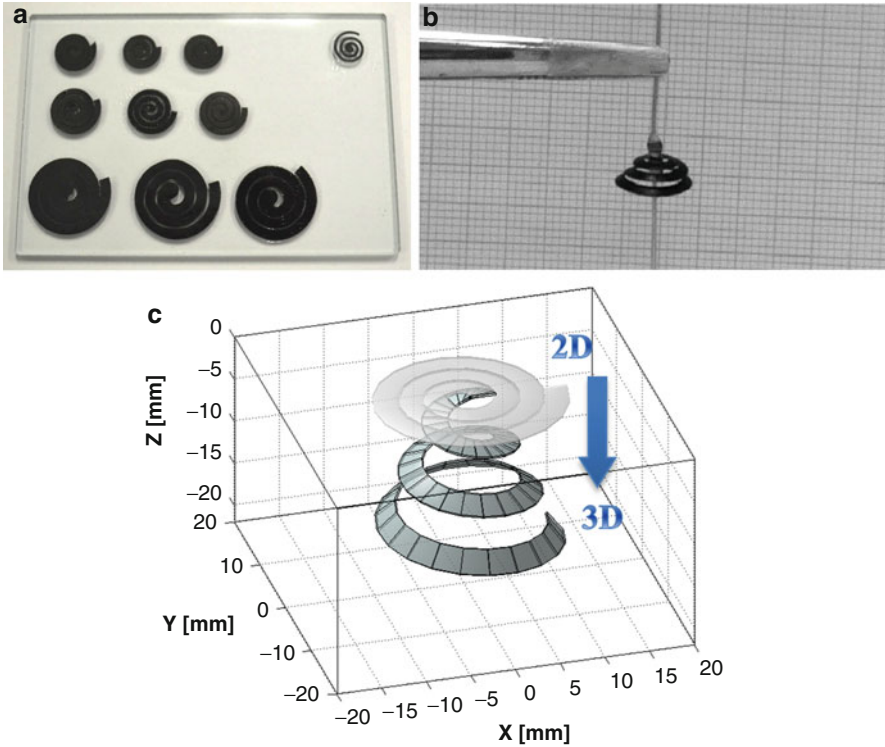


Fig. 24 The lamina emergent mechanisms based on the tri-layer configuration with different dimensions and its operation (Mutlu et al. 2011)

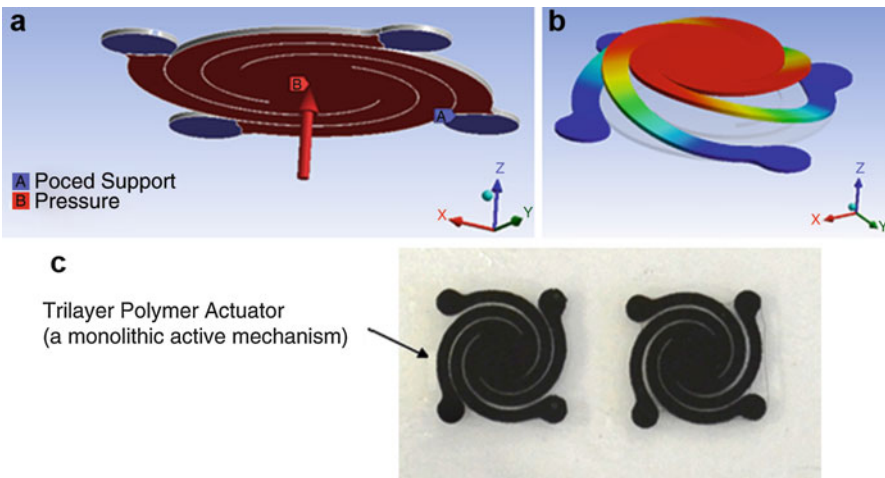
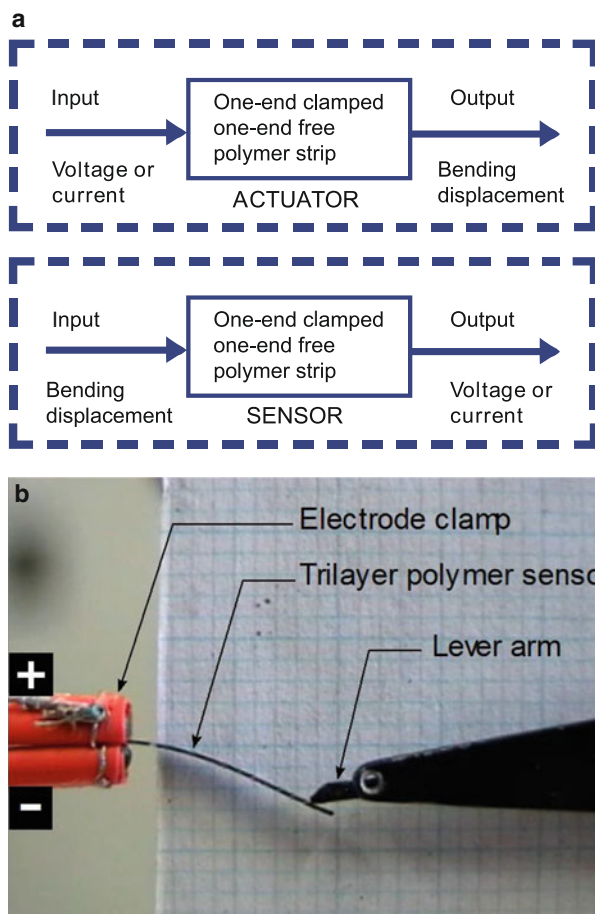


Fig. 25 A micro active-compliant lamina emergent mechanism as a linear positioner based on the tri-layer actuation configuration

Fig. 26 (a) Schematic representation of the actuation and sensing principles for the polymer transducers. (b) Configuration of a tri-layer polymer sensor (Alici et al. 2008)



the conjugated polymer is controlled simultaneously. The change in the potential difference and the change in corresponding electric energy consumed during the tactile sensing are linearly proportional to the mass of the object.

These mechanical displacement and/or force sensors, when miniaturized appropriately, can be embedded in flexible structures and can be used in biomedical applications such as implants and wearable sensing systems.

4 Device Configurations Based on PEDOT/PSS

Conducting polymer poly(3,4-ethylenedioxythiophene)/poly(styrene sulfonate) (PEDOT/PSS) which is a p-doped and water-soluble polymer is usually configured as a thin film using spin and spray coating, casting, ink-jet, screen and extrusion printing, photolithography and dry etching, subtractive patterning, and other

methods on flexible substrates. Blending with PSS makes PEDOT more conductive and processable. When reinforced with nanoparticles such as graphene, their electrical and thermal properties can be further improved in order to widen their applications (Ouyang et al. 2005; Nikolou and Malliaras 2008; Takano et al. 2012; Otero et al. 1992). The high conductivity of PEDOT/PSS has been exploited for optoelectronic devices, electrochromic displays, organic solar cells, polymer LEDs, actuators, and sensors. PEDOT/PSS films fabricated using one of those techniques are used as the electrodes of organic thin-film electronic components such as diodes, triodes, transistors, and others (Chen 2005). In this configuration, an electrolyte layer is employed to connect two PEDOT/PSS films. In another study (Mire et al. 2011), PEDOT/PSS conducting polymers are used to make conductive tracks embedded onto and into biopolymer films such as hydrogels, to be used as the electrodes of any functional devices. Similar to the configurations of PPy-based actuators presented in the previous sections, PEDOT/PSS-based thin film (Okuzaki et al. 2009a) and bilayer and tri-layer actuators have been proposed in the literature (Li et al. 2014; Okuzaki et al. 2009a, b, 2013, 2014; Taccola et al. 2013; Takahashi et al. 2005; Takano et al. 2012; Ikushima et al. 2010; Kim et al. 2013; Lee et al. 2005).

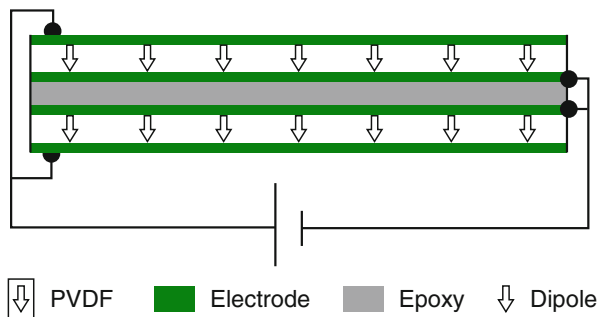
As an example to the thin-film configurations, Zainudeen et al. (2007) synthesized double (PEDOT/PPy)- or triple-layer (PPy/PEDOT/PPy) actuators consisting of PEDOT and PPy thin layers, which operate like a single-layer PPy actuator. Both polymers are electrochemically doped with dodecyl benzenesulfonate (DBS) anions. They suggest that these composite thin-film topologies improve the performance (i.e., mechanical output) of the film PPy actuators.

Taccola et al. (2013) have employed the spin-coating technique to build bilayer polymer actuators, which are in the form of microfingers, consisting of a PEDOT/PSS film spin-coated with SU-8, which is the structural passive layer in the bilayer configuration.

Okuzaki et al. (2009a) used Joule heating to desorb the water vapor to contract (i.e., actuate) a PEDOT/PSS film with a thickness of 21 μm , which generated approximately 2 % strain under 35 V. The electric current passing through the film and the surface temperature of the film were measured as 9 mA and 38 $^{\circ}\text{C}$, respectively, while generating this strain. The film returned to its initial length when the electrical input was turned off and the relative humidity of the environment/air reached 50 %. In another study, Okuzaki et al. (2013) used the PEDOT/PSS films as linear actuators, which showed significant contraction, which was due to the release of water vapor molecules absorbed in the film. These films were used to articulate (i) a lever to increase its mechanical advantage resulting in a leverage actuator and (ii) a Braille cell to demonstrate their suitability in establishing functional devices.

Lee et al. (2005) employed the PEDOT/PSS treated with a dimethyl sulfoxide (DMSO) solvent as the electrodes of all polymer bimorph cantilevers in which the piezoelectric polymer poly(vinylidene fluoride) (PVDF) was used as the active layers, as shown in Fig. 27. They compared the mechanical output of the bimorph cantilevers with the PEDOT/PSS (DMSO) electrodes and that of the inorganic electrodes such as platinum (Pt) and indium tin oxide (ITO). The cantilever with

Fig. 27 Schematic representation of the bimorph piezoelectric actuator where PEDOT/PSS (DMSO) electrodes are used to activate the bimorph actuator (Lee et al. 2005)



the PEDOT/PSS (DMSO) electrodes outperformed the others, under the same input voltage of 40 V, not only in the mechanical output but also in the stable operation with no damage due to the high deformation and operation frequency.

Recently, Kim et al. (2013) used PEDOT/PSS as the polymeric electrodes deposited on the top and bottom surfaces of the freeze-dried bacterial cellulose absorbed with the ionic liquids BMIM-Cl and EMIM-BF₄ to build a tri-layer actuator, similar to the configuration of the tri-layer PPy-based actuators. The actuator has generated a larger tip displacement than the same actuator configuration with metallic electrodes. Similarly, Ikushima et al. (2010) built a tri-layer actuator for autofocus micro lens applications, using PEDOT/PSS as the polymeric electrodes deposited on both surfaces of poly(vinylidene fluoride) (PVDF) film absorbed with an ionic liquid. They used polyethylene oxide (PEO) to enhance the electrical conductivity and breaking strain of the PEDOT/PSS films. Similarly, Okuzaki et al. (2014) assembled ionic liquid/polyurethane (IL/PU) gels with a thickness of 100 μm between two layers of PEDOT/PSS as the polymeric electrodes each with a thickness of 14 μm in order to establish a tri-layer polymer actuator. An actuator sample with the dimensions of 25 mm × 5 mm × 0.13 mm generated 0.32 % strain at 2 V. Recently, Li et al. (2014) prepared PEDOT/PSS/Xylitol (Xyl) films by casting as the soft electrodes of a tri-layer configuration consisting of ionic liquid/polyurethane (IL/PU) gels sandwiched between the PEDOT/PSS/ Xyl films. Compared to their previous study (Okuzaki et al. 2014), they used the Xylitol to weaken hydrogen bonds between PSS of colloidal particles and to increase the mobility of charge carriers between the particles. 0.15 % strain under 2 V was estimated for an actuator sample with the dimensions of 25 mm × 5 mm × 0.128 mm. Compared to the performance of the actuator in their previous study (Okuzaki et al. 2014), this new actuator could operate with frequencies up to 50 Hz.

5 Critical Research Issues and Outlook

Significant research work should be undertaken before conducting polymer transducers which can be used in establishing functional devices, beyond the prototypes built and tested in research environments.

Conducting polymers actuators have for a long time been considered as being too slow for use in many applications; they can take seconds or even tens of seconds to fully expand or contract (Smela and Gadegaard 2001) unless steps are taken to increase their rate of actuation. Over the years several different strategies have been employed to increase strain rates. However, although these approaches have been highly effective in increasing the speed of microactuators, this has still to be realized for larger-scale actuators.

The rate of actuation of conducting polymers can be limited by the diffusion of ions (Wang and Smela 2009) or holes (Kaneto et al. 1984; Tezuka and Aoki 1989; Tezuka et al. 1999) depending upon the device geometry. For bilayer devices actuation typically occurs at or near the surface of the conducting polymer film in contact with the electrolyte, with the volume of polymer capable of undergoing actuation depending upon the ability of ions to penetrate the polymer network. The state of the polymer network has a great influence on the rate of ion movement (Wang and Smela 2009); ion movement is slower in dense nonporous films compared to more open and porous networks. Strategies aimed at increasing the rate of ion diffusion into/out of the polymer have led to increases in actuation rates.

A simple strategy for increasing actuation rates is to employ thinner films (Melling et al. 2013). This ensures that the full thickness of the film is able to actuate. Another strategy has been to increase the porosity of polymer films by patterning them with arrays of holes (Lee et al. 2012). This approach increases the number and size of ion channels allowing quicker and deeper ion transport into the polymer film. Further improvements in actuator speeds have come as a result of the tri-layer structure, where the ion source is sandwiched between two thin conducting polymer films. This configuration ensures that the ions have shorter distances to move to fully penetrate and actuate the polymer. Increased strain rates have also resulted from the use of solid polymer electrolytes incorporated into the conducting polymer as part of an interpenetrating polymer network (Plesse et al. 2005). Here, the solid polymer electrolyte acts as the ion source, compensating redox charge on the neighboring conducting polymer network to comply with the requirement of charge neutrality. Since the polyelectrolyte is conveniently located only nanometers away, being part of a co-network, actuation rates are greatly increased rates. Using this approach Maziz et al. have recently produced microactuators that can operate at frequencies close to 1000 Hz (Maziz et al. 2014).

Strain rates have also been increased by employing an electrical potential greater than that required to fully reduce/oxidize the polymer. This increases the electric field within the polymer, accelerating the ions to greater speeds, and hence increases the rate of expansion. Unfortunately, the potential range that can be employed is restricted; if it is too large, decomposition of the polymer can occur, resulting in deterioration in performance and ultimately failure of the device. One way of overcoming this problem is to apply the driving potential for a small fraction of the actuation cycle to produce increased actuation rates while minimizing the risk of decomposition (Madden et al. 2000).

The bulk of the expansion of a conducting polymer occurs within in moments after the electric switching potential is applied (Melling et al. 2013). Therefore, if an

expansion of 50–80 % of the maximum expansion is acceptable for a given application, an increase in reversible expansion rate can be obtained, by accepting a lower expansion.

By shortening the distances (dimensions) that the ions need to move to compensate redox charge generated within the polymer, increased actuation rates can be achieved. Improvements brought about by scaling down device dimension are clearly of greatest benefit in the field of microactuators; however, for macroscale actuators to have similar benefits, they would need to be comprised of a large number of microactuators. The use of many small actuators working together to produce bulk movements is more closely analogous to muscle tissue. Through the implementation of clever design, such structures might be fabricated, in the future.

The deterioration in performance of conducting polymers with time is another critical issue that must be addressed if they are to be used in devices that are expected to undergo thousands/tens of thousands of cycles in service. For applications that require accurate positioning, electrochemical creep can lead to a positional drift, making the device ineffective (Madden et al. 2007). Increasing the strength of the conducting polymer, for example, by increasing cross-linking, reduces creep, but it also decreases the strain and strain rates (Tominaga et al. 2011). However, this decrease in actuation strain and strain rates may be the result of other factors such as electronic effects associated with N-cross-linking. The use of solid polymer electrolytes as interpenetrating polymer networks may be the key to producing more robust actuators that are capable of greater positional control (Festin et al. 2013, 2014). A better understanding of the relationship between network structure, electroactive performance, and strength is needed to produce mechanically strong conducting polymers without detrimental effects on performance.

The construction of macroscale actuators from large numbers (arrays or modules) of microactuators would not only lead to faster, stronger, and more efficient actuators but also result in them being more robust. Here, the failure of several individual microscale actuators would not result in device failure since the majority of the micro-devices would continue to function. If the device is engineered to a specification that exceeds the demands of the application, it can be operated at a lower specification resulting in an increased lifetime of service.

Another critical issue associated with the mechanical strength of conducting polymer actuators is the ability to modulate their strength/stiffness. The ability to modulate the stiffness (Young's modulus of elasticity) would allow variable stiffness devices to be developed that can be flexible or stiff as required. The Young's modulus of conducting polymers such as polypyrrole's is known to undergo a significant change between the fully reduced and oxidized states (Chiarelli et al. 1995; Murray et al. 1997). This innate property of conducting polymers might be a good starting point in the development of variable stiffness actuators.

Such devices would find numerous applications. In the case of swimming fishlike robots, flexible actuators can produce larger bending angles, whereas those with greater flexural rigidity can produce larger forces and quicker movements. Another example would be the development of flexible surgical devices such as guide wires that are capable of being safely guided along a complex three-dimensional path to

reach the intended target. Once the target has been reached, the end of the device could be made (out of necessity) to change its stiffness to tether the device and to apply forces, e.g., to grasp and excise tissue.

Increased understanding of the actuation and sensing mechanisms by physicists, chemists, and engineers (i.e., the development of physical and chemical models) will enable materials scientists to develop conducting polymers with improved properties. Conducting polymer actuators and sensors with improved properties may come as a result of improvements made to existing materials or through the development of completely new types of conducting polymers. Engineers, armed with improved forms of conducting polymers, will then increasingly use them in devices. In turn engineers can contribute to the development of the field by devising ingenious mechanisms employing scaled-down sets or arrays of actuators. Clearly a multidisciplinary approach will continue to be a requirement for the successful design of the conducting polymer actuators of the future.

Acknowledgments This work is partly supported by ARC Centre of Excellence for Electromaterials (ACES) (Grant Nos. CE0561616 and CE140100012). The authors wish to acknowledge that some of relevant studies in the published literature likely have not been included in this chapter due to purely the authors' oversight of those publications.

References

- Alici G (2009) An effective modelling approach to estimate nonlinear bending behaviour of cantilever type conducting polymer actuators. *Sens Actuators B Chem* 141:284–292
- Alici G, Higgins MJ (2009) Normal stiffness calibration of microfabricated tri-layer conducting polymer actuators. *Smart Mater Struct* 18:065013
- Alici G, Huynh NN (2007) Performance quantification of conducting polymer actuators for real applications: a microgripping system. *Mechatronics IEEE/ASME Trans* 12:73–84
- Alici G, Spinks G, Huynh NN, Sarmadi L, Minato R (2007) Establishment of a biomimetic device based on tri-layer polymer actuators – propulsion fins. *Bioinspir Biomim* 2:S18
- Alici G, Spinks GM, Madden JD, Yanzhe W, Wallace GG (2008) Response characterization of electroactive polymers as mechanical sensors. *Mechatronics IEEE/ASME Trans* 13:187–196
- Andrews MK, Jansen ML, Spinks GM, Zhou D, Wallace GG (2004) An integrated electrochemical sensor–actuator system. *Sens Actuators A Phys* 114:65–72
- Baughman RH (1996) Conducting polymer artificial muscles. *Synth Met* 78:339–353
- Baughman RH, Shacklette LW, Elsenbaumer RL, Plichta EJ, Becht C (1991) Molecular electronics. In: Lazarev PI (ed). Kluwer, Dordrecht, pp 267–289
- Bay L, West K, Sommer-Larsen P, Skaarup S, Benslimane M (2003) A conducting polymer artificial muscle with 12 % linear strain. *Adv Mater* 15:310–313
- Burriss E, Alici G, Spinks G, McGovern S (2011) Modelling and performance enhancement of a linear actuation mechanism using conducting polymers. In: Cetto J, Filipe J, Ferrier J-L (eds) *Informatics in control automation and robotics*. Springer, Berlin/Heidelberg, pp 63–78
- Carpi F, Smela E (2009) Biomedical applications of electroactive polymer actuators. Wiley, Chichester
- Carpi F, Frediani G, Turco S, De Rossi D (2011a) Bioinspired tunable lens with muscle-like electroactive elastomers. *Adv Funct Mater* 21:4152–4158
- Carpi F, Kombluh R, Sommer-Larsen P, Alici G (2011b) Electroactive polymer actuators as artificial muscles: are they ready for bioinspired applications? *Bioinspir Biomim* 6:045006

- Chen M (2005) Printed electrochemical devices using conducting polymers as active materials on flexible substrates. *Proc IEEE* 93:1339–1347
- Chiarelli P, De Rossi D, Della Santa A, Mazzoldi A (1994) Doping induced volume change in a π -conjugated conducting polymer. *Polym Gels Networks* 2:289–297
- Chiarelli P, Della Santa A, De Rossi D, Mazzoldi A (1995) Actuation properties of electrochemically driven polypyrrole free-standing films. *J Intell Mater Syst Struct* 6:32–37
- Christophersen M, Shapiro B, Smela E (2006) Characterization and modeling of PPy bilayer microactuators: part 1. Curvature. *Sens Actuators B* 115:596–609
- Conzuelo LV, Arias-Pardilla J, Cauch-Rodríguez JV, Smit MA, Otero TF (2010) Sensing and tactile artificial muscles from reactive materials. *Sensors* 10:2638–2674
- Della Santa A, De-Rossi D (1996) Intravascular microcatheters steered by conducting polymer actuators. In: *Engineering in medicine and biology society, 1996. Bridging disciplines for biomedicine. Proceedings of the 18th annual international conference of the IEEE*. Amsterdam, 5:2203–2204
- Della Santa A, De Rossi D, Mazzoldi A (1997) Performance and work capacity of a polypyrrole conducting polymer linear actuator. *Synth Met* 90:93–100
- Ding J, Liu L, Spinks GM, Zhou D, Wallace GG, Gillespie J (2003) High performance conducting polymer actuators utilising a tubular geometry and helical wire interconnects. *Synth Met* 138:391–398
- Eamex Hp In. Available: <http://eamex.co.jp/>. Accessed on 7 Nov 2014
- Fang Y, Tan X (2010) A novel diaphragm micropump actuated by conjugated polymer petals: fabrication, modeling, and experimental results. *Sens Actuators A Phys* 158:121–131
- Fay C, Lau KT, Beirne S et al (2010) Wireless aquatic navigator for detection and analysis (WANDA). *Sens Actuators B* 150:425–435
- Festin N, Maziz A, Plesse C, Teysié D, Chevrot C, Vidal F (2013) Robust solid polymer electrolyte for conducting IPN actuators. *Smart Mater Struct* 22:104005
- Festin N, Plesse C, Pirim P, Chevrot C, Vidal F (2014) Electro-active interpenetrating polymer networks actuators and strain sensors: fabrication, position control and sensing properties. *Sens Actuators B Chem* 193:82–88
- Gaihre B, Alici G, Spinks GM, Cairney JM (2012) Pushing the limits for microactuators based on electroactive polymers. *Microelectromech Syst J* 21:574–585
- Gaihre B, Ashraf S, Spinks GM, Innis PC, Wallace GG (2013) Comparative displacement study of bilayer actuators comprising of conducting polymers, fabricated from polypyrrole, poly(3,4-ethylenedioxythiophene) or poly(3,4-propylenedioxythiophene). *Sens Actuators A Phys* 193:48–53
- Gallardo-Alvarado J, Alici G, Rodríguez-Castro R (2012) A novel three degrees of freedom partially decoupled robot with linear actuators. *Robotica* 30:467–475
- Gandhi MR, Murray P, Spinks GM, Wallace GG (1995) Mechanism of electromechanical actuation in polypyrrole. *Synth Met* 73:247–256
- Grande H, Otero TF (1999) Conformational movements explain logarithmic relaxation in conducting polymers. *Electrochim Acta* 44:1893–1900
- Han G, Shi G (2004a) Conducting polymer electrochemical actuator made of high-strength three-layered composite films of polythiophene and polypyrrole. *Sens Actuators B Chem* 99:525–531
- Han G, Shi G (2004b) High-response tri-layer electrochemical actuators based on conducting polymer films. *J Electroanal Chem* 569:169–174
- Hara S, Zama T, Sewa S, Takashima W, Kaneto K (2003a) Highly stretchable and powerful polypyrrole linear actuators. *Chem Lett* 32:576–577
- Hara S, Zama T, Sewa S, Takashima W, Kaneto K (2003b) Polypyrrole-metal coil composites as fibrous artificial muscles. *Chem Lett* 32:800–801
- Hara S, Zama T, Ametani A, Takashima W, Kaneto K (2004a) Enhancement in electrochemical strain of a polypyrrole-metal composite film actuator. *J Mater Chem* 14:2724–2725
- Hara S, Zama T, Takashima W, Kaneto K (2004b) Artificial muscles based on polypyrrole actuators with large strain and stress induced electrically. *Polym J* 36:151–161

- Hara S, Zama T, Takashima W, Kaneto K (2004c) Gel-like polypyrrole based artificial muscles with extremely large strain. *Polym J* 36:933–936
- Hara S, Zama T, Takashima W, Kaneto K (2004d) Polypyrrole–metal coil composite actuators as artificial muscle fibres. *Synth Met* 146:47–55
- Hara S, Zama T, Takashima W, Kaneto K (2004e) TFSl-doped polypyrrole actuator with 26 % strain. *J Mater Chem* 14:1516–1517
- Hara S, Zama T, Takashima W, Kaneto K (2005a) Gel-like polypyrrole based artificial muscles with extremely large strain. *Polym J* 36:933–936.
- Hara S, Zama T, Takashima W, Kaneto K (2005b) Free-standing gel-like polypyrrole actuators doped with bis(perfluoroalkylsulfonyl)imide exhibiting extremely large strain. *Smart Mater Struct* 14:1501–1510.
- Hara S, Zama T, Takashima W, Kaneto K (2005c) Free-standing polypyrrole actuators with response rate of 10.8%/s. *Synth Met* 149(2-3): 199–201.
- Hara S, Zama T, Tanaka N, Takashima W, Kaneto K (2005d) Artificial fibular muscles with 20% strain based on polypyrrole-metal coil composites. *Chem Lett* 34:784–785.
- Hutchison AS, Lewis TW, Moulton SE, Spinks GM, Wallace GG (2000) Development of polypyrrole-based electromechanical actuators. *Synth Met* 113:121–127
- Ikushima K, John S, Ono A, Nagamitsu S (2010) PEDOT/PSS bending actuators for autofocus micro lens applications. *Synth Met* 160:1877–1883
- Jager EWH, Smela E, Inganäs O, Lundström I (1999) Polypyrrole micro actuators. *Synth Met* 102:1309–1310
- Jager EWH, Inganäs O, Lundström I (2000) Microrobots for micrometer-size objects in aqueous media: potential tools for single-cell manipulation. *Science* 288:2335–2338
- Jager EWH, Masurkar N, Nworah NF, Gaihre B, Alici G, Spinks GM (2013) Patterning and electrical interfacing of individually controllable conducting polymer microactuators. *Sens Actuators B Chem* 183:283–289
- James T, Patrick A, Timothy F, Angela C, Del Mike Z, Ian H (2007) The application of conducting polymers to a biorobotic fin propulsor. *Bioinspir Biomim* 2:S6
- John SW, Alici G, Cook CD (2008) Validation of resonant frequency model for polypyrrole trilayer actuators. *Mechatron IEEE/ASME Trans* 13:401–409
- John SW, Alici G, Spinks GM, Madden JD, Wallace GG (2009) Towards fully optimized conducting polymer bending sensors: the effect of geometry. *Smart Mater Struct* 18:085007
- Kaneko M, Fukui M, Takashima W, Kaneto K (1997) Electrolyte and strain dependences of chemomechanical deformation of polyaniline film. *Synth Met* 84:795–796
- Kaneto K, Ura S, Yoshino K, Inuishi Y (1984) Optical and electrical properties of electrochemically doped N- and P-type polythiophenes. *Jpn J Appl Phys Part 2 Lett* 23:189–191
- Kim S-S, Jeon J-H, Kee C-D, Oh I-K (2013) Electro-active hybrid actuators based on freeze-dried bacterial cellulose and PEDOT:PSS. *Smart Mater Struct* 22:085026
- Krogh M, Jager E (2007) Medical devices and methods for their fabrication and use. Google Patents
- Lee CS, Joo J, Han S, Koh SK (2005) An approach to durable PVDF cantilevers with highly conducting PEDOT/PSS (DMSO) electrodes. *Sensors Actuators A Phys* 121:373–381
- Lee KKC, Herman PR, Shoa T, Haque M, Madden JDW, Yang VXD (2012) Microstructuring of polypyrrole by maskless direct femtosecond laser ablation. *Adv Mater* 24:1243–1246
- Li Y, Tanigawa R, Okuzaki H (2014) Soft and flexible PEDOT/PSS films for applications to soft actuators. *Smart Mater Struct* 23:074010
- Lu W, Smela E, Adams P, Zuccarello G, Mattes BR (2004) Development of solid-in-hollow electrochemical linear actuators using highly conductive polyaniline. *Chem Mater* 16:1615–1621
- Madden JD, Cush RA, Kanigan TS, Brenan CJ, Hunter IW (1999) Encapsulated polypyrrole actuators. *Synth Met* 105:61–64
- Madden JD, Cush RA, Kanigan TS, Hunter IW (2000) Fast contracting polypyrrole actuators. *Synth Met* 113:185–192

- Madden JDW, Schmid B, Hechinger M, Lafontaine SR, Madden PGA, Hover FS, Kimball R, Hunter IW (2004) Application of polypyrrole actuators: feasibility of variable camber foils. *Ocean Eng IEEE J* 29:738–749
- Madden JD, Rinderknecht D, Anquetil PA, Hunter IW (2007) Creep and cycle life in polypyrrole actuators. *Sens Actuators A Phys* 133:210–217
- Martinez JG, Otero TF (2012) Biomimetic dual sensing-actuators: theoretical description. Sensing electrolyte concentration and driving current. *J Phys Chem B* 116:9223–9230
- Martinez JG, Otero TF (2014) Mechanical awareness from sensing artificial muscles: experiments and modeling. *Sens Actuators B Chem* 195:365–372
- Maziz A, Plesse C, Soyer C, Chevrot C, Teyssié D, Cattani E, Vidal F (2014) Demonstrating kHz frequency actuation for conducting polymer microactuators. *Adv Funct Mater* 24:4851–4859
- Mazzoldi A, De Rossi D (2000) Conductive-polymer-based structures for a steerable catheter. *Proceeding SPIE 3987, smart structures and materials 2000: Electroactive polymer actuators and devices (EAPAD)*. Newport Beach, CA, 3987:273–280
- Mazzoldi A, Degl'innocenti C, Michelucci M, De Rossi D (1998) Actuating properties of polyaniline fibers under electrochemical stimulation. *Mater Sci Eng C* 6:65–72
- McGovern S, Alici G, Truong V-T, Spinks G (2009) Finding NEMO (novel electromaterial muscle oscillator): a polypyrrole powered robotic fish with real-time wireless speed and directional control. *Smart Mater Struct* 18:095009
- Melling D, Wilson S, Jager EWH (2013) The effect of film thickness on polypyrrole actuation assessed using novel non-contact strain measurements. *Smart Mater Struct* 22:104021
- Mire CA, Agrawal A, Wallace GG, Calvert P, In Het Panhuis M (2011) Inkjet and extrusion printing of conducting poly(3,4-ethylenedioxythiophene) tracks on and embedded in biopolymer materials. *J Mater Chem* 21:2671–2678
- Murray P, Spinks GM, Wallace GG, Burford RP (1997) In-situ mechanical properties of tosylate doped (pTS) polypyrrole. *Synth Met* 84:847–848
- Mutlu R, Alici G (2010a) Artificial muscles with adjustable stiffness. *Smart Mater Struct* 19:045004
- Mutlu R, Alici G (2010b) A multistable linear actuation mechanism based on artificial muscles. *J Mech Des* 132:111001–111001
- Mutlu R, Alici G, Weihua L (2011) Kinematic modeling for artificial flagellum of a robotic bacterium based on electroactive polymer actuators. In: *Advanced intelligent mechatronics (AIM)*, 2011 IEEE/ASME international conference on, 3–7 July 2011. Budapest, pp 440–445
- Mutlu R, Alici G, Xiang X, Li W (2014) An active-compliant micro-stage based on EAP artificial muscles. In: *Advanced intelligent mechatronics (AIM)*, 2014 IEEE/ASME international conference on, 8–11 July 2014. Besançon, pp 611–616
- Nikolou M, Malliaras GG (2008) Applications of poly(3,4-ethylenedioxythiophene) doped with poly(styrene sulfonic acid) transistors in chemical and biological sensors. *Chem Rec* 8:13–22
- Okuzaki H, Suzuki H, Ito T (2009a) Electrically driven PEDOT/PSS actuators. *Synth Met* 159:2233–2236
- Okuzaki H, Suzuki H, Ito T (2009b) Electromechanical properties of poly(3,4-ethylenedioxythiophene)/poly(4-styrene sulfonate) films. *J Phys Chem B* 113:11378–11383
- Okuzaki H, Hosaka K, Suzuki H, Ito T (2013) Humidity-sensitive conducting polymer films and applications to linear actuators. *React Funct Polym* 73:986–992
- Okuzaki H, Takagi S, Hishiki F, Tanigawa R (2014) Ionic liquid/polyurethane/PEDOT:PSS composites for electro-active polymer actuators. *Sens Actuators B Chem* 194:59–63
- Otero TF, Cortés MT (2003a) Artificial muscles with tactile sensitivity. *Adv Mater* 15:279–282
- Otero TF, Cortés MT (2003b) A sensing muscle. *Sens Actuators B Chem* 96:152–156
- Otero TF, Cortés MT (2004) Artificial muscle: movement and position control. *Chem Commun* 3:284–285
- Otero TF, Martinez JG (2012) Artificial muscles: a tool to quantify exchanged solvent during biomimetic reactions. *Chem Mater* 24:4093–4099
- Otero TF, Martinez JG (2015) Physical and chemical awareness from sensing polymeric artificial muscles. *Experiments and modeling. Prog Polym Sci* 44:62–78

- Otero TF, Angulo E, Rodríguez J, Santamaría C (1992) Electrochemomechanical properties from a bilayer: polypyrrole/non-conducting and flexible material – artificial muscle. *J Electroanal Chem* 341:369–375
- Otero TF, Grande H, Rodríguez J (1997) Role of conformational relaxation on the voltammetric behavior of polypyrrole. Experiments and mathematical model. *J Phys Chem B* 101:8525–8533
- Otero TF, Cortés MT, Arenas GV (2007) Linear movements from two bending triple-layers. *Electrochim Acta* 53:1252–1258
- Otero TF, Martínez JG, Arias-Pardilla J (2012a) Biomimetic electrochemistry from conducting polymers. A review: artificial muscles, smart membranes, smart drug delivery and computer/neuron interfaces. *Electrochim Acta* 84:112–128
- Otero TF, Sanchez JJ, Martínez JG (2012b) Biomimetic dual sensing-actuators based on conducting polymers. Galvanostatic theoretical model for actuators sensing temperature. *J Phys Chem B* 116:5279–5290
- Otero TF, Martínez JG, Zaifoglu B (2013) Using reactive artificial muscles to determine water exchange during reactions. *Smart Mater Struct* 22:104019
- Otero TF, Martínez JG, Fuchiwaki M, Valero L (2014) Structural electrochemistry from freestanding polypyrrole films: full hydrogen inhibition from aqueous solutions. *Adv Funct Mater* 24:1265–1274
- Ouyang J, Chu CW, Chen FC, Xu Q, Yang Y (2005) High-conductivity poly(3,4-ethylenedioxythiophene):poly(styrene sulfonate) film and its application in polymer optoelectronic devices. *Adv Funct Mater* 15:203–208
- Pei Q, Inganaes O (1993) Electrochemical applications of the bending beam method. 2. Electroshrinking and slow relaxation in polypyrrole. *J Phys Chem* 97:6034–6041
- Pei Q, Inganlås O (1992) Conjugated polymers and the bending cantilever method: electrical muscles and smart devices. *Adv Mater* 4:277–278
- Plesse C, Vidal F, Randriamahazaka H, Teyssié D, Chevrot C (2005) Synthesis and characterization of conducting interpenetrating polymer networks for new actuators. *Polymer* 46:7771–7778
- Pyo M, Bohn CC, Smela E, Reynolds JR, Brennan AB (2003) Direct strain measurement of polypyrrole actuators controlled by the polymer/gold interface. *Chem Mater* 15:916–922
- Sansinena JM, Olazabal V, Otero TF, Polo Da Fonseca CN, De Paoli M-A (1997) A solid state artificial muscle based on polypyrrole and a solid polymeric electrolyte working in air. *Chem Commun* 22:2217–2218
- Santa AD, Mazzoldi A, De Rossi D (1996) Steerable microcatheters actuated by embedded conducting polymer structures. *J Intell Mater Syst Struct* 7:292–300
- Sfakiotakis M, Lane DM, Davies JBC (1999) Review of fish swimming modes for aquatic locomotion. *Ocean Eng IEEE J* 24:237–252
- Shoa T, Madden JD, Munce NR, Yang VXD (2009) Steerable catheters. In: Carpi F, Smela E (eds) *Biomedical applications of electroactive polymer actuators*. Wiley, Chichester, pp 229–248
- Shoa T, Madden JDW, Mirfakhrai T, Alici G, Spinks GM, Wallace GG (2010) Electromechanical coupling in polypyrrole sensors and actuators. *Sens Actuators A Phys* 161:127–133
- Smela E, Gadegaard N (2001) Volume change in polypyrrole studied by atomic force microscopy. *J Phys Chem B* 105:9395–9405
- Smela E, Kallenbach M, Holdenried J (1999) Electrochemically driven polypyrrole bilayers for moving and positioning bulk micromachined silicon plates. *Microelectromech Syst J* 8:373–383
- Spinks GM, Alici G, McGovern S, Xi B, Wallace GG (2009) Fundamental mechanisms of actuation in conducting polymers. In: Carpi F, Smela E (eds) *Biomedical applications of electroactive polymer actuators*. Wiley, Chichester, pp 195–228
- Taccola S, Greco F, Mazzolai B, Mattoli V, Jager EWH (2013) Thin film free-standing PEDOT:PSS/SU8 bilayer microactuators. *J Micromech Microeng* 23:117004
- Takahashi T, Ishihara M, Okuzaki H (2005) Poly(3,4-ethylenedioxythiophene)/poly(4-styrenesulfonate) microfibers. *Synth Met* 152:73–76

- Takano T, Masunaga H, Fujiwara A, Okuzaki H, Sasaki T (2012) PEDOT nanocrystal in highly conductive PEDOT:PSS polymer films. *Macromolecules* 45:3859–3865
- Takashima W, Uesugi T, Fukui M, Kaneko M, Kaneto K (1997) Mechanochemoelectrical effect of polyaniline film. *Synth Met* 85:1395–1396
- Tezuka Y, Aoki K (1989) Direct demonstration of the propagation theory of a conductive zone in a polypyrrole film by observing temporal and spatial variations of potentials at addressable microband array electrodes. *J Electroanal Chem* 273:161–168
- Tezuka Y, Aoki K, Ishii T (1999) Alternation of conducting zone from propagation-control to diffusion-control at polythiophene films by solvent substitution. *Electrochim Acta* 44:1871–1877
- Tominaga K, Hamai K, Gupta B, Kudoh Y, Takashima W, Prakash R, Kaneto K (2011) Suppression of electrochemical creep by cross-link in polypyrrole soft actuators. *Phys Procedia* 14:143–146
- Valero L, Arias-Pardilla J, Cauich-Rodríguez J, Smit MA, Otero TF (2011) Characterization of the movement of polypyrrole–dodecylbenzenesulfonate–perchlorate/tape artificial muscles. Faradaic control of reactive artificial molecular motors and muscles. *Electrochim Acta* 56:3721–3726
- Valero L, Otero TF, Martínez JG (2014) Exchanged cations and water during reactions in polypyrrole macroions from artificial muscles. *ChemPhysChem* 15:293–301
- Velmurugu Y, Skaarup S (2005) Ion and solvent transport in polypyrrole: experimental test of osmotic model. *Ionics* 11:370–374
- Wallace GG, Smyth M, Zhao H (1999) Conducting electroactive polymer-based biosensors. *TrAC Trends Anal Chem* 18:245–251
- Wang X, Smela E (2009) Color and volume change in PPy(DBS). *J Phys Chem C* 113:359–368
- Wang E, Liu Y, Samec Z, Dvořák C (1990) Charge transfer across a conducting polypyrrole membrane separated by two electrolyte solutions. *Electroanalysis* 2:623–629
- Wang X, Shapiro B, Smela E (2004) Visualizing ion currents in conjugated polymers. *Adv Mater* 16:1605–1609
- Wilson SA, Jourdain RPJ, Zhang Q et al (2007) New materials for micro-scale sensors and actuators: an engineering review. *Mater Sci Eng R Rep* 56:1–129
- Wu Y, Zhou D, Spinks GM, Innis PC, Megill WM, Wallace GG (2005) TITAN: a conducting polymer based microfluidic pump. *Smart Mater Struct* 14:1511–1516
- Wu Y, Alici G, Spinks GM, Wallace GG (2006) Fast trilayer polypyrrole bending actuators for high speed applications. *Synth Met* 156:1017–1022
- Wu Y, Alici G, Madden JDW, Spinks GM, Wallace GG (2007) Soft mechanical sensors through reverse actuation in polypyrrole. *Adv Funct Mater* 17:3216–3222
- Zainudeen UL, Careem MA, Skaarup S (2007) Actuators based on pedot and PPy conducting polymer bilayers and trilayers. In: *Industrial and information systems, 2007. ICIS 2007. International conference on*, 9–11 Aug 2007. Peradeniya, pp 461–464
- Zhou D, Wallace GG, Spinks GM, Liu L, Cowan R, Saunders E, Newbold C (2003) Actuators for the cochlear implant. *Synth Met* 135–136:39–40

Edwin W. H. Jager, Ali Maziz, and Alexandre Khaldi

Contents

1	Introduction: Why Microfabricating?	294
2	Facilities and Equipment	295
3	General Microfabrication Principles	296
4	Patterning and Subtractive Techniques	296
5	Additive Techniques	299
5.1	Chemical and Physical Vapour Deposition	299
5.2	Deposition of Conducting Polymers	300
5.3	Spin Coating	302
6	Microfabricating CP Actuators	302
6.1	Microactuator Using Bulk Volume Change	302
6.2	Bilayer Actuators	303
6.3	Trilayer Actuators	305
6.4	IPN Actuators	306
7	Integration of CP Actuators in Complex Devices	308
8	Interfacing and Actuation	312
9	Specifications, Performance, and Applications	314
10	Conclusion and Future Work	315
	References	315

Abstract

In this chapter, first some basic principles of photolithography and general microfabrication are introduced. These methods have been adapted to fit the microfabrication of conducting polymer actuators, resulting in a toolbox of techniques to engineer microsystems comprising CP microactuators, which will be explained in more detail. CP layers can be patterned using both subtractive and additive techniques to form CP microactuators in a variety of configurations

E.W.H. Jager (✉) • A. Maziz • A. Khaldi

Department of Physics, Chemistry and Biology (IFM), Linköping University, Linköping, Sweden
e-mail: edwin.jager@liu.se; ali.maziz@liu.se; alexandre.khaldi@liu.se

including bulk expansion, bilayer, and trilayer actuators. Methods to integrate CP microactuators into complex microsystems and interfaces to connect them to the outside world are also described. Finally, some specifications, performance, and a short introduction to various applications are presented.

Keywords

Actuation principle • Bilayer actuators • Cell-clinics • Conducting polymer actuators • Applications • Chemical and physical vapour deposition • Facilities and equipment • Integration in complex devices • Oxidative coupling • Patterning and subtractive techniques • Performance • Specifications • Spin coating • Trilayer actuators • Vapour phase polymerization • Dry etching technique • Electrochemical synthesis • Flexible printed circuit boards • Interpenetrating polymer network actuator • Photomasks • PPy • PPy bulk microactuator • Sacrificial layer technique • Soft lithography • Solid polymer electrolyte • Spin coating • Volume change • Wet etching

1 Introduction: Why Microfabricating?

As explained in more detail in the previous chapters, conducting polymers (CPs) undergo a volume change upon electrochemical oxidation or reduction by applying a low potential of 1–2 V. The volume change is predominantly caused by the insertion or ejection of ions and solvent into the polymer matrix (Pei and Inganäs 1992). This volume change is used to build actuators in different modes and devices, including microrobots (Jager et al. 2000a). Since the volume change is based on ion and solvent motion, the CP actuators need an ion source/sink to operate. This may be an external salt solution or an ionic liquid embedded in a polymer matrix that allows operation in normal atmosphere and also results in a major increase in cycle life time (Lu et al. 2002; Zhou et al. 2003; Vidal et al. 2004). As the actuation principle is based on ion and solvent movement into the polymer matrix, this ion diffusion is limiting the actuation rate. In order to achieve reasonably fast actuation, thin CP layers would be needed and the actuators should thus be microfabricated (Baughman et al. 1991; Jager et al. 2000b).

Not only physical limitations push for microfabricated CP actuators but also various applications require soft, low power/voltage, and compliant microactuators. Applications in fields such as MEMS/microsystem technology to power microUAV (Khaldi et al. 2011a), in microfluidics and Lab-on-a-Chip applications as small, integrated valves (Göttsche 2007), as actuators in microrobotics (Jager et al. 2000a) and medical devices such as catheters (Jager 2010), and in cell biology to manipulate and stimulate (single) cells (Jager et al. 2002; Svennersten et al. 2011), all have pushed the development of CP microactuators.

2 Facilities and Equipment

As the feature size, i.e., layer thickness and lateral dimensions, of the microactuators is reduced to the micrometer scale, higher demands are set to the processing environment and processing equipment. The minimal feature size has reached the same order of magnitude as (dust) particles, thus contamination with particles during the processing has to be avoided. Therefore, microfabrication is performed in a so-called clean room, a processing lab, or production area where the air is filtered from particles using HEPA filters and a laminar air flow prevents contamination from external sources. Clean rooms are classified according to cleanliness, i.e., the number of particles per volume. Often they are still referred to as class, e.g., 1000 or 10,000 (no of particles $\geq 0.5 \mu\text{m}/\text{ft}^3$) according to the old Federal Standard 209E, but this has been replaced by the ISO 14644-1 standard. An ISO 6 clean room is equivalent to a class 1000 clean room and ISO 7 to class 10,000. Most CP microfabrication is performed in clean rooms of class 100 (ISO 5) to class 10,000 (ISO 7). In addition to a controlled particle level, a clean room also has a well-controlled temperature and humidity to assure a good reproducibility of the processing, for instance, of the photoresist layers. This is also an advantage for the processability of the CPs.

As the construction and maintenance of a clean room requires a huge capital investment, it is also possible to do the processing of CP microfabrication using other means of providing a contamination controlled environment, such as laminar flow benches with HEPA filters.

Microfabrication also requires specialized equipment, most importantly a mask aligner. Often a microdevice comprises many different layers and structures that have to be aligned to each other with micrometer precision. For this, the mask aligner is used. A range of equipment for deposition of the various materials is needed: spin coaters for deposition of solution processable materials (such as photoresist and polymers), thermal evaporators, chemical vapour deposition (CVD) equipment, and sputtering systems. Some materials might need thermal treatments a post-processing requiring hot plates or (high T) ovens. After deposition, the layers need to be patterned for instance using dry etching methods for which a reactive ion etching (RIE) system may be used. Finally wet benches are required for development of the photoresist, wet chemical etching, and photoresist stripping after processing.

During and after the processing, the samples need to be inspected and characterized requiring equipment for characterization including optical microscopes, surface profilers, SEM, and ellipsometers. For more detailed information on clean room design and functionality as well as the equipment, we refer to text books such as Chang and Sze (1996) and Madou (1997).

In addition to the more classical microfabrication equipment, more recently developed methods like laser ablation and 3D printing require their own dedicated equipment.

3 General Microfabrication Principles

The microfabrication process starts by making a design of the microdevice including the CP microactuators using dedicated CAD software for photomask or circuit layout editing, or general drawing programs such as CorelDraw and Adobe Illustrator. During the CAD design phase, the device is divided into multiple layers. The design is then transferred to a photomask. One mask is needed for each separate layer of device, for instance, one for the metal layers including contact pads, one for the CP. As a photomask, either Cr masks or printed masks can be used. Cr masks are commonly used in microfabrication and the electronics industry. They are made of highly opaque Cr structures on highly transparent optical glass, have very high, sub-micron resolution, and when handled properly are very durable but are slightly expensive. The recent developments of high-resolution printers have also made printed photomasks a suitable option. The major advantage of printed photomask is the relatively low price, but resolution is limited typically down to 20–50 μm only, but this is often good enough for many CP-microactuator applications. Opacity of the plastic foil (small embedded particulates, granulometry) and limited opaqueness of the printed ink are other drawbacks. Photomasks can be made in house using a pattern generator or ordered from specialized photomask print shops.

Once the photomasks have been made, the traditional photolithography-based microfabrication typically comprises four steps:

1. Pattern transfer
2. Deposition/Additive techniques
3. Subtractive techniques
4. Remove photoresist

These steps are then repeated for each layer of the device.

In soft lithography, first a master or template is made (Xia and Whitesides 1998). This is commonly done using traditional microfabrication as mentioned above, for instance, a SU8 pattern on a Si wafer. Next a negative copy or stamp of the master is formed. PDMS is poured on the master, cured, and peeled, forming the PDMS stamp. This stamp can be used to pattern the layers similar to photolithography, to directly pattern similar to printing, by soft embossing, or used as a structural material, especially in microfluidics. For more details, we refer to reviews such as Xia and Whitesides (1998).

Technological advances have created a plethora of other, often direct, patterning methods with reasonable (tens to hundreds of micrometer) lateral resolutions. These include screen printing, inkjet printing, 3D printing or additive fabrication, and laser ablation.

4 Patterning and Subtractive Techniques

Direct or indirect patterning techniques can be used to microfabricate conjugated polymer devices. Indirect patterning is one commonly used technique in microelectronics industry and can be used for conjugated polymer patterning as well. This

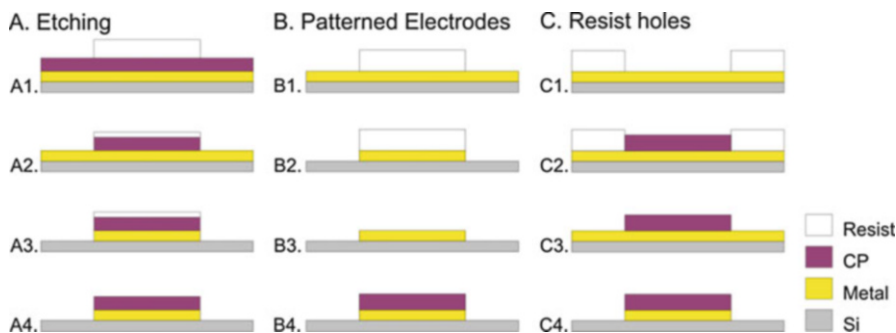


Fig. 1 Three different methods to pattern the CP layers. (A) Etching, e.g., using RIE: **A1** deposition of the patterned photoresist, **A2** etching of the CP layer, **A3** (wet chemical) etching of the metal layer, and finally **A4** stripping of the photoresist. (B) Patterned electrodes: **B1** deposition of the patterned photoresist, **B2** (wet chemical) etching of the metal layer, **B3** stripping of the photoresist, **B4** electrosynthesis of CP on the patterned metal electrode. (C) Resist holes: **C1** deposition of the patterned photoresist, **C2** electrosynthesis of CP in the patterned photoresist layer, **C3** stripping of the photoresist, **C4** (wet chemical) etching of the metal layer, depending on the etchant a protective photoresist layer similar to **A2** might be needed in this step

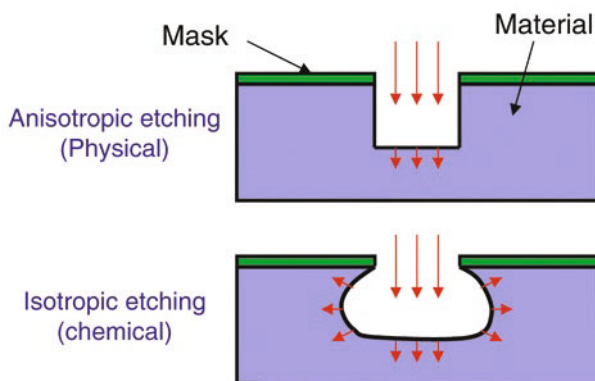
technique is composed of two steps: the first step uses photolithography to transfer the pattern and the second step is etching of the polymer layer to define the pattern.

A photoresist layer is deposited, generally by spin coating, on the layer to be patterned and exposed selectively through a mask transferring the micro-sized areas. The area of photoresist to remove is then solubilized in the proper solvent. One important consideration to take into account with polymers which is not present in classic inorganic semiconductor is the dimensional swelling effect. This swelling effect can create some failures in the underlying polymer layer or the photoresist, such as cracks which then will be transferred in the layer to be patterned due to the etching process. A photoresist containing a solvent of a formulation compatible with the polymer to be patterned should be selected. Photoresists known to work well with CPs are, for instance, the Shipley Microposit S1800 series.

Next, the etching step will be performed (see Fig. 1A). To be able to microfabricate conjugated polymer actuators, it is important to be able to remove the active layers with a controlled rate. The selectivity of the etching or etch rate of the CP layer compared to its protective photoresist layer should be as high as possible, taking into account the thickness of photoresist that can be deposited.

Wet etching is a technique of materials' degradation and/or solubilization. Wet etching is commonly used in microfabrication for instance to pattern metals or etch structures into silicon. This technique is particularly useful to pattern the other layers that might compose the architecture of the final targeted device. For instance, wet etching is often used to pattern the gold layer of a bilayer CP actuator (see Fig. 1). Recently, a wet etching recipe to pattern conjugated polymers has been presented, thus further increasing the toolbox of methods to fabricate CP microactuators (Taccolla et al. 2013).

Fig. 2 Different types of etch profile depending on the etch method used



The dry etching technique is more commonly used in order to get well-defined patterns with straight sidewalls. There exist several techniques to dry etch different types of materials. Reactive ion etching (RIE) is one of the most useful techniques to etch polymers (Taylor and Wolf 1980). Commonly a mixture of O_2 and CF_4 gases are used to etch polymers, where CF_4 allows increasing the reactive free radicals density in the plasma. Deep RIE, also named Bosch process or sputter etching, is also commonly used to etch the inorganic semiconducting materials and results in more vertical etched walls.

The etching profile can show different types of isotropy (Fig. 2) depending on its physical or chemical nature. Chemical etching leads to isotropic etching while physical (bombardment) etching leads to highly anisotropic structures.

A second way to (directly) pattern CPs is to electropolymerize on top of a patterned metal electrode (Fig. 1B). First, the microelectrode is formed, e.g., by (wet chemical) etching or lift-off, and then the CP is synthesized from solution as described in Sect. 5.2 directly on the electrode surface, resulting in in-situ patterning. Another way to achieve in-situ patterning of CP layers is to electropolymerize the CP layer in “resist holes” (Fig. 1C). A resist layer is patterned with openings, or holes, that expose the underlying metal layer to the polymerization solution. The CP layer can then be grown in this hole. Care has to be taken that the photoresist layer is thicker than the intended CP layer, otherwise the CP will grow over the edges of the photoresist, resulting in a poor pattern definition.

Recently, some more of direct patterning techniques have been developed, especially using printing methods. The CP layers can be deposited by inkjet printing, screen printing, or reel-to-reel printing. Additive fabrication or 3D printing can give resolution of pattern of $100\ \mu\text{m}$. This technique has still not been used for printing conjugated polymers itself but fabricate good 3D support structures with a well-controlled architecture.

Finally, laser ablation or laser cutting allows the fabrication of pattern with a resolution of down to $50\ \mu\text{m}$. It has been used to demonstrate the first conjugated microactuator working in air (Alici et al. 2009).

Although not truly a subtractive method, overoxidation is useful technique for patterning conducting polymers. Overoxidation is an irreversible loss of electrical conductivity due to breakage of the conjugation in the polymer backbone (Tehrani et al. 2005). The overoxidation can be done locally on microsized areas using fast, inexpensive printing techniques such as screen printing or dipping the sample covered with a photoresist pattern in an electrolyte. It is important to notice that with this technique the overoxidized polymer is not physically removed. Only the conductivity is destroyed and the material becomes part of the structure in the final targeted micropatterned device. It can for instance be useful to pattern conductive lines (Faxälv et al. 2014).

5 Additive Techniques

In addition to the mentioned common methods for patterning conducting polymers, i.e., lithography and etching, further development of the structures and pattern transfer may require some additive thin-film deposition techniques which involve that solids such as metals and polymers are deposited onto a substrate. Here we will describe some additives techniques commonly used in microelectronics and that can be utilized in devices comprising CP microactuators. The thin-film deposition may be done through liquid-phase chemical techniques, gas-phase chemical processes, glow discharge processes or evaporation methods (Glocker et al. 1995). Two major categories can be distinguished according to the nature of deposition process: depositions that occur through chemical reactions (Chemical Vapour deposition CVD, liquid phase epitaxy, thermal oxidation) or depositions that happen through a physical reaction (physical vapour deposition (PVD) processes or casting from solution). For more detailed information on the various methods, we refer to microfabrication handbooks such as (Chang and Sze 1996; Madou 1997).

5.1 Chemical and Physical Vapour Deposition

CVD and PVD are probably the two most used methods for thin-film deposition, each one providing interesting features and benefits. CVD is very versatile and can be used to deposit a large variety of elements and compounds and to produce solid materials over large areas with high purity. Typically, CVD refers to a chemical process where one or more gaseous precursors are transported to the reaction chamber and react and/or decompose on a substrate surface to produce a thin film. The precursors are activated thermally; sometimes assisted using, for instance, radio-frequency radiation in what is called plasma-enhanced CVD (PECVD). However, the use of high process temperatures is usually not recommended for structures that already comprise micropatterned CP or other polymers on substrate.

On the other hand, PVD involves purely physical processes, such as high-vacuum evaporation or plasma sputter bombardment, in which material is released from a source and transferred to the substrate. In thermal evaporation, the source material is

sublimed which thereafter condenses on the substrate. In sputtering a target, the material to be deposited is bombarded by inert gas ions that physically remove the material atoms which in their turn are deposited on the substrate. There are some advantages that make PVD more attractive for some applications comprising patterning of conducting polymers. The PVD process can be carried out at lower-deposition temperatures, but deposition rates are typically lower. Also, it is a more environment friendly, simpler, and cheaper process than CVD.

5.2 Deposition of Conducting Polymers

The properties of conducting polymer are strongly dependent on their synthesis conditions. To achieve a good conductivity, it is required that the conjugated nature of the monomer is conserved in the repeating unit during the polymerization process, which strongly limits both the choice of monomer and the choice of the deposition pathway. As explained in more detail in the previous chapters, the polymerization of designated conducting polymer monomers can be carried in many ways. However, the most widely used technique is the oxidative coupling involving the oxidation of monomers via chemical or electrochemical routes (Chao and March 1988; Diaz et al. 1986; Machida et al. 1989; Rapi et al. 1988).

The simplicity, high selectivity, and reproducibility have made electrochemical synthesis the preferred method to synthesize conducting polymers for actuator applications. It has the advantage of producing the material on an electrode facilitating further analysis and hence eliminating processability problems. Moreover, the electrochemical route has the advantage to allow a good control of the polymer thickness, morphology, and degree of the polymer doping by controlling the synthesis parameters such as the quantity of charge passed during the deposition process. The electrosynthesis is usually achieved using a two- or three-electrode system through the electro-oxidation of a given monomer (e.g., pyrrole or 3,4-ethylenedioxythiophene) in a solution containing a supporting electrolyte (Fig. 3). This maybe an inert organic solvent, such as propylene carbonate with, e. g., bis(trifluoromethane)sulfonimide lithium (LiTFSI) or an aqueous electrolyte, typically sodium dodecylbenzenesulfonate (NaDBS). As mentioned, conducting polymers are deposited on conducting substrates, such as gold, stainless steel, platinum, indium-tin oxide (ITO)-coated glass, or more recently conducting polymers-coated membranes (Temmer et al. 2013). The electrochemical polymerization process can be performed using different ways of application of the current or the potential to the conducting substrate. The simplest electrochemical methods include potentiostatic or galvanostatic (constant potential and constant current, respectively) methods, but potentiodynamic methods have also been employed.

Conjugated polymers can often also be synthesized using a chemical oxidative polymerization. Distinct advantages of the chemical route over electrochemical synthesis are that there is no need for electrochemical instruments such as a potentiostat and that also nonconductive surfaces can be coated. Moreover, chemical polymerization is known to be simple and fast method and strongly recommended if

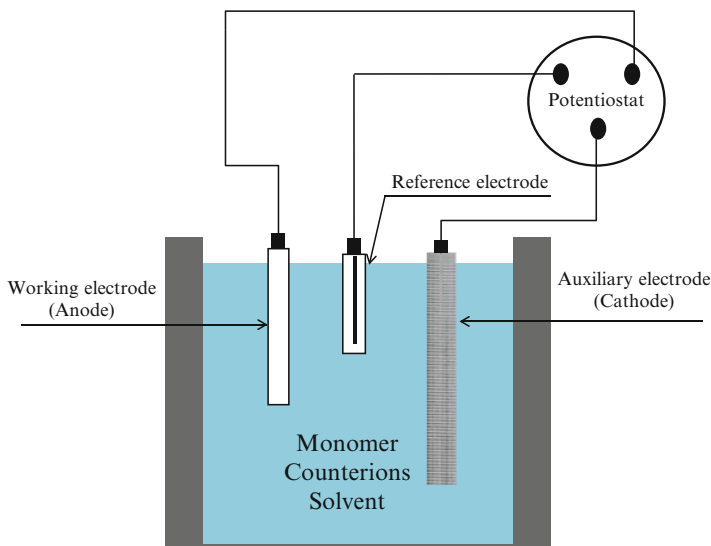


Fig. 3 A three-electrode electrochemical polymerization cell. The sample, for instance the Si wafer with the microdevices is connected as the working electrode

large amounts of conjugated polymer are needed. In typical chemical polymerization, an oxidizing reagent such as iron (III) chloride is used in aqueous or nonaqueous solvents (Kanazawa et al. 1979; Sugimoto et al. 1986) to produce polymer in the conducting form. Although other oxidizing agents can be used as well (Castillo-Ortega et al. 1989), iron (III) chloride was found to be one of the most efficient oxidants for pyrrole or EDOT polymerization because of high polymerization yield. In chemical synthesis, however, it is difficult to get a direct control over the polymer deposition that results in a lack of accuracy and reproducibility.

An alternative chemical synthesis method to conventional solution-based CP deposition is the so-called vapour phase polymerization (VPP) technique (Mohammadi et al. 1986; Kim et al. 2003; Winther-Jensen and West 2004; Winther-Jensen et al. 2005; Fabretto et al. 2008). There is much interest in this method because it provides high control over CP film thickness, uniformity, and density. Typically, the formation of conjugated polymers is carried out directly on the surface of the substrate in a two-step process. First, the oxidant such as iron tosylate in *n*-butanol is applied on the substrate using solvent coating processes and then the coated surface is exposed to a reactive CP monomer vapour. PEDOT films have been reported to have with conductivities as high as approximately $3400 \text{ S}\cdot\text{cm}^{-1}$ or S cm^{-1} for a thickness of 60 nm, which is equivalent to commercially available indium tin oxide (ITO) (Fabretto et al. 2012).

CP processing using commonly employed deposition methods such as spin-coating, solvent-casting, or ink-jet printing is virtually impossible since these conjugated polymers are relatively insoluble in most solvents. To overcome this problem, alternative synthetic routes have been proposed which involve the attachment

of soluble functional groups to the polymer or doping with stabilizing polyelectrolytes (Cao et al. 1992; Heywang and Jonas 1992; Hide et al. 1996; Kobayashi et al. 1985). An aqueous dispersion of poly(3,4-ethylenedioxythiophene)-poly(styrenesulfonate) (PEDOT:PSS) is commercially available under the brand names Baytron P or Clevios P.

5.3 Spin Coating

In spin coating, a material is processed from a solution, and this method is typically used for passive polymers that form structural layers in the device such as SU8 and polyimide. The solution is cast on a fast rotating substrate that ensures a well-defined and reproducible layer thickness. The spin-coated layer can be photopatternable meaning that the layer can be patterned using UV radiation that either cross-links or destroys the exposed areas. Negative and positive photoresists, although not a structural layer, are examples of UV patternable polymers. If not photopatternable, dry etching methods combined with photolithography are typically employed to shape the structural layers.

Also some conducting polymers can be deposited using spin coating. Especially PEDOT:PSS (also known under the brand names Baytron P and Clevios P) is often deposited from dispersion. Recently, spin coating the electromechanically active CP layer has been demonstrated for the first time (Taccola et al. 2013).

6 Microfabricating CP Actuators

Using a combination of the previously described patterning, additive, and/or subtractive methods, CP actuators have been down scaled to micrometer sizes and designed in a variety of configurations: microactuators that use the bulk volume change (Sect. 6.1); bending bilayer or unimorph microactuators (Sect. 6.2); and bending trilayer or bimorph actuators (Sects. 6.3 and 6.4). In the bulk and bilayer microactuators, typically an external electrolyte is used as the ion source/sink. However, this restricts the actuators from operating in air. Therefore, trilayer microactuators have been developed, where an electrolyte containing layer is sandwiched between two CP actuating layers, either as a three layered actuator (Sect. 6.3) or as an interpenetrating polymer network actuator (Sect. 6.4). Buckling microactuators are similar in processing and operation as the bilayer or trilayer bending actuators, but they have been attached or clamped on at least two sides.

6.1 Microactuator Using Bulk Volume Change

The simplest CP microactuator is a micropatterned structure that is fixed on the substrate, in contrast to the bending actuators that can freely move. Electrochemical stimulation will cause its volume to increase, i.e., to actuate. These bulk actuators are

typically microfabricated by electrochemical synthesis on patterned electrodes (Berdichevsky and Lo 2003; Yamada et al. 1998) or in photoresist or SU8 holes (Svennersten et al. 2011; Wang et al. 2008) as explained in Fig. 1.

6.2 Bilayer Actuators

The traditional method to microfabricate freely moving actuators is to use a sacrificial layer. This method is also used for CP microactuators (Smela et al. 1993; Jager et al. 2000a). On the substrate, first a so-called sacrificial layer is deposited and patterned (Fig. 4A). On top of the sacrificial layer, the structural and CP layers are deposited and patterned. In the last step the sacrificial layer is removed and the actuator is released. If the actuator is to remain on the substrate, the actuator has to only partially cover the sacrificial layer so that it is also still attached to the substrate. It is also possible to completely remove the actuators from the substrate (Taccola et al. 2013), which is common practice for IPN microactuators (Sect. 6.3). In those cases, the sacrificial layer or intermediate layer is larger than the actuator size.

As a variant thereof one can, instead of removing a sacrificial layer, completely etch the substrate to release the actuators (Smela et al. 1999). First, the CP microactuators are patterned using the previous described methods (Fig. 4B). Thereafter, the backside of the substrate is patterned and the substrate is etched until it reached the actuator. Possibly an etch-stop has to be employed. This method allows to fabricate any structure or device on a substrate that thereafter can be (re-)positioned by the CP microactuator (Smela 1999a).

A modification of the latter method was developed by Krogh and Jager to gain access to both sides of the actuator during fabrication in order to minimize contamination with different processing solutions that were needed during the fabrication (Jager and Krogh 2003). The reduction of contamination of processing solutions is especially important for applications such as medical devices. The sacrificial layer and substrate methods are based on bottom up fabrication, i.e., layers are added successively onto the substrate thus building the actuator or device. In this membrane method, first the passive structural layer of the CP microactuator is deposited on the substrate, and the substrate is partially bulk etched forming a membrane (Fig. 4C). This membrane can now be accessed on both sides, for instance, to sequentially deposit the PPy active layer and a polyurethane blood-compatible polymer coating on the opposing sides of the membrane, forming a three-layered unimorph microactuator. In the final step, the actuator can be cut out of the frame using, e.g., laser ablation.

The sacrificial layer techniques can be difficult to apply as they require a delicate choice of materials and etching methods that might not be compatible with the CPs. Also, the method introduces a step and thus a weak spot in the actuator (see Fig. 4A4). Therefore, a new method was developed that utilizes the poor adhesion between two materials, e.g., between Au and Si, the so-called differential adhesion method (Smela et al. 1995). First, an adhesive frame is patterned on the substrate that surrounds the actuator, except for an anchoring point (Fig. 4D). In the case of Si and

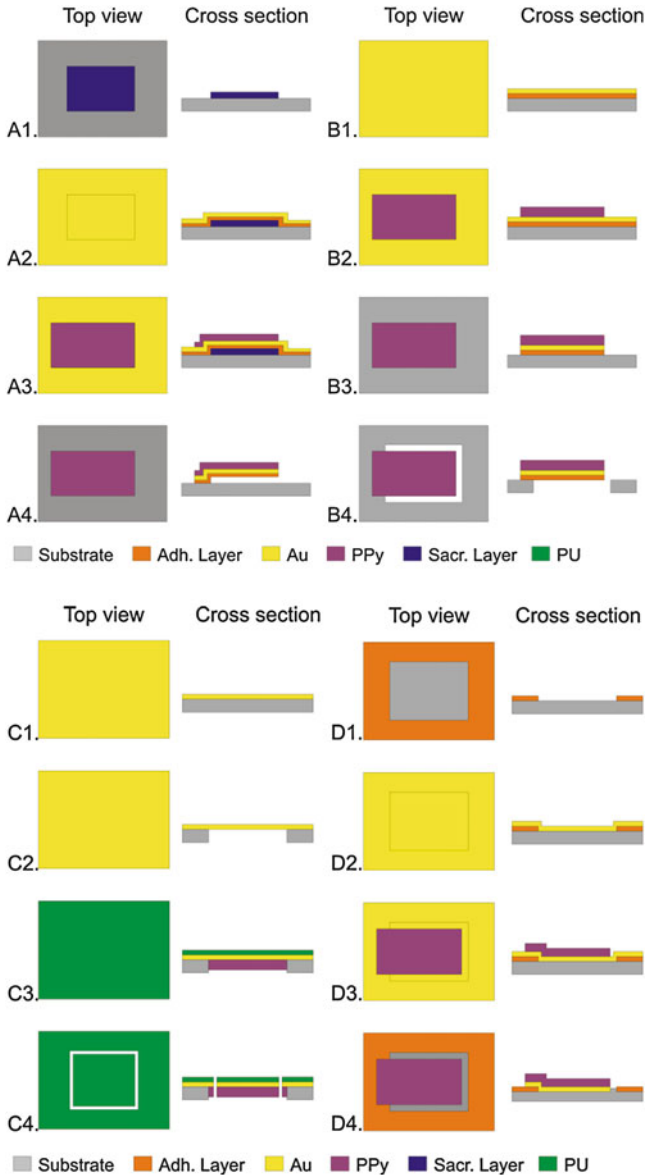


Fig. 4 Schematic overview of the different fabrication methods for bilayer actuators: (A1–A4) Sacrificial layer, (B1–B4) bulk etching of the substrate, (C1–C4) membrane fabrication, and (D1–D4) Differential adhesion. A1 Deposition and patterning of sacrificial layer on the substrate. A2 Deposition of the adhesion and Au structural layers. A3 Deposition and patterning of the PPy layer. A4 Patterning and etching of the final PPy microactuator structure and etching of the sacrificial layer, resulting in a free microactuator. B1 Deposition of the adhesion and Au structural layers. B2 Deposition and patterning of the PPy layer. B3 Patterning and etching of the final PPy microactuator structure. B4 Bulk etching of the substrate to release the microactuator. C1

Au, Ti or Cr is used as the adhesion promoting layer. On this patterned adhesive layer, the passive structural layer, e.g., Au, is deposited. Next, the active PPy layer is deposited and patterned and any eventual further processing is performed. Finally, the differential adhesion layer (e.g., Au) is etched. After this etching, the actuator is no longer attached to the adhesive frame. It is only attached to the substrate at the anchor point. Elsewhere, it is held onto the substrate only by the poor adhesive forces to the substrate surface. When the CP microactuator is actuated for the first time, it pulls itself free from the surface. A limitation of the differential adhesion method is that it is restricted to a few material combinations, such as Au and Si. Figure 5 shows a microfabricated self-assembling octahedron with PPy/Au bilayer hinge microactuators and SU8 rigid plates on a Si wafer. The octahedron can be reversibly folded and unfolded.

6.3 Trilayer Actuators

Trilayer actuators architecture have been proposed in 1996 by Baughman (1996) to allow their operation in air because the middle layer acts as an ion reservoir necessary for oxidation-reduction process. Several of these macroactuator architectures have been realized using classical electrodeposition methods of CP. This architecture has been downscaled to microsized structures for the first time in 2009 by G. Alici et al. (2009). They used the laser ablation to cut the PPy/PVDF/PPy trilayer actuators into microbeam shapes. They were able to fabricate trilayer microactuators with a size of $850 \times 250 \times 170 \mu\text{m}^3$ using this technique.

In these first trilayer microactuators, thick commercial PVDF membranes were utilized as the electrolyte storage layer. In order to further miniaturize the actuator while keeping acceptable form factors (length to width and width to thickness ratios) and increase the bending angle, porous PVDF thin films were synthesized with a thickness of $32 \mu\text{m}$ (Gaihre et al. 2011b). It has been possible to decrease the size of the microactuator to $200 \times 50 \times 48 \mu\text{m}^3$ (Fig. 6). They also demonstrated that when the size of the microactuators decreases, the produced strain energy by unit of mass or volume is higher (Gaihre et al. 2012).

The trilayer microactuators were simple, single bending actuators. A new method of fabrication has been described by Jager et al. to pattern the microtrilayer actuators using photolithography to allow for individual control of multiple actuators on a single device (Jager et al. 2013b). This method starts with patterning the conducting electrode and actuator structures using wet chemical etching followed by

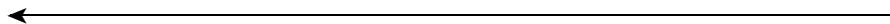


Fig. 4 (continued) Deposition of Au structural layer on substrate. **C2** Bulk etching of the substrate, giving the Au membrane. **C3** Deposition of PPy on bottom side and polyurethane layer on top side. **C4** Cutting out the PPy microactuator from the substrate frame. **D1** Deposition and patterning of the adhesion layer (e.g., Cr or Ti) on the substrate (e.g., Si). **D2** Deposition of Au structural layer. **D3** Deposition and patterning of the PPy layer. **D4** Patterning and etching of the final microactuator structure. The PPy microactuator will release itself from the substrate during the first cycles due to the poor Au-Si adhesion

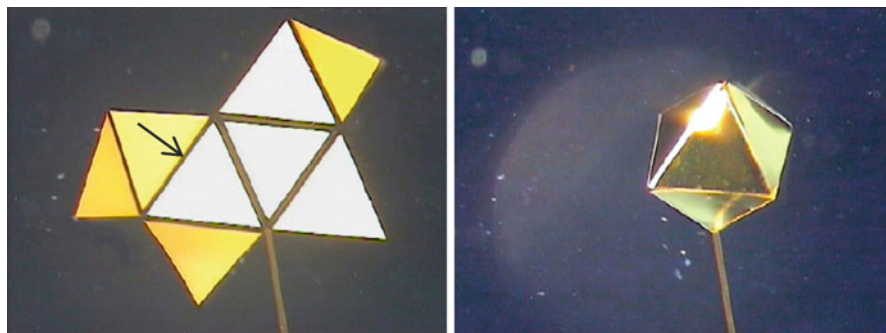


Fig. 5 Folding of a micromachined octahedron with PPy/Au bilayer microactuator hinges on a Si wafer. One of the microactuators is indicated by an *arrow*. The octahedron can be reversibly folded and unfolded (Reproduced from Wilson et al. (2007))

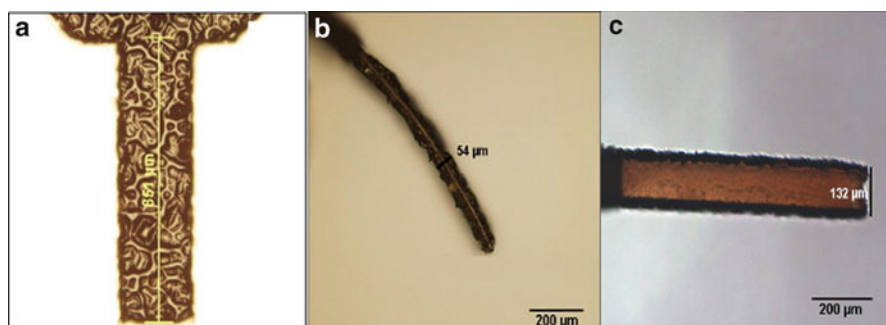


Fig. 6 Top view of (a) 851 μm long PPy trilayer microactuator and cross sections of PPy trilayer microactuators with thicknesses of (b) 54 μm and (c) 132 μm (Reproduced from Gaihre et al. (2011a))

electrochemical synthesis of the active PPy layers. These systems are still under development and could lead to integration in soft robotics and biomedical applications.

6.4 IPN Actuators

The diffusion phenomena of ions and solvents into the CP are the rate-limiting step in the actuation performance. Therefore, high actuation speed can be achieved either by increasing the ionic conductivity, i.e., to obtain high ion diffusion rate through the solid polymer electrolyte (SPE) and/or reducing the distance between the electroactive layers, i.e., the ion diffusion distance is minimized by decreasing the thickness of the SPE (Madden et al. 2000; Wu et al. 2006; Gaihre et al. 2011b). The SPE has consequently an important role in miniaturization of these

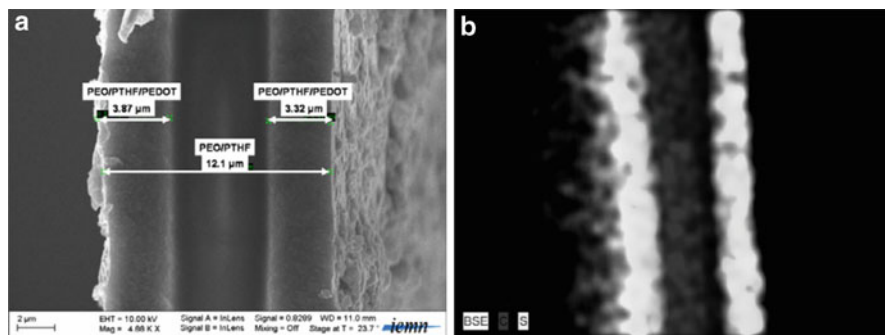


Fig. 7 (a) SEM image of the PEO-PTHF IPN cross section without ionic liquid. (b) The host matrix and PEDOT electrodes are clearly distinguished by EDS mapping analysis on sulphur atoms (Reproduced from Khaldi et al. (2011b))

electrochemomechanical systems and hinder further progress in the integration conducting polymer actuators into microsystems. Interpenetrating polymer networks (IPNs) are an interesting candidate as SPE for electrochemomechanical devices as they can combine a variety of physical properties needed for the device, including elasticity, mechanical strength, and ionic conductivity (Klempner et al. 1994; Sperling 2004). IPNs are described as a combination of two or more cross-linked polymers. The entanglement of the two networks ensures a good interpenetration of the mixed components and thus a radical improvement of the dimensional and morphological stability. By an appropriate choice of the two IPN polymer partners, it is possible to combine the rubbery properties of the first partner with the ionic conduction properties of the second one. When a CP such as PEDOT is incorporated in such an IPN, it can be turned into an actuator (Vidal et al. 2003, 2004; Plesse et al. 2005).

Microfabricated conducting IPN actuators were demonstrated for the first time at Cergy-Pontoise University by Vidal and co-workers (Khaldi et al. 2011b; Maziz et al. 2014). They developed new IPN membranes based on poly(ethylene oxide) (PEO) and either polytetrahydrofuran (PTHF) or nitrile butadiene rubber (NBR). In the SPE IPN membrane, one polymer network is mainly used as the SPE, i.e., PEO, whereas the second one provides the good mechanical properties needed for the devices. They have reduced the IPNs thicknesses using either a hot pressing method, resulting in 12 μm thin PEO-PTHF IPN layer (Khaldi et al. 2011b) or by spin-coating the PEO-NBR starting material mixture, resulting in tunable thickness from 30 μm down to 600 nm (Maziz et al. 2014). Two electroactive PEDOT layers were thereafter interpenetrated using chemical polymerization in both faces of the IPNs, leading to a pseudotrilayer configuration. The developed synthetic pathway ensures a nonhomogeneous distribution of PEDOT throughout the film thickness, i.e., PEDOT layers are interpenetrated only partially in the IPNs as two separate and parallel electrodes, mimicking a trilayer configuration (see Fig. 7).

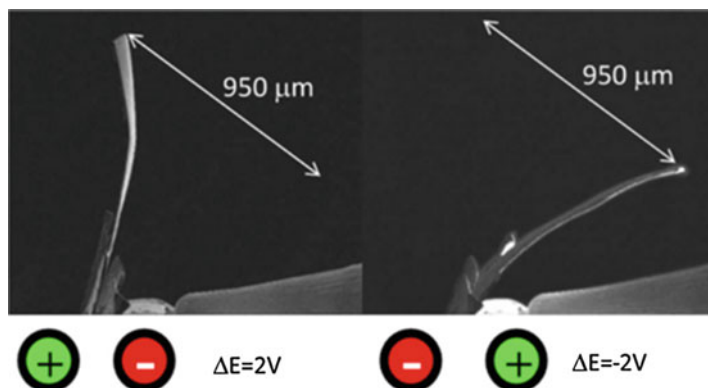


Fig. 8 Two SEM images showing the maximum bending positions of an IPN microactuator ($900 \times 300 \times 17 \mu\text{m}^3$) at 10^{-4} mTorr operating at 5×10^{-2} Hz, ± 2 V (Reproduced from Khaldi et al. (2011b))

The lateral patterning of these materials was then carried out using photolithography techniques and reactive ion etching (RIE) that have been adapted and designed for the development of microactuators (Fig. 9). A Plasma of CF_4/O_2 was used to pattern first $900 \mu\text{m}$ long, $300 \mu\text{m}$ wide freestanding microbeam actuators. These microbeams were immersed in EMITFSI ionic liquid to obtain an active actuator that can operate in open air. The microactuator showed a displacement of $950 \mu\text{m}$ corresponding to a strain of 1.11 %, a curvature of $1.045 \times 10^{-3} \text{ m}^{-1}$ and a bending angle of 63° under an applied voltage of ± 2 V (Fig. 8). Moreover, batch microfabrication has been also demonstrated (Khaldi et al. 2012) as well as actuation under low vacuum from 5.10^{-2} to 30 Hz.

By downscaling the thickness of the SPE using spin-coating, large displacements of $200 \mu\text{m}$ at a frequencies as high as 930 Hz, corresponding to the fundamental resonance frequency, were achieved for $690 \mu\text{m}$ long, $45 \mu\text{m}$ wide, and $12 \mu\text{m}$ thick microbeam IPN actuators under low-voltage stimulation (± 4 V) (Maziz et al. 2014). Figure 9 shows the microfabrication steps and two SEM images of the finished devices. The translation of small-ion motion into large mechanical deformation has been used as a tool to demonstrate that small-ion vibration can still occur at frequency above 1000 Hz in conjugated polymer electrochemomechanical systems.

7 Integration of CP Actuators in Complex Devices

Some efforts have been done to integrate the CP microactuators in functional devices. The biocompatibility of conjugated polymers makes them interesting in order to fabricate biomedical devices and their mechanical properties interesting to build soft robots. Some bilayer materials working in solution have been used to open and close a valve of a PDMS microfluidic channel. The first-demonstrated CP microvalve used a PPy/Au bilayer hinge to rotate rigid plate inside a silicone rubber

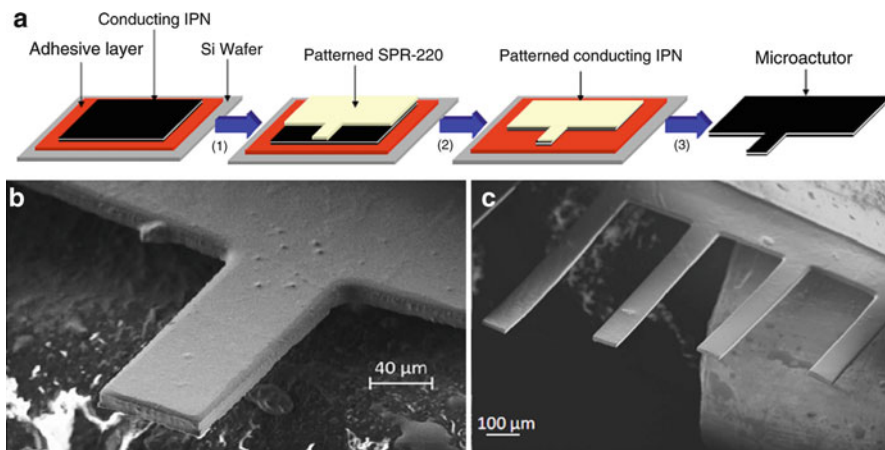


Fig. 9 (A) A schematic of the microfabrication process of a conducting IPN microactuator: A-(1) adhesion of the conducting IPN onto the PVA layer and patterning of the photoresist, A-(2) dry etching of the unprotected parts of the conducting IPN in O₂/CF₄ 90/10 plasma, A-(3) dissolution of the residual photoresist layer and lift-off of the patterned conducting IPN. (B) A conducting IPN microactuator obtained after patterning and lift-off ($200 \times 100 \times 20 \mu\text{m}^3$) (C) collective fabrication of conducting IPN microactuators (Reproduced from Khaldi et al. (2012))

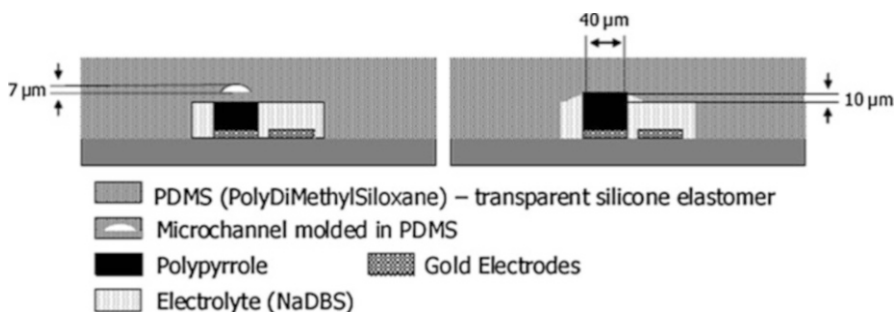


Fig. 10 A sketch of the principle of the PPy bulk microactuator operating as a valve to close a PDMS microchannel (Reproduced from Berdichevsky and Lo (2003))

(polydimethylsiloxane, PDMS) microfluidic channel (Pettersson et al. 2000). The PPy actuators were made on a Si substrate, and the microfluidic circuitry was made separately in a PDMS slab. The PDMS slab was thereafter bonded on the Si substrate resulting in a microfluidic system with built-in PPy microactuator valves. The liquid flow was to be stopped by lifting the PPy-actuated plates.

Figure 10 shows an alternative microfluidic device in PDMS that employed PPy microactuators as a valve (Berdichevsky and Lo 2003). Here the bulk volume change was used to operate as microvalve. The microfluidic channel made in PDMS was mounted on top of an electrode covered with a thick layer of PPy.

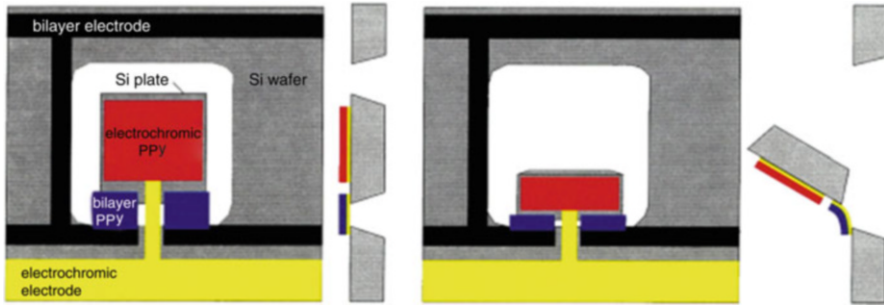


Fig. 11 PPy bilayer microactuators are able to move electrochromic pixels made on a Si substrate (Reproduced from Smela (1999a))

When activated, the volume of the PPy expanded and pushed against the thin PDMS bottom of the microchannel. This thin bottom then bulged upwards, pinching off the flow.

An interesting demonstration of integrating CP microactuators has been made by Smela and coworkers (Smela et al. 1999). They showed that PPy microactuators could be integrated with silicon micromachining and, for instance, could be used to lift Si-plates freed using bulk etching (Fig. 4B). To demonstrate the versatility, they have built electrochromic pixels that could be lifted out of plane (Fig. 11), thus showing that potentially anything made on Si can be moved with CP microactuators (Smela 1999a).

The first complex microdevice that comprised multiple, individually controllable CP microactuators was the microrobot developed by Jager et al. to perform micro-manipulations of single cells (Jager et al. 2000a). It was designed as an articulated microarm composed of 7 PPy bilayer actuators as hinges. They demonstrated precise manipulation of a 100 μm glass bead (Fig. 12). The same group also showed that it is possible to integrate microelectrodes, lids, and microcavities, which were either etched into the glass substrate or made of SU8 on the substrate, with PPy bilayer hinge microactuators, resulting in so-called “cell-clinics” (Jager et al. 2002).

As mentioned in previous chapters, CP actuators need a counter and preferably even a reference electrode to operate. As a first step towards an all integrated or all-polymer system, microactuators with all electrodes integrated on a single chip have been also developed (Jager et al. 1999). The on-chip electrodes permit electronic control of the movable microelectrodes, allowing their movement out of a surface. Thus, it is possible to control the approach of one electrode to a particular object. This tool is expected to be useful in fields such as single-cell studies or neurophysiology.

Some efforts have been realized to turn the microactuators working in air into various devices. It has been shown that an articulated finger (Jager et al. 2013a) can be built from thin film PVDF PPy trilayer actuators (Fig. 13).

As showed previously various objects have been attached to CP actuator such as Si plates. CP actuators have also good adhesion to SU-8 photoresist. Khaldi and

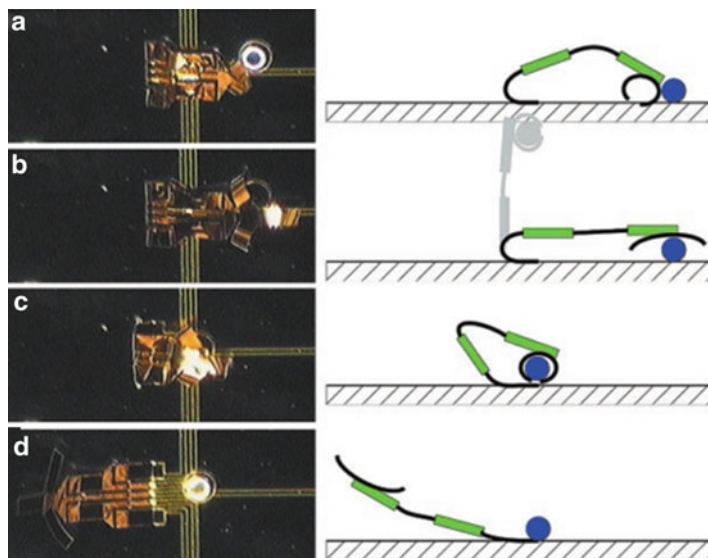


Fig. 12 (a through d) A sequence of pictures (*left*) showing the manipulation of a 100- μm glass bead by the robotic arm and schematic illustrations thereof (*right*). The robot was composed of an “arm” with three fingers, an “elbow,” and a “wrist” each composed of two actuators (Reproduced from Jager et al. (2000a))

Fig. 13 Articulated finger built from thin-film PVDF PPy trilayer actuators with integrated contact pads



coworkers have used that to fabricate biomimicking insect wings. They fabricated artificial wings of SU8 and glued IPN microactuators to them to operate the wings. They showed that the IPN microactuator has enough force to put a wing in motion at a frequency of 24 Hz with a bending amplitude of 20° (Khaldi et al. 2011a). Figure 14 shows an IPN microactuator actuating such an artificial wing with a bending amplitude of 60° at 16 Hz demonstrating the potential of CP actuators to power micro-UAVs (unmanned aerial vehicles or drones). Micro-UAVs would need a higher flapping wing frequency to lift; however, this result shows a proof-of-concept.

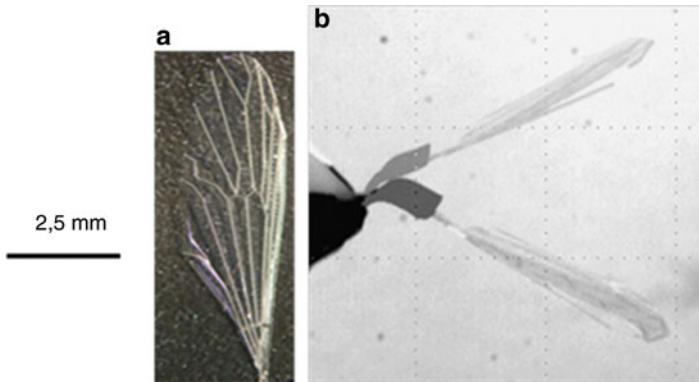


Fig. 14 (a) An artificial wing made of SU8 (b) Flapping SU8 wing movement at a resonant frequency of 16 Hz, under applied voltage of ± 2 V and with a bending angle of 60°

Further development such as downscaling the size of the wing and increasing the resonance frequency of the system is currently ongoing. For instance, a drastic increase of the resonance frequency to approximately 1 kHz was recently presented (Maziz et al. 2014).

8 Interfacing and Actuation

The lack of proper electrical connections and interfacing systems to CP microfabricated air working actuators have been major obstacles hindering further progress of these smart devices into microsystems and microrobotics applications. Macroscopic electrical connections, such as Kelvin clips, alligator clips, or home-made tweezers (Alici et al. 2009; Khaldi et al. 2011b; Jager et al. 2013b), have been applied to devices, but they are poorly adapted for these micrometer scale devices. These connection methods use a mechanical force to establish a sufficient electrical contact between the CP microactuator and the power supply. Since the CP actuators are microfabricated and thus relatively small and especially thin and fragile, the macroscopic electrical connections can cause short-circuiting and therefore damage the microactuator. To overcome the problem of short circuits due to high forces when using clips or tweezers, Jager et al. developed a new interfacing method for PPy trilayer microactuators that can be individually controlled (Jager et al. 2013b). The millimetre-sized PPy actuators were first patterned on a PVDF membrane to form an actuator unit comprising three individually controllable actuators. The new interface was based on a commercial flexible printed circuit board (FPCB) that comprised the electronic circuit into which the microactuator unit was embedded by simply inserting and folding the flexible interface (Fig. 15). The contact pads were automatically aligned to the actuator unit.

For systems that operate on a chip, such as microvalves and the microrobot, probe needles (attached to a micromanipulator) and wire bonding are well-established

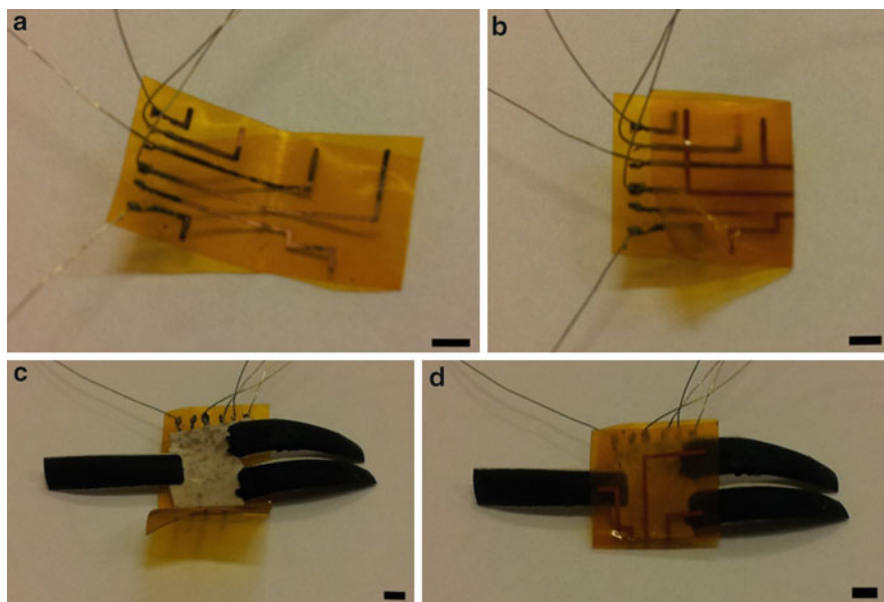


Fig. 15 An interface based on flexible printed circuit boards (FPCB) for contacting CP (micro-)actuators in the open (**a**) and closed (**b**) position. The actuator unit is placed in the open FPCB interface with the actuators aligned to the Cu leads (**c**). Thereafter, the FPCB interface is folded around the actuator unit to provide contact to both sides of the actuators (**d**). Scale bars 2 mm (Reproduced from Jager et al. (2013b))

alternatives that are standardly employed in the microelectronics industry standard and have been used for CP microactuators too. Probe needles can provide easy and quick electrical connections to the microactuators if one integrates contact or bond pads in the design. Wire bonding provides a permanent contact.

The control and operation of the microfabricated CP actuators are typically achieved by an external potentiostat instrument and accompanying software. This allows for applying well-controlled stimulation parameters as well as addressing of multiple actuators. The actuators can be operated with in a two-electrode or three-electrode configuration. In the trilayer and IPN actuators, typically a two-electrode addressing is used. A simple operation by using a battery to provide the power needed to drive the actuators is also possible. Prakash et al. have developed an integrated potentiostat for driving electrochemical actuation of conjugated polymers on a common CMOS substrate for cell-based sensing (Prakash et al. 2008). This approach eliminated for the first time the need of an external potentiostat, i.e., the integrated microsystem comprised on-chip working, counter- and reference electrodes fabricated on top of the necessary control circuitry. The integrated control technique enables a complete miniaturization including a direct battery-powered and independent control of the CP microactuators. Also the abovementioned FPCB interface is intended to provide fully integrated control. In future devices both batteries and control circuitry are going to be mounted on the FPCB.

9 Specifications, Performance, and Applications

Currently there is no standardized CP microactuator (yet). Therefore, it is difficult to supply a general answer to question what the performance of these CP microactuators is. The performance depends to a large extent to the specifications and design, which in turn are set by the application in mind but also by the technological possibilities. In this section, we have collected some data from various CP microactuator technologies. The data is far from comprehensive and provides only an overview of typical performance. It should also be pointed out that the requirements of the application can set contradictory specifications on the design of the CP microactuator. For instance, in order to achieve a fast actuation, the CP layer should be thin, but to get a large force the layer should be thick. So optimisation towards an optimal application specific design is needed.

Bulk CP actuators have a perpendicular expansion of 10–30 %, which is 1–15 μm depending on the layer thickness. Since they mostly consist of thick CP layers, the actuations speeds are low, 10–100 s. The lateral dimensions are 20–100 μm and thickness range is 5–50 μm . See for instance Smela and Gadegaard (1999), Melling et al. (2013), Svennersten et al. (2011), and Carlsson et al. (2007).

Due to the much thinner CP layers, the speed of PPy/Au bilayer microactuators is higher, usually 0.1–10 Hz. The thickness of the PPy layer is often around ~ 1 μm and Au ~ 100 nm, but thinner layers have been used too. PPy microactuators with lateral sizes down to 10×40 μm^2 have been fabricated. These microactuators can have a curvature of 5.6 μm or larger and can bend more than 360° . They are also relatively strong. They have been shown to lift $40,000\times$ their own weight. For more information, see, for instance, Smela et al. (1999), Smela (1999b), and Jager et al. (2000b).

PPy trilayers microactuators have been laser cut with lateral sizes down to 200 μm long and 50 μm wide. They have been made with a commercial PVDF membrane or spin-coated PVDF thin film, having a total actuator thickness of 126 and 48 μm , respectively. Since they are composed of a slightly thicker PPy layer than the bilayer microactuators, their speeds are lower too, 0.1–0.6 Hz. The measured blocking force is up to ~ 600 μN (see Gaihre et al. 2011b, 2012).

The IPN microactuators have so far only be presented employing PEDOT as the electroactive polymer. The actuation speed of such PEDOT/IPN trilayer microactuators has recently reached a stunning 1500 Hz by employing thin films, with a total actuator thickness as thin as 6 μm . Lateral sizes down to 10×50 μm^2 have been presented. These actuators have shown bending angle around 60° and blocking forces in the range of 1–10 μN (Khaldi et al. 2011b; Maziz et al. 2014).

Although there have been many advanced demonstrations, prototypes, and application proposals, to the best of our knowledge, commercial products have not been introduced to the market yet. Demonstrations of applications span a wide range from artificial flying insects (Khaldi et al. 2011a), microfluidics, and Lab-on-a-Chip (Göttsche 2007) to medical devices such as steerable catheters (Immerstrand et al. 2002; Shoa et al. 2010; Wilson et al. 2007). A more detailed description of the various microactuator applications is given in a following chapter that describes CP application.

10 Conclusion and Future Work

During the last two decades, the CP microactuator technology has been tremendous progress from concept to a plethora of devices. They can be fabricated using variety of methods and technologies and integrated with other microcomponents. The CP microactuator technology is both versatile and exciting, and it is an enabling technology for many applications as already shown by the width of presented possible applications. So far mostly components or simple devices relying on external control have been presented.

In the near future, further development in new soft microelectrochemical devices based on conjugated polymer actuators will require their complete conception, operation, and interfacing systems all integrated on a single substrate to allow easy and independent operation. This still poses a real challenge that remains to be overcome. Also, it would be of great interest to develop microactuators with linear actuation to further extend the tool box of CP microactuator devices.

References

- Alici G, Devaud V, Renaud P, Spinks G (2009) Conducting polymer microactuators operating in air. *J Micromech Microeng* 19:025017
- Baughman RH (1996) Conducting polymer artificial muscles. *Synth Met* 78:339–353
- Baughman RH, Shacklette LW, Elsenbaumer RL, Plichta EJ, Becht C (1991) Micro electromechanical actuators based on conducting polymers. In: Lazarev PI (ed) *Molecular electronics*. Kluwer, Dordrecht, pp 267–289
- Berdichevsky Y, Lo Y-H (2003) Polymer microvalve based on anisotropic expansion of polypyrrole. In: *Proceedings - Materials Research Society Symposium*. Boston, United States, 782: pp 101–107
- Cao Y, Smith P, Heeger AJ (1992) Counter-ion induced processibility of conducting polyaniline and of conducting polyblends of polyaniline in bulk polymers. *Synth Met* 48:91–97
- Carlsson D, Jager E, Krogh M, Skoglund M (2007) Systems, device and object comprising electroactive polymer material, methods and uses relating to operation and provision thereof. Patent WO2009038501
- Castillo-Ortega M, Inoue M, Inoue M (1989) Chemical synthesis of highly conducting polypyrrole by the use of copper (II) perchlorate as an oxidant. *Synth Met* 28:65–70
- Chang CY, Sze SM (1996) *ULSI technology*. McGraw-Hill, Singapore
- Chao T, March J (1988) A study of polypyrrole synthesized with oxidative transition metal ions. *J Polym Sci Part A Polym Chem* 26:743–753
- Diaz A, Bargon J, Skotheim T (1986) *Handbook of conducting polymers*, vol 1. Marcel Dekker, New York, p 81
- Fabretto M, Zuber K, Hall C, Murphy P (2008) High conductivity PEDOT using humidity facilitated vacuum vapour phase polymerisation. *Macromol Rapid Commun* 29:1403–1409
- Fabretto MV, Evans DR, Mueller M, Zuber K, Hojati-Talemi P, Short RD, Wallace GG, Murphy PJ (2012) Polymeric material with metal-like conductivity for next generation organic electronic devices. *Chem Mater* 24:3998–4003
- Faxälv T, Bolin M, Jager EWH, Lindahl TL, Berggren M (2014) Lab on a Chip 14:3043.
- Gaihre B, Alici G, Spinks GM, Cairney JM (2011a) Effect of electrolyte storage layer on performance of PPy-PVDF-PPy microactuators. *Sens Actuators B* 155:810–816
- Gaihre B, Alici G, Spinks GM, Cairney JM (2011b) Synthesis and performance evaluation of thin film PPy-PVDF multilayer electroactive polymer actuators. *Sens Actuators A* 165:321–328

- Gaihre B, Alici G, Spinks GM, Cairney JM (2012) Pushing the limits for microactuators based on electroactive polymers. *J Microelectromech Syst* 21:574–585
- Glocker DA, Shah SI, Westwood WD (1995) Handbook of thin film process technology. Institute of Physics Publishing, Philadelphia
- Götsche T (2007) Highly integrated oral drug delivery system with valve based on electro-active-polymer. In: IEEE MEMS 2007, Kobe, pp 461–464
- Heywang G, Jonas F (1992) Poly (alkylenedioxythiophene)s – new, very stable conducting polymers. *Adv Mater* 4:116–118
- Hide F, Diaz-Garcia MA, Schwartz BJ, Andersson MR, Pei Q, Heeger AJ (1996) Semiconducting polymers: a new class of solid-state laser materials. *Science* 273:1833–1836
- Immerstrand C, Peterson KH, Magnusson K-E, Jager E, Krogh M, Skoglund M, Selbing A, Inganäs O (2002) Conjugated-polymer micro- and milliaactuators for biological applications. *MRS Bull* 27:461–464
- Jager EWH (2010) Chapter 8, Conjugated polymers as actuators for medical devices and microsystems. In: Leger J, Carter S, Berggren M (eds) *Iontronics – ionic carriers in organic electronic materials and devices*. CRC Press, Boca Raton, pp 141–162
- Jager E, Krogh M (2003) Method for producing a micromachined layered device. Patent WO2004092050
- Jager EWH, Smela E, Inganäs O (1999) On-chip microelectrodes for electrochemistry with moveable PPy bilayer actuators as working electrodes. *Sens Actuators B Chem* 56:73–78
- Jager EWH, Inganäs O, Lundström I (2000a) Microrobots for micrometer-size objects in aqueous media: potential tools for single cell manipulation. *Science* 288:2335–2338
- Jager EWH, Smela E, Inganäs O (2000b) Microfabricating conjugated polymer actuators. *Science* 290:1540–1545
- Jager EWH, Immerstrand C, Petersson KH, Magnusson K-E, Lundström I, Inganäs O (2002) The cell clinic: closable microvials for single cell studies. *Biomed Microdevices* 4:177–187
- Jager EWH, Masurkar N, Nworah NF, Gaihre B, Alici G, Spinks GM (2013a) Individually controlled conducting polymer tri-layer microactuators. In: *Transducers 2013, Barcelona, 16–20 June 2013*, pp 542–545
- Jager EWH, Masurkar N, Nworah NF, Gaihre B, Alici G, Spinks GM (2013b) Patterning and electrical interfacing of individually controllable conducting polymer microactuators. *Sens Actuators B* 183:283–289
- Kanazawa KK, Diaz A, Geiss RH, Gill WD, Kwak JF, Logan JA, Rabolt JF, Street GB (1979) ‘Organic metals’: polypyrrole, a stable synthetic ‘metallic’ polymer. *J Chem Soc Chem Commun* 19:854–855
- Khalidi A, Plesse C, Soyer C, Cattani E, Vidal F, Chevrot C, Teyssié D (2011a) Dry etching process on a conducting interpenetrating polymer network actuator for a flapping fly micro robot. In: *ASME 2011 international mechanical engineering congress and exposition, IMECE 2011, vol 2, Denver*, pp 755–757
- Khalidi A, Plesse C, Soyer C, Cattani E, Vidal F, Legrand C, Teyssié D (2011b) Conducting interpenetrating polymer network sized to fabricate microactuators. *Appl Phys Lett* 98:164101
- Khalidi A, Plesse C, Soyer C, Chevrot C, Teyssié D, Vidal F, Cattani E (2012) Patterning process and actuation in open air of micro-beam actuator based on conducting IPNs. In: *Proceedings of SPIE – The International Society for Optical Engineering, San Diego, USA, vol 8340*
- Kim J, Kim E, Won Y, Lee H, Suh K (2003) The preparation and characteristics of conductive poly (3, 4-ethylenedioxythiophene) thin film by vapor-phase polymerization. *Synth Met* 139:485–489
- Klempner D, Sperling LH, Utracki LA (1994) *Interpenetrating polymer networks*. An American Chemical Society Publication, Washington, DC
- Kobayashi M, Colaneri N, Boysel M, Wudl F, Heeger A (1985) The electronic and electrochemical properties of poly (isothianaphthene). *J Chem Phys* 82:5717–5723
- Lu W, Fadeev AG, Qi B et al (2002) Use of ionic liquids for -conjugated polymer electrochemical devices. *Science* 297:983–987

- Machida S, Miyata S, Techagumpuch A (1989) Chemical synthesis of highly electrically conductive polypyrrole. *Synth Met* 31:311–318
- Madden JD, Cush RA, Kanigan TS, Hunter IW (2000) Fast contracting polypyrrole actuators. *Synth Met* 113:185–192
- Madou M (1997) Fundamentals of microfabrication. CRC Press, Boca Raton
- Maziz A, Plesse C, Soyer C, Chevrot C, Teyssié D, Cattan E, Vidal F (2014) Demonstrating kHz frequency actuation for conducting polymer microactuators. *Adv Funct Mater* 24:4851–4859
- Melling D, Wilson S, Jager EWH (2013) The effect of film thickness on polypyrrole actuation assessed using novel non-contact strain measurements. *Smart Mater Struct* 22:104021
- Mohammadi A, Hasan M-A, Liedberg B, Lundström I, Salaneck W (1986) Chemical vapour deposition (cvd) of conducting polymers: polypyrrole. *Synth Met* 14:189–197
- Pei Q, Inganäs O (1992) Conjugated polymers and the bending cantilever method: electrical muscles and smart devices. *Adv Mater* 4:277–278
- Pettersson F, Jager EWH, Inganäs O (2000) Surface micromachined polymer actuators as valves in PDMS microfluidic system. In: Dittmar A, Beebe D (eds) IEEE-EMBS special topic conference on microtechnologies in medicine & biology, Lyon, 12–14 Oct 2000, pp 334–335
- Plesse C, Vidal F, Randriamahazaka H, Teyssié D, Chevrot C (2005) Synthesis and characterization of conducting interpenetrating polymer networks for new actuators. *Polymer* 46:7771–7778
- Prakash SB, Urdaneta M, Christophersen M, Smela E, Abshire P (2008) In situ electrochemical control of electroactive polymer films on a CMOS chip. *Sens Actuators B* 129:699–704
- Rapi S, Bocchi V, Gardini G (1988) Conducting polypyrrole by chemical synthesis in water. *Synth Met* 24:217–221
- Shoa T, Madden JD, Munce NR, Yang V (2010) Analytical modeling of a conducting polymer-driven catheter. *Polym Int* 59:343–351
- Smela E (1999a) A microfabricated movable electrochromic “pixel” based on polypyrrole. *Adv Mater* 11:1343–1345
- Smela E (1999b) Microfabrication of PPy microactuators and other conjugated polymer devices. *J Micromech Microeng* 9:1–18
- Smela E, Gadegaard N (1999) Surprising volume change in PPy(DBS): an atomic force microscopy study. *Adv Mater* 11:953–957
- Smela E, Inganäs O, Pei Q, Lundström I (1993) Electrochemical muscles: micromachining fingers and corkscrews. *Adv Mater* 5:630–632
- Smela E, Inganäs O, Lundström I (1995) Controlled folding of micrometer-size structures. *Science* 268:1735–1738
- Smela E, Kallenbach M, Holdenried J (1999) Electrochemically driven polypyrrole bilayers for moving and positioning bulk micromachined silicon plates. *J Microelectromech Syst* 8:373–383
- Sperling LH (2004) Interpenetrating polymer networks. Wiley Online Library, Washington, DC
- Sugimoto R-I, Takeda S, Gu H, Yoshino K (1986) Preparation of soluble polythiophene derivatives utilizing transition metal halides as catalysts and their property. *Chem Express* 1:635–638
- Svennersten K, Berggren M, Richter-Dahlfors A, Jager EWH (2011) Mechanical stimulation of epithelial cells using polypyrrole microactuators. *Lab Chip* 11:3287–3293
- Taccola S, Greco F, Mazzolai B, Mattoli V, Jager EWH (2013) Thin film free standing PEDOT:PSS/SU8 bilayer microactuators. *J Micromech Microeng* 23:117004
- Taylor GN, Wolf TM (1980) Oxygen plasma removal of thin polymer films. *Polym Eng Sci* 20:1087
- Tehrani P, Robinson ND, Kugler T, Remonen T, Hennerdal LO, Häll J, Malmström A, Leenders L, Berggren M (2005) Patterning polythiophene films using electrochemical over-oxidation. *Smart Mater Struct* 14:N21–N25
- Temmer R, Maziz A, Plesse C, Aabloo A, Vidal F, Tamm T (2013) In search of better electroactive polymer actuator materials: PPy versus PEDOT versus PEDOT–PPy composites. *Smart Mater Struct* 22:104006

- Vidal F, Popp JF, Plesse C, Chevrot C, Teyssie D (2003) Feasibility of conducting semi-interpenetrating networks based on a poly (ethylene oxide) network and poly (3, 4-ethylenedioxythiophene) in actuator design. *J Appl Polym Sci* 90:3569–3577
- Vidal F, Plesse C, Teyssie D, Chevrot C (2004) Long-life air working conducting semi-IPN/ionic liquid based actuator. *Synth Met* 142:287–291
- Wang X, Berggren M, Inganäs O (2008) Dynamic control of surface energy and topography of microstructured conducting polymer films. *Langmuir* 24:5942–5948
- Wilson SA, Jourdain RPJ, Zhang Q et al (2007) New materials for micro-scale sensors and actuators: an engineering review. *Mater Sci Eng R Rep* 56:1–129
- Winther-Jensen B, West K (2004) Vapor-phase polymerization of 3, 4-ethylenedioxythiophene: a route to highly conducting polymer surface layers. *Macromolecules* 37:4538–4543
- Winther-Jensen B, Breiby DW, West K (2005) Base inhibited oxidative polymerization of 3, 4-ethylenedioxythiophene with iron (III) tosylate. *Synth Met* 152:1–4
- Wu Y, Alici G, Spinks GM, Wallace GG (2006) Fast trilayer polypyrrole bending actuators for high speed applications. *Synth Met* 156:1017–1022
- Xia Y, Whitesides GM (1998) Soft lithography. *Angew Chem Int Ed* 37:550–575
- Yamada K, Kume Y, Tabe H (1998) A solid-state electrochemical device using poly(pyrrole) as micro-actuator. *Jpn J Appl Phys Part 1 Regul Pap Short Notes Rev Pap* 37:5798–5799
- Zhou DZ, Spinks GM, Wallace GG, Tiyapiboonchaiya C, Macfarlane DR, Forsyth M, Sun JZ (2003) Solid state actuators based on polypyrrole and polymer-in-ionic liquid electrolytes. *Electrochim Acta* 48:2355–2359

Daniel Melling and Edwin W. H. Jager

Contents

1	Introduction	320
2	Characterization Techniques	321
2.1	Bending Actuators	321
2.2	Linear Actuators	326
2.3	Other Characterization Methods	334
3	Actuation Metrics	343
3.1	Volume Change	345
3.2	Speed	347
4	Conclusion	348
	References	349

Abstract

This chapter outlines the various methods that have been developed in the past three decades to characterize the electroactive performance of conducting polymers (CP) to provide fundamental metrics such as strain, strain rate, stress, force, modulus of elasticity, and work capacity. In addition to providing metrics, these characterization techniques have served as valuable tools for studying CPs, providing a greater understanding of the actuation process, optimizing synthesis conditions, and geometric parameters for optimal device performance. The issues associated with the determination of metrics and the need for standardization are discussed.

D. Melling (✉)

Institute for Medical Science and Technology, University of Dundee, Dundee, UK

e-mail: d.melling@dundee.ac.uk

E.W.H. Jager

Department of Physics, Chemistry and Biology (IFM), Linköping University, Linköping, Sweden

Biosensors and Bioelectronics, Linköping University, Linköping, Sweden

e-mail: edwin.jager@liu.se

Keywords

Mechanical characterization • Actuator metrics • Actuator performance • Standardization

1 Introduction

Since the earliest demonstrations of the electrochemomechanical volume change of conjugated polymers, researchers have attempted to quantify their expansion and contraction in terms of strain. Unfortunately, the earliest estimates of the magnitude of their strain varied greatly from <1 % to 120 % for nominally identical systems (Smela and Gadegaard 2001). These apparent discrepancies highlight the need to reliably characterize actuation performance and calculate performance metrics. The accurate and meaningful characterization of conducting polymer actuators is crucial to the development of new forms of CP with improved performance, their optimization, and the development of applications.

These differences were no doubt due to: differences in synthesis conditions, differences in the sample geometry/dimensions, differences in the way the samples were actuated, and differences in the way the strains were measured and calculated. These differences make it very difficult to compare the metrics obtained by one research group with another even when all of the conditions are clearly stated along with the metrics.

Since the early 1990s, a number of approaches to the characterization actuator performance have come into focus and have proved highly effective in increasing our understanding of the actuation mechanism, the importance of synthesis and cycling conditions, and device geometry. Essentially, three different approaches have been developed in order to characterize one of the three actuation modes of CPs: bending, linear, or bulk actuation (Fig. 1). Given that no single test method currently in use can provide metrics for all three actuation modes, there would appear to be a need for a range of test methods.

The type of device being developed will determine the approach adopted for characterization. For example, the most appropriate characterization technique for developing devices employing bending bilayer or trilayer actuators would be a setup for studying bending actuators (Maw et al. 2001) for obvious reasons. Test methods developed for the characterization of linear actuators would be most suitable for the development of free-standing film actuators (Hara et al. 2004a) or fiber actuators (Hara et al. 2004b; Smela et al. 2005; Plesse et al. 2010). Characterization techniques that can furnish the out-of-plane strain metrics of films would be the most appropriate techniques to use in the development of out-of-plane actuation for bulk expansion actuators such as microfluidic valves (Berdichevsky and Lo 2003) or microactuators for the mechanostimulation of cells (Svennersten et al. 2011).

The characterization techniques currently in use will be outlined in the following sections and illustrated with examples taken from both the early and recent literature to illustrate the range of metrics that can be obtained and their use in increasing our

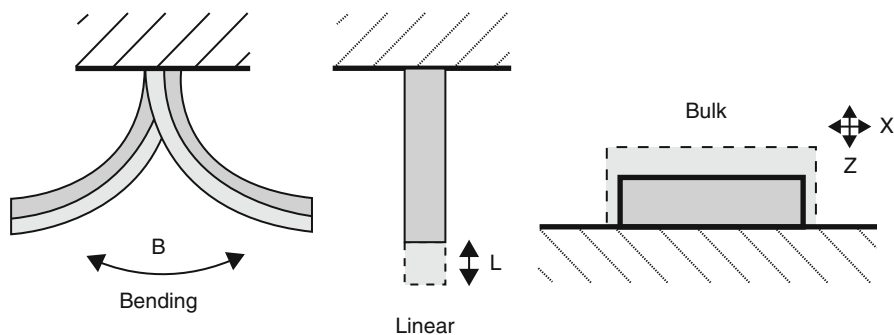


Fig. 1 Typical actuation modes used for the characterization of EAPs

understanding of the actuation process and devices. For readers who are new to the field of CP actuators, you will begin to appreciate the complexity of the actuation process and come to an increasing realization that there is still a great need for the standardization of characterization techniques and the calculation of metrics.

2 Characterization Techniques

2.1 Bending Actuators

One of the first approaches used to characterize actuation of conducting polymer (CP) actuators was developed by Pei and Inganäs (1992, 1993). Their approach enabled the in-plane strain of bending actuators to be estimated using the mathematical approach developed by Timoshenko for modeling a bimetal thermostat (Timoshenko 1925). This approach has been widely adopted by other research groups and has become known as ‘the bending-beam method’. Their approach resulted in the first reasonable estimates of in-plane strain for polypyrrole (PPy) bilayers doped with different dopants of up to 3.4 % and polyaniline (PA) bilayers of 1 %. For polypyrrole dodecylbenzenesulfonate, PPy(DBS), bilayers the in-plane strain was calculated to be 0.35 %. Smela et al. (1999) refined these estimates to take into account the difference in Young’s modulus of elasticity of CP between the reduced and oxidized states, obtaining estimates for the in-plane strain of PPy(DBS) of ~ 2 % (Smela et al. 1999). More recently, this approach has been extended to the study of multilayer actuators (Du et al. 2010).

The movement of bending CP actuators can be followed by measuring the change in the geometric parameters illustrated in Fig. 2. These include the x and y coordinates (displacement) of the tip, the angle which the tip moves through (angular displacement, θ), the length of the curved path traced out by the tip (the tip travel distance, TTD), and the radius of curvature (R). Different researchers have developed different setups to experimentally determine these parameters. Some setups employ video cameras to capture the bending movement (Fig. 3) (Maw et al. 2001, 2005),

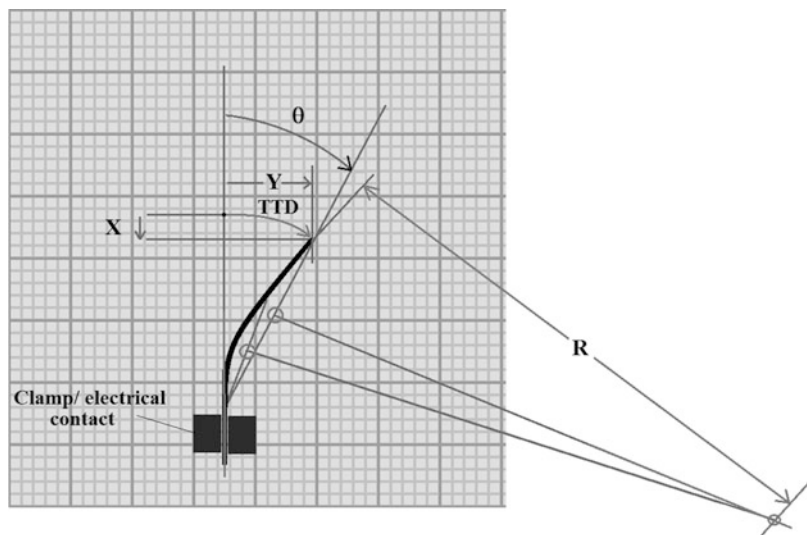


Fig. 2 The range of geometric parameters employed to study bending actuators

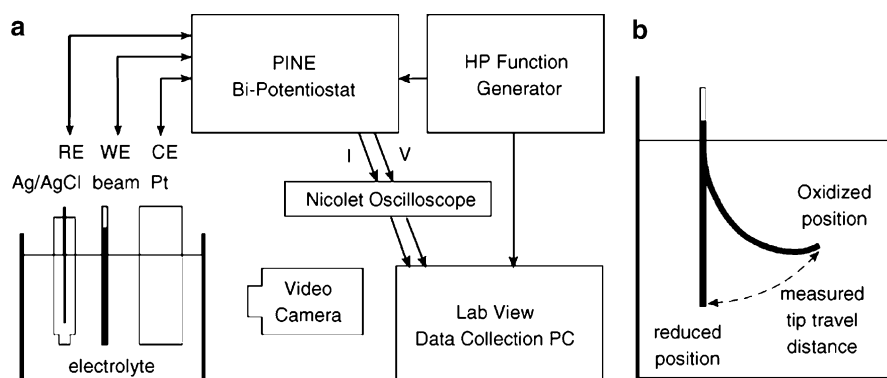


Fig. 3 (a) The setup used by Maw to characterize the actuation of a bilayer actuator. (b) The geometric parameter used to characterize bending actuation (Reprinted from Maw et al. (2005))

while others have employed laser micrometry to determine tip displacements (Kaneko and Kaneto 1998). Sugino et al. have employed laser micrometry to determine the strain difference (Fig. 4) (Sugino et al. 2009). This strain metric is simple to determine and has become widely employed by other researchers. These setups allow the bending movement to be characterized while undertaking electrochemical experiments typically used to study CP.

The characterization of bending CP actuators has greatly increased understanding of the actuation process. In addition, it has allowed the optimum synthesis and geometric conditions to be determined. It remains the method of choice for

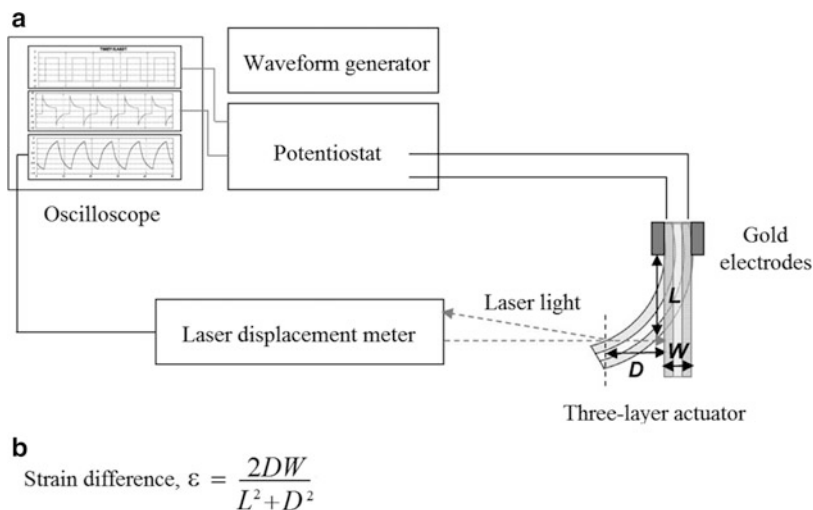


Fig. 4 (a) Laser micrometry setup employed by Sugino et al. (b) Mathematical relation used to calculate strain difference. Note: free length, L , is the length from the fixed end of the gold electrodes to the point where the laser irradiates the actuator strip (Reprinted from Sugino et al. (2009))

characterizing the actuation performance of bilayer and trilayer actuators, being a relatively simple yet highly effective approach for the optimization of bending actuators.

CP are sensitive to a wide range of synthesis parameter, such as deposition potential and current density, the type and concentration of dopant, and stimulation salts, polymerization temperature, solvent, monomer concentration, electrode, and pH (Maw et al. 2005). CPs that have been deposited under different synthesis conditions can be considered to be distinctly different materials, albeit within a family.

Maw et al. investigated the effects of varying the deposition current density (DCD) on the bending behavior of PPy(DBS) bilayer beam actuators and showed that bending can be controlled during both manufacture and use. Beams were synthesized using current densities ranging from 0.4 to 40 mA/cm² with the deposition duration ranging from 50 to 5000 s, depending on the DCD. Interestingly, all of the beams curled during polymerization with the PPy-coated surface facing outwards. A plot of beam tip movement versus DCD (Fig. 5) reveals that beams coated at lower DCD values curled more.

After deposition the films were cycled 15 times between +0.4 V and -1.1 V at 150 mV/s. In general, the beams curled film-side in during oxidation and straightened or back-curved with the film-side out during reduction, indicating that the PPy (DBS) contracted during oxidation and expanded during reduction. These first

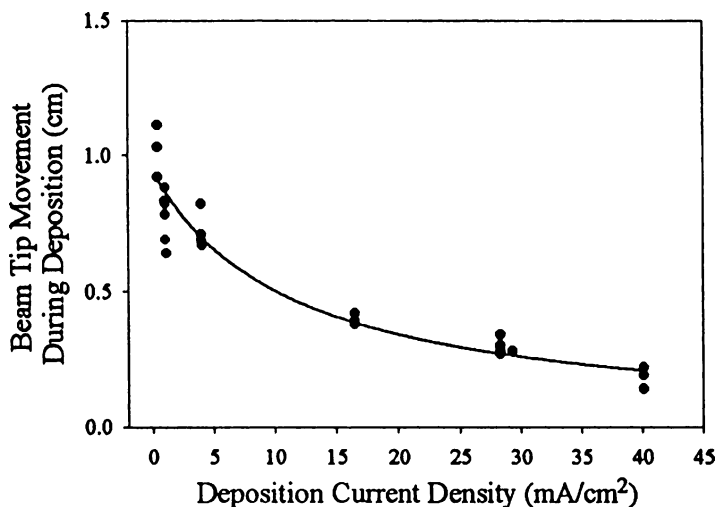


Fig. 5 Movement of the beam tip during deposition versus DCD (Reprinted from Maw et al. (2001))

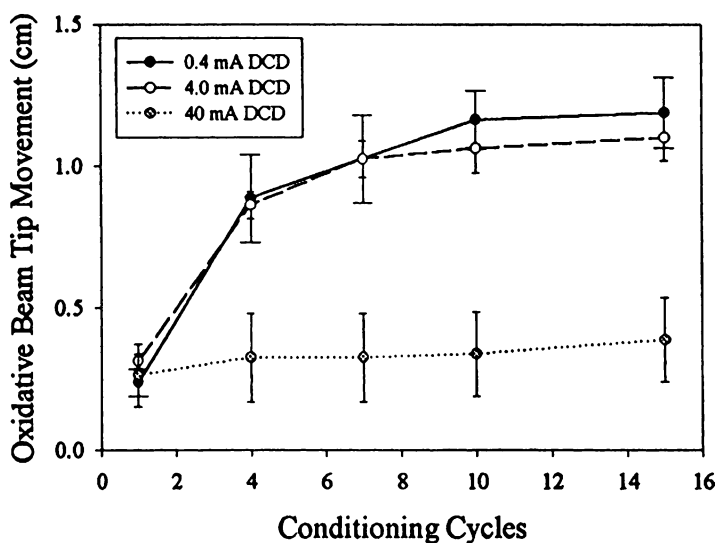


Fig. 6 Beam tip movements of the conditioning cycles during the oxidation scans (Reprinted from Maw et al. (2001))

15 “conditioning” cycles reveal that low DCD values favor more extensive and rapid curling (Fig. 6). However, they also require a longer break-in period. In all cases, the movement extent was shown to be proportional to the amount of charge exchanged (Fig. 7).

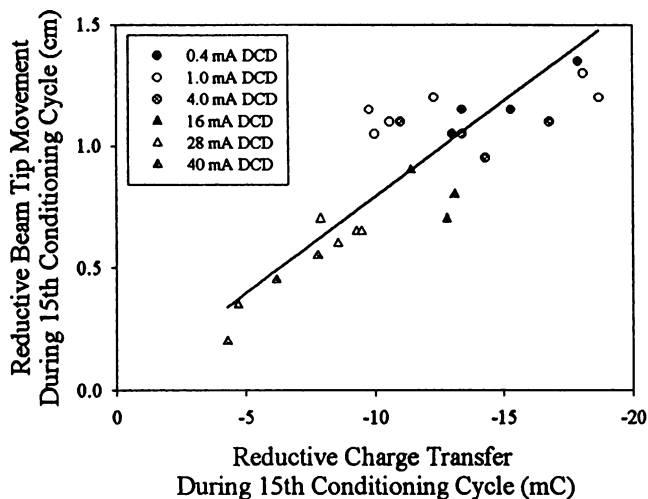


Fig. 7 Maximum extent of the beam tip movement during the reduction scan in the 15th conditioning cycle versus the reductive charge transfer during the cycle (Reprinted from Maw et al. (2001))

After the conditioning cycles the beams were cycled with five voltage steps of +0.4 V (10 s) and -1.1 V (10 s). These voltage steps also revealed that low DCD beams transfer charge more easily, resulting in more curling at a given level of voltage stimulation.

Current stepping showed that control over the extent and speed of curling can be well managed by controlling the charge transfer, with beam bending being approximately proportional to the amount of charge transferred, and this appears to be independent of DCD. However, the proportionality between beam bending and charge transfer does depend on DCD when percentage of charge transfer (compared to its natural maximum, found during voltage stimulation) is used. As mentioned, these experiments illustrate nicely that albeit within a family, even having the same composition, PPy(DBS), different synthesis conditions (DCD) result in distinctly different materials with different performance (Otero et al. 2000).

Alici et al. have characterized bending actuators for real-life applications such as a micro-gripping system (Alici and Huynh 2007). They were able to use their experimental setup to show that the higher the input voltage the larger the tip displacement and that the force decreases linearly with the input frequency. However, an input voltage is eventually reached above which the displacement plateaus out (Festin et al. 2013). The speed (rate of deformation) has also been shown to increase with input voltage (Madden et al. 2000; Plesse et al. 2005). They also used their setup to characterize the actuators nonlinear behavior, hysteresis, and creep. Hysteresis was negligibly small in the device; however, creep caused significant positioning inaccuracy, if not properly identified and compensated. They developed

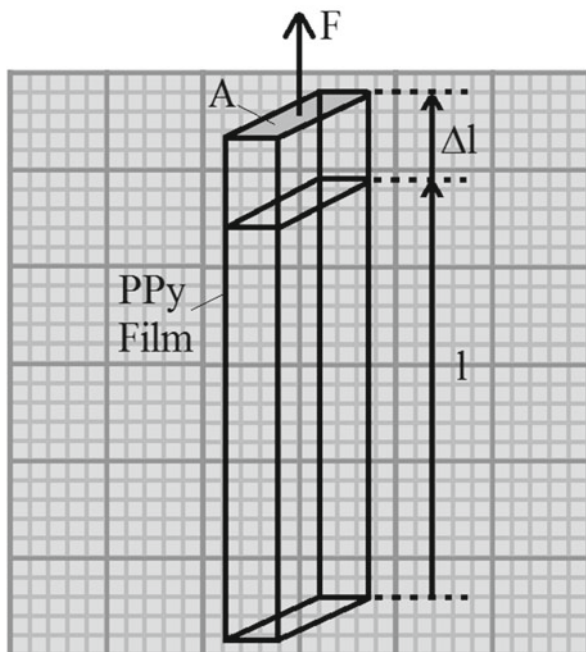
mathematical models to describe both the movement (Bending motion model) and the force (Force output model) that can be generated by a robotic finger (trilayer actuator) and use their setup to test the models and demonstrated excellent agreement between theoretical and experimental results.

Otero et al. have used two bending trilayer actuators to produce a device that can function simultaneously as an actuator and a sensor (Otero et al. 2007). As an actuator, the device can perform longitudinal movements (up to 60 % linear displacement) and mechanical work (lift a trailing weight) under electrical stimulus, and as a sensor, responding with a change of the consumed electrical energy to any change of the experimental external variables acting on the driving electrochemical reaction. The moving device has the capability to sense changes in the weight, salt concentration, or driving current simultaneously while moving. Hence, CPs are simultaneous sensing actuators (Fernández-Otero et al. 2010; Córdova et al. 2013). Bending bilayers can also be used as a tool in the quantification of the number of solvent molecules accompanying the actuation of CPs (Otero and Martinez 2012; Otero et al. 2013).

2.2 Linear Actuators

The typical metrics used to characterize linear actuators are tensile stress (σ), axial strain (ϵ), and Young's modulus of elasticity (E) (see Fig. 8) determined using either isometric (constant length) or isotonic (constant load) conditions (Della Santa et al. 1997b). Here the stress is defined as the force (F) per unit area (A) and the strain defined as the ratio of the change in length (Δl) over the initial length (l). The Young's modulus of elasticity (E), a measure of the stiffness of the material, is defined as the ratio of the stress and strain ($E = \sigma/\epsilon$). Other metrics include the work capacity (W) (the area below the horizontal load line in the stress–strain plane) and the average power (P) (the ratio of the work per cycle and the half period ($T/2$) of the cycle).

Some of the first studies of free-standing CP films as linear actuators were performed by Chiarelli et al. using the apparatus shown in Fig. 9 (Chiarelli et al. 1995). Here the electrochemical cell contains a clamp to mechanically fix the lower extremity of the free-standing strip of PPy doped with benzene sulphonate (PPy(BS) or Lutamer[®]), 90 mm \times 1 mm \times 32 μ m. A thin gold disk, clamped to the lower extremity of the PPy strip, provides the electrical connection to the potentiostat which provides appropriate voltage and/or current waveforms under computer control. The upper extremity of the strip can be connected to either a displacement sensor for the determination of sample length change or a servo-actuator for the determination of sample elastic modulus. Only 50 mm of the sample strip is immersed in the electrolyte solution. The electrochemical cell is a three-electrode system with the sample strip forming the WE, platinum CE, and saturated calomel (SCE) RE. The relaxed elastic modulus (E_r) is found by applying sudden steps of length to the sample and determining its elastic modulus once force changes have completely stabilized, which occurs 5 s after each length step. During the length



Metric:	Stress (σ)	Strain (ϵ)	Young Modulus of Elasticity (E)	Work Capacity (W)	Average Power (P)
Expression:	$\sigma = F/A$	$\epsilon = \Delta l/l$	$E = \sigma/\epsilon$	$W = \sigma \epsilon/2$	$P = W/(T/2)$

Fig. 8 Common metrics employed in the study of linear actuators. Illustration depicts isotonic loading of the free-standing PPy film

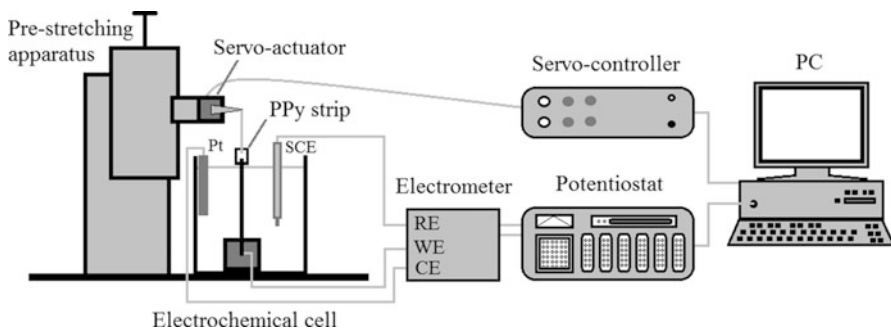


Fig. 9 Setup used by Chiarelli and Della Santa et al. for characterizing the linear actuation of free-standing PPy(BS) films (Reprinted (adapted) from Della Santa et al. (1997b))

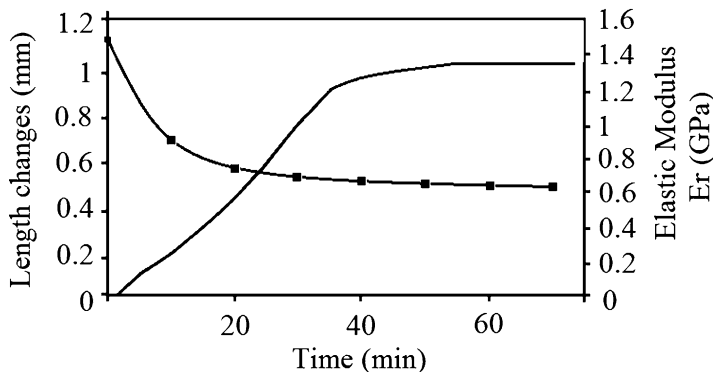


Fig. 10 Free-swelling curve: length (—) and relaxed elastic modulus (—■) versus time of a PPy sample after its immersion in 0.01 M sodiumbenzenesulfonate in acetonitrile (95 % volume) and de-ionized water (5 % volume) (Reprinted from Chiarelli et al. (1995))

change experiments, a 1 g counter load was applied to the displacement transducer to just maintain the sample straight.

Chiarelli et al. used the setup to quantitatively measure isotonic length and relaxed modulus changes during “free-swelling” conditions and subsequently during cyclic voltammetry and square-wave amperometry. Large changes in length and elastic modulus were observed by simply immersing dried samples in electrolyte over a period of 80 min (Fig. 10). Dimensional and elastic changes were seen to be large during the first cycle (linear strain (ϵ) = 2 %, reduced elastic modulus (E_r) = 80 %) but decrease progressively due to irreversible changes until they stabilize by the 20th cycle (ϵ = 0.6 %, E_r = 0 %). Good proportionality between length changes and exchanged charge was seen. A value of 0.25 C was found to be the maximum charge the sample could exchange without deterioration. A nonhomogeneous electrochemical behavior was observed with the length portion nearest to the electrical supply being most active. These authors recommended the use of a trapped bulk dopant for improving material stability and scaling down of film thickness to make the electromechanical time response lower, i.e. produce quicker actuations.

Using the same setup Della Santa et al. characterized the performance of a linear free-standing PPy(BS) film actuator of the same dimensions cycled in 0.1 M NaBS (95 % acetonitrile/5 % water) (Della Santa et al. 1997b). Figure 11 shows that 1 % displacement (linear strain) is achievable. An increase in exchanged charge above 0.25 C can further increase the linear strain but drastically decreases sample life. An overlay of the isotonic strain and isometric stress (recorded separately) is shown in Fig. 12. The peak-to-peak force is 10 g, which corresponds to an equivalent stress of 3.25 MPa. A working density of 73 KJ/M³, greater than in human muscle or other bending actuators, is achievable for these linear actuators. However, due to their low response times, the average power achievable is much less.

Using this approach to characterization, Della Santa et al. developed a model for linear actuation and verified this with respect to the experimental data

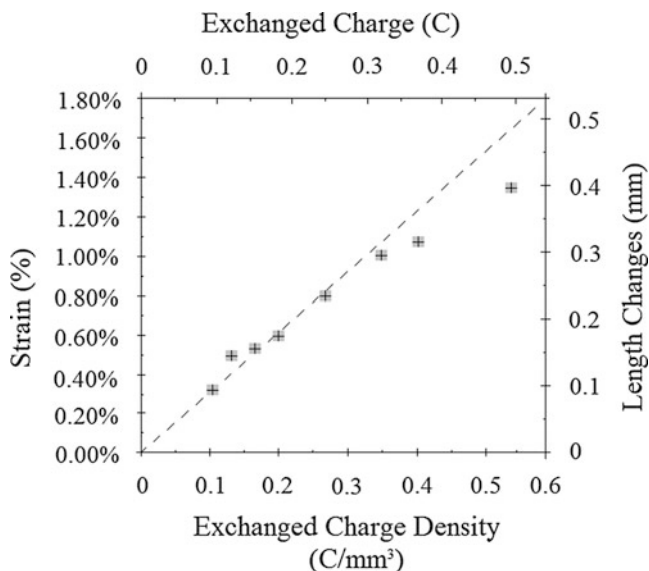


Fig. 11 Isotonic length changes versus exchanged charge during different current square wave stimulations of the PPY sample. Both quantities are also shown as normalized with respect to the active length and active volume of the sample (Reprinted from Della Santa et al. (1997b))

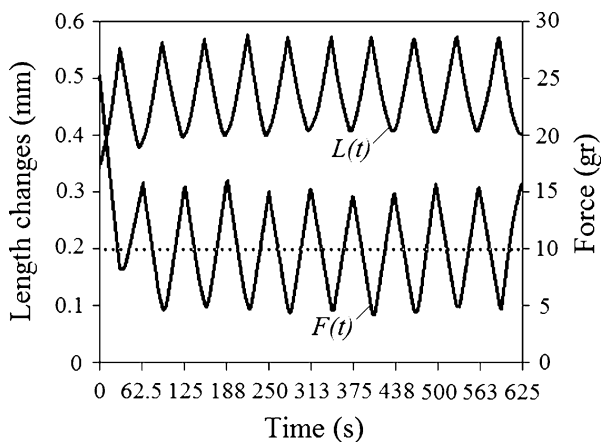


Fig. 12 Isotonic length changes ($L(t)$) and isometric developed forces ($F(t)$) of the PPY sample during the same square wave stimulation ($I = 5$ mA, $T = 62.5$ s, $Q = 0.156$ C). During the reduction semi-cycle, the sample elongates under isotonic conditions, whereas it develops a negative force with respect of the offset prestretching force (dotted line) under isometric conditions. The length changes refer to a sample whose wet, electrochemically active portion is 30 mm long (Reprinted from Della Santa et al. (1997b))

(Della Santa et al. 1997a). They recommended that solid polymer electrolytes be developed having good electrochemical and mechanical coupling to the CP and the implementation of microactuators either in series or in parallel to increase the force or the displacement, respectively.

Other researchers have employed a similar experimental setup employing a laser displacement sensor to measure the linear displacement of free-standing CP films (Hara et al. 2004a). The application of an isotonic load to PPy leads to an elastic deformation and creep. Here creep refers to the strain that occurs subsequent to the immediate spring-like deformation when a step in load is applied. Much of what is referred to as creep is recoverable, but some is plastic deformation and is not recoverable. The extent of these elastic and creep displacements is important as they will often determine the maximum acceptable load. Kaneto et al. used this setup to investigate the actuation and creeping of PPy in ionic liquids (Kaneto et al. 2011). They observed that the electrochemomechanical strain (ECMS) was initiated by both reduction (3 %) and solvent swelling (15–20 %) in ionic liquids, producing blocking stresses of 1.7 MPa. Creeping of the films was observed at tensile loads larger than 0.5 MPa and displayed scan rate dependence. The electrochemical strain of samples actuated in a mixed solution of ionic liquid and propylene carbonate was initially 15 % becoming negligible after several cycles. This has been attributed to the loss of electrochemical activity and conductivity upon swelling with propylene carbonate.

Using the same setup, Tominaga et al. showed that the electrochemical creep of PPy could be decreased by increasing the strength of the actuators through increasing crosslinking within the polymer network (Tominaga et al. 2011). Tominaga employed “dipyrrole alkane” monomer units, containing two pyrrole rings linked by a linear alkyl chain via their nitrogen atoms. Subsequent copolymerization of Py monomer with dipyrrole alkane monomer leads to an increase in crosslinking and a decrease in the electromechanical creep with increasing dipyrrole alkane content. Unfortunately, the decrease in creep also resulted in a decrease in reversible strain. Melling et al. have observed an increase in electrochemical creep due to decreasing crosslinking by increasing blocking of the beta-positions in the PPy network through the copolymerization of Py and 3,4-dimethyl-1H-pyrrole (Melling et al. 2011, 2015).

Information regarding the appropriate operating load, extent of creep, and cycle life has been obtained by Madden et al. These authors performed a series of experiments on free-standing polypyrrole (PPy(PF₆)) film actuators using isotonic testing apparatus (ITA) to investigate creep, passive, and active cycle life (Madden et al. 2007).

This apparatus, shown in Fig. 13, is composed of two modules: an upper module containing force and displacement sensors, the actuators, the upper clamp and probe; a lower module composed of a lower clamp and bath.

Figure 14 depicts two creep responses taken on one sample. During these tests the stress is stepped from 2 to 20 MPa, where it is held for 100 min, and then returned to 2 MPa while recording strain. The lower curve results from the same test performed

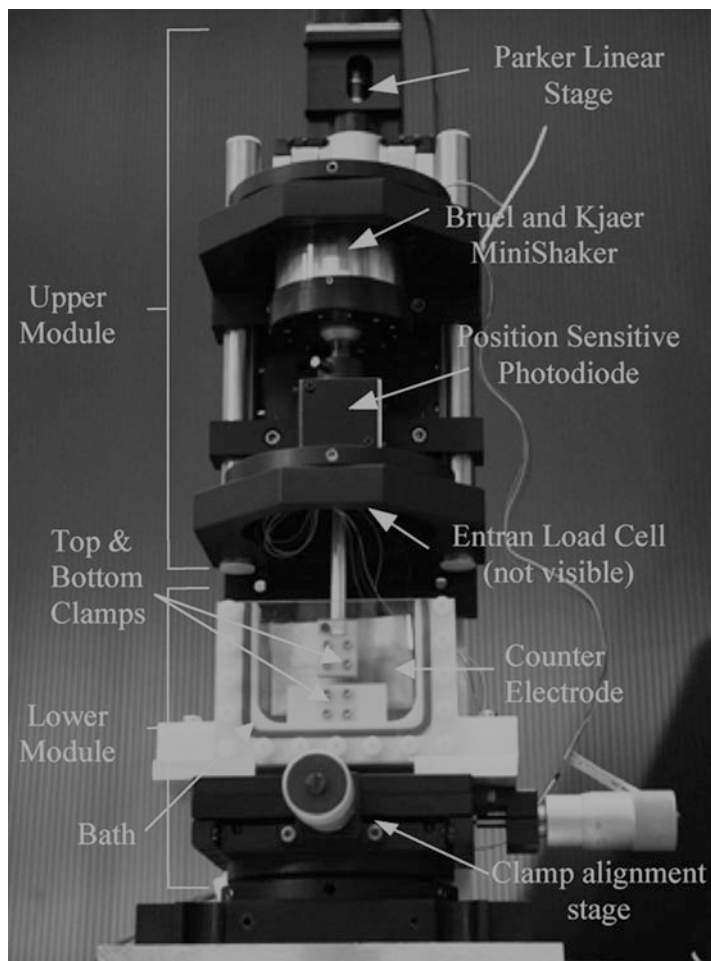


Fig. 13 Testing apparatus and a solution containing bath (Reprinted from Madden et al. (2007))

6 days later. Note that the rate of creep is reduced by a factor of 3 from the original measurement. This reduction in creep may be due to a gradual stretch alignment of the film in the axial direction, making deformation more difficult. In a time invariant system the responses should be identical, but instead clearly demonstrate that the film mechanical properties are dependent on the load history.

The polypyrrole creep response is clearly history dependent and nonlinear at the very high loads employed in this study. The sequence of results for the same sample displayed in Fig. 14 shows that after enduring high stresses over significant periods of time (~ 100 min), creep can be substantially reduced. This effect may be useful as

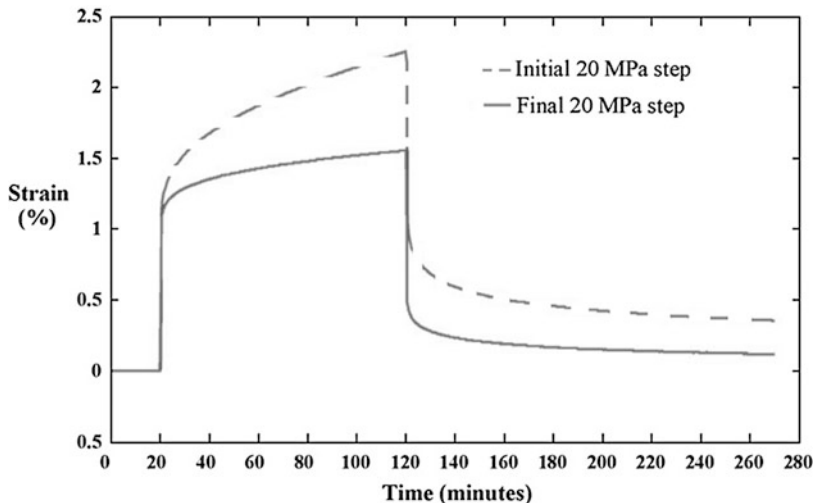


Fig. 14 History dependence of creep in a single (one sample) polypyrrole film. An initial load of 2 MPa is applied. Stress is then increased to 20 MPa for 100 min and returned to 2 MPa for the final 150 min. The dashed-curve data was taken 2 days after immersion of the sample in propylene carbonate, and the solid-curve data was obtained a further 6 days later. Measurements were performed at 24 °C (Reprinted from Madden et al. (2007))

a pretreatment in cases where high load operation is required with minimal creep, although exposure to high loads could also reduce electrochemically induced strain.

Temperature has a large influence on the speed of passive mechanical response/creep. Figure 15 shows the response at 44 °C and 24 °C. The creep is much faster at the higher temperature. This is most evident when the static modulus (ratios of total stress and strain) is plotted versus time on a log–log scale in Fig. 15. The similarity of the two curves in the log–log domain suggests that time–temperature equivalence may apply. If operation is expected at a variety of temperatures then the need for compensation under position control will be greater at higher temperatures, and the time over which loads can be held will be shorter. This will be important for operation *in vivo*, for example, where creep will be accelerated relative to room temperature.

Another failure mechanism is fatigue, which is induced in response to passive cycling (the cyclic application of a load without the application of an electrical potential). Samples soaked in polypropylene carbonate held for 6000 min at 10 MPa and a dynamic load of ± 4 MPa was applied at 3 Hz. Samples subjected to one million cycles show no apparent fatigue, suggesting that loading is not limiting cycle life.

Films cycled by applying square wave electrical potentials do show a drop in active strain with cycle number. Figure 16 shows that strain amplitude decreases from 2 % to 1 % after 7000 cycles and an increased rate of creep is also observed during actuation. When the potential range is reduced such that the initial strain

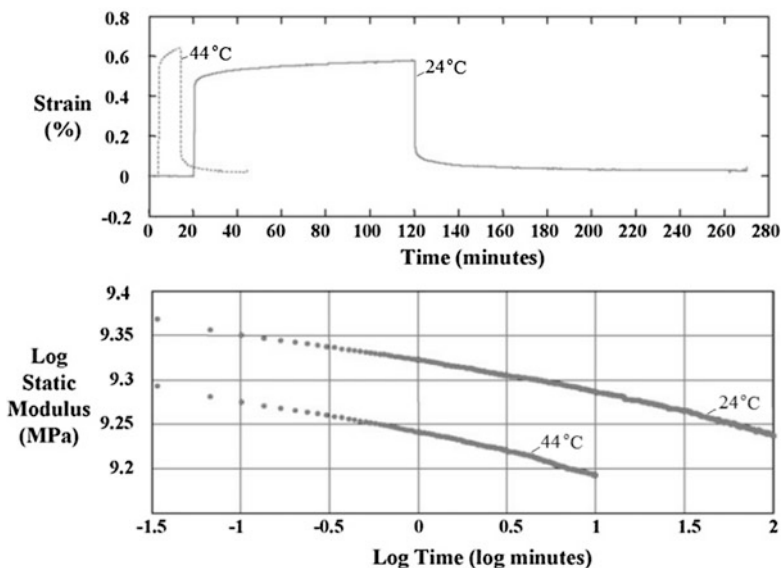


Fig. 15 Temperature dependence of creep. Stress is stepped between 2 and 10 MPa in a sample at 44 °C and 24 °C. The 10 MPa stress is held for 10 min at 44 °C and 100 min at 24 °C, after which stress is returned to 2 MPa. The *top* plot is the strain versus time; the *bottom* plot is the ratio of stress to strain over time (Reprinted from Madden et al. (2007))

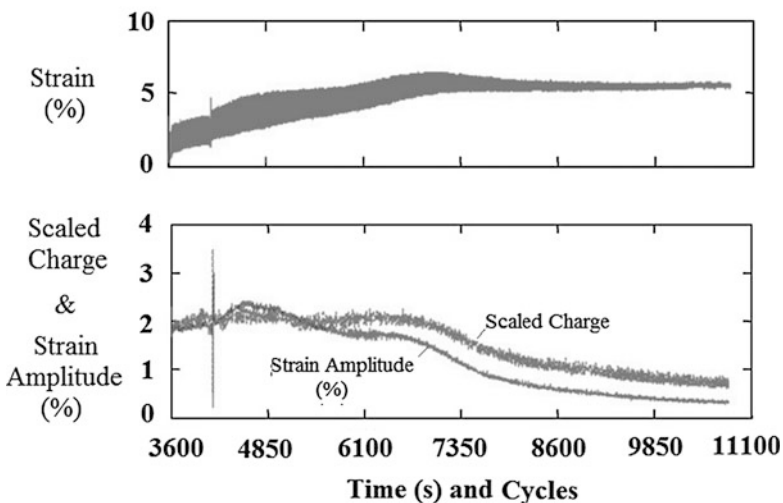


Fig. 16 Final 7000 cycles of a 10,600 cycle active test performed at 0.24 Hz and at 2.5 MPa. The *top* plot depicts strain versus cycles. The *bottom* plot shows the 0.24 Hz strain amplitude and charge density amplitude as functions of time. The charge density is scaled by an estimated strain to charge ratio of $2.5 \times 10^{-10} \text{ m}^3 \text{ C}^{-1}$ to show the correlation between charge density and strain (Reproduced from Madden et al. (2007))

amplitude is 1.5 %, the strain drops to 1 % after 32,000 cycles. An increase in the frequency of actuation (0.25–1 Hz) therefore leads to an increase in the life time of the actuator. The reduction in strain amplitude correlates with a decrease in charge transferred, suggesting degradation of the polymer is the cause of the loss in strain amplitude.

2.3 Other Characterization Methods

2.3.1 Profilometry

Profilometry is a metrological technique that measures changes in the heights of surface features by scanning them with a stylus maintained in contact with the surface (Fig. 17). This has led to it being used to measure the change in film thickness during electrochemical cycling and can be used to characterize bulk actuation.

Gadegaard et al. used a profilometer to study the actuation of polypyrrole films doped with dodecylbenzenesulphonate, PPy(DBS) (Smela and Gadegaard 2001). They observed an increase in thickness of 26 % during the first reduction. During oxidation, the thickness decreased but remained 6.5 % larger than in the as-deposited oxidized state (Fig. 18). Both bilayer and profilometry measurement techniques show irreversible behavior during the first redox cycle, but the behavior of the film is different in the x - y and z directions. They also observed a 19 % increase in the thickness of a 16.8 μm PPy(DBS) film in the reduced state compared to the oxidized state. This was much larger than expected from measurements of free-standing films or bilayers, both of which reveal in-plane dimensional changes.

Profilometry also revealed that dry PPy(DBS) films undergo considerable swelling ($\sim 11\%$) when immersed in aqueous 0.1 M NaDBS electrolyte. This supports the work of Bay et al. who showed that the ionic composition of the polymer generates an osmotic pressure (Bay et al. 2001; Velmurugu and Skaarup 2005). The solvent is distributed between the polymer matrix and the surrounding electrolyte; water is

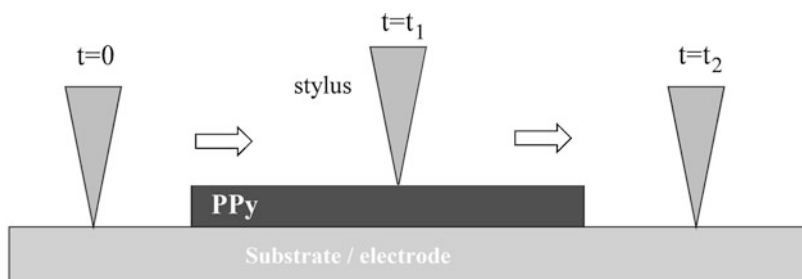
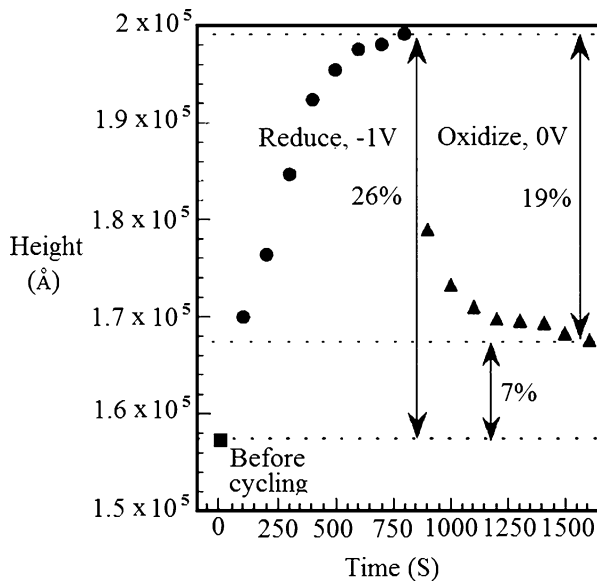


Fig. 17 Illustration of the thickness measurement method by mechanical profilometry, performed with the samples immersed in the electrolyte (not shown) (Reprinted (adapted) with permission from Wang and Smela (2009a). Copyright (2009) American Chemical Society)

Fig. 18 The change in height of a $16.8\ \mu\text{m}$ PPy(DBS) film over time. The volume in the oxidized state under electrochemical cycling did not return to the same volume before cycling; there was an irreversible increase in height. This corresponds to an irreversible volume change in a direction out of the plane of the film (z-direction) (Reprinted (adapted) with permission from Smela and Gadegaard (2001). Copyright (2001) American Chemical Society)



driven into the polymer to counteract differences in water activity between the two phases.

A serious complication of using profilometry to measure volume change becomes apparent when attempting to make measurements on thin films ($<10\ \mu\text{m}$). Here the applied force from the stylus can lead to anomalous results such as a smaller PPy (DBS) film thickness in the expanded (reduced) state than in the contracted (oxidized) state. This is due to the lower stiffness (Young's modulus of elasticity) in the reduced state compared to the oxidized state resulting in the stylus sinking into the softer polymer. This is not a problem for relatively thick films provided absolute values are not required; profilometry can serve as a useful tool to observe the actuation of thick conducting polymer films.

Wang et al. combined profilometry and optical measurements to investigate the optical-mechanical-electrochemical coupling in PPy(DBS) during electrochemical switching (Wang and Smela 2009a, b). They used a special experimental geometry (Fig. 19) in which the top surface of the PPy film is covered by a transparent ion barrier, which constrains the charge-compensating cations to enter the film only at the edges. Since the ion barrier is transparent, any color change in the underlying PPy(DBS) film can be observed from above.

The out-of-plane strain of an ion barrier-covered PPy(DBS) film is shown in Fig. 20a during reduction for the first time at $-1.0\ \text{V}$. The gray line shows the thickness of the as-deposited PPy with the overlying SU8 layer. The slow ion velocity during the first reduction scan, which took approximately 4 min, allowed snapshots of the process to be taken since the height profiles were completed in only 2 s. The thin black lines in Fig. 20a are profiles taken 40 s apart, and the thick black

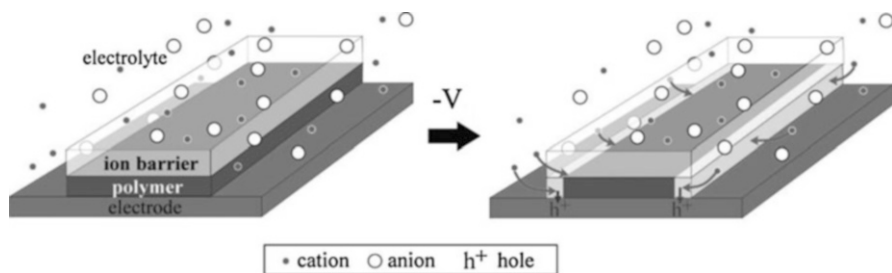


Fig. 19 Device configuration that makes ion transport the rate limiting step during electrochemical switching of a conjugated polymer. The polymer is patterned into a long, narrow stripe over an electrode and is covered on the top side with a transparent ion-blocking layer (vertical dimensions exaggerated for clarity). Ions enter and exit the polymer from the long edges. The color of the film varies with its oxidation level, which cannot change until charge-compensating ions arrive or leave (Reprinted (adapted) with permission from Wang and Smela (2009a). Copyright (2009) American Chemical Society)

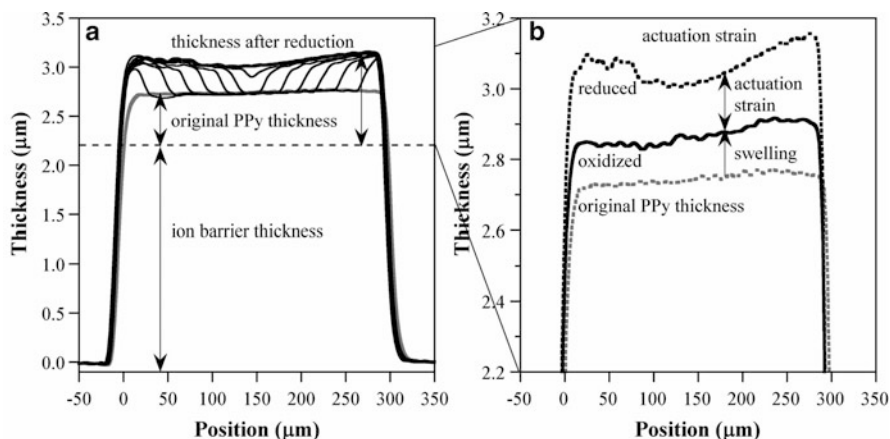


Fig. 20 (a) Height changes during the first-ever reduction (-1 V vs. Ag/AgCl). Shown are the as-deposited PPy + SU8 thickness (*gray line*), thickness snapshots taken every 40 s during the reduction process (*thin black lines*), and the completely reduced thickness (*thick black line*). The unchanging ion barrier thickness is indicated schematically by the *dashed line* (in actuality the SU8 is above, not below, the PPy.) (b) Magnified view of the subsequent height changes during later actuation cycles (Reprinted with permission from Wang and Smela (2009a). Copyright (2009) American Chemical Society)

line shows the final, completely reduced state, which was 55 % thicker than the as-deposited film.

The height increased stepwise to a value corresponding to the maximum ion concentration in the PPy, and the steps traveled from the edges of the film to the center. The thickness at the edges did not increase further as the front advanced.

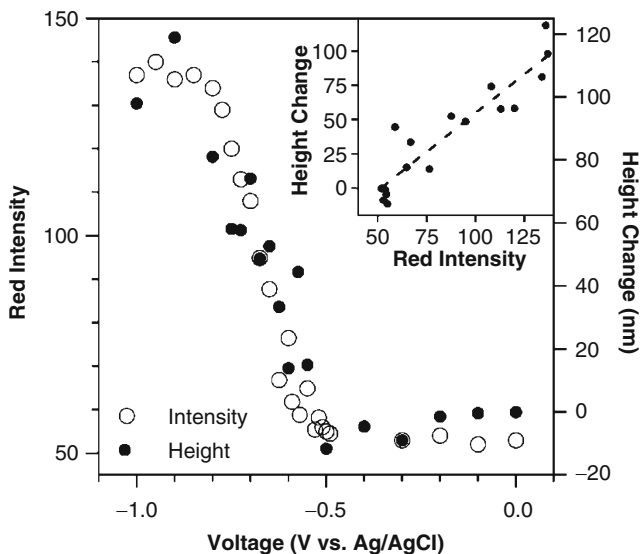


Fig. 21 Red channel intensity (*open circles*, left axis) of an uncovered PPy film that was 400 nm thick as deposited and thickness change (*black points*, right axis) in an SU8-covered PPy film that was 420 nm thick as deposited versus the applied reduction potential after stepping from 0 V and holding for several minutes. The *inset* shows the height change versus the red channel intensity between 0 and -1 V, with a linear fit of $y = -59 + 1.14x$, $R = 0.93$ (Reprinted with permission from Wang and Smela (2009a). Copyright (2009) American Chemical Society)

Upon reoxidation (shown in the close-up Fig. 20b), the PPy thickness did not return back to its original, as-deposited value.

A quasi-irreversible swelling occurred in the first cycle: The oxidized state was 25 % thicker than the as-deposited film. This irreversible swelling is consistent with results obtained on uncovered PPy(DBS) films with atomic force microscopy (Smela and Gadegaard 2001) and with the hypothesis that water enters the film during the first reduction scan and remains in the film during reoxidation. (This may also be the case for some fraction of the cations since the charge consumed during the first reduction scan is larger than in later scans.) In subsequent cycles, the height changed reproducibly between the reduced state value and the oxidized state value, with a reversible actuation strain, based on the oxidized film thickness, of 28 %.

The cation concentration determines the volume of the polymer and is also directly related to the oxidation level of the polymer, which in turn determines its color. During electrochemical reduction, the edges of the film lighten, and this light color travels as a front to the center of the film. At the same time, the height of the film increases when and where the color lightens, and the increase in height is directly proportional to the change in color intensity (Fig. 21). This means that the increasing in film thickness can be followed optically, as a noncontact measurement.

The use of profilometry, along with this special experimental geometry, has led to a greater understanding of in-plane ion movement with the development of physics

models (Wang et al. 2009). The future development of a method for studying out-of-plane ion movement would further aid the understanding of ion movement and refinement of the physical model developed by Wang et al.

Stylus based profilometers such as the Dektak have not been designed for operation in a liquid. Typically, (a portion of) the stylus tip is inserted in the electrolyte and the drag on the stylus during the scanning may influence the measurement creating a possible error source in these setups. Therefore, Svennersten et al. did *ex situ* measurement of the perpendicular expansion using a Dektak (Svennersten et al. 2011). They were able to follow the volume change having a ~ 10 % perpendicular expansion. However, even though the measurement time outside the electrolyte was only a few seconds, it did later show that these numbers might actually be underestimated due to evaporation of the solvent from the film. *In situ* volume change measurements in liquid using an optical profiler with a dip-down objective showed higher numbers, up to 30 % (Jager 2011, unpublished results).

2.3.2 Atomic Force Microscopy

Atomic force microscopy (AFM) has been also been used to examine the actuation of polypyrrole films doped with dodecylbenzenesulfonate (PPy(DBS)) (Smela and Gadegaard 1999, 2001; Gelmi et al. 2010). AFM is a similar characterization technique to profilometry that measures very small changes in height by scanning (raster) the surface using a small cantilever arm. The cantilever tip force employed in AFM is so small that the serious complication observed for thin films using surface profilometry are not observed and it can be used in a liquid environment. The setup developed by Smela et al. is shown in Fig. 22. The films were photolithographically patterned to allow the scan to start on the substrate, go over the film, and return back to the substrate, giving an absolute height measurement (Fig. 23).

This technique allows the real-time volume change to be mapped *in situ* in the out-of-plane direction. This has shown that the PPy(DBS) film thickness increased by over 35 % in the reduced state compared to the oxidized state (Fig. 24). This compares with an in-plane strain of 2 % found in prior studies using bilayers, showing that the volume change of PPy(DBS) is anisotropic. The anisotropic strain of PPy(DBS) supports the view that it has a lamella structure with planes orientated parallel to the substrate (Wernet et al. 1985).

The height change depended on film thickness as well as the width of the photolithographically patterned feature (Fig. 25). An optimal thickness was observed at which maximum expansion occurred. For both the 10 and 30 μm width features, an optimum expansion of 1.5 μm was observed. For thinner and thicker films, the expansion was smaller. This might be the result of structural changes that have been reported by Naoi et al. for PPy(DBS) above ~ 0.33 μm (Naoi et al. 1995).

The AFM setup can also be used to determine the polymer response and strain rate; During reduction, 80 % of the volume change occurred within the first 12 s, with an initial strain rate (slope) of 57.5 nm/s (3 %/s). During oxidation, 80 % of the volume change took 11 s and the initial strain rate was -84.3 nm/s (-4.5 %/s).

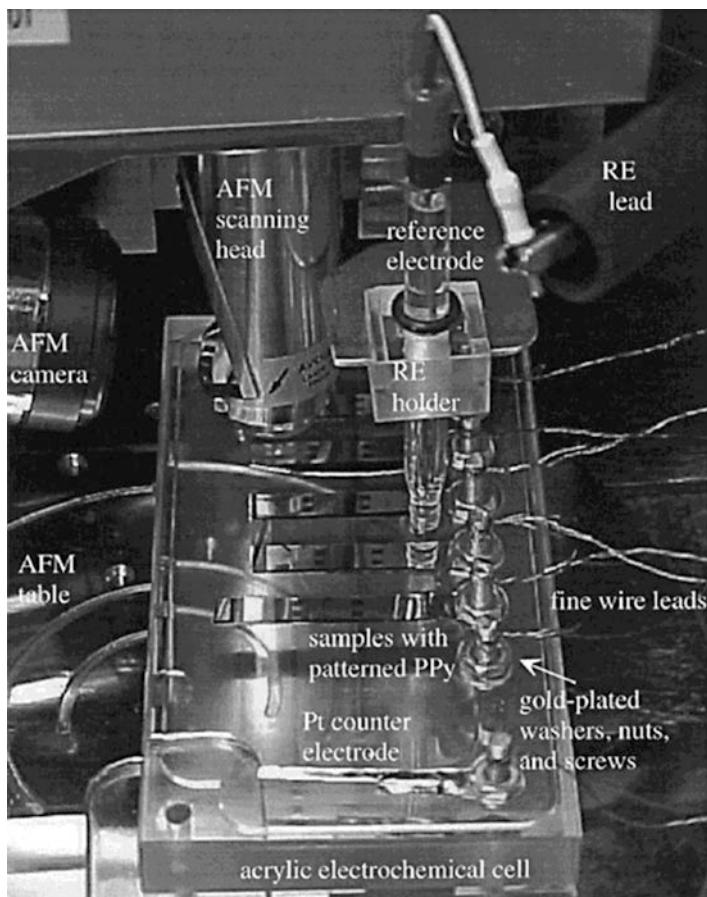


Fig. 22 Experimental setup showing the electrochemical cell under the AFM scanning head, the samples of patterned PPy on Au-coated silicon and the counter and reference electrodes (Reproduced from Smela and Gadegaard (1999))

After the first 11–12 s, the strain rate changes abruptly to 0.7 nm/s (0.04 %/s) for reduction and -0.45 nm/s (-0.02 %/s) for oxidation (Smela and Gadegaard 2001).

2.3.3 Laser-Scanning Micrometry

The characterization of CP films has been undertaken by Melling et al. using laser-scanning micrometry (LSM) (Melling et al. 2013, 2015). Their setup comprises of a three-electrode electrochemical cell, potentiostat, and LSM. CP films are grown on the surface of a gold wire working electrode (WE) which has been positioned to vertically cut the plane of the LSM. The LSM and electrochemical cell is shown schematically in Fig. 26.

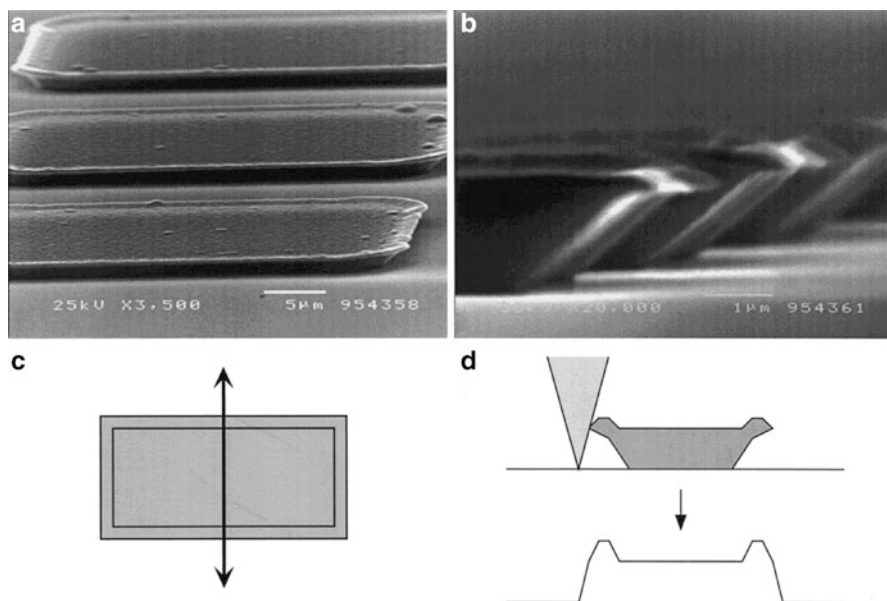


Fig. 23 SEM photograph of 30 nm wide PPy(DBS) rectangles: (a) oblique view (b) close-up side view (c) illustration of scans (d) illustration of the profile resulting from a scan of a feature with the cross-section shown in (b) (Reproduced from Smela and Gadegaard (1999))

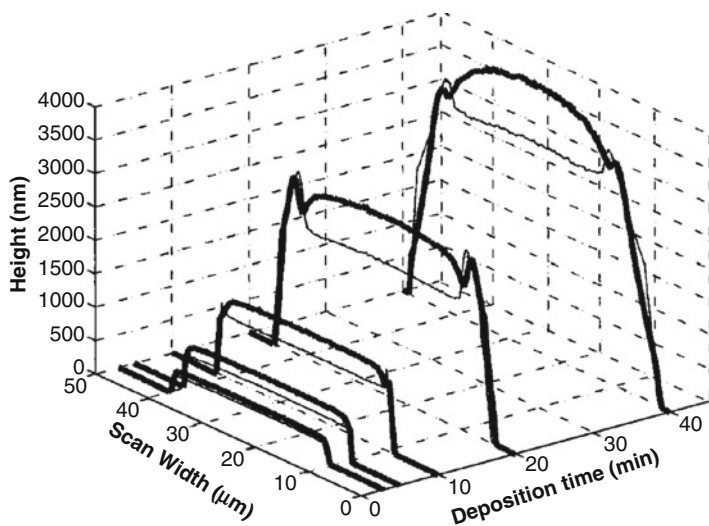


Fig. 24 Horizontal cuts for PPy(DBS) films of different thickness in the oxidized (*thin lines*) and reduced (*thick lines*) states (Reprinted with permission from Smela and Gadegaard (2001). Copyright (2001) American Chemical Society)

Fig. 25 Expansion as a function of film thickness. PPy(DBS) rectangles with two widths were examined: 10 and 30 μm (Reprinted with permission from Smela and Gadegaard (2001). Copyright (2001) American Chemical Society)

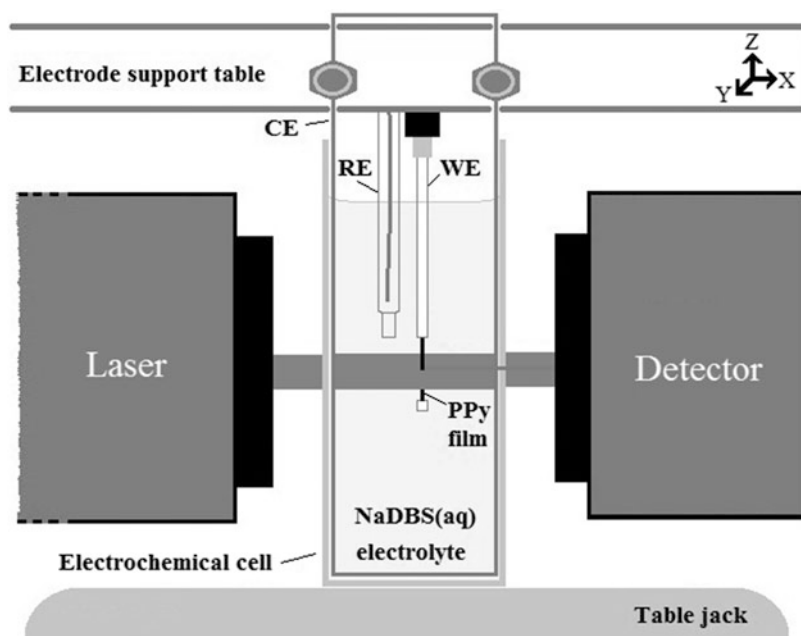
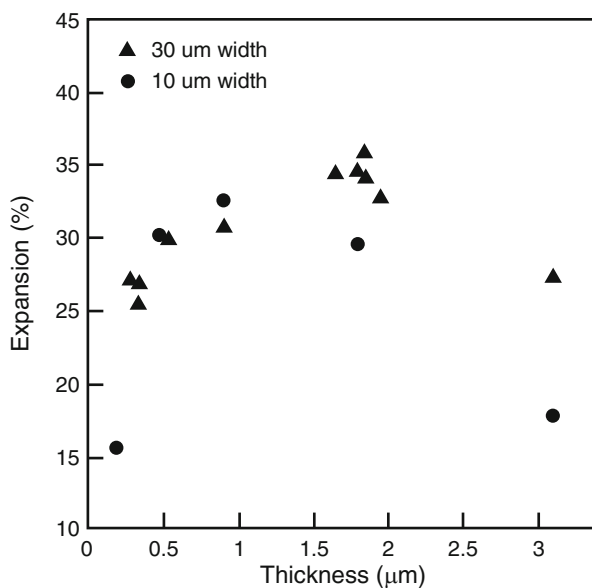


Fig. 26 A depiction of the electrochemical cell arrangement used to make actuation measurements. The scanning laser passes through the transparent electrochemical cell undisturbed until it meets the PPy coated AuWE which blocks its path and casts a shadow on the detector equal to its diameter (Reproduced from Melling et al. (2013) © IOP Publishing. Reproduced by permission of IOP Publishing. All rights reserved)

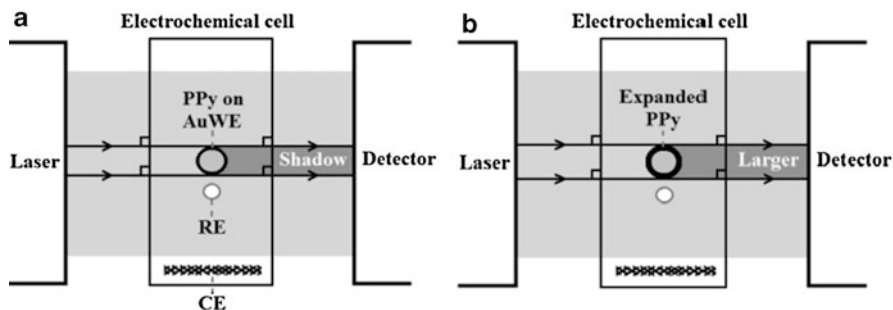


Fig. 27 Plan views of the LSM setup shown on Fig. 26 illustrating the principle of dimensional measurement using the LSM. (a) The shadow cast by the cross-section of the PPy coated AuWE. (b) The increase in the shadow due to the increase in the diameter caused by the expansion of the polymer film (Reproduced from Melling et al. (2013) © IOP Publishing. Reproduced by permission of IOP Publishing. All rights reserved)

The principle of operation is illustrated in Fig. 27. The LSM repeatedly scans a line in one direction at high speed. A gold wire working electrode (AuWE) coated with a PPy film inserted in the beam casts a ‘shadow’, equal to its diameter, onto the LSM detector. As the dimensions of the polymer film change during deposition or actuation, the shadow cast on the detector changes accordingly. By noting the initial diameter of a cross-section of the Au wire, PPy film thicknesses can be calculated along with a variety of other performance metrics. This data is recorded simultaneously with electrochemical data from experiments controlled by the potentiostat and associated software (GPES).

The growth of CP films can be monitored in real-time films allowing precise control over film thickness (Fig. 28). This ensures that actuation of different CP films of the same thickness can be compared. This is necessary for fair comparison as the actuation of CP films is thickness dependant (Melling et al. 2013).

After the polymerization solution has been exchanged for an actuating solution, the CP films are actuated until actuations stabilize. The first three cycles (conditioning cycles) and cycles 102–104 (steady state cycles) obtained using the LSM setup for PPy(DBS) film are shown in Fig. 29. The out-of-plane (diametrical/radial) strain and strain rate of films can then be determined from the recorded sequence along with electrochemical data recorded by the potentiostat and associated software.

The actuation sequence shown in Fig. 30 for PPy(DBS) shows two components to the expansion, a reversible and an irreversible component. The irreversible component can be attributed to processes such as solvent swelling and electrochemical creep (Smela and Gadegaard 2001). The first cycle is known to display a large strain, greater than the subsequent cycles in the sequence (Wang and Smela 2009a). This has been attributed to the irreversible movement of solvent and ions into the polymer during the first cycle. It can take many tens of cycles before for the actuations become fully reversible. LSM has been used to study the effects variables such as film thickness (Fig. 30), cycling rate, and electrolyte concentration amongst others (Martinez et al. 2014; Melling et al. 2013).

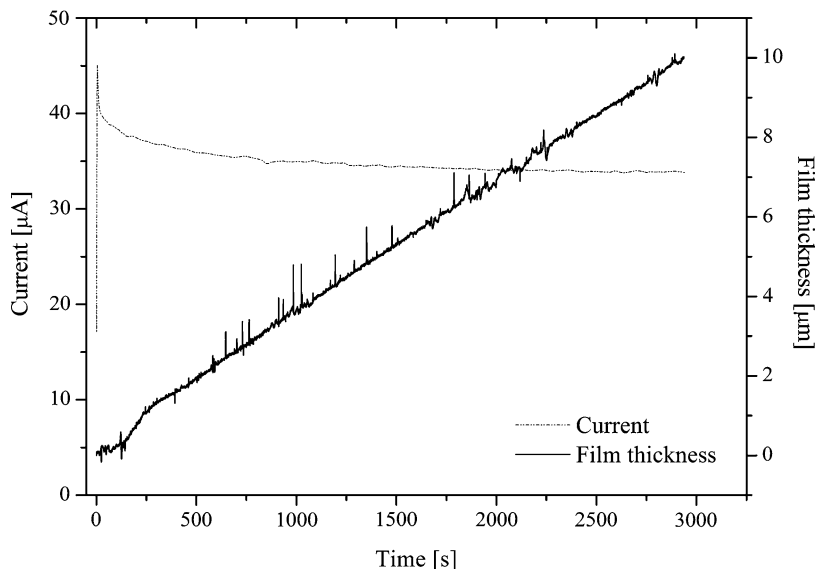


Fig. 28 Graphs showing the current and film thickness recorded during the polymerization of a 10 μm PPY film. Growth is essentially linear with slight instability and “spiking.” Spiking is contributed to the presence of particulate matter in the unfiltered polymerization solutions (Reproduced from Melling et al. (2013) © IOP Publishing. Reproduced by permission of IOP Publishing. All rights reserved)

The LSM approach is a relatively simple noncontact technique; unlike profilometry it is not subject to tip force errors. Furthermore, the films are not loaded which can be both an advantage and drawback in the characterization of the films. It characterizes the out-of-plane strain metrics of CP films. When combined with other characterization techniques that can provide in-plane or linear metrics, e.g. a tensile tester, it can be used to fully characterize CP films in both directions simultaneously.

3 Actuation Metrics

The actuation of CPs is a complex process involving many interrelated materials properties (Fig. 31). To fairly compare the actuation performance of one type of CP or device with another all of the parameters employed during the determination of a metric should be given such as the synthesis conditions (e.g., the dopant and solvent used); the cycling conditions (e.g., the scan rate, numbers of precycling); and the variable being measured (e.g., the in-plane or out-of-plane strain). Furthermore, given the large number of variables and values that these can take, it would greatly aid comparison if these variables were fixed at standard values. For example: the monomer and dopant concentrations used during polymerization might be fixed at 0.10 M; the temperature employed during synthesis and actuation could be fixed at 23 $^{\circ}\text{C}$ (or perhaps 37 $^{\circ}\text{C}$ for medical applications). What values the parameters

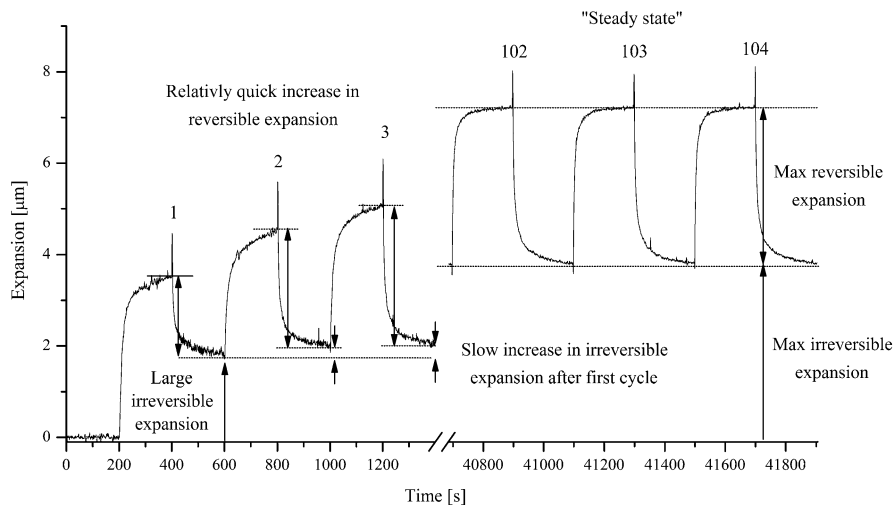


Fig. 29 Changes in reversible expansion and irreversible expansion with cycle number for a 10 μm film of PPy(DBS). Note: the reversible component stabilizes relatively quickly and reaches its maximum early on in the sequence, typically by cycle 10. After a large increase during the first cycle, the irreversible expansion displays a slower more gradual increase, reaching a stable maximum between 70 and 80 cycles (Reproduced from Melling et al. (2013) © IOP Publishing. Reproduced by permission of IOP Publishing. All rights reserved)

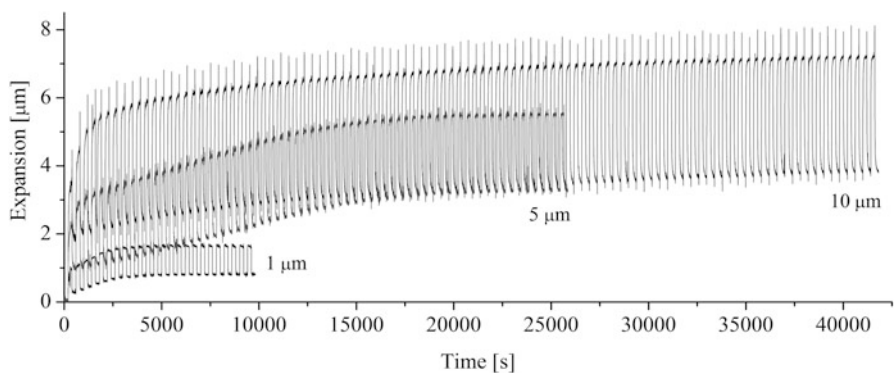
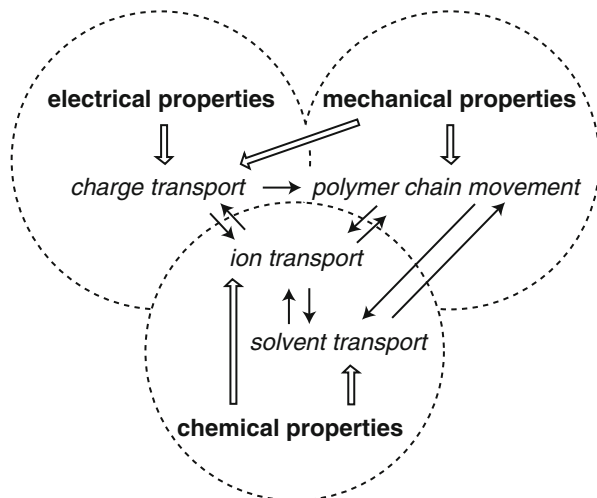


Fig. 30 Overlay of typical sequences obtained for 1, 5, and 10 μm PPy(DBS) films (Reproduced from Melling et al. (2013) © IOP Publishing. Reproduced by permission of IOP Publishing. All rights reserved)

should be fixed at will require agreement internationally between research groups working in the field or ISO standardization. This process is currently being undertaken by researchers coordinated by the European Scientific Network for Artificial Muscles (ESNAM, www.esnam.eu) and EuroEAP society (www.euroeap.eu).

Fig. 31 The interrelationship between materials properties of CPs (Reproduced from Smela (2003))



To illustrate the challenge of standardization, the remainder of this chapter will highlight a number of difficulties associated with the measurement of metrics. The standardization of metrics will require: standardization of the way that they are measured and calculated; that synthesis, geometric, and cycling parameters are known and ideally fixed. In addition, great care will need to be exercised to ensure that the metrics are relevant and not misleading.

3.1 Volume Change

The direct measurement of *volume* change is seldom undertaken as this would require the change in all three dimensions to be determined at the same time; it is much easier to measure the change in a single dimension. Furthermore, the change in length, thickness, or bending angle is of greater relevance to the operation of an actuator. For example, the change in length of a linear actuator will be more relevant than the change in its volume.

Changes in dimensions can be quoted as either an absolute or relative metric. For example: expansion is an absolute metric, typically quoted in μm or mm , which gives the movement in a specified direction; strain is a relative metric, typically quoted as a percentage or fraction, which relates the expansion to an 'initial' fixed dimension. Both of which can have their uses. However, the direction in which the expansion or strain is measured should be clearly specified, e.g., in-plane (x-y direction, parallel to the plane of the film) strain and out-of-plane (z-direction, perpendicular to the plane of the film) strain. In addition, how the strains have been calculated, e.g., relative to the as-synthesized passive length or relative to the stable length after precycling, should be clearly specified. Furthermore, it should be clearly stated whether the metric quoted is: a reversible or irreversible expansion or

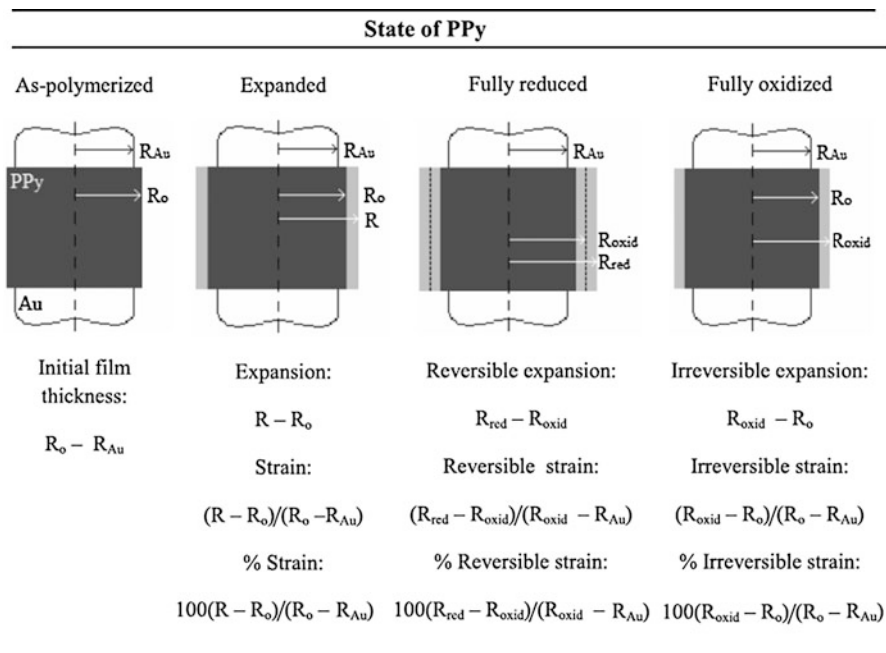


Fig. 32 Expressions used to calculate expansion and strain metrics. Key: AuWE (gold working electrode), R (general term for radius), RAu (radius of AuWE), Ro (initial radius of the “as-polymerized” PPy film C RAu), Rred (radius of the fully reduced PPy film C RAu), Roxid (radius of the fully oxidized PPy film C RAu) (Reproduced from Melling et al. (2013) © IOP Publishing. Reproduced by permission of IOP Publishing. All rights reserved)

strain; undertaken during reduction or oxidation half-cycle; the expansion or strain in the first cycle (known to be anomalous) or a later (stable) cycle.

The calculations used to determine the out-of-plane reversible and irreversible expansion and strain metrics of the CP films during the oxidation and reduction half-cycles via LSM micrometry (see Sect. 2.3.3) are given in Fig. 32 as an example.

Furthermore, if strains are calculated for a given half-cycle relative to the film thickness at the start of the half-cycle, as opposed to the as-deposited film thickness, for films that display an irreversible strain, e.g., PPy(DBS) films, this can be misleading. Here the reference (oxidized) film thickness is not fixed during early cycles, increasing due to irreversible process such as solvent swelling and creep. If the film thickness at the start of the cycle is used to calculate the reversible strain, the film can appear to undergo a *decrease* in reversible strain/performance between the early cycles and later cycles simply because the reference thickness is increasing (see Fig. 33). If the reversible strain is calculated relative to the as-deposited film thickness, the reversible strain can be seen to remain *constant* between the early cycles and later stable state cycles. In such circumstances, care needs to be exercised to not draw the wrong conclusions, for example, attributing a decrease in reversible

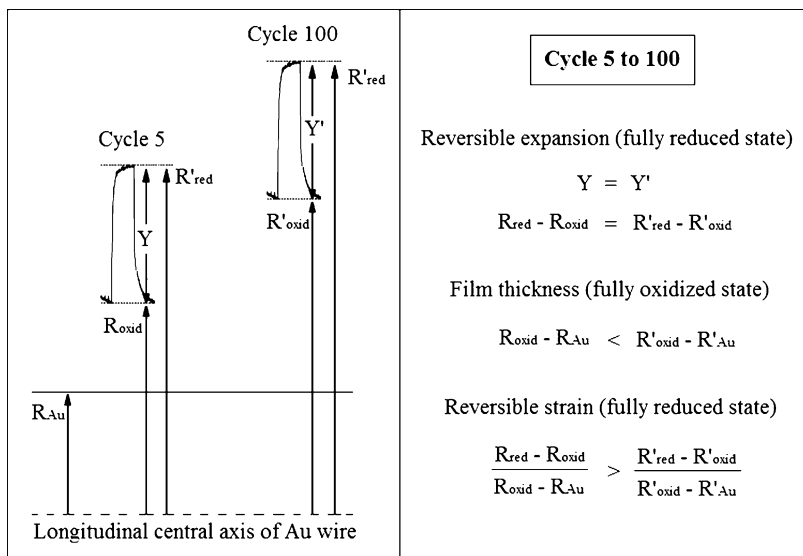


Fig. 33 Comparison of reversible expansion and reversible strain between cycles 5 and 100. Note: Although the *reversible expansion* is the same in cycle 5 and 100, the *reversible strain* decreases on going from cycle 5 to 100 due to the increase in film thickness

strain between the early and later stable state cycles to changes occurring in the CP such as chemical decomposition.

3.2 Speed

The maximum rate of expansion or strain can be assessed using different metrics. For CP films, the maximum expansion and strain rates and the time to 90 % maximum expansion have been used as metrics. Figure 34 shows how to calculate these metrics for CP films.

The maximum expansion and strain occurs just after the film is electrically switched and is given by the tangent drawn to the curve of maximum gradient. This metric has the advantage of being independent of the cycling rate. However, it requires that a relatively fast sampling rate (small data point interval) be used.

The time it takes to reach 90 % of the maximum expansion is a metric that measures the average speed over a specified time period. First of all using the number 90 % is quite arbitrary. Moreover, unfortunately this time period is not fixed when measuring the same CP film but depends upon several factors such as the film thickness and the cycling rate. In this respect, the maximum rate of expansion can be seen as a more reliable metric for assessing the rate of volume change. In addition, if a low cycling rate is employed, 90 % of the maximum film thickness occurs during the slow expansion phase that occurs in the later part of the half-cycle. This corresponds to the slower osmotic movement of solvent molecules as opposed

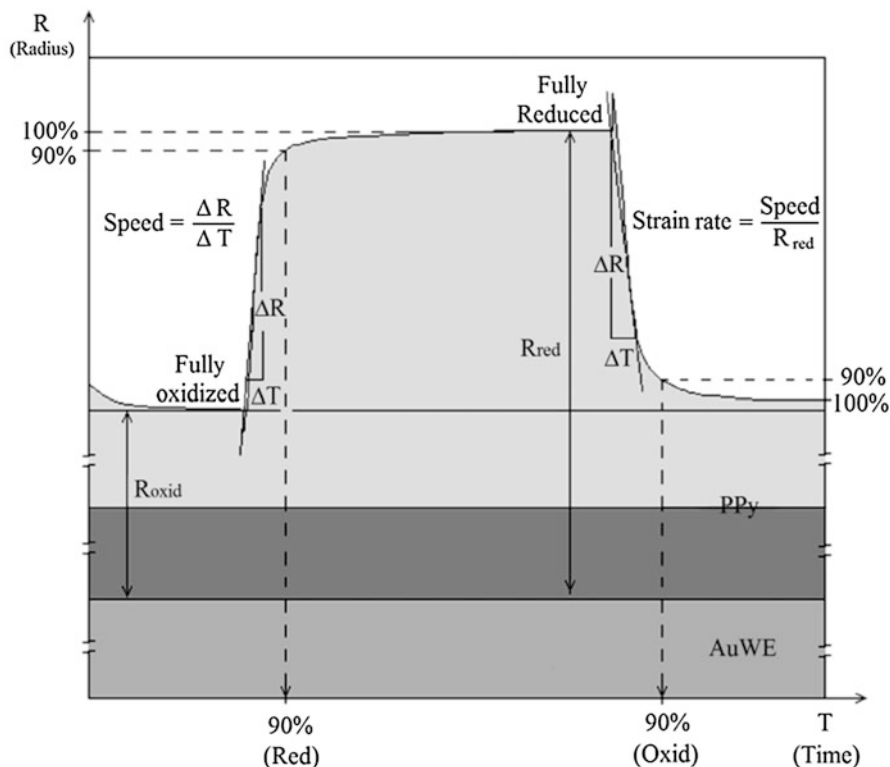


Fig. 34 Metrics used to represent how fast the PPy films actuate: expansion rate (speed), strain rate, and time taken to reach 90 % maximum reversible expansion (Reproduced from Melling et al. (2013) © IOP Publishing. Reproduced by permission of IOP Publishing. All rights reserved)

to the earlier fast expansion phase associated with the insertion of ions. The shallow gradient in the slow expanding phase mean that small variations (electrochemical noise) in the actuation profile can lead to large variations between replicate samples.

4 Conclusion

The different approaches to the characterization of CP EAPs outlined in this chapter have been developed to characterize one of the actuation modes commonly employed in devices. These are capable of yielding reliable and accurate metrics provided that all of the know variables that impact on the actuators performance are known and under control. When metrics are quoted, it should be clear exactly how they were determined and calculated. Otherwise, they will be of little value or misleading. However, even when these conditions are clearly stated, it will be difficult to compare the results measured under one set of conditions with those measured under another. Hence, there exists a great need for standardization within

the CP EAP community. Standard approaches to characterization, the conditions under which they are taken, and how they are measured and presented are needed and to be adopted by all researchers in the field. In addition, the development of a single approach that is capable of simultaneously characterizing various actuation modes, e.g., linear and perpendicular strain, or bending and bulk volume change is desirable. Such an approach would allow actuators to be studied while undertaking the full range of movements that they will display during use.

Standardization would increase the confidence of engineers to use these materials in their devices and advance the field of CP EAPs. Whatever the future holds the standardization of characterization and the calculation of metrics remains essential to our understanding of the basic science, improving performance of materials and their use in devices.

References

- Alici G, Huynh NN (2007) Performance quantification of conducting polymer actuators for real applications: a microgripping system. *IEEE/ASME Trans Mechatron* 12:73–84
- Bay L, Jacobsen T, Skaarup S, West K (2001) Mechanism of actuation in conducting polymers: osmotic expansion. *J Phys Chem B* 105:8492–8497
- Berdichevsky Y, Lo YH (2003) Polymer microvalve based on anisotropic expansion of polypyrrole. *MRS Online Proc Libr* 782:101–107
- Chiarelli P, Della Santa A, De Rossi D, Mazzoldi A (1995) Actuation properties of electrochemically driven polypyrrole free-standing films. *J Intell Mater Syst Struct* 6:32–37
- Córdova FG, Ismail YA, Martínez JG, Al Harrasi AS, Otero TF (2013) Conducting polymers are simultaneous sensing actuators. In: *Proceedings of SPIE – The International Society for Optical Engineering*, vol 8687
- Della Santa A, De Rossi D, Mazzoldi A (1997a) Characterization and modelling of a conducting polymer muscle-like linear actuator. *Smart Mater Struct* 6:23–34
- Della Santa A, De Rossi D, Mazzoldi A (1997b) Performance and work capacity of a polypyrrole conducting polymer linear actuator. *Synth Met* 90:93–100
- Du P, Lin X, Zhang X (2010) A multilayer bending model for conducting polymer actuators. *Sens Actuators A* 163:240–246
- Fernández-Otero T, Vázquez G, Valero L (2010) Conducting polymers as simultaneous sensor-actuators. In: *Proceedings of SPIE – The International Society for Optical Engineering*, vol 7642
- Festin N, Maziz A, Plesse C, Teysié D, Chevrot C, Vidal F (2013) Robust solid polymer electrolyte for conducting IPN actuators. *Smart Mater Struct* 22(10), Art. No. 104005
- Gelmi A, Higgins MJ, Wallace GG (2010) Physical surface and electromechanical properties of doped polypyrrole biomaterials. *Biomaterials* 31:1974–1983
- Hara S, Zama T, Takashima W, Kaneto K (2004a) Artificial muscles based on polypyrrole actuators with large strain and stress induced electrically. *Polym J* 36:151–161
- Hara S, Zama T, Takashima W, Kaneto K (2004b) Polypyrrole-metal coil composite actuators as artificial muscle fibres. *Synth Met* 146:47–55
- Kaneko M, Kaneto K (1998) Electrochemomechanical deformation of polyaniline films doped with self-existent and giant anions. *React Funct Polym* 37:155–161
- Kaneto K, Shinonome T, Tominaga K, Takashima W (2011) Electrochemical creeping and actuation of polypyrrole in ionic liquid. *Jpn J Appl Phys* 50(9), PART 1, Art. No. 091601
- Madden JD, Cush RA, Kanigan TS, Hunter IW (2000) Fast contracting polypyrrole actuators. *Synth Met* 113:185–192

- Madden JD, Rinderknecht D, Anquetil PA, Hunter IW (2007) Creep and cycle life in polypyrrole actuators. *Sens Actuators A* 133:210–217
- Martinez JG, Otero TF, Jager EWH (2014) Effect of the electrolyte concentration and substrate on conducting polymer actuators. *Langmuir* 30:3894–3904
- Maw S, Smela E, Yoshida K, Sommer-Larsen P, Stein RB (2001) The effects of varying deposition current density on bending behaviour in PPy(DBS)-actuated bending beams. *Sens Actuators A* 89:175–184
- Maw S, Smela E, Yoshida K, Stein RB (2005) Effects of monomer and electrolyte concentrations on actuation of PPy(DBS) bilayers. *Synth Met* 155:18–26
- Melling D, Wilson SA, Berggren M, Jager EWH (2011) Altering the structure of polypyrrole and the influence on electrodynamic performance. In: *Proceedings of SPIE – The International Society for Optical Engineering*, vol 7976
- Melling D, Wilson SA, Jager EWH (2013) The effect of film thickness on polypyrrole actuation assessed using novel non-contact strain measurements. *Smart Mater Struct* 22(10), Art. No. 104021
- Melling D, Wilson SA, Jager EWH (2015) Controlling the electro-mechanical performance of polypyrrole through 3- and 3,4-methyl substituted copolymers. *RSC advances* 5:84153–84163
- Naoi K, Oura Y, Maeda M, Nakamura S (1995) Electrochemistry of surfactant-doped polypyrrole film(I): formation of columnar structure by electropolymerization. *J Electrochem Soc* 142:417–422
- Otero TF, Martinez JG (2012) Artificial muscles: a tool to quantify exchanged solvent during biomimetic reactions. *Chem Mater* 24:4093–4099
- Otero TF, Huerta FJ, Cheng S-A, Alonso D, Villanueva S (2000) Modulation of EAP properties through the variables of synthesis. *Proc SPIE Int Soc Opt Eng* 3987:148–158
- Otero TF, López Cascales JJ, Vázquez Arenas G (2007) Mechanical characterization of free-standing polypyrrole film. *Mater Sci Eng C* 27:18–22
- Otero TF, Martínez JG, Zaifoglu B (2013) Using reactive artificial muscles to determine water exchange during reactions. *Smart Mater Struct* 22(10), Art. No. 104019
- Pei Q, Inganäs O (1992) Electrochemical applications of the bending beam method. 1. Mass transport and volume changes in polypyrrole during redox. *J Phys Chem* 96:10507–10514
- Pei Q, Inganäs O (1993) Electrochemical applications of the bending beam method. 2. Electroshrinking and slow relaxation in polypyrrole. *J Phys Chem* 97:6034–6041
- Plesse C, Vidal F, Randriamahazaka H, Teyssié D, Chevrot C (2005) Synthesis and characterization of conducting interpenetrating polymer networks for new actuators. *Polymer* 46:7771–7778
- Plesse C, Vidal F, Teyssié D, Chevrot C (2010) Conducting polymer artificial muscle fibres: toward an open air linear actuation. *Chem Commun* 46:2910–2912
- Smela E (2003) Conjugated polymer actuators for biomedical applications. *Adv Mater* 15:481–494
- Smela E, Gadegaard N (1999) Surprising volume change in PPy(DBS): an atomic force microscopy study. *Adv Mater* 11:953–957
- Smela E, Gadegaard N (2001) Volume change in polypyrrole studied by atomic force microscopy. *J Phys Chem B* 105:9395–9405
- Smela E, Kallenbach M, Holdenried J (1999) Electrochemically driven polypyrrole bilayers for moving and positioning bulk micromachined silicon plates. *J Microelectromech Syst* 8:373–383
- Smela E, Lu W, Mattes BR (2005) Polyaniline actuators: part 1. PANI(AMPS) in HCl. *Synth Met* 151:25–42
- Sugino T, Kiyohara K, Takeuchi I, Mukai K, Asaka K (2009) Actuator properties of the complexes composed by carbon nanotube and ionic liquid: the effects of additives. *Sens Actuators B* 141:179–186
- Svennersten K, Berggren M, Richter-Dahlfors A, Jager EWH (2011) Mechanical stimulation of epithelial cells using polypyrrole microactuators. *Lab Chip* 11:3287–3293
- Timoshenko S (1925) Analysis of bi-metal thermostats. *J Opt Soc Am* 11:233–255

- Tominaga K, Hamai K, Gupta B, Kudoh Y, Takashima W, Prakash R, Kaneto K (2011) Suppression of electrochemical creep by cross-link in polypyrrole soft actuators. *Phys Procedia* 14:143–146
- Velmurugu Y, Skaarup S (2005) Ion and solvent transport in polypyrrole: experimental test of osmotic model. *Ionics* 11:370–374
- Wang X, Smela E (2009a) Color and volume change in PPy(DBS). *J Phys Chem C* 113:359–368
- Wang X, Smela E (2009b) Experimental studies of ion transport in PPy(DBS). *J Phys Chem C* 113:369–381
- Wang X, Shapiro B, Smela E (2009) Development of a model for charge transport in conjugated polymers. *J Phys Chem C* 113:382–401
- Wernet W, Monkenbusch M, Wegner G (1985) On structure and properties of Polypyrrole Alkyl-Sulf(on)Ates. *Mol Cryst Liq Cryst* 118:193–197

Meisam Farajollahi, Gursel Alici, Mirza Saquib Sarwar, and John D. W. Madden

Contents

1	The Basics: Underlying Physical Phenomena and the First-Order Models Used to Describe Them	354
1.1	Relationship Between Strain and Charge	355
1.2	Effect of Polymer Anisotropy on the Strain-to-Charge Ratio	356
1.3	Stress–Strain Relationship	357
1.4	State of Charge-Dependent Modulus	357
1.5	Creep and Stress Relaxation	357
1.6	Bending Structures: Tri-layer Equations	359
1.7	Inertial Effects and Rate Limits: Resonance	361
1.8	Charge–Voltage Relationship	362
1.9	Electronic and Ionic Conductivity Variation with State of Charge	363
1.10	Rate-Limiting Factors	364
1.11	Modeling Diffusion and Diffusion-Like Processes	366
1.12	Electromechanical Coupling and Efficiency	368
2	Conducting Polymer Sensors	369
2.1	Sensor Mechanisms	370

M. Farajollahi

Mechanical Engineering, Advanced Materials and Process Engineering Lab, University of British Columbia, Vancouver, BC, Canada

e-mail: m.farajollahi@mech.ubc.ca

G. Alici

School of Mechanical, Materials, and Mechatronic Engineering, ARC Australian Centre of Excellence for Electromaterials Science, University of Wollongong, Wollongong, NSW, Australia

e-mail: gursel@uow.edu.au

M.S. Sarwar • J.D.W. Madden (✉)

Electrical and Computer Engineering, Advanced Materials and Process Engineering Lab, University of British Columbia, Vancouver, BC, Canada

e-mail: mirzas@ece.ubc.ca; jmadden@ece.ubc.ca

3	System Identification Techniques Applied to Conducting Polymer Actuators and Sensors	372
3.1	Case Study: Identification of Transfer Function Models for EAP Sensors, A Black Box Model	373
3.2	Case Study: Identification of a Transfer Function Model for EAP Actuators, A Black Box Model	376
3.3	Case Study: Identification of a Transfer Function Models for EAP Actuators, A Gray Box Model	378
4	Overview	379
	References	380

Abstract

Conducting polymer actuators and sensors employ the coupling between electrochemistry and mechanics. The aim of this chapter is to equip the reader with the basic models needed in order to assess the feasibility of using conducting polymers, design devices, describe the device response, and predict behavior. The chapter begins with an overview of the basic observations and phenomena on which physical models are based, briefly describes models employed, and gives some references to literature presenting the models. The use of system identification techniques is then presented, and it is shown that these can very effectively be employed to create and validate models, as well as extract physical phenomena and enable predictions.

Keywords

Black box model • Conducting polymer actuators • Conducting polymer sensors • Charge density • Bending structures • Charge-dependent modulus • Charge–voltage relationship • Creep and stress relaxation • Diffusion models • Electromechanical coupling and efficiency • Electronic and ionic conductivity • Gray box model • Inertial effects–rare limits • Polymer anisotropy • Rate-limiting factors • Strain and charge • Stress–strain relationship • Mechanisms • Diffusion models • Donnan potential • Electrokinetic effect • Electromechanical coupling • Electronic conductivity • Ion mobility • Kelvin–Voigt model • Maxwell model • Nernst equation • Resonance frequency • Standard linear solid model • Volumetric capacitance • Wiechert model

1 The Basics: Underlying Physical Phenomena and the First-Order Models Used to Describe Them

The first section gives an overview of many of the basic models that have been employed to describe the electrical, electrochemical, mechanical, and electromechanical properties of conducting polymer actuators.

1.1 Relationship Between Strain and Charge

The key observation that underpins most models of conducting polymer actuators and also influences sensor descriptions is that the deformation of the polymer is proportional to the amount of charge transferred. Early work using relatively dense (nonporous) polypyrrole showed that expansion is observed when ions are inserted. This ion insertion occurs as the polymer is charged (or discharged) electrochemically (Pei and Ingnas 1993). Ionic charge is balanced by electronic charge (usually positive) on the polymer backbone. Figure 1 is a qualitative description of the expansion and contraction of the polymer due to oxidation and reduction.

Typically, only one ion is mobile within the polymer. This can be achieved, for example, by employing a combination of a large and small ion in the electrolyte so that the large, bulky ion effectively does not penetrate or remains immobile within the matrix. The mobile ion moves in or out of the polymer to balance electronic charge on the backbone. This relationship between ion content and deformation is expressed most simply through an empirical strain-to-charge ratio, α , which relates strain, ε , in one axis and the charge per volume, ρ :

$$\varepsilon = \alpha\rho. \quad (1)$$

The strain-to-charge ratio is in fact more precisely the strain-to-charge density ratio and has units of m^3/C . Charge density and ion concentration in moles per liter are simply related through Faraday's number, F (for monovalent ions, $\rho = 1000FC$ when concentration is in moles per liter, and other units are mks).

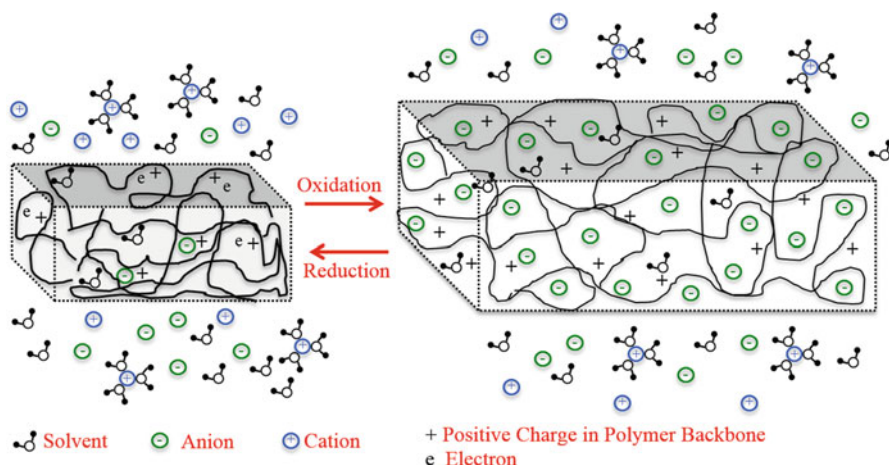


Fig. 1 Expansion and contraction of a conducting polymer surrounded by electrolyte as a result of oxidation and reduction. In this case, only the anions are mobile within the polymer. The scale of change is exaggerated

The relationship between charge and strain was first proposed (Baughman et al. 1991) to describe changes in dimension observed upon insertion of ions within polyacetylene as a result of electrochemical doping and provides a reasonable first-order description. Values of the strain-to-charge ratio, α , are typically on the order of 0.3 to $5 \times 10^{-10} \text{ m}^3/\text{C}$ (Cole 2006; Madden 2000). There is some frequency dependence (Madden et al. 2002a), potential dependence, and hysteresis (Bahrami-Samani et al. 2008) in the volume and length changes associated with electrochemical charging and discharging, and as a result, Eq. 1 is not a perfect description. The charge density, ρ , represents only the charge that is stored within the polymer and associated with ion transfer. Other reactions that consume charge without inserting ions (e.g., parasitic electrochemical reactions such as hydrolysis at the surface of electrodes) do not count toward the charging. A more general expression for the active strain resulting from insertion charge with multiple ions being mobile is

$$\varepsilon_{i,\text{active}}(t, V) = \alpha_i(t, V) \cdot \rho_{\text{stored}} \cdot \gamma_i, \quad (2)$$

where t represents time and V is a voltage describing electrochemical state. The total strain is the sum of strains due to each mobile ion, summed over the subscript i , with γ_i representing the fraction of the charge balance achieved by the insertion or removal of a particular ion.

It is tempting to declare that the larger the ion inserted, the larger the strain to charge. From a modeling perspective, ideally one would like to relate the strain-to-charge ratio to the physical volume of the mobile ion. The strain-to-charge density ratio for a given ion is close in value to the estimated ion volume plus solvation sphere, divided by fundamental charge and by three (to account for the contribution in one axis). However, correlations between ion size and strain to charge have proven to be weak (Kaneko et al. 1997).

1.2 Effect of Polymer Anisotropy on the Strain-to-Charge Ratio

In polyaniline (Herod and Schlenoff 1993) and polypyrrole (Pytel et al. 2006; Pytel 2007), expansion is primarily perpendicular to the chain direction. Thus stretch alignment of conducting polymers leads to anisotropic expansion upon ion insertion, in addition to anisotropy in mechanical and electrical properties. Chain alignment can be achieved by stretch alignment (Herod and Schlenoff 1993), rolling (Pytel et al. 2006), and spinning (Spinks et al. 2006; Smela et al. 2005) or even simply by the process of electrodeposition on a conductive substrate (Smela and Gadegaard 1999). The effect can be inserted using a tensor form of the strain-to-charge ratio, analogous to the treatment of piezoelectric coefficients. This has yet to be done.

1.3 Stress–Strain Relationship

Total strain at constant temperature is the sum of strain resulting from active charging and that resulting from changes in load. In the simplest models, this load-related strain is described using an elastic model, with the material having an effective spring constant, or an intrinsic modulus, E , so that the strain resulting from load, $\varepsilon_{\text{load}}$, is proportional to stress, σ , when load is uniaxial and strain is small ($\ll 10\%$):

$$\varepsilon_{\text{load}} = \frac{\sigma}{E}. \quad (3)$$

Typically if a material is stretched in one axis, it will contract in the perpendicular directions, with the ratio of perpendicular contraction to extension being described by Poisson's ratio. It is expected to be between 0.3 and 0.4, but can be ~ 0.5 (constant volume condition) when the polymer is in a gel-like state. The response to stress in three axes on the strain in one axis (e.g., x) in an isotropic material at small strain is given by

$$\varepsilon_{x,\text{load}}(t) = \frac{\sigma_x}{E(t)} - \nu \frac{\sigma_y}{E(t)} - \nu \frac{\sigma_z}{E(t)}. \quad (4)$$

1.4 State of Charge-Dependent Modulus

As might be expected with the insertion of ions, along with solvent, change of the conducting polymer's charge state is associated with changes in modulus (Fig. 2) (Shoa et al. 2010c; Bahrami-Samani et al. 2008).

The modulus dependence on potential will be a function of the synthesis methods and electrolytes used. There can also be a time dependence perhaps resulting from ion and solvent diffusion times.

Providing creep is not large (i.e., loads are less than ~ 10 MPa) and time is allowed for complete charging of the polymer; the change in strain, $\Delta\varepsilon$, at steady state for uniaxial load can be represented using (Spinks et al. 2002)

$$\Delta\varepsilon = \left(\frac{\sigma_{\text{initial}}}{E_{\text{initial}}} - \frac{\sigma_{\text{final}}}{E_{\text{final}}} \right) + \alpha\rho. \quad (5)$$

1.5 Creep and Stress Relaxation

A perfectly elastic material responds instantly to a change in stress. In practice in polymers, there is also some time-dependent response as molecules reorient or slide past one another.

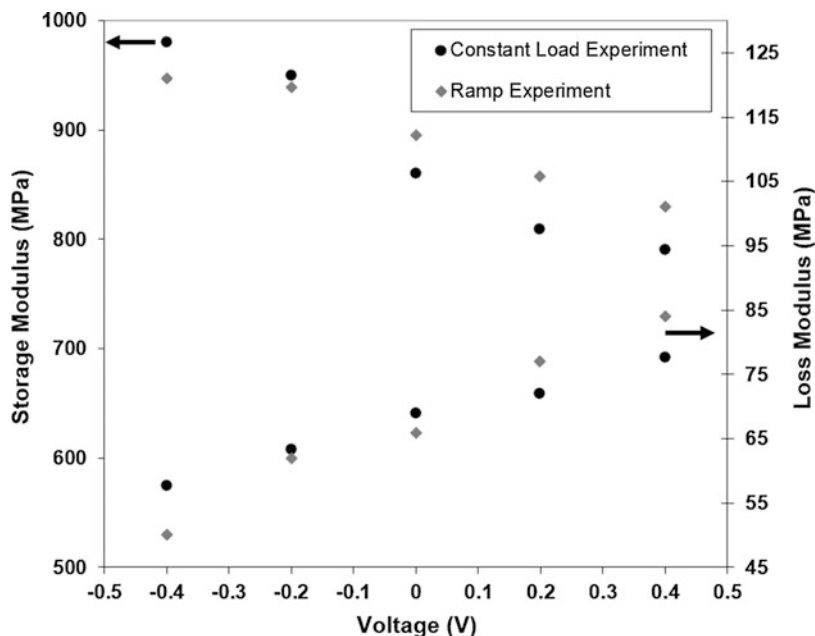


Fig. 2 Storage and loss modulus as a function of polymer potential (versus Ag/AgCl in 3 M NaCl) (Reprinted from Shoa et al. (2010c) with permission from Elsevier)

Creep describes gradual extension under load, while stress relaxation is the drop in force seen in a sample after it is extended. A number of linear viscoelastic models have been used to describe creep and stress relaxation in polymers some of which are shown in Fig. 3. In these models viscous elements are employed, in which strain rate is proportional to stress. The viscous elements are applied in series and in parallel with elastic elements. For example, the Kelvin–Voigt model shown in Fig. 3b employs a parallel combination of a spring and a dashpot. Once scaled by dimensions, this model enables the determination of the storage and loss components of the elastic modulus, also referred to as the real and imaginary components of Young’s modulus, and is typically extracted from frequency response measurements (Shoa et al. 2010c). The use of a spring in series with the Kelvin–Voigt configuration, or a spring in parallel with a series spring–dashpot (the standard model, Fig. 3e), describes the immediate step in displacement seen upon application of a load (short-time elastic response), followed by a gradual, but decaying extension or “creep” (Madden et al. 2001). In reality the material often has multiple relaxation time constants, so one time constant does not always provide a good description (Della Santa et al. 1996). Some sophisticated models have included both electromechanical coupling and linear viscoelastic effects (Della Santa et al. 1997; Nguyen et al. 2014).

A more complete model considers the effect of time or frequency, state of charge or potential, electrolyte, solvent content, and temperature on the mechanical

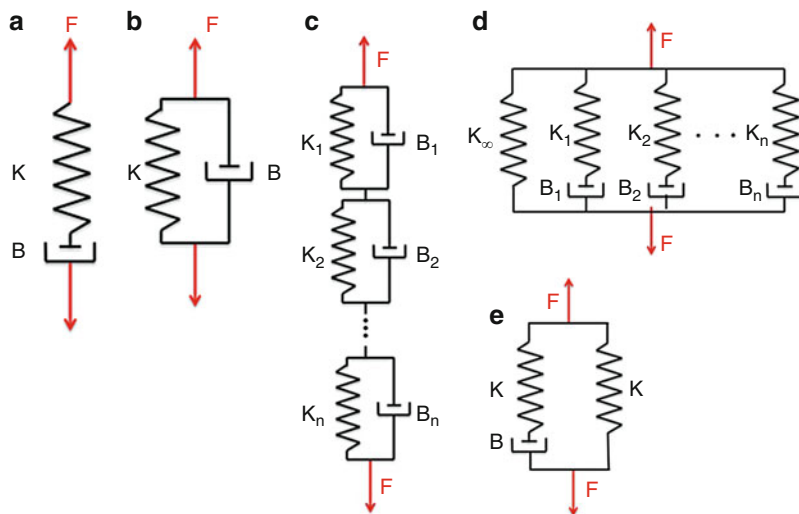


Fig. 3 Common viscoelastic models: (a) Maxwell, (b) Kelvin–Voigt, (c) Wiechert, (d) Kelvin, and (e) standard linear solid

properties of the material. Synthesis conditions have a dramatic effect on the properties of conducting polymers – both electrical (Kohlman and Epstein 1998; Yamaura et al. 1992) and mechanical (Zama et al. 2005; Hara et al. 2004). Interestingly, creep can be accelerated during the passage of current (Madden et al. 2002a; Zheng et al. 2011). This effect is significant at high loads (>5 MPa), but has not been modeled. These additional considerations may not be necessary, depending on the degree of accuracy needed and the range of applied potentials used, with good descriptions having been reported that do not include the effects of creep and modulus changes, for example (Shoa et al. 2011).

The mechanical behavior of a conducting polymer can be a function of oxidation state, time, and even charging rate (Madden et al. 2002a, 2007; Bahrami-Samani et al. 2008). Some of these effects have been included in nonlinear models (Nguyen et al. 2014).

1.6 Bending Structures: Tri-layer Equations

Often, conducting polymer actuators are in the form of bending structures and in particular tri-layers – with two layers of conducting polymer separated electrically but connected ionically by a porous polymer such as PVDF or polyethylene oxide/butadiene rubber block copolymer (Fig. 4) (Yao et al. 2008; Arias-Pardilla et al. 2011; Maziz et al. 2014).

This geometry can enable large amplification of deformation, similar to geometries used to amplify thermal expansion and the strains of piezoceramics. Analytical

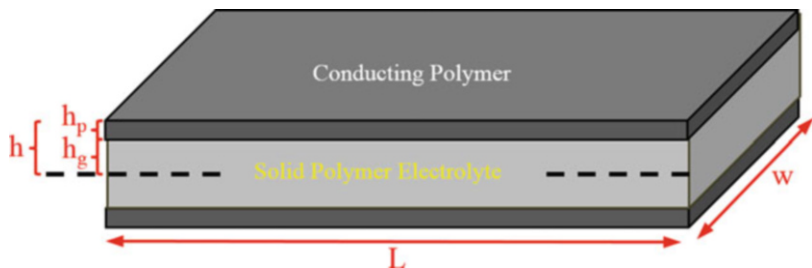


Fig. 4 Tri-layer actuator configuration and dimension

models can often be used effectively to describe the deformation of these structures. For example, if the separator layer is of very low bending stiffness compared to the conducting polymer and the layer of conducting polymer is thin compared to the overall tri-layer thickness, $2h$, then the active (free) strain, $\alpha\rho$, produced by the conducting polymer can be related to the curvature, K , and beam deflection using the relation

$$\frac{K}{\rho} = \frac{\alpha}{h}. \quad (6)$$

The bending radius is K^{-1} . Typically, the tri-layer can be deflected both up and down, and thus the total free strain is expected to be twice the estimate made above. (This situation occurs when the conducting polymer layers in a flat tri-layer are both at an intermediate state of oxidation.) The deflection of the beam from its zero position is approximately

$$\delta = \frac{KL^2}{2}, \quad (7)$$

providing that the deflection is less than the length, L , of the beam. The peak force (at zero displacement) for this case in terms of beam width, W ; separator thickness, h_g ; conducting polymer elastic modulus, E_p ; and polymer thickness, h_p , is

$$\frac{F}{\rho} = \frac{2E_p\alpha W h_g h_p}{L}. \quad (8)$$

The simple relations can be useful in making design estimates.

For a symmetric tri-layer, accounting now for the stiffness of the separator, the curvature, K , achieved (with no load applied) is given by

$$\frac{K}{\rho} = \frac{3\alpha}{2h_g} \left[\frac{(1+\gamma)^2 - 1}{(1+\gamma)^3 + (1/e - 1)} \right], \quad (9)$$

where $2h_g$ is the separator thickness; γ is the ratio of the polymer to the separator thickness, h_p/h_g ; and e is the ratio of the conducting polymer modulus to the separator modulus, E_p/E_g (Madden 2003).

The force generated in a beam of length, L , and width, W , as a function of curvature and charge density is

$$F = C_{\text{spring}} \cdot K + C_{\text{charge}} \cdot \rho, \quad (10)$$

with

$$C_{\text{spring}} = \frac{2WE_p}{3L} h_g^3 \left[\left(1 + \frac{h_p}{h_g} \right)^3 - 1 + \frac{E_g}{E_p} \right] \quad (11)$$

and

$$C_{\text{charge}} = \frac{E_p \alpha}{L} W h_g^2 \left[\left(1 + \frac{h_p}{h_g} \right)^2 - 1 \right]. \quad (12)$$

Encapsulation layers may need to be added or other geometries used. In such cases, equations can be derived using the balance of forces and moments, as has been done, for example, with tubular geometries used in making tri-layer catheters (Shoa et al. 2010a). For more complex geometries, or where a fast time response is needed, numerical methods are often more useful – including the use of thermal expansion coefficients as an analog to the strain-to-charge ratio (Metz et al. 2006).

The active and passive contributions to strain have now been discussed. The following sections enumerate rate-limiting factors including inertia and electrical impedance.

1.7 Inertial Effects and Rate Limits: Resonance

Typically rate of actuation is limited by the speed at which ions and electrons can be inserted or removed from the polymer. On occasion, however, it is inertial effects that limit the rate of response or – when operating at resonance – allow amplification of deflection and speed. If the load driven by a polymer actuator is a mass, m – much larger than the mass of the actuator – and the actuator has an effective spring constant, k , then resonance frequency is often as simple as

$$f = \frac{1}{2\pi} \sqrt{\frac{k}{m}} \quad (13)$$

Amplitude can be enhanced at resonance, provided that the system is underdamped. Beyond this frequency the amplitude drops rapidly (by a factor of

100 × per decade in frequency). In the case of a symmetric rectangular tri-layer with a mass, m_t , at the tip and its own mass, m , the resonance frequency is (John et al. 2008c)

$$f_n^2 = \frac{1}{4\pi^2} \frac{3\beta^4}{3m + \beta^4 m_t} \frac{EI}{l^3}, \quad (14)$$

$$m = 2LW h_g \rho_{PVDF} + 2LW (h - h_g) \rho_{PPy}, \quad (15)$$

$$EI = 2W \left(\frac{h_g^3}{3} E_{PVDF} + \frac{h^3 - h_g^3}{3} E_{PPy} \right), \quad (16)$$

where β is the resonant frequency mode (1.875 for natural frequency), EI is the flexural rigidity of the beam, ρ is the density, and A is the cross-sectional area.

1.8 Charge–Voltage Relationship

The next step is describing the relationship between applied voltage and charge. Conducting polymers are known to be very high-capacitance electrodes, sometimes used in supercapacitors. The equilibrium response (e.g., when all charging currents have died down following a change in voltage) is described most simply to first order by the capacitive relationship:

$$\rho = C_V V, \quad (17)$$

where C_V is the capacitance per unit volume and V is the change in voltage applied to the electrode, resulting in a change in stored charge, ρ . The mechanical analogy is of a water tank filled from the bottom, where higher pressure (voltage) is needed to fill the tank to a higher level (charge). Unlike a conventional capacitor, the charge is stored within the volume of the polymer. This model works well to describe the equilibrium response of highly conductive polypyrrole over relatively wide potential ranges (Wing Yu Lam 2011). One way of picturing this volumetric capacitance is as electronically conducting monolayer sheets resulting from 2D stacks of polypyrrole chains, separated by regions containing dopant ions as well as solvent. This type of ordering – over a range of nanometers – is suggested by X-ray diffraction results (Nogami et al. 1994; Warren and Madden 2006a). The highly electronically conducting layers of polymer may act as planar electrodes as in electrical double-layer capacitors and thus charge in a manner similar to single-carbon layer sheets in graphene supercapacitor.

The linear model does not describe the observed voltage–charge or voltage–current relationships in disordered forms of conducting polymer (including disordered polypyrrole) and in ordered polypyrrole approaching the undoped state. These appear to be more battery-like in their behavior. The Nernst equation has often

been used to describe the charging response. Otero has suggested that even in a capacitive region, as seen, for example, in highly ordered conducting polymers, the relationship between voltage and charge can be interpreted as the superposition of oxidation state changes. Here, the polymer backbone which has, for example, N pyrrole monomers is seen to go through a near continuum of oxidation states (from zero charge to approximately $+ N/3$). Each addition of charge is viewed as a redox reaction. This interpretation may be valid, particularly when the conducting polymer is in an effectively insulating state, and charges on the backbone are well screened from each other, so that the assumption of noninteracting particles that is central to the Nernst equation is valid. A model that is relatively independent of the underlying physical mechanism and has been used to describe battery and carbon electrode responses treats the electrode as being a voltage-dependent (nonlinear) capacitor at equilibrium:

$$\rho(V) = C_V(V)V. \quad (18)$$

This model does not account for hysteresis that might be observed in ion insertion and extraction.

The full device model contains two electrodes – one or both of which can be conducting polymers. Generally the counter electrode is also a conducting polymer or a highly capacitive electrode such as carbon paper. In this case the equilibrium electrical model is two capacitors in series.

1.9 Electronic and Ionic Conductivity Variation with State of Charge

Unusual electrochemical behavior in conducting polymers may result from abrupt changes in electronic and ionic conductivity as a function of potential (oxidation state) (Tezuka 1997; Kohlman and Epstein 1998; Wang et al. 2004; Warren and Madden 2006b). These are observed particularly strongly at reduced states where the polymer backbone is relatively uncharged and the density of carriers is small. Electronic conductivity is seen to drop dramatically at low oxidation states. Ion mobility can also become slow, with drops seen in reduced states of hexafluorophosphate-doped polypyrrole (Tso et al. 2007) and in polyaniline (Skotheim et al. 1998). There may be a compaction of the polymer (Otero and Padilla 2004) making ion transport more difficult. Phase front (Wang et al. 2004) and lumped element transmission lines where conductivity is a sigmoidal function of oxidation state (Warren and Madden 2006b) have been used to account for transitions in ionic and electronic conductivities. Very slow scanning of potential can in some cases result in a more purely capacitive response even in highly reduced (nearly undoped) polypyrrole (Wing Yu Lam 2011), suggesting that slow transport of electronic charges and/or ions is masking the equilibrium response. The nonlinear effects can be avoided by operating in potential ranges where their effect is small (Shoa et al. 2007).

1.10 Rate-Limiting Factors

Like any practical battery or capacitor, charging is not immediate and, since strain is proportional to charge, neither is actuation. Typically it is charging rate that limits frequency response simply because the electrodes store charge at extremely high densities. Even small resistances can then lead to long charging times (as expressed by the resistor–capacitor or RC charging time). A simple electrical equivalent circuit is shown in Fig. 5a in which two capacitors are in series with the separator and contact resistances R_S and R_C . Here the total contact resistance is represented by the one resistor.

Particularly at potential extremes, reactions are occurring in solutions that tend to discharge the polymer (over seconds to hours). These can be represented as voltage-dependent resistors in parallel with the capacitances of the electrodes, as shown in Fig. 5b. Often such a model is sufficient to provide a good description of the charging rate of conducting polymers. However, when electronic or ion paths within the electrodes are long, a more involved circuit description is needed. Overall, there are a number of electrical rate-limiting factors, including:

- The resistance to ion transport of the separator, R_s , which depends on the ionic conductivity of the separator and its dimensions
- Contact resistance between the metal and the conducting polymer, R_c
- The resistance to field-driven ion movement (known as ion migration or drift) through the polymer
- Diffusion of ions in and out of the polymer
- The electronic resistance along the length of the polymer, R_e

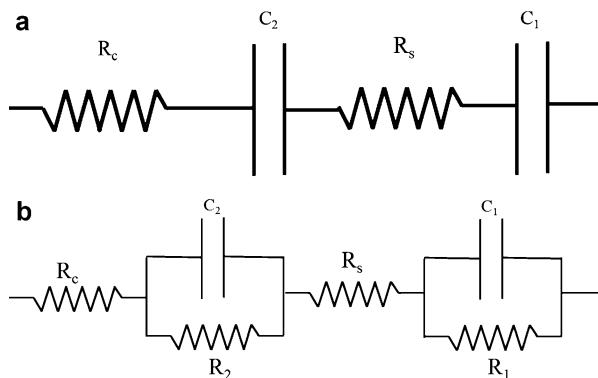
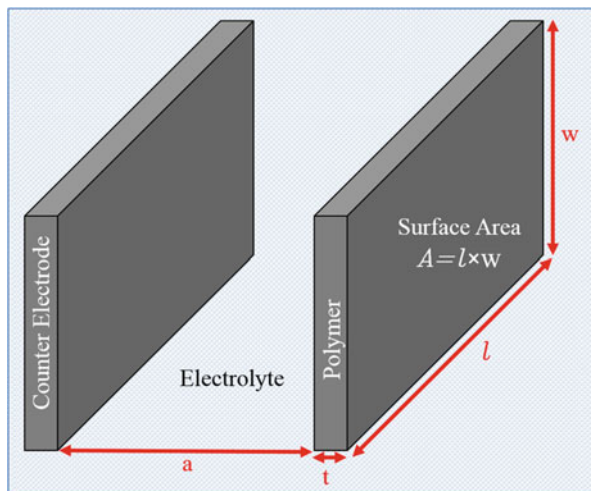


Fig. 5 Simple electrical equivalent circuit diagrams. (a) Each capacitor represents one electrode – which could each, for example, be two sheets of conducting polymer. The contact resistance R_c represents the sum of electrical contact resistances at both electrodes. R_s is the electrolyte or separator resistance. The other two resistors, shown in (b), represent loss of charge due to parasitic reactions. In the literature, typically the equivalent circuit either describes only one electrode or lumps both electrodes into one capacitance. Often, solution and contact resistances are also lumped together

Fig. 6 Dimension of the polymer actuator. Electrical contact to the polymer is made at one end of the polymer film of length l (Adapted from Madden et al. (2002a))



Diffusion is also expected to be relevant when concentrations are low (Tso et al. 2007) or multiple ions of similar diffusion coefficient but opposing charge are present.

In electrical systems, it is common to describe the time to charge a capacitor using the product of resistance and capacitance, or RC . In designing and troubleshooting device performance, it is useful to consider the various time constants. In the case of symmetric conducting polymer electrodes that face each other, as shown in Fig. 6, with a capacitance, C , per electrode and a capacitance per volume of the polymer electrode, C_V , and assuming the ionic conductivity, $\sigma_i \ll \sigma_e$, and the electronic conductivity, the time constants are (Madden et al. 2002b):

- Contact resistance: $\tau_c = R_c C$.
- Solution resistance: $\tau_s = R_s C = \frac{a}{\sigma_s l w} \frac{C_V l w t}{2} = \frac{C_V t a}{2 \sigma_s}$
(here there are two capacitors in series, each of $C = C_V l w t$).
- Ionic resistance of the electrode: $\tau_i = R_i C = \frac{t}{\sigma_i w l} \frac{C_V l w t}{2} = \frac{C_V t^2}{2 \sigma_i}$.
- Electrical resistance of the polymer: $\tau_e = R_e C = \frac{1}{\sigma_e w t} \frac{C_V l w t}{2} = \frac{C_V l^2}{2 \sigma_e}$.
- Diffusion within the electrode: $\tau_D = \frac{l^2}{D}$,

where D is the diffusion coefficient of the active ion in the polymer.

It is not uncommon for contact resistance, R_c , to be several ohms (or even kilohms if care is not taken to ensure intimate contact). Solution resistance can also be 10 Ω or greater depending on size of the electrodes and separation, and the ionic conductivity of a separator used to keep electrodes apart is low. Ionic conductivities of aqueous solutions used in actuators can be as high as ~ 10 S/m. Common separator ionic resistances range from ~ 3 to 100 Ω/cm^2 in acetonitrile at room temperature (Izadi-Najafabadi 2006). The resistance of ion transport through the

polymer can be measured using a four-point ionic conductivity measurement apparatus (Fekri 2011; Ehrenbeck and Juttner 1996; Yoo et al. 2011). Values of this conductivity in low-temperature grown, highly ordered polypyrrole are in the order of 10^{-3} to 10^{-4} S/m and depend on solvent content. The effective resistance can be lowered by making the electrodes more porous to ions, reducing the impedance due to the polymer chains (Fekri et al. 2014; Maziz et al. 2014).

The ionic conductivity and the related diffusion coefficient within dense polymer drop considerably at low doping states, at least in cation-containing polymers (Skotheim et al. 1998; Warren and Madden 2006a, b; Tso et al. 2007), due to drop in concentration of carriers, but also due to other effects, which may include the densification or “compaction” (Otero and Padilla 2004) of the polymer. Work has been done by Otero and colleagues to describe and model this compaction effect (Otero and Padilla 2004). Further complicating matters, exposure to elevated temperatures, and time can also lead to a drop in transport rates (Cole and Madden 2005; Shoa et al. 2007; Cole 2006), presumably due to structural compaction – an effect that has not been modeled.

Electronic conductivity can be as high as 10^5 S/m (10^3 S/cm) in stretch-aligned polypyrrole and polyaniline, as well as in solution-processable PEDOT. Typical values of conductivity seen in actuators are in the range of 10^3 – 10^4 S/m, 2–3 orders of magnitude lower than is achieved in metals. As the neutral doping state is approached, conductivity drops markedly and can be lower than 100 S/m (Warren and Madden 2006a).

In general, fast actuation (1 Hz or greater) requires that the distances ions travel through the device are small (usually <10 μm for the electrodes, less than 250 μm for the separator) and that electronic conduction paths also are relatively short (<100 mm).

1.11 Modeling Diffusion and Diffusion-Like Processes

Ion transport within conducting polymers is much slower than in liquid electrolytes and is typically also much slower than electron transport. As a result, it often becomes the rate-limiting factor. There are three situations where diffusion models are used:

1. To describe ion flux resulting from a concentration gradient
2. To describe the distributed nature of ionic resistance and capacitance within the conducting polymer
3. In poro-elastic models, where fluid storage and resistance to flow in pores within the polymer are modeled (Mazzoldi et al. 1999)

In the second case, the conducting polymer is viewed as having both a local capacitance per volume and a local resistance to ion flux. In all cases the diffusion equation can be used to mathematically model the response. The electrochemical response for the first two cases can be represented in discrete circuit elements by an

RC (resistor–capacitor) transmission line. In the limit of increasing the element number to infinity and reducing the values of R and C to zero, the transmission line description becomes a continuum, equivalent to the diffusion equation. Since free strain is proportional to local charge density at any point within the polymer, both charge and strain can be mapped as a function of position using the transmission line.

A transmission line diffusion element, Z_D , can be used as part of an equivalent circuit model. In the frequency domain, it is represented by an element that is a function of $f^{-1/2}$, where f is frequency (or $s^{-1/2}$ in the Laplace domain). This type of response can then be detected on a Nyquist plot (imaginary vs. real components of a frequency response) as a region of slope of -45° . The response to a step in concentration (or applied voltage) is a function of the inverse square root of time, $t^{-1/2}$, as, for example, has been used by Pei and Inganas (Pei and Inganas 1992) to model the deflection of a tri-layer.

When diffusion occurs over a finite distance – for example, through the finite thickness of a conducting polymer film – there are closed-form descriptions of the impedance. These have been used in a number of models in combination with other circuit elements (e.g., to represent solution resistance and electrical resistance) to describe the overall electrical impedance and the actuation response both for the entire actuator (Shoa et al. 2008; Nguyen et al. 2012; Fang et al. 2008a; Khalili et al. 2015) and locally (Shoa et al. 2011; Warren and Madden 2006b). Figure 7a, for

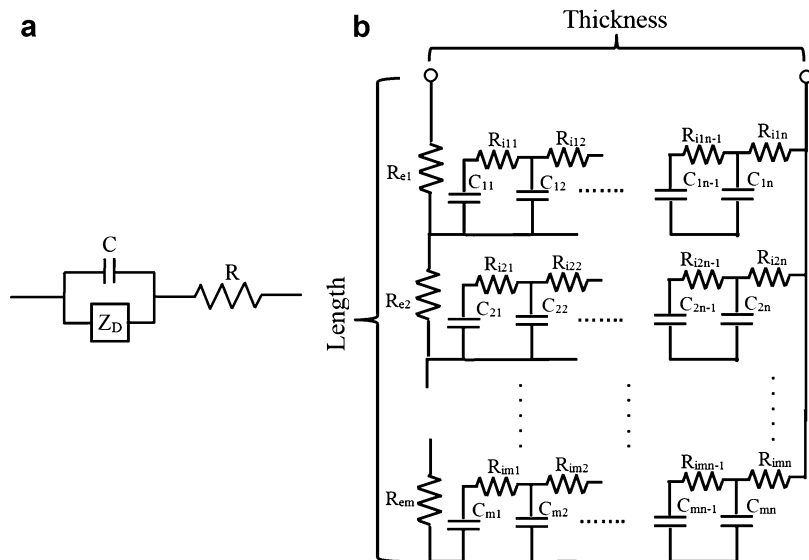


Fig. 7 (a) Lumped circuit model approximation of transport described by the diffusion equation. Such a response can be the result of concentration gradients or combined ionic resistance and distributed capacitance. (b) Example of an equivalent circuit model including a finite diffusion element, a series resistance, and capacitance at the interface between the solution and the polymer

example, depicts a model impedance in which a finite diffusion element (Z_D) is in series with a solution resistance/contact resistance, R , and is in parallel with the double-layer capacitance, C , formed by ions assembling at the electrolyte/solution interface (Madden 2000; Madden et al. 2002b). If electrical resistance, R_e , is also important, two-dimensional transmission lines can be used to model the response, as seen in Fig. 7b (Shoa et al. 2008; Nguyen et al. 2012). Here the RC transmission lines extending from left to right model ion transport and the distributed storage of the ions by capacitive coupling with the electronically conducting polymer. This models ion transport through the thickness, with resistance to electrical transport being considered negligible. Each RC transmission represents a section of the RC line that is separated from others by an electronic resistance, R_e . This electronic resistance describes the drop in voltage along the film length resulting from current that is assumed to be originating from contact points at the top or bottom.

As with electronic conductivity, ion conductivity and diffusion coefficient can vary with oxidation state in conducting polymers, making the models nonlinear (Ariza and Otero 2005; Tso et al. 2007). In this situation – which can be evident in the reduced state of polypyrrole, for example – frequency domain approaches cannot be used alone, as they are only valid over linear regions of response. Elisabeth Smela and her team have generated beautiful experimental results and numerical models of the effects of this nonlinearity (Wang et al. 2004, 2009), which have also been modeled using oxidation state dependence in transmission lines (Farajollahi et al. 2015; Warren and Madden 2006b). Toribio Otero and his team have used molecular dynamics to model the change in polymer conformation and degree of “compaction” with oxidation state (López Cascales and Otero 2004).

1.12 Electromechanical Coupling and Efficiency

Electromechanical coupling is the ratio of mechanical energy out to electric energy in, while efficiency relates the net mechanical energy out per cycle divided by the net electrical energy into the device per cycle. Although the electromechanical coupling tends to be low in conducting polymer actuators – often $< 1\%$ (Madden 2000) – the efficiency of converting electrical energy to mechanical work should in principle be higher since much of the input energy is stored and can be recovered. In terms of current per volume, $\hat{\rho}$, voltage applied, V ; time, t ; stress, σ ; strain rate, $\dot{\epsilon}$, and strain to charge, α , the efficiency, e , per cycle of period, T , is given by

$$e = \frac{\int_0^T \sigma d\epsilon}{\int_0^T V \hat{\rho} dt} = \frac{\int_0^T \sigma (\dot{\sigma}/E + \alpha \dot{\rho}) dt}{\int_0^T V \hat{\rho} dt}, \quad (19)$$

where the right-hand expression separates the elastic and charge insertion-related components of strain. The efficiency is dependent on path taken and on whether or not electrical energy is recovered.

To obtain an estimate of the magnitude of the electromechanical coupling, consider contraction under fixed load following the application of a step in potential from zero volts of magnitude, V , estimated from Eq. 19 over $\frac{1}{2}$ a cycle (Madden et al. 2001; Madden 2000):

$$\sim \frac{\sigma\alpha}{V}. \quad (20)$$

Plugging in typical values to the equation (the applied voltage difference is 0.5 V, the stress is 10 MPa, and the strain-to-charge ratio is $5 \times 10^{-10} \text{ m}^3/\text{C}$), the coupling is 1 %. If voltage were ramped up slowly instead of stepped, then this coupling could be doubled to 2 %. When significantly higher efficiency is desired, then there is a need to recover input electrical energy. 90 % recovery of the stored energy would make it possible to achieve efficiency similar to muscle. Such recovery has not been attempted. The expression suggests that coupling can be greater than 1 % for small applied potentials.

In order to perform net mechanical work over a full cycle, load must be changed. The application of a load leads to elongation and work on the actuator rather than by the actuator. As mentioned above, elastic modulus also changes with oxidation state. A full treatment of both efficiency and electromechanical coupling must account for these factors. Experimentally this is achieved in natural muscles by using the work loop method, in which a periodically varying load is applied (Josephson 1993).

A full analysis of electromechanical coupling and efficiency in conducting polymer actuators would also consider the microscopic reversibility and energy storage. Early work by Takashima and Kaneto shows that conducting polymers act as sensors as well as actuators (Takashima et al. 1997). A model that considers the sensor–actuator nature has been proposed and is based on the strain-to-charge ratio as an indicator of the mechanical to electrical coupling (Shoa et al. 2010b). The sensor aspect is now discussed.

2 Conducting Polymer Sensors

Takashima et al. (1997, 2007) and then Wu et al. (2007) found that films and tri-layer sensors produce voltage and/or current in response to the application of force and displacement. Actuation and strain responses are likely related through the strain-to-charge ratios (Wu et al. 2007; Shoa et al. 2010b; Madden 2000), as might be expected through microscopic reversibility (Onsager 1931) (analogous to the piezoelectric coefficient for piezoelectric materials). Just as actuation strain is relative to charge density via the actuation strain-to-charge ratio, α , so it is proposed that the sensor voltage, V_s , is related to the applied stress, σ , via the sensor strain-to-charge ratio, α_s :

$$\Delta V = \alpha_s \cdot \sigma. \quad (21)$$

In analogy to the piezoelectric coefficient, we propose that the α terms be referred to as piezoionic coefficients. One aspect that is not always consistent with the model is the DC response – predicted to be steady for a step in stress – but in some cases tending to zero at long times and low frequencies (John et al. 2008a, 2009), perhaps due to parasitic reactions on metallic contact electrodes or even transport of a second ion.

Rigorous characterization work has been carried out to describe sensor response in tri-layers, but the physical mechanisms are still a source of debate. Both these aspects are now discussed.

A distinct sensor response is reported by Otero and his team (Otero and Cortés 2003; Otero 2008), wherein under constant current application, an increase in voltage is observed when actuator loading is increased. This type of sensor is not described here.

2.1 Sensor Mechanisms

Two plausible mechanisms have been presented to explain the sensor response. The first relies on changes in concentration of ions within the polymer – relative to the surroundings – as the polymer is mechanically deformed. The second assumes that there is an elastic energy required to insert ions into the polymer and that this insertion energy, which depends on the volume per ion (and equivalently the strain-to-charge ratio), is modified by the application of an external load. Increase of volume of the film via the applied tensile load makes it easier to insert ions. A third possibility is through the electrokinetic effect, with fluid flux within the polymer in response to applied stress also transporting ions and generating a potential. This effect has not been explored to describe sensing in conducting polymers.

A qualitative description of the sensor response is illustrated in Fig. 8, which depicts a polymer with chains that are charged (red +) sitting in an electrolyte with, in this example, large cations (too large to enter) and smaller anions (mobile in both phases). The material is compressed, leading to an increase in anion concentration relative to the external electrolyte and also a stress on the mobile ions, both factors driving a net expulsion of the mobile anions. Charges on the polymer backbone remain along with any large immobile dopants (not shown in this case). As a result, the deformation induces a separation of charge and the generation of a voltage difference.

In the first approach to explaining the sensor response, compression of the polymer containing a certain number of ions leads to an increase in the concentration of these ions relative to the surroundings. This in turn may lead to a change in surface potential as more ions leave per unit surface area in a given time, changing the balance of charge at the interface. The potential developed is known as the Donnan potential. For small deformations, the relationship between induced voltage, ΔV , and relative change in volume, $\Delta v/v$, is

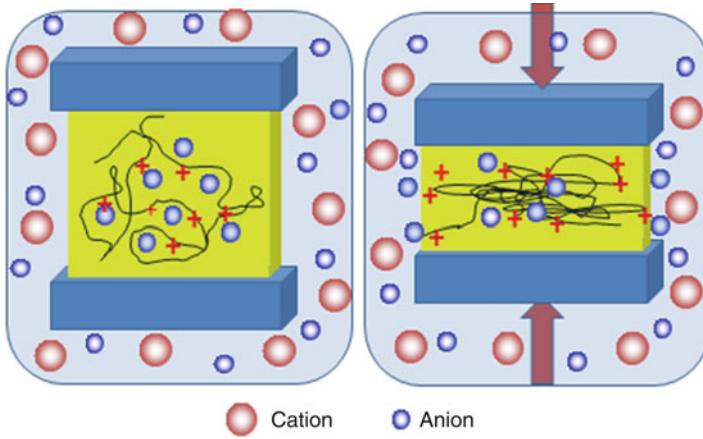


Fig. 8 The compression (*right*) of a charged polymer (*yellow area with black chains positively charged*) containing mobile ions and in contact with an electrolyte (*light blue*) leads to the expulsion of ions and the generation of a potential due to the separation of charge at the interface. The expulsion may be the result of imbalance in concentration (Donnan potential) or elastic forces squeezing the ions out

$$\Delta V = \pm \frac{kT}{e} \frac{\Delta v}{v} \quad \text{or} \quad \Delta V = \pm 25 \text{ mV} \frac{\Delta v}{v} \quad (\text{at } 20^\circ\text{C}), \quad (22)$$

where it is assumed that relative change in concentration is equal to the relative change in volume and that there is a single fundamental charge, e , per ion. The sign is negative when anions are mobile and positive when cations are mobile. T is absolute temperature and k is Boltzmann's constant. Volume change can be related to strain assuming that Poisson's ratio is known. Although no systematic attempt to match this equation to experimental results has been made, inspection of the reported values (Takashima et al. 1997, 2007; Wu et al. 2007; Shoa et al. 2010b) shows that the equation correctly predicts the sign of the sense voltage and provides magnitudes that are approximately consistent with published observations. For example, in the work by Shoa (Shoa et al. 2010b), a tensile strain of +0.22 % is applied in one axis, and assuming a Poisson's ratio of 0.3 with $\frac{\Delta V}{V} = \epsilon_x - \nu\epsilon_y - \nu\epsilon_z$, the predicted and generated voltages of -0.02 mV match within uncertainty. The Donnan equilibrium approach does not predict how a change in concentration will change volume and thus does not relate actuation and sensing. The strain-to-charge ratio/piezoionic coefficient is an empirical relationship that does link concentration and strain (and potentially volume).

Shoa et al. (2010b) suggest a microscopic model to link sensing and actuation via the piezoionic coefficient. The origin of the sensor voltage in this view is the balance between mechanical stresses that are pushing ions out of the solid polymer and electrostatic forces developed at the surface to hold them in. In this approach the balance of mechanical and electrical forces suggests $\Delta V = \sigma \cdot \alpha_s$, as in Eq. 21.

Here the piezoionic coefficient is interpreted as the effective strain per charge inserted (including solvation), which can be estimated from the effective ion volume and its charge. Its value is found to be on the order of 10 to $500 \times 10^{-12} \text{m}^3/\text{C}$ (Madden 2000; Cole and Madden 2005) from actuation. Actuation and sensing have been shown to be governed by a consistent value of piezoionic coefficient (Wu et al. 2007; Shoa et al. 2010b).

The Donnan and electromechanical coupling models predictions match when $\alpha_s \cdot Y \sim kT/e$, where Y is the elastic modulus of the polymer (using Hooke's Law $\sigma = Y \cdot \varepsilon$), which is the case in hexafluorophosphate-doped polypyrrole since $Y \sim 8 \times 10^8 \text{ pa}$ (Shoa et al. 2010b) and $\alpha \sim 0.3 \times 10^{-10} \text{m}^3/\text{C}$ (Shoa et al. 2010b). Further work is needed to distinguish or relate these two effects, possibly by studying the sensing and actuation in polymers of various elastic moduli and temperatures.

Charge transferred by the sensor per volume, $\Delta\rho$, can be predicted from the sensor voltage (at open circuit ΔV_s) and the effective capacitance per volume, C_V , approximately 10^8F/m^3 (Madden et al. 2002b) of the electrode at the operating electrochemical potential:

$$\Delta\rho = C_V \Delta V_s \quad (23)$$

The larger the volume of conducting polymer, the more charge that can be extracted. Current from the sensor is limited by the internal resistance (Shoa et al. 2010b) (in general impedance) of the electrochemical cell, as in a battery or supercapacitor. Contact resistance between the conducting polymer and metal contact, electronic resistance of the conducting polymer, ionic resistance of the electrolyte, and the effective diffusion coefficient of ions in the conducting polymer can all limit current just as they do in supercapacitors and actuators (Madden et al. 2002b). The discussion above of models of electromechanical coupling in the actuator also applies to the sensor – with the implication that while the sensor can generate a lot of charge, it is not an effective generator.

3 System Identification Techniques Applied to Conducting Polymer Actuators and Sensors

A model of a system is needed to predict and understand the behavior of the system. The model is employed to design control algorithms to improve the performance of the system they are describing, make the system insensitive to parameter changes and external disturbances, and increase its speed of response. It is cost and time effective, flexible, and safe to have an accurate enough model of a dynamic system such as electroactive actuators and sensors. A valid model is used to optimize the configuration, design, and operation and performance metrics of a system without needing a real system. The model can be in the form of differential or difference equations, graphs (Bode plots and time-domain response data), state-space equations, verbal commands (neural network, fuzzy logic), transfer functions, and the like. They can be linear, nonlinear (needs to be linearized in order to use various

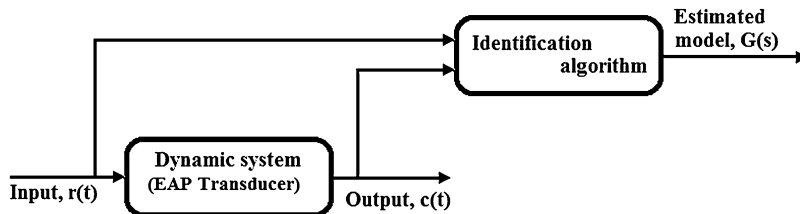


Fig. 9 Schematic representation of model identification

system identification and validation techniques), parametric, or nonparametric. Depending on the purpose, one of these models can be chosen, identified, and validated. Detailed explanation on system modeling and identification can be found in some classical textbooks (Johansson 2003; Ljung 1999).

The models can be white box, gray box, and black box. White box models are derived using physical laws and principles. Their parameters are identified from experimental data. However, these models are overly complex and usually not realistic to build and use. Gray box models which are partially based on physical laws and principles use the experimental data to complete the rest of the model and subsequently validate them. On the other hand, a black box model which is the most commonly used model structure describes an output–input relationship, without explaining the physical phenomena behind the identified model.

It must be noted after a model is identified, a new set of experimental data is required to validate it in order to have confidence in its accuracy for the purpose or application it is established for. Establishing a valid model is one of the scientific and reliable tools researchers or practitioners use to undertake system analysis and design and optimize the system configuration and performance in order to establish and validate various concepts and ideas. To this end, significant research has been dedicated to the modeling and identification of EAP transducers. The procedure for model identification, which aims to obtain a mathematical model from input–output data, is depicted in Fig. 9.

The examples presented below employ linear system identification techniques in which superposition and scaling are assumed. These enable conversion between the frequency and time-domain models. Nonlinearities in conducting polymers can arise from significant potential-dependent ionic and electronic conductivities, for example. In cases where nonlinearities are significant, it may nevertheless be appropriate to apply linear techniques over certain ranges of voltage, strain, or charge state where response is effectively linear.

3.1 Case Study: Identification of Transfer Function Models for EAP Sensors, A Black Box Model

Following the basic procedure in Fig. 9, the transfer function model and its identification for a tri-layer polypyrrole-type conducting polymer sensor are accomplished

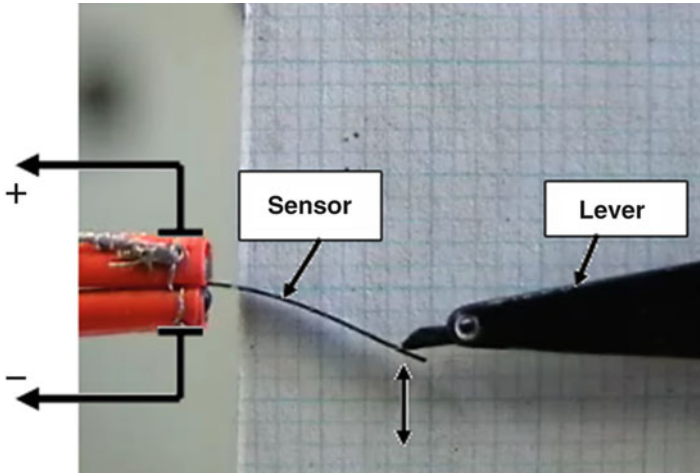


Fig. 10 Configuration of the sensor and mechanical exciter (Adapted from Alici et al. (2008))

Table 1 The transfer function models for three EAP sensors

Voltage/displacement Transfer functions, $G(s)$	Current/displacement Transfer functions, $G(s)$	Sensor dimensions
$14.15 \frac{s+0.6144}{(s+54)(s+3.0215)}$	$16.81 \frac{s+0.2705}{(s+52.295)(s+2.824)}$	$7.5 \times 1 \times 0.17$ mm
$16.12 \frac{s+1.2416}{(s+75.394)(s+5.132)}$	$21.23 \frac{s+0.5142}{(s+66.777)(s+3.898)}$	$10 \times 1 \times 0.17$ mm
$5.892 \frac{s+0.875}{(s+28.059)(s+3.66)}$	$10.07 \frac{s+0.3634}{(s+31.313)(s+3.098)}$	$12.5 \times 1 \times 0.17$ mm

under a sinusoidal displacement input and the voltage generated and current passing between the two outer polypyrrole layers as the output (Alici et al. 2008). The sensor is configured such that its one end was clamped and the other free end was excited through a mechanical exciter, as shown in Fig. 10. The details of this work are in Alici et al. (2008). The voltage generated and current passing were measured to model the output–input behavior of the sensors through their experimental current/displacement and voltage/displacement frequency responses (Alici et al. 2008; Wu et al. 2007). The identified transfer functions for the three sensors with the dimensions of $7.5 \times 1 \times 0.17$ mm, $10 \times 1 \times 0.17$ mm, and $12.5 \times 1 \times 0.17$ mm are shown in Table 1.

Another set of experimental output is used to validate the model. To this aim, the transfer function identified for the sensor $7.5 \times 1 \times 0.17$ mm was employed to estimate the voltage output of the sensor at different frequencies, which are shown in Fig. 11. The close correspondence between the experimental and estimated voltage outputs demonstrates that the transfer function model of the sensor is accurate enough to estimate its electrical output.

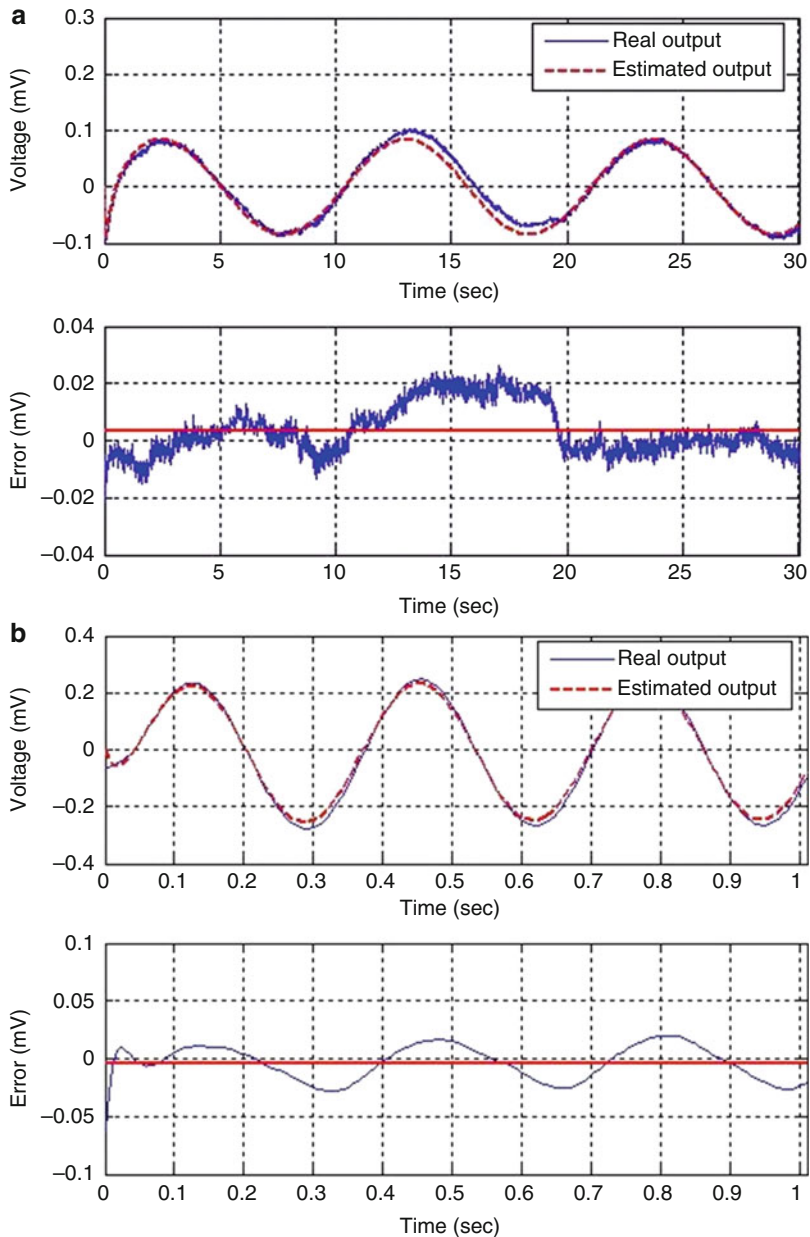


Fig. 11 Comparison of the experimental and estimated voltage outputs for the sensor ($7.5 \times 1 \times 0.17$ mm) under different input frequencies: (a) 0.1 Hz and (b) 3 Hz (Adapted from Alici et al. (2008))

3.2 Case Study: Identification of a Transfer Function Model for EAP Actuators, A Black Box Model

Using the system identification technique, the transfer function model of the tri-layer EAP actuators has been identified from the output–input data for the purposes of (i) obtaining the resonant frequency model of the actuators, from which the mechanical properties of the actuators can be estimated (John et al. 2008c), and (ii) controlling the position of the actuators using either a feedback control system or an open-loop control system such as inversion-based feed-forward control system (Fang et al. 2008b; John et al. 2010; Yao et al. 2008). As the tri-layer actuator in the form of a cantilever beam, its resonant frequency model for a mass, m_t , at its tip and its own mass m are given by

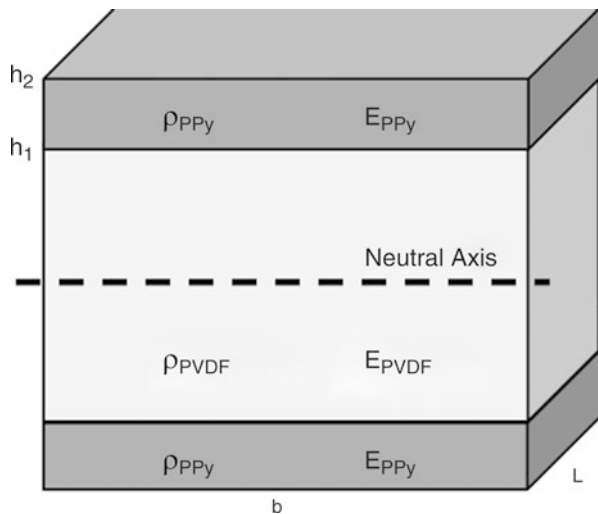
$$f_n^2 = \frac{1}{4\pi^2} \frac{3\beta^4}{3m + \beta^4 m_t} \frac{EI}{l^3} \quad (24)$$

$$m = 2lbh_1\rho_{PVDF} + 2lb(h_2 - h_1)\rho_{PPy} \quad (25)$$

$$EI = 2b \left(\frac{h_1^3}{3} E_{PVDF} + \frac{h_2^3 - h_1^3}{3} E_{PPy} \right) \quad (26)$$

where β is the resonant frequency mode (1.875 for natural frequency), EI is the flexural rigidity of the beam, ρ is the density, and A is the cross-sectional area. The parameters in the flexural rigidity EI and m are the height of the PVDF, h_1 , and the polypyrrole, h_2 , from the neutral axis, as shown in Fig. 12. The elastic moduli of the polypyrrole and PVDF are E_{PPy} and E_{PVDF} , respectively, and the densities are ρ_{PPy} and ρ_{PVDF} .

Fig. 12 Description of the actuator parameters



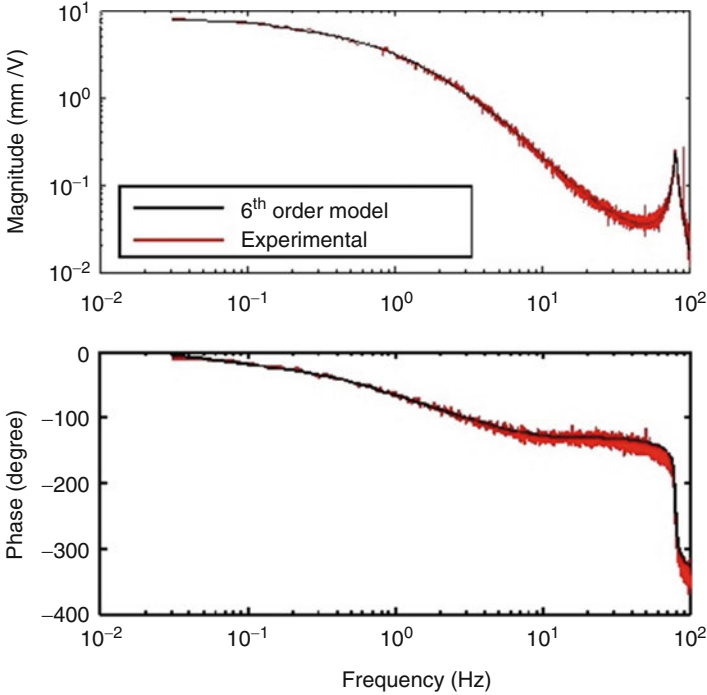


Fig. 13 Estimated and experimental voltage/displacement frequency response for the actuator with the dimensions of $10 \times 2 \times 0.17$ mm (Adapted from John et al. (2008b))

After some iterations, a six-ordered model with a pure time delay of 2 ms primarily due to the data acquisition system has fitted well to the frequency response data of an actuator with dimensions of $\sim 10 \times 2 \times 0.17$ mm, as shown in Fig. 13 (John et al. 2008b). The identified model which is a black box model describing the relationship between the input voltage and the tip displacement is obtained as

$$G(s) = e^{-0.002s} \frac{0.29(s + 1.3)(s + 126)(s + 1619)(s^2 + 2564s + 3.2 \times 10^6)}{(s + 0.88)(s + 4.6)(s + 34)(s + 898)(s^2 + 28s + 2.5 \times 10^6)} \quad (27)$$

For the experimental model in Fig. 13, white Gaussian noise was used as the input signal to excite the dynamics of the actuator, whose displacement as the output signal was measured using a laser displacement sensor focused 0.5 mm from its tip. The fast Fourier transform method was employed to obtain the transfer function in Eq. 27. The validity of this model was realized under a dynamic signal shown in Fig. 14 (John et al. 2008b). It must be noted the model validation is the last step in a typical system identification procedure.

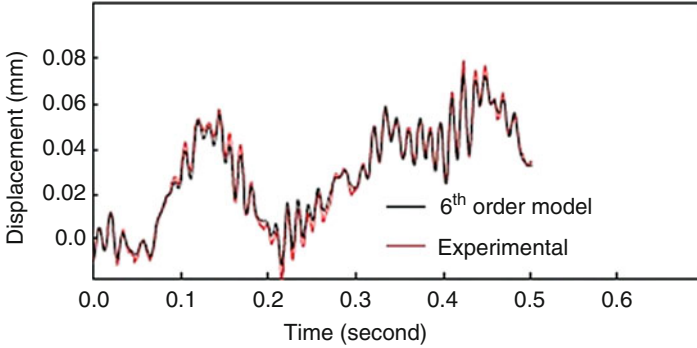


Fig. 14 Estimated and experimental displacement response of the actuator with the dimensions of $10 \times 2 \times 0.17$ mm under a dynamic signal (Adapted from John et al. (2008b))

3.3 Case Study: Identification of a Transfer Function Models for EAP Actuators, A Gray Box Model

In a recent study (Nguyen et al. 2014), starting with the diffusive impedance of a conducting polymer actuator, electrical, mechanical, and viscoelastic properties of a tri-layer conjugated polymer actuator are combined into an advanced mathematical model, which describes the relationship between the curvature of the actuator and an applied voltage, expressed as

$$\frac{k(s)}{V(s)} = K_c \frac{\tan h\left(\sqrt{\frac{2R_c}{Z_i(s)}}L\right)}{s\sqrt{2R_c Z_i(s)}} \quad (28)$$

where

$$K_c = \frac{3\alpha}{2h_{PVDF}hWL} \frac{\left(1 + \frac{h}{h_{PVDF}}\right)^2 - 1}{\left(1 + \frac{h}{h_{PVDF}}\right)^3 \frac{e_2(1 + k_2s)(1 + k_0 + k_1s)}{e_0(k_0 + k_2s)} - 1} \quad (29)$$

It is found that this model can be represented as a ratio of two polynomials, as follows:

$$G(s) = \frac{\sum_{i=0}^{N-1} b_i s^i}{\sum_{i=0}^N a_i s^i} \quad (30)$$

The parameters a_i and b_i depend on the dimensions, viscoelastic properties of the actuator materials, diffusion coefficient, total capacitance, and strain-to-charge

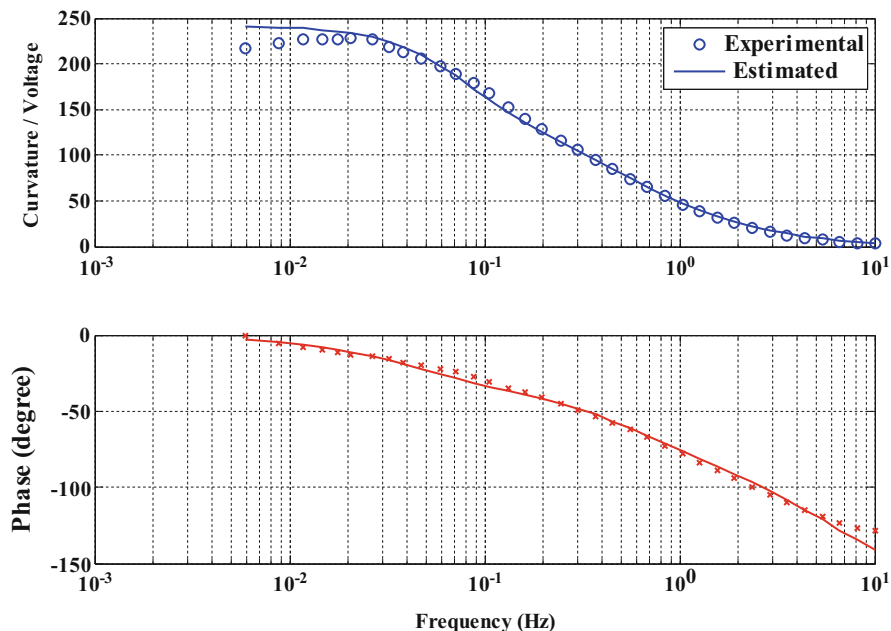


Fig. 15 Experimental and theoretical frequency responses of the actuator under 0.5 V to identify the unknown parameters in the gray box model in Eq. 28 (Adapted from Nguyen et al. (2014))

density ratio. After substituting the numerical values of the parameters into the model Eqs. 29 and 30, six parameters remained to be identified from the experimental frequency response of the actuator. The smaller is the number of parameters to be identified from the experimental data, the closer is the model to be a white box model to explain the physical phenomena behind the operation of the actuator. This is a very good example to the gray box model of the actuators. Based on the close match between the experimental and theoretical frequency of the actuators, as shown in Fig. 15, the six parameters are identified. This model enabled open-loop control of tip displacement of the actuator – i.e., without using feedback from an external sensor, but rather invert this model to control the position (Nguyen et al. 2012).

4 Overview

Physical models and equivalent circuit representations for conducting polymer actuators and sensors are presented, including mechanical, electrical, and electro-mechanical descriptions. The underlying concept of most models is that strain is proportional to charge density, and sense voltage is proportional to stress. Dynamics are determined by the rate of charge transfer, as well as the mechanical properties of

the actuator. The speed of charging is limited by internal resistance including solution resistance of the electrolyte or separator, electrical resistance of the polymer, and ionic resistance through the film. Diffusion can also determine speed of response, particularly at low doping levels. Contact resistance can also be significant. The product of resistance and capacitance provides a characteristic time of response, whether the resistance and capacitance are in series or distributed as in an *RC* transmission line. Identification of the prime rate-limiting factors through estimation of the relative time constants can help focus the simulations on the physically relevant factors.

System identification techniques provide a rigorous approach for finding and validating models, as well as estimating physical parameters. Examples are presented of black box and gray box models and their implementation and validation. In the examples presented, models are fit to the measured frequency response. Validation is then achieved by showing accuracy in predicting time-domain responses and verifying the physical validity of the estimates in the case of gray box models. The models can provide exceptional accuracy in prediction without substantial mathematical complexity. Open-loop control of the actuators is demonstrated.

References

- Alici G et al (2008) Response characterization of electroactive polymers as mechanical sensors. *IEEE/ASME Trans Mechatron* 13(2):187–196
- Arias-Pardilla J et al (2011) Self-supported semi-interpenetrating polymer networks as reactive ambient sensors. *J Electroanal Chem* 652(1-2):37–43
- Ariza MJ, Otero TF (2005) Ionic diffusion across oxidized polypyrrole membranes and during oxidation of the free-standing film. *Colloids Surf A Physicochem Eng Asp* 270-271:226–231
- Bahrami-Samani M et al (2008) Quartz crystal microbalance study of volume changes and modulus shift in electrochemically switched polypyrrole. *Thin Solid Films* 516(9):2800–2807
- Baughman RH et al (1991) Electromechanical actuators based on conducting polymers. In: *Molecular electronics*. Kluwer, Dordrecht, pp 267–289
- Cole M (2006) Feasibility of miniature polypyrrole actuated valves. UBC, Vancouver, BC, Canada, <https://open.library.ubc.ca/cIRcle/collections/ubctheses/831/items/1.0101166>
- Cole M, Madden JD (2005) The effect of temperature on polypyrrole actuation. MRS, Boston, pp 105–110
- Della Santa A et al (1996) Conducting polymer electromechanics: a continuum model of passive mechanical properties. In: *Third ICIM/ECSSM*. pp 371–376
- Della Santa A, DeRossi D, Mazzoldi A (1997) Characterization and modeling of a conducting polymer muscle-like linear actuator. *Smart Mater Struct* 6:23–34
- Ehrenbeck C, Juttner K (1996) Ion conductivity and permselectivity measurements of polypyrrole membranes at variable states of oxidation. *Electrochim Acta* 41(11):1815–1823
- Fang Y, Tan X, Shen Y et al (2008a) A scalable model for trilayer conjugated polymer actuators and its experimental validation. *Mater Sci Eng C* 28(3):421–428
- Fang Y, Tan X, Alici G (2008b) Robust adaptive control of conjugated polymer actuators. *IEEE Trans Contr Syst Technol* 16(4):600–612
- Farajollahi M et al (2015) Non-linear two-dimensional transmission line models for electrochemically driven conducting polymer actuators. *IEEE/ASME Transactions on Mechatronics*, Vol. 21, 2016

- Fekri N (2011) Influence of porosity on charging speed of polypyrrole supercapacitors. UBC, Vancouver, BC, Canada
- Fekri N et al (2014) Influence of porosity on charging speed of polypyrrole. *Synth Met* 187:145–151
- Hara S et al (2004) Gel-like polypyrrole based artificial muscles with extremely large strain. *Polym J* 36(11):933–936
- Herod TE, Schlenoff JB (1993) Doping induced strain in polyaniline: stretchoelectrochemistry. *Chem Mater* 5:951–955
- Izadi-Najafabadi A (2006) Carbon nanotube and polypyrrole supercapacitors. UBC, Vancouver, BC, Canada
- Johansson R (2003) System modeling and identification. Prentice Hall, Englewood Cliffs, New Jersey
- John S, Alici G, Spinks G et al (2008a) Sensor response of polypyrrole trilayer benders as a function of geometry. In: Bar-Cohen Y (ed) *Electroactive polymer actuators and devices*. SPIE conference, San Diego, CA, USA, pp 692721–1–692721–9
- John S, Alici G, Cook C (2008b) Frequency response of polypyrrole trilayer actuator displacement. In: Bar-Cohen Y (ed) *Electroactive polymer actuators and devices*. SPIE conference, San Diego, CA, USA, pp 69271T–69271T–8
- John SW, Alici G, Cook CD (2008c) Validation of resonant frequency model for polypyrrole trilayer actuators. *IEEE/ASME Trans Mechatron* 13(4):401–409
- John SW et al (2009) Towards fully optimized conducting polymer bending sensors: the effect of geometry. *Smart Mater Struct* 18(8):1–8
- John SW, Alici G, Cook CD (2010) Inversion-based feedforward control of polypyrrole trilayer bender actuators. *IEEE/ASME Trans Mechatron* 15(1):149–156
- Josephson RK (1993) Contraction dynamics and power output of skeletal muscle. *Annu Rev Physiol* 55:527–546
- Kaneko M et al (1997) Electrolyte and strain dependences of chemomechanical deformation of polyaniline film. *Synth Met* 84:795–796
- Khalili N, Naguib HE, Kwon RH (2015) Transmission line circuit model of a PPy based trilayer mechanical sensor. In: SPIE conference on electroactive polymer actuators. pp 94302E1–94302E–9
- Kohlman RS, Epstein AJ (1998) Insulator-metal transition and inhomogeneous metallic state in conducting polymers. In: Skotheim TA, Elsenbaumer RL, Reynolds JR (eds) *Handbook of conducting polymers*. Marcel Dekker, New York, pp 85–122
- Ljung L (1999) System identification- theory for the user second. Prentice Hall, Englewood Cliffs, New Jersey
- López Cascales JJ, Otero TF (2004) Molecular dynamic simulation of the hydration and diffusion of chloride ions from bulk water to polypyrrole matrix. *J Chem Phys* 120(4): 1951–1957
- Madden JDW (2000) Conducting polymer actuators. MIT, Cambridge, MA, USA
- Madden PGA (2003) Development and modeling of conducting polymer actuators and demonstration of a conducting polymer-based feedback loop. MIT, Cambridge, MA, USA
- Madden JDW, Madden PGA, Hunter IW (2001) Polypyrrole actuators: modeling and performance. *SPIE* 4329:72–83
- Madden JD et al (2002a) Load and time dependence of displacement in a conducting polymer actuator. *Mater Res Soc Proc* 698(EE4.3):137–144
- Madden JDW, Madden PG, Hunter IW (2002b) Conducting polymer actuators as engineering materials. In: Bar-Cohen Y (ed) *SPIE conference on electroactive polymer actuators*, vol 4695. SPIE conference, San Diego, CA, USA, pp 176–190
- Madden JDW et al (2007) Creep and cycle life in polypyrrole actuators. *Sens Actuators A* 133 (1):210–217
- Maziz A et al (2014) Demonstrating kHz frequency actuation for conducting polymer microactuators. *Adv Funct Mater* 24(30):4851–4859

- Mazzoldi A, Della Santa A, De Rossi D (1999) Conducting polymer actuators: properties and modeling. In: Polymer sensors and actuators. Osada Y, De Rossi DE (eds). Springer, Heidelberg
- Metz P, Alici G, Spinks GM (2006) A finite element model for bending behaviour of conducting polymer electromechanical actuators. *Sens Actuators A* 130-131:1–11
- Nguyen CH, Alici G, Wallace GG (2012) Modeling trilayer conjugated polymer actuators for their sensorless position control. *Sens Actuators A* 185:82–91
- Nguyen CH, Alici G, Wallace G (2014) An advanced mathematical model and its experimental verification for trilayer conjugated polymer actuators. *IEEE/ASME Trans Mechatron* 19 (4):1279–1288
- Nogami Y, Pouget J-P, Ishiguro T (1994) Structure of highly conducting PF6-doped polypyrrole. *Synth Met* 62:257–263
- Onsager L (1931) Reciprocal relations in irreversible processes. I. *Phys Rev* 37:405–426
- Otero TF (2008) Reactive conducting polymers as actuating sensors and tactile muscles. *Bioinspir Biomim* 3(3):1–9
- Otero TF, Cortés MT (2003) A sensing muscle. *Sens Actuators B* 96(1-2):152–156
- Otero TF, Padilla J (2004) Anodic shrinking and compaction of polypyrrole blend: electrochemical reduction under conformational relaxation kinetic control. *J Electroanal Chem* 561:167–171
- Pei Q, Ingnas O (1992) Electrochemical applications of the bending beam method. 1. Mass transport and volume changes in polypyrrole during redox. *J Phys Chem* 96:10507–10514
- Pei Q, Ingnas O (1993) Electrochemical applications of the bending beam method; a novel way to study ion transport in electroactive polymers. *Solid State Ion* 60:161–166
- Pytel RZ (2007) Artificial muscle morphology: structure/property relationships in polypyrrole actuators. MIT, Cambridge, MA, USA
- Pytel RZ, Thomas EH, Hunter IW (2006) Anisotropy of electroactive strain in highly stretched polypyrrole actuators. *Chem Mater* 18(4):861–863
- Shoa T et al (2007) Polypyrrole operating voltage limits in aqueous sodium hexafluorophosphate. *Proc SPIE* 6524:652421–652421–8
- Shoa T et al (2008) Rate limits in conducting polymers. *Adv Sci Technol* 61:26–33
- Shoa T et al (2010a) Analytical modeling of a conducting polymer-driven catheter. *Polym Int* 59 (3):343–351
- Shoa T, Madden JDW et al (2010b) Electromechanical coupling in polypyrrole sensors and actuators. *Sens Actuators A* 161(1-2):127–133
- Shoa T, Mirfakhrai T, Madden JDW (2010c) Electro-stiffening in polypyrrole films: dependence of young's modulus on oxidation state, load and frequency. *Synth Met* 160(11-12):1280–1286
- Shoa T et al (2011) A dynamic electromechanical model for electrochemically driven conducting polymer actuators. *IEEE/ASME Trans Mechatron* 16(1):42–49
- Skotheim TA, Elsenbaumer RL, Reynolds JR (1998) Handbook of conducting polymers. Marcel Dekker, New York
- Smela BE, Gadegaard N (1999) Surprising volume change in PPy (DBS): an atomic force microscopy study. *Adv Mater* 11(11):953–957
- Smela E, Lu W, Mattes BR (2005) Polyaniline actuators part 1: PANI(AMPS) in HCl. *Synth Met* 151:25–42
- Spinks GM et al (2002) Strain response from polypyrrole actuators under load. *Adv Funct Mater* 12 (6-7):437–440
- Spinks GM et al (2006) Carbon-nanotube-reinforced polyaniline fibers for high-strength artificial muscles. *Adv Mater* 18(5):637–640
- Takashima W et al (1997) Mechanochemoelectrical effect of polyaniline. *Synth Met* 85:1395–1396
- Takashima W, Hayasi K, Kaneto K (2007) Force detection with Donnan equilibrium in polypyrrole film. *Electrochem Commun* 9(8):2056–2061
- Tezuka Y (1997) Concentration profiles of conducting species in polypyrrole films in cyclic voltammetry by means of a diode array detector. *J Electroanal Chem* 425:167–172
- Tso CH, Madden JD, Michal CA (2007) An NMR study of PF6-ions in polypyrrole. *Synth Met* 157 (10-12):460–466

- Wang X, Smela E, Shapiro B (2004) Understanding ion transport in conjugated polymers. In: Bar-Cohen Y (ed) Smart structures and materials 2004: electroactive polymer actuators and devices (EAPAD), vol 5385, pp 146–154
- Wang X, Shapiro B, Smela E (2009) Development of a model for charge transport in conjugated polymers. *J Phys Chem C* 113(1):382–401
- Warren MR, Madden JDW (2006a) A structural, electronic and electrochemical study of polypyrrole as a function of oxidation state. *Synth Met* 156(9–10):724–730
- Warren MR, Madden JDW (2006b) Electrochemical switching of conducting polymers: a variable resistance transmission line model. *J Electroanal Chem* 590(1):76–81
- Wing Yu Lam J (2011) Influences of growth conditions and porosity on polypyrrole for supercapacitor electrode performance. UBC, Vancouver, BC, Canada
- Wu Y et al (2007) Soft mechanical sensors through reverse actuation in polypyrrole. *Adv Funct Mater* 17(16):3216–3222
- Yamaura M, Sato K, Iwata K (1992) Memory effect of electrical conductivity upon the counter-anion exchange of polypyrrole films. *Synth Met* 48(3):337–354
- Yao Q, Alici G, Spinks GM (2008) Feedback control of tri-layer polymer actuators to improve their positioning ability and speed of response. *Sens Actuators A* 144(1):176–184
- Yoo DS et al (2011) Multiple time constant modelling of a printed conducting polymer electrode. *Electrochim Acta* 56(13):4711–4716
- Zama T et al (2005) Comparison of conducting polymer actuators based on polypyrrole doped with BF₄⁻, PF₆⁻, CF₃SO₃⁻, and ClO₄⁻. *Bull Chem Soc Jpn* 78(3):506–511
- Zheng W et al (2011) Artificial muscles based on polypyrrole/carbon nanotube laminates. *Adv Mater* (Deerfield Beach, Florida) 23(26):2966–2970

Keiichi Kaneto, Edwin W. H. Jager, Gursel Alici, and
Hidenori Okuzaki

Contents

1	Bending Actuators	386
1.1	Diaphragm Pumps	386
1.2	Swimming Devices	389
1.3	Flexural-Jointed Gripper	390
2	Microactuators and Biomedicine	391
2.1	Microdevices	391
2.2	Microfluidics and Drug Delivery	393
2.3	Biocompatibility	395
2.4	Cell Biology	395
2.5	Medical Devices	398

K. Kaneto

Kyushu Institute of Technology, Eamex Co. Ltd, Chuoku, Fukuoka, Japan

Osaka Institute of Technology, Eamex Co. Ltd., Osaka, Japan

e-mail: keiichi.kaneto@oit.ac.jp

E.W.H. Jager

Department of Physics, Chemistry and Biology (IFM), Linköping University, Linköping, Sweden

Biosensors and Bioelectronics, Linköping University, Linköping, Sweden

e-mail: edwin.jager@liu.se

G. Alici

School of Mechanical, Materials, and Mechatronic Engineering, ARC Centre of Excellence for Electromaterials Science, University of Wollongong, Wollongong, NSW, Australia

e-mail: gursel@uow.edu.au

H. Okuzaki (✉)

Interdisciplinary Graduate School of Medicine and Engineering, University of Yamanashi, Kofu, Yamanashi, Japan

e-mail: okuzaki@yamanashi.ac.jp

3	Linear Actuators	400
3.1	Braille Cell	401
3.2	Humidity-Sensitive Linear Actuators	402
3.3	Origami Actuators	405
4	Conclusion	406
	References	408

Abstract

Artificial muscles are the longtime dream of human being to replace the existing engines, motors, and piezoelectric actuators because of the low-noise, environment-friendly, and energy-saving actuators (or power force generators). This chapter describes applications of conducting polymers (CPs) to EAPs such as bending actuators, microactuators, and linear actuators. The bending actuators were applied to diaphragm pumps, swimming devices, and flexural-jointed grippers with the trilayer configurations. On the other hand, the microactuators have the advantage of short diffusion times and thus fast actuation. Since the CP actuators operate in any salt solutions, such as a saline solution, cell culture media, and biological liquid, the PPy microactuators have potential applications in microfluidics and drug delivery, cell biology, and medical devices. Furthermore, the linear actuators were developed for the applications to the Braille cells, artificial muscles for soft robots.

Keywords

Bending actuators • Diaphragm pumps • Flexural-jointed gripper • Swimming devices • Braille cell • Cell clinic • Conducting polymer microactuators • Biocompatibility • Cell biology • Medical devices • Microdevices • Microfluidics and drug delivery • Electroactive scaffold • Fluid micropump • Linear actuators • Humidity sensitive • Origami actuators • Microanastomosis connector • Microhinges • NEMO • Shape memory alloy (SMA) actuators • Tube-in-tube actuator node (TITAN) • WANDA

1 Bending Actuators

In general, volume changes of the CPs caused by electrochemical or chemical doping and dedoping are small, less than 10 %. The bending actuators with bilayer or trilayer structure are of great advantage to display fast and large bending deformation since the small volume changes in the CP thin layer caused by rapid transportation of solvated ions can be directly observed with the bending beam method.

1.1 Diaphragm Pumps

The pump based on a petal-shaped diaphragm (it is multi-piece as opposed to other single-piece diaphragm pumps) is shown in Fig. 1. The diaphragm of this pump, fabricated through PDMS-based MEMS processes, is made of trilayer polymer

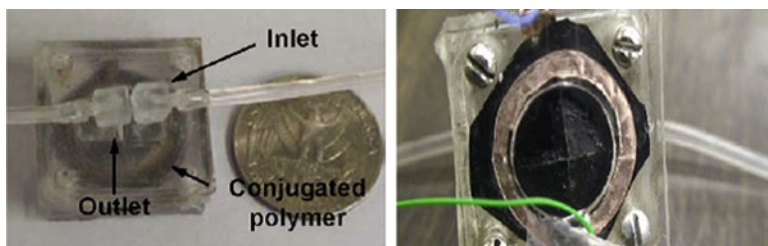


Fig. 1 A view of the micropump articulated with the petal-shaped diaphragm made of trilayer polymer substrate (Reprinted with permission from Fang and Tan (2010). Copyright (2010) Elsevier Limited)

actuators, which can provide a significantly large diaphragm deformation and consequently a flow rate as high as 1260 $\mu\text{l}/\text{min}$.

Wu et al. (2005) employed the trilayer configuration to establish another pumping concept, whose operation principle and sequence are illustrated in Fig. 2. Its configuration called “The Tube-In-Tube Actuator Node (TITAN)” is based on the concentric arrangement of the polypyrrole actuators which induce a peristaltic action to move the fluid through an inner channel in a single unit. This low-cost, low-power valveless pump provides flow rates of up to 2.5 $\mu\text{l}/\text{min}$ against a back pressure of 50 mbar in a 30 mm active segment.

Figure 3a shows schematic drawing of diaphragm pump using PPy films (Eamex HP). When the bias was applied with the polarity, namely, upper PPy film was biased positively and the lower negatively, the upper PPy film expanded to suck fluid from the left hand side, and the lower shrunk to expel fluid to right hand side. If both pumps were connected and valves were equipped properly, the bias with alternate polarity drove each diaphragm pump oppositely, and then, the fluid flowed in one direction. Figure 3b shows the prototype diaphragm pump with the diaphragm diameter of 30 mm. When the diaphragm pump was operated at 2 V, 200 mA, and 1 Hz, the pump demonstrated to flow the fluid with the rate of 70 ml/min. A problem of the diaphragm pump was that the electrolyte solution leaked to the fluid area through the PPy films. Seal coating of PPy film with thin polymer film reduced the output power. The fluid can be the electrolyte solution, and then, the pump is used as the closed cycle unit like a heat pipe.

Figure 4 shows the prototype heat pipe and PPy diaphragm pump (Eamex HP) designed for cooling a central processing unit (CPU) in personal computers. The dimension of diaphragm pump was 25 mm square and 10 mm thickness. The heat pipe was assembled with ten thin tubes in a rectangular rod with length of 150 mm, width of 9.2 mm, and thickness of 1.8 mm as shown in Fig. 4. The heat pipe transferred 30 W with the operation frequency of 0.5 Hz at 1.5 V. The coolant came and went in the thin tube, which can be seen in the demonstration at Eamex HP.

A fluid micropump with the other structure (Naka et al. 2010), namely, peristaltic movement, was fabricated using PPy films. The micropump was composed with two serially arranged open-close micropumps without valves. The serial micropumps were driven alternatively to push the fluid in one direction by taking the synchronous

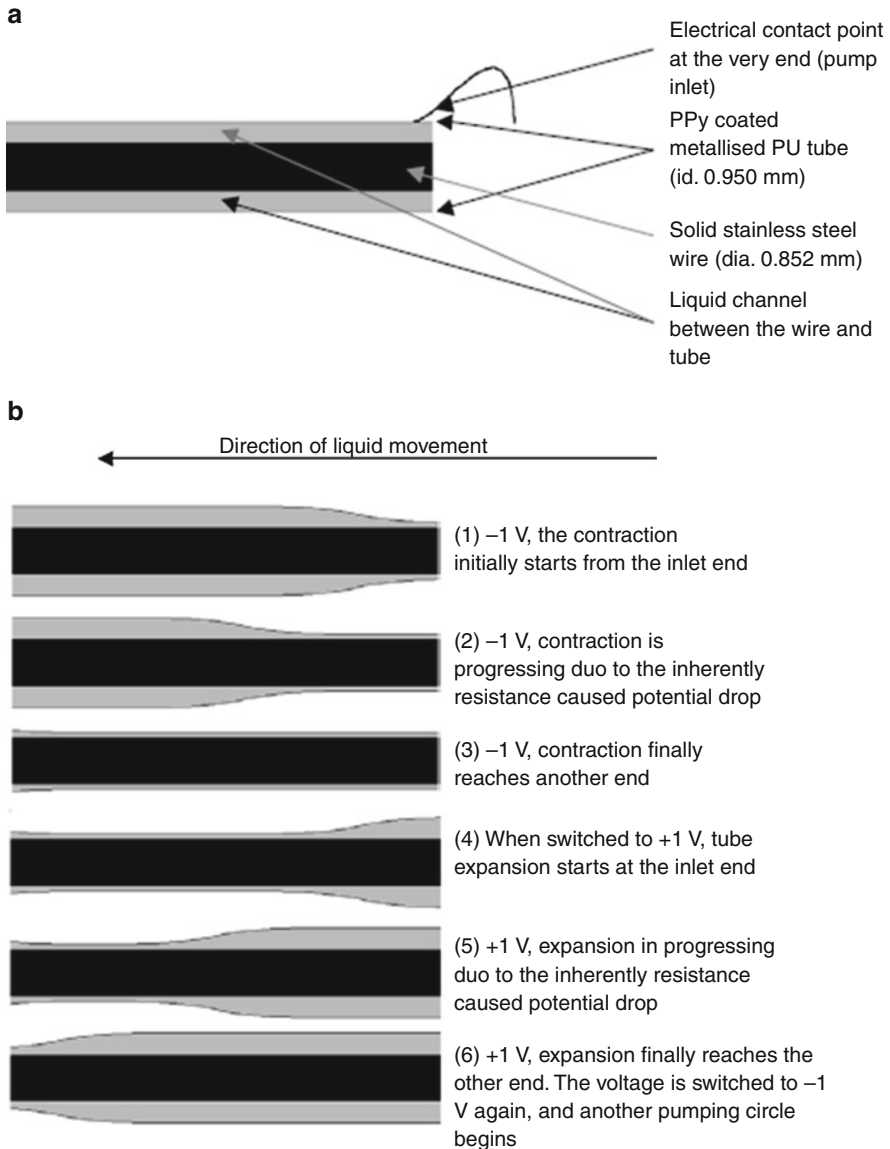


Fig. 2 A schematic view of the valve pump activated with trilayer polymer actuators (Reprinted with permission from Wu et al. (2005). Copyright (2005) Institute of Physics)

timing. The micropump is suitable to pump high viscous fluids with precise control of the flow rate in the wide range. It has also been found that the energy consumption rate of the micropump is markedly lower than those of conventional ones (Naka et al. 2010).

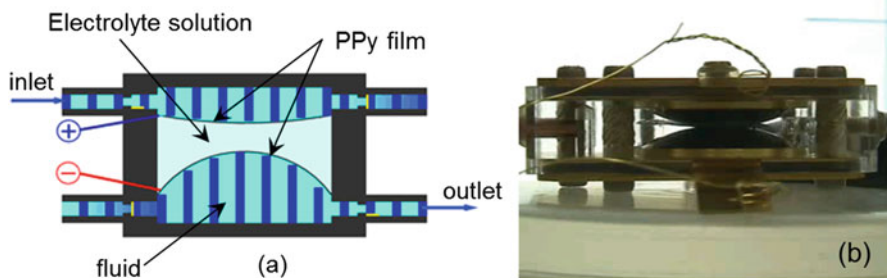


Fig. 3 (a) Schematic drawing of diaphragm pump and (b) photograph of the prototype diaphragm pump (Reproduced from (Eamex HP, <http://eamex.co.jp/>))

Fig. 4 A prototype heat pipe fabricated with the PPy diaphragm pump (Reproduced from (Eamex HP, <http://eamex.co.jp/>))

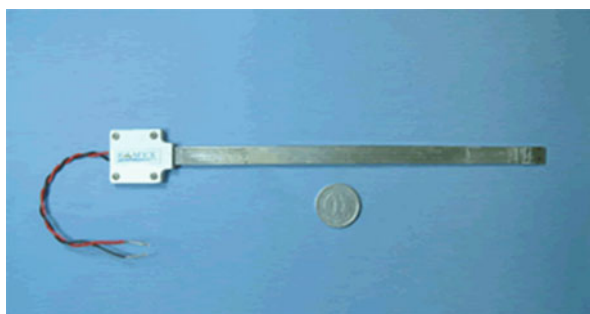
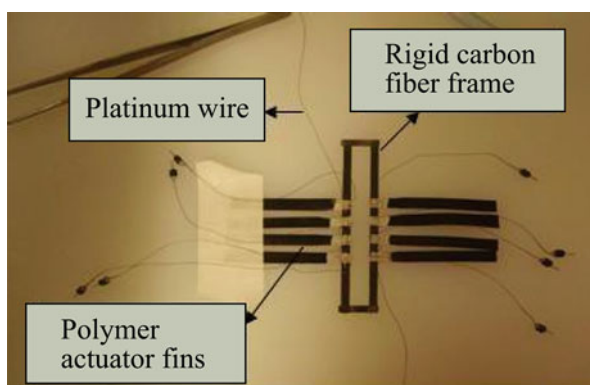


Fig. 5 A view of the prototype swimming device articulated with trilayer polymer actuator Alici et al. (2007)



1.2 Swimming Devices

Based on the large deflection of the trilayer configuration, a number of swimming devices have been proposed by the research group from the University of Wollongong. The first of such devices (Alici et al. 2007) shown in Fig. 5 has eight fins (i.e., trilayer polymer actuators) installed along both sides of a rigid body to move the device in a direction perpendicular to the longitudinal axis of the body. The rigid

Fig. 6 NEMO the fish articulated with trilayer actuators and its caudal fin arrangement (Reprinted with permission from McGovern et al. (2009). Copyright (2009) Institute of Physics)

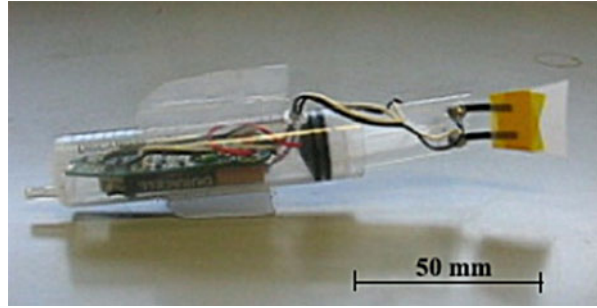


Fig. 7 WANDA the fish articulated with trilayer actuators and its caudal fin arrangement (Fay et al. 2010; Carpi et al. 2011). It must be noted that the body and caudal fin of WANDA have been optimized to minimize the drag and increase its swimming efficiency, compared to NEMO

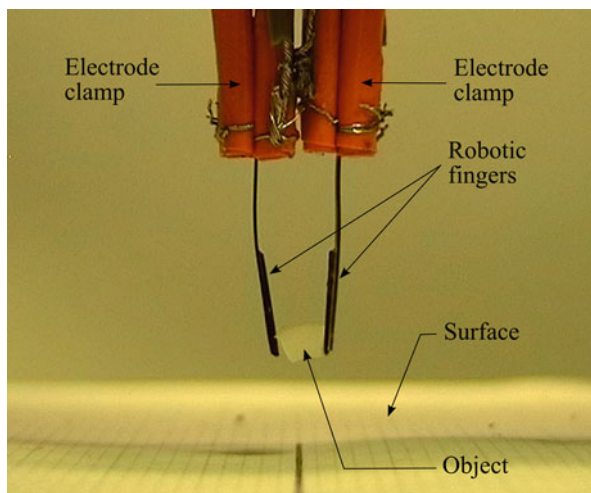
body is made of pregunated carbon fiber strips of 0.3 mm thickness and hardened with resin. The device can be considered like a box fish having a carapace (rigid body) with side or paired fins running through the rigid body, like a fish having pectoral fins (Sfakiotakis et al. 1999). The fins or polymer benders behave as individually controlled flexible membranes. Each fin is activated with sinusoidal inputs such that there is a phase lag between the movements of the successive fins, and the frequency and amplitude of the input can be changed to create enough thrust force for propulsion.

Following the success of this device, the same group proposed a number of swimming devices called NEMO (McGovern et al. 2009) and WANDA (Fay et al. 2010), autonomously powered and controlled robotic fish, which use the trilayer actuators as the caudal fins to propel the fish, as illustrated in Figs. 6 and 7, respectively. WANDA had an overall length of 24 cm and real-time wireless speed and directional control with an onboard camera and a power source. The aim has been to replicate some biomechanical aspects of fish swimming in establishing such devices. Although the actuators are kinematically compatible with the envisioned design concept to provide the biomimetics of movement, they are not fully compatible from kinetics points of view in order to generate enough thrust force for efficient propulsion.

1.3 Flexural-Jointed Gripper

The trilayer actuator configuration has been used as the active flexural joints of a two-finger gripper, as depicted in Fig. 8 (Alici and Huynh 2007). Each finger has the

Fig. 8 A view of a two-finger gripper articulated with trilayer polymer actuators (Alici and Huynh 2007)



dimensions of (5-mm actuator + 5-mm rigid link) \times 1 mm \times 0.17 mm. The conducting polymer part of the finger works as an actuator and a flexure joint called *active flexure (acti-flex)* joint, while the carbon fiber attached to the end of the polymer serves as a rigid link for the finger. The gripper can lift and handle as much as 50 times of its total mass under 1.5 V.

2 Microactuators and Biomedicine

Since the volume change mechanism depends on the insertion and de-insertion of ions and solvent in the polymer matrix, microscale actuators have the advantage of short diffusion times and thus fast actuation. In addition the microfabricating conducting polymer (CP) actuators can result in novel applications that are not possible with other technologies.

The CPs need an electrolyte, a source/sink for ions and solvent, in order to operate. This can in principle be any salt solution, such as a saline solution, cell culture media, and biological liquid such as blood, saliva, and urine. This makes applications in biology and medicine interesting and possible. Many applications and application demonstrators employing CP microactuators have been developed over the years, but commercial products are currently not yet available.

2.1 Microdevices

Using microfabrication (see ► [Chap. 15, “Conducting Polymers as EAPs: Physical Description and Simulation”](#)), Smela et al. developed the first CP microactuators. They were bilayers of Au and PPy(DBS) that gave a simple bending motion (Smela et al. 1993). In the years following this first demonstration, the complexity of the

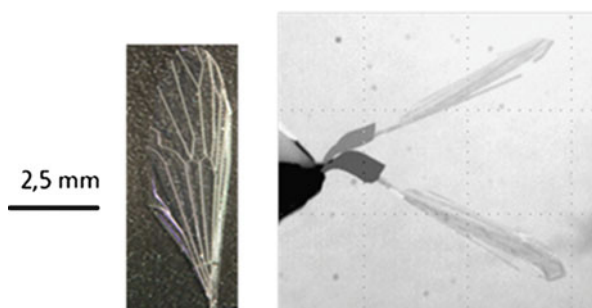
devices is enhanced by adding additional elements including rigid plates (Smela et al. 1995), multiple actuators (Jager et al. 2000a), and sensors (Jager et al. 2002), resulting in multifunctional microdevices.

The PPy/Au bending bilayers (Smela et al. 1993; Zhou et al. 2004; Lee et al. 1994) are one of the basic microactuator structures. These bilayer actuators have been primarily used as microhinges. Smela et al. fabricated 30 μm by 30 μm hinges to which 90 μm by 90 μm rigid plates made of a photopatternable polymer were attached (Smela et al. 1995). By actuating the hinges, the plates could be rotated 180°, resulting in an active surface of which the properties could be changed dynamically. Next, six plates were interconnected by multiple hinges. Upon activation of the hinges, the plates self-assembled into a cube of 300 μm by 300 μm by 300 μm . Reversing the applied potential unfolded the cubes. Also, Si plates, fabricated from the substrate and containing additional electronic elements such as an electrochromic pixel, have been lifted using the PPy/Au bilayer microhinges (Smela 1999; Smela et al. 1999).

While the bilayer microactuators typically use an external electrolyte, trilayer microactuators have been developed to allow for in-air operation (see previous chapters). The first microfabricated trilayer actuator used a commercial PVDF membrane as the intermediate, electrolyte-storing layer, and the fabrication was similar to the macroscopic versions except that it was cut out having micrometer lateral dimensions (500–900 μm long, 160–350 μm wide) using laser ablation (Alici et al. 2009). The main limiting factor was the actuator thickness, approximately 170 μm . This was later reduced to 54 μm resulting in an increase of deflection (Gaihre et al. 2011). However, these trilayer actuators were still simple, bending actuators. The next step is to integrate them into small microgrippers, which required patterning and individual control of multiple trilayer actuators as recently demonstrated (Jager et al. 2013).

The other trilayer actuator technology that is based on IPNs has also been microfabricated using photolithography and reactive ion etching (Khaldi et al. 2011b). The IPN microactuators (900 \times 300 \times 17 μm^3) showed a displacement of 950 μm . These IPN microactuators have thereafter been combined with passive SU8 structures that are integrated into a single device that can be easily released after fabrication using lift-off (Khaldi et al. 2011a). The IPN microactuators are envisioned to drive the flapping wings of an artificial insect. The integrated SU8 structures form bioinspired wings (Fig. 9). Recently, they have improved the

Fig. 9 *Top:* two still pictures of SU8 wings driven by the IPN microactuator. *Bottom:* close up of the SU-8 wings that mimic venation of crane fly wings



fabrication and showed ultrathin robust IPN microactuators that could actuate at frequencies of more than 1 kHz, bringing the micro-aerial vehicle closer to realization (Maziz et al. 2014).

A device for tactile sensing has been proposed by Yamada and coworkers. PPy was deposited on comb-shaped microelectrodes and covered with a polyethylene glycol solid polymer electrolyte containing LiClO_4 salt. The 30 μm PPy layer expanded 2 μm in 30 s, which, according to the authors, should be enough to be sensed (Yamada et al. 1998).

2.2 Microfluidics and Drug Delivery

The small size and fact that they can operate in a liquid environment make CP microactuators interesting for applications in microfluidics and drug delivery. The CP-actuated valves can be designed using different mechanical principles such as bilayer hinges, buckling actuators, and bulk-swelling layers.

The first demonstrated microvalve employed CP microactuators, used as a PPy/Au bilayer hinge to rotate a rigid plate inside a PDMS microfluidic channel (Pettersson et al. 2000). The PPy actuators were made on a Si substrate and the microfluidic circuitry was made in a PDMS slab. PDMS was thereafter bonded on the Si substrate resulting in a microfluidic system. By lifting the plate, the flow was to be stopped.

HSG-IMIT and Micromuscle AB developed valve to control the flow of an implantable drug delivery device called Intellidrug (Göttsche et al. 2006; Göttsche and Haeberle 2009). The Intellidrug device had the same size as two molar teeth and was aimed to control the release of a drug (on/off) into the mucosal tissue in the mouth. The small size of the implant and application required a low power consumption of the valve. Only PPy microactuators had the required low power consumption and low-driving voltage with regard to size (Göttsche and Haeberle 2009). For safety reasons a “normally closed valve” design was employed. The valve was designed as a buckling membrane valve over an orifice. The first generation valve had the microfluidic in- and outlets, PPy/Au membrane, CE, and RE integrated into a single Si chip (Fig. 10a). However, the membrane did not close perfectly in the off state, due to the irreversible volume change of PPy in the first cycle. The second-generation valve consisted of a freestanding Au/PPy bilayer membrane that was clamped between the fluidic circuitry comprising the orifice and the container that contained the electrolyte and CE (Fig. 10b). A separate electrolyte was used in contact with the “back side” of the membrane, i.e., the PPy side, in order to separate the actuation from the liquid flow. A membrane deflection of $200 \pm 50 \mu\text{m}$ was achieved and the flow could be controlled. The relatively large periodicity of the on/off switching suited the application.

The large perpendicular volume change of PPy has also been employed to operate a microvalve (Berdichevsky and Lo 2004). Like the device of Peterson et al., the microfluidic circuitry was made in PDMS and consisted of fluidic channel and an electrolyte chamber separated by a thin membrane. The PDMS slab was mounted on

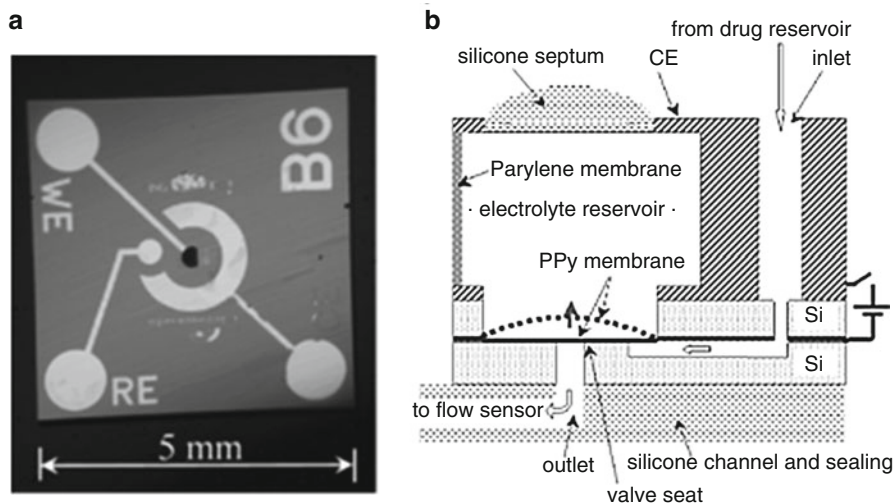


Fig. 10 (a) Photograph of the PPy buckling valve chip and (b) a sketch of the buckling PPy membrane valve used in the Intellidrug device (Reproduced from Götsche and Haerberle (2009))

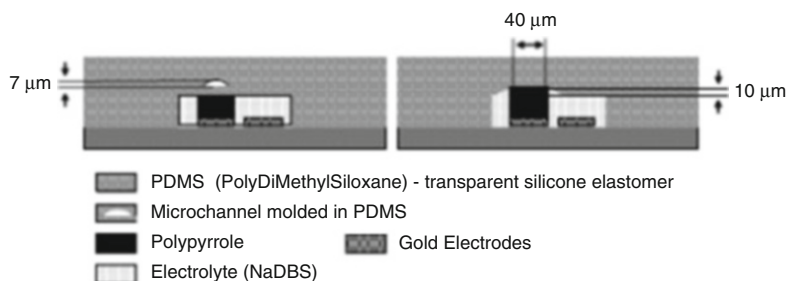


Fig. 11 A schematic figure illustrating the operation of the bulk PPy microvalve to open and close the microchannel (Reproduced from Berdichevsky and Lo (2004))

top of a glass substrate that comprised the PPy actuator, CE, and RE. Upon activation, the volume of the PPy expanded and pushed against the thin bottom of the PDMS channel, bulging it upward and thus pinching off the flow (Fig. 11).

A so-called smart pill, or drug delivery capsule, is developed by Madou and coworkers. In the first generation, the bulk volume change of PPy was proposed to control the orifice of the cavity, but showed to be unfeasible (Low et al. 2000). The small drug capsule now comprises a lid that can be opened and closed (Xu et al. 2006) utilizing the same principle of moving plates by using PPy/Au bilayer microactuators as developed by Smela (Smela et al. 1995) and Jager (Jager et al. 2002).

Not only liquid flow can be controlled using CP microactuators but also the wettability of a surface as demonstrated by Wang et al. (2008). They fabricated a

surface containing thick SU8 micropillars surrounded by PPy. When they applied a potential, the PPy layer between the SU8 pillars expanded, altering the surface from being hydrophobic (a droplet was laying on the SU8 micropillars, fakir situation) to hydrophilic (the droplet was wetting the entire surface).

2.3 Biocompatibility

The fact that CP actuators can operate in saline solution does not warrant that they can also safely interact with cells and tissue. There is a range of literature indicating that cells are viable on CP surfaces, for instance (Wong et al. 1994; Schmidt et al. 1997; Fonner et al. 2008), and even few papers that focus on cell viability for CP actuators (Lundin et al. 2011; Gelmi et al. 2014b). However, cell viability does not guarantee biocompatibility or even, more challenging, blood compatibility.

Extensive bio- and blood compatibility testing was done by the spin-off company Micromuscle AB for PPy and the microanastomosis connector (Sect. 2.5). PPy and the connector device passed basic biocompatibility testing, including cytotoxicity, irritation, acute systemic toxicity, and hemolysis. In addition they performed a small implantation study of the connector in a rat model. After 3 months, the devices showed not to be causing blood clotting or other obstruction, indicating blood- and biocompatibility. They also studied whether the devices caused coagulation using a Chandler looping setup comparing both heparinized (in order to increase blood compatibility) and untreated, as fabricated PPy connectors. The latter study indicated little difference in coagulation between both the heparinized and unheparinized PPy connectors and commercial stents (Jager 2010). The company also demonstrated that ethylene oxide sterilization, the golden standard in the medical device industry, does not affect the performance of the PPy actuators.

2.4 Cell Biology

The small size of these actuators makes them well suited to interact with cells, for instance, to manipulate cells. This was demonstrated by Smela et al. by grabbing small sand grains in the previously mentioned folding boxes (Smela et al. 1995) and Jager et al. by grabbing microscale objects using curling bilayer actuators (Jager et al. 2000b). The latter team also developed a microrobotic arm to manipulate microscale objects. The microrobotic arm, 670 μm long and 250 μm wide, consisted of two hinges as an “elbow joint,” two hinges as a “wrist,” and three hinges as fingers of a “hand,” all interconnected by rigid elements of SU8 (Jager et al. 2000a). The joints were individually controlled. Using this arm a 100 μm bead could be moved over a surface (Fig. 12). They also demonstrated actuation in the same plane as the substrate and the tapping, or rather shooting, of a microbead similar to a ball in pinball machine (Jager et al. 2001).

The “cell clinic” was developed to study single cells, for instance, signaling pathways or intracellular responses to external stimuli (Jager et al. 2002). The cell

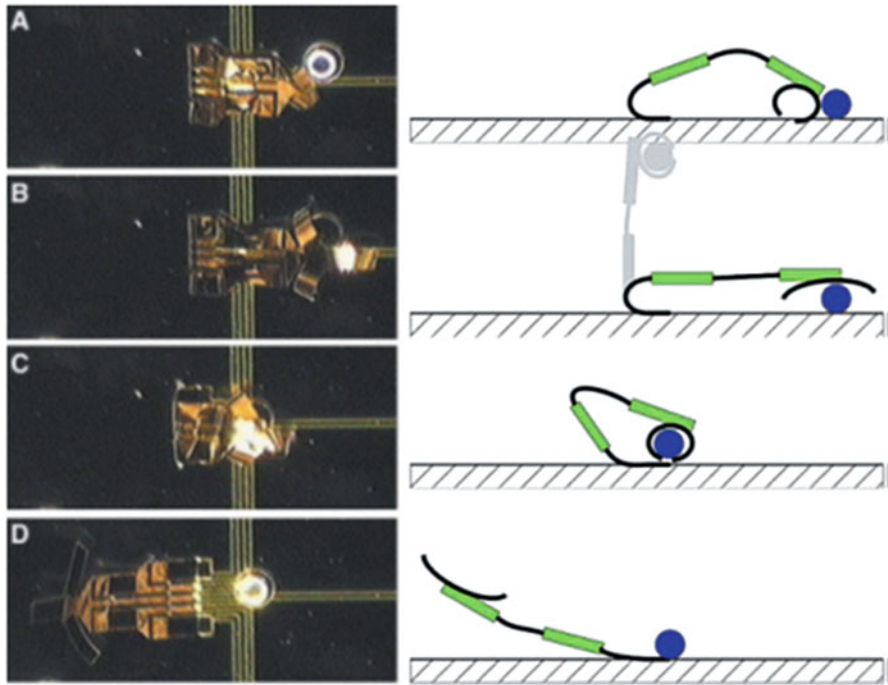


Fig. 12 A sequence of pictures (*left*) showing the grabbing and lifting of a 100 μm glass bead by a PPy-actuated microrobotic arm. A schematic drawing of the sequence is shown to the *right*. The robotic arm has an “elbow,” a “wrist,” and three “fingers” placed 120° from each other. The pictures do not show the fact that the bead is actually lifted from the surface before it is placed at the base of the robot arm. We have illustrated this in gray in the second sketch to the right (Reproduced from Jager et al. (2000a))

clinic consisted of a microfabricated cavity $100 \times 100 \times 20 \mu\text{m}^3$ made of SU8 to contain a cell or cells, which could be opened and closed with a lid ($150 \times 150 \mu\text{m}^2$) that was actuated by two PPy hinges of $100 \times 50 \mu\text{m}^2$. On the bottom of the cavity, a pair of Au electrodes (each $10 \times 80 \mu\text{m}^2$) was positioned to do impedance measurements. The PPy actuator hinges, lid, and electrodes were all monolithically fabricated on a common substrate. *Xenopus laevis* melanophore cells were seeded in the cavities (and on the device). These cells have pigment granules that aggregate and disperse upon (bio-)chemical stimulation. Impedance measurements by means of the electrode pair were used to follow this intracellular event.

The cell clinic has paved the way for further cell-based sensing (Urdaneta et al. 2005). In this device, the same scheme of fabricating the cavities is used: a thick rim on top of a Si-based sensor system forms the microvial. The device will also include an on-chip potentiostat (Prakash et al. 2008) and on-chip CE and RE (Jager et al. 1999).

CP microactuators have also been used to mechanically stimulate cells (Svennersten et al. 2011). Svennersten et al. developed a microchip comprising

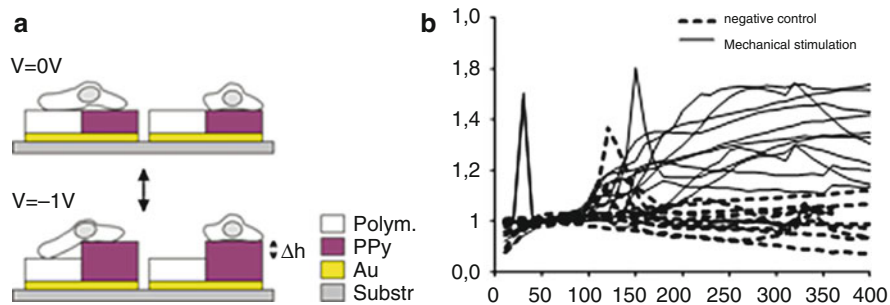


Fig. 13 (a) An illustration of the principle of in vitro mechanical stimulation using PPy microactuators. Cells attached on both the polymer and PPy are stretched when actuated, while cells on PPy or polymer only are not stretched. (b) Fluorescence signal from the intracellular Ca^{2+} signaling showing a concentration increase in the stretched cells and no increase in the non-stretched cells. See (Svennersten et al. 2011) for more details

PPy microactuators to mechanically stimulate, or stretch, single cells (Fig. 13a). The microchip was designed as alternating, 100 μm wide lines of PPy ($\sim 11.0 \mu\text{m}$ thick) and the passive material SU-8 ($\sim 10.0 \mu\text{m}$). Upon activation the PPy lines expanded perpendicularly by $\sim 1.0 \mu\text{m}$ and stretched the cells that are adhered to both the PPy and SU-8, while cells that are adhered on only PPy or SU-8 are not mechanically stimulated. In addition three different control areas were integrated on the chip. Renal epithelial (MDCK) cells, which are responsive to mechanical stimuli and physiologically relevant, were seeded and showed good adhesion and spreading on the PPy and SU8 surfaces. The MDCK cells were mechanically stimulated by activating the PPy microactuators for 300 s. This mechanical stimulation resulted in an increase in intracellular Ca^{2+} of the cells adhered to the actuators, which could be followed in real time (Fig. 13b). The intracellular Ca^{2+} increase was slow but followed to the expansion profile of PPy microactuators well. The gradual intracellular Ca^{2+} increase was absent in the cells that adhered on PPy only, thus further indicating that the Ca^{2+} signal was indeed mechanically induced. The authors showed that the Ca^{2+} response was caused by an autocrine ATP signaling pathway associated with mechanical stimulation of the cells, one of the most important mechanosensing mechanisms in MDCK cells.

Myocardial infarction, or heart attack, is the interruption of blood supply to a part of the heart that causes heart cells to die, resulting in scar tissue formation and impaired cardiac function. In order to restore function, bypass surgery or ultimately heart transplantation is needed, both of which are associated with serious complications. Therefore, new strategies to help regenerate the injured heart are necessary. One such strategy is an electroactive scaffold that is currently being developed by Gelmi and coworkers for cardiac tissue engineering applications utilizing a similar mechanical stimulation of cells as the previous device (Gelmi et al. 2014a). An electrospun scaffold, which mimics the extracellular matrix, is coated with PPy that provides a mechanical stimulation to stem cells seeded on the scaffold to increase the

differentiation ratio of stem cells into cardiomyocytes and thus increase the formation of novel cardiac tissue.

2.5 Medical Devices

Owing to the small size, CP actuators have often been proposed to drive steerable guide wires and catheters to facilitate maneuvering such devices through the vascular system. Lee et al. mounted one or two opposing pairs of PPy actuators on the tip of a 0.5 mm OD catheter; see Fig. 14a (Lee et al. 2009). Upon activation in a nonphysiological 1 M NaPF₆ solution, they achieved bending curvatures up to 0.06 m⁻¹.

Micromuscle AB developed an alternative design where PPy is applied only on one side of the coil that constitutes the tip of a guide wire (Krogh and Jager 2005). When a potential was applied, the PPy volume increased resulting in an increased curvature of the tip. A full 360° circular motion of the tip can be achieved by rotating the guide wire, which is common practice using standard fixed curvature guide wires. Figure 14b shows the PPy-activated guide wire in a mock-up vascular system using the surrounding salt solution as the electrolyte.

The same company also developed a microanastomosis connector aimed at reconnecting the two ends of a small blood vessel (1–3 mm diameter) that is separated either by trauma or by a surgical procedure, as an alternative to cumbersome micro-suturing (Immerstrand et al. 2002). The connector was shaped as a rolled-up sheet consisting of a blood-compatible polyurethane, Au (including a micropattern to control the bending direction (Krogh et al. 2001)), and PPy layer. Using a low voltage, the connector was shrunk, i.e., the sheet is rolled more tightly. Thereafter, the connector was inserted in both ends of the cut blood vessel (Fig. 15). Removing the applied voltage, the connector expanded by unrolling the sheet and held the two vessel ends together, while the vessel could heal.

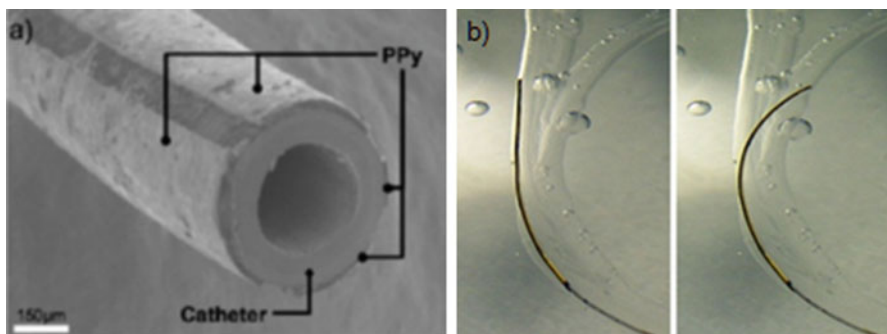


Fig. 14 (a) SEM image showing the four PPy actuators on a catheter tip (Reproduced from Lee et al. (2009)) (b) An active guide wire with a PPy-actuated bending tip maneuvering in mock-up vessels (Reproduced from Wilson et al. (2007))

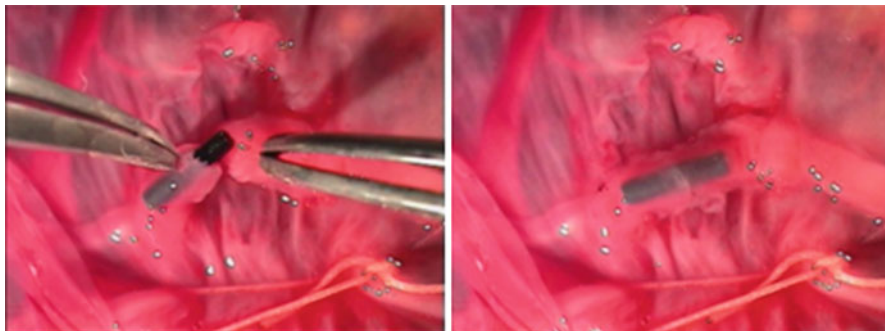


Fig. 15 Ex vivo surgery of the microanastomosis connector. The microanastomosis connector is an implantable medical device intended for reconnecting millimeter-sized blood vessels (Reproduced from Wilson et al. (2007))

During coronary angioplasty, a narrowed coronary artery is widened using a dilation balloon, and often, in addition, a stent is inserted to keep the stenotic area open. As special case is bifurcation stenting, when two stents are positioned around a side branch, one stent in the main artery and one in the side branch using a two-guide-wire system. The first stent has an opening through which the second stent is to be placed. It is therefore important that the first stent is positioned correctly, with the opening over the side branch. For this purpose, a rotating balloon system was developed (Gumm 2002). When inflating the first dilation balloon, the pivot points at both ends of the balloon had to be sealed to mechanically lock the balloon in the correct place and to prevent it from further rotation as well as to be able to pressurize the balloon to unfold and deploy the stent. A PPy-based balloon seal for this bifurcation stenting system was developed by Micromuscle and Boston Scientific (Carlsson et al. 2007; Jager et al. 2007). The seal (nrs. 230, 232 in Fig. 16) consisted of a metal ring with a thick (40–70 μm) layer of PPy and is mounted on a balloon shaft (nrs. 212, 214) on the narrow section of the dilation balloon (nr. 216). The counter electrode (nr. 257) was integrated on the same shaft, in the balloon lumen. The PPy seal was tested in a dilation balloon test system using a standard physiological saline solution. Activation of the PPy resulted in expansion up to 30 % of the PPy layer. This expansion was sufficient to close the gap between the shaft (nr. 230 or 232) and balloon pivot point (nr. 220 or 222), locking the balloon in place and preventing rotation. The developed PPy seal tolerated balloon inflation pressures up to 24 atm, exceeding the clinically applied pressures of 12–20 atm while preventing leaking of the balloon. The PPy seal was further optimized with respect to maximum expansion and speed altering synthesis conditions, dopants, temperature, applied potential, and electrolyte concentration and composition (Carlsson et al. 2007). This resulted in a the maximum expansion of 15 μm for a 50 μm thick PPy ring activated at -1.3 V in 0.3 M LiCl at a temperature of 37 °C. The expansion speed increased as well: an expansion of 11 μm was achieved in the first few seconds.

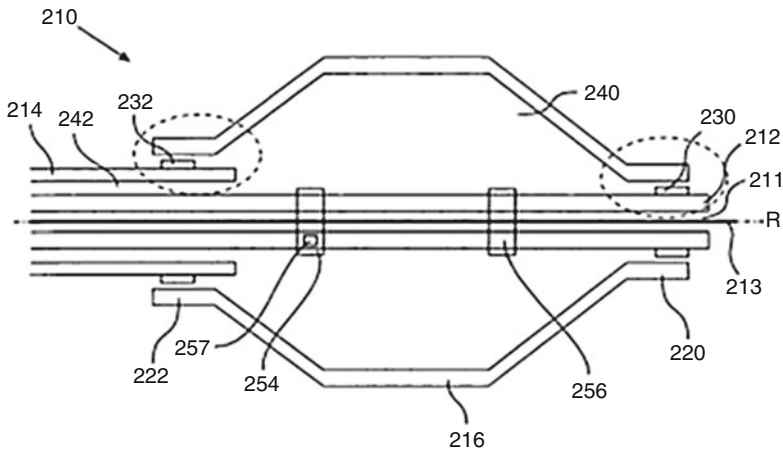


Fig. 16 Sketch of the rotating balloon system, comprising a PPy seal (230, 232) (Reproduced from Jager et al. (2007))

In order to facilitate the insertion procedure of cochlear implants, the University of Wollongong has developed a cochlear electrode array that can electroactively change its curvature. They added PPy actuator to a standard cochlear electrode array (Zhou et al. 2004). The PPy actuator was a trilayer actuator consisting of PPy/Pt/PVDF/Pt/PPy, with the PVDF pores filled with a propylene carbonate-based electrolyte. They were able to show bending close to 180°.

The same group also presented a design for a wearable sleeve that can provide a gentle massaging prevention of lymphedema (Zheng et al. 2013). The actuating sleeve consisted of stretchable PPy/rubber composite with a corrugated pattern. This stretchable PPy actuator could generate 1 % strain even when stretched up to 25 %.

Finally, trilayer PPy actuator strips PPy ($3 \times 20 \text{ mm}^2$) have been implanted and wrapped around the right ventricle of a rat model to investigate whether the contraction of the PPy actuators could assist the contraction of the heart as an alternative to cardiac tissue engineering using stem cells. The authors claim that the trilayer PPy actuator strips were able to significantly augment right ventricular contraction (Ruhparwar et al. 2014).

3 Linear Actuators

Since the CPs with superior mechanical properties such as high Young's modulus ($\sim 1 \text{ GPa}$) and tensile strength ($\sim 100 \text{ MPa}$) can generate large stress (up to 34 MPa) under low voltages ($\sim 2 \text{ V}$) (Madden et al. 2004), the linear actuators utilizing the CPs is one of the promising candidates for the applications to artificial muscles and electromechanical devices.

3.1 Braille Cell

The linear stroke polymer actuator has been proposed by Ding et al. (2003). It is based on hollow PPy fibers with a helical wire interconnect. They report that this actuator configuration, which provides up to 5 % axial strain, usable strains ($>1\%$) to at least 8 MPa, and peak strain rates of up to 13 %/s, can be used in the applications typified by a Braille display. In fact, the same research group has established a prototype electronic Braille cell with eight pins individually switched by this actuator configuration, as shown in Fig. 17.

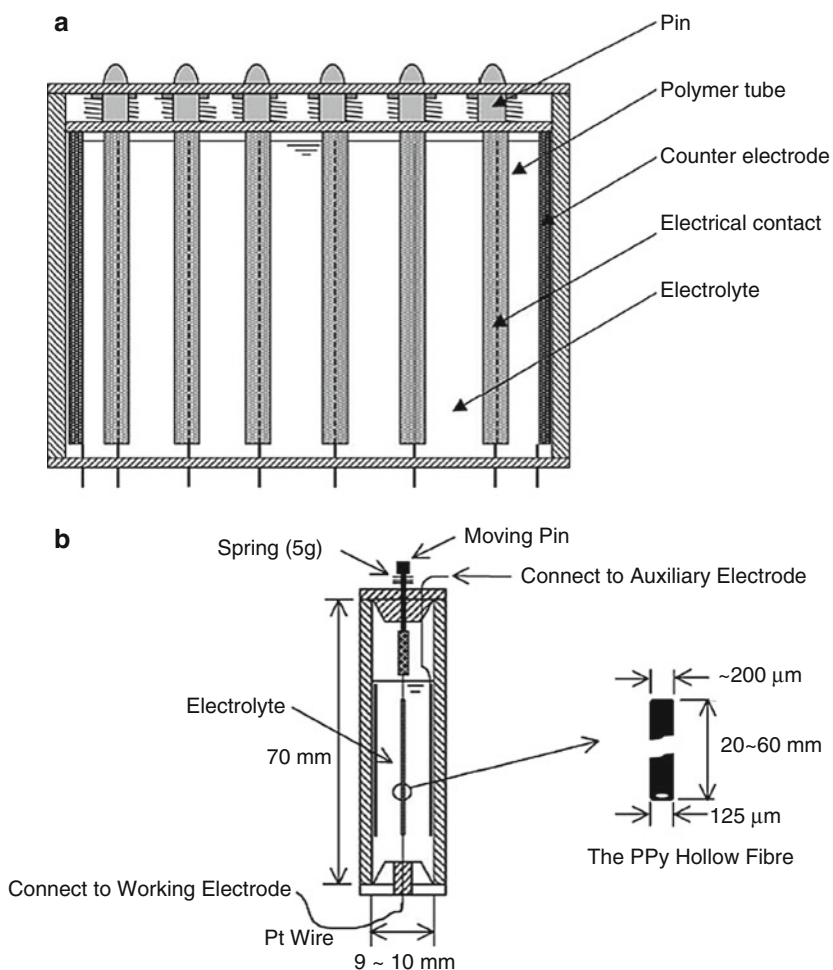


Fig. 17 A prototype electronic Braille cell with eight pins individually articulated the linear stroke polymer actuator (Reprinted with permission from Ding et al. (2003). Copyright (2003) Elsevier Limited)

Vidal et al. demonstrated linear actuators consisting of an interpenetrating network (IPN) matrix in which 3,4-ethylenedioxythiophene (EDOT) was chemically polymerized, leading to the formation of a PEDOT gradient similarly to the trilayer device (Vidal et al. 2006). The resulting IPN actuator showed linear displacement of 0.87 mm in air under 3.5 V. Furthermore, IPN hollow fiber actuator operated in air with linear strains up to 3 % and forces above 300 mN (Plesse et al. 2010).

3.2 Humidity-Sensitive Linear Actuators

Poly(3,4-ethylenedioxythiophene) doped with poly(4-styrenesulfonate) (PEDOT/PSS), commercially available in the form of water dispersion of colloidal particles, has attracted considerable attention because of its superior electrical and thermal stability especially in the conductive state, which provides potential applications such as antistatic coatings, capacitors, hole transport layers of organic light-emitting diodes, and transparent electrodes of touch panels and solar cells (Okuzaki 2012). The films made of PEDOT/PSS contracted in air under application of an electric field, the mechanism of which is explained by desorption of water vapor caused by Joule heating (Okuzaki et al. 2009) similarly to the PPys (Okuzaki and Kunugi 1996, 1997, 1998; Okuzaki et al. 1997, 1998a, b). Here, the electric field is capable of controlling the sorption equilibrium, and the PEDOT/PSS can sorb and desorb water vapor in response to ON and OFF of the electric field as it were breathing (Fig. 18; Okuzaki et al. 2010).

Under isometric conditions, the PEDOT/PSS film generates a contractile stress of 17 MPa which is 50 times larger than that of the real muscles (0.35 MPa). The maximum contraction of the PEDOT/PSS film increases with increasing both PSS content and relative humidity (RH), where the value attains as high as 7 % at 70 % RH for the film with 93 % of PSS (Okuzaki et al. 2013b). Figure 19 shows a linear actuator in which both ends of the PEDOT/PSS film (50 mm long, 2 mm wide, and 16 μm thick) were clamped by two Au-plated chucks as electrodes. Upon application of an electric field, a shaft slides up against a compressive force of a spring due to the film contraction where the bottom chuck is movable lifting up the shaft. When the electric field is turned off, the shaft rapidly slides down to the initial position in the course of the film expansion with the help of an expansive force of the spring. Since the linear actuator operates in ambient air without electrochemical reactions in an electrolyte solution or redox gas atmosphere, high reproducibility of motion may be achieved.

To examine durability of the film, a cycle of turning 10 V on for 5 s and off for 15 s was repeated at 50 % RH. It is found that the contractile strain slightly decreases to about 80 % of the initial strain until 10^3 cycles due to a creep of the film which increases the resistance and decreases the electric current (Okuzaki et al. 2013b). After 10^3 cycles, the film gradually contracts probably due to the rearrangement of polymer chains, which may partly recover the film contraction. After 8×10^4 cycles, the film finally breaks where both contractile strain and electric current are kept constant from 10^3 cycles until breaking, suggesting the PEDOT has superior stability

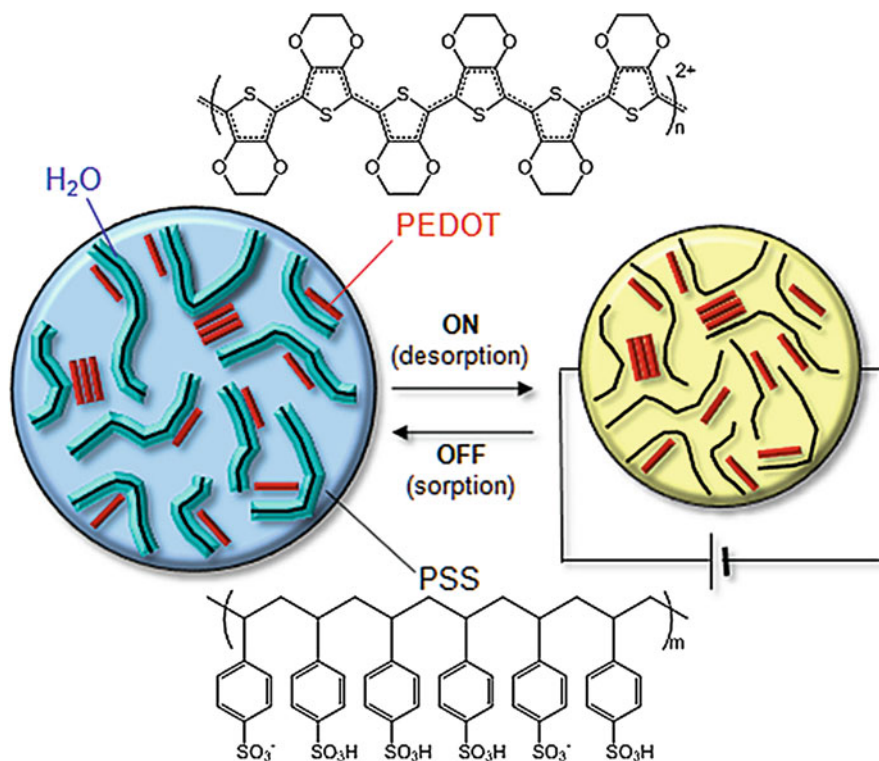


Fig. 18 Time profiles of biomorphic origami robot in action measured at 25 °C and 50 % RH

of electrical conductivity. The stress concentrates, and deformation or breaking may take place at structural defects, such as microvoids or microfractures formed during the casting. On the other hand, reproducibility and reliability may deteriorate at higher RH, where creep of the film becomes more remarkable because of the plasticization of PSS chains.

On the other hand, the PEDOT/PSS films can also be applied to a Braille cell consisting of six linear actuators, keyboard, and controller. As shown in Fig. 20, the Braille cell can display Japanese characters of “Ya,” “Ma,” “Na,” and “Shi” by driving the individual linear actuators. Similarly, shape memory alloy (SMA) actuators are driven by electrical Joule heating where deformation is caused by thermal phase transition between austenitic and martensitic phases. However, it is difficult to control not only phase transition temperature decided by the composition of alloys but also intermediate states between the two phases. In contrast, the PEDOT/PSS actuator can provide various contraction states according to the applied voltage. We should emphasize here that the PEDOT/PSS films exhibit electromechanical performance with large contractile strain in ambient atmosphere without using an electrolyte solution and counter/reference electrodes where the electric field is capable of controlling the equilibrium of water vapor sorption. Furthermore, the PEDOT/PSS



Fig. 19 Photographs of linear actuator utilizing PEDOT/PSS film (Reproduced from Okuzaki et al. (2013a))

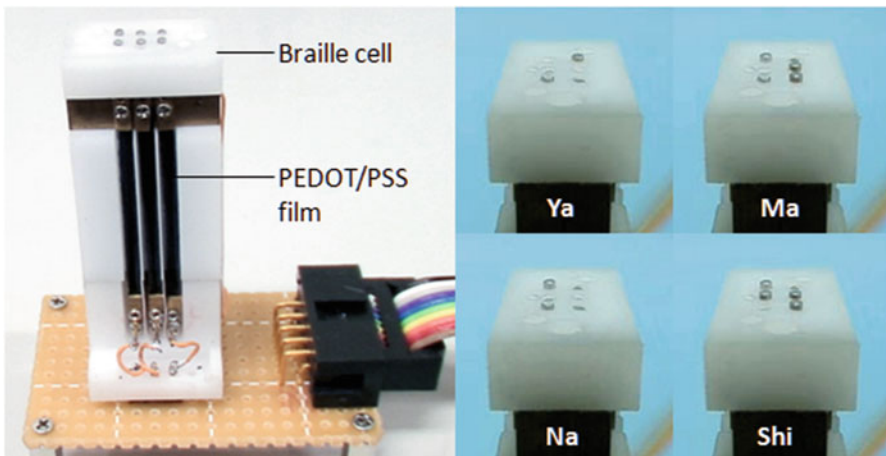


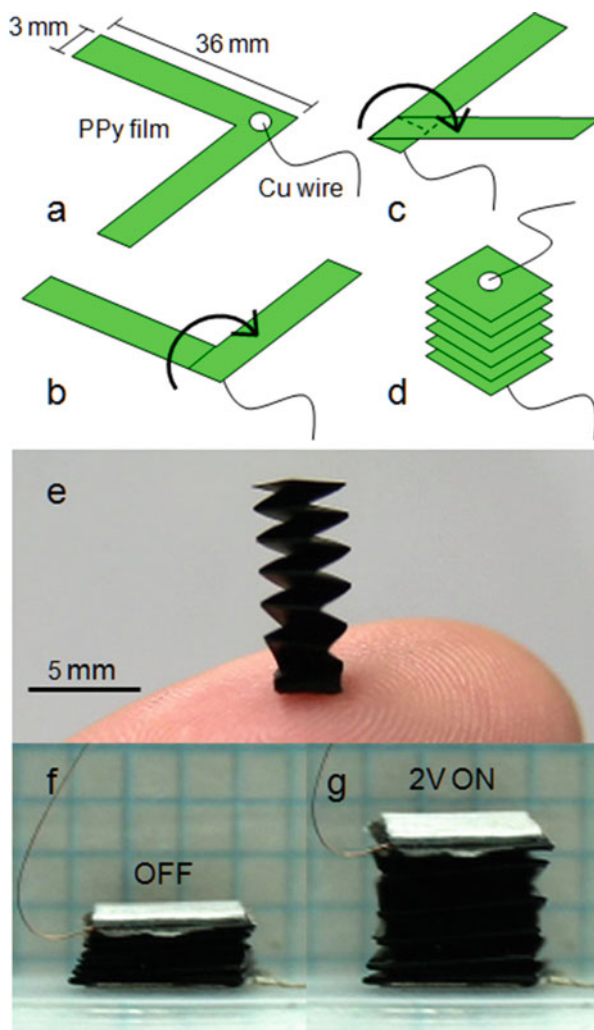
Fig. 20 Photographs of Braille cell using PEDOT/PSS linear actuators

actuator operates at voltages 1 or 2 orders of magnitude lower than dielectric elastomers and piezoelectric actuators because the dimensional change of the film is caused not by the electric current but the electric field.

3.3 Origami Actuators

Differing from 1D fiber and 2D film actuators, the origami actuator has its 3D structure constructed by folding a conductive polymer film. A procedure to fabricate the accordion-shaped origami actuator is schematically shown in Fig. 21 (Okuzaki et al. 2008, 2013a). A film made from electrochemically synthesized PPy doped with tetrafluoroborate is cut into an *L* shape (36 mm long, 3 mm wide, 20 μm thick in one side), and a copper wire is attached to the corner with a silver paste (Fig. 21a). After turning the film over, one side is folded to the opposite side (Fig. 21b), and then the other side is folded in the same manner (Fig. 21c). By alternately folding each side of the film six times, the PPy film is folded into the figure of an accordion shape, and

Fig. 21 Schematic illustrating the fabrication process (a–d) of accordion-shaped origami actuator and the photographs before annealing (e) and after annealing under 0 V (f) and 2 V (g) (Reproduced from Okuzaki et al. (2008, 2013b))



then a copper wire is attached on its top (Fig. 21d). Figure 21e shows a photograph of the as-folded accordion-shaped origami actuator before annealing. The resulting origami actuator is sandwiched between two glass plates and annealed at 140 °C for 1 h in air to crease properly (Fig. 21f).

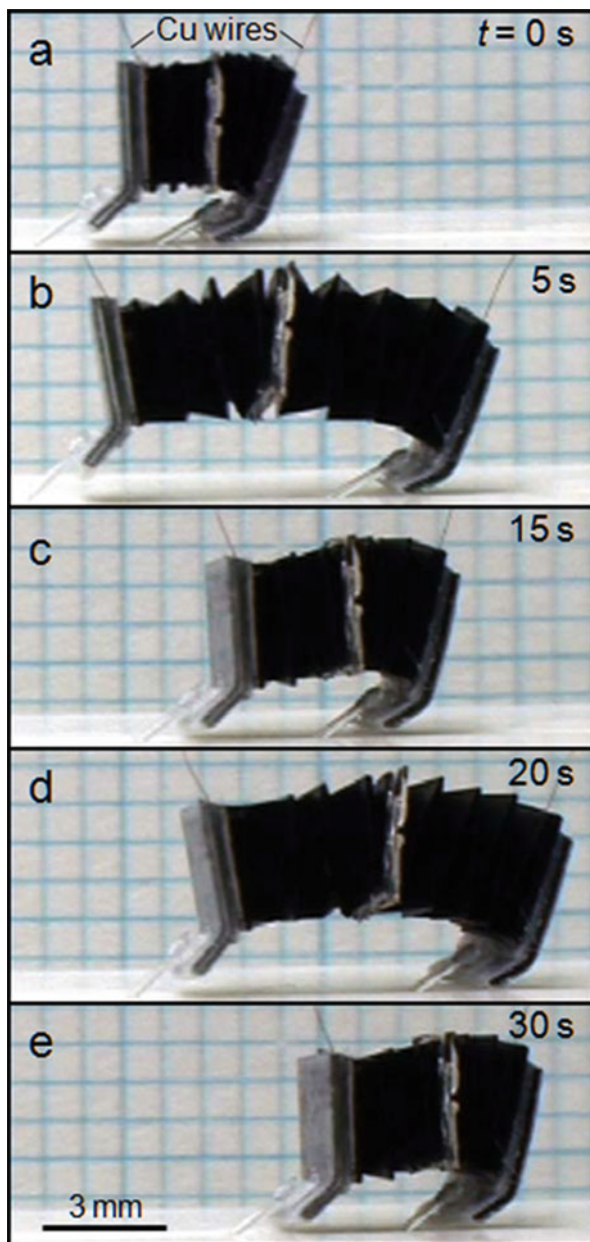
It is seen that the origami actuator exhibits rapid and significant expansion upon application of the electric field (Fig. 21g). The maximum strain attains 147 % at 2 V, which is 2 orders of magnitude larger than the film contraction caused by desorption of water vapor due to Joule heating. The mechanism is based on unfolding of the creases that results in the significant expansion of the origami actuator (Okuzaki et al. 2008). At the creases formed by folding the PPy film, the force to fold balances with that to unfold, thereby exhibiting spring characteristics. This balancing of forces also determines the length of the origami actuator. The application of an electric field causes desorption of water vapor and contraction of the film, leading to an increase in the elastic modulus making the film more difficult to be deformed. Therefore, a force to unfold the creases allows the angles to be extended, thereby expanding the origami actuator. The expansive force measured under isometric conditions attained 24 kPa at 2 V, that is, 2 orders of magnitude smaller than the film actuator contractile forces (6.1 MPa) (Okuzaki and Funasaka 2000). Thus, the origami actuator demonstrates extremely large strains with over 100 % trade-off with small stresses, ascribed to the small value of spring constant of the origami actuator (14 kPa).

On the basis of origami technology, a biomorphic origami robot is fabricated by connecting two accordion-shaped origami actuators in series and a pair of plastic plates acting as pawls attached to the ends (Fig. 22). Upon application of DC 3 V for 5 s through copper wires attached to the ends (Fig. 22a), the front pawl can slide forward due to the expansion of the accordion, but the rear hook is prevented by the teeth of the ratchet formed on the substrate from sliding backward (Fig. 22b, d). When the electric field is turned off for 10 s, the rear hook can move forward due to the contraction of the accordion, but the front hook is prevented from sliding backward (Fig. 22c, e). Thus, the origami robot moves forward with a caterpillar-like motion by repeated expansion and contraction at a measured velocity of 2 cm/min (Okuzaki et al. 2008, 2013a). Unlike EAP actuators using conductive polymers, polymer gels, or carbon nanotubes, the origami robot walked in air without using an electrolytic solution or counter and reference electrodes. Furthermore, this system can work at voltages 1 or 2 orders of magnitude lower than piezoelectric actuators or dielectric elastomers because the dimensional change is caused not by the electric current but the electric field. Moreover, various conductive polymers or their derivatives that undergo dimensional changes due to the sorption of water vapor can be employed on the same principle.

4 Conclusion

A variety of applications of EAP actuators using CPs was described in this chapter. The diaphragm pumps using bending actuators, capable of flowing the fluid continuously, were applied to the heat pipe for cooling the electronic devices.

Fig. 22 Time profiles of biomorphic origami robot in action measured at 25 °C and 50 % RH (Reproduced from Okuzaki et al. (2008, 2013b))



The swimming devices with bending actuators powered and controlled robotic fish as the caudal fins. The microrobotic arm made of the PPy microactuators could grab and lift a glass bead. Based on the unique characteristics of low activation voltage and biocompatibility, the bending actuators can be used as the steerable catheters, guide

wires, and microanastomosis connectors for the biological and medical applications. Furthermore, the Braille cells were fabricated by using the hollow PPy fibers with a helical wire interconnect or humidity-sensitive PEDOT/PSS linear actuators. The results allowed us to conclude that the EAP actuator using CPs would be one of the promising candidates for the soft actuators and artificial muscles for the practical applications.

References

- Alici G, Huynh NN (2007) Performance quantification of conducting polymer actuators for real applications: a microgripping system. *IEEE/ASME Trans Mechatron* 12:73–84
- Alici G, Spinks G, Huynh NN, Sarmadi L, Minato R (2007) Establishment of a biomimetic device based on tri-layer polymer actuators – propulsion fins. *Bioinspir Biomim* 2:S18
- Alici G, Devaud V, Renaud P, Spinks G (2009) Conducting polymer microactuators operating in air. *J Micromech Microeng* 19:025017
- Berdichevsky Y, Lo Y-H (2004) Polymer microvalve based on anisotropic expansion of polypyrrole. In: *Materials Research Society symposium-proceedings, 2003, vol 782*, Materials Research Society, Boston, p A4.4.1
- Carlsson D, Jager E, Krogh M, Skoglund M (2007) Systems, device and object comprising electroactive polymer material, methods and uses relating to operation and provision thereof. Patent WO2009038501
- Carpi F, Kombluh R, Sommer-Larsen P, Alici G (2011) Electroactive polymer actuators as artificial muscles: are they ready for bioinspired applications? *Bioinspir Biomim* 6:045006
- Ding J, Liu L, Spinks GM, Zhou D, Wallace GG, Gillespie J (2003) High performance conducting polymer actuators utilising a tubular geometry and helical wire interconnects. *Synth Met* 138:391–398
- Eamex HP. <http://www.eamex.co.jp/features/koubunshi/koubunshi/>
- Fang Y, Tan X (2010) A novel diaphragm micropump actuated by conjugated polymer petals: fabrication, modeling, and experimental results. *Sens Actuators A* 158:121–131
- Fay C, Lau KT, Beirne S et al (2010) Wireless aquatic navigator for detection and analysis (WANDA). *Sens Actuators B* 150:425–435
- Fonner JM, Forciniti L, Nguyen H, Byrne JD, Kou YF, Syeda-Nawaz J, Schmidt CE (2008) Biocompatibility implications of polypyrrole synthesis techniques. *Biomed Mater* 3:034124
- Gaihre B, Alici G, Spinks GM, Cairney JM (2011) Effect of electrolyte storage layer on performance of PPy-PVDF-PPy microactuators. *Sens Actuators B* 155:810–816
- Gelmi A, Ljunggren M, Rafat M, Jager EWH (2014a) Bioelectronic nanofibre scaffolds for tissue engineering and whole-cell biosensors. *Biosensors 2014*. Melbourne
- Gelmi A, Ljunggren M, Rafat M, Jager EWH (2014b) Influence of conductive polymer doping on the viability of cardiac progenitor cells. *J Mater Chem B* 2:3860–3867
- Göttsche T, Haeberle S (2009) Chapter 15. Integrated oral drug delivery system with valve based on polypyrrole. In: Carpi F, Smela E (eds) *Biomedical applications of electroactive polymer actuators*. John Wiley & Sons, Chichester, UK
- Göttsche T, Kohnle J, Schumacher A, Kattinger G, Jager E, Krogh M (2006) Ventil. Patent DE102006005517
- Gumm D (2002) Rotating stent delivery system for side branch access and protection and method of using same. Patent WO03/017872
- Immerstrand C, Peterson KH, Magnusson K-E, Jager E, Krogh M, Skoglund M, Selbing A, Inganäs O (2002) Conjugated-polymer micro- and milliaactuators for biological applications. *MRS Bull* 27:461–464

- Jager EWH (2010) Chapter 8, Conjugated polymers as actuators for medical devices and microsystems. In: Leger J, Carter S, Berggren M (eds) *Iontronics – ionic carriers in organic electronic materials and devices*. CRC Press, Boca Raton, pp 141–162
- Jager EWH, Smela E, Inganäs O (1999) On-chip microelectrodes for electrochemistry with moveable PPy bilayer actuators as working electrodes. *Sens Actuators B* 56:73–78
- Jager EWH, Inganäs O, Lundström I (2000a) Microrobots for micrometer-size objects in aqueous media: potential tools for single cell manipulation. *Science* 288:2335–2338
- Jager EWH, Smela E, Inganäs O (2000b) Microfabricating conjugated polymer actuators. *Science* 290:1540–1545
- Jager EWH, Inganäs O, Lundström I (2001) Perpendicular actuation with individually controlled polymer microactuators. *Adv Mater* 13:76–79
- Jager EWH, Immerstrand C, Petersson KH, Magnusson K-E, Lundström I, Inganäs O (2002) The cell clinic: closable microvials for single cell studies. *Biomed Microdevices* 4:177–187
- Jager E, Carlsson D, Krogh M, Skoglund M (2007) Electroactive polymer actuator devices and systems comprising such devices. Patent WO2008113372
- Jager EWH, Masurkar N, Nworah NF, Gaihre B, Alici G, Spinks GM (2013) Patterning and electrical interfacing of individually controllable conducting polymer microactuators. *Sens Actuators B* 183:283–289
- Khalidi A, Plesse C, Soyer C, Cattan E, Vidal F, Chevrot C, Teyssié D (2011a) Dry etching process on a conducting interpenetrating polymer network actuator for a flapping fly micro robot. In: ASME 2011 international mechanical engineering congress and exposition, IMECE 2011, vol 2, Denver, pp 755–757
- Khalidi A, Plesse C, Soyer C, Cattan E, Vidal F, Legrand C, Teyssié D (2011b) Conducting interpenetrating polymer network sized to fabricate microactuators. *Appl Phys Lett* 98:164101
- Krogh M, Jager E (2005) Medical devices and methods for their fabrication and use. Patent WO2007057132
- Krogh M, Inganäs O, Jager E (2001) Fibre-reinforced microactuator. Patent WO03039859
- Lee AP, Hong KC, Trevino J, Northrop MA (1994) Thin film conductive polymer for microactuator and micromuscle applications. In: Dynamic and systems and control session, international mechanical engineering congress, vol DSC-2. ASME Publications, Chicago, pp 725–732
- Lee KKC, Munce NR, Shoa T, Charron LG, Wright GA, Madden JD, Yang VXD (2009) Fabrication and characterization of laser-micromachined polypyrrole-based artificial muscle actuated catheters. *Sens Actuators A* 153:230–236
- Low L-M, Seetharaman S, He K-Q, Madou MJ (2000) Microactuators toward microvalves for responsive controlled drug delivery. *Sens Actuators B* 67:149–160
- Lundin V, Herland A, Berggren M, Jager EWH, Teixeira AI (2011) Control of neural stem cell survival by electroactive polymer substrates. *PLoS One* 6:e18624
- Madden JDW, Vandesteeg NA, Anquetil PA, Madden PGA, Takshi A, Pytel RZ, Lafontaine SR, Wieringa PA, Hunter IW (2004) Artificial muscle technology: physical principles and naval prospects. *IEEE J Ocean Eng* 29:706–728
- Maziz A, Plesse C, Soyer C, Chevrot C, Teyssié D, Cattan E, Vidal F (2014) Demonstrating kHz frequency actuation for conducting polymer microactuators. *Adv Funct Mater* 24:4851–4859
- McGovern S, Alici G, Truong V-T, Spinks G (2009) Finding NEMO (novel electromaterial muscle oscillator): a polypyrrole powered robotic fish with real-time wireless speed and directional control. *Smart Mater Struct* 18:095009
- Naka Y, Fuchiwaki M, Tanaka K (2010) A micropump driven by a polypyrrole-based conducting polymer soft actuator. *Polym Int* 59:352–356
- Okuzaki H (ed) (2012) PEDOT: material properties and device applications. Science & Technology, Tokyo
- Okuzaki H, Funasaka K (2000) Electromechanical properties of a humido-sensitive conducting polymer film. *Macromolecules* 33:8307–8311

- Okuzaki H, Kunugi T (1996) Adsorption-induced bending of polypyrrole films and its application to a chemomechanical rotor. *J Polym Sci Part B Polym Phys* 34:1747–1749
- Okuzaki H, Kunugi T (1997) Adsorption-induced chemomechanical behavior of polypyrrole films. *J Appl Polym Sci* 64:383–388
- Okuzaki H, Kunugi T (1998) Electrically induced contraction of polypyrrole film in ambient air. *J Polym Sci Part B Polym Phys* 36:1591–1594
- Okuzaki H, Kuwabara T, Kunugi T (1997) A polypyrrole motor driven by sorption of water vapor. *Polymer* 38:5491–5492
- Okuzaki H, Kuwabara T, Kunugi T (1998a) Theoretical study of sorption-induced bending of polypyrrole films. *J Polym Sci Part B Polym Phys* 36:2237–2246
- Okuzaki H, Kuwabara T, Kondo T (1998b) Role and effect of dopant ion on sorption-induced motion of polypyrrole films. *J Polym Sci Part B Polym Phys* 36:2635–2642
- Okuzaki H, Saido T, Hara Y, Yan H (2008) A biomorphic organic actuator fabricated by folding a conducting paper. *J Phys Conf Ser* 127:12001
- Okuzaki H, Suzuki H, Ito T (2009) Electromechanical properties of poly(3,4-ethylenedioxythiophene)/poly(4-styrenesulfonate) films. *J Phys Chem B* 113:11378–11383
- Okuzaki H, Hosaka K, Suzuki H, Ito T (2010) Effect of temperature on humido-sensitive conducting polymer actuators. *Sens Actuators A* 157:96–99
- Okuzaki H, Hosaka K, Suzuki H, Ito T (2013a) Humido-sensitive conducting polymer films and applications to linear actuators. *Rect Funct Polym* 73:986–992
- Okuzaki H, Kuwabara T, Funasaka K, Saido T (2013b) Humidity-sensitive polypyrrole films for electro-active polymer actuators. *Adv Funct Mater* 23:4400–4407
- Pettersson F, Jager EWH, Inganäs O (2000) Surface micromachined polymer actuators as valves in PDMS microfluidic system. In: Dittmar A, Beebe D (eds) IEEE-EMBS special topic conference on microtechnologies in medicine and biology, Lyon, 12–14 Oct 2000, pp 334–335
- Plesse C, Vidal F, Teyssié D, Chevrot C (2010) Conducting polymer artificial muscle fibres: toward an open air linear actuation. *Chem Commun* 46:2910–2912
- Prakash SB, Urdaneta M, Christophersen M, Smela E, Abshire P (2008) In situ electrochemical control of electroactive polymer films on a CMOS chip. *Sens Actuators B* 129:699–704
- Ruhparwar A, Piontek P, Ungerer M et al (2014) Electrically contractile polymers augment right ventricular output in the heart. *Artif Organs*. doi:10.1111/aor.12300 (in press)
- Schmidt CE, Shastri VR, Vacanti JP, Langer R (1997) Stimulation of neurite outgrowth using an electrically conducting polymer. *Proc Natl Acad Sci U S A* 94:8948–8953
- Sfakiotakis M, Lane DM, Davies JBC (1999) Review of fish swimming modes for aquatic locomotion. *IEEE J Ocean Eng* 24:237–252
- Smela E (1999) A microfabricated movable electrochromic “pixel” based on polypyrrole. *Adv Mater* 11:1343–1345
- Smela E, Inganäs O, Pei Q, Lundström I (1993) Electrochemical muscles: micromachining fingers and corkscrews. *Adv Mater* 5:630–632
- Smela E, Inganäs O, Lundström I (1995) Controlled folding of micrometer-size structures. *Science* 268:1735–1738
- Smela E, Kallenbach M, Holdenried J (1999) Electrochemically driven polypyrrole bilayers for moving and positioning bulk micromachined silicon plates. *J Microelectromech Syst* 8:373–383
- Svennersten K, Berggren M, Richter-Dahlfors A, Jager EWH (2011) Mechanical stimulation of epithelial cells using polypyrrole microactuators. *Lab Chip* 11:3287–3293
- Urdaneta M, Liu Y, Christopherson M, Prakash S, Abshire P, Smela E (2005) Integrating conjugated polymer microactuators with CMOS sensing circuitry for studying living cells. In: *Smart structures and materials; electroactive polymer actuators and devices (EAPAD)*, vol 5759, San Diego, pp 232–240
- Vidal F, Plesse C, Palaprat G, Kheddar A, Citerin J, Teyssié D, Chevrot C (2006) Conducting IPN actuators: from polymer chemistry to actuator with linear actuation. *Synth Met* 156:1299–1304
- Wang X, Berggren M, Inganäs O (2008) Dynamic control of surface energy and topography of microstructured conducting polymer films. *Langmuir* 24:5942–5948

- Wilson SA, Jourdain RPJ, Zhang Q et al (2007) New materials for micro-scale sensors and actuators an engineering review. *Mater Sci Eng R Rep* 56:1–129
- Wong JY, Langer R, Ingber DE (1994) Electrically conducting polymers can noninvasively control the shape and growth of mammalian cells. *Proc Natl Acad Sci U S A* 91:3201–3204
- Wu Y, Zhou D, Spinks GM, Innis PC, Megill WM, Wallace GG (2005) TITAN: a conducting polymer based microfluidic pump. *Smart Mater Struct* 14:1511
- Xu H, Wang C, Wang C, Zoval J, Madou M (2006) Polymer actuator valves toward controlled drug delivery application. *Biosens Bioelectron* 21:2094–2099
- Yamada K, Kume Y, Tabe H (1998) A solid-state electrochemical device using poly(pyrrole) as micro-actuator. *Jpn J Appl Phys* 37:5798–5799
- Zheng W, Alici G, Clingan PR, Munro BJ, Spinks GM, Steele JR, Wallace GG (2013) Polypyrrole stretchable actuators. *J Polym Sci Part B Polym Phys* 51:57–63
- Zhou JWL, Chan H-Y, To TKH, Lai KWC, Li WJ (2004) Polymer MEMS actuators for underwater micromanipulation. *IEEE/ASME Trans Mechatron* 9:334–342

Conducting Polymers as EAPs: How to Start Experimenting with Them

17

José G. Martinez, Cedric Plesse, Frederic Vidal, and Wen Zheng

Contents

1	Introduction	414
2	Bilayer and Trilayer Actuators Operating in a Liquid Electrolyte	416
2.1	Bilayer and Trilayer Actuators Fabrication	416
2.2	Characterizations of Bilayer and Trilayer Actuators Operating in a Liquid Electrolyte	420
3	Trilayer Actuators Operating in Open Air	422
3.1	Fabrication Based on PVDF Membrane	422
3.2	Fabrication Based on Conducting IPNs	424
3.3	Electrochemical and Mechanical Characterizations of Air-Operating Devices	428
4	Conclusion	434
	References	434

Abstract

The goal of this chapter is to give initial practical information on experimentation with conducting polymer based actuators. The chapter is dedicated to all kind of audience, from confirmed researchers starting in the field of EAPs to teachers wanting to propose practical works on such materials. It will focus on bi(tri)layer bending actuators operating in liquid electrolyte and on two kinds of trilayer

J.G. Martinez

Center for Electrochemistry and Intelligent Materials (CEMI), Universidad Politécnica de Cartagena, Cartagena, Spain

e-mail: jgabriel.martinez@upct.es

C. Plesse • F. Vidal (✉)

Université de Cergy-Pontoise, Cergy-Pontoise cedex, France

e-mail: Cedric.plesse@u-cergy.fr; frederic.vidal@u-cergy.fr

W. Zheng

School of Mechanical Engineering, Shanghai Jiao Tong University, Shanghai, China

e-mail: zhengwen@sjtu.edu.cn

bending devices able to operate in open-air. Experimental details will be provided on how to fabricate each of them step by step giving examples. Electrical and electromechanical characterizations will be also described from basic measurements to some more complicated concepts.

Keywords

Bilayer and trilayer actuators • Characterizations of • Electrochemical cell • Experimental procedure • Materials • Conducting polymers (CPs) • Liquid electrolyte • Open air • Cyclic voltammetry • Dibutyltin dilaurate • Electronic conducting polymers (ECPs) • Interpenetrating polymer network (IPN) • Poly(3,4-ethylenedioxythiophene) (PEDOT) • Polypyrrole (PPY) • Actuation mechanism of • Electrogeneration of • Electropolymerization of pyrrole monomer • Oxidation and reduction reaction of • Polyvinylidene fluoride (PVDF) • Solid polymer electrolyte (SPE) membrane • Force characterizations • IPNs • Load curves and metrics • PVDF membrane • Strain characterizations

1 Introduction

Electronic Conducting Polymers (ECPs) as polypyrrole (PPY) or poly(3,4-ethylenedioxythiophene) (PEDOT) are chemically reactive polymers. In particular when they are oxidized or reduced, the electrochemical reaction promotes reversible volume changes in the ECPs. Indeed during the redox reactions in electrolytic solution electrons are extracted from (or injected to) the polymer chains and ions and solvent are exchanged with the electrolyte to keep charge and osmotic balance inside the ECP film (Fig. 1). This ion expulsion/inclusion motions during redox processes is believed to be the main factor which is responsible of the dimensional changes (Smela 2003; De Paoli 1997; Baughman 1996; Shimoda and Smela 1998; Smela and Gadegaard 1999; Otero and Cortés 2003; Otero 2013).

The volume variation during the redox process can be used to get out of plane movement by designing actuators with a bilayer configuration. Bilayer actuators are laminates of ECP and passive or “non-volume changing” thin film i.e., a tape, in which the relative expansion or contraction, under electrochemical control, of the conducting polymer film with respect to the second layer leads to the bending of the device (Fig. 2a). Trilayer actuators (Fig. 2b) can be also fabricated, comprising an electrochemically passive layer sandwiched by two ECP layers. Both conducting layers are connected to the electrical generator. When applying a potential, one layer will contract whereas the second ECP layer will expand leading to a larger bending

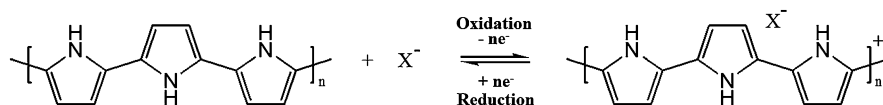


Fig. 1 The oxidation and reduction reaction of polypyrrole

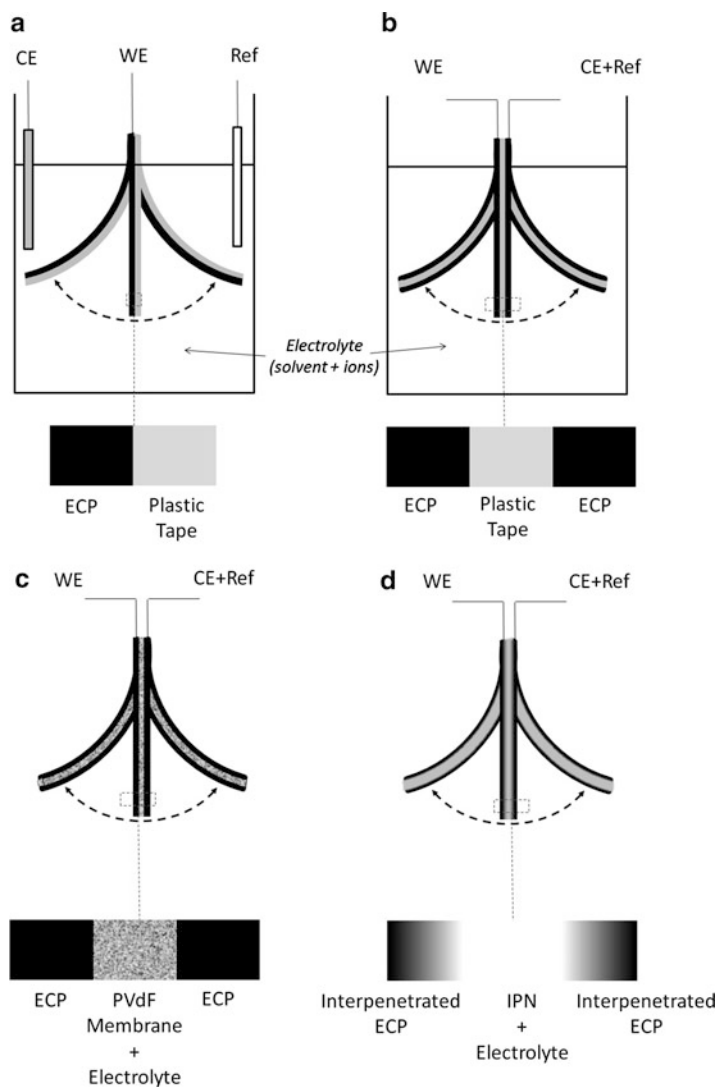


Fig. 2 Schematic structure of bending actuators. (a) bilayer and (b) trilayer actuators operating in liquid electrolyte. (c) trilayer and (d) pseudo-trilayer actuators containing their own electrolyte and operating in open-air. *WE* working electrode, *CE* counter-electrode. *Ref.* reference electrode. *ECP* electronic conducting polymer, *PVDF* Polyvinylidene fluoride. *IPN* interpenetrating polymer network

movement. The described trilayer actuators (Fig. 2b) operate only within liquid electrolytes that provide the ionic species necessary for the redox reaction. However such devices can operate in open air if the passive layer is designed as an ion reservoir membrane. The ion reservoir can be either a porous PVDF membrane

filled by the electrolytic solution (Fig. 2c) or a polymer membrane based on a complex macromolecular architecture as an interpenetrating polymer network (IPN) swollen by the electrolyte solution (Fig. 2d).

In this chapter the full description of the four kinds of actuators synthesis and characterization is given. The two first actuators should be operated in an electrolytic medium (Fig. 2a, b) whereas the two last described devices can be operated in open air (Fig. 2c, d). To allow quick starting experiments with such devices we focus only on synthetic ways which can be easily carried out either in an electrochemistry lab or in a chemistry lab. The synthesis of the three first multi-layered actuators can be done in electrochemistry labs since their fabrication does not require any organic/polymer synthesis but only commercial membranes, pyrrole monomers and potentiostats for the electropolymerization step. The actuator based on IPN macromolecular architecture can be fabricated in a standard polymer laboratory since the conducting polymer and the ion reservoir membrane are synthesized chemically. Beyond the synthesis description, it is also mentioned in this chapter the characterization methods that are absolutely essential which can be easily implemented. The electrical, strain and forces responses versus electrical stimulation can thus be determined which allow comparing the actuator performances. It is noteworthy to mention here that ECP actuators only require small voltage input, mostly in the range of 1–2 V. High stimulation voltage will cause over oxidation and damage the conducting polymer. All those actuators can be activated via a potentiostat in a two or three electrodes cell configuration or via a simple DC generator.

2 Bilayer and Trilayer Actuators Operating in a Liquid Electrolyte

2.1 Bilayer and Trilayer Actuators Fabrication

In this section, we will focus on bilayers conducting polymer/commercial (office) tape. Similar procedures can be followed for the fabrication of the rest of bilayers, only adding the process of fabrication of the passive layer and modifying the attachment procedure (Otero et al. 1992; Pei and Inganas 1992). Passive layers as a thin layer of sputtered metal (Smela et al. 1993; Jager et al. 2000a, b), a piece of paper (Deshpande et al. 2005a, b), a plastic (Higgins et al. 2003) or a solid electrolyte (Baughman 1996; Alici et al. 2011) can be used. The process of fabrication of conducting polymer/commercial (office) tape bilayer artificial muscle consists of the following different steps.

2.1.1 Materials

Many different materials can be used to build bilayer artificial muscles. Here, for simplicity, we will focus on doped polypyrrole electrogenerated and characterized in presence of LiClO_4 /commercial (office) tape bilayer artificial muscles. For that, pyrrole (Fluka) was purified by distillation under vacuum using a diaphragm vacuum pump MZ 2C SCHOTT and stored under nitrogen atmosphere at $-10\text{ }^\circ\text{C}$.

Anhydrous lithium perchlorate salt (Fluka) and acetonitrile (Panreac, HPLC grade) were used as received. Ultrapure water was attained from a Millipore Milli-Q equipment. Office tape (Marco[®]) and Nail Paint (MaxFactor[®]) were used as received.

2.1.2 Experimental Procedure

An easy and reproducible way to obtain polypyrrole films it is through electrogeneration (Fig. 3).

1. Electrogeneration of PPy can be carried out from 0.2 M pyrrole and 0.1 M LiClO₄ acetonitrile solution including 2 % of water content in order to avoid parallel chemical polymerization (Otero and Rodriguez 1993). The working electrode was an AISI 304 stainless steel plate (the low adherence of the generated polymer allows to remove quite thin films from it to get self-supported electrodes or films for the construction of different devices) having 4 cm² of surface area. As counter electrodes two similar stainless steel electrodes were used, one by side of the working electrode and at the same distance (0.5 cm) in order to get a uniform electric field. A Metrohm Ag/AgCl (3 M KCl) electrode was used as reference electrode. The electrogeneration was performed by consecutive square potential waves between -0.322 V (kept for 2 s) and 0.872 V (kept for 8 s) in order to control the film morphology and adherence. The overall polymerization charge (anodic minus cathodic charges) was 28 °C (Otero et al. 1992).
2. The PPy film is carefully removed from the metallic background electrode cutting the borders (Fig. 4b, c) to get the free-standing conducting polymer film (Fig. 4d).
3. To cut a suitable piece from the self-supported conducting polymer film, with the desired dimensions (Fig. 4e, f) and characterize it (obtaining its mass, dimensions. . .).
4. To attach the free standing polymer film to any commercial (office) tape ensuring proper adhesion (Fig. 4g) and to apply mechanical pressure with a rounded surface during enough time and with proper mechanical pressure to ensure the proper attachment (Fig. 4h).
5. To cut the borders of the tape (Fig. 4i) and to remove non-attached parts (Fig. 4j) getting a bilayer artificial muscle (Fig. 4k).
6. To ensure the electrical contact between the bilayer artificial muscle and the current generator. This can be done, for example, employing a metallic clamp (Fig. 4l).
7. To paint the bilayer artificial muscle close to the electrical contact to avoid the electrolyte ascension through capillarity to the metallic clamp (Fig. 4m). Let the

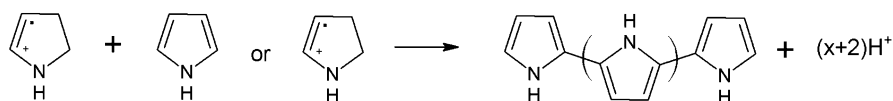


Fig. 3 Polymerization of pyrrole monomer resulting in polypyrrole

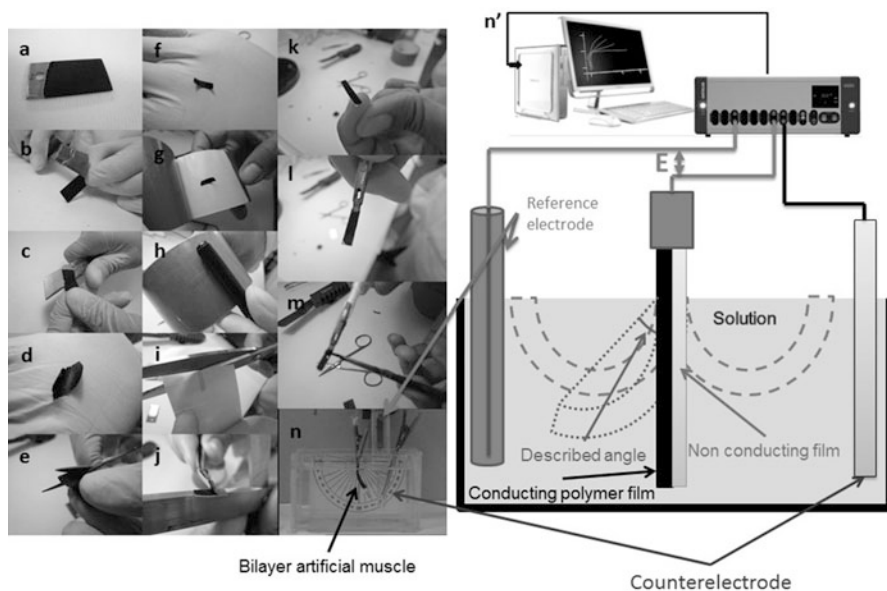


Fig. 4 Fabricating a bilayer artificial muscle: **(a)** Electrogenerated conducting polymer film; **(b)** Cutting the borders; **(c)** Removing the conducting polymer film from the metallic electrode used during the electrogeneration; **(d)** Free-standing conducting polymer film; **(e)** Cutting a smaller sample; **(f)** Small free-standing conducting polymer film ready to fabricate the bilayer; **(g)** Attaching the free-standing polymer film to the conventional tape; **(h)** Mechanical pressure over the bilayer to ensure the proper attachment; **(i)** Cutting the borders of the tape; **(j)** Removing the isolating parts no attached to the bilayer; **(k)** Bilayer artificial muscle; **(l)** Ensuring the electrical contact with a metallic clamp; **(m)** Painting the bilayer artificial muscle with paint to fill the pores and avoid the electrolyte contact with the metallic clamp by capillarity; **(n)** Electrochemical cell used during bilayer artificial muscle actuation. **(n')** scheme of the connections of the electrochemical cell

paint dry. Such paint should be insoluble in the solvent it is going to be used and with a proper viscosity so it is able to penetrate into the pores of the conducting polymer film. In the example nail paint soluble in acetone was used.

8. To set the electrochemical cell for the experiments (Fig. 4n, n'), including a reference electrode to set a reference for the potential and a counter electrode to close the electrical circuit. In the electrochemical cell, it is possible to use any kind of electrolyte: almost any kind of salt (LiClO_4 , for example, in a high enough concentration (>0.01 M) to avoid limitations induced by the impedance of the electrolyte or the diffusion of counterions from the bulk solution to the polymer surface) allowing the exchange of counterions in water (other solvents may dissolve the commercial tape or not ensure the proper attachment between the layers). Potential and current limits depend on the conducting polymer used. For polypyrrole actuators the potential range can be quite large: From -2.5 to 1.0 V versus Ag/AgCl (Otero et al. 2013; Otero and Martinez 2014)

When bilayers are used, a counter-electrode is required to close the electrical circuit allowing the current flow (Fig. 4n'). A big amount of energy is wasted on such counter-electrode, where parallel electrochemical reactions such as solvent dissociation occur, resulting in most of the cases in pH variations and new chemicals able to migrate through the solution and interfering with the actuator, even influencing its degradation (Arias-Pardilla et al. 2012).

2.1.3 Additional Experiments

In order to avoid the counter-electrode and its inconveniences, trilayer structures were proposed. The process of fabrication it is the same than for the bilayer. The only difference is that a two sided sticky polymeric tape (any commercial one is valid when water is used as solvent) is needed in order to stick the free-standing polymer film in the two sides of the tape (Fig. 5; Otero and Cortes 2000; Han and Shi 2004; Alici and Huynh 2006; John et al. 2008; Yao et al. 2008; Zainudeen et al. 2008; García-Córdova et al. 2011). The same current is used to promote opposite bending movements in each of the conducting polymer films. One of the films acts as anode, swelling (or shrinking, it depends on the prevalent ionic exchange (Fuchiwaki and Otero 2014; Otero and Martinez 2014)) during oxidation and the other acts as cathode, shrinking (or swelling) during reduction when the same current is passed through each of the conducting polymer films trailing the bilayer in the same

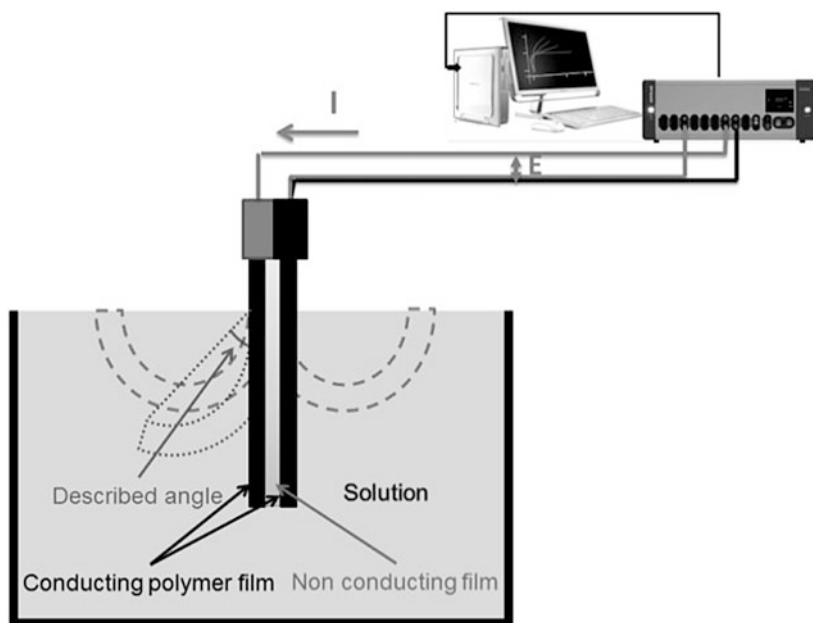


Fig. 5 Electrochemical cell employed to study a trilayer conducting polymer/non-conducting polymer/conducting polymer artificial muscle

direction. When the current direction is changed the film swelling shrinks and the film shrinking swells, moving in the opposite direction.

2.2 Characterizations of Bilayer and Trilayer Actuators Operating in a Liquid Electrolyte

For both, bilayer and trilayer devices, the experimental setup is quite similar (Figs. 3 and 4). The actuator is immersed in a liquid electrolyte, ensuring proper electrical conductivity (a metallic clamp can be used for example, as mentioned before). In the case of the bilayer device, a reference electrode and a counter-electrode are needed. These electrodes need to have proper connections too. Each of the electrodes are directly connected to the proper inputs of a potentiostat-galvanostat, able to apply and measure simultaneously current and potential waves. Applied waves are controlled by a computer. The measured signals are also recorded. For the three-layer device, the reference electrode and counter-electrode inputs of the potentiostat are shortcut and connected directly to the second active layer of conducting polymer. The connections of the two different conducting polymer layers must be independent, ensuring proper isolation between them.

2.2.1 Initial Experiments

Once the setup is ready, it is possible to start moving the actuator. For that, some initial experiments are required in order to know its basic characteristics, as the potential range, the maximum charge that can be applied and the sense and amplitude of the movement. One of the most used electrochemical techniques allowing detecting such basic characteristics is cyclic voltammetry. This technique consists on applying a potential sweep between a cathodic potential limit (most negative potential set for the experiment) and an anodic potential limit (most positive potential set for the experiment) varying the potential at a constant rate. Once a potential limit is achieved, the potential sweep goes on in the opposite way to the other potential limit at the same rate (symmetrical triangular potential wave), Fig. 6a. This is repeated as many times as necessary, usually to achieve a stationary response. During the potential sweep, the current flowing at any time is recorded (Fig. 6b) and usually presented as a function of the applied potential. Both, anodic (from the cathodic potential limit to the anodic one) and cathodic (from the anodic potential limit to the cathodic one) sweeps are usually presented over the same potential axes giving, in many cases-when the study is in the steady state- a closed loop (Fig. 6c).

Cyclic voltammetry allows characterizing the electrochemical properties of the actuator. From the consumed charge during cyclic voltammetry it is possible to detect parallel reactions occurring in the material not promoting actuation and possibly influencing the degradation of the actuator (Martinez et al. 2014). As far as such parallel reactions are not present, the potential range can be enlarged with the subsequent increment of the consumed charge and actuation (Otero and Martinez 2014). If the cell containing the electrolyte is transparent (plastic or glass), the movement can be video recorded while the electrochemical experiments are

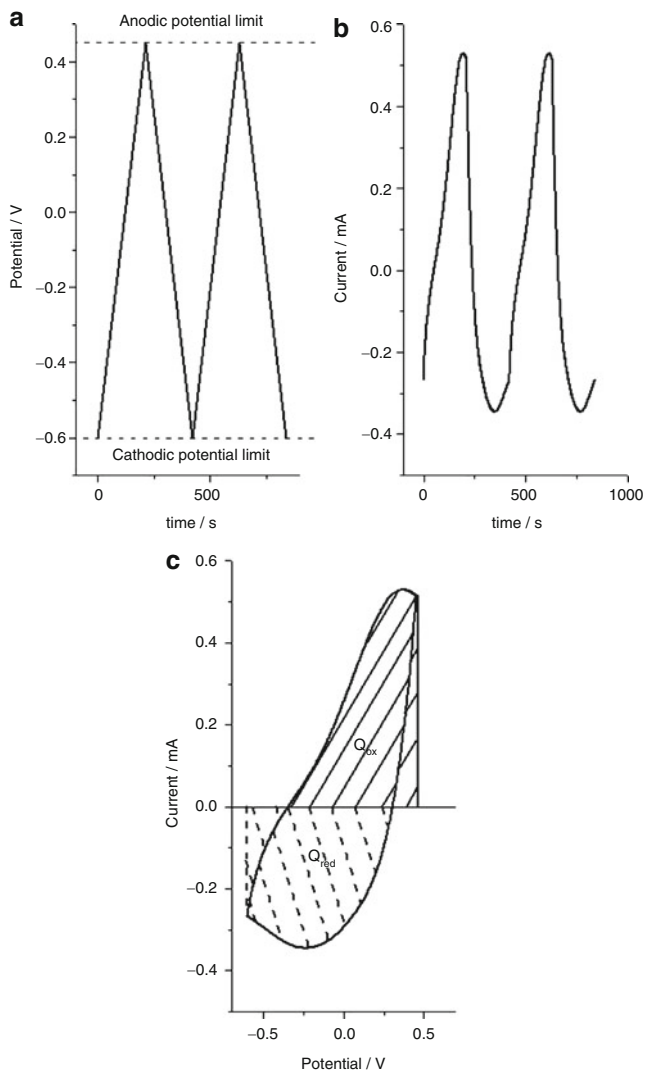


Fig. 6 Cyclic voltammetry. (a) Symmetrical triangular potential wave applied to the working electrode. (b) Measured current when the potential wave in (a) is applied. (c) Cyclic voltammogram

performed, so the rate of the movement, the amplitude of the movement and the relationship with the consumed charge or the applied potential can be attained. So far, linear relationships have been attained between the measured angle variation of the bilayer end and the consumed charge. Up to 14° can be moved when 1 mC of charge is applied ($\text{angle}^\circ = 14 \cdot \text{charge (mC)}$) (Otero and Martinez 2012). From the curvature of the movement it is possible to get very useful variables as stress and

strain (Verdu et al. 2005). Also, it is possible to use a universal test frame machine (Otero and Martinez 2014).

3 Trilayer Actuators Operating in Open Air

3.1 Fabrication Based on PVDF Membrane

A classical bending actuator usually consists of five layers. The middle layer plays as insulator and acts as an ion reservoir. The conductor layer, usually metals, was coated on both sides. Finally, electronic conducting polymers (ECPs), which provide actuation, were deposited onto metal layer chemically or electrochemically (Fig. 7a).

When applying a positive potential, electrons will flow out from ECPs, in order to keep charge neutrality, anions are incorporated into polymer matrix which will cause expansion. When applying a negative potential, the reverse process will happen and cause shrinkage. A multi-layer bending actuator is based on such mechanism (Fig. 7b). In most cases, the middle layer is porous polymer. There are two main reasons for that: firstly, such a porous structure will allow ions and solvent travel between two active layers during actuation. Secondly, the porous structure will hold electrolyte and allow such multi-layers structure operated in the air for a certain time of period.

3.1.1 Materials

AR grade of Propylene carbonate (from Aldrich), lithium trifluoromethanesulfonimide (from 3 M), tetrabutylammonium hexafluorophosphate (from Sigma), anhydrous iron III chloride (Acros) were used as received. Pyrrole (from Merck, also AR grade) and 3,4-ethylenedioxythiophene (H C Starck) were distilled and stored under Nitrogen environment at $-20\text{ }^{\circ}\text{C}$ before using. Polyvinylidene fluoride (ImmobilisonTM, Millipore) membrane of $0.45\text{ }\mu\text{m}$ pore size, 75 % of porosity and $110\text{ }\mu\text{m}$ thickness was chosen as middle layer of bending actuators. 40 nm thick of gold/platinum was sputtering coated on both side before using.

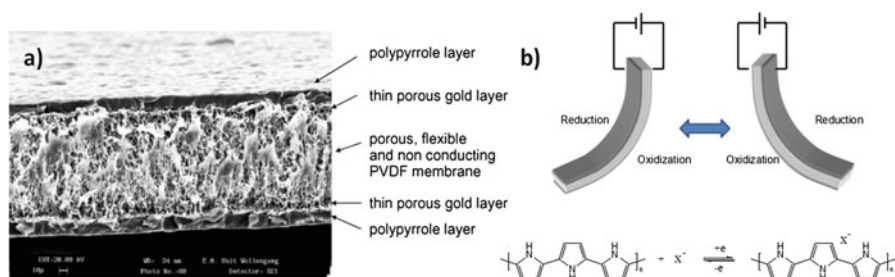


Fig. 7 (a) A typical multi-layer actuators based on PVDF membranes (Wu et al. 2006). (b) Illustration of the actuation mechanism of multi-layer polypyrrole actuator. *Up*: bending upon application of a voltage. *Down*: the oxidation and reduction reaction of PPy

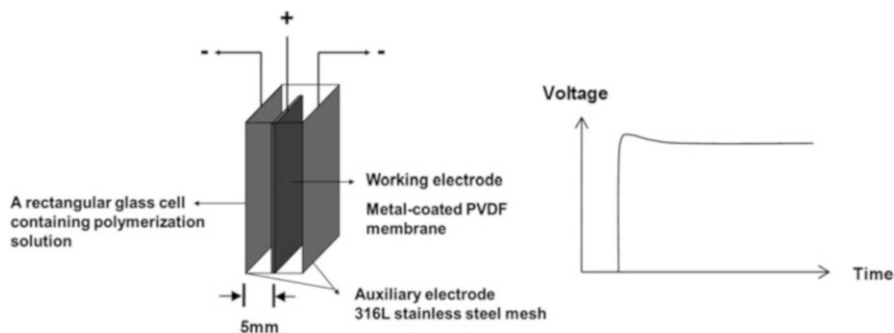


Fig. 8 A typical two electrode deposition cell (*left*) and voltage response (*right*) under constant current during electrochemical deposition. When set up polymerization cell, ideally working electrode is parallel to counter electrode, and the distance between those electrodes is in the range of 5 mm

3.1.2 Experimental Procedure

1. A common polymer middle layer is polyvinylidene fluoride (PVDF) with 0.1~0.45 μm pore size. Metals, normally gold or platinum, are sputtering coated with a thickness of 40 nm.
2. Conducting polymers such as polypyrrole is electrochemically deposited from electrolyte. Typically, 0.05~0.1 M lithium trifluoromethanesulfonimide (Li.TFSI) or tetrabutylammonium hexafluorophosphate (TBA.PF₆) and 0.06 M Pyrrole are dissolved into propylene carbonate (PC), 0.5 % (by whole electrolyte weight) of de-ionized water was added in and whole electrolyte purged with nitrogen for 10~20 min before use. The electrochemical polymerization of pyrrole is taken under $-25\text{ }^{\circ}\text{C}$ to $-28\text{ }^{\circ}\text{C}$ for 8~10 h under 0.1 mA/cm² by using a two electrode cell (Fig. 8).
3. After polymerization, whole pieces of actuators are rinsed by 0.1MLiTFSI/PC electrolyte to remove the remaining pyrrole monomer.
4. Actuator samples are usually stored in 0.1 M LiTFSI/PC solution. Before using, wipe dry using filter paper.

3.1.3 Alternative Experiments

Based on such multilayer structures, several works have been done to each layer to (a) removing the metal layer; (b) improving tip actuation performance; (c) extending cycle life (Temmer et al. 2013; Gaihre et al. 2011; Naficy et al. 2013). Recently, a novel way has been developed by Temmer and his colleagues for the fabricating PVDF based tri-layer actuators. The idea is that metal layer can be replaced by poly (3,4-ethylenedioxythiophene) (PEDOT), a classic conducting polymer but with high conductivity, high porosity and also be able to provide actuation. PEDOT was chemically synthesised on both side of PVDF membrane and then PPy was electrochemically deposited afterwards. As PEDOT is quite porous, PEDOT interlock to both PPy and PVDF, which form composites and avoid delamination.

The fabrication of PEDOT coated PVDF could be done as follows:

1. Permeating PVDF with EDOT monomer, tap drying with filtration paper to remove extra monomers.
2. Immersing saturated PVDF into oxidant agent. 60 °C of 1.5 M anhydrous FeCl₃ aqueous solution e.g.,
3. After certain time, 2 min for instance, the whole piece of PVDF will turned dark;
4. Rinse whole piece of membrane repeatedly with methanol to remove residual monomers.
5. Dry the whole piece in oven for 1 h under 40 °C.

After receiving PEDOT coated PVDF, PPy could be then deposited electrochemically on both sides as procedures described before.

PVDF layer is also very critical to actuation performance. A typical Phase-inversion process can be adopted to home-made PVDF as desired thickness and pore size (Gaihre et al. 2011). Improvement on ion transfer and reducing the mechanical resistance of PVDF layer will benefit the actuation performance.

As mentioned, such multilayer actuators can only operate few hours in the air or few minutes in fresh water due to the electrolyte evaporating or dissolving. An attempt to increase cycle life in air is using electrolyte with high boiling point and non-water soluble electrolyte, such as ionic liquid. Alternately, a convenient way to achieve longer operation life time is encapsulating whole piece of actuator. Usually apply that encapsulating/coatings while actuators still hold certain amount of electrolyte. General rules of selecting encapsulating agents are: (1) Coating material and carrying agent can not react with electrolyte and any layer of actuators; (2) Coating must prohibit electrolyte from evaporation or any leaking, be capable to provide thin, dense and porous-free layers to reduce actuation resistance; (3) encapsulating materials are flexible enough and should not jeopardize the actuation performance too much. Poly (styrene-*b*-isobutylene-*b*-styrene) (SIBS) (Naficy et al. 2013), natural rubber or even nail polish (contains nitrocellulose and butyl acetate) (Spinks 2013) are good candidates to achieve those goals. Approaches of applying encapsulating process can be spray coating, dip coating and brushing painting etc.

3.2 Fabrication Based on Conducting IPNs

Open-air bending actuators can also be obtained as pseudo-trilayer devices where the conducting polymer electrodes are interpenetrated in the both faces of a solid polymer electrolyte (SPE) membrane. Since the electrodes are entangled in the SPE, the resulting material avoids any delamination issue during actuation. If an ionic liquid is used as electrolyte, very high lifetime can be obtained (Vidal et al. 2004). The typical procedure requires (1) to synthesize the SPE membrane first and then (2) to incorporate the conducting polymer electrodes.

The SPE membrane is synthesized with an interpenetrating polymer network (IPN) architecture. IPNs are defined as the combination of two (or more) crosslinked polymer synthesized in the presence of each other (Klempner et al. 1994). If co-continuous morphology is reached a combination of the properties of each

polymer partner can be obtained in the final materials. For actuator application, one network will act as the ionic conducting medium and the second one will insure relevant mechanical properties. Several types of IPN membranes can be easily synthesized (Gauthier et al. 2007; Plesse et al. 2007, 2010; Vidal et al. 2013; Goujon et al. 2011; Festin et al. 2013). In the following, the IPN membrane will be composed of poly(ethyleneoxide) (PEO) network interpenetrated in a polytetrahydrofurane (PTHF) network (Plesse et al. 2011) The first one is obtained by free radical copolymerization of polyethylene glycol methacrylate (PEGM) and dimethacrylate (PEGDM). The second one is obtained by polyaddition between the terminal hydroxyl functions of a linear PTHF with isocyanate function of Desmodur N3300.

3.2.1 Materials

Polytetrahydrofurane (PTHF, Terathane[®] Mw = 2,900 g.mol⁻¹), Methoxy poly(ethylene glycol) methacrylate (PEGM475 Mw = 475 g.mol⁻¹), poly(ethylene glycol) dimethacrylate (PEGDM750, Mw = 750 g.mol⁻¹; PEGDM550, Mw = 550 g.mol⁻¹), dibutyltin dilaurate (DBTDL 95 %), obtained from Aldrich were used without further purification. 3,4-ethylenedioxythiophene (EDOT) (Bayer) was distilled under reduced pressure at 130 °C prior to be used but could be used as received for practical works. Toluene (VWR), methanol (VWR), lithium perchlorate (Aldrich), anhydrous iron III chloride (Acros), and Desmodur[®] N3300 (5.2 10⁻³ mol of NCO for 1 g of Desmodur[®]) (Bayer) were used without further purification. Dicyclohexylperoxidicarbonate (DCPD) (Groupe Arnaud) was used as received.

3.2.2 Experimental Procedure

1. The 50/50 wt% PEO/PTHF is prepared according to the following procedure. In a flask are introduced (Fig. 9):

- PolyTHF 2900 (Terathane 2,900 g.mol⁻¹) : 0.5 g
- Desmodur N3300: 106 mg

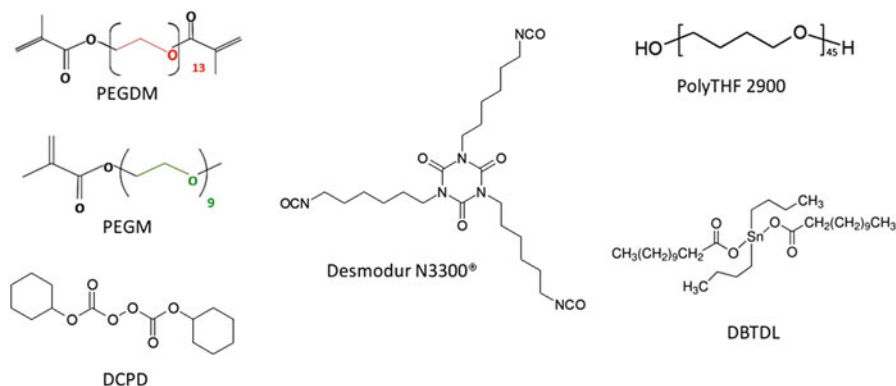


Fig. 9 Chemical structures of reactants used for the synthesis of PEO/PTHF IPN

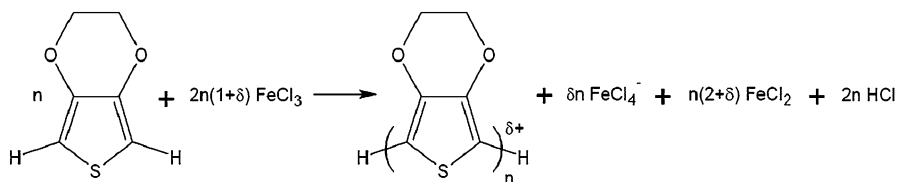


Fig. 10 Chemical oxidative polymerization of EDOT into PEDOT

- Polyethyleneglycol dimethacrylate (PEGDM $750 \text{ g}\cdot\text{mol}^{-1}$): 0.125 g
- Polyethyleneglycol methacrylate (PEGM $475 \text{ g}\cdot\text{mol}^{-1}$): 0.375 g
- Dicyclohexyl Peroxydicarbonate (DCPD): 16 mg
- Toluene: around 1 mL in order to obtain a transparent and homogeneous solution.

The mixture is stirred under inert atmosphere (argon) for 30 min. Dibutyltin dilaurate is then added ($16 \mu\text{L}$, $[\text{DBTDL}]/[\text{OH}] = 0.1$) and the mixture is poured into a mould made of two glass plates ($10 \times 10 \text{ cm}^2$) separated by a $250 \mu\text{m}$ thick Teflon[®] gasket. The mould is then heated at $50 \text{ }^\circ\text{C}$ for 1 h followed by a post-curing step at $80 \text{ }^\circ\text{C}$ for 1 h. The PEO/PTHF IPN is then carefully unmolded, dried under vacuum at $50 \text{ }^\circ\text{C}$.

2. PEO/PTHF IPN are cut into smaller pieces ($2 \times 1 \text{ cm}^2$) with scissors for the following steps. The weighted PEO/PTHF pieces are then dipped in neat EDOT to reach a swelling ratio of 120 %. Typically, swollen samples are removed from the EDOT flask, carefully wiped off and weighted. The swelling ratio is calculated according to the following equation:

$$SR\% = \frac{m(t) - m_0}{m_0} \times 100$$

Where m_0 and $m(t)$ are the weight of the sample before and after swelling.

When the desired swelling ratio is reached, the samples are immersed into FeCl_3 1,5 M/ H_2O solution ($40 \text{ }^\circ\text{C}$, 3 h) for the oxidative polymerization step of EDOT into PEDOT (Fig. 10).

The films are then washed several times with methanol until the yellow colour disappears completely, i.e., excess of FeCl_3 is removed.

3. The edges of the sample are cut off in order to separate the two faces and to avoid short-circuits.
4. After drying (1 h at $50 \text{ }^\circ\text{C}$ under vacuum), the samples are immersed overnight in electrolytic solution (LiClO_4 1 M/Propylene carbonate) or ionic liquid (EMITFSI) for 1 week at least and can now be used as an actuator (Fig. 11). The electrolyte content should rise above 100 % versus the dry sample in order to get high ionic conductivity.

3.2.3 Additional Experiments

The PEO/PTHF IPN polymerization/crosslinking kinetics can be followed by FT-IR spectroscopy with the disappearance of methacrylate and isocyanate vibration bands

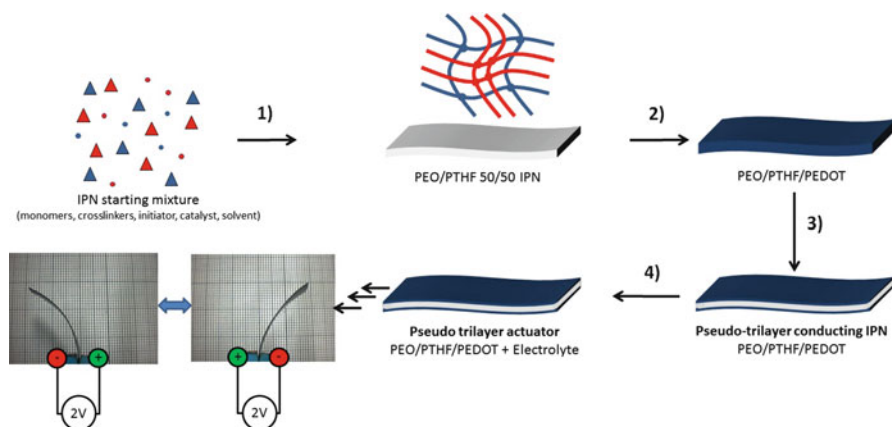


Fig. 11 Elaboration pathway of conducting IPN actuators operating in open-air

according to (Plesse et al. 2007). Since in ionic actuator the response speed is limited by ion diffusion, i.e., ionic conductivity and diffusion distance, it is possible to increase the response speed of the resulting actuators by decreasing the IPN thickness (thinner Teflon gasket). However it becomes necessary to adapt the oxidative polymerization step (step 2) in order to avoid too thick interpenetrated PEDOT electrodes that would result in short-circuits.

In step (3) or (4), a rough estimation of the pseudo-trilayer configuration can be obtained by measuring the electrical resistance along the surface (R_s) and across the thickness (R_e). R_s below 20 Ω and R_e above 1 kohms can be expected for a sample synthesized according to the previous conditions.

Another check of the pseudo-trilayer configuration can be deduced from electrical response of the device under chronoamperometric measurements (Fig. 12). Typically under $\pm \Delta E$ square wave potential stimulation, the device behaves like a supercapacitor that will charge and discharge along with cycles. The sample response follows a time constant $\tau = RC$, with R the ionic resistance through the membrane and C the total capacitance of the sample being equal to the half of the capacitance of each electrode (Randriamahazaka et al. 2005). The current response presents a peak current followed by a decrease of the electron flow since the sample approaches to its charged state. When current reaches zero the redox process is over, i.e., one electrode is fully oxidized and the other one fully reduced. In the case of short-circuits between the two interpenetrated electrodes a leakage current will remain meaning that electrons can go through the thickness of the sample. The amount of the leakage current can be an indicator of the extent of the pseudo-trilayer configuration loss. As mentioned above, if an increase of the actuator speed is desired, samples can be synthesized as thin conducting IPNs. The decrease of the IPN thickness will result in a decrease of R while the decrease of the conducting polymer thickness will result in a decrease of total capacitance C . As a consequence the time constant τ should decrease drastically leading to fast electrical response.

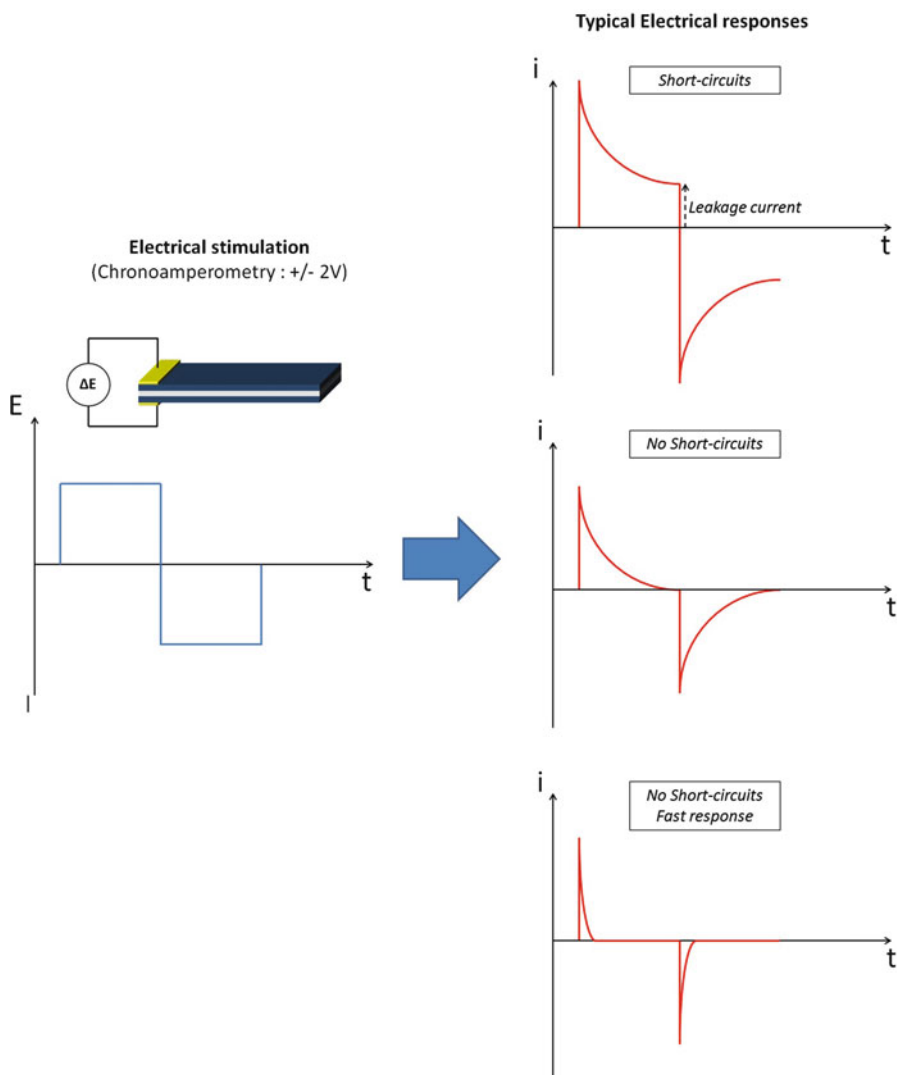


Fig. 12 Typical electrical responses of conducting IPN actuators under two electrode potentiostatic experiments in open-air

3.3 Electrochemical and Mechanical Characterizations of Air-Operating Devices

The electromechanical actuation tests were ideally performed using a potentiostat to control the applied voltage or current and the type of signal (sinusoidal, triangle and square wave). As for trilayer devices operating in electrolyte medium, the working electrode input of the potentiostat is connected to one electrode of the actuator while

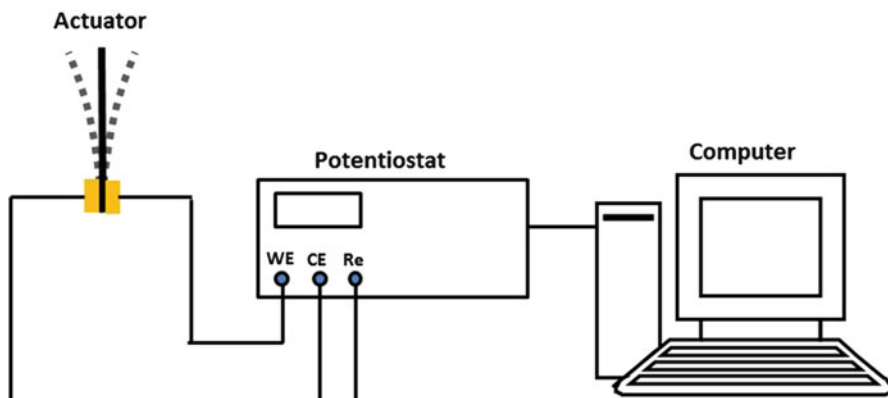


Fig. 13 Schematic diagram of experiment set-up for actuator tested in air. Different potential steps like step, sinusoidal wave or triangle wave could be applied to drive actuation

the reference electrode and counter electrode inputs are shortcut and connected directly to second active layer. The connections of the two different conducting polymer electrodes must be independent, ensuring proper isolation between them (Fig. 13). Usually the applied potential is in the range of -2 to 2 V. High voltage will damage the conducting polymer layers. The two limit parameters that used to be measured for bending actuators are the free strain and the blocking force.

3.3.1 Strain Characterizations

Measurements of strain data can be done according to several protocols (Fig. 14). The cheapest and simplest one requires graph paper and a video camera. This method allows extracting easily all the data but can be time consuming if strain versus time curves are wanted. Moreover, accuracy of the data may be limited by image resolution and/or frame rate of the camera. The second method requires using a laser displacement sensor. While this setup is more expensive it allows extracting accurate data and getting easily strain evolution as a function of time/voltage.

Free strain characterization of bending actuators is performed under zero load conditions but, unlike linear actuators, measurements are usually not trivial. Several types of data, related to each other, can be recorded at maximum positions or as a function of time: typically from the simplest to the most complicated i.e., displacement $D(t)$, bending angle $\theta(t)$, curvature $\rho(t)$ or curvature radius $r(t)$ and strain difference between the two ECP electrodes $\Delta\varepsilon(t)$. All these metrics can be followed as a function of the consumed charge.

Tip displacement $D(t)$ is usually in the range of mm to cm for cm scale samples. This is the simplest metrics of bending actuators and may allow quick and precise comparison between different actuators if they are presenting exactly the same geometry. Indeed D is an extrinsic data, i.e., it is dependent on device dimensions: a greater L leading to a greater D . In the same way, thicker samples will present lower D when compared to thinner actuators. Bending angle $\theta(t)$ may also provide

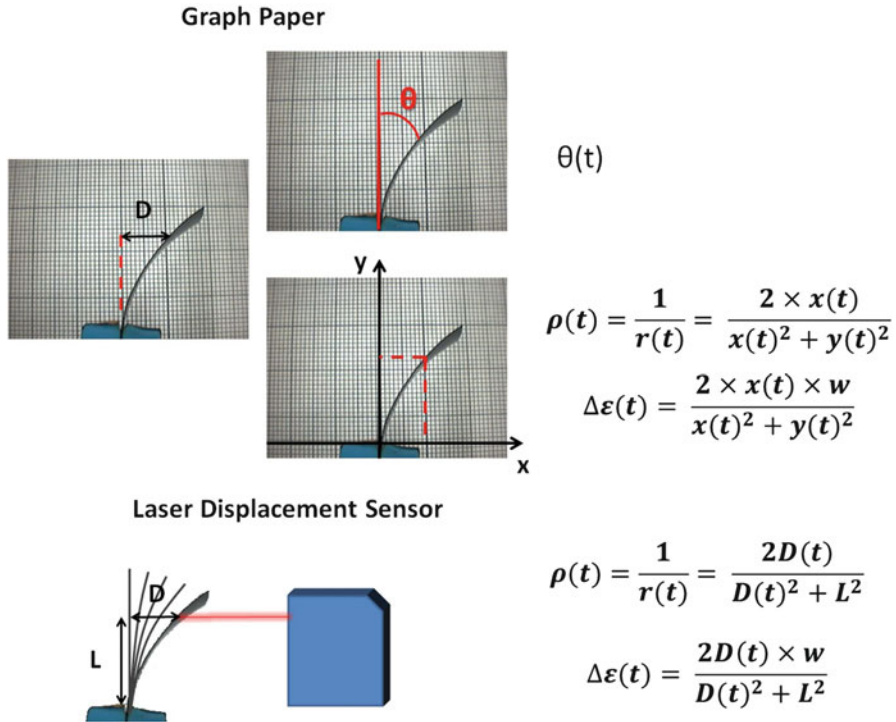


Fig. 14 Typical protocols to extract data on strain. *w*: thickness of the actuator

good estimation of actuator performance but may be also dependent of the actuator length.

Another classical way to describe material bending is the curvature ρ or the curvature radius r , being the inverse of the first one. It can be used to quantify more precisely the circular arc described by the bending actuator. The higher is the curvature (the smaller is the curvature radius), the greater is the strain performance of the actuator. It can be calculated using either the graph paper or the laser displacement sensor. The main difference between the two methods is that the graph paper one will follow a precise point and *x* et *y* coordinates are both varying as a function of time. Using the laser displacement sensor the *y* coordinate is not changing since the laser remains at a constant distance *L* of the clamped beam and is measuring *D(t)*. The numerical values obtained according to these two methods are very close. The limitation of curvature measurement appears if curvature is not constant along the length. This case often appears with conducting polymer actuators due to ohmic drop along the length. Moreover this measurement gives once again only data of the whole device and is dependent of the actuator thickness. For the same intrinsic deformation of the electroactive layer, a thinner actuator will lead to larger curvature of the device.

In order to obtain intrinsic metrics the deformation of the conducting polymer electrodes can be calculated from the previous data. Indeed several equations relate

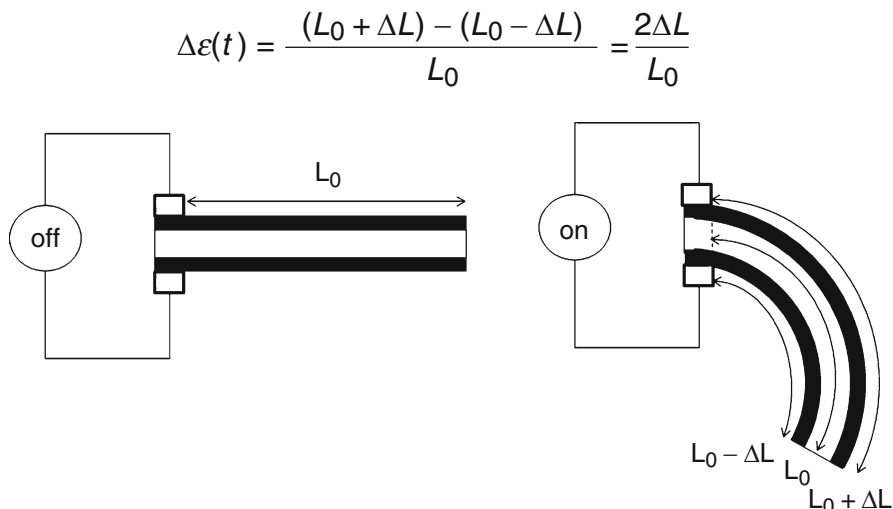


Fig. 15 Schematic representation of the length changes of both electrodes, i.e., the strain difference

the *out-of-plane* displacement of the actuator to the in-plane strain of the electrodes. The strain difference between the two electrodes in the bend state of the actuator can provide direct calculation of the total ECP strain capability which will be independent of the actuator geometry. Starting from an initial length L_0 for each layer, the length of each active layer will be changed during actuation (Fig. 15). One will contract ($L_0 - \Delta L$) while the second one will expand ($L_0 + \Delta L$). In other words, with only one half displacement one can extract the two limit lengths of the electrodes which is nothing else that the ECP total strain, from the reduced to the oxidized state: The intrinsic strain difference can be obtained from the following equation taking into account the displacement $D(t)$ and the actuator length L and thickness w (Sugino et al. 2009):

$$\Delta\varepsilon(t) = \frac{2 \times w \times D(t)}{L^2 + D(t)^2}$$

3.3.2 Remarks

It is worthwhile to point out that, in most cases, increasing input frequencies will result in diminishing of tip displacement. As the migration rate of ions can't catch up switching frequency. However, in a certain range, such increasing of frequencies leads to a sharp-instant increasing of tip movement, which indicates that the actuation process coincident with natural frequencies of multi-layer bending actuators. It is a unique observation in most actuation experiments and has great application potentials (Wu et al. 2006; McGovern et al. 2008, 2009; Plesse et al. 2011; Maziz et al. 2014).

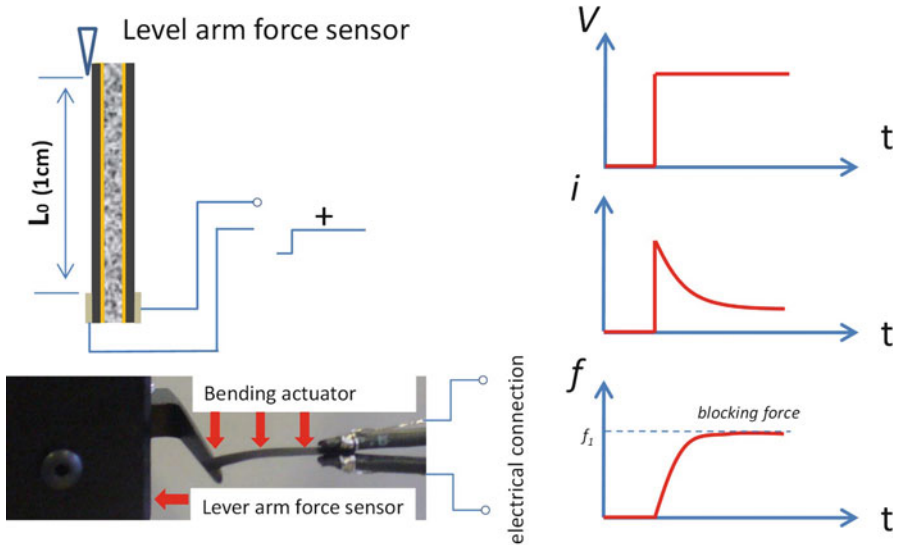


Fig. 16 Typical experiment set up (*left*) for force and electrical responses (*right*) of bending actuators by applying two electrode system in open-air. As indicated, generally a step voltage stimulation is used and the force detecting tip is usually 1 cm offset from electrical connection part

3.3.3 Force Characterizations

Tip force measurement can be done by introducing a dual-mode lever arm system with 50 mN loading cell from Aurora Scientific Inc. (also can be other force detecting instrument). During test, simply place actuator tip against to level arm sensor tip (also illustrated in Fig. 16). Samples are commonly cut into 2 mm wide and 1 cm long. The force output will be recorded by applying a constant voltage. Please note that, the force value gained from such process is “blocking force”. Tracking dynamic force during actuation is quite complex, therefore, using blocking force to compare simply performance among different actuators is recommended.

3.3.4 Remarks

The blocking force for such dimension is usually in the range of mN. However force is not intrinsic for benders since it will depend on the length of the sample. Indeed, the longer is the actuator the lower will be the blocking force. The force moment or torque can then be calculated. It can be obtained by multiplying the measured blocking force by the length of the actuator:

$$\vec{M} = \vec{F} \times \vec{L}$$

This moment is reported in unit of N.m and is measuring the rotational force. It does not depend on the length anymore since shorter or longer benders should produce the same moment, but will still depend on the width of the sample.

3.3.5 Load Curves and Other Metrics

It must be pointed out here that free strain and blocking force are the limit performances of the actuator. In such cases, the output mechanical work is equal to zero. If a measure of the mechanical work must be obtained, load curves can be built. Load curves can be built by reporting the force as a function of the displacement. The intersection with axis is then corresponding to the blocking force (no displacement) and free/max displacement (no force). Intermediate points can be measured by decreasing the initial load of the loading cell. As soon as the preload force is below the blocking force, a displacement of the actuator will be observed. By choosing several preload forces, load curves will be obtained (Fig. 17). The maximum output work (unit: Joule) of an actuator can be determined as the maximum area below the load curve: force (N) multiplied by displacement (m). Dividing this value by the total volume of the sample will provide work density (J/vol). The efficiency (%) of the conversion from electrical energy input E_{in} to mechanical work W_{out} can also be calculated:

$$\text{Conversion Efficiency}(\%) = \frac{W_{out}}{E_{in}} \times 100$$

With $E_{in} = i.V.t$, (i the current, V the applied potential and t the time).

NB: it must be pointed out that the most part of the input energy is stored through the redox process during actuation. By short-circuiting the two electrodes, a large part of the consumed electrical input can then be recovered.

Finally other comparative metrics such as strain rate (%/s) or lifetime can also be determined through adequate experiments or calculations.

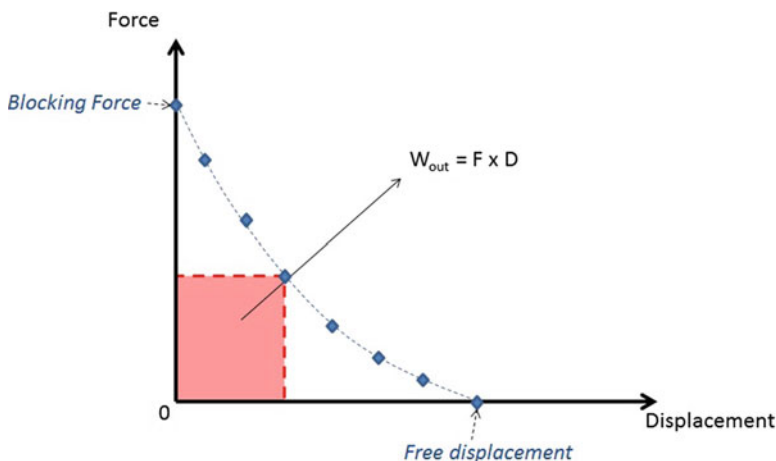


Fig. 17 Load curve of an actuator allowing to obtain output work (J) of the actuator

4 Conclusion

This chapter has been dedicated to all people wanting to make their first step in the field of ionic EAP: researcher, teacher or even students. This chapter tried to gather useful and precise experimental details on how to fabricate and to characterize actuators based on such astonishing materials.

Acknowledgments Authors acknowledge financial support of ESNAM, the European Scientific Network for Artificial Muscles (MP1003).

References

- Alici G, Huynh NN (2006) Predicting force output of trilayer polymer actuators. *Sensors Actuators A Phys* 132(2):616–625, Available at <http://linkinghub.elsevier.com/retrieve/pii/S0924424706001646>. Accessed 23 Jan 2014
- Alici G, Punning A, Shea HR (2011) Enhancement of actuation ability of ionic-type conducting polymer actuators using metal ion implantation. *Sensors Actuators B Chem* 157(1):72–84
- Arias-Pardilla J et al (2012) Biomimetic sensing-actuators based on conducting polymers. In: Motheo A de J (ed) *Fundamentals and applications of conducting polymers*. Intech, Rijeka
- Baughman RH (1996) Conducting polymer artificial muscles. *Synth Met* 78(3):339–353, Available at <http://linkinghub.elsevier.com/retrieve/pii/S1169833011000494>. Accessed 12 Dec 2013
- De Paoli MA (1997) Conductive polymers synthesis and electrical properties. In: Nalwa HS (ed) *Handbook of organic conductive molecules and polymers*, vol 2, *Conductive polymers synthesis and electrical properties*. Wiley, Chichester
- Deshpande SD, Kim J, Yun SR (2005a) New electro-active paper actuator using conducting polypyrrole: actuation behaviour in LiClO_4 acetonitrile solution. *Synth Met* 149(1):53–58, Available at www.files.654/full_record.html
- Deshpande SD, Kim J, Yun SR (2005b) Studies on conducting polymer electroactive paper actuators: effect of humidity and electrode thickness. *Smart Mater Struct* 14(4):876–880
- Festini N et al (2013) Robust solid polymer electrolyte for conducting IPN actuators. *Smart Mater Struct* 22(10):104005, Available at <http://stacks.iop.org/0964-1726/22/i=10/a=104005?key=crossref.47e2a9409c308596ea5b13424f707d23>. Accessed 27 Sept 2013
- Fuchiwaki M, Otero TF (2014) Polypyrrole–para-phenolsulfonic acid/tape artificial muscle as a tool to clarify biomimetic driven reactions and ionic exchanges. *J Mater Chem B* 2(14):1954–1965, Available at <http://pubs.rsc.org/en/content/articlelanding/2014/tb/c3tb21653e>
- Gaihre B et al (2011) Synthesis and performance evaluation of thin film PPy-PVDF multilayer electroactive polymer actuators. *Sensors Actuators A Phys* 165(2):321–328
- García-Córdova F et al (2011) Biomimetic polypyrrole based all three-in-one triple layer sensing actuators exchanging cations. *J Mater Chem* 21(43):17265–17272, Available at <http://pubs.rsc.org/en/content/articlelanding/2011/jm/c1jm13374h>
- Gauthier C et al (2007) Polybutadiene/poly(ethylene oxide) based IPNs, part II: mechanical modelling and LiClO_4 loading as tools for IPN morphology investigation. *Polymer* 48(26):7476–7483, Available at <http://linkinghub.elsevier.com/retrieve/pii/S0032386107010105>. Accessed 22 Feb 2013
- Goujon LJ et al (2011) Flexible solid polymer electrolytes based on nitrile butadiene rubber/poly(ethylene oxide) interpenetrating polymer networks containing either LiTFSI or EMITFSI. *Macromolecules* 44(24):9683–9691, Available at <http://pubs.acs.org/doi/abs/10.1021/ma201662h>. Accessed 22 Feb 2013

- Han GY, Shi GQ (2004) High-response tri-layer electrochemical actuators based on conducting polymer films. *J Electroanal Chem* 569(2):169–174
- Higgins SJ et al (2003) Grafting and electrochemical characterisation of poly-(3,4-ethylenedioxythiophene) films, on nafion and on radiation-grafted polystyrenesulfonate-polyvinylidene fluoride composite surfaces. *J Mater Chem* 13(10):2485–2489
- Jager EWH, Inngan O, Lundstrom I (2000a) Microrobots for micrometer-size objects in aqueous media: potential tools for single-cell manipulation. *Science* 288(5475):2335–2338, Available at www.files.781/full_record.html
- Jager EWH, Smela E, Inngan O (2000b) Microfabricating conjugated polymer actuators. *Science* 290(5496):1540–1545, Available at www.files.708/full_record.html
- John S, Alici G, Cook C (2008) Frequency response of polypyrrole trilayer actuator displacement. In: Bar-Cohen Y (ed) *Electroactive polymer actuators and devices (eapad) 2008*. SPIE-Int Soc Optical Engineering, Bellingham
- Klempner D, Sperling LH, Utracki LA (eds) (1994) *Interpenetrating polymer networks*. American Chemical Society, Washington, DC, Available at <http://pubs.acs.org/doi/book/10.1021/ba-1994-0239>. Accessed 26 July 2014
- Martinez JG, Otero TF, Jager EWH (2014) Effect of the electrolyte concentration and substrate on conducting polymer actuators. *Langmuir* 30(13):3894–3904. doi:10.1021/la404353z
- Maziz A et al (2014) Demonstrating kHz frequency actuation for conducting polymer microactuators. *Adv Funct Mater* p.n/a–n/a. Available at 10.1002/adfm.201400373. Accessed 30 May 2014
- McGovern ST et al (2008) Fast bender actuators for fish-like aquatic robots. In: Bar-Cohen Y (ed). pp 69271L–69271L–12. Available at <http://proceedings.spiedigitallibrary.org/proceeding.aspx?articleid=1330542>. Accessed 26 July 2014
- McGovern S et al (2009) Finding NEMO (novel electromaterial muscle oscillator): a polypyrrole powered robotic fish with real-time wireless speed and directional control. *Smart Mater Struct* 18(9):095009, Available at <http://stacks.iop.org/0964-1726/18/i=9/a=095009?key=crossref.9865bb3d58a7987ae6b5593c83813c68>. Accessed 10 May 2014
- Naficy S et al (2013) Evaluation of encapsulating coatings on the performance of polypyrrole actuators. *Smart Mater Struct* 22(7):075005, Available at <http://stacks.iop.org/0964-1726/22/i=7/a=075005?key=crossref.235ad5fac96cc7e3eca2dc4f404f6b75>. Accessed 26 July 2014
- Otero TF (2013) Biomimetic conducting polymers: synthesis, materials, properties, functions, and devices. *Polym Rev* 53(3):311–351, Available at <http://www.tandfonline.com/doi/abs/10.1080/15583724.2013.805772>
- Otero TF, Cortes MT (2000) Electrochemical characterization and control triple-layer muscles. In: BarCohen Y (ed) *Smart structures and materials 2000: electroactive polymer actuators and devices (eapad)*. SPIE-Int Soc Optical Engineering, Bellingham, pp 252–260
- Otero TF, Cortés MT (2003) Artificial muscles with tactile sensitivity. *Adv Mater* 15(4):279–282, Available at <http://doi.wiley.com/10.1002/adma.200390066>. Accessed 3 Feb 2014
- Otero TF, Martinez JG (2012) Artificial muscles: a tool to quantify exchanged solvent during biomimetic reactions. *Chem Mater* 24(21):4093–4099. doi:10.1021/cm302847r
- Otero TF, Martinez JG (2014) Ionic exchanges, structural movements and driven reactions in conducting polymers from bending artificial muscles. *Sensors Actuators B Chem* 199:27–30, Available at <http://www.sciencedirect.com/science/article/pii/S0925400514003293>
- Otero T, Rodriguez J (1993) Polypyrrole electrogeneration at different potentials in acetonitrile and acetonitrile water solutions. *Synth Met* 55(2–3):1418–1423
- Otero TF et al (1992) Electrochemomechanical properties from a bilayer: polypyrrole/non-conducting and flexible material – artificial muscle. *J Electroanal Chem* 341(1–2):369–375, Available at http://sawwok5.fecyt.es/apps/full_record.do?product=WOS&search_mode=GeneralSearch&qid=8&SID=S1oEG1hEe4278aHl8P8&page=1&doc=3
- Otero TF et al (2013) Biomimetic structural electrochemistry from conducting polymers: processes, charges, and energies. Coulouvtammetric results from films on metals revisited. *Adv Funct*

- Mater 23(31):3929–3940, Available at <http://onlinelibrary.wiley.com/doi/10.1002/adfm.201203502/abstract>
- Pei Q, Inganas O (1992) Conjugated polymers and the bending cantilever method – electrical muscles and smart devices. *Adv Mater* 4(4):277–278
- Plesse C et al (2007) Poly(ethylene oxide)/polybutadiene based IPNs synthesis and characterization. *Polymer* 48(3):696–703, Available at <http://linkinghub.elsevier.com/retrieve/pii/S0032386106013085>. Accessed 22 Feb 2013
- Plesse C et al (2010) Conducting polymer artificial muscle fibres: toward an open air linear actuation. *Chem Commun (Camb)* 46(17):2910–2912, Available at <http://www.ncbi.nlm.nih.gov/pubmed/20386819>. Accessed 22 Feb 2013
- Plesse C et al (2011) Polyethylene oxide–polytetrahydrofuran–PEDOT conducting interpenetrating polymer networks for high speed actuators. *Smart Mater Struct* 20(12):124002, Available at <http://stacks.iop.org/0964-1726/20/i=12/a=124002?key=crossref.d7022dabd7990579af8243e043ba93e3>. Accessed 31 July 2013
- Randriamahazaka H et al (2005) Charging/discharging kinetics of poly(3,4-ethylenedioxythiophene) in 1-ethyl-3-methylimidazolium bis-(trifluoromethylsulfonyl)imide ionic liquid under galvanostatic conditions. *Electrochim Acta* 50(21):4222–4229
- Shimoda S, Smela E (1998) The effect of pH on polymerization and volume change in PPy(DBS). *Electrochim Acta* 44(2–3):219–238, Available at <http://www.sciencedirect.com/science/article/pii/S0013468698000486>
- Smela E (2003) Conjugated polymer actuators for biomedical applications. *Adv Mater* 15(6):481–494, Available at <http://doi.wiley.com/10.1002/adma.200390113>
- Smela E, Gadegaard N (1999) Surprising volume change in PPy(DBS): an atomic force microscopy study. *Adv Mater* 11(11):953–956
- Smela E et al (1993) Electrochemical muscles – micromachining fingers and corkscrews. *Adv Mater* 5(9):630–632, Available at www.files/767/full_record.html
- Spinks GM (2013) Encapsulating conductive polymer actuators-part I. Available at <http://www.youtube.com/watch?v=gzwxqHXmpx4>
- Sugino T et al (2009) Actuator properties of the complexes composed by carbon nanotube and ionic liquid: the effects of additives. *Sensors Actuators B Chem* 141(1):179–186, Available at <http://linkinghub.elsevier.com/retrieve/pii/S0925540050900478X>. Accessed 27 Jan 2014
- Temmer R et al (2013) In search of better electroactive polymer actuator materials: PPy versus PEDOT versus PEDOT–PPy composites. *Smart Mater Struct* 22(10):104006, Available at <http://stacks.iop.org/0964-1726/22/i=10/a=104006?key=crossref.223bd7eebc19f96bf72903adbd2b1297>. Accessed 27 Sept 2013
- Verdu R et al (2005) Mechanical characterization of the life cycle of artificial muscles through stereoscopic computer vision and active contours. In *2005 international conference on image processing (ICIP), vols 1–5*. IEEE, New York, pp 3705–3708
- Vidal F et al (2004) Long-life air working conducting semi-IPN/ionic liquid based actuator. *Synth Met* 142(1–3):287–291, Available at <http://linkinghub.elsevier.com/retrieve/pii/S0379677903004831>. Accessed 6 Feb 2013
- Vidal F et al (2013) Influence of the poly(ethylene oxide)/polybutadiene IPN morphology on the ionic conductivity of ionic liquid. *Eur Polym J* 49(9):2670–2679, Available at <http://linkinghub.elsevier.com/retrieve/pii/S0014305713002577>. Accessed 30 Sept 2013
- Wu Y et al (2006) Fast trilayer polypyrrole bending actuators for high speed applications. *Synth Met* 156(16–17):1017–1022, Available at <http://linkinghub.elsevier.com/retrieve/pii/S0379677906001731>. Accessed 12 Dec 2013
- Yao Q, Alici G, Spinks GA (2008) Feedback control of tri-layer polymer actuators to improve their positioning ability and speed of response. *Sensors Actuators A Phys* 144(1):176–184
- Zainudeen UL, Careem MA, Skaarup S (2008) PEDOT and PPy conducting polymer bilayer and trilayer actuators. *Sensors Actuators B Chem* 134(2):467–470

Section IV

Electroresponsive Carbon-Based Materials

Electrochemically Driven Carbon-Based Materials as EAPs: Fundamentals and Device Configurations

18

Janno Torop, Anna-Liisa Peikolainen, Alvo Aabloo, Mihkel Koel, Kinji Asaka, and Ray H. Baughman

Contents

1	Research Motivation and Application	440
2	Carbon Material-Based EAPs: Device Configuration	441
3	Characterization of Bending Actuation of Carbon Material-Based EAPs	442
4	The Electrochemistry Behind the Actuation of Carbon Material-Based EAPs	443
5	Carbon Nanotubes Can Twist: Leap to Nanogears	444
6	Carbide-Derived Carbon: Actuation Hidden Inside Small Pores	446
7	All the Carbons Are Not the Same: Essential Differences Between Carbon Nanotubes and Porous Amorphous Carbon	450
8	Conclusion	451
	References	451

Abstract

The varieties of different carbon structures offer a great basis for EAPs. They are most widely used electrode materials in low-voltage actuation generation. So far, carbon nanotubes (CNTs) have gained unrivaled attention. Their popularity is

J. Torop • A.-L. Peikolainen • A. Aabloo (✉)

Intelligent Materials and Systems Lab, Institute of Technology, University of Tartu, Tartu, Estonia
e-mail: janno.torop@ut.ee; anna.liisa.peikolainen@ut.ee; alvo.aabloo@ut.ee

M. Koel

Department of Chemistry, Tallinn University of Technology, Tallinn, Estonia
e-mail: mihkel.koel@ttu.ee

K. Asaka

Inorganic Functional Material Research Institute, National Institute of Advanced Industrial Science and Technology (AIST), Ikeda, Osaka, Japan
e-mail: asaka-kinji@aist.go.jp

R.H. Baughman

The Alan G. MacDiarmid NanoTech Institute, University of Texas at Dallas, Richardson, TX, USA
e-mail: rbaughman@utdallas.edu; Ray.Baughman@utdallas.edu

reflected in a production capacity that presently exceeds several thousand tons per year. In addition to carbon nanotubes, other electrically conductive carbon allotropes that contain electron-rich conjugated double bonds can be also successfully used as actuator electrodes. The following chapter focuses on most common carbon material-based EAPs. More specifically, on graphite which consists of multiple stacked conducting layers of graphene, on porous amorphous carbons, on fullerenes (C₆₀, C₇₀) and on carbon nanotubes (CNT). The porous amorphous carbons will include activated carbons, carbon nanofibers and filaments, carbide-derived conductive carbons synthesized from different precursors, and carbon aerogels. The chapter introduces these carbons as independently standing actuators or as materials for actuator electrodes and presents different approaches toward actuator fabrication. The ability to manipulate the morphology of these carbons, thus tuning the mechanical performance of the actuators, is also discussed. Essential differences in electrochemical, electro(chemo)mechanical properties and overall device configuration of carbon material-based actuators compared to other EAPs will be revealed.

Keywords

Electroactive materials • High surface area carbon • Electric double-layer • Ionic liquids

1 Research Motivation and Application

An EAP actuator is a device that performs a mechanical transformation in response to an input signal, prevailing to electric stimuli (Kosidlo et al. 2013). Except for electrolyte-filled independent carbon nanostructures such as torsional CNT bundles (Foroughi et al. 2011), a typical EAP consists of two electrode layers and with one separating layer between them (Wilson et al. 2007). By this simplification most common EAP electrodes can be classified further into two categories: (a) fully carbon-based (Li et al. 2011) and (b) polymer/ionic liquid-modified electrodes (Asaka et al. 1995; Torop et al. 2011). The polymer referred here mainly acts as an additive for better film formation and adhesion to electrolyte layer (Zheng et al. 2011). Usually, the carbon nanomaterial electrodes are prepared by casting, by filtration, or by self-assembly methods (Giménez et al. 2012; Takeuchi et al. 2010). The whole actuators are then fabricated by hot pressing of the as-prepared electrode and electrolyte layers or by dip coating of electrolyte layers into the carbon nanomaterial gel (Kaasik et al. 2013; Palmre et al. 2012).

As the actuation performance of aforementioned EAPs is mainly dominated by electrochemical and electromechanical processes of the electrode layer, the electrode material and structure become more crucial to specific applications. The recent discovery of one-dimensional carbon nanotube and two-dimensional graphene has created a revolution not only in EAP field but in all functional nanomaterials (Castro Neto et al. 2009; Zhu et al. 2010). Therefore, unique structures of newly described carbon materials offer a basis to develop in near future singular electrical and

mechanical devices at sophisticated level. Although the detailed effects occurring down to ion scale in those carbon nanomaterial electrodes are still not very clear, the outstanding actuation performance presented so far give us tremendous motivation to meet the challenge in understanding the mechanisms and thus developing more advanced actuator materials (Weiss et al. 2012; Zhu et al. 2011).

Despite the increasing popularity of low-voltage carbon material-based EAPs, there are some issues that are not completely solved. Main drawbacks are related to the complexity of the manufacturing process. The lack of reproducibility in both mechanical and electrical properties of formed actuators, short lifetime, and insufficient control and guidance of the actuator movement restrict further breakthrough. Stable actuators with high response speed and with relatively high output power are still a challenge.

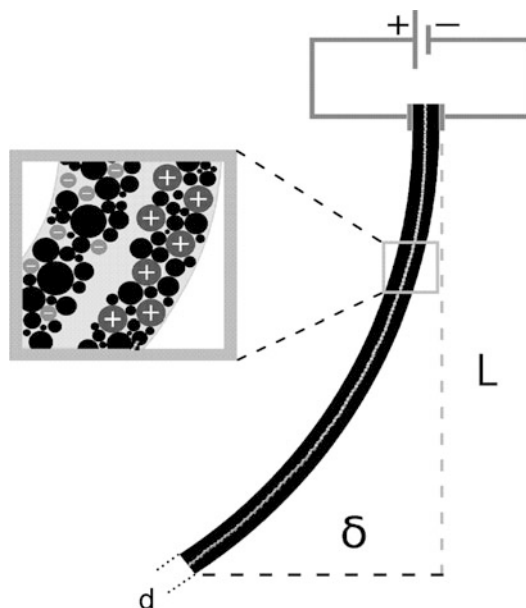
2 Carbon Material-Based EAPs: Device Configuration

There are several methods for fabrication of carbon-based actuators: (a) direct assembly process (Akle et al. 2006), where the layers of electrodes and membrane are fabricated separately followed by sandwiching the membrane layer between the layers of electrodes by hot pressing (Palmre et al. 2010), and (b) spray painting (Must et al. 2013), where activated carbon powder is mixed with ionomer solution and the suspension is sprayed directly onto the membrane. Printing techniques have also been applied allowing higher reproducibility and precision in fabricating micro-size actuators. By printing layer by layer, the electrode suspension is applied to a substrate, then the layer of polymer electrolyte is printed on top of the electrode layer, and the final layer of the trilaminar sheet is carbon-based electrode layer. However, microprinting technology for creating complex patterns is not so widespread in the field of actuators as in the field of supercapacitors (Pech et al. 2010).

The overall electroactivity of carbon-based actuators, including CNTs, CDCs, or activated carbons, predicates on two main actuation mechanisms. The first principle is based on the electronic (metallic) conductivity of carbon material. Actuators of such type need high electrical potential (field) for actuation. Actuation occurs due to carbon-carbon interaction change due to high electrical field and increased temperature (electrothermal effect) (Liu et al. 2014; Zhang et al. 2014). Another principle is diffusion of ions and ion pairs induced by applied low potential as shown in Fig. 1. These transducers usually combine carbon materials with polymer matrix and some ionic conducting media. They seem to have much more possible applications in the near future (Asaka et al. 2013).

The twisting nanotube yarn actuators based on first principle mentioned above enable fully dry torsional actuation as the main driving mechanisms are based on electrothermal and/or photothermal effects. These actuators do not require electrolyte, counter electrode, or extra package as it is needed for electrochemically driven actuators (Chun et al. 2014). Indeed, the electroactivity of nanotube yarns were firstly described in setup where bundled fibers were immersed in electrolyte; the overall capability of twisting of actuators was demonstrated later without ion

Fig. 1 Displacement of trilayer actuator under applied voltage (cross-sectional view). *Inset* shows a schematic distribution of electrolyte ions along the carbonaceous electrodes



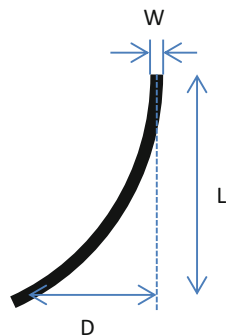
adsorption required. Immersing a twisted MWCNT yarn and a counter electrode in an electrolyte and applying a voltage between these electrodes cause the yarn to partially untwist (Foroughi et al. 2011). Vertically suspended actuating yarn was fully immersed in the electrolyte (0.2 M tetrabutylammonium hexafluorophosphate (TBA-PF₆) in acetonitrile) and supported a paddle at its lower end.

Most common types of three-layered composite actuators can be easily formed into various shapes and miniaturized while maintaining actuating properties. The properties of the actuators can be engineered with potential to be integrated into microelectromechanical systems and sensors as control devices to produce smart systems (Pugal et al. 2010).

3 Characterization of Bending Actuation of Carbon Material-Based EAPs

As most of the IEAP materials, carbon material-based EAPs are a trilayer type of banding actuators. The width of the actuator is at least order of magnitude larger than the thickness, and the length is at least few times larger than the width. When voltage is applied between the opposite faces of such a trilayer strip, the different expansion or contraction of the two electrodes produces an easily perceived large bending of the ribbon. Though the bending of the IEAP actuator is effective and visible, the mathematical characterization of this mechanical behavior is not straightforward. The two most widely used measures for characterizing bending actuators are their strain and bending moment in a cantilever configuration. The former describes the

Fig. 2 Strain difference definition



lateral expansion of the electrodes, while the latter characterizes the ability of the actuator to perform mechanical work. Both are adopted from the classical mechanics of a cantilever beam. The theory was developed in the seventeenth to eighteenth centuries by Galilei, Bernoulli, Euler, and many of their followers (Timoshenko 1983).

It has been accepted that bending actuator is characterized by strain difference ε (Sugino et al. 2009)

$$\varepsilon = \frac{2DW}{L^2 + W^2}, \quad (1)$$

where D is half of the peak-to-peak displacement, W is the thickness of the actuator, and L is the distance from the clamped beam to the projection of the measurement spot (Fig. 2).

It has to be noted out; the cantilever beam is an approximation as electrodes do not expand/contract equally. However, it is a good basis to compare performance of different actuators from engineering point of view.

4 The Electrochemistry Behind the Actuation of Carbon Material-Based EAPs

The electrode materials consisting of carbon-based electrodes can be divided into two main categories in terms of electrochemical point of view: (a) the materials undergoing faradaic charge-transfer reactions during operation or (b) materials where faradaic charge-transfer reactions do not occur or can be considered as negligible (Imaizumi et al. 2012; Otero et al. 2013; Torop et al. 2014b).

Faradaic reactions tend to occur when carbon material is modified with conjugated polymers or with pseudocapacitive additives like RuO_2 and MnO (Giménez et al. 2012; Sugino et al. 2009). Metal oxides have usually high resistance; therefore, oxide powders in electrode layer are often modified with pure, SWCNTs, or CNTs. This turns them hybrid actuators, where redox and non-redox behavior appear

(Terasawa et al. 2012b). Oxide-based electrode layers can be covered also with highly conductive noble-metal layers (Akle et al. 2007).

Microporous carbon is one of the most widely used electrode material for IEAP due to its electrochemical inertness and a wide diversity of available forms, ranging from powders to fibers, cloths, monoliths, nanoscale structures, etc. (Presser et al. 2011). In order to explain the charge accumulation and dimensional effects, Baughman and coworkers first described and proposed electrochemical actuation of CNTs when applying voltages in electrolytes against a counter electrode. They relied on a “charge injection” model (Baughman 1999).

According to this model, the actuation is attributed to the dimensional changes in covalently bonded directions caused by the charge injection, which originate from quantum and double-layer electrostatic effects. However, the induced strain of bucky-gel actuators is comparable to that or is even larger than that of SWNT sheet-based actuators in spite of the fact that the SWNT contents in the bucky-gel electrodes are from 13 to 20 wt%. Hence, it was considered that the bending motion of the actuator in response to voltages takes place by dimensional changes at microscale of the soft electrode layers due to the difference in the size of the transport ions from the electrodes.

5 Carbon Nanotubes Can Twist: Leap to Nanogears

Macroscopic mechanical gears are widespread to generate and control rotational movement and produce useful work in numerous mechanical devices such as in clocks, watches, transmissions, car, trains, and robots. Recently, Foroughi et al. showed that an electrolyte-filled twist-spun MWNT yarn, much thinner than a human hair, functions as a torsional artificial muscle in a simple three-electrode electrochemical system, providing a reversible $15,000^\circ$ rotation and 590 rpm (Foroughi et al. 2011). These yarns have usually diameter in few micrometers. The design and synthesis of molecular systems at nanoscale level that work as gears have attracted a lot of interest and is still a challenge. The idea of carbon nanotube-based gears came from previous progress in fullerene science and technology (Han et al. 1997). The finding of the reaction of benzyne with C60 stimulated the idea of nanogears, which consists of carbon nanotubes and benzynes.

Multiwalled and single-walled nanotubes and fibers have been successfully prepared, and rapid advances have been made in controlling tube diameter, length, chirality, and the number of concentric shells. Immersing a twisted MWNT yarn and a counter electrode in electrolytes and applying a voltage between these electrodes caused the yarn to partially untwist. Observed contraction of yarns was supposed to be largely driven by internal pressure associated with ion insertion. This system has shown great efficiency in torsional rotation with fast actuation rate. However, it relies on the use of electrolytes. As a result, the actuating system is restricted to a wet environment. In practical aspect, the electrolytes limit operating temperature, voltage, and actuation rate. In addition, due to working electrolytes and required special

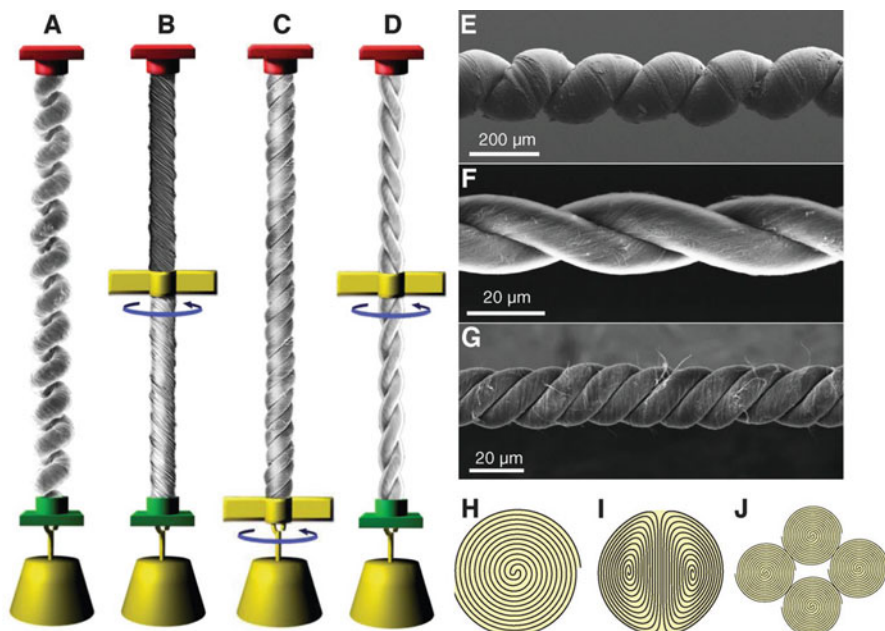


Fig. 3 Muscle configurations and yarn structures for tensile and torsional actuation. Tensile load and paddle positions for (a) a two-end-tethered, fully infiltrated homochiral yarn; (b) a two-end-tethered, bottom-half-infiltrated homochiral yarn; (c) a one-end-tethered, fully infiltrated homochiral yarn; and (d) a two-end-tethered, fully infiltrated heterochiral yarn. The depicted yarns are coiled, noncoiled, four ply, and two ply, respectively. Arrows indicate the observed direction of paddle rotation during thermal actuation. Red and green yarn-end attachments are tethers, meaning they prohibit end rotation; red attachments also prohibit translational displacement. SEM micrographs of (e) a fully infiltrated homochiral coiled yarn, (f) a neat two-ply yarn, and (g) a neat four-ply yarn. Illustration of ideal cross sections for (h) Fermat, (i) dual-Archimedean, and (j) infiltrated four-ply Fermat yarns (Reproduced from Lima et al. 2012)

packing, additional weight and volume reduce the overall work density of the system.

In 2012, Lima et al. reported an electrolyte-free guest-filled twist-spun MWNT yarn artificial muscle that spun a rotor at an average of 11,500 rpm, achieving 20 times higher than previously demonstrated by Foroughi et al. a year before (Lima et al. 2012) (Fig. 3). Similarly, the system delivered 3 % tensile contraction at 1200 cycles/min and provided up to 27.9 kW/kg of mechanical power density during muscle contraction, which is 85 times higher than that for natural skeletal muscle. More than a million cycles of tensile and torsional actuation have been performed without a significant loss of performance. Electrical, chemical, or photonic excitation of hybrid yarns changes guest paraffin wax dimensions and generates torsional rotation and contraction of the yarn host. Compared with alternative actuation materials, CNTs exhibit a series of advantages. Among others, actuation under low voltages, fast-response rate, and millions of cycle life are especially

significant benefits. Also, fuel cell-powered CNT artificial muscle was demonstrated as well as CNT yarn-based actuator with extremely efficient torsional actuation. Unique electronic properties, large surface area, high mechanical strength, and excellent chemical and thermal stability account for such advantages for CNT-based actuators.

6 Carbide-Derived Carbon: Actuation Hidden Inside Small Pores

The mechanism of charge-induced volumetric actuation involves several processes including ionic transport and electrochemical effects. One remarkable example of electrochemical reaction-driven actuator system is faradaic reactions causing oxidation and reduction of the conjugated polymer backbone and where ion movements produce dimensional changes of typically up to 25 % (Conzuelo et al. 2010; Jager 2000; Melling et al. 2013).

In the field of carbonaceous actuators, several processes related to volume change may appear simultaneously. Unlike the graphene-based actuators, where the theoretical calculation show the directional large volume expansion perpendicular to its basal plane direction (Kong and Chen 2014), the amorphous carbon-based actuators show the charge-induced expansion rate around 1.5 %, confirmed via dilatometry studies (Hantel et al. 2011). As reported, the graphene layers could expand up to >700 % when intercalated by solvated ions $\text{Li}^+(\text{PC})_y$. However, the expansion of graphene layers is mainly related to reversible electrochemical intercalation reaction and can be confirmed by corresponding cyclic voltammograms (Balke et al. 2010).

On the contrary, the charge/discharge processes contributing to electrochemical capacitance and electrochemical strain generation of porous carbon electrodes can be separated into two processes: fast (charge transfer) and slow (diffusion) processes could be identified. They both contribute to the capacitance as well for strain generation. The fast process is assigned to the double-layer charging, whereas the slow process is assigned to ion migration into the carbon pores or through the porous carbon matrix (Arruda et al. 2013; Kaasik et al. 2013).

By the electrochemical point of view, another criterion should be taken account when comparing “fast” and “slow” processes. While keeping driving voltage lower than 2 V, the electrochemical reactions will not occur in carbon-based actuators using nonaqueous solvents or ionic liquids (Jänes et al. 2004; Torop et al. 2009). However, in aqueous media the electrochemical oxidation of carbon-based electrodes appear already at +0.6 V (vs. Ag/AgCl reference) and may lead to intense gas evolution (Xi et al. 2009).

While developing reliable carbonaceous actuator materials, many groups have been modifying their actuator performance in terms of electrochemical processes. They have been demonstrating a successful separation of the concurring processes in actuators, thus, offering fundamental insights for future development (Giménez et al. 2012; Jo et al. 2013).

Previous studies have shown that CDC materials, particularly thin-shaped microporous carbon sheets, may have considerable resizing, contraction, and expansion, in variable electric field. Unlike piezoelectric or electrostrictive ceramics and magnetostrictive materials which require high voltage or magnetic field for activation, electrically driven microporous carbon film actuators operate at much lower and more readily implemented voltage values (Carpi and Smela 2009). Dilatometric studies on different porous TiC-derived carbon electrodes revealed that generated stress and strain of actuators were directly dependent on the specific surface area and pore size distribution of CDC used in electrode layer (Hantel et al. 2011; Ruch et al. 2010; Torop et al. 2009). Actuators made from different precursor CDC powders have demonstrated both different displacement performances and energy consumptions according to the amount of mesopores introduced in the electrode layer. Interestingly, both the dilatometric investigations and research on electroactive response of CDC composites confirmed the important role of carbon pore size on the volumetric and resizing effects. Microporous carbons have shown sufficient performance regarding response time and amplitude of motion, which both are desired properties in the case of the actuator while compared to carbon black or other porous carbons (Must et al. 2013; Torop et al. 2014b; Fig. 4).

The conductivity of the electrode is crucial factor for fast-response actuators. Unfortunately without improvements in the electrode conductivity, the porous carbons are not able to work at excitation frequencies higher than 1 Hz (Palmre et al. 2012; Sugino et al. 2009). One way is to tune the properties of carbon by choosing suitable precursors and synthesis conditions; however, as discussed above, another approach to enhance the electrical conductivity of carbon-based electrodes is to combine amorphous carbon with carbon having higher electrical conductivity, such as CNTs with CDC, CNTs, or vapor-grown carbon nanofibers with activated carbon nanofibers or with carbon black.

Carbon-polymer composite ionic actuators with five different ratios of SWCNTs to CDC in electrodes were fabricated, and their electromechanical, electrochemical, and mechanical properties were studied by Palmre et al. (2012). Increasing the

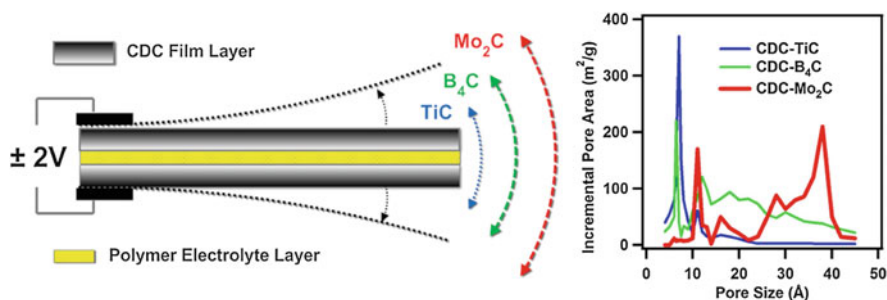


Fig. 4 Demonstration of porosity-dependent bending displacement using microporous, micro-mesoporous, and mesoporous carbons (Reproduced from Torop et al. 2014b)

content of SWCNTs in the composite electrodes increased considerably the conductivity of electrode and the stiffness (Young's modulus) of the actuators. The addition of SWCNTs into the electrodes caused a significant improvement in bending strain response. At higher actuation frequencies (0.5–50 Hz), the improvement can be mainly attributed to enhanced electrode conductivity and increased mesoporosity, i. e., quicker and higher electrolyte ion accessibility into porous matrix of the electrodes. At the low-frequency range (5 mHz–0.5 Hz), the SWCNT/CDC (50/50) actuator showed by far the highest bending strain among the samples (up to 0.85 %), which compared to the pure CDC electrodes with maximum strain of 0.35 % is an improvement of more than two times. The SWCNT/CDC (50/50)-actuator also showed the best combination in terms of stress (bending force) and maximum strain output. A strong co-effect of the specific capacitance and Young's modulus on the bending strain was observed at the lower frequency range. A correlation between the mentioned parameters was derived, which indicates that the superior performance of SWCNT/CDC (50/50) electrodes is due to a unique ratio of micro- and mesoporosity in the electrodes combined with moderately high stiffness of carbon matrix. Capacitance of the actuator decreased with increasing content of carbon with higher electrical conductivity and lower specific surface area.

Unexpectedly, impregnating carbon black with vapor-grown carbon fibers (VGCFs) did not reduce capacitance of the actuator according to Terasawa et al. On the contrary, the addition of VGCF improved both the electrical conductivity of carbon black electrodes and the capacitance of the actuator (Terasawa and Takeuchi 2014; Terasawa et al. 2012a). The enhancement is proposed to be due to high degree of entanglement of VGCF, which forms an open network of mesopores allowing IL ions an easy access to carbon black. The strain has an optimum at carbon black/VGCF ratio 50 %/50 % similar to CDC/SWCNT-based electrodes; however, the strain for carbon black/VGCF actuator with EMI[BF₄] as an electrolyte is higher than for the actuator based on SWCNTs, 0.46 % versus 0.43 %, respectively.

Compared to numerous studies on carbon nanotube-conducting polymer composites, there are only a few publications referring to the use of amorphous carbon-conducting polymer composites in actuators (Kaasik et al. 2011; Palmre et al. 2009). Controlled heat treatment allows for the manipulation of the porosity of amorphous carbons leading to materials with large specific surface areas and subsequently a large contact area between the carbon electrode and electrolyte. Coconut-based activated carbon powder in actuators prepared by Palmre et al. had a specific surface area of 1900 m²g⁻¹ and an electrical conductivity of ≈50 mS cm⁻¹. However, it is considered that the preferred BET-specific surface area for amorphous carbon used in the actuator electrodes is in the range of 500–1500 m²g⁻¹. A lower specific surface area diminishes the capacitive properties due to a low area capable of forming an electrochemical double layer (area in contact with an electrolyte). In contrast, an extremely high specific surface area, exceeding 3000 m²g⁻¹, deteriorates the performance of the electrode due loss of carbon atoms from the carbon structure during activation accompanying lowering the density of electron-conducting regions; in addition, the materials having

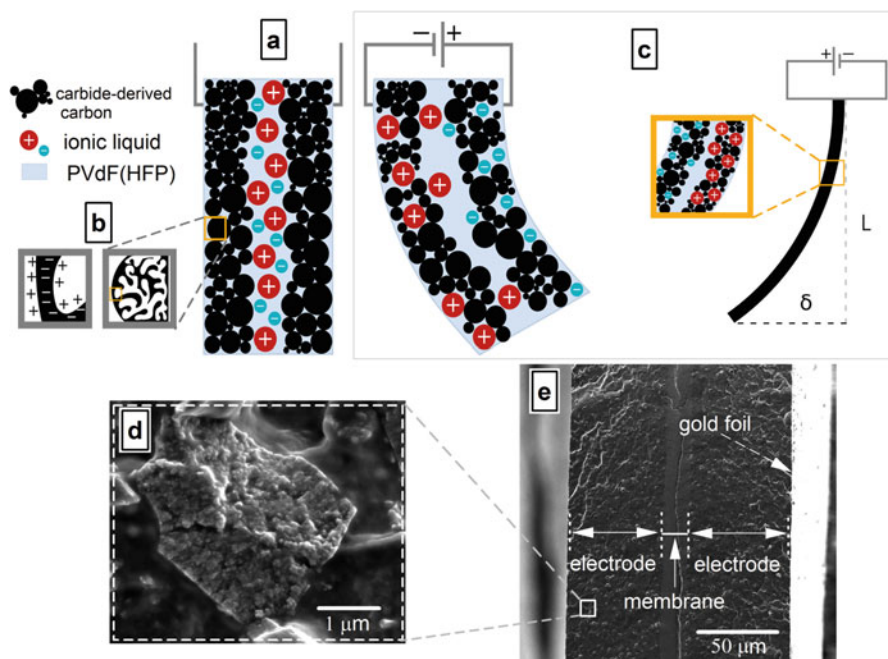


Fig. 5 (a) Cross-sectional model of nanoporous carbide-derived carbon-based actuator. (b) Simplified notation of electrical double-layer formation inside porous CDC during charging. (c) Bending displacement of actuator under applied voltage. (d, e) SEM images of cross section of actuators with polymer-supported and gold-foil-modified CDC electrodes (Reproduced from Torop et al. 2012)

exceptionally high surface area are inherently less stable over long-term use (Arulepp et al. 2006).

Response improvement of porous carbon actuators was demonstrated by Torop et al. while using thin gold foil at outer electrode surface to avoid potential drop along the porous carbon electrode surface (Torop et al. 2012). The gold-foil-modified actuators did not only show fast response to applied voltage, but they also required remarkably lower operating voltage – as low as ± 0.25 V compared to conventional porous carbon actuators which operate at voltage range of ± 2 V (Fig. 5). Hot-pressed additional 100 nm thick gold layer ensured better conductivity of polymer-supported CDC electrodes while still maintaining the bending elasticity of the actuator. Electrochemical impedance measurements confirmed that relaxation time constant of gold-foil-modified actuator decreased more than one order of magnitude while compared with pure CDC actuator, thus allowing faster charge/discharge cycles. Gold-foil-modified CDC actuators obtained the strain level of 2.2 % when rectangular voltage ± 2 V was applied with frequency 0.5 Hz. As a comparison, the actuator with the same composition except the additional gold foil had a strain below 1 % at the same voltage cycle.

7 All the Carbons Are Not the Same: Essential Differences Between Carbon Nanotubes and Porous Amorphous Carbon

The electrochemical, electromechanical (and chemomechanical) properties of amorphous carbon-based actuators are derived from their molecular origin (Jänes et al. 2007; Torop et al. 2009). For the same reason, the behavior of CNT-based actuators is different compared to ones based on amorphous carbon. There are two substantial differences between amorphous carbons and carbon nanotubes: Firstly, CNTs have higher electrical conductivity than porous amorphous carbons due to conjugation of carbon atoms. Secondly, the specific surface area of CNTs is significantly lower compared to most representatives of amorphous carbons leading to lower specific capacitance of the actuator device (Sugino et al. 2009).

Unlike porous amorphous carbons, the high ratio of the external surface area to the total surface area of CNTs provides fast adsorption/desorption of electrolyte ions associated with the process of the formation of the electric double layer due to no ion-sieving effect occurring (Arulepp et al. 2006). Sorption of ions onto external surface area of CNTs makes the double-layer capacitance of CNT-based actuators less dependent on the ionic liquid species (ion dimensions) than the capacitance of amorphous carbon-based actuators, where the ion transport into the pores depends on the pore size and the size of electrolyte ions. The frequency dependence of generated strain has been attributed to the electrochemical kinetics; different deflection amplitudes are the result of different ionic conductivities of IL species (Imaizumi et al. 2012).

Another characteristic property of CNT-based actuators is their high Young's modulus. It is remarkably higher compared to amorphous carbon-based actuators and almost eight times higher compared to CDC-based actuator (Table 1; Palmre et al. 2012). The Young's modulus of ACNF-based actuators is similar to actuators from SWCNTs, but the extremely larger specific area ($2000 \text{ m}^2 \text{ g}^{-1}$) of ACNF results in higher specific capacitance for ACNF-based actuators. The strain of SWCNT actuators is larger than the strain of ACNF-based actuators being in a good agreement with the sorption speed theory described above (Terasawa et al. 2012a).

Table 1 A summary of measured properties of different SWCNT/CDC actuators

Actuator notation ^a	Maximum strain (%)	Stress at max. strain (MPa)	Young's modulus (MPa)	Electrode conductivity (S/cm)
SWCNT (100)	0.587	1.57	268	2.42
SWCNT/CDC (75/25)	0.514	0.89	173	0.93
SWCNT/CDC (50/50)	0.851	1.38	162	0.3
SWCNT/CDC (25/75)	0.595	0.89	149	0.19
CDC (100)	0.345	0.11	32	0.16

^awt% of the electrode components in parentheses

A disadvantage that must be overcome when CNT-based actuator electrodes are fabricated is poor dispersibility of CNTs due to strong van der Waals forces and electrostatic interactions between the nanotubes forming entangled bundles and aggregates in the polymer (Fukushima and Aida 2007). Whereas the suspension of amorphous carbon-based electrodes can be mixed using a magnetic stirrer, CNTs require special approach. In order to obtain homogeneous CNT suspensions, first the CNT bundles in the suspension should be disentangled by sonication, and then the stabilization of the solution is necessary to keep the tubes untangled (Punning et al. 2014). This might need applying amphiphilic polymers or surfactants or chemical functionalization of the nanotubes which affects the electrical conductivity of the composite electrode (Torop et al. 2014a).

Carbon nanotubes are synthesized using metal catalysts, which are later difficult to remove from the nanotubes to assure high purity. These impurities develop pseudocapacitive properties of CNT-based actuators. The trend in carbon-based actuators is to find alternatives to CNTs, especially to SWCNTs, mostly because of their high cost. CNTs have still unique properties and by far better electrical conductivity compared to amorphous carbons, and rather than replacing, the combination of CNTs with different types of amorphous carbons in electroactive carbon-polymer composite actuators is the prospect.

8 Conclusion

The studies in different carbonaceous materials have pointed out that actuators with hierarchical displacement/strain characteristics can be prepared from wide selection of precursor carbons available. The tunability of the morphology of carbons and thus the ability to tune the mechanical performance of the actuators are the main focus in this research. Essential differences in electrochemical, electro(chemo)mechanical properties allow to build several actuator systems with bending, linear, and twisting motion. For example, in case of amorphous carbons, the overall device displacement is determined by porosity of final carbon material which affects the speed and bending range. This unique property together with their facile preparation method, flexibility, remarkable specific capacitance, and low-driving voltage enables the amorphous carbon-based actuators in application to many areas where other EAPs can be complemented.

References

- Akle BJ, Bennett MD, Leo DJ (2006) High-strain ionomeric–ionic liquid electroactive actuators. *Sensors Actuators A Phys* 126:173–181
- Akle BJ, Bennett MD, Leo DJ, Wiles KB, McGrath JE (2007) Direct assembly process: a novel fabrication technique for large strain ionic polymer transducers. *J Mater Sci* 42:7031–7041
- Arruda TM, et al (2013) In situ tracking of the nanoscale expansion of porous carbon electrodes. *Energy Environ Sci* 6:225

- Arulepp M, et al (2006) The advanced carbide-derived carbon based supercapacitor. *J Power Sources* 162:1460–1466
- Asaka K, Oguro K, Nishimura Y, Mizuhata M, Takenaka H (1995) Bending of polyelectrolyte membrane-platinum composites by electric stimuli I. Response characteristics to various waveforms. *Polym J* 27:436–440
- Asaka K, Mukai K, Sugino T, Kiyohara K (2013) Ionic electroactive polymer actuators based on nano-carbon electrodes. *Polym Int* 62:1263–1270
- Balke N, Jesse S, Morozovska AN, Eliseev E, Chung DW, Kim Y, Adamczyk L, García RE, Dudney N, Kalinin SV et al (2010) Nanoscale mapping of ion diffusion in a lithium-ion battery cathode. *Nat Nanotechnol* 5:749–754
- Baughman RH (1999) Carbon nanotube actuators. *Science* (80-) 284:1340–1344
- Carpi F, Smela E (2009) Biomedical applications of electroactive polymer actuators. *Biomedical applications of electroactive polymer actuators*. John Wiley & Sons, Ltd., Chichester. doi:10.1002/9780470744697
- Castro Neto AH, Peres NMR, Novoselov KS, Geim AK (2009) The electronic properties of graphene. *Rev Mod Phys* 81:109–162
- Chun et al (2014) Hybrid carbon nanotube yarn artificial muscle inspired by spider dragline silk. *Nat Commun* 5:3322
- Conzuelo LV, Arias-Pardilla J, Cauch-Rodríguez JV, Smit MA, Otero TF (2010) Sensing and tactile artificial muscles from reactive materials. *Sensors (Basel)* 10:2638–2674
- Foroughi J, et al (2011) Torsional carbon nanotube artificial muscles. *Science* 334:494–497
- Fukushima T, Aida T (2007) Ionic liquids for soft functional materials with carbon nanotubes. *Chemistry* 13:5048–5058
- Giménez P, et al (2012) Capacitive and faradic charge components in high-speed carbon nanotube actuator. *Electrochim Acta* 60:177–183
- Han J, Globus A, Jaffe R, Deardorff G (1997) *Nanotechnology* 8:95–102
- Hantel MM, Presser V, Kötz R, Gogotsi Y (2011) In situ electrochemical dilatometry of carbide-derived carbons. *Electrochem Commun* 13:1221–1224
- Imaizumi S, Kato Y, Kokubo H, Watanabe M (2012) Driving mechanisms of ionic polymer actuators having electric double layer capacitor structures. *J Phys Chem B* 116:5080–5089
- Jager EWH (2000) Microfabricating conjugated polymer actuators. *Science* (80-) 290:1540–1545
- Jänes A, Permann L, Arulepp M, Lust E (2004) Electrochemical characteristics of nanoporous carbide-derived carbon materials in non-aqueous electrolyte solutions. *Electrochem Commun* 6:313–318
- Jänes A, Kurig H, Lust E (2007) Characterisation of activated nanoporous carbon for supercapacitor electrode materials. *Carbon N Y* 45:1226–1233
- Jo C, Pugal D, Oh I-K, Kim KJ, Asaka K (2013) Recent advances in ionic polymer–metal composite actuators and their modeling and applications. *Prog Polym Sci* 38:1037–1066
- Kaasik F, Torop J, Peikola A-L, Koel M, Aabloo A (2011) Carbon aerogel based electrode material for EAP actuators. In: Bar-Cohen Y, Carpi F (eds) *Proceedings of SPIE – the international society for optical engineering*, San Diego, California, 7976, p. 797600–797600–8
- Kaasik F, et al (2013) Anisometric charge dependent swelling of porous carbon in an ionic liquid. *Electrochem Commun* 34:196–199
- Kong L, Chen W (2014) Carbon nanotube and graphene-based bioinspired electrochemical actuators. *Adv Mater* 26:1025–1043
- Kosidlo U, et al (2013) Nanocarbon based ionic actuators—a review. *Smart Mater Struct* 22:104022
- Li J, et al (2011) Superfast-response and ultrahigh-power-density electromechanical actuators based on hierarchical carbon nanotube electrodes and chitosan. *Nano Lett* 11:4636–4641
- Lima MD, et al (2012) Electrically, chemically, and photonically powered torsional and tensile actuation of hybrid carbon nanotube yarn muscles. *Science* 338:928–932
- Liu Q, et al (2014) Nanostructured carbon materials based electrothermal air pump actuators. *Nanoscale* 6:6932–6938

- Melling D, Wilson S, Jager EWH (2013) The effect of film thickness on polypyrrole actuation assessed using novel non-contact strain measurements. *Smart Mater Struct* 22:104021
- Must I, et al (2013) Mechanoelectrical impedance of a carbide-derived carbon-based laminate motion sensor at large bending deflections. *Smart Mater Struct* 22:104015
- Otero TF, Alfaro M, Martinez V, Perez MA, Martinez JG (2013) Biomimetic structural electrochemistry from conducting polymers: processes, charges, and energies. Coulovoltammetric results from films on metals revisited. *Adv Funct Mater* 23:3929–3940
- Palmre V, et al (2009) Nanoporous carbon-based electrodes for high strain ionomeric bending actuators. *Smart Mater Struct* 18:095028
- Palmre V, et al (2010) Ionic polymer metal composites with nanoporous carbon electrodes. In: *Electroactive polymer actuators and devices (EAPAD) 2010*. SPIE – The International Society for Optical Engineering. San Diego, California, p. 76421D (9 pp)
- Palmre V, et al (2012) Impact of carbon nanotube additives on carbide-derived carbon-based electroactive polymer actuators. *Carbon N Y* 50:4351–4358
- Pech D, et al (2010) Elaboration of a microstructured inkjet-printed carbon electrochemical capacitor. *J Power Sources* 195:1266–1269
- Presser V, Heon M, Gogotsi Y (2011) Carbide-derived carbons – from porous networks to nanotubes and graphene. *Adv Funct Mater* 21:810–833
- Pugal D, Jung K, Aabloo A, Kim KJ (2010) Ionic polymer-metal composite mechanoelectrical transduction: review and perspectives. *Polym Int* 59:279–289
- Punning A, et al (2014) *J Intell Mater Syst Struct* 25:2267–2275. doi:10.1177/1045389X14546656
- Ruch PW, et al (2010) A dilatometric and small-angle X-ray scattering study of the electrochemical activation of mesophase pitch-derived carbon in non-aqueous electrolyte solution. *Carbon N Y* 48:1880–1888
- Sugino T, Kiyohara K, Takeuchi I, Mukai K, Asaka K (2009) Actuator properties of the complexes composed by carbon nanotube and ionic liquid: the effects of additives. *Sensors Actuators B Chem* 141:179–186
- Takeuchi I, et al (2010) Electrochemical impedance spectroscopy and electromechanical behavior of bucky-gel actuators containing ionic liquids. *J Phys Chem C* 114:14627–14634
- Terasawa N, Takeuchi I (2014) Li ion/vapor grown carbon fiber polymer actuators show higher performance than single-walled carbon nanotube polymer actuators. *J Mater Chem A* 2:130
- Terasawa N, Mukai K, Asaka K (2012a) Superior performance of a vapor grown carbon fiber polymer actuator containing ruthenium oxide over a single-walled carbon nanotube. *J Mater Chem* 22:15104
- Terasawa N, Mukai K, Yamato K, Asaka K (2012b) Superior performance of manganese oxide/multi-walled carbon nanotubes polymer actuator over ruthenium oxide/multi-walled carbon nanotubes and single-walled carbon nanotubes. *Sensors Actuators B Chem* 171–172:595–601
- Timoshenko S (1983) *History of strength of materials*. New York, NY: Dover
- Torop J, et al (2009) Nanoporous carbide-derived carbon material-based linear actuators. *Materials* 3:9–25
- Torop J, et al (2011) Flexible supercapacitor-like actuator with carbide-derived carbon electrodes. *Carbon N Y* 49:3113–3119
- Torop J, et al (2012) Nanoporous carbide-derived carbon based actuators modified with gold foil: prospect for fast response and low voltage applications. *Sensors Actuators B Chem* 161:629–634
- Torop J, Aabloo A, Jager EWH (2014a). Novel actuators based on polypyrrole/carbide-derived carbon hybrid materials. *Carbon N Y* 80:387–395
- Torop J, et al (2014b) Microporous and mesoporous carbide-derived carbons for strain modification of electromechanical actuators. *Langmuir* 30:2583–2587
- Weiss NO, et al (2012) Graphene: an emerging electronic material. *Adv Mater* 24:5782–5825
- Wilson SA, et al (2007) New materials for micro-scale sensors and actuators. *Mater Sci Eng R Rep* 56:1–129

-
- Xi B, et al (2009) Electrochemical pneumatic actuators utilising carbon nanotube electrodes. *Sensors Actuators B Chem* 138:48–54
- Zhang X, et al (2014) Photoactuators and motors based on carbon nanotubes with selective chirality distributions. *Nat Commun* 5:2983
- Zheng W, et al (2011) Artificial muscles based on polypyrrole/carbon nanotube laminates. *Adv Mater* 23:2966–2970
- Zhu Y, et al (2010) Graphene and graphene oxide: synthesis, properties, and applications. *Adv Mater* 22:3906–3924
- Zhu S-E, et al (2011) Graphene-based bimorph microactuators. *Nano Lett* 11:977–981

Electrothermally Driven Carbon-Based Materials as EAPs: Fundamentals and Device Configurations

19

Javad Foroughi, Geoffrey M. Spinks, John D. W. Madden,
Ray H. Baughman, and Seon Jeong Kim

Contents

1	Introduction	456
2	Carbon Nanotube Yarns, Hybrid Yarns, and Coiled Yarns	457
2.1	Yarn Fabrication	457
2.2	Hybrid Yarn Muscles	459
3	Device Configurations	461
4	Torsional Actuation Performance	462
4.1	Wax-Filled Single-Ply Yarn Muscles	462
4.2	Overdamped Hybrid Yarn Muscles	463
5	Tensile Actuation Performance	465
5.1	Neat-Twisted Yarns	465
5.2	Wax-Filled Twisted and Coiled Yarns	466
6	Conclusion	468
	References	470

J. Foroughi (✉) • G.M. Spinks

ARC Centre of Excellence for Electromaterials Science, Intelligent Polymer Research Institute,
University of Wollongong, North Wollongong, NSW, Australia
e-mail: foroughi@uow.edu.au; gspinks@uow.edu.au

J.D.W. Madden

Electrical and Computer Engineering, Advanced Materials and Process Engineering Lab,
University of British Columbia, Vancouver, BC, Canada
e-mail: jmadden@ece.ubc.ca

R.H. Baughman

The Alan G. MacDiarmid NanoTech Institute, University of Texas at Dallas, Richardson, TX, USA
e-mail: rbaughman@utdallas.edu; Ray.Baughman@utdallas.edu

S.J. Kim

Center for Self-Powered Actuation and Department of Biomedical Engineering, Hanyang
University, Seoul, South Korea
e-mail: sjk@hanyang.ac.kr

Abstract

Inserting twist into carbon nanotube fibers has enabled novel actuation mechanisms that result in both rotating and linear translational movement. Heating the carbon nanotube fibers generates a volume increase that drives a partial untwist of the fiber. The process is reversible upon cooling with the aid of a return spring mechanism. The actuation can be magnified by incorporation of a guest material, such as paraffin wax. The torsional stroke and/or torque can be used to perform useful work, such as the rotation of an attached paddle for fluid mixing. Various device configurations are possible and can be modeled by torsion mechanics. Tensile contraction also occurs during fiber untwist and can be greatly magnified by overtwisting the yarns to form spring-like coils. The high conductivity of the carbon nanotube yarns facilitates the convenient electrical heating and control giving high stroke, long-life, and rapid tensile and torsional actuation. This chapter summarizes the methods to produce guest-filled carbon nanotube yarns and the configurations that can be employed to generate either torsional or tensile actuation.

Keywords

Artificial muscles • Carbon nanotube • Electrothermally actuators • MWNT yarn

1 Introduction

Actuating materials, or “artificial muscles,” continue to attract a great deal of interest because of the need to provide compact, lightweight means to mechanically power everything from robots, exoskeletons, and medical prosthetics to micro-fluidic circuits and micro-tools. Carbon nanotube actuators have been known for some time (Baughman et al. 1999), but performance limitations have restricted application. The recent discoveries that carbon nanotube yarns generate giant torsional (rotational) actuation (Foroughi et al. 2011) and the conversion of torsion actuation to powerful tensile actuation in coiled yarns (Lima et al. 2012) have increased the performance and potential application areas for carbon nanotube actuators. The properties of the carbon nanotubes (CNTs) combined with the extreme twist insertion in CNT yarns are the source of the large torsional and tensile actuation strokes.

The first observation of torsional actuation in CNT yarns was an accidental discovery that occurred during routine electrochemical characterization of yarn capacitance. A single piece of yarn immersed in liquid electrolyte and connected at one end to a potentiostat was observed to slowly rotate as the electrochemical potential applied to the yarn was changed. The direction of yarn rotation depended on voltage scan direction. The first systematic studies of the phenomenon also used electrochemical stimulation and led to the discovery of giant torsional actuation strokes of up to 250°/mm rotation per actuating yarn length with speeds of 600 rpm (Foroughi et al. 2011). These large torsional actuation strokes were at least 1,000 times higher than for previously reported torsional actuators based on shape memory

alloys and ceramic piezoelectric materials. These initial studies also demonstrated that the torsional actuation was a result of yarn volume increase that accompanies electrochemical charging. Subsequent work led to non-electrochemical means to generate yarn volume change, such as simple absorption of solvent or, more usefully, the electrothermal expansion of an incorporated guest material. The latter enabled fully dry torsional actuation systems that did not require the electrolyte, counter electrode, and packaging needed for electrochemically driven actuators.

In this chapter, we review the methods used to fabricate CNT hybrid yarns and describe configurations used to demonstrate and optimize both torsional and tensile actuation. Although actuation can be stimulated electrochemically, optically, chemically, and thermally, we here concentrate on the electrothermal method for actuating the CNT yarns.

2 Carbon Nanotube Yarns, Hybrid Yarns, and Coiled Yarns

Carbon multiwalled nanotube (MWNT) forests that can be drawn to produce sheets of oriented CNTs were used to prepare CNT yarns. The CNTs were grown by chemical vapor deposition using acetylene (C_2H_2) gas and a silicon wafer coated with a 1–3 nm thick iron catalyst layer by e-beam evaporation (Fig. 1a). This substrate was heated to 700 °C in a mixture of 750 sccm Ar and 100 sccm H_2 . A nanotube forest consisting of ~ 400 μm high-carbon MWNTs was grown in 2–5 min after introduction of 50 sccm of C_2H_2 to this gas mixture. Transmission and scanning electron microscope (SEM) images indicate that the MWNTs have an outer diameter of ~ 12 nm, contain ~ 9 walls, and form large bundles. Thermogravimetric analysis shows that the content of noncombustible material, such as residual catalyst, in the drawn nanotubes is below 1 wt% (Zhang et al. 2004, 2005).

2.1 Yarn Fabrication

CNT yarns could be readily prepared in three different scroll geometries, Fermat, Archimedean, and dual Archimedean (Lima et al. 2011), and with controlled diameter and twist angle. Twist insertion during sheet draw from a forest provides a Fermat scroll (Fig. 2h) or an Archimedean scroll, depending upon whether the applied stress on the spinning triangle is symmetric or highly asymmetric, respectively. Alternatively, symmetrically twisting a pre-drawn nanotube sheet suspended between two rigid end supports generates a dual-Archimedean scroll (Fig. 2i). The yarn diameter could be conveniently varied from ~ 10 to ~ 30 μm by changing the drawn forest width from ~ 0.5 to ~ 5 cm. Much larger diameter dual-Archimedean yarns were typically fabricated by stacking 20–40 sheets (1.0–2.5 cm wide and 5–17 cm long) between rigid rods and inserting twist using an electric motor, while one end of the sheet stack supported a 5 g weight that was tethered to prohibit rotation. Approximately 150 turns were necessary to collapse a 5 cm long sheet stack into a 4.5 cm long yarn having dual-Archimedean structure.

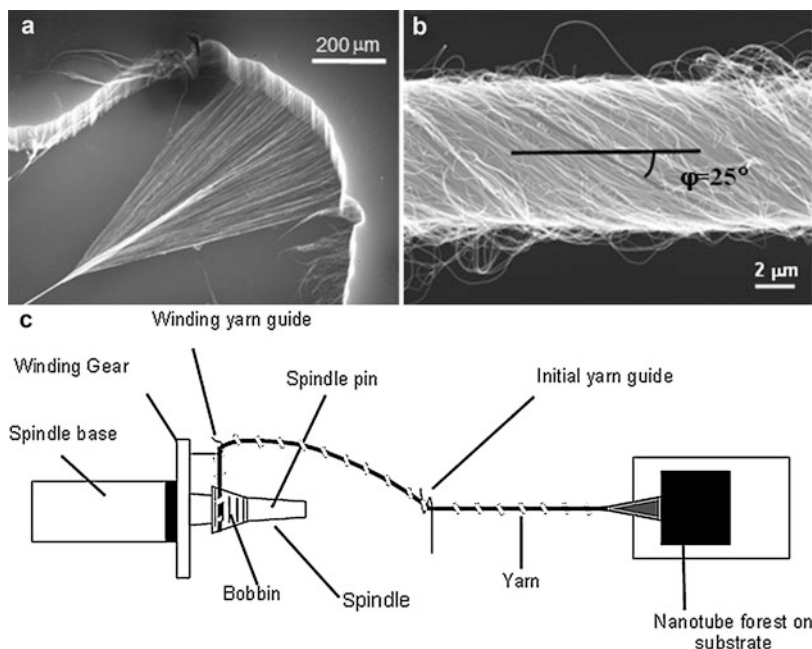
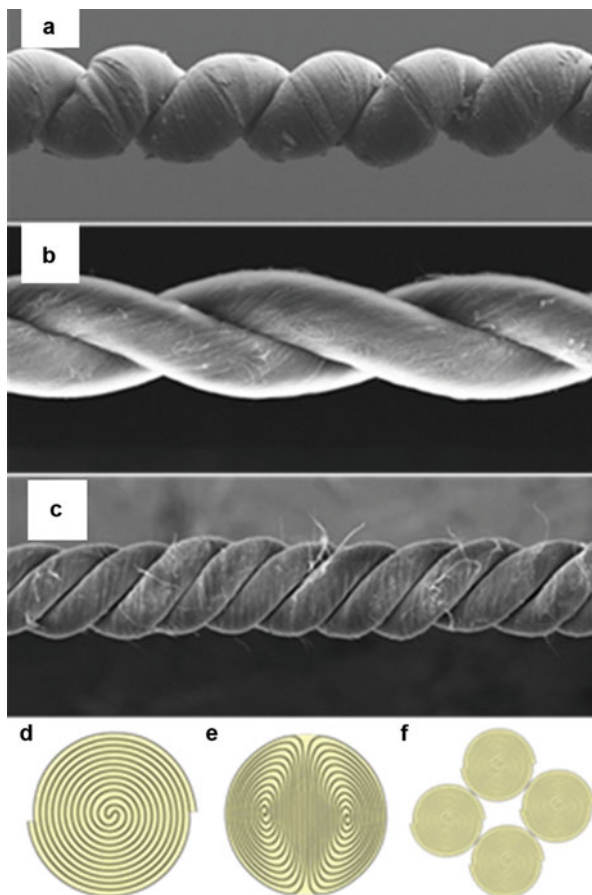


Fig. 1 (a) SEM micrograph of an MWNT forest being twist spun into a CNT yarn, (b) SEM micrograph of a carbon nanotube yarn that was symmetrically twist spun from a MWNT forest, and (c) schematic illustration for the spinning of an MWNT yarn from a MWNT forest (From Zhang et al. (2004). Reprinted with permission from AAAS)

The amount of inserted twist can be used to modify yarn properties. Yarn diameter (d) and the bias angle (α) between the nanotube orientation on the yarn surface and the yarn direction were measured by SEM. Typical values of d and α are $\sim 10\text{--}20\ \mu\text{m}$ and 25° , respectively, for an inserted twist T of 20,000 turns/m of yarn. For Fermat yarns, the theoretical relationship $\alpha = \tan^{-1}(\pi dT)$ is consistent with observations, despite the complex nature of the actual yarn structure. According to the direction of twist insertion, yarns are classified as S or Z yarns (for clockwise and anticlockwise twist insertion, respectively). Plyed yarns could also be prepared simply by folding a highly twisted yarn upon itself. The two yarn pieces spontaneously wrap to form a stable ply. The ply twist is in the opposite direction to the yarn twist, so the yarn is called heterochiral (as opposed to homochiral).

Coiled yarns were typically fabricated by inserting additional twist at constant yarn tension until the yarn contracted to 30–40 % of its original length. For a dual-Archimedean yarn made under 4 g load by twist insertion in a stack of 40 co-oriented, 9 mm wide, 15 cm long sheets, coiling started at ~ 580 turns, and the yarn was completely coiled after ~ 620 turns.

Fig. 2 The structures of MWNT yarns used for tensile and torsional actuation. SEM micrographs of (a) a fully infiltrated coiled yarn, (b) a neat two-ply yarn, and (c) a neat four-ply yarn. Illustration of ideal cross sections for (d) Fermat, (e) dual-Archimedean, and (f) infiltrated four-ply Fermat yarns (From Lima et al. (2012). Reprinted with permission from AAAS)



2.2 Hybrid Yarn Muscles

Various “hybrid” yarns were prepared by incorporating a guest material into the pore space between MWNT bundles. In most studies, the incorporated guest was Sigma-Aldrich 411671 wax, which comprises a mixture of alkanes. This wax fully melts at ~ 83 °C, expands by ~ 20 % between 30 °C and 90 °C during solid-state transitions and melting, and provides ~ 10 % additional volume expansion between 90 °C and 210 °C (Lima et al. 2012).

MWNT yarns were typically infiltrated with sufficient paraffin wax to fill internal pores, while avoiding formation of non-infiltrated surface wax. Using the “hot wire method,” a two-end-tethered, twist-spun yarn, under constant tensile load, was electrically heated to above the melting point of the paraffin wax and then contacted with a small amount of solid paraffin. The paraffin quickly spread through the yarn volume. Since excess paraffin on the yarn surface degrades actuation, the yarn was

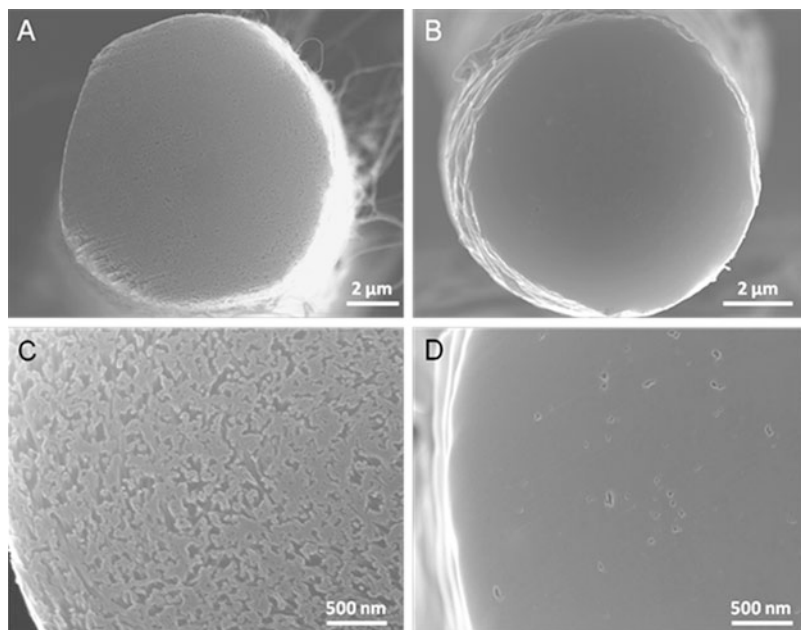


Fig. 3 SEM micrographs of the cross section of a non-coiled Fermat carbon nanotube yarn before (a, c) and after (b, d) wax infiltration. Pores shown in the high-magnification image of the neat yarn (c) are not visible in the corresponding image for the wax hybrid yarn (d). The diameter of the wax hybrid yarn ($8.2 \pm 0.3 \mu\text{m}$) was less than that of the neat yarn ($10.4 \pm 0.3 \mu\text{m}$) because additional twist was inserted in the yarn before wax solidification (From Lima et al. (2012). Reprinted with permission from AAAS)

electrically heated to above the evaporation temperature of the paraffin ($\sim 233^\circ\text{C}$) until no excess paraffin was observed on the yarn surface. Another wax infiltration method is to slowly immerse a two-end-tethered, as-spun yarn into melted paraffin ($\sim 0.1 \text{ cm/s}$), which the yarn is under constant tensile load. Other guest materials could also be incorporated into the CNT yarns by the immersion method. In one example, mixtures of paraffin wax and polystyrene-poly(ethylene-butylene)-polystyrene (SEBS) copolymer were dissolved in toluene and yarn immersed in this solution (Chun et al. 2014).

The extent of guest infiltration was determined by SEM microscopy of the yarn's cross section (Fig. 3). Neat and paraffin wax hybrid MWNT yarns were cut along their diameters using Ga ions (5 nA beam current) in a focused ion beam (FIB, Nova 2000) operated at 30 kV. The obtained cross sections were cleaned (via ion polishing) by etching several micrometers of yarn length with consecutively decreasing ion currents ranging from 3.0 to 0.3 nA. These cut yarns were next transferred to a Zeiss Supra 40 SEM in order to perform microscopy (at 15 kV). The SEM micrographs of Fig. 3 show that the porosity of the neat yarn has been largely eliminated by wax infiltration using the above slow immersion method.

3 Device Configurations

The basic configuration to demonstrate torsional actuation is simple. In the first electrochemical experiments, a vertically suspended actuating yarn was fully immersed in the electrolyte (0.2 M tetrabutylammonium hexafluorophosphate, TBAPF₆, in acetonitrile) with counter and reference electrodes. The yarn supported a paddle at its lower end (Fig. 4a). In this configuration reversible torsional actuation during a voltage cycle was approached only after many cycles, which progressively decrease torsional stroke. To improve reversibility, the yarn was tethered at both ends to prohibit end rotation (Fig. 4b) and used only part of the yarn as a torsional muscle (e.g., by immersing only part of the yarn in the electrolyte or filling only one half of the yarn with wax). Though torsional actuation decreased, reversibility improved since the non-actuating length of the yarn functioned as a torsional spring to return the paddle to starting angle. In this configuration the nonuniformity of actuation is essential, since a uniformly actuated yarn cannot produce torsional rotation in the two-end-tethered configuration.

Analysis of the torsional stroke involves consideration of the actuator geometry and method of tethering. First consider a vertically hanging yarn of length L_A that is clamped at the top end and free to rotate at the opposite end, where a paddle is attached (Fig. 4c). The actuating yarn generates a rotation per yarn length of $\Delta\theta$ when activated (electrochemically charged or heated) while tethered at only one end. The rotation at any distance x from the tethered end is simply $\phi(x) = x\Delta\theta$. Clamping the yarn at both ends restricts rotation at all points along the yarn by generating equal

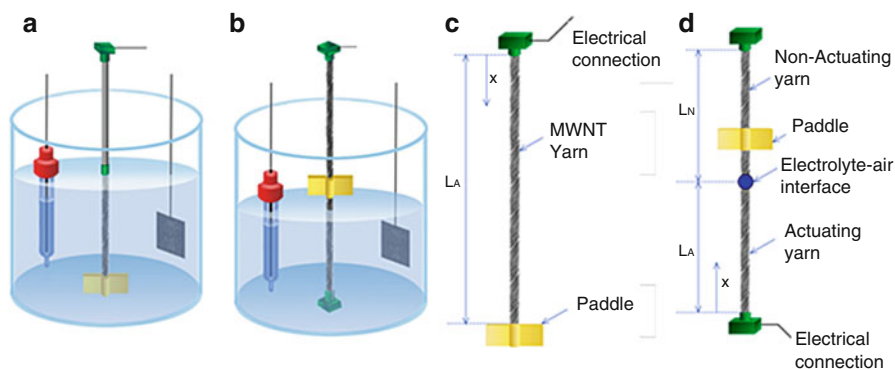


Fig. 4 (a, b) Illustration of electrochemical cell configurations used for characterizing torsional actuation or the combination of torsional and tensile actuation, where the reference electrode, actuating MWNT yarn electrode, and Pt mesh counter electrode are from left to right. (c) A one-end-tethered yarn configuration in which a paddle, located at yarn end, rotates in the electrolyte. (d) A yarn configuration in which the yarn is two-end tethered to prevent torsional rotation and the paddle is located far from the yarn ends. In b and d the top yarn support is a force/distance transducer that maintains constant tensile force on the yarn and measures the axial length change as the paddle rotates in air (in other cases, the electrolyte level was raised to submerge the paddle) (From Foroughi et al. (2011)). Reprinted with permission from AAAS)

and opposite torques in the actuating and non-actuating segments, as illustrated in Fig. 4d. The net rotation, $\phi(x)$ occurring at any point x along the yarn is given by:

Rotation in actuating yarn segment:

$$0 \leq x \leq L_A \quad \phi(x) = (x\Delta\theta) \left(\frac{\beta}{\beta + \gamma} \right) \quad (1)$$

Rotation in non-actuating yarn segment:

$$L_A \leq x \leq (L_A + L_N) \quad \phi(x) = (L_A\Delta\theta) \left(\frac{L_A + L_N - x}{L_N} \right) \left(\frac{\beta}{\beta + \gamma} \right) \quad (2)$$

where β is the ratio of the torsional modulus of the actuating and non-actuating yarn and γ is the ratio of the actuating yarn length to non-actuating yarn length. The above described $\Delta\theta$ is a fundamental torsional parameter that is directly related to the mechanism of torsional actuation. This parameter can be used to derive torsional rotation for yarns in various configurations. As simple examples, $\phi_f = L_A\Delta\theta$ for the free-end rotation for one-end tethering, and $\phi_{\max} = \frac{1}{4} L_A\Delta\theta$ for the maximum rotation in the two-end-tethered configuration (which occurs at the midpoint of a half-active yarn), when β is approximated to be one.

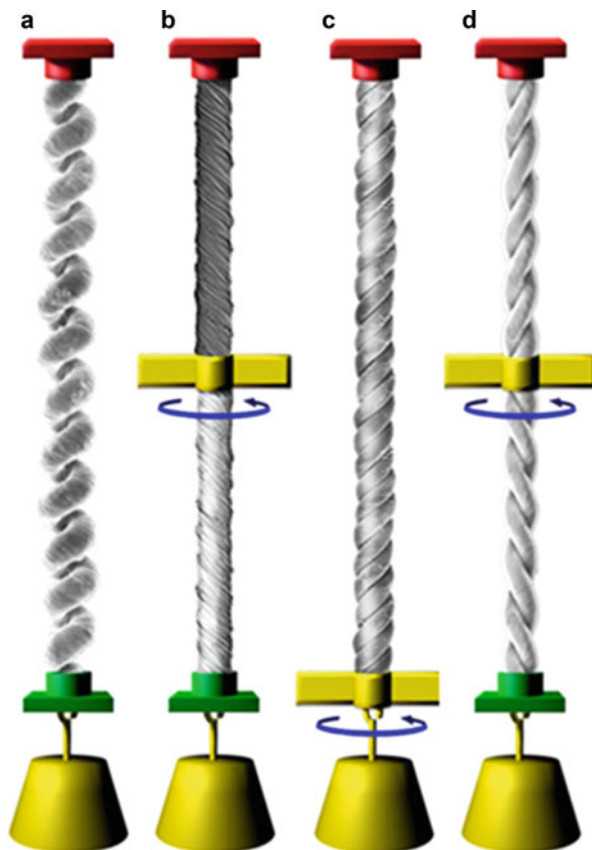
Additional configurations for yarn actuation are illustrated in Fig. 5. As described above, overtwisting of yarns produces coils that can be shape fixed by the incorporation of solid guest. In addition, multiple yarns can be plied together. Finally, yarns that are tethered at both ends can be configured as either homochiral or heterochiral. In the former, the twist direction is uniform along the entire length and torsional actuation is only possible when part of the yarn is activated. In the heterochiral configuration, the system consists of two yarns having opposite twist. Now torsion is possible when the both parts of the yarn are activated.

4 Torsional Actuation Performance

4.1 Wax-Filled Single-Ply Yarn Muscles

Very fast, highly reversible electrothermal torsional actuation was demonstrated half-wax-infiltrated homochiral Fermat yarn that was tethered at both ends and rotated a paddle at yarn midpoint (Fig. 5b configuration). The hybrid yarn accelerated a 16.5 times heavier paddle to a full-cycle-averaged 11,500 rotations per minute – first in one direction and then in reverse (Fig. 6a). Over two million actuation cycles were observed without significant degradation. Even though actuation temperature was far above the wax melting, this high cycle life resulted because the unactuated yarn segment acted as a torsional “return spring.” Figure 6b shows the dependence of torsional rotation on input electrical power and applied tensile load for a similar yarn that rotated a 150 times heavier paddle for a million highly reversible cycles. Increasing tensile load increased rotation speed from 5,500 rpm to a maximum of 7,900 rpm.

Fig. 5 Muscle configurations for tensile and torsional actuation in wax-filled hybrid CNT yarns. Tensile load and paddle positions for (a) a two-end-tethered fully infiltrated homochiral yarn; (b) a two-end-tethered, bottom-half-infiltrated homochiral yarn; (c) a one-end-tethered, fully infiltrated homochiral yarn; and (d) a two-end-tethered, fully infiltrated heterochiral yarn. The depicted yarns are coiled, non-coiled, four ply, and two ply, respectively. *Arrows* indicate the observed direction of paddle rotation during thermal actuation. *Red* and *green* yarn-end attachments are tethers, meaning they prohibit end rotation; *red* attachments also prohibit translational displacement (From Lima et al. (2012). Reprinted with permission from AAAS)



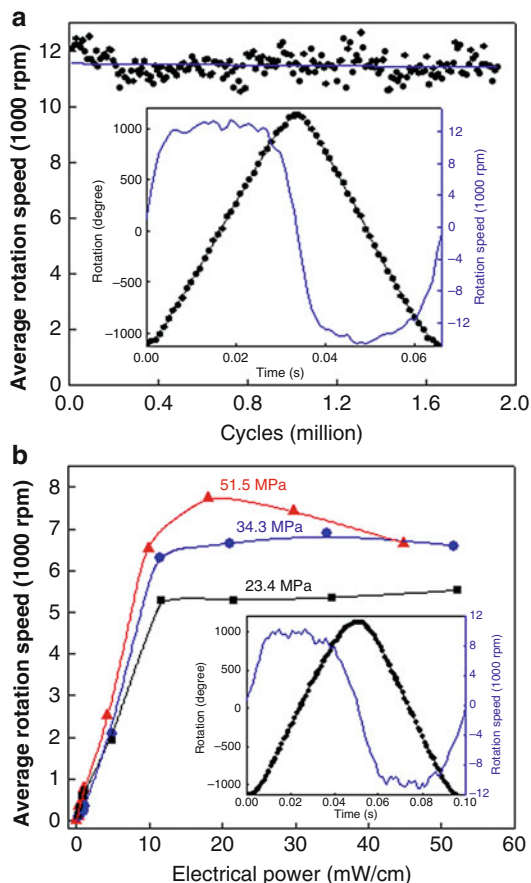
Highly reversible actuation was also achieved in one-end-tethered (Fig. 5c) and heterochiral systems (Fig. 5d) when the applied temperature was kept below the wax melting point. In such cases, the elastic deformation of the solid wax acted as the return mechanism. Actuation for these configurations became increasingly irreversible at higher temperatures, especially when mechanical load was large, and cycling to above temperatures where melting is complete caused large permanent untwist. This problem does not arise for two-ply yarns where ply and yarn directions are opposite – since the sum of yarn twist and the twist of yarn plying is conserved during heating.

4.2 Overdamped Hybrid Yarn Muscles

Rapid heating of the wax-filled CNT yarns results in rapid acceleration of attached paddles. Such systems are underdamped oscillators (Chun et al. 2014) when

Fig. 6 Torsional actuation for two-end-tethered, wax-infiltrated yarns.

(a) Average rotation rate versus cycle number for a 6.9 cm long, half-infiltrated, homochiral Fermat yarn (10 μm diameter and $\sim 22,000$ turns/m twist), when excited by a 15 Hz, 40 V/cm, square-wave voltage using 50 % duty cycle and 41 MPa applied load. Each point on the graph is the average speed over 120 cycles. Inset: rotation angle and rotation speed versus time for one complete cycle. (b) Average rotation rate versus applied electrical power for different tensile loads when using the yarn in (a) and a heavier paddle. Inset: rotation angle and speed versus time for 51.5 MPa load (From Lima et al. (2012). Reprinted with permission from AAAS)



heated using a square-wave electric pulse (Fig. 7a). Replacing the wax guest material with a blend of paraffin wax with polystyrene-poly(ethylene-butylene)-polystyrene (SEBS) copolymer was used to tune damping. By using an 80 % wax, 20 % SEBS blend as yarn guest (which maximized viscoelastic loss), an overdamped dynamic response (Fig. 7a, b) was achieved, which provided the results of Fig. 7c. These results show a tenfold reduction in the time needed to achieve the final rotation angle compared with that for solely wax-filled yarns. The overdamped system generated rotation speeds of 9,800 rpm without noticeable oscillation for 40,000 cycles when excited by a 0.5 Hz square-wave voltage. Figure 7d shows that the damping ratio for torsional oscillations is correlated with the maximum high temperature damping loss coefficient $\tan \delta$ for the wax/SEBS mixture.

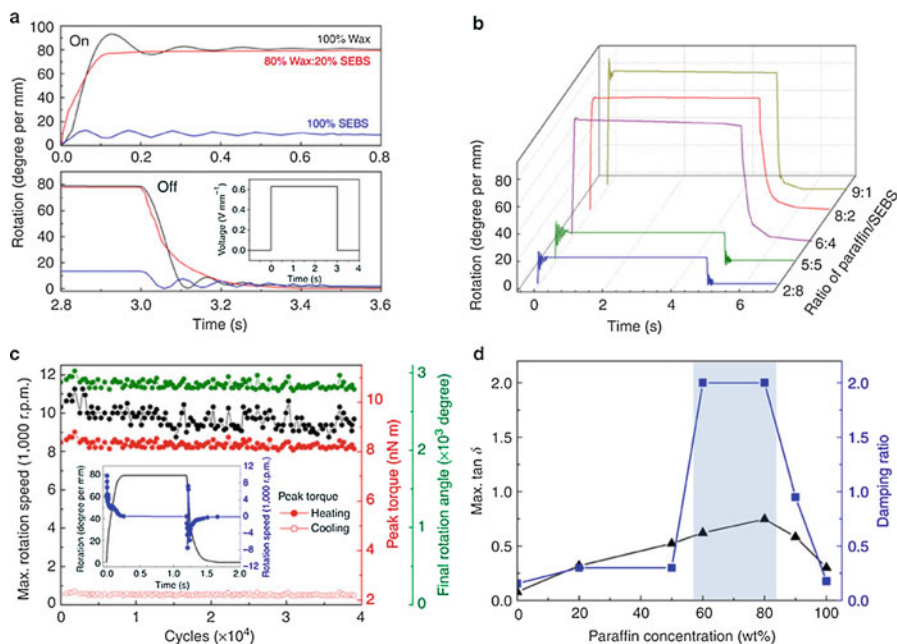


Fig. 7 (a) Torsional rotation versus time for hybrid yarn artificial muscles that are powered using the square-wave voltage input that is shown in the inset. The plots are for when the drive voltage is turned on (*top*) and turned off (*bottom*). The percent wax in the wax-SEBS yarn guest for the different hybrid yarns is as follows: 100 % wax (*black line*), 80 % wax (*red line*), and 0 % wax (*blue line*). (b) Rotation angle versus time for five different hybrid yarns with different ratios of wax to SEBS; (c) maximum rotation speed (*black solid circles*), final rotation angle (*green solid circles*), and peak torque (*red solid circles*) versus cycle number for a hybrid yarn containing 8:2 wax-SEBS yarn guest, when excited by a 0.5 Hz square-wave voltage to 0.63 V/mm using 50 % duty cycle. The open circles provide the peak torque during the cooling part of the torsional actuation cycle. Inset: rotation angle and rotation speed versus time for one complete cycle. (d) The maximum high temperature damping loss coefficient $\tan \delta$ and the damping ratio for torsional relaxation on torsional oscillations as a function of wt% paraffin wax in the wax-SEBS mixture within the hybrid yarn muscle. The *blue* area indicates the wt% of wax where overdamped torsional response is obtained (Reprinted by permission from Macmillan Publishers Ltd: [Nature Communications] (Chun et al. 2014), copyright (2014))

5 Tensile Actuation Performance

5.1 Neat-Twisted Yarns

Experimental data on tensile actuation versus twist insertion for neat non-coiled MWNT yarns shows the importance of twist on thermal contraction (Fig. 8). Although only small actuation strains of less than 0.1 % were observed in these neat, non-coiled Fermat yarns, a clear increase in thermal contraction was evident in yarns prepared with higher twist. With increase of inserted twist from $\sim 9,650$ to

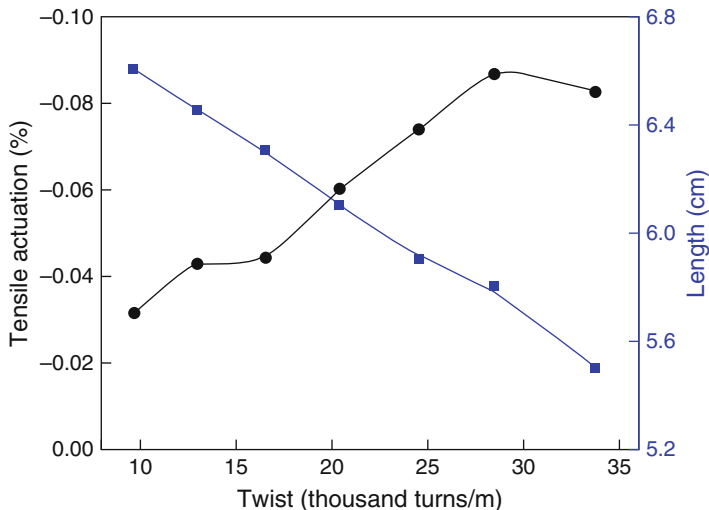


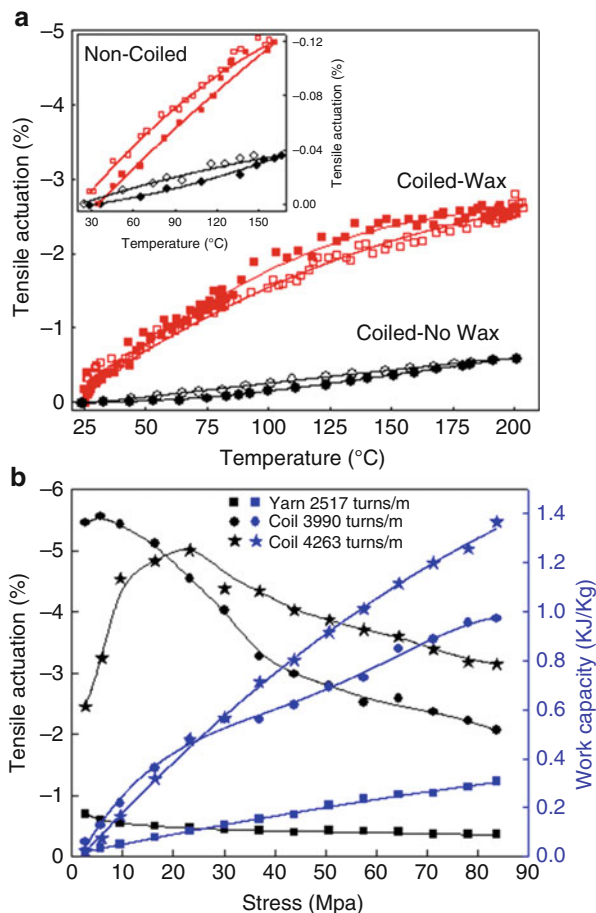
Fig. 8 Tensile actuation as a function of inserted twist for a neat 13.5 μm diameter Fermat yarn. The amount of steady-state electrical power applied to obtain yarn contraction was constant ($85 \pm 2.6 \text{ mW/cm}$) when normalized to the measured yarn length for each degree of twist, so the input power per yarn weight was also constant. Mechanical load was constant and corresponded to 72 MPa. The lines are guides for the eyes (From Lima et al. (2012). Reprinted with permission from AAAS)

$\sim 28,130$ turns/m, the magnitude of tensile actuation at constant applied power increased ~ 2.8 times (from $\sim 0.03\%$ to $\sim 0.086\%$). However, when the start of coiling was first observed (at 33,800 turns/m), there was small decrease in thermal contraction, which might be due to the predominance of non-coiled yarn segments in providing contraction when there is little coiling and the effect of introduced coiling on decreasing modulus.

5.2 Wax-Filled Twisted and Coiled Yarns

Tensile contractions versus temperature for non-coiled and coiled CNT yarn, before and after wax infiltration, are compared in Fig. 9. Wax infiltration greatly enhanced tensile contraction for all yarns. When heated from ambient to 175°C , twisted neat CNT yarns contracted -0.4% , while the equivalent wax-filled hybrid yarn contracted -2.2% (Fig. 9a). Yarn coiling has an even greater impact on tensile actuation when both yarns are wax filled. In this case, coiling increased tensile by a factor of ~ 10 compared with that for non-coiled yarns over the same temperature range (Fig. 9a, b). The 10X to 20X stroke amplification due to coiling is much larger than the $\sim 3\text{X}$ higher fiber length in a coiled yarn than in a twisted yarn having the same overall length. Such large amplification follows from coupling between yarn torsional actuation and coil tensile actuation and is analogous to the relationship

Fig. 9 Thermal tensile actuation for two-end-tethered homochiral yarns. **(a)** Tensile actuation strain versus temperature before (*black*) and after (*red*) wax infiltration for a coiled, dual-Archimedean yarn having 130 μm initial diameter, an inserted twist of $\sim 4,000$ turns/m (per length of the precursor sheet stack), and an applied stress of 6.8 MPa. Inset: corresponding actuation data before (*black*) and after (*red*) wax infiltration for a non-coiled Fermat yarn having 16 μm initial diameter, $\sim 20,000$ turns/m twist, and an applied stress of 4.8 MPa. **(b)** The stress dependence of steady-state tensile actuation and contractile work (*black* and *blue* data points, respectively) produced by Joule heating (0.189 V/cm) for a 150 μm diameter, wax-filled dual-Archimedean yarn having different levels of inserted twist (From Lima et al. (2012). Reprinted with permission from AAAS)



between wire twisting and the elongation of a helical wire spring (Haines et al. 2014).

Applied tensile load had a significant effect on both actuator stroke and work capacity during contraction. Figure 9b shows the stress dependence of actuator stroke and work capacity for different amounts of twist insertion in a wax-infiltrated, 150 μm diameter, dual-Archimedean yarn that is two-end tethered. Applying high stress decreases stroke, due to the yarn's lower Young's modulus in the contracted state (containing molten wax) and correspondingly larger elastic elongation under load than the initial state. The stroke for highly coiled yarn decreases at low stresses, which is consistent with contact between adjacent coils hindering contraction. Figure 9b shows that there is an optimal amount of coiling that maximizes either stroke or work during contraction for the wax hybrid yarn. A maximum contraction of 5.6 % was observed at 5.7 MPa stress for a coiled Fermat yarn having intermediate twist. Adding 6.8 % more twist to the coiled yarn increased

the stress of maximum contraction (16.4 MPa for 5.1 % strain) and the maximum measured contractile work (1.36 kJ/kg at 84 MPa), which is 29 times the work capacity of natural muscle (Peterson and Bronzino 2008). Subsequently reducing twist by 41 % eliminated coiling and reduced maximum contraction and contractile work to low values (0.7 % and 0.31 kJ/kg, respectively).

Very fast tensile actuation could be achieved by rapid heating and cooling. A two-end-tethered, wax-filled, coiled Fermat yarn actuated using a 20 Hz, 18.3 V/cm square wave at 50 % duty produced 3 % stroke at 1,200 cycles per minute. This system operated stably for over 1.4 million cycles (Fig. 10a) with the yarn lifting 17,700 times its own weight during each contraction. Fast passive cooling in 25 ms resulted from the small yarn and coil diameters (11.5 μm and 20 μm , respectively). A much longer cooling time of ~ 2.5 s was required for the 150 μm diameter, partially coiled, dual-Archimedean yarn of Fig. 10c. Rapid heating produced contractions of 10 % under 5.5 MPa stress. However, the comparatively slow cooling resulted in a low contractile power density when both heating and cooling times are considered (0.12 kW/kg). The higher applied stress applied to the Fermat hybrid yarn of Fig. 10b compared with Fig. 10a increased the work during contraction (0.836 kJ/kg) and provided a power output of 27.9 kW/kg, which is 85 times the peak output of mammalian skeletal muscles (0.323 kW/kg) (Josephson 1993) and 30 times the measured power density of previous carbon nanotube muscles (Foroughi et al. 2011). However, the high applied electrical power reduced cycle life by causing excessive heating and corresponding slow paraffin evaporation.

6 Conclusion

The development of twisted and coiled carbon nanotube yarns has provided novel high-performance torsional and tensile actuators. The first generation of torsional CNT yarns artificial muscles were operated by electrochemical double-layer charge injection, like for carbon nanotube supercapacitors. The extreme twist insertion in these CNT yarns, combined with the volume expansion occurring during electrochemical charging, generated giant torsional actuation strokes of up to 250 $^\circ/\text{mm}$ with speeds of 600 rpm. The experimentally derived peak power output per weight of electrochemically actuating yarn was 71 W/kg.

The practical limitations of the electrochemical CNT yarn actuators were overcome in the second-generation hybrid materials that used an incorporated guest material to generate the required volume change. Such systems could operate in air or in liquids and did not require the electrolyte, additional electrodes, and packaging needed for the electrochemical systems. Hybrid yarns could be conveniently controlled using electrothermal means by taking advantage of the highly conducting CNT yarn host. The maximum torsional strokes of $\sim 60^\circ/\text{mm}$ for these electrothermally actuated CNT yarns containing paraffin wax guest were smaller than the largest strokes obtained electrochemically. However, rotation speeds were considerably higher (up to 11,500 rpm), and the systems operated stably for more than one million cycles.

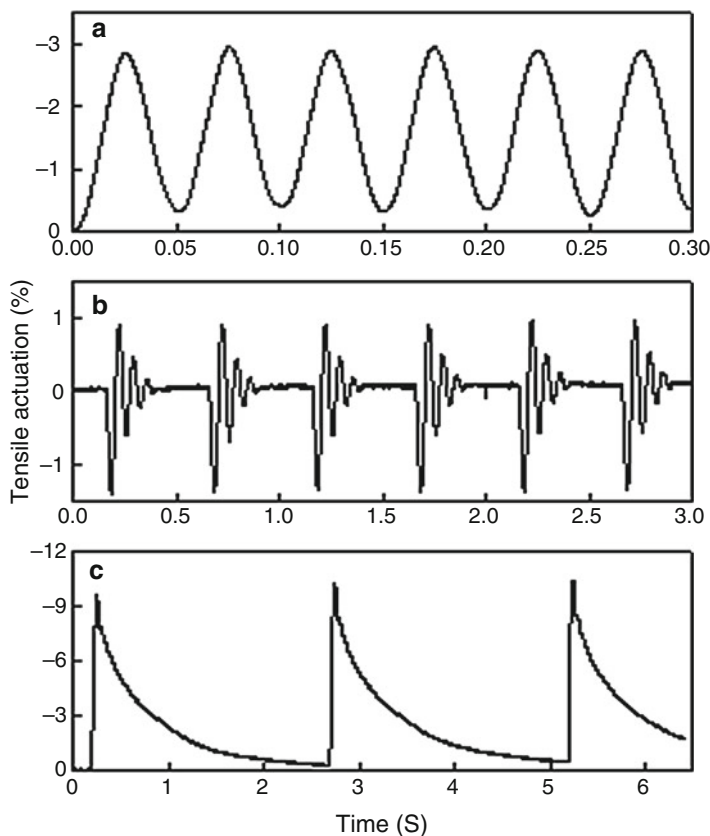


Fig. 10 Electrothermal tensile actuation for two-end-tethered, homochiral, wax-filled coiled CNT yarns. **(a)** Tensile actuation strain versus time after 1,400,000 reversible cycles for an 11.5 μm diameter, coiled Fermat yarn having $\sim 25,000$ turns/m twist when driven by a 18.3 V/cm, 20 Hz symmetric square-wave voltage while lifting a load that provided a 14.3 MPa stress. **(b)** Tensile actuation for the yarn of **(a)** with 109 MPa applied tensile stress when driven at 3 % duty cycle by 15 ms, 32 V/cm square-wave voltage pulses having a period of 500 ms. **(c)** Tensile strain versus time for a 150 μm diameter, dual-Archimedean yarn with 3,990 turns/m of inserted twist per precursor sheet stack length, when supporting a 5.5 MPa tensile stress and driven by a 15 V/cm square wave having 50 ms pulse duration and 2.5 s period (From Lima et al. (2012). Reprinted with permission from AAAS)

Tensile actuation was also demonstrated in all twisted CNT yarns, while stroke, work, and power outputs were dramatically increased by incorporation of yarn guest and by overtwinning the yarn to form coils. Fast, highly reversible tensile actuation was demonstrated for paraffin-wax-filled yarns. Strokes of up to 10 % were observed in coiled, wax-filled yarns. For small diameter yarns, actuation at 1,200 cycles per minute giving 3 % stroke was demonstrated for over 1.4 million cycles. In the tensile mode, power outputs during contraction reached 27.9 kW/kg or 85 times that of skeletal muscle.

These performance characteristics make CNT-twisted yarn muscles attractive for high-value applications requiring small weights of CNT yarn, since CNT yarns are presently expensive. To avoid this cost problem, technological advances have been very recently extended to twisted and coiled, highly oriented polymer fibers, such as fishing line and sewing thread (Haines et al. 2014). While impressive performance has been demonstrated to date, further work is needed to improve the energy conversion efficiency. At present, the highest realized efficiency for conversion of electrical energy to mechanical energy is $\sim 0.5\%$ for CNT hybrid yarns and $\sim 2\%$ for coiled polymer fibers. Another problem for certain applications is the high operating temperatures needed to obtain giant strokes.

References

- Baughman RH, Cui C, Zakhidov AA et al (1999) Carbon nanotube actuators. *Science* 284:1340–1344
- Chun K-Y, Kim SH, Shin MK et al (2014) Hybrid carbon nanotube yarn artificial muscle inspired by spider dragline silk. *Nat Commun* 5:3322
- Foroughi J, Spinks GM, Wallace GG et al (2011) Torsional carbon nanotube artificial muscles. *Science* 334:494–497
- Haines CS, Lima MD, Li N et al (2014) Artificial muscles from fishing line and sewing thread. *Science* 343:868–872
- Josephson RK (1993) Contraction dynamics and power output of skeletal-muscle. *Annu Rev Physiol* 55:527–546
- Lima MD, Fang S, Lepró X et al (2011) Biscrolling nanotube sheets and functional guests into yarns. *Science* 331:51–55
- Lima MD, Li N, Jung De Andrade M et al (2012) Electrically, chemically, and photonically powered torsional and tensile actuation of hybrid carbon nanotube yarn muscles. *Science* 338:928–932
- Peterson DR, Bronzino JD (2008) *Biomechanics; principles and applications*. Scitech Book News. Ringgold Inc, Portland
- Zhang M, Atkinson KR, Baughman RH (2004) Multifunctional carbon nanotube yarns by downsizing an ancient technology. *Science* 306:1358–1361
- Zhang M, Fang S, Zakhidov AA et al (2005) Strong, transparent, multifunctional, carbon nanotube sheets. *Science* 309:1215–1219

Electrochemically and Electrothermally Driven Carbon-Based Materials as EAPs: How to Start Experimenting with Them

20

Indrek Must, Geoffrey M. Spinks, and Alvo Aabloo

Contents

1	Introduction	472
2	The Choice of Materials	473
2.1	Electrothermally Driven Actuators	473
2.2	Electrochemically Driven Actuators	474
3	Electrical Control	475
3.1	Control for Electrothermally Driven Actuators	475
3.2	Control for Electrochemically Driven Actuators	476
3.3	Working Voltage and the Effect of Ambient Humidity	479
4	Characterization of the Actuators	480
4.1	Electrical Characterization	481
4.2	Mechanical Characterization	481
4.3	Electromechanical Characterization	482
	References	484

Abstract

Carbon is a distinctive electrode material for actuators, as it is available in a wide variety of forms, ranging from monoliths to powders, fibers, and yarns. The diversity in the properties of different carbonaceous materials is also expressed in a variety of actuation mechanisms. This chapter considers two classes of actuators – electrochemically and electrothermally driven actuators – which both make use of carbonaceous materials as active elements. In both of the listed types of actuators, carbon is especially advantageous because of its chemical and

I. Must (✉) • A. Aabloo

IMS lab, Institute of Technology, University of Tartu, Tartu, Estonia

e-mail: indrekm@ut.ee; alvo.aabloo@ut.ee

G.M. Spinks

ARC Centre of Excellence for Electromaterials Science, Intelligent Polymer Research Institute,
University of Wollongong, North Wollongong, NSW, Australia

e-mail: gspinks@uow.edu.au

thermal inertness and also because of its high intrinsic electrical conductivity. The working principles of different actuators, having carbonaceous electrodes, are drastically different and so are the optimization criteria for selecting a particular type of carbon for a particular type of actuator. This chapter is to explain some important practical considerations for successful experimentation with the carbon-based actuators. Special attention is bestowed on the choice of materials and the choice of appropriate electrical driving signal. The effects caused by the ambient environment are discussed. Finally, a selection of commonly used characterization methods is suggested.

Keywords

Actuators • Electrochemical impedance spectroscopy (EIS) • Electrochemically driven actuators • Voltage vs. current control • Electromechanical characterization • Electrothermally driven actuators • Ionic liquids (IL) • Pulse-width-modulated (PWM) control signal

1 Introduction

When starting experimentation with any type of actuator, their particularly distinctive characteristics, and possible multifunctional nature, should be considered, as they can be essential in consideration of possible applications and characterization methods for the particular types of actuators.

In the electrothermally driven actuators, synergistic effect between a carbon filament as the host material and a polymeric filler, having large thermal expansion coefficient, is achieved. These systems have only recently been described (Lima et al. 2012) and are based on electrochemically driven carbon nanotube yarn torsional actuators (Foroughi et al. 2011). The electrothermal systems also utilize carbon nanotube yarns but incorporate a guest material as filler. Electric heating causes guest volume expansion that then produces a combination of yarn torsion and lengthwise contraction.

Whereas electrothermally driven actuators, although more straightforward in their construction, have gained their popularity primarily during the past few years' time, the electrochemically driven actuators, having carbonaceous electrodes, have been first proposed in 1999 (Baughman et al. 1999). The working principle of the electrochemically driven actuators involves many concurrent mechanisms, the ratio of which is still under dispute to date. It is generally accepted that the strain difference between the oppositely charged electrodes is related to the shift in the local concentration of the electrolyte ions that accompanies with the buildup of electric double-layer (Kosidlo et al. 2013).

The introduction of carbonaceous electrode materials for the electrochemically driven actuators intersected two classes of electrochemical devices that were considered as being separate beforehand – the electromechanical actuators and the electric double-layer capacitors (also known as supercapacitors). Although the

conventional supercapacitors and the “conventional” electrochemically driven actuators have notable differences in their particular optimization parameters, their governing physical processes are virtually identical.

The similarity between the carbonaceous, electrochemically driven actuators, and the supercapacitors is particularly noteworthy. Among the wide range of existing types of “smart” actuators, whose working principle involves electro-osmosis of ions in the extent of a layered microporous laminate, the actuators with carbonaceous electrodes resemble the most to the supercapacitors. The high level of similarity is anticipated, as identical carbonaceous materials can be used in construction of either of the two devices – a supercapacitor (Simon et al. 2013) or an actuator (Kosidlo et al. 2013). After the introduction of carbon as the superior active material for the electrochemically activated actuators in 1999, the emerged types of actuators resembled to a great extent to the supercapacitors, which had been in commercial production for many decades already – since 1978 (Miller 2007). It has been demonstrated that (a) the electrochemically driven actuators have a decent energy-storage capability (Torop et al. 2009, 2011) and (b) opportune employment of the capacitive nature of the electrochemically driven actuators gives completely new functionalities to these laminates, originally intended for use as actuators (Must et al. 2013). In order to emphasize the capacitive nature of the electrochemically driven actuators, “actuating” and “charging” of this type of actuators are used as synonyms in this chapter.

The capacitive nature of the electrochemically driven actuators with carbonaceous electrodes is of particular importance to consider when starting experimentation with this type of actuators – the capacitive properties of the actuators determine the most suitable driving waveform and characterization methods.

2 The Choice of Materials

2.1 Electrothermally Driven Actuators

The electrothermally driven actuators benefit the most from carbons that have directional nanostructures, resulting in high mechanical yield strength, but also in sufficient electrical conductivity along the nanostructure direction. Twisted yarns of multiwalled carbon nanotubes are the most extensively studied of these relatively new actuator materials. Twisting the multiwalled CNTs adds considerable strength (Zhang et al. 2004), but the method of preparation also allows the ready addition of guest materials incorporated within the continuously twisted CNT bundles (Lima et al. 2011). Electrothermally activated hybrid CNT yarns have been produced by infiltrating twisted CNT yarns with molten paraffin wax. The yarns were prepared by drawing from a “forest” of CNTs produced by chemical vapor deposition. The drawn CNT sheet consists of interconnected and oriented multiwalled CNTs. Twist insertion produces the twisted yarn that is stable. “Overtwisting” generates a coiled yarn structure that is generally not stable when released. Dipping the yarn into molten wax fills the pore space with paraffin. Solidification of the wax by cooling can fix the

coiled structure when released. Other guest materials have also been incorporated into the twisted and coiled CNT yarns, including synthetic rubbers (Chun et al. 2014). Other host materials have also been recently reported like niobium nanowire yarns (Mirvakili et al. 2013).

2.2 Electrochemically Driven Actuators

In the selection of carbons for use as the electrode material in electrochemically driven actuators, the primary factor of choice is the specific surface area of the carbons. Generally, an actuator that has higher capacitance also has higher actuation performance; however, this principle is valid in the extent of the same electrode material only (Palmre et al. 2009).

The operating voltage of electrochemically driven actuators is low, in the range of several volts, but the driving currents are high. Due to high driving current, the electrochemically driven actuators demand high electronic conductivity along its electrodes. Activated carbon electrode materials with nondirectional nanostructures have only moderate bulk conductivity – for example, it is in the order of several tens of S cm^{-1} for carbide-derived carbons (Chmiola et al. 2006) or several S cm^{-1} for carbons derived from carbon aerogels (Simon et al. 2013). The conductivity of an actual electrode is considerably lower than that of the corresponding bulk electrode material – the conductivity is reduced due to contact resistance between the carbon grains next to each other and due to the use of binder polymer, which can form an insulation layer between the carbon grains (Must et al. 2012). In case of electrothermally driven actuators, low conductivity of the filament can merely limit its heating and actuation rate. In contrast, an electrode on an electrochemically driven actuator can be seen as a finite transmission line, significantly slowing down the signal propagation along its electrodes. In case of some particular configurations for the electrochemically driven actuators, such as the cantilevered laminate configuration, insufficient electronic conductivity along the actuator's electrodes can reduce or even exclude the contribution of some parts of the actuator to the total actuation.

The limited electronic conductivity of the activated carbon electrodes can be compensated by the use of thin and compliant current collector layers. The use of current collectors, having metallic conductivity, drastically increases the actuation speed (Torop et al. 2012). Due to the corrosive property of the electrolytes, especially under voltage applied to the system, the current collectors (but also the terminals connecting to the power supply) must be inert – gold and platinum are proven as stable current collector (and connector terminal) materials in long-term use. The thickness of the current collector layers is critical – on one hand, the current collector must be as thin as possible to achieve compliance to the electrode, but a current collector of nanoscale thickness can heat up as a result of high electrical currents involved during charging on the other. Monolithic sheets of metal, glued on top of the actuator's electrodes in the prebuckled state, provide the highest level of conductivity (Must et al. 2014a).

The use of carbon nanotubes, preferably of single-walled type, is one of the proposed solutions in construction of an efficient actuator without metal current collectors (Mukai et al. 2009). The omission of metallic current collectors is a considerable advantage, as it makes possible to construct completely metal-free actuators.

Ionic liquids (IL) are common electrolytes for use in ionic and capacitive actuators operable in air. IL fills the porous structure of the carbonaceous electrodes and the interconnected porous network in the polymeric separator in-between the electrodes. IL-incorporated polymer can be required also as a binder in the electrodes. As an advantageous property, carbon nanotubes form a highly viscous gel – a so-called “bucky-gel,” when mixed with ionic liquids (Fukushima et al. 2005; Fukushima et al. 2003). The “bucky-gel” electrodes do not require addition of any polymeric binder, which, in turn, helps to retain good electrical conductivity along the electrodes.

3 Electrical Control

The selection of an appropriate waveform for driving electrochemically and electrothermally driven actuators is essential to achieve their full actuation capability and to prevent them from degradation. To date, both types of actuators under consideration in this chapter lack practice of use in industrial applications, even at the prototype level. Consequently, standard control methods have not yet been established for these types of actuators. The control signals that have been used in the scientific works on the “smart” electroactive actuators to date are selected primarily with the purpose to facilitate convenient comparison of the newly prepared actuators with the previously available ones.

The equivalent electrical circuit is the primary concern in the selection of an appropriate waveform to drive any type of actuator. This chapter is to give an overview of the electrical control methods for electrochemically and electrothermally driven actuators, in consideration of their equivalent electrical circuits.

3.1 Control for Electrothermally Driven Actuators

Joule heating of the host material – possibly carbon nanotube fibers – governs the actuation response of the electrothermally driven actuators. The electrical equivalent circuit for an electrothermally driven actuator is a resistor, which undergoes linear or rotary motion, when energy is dissipated on it.

In vacuo carbon nanotube fibers can be electrothermally heated to in excess of 2000 °C and generate around 7 % tensile contraction. Maximum temperatures are restricted to much lower values when operated in air due to thermal degradation and oxidation. With wax incorporated as yarn guest material, the maximum operating temperature is ~250 °C and limited by thermal evaporation of wax. Electrothermal actuation can be very rapid during heating cycles, but overall cycle rates are typically limited by cooling (Lima et al. 2012). Usually passive cooling is used and cooling

rates dependent on fiber diameter. For example, full heating and cooling at 20 Hz has been demonstrated for an 11.5- μm diameter wax-filled CNT coiled yarn generating 3 % contraction on heating. In contrast, a 150- μm diameter wax-filled CNT coiled yarn heated with a 50-ms pulse generated 10 % contraction but needed more than 2 s to cool and expand. In these cases, pulse heating with tailored duty cycles is effective means for controlling strain and strain rate during both heating and cooling (Chun et al. 2014).

A number of allotropes of carbon, including carbon nanotubes, exhibit semiconductor-like electrical conductivity – their temperature coefficient of electrical conductivity is negative (Simsek et al. 2007). Consequently, it is suggested that feedback on electrical current and temperature can be required in controlling the electrothermally driven actuators with carbon as a heating element to prevent burn-out failure.

3.2 Control for Electrochemically Driven Actuators

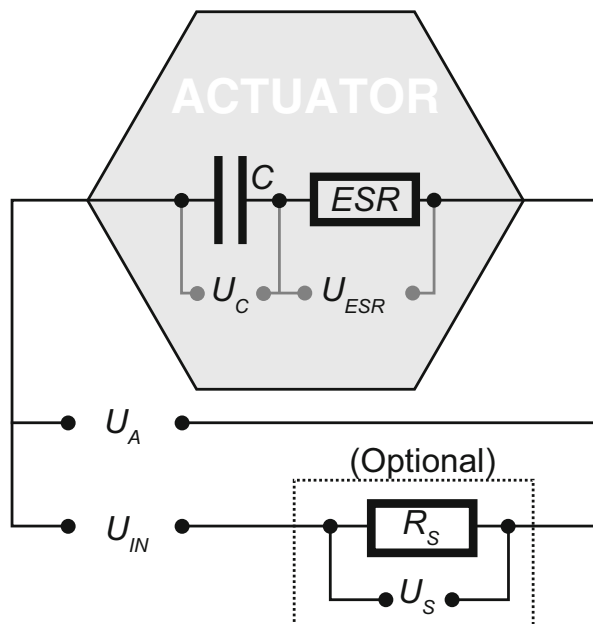
Whereas all of the electric energy that is injected into an electrothermally driven actuator is dissipated into heat to produce actuation, an electrochemically driven actuator, instead, stores the majority of the injected electric energy reversibly. Consequently, the applicable control strategies and the equivalent electrical circuits are unlike for these types of actuators. This chapter first introduces a simplified equivalent electrical circuit for the carbon-based, ionic, and capacitive actuators. Thereupon, the waveforms, commonly used to drive this type of actuators, are characterized. Additionally, the properties of the ionic actuators, involving liquid electrolytes, are significantly affected by the surrounding environment, particularly by the relative humidity level.

3.2.1 Equivalent Electrical Circuit

It was mentioned above that an electrochemically driven actuator is capacitive in its nature. The equivalent circuit for an electrochemically driven actuator can be therefore described as a capacitor C having an internal equivalent series resistance (ESR). This equivalent circuit for the ionic and capacitive actuators, illustrated as a hexagon in Fig. 1, is highly simplified, but it carries huge practical value in designing appropriate setups for their characterization and also their use in potential applications.

The equivalent circuit given in Fig. 1 could not be used to describe all existing types of ionic actuators. For example, the ionic polymer-metal composite (IPMC) actuators require addition of an extra resistor in parallel with the capacitor C in their equivalent electric circuit to concord with the experimentally obtained data (Punning et al. 2009). Instead, the value of conductance in parallel with the capacitance has been found to be inconsiderably small in case of electrochemically driven actuators with carbon-based electrodes (Must et al. 2011).

Fig. 1 Simplified equivalent circuit of an ionic and capacitive actuator



3.2.2 Rectangular Voltage

Rectangular voltage input is the most straightforward control method; hence, it is widely used in characterization of the electrochemically driven actuators. This method also requires minimal hardware to be used – just a mechanical switch is sufficient for waveform generation. Rectangular voltage input signal (U_{IN} in Fig. 1) results in the formation of a sharp peak in electric current at the switching moment, followed by an exponential decrease in the current. The electric current can be measured using an external current-measuring (shunt) resistor R_S (Fig. 1). The value of R_S adds up to the ESR of the actuator. On one hand, the series connection of the resistor R_S and the ESR of the actuator can slow down charging of the capacitor C , but it imposes a limit on the maximum peak value of electric current on the other. Consequently, the shunt resistor R_S with an appropriately chosen value acts as a simple, but effective and fail-proof, protective measure against, for example, possible short-circuiting of the actuator. The use of rectangular voltage yields the highest (momentary) deflection rate immediately after the application of the voltage, but, as a drawback, the corresponding value of the electric current can exceed the maximum tolerable limit, potentially degrading the actuator.

3.2.3 Sinusoidal Voltage

The second commonly used waveform for driving ionic and capacitive actuators is sinusoidal voltage at variable frequency or amplitude. Harmonic analysis is especially advantageous for characterization and subsequent comparison of the performance of particular types of actuators, or evaluation of different actuator geometries. In case of an actuator with non-Faradaic, carbonaceous electrodes, sinusoidal

voltage input also results in sinusoidal transient course of electric current and deflection, yet of variable amplitude and phase. The frequency response between voltage and electric current enables to elaborate on the precise equivalent electric circuit of the actuator, which is essential for improving the manufacturing process of the actuators, or characterization of the performance of the actuators at varying environmental conditions (Takeuchi et al. 2010; Must et al. 2014c).

3.2.4 Voltage Versus Current Control

The soft actuators are especially advantageous for use in soft robotics applications, which benefit the most from the actuator's (a) capability for high strains and (b) compliance to different environments and surface textures (Ilievski et al. 2011). Considering the particularly potential applications, the time needed for an actuator to transform from its initial shape into its desired final shape is one of its most important characteristics. As a comparison, precise control over the transitory position and actuation speed can be of secondary importance in soft robotics applications.

The actuation rate of an ionic and capacitive actuator is in a direct correlation with its charging rate. Consequently, the fastest actuation is achieved when the actuator is charged at its maximum endurable rate during the whole actuation cycle. Neither rectangular or sinusoidal voltage drive the actuators at the highest rate during one actuation cycle, as the value of electric current varies between its peak and zero value. The peak value of current can exceed the maximum value tolerable by an actuator, whereas, for most of the time, the actuator is driven at a rate that is considerably below its optimum value. Consequently, sinusoidal and rectangular voltage are not optimal for driving the ionic and capacitive actuators, as (a) full bending speed of the actuator is not achieved, and, at the same time, (b) the actuator can degrade rapidly due to possible overcurrent (Must et al. 2014b).

The considerations given above suggest that in real-world applications, it is advantageous to charge the ionic and capacitive actuators at constant current. There are two major competing approaches for current control: (a) by regulating the input voltage and (b) by modulating the input voltage of constant level. In the latter approach, time-averaged current is regulated. The following section considers modulation technique for driving the ionic and capacitive actuators.

3.2.5 Modulation Technique

Must et al. (2014a, b) recently proposed pulse-width-modulated (PWM) control signal. PWM signal consists of charging impulses of length T_c applied every time interval T_{PWM} ; and the duty cycle is defined as T_c/T_{PWM} . During the period T_o between the consecutive pulses ($T_o = T_{PWM} - T_c$), the input terminals are disconnected, having high-impedance state. The notations are given in Fig. 2.

The amount of electric charge, stored into an ionic and capacitive actuator, determines its transient strain level (Must et al. 2014a). When the input voltage is regulated, the charging extent could only be determined by integration of the charging current in time. A capacitive actuator offers one more method to determine its charging and strain levels – by measuring the open-circuit voltage on the capacitor's terminals. In case of voltage-regulated driving signal, the voltage on the capacitor C could not be registered

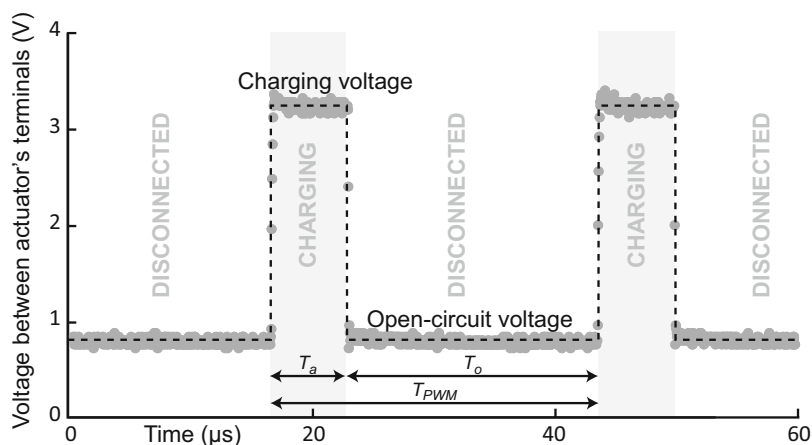


Fig. 2 Transient voltage of a PWM-driven ionic and capacitive actuator

because of the voltage drop on the ESR. Hence, the transitory voltage on the actuator's terminals, U_A (Fig. 1), does not convey useful information on the instantaneous state of the actuator during charging. Instead, when modulated driving signal is used, the voltage on the actuator's terminals, U_A , is equal to the voltage on the capacitor $C - U_C$ during the inactive period T_o of the modulated input signal (Fig. 2). Therefore, the charging extent can be accurately measured during every period T_o during the actuation cycle (Must et al. 2014b).

Modulated input signals also offer some additional advantages. In addition to charging, also short-circuiting can be performed using modulated input signals, increasing power-economy of the actuators in turn. When analog input signals are used to drive the actuators, current is drawn from the power source for both increasing and decreasing the charging level. When the actuator's electrodes are connected to an identical potential during the active cycle, T_a , the charging level of the actuator is decreased, without consuming energy from its power supply (Must et al. 2014b).

Modulated signals are particularly beneficial for driving ionic and capacitive actuators in real-world applications, as efficient, complex, bipolar, modulated input signals can be easily generated using low-cost, widely available microcontrollers (Must et al. 2014a).

3.3 Working Voltage and the Effect of Ambient Humidity

The ionic actuators with carbonaceous electrodes are considered, as a rule, as being non-Faradaic, i.e., the electromechanical effects are governed by the electrochemical double-layer buildup at the electrode-electrolyte boundary (Kosidlo et al. 2013). The absence of Faradaic charge-transfer reactions, which can deteriorate the actuator's performance in the long run, can be assured by not exceeding the electrochemical stability window (ESW) of the electrolyte.

Operating voltage is a characteristic that is often used to describe the electrochemically driven actuators. However, it is not correct to assert that the voltage on the actuator's terminals, U_A , during its charging must not exceed some fixed value that is unique for the particular type of actuator, built from the particular materials. As it is shown in Fig. 1, the voltage U_A is a sum of the voltage drop on the capacitor – U_C – and the voltage drop on the ESR – U_{ESR} . Only the voltage drop on the capacitor, U_C , should not exceed the ESW value of the electrolyte. An actuator with a high value of ESR can be driven using voltage U_A that considerably exceeds the ESW of the electrolyte. Using analog driving signals, only the voltage U_A can be registered. In contrast, the voltage U_C can be directly measured during the charging cycle by using modulated driving signals, as described in Sect. 3.4.5.

The ESW of ILs, which are commonly used as electrolytes in the electrochemically activated actuators, is exceptionally high – in the range of 4.1–6.0 V (Lazzari et al. 2013), however, in their completely water-free form. If an IL electrolyte contains water even at trace quantities (around 1000 ppm), its ESW is limited by the ESW of water – that being only 1.23 V. ESW is a parameter of the electrolyte inside the actuator, but it does not describe an actuator as an electrochemical system, having a considerable ESR.

The content of water, absorbed by an actuator from the ambient environment, does not only limit the actuator's open-circuit voltage U_C , but it can have a drastic effect on the actuator's performance at voltages below the ESW limit, imposed by the electrolyte. If the actuator contains hygroscopic constituents, it undergoes reversible sorption of water, in turn changing its electrical and electromechanical parameters (Kikuchi and Tsuchitani 2009; Must et al. 2014c). The effect of ambient humidity on the actuators depends on the particular choice of constituent materials, especially the electrolyte and the separator polymer. A carbonaceous electrode with a functionalized surface can also be hydrophilic. The humidity absorption by an actuator is not necessarily a disadvantage. Water content decreases viscosity and hence increases the conductivity of the IL electrolyte, improving the frequency-response of the actuator in turn (Must et al. 2014c). As a disadvantage, the efficiency of the actuator is decreased at high water content levels (Must et al. 2014c).

There is a choice – to seal an actuator entirely against any water absorption or to expose the whole actuator directly to ambient air. In the research on the ionic actuators to date, the latter choice has been a more prevalent approach, as the sealing technology capable of fully preventing water absorption in long term is not available for soft elastomeric materials undergoing large strain, the soft actuators being among these (Must et al. 2014a).

4 Characterization of the Actuators

The development of novel electromechanically active materials also demands suitable methods for characterization of their actuation performance. Actuators can be constructed in a variety of configurations – bending, linear length change (Torop et al. 2009; Ghaffari et al. 2013), and torsional actuation (Foroughi et al. 2011) being

the most common. The choice of the particular characterization method depends on the actuator's configuration.

Characterization of actuators involves measurement of (a) electrical, (b) mechanical, and (c) electromechanical properties. Electromechanical measurements can be divided into isometric, isotonic, and unobstructed actuation configuration. Additionally, (d) mechanoelectrical measurements are often performed to characterize the sensorial properties of the actuators. For reasons of space, mechanoelectrical characterization is not covered in this chapter.

4.1 Electrical Characterization

Electric conductivity along the carbon filament in case of the electrothermally driven actuators, and along individual electrodes in case of the electrochemically driven actuators, is an important characteristic that has a large impact on the speed of the actuators, as it is explained in Sect. 2.2. Conductivity of an electrode can be measured using four-point measurement setup. Alternatively, voltage drop along an electrode during actuation can be used to estimate its conductivity (Kruusamäe et al. 2012).

Electrochemical impedance spectroscopy (EIS) is an indispensable method for characterization of the electrochemically driven actuators. Good electrical contact between the adjacent carbon particles can be assured by measuring the electrode's impedance – it shows only resistive component in case of a good contact. However, if the electrode under characterization is a part of a three-layered laminate, the measured impedance also includes a contribution from the opposite electrode – an apparent capacitive component appears on a factually resistive electrode (Kruusamäe et al. 2012). EIS data measured between the opposite electrodes of an actuator laminate (that is, cross-electrode impedance) can be used to elaborate on the equivalent electrical circuit, which gives valuable information on the ion-transport efficiency of the actuator in turn (Must et al. 2011; Takeuchi et al. 2010). It has been demonstrated that a laminate with exceptional electromechanical properties has cross-electrode impedance that is very similar to the laminates acting as supercapacitors, being optimized exclusively for energy storage (Must et al. 2014a). Consequently, high level of ionic conductivity between the opposite electrodes and high electronic conductivity along the individual electrodes results in fast and efficient actuation.

4.2 Mechanical Characterization

Mechanical properties of the actuator materials can be characterized without any electrical signal applied. The typical stress range for electrothermally and electrochemically driven actuators is different. The electrothermally driven actuators are preferably operated in the stress range that approaches to the ultimate tensile strength of the actuating fibers, which makes their load-bearing capacity as an essential

parameter. The electrothermally driven actuators are, in contrast, typically applied at stress range that is much below their tensile strength. The electrochemically driven actuators are viscoelastic materials; therefore, their elastic property could not be described using a single value for elastic modulus. What is more, the elastic properties of soft polymeric materials change with temperature. The elastic properties can be characterized using dynamic mechanical analysis (Kruusamäe et al. 2014).

4.3 Electromechanical Characterization

The frequency response of strain and force is one of the primary characteristics for the actuators. As a standard set of experiments, the following parameters of an actuator are registered: (a) frequency dependence in case of free, unobstructed actuation, (b) frequency dependence of isometric (blocking) force, and (c) stress-dependence of isotonic strain.

A couple of additional aspects must be considered in characterization of electromechanical response. The electrochemically driven actuators can also heat up during the working cycle. In contrast to the electrothermally driven actuators, this effect is usually not desired in case of the electrochemically driven actuators, as the actuator's constituents can significantly change their mechanical and electrical properties. In an extreme case, the temperature of the separator polymer can increase over its melting point, causing the actuator to short-circuit in turn.

As the electrochemically driven actuators have viscoelastic properties and contain liquid electrolyte, it can undergo back-relaxation in long run (Kruusamäe et al. 2014; Vunder et al. 2012).

As explained in Sect. 3.5, also humidity absorption can change the electromechanical properties of an actuator considerably. Therefore, measurement of both – ambient temperature and relative humidity level – is necessary for proper electromechanical characterization of the actuators.

4.3.1 Unobstructed, “Free” Actuation

The most commonly used metric for characterization of the actuators is the level of electrically induced “free” strain, ε , in case of unobstructed actuation. The strain measurement is the most straightforward in case of linear actuators (Ghaffari et al. 2013), where the level of strain relates to the initial length, l , and the change in length, Δl , of the actuating element as:

$$\varepsilon = \frac{\Delta l}{l}. \quad (1)$$

The strain levels are usually quite moderate, in the order of several percent in case of electrochemically driven actuators. Moderate strain levels can be amplified into large dimensional change by constructing an actuator in the cantilever configuration.

Free-bending actuation is commonly measured using a laser displacement meter, pointed on the free end of the cantilevered actuator. The laser displacement meter's output is converted to the actuator's strain difference, $\Delta\varepsilon$, using a dedicated formula, referred to as the Sugino's formula (Sugino et al. 2009):

$$\Delta\varepsilon = \frac{2DW}{L^2 + D^2}, \quad (2)$$

where D is actuator's displacement, L is distance from the cantilever's fixing point to the measurement point, and W is actuator's thickness. It must be underlined that the value derived from the Sugino's formula is the difference between strains at the opposite electrodes, but not the absolute strain of the electrodes (Punning et al. 2016).

The use of laser displacement meter does not allow characterization of nonhomogenous bending profiles – the actuator is expected to have always-uniform curvature; this presumption could not apply in case of an actuator having insufficient electrode conductivity. Additionally, a laser displacement meter could not be used in case of large deflections. In case of nonhomogenous bending profiles and large bending amplitudes, actuation can be characterized by filming the cross-section of an actuator using a camera. Preferably, the camera should be equipped with a lens of long focal length. When the actuator is illuminated from the side opposite to the camera, a single, high-contrast curve, corresponding to the cross-section of the actuator, is registered by the camera. The curvature of the actuator is extracted frame-by-frame using an image recognition software. The actuator's profile can be divided into vectors, and its transient behavior can be analyzed (Vunder et al. 2012).

In the case of homogenous bending profiles, division of the actuator lengthwise into vectors is not necessary, and the cross-section of an actuator can be fitted with an arc (Must et al. 2014a). In such case, strain difference is expressed as

$$\varepsilon = -ky, \quad (3)$$

where k is curvature and y is half of the thickness of the actuator laminate. It must be considered, however, that the strain value calculated by Eq. 3 corresponds to absolute strain value of the electrodes only if the neutral layer remains in the center of the actuator during actuation.

4.3.2 Blocking Force

Blocking force is measured using isometric load cells that are attached so as to prohibit any actuator movement. For bending type electrochemical actuators, the load cell is attached in perpendicular to the actuator. Carbon nanotube mats have also been activated electrochemically in tensile mode. A load cell was used to measure isometric stress generated during voltage pulsing (Madden et al. 2006). The study demonstrated fast charging generating over 1 MPa stress in just a few milliseconds.

4.3.3 Isotonic Strain Measurement

Tensile actuators are commonly characterized in terms of their strain capacity when subjected to fixed tensile loads. The strain is referred to as the isotonic strain and is typically dependent on the applied load (Spinks and Truong 2005). The test involves using a force/length measurement system with feedback control. The system adjusts the sample length during activation so as to maintain a constant applied force. Unoriented mats of single-walled or multiwalled carbon nanotubes typically generate up to 0.3 % expansion strains with only a small dependence on applied load when activated electrochemically. Twisted carbon nanotube yarns, in contrast, produce contractions of up to 0.5 % by electrochemical or electrothermal activation. The latter can be increased by an order of magnitude by overtwisting to form coiled yarns (Lima et al. 2012).

References

- Baughman RH, Cui C, Zakhidov AA, Iqbal Z, Barisci JN, Spinks GM, Wallace GG, Mazzoldi A, De Rossi D, Rinzler AG, Jaschinski O, Roth S, Kertesz M (1999) Carbon nanotube actuators. *Science* 284(5418):1340–1344
- Chmiola J, Yushin G, Gogotsi Y, Portet C, Simon P, Taberna PL (2006) Anomalous increase in carbon capacitance at pore sizes less than 1 nanometer. *Science* 313(5794):1760–1763
- Chun K, Kim SH, Shin MK, Kwon CH, Park J, Kim YT, Spinks GM, Lima MD, Haines CS, Baughman RH (2014) Hybrid carbon nanotube yarn artificial muscle inspired by spider dragline silk. *Nat Commun* 5:3322
- Foroughi J, Spinks GM, Wallace GG, Oh J, Kozlov ME, Fang S, Mirfakhrai T, Madden JD, Shin MK, Kim SJ, Baughman RH (2011) Torsional carbon nanotube artificial muscles. *Science* 334(6055):494–497
- Fukushima T, Kosaka A, Ishimura Y, Yamamoto T, Takigawa T, Ishii N, Aida T (2003) Molecular ordering of organic molten salts triggered by single-walled carbon nanotubes. *Science* 300(5628):2072–2074
- Fukushima T, Asaka K, Kosaka A, Aida T (2005) Fully plastic actuator through layer-by-layer casting with ionic-liquid-based Bucky gel. *Angew Chem* 117(16):2462–2465
- Ghaffari M, Kinsman W, Zhou Y, Murali S, Burlingame Q, Lin M, Ruoff R, Zhang Q (2013) Aligned nano-porous microwave exfoliated graphite oxide ionic actuators with high strain and elastic energy density. *Adv Mater* 25(43):6277–6283
- Ilievski F, Mazzeo AD, Shepherd RF, Chen X, Whitesides GM (2011) Soft robotics for chemists. *Angew Chem* 123(8):1930–1935
- Kikuchi K, Tsuchitani S (2009) Effects of environmental humidity on electrical properties of ionic polymer-metal composite with ionic liquid. In: *Proceedings of the ICCAS-SICE 2009, IEEE, Fukuoka*, pp 4747–4751
- Kosidlo U, Omastová M, Micusík M, Ćirić-Marjanović G, Randriamahazaka H, Wallmersperger T, Aabloo A, Kolaric I, Bauernhansl T (2013) Nanocarbon based ionic actuators – a review. *Smart Mater Struct* 22(10):104022
- Kruusamäe K, Punning A, Aabloo A (2012) Electrical model of a carbon-polymer composite (CPC) collision detector. *Sensors* 12(2):1950–1966
- Kruusamäe K, Mukai K, Sugino T, Asaka K (2014) Impact of viscoelastic properties on bucky-gel actuator performance. *J Intell Mater Syst Struct* 25(18), 2235–2245
- Lazzari M, Arbizzani C, Soavi F, Mastragostino M (2013) EDLCs Based on solvent free ionic liquids. In: Béguin F, Frackowiak E (eds) *Supercapacitors: materials, systems, and applications*. Wiley, Weinheim, pp 289–306

- Lima MD, Fang S, Lepro X, Lewis C, Ovalle-Robles R, Carretero-Gonzalez J, Castillo-Martinez E, Kozlov ME, Oh J, Rawat N, Haines CS, Haque MH, Aare V, Stoughton S, Zakhidov AA, Baughman RH (2011) Biscrolling nanotube sheets and functional guests into yarns. *Science* 331(6013):51–55
- Lima MD, Li N, Jung de Andrade M, Fang S, Oh J, Spinks GM, Kozlov ME, Haines CS, Suh D, Foroughi J, Kim SJ, Chen Y, Ware T, Shin MK, Machado LD, Fonseca AF, Madden JD, Voit WE, Galvao DS, Baughman RH (2012) Electrically, chemically, and photonically powered torsional and tensile actuation of hybrid carbon nanotube yarn muscles. *Science* 338(6109):928–932
- Madden JD, Barisci JN, Anquetil PA, Spinks GM, Wallace GG, Baughman RH, Hunter IW (2006) Fast carbon nanotube charging and actuation. *Adv Mater* 18(7):870–873
- Miller J (2007) A brief history of supercapacitors. *Battery Energy Storage Technol* 2007:61–78
- Mirvakili SM, Pazukha A, Sikkema W, Sinclair CW, Spinks GM, Baughman RH, Madden JD (2013) Niobium nanowire yarns and their application as artificial muscles. *Adv Funct Mater* 23(35):4311–4316
- Mukai K, Asaka K, Sugino T, Kiyohara K, Takeuchi I, Terasawa N, Futaba DN, Hata K, Fukushima T, Aida T (2009) Highly conductive sheets from millimeter long single walled carbon nanotubes and ionic liquids: application to fast moving, low voltage electromechanical actuators operable in air. *Adv Mater* 21(16):1582–1585
- Must I, Kruusamäe K, Johanson U, Tamm T, Punning A, Aabloo A (2011) Characterisation of electromechanically active polymers using electrochemical impedance spectroscopy. In: Kanoun O (ed) *Lecture notes on impedance spectroscopy*, vol 2. CRC Press, London, pp 113–121
- Must I, Johanson U, Kaasik F, Põldsalu I, Punning A, Aabloo A (2013) Charging supercapacitor-like laminate with ambient moisture: from humidity sensor to energy harvester. *Phys Chem Chem Phys* 15(24):9605–9614
- Must I, Kaasik F, Põldsalu I, Mihkels L, Johanson U, Punning A, Aabloo A (2015) Ionic and capacitive artificial muscle for biomimetic soft robotics. *Adv Eng Mater* 17(1):84–94
- Must I, Kaasik F, Põldsalu I, Mihkels L, Johanson U, Punning A, Aabloo A (2014b). Pulse-width-modulated charging of ionic and capacitive actuators. In: *Proceedings of the IEEE/ASME international conference on advanced intelligent mechatronics (AIM) 2014*, IEEE, Besançon, pp 1446–1451
- Must I, Vunder V, Kaasik F, Põldsalu I, Johanson U, Punning A, Aabloo A (2014a) Ionic liquid-based actuators working in air: the effect of ambient humidity. *Sens Actuator B-Chem* 202:114–122
- Palmre V, Brandell D, Mäeorg U, Torop J, Volobujeva O, Punning A, Johanson U, Kruusmaa M, Aabloo A (2009) Nanoporous carbon-based electrodes for high strain ionomeric bending actuators. *Smart Mater Struct* 18:095028
- Punning A, Johanson U, Anton M, Aabloo A, Kruusmaa M (2009) A distributed model of ionomeric polymer metal composite. *J Intell Mater Syst Struct* 20(14):1711–1724
- Punning A, Vunder V, Must I, Johanson U, Anbarjafari G, Aabloo A (2016). In situ scanning electron microscopy study of strains of ionic electroactive polymer actuators. *J Intell Mater Syst Struct* 27(8):1061–1074
- Simon P, Taberna P, Béguin F (2013) Electrical double-layer capacitors and carbons for EDLCs. In: Béguin F, Frackowiak E (eds) *Supercapacitors: materials, systems, and applications*. Wiley, Weinheim, pp 131–165
- Simsek Y, Ozyuzer L, Seyhan AT, Tanoglu M, Schulte K (2007) Temperature dependence of electrical conductivity in double-wall and multi-wall carbon nanotube/polyester nanocomposites. *J Mater Sci* 42(23):9689–9695
- Spinks GM, Truong V (2005) Work-per-cycle analysis for electromechanical actuators. *Sens Actuator A-Phys* 119(2):455–461
- Sugino T, Kiyohara K, Takeuchi I, Mukai K, Asaka K (2009) Actuator properties of the complexes composed by carbon nanotube and ionic liquid: the effects of additives. *Sens Actuator B-Chem* 141(1):179–186

- Takeuchi I, Asaka K, Kiyohara K, Sugino T, Mukai K, Randriamahazaka H (2010) Electrochemical impedance spectroscopy and electromechanical behavior of Bucky-gel actuators containing ionic liquids. *J Phys Chem C* 114(34):14627–14634
- Torop J, Arulepp M, Leis J, Punning A, Johanson U, Palmre V, Aabloo A (2009) Nanoporous carbide-derived carbon material-based linear actuators. *Materials* 3(1):9–25
- Torop J, Palmre V, Arulepp M, Sugino T, Asaka K, Aabloo A (2011) Flexible supercapacitor-like actuator with carbide-derived carbon electrodes. *Carbon* 49(9):3113–3119
- Torop J, Sugino T, Asaka K, Jänes A, Lust E, Aabloo A (2012) Nanoporous carbide-derived carbon based actuators modified with gold foil: prospect for fast response and low voltage applications. *Sens Actuator B-Chem* 161(1):629–634
- Vunder V, Punning A, Aabloo A (2012) Mechanical interpretation of back-relaxation of ionic electroactive polymer actuators. *Smart Mater Struct* 21(11):115023
- Zhang M, Atkinson KR, Baughman RH (2004) Multifunctional carbon nanotube yarns by downsizing an ancient technology. *Science* 306(5700):1358–1361

Section V

Piezoelectric and Electrostrictive Polymers

Reimund Gerhard

Contents

1	Introduction	490
2	First Principles of Piezoelectricity	490
3	Spring Model for Piezoelectricity in Heterogeneous Dielectrics with Fixed Electric Charges of Both Polarities	493
4	Nonuniform Strains and Higher-Order Effects: Bending Piezoelectricity, Flexoelectricity, Electrostriction, etc.	500
4.1	Flexoelectricity, Bending, and Torsional Piezoelectricity	500
4.2	Electrostriction and Dielectrostriction	501
4.3	Concluding Remarks	504
	References	505

Abstract

In this chapter, fundamental aspects of piezoelectricity and electrostriction in dielectric materials and especially in polymers will be outlined. In order to make the introduction into the subject easier to access, basic and schematic ways of describing the complex matter have been chosen instead of an elaborate or comprehensive theoretical approach. For more detailed and more precise information, the interested reader is referred to the large volume of available original and review literature and to other relevant chapters of this book.

Keywords

Affine deformation • Bend • Dielectrostriction • Direct piezoelectricity • Electric polarization • Electromechanical materials • Electrostriction • Flexoelectricity • Gibbs free energy • Inverse piezoelectricity • *Non-affine* deformation •

R. Gerhard (✉)

Applied Condensed-Matter Physics, Institute of Physics and Astronomy, Faculty of Science,
University of Potsdam, Potsdam-Golm, Germany
e-mail: reimund.gerhard@uni-potsdam.de

Piezoelectricity • Bending • Discovery • Principles of • Torsional • Splay • Spring model • Strain • Twist • Two-domain Heckmann diagram

1 Introduction

Pierre and Jacques Curie discovered piezoelectricity in 1880 on crystals of Rochelle or Seignette salt (potassium sodium tartrate tetrahydrate, $\text{KNaC}_4\text{H}_4\text{O}_6 \cdot 4\text{H}_2\text{O}$) (Curie and Curie 1880). The term *piezoelectricity* contains the two Greek words *πιεζειν* (to press or to compress) and *ηλεκτρον* (amber, i.e., the first example of an electrically charged object) and thus means pressure-induced electrostatic charge. In addition to direct piezoelectricity (electric displacement induced by mechanical stress), there is also an inverse piezoelectricity (mechanical strain induced by electrical stress). Thermodynamics requires not only that there is reciprocity between direct and inverse piezoelectricity but also that the relationship between cause and effect is linear so that the direct and inverse piezoelectric coefficients should be identical and constant. If the generated mechanical strain depends on the square of the applied electric field, the relevant property is named *electrostriction* and is found in all materials, irrespective of their inherent symmetries. The inverse effect of a strain- or stress-induced change in the dielectric properties is now sometimes called *dielectrostriction* (Lee and Shkel 2004).

Piezoelectricity in natural and synthetic polar polymers was pioneered by Fukada (Fukada 2000) (and references therein) and by Kawai (Kawai 1969) in the 1960s. During the 1990s, nonpolar polymers with quasi-permanent electrically charged internal cavities were also found to be piezoelectric – at least according to the thermodynamical definitions and for all practical purposes. Such bipolar electrets are now usually called *ferroelectrets* (Gerhard(-Multhaupt) 2002; Bauer et al. 2004) (and references therein) or piezoelectrets. Last, but not least, very soft, essentially incompressible elastomers also show electromechanical and mechano-electrical transduction (Carpi et al. 2008), but they are not piezoelectric, as their observed macroscopic behavior is not linear. They may, however, behave almost linearly over limited ranges if a constant, rather large, electrical or mechanical bias is applied in addition to the transducer input signal that varies with time.

2 First Principles of Piezoelectricity

In the late nineteenth century, scientists quickly adopted the seminal publications of the Curie brothers. Consequently, piezoelectricity and electrostriction were first discovered and investigated on inorganic, mono- or polycrystalline materials (Katzir 2006). Therefore, the theoretical treatment of the relevant electromechanical properties has been based on the physics and in particular on the structure and the anisotropy of crystals (Newnham 2005; Tichý et al. 2010). Semicrystalline or amorphous polymers are usually less anisotropic than crystals, and the symmetry

breaking, as well as the anisotropy that is required for piezoelectricity, can usually only be achieved by means of structural and electrical preparation (e.g., stretching or foaming plus charging or poling).

The thermodynamical derivation of piezoelectricity includes two steps: (1) The relevant mechanical or electrical quantities are calculated as partial derivatives of the Gibbs free energy with respect either to one of the two mechanical or to one of the two electrical observables, respectively. (2) The second partial derivative of the Gibbs free energy with respect to the *other* domain (electrical or mechanical, respectively) yields one of the piezoelectric coefficients. Because there is one intensive (force-like or voltage-like) observable, namely, mechanical stress and electrical field, and one extensive (displacement-like) observable, namely, mechanical strain and electrical displacement, in each of the two domains, we have four possible combinations of one mechanical and one electrical observable in total. Thus, we obtain four different piezoelectric coefficients that are usually abbreviated as d , e , g , and h . As the sequence of the two partial derivations can be reversed, we arrive at two different expressions for each coefficient: one for *direct* piezoelectricity (mechanical stimulus leads to an electrical response) and one for *inverse* or *converse* piezoelectricity (electrical stimulus leads to a mechanical response). For example, the piezoelectric d coefficient is given by the two alternative terms:

$$d = \frac{\partial D}{\partial T} = \frac{\partial S}{\partial E}, \quad (1)$$

one for direct and one for inverse piezoelectricity, respectively. The reciprocity is also seen in the units of measurement: Coulomb per Newton (C/N) or Meter per Volt (m/V), respectively. Both units are actually identical, as can be easily seen if “C/N” is multiplied by “m” in the numerator and the denominator, and if “Nm” is then replaced by “Ws = VAs = VC” so that “Cm/(VC)” can be reduced to “m/V.”

Most of the relevant equations can be easily found in the literature (e.g., (Tichý et al. 2010; Sherrit and Mukherjee 2012) and references therein) and do not have to be repeated here. Instead, a detailed schematic is shown in Fig. 1 which has been developed as a two-domain diagram after the original three-domain schematic proposed by Gustav Heckmann already in 1925 (Heckmann 1925). In the modified two-domain Heckmann diagram, the four direct and the four inverse piezoelectric coefficients, as well as the respective tensors for elasticity and dielectric behavior, are shown as arrows that point from the cause to the effect (or from the denominator of the respective partial derivative to its numerator). It should be noted that the two mechanical observables can be represented by vectors with six components, while the two electrical observables are three-dimensional vectors so that the piezoelectric coefficients are in general components of a 3×6 or a 6×3 tensor (one is the transpose of the other). The relevant component of the piezoelectric tensor depends on the choice of the vector components of the mechanical and the electrical observable. For the elastic modulus and the elastic compliance, a 6×6 tensor and its transpose is required, while the dielectric permittivity and the (di)electric modulus (Richert 2005) can be written as a 3×3 tensor and its transpose.

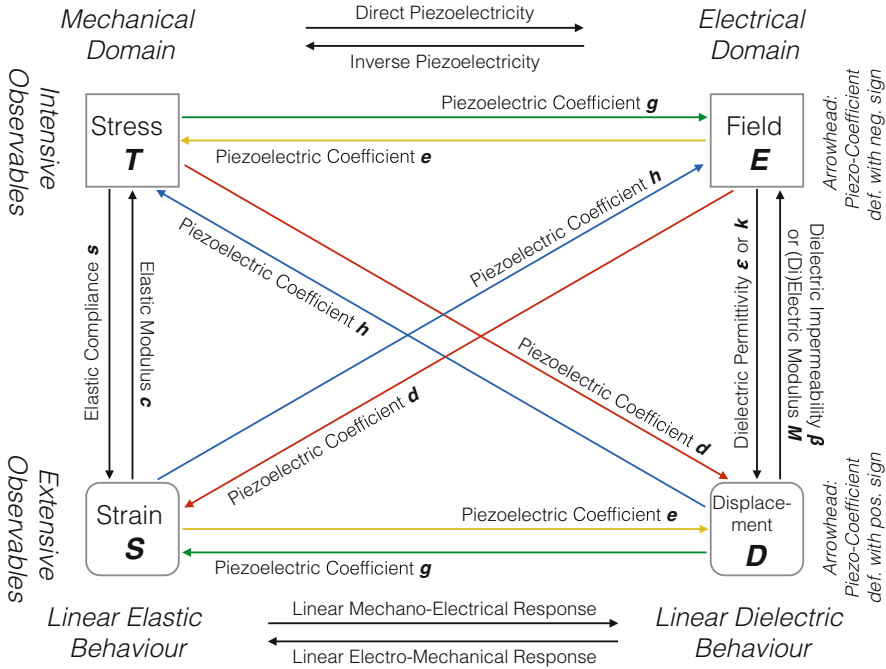


Fig. 1 Two-domain Heckmann diagram (Heckmann 1925) illustrating the *linear* mechano-electrical and electromechanical effects (i.e., direct and inverse piezoelectricity, respectively) in dielectric materials. The four relevant piezoelectric coefficients d , e , g , and h are shown as horizontal or diagonal arrows in red, yellow, green, and blue, respectively, while the linear elastic and dielectric parameters are included as vertical black arrows

From the two-domain Heckmann diagram of Fig. 1, we can also find the signs of the respective piezoelectric coefficients that follow from the definition of Gibbs free energy and the respective derivatives: All arrows that end in the upper half of the diagram (i.e., at intensive observables) represent a coefficient with a minus sign in its definition, while all the arrows that have their tips in the lower half of the diagram stand for coefficients with a positive sign. Furthermore, relationships between the different piezoelectric coefficients can be obtained by making a “detour” when going from the cause to the effect: Thus, the piezoelectric d coefficient is given by the product of the dielectric permittivity ϵ and the piezoelectric g coefficient, etc.

For device applications, the efficiency is often characterized by the electromechanical coupling factor k , the square of which is given by the ratio of the available output energy to the input energy that has been provided. The mechanical and electrical energies can be taken from the Gibbs free energy function and then be expressed via the relevant material coefficients. In case of a mechano-electrical transducer, for example, we obtain $k^2 = (ED)/(ST)$, and the ratios of the observables can be replaced by piezoelectric coefficients, as well as by elastic and dielectric constants according to the above two-domain Heckmann diagram to yield,

e.g., $k^2 = d \cdot h = e \cdot g = d^2/(\epsilon \cdot s) = e^2/(c \cdot \epsilon)$, etc. Here, the pertinent tensor components are again to be chosen according to the respective input and output vector components, while the piezoelectric coefficients can be replaced by each other according to the above “detour” rule where going along the direction of an arrow leads to a factor in the *numerator*, while going against the direction of an arrow leads to a factor in the *denominator*. Experimental determination of the frequency-dependent coupling factor k is possible with an all-electrical method (a combination of dielectric spectroscopy and electromechanical resonances) that also yields the respective components of the elastic modulus c and the piezoelectric coefficient d (Mellingner 2003).

3 Spring Model for Piezoelectricity in Heterogeneous Dielectrics with Fixed Electric Charges of Both Polarities

Electromechanical and mechano-electrical transduction is often based on inverse and direct piezoelectricity, respectively. According to the definition of the piezoelectric d coefficient (cf. Eq. 1 and Fig. 1 above), *direct* piezoelectricity is the linear change of the electrical displacement D caused by mechanical stress T , while *inverse* piezoelectricity is the linear change of the mechanical strain S due to electrical stress E . Here, either the electric field E or the mechanical stress T has to be kept constant, respectively. Under this condition, the electric displacement D may be replaced by the electric polarization P in the definition of the direct d coefficient: $d = \partial P/\partial T$, which may also be written in tensor notation as $P_j = d_{jkl}T_{kl}$ (Newnham 2005).

The electric polarization P may in turn be defined as the density of dipoles in a material where the individual dipoles can be identified as two electric charges of opposite polarity, but equal magnitude, that are separated by a given distance. Putting these definitions together, it is possible to write the direct piezoelectric coefficient d as the sum of linear changes in the dipole moments themselves (“primary piezoelectricity”) and of linear changes in the density of these dipoles (“secondary piezoelectricity”). In an elastically uniform material or material system, the deformation under mechanical stress is affine, and the two effects cancel each other so that no piezoelectricity is observed, as illustrated in Fig. 2. Consequently, piezoelectricity requires an elastically nonuniform dielectric with at least two different phases and with electric charges at or near their interfaces.

We consider a very general two-phase system with a *dipole* phase “D” and a *matrix* phase “M.” The dipole phase may consist of any type of nanoscopic, microscopic, or macroscopic dipoles such as ionic charges of opposite polarity in the lattice of an inorganic solid, polar molecules or polar molecular units, ionic crystalline particles, polymer crystallites in a semicrystalline polymer, particles with charges of opposite polarity on their opposing faces, cavities with internal surface charges of one or both polarities, etc. The matrix phase may be the material between or around ionic charges, the polymer matrix of a composite, the amorphous phase of

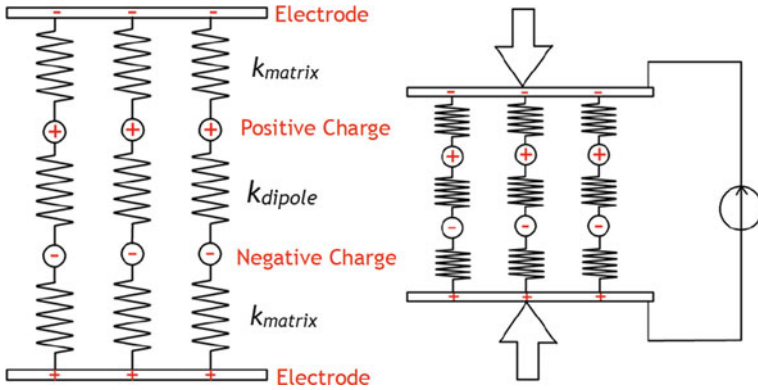


Fig. 2 Affine deformation of an elastically homogeneous dielectric with $k_{matrix} = k_{dipole}$ leads to no relative change (i.e., no signal)

a semicrystalline polymer, the cell walls of a polymer foam, etc. We consider all these materials and material systems in the same way, with only the length scales of the two phases and their deformations different. This concept can be represented by the arrangement of charges and springs outlined in Fig. 2 (Gerhard 2014).

The overall polarization \vec{P} in a material of volume V is given by the vector sum of its N dipole moments $\vec{\mu}_i$:

$$\vec{P} = \frac{1}{V} \sum_{i=1}^N \vec{\mu}_i. \tag{2}$$

The individual dipoles $\vec{\mu}_i$ are defined by their bipolar charge q_i and their length vector \vec{l}_i as $\vec{\mu}_i = q_i \vec{l}_i$. Inserting this definition into Eq. 2, we obtain

$$\vec{P} = \frac{1}{V} \sum_{i=1}^N q_i \vec{l}_i. \tag{3}$$

Applying a stress component T (e.g., a uniaxial pressure p) to the material and its polarization, we find the following linear response that is usually called direct piezoelectricity and described by the d coefficient:

$$\frac{\partial \vec{P}}{\partial T} = -\frac{1}{V^2} \frac{\partial V}{\partial T} \sum_{i=1}^N q_i \vec{l}_i + \frac{1}{V} \sum_{i=1}^N q_i \frac{\partial \vec{l}_i}{\partial T}. \tag{4}$$

If we now consider the special case of a thin slab or film with an area A and a uniform thickness t subjected to compression (or rarefaction) in its thickness direction (T_{33}), Eq. 4 becomes

$$\frac{\partial P_3}{\partial T_{33}} = -\frac{1}{At^2} \frac{\partial t}{\partial T_{33}} N_{qd} l_D + \frac{1}{At} N_{qd} \frac{\partial l_D}{\partial T_{33}}. \tag{5}$$

Here, the individual dipole lengths \vec{l}_i have been replaced by the average dipole length l_D perpendicular to the slab surface so that the vector sum can be rewritten as the product of the number of dipoles and the average length of each dipole in the thickness or (3) direction of the slab or film.

The first term on the right-hand side of Eq. 5 contains the deformation of the matrix with stiff dipoles. Therefore, the derivative $\partial t/\partial T_{33}$ is given by the ratio t/Y_M of the slab thickness and the elastic modulus Y_M of the matrix. The second term on the right-hand side corresponds to the deformation (or to the change in the perpendicular components of the dipole moments upon rotation) that the dipoles themselves undergo within a non-deformable matrix. Here, the derivative $\partial l_D/\partial T_{33}$ is given by the ratio l_D/Y_D of the average dipole length l_D and the elastic modulus Y_D of the dipole phase. We thus obtain

$$\begin{aligned} \frac{\partial P_3}{\partial T_{33}} &\approx -\frac{1}{At} N_{qd} \frac{l_D}{Y_M} + \frac{1}{At} N_{qd} \frac{l_D}{Y_D} \\ &\approx -\frac{\sigma}{t} \frac{l_D}{Y_M} + \frac{\sigma}{t} \frac{l_D}{Y_D}, \end{aligned} \tag{6}$$

where the combined charge N_{qd} on all dipoles per area A has been replaced by the bipolar charge density σ on the interfaces between dipole phase and matrix phase.

The elastic moduli Y_M of the matrix phase and Y_D of the dipole phase can also be calculated from the spring constants k_{matrix} and k_{dipole} in Figs. 2, 3, and 4, respectively, if the particular geometrical arrangement of the springs is taken into account.

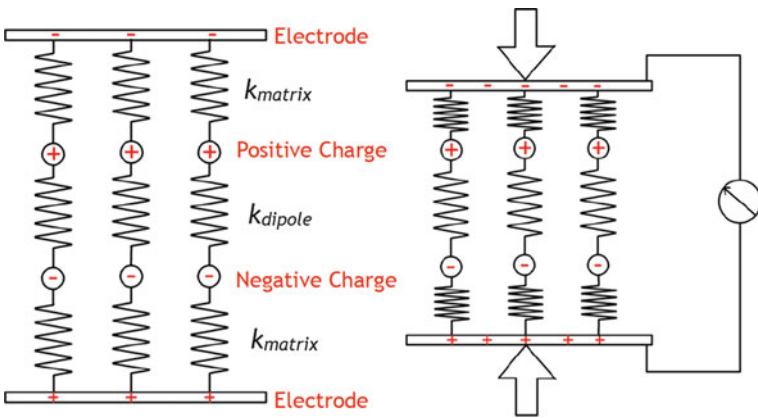


Fig. 3 *Non-affine* deformation of an elastically heterogeneous dielectric with $k_{matrix} \ll k_{dipole}$ leads to a dipole-density change (negative signal; so-called secondary piezoelectricity)

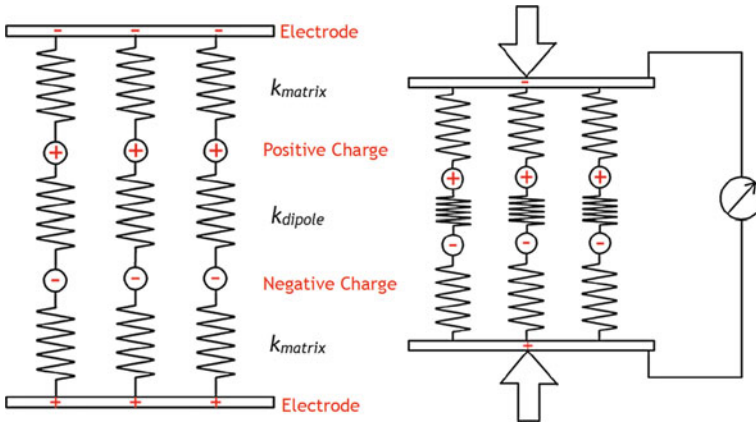


Fig. 4 Non-affine deformation of an elastically heterogeneous dielectric with $k_{matrix} \gg k_{dipole}$ leads to a dipole-moment change (positive signal; so-called primary piezoelectricity)

According to Eq. 6, direct piezoelectricity can be separated into a matrix (or dipole-density) effect (“secondary piezoelectricity”) and a dipole-moment effect (“primary piezoelectricity”). The two alternative situations are illustrated in Figs. 3 and 4, respectively. However, if the matrix and dipole phases have the same elastic modulus (i.e., spring constant), no piezoelectricity is observed (affine deformation). This situation has been illustrated in the spring model of Fig. 2 above where the electrode charges do not change upon deformation.

In real piezoelectric materials, one phase will be stiffer and the other softer so that a nonzero response is observed. Equation 6 tells us how to design piezoelectric materials with two or more phases such as ferroelectrets from cellular foams (the dipole phase typically consists of air-filled foam cells or cavities) or Maxwell–Wagner piezoelectrets from particle–polymer composites (in which the dipole phase may consist, e.g., of hard particles that cannot be compressed very much).

Equation 6 is an approximate expression for the piezoelectric “thickness” coefficient $d_{33} = \partial P_3 / \partial T_{33} \approx -1 / (At) Nq_D l_D / Y_M + 1 / (At) Nq_D l_D / Y_D$ that describes the longitudinal direct piezoelectricity in the thickness direction of a slab or film. If the combined charge Nq_D on all dipoles per area A is replaced by the bipolar interfacial charge density σ , the second line of Eq. 6 yields the expression $d_{33} \approx -(\sigma/t)(l_D/Y_M) + (\sigma/t)(l_D/Y_D)$. It should be kept in mind that all dipoles are assumed to be perpendicular to the surface of the slab or film in this model. Furthermore, the dipoles can only be deformed along their respective axes (i.e., only the projection of dipole rotations onto the vertical axis is taken into account). Therefore, all other deformation mechanisms that may contribute to the piezoelectric response of a real material are not realistically modeled in the essentially one-dimensional “charges + springs” concept.

The first line of Eq. 5 can be written as a relation that may be easily compared to experimental data if the combined moments $N_{d_D} l_D$ of all dipoles per volume $V = At$ are again replaced by the overall polarization P_3 :

$$d_{33} \approx -\frac{P_3}{Y_M} + \frac{P_3}{Y_D}. \quad (7)$$

Equation 7 includes the prediction that the ratio of the piezoelectric d_{33} coefficient and the remanent polarization $P_3 = P_r$ should be approximately equal to the elastic compliance $1/Y_M$ of the matrix phase for the dipole-density effect or to the elastic compliance $1/Y_D$ of the dipole phase for the dipole-moment effect, respectively (or inversely proportional to the respective elastic modulus). First results assembled from the literature and from our own experimental data on PVDF and on cellular-foam PP and tubular-channel FEP ferroelectrets (Altafim et al. 2009) are shown in Fig. 5 (Qiu et al. 2013, 2014). They provide experimental evidence that the direct piezoelectric thickness coefficient of polymer materials can indeed be roughly approximated by the product of the remanent polarization in the poled material and of its overall elastic compliance. Additional data from the literature on other

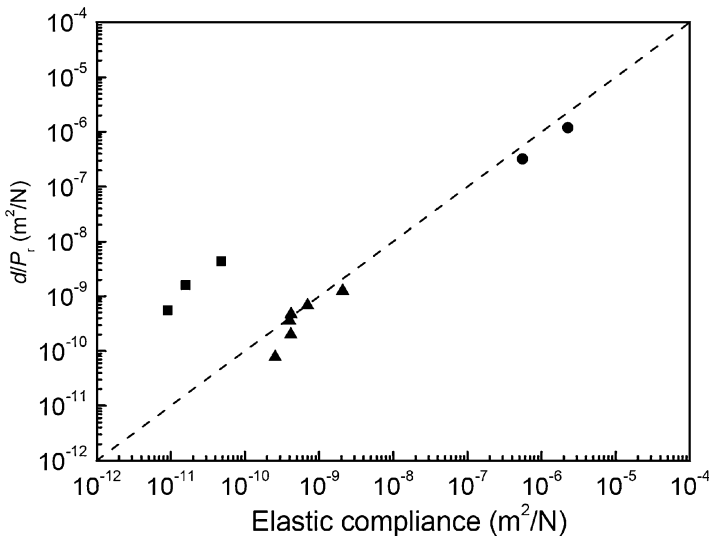


Fig. 5 The ratio of the relevant component of the piezoelectric coefficient d and the respective polarization P_r is plotted vs. the reciprocal of the respective elastic modulus Y (i.e., the relevant component of the elastic compliance). From left to right: Literature data for *inorganic ferroelectrics* (squares): barium titanate (BaTiO_3), lead zirconate titanate (PZT), and lead zirconate niobate (PZN). *Ferroelectric polymers* (triangles): polyamide-11 (PA-11), poly(vinylidene cyanide-vinyl acetate) (P(VDCN-VAc)), polyurea-5, poly(vinylidene fluoride (PVDF)), poly(vinylidene fluoride-trifluoroethylene) (P(VDF-TrFE)), and poly(vinylidene-hexafluoropropylene) (P(VDF-HFP)). *Polymer ferroelectrets* (circles): cellular polypropylene (cellular-PP) and tubular-channel poly (fluoro-ethylene-propylene) (FEP) (Qiu et al. 2014)

piezoelectric polymers and on a few inorganic ferroelectrics are also included in Fig. 5 and do not always agree with the approximate prediction of Eq. 7 (cf. also (Qiu et al. 2014)).

It is, however, not surprising that the prediction is in general only approximately fulfilled for the polymeric piezoelectrics and seems to break down completely for the inorganic piezoelectrics. The model apparently works best for polymers in which the elastic compliance of the phase that is essential for piezoelectricity clearly dominates the overall compliance (i.e., the soft amorphous matrix in semicrystalline polymers above their respective glass-transition temperatures or the gas-filled cavities in polymer ferroelectrets, respectively). When looking at the spring model and its comparison with selected experimental data from the literature (cf. Fig. 5), the following points should be taken into account:

1. The experiments for determining the respective piezoelectric and elastic constants are usually quite different, and the values for the remanent polarizations are often obtained from electrical measurements during poling and may thus not be identical to the dipole polarization that can be exploited for piezoelectricity.
2. Depending on the sample geometry and the experimental mode, it may be necessary to correct the piezoelectric coefficients – in particular in polymeric samples and in relation to the remanent polarization – for effects of the electrode geometries under strain (Kepler 1978; Kepler and Anderson 1980).
3. For PVDF and for other semicrystalline polar polymers, there are several different molecular and interfacial mechanisms that may lead to piezoelectricity, and their relative quantitative contributions are still not fully understood (Broadhurst and Davis 1984; Rollik et al. 1999; Katsouras et al. 2015). And in polyamide-11, one of the odd-numbered polyamides and, in other semicrystalline polymers, a rigid amorphous phase has been found to modify the mechanical deformation and thus also the piezoelectric response (Frübing et al. 2006).
4. In inorganic piezoelectrics, several ions in the crystalline lattice may contribute to the relevant dipole moments, and their relative movement under macroscopic mechanical (or electrical) stress is probably not just a simple displacement in the thickness direction of the respective sample.

Clearly, further research is required in order to better understand the microscopic and macroscopic structure–property relationships (e.g., by probing the “elasticity” of the dipoles directly with high-speed X-ray techniques) and to obtain useful guidelines for material selection and design, as well as for specific applications.

In order to conclude the above discussion of the spring model in which electric charges of both polarities are coupled to materials with nonuniform elastic behavior, a comparative overview of electroactive dielectric materials that exhibit piezoelectricity and/or electrostriction is presented in Table 1. The table was developed in order to summarize the possible roles of electric charges, their coupling to materials, and their interplay with elastic heterogeneities at different length scales (Gerhard 2014). Most of the fundamental material concepts listed in Table 1 are known as various types of *electrets* as indicated, but often also under other technical terms.

Table 1 Comparison of electromechanical materials and their fundamental modes of operation (Modified and amended from the Whitehead Memorial Lecture 2014 (Gerhard 2014))

Electroactive dielectric material	Anchoring of trapped charges	Elastic heterogeneity of material	Additional specific essential features
Electro-electret (dielectric-elastomer actuator, sensor or energy harvester)	External voltage induces charges on compliant electrodes	Compression/rarefaction of elastomer (charges stay on soft electrodes)	Incompressibility leads to change in length/width or to bending
Space-charge electret (film, plate, fiber, etc.) a.k.a. “electrophore”	Trapping on/in polymer film (image charges on electrodes)	Polymer + backplate (harder part) plus air-filled cavities (much softer part)	Mainly uniaxial pistonlike motion perpendicular to film plane
Ferro- or piezoelectret (heterogeneous system with cavities/inclusions)	Charges of both polarities deeply trapped at/near internal interfaces	Polymer walls or films enclose cavities, droplets, or various particles	“Devices <i>inside</i> a material” instead of “devices <i>from</i> various materials”
Ferro-, and/or pyro-, and/or piezoelectric polymer electret	Charges in polar chemical bonds form molecular dipoles	Crystallites with oriented dipoles move inside amorphous phase	Interfacial charge and amorphous phase can modify the observed effects
Piezo/pyroelectric composite (inorganic ferroelectric particles in polymer matrix)	Ions in crystalline particles form ionic dipoles upon symmetry breaking	Ionic dipoles deform/rotate with mechanical (electrical) stress	Ferroelectric matrix polymer may compensate piezo- or pyroelectric effect
Piezo/pyroelectric crystal or ceramic (lattice with spontaneous polarization)	Ions in crystalline lattice form ionic dipoles upon symmetry breaking	Ionic dipoles deform/rotate with mechanical (electrical) stress	Often also ferroelectric (hysteresis, remanence, coercive field)

A fundamental difference between ferroelectret polymers and ferroelectric polymers is the large elastic anisotropy of the ferroelectrets which can usually be easily deformed (compressed or expanded) in the thickness direction, but not laterally! Ferroelectric polymers are, however, essentially incompressible, which leads to a strong coupling between the longitudinal piezoelectricity in the thickness direction and the transverse piezoelectricity that couples lateral elastic deformations with changes of the vertical electric polarization.

In this context, the possibility to “tune” the piezo- and pyroelectricity of specific composites (Ploss et al. 2000) by means of separate poling of the inorganic particles and of the polymer crystallites should also be mentioned. In addition, piezo-, pyro-, and ferroelectric polymers such as PVDF and its relevant copolymers may be optimized by controlling the poling of the amorphous and of the crystalline phase, as well as of the interface between them (Maxwell–Wagner interface polarization) separately (Rollik et al. 1999). Furthermore, it is possible to follow the examples of the “classical” electret transducers (with polymeric *space-charge electrets*) or of the dielectric-elastomer transducers (sometimes also called *electro-electrets*) and to

replace charge layers in or on polymers with electrodes (Rychkov et al. 2014) in order to arrive at materials and devices that are easier to manufacture, to optimize, and to control.

4 Nonuniform Strains and Higher-Order Effects: Bending Piezoelectricity, Flexoelectricity, Electrostriction, etc.

The influences of nonuniform strains on the electric polarization in materials with molecular dipoles and the possibly resulting piezoelectric effects were first considered for liquid crystalline (LC) materials (Meyer 1969; Helfrich 1971). The arrangements of the individual LC molecules are classified according to the orientation distribution of the so-called molecule “director,” a vector that represents the main axis of the molecule in question, but not necessarily its dipole moment! Basically, three nonuniform deformation modes can be identified: (1) “Splay” is a deformation, in which the directors of the individual LC molecules assume a radial fanlike pattern with their tips further away from each other than their ends. (2) “Bend” is a deformation, in which the LC directors are arranged like the rail cars of the trains on parallel tracks in a curve. (3) “Twist” is an LC director arrangement, in which the directors of subsequent LC-molecule layers are rotated either all clockwise or all counterclockwise relative to each other. Combinations of the three fundamental deformation modes are also known. Many additional details and the state of the art may be found in the pertinent literature and on the Internet, e.g., in Andrienko (2006).

4.1 Flexoelectricity, Bending, and Torsional Piezoelectricity

A liquid crystal (LC) in which the electric dipoles point in the same direction as the respective LC directors should exhibit not only a nonuniform strain but also a piezoelectric response when it undergoes one or more of the three nonuniform deformation modes that are identified as “splay,” “bend,” and “twist.” Accordingly, three different modes of piezoelectricity from nonuniform strain distributions were postulated for liquid crystals (Meyer 1969), but it was not clear whether the resulting piezoelectric effects were large enough to be observed in real experiments (Helfrich 1971). In the meantime, since the early concepts, a whole new field – flexoelectricity in liquid crystals (Buka and Éber 2013) – has developed from the pioneering work of Meyer and Helfrich on “splay” and “bend” deformation in liquid crystals.

At the same time, flexoelectricity has also been thoroughly investigated on solid crystals (see, e.g., Tagantsev 1991; Zubko et al. 2013) and references therein) and on fluoropolymers containing molecular dipoles (Baskaran et al. 2011, 2012). In particular, very thin (nanometer scale) films of crystalline solids may exhibit the required high strain nonuniformity upon bending. Poling is not always required for flexoelectricity in polymers, as the necessary symmetry breaking can be generated by the nonuniform strain upon flexure. It is, however, very important to determine

the strain profiles accurately so that free-standing polymer films are preferable (Chu and Salem 2012). A comparison of flexoelectricity in VDF-based paraelectric and ferroelectric copolymers, as well as relaxor-ferroelectric terpolymers, points towards a more complex behavior than had been expected from considering only the dielectric properties of the respective materials (Poddar and Ducharme 2013).

Significant bending piezoelectricity of polymer films with a nonuniform polarization profile across their thickness had already been known for quite some time (e.g., (Fukada et al. 1987)). Here, the nonuniform strain can be matched with the nonuniform profile of the dipole polarization so that both effects reinforce each other. The required films can be prepared from piezoelectric polymers, e.g., by gluing a poled and a non-poled film or two oppositely poled films together or by limiting the poled volume to one half of the specimen thickness by means of an electron-beam-deposited charge layer in the middle of the film (Gross et al. 1987; Yang et al. 1994). The resulting polymeric monomorph and bimorph devices, as well as their preparation, investigation, and application, were briefly reviewed some time ago (Bauer-Gogonea et al. 1999). Multilayer arrangements in monolithic or sandwich form were also discussed in this context. It seems that the “older” bending piezoelectricity and the “newer” flexoelectricity in polymers overlap to quite a large extent, but a more detailed picture can only be obtained from more comprehensive investigations and from a detailed analysis of the older research.

Torsional piezoelectricity, which is closely related to the “twist” deformation mode of liquid crystals, has also been achieved via clever combinations of patterned electrodes and suitable piezoelectric-tensor geometries in ferroelectric ceramics (Fuda and Yoshida 1994). With particular emphasis on aeronautical and space applications, the possibilities of engineering “smart” or “intelligent” piezoelectric sensors and sensor systems with various deformation modes by means of patterned electrodes and structured piezoelectrics were reviewed quite extensively (Chee et al. 1998; Chopra 2002) for inorganic materials. Nevertheless, the extensive and attractive possibilities of materials engineering and in particular of “electrical” patterning via selective poling and/or by means of suitable electrode geometries have not been fully exploited yet – in particular with respect to soft electroactive polymers and polymer composites.

4.2 Electrostriction and Dielectrostriction

In material physics which was historically dominated by the investigation of inorganic and crystalline materials, electrostriction (i.e., the *quadratic* electromechanical coupling effect in materials) is defined by the tensor equations (Newnham 2005; Newnham et al. 1997):

$$S_{ij} = \gamma_{ijkl} E_k E_l = Q_{ijkl} P_k P_l \quad (8)$$

for the electric-field and the dielectric-polarization dependence with the fourth-rank electrostriction tensors γ_{ijkl} and Q_{ijkl} , respectively. Electrostriction should not be

mixed up with the *linear* electromechanical effect of inverse piezoelectricity that is given, e.g., by $S_{ij} = d_{ijk}E_k = g_{ijk}P_k$ for the electric-field and the dielectric-polarization dependence, respectively (Sherrit and Mukherjee 2012), and that is discussed in Sects. 2 and 3.

Unfortunately, even today, inverse (or converse) piezoelectricity is still sometimes called electrostriction because the name “electrostriction” suggests the “electromechanical” direction (electrical stimulus leads to mechanical response), while “piezoelectricity” seems to refer only to the opposite “mechano-electrical” direction. In order to avoid the misleading use of the term, it should be kept in mind that our modern terminology is based on phenomenological thermodynamical relations so that the *linear* effects of direct and inverse piezoelectricity must be identical due to the mathematically required reciprocity.

To make things even more complicated, the historical definition of electrostriction, which was developed in physical chemistry already in the late nineteenth century, is given by the Drude–Nernst equation (Drude and Nernst 1894) and describes the volume contraction ΔV_{el} in an electric medium of relative static dielectric permittivity ϵ_r upon introduction of an ionic charge with the number z and the effective radius r :

$$\Delta V_{el} = -\frac{(ze)^2}{2r\epsilon_r} \frac{\partial(\ln\epsilon_r)}{\partial p}. \quad (9)$$

Equation 9 is given in modern notation (IUPAC 1997), as it is still employed in the physical chemistry of fluids – in particular at high pressures. Here, the derivative of $\ln\epsilon_r$ with respect to pressure p is sometimes used separately as another quantity that has also been named “coefficient of electrostriction” – this time indicating the deformation dependence of the dielectric response and thus defining another nonlinear “mechano-electrical” parameter. Consequently, the term “electrostriction” can still be sometimes found as a description of the strain-induced changes of the dielectric permittivity. Fortunately, the new term “dielectrostriction” has been proposed for the strain or stress dependence of the dielectric permittivity in solid materials (Lee and Shkel 2004; Lee et al. 2005), and its analogy to the stress- or strain-induced optical birefringence in dielectric materials has been pointed out: Just as the dielectric permittivity at optical frequencies is given by the square of the respective refractive index, the dielectrostriction at optical frequencies is usually known as birefringence.

An assignment of the respective terms according to presently suggested usage is provided in Table 2. It should be noted that the definitions of the four terms do *not* indicate any underlying mechanisms for the observed effects, i.e., they are just phenomenological. A first step towards the understanding of the physics behind the electromechanical (and mechano-electrical) effects in dielectric materials is provided by the above-discussed spring model (cf. Sect. 3). An even less complex (and thus also less explanatory) concept of electrostriction in dielectrics with compliant electrodes is obtained if the Coulomb force F on an electric charge q in an electric field E is translated into a mechanical stress T on a planar charge distribution σ :

Table 2 Linear and quadratic, and direct and inverse effects that connect the mechanical (elastic) and electrical (dielectric) domains in materials directly (mechanical stimulus \rightarrow electrical response) and inversely (electrical stimulus \rightarrow mechanical response)

Direction	Linear effect	Quadratic effect
Direct effect	Direct piezoelectricity (d, e, g, h)	Dielectrostriction /stress birefringence
Inverse effect	Inverse piezoelectricity (d, e, g, h)	Electrostriction (γ)

$$F = qE \Leftrightarrow T = \sigma E. \quad (10)$$

If there are no quasi-permanent charges or dipoles in the material, the charge density σ on the electrodes is generated by the electric field acting on them due to the applied voltage: $\sigma = \epsilon_0 \epsilon E$. Consequently, we find

$$T = \epsilon_0 \epsilon E^2 \quad (11)$$

for the electrically induced mechanical stress (so-called Maxwell stress) in this case. Depending on the elastic or Young's modulus Y of the uniform dielectric material, the resulting strain S is given by $S = T/Y$ and thus finally by

$$S = \epsilon_0 \frac{\epsilon}{Y} E^2. \quad (12)$$

In the derivation of Eq. 12, it is obvious that the electric field is required twice, once for inducing and maintaining the charges in the electrodes ("electro-electret") and once more for pulling the same charges towards each other, which leads to the observed Maxwell stress T that depends on the square of the electric field E . If the three parameters on the right-hand side of Eq. 12 are lumped into the electrostriction constant γ , a scalar version of Eq. 8 for the electrostriction strain S is obtained. If the dielectric medium between the compliant electrodes is assumed to have liquid-like incompressibility, the strain between the electrodes translates not only into a thickness reduction but also into a lateral expansion that can be used for actuation.

In order to arrive at transducers with almost linear characteristics, a rather large DC bias field E_{DC} can be applied between the electrodes together with the much smaller time-varying AC signal field E_{AC} . The total field is then given by $E = E_{DC} + E_{AC}$ and its square by $E^2 = E_{DC}^2 + 2E_{DC}E_{AC} + E_{AC}^2$. If the DC field is for instance at least one order of magnitude larger than the amplitude of the AC field, the third term will always be less than five percent of the second term so that the nonlinearity is rather small and the dependence of the overall field on the signal may be considered as being more or less linear. In addition to the linearization of the actuation field, the stress-strain behavior of the dielectric material can also be set to a favorable operating point with a quasi-linear stress-strain dependence by pre-stretching the (soft) dielectric in a well-controlled manner.

Several less elementary derivations of the electrically induced mechanical strains or stresses in dielectric materials can be found in the literature: Noncompliant electrodes lead to a reduction of the stress by a factor of up to 2. Furthermore, the

assumption of a poling-induced dipole polarization as in polar electrets yields a thickness reduction during poling which has indeed been observed on piezoelectric PVDF films (Anderson 1986). The nonlinear electric-field or dielectric-polarization dependence of electrostriction can also be used to explain linear piezoelectricity in poled dielectrics with their quasi-permanent dipole polarization (Newnham 2005; Furukawa and Seo 1990) that in turn shows a nonlinear dependence on the electric poling field (hysteresis) in all ferroelectric materials and even in ferroelectrets (Qiu et al. 2013, 2014).

4.3 Concluding Remarks

Nonlinearities play essential roles not only in the poling of electrets and ferroelectric materials (hysteresis, etc.) but also in their piezoelectric and electrostrictive behavior. In addition, piezoelectricity and electrostriction also lead to nonlinearities in the dielectric response of the respective materials (for a general introduction, see Richert (2010)). Consequently, the pressure dependence and the nonlinearities of the dielectric response have been foci of attention in the area of piezoelectricity and electrostriction in inorganic (Zhang et al. 1988) and polymeric (Furukawa et al. 1987; Bauer et al. 2005) dielectrics. Nonlinear effects are also particularly important at large electric fields or deformations (see, e.g., the recent review on the deformation of soft dielectrics (Zhao and Wang 2014) and refs. therein).

The closely related phenomena of the pyroelectric and electrocaloric effects in which the thermal and the electrical domains are coupled directly and inversely, respectively, have not been mentioned or discussed here at all. Ferroelectricity, one of the nonlinear dielectric phenomena that brings pyro- and piezoelectricity with it, has only been briefly touched upon wherever necessary. The relevant dielectric materials with ferro-, pyro-, and piezoelectricity usually also exhibit nonlinear optical (NLO) effects, as well as linear (or Pockels) and nonlinear (or Kerr) electro-optical (EO) effects that are analogous to the linear (piezoelectricity) and nonlinear (electrostriction) electromechanical effects introduced here. Finally, the direct and inverse coupling of the magnetical domain with the mechanical, thermal, electrical, and optical domains yields several additional phenomena that are being investigated and exploited for applications. Fundamental aspects of the whole range of observed or predicted phenomena may be found, e.g., in the book of Newnham (2005).

Last, but not least, it should be noted that only a macroscopic, phenomenological picture of practical and engineering relevance could be provided in this brief introduction. More detailed concepts and theoretical models of material behavior at microscopic or even nanoscopic and molecular scales which help to understand the underlying mechanisms of piezoelectricity and electrostriction better are found in the literature and in other chapters of this book. Between the present phenomenological description and rigorous quantum-physical theories, there is a large spectrum of conceptual approaches to the always exciting world of electromechanical coupling in dielectric materials. The coexistence of so many different models and

descriptions may remind us that we do not know the absolute truth, but only have more or less accurate (and less or more defective) approximations to a full understanding of the wealth of natural phenomena.

Acknowledgments The author is very much indebted to Ruy Altafim, Heitor Basso, Siegfried Bauer, Simona Bauer-Gogonea, the late Dilip Das-Gupta, Takeo Furukawa, the late Bernhard Gross, Sidney Lang, the late Guilherme Leal Ferreira, Axel Mellinger, the late Martin Perlman, Xunlin Qiu, Wei Ren, Dmitry Rychkov, Gerhard Sessler, Zhongfu Xia, and Werner Wirges for many years of fruitful collaborations and stimulating discussions on the topics of this chapter.

References

- Altafim RAP, Qiu X, Wirges W, Gerhard R, Altafim RAC, Basso HC, Jenninger W, Wagner J (2009) Template-based fluoroethylenepropylene piezoelectrets with tubular channels for transducer applications. *J Appl Phys* 106:014106
- Anderson RA (1986) Mechanical stress in a dielectric solid from a uniform electric field. *Phys Rev B* 33:1302–1306
- Andrienko D (2006) Introduction to liquid crystals. Max-Planck Institute of Polymer Research, International Max-Planck Research School “Modelling of Soft Matter” http://www.mpip-mainz.mpg.de/%7Eandrienk/lectures/IMPRS/liquid_crystals.pdf. Cited 19 Dec 2015
- Baskaran S, He X, Chen Q, Fu JY (2011) Experimental studies on the direct flexoelectric effect in α -phase polyvinylidene fluoride films. *Appl Phys Lett* 98:242901
- Baskaran S, He X, Wang Y, Fu JY (2012) Strain-gradient-induced electric polarization in α -phase polyvinylidene fluoride films. *J Appl Phys* 111:014109
- Bauer S, Gerhard(-Mulhaupt) R, Sessler GM (2004) Ferroelectrets: soft electroactive foams for transducers. *Phys Today* 57(2):37–42
- Bauer S, Bauer-Gogonea S, Ploss B, Ploss B (2005) Nonlinear dielectric response of poled amorphous polymer dipole glasses. *J Non-Cryst Sol* 351:2759–2763
- Bauer-Gogonea S, Bauer S, Gerhard(-Mulhaupt) R (1999) Monomorphs, bimorphs, and multimorphs from polar polymer electrets. *Braz J Phys* 29:306–317
- Broadhurst MG, Davis GT (1984) Physical basis for piezoelectricity in PVDF. *Ferroelectrics* 60:3–13
- Buka A, Éber N (2013) Flexoelectricity in liquid crystals – theory, experiments and applications. Imperial College Press, London
- Carpi F, De Rossi D, Kornbluh R, Pelrine R, Sommer-Larsen P (2008) Dielectric elastomers as electromechanical transducers: fundamentals, materials, devices, models and applications of an emerging electroactive polymer technology. Elsevier, Oxford/Amsterdam
- Chee CYK, Tong L, Steven GP (1998) A review on the modelling of piezoelectric sensors and actuators incorporated in intelligent structures. *J Intell Mater Syst Struct* 9:3–19
- Chopra I (2002) Review of state of art of smart structures and integrated systems. *AIAA J* 40:2145–2187
- Chu B, Salem DR (2012) Flexoelectricity in several thermoplastic and thermosetting polymers. *Appl Phys Lett* 101:103905
- Curie J, Curie P (1880) Développement par compression de l'électricité polaire dans les cristaux hémédres à faces inclinées (Development of polar electricity through compression in hemihedral crystals at inclined faces). *Bull Soc Minéral Fr* 3:90–93
- Drude P, Nernst W (1894) Über Elektrostriktion durch freie Ionen (About electrostriction via free ions). *Z Phys Chem Leipzig* 15:79–85
- Frübing P, Kremmer A, Gerhard(-Mulhaupt) R, Spanoudaki A, Pissis P (2006) Relaxation processes at the glass transition in polyamide 11: from rigidity to viscoelasticity. *J Chem Phys* 125:214701

- Fuda Y, Yoshida T (1994) Piezoelectric torsional actuator. *Ferroelectrics* 160:323–330
- Fukada E (2000) History and recent progress in piezoelectric polymers. *IEEE Trans Ultrason Ferroelectr Freq Contr* 47:1277–1290
- Fukada E, Sessler GM, West JE, Berraisoul A, Günther P (1987) Bending piezoelectricity in monomorph polymer films. *J Appl Phys* 62:3643–3646
- Furukawa T, Seo N (1990) Electrostriction as the origin of piezoelectricity in ferroelectric polymers. *Jpn J Appl Phys* 29:675–680
- Furukawa T, Nakajima K, Koizumi T, Date M (1987) Measurements of nonlinear dielectricity in ferroelectric polymers. *Jpn J Appl Phys* 26:1039–1045
- Gerhard R (2014) A matter of attraction: electric charges localised on dielectric polymers enable electromechanical transduction. In: Annual Report, IEEE Conference on Electrical Insulation and Dielectric Phenomena. IEEE, New York, pp 1–10, doi:10.1109/CEIDP.2014.6995800
- Gerhard(-Mulhaupt) R (2002) Less can be more – holes in polymers lead to a new paradigm of piezoelectric materials for electret transducers. *IEEE Trans Dielectr Electr Insul* 9:850–859
- Gross B, Gerhard(-Mulhaupt) R, Berraisoul A, Sessler GM (1987) Electron-beam poling of piezoelectric polymer electrets. *J Appl Phys* 62:1429–1432
- Heckmann G (1925) Die Gittertheorie der festen Körper (Lattice theory of solids). *Ergebnisse der exakten Naturwissenschaften (Springer Tracts in Modern Physics)* 4:100–153. doi:10.1007/978-3-642-94259-4_5, in particular the diagram on page 140
- Helfrich W (1971) The strength of piezoelectricity in liquid crystals. *Z Naturforsch* 26a:833–835
- IUPAC (1997) Compendium of chemical terminology, 2nd edn (“Gold Book”), compiled by AD McNaught, A Wilkinson. Blackwell, Oxford. XML on-line corrected version: <http://goldbook.iupac.org> (2006) created by M Nic, J Jirat, B Kosata; updates compiled by A Jenkins, last update: 2014-02-24, version: 2.3.3., ISBN 0-9678550-9-8. doi:10.1351/goldbook.DT07364
- Katsouras I, Asadi K, Li M, van Driel TB, Kjaer KS, Zhao D, Lenz T, Gu Y, Blom PWM, Dmajanovic D, Nielsen MM, de Leeuw DM (2015) The negative piezoelectric effect of the ferroelectric polymer poly(vinylidene fluoride). *Nat Mater*. doi:10.1038/nmat4423
- Katzir S (2006) The beginnings of piezoelectricity – a study in mundane physics. *Boston Studies in Philosophy and Science*, vol 246. Springer, Dordrecht. doi:10.1007/978-1-4020-4670-4
- Kawai H (1969) The piezoelectricity of poly(vinylidene Fluoride). *Jpn J Appl Phys* 8:975–976
- Kepler RG (1978) Piezoelectricity, pyroelectricity, and ferroelectricity in organic materials. *Ann Rev Phys Chem* 29:497–518
- Kepler RG, Anderson RA (1980) Piezoelectricity in polymers. *CRC Crit Rev Sol State Mater Sci* 9:399–447
- Lee HY, Shkel YM (2004) The dielectrostriction effect for NDE of polymeric materials. *Proc SPIE* 5391:211–218
- Lee HY, Peng Y, Shkel YM (2005) Strain-dielectric response of dielectrics as foundation for electrostriction stresses. *J Appl Phys* 98:074104
- Mellinger A (2003) Dielectric resonance spectroscopy: a versatile tool in the quest for better piezoelectric polymers. *IEEE Trans Dielectr Electr Insul* 10:842–861
- Meyer RB (1969) Piezoelectric effects in liquid crystals. *Phys Rev Lett* 22:918–921
- Newnham RE (2005) Properties of materials: anisotropy, symmetry, structure. Oxford University Press, Oxford/New York
- Newnham RE, Sundar V, Yimnirun R, Su J, Zhang QM (1997) Electrostriction: nonlinear electro-mechanical coupling in solid dielectrics. *J Phys Chem* 101:10141–10150
- Ploss B, Ploss B, Shin FG, Chan HLW, Choy CL (2000) Pyroelectric or piezoelectric compensated ferroelectric composites. *Appl Phys Lett* 76:2776–2778
- Poddar S, Ducharme S (2013) Measurement of the flexoelectric response in ferroelectric and relaxor polymer thin films. *Appl Phys Lett* 103:202901
- Qiu X, Holländer L, Wirges W, Gerhard R, Basso HC (2013) Direct hysteresis measurements on ferroelectret films by means of a modified Sawyer-Tower circuit. *J Appl Phys* 113:224106
- Qiu X, Wirges W, Gerhard R (2014) Polarisation and hysteresis in tubular-channel fluoropolyethylene-copolymer ferroelectrets. *Ferroelectrics* 472:100–109

- Richert R (2005) Dielectric modulus: experiment, application, and interpretation. Arizona State University, Tutorial “Broadband Dielectric Spectroscopy and its Applications” <http://www.uni-leipzig.de/~ids2012/tutorials/richert2005.pdf>. Cited 20 Dec 2015
- Richert R (2010) Non-linear effects in physics of dielectrics. Arizona State University, Tutorial “Broadband Dielectric Spectroscopy and its Applications” <http://www.uni-leipzig.de/~ids2012/tutorials/richert2010.pdf>. Cited 23 Dec 2015
- Rollik D, Bauer S, Gerhard (-Mulhaupt) R (1999) Separate contributions to the pyroelectricity in poly(vinylidene fluoride) from the amorphous and crystalline phases, as well as from their interface. *J Appl Phys* 85:3282–3288
- Rychkov D, Altafim RAP, Gerhard R (2014) Unipolar ferroelectrets – following the example of the electret microphone more closely. In: Annual Report, IEEE Conference on Electrical Insulation and Dielectric Phenomena. IEEE, New York, pp 860–862. doi:10.1109/CEIDP.2014.6995907
- Sherrit S, Mukherjee BK (2012) Review of techniques for characterizing piezoelectric/electrostrictive material for transducer applications. In: Bharadwaja, SSN, Dorey, RA (eds) Dielectric and ferroelectric reviews. Research Signpost, Scarborough, Canada, pp 175–244. <http://arxiv.org/pdf/0711.2657.pdf>
- Tagantsev AK (1991) Polarization in crystals and its response to thermal and elastic perturbations. *Phase Trans* 35:119–203
- Tichý J, Erhart J, Kittinger E, Přivratská J (2010) Fundamentals of piezoelectric sensors. Springer, Berlin/Heidelberg
- Yang GM, Bauer-Gogonea S, Sessler GM, Bauer S, Ren W, WWirges W, Gerhard(- Mulhaupt) R (1994) Selective poling of nonlinear optical polymer films by means of a monoenergetic electron beam. *Appl Phys Lett* 64:22–24
- Zhang QM, Pan WY, Jang SJ, Cross LE (1988) The pressure dependence of the dielectric response and its relation to the electrostriction. *Ferroelectrics* 88:147–154
- Zhao X, Wang Q (2014) Harnessing large deformation and instabilities of soft dielectrics: theory, experiment and application. *Appl Phys Rev* 1:021304
- Zubko P, Catalan G, Tagantsev AK (2013) Flexoelectric effect in solids. *Annu Rev Mater Res* 43:387–421

Ji Su and Yoshiro Tajitsu

Contents

1	Introduction	510
2	Representative Ferroelectric and Piezoelectric Polymeric Materials	511
2.1	Poly(vinylidene fluoride)(PVDF or PVF ₂) and Its Copolymers	511
2.2	Odd-Numbered Polyamides: Nylons	514
2.3	Ferroelectric and Piezoelectric Polymer-Polymer Composite Systems	517
2.4	Summary of Ferroelectricity and Piezoelectricity of the Polymers	519
3	Shear Piezoelectric Polymers	520
3.1	Shear Piezoelectricity in Polymers	520
3.2	Piezoelectricity in PLLA	520
4	Electrostrictive Polymers	523
4.1	High-Energy-Electron Irradiated (HEEI) P(VDF-TrFE) Copolymers	524
4.2	Electrostrictive Graft Elastomers (G-Elastomers)	525
4.3	P(VDF-TrFE)-Based Terpolymers	526
4.4	Other PVDF-Based Copolymers	527
5	Remarks	528
	References	528

Abstract

In this chapter a brief introduction on piezoelectric polymers and electrostrictive polymers is presented, and some representative polymers are given with their essential properties. The information should provide knowledge for readers to know the origin of modern research on piezoelectric and electrostrictive polymers and recent advances in this area.

J. Su (✉)

Advanced Materials and Processing Branch, NASA Langley Research Center, Hampton, VA, USA
e-mail: ji.su-1@nasa.gov

Y. Tajitsu

Faculty of Engineering Science, Kansai University, Osaka, Japan
e-mail: kenji_imoto@imonet.jp

Keywords

Electrostrictive graft elastomers (G-elastomers) • Electrostrictive polymers • Electrostrictive graft elastomers • HEEI P(VDF-TrFE) copolymers • P(VDF-TrFE)-based terpolymers • PVDF-based copolymers • Ferroelectric and piezoelectric polymers (*see* piezoelectric polymers) • High-energy-electron irradiated (HEEI) P(VDF-TrFE) copolymers • Human-machine interface (HMI) • Odd-numbered nylons • Annealing temperature • Molecular structures and ferroelectricity of odd-numbered nylons • Piezoelectric polymers • Mechanisms • Properties • PVDF (*see* Poly(vinylidene fluoride) (PVDF)) • Shear piezoelectric polymers • Poly(vinylidene fluoride) (PVDF) • Curie transition temperature • Melting temperature • Nylon 11-PVDF blends • Odd-numbered polyamides (nylons) • PVDF-nylon 11 bilaminates • Structures of piezoelectric PVDF • Poly-L-lactic acid (PLLA) • PLLA film as practical sensing material • Origin of piezoelectricity

1 Introduction

Piezoelectric and ferroelectric polymers have been recognized as a new class of electroactive materials when the significant piezoelectricity in polyvinylidene fluoride (PVDF or PVF₂) was discovered by Kawai (1969). Since then, a variety of new piezoelectric polymers have been developed including copolymers of vinylidene fluoride and trifluoroethylene, P(VF₂-TrFE), odd-numbered nylons, composite polymers, etc. These materials offer options of material selections for sensor and actuator technologies that need lightweight electroactive materials.

A material is defined as being piezoelectric if the material is polar and the polarization is reorientable or switchable under an external electric field. The piezoelectric response of materials was discovered by the Curies in 1880. They found that some crystals can convert mechanical energy into electrical energy. In 1881, W. G. Hankel contended that the response must obey certain laws of its own (like other intrinsic properties of materials), and Hankel proposed the term “piezoelectricity” (1881), which means pressure-electricity [since *piezo* means press in Greek], to describe the property. Later, a classical theory for single crystals was developed by W. Voigt (1890) and others. According to the classical theory for single crystals, among the 32 crystal classes, 20 with non-centrosymmetry can be piezoelectrically active. Ten of these 20, which have neither a reflection plane nor a twofold axis perpendicular to a particular direction, can possess a net intrinsic dipole moment in their crystal unit cell and thus exhibit pyroelectricity. A crystal is defined to be ferroelectric when the intrinsic dipole moments in the crystal can reverse their direction, following the application of a sufficiently high external electric field (Takase 1991). Figure 1 shows a simple box relationship to distinguish ferroelectricity, piezoelectricity, and pyroelectricity by nature of crystal materials.

The origins of the piezoelectricity of polymers are still not completely understood. Contributions of dimension change and polarization as well as the electrostriction effects (Furukawa and Seo 1990) are widely accepted. It is also suggested by several

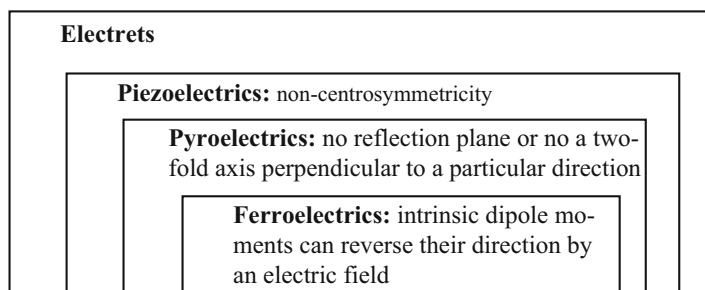


Fig. 1 A simple method to distinguish ferroelectricity, piezoelectricity, and pyroelectricity by nature of crystal materials

Table 1 Contributions from various mechanisms to the piezoelectricity

	Percentage of total response					
	d_p			p_y		
	B et al.	W-H	P-T	B et al.	W-H	P-T
Electrostriction	34	22	45	27	0	76
Dipole libration	10	—	—	23	—	—
Dimensional change of sample	56	78	55	50	47	24
Dimensional change of crystal	—	—	—	—	53	—

^aThe coefficient considered was the piezoelectric stress coefficient, e_{31} .

B et al., Broadhurst et al. 1978; W-H, Wada and Hayakawa; and P-T, Purvis and Taylor

researchers that space charges' effects should also be considered as another significant factor (Borbman et al. 1971). Space charges can have two effects on the spontaneous polarization, P_s , by direct contribution to polarization and modification of the local field during the poling process, which gives rise to local heterogeneity. Table 1 provides a summary of these contributors (Wada and Hayakawa 1976; Broadhurst et al. 1978).

Due to the complicated nature of the piezoelectric properties of polymeric materials, it is extremely difficult to exactly determine which theoretical model is closest to presenting the real mechanisms. However, the theoretical models proposed by researchers are useful in providing insight into the physical basis of the observed piezoelectricity.

2 Representative Ferroelectric and Piezoelectric Polymeric Materials

2.1 Poly(vinylidene fluoride)(PVDF or PVF₂) and Its Copolymers

The discovery of significant piezoelectric response of PVDF films which were mechanically stretched followed by electrical poling initiated comprehensive investigations of structures and morphologies of the polymer. The investigations led to

several significant accomplishments in understanding the intrinsic mechanisms of the ferroelectric and piezoelectric properties of PVDF. The understanding of the nature of ferroelectricity and piezoelectricity in PVDF, including the formation of polymorphic crystal structures, the control of semicrystalline morphology, and the thermal stability of crystal phases, as well as the effects of these on the ferroelectric and piezoelectric properties, guided the development of a series of PVDF-based copolymers with trifluoroethylene. The development of copolymers of poly(vinylidene fluoride-trifluoroethylene) provided a class of ferroelectric and piezoelectric polymeric materials. Systematic studies of the class of polymers have resulted in a more comprehensive understanding of the mechanisms of ferroelectricity and piezoelectricity of this type of polymers, especially the phase transition phenomena. Several review papers have been separately published by Wada and Hayakawa (1976), Furukawa (1989), Davis (1992), Lovinger (1982), and Kepler and Anderson (1978, 1992).

2.1.1 Structures of Piezoelectric PVDF

The repeat unit in the molecular structure of PVDF is $-\text{CF}_2-\text{CH}_2-$. The $-\text{CF}_2$ groups are perpendicular to the axis of the molecular chain direction and are primary dipoles contributing to the remnant polarization. When the molecules crystallize, four primary crystal phases can be formed. They are phase (I), or all-trans (TT) phase; phase (II), or trans-gauche-trans-gauche' (TGTG') phase; phase (III); and phase (IV), or trans-trans-trans-gauche-trans-trans-trans-gauche' (TTTGTTG') phase. The TGTG' conformation of phase (II) is a nonpolar one. The other three phases are polar. However, phase (I) is the most stable polar phase. Phase (II) and phase (I) are the two most commonly studied and understood phases since phase (II) is the primary thermodynamically stable phase, while phase (I) is the desired phase for electromechanical activities (ferroelectricity and piezoelectricity). Figure 2 shows a schematic representation of the view parallel to the chain axis in a crystal unit for a comparison of nonpolar phase (II) and polar phase (I). As can be seen, the dipole cancellation due to the opposite orientation of the equal polar groups happens in

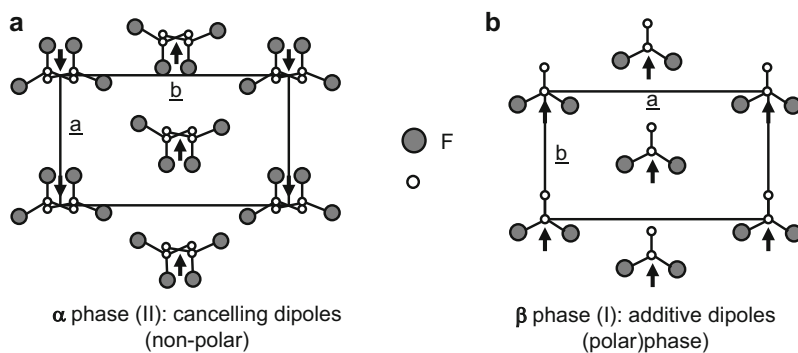


Fig. 2 A schematic comparison of the view parallel to the chain axis in the crystal units of (a) nonpolar α -phase (II) and (b) polar β -phase (I)

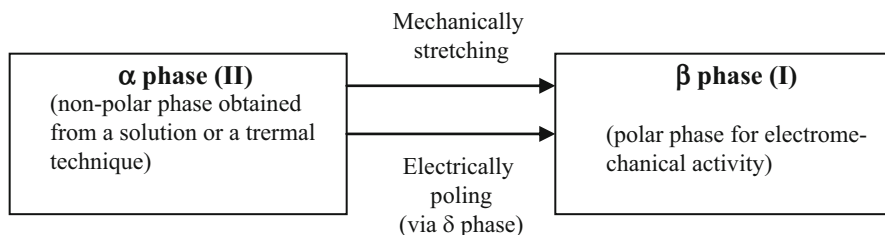


Fig. 3 A block chart demonstrating the routes to make polar β -phase (I) PVDF from nonpolar α -phase (II) PVDF

phase (II), while the dipoles in phase (I) are all aligned in one direction. Phase (I) and phase (II) are also named as β -phase and α -phase, respectively.

In order to make phase (I) PVDF, mechanical stretching, electrical poling, and combination of the mechanical and electrical processing are commonly utilized to transfer thermodynamically stable and nonpolar phase (II) PVDF to electromechanically active polar phase (I). Figure 3 provides a block chart demonstrating the routes to make polar phase (I) PVDF from nonpolar phase (II) PVDF.

In the as-mechanically stretched PVDF film, the polar axis, i.e., the dipole moment axis, is randomly oriented to the stretching direction. An electrical poling treatment is needed to make the dipole axis reorient to align predominantly along the poling z-axis, that is, perpendicular to the film's plane. The field-induced dipole alignment in phase (I) crystals has been investigated by Raman spectroscopy, x-ray diffraction, and infrared dichroism (Wada and Hayakawa 1981).

Lando and Doll reported, in 1968, that copolymers of the VF phase, $-(\text{CH}_2\text{-CF}_2)-$ and VF_2 , $-(\text{CHF-CF}_2)-$, when the VF_2 content is more than 17 mol%, accommodate the more extended all-trans conformation, which is similar to phase (I) PVDF. Yagi et al. synthesized the copolymers with various relative mole compositions (50–80 mol%) in 1979 (Yagi et al. 1980). Because of the advantage of being crystallized directly into the planar zigzag (all-trans) conformation, which is similar to phase (I) PVDF, the ferroelectricity and piezoelectricity of these copolymers have been extensively studied (Lovinger et al. 1983). Ferroelectric transition phenomena have been observed in investigations of the copolymers. Curie transition temperatures of the copolymers were found to be dependent on the relative compositions of VF_2 and VF_3 . The higher the VF_2 content, the higher the Curie transition temperature. If the VF_2 content is higher than 81 mol%, the Curie transition disappears because the transition temperature of such copolymers is higher than the melting temperature, which also explains why PVDF homopolymer does not show a Curie transition (Yamada et al. 1982). Table 2 provides the melting temperatures and the Curie transition temperatures of various copolymers and PVDF homopolymers.

2.1.2 Piezoelectricity of PVDF

The piezoelectric properties of semicrystalline polymers, such as PVDF and its copolymers, are determined by the remnant polarization in the materials and the

Table 2 Melting and Curie transition temperatures of PVDF and its copolymers

	PVDF	52 mol% copolymer	65 mol% copolymer	78 mol% copolymer	80 mol% copolymer
T_m (°C)	182	160	152	153	151
T_c (°C)	198 ^a	67	92	132	141
ΔT (°C) ($T_m - T_c$)	-16 ^b	93	60	19	10

^aExtrapolated^bEstimated

mechanical properties. The remnant polarization primarily depends on the crystallinity, or the content, of polar crystals and the alignment of the polar crystal domains. The most popular method to increase crystallinity is thermal treatment, or annealing. The annealing temperature should be significantly above the glass transition temperature and below the melting temperature and Curie transition temperature if the Curie transition temperature is lower than the melting temperature. In the effective temperature range, the higher the temperature, the better the annealing effect. The method to generate the good alignment of polar crystal domains, that is, the remnant polarization, is electrical poling. Three primary factors are important for poling the materials to achieve high remnant polarization: poling temperature, poling field, and poling time. Generally, higher poling temperature, higher poling field, and longer poling time result in higher remnant polarization. Usually an optimization of the three primary factors is needed for the best poling effect. A well-poled (at room temperature) uniaxially stretched (five times) PVDF film usually can offer the remnant polarization, P_r , of 50 mC/m² and the piezoelectric strain coefficient, d_{31} , of 25 pC/N at room temperature. The piezoelectric response of a poled PVDF depends on the temperature. When the temperature is below its glass transition temperature, T_g , which is around -50 °C, the piezoelectric strain coefficient is very small (less than 2 pC/N). As the temperature increases to be higher than its T_g , the piezoelectric strain coefficient increases obviously to reach the maximum around room temperature. As the temperature keeps increasing, the piezoelectric coefficient starts to decrease around 50 °C due to the thermal depolarization (Su et al. 1995).

2.2 Odd-Numbered Polyamides: Nylons

Another class of representative ferroelectric and piezoelectric polymers is odd-numbered polyamides (nylons). Hydrogen bonding formed by -NH and -C=O groups provides essential polar elements in the polymer for piezoelectricity. The significant piezoelectric properties of nylon 11 was studied and reported in the early 1980s (Newman et al. 1980; Mathur et al. 1988). Its ferroelectricity was predicted based on a study on its chemical structures and crystal phases. However, the synopsis of ferroelectricity in nylons was not confirmed until 1991 when Scheinbeim et al.

reported a typical ferroelectric hysteresis loop from the electric displacement, D , versus the applied electric field, E , test of a specially treated nylon 11 films. The film was produced by a melt-quenched and cold-stretching method. The melt-quenched and cold-stretched nylon 11 not only exhibits the ferroelectric switching mechanism but also increased its piezoelectric property significantly compared to that previously reported, especially at an elevated temperature (Lee and Takase 1991). The discovery has led to a series of achievement in the research on the ferroelectricity and piezoelectricity of odd-numbered nylons including nylon 9, nylon 7, and nylon 5 in Scheinbeim's group.

2.2.1 Molecular Structures and Ferroelectricity of Odd-Numbered Nylons

The alpha-phase crystal structure of nylon 11, suggested by Slichter (1959), is polar. The molecular conformation of the proposed structure is all-trans, and for an odd-numbered nylon, this entails a net dipole moment per chain. Figure 4 shows the molecular structures of odd-numbered nylons and even-numbered nylons (Lee 1991; Su et al. 1995). As can be seen, in odd-numbered nylons, the electric dipoles formed by amide groups (H-N-C=O) with a dipole moment of 3.7 Debyes are sequenced in a way that all the dipoles are in the same direction synergistically. Therefore, the net dipole moment can be formed in one direction. While in even-numbered nylons, the amide group dipoles are in two ways if one is in one direction, the next one will be in the opposite direction, alternately. This results in an intrinsic cancellation of the dipole moments, as demonstrated schematically in the figure.

The remnant polarization of the ferroelectric odd-numbered nylons is a function of the number, which is decisive to the electric dipole density. The smaller the number, the higher the dipole density. This is because the number represents the

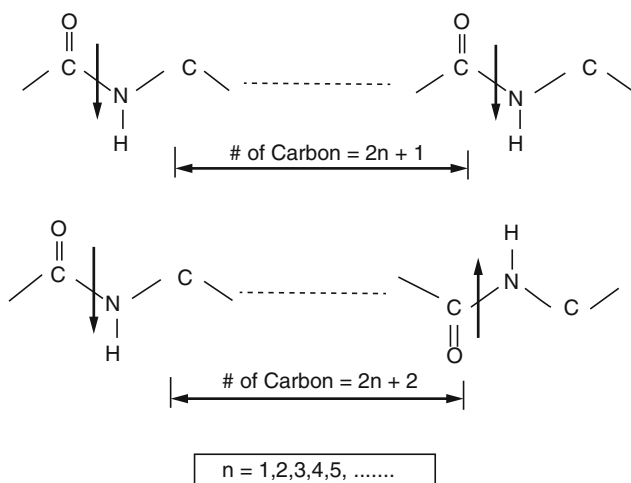


Fig. 4 Schematics of molecular structures of odd-numbered nylons and even-numbered nylons (Adapted from J. Su)

Table 3 Dipole density and remnant polarization of odd-numbered nylons

	N-3	N-5	N-7	N-9	N-11
Molecular weight of repeat unit	71.1	99.1	127.2	155.2	183.3
Dipole density (D/100A ³)	4.30	2.92	2.12	1.65	1.40
Remnant polarization (mC/m ²)	180 ^a	125	86	68	56

^aPredicted

number of carbons contained in a repeat unit in polyamide molecules; therefore, the concentration of amide groups and hydrogen bonds in the polymer increases when the number goes down since there is one amide group in a repeat unit. The interrelationship between the number of dipole per unit molecular weight and the remnant polarization is tabulated in Table 3 as reported by Mei and Scheinbeim (1993).

2.2.2 Piezoelectricity of Some Representative Odd-Numbered Nylons

Similar to the piezoelectric properties of PVDF, the piezoelectric properties of odd-numbered nylons, as semicrystalline polymers, are determined by the remnant polarization in the materials and the mechanical properties. The remnant polarization primarily depends on the crystallinity, or the content, of polar crystals and the alignment of the polar crystal domains. Thermal annealing is the most popular method to increase the crystallinity. For odd-numbered nylons, the annealing temperature should be significantly above the glass transition temperature and below the melting temperature. In the effective temperature range, the higher the temperature, the better the annealing effect. The method to generate the good alignment of polar crystal domains, that is, the remnant polarization, is electrical poling. Three primary factors are important for poling the materials to achieve high remnant polarization: poling temperature, poling field, and poling time. Generally, higher poling temperature, higher poling field, and longer poling time result in higher remnant polarization. Usually an optimization of the three primary factors is needed for the best poling effect. For instance, a well-poled (at room temperature) melt-quenched and uniaxially stretched (3.5 times) nylon 11 film usually can possess a remnant polarization, P_r , of 50 mC/m² and offer a piezoelectric strain coefficient, d_{31} , of 2.8 pC/N at room temperature (Lee et al. 1991a, b). The d_{31} is much less than that of PVDF at room temperature since the piezoelectric response of a poled nylon 11 also depends on the temperature and the room temperature is below its glass transition temperature which is around 70 °C. As the temperature increases to be higher than its T_g , the piezoelectric strain coefficient increases to be as high as 9 pC/N (Takase et al. 1991)

Takase et al. also reported, in 1991, that the annealing treatment of the poled nylon 11 and nylon 7 demonstrated both enhanced piezoelectric strain coefficient and improved piezoelectric stability. These make the odd-numbered nylons possess high and stable piezoelectric properties at high temperatures (up to 200 °C), which is

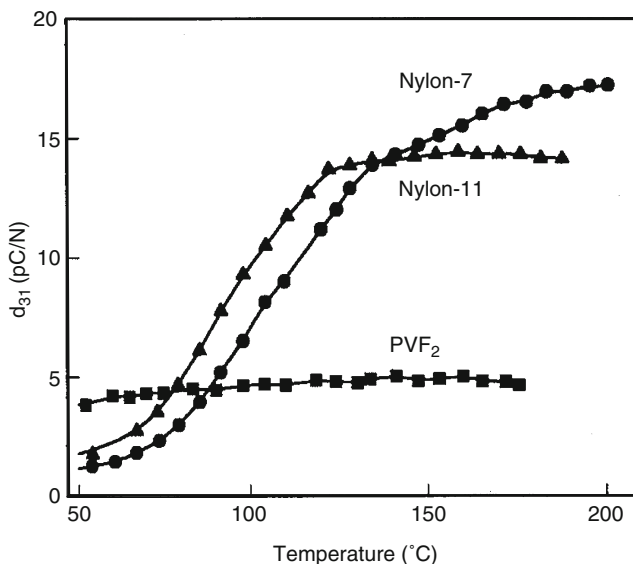


Fig. 5 Temperature dependence of piezoelectric strain coefficient, d_{31} , of the poled and annealed nylon 11 and nylon 7 in comparison with that of poled and annealed PVDF (Adapted from Y. Takashi et al.)

a significant advantage over PVDF which will melt at the temperature. Figure 5 shows a comparison of temperature dependence of the piezoelectric strain coefficients of annealed nylon 11, nylon 7, and PVDF.

2.3 Ferroelectric and Piezoelectric Polymer-Polymer Composite Systems

The existence of the two classes of ferroelectric and piezoelectric polymers, PVDF and its copolymers and odd-numbered nylons, makes it possible to develop polymer-polymer composite systems. Ferroelectric and piezoelectric PVDF-nylon 11 bilaminates and nylon 11-PVDF blends were studied by Su (1992) and Gao et al. (1999), respectively. Significant enhancements in ferroelectric and piezoelectric properties were observed in both polymer-polymer composite systems. Interfacial polarization plays an important role for the enhancement.

2.3.1 PVDF-Nylon 11 Bilaminates

The development of the two ferroelectric and piezoelectric polymers – PVDF and odd-numbered nylons – provides a possibility to make all polymer ferroelectric and piezoelectric composite system. Using PVDF and nylon 11, Su et al. developed nylon 11-poly(vinylidene fluoride) bilaminates by a co-melt-pressed-stretched process in 1992 (Su et al.). The bilaminate exhibits a typical ferroelectric D-E hysteresis

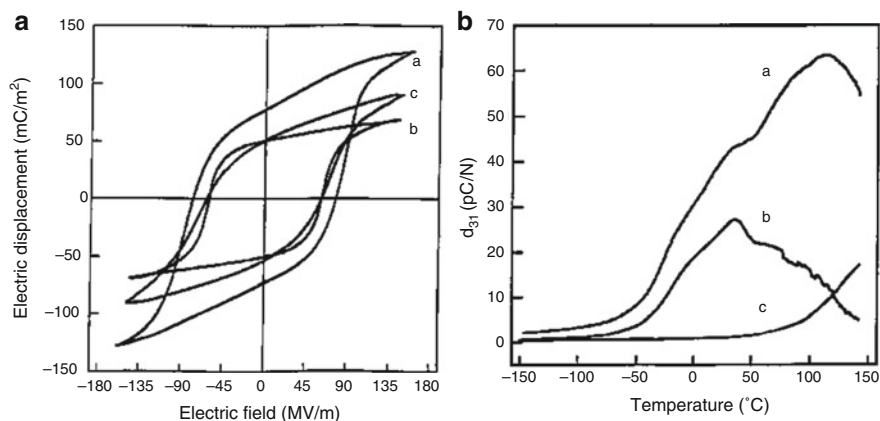


Fig. 6 (a) Curves of electric field displacement, D , versus applied electric field, E , (D - E) and (b) temperature dependence of the piezoelectric strain coefficient, d_{31} , for (a) PVDF-nylon 11 bilaminate, (b) PVDF, and (c) nylon 11 films (Adapted from J. Su et al.)

loop with significantly enhanced remnant polarization, P_r , of 75 mC/m^2 , which is 44 % higher than those of the individual institutes, nylon 11 or PVDF. The results of D - E hysteresis ferroelectric characterization of a 1:1 bilaminate is shown in Figure 6a in comparison with those of individual PVDF and nylon 11. The piezoelectric strain coefficients including strain coefficient d_{31} , stress coefficient e_{31} , and hydrostatic coefficient d_h also show significant enhancement. The enhancement in the piezoelectricity becomes more obvious at the elevated temperature over the glass transition temperature of nylon 11. Figure 6b shows the temperature dependence of the piezoelectric strain coefficient, d_{31} , of PVDF-nylon 11 bilaminate having a 1:1 ratio in comparison with that of individual nylon 11 or PVDF.

The mechanism resulting in the enhancement was found to be attributed to the interfacial space-charge accumulation and the asymmetric distribution of the accumulated space charges along the direction across the interface between the two constituents (Chen et al. 1994). The remnant polarization and piezoelectric coefficients of the bilaminates are a function of the fraction of the two constituents.

2.3.2 Nylon 11-PVDF Blends

In 1999, Gao et al. reported the development of nylon 11-PVDF blends which also exhibit a significantly enhanced remnant polarization, P_r . The P_r of the blend with the 50–50 composition is 85 mC/m^2 , which is more than 60 % higher than those of individual nylon 11 or PVDF with the P_r of 52 mC/m^2 (Gao et al. 1999 and Gao and Scheinbeim 2000). The curves of the electric field displacement, D , versus the applied electric field, E , are shown in Fig. 7. The same paper also reported that the dependence of the ferroelectricity of the blends depends on the fraction of the two constituents and that the enhancement might also be attributed to the space-charge accumulation and distribution (Su et al. 1995). The piezoelectric strain coefficient,

Fig. 7 Curves of electric field displacement, D , versus applied electric field, E , (D - E) (I, nylon 11; II, PVDF films; and III, nylon 11/PVDF 50:50 blend) (Adapted from Q. Gao et al.)

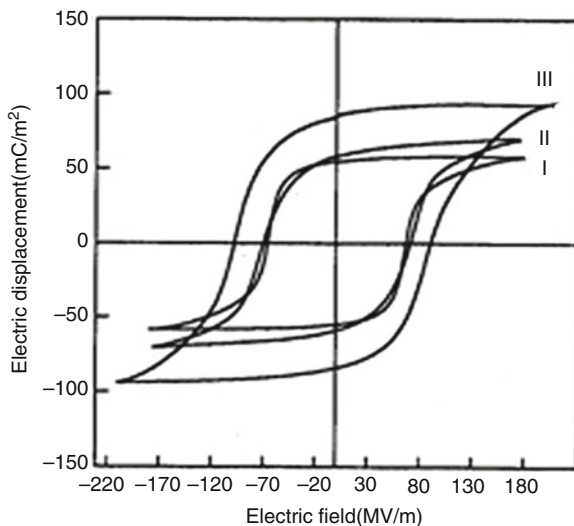


Table 4 Summary of ferroelectric and piezoelectric properties

	PVDF	Nylon 11	Nylon 7	Bilaminate 1:1 (nylon:PVDF) (thickness ratio)	Blend 20:80 (nylon:PVDF) (weight ratio)
P_r (mC/m ²)	52	52	86	75	85
d_{31} at 25 °C	25	3	2	41	—
d_{31} at 110 °C	12	9	7	62	34
d_{31} at 150 °C	4	13	15	53	52
d_{31} at 180 °C	—	13	18	—	—

d_{31} , of nylon 11-PVDF blend films also shows a significant enhancement when compared with the individual nylon 11 or PVDF films. The coefficient depends on the fraction of the two constituents in blends.

2.4 Summary of Ferroelectricity and Piezoelectricity of the Polymers

To summarize the ferroelectric and piezoelectric properties of the discussed polymers, some important ferroelectric and piezoelectric parameters are tabulated in Table 4. As discussed in the previous sections, the ferroelectric and piezoelectric properties of polymeric and polymeric composite systems depend on various factors, such as crystallinity, poling conditions, glass transition temperature, and before and after electrical poling treatments (electrical, mechanical, and thermal treatments). In addition to the factors mentioned above, for composite systems, laminates or blends, fraction of constituents, and interfacial polarization are also important. Therefore, the

properties tabulated may vary due to the dependence of the ferroelectric properties and piezoelectric properties on these factors and the dependence of the factors on the material preparation methods. However, the tabulated summary should provide a reference for the selection of materials for applications or a guideline for developing new ferroelectric and piezoelectric polymeric materials.

3 Shear Piezoelectric Polymers

The study of the shear piezoelectric polymers has advanced in the last few decades, and their practical application to sensor and actuator devices has progressed. In this section, the fundamental properties and applications of shear piezoelectric polymers are discussed.

3.1 Shear Piezoelectricity in Polymers

At present, polymers that have chirality and a helix structure, such as α -helix polypeptides and optically active polymers, are well known to exhibit shear piezoelectricity (Fukada 2000). The following are the important discoveries in the history of shear and tensile piezoelectric polymers. The piezoelectricity of polymers was first investigated for wood and cellulose in 1955 and bone in 1957 (Nalwa and Fukada 1995). Both materials exhibited shear piezoelectricity. Later, tensile piezoelectricity in the axial direction was found in the bone and tendon in 1964 (Fukada 2006). Pyroelectricity in the axial direction was discovered in 1966 (Lang 2005). Tensile piezoelectricity in poly(vinylidene fluoride) (PVDF) was discovered by Prof. Kawai in 1969 (Galetti et al. 1988). Shear piezoelectricity in poly-L-lactic acid (PLLA) was found in 1991 (Carpi and Smela 2009). In 2012, Prof. Li of the University of Washington discovered ferroelectricity in the aorta wall. At present, we indicate PVDF and PLLA are considerable to be suitable polymer materials for forming practical elements. The piezoelectric d-constants of various piezoelectric polymers are summarized in Table 5 (Galetti et al. 1988; Nalwa and Fukada 1995; Fukada 2000; Lang 2005; Fukada 2006).

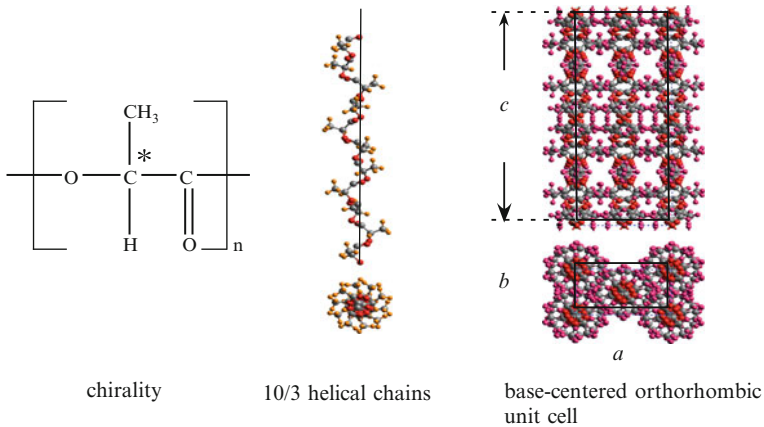
3.2 Piezoelectricity in PLLA

Poly-L-lactic acid is a chiral polymer with two optical isomers, and its chain molecules form a helical structure owing to its chirality. One is PLLA and the other is poly-D-lactic acid (PDLA). The helical structure of PLLA is right handed, whereas the helical structure of PDLA is left handed. The shear piezoelectric constant of PLLA is high compared with those of other shear piezoelectric polymers, as shown in Table 5.

Table 5 Piezoelectricity is universally observed in natural polymers: wood, bamboo, silk, bone, tendon, skin, teeth, horn, blood vessel, muscle, and shell

Biopolymers	pC/N	Synthetic polymers	pC/N
Polysaccharides		Polypeptides (shear)	
Cellulose	0.1	Poly- γ -methyl-L-glutamate (PMLG)	3
Chitin	1.5	Optically active polymers (shear)	
Amylose	3.0	Poly-L-lactic acid (PLLA)	8
Proteins			
Keratin	1.8	Polar polymers (tensile)	
Collagen	4.0	Polyvinylidene fluoride (PVDF)	20
Fibrinogen	2.5	Porous electret (tensile)	
DNA ($-100\text{ }^{\circ}\text{C}$)	0.01	Porous polypropylene (pPP)	400

(Galetti et al. 1988; Nalwa and Fukada 1995; Fukada 2000; Lang 2005; Fukada 2006)

**Fig. 8** Macroscopic symmetry of polymer film

3.2.1 Origin of Piezoelectricity of PLLA

It is well known that the macro-piezoelectricity of a PLLA film is based on the piezoelectricity of the crystal state, which originates from the crystal structure of PLLA. The PLLA crystal structure is based on a base-centered orthorhombic unit cell, as shown in Fig. 8 (Aleman et al. 2001; Kobayashi et al. 1995). Its point group is D_2 and there are three independent shear piezoelectric tensors, d_{14} , d_{25} , and d_{36} . Also, it contains two 10/3 helical chains in a PLLA crystal unit. The origins and ultimate causes of piezoelectricity are the cooperative motion of permanent dipoles existing on the helical chain molecules of PLLA (Tajitsu 2002). Actually, shear stress is applied to the chain molecules in PLLA with a 10/3 helical structure through its side chain. All the atoms in the chain molecules are displaced. In particular, the plane on which the CO bond and carboxyl bond (C=O) exist is rotated, as shown in

Fig. 8. As a result, the C=O bond, which has a larger dipole moment than the other bond, is displaced. The rotation of the C=O bond changes the polarization of the entire long-chain molecule, resulting in the shear piezoelectricity of PLLA. Thus, the macroscopic piezoelectricity of a drawn PLLA film is a result of its intrinsic piezoelectricity due to its crystal state. However, in general, translational symmetry does not exist in a PLLA film because of its complex high-order structure (Tajitsu 2010). In other words, amorphous components are always present in the complex high-order structure. No one-to-one correspondence has been found between macro-piezoelectric properties and crystal characteristics. The mechanism of macroscopic piezoelectricity is made complicated by the existence of the complex high-order structure. We emphasize that the point group in the macroscopic state is different from that in the crystal state (Tajitsu 2013).

Pyroelectricity is not anticipated in PLLA crystal owing to its D_2 symmetry. The existence of pyroelectricity is a very important factor in human-machine interface (HMI) applications for the following reason. If a piezoelectric sensor material exhibits pyroelectricity, then it immediately detects heat from a finger when it is used as an HMI; therefore, it is not possible to distinguish whether the signal originates from the pressure or the heat of the operator's hand. Stable PLLA films with a sufficiently high piezoelectric constant to be used for sensing applications have been successfully produced and further developed into potential HMI devices.

3.2.2 PLLA Film as a Practical Sensing Material

PLLA films, with a larger shear piezoelectric constant than the other polymers in Table I and non-pyroelectricity, are greatly anticipated to be used as sensors and actuators for realizing unconventional HMIs because of their excellent flexibility and transparency. A PLLA sensor has been combined with a projected capacitive touch panel to realize a deformation-sensitive touch panel (Ando et al. 2012). The touch sensor comprises a PLLA film, and the electrode of the touch sensor has a diamond structure. A polycarbonate (PC) plate is used as the surface plate of the touch panel. The electrode consists of three layers, as shown in Fig. 9 (Ando et al. 2013). On layer 1, an RX electrode was

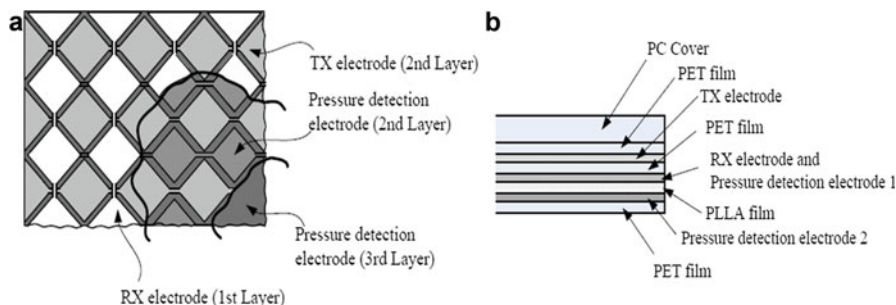


Fig. 9 Deformation- and touch-sensing electrode: (a) plan view and (b) layered structure

Fig. 10 Prototype deformation detection touch panel



formed. On layer 2, a TX electrode was formed. One electrode was formed directly under the RX electrode, the TX electrode and the RX electrode.

Electrodes adjoin each other. On layer 3, another electrode was formed, and this electrode was separated into four portions. This sensor detects the moment of deformation. Furthermore, using an integrated circuit, the sensor can also detect absolute displacement. Figure 10 shows a prototype deformation detection touch panel (Ando et al. 2013).

4 Electrostrictive Polymers

A material is considered as an electrostrictive material when it demonstrates a parabolic strain-electric field relationship due to the interaction between the internal polar domains and the applied electric field. The electrostrictive coefficient of polymers with relatively low elastic modulus may become quite large (Newnham et al.). Scheinbeim et al. firstly reported the significantly high electrostrictive property of polyurethane (PU) in 1994. Thereafter, several other polymers that demonstrated high electrostrictive properties have been reported. It has been shown that the electrostrictive response of ferroelectric polymers can be markedly enhanced through either a route of high-energy electron radiation or a route of molecular engineering since both of the routes, physical and chemical, can introduce changes of molecular conformation, and the molecular conformation results in, consequently, large electrostrictive strain and other electroactive responses. The representative recently developed electrostrictive polymers include high-energy-electron irradiated (HEEI) P(VDF-TrFE) copolymers (Zhang et al. 1998), electrostrictive graft elastomers (G-elastomer) (Su et al. 2000), and P(VDF-TrFE)-based terpolymers (Bharti et al. 2000; Mabboux and Gleason 2002). This section will summarize recent progress for polymers with high electrostriction.

4.1 High-Energy-Electron Irradiated (HEEI) P(VDF-TrFE) Copolymers

One of the approaches to significantly increase the electrostrictive response with a high force level and high elastic energy density in polymers is to work with polymers with a higher dielectric constant. Recently, it has been shown that in HEEI P (VDF-TrFE) copolymers, the dielectric constant of near 60 can be achieved at room temperature range, and, as a consequence, a high electrostrictive strain of about 5 % under 150 MV/m field has been demonstrated (Zhang et al. 1998; Zhao et al. 1998; Cheng et al. 1999b). For the HEEI copolymer, Q_{33} is found in the range between -4 and -15 m^2/C (the electrostrictive M coefficient is greater than 2×10^{-18}) (Cheng et al. 2000), depending on the sample processing conditions. The strain response does not change appreciably with temperature.

The basis for such a large electrostriction in the HEEI P(VDF-TrFE) copolymers is the large change in the lattice strain as the polymer goes through the transformation from the paraelectric-like to ferroelectric-like phases. Besides the large strain response at F-P transition, there is another interesting feature associated with the F-P transition – the possibility that a very large electromechanical coupling factor ($k \sim 1$) can be obtained near a first-order F-P transition temperature (Zhang et al. 1995). Here, the irradiation effect is to introduce defect structures in the polymer to move the transformation process to near room temperature, eliminate the hysteresis in the polarization response to the applied field, and broaden the transformation temperature region so that a high electrostriction can be obtained over a relatively broad temperature range.

Of special interest is the finding that in the electron irradiated P(VDF-TrFE) copolymers, large anisotropy in the strain responses exists along and perpendicular to the chain direction, as can be deduced from the change in the lattice parameters between the polar and nonpolar phases. Therefore, the transverse strain can be tuned over a large range by varying the film processing conditions. For unstretched films, the transverse strain is relatively small ($\sim +1$ % at ~ 100 MV/m), while the amplitude ratio between the transverse strain and longitudinal strain is less than 0.33 (Cheng et al. 1999a, b). This feature is attractive for devices utilizing the longitudinal strain such as ultrasonic transducers in the thickness mode and actuators and sensors making use of the longitudinal electromechanical responses of the material. On the other hand, for stretched films, a large transverse strain (x_1) along the stretching direction can be achieved. A transverse strain of about +4.5 % can be achieved in the HEEI copolymer under an electric field of 85 MV/m (Huang et al. 2004).

The electromechanical coupling factor, k_{33} , for the HEEI copolymers can be as high as 0.3 at near room temperature and under an electric field of 80 MV/m. The k_{33} is comparable to that obtained in a single-crystal P(VDF-TrFE) copolymer. More interestingly, k_{31} of 0.65 can be obtained in a stretched copolymer (Cheng et al. 2001), which is much higher than values measured in piezopolymers (Omote et al. 1997). The frequency response of the electrostrictive strain of the irradiated copolymer was studied, and it was found that the high strain response can be maintained at least to 100 kHz, the upper limit of the study (Xu et al. 2002).

One principal effect of the high-energy irradiation is network formation (cross-linking) (Bharti et al. 2000). Casalini and Roland used a free-radical cross-linker and coagent to form a three-dimensional network of P(VDF-TrFE) copolymer with high cross-link density and showed that in such a P(VDF-TrFE) network, a thickness strain of more than -10% can be induced under a field of 9 MV/m when measured under DC condition (Casalini and Roland 2001). It was suggested that the large strain is from the rotation of the small ferroelectric crystals, created due to the high density of cross-linking which greatly reduces the crystallite sizes, under external field.

The polarization hysteresis loop measured at room temperature for the P(VDF-TrFE) 68/32 mol% copolymer changes with the irradiation dose (Cheng et al. 2002). With increased dosage, the near square polarization hysteresis loop, characteristic for a normal ferroelectric material, is transformed to a slim polarization loop (at 75 Mrads). At very high dose (175 Mrads), the polymer becomes a linear dielectric in which the crystallinity is near zero.

4.2 Electrostrictive Graft Elastomers (G-Elastomers)

Su et al. (1999, 2003) reported the observation of a high strain (thickness strain $\sim 4\%$) in a grafted elastomer. The induced strain in the electrostrictive G-elastomer exhibits a quadratic dependence with the applied electric field. The graft elastomer consists of two components, a flexible backbone polymer and grafted crystalline polar groups. The flexible backbone polymer provides the amorphous chains for the formation of the three-dimensional network that is physically cross-linked by the grafted crystalline moieties. The grafted polar crystalline moieties also provide the electric field-responsive mechanism for the electric field-induced dimensional change or electromechanical properties. In the electrostrictive G-elastomer studied, the flexible backbone polymer is a copolymer of chlorotrifluoroethylene and trifluoroethylene, while the grafted polar crystalline polymer is a copolymer of vinylidene fluoride and trifluoroethylene (P(VDF-TrFE)). The electric field-induced longitudinal strain was measured at room temperature.

In the case of polymeric elastomers exhibiting a large electric field-induced strain, two intrinsic mechanisms are considered as primary contributors: electrostriction and the Maxwell stress effect. The contributions from both mechanisms exhibit a quadratic dependence with an applied electric field. For the newly developed electrostrictive graft elastomers, more than 95 % of the electric field-induced strain response is contributed by the electrostriction mechanism, while the contribution from the Maxwell stress effect is less than 5 %. Due to the relatively high elastic modulus (~ 0.55 GPa), the grafted elastomer also exhibits a high elastic energy density of 0.44 MJ/m³.

Su et al. reported, in 2003, that the electric field-induced strain of the elastomer can be controlled by thermal annealing treatment, which can increase the crystallinity of the grafted electric field-responsive domains. The higher crystallinity is achieved, the higher electric field-induced strain is obtained. Since the mechanism

of the electromechanical response in an electrostrictive graft elastomer is hypothesized to involve rotation of the polar crystal domains under an applied electric field, the overall electric field-induced strain should critically depend on the number or size of the polar domains and, therefore, the degree of crystallinity. Accordingly, the electric field-induced strain of the elastomers significantly increases with annealing treatment. In general, the strain responses increase with total crystallinity. At a given crystallinity, however, the elastomer containing more grafted polar domains gives a higher response. It is thought that the crystal size and distribution may also affect the overall electromechanical response.

To understand the mechanisms of the electrostriction in the G-elastomers, a model has been established (Wang et al. 2003). The model simulation indicated that the mechanisms of the electric field-induced strain in the electrostrictive G-elastomers are attributed to the rotation of the polar crystal domains that formed by grafted molecular chains and the reorientation of the flexible backbone chains when an electric field is applied.

4.3 P(VDF-TrFE)-Based Terpolymers

Although high-energy irradiations can be used to convert the normal ferroelectric P(VDF-TrFE) into a relaxor ferroelectrics with high electrostriction, the irradiation also introduces many undesirable defects to the copolymer, such as the formation of cross-linkings, radicals, and chain scission (Bharti et al. 1999, 2000; Mabboux and Gleason 2002). From the basic ferroelectric response point of view, the defect modification of the ferroelectric properties can also be realized by introducing randomly in the polymer chain a third monomer, which is bulkier than VDF and TrFE. Furthermore, by a proper molecular design which enhances the degree of molecular level conformational changes in the polymer, the terpolymer can exhibit a higher electromechanical response than the high-energy-electron irradiated copolymer, as will be shown by the terpolymers containing small amount of chlorofluoroethylene (CFE, $-\text{CH}_2\text{-CFCl}-$) as the termonomer. The high electrostrictive response was also observed in several other ferroelectric fluoroterpolymers such as P(VDF-TrFE-CTFE) (CTFE, chlorotrifluoroethylene) and P(VDF-TrFE-HFP). To facilitate the discussion and comparison with the irradiated P(VDF-TrFE) copolymer, the composition of the terpolymers (use P(VDF-TrFE-CFE) as an example) is labeled as $\text{VDF}_x\text{-TrFE}_{1-x}\text{-CFE}_y$, where the mole ratio of VDF/TrFE is $x/1-x$ and y is the mol.% of CFE in the terpolymer.

For the 62/38/4 mol% terpolymer P(VDF-TrFE-CFE), under a field of 130 MV/m, the thickness strain of -4.5% can be achieved, which is comparable to that observed in the irradiated copolymers. The high elastic modulus in this P(VDF-TrFE-CFE) terpolymer ($Y \sim 1.1$ GPa for unstretched films) results in a high elastic energy density, $YS^2/2$, ~ 1.1 J/cm³. The longitudinal coupling factor, k_{33} , can be as high as 0.55 (Xia et al. 2002).

By increasing the ratio of VDF/TrFE in the terpolymer, the electric field-induced strain level can be raised due to the fact that the lattice strain between the polar conformation and nonpolar conformations increases with the VDF/TrFE ratio.

The thickness strain of the P(VDF-TrFE-CFE) terpolymer at composition of 68/32/9 mol% can be as high 7 %, which is by far the highest among all the high-energy-electron irradiated copolymers and terpolymers investigated (measured at frequencies equal to or higher than 10 Hz) (Xia et al. 2002; Huang et al. 2004; Cheng et al. 2001; Xu et al. 2001). The transverse strain response of this terpolymer was also characterized. The transverse strain x_1 of uniaxially stretched film is usually higher than the transverse strain of a non-stretched film. The transverse strain perpendicular to the stretching direction is negative. Using the relationship

$$x_v = x_3 + x_1 + x_2$$

where x_1 and x_2 are the transverse strains, the volume strain can be determined, and it was found that for the terpolymer of P(VDF-TrFE-CFE), the volume strain is very small (on the order of 10 % of the thickness strain x_3). This is different from the irradiated copolymers, which exhibit quite high volume strain and suggests different mechanisms for generating electrostrictive strain in the two classes of polymers.

In addition to the terpolymer of P(VDF-TrFE-CFE), ferroelectric fluoroterpolymers with other monomers such as chlorotrifluoroethylene (CTFE), hexafluoropropylene (HFP), vinyl chloride (VC), and chlorodifluoroethylene (CDFE) (Xu et al. 2001; Chung and Petchsuk 2001; Chung and Petchsuk 2002; Garrett et al. 2003) have also been developed. Among these terpolymers, P(VDF-TrFE-CTFE) was investigated in some details regarding their electromechanical response, and the results show that although very large thickness strain was reported when measured at near DC (static) condition (strain of 1.2 % under 20 MV/m, for example, corresponding an electrostrictive coefficient $M = 3 \times 10^{-17} \text{ m}^2/\text{V}^2$, $S = \text{ME}^2$), the strain response measured at non-DC condition is lower than that from the terpolymer of P(VDF-TrFE-CFE) (Xu et al. 2001; Buckley et al. 2002).

4.4 Other PVDF-Based Copolymers

In addition to the three classes of electrostrictive polymers, several other PVDF-based electrostrictive polymers have also been reported, including poly(vinylidene fluoride-hexafluoropropylene) (P(VDF-HFP)) and poly(vinylidene fluoride-chlorotrifluoroethylene) (P(VDF-CTFE)) copolymers. The research work on these electrostrictive polymers was primarily conducted by Gerhard-Muthaupt's group at the University of Potsdam, Scheinbeim's group at Rutgers University, and Zhang's group at the Pennsylvania State University, respectively.

The electrostrictive performance of P(VDF-HFP) copolymer films under different thermal treatments was investigated (Lu et al. 2000; Jayasuriya et al. 2001). Although the copolymer exhibits a large polarization hysteresis loop, it is found

that the quenched copolymer sample is at electrostrictive state with a relatively high strain response. The strain measurements were carried out at near static condition, and the mechanism responsible for such a large strain response was not known.

The electrostrictive behavior of P(VDF-CTFE) copolymers was investigated (Li et al. 2004; Li et al. 2006). A high electromechanical response was obtained in these copolymer films. As other PVDF-based polymers, the processing condition plays a very critical role on its properties. For a well-stretched and annealed P(VDF-CTFE) 88/12 copolymer film, a longitudinal electrostrictive strain as much as 5.5 % was obtained. A linear relationship between the strain response and the P^2 was observed, which indicates the electrostrictive nature of the electromechanical response in P(VDF-CTFE) copolymers. The corresponding electric field-related electrostrictive coefficient for the copolymer film is obtained as $M_{33} = -1.23 \pm 0.02 \times 10^{-18} \text{ (m}^2/\text{V}^2\text{)}$ (Li et al. 2006).

5 Remarks

Electroactive polymers, particularly, piezoelectric and electrostrictive polymer, and their applications are still relatively new research fields. Due to some advantages of electroactive polymers over electroactive ceramics, such as being lightweight and having good process ability, low cost, and mechanical and electrical toughness, these research fields have been drawing more and more attention to researchers worldwide since significant ferroelectric and piezoelectric properties of poly(vinylidene fluoride) (PVDF or PVF₂) were discovered and reported in 1969. In recent year, electrostrictive polymers have demonstrated very impressive electroactive properties, especially the large electric field-induced strain combined with relatively high mechanical modulus. The properties make electrostrictive polymers very promising materials for electromechanical applications. The information provided here may serve as a guideline for readers for understanding the nature of the piezoelectric and electrostrictive polymers and for developing techniques to tailor or control the piezoelectric and electrostrictive properties as desired.

References

- Aleman C, Lotz B, Puiggali J (2001) Crystal structure of the alpha-form of poly(L-lactide). *Macromolecules* 34:4795–4801
- Ando M, Kawamura H, Tajitsu Y et al (2012) Film sensor device fabricated by a piezoelectric poly-L-lactic acid film. *Jpn J Appl Phys* 51:09LD14-1
- Ando M, Kawamura H, Tajitsu Y et al (2013) A deformation detection touch panel using a piezoelectric poly(L-lactic acid) film. In: *Proceedings of the 20th international display workshop*, Sapporo Convention Center, Sapporo, 4–6 Dec 2013
- Bergman J et al (1971) Pyroelectricity and optical second harmonic generation in polyvinylidene fluoride films. *Appl Phys Lett* 18:203
- Bharti V et al (1999) High electrostrictive strain under high mechanical stress in electron irradiated poly(vinylidene fluoride–trifluoroethylene) copolymer. *Appl Phys Lett* 75:2653

- Bharti V et al (2000) Polarization and structural properties of high energy electron irradiated P(VDF-TrFE) copolymer films. *J Appl Phys* 87:452–461
- Broadhurst M et al (1978) Piezoelectricity and pyroelectricity in polyvinylidene fluoride—A model. *J Appl Phys* 49:4992
- Buckley GS et al (2002) Electrostrictive properties of poly(vinylidene fluoride–trifluoroethylene–chlorotrifluoroethylene). *Chem Mater* 14(6):2590–2593
- Carpi F, Smela E (eds) (2009) Biomedical applications of electroactive polymer actuators. Wiley, Chichester
- Casalini R, Roland M (2001) Highly electrostrictive poly(vinylidene fluoride–trifluoroethylene) networks. *Appl Phys Lett* 79:2627
- Chen G et al (1994) FTIR-ATR studies of drawing and poling in polymer bilaminate films. *J Polym Sci Part B Polym Phys* 32:2065
- Cheng Z et al (1999a) Transverse strain responses in electrostrictive poly(vinylidene fluoride–trifluoroethylene) films and development of a dilatometer for the measurement. *J Appl Phys* 86:2208
- Cheng Z et al (1999b) Transverse strain responses in the electrostrictive P(VDF-TrFE) copolymer. *Appl Phys Lett* 74:1901–1903
- Cheng Z et al (2000) Effect of high energy electron irradiation on the electromechanical properties of poly(vinylidene fluoride–trifluoroethylene) 50/50 and 65/35 copolymers. *IEEE Trans Ultrason Ferroelectr Freq Control* 47:1296
- Cheng Z et al (2001) Electrostrictive poly(vinylidene fluoride–trifluoroethylene) copolymers. *Sensor Actuators A Phys* 90:138
- Cheng Z et al (2002) Structural changes and transitional behavior studied from both micro- and macroscale in the high-energy electron-irradiated P(VDF-TrFE) copolymer. *Macromolecules* 35:664
- Chung, Petchsuk (2001) Ferroelectric polymers with large electrostriction; based on semicrystalline VDF/TrFE/CTFE terpolymers. *Ferroelectr Lett Sec* 28:5–6
- Chung, Petchsuk (2002) Synthesis and properties of ferroelectric fluoroterpolymers with curie transition at ambient temperature. *Macromolecules* 35(20):7678–7684
- Curie J, Curie P (1880) Development by pressure of polar electricity in hemihedral crystals with inclined faces. *Bull Soc Min de France* 3:90
- Davis G (1992) Piezoelectric and pyroelectric polymers. In: Wong CP (ed) *Polymers for electronic and photonic applications*. Academic Press, Boston
- Fukada E (2000) History and recent progress in piezoelectric polymers. *IEEE Trans Ultrason Ferroelectr Freq Control* 47:1110–1119
- Fukada E (2006) Recent developments of polar piezoelectric polymers. *IEEE Trans Dielectr Electr Insul* 13:1110–1119
- Furukawa T (1989) Ferroelectric properties of vinylidene fluoride copolymers. *Phase Transit* 18:143
- Furukawa T, Seo N (1990) Electrostriction as the origin of piezo-electricity in ferroelectric polymers. *Jpn J Appl Phys* 29(4):675
- Galetti P et al (eds) (1988) Piezoelectric and ferroelectric properties of P(VDF-TrFE) copolymers and their application to ultrasonic transducers. In: *Medical applications of piezoelectric polymers* Gordon and Breach, New York
- Gao G, Scheinbeim (2000) Dipolar intermolecular interactions, structural development, and electromechanical properties in ferroelectric polymer blends of nylon-11 and poly(vinylidene fluoride). *J Macromol* 33:7546
- Gao Q et al (1999) Ferroelectric properties of nylon 11 and poly(vinylidene fluoride) blends. *J Polym Sci Part B Polym Phys* 37:3217
- Garrett J et al (2003) Electrostrictive behavior of poly(vinylidene fluoride–trifluoroethylene–chlorotrifluoroethylene). *Appl Phys Lett* 83:1190
- Hankel W (1881) Über die aktinoud piezoelektrischen eigen schaften des bergkrystalles und ihre beziehung zi den thermoelektrischen. *Abh Sachs* 12:451

- Huang et al (2004) Poly(vinylidene fluoride-trifluoroethylene) based high performance electroactive polymers. *IEEE Trans Dielec Elec Insul* 20:299–311
- Jayasuriya et al (2001) Crystal-structure dependence of electroactive properties in differently prepared poly(vinylidene fluoride/hexafluoropropylene) copolymer films. *J Polym Sci Part B Polym Phys* 39(22):2793–279
- Kawai H (1969) The piezoelectricity of poly (vinylidene fluoride). *Jpn J Appl Phys* 8:975
- Kepler R, Anderson R (1978) Ferroelectricity in polyvinylidene fluoride. *J Appl Phys* 49:1232
- Kepler R, Anderson R (1992) Ferroelectric polymers. *Adv Phys* 41(1):1
- Kobayashi J, Fukada E, Shikunami Y et al (1995) Structural and optical properties of polylactic acid. *J Appl Phys* 77:2957–2972
- Lang SB (2005) Guide to the literature of piezoelectricity and pyroelectricity. *Ferroelectrics* 321:91–204
- Lee (1991) Ferroelectricity and piezoelectricity of odd-numbered nylons. PhD Thesis, Rutgers, The State University of New Jersey
- Lee J et al (1991a) Ferroelectric polarization switching in nylon-11. *J Polym Sci Part B Polym Phys* 29:273
- Lee J et al (1991b) Effect of annealing on the ferroelectric behavior of nylon – 11 and nylon – 7. *J Polym Sci Part B Polym Phys* 29:279
- Li Z et al (2004) Recrystallization study of high-energy electron-irradiated P(VDF–TrFE) 65/35 copolymer. *Macromolecules* 37:79–85
- Li Z et al (2006) Electromechanical properties of poly(vinylidene-fluoride–chlorotrifluoroethylene) copolymer. *Appl Phys Lett* 88:062904
- Lovinger A (1982) Chapter 5: Poly(Vinylidene fluoride). In: Bassett DC (ed) *Development in crystalline polymers I*. Applied Science, London
- Lovinger A et al (1983) Curie transitions in copolymers of vinylidene fluoride. *Ferroelectrics* 50:227
- Lu et al (2000) Giant electrostrictive response in poly(vinylidene fluoride-hexafluoropropylene) copolymers. *IEEE Transactions on Ultrasonics, Ferroelectrics, and Frequency Control* 47(6):1291–1295
- Mabboux, Gleason (2002) NMR characterization of electron beam irradiated vinylidene fluoride-trifluoroethylene copolymers. *J Fluorine Chem* 113(1):27–35
- Mathur S et al (1988) Piezoelectricity in uniaxially stretched and plasticized nylon 11 films. *J Polym Sci Part B Polym Phys* 26:447
- Mei, Scheinbeim (1993) Ferroelectricity and piezoelectricity of odd-numbered nylons. *Ferroelectrics* 144:51
- Nalwa H, Fukada E (eds) (1995) *Ferroelectric polymers*. Marcel dekker, New York
- Newman B et al (1980) The piezoelectricity of poly(vinylidene fluoride). *J Appl Phys* 51:5161
- Omote et al (1997) Temperature dependence of elastic, dielectric, and piezoelectric properties of “single crystalline” films of vinylidene fluoride trifluoroethylene copolymer. *J Appl Phys* 81:2760
- Scheinbeim J et al (1991) Effect of water content on the piezoelectric technical report properties of nylon 11 and nylon 7. *J Polym Sci Part B Polym Phys* 24:1791
- Scheinbeim J, Newman B (1993) Electric field-induced changes in odd-numbered nylons. *Trip* 1:394
- Slichter (1959) Molecular motion in polyamides. *J Polym Sci A* 35(128):77–92
- Su (1992) Ferroelectricity and piezoelectricity of nylon 11-PVF2 bilaminates. Internal Technical report, Rutgers, The State University of New Jersey
- Su J et al (1999) Electrostrictive graft elastomers and applications. In: *Proceedings of MRS Symposium, vol 600*, pp 131–136, MRS Conference Publication
- Su J et al (2003) Electrostrictive graft elastomers, U.S. Patent No. 6,515,077, 4
- Su J et al (1995) Ferroelectric and piezoelectric properties of nylon 11/poly(vinylidene fluoride) bilaminate films. *J Polym Sci Part B Polym Phys* 33:85

- Tajitsu Y (2002) Giant optical rotatory power and light modulation by polylactic acid film. In: Zhang Q, Fukada E (eds) Materials research society symposium proceedings book, vol 698, pp 125–136. MRS Publication, Cambridge University Press, Cambridge
- Tajitsu Y (2010) Basic study on controlling piezoelectric motion of chiral polymeric fiber. *IEEE Transactions Dielectr Electr Insul* 17:1050–1055
- Tajitsu Y (2013) Fundamental study on improvement of piezoelectricity of poly(l-lactic acid) and Its application to film actuators *IEEE transactions of ultrasonics. Ferroelectr Freq Control* 60:1625–1629
- Takase Y (1991) Electric properties of polymers. Unpublished internal Lecture Text Book, Rutgers University
- Takase Y et al (1991) High-temperature characteristics of nylon-11 and nylon-7 piezoelectrics. *Macromolecules* 24:6644
- Voigt W (1890) General theory of the piezo and pyroelectric properties of crystals. *Abh Gott* 36:1
- Wang Y et al (2003) Two-dimensional computational model for electrostrictive graft elastomer. *Proc SPIE* 5051:100–111, SPIE Publisher
- Wada Y, Hayakawa R (1976) Piezoelectricity and pyroelectricity of polymers. *Jpn J Appl Phys* 15:2041
- Wada Y, Hayakawa R (1981) A model theory of piezo- and pyroelectricity of poly(vinylidene fluoride) electret. *Ferroelectrics* 32:115
- Xia F et al (2002) High electromechanical responses in a P(VDF–TrFE–CFE) terpolymer. *Adv Mater* 14:1574
- Xu H et al (2001) Ferroelectric and electromechanical properties of P(VDF–TrFE–CTFE) terpolymer. *Appl Phys Lett* 78:2360
- Xu TB et al (2002) High-performance micromachined unimorph actuators based on electrostrictive P(VDF–TrFE) copolymer. *Appl Phys Lett* 80:1082
- Yagi T et al (1980) *Polym J* 12:209
- Yamada T et al (1982) Piezoelectricity of a high-content lead zirconate titanate/polymer composite. *J Appl Phys* 53:4328–4332
- Zhang QM et al (1995) Characteristics of the electromechanical response and polarization of electric field biased ferroelectrics. *J Appl Phys* 77:2549
- Zhang QM et al (1998) Giant electrostriction and relaxor ferroelectric behavior in electron irradiated P(VDF–TrFE). *Science* 280:2101
- Zhao X et al (1998) Electromechanical properties of electrostrictive P(VDF–TrFE) copolymer. *Appl Phys Lett* 73:2054

Siegfried Bauer and Simona Bauer-Gogonea

Contents

1	Introduction	534
2	Printing of Piezoelectric Polymers	535
3	Piezoelectric Polymer-Based Electronic Skins	538
4	Loudspeakers, Tactile Sensors with Haptic Feedback, and Braille Displays	539
5	Electromechanical Energy Harvesting with Piezoelectric Polymers	542
6	Discussion and Conclusion	544
	References	545

Abstract

This chapter presents a brief overview on sensor and transducer applications of piezoelectric and electrostrictive polymers. Piezoelectric and electrostrictive polymers are smart electromechanical materials which have already found commercial applications in various transducer configurations. Novel applications may arise in the emerging fields of autonomous robots, electronic skin, and flexible energy generators. This chapter focuses on recent device demonstrations of piezoelectric and electrostrictive polymers in these novel fields of research to stimulate and to facilitate the exchange of ideas between disciplines. The applications considered include piezoelectric sensors for electronic skin, piezoelectric loudspeakers and transducers for mechanically flexible energy harvesters, as well as electrostrictive transducers for haptic feedback in displays.

Keywords

Piezoelectric sensors • Flexible electronics • Electronic Skin • Loudspeakers • Haptic feedback • Braille displays • Energy harvesting

S. Bauer (✉) • S. Bauer-Gogonea
Soft Matter Physics, Johannes Kepler University Linz, Linz, Austria
e-mail: sbauer@jku.at; simona.bauer-gogonea@jku.at

1 Introduction

Piezoelectricity is a common feature of diverse polymers, but the effect is usually small and not of sufficient magnitude to be applied technically (Bauer 1996; Fukada 2000; Qiu 2010). The situation changed in the late 60s, where a strong piezoelectric effect was found in the synthetic fluoropolymer polyvinylidene fluoride (PVDF) (Kawai 1969). Kawai's discovery was immediately complemented by the finding of pyroelectricity and optical second harmonic generation in PVDF only 2 years later (Bergman et al. 1971; Nakamura and Wada 1971). These initial papers triggered a wealth of device-oriented works with ferroelectric polymers from the PVDF family, starting with pyroelectric infrared sensors (Glass et al. 1971) and a pyroelectric xerography process (Bergman et al. 1972). PVDF and its copolymers display moderate piezoelectric effects, as compared to piezoelectric ceramics (Li et al. 2014) and ferroelectrets (Bauer et al. 2004). Despite the moderate piezoelectric effect in ferroelectric polymers, commercially successful devices emerged in many niches, such as hydrophones, clamp-on transducers for the detection of transient pressure signals, and piezoelectric ignition systems for measuring the mechanical properties of materials under shock loading (Bauer and Bauer 2008).

The materials base of ferroelectric polymers was significantly enlarged by the discovery of relaxor ferroelectric polymers with a strong electrostrictive response in electron beam-irradiated poly(vinylidene-trifluoroethylene) P(VDF-TrFE) copolymers (Zhang et al. 1998). State of the art relaxor ferroelectric polymers rely on terpolymers of PVDF with trifluoroethylene and 1, 1-chlorofluoroethylene (CFE) or chlorotrifluoro ethylene (CTFE). They enable applications in Braille displays or haptic feedback-based sensor devices (Bauer 2012). In terms of material processing, printing became a focus of recent research, paving a way to easily process piezoelectric polymers on large areas on a wide range of support materials (Zirkel et al. 2011; Pabst et al. 2012).

In this book chapter, we will not discuss established applications of ferroelectric polymers; we rather briefly present novel devices arising in emerging research fields such as autonomous robots, electronic skin, and flexible electromechanical energy harvesters (Chortos and Bao 2014; Hammock et al. 2013; Bauer et al. 2014). Instead of providing an in-depth coverage of the topic, we have selected a few recent device applications to give the reader a flavor of current research. For a thorough review of piezoelectric polymers in electromechanical transducers, the reader is referred to the work by Ramadan et al. (2014). The chapter is organized as follows. In Sect. 2, we briefly introduce printing for processing piezoelectric polymer films on large area flexible substrates. We continue the discussion in Sect. 3 with a description of electronic skins based on piezoelectric sensing. In Sect. 4, we summarize applications of piezoelectric polymers for loudspeakers, tactile sensors with haptic feedback systems, and Braille displays, before we proceed in Sect. 5 with a discussion of electromechanical energy harvesting systems based on piezoelectric polymers. In the conclusion, Sect. 6, we briefly emphasize the diversity of current device-oriented research with piezoelectric and electrostrictive electroactive polymers, with the aim

to demonstrate the huge technological potential offered by these materials and the challenges for future research.

2 Printing of Piezoelectric Polymers

Printed electronics promises to change the fabrication of electronic devices, enabling sustainable production at low-cost and large volume on flexible or elastic substrates (Parashkov et al. 2005). One of the challenges in the printing of piezoelectric polymers is the formulation of an environmentally friendly ink for the P(VDF-TrFE) copolymers (Zirkl et al. 2011). P(VDF-TrFE) is advantageous over PVDF for printing, because carefully chosen curing steps directly support the formation of the crystalline piezoelectric β -phase. An environmentally friendly P(VDF-TrFE) ink employs a mixture of *g*-butyrolactone and acetone to dissolve the polymer granules (Zirkl et al. 2011). After the complete dissolution of the polymer granules, acetone was removed from the solution. With an 18 wt% solution, optimum printing results were obtained by screen printing the polymer on different flexible substrates. The process flow for the production of a printed piezoelectric active matrix sensor array consists of consecutive screen printing steps of the bottom electrodes, the piezoelectric polymer sensor layer, and top electrodes (Fig. 1a–c). Further printing steps form the electrochemical transistors for impedance matching and multiplexing (Fig. 1d–f). With a careful choice of materials, such a complex device could be fabricated with five functional inks only.

Printing of P(VDF-TrFE) on different flexible substrates forms the base of the PYZOFLEX[®] technology, currently developed at Joanneum Research in Austria (Pyzoflex 2015). In combination with advanced hardware and software components, transparent self-sensing deformable surfaces are achieved (Fig. 2), enabling a variety of applications, for example, transparent covers for tablets supporting complex 2.5D deformations for enhanced visualization, but also high degree of freedom input controllers (Rendl et al. 2014). This example shows that device-related research is an interdisciplinary endeavor, requiring intense cooperation between material scientists, hardware developing engineers, and software programming computer scientists. Challenges for future research include improvements in the transparency of the printed piezoelectric devices.

Touch panels for mobile or home appliances must work in different environments. They must withstand operation in sunlight, or when used in the kitchen or bathroom, they must endure moisture. An alternative to the printing of ferroelectric P(VDF-TrFE) polymers is the direct use of PVDF as a functional substrate. PVDF is easily available in sheets at low cost. Transparent PVDF touch panels with printed graphene electrodes that work in moist environments and even under water were demonstrated (Vuorinen et al. 2014). In comparison to nontransparent devices, the pyroelectric response to visible light is significantly reduced. By employing functional substrates and printing, low-cost and high-throughput manufacturing of large area touch panels seems feasible.

An all-inkjet-printed piezoelectric polymer actuator for microfluidic environments (Pabst et al. 2014) illustrates the wide range of possibilities for manufacturing

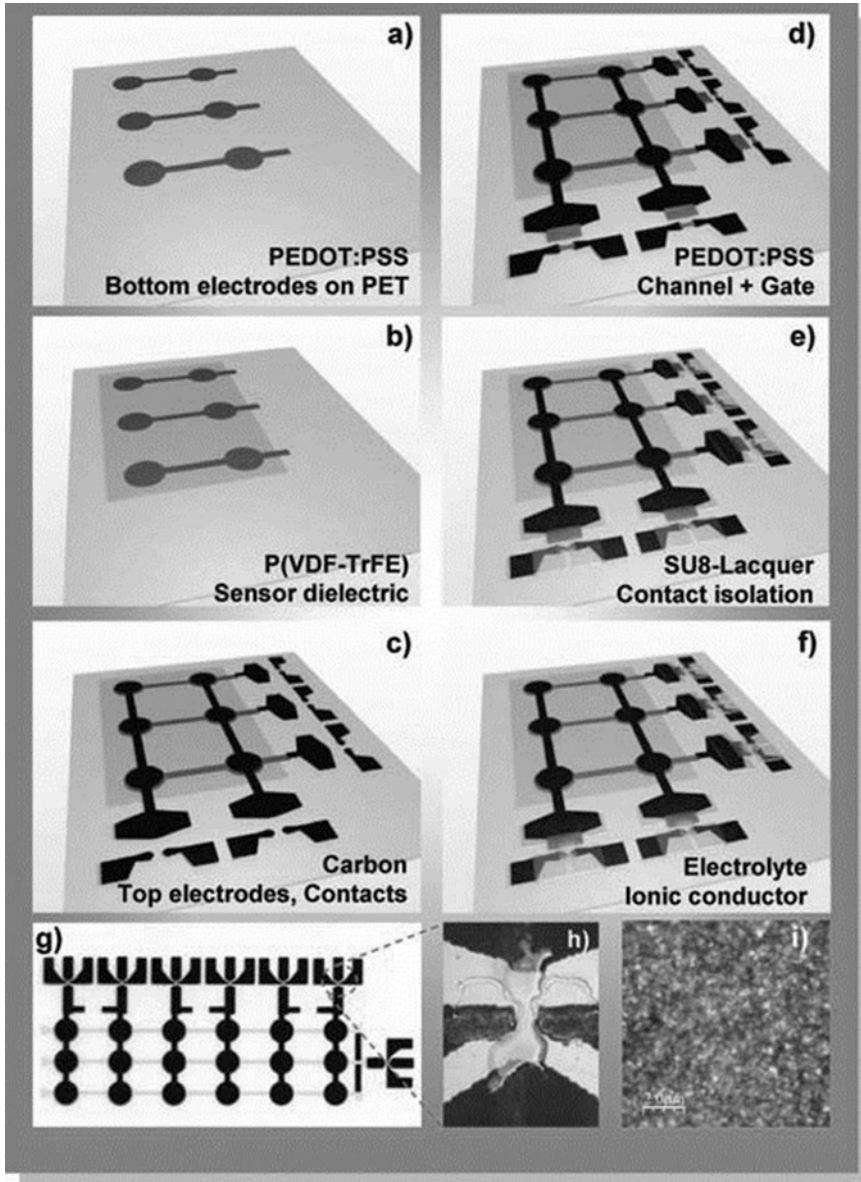


Fig. 1 Process flow for the fabrication of printed piezoelectric active matrix sensor arrays. (a) Screen printing of the bottom electrodes, (b) screen printing of the piezoelectric sensor layer, (c) screen printing of the top electrodes, (d–f) printing processes for producing the transistors, consisting of gate and channel (d), separation layer, (e) and polymeric electrolyte (f). (g) Photograph of a printed 3×6 sensor array with impedance matching transistors. (h) and (i) show details of the transistor and an atomic force microscope height image of the P(VDF-TrFE) layer, with a rms-roughness of 4.5 nm. Printing is a versatile tool for the fabrication of large area piezoelectric transducers on a wide range of flexible support materials (Reprinted with permission (Zirkel et al. 2011))

Fig. 2 Example of a fully flexible, transparent piezoelectric thin film surface called FlexSense. The top photograph illustrates the printed piezoelectric sensor. With a sophisticated electronic readout and algorithm, the 3D shape of the surface is captured in real time (bottom photograph) (Reprinted with permission (Rendl et al. 2014))

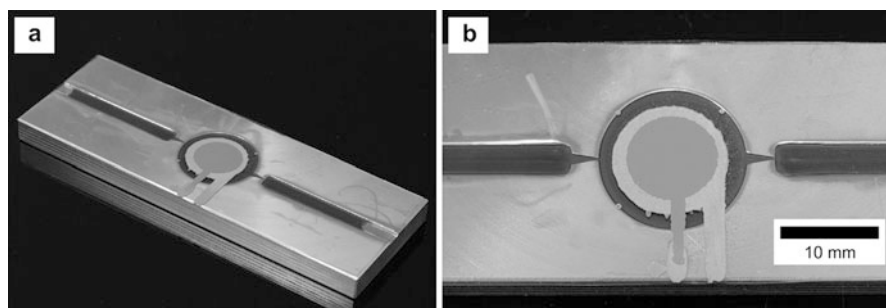
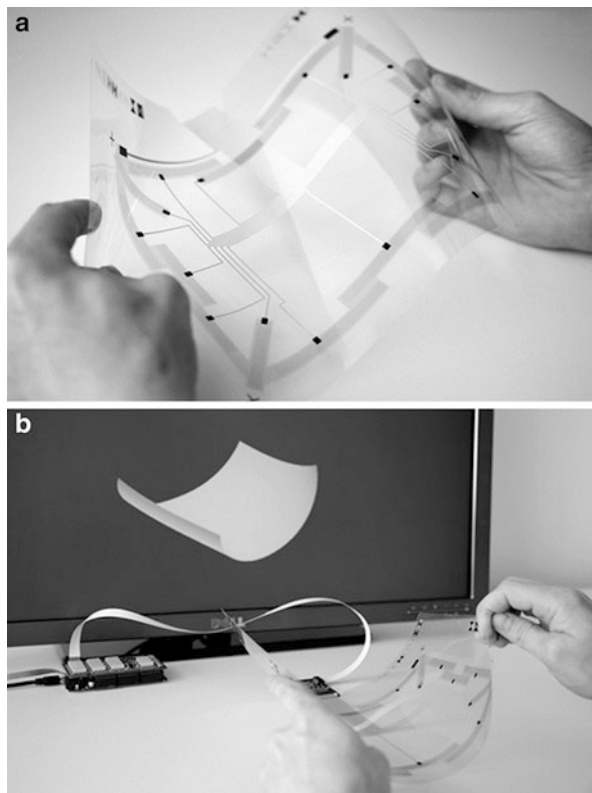


Fig. 3 Two views of an inkjet-printed P(VDF-TrFE) membrane actuators for micropumps for microfluidic lab-on-the-chip systems. The images illustrate the wide range of possibilities for printed piezoelectric device manufacturing (Reprinted with permission (Pabst et al. 2014))

piezoelectric devices by printing techniques (Fig. 3). The microactuators employ inkjet-printed silver electrodes and an inkjet-printed piezoelectric P(VDF-TrFE) layer (Pabst et al. 2012, 2014). Challenges in current research are gaining insight into the optimization of the morphology of the printed ferroelectric polymer films to obtain highly reproducible piezoelectric properties and environmental stability.

The examples shown illustrate the potential of printing in the fabrication of piezoelectric large area devices. With suitable environmentally friendly inks, the technology may pave the way for piezoelectric devices anywhere.

3 Piezoelectric Polymer-Based Electronic Skins

Human skin is a fascinating example of a large area sensory system, allowing us to sense temperature, humidity, touch, pressure, and vibration. Scientists are inspired by this natural model system and work on artificial electronic sensor surfaces (Lacour et al. 2005) that will ultimately enable robots with a sense of feeling (Chortos and Bao 2014; Hammock et al. 2013; Bauer et al. 2014). A full coverage of this topic is beyond the scope of this chapter, so here we focus on illustrating the huge potential for piezoelectric polymers in electronic skin development with two selected research examples.

Ferroelectric polymers from the PVDF family are multifunctional; they simultaneously react to both temperature and pressure changes. In electronic skin applications, this may cause problems, because temperature and pressure changes cannot be discriminated, so one parameter, either temperature or pressure, must be kept constant when ferroelectric polymer sensors are employed. By design of a nanocomposite material made of ceramic ferroelectric nanoparticles embedded in a polymeric ferroelectric matrix, it is possible to overcome this limitation of ferroelectric polymer sensors (Ploss et al. 2000; Graz et al. 2009), enabling a monolithically integrated bifunctional sensor frontplane to large area electronic skins (Fig. 4). While the sign of the pyroelectric coefficient p_3 is the same in both polymers and ceramics, the sign of the piezoelectric d_{33} coefficient differs between polymers and ceramics. Bifunctionality to pressure and temperature changes is thus achieved by independently adjusting the polarization directions in the nanoparticles and the ferroelectric polymer in a two-step poling process. This enables sensor elements that are only piezoelectric or pyroelectric. Challenges of current research are the development of environmentally friendly nanoceramics and inks for producing such composites by printing.

Piezoelectric polymers are not only employable in the form of thin films, for applications in textiles, or on skin, it may be advantageous to have them in the form of sheets of fibers (Persano et al. 2013). Electrospinning of P(VDF-TrFE) produces arrangements of fibers where the polymer chains are preferentially aligned (Fig. 5a).

Such fiber mats (Fig. 5b) display piezo- and pyroelectric responses and can be used to detect small pressure changes on the order of 0.1 Pa. The fiber arrays are extremely flexible and can be easily wrapped around a human finger (Fig. 5c), giving opportunities to monitor human motions. Fiber preparation is challenging, and optimization of the piezoelectric properties of the fibers provides avenues for future research.

Piezoelectric polymers in the form of aligned fiber mats offer a huge potential for integration into textiles, on and even within the body, enabling applications in monitoring vital signals for healthcare applications or sports.

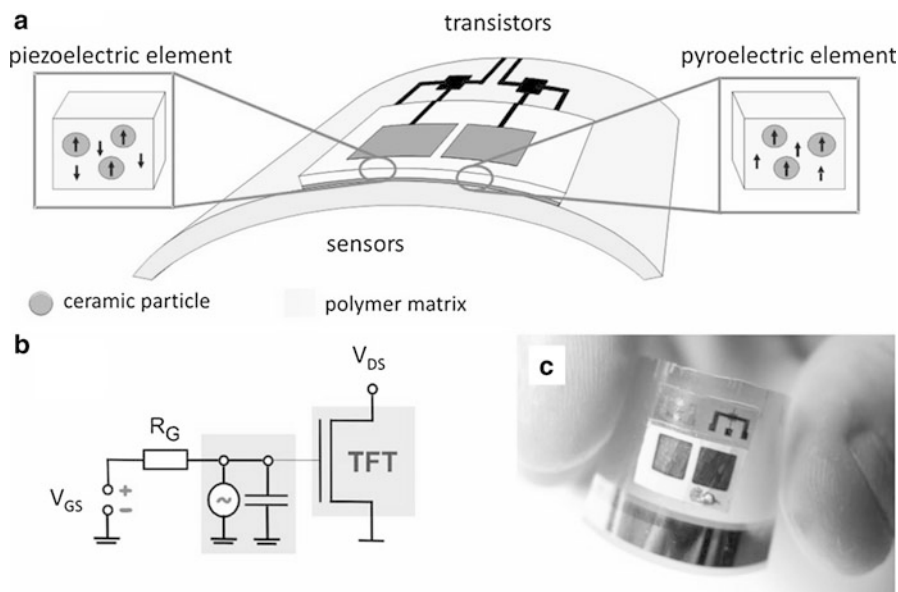


Fig. 4 (a) Scheme of a flexible ferroelectric ceramic polymer nanocomposite layer, laminated on a flexible transistor backplane. In the piezoelectric sensor pixel, the polarization in the ceramic nanoparticles and polymer are antiparallel, while in the pyroelectric, pixel polarizations are parallel. (b) Equivalent circuit of a sensing pixel. (c) Photograph of a simple prototype with one temperature and one pressure sensor (Reprinted with permission (Graz et al. 2009))

4 Loudspeakers, Tactile Sensors with Haptic Feedback, and Braille Displays

The converse piezoelectric effect in ferroelectric polymers is used to advantage in large area loudspeakers. Many different configurations of piezoelectric polymer loudspeakers were developed; we have chosen two examples to illustrate the potential of such flexible devices. In the first design, polyethersulfone with a polythiophene electrode layer forms the transparent support (Sugimoto et al. 2009). The piezoelectric polymer is PVDF, pasted across the whole surface of the support substrate. Polythiophene top electrodes finish the loudspeaker (Fig. 6).

The loudspeaker works best in a bend form with both edges fixed, leading to effective vibration and sound emission. Transparent loudspeakers provide avenues for future research, especially in the design and optimization of transparent bottom and top electrode materials compatible with piezoelectric polymers (Xu et al. 2014).

In the second design, paper is the support structure, while P(VDF-TrFE) is used as the piezoelectric polymer, because it directly crystallizes into the piezoelectric β -form (Hübler et al. 2012).

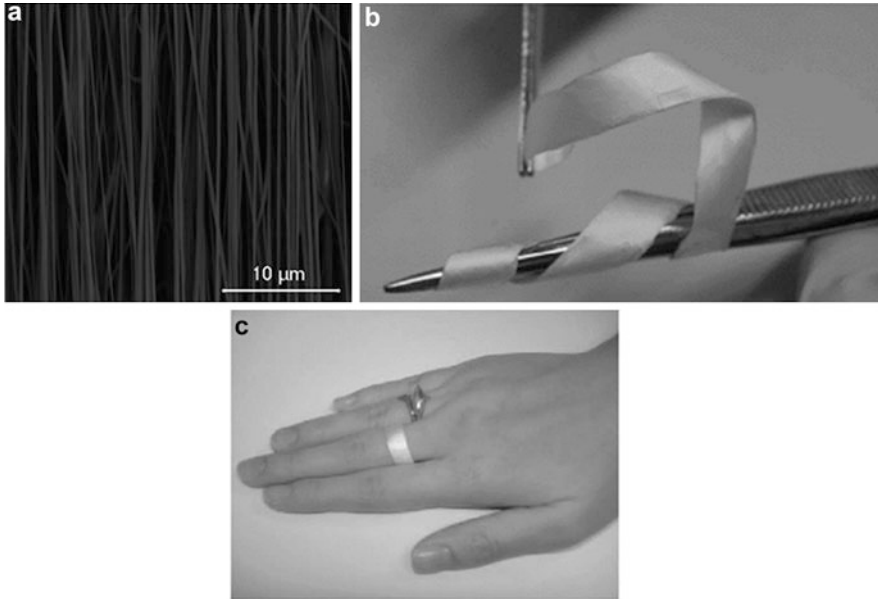
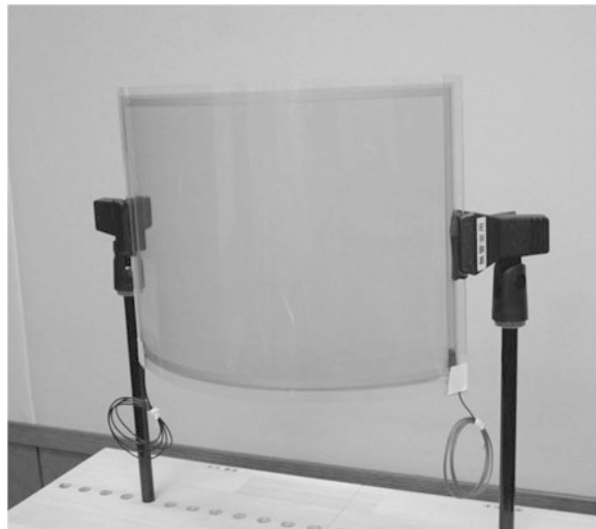


Fig. 5 (a) Scanning electron micrograph image of piezoelectric polymer fiber arrays (scale bar is 10 μm), (b) Photograph of the highly aligned piezoelectric fibers, (c) Photograph of a flexible piezoelectric nanofiber device wrapped around a finger (Reprinted with permission (Persano et al. 2013))

Fig. 6 Photograph of a transparent piezoelectric PVDF loudspeaker on polyethersulfone support with polythiophene electrode layers (Reprinted with permission (Sugimoto et al. 2009))



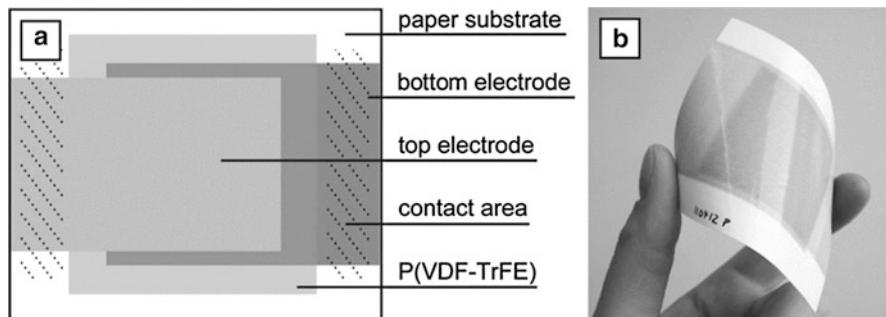


Fig. 7 (a) Scheme of a piezoelectric polymer loudspeaker on a paper support, with printed polymeric bottom and top electrodes of PEDOT:PSS. (b) Photograph of a loudspeaker prototype to illustrate the flexibility of the device (Reprinted with permission (Hübler et al. 2012))

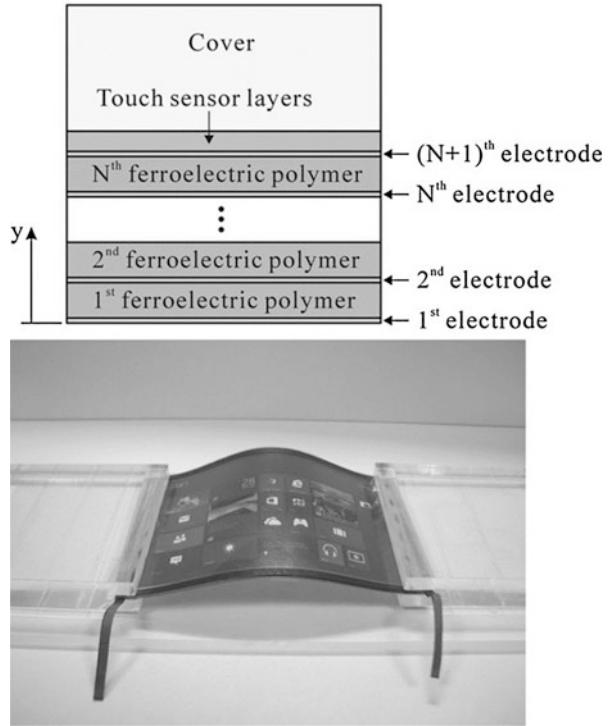
All functional layers were produced by screen and stencil printing on conventional paper, demonstrating the ability of the technology for producing low-cost devices for mass market applications (Fig. 7a). Paper is an environmentally friendly and recyclable support material (Tobjörk and Österbacka 2011), available at much lower costs than polymer substrates like poly (ethylene terephthalate). Disadvantageous is the porous surface of paper with a very large surface roughness. It is remarkable that printed piezoelectric films on paper show a significant piezoelectric response, enabling the loudspeaker to emit sound with an acceptable level up to 80 dB. With printed polymeric PEDOT:PSS electrodes, the whole loudspeaker became highly flexible (Fig. 7). Avenues for future research are broad, both in the design of the speakers and in the optimization of the sound emission.

Relaxor ferroelectric polymers produce large strains up to 5 % under large electric fields of $150 \text{ V}/\mu\text{m}$ without the necessity of poling. Such polymers are very interesting for the development of tactile-feedback devices on various substrates; a potential mass application are flexible touch screens in future mobile appliances (Ju et al. 2014). Currently, such applications are hindered by the need of high voltages to drive the relaxor ferroelectric transducers. To overcome this limitation, it is necessary to develop multilayer ferroelectric relaxor film structures (Fig. 8a).

When used in displays, such structures must also be transparent. Initial studies showed promising results with a flexible tactile-feedback touch screen employing a single layer P(VDF-TrFE-CTFE) vibrator. The resonance frequency of the tactile-feedback touch screen was designed to be in the frequency range of 200–240 Hz, this is the frequency range where human fingertips are most sensitive. Piezoelectric and relaxor ferroelectric polymers seem to be ideal materials for the development of tactile sensors with haptic feedback, but there is still a lot of research necessary to come to practical market compatible solutions.

The large strain of relaxor ferroelectric polymers, coupled with a high elastic modulus, makes these materials attractive to replace low strain piezoceramics in refreshable Braille displays (Ren et al. 2008). It is desirable to use small diameter

Fig. 8 (top) Cross-sectional view of a transparent multilayered ferroelectric relaxor film vibrator under a cover with capacitive touch sensitive layers. (bottom) Photograph of a tactile-feedback touch screen with a single layer P(VDF-TrFE-CTFE) vibrator (Reprinted with permission (Ju et al. 2014))



actuators to move the pins in such displays. P(VDF-TrFE-CFE) seems to be an ideal material for the fabrication of such actuators, because it provides the high strain and actuation force required under modest driving voltages (Levard et al. 2012). Tubular actuators rolled in a 2 mm diameter tube from a bilayer structure of 6 μm thick relaxor ferroelectric P(VDF-TrFE-CFE) films (Fig. 9a) showed a large strain of 4 % with a blocking force of 1 N with a relatively moderate driving voltage of 600 V.

Such actuators work in a very compact Braille cell design with 3×2 elements (Fig. 9b). Although promising, future research is required to develop the technology further, by optimizing the rolled actuators, by developing strategies to prevent premature failures, and by guaranteeing a suitable product lifetime.

5 Electromechanical Energy Harvesting with Piezoelectric Polymers

Mechanical energy is an abundant energy source; it is available on large and small scales, ranging from ocean waves, to wind, to machine vibrations and human gait (Paradiso and Starner 2005; Kornbluh et al. 2012). Conversion of mechanical

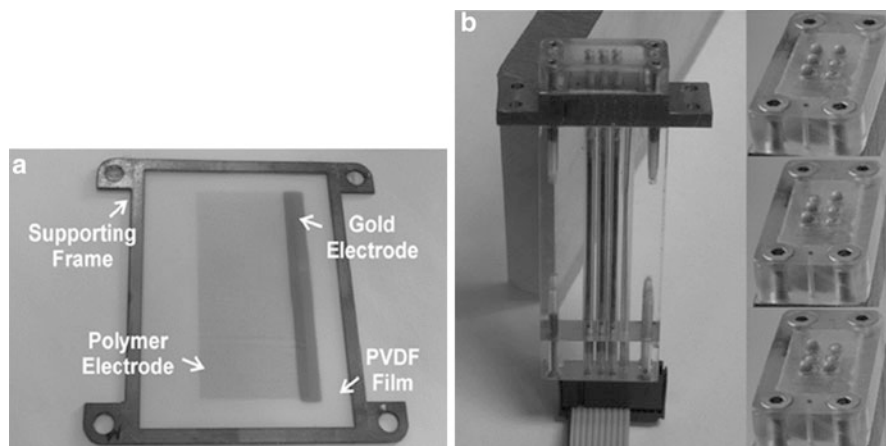


Fig. 9 (a) Design of the rolled tube actuator based on a bilayer structure of relaxor ferroelectrics embedded between two electrodes. (b) Photograph of the developed prototype Braille cell element with close-up views of the six pins spelling “PSU” (Reprinted with permission (Levard et al. 2012))

energy currents into other more useful energy currents employed in our technical world, like electricity, promises autonomous and self-powered electronic devices, for example, for wireless sensor networks, electronic skin, or mobile appliances. Piezoelectric polymers display relatively low piezoelectric and electromechanical coupling coefficients compared to inorganic piezoelectric materials, so they are interesting for electromechanical energy harvesting only when flexibility becomes an important design criterion. Piezoelectric energy harvesting is currently a booming field (Bowen et al. 2014; Li et al. 2014; Toprak and Tigli 2014), and piezoelectric polymers play a vital role in the development of mechanically flexible prototype and demonstrator devices (Ramadan et al. 2014). Several excellent reviews cover the recent progress in piezoelectric energy harvesting, here we discuss one particular example of a piezoelectric polymer-based insole energy harvester to drive a pedometer in order to highlight the prospect of electroactive polymers in mechanical energy harvesting from human gait (Ishida et al. 2013).

PVDF is used in the insole pedometer design (Fig. 10a). To enhance the effective area of the PVDF sheets inside the shoe sole, rolled transducers are employed (Fig. 10b). The PVDF transducers generate electrical energy during human gait, and the produced energy drives the electronic circuitry of the pedometer. The steps during walking are counted by the electrical pulses delivered by one of the PVDF rolls. The PVDF harvester produces a mean electrical power of 12 μ W. The pedometer electronics works with very low power 2 V organic electronic circuitry.

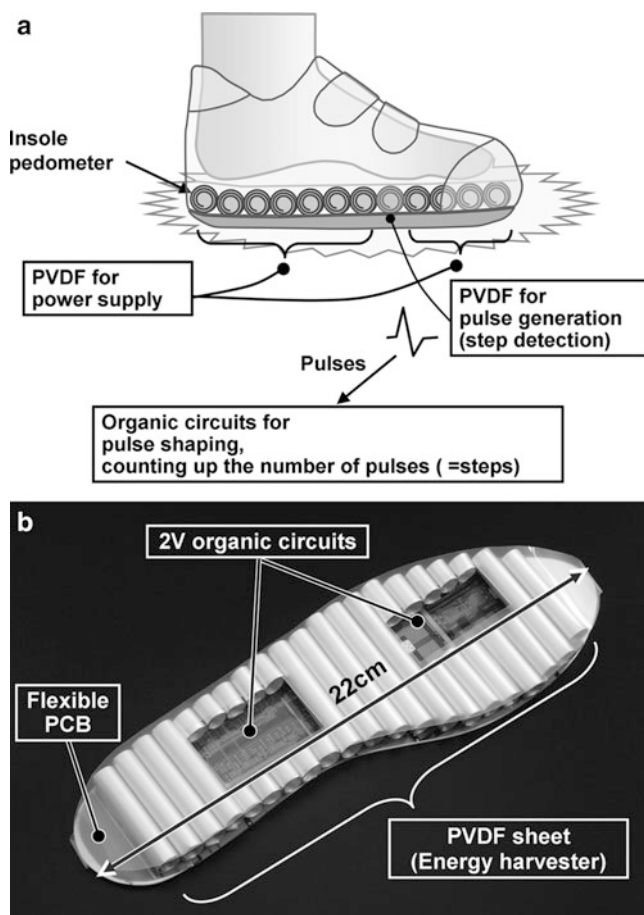


Fig. 10 (a) Scheme of the piezoelectric polymer-based insole pedometer. Rolled PVDF transducers are employed for electromechanical energy conversion. Pulses of one of the rolled transducers are used to count the steps with a 2 V low power electronic circuit. (b) Photograph of the developed prototype (Reprinted with permission (Ishida et al. 2013))

6 Discussion and Conclusion

After the discovery of significant piezoelectricity in polymers in the late 60s, they were immediately considered for applications in the early 70s. Interest faded in the early 80s due to problems in producing reproducible devices. After solving these initial problems by developing efficient poling procedures and suitable electrical contacting methods, piezoelectric polymers became a commercial success in many niche applications. Science progresses in waves, and currently, we face a very active research phase where piezoelectric and relaxor ferroelectric polymers are employed

to develop a wealth of novel devices in emerging and booming areas, such as robotics, electronic skin, and energy harvesting. The demonstrators and prototypes discussed in this chapter show the significant potential of piezoelectric and relaxor ferroelectric electroactive polymer technology for innovative systems with a diversity of uses, such as large area transparent touch surfaces, loudspeakers, tactile sensors with haptic feedback, and Braille displays. Research on electroactive polymers is a cross-disciplinary endeavor, where the combined expertise of materials scientists, engineers, and computer scientists is required to develop new products for mobile appliances, healthcare monitoring, and sports. In the future, we may see piezoelectric and electroactive polymer technology virtually everywhere and not only in niches, as we are familiar with today.

Acknowledgment Work supported by ESNAM, the European Research Council under the Advanced Grant SoftMap and the Austrian Science Funds.

References

- Bauer S (1996) Poled polymers for sensors and photonics applications. *J Appl Phys* 80:5531–5558
- Bauer F (2012) Review on the properties of the ferrorelaxor polymers and some new developments. *Appl Phys A* 107:567–573
- Bauer S, Bauer F (2008) Piezoelectric polymers and their applications. In: Heywang W, Lubitz K, Wersing W (eds) *Piezoelectricity: evolution and future of a technology*, vol 114, Springer series in materials science. Springer, Berlin/Heidelberg, pp 157–177
- Bauer S, Gerhard-Multhaupt R, Sessler GM (2004) Ferroelectrets: soft electroactive foams for transducers. *Phys Today* 57(2):37–43
- Bauer S, Bauer-Gogonea S, Graz I, Kaltenbrunner M, Keplinger C, Schwödauer R (2014) 25th anniversary article: a soft future: from robots and sensor skin to energy harvesters. *Adv Mater* 26:149–162
- Bergman JG, McFee JH, Crane GR (1971) Pyroelectricity and optical second harmonic generation in polyvinylidene fluoride films. *Appl Phys Lett* 18:203–205
- Bergman JG, Crane GR, Ballman AA, O'Bryan HM Jr (1972) Pyroelectric copying process. *Appl Phys Lett* 21:497–499
- Bowen CR, Kim HA, Weaver PM, Dunn S (2014) Piezoelectric and ferroelectric materials and structures for energy harvesting applications. *Energy Environ Sci* 7:25–44
- Chortos A, Bao Z (2014) Skin-inspired electronic devices. *Mater Today* 17:312–331
- Fukada E (2000) History and recent progress in piezoelectric polymers. *IEEE Trans Ultrason Ferroelectr Freq Control* 47:1277–1290
- Glass AM, McFee JH, Bergman J Jr (1971) Pyroelectric properties of polyvinylidene fluoride and its use for infrared detection. *J Appl Phys* 42:5219–5222
- Graz I, Krause M, Bauer-Gogonea S, Bauer S, Lacour SP, Ploss B, Zirkl M, Stadlober B, Wagner S (2009) Flexible active-matrix cells with selectively poled bifunctional polymer/ceramic nanocomposite for pressure and temperature sensing skin. *J Appl Phys* 106:034503-1–034503-5
- Hammock ML, Chortos A, Tee BC-K, Tok JB-H, Bao Z (2013) 25th anniversary article: the evolution of electronic skin (E-skin): a brief history, design considerations, and recent progress. *Adv Mater* 25:5997–6038
- Hübner AC, Bellmann M, Schmidt GC, Zimmermann S, Gerlach A, Haentjes C (2012) Fully mass printed loudspeakers on paper. *Org Electron* 13:2290–2295

- Ishida K, Huang T-C, Honda K, Shinozuka Y, Fuketa H, Yokota T, Zschieschang U, Klauk H, Tortissier G, Sekitani T, Toshiyoshi H, Takamiya M, Someya T, Sakurai T (2013) Insole pedometer with piezoelectric energy harvester and 2 V organic circuits. *IEEE J Solid State Circuits* 48:255–264
- Ju W-E, Moon Y-J, Park C-H, Choi ST (2014) A flexible tactile-feedback touch screen using transparent ferroelectric polymer film vibrators. *Smart Mater Struct* 23:074004-1–074004-10
- Kawai H (1969) The piezoelectricity of poly (vinylidene fluoride). *Jpn J Appl Phys* 8:975–976
- Kornbluh RD, Pelrine R, Prahlah H, Wong-Foy A, McCoy B, Kim S, Eckerle J, Low T (2012) Dielectric elastomers: stretching the capabilities of energy harvesting. *MRS Bull* 37:246–253
- Lacour SP, Jones J, Wagner S, Li T, Suo Z (2005) Stretchable interconnects for elastic electronic surface. *Proc IEEE* 93:1459–1467
- Levard T, Diglio PJ, Lu S-G, Rahn CD, Zhang Q-M (2012) Core-free rolled actuators for Braille displays using P(VDF–TrFE–CFE). *Smart Mater Struct* 21:012001-1–012001-7
- Li H, Tian C, Deng ZD (2014) Energy harvesting from low frequency applications using piezoelectric materials. *Appl Phys Rev* 1:041301-1–041301-20
- Nakamura K, Wada J (1971) Piezoelectricity, pyroelectricity, and the electrostriction constant of poly (vinylidene fluoride). *J Polym Sci A* 29:161–173
- Pabst O, Perelaer J, Beckert E, Schubert US, Eberhardt R, Tünnermann A (2012) All-inkjet-printed piezoelectric polymer actuators: characterization and applications for micropumps in lab-on-a-chip. *Org Electron* 14:3423–3429
- Pabst O, Hölzer S, Beckert E, Perelaer J, Schubert US, Eberhardt R, Tünnermann A (2014) Inkjet printed micropump actuator based on piezoelectric polymers: device performance and morphology studies. *Org Electron* 15:3306–3315
- Paradiso JA, Starner T (2005) Energy scavenging for mobile and wireless electronics. *IEEE Pervasive Comput* 4(1):18–27
- Parashkov R, Becker E, Riedl T, Johannes H-H, Kowalsky W (2005) Large area electronics using printing methods. *Proc IEEE* 93:1321–1329
- Persano L, Dagdeviren C, Su Y, Zhang Y, Girando S, Pisignano D, Huang Y, Rogers JA (2013) High performance piezoelectric devices based on aligned arrays of nanofibers of poly(vinylidene fluoride-co-trifluoroethylene). *Nat Commun* 4:1633-1–1633-10
- Ploss B, Ploss B, Shin FG, Chan HLW, Choy CL (2000) Pyroelectric or piezoelectric compensated ferroelectric composites. *Appl Phys Lett* 76:2776–2778
- Pyzoflex Technology. <http://www.joanneum.at/de/materials/forschungsbereiche/pyzoflexr.html>. Accessed 8 Feb 2015
- Qiu X (2010) Patterned piezo-, pyro- and ferroelectricity in poled polymer electrets. *J Appl Phys* 108:011101-1–011101-19
- Ramadan KS, Sameoto D, Evoy S (2014) A review of piezoelectric polymers as functional materials for electromechanical transducers. *Smart Mater Struct* 23:033001-1–033001-26
- Ren K, Liu S, Lin M, Wang Y, Zhang QM (2008) A compact electroactive polymer actuator suitable for refreshable Braille display. *Sens Actuators A* 143:335–342
- Rendl C, Kim D, Fanello S, Parzer P, Rhemann S, Taylor J, Zirkl M, Scheipl G, Rothländer T, Haller M, Izadi S (2014) FlexSense: a transparent self-sensing seformable surface. In: *Proceedings of the 27th annual ACM symposium on User interface software and technology*, ACM Digital Library, New York pp 129–138
- Sugimoto T, Ono K, Ando A, Kurozumi K, Hara A, Morita Y, Miura A (2009) PVDF-driven flexible and transparent loudspeaker. *Appl Acoust* 70:1021–1028
- Tobjörk D, Österbacka R (2011) Paper electronics. *Adv Mater* 23:1935–1961
- Toprak A, Tigli O (2014) Piezoelectric energy harvesting: state-of-the-art and challenges. *Appl Phys Rev* 1:031104-1–031104-14
- Vuorinen T, Zakrzewski M, Rajala S, Lupo D, Vanhala J, Palovuori K, Tuukanen S (2014) Printable, transparent, and flexible touch panels working in sunlight and moist environments. *Adv Funct Mater* 24:6340–6347

- Xu S, Man B, Jiang S, Liu M, Yang C, Chen C, Zhang C (2014) Graphene–silver nanowire hybrid films as electrodes for transparent and flexible loudspeakers. *CrystEngComm* 16:3532–3539
- Zhang QM, Bharti V, Zhao X (1998) Giant electrostriction and relaxor ferroelectric behavior in electron-irradiated poly(vinylidene-trifluoroethylene) copolymer. *Science* 280:2101–2104
- Zirkel M, Sawatdee A, Helbig U, Krause M, Scheipl G, Kraker E, Andersson Ersman P, Nilsson D, Platt D, Bodö P, Bauer S, Domann G, Stadlober B (2011) An all-printed ferroelectric active matrix sensor network based on only five functional materials forming a touchless control interface. *Adv Mater* 23:2069–2074

Section VI

Polymer Electrets and Ferroelectrets

Ingrid Graz and Axel Mellinger

Contents

1	Introduction	552
2	A Short History of Electrets	552
3	Polymer Electrets: A Classification	553
3.1	Charge Electrets	553
3.2	Ferroelectrets	554
3.3	Dipole Electrets	556
4	Charge Stability in Electrets	557
5	Conclusion	558
	References	558

Abstract

Electrets are dielectric materials capable of quasi-permanently storing electric charges at their surface or in their bulk. This chapter presents a brief history of electret research, followed by a classification and introduction of the most important electret materials. The chapter also discusses ferroelectrets and recent developments in charge stability.

Keywords

Electret • Polymer • Ferroelectret • Dipole • Charge • Stability

I. Graz (✉)

Soft Matter Physics, Johannes Kepler University Linz, Linz, Austria

e-mail: Ingrid.graz@jku.at

A. Mellinger

Department of Physics, Central Michigan University, Mount Pleasant, MI, USA

e-mail: axel.mellinger@cmich.edu

1 Introduction

Electrets are dielectric materials capable of quasi-permanently storing electric charges at their surface or in their bulk (Sessler 1987). The term “quasi-permanent” signifies that the characteristic time constants for the decay of the charges are much longer than the time period over which studies are performed with the electret. The electret charges are either real excess charges (charge electrets) or result from oriented dipoles (dipole electrets). Ferroelectrets are a member of the electret family (charge electrets) based on nonpolar polymers with a porous foam structure with open or closed cells where the internal surfaces carry positive and negative charges. The multitude and diversity of electret materials with their different properties, depending on the charge localization and their internal structure, renders them very powerful electroactive polymers. In this chapter, we give a short history of electret research (Sect. 2), followed by a classification and introduction of the most important electret materials (Sect. 3). Ferroelectrets are discussed in Sect. 3.2. Section 4 deals with the recent developments in charge stability.

2 A Short History of Electrets

Effects of quasi-permanent charge storage or dipole charge orientation have been observed since the ancient Greeks. In 1732, electret properties were described by S. Gray (1732) as a “perpetual attractive power” after generating static electricity of waxes by contact electrification by cooling of the melts in iron ladles. The term “electret” was introduced in 1885 by Oliver Heaviside (1885) from a purely theoretical point of view as the electrostatic analog to a magnet. In the 1920s, systematic research was initiated by Mototaro Eguchi in Japan studying carnauba wax and resins (Eguchi 1925). He exposed molten wax to a strong electric field while simultaneously cooling and solidifying the samples, and found them to exhibit a strong negative charge. In the following years, electret research picked up momentum when polymers were identified as promising materials for charge storage (Gutmann 1948). In the 1960s and early 1970s, poly(tetrafluoroethylene) (PTFE) (Sessler and West 1962) and its copolymers were found to exhibit excellent charge stability and strong piezo- and pyroelectric effects were demonstrated in poly(vinylidene fluoride) (PVDF) (Kawai 1969; McFee et al. 1972), respectively. A decade later, amorphous polymer electrets moved into the focus of electret research due to their large nonlinear optical effects (Singer et al. 1986). In 1986, heterogeneous, charged cellular polymer electrets with outstanding piezoelectric properties were introduced as a novel class of electrets (Patent 1986). These materials are called ferroelectrets to emphasize that they exhibit a spontaneous electric polarization that can be switched by an external electric field (Bauer et al. 2004). With the advent of flexible electronics in the new millennium, foil electrets and ferroelectrets found applications in various types of sensors (Graz et al. 2006; Huang et al. 2007). In recent years, growing interest in energy harvesting from motion has provided a new spin to the field (Jean-Mistral et al. 2012; Wang et al. 2013), clearly demonstrating

that there are still unexplored routes for electret research. Novel applications such as ultraconformable electronics also demand more and more tailored material properties such as stretchability (Zhang et al. 2014).

3 Polymer Electrets: A Classification

The short excursion into the history of electret research already shows that there are numerous different material types and materials with the ability to quasi-permanently store charges. Depending on the charge carrier type, electrets are divided into charge electrets and dipole electrets. The following section introduces both concepts and the most important polymers belonging to each category.

3.1 Charge Electrets

Figure 1 shows a schematic overview of different charge electret types. Homogeneous charge electrets based on highly insulating nonpolar or weakly polar and elastically isotropic polymers with very small dielectric losses exhibit a quasi-permanent excess charge trapped either at their surface (surface charge electrets) (Fig. 1a) or within their volume (space charge electrets) (Fig. 1b). Charges trapped within the bulk can be observed in amorphous or crystalline phases and in semi-crystalline polymers also at the interfaces between amorphous and crystalline regions (Maxwell-Wagner effect) (Rollik et al. 1999).

Polytetrafluoroethylene (PTFE) and its copolymers fluoroethylenepropylene (FEP), perfluoroalkoxy (PFA), and amorphous PTFE, a perfluorinated dioxole (Teflon[®] AF), are the best electret materials for storing negative charges due to the large electronegativity of the F atom and the highly symmetrical CF_2 group with its

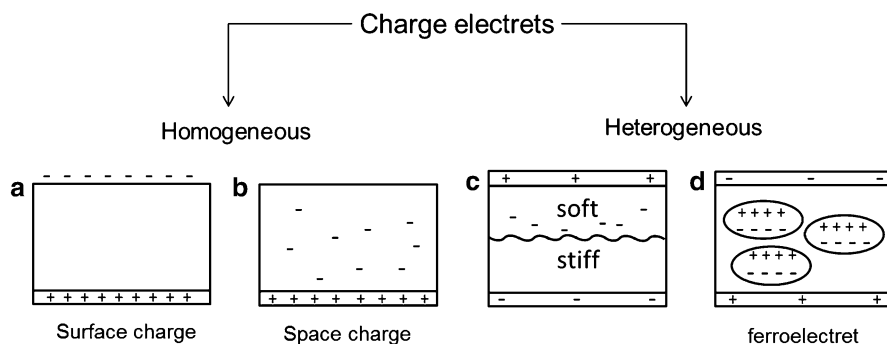


Fig. 1 Schematic view of classification of charge electrets: Homogeneous polymers that carry excess charges at the surface (a) or within the bulk or volume (b) Heterogeneous charge electrets consist of a soft and a hard part. The noncentrosymmetry is either due to the sample geometry (c) or a result of bipolar charging (d)

small polarizability. They are further capable to retain the charges up to 200 °C (Van Turnhout 1975). Other widely used nonpolar or weakly polar polymers such as polyethylene (PE), polypropylene (PP), or poly(ethylene terephthalate) (PET) do not exhibit comparable electret properties, whereas cyclo-olefines are remarkable nonfluorinated electrets especially for positive charging with charge stability up to 160 °C (Sessler et al. 1997). Low k-dielectric materials are another promising group of electrets. The silicon-based benzocyclobutene (BCB) and the perfluorinated cyclobutene (PFCB) show excellent electret properties for both negative and positive charges with their delocalized electrons (Farona 1996; Kennedy et al. 1995).

Discovered by Jacques Curie and Pierre Curie in 1880 (Curie and Curie 1880), piezoelectricity describes the strain-induced electrical polarization observed in noncentrosymmetrical crystals. Being a prerequisite for piezoelectricity, noncentrosymmetry refers to the lack of an inversion center in the crystal's unit cell. Out of the 32 point groups (for 230 potential crystal arrangements in 7 axial systems), 21 are noncentrosymmetrical, and all except one exhibit piezoelectric properties. In order to render charge electrets piezoelectric, strategies to introduce noncentrosymmetry are required. In contrast to crystals where symmetry is broken on the atomic scale, heterogeneous charge electret systems utilize an engineered macroscopically noncentrosymmetrical charge distribution by combining soft and hard electrets (Bauer 2006; Qiu 2010). Figure 1c, d schematically shows two electret film assemblies consisting of an elastically “soft” and a “hard” charge electret, with charges at the interface between the two materials. These nonuniform or heterogeneous electret systems are either built up in layers (of different stiffness) or as a composite where the matrix and the inclusions have different mechanical properties to obtain elastic anisotropies. In layered heterogeneous electret systems, piezoelectric-like behavior results from the geometry: When charges at the interface at the soft and hard layers are displaced, a change in charges at the surface is induced (Fig. 1c). Figure 1d shows the foam-like structure of a ferroelectret, another class of heterogeneous space charge electrets, where the opposite charges located in the soft inclusions within a harder matrix result in a symmetry breaking, thus exhibiting a very large piezoelectric d_{33} coefficient. (For more information see Sect. 3.2)

3.2 Ferroelectrets

Heterogeneous voided electrets – now frequently called ferroelectrets – were first described in the late 1980s (Savolainen et al. 1989), but research did not pick up until a decade later. They were initially prepared from closed cell polypropylene foams (Fig. 2a). To render these insulating polymer-systems electroactive, they are exposed to high electric fields (often exceeding 100 MV/m), which induces microscopic dielectric barrier discharges within the voids (Lindner et al. 2002; Qiu et al. 2007; Harris and Mellinger 2014). These microdischarges lead to a charge separation and the voids' surfaces become oppositely charged forming macrodipoles (Fig. 2b).

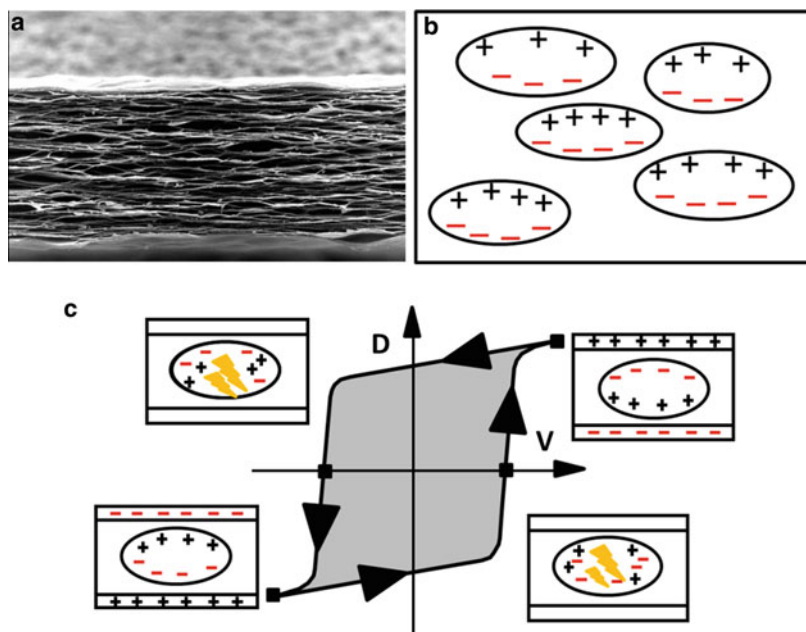


Fig. 2 Scanning electron microscope image showing a PP foam ferroelectret cross-section (a) (courtesy of Mika Pajannen, VTT, Finland) and schematic depiction of engineered macrodipoles within the voids of the ferroelectret (b) and hysteresis loop exhibited when switching of the macrodipoles orientation (c) (After Bauer et al. 2004)

These engineered macrodipoles can be switched in high electric fields similar to the dipole orientation in ferroelectric materials exhibiting hysteresis loops in displacement as function of applied electric field (Fig. 2c) (Wegener and Bauer 2005; Qiu et al. 2013). Their ferroelectric-like properties (Sessler and Hillenbrand 1999; Neugschwandtner et al. 2001), especially their very strong piezoelectric effect, with d_{33} coefficients up to 1000 pC/N (Zhang et al. 2006) by far exceeding those of piezoelectric ceramics such as BaTiO_3 , makes them very promising materials for various applications such as pressure sensors, radiation dosimeters, or ultrasound transducers. With their low acoustical impedance enabling very good coupling to air, these novel ferroic materials are highly suitable for microphones and loudspeakers.

In recent years, the family of ferroelectrets has been extended from foam systems to engineered voided structures featuring materials such as PTFE and FEP. These novel heterogeneous space charge systems are characterized by their extremely high piezoelectric coefficients (Zhang et al. 2006) along with improved charge stability to temperatures above 120°C (Hu and von Seggern 2006; Zhang et al. 2007) as well as mechanical compliance enabling new applications (Zhang et al. 2014). For more details see Sect. 4.

3.3 Dipole Electrets

In contrast to charge electrets with their stored real charges, dipole electrets are characterized by a preferential orientation of their molecular dipoles. Here amorphous and semicrystalline dipole electrets are distinguished. Amorphous dipole electrets are characterized by a quasi-permanent dipole polarization in the amorphous phases (Fig. 3a), whereas semicrystalline ones show a permanent dipole orientation in the crystalline phases and additionally contain Maxwell-Wagner compensation charges at the interfaces between amorphous and crystalline regions for stabilizing the polarization (Fig. 3b) (Mopsik and Broadhurst 1975; Broadhurst et al. 1978; Sessler et al. 1992).

3.3.1 Amorphous Dipole Electrets

Amorphous dipole electrets exhibit preferentially oriented molecular or microscopic dipoles (Mopsik and Broadhurst 1975), where the orientation is achieved by means of poling. All electrets need to be charged, poled, or both, requiring large electric fields applied to the electret material. For more details see ► [Chap. 25, “Polymer Electrets and Ferroelectrets as EAPs: Materials”](#) of this book. The incorporation of molecular dipoles in amorphous polymers is based on different concepts illustrated in Fig. 3a. In the most simple approach (termed a guest-host system), a nonpolar polymer host is doped with molecular dipoles (3a i) (Singer 1986). Alternatively, polymers can carry dipoles attached to their side chains (Fig. 3a ii) or separated by spacer groups in the main chain (Fig. 3a iii) (Stockmayer 1967; Riande and Saiz 1992). Only a few amorphous dipole electrets show piezoelectric and pyroelectric responses. Amongst them are nonlinear optical polymers with very large dipole

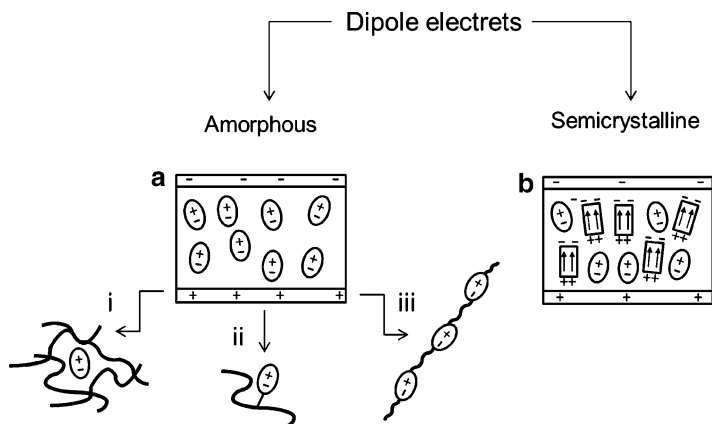


Fig. 3 Schematic view of the classification of dipole electrets: Amorphous dipole electrets (**a**) must contain preferentially oriented molecular dipoles that are either located as guest charges in the polymer (*i*), attached to the side (*ii*), or located in the main chain (*iii*). Semicrystalline dipole electrets (**b**) exhibit both oriented molecular dipoles and Maxwell-Wagner compensation charges at the interfaces to the crystalline regions

moments. Here the chromophores form the molecular dipoles with acceptor-donor groups linked by delocalized π -electrons. Typically, chromophores are very stable at high temperatures and light intensities. An example for a nonlinear guest-host polymer is a poly(methylmethacrylate) (PMMA) based network forming polymer with dissolved chromophore, Disperse Red 1, side groups (Singer et al. 1986). More details on nonlinear optical polymers can be found elsewhere (Bauer-Gogonea and Bauer 2001). Another interesting amorphous dipole electret with a large dipole moment in its repeat unit is vinylidene cyanide vinylacetate copolymer (P(VDCN-VAc) (Norwood et al. 1992) or poly(styrenemaleic anhydride)/Disperse Red 1 P (S-MA)DR1) side chain polymer (Ahlheim and Lehr 1994).

3.3.2 Semicrystalline Dipole Electrets

In semicrystalline dipole electrets, polar crystallites are present in addition to the polar amorphous phase (Fig. 2b). In the technically most interesting semicrystalline dipole electrets such as polyvinylidene fluoride (PVDF) and its copolymers with trifluoroethylene (P(VDF-TrFE)) (Lovinger 1983) or hexafluoropropylene (P(VDF-HFP)), odd Nylons 7 and 11, polyureas, polyurethanes (PU), and some liquid crystalline polymers, the crystallites are ferroelectric (Vasudevan et al. 1979; Hattori et al. 1996). The terpolymer poly(vinylidene-fluoride–trifluoroethylene–chlorotrifluoroethylene) (P(VDF-TrFE-CTFE)) has been shown to have relaxor ferroelectric properties as the CTFE group destabilizes the long-range order of the ferroelectric phase (Xu et al. 2001).

4 Charge Stability in Electrets

The key property of charge electrets is the extremely long lifetime of the surface or bulk charge. From measurements at elevated temperature, room temperature lifetimes in the range of 10^3 to 2.6×10^5 years have been extrapolated (Xia and Gerhard-Multhaupt 1999; Xia et al. 2003). A commonly held view is that these charges are held in “traps” with an energy depth of at least 1 eV, since charges in shallower traps (trap depth $\ll 1$ eV) have a high thermal activation rate. Małecki suggested a rate equation model (Małecki 1999), where carrier annihilation at the electrode and by free, implanted charges causes a transition from a short-term, exponential decay – resulting from ohmic conductivity – to a long-term linear decay over thousands of years. This model requires the presence of deep traps to minimize thermal activation of charge carriers.

Meunier et al. calculated trap energies resulting from impurities that are commonly present in the type of polyethylene used for cable insulation (Meunier et al. 2001) and found charge carrier densities of up to 10^{17} cm^{-3} with lifetimes of 30,000 years. Some of the impurities have been identified through their luminescence spectra (Teyssedre et al. 2001).

The “traditional” tool to investigate charge stability and energetic trap depths is the thermally stimulated discharge method (Van Turnhout 1999). However, this technique is limited to trap depths below 1.5 eV, since the high temperatures required

to free charges from deeper traps lead to thermal decomposition of the material under investigation. In recent years, photostimulated discharge (PSD) spectroscopy (Brodrribb et al. 1975), a technique where charge carriers are excited out of their traps by absorption of monochromatic visible or UV radiation, has provided some experimental evidence for the existence of “deep” traps (Mellinger et al. 2004; Yue et al. 2013). A significant case of state-selective detrapping was found in cellular polypropylene, a well-known ferroelectret (Mellinger et al. 2003). The material exhibits three PSD current maxima at 276, 223, and 198 nm, which can be (at least partially) selectively bleached by irradiation at the respective wavelengths. During UV irradiation, the piezoelectric activity of the ferroelectret was monitored in situ using dielectric resonance spectroscopy. No change in its d_{33} coefficient was found during irradiation at 276 and 223 nm, whereas irradiation below 210 nm resulted in a gradual reduction of d_{33} . As the piezoelectric properties are caused by charges trapped on the inner surfaces of the voids, this observation directly links these charges to the 6.2 eV traps corresponding to the 198 nm maximum in the PSD spectrum. This experimental proof of charges in deep traps, responsible for the astonishing stability of electrets, allows a deeper understanding and enables new directions of electret research.

5 Conclusion

Electrets and ferroelectrets are a class of EAPs comprising a variety of very different materials such as amorphous, semicrystalline, closed- or open cell foams, or heterogeneous layered polymers, waxes, and elastomers. This plethora of polymer electrets exhibits along with its main ability to store charges a range of electroactive properties such as piezo- and pyroelectricity or switchable polarization. Novel heterogeneous systems with improved charge retention at elevated temperatures and the understanding of charge trapping mechanisms are key foci of ongoing research. With this growing knowledge and novel evolutions of materials, the number of potential applications in pressure/temperature sensors, microphones, or energy harvesting is increasing, paving a bright future for electrets.

References

- Ahlheim M, Lehr F (1994) Electrooptically active polymers. Non-linear optical polymers prepared from maleic anhydride copolymers by polymer analogous reactions. *Macromol Chem Phys* 195:361–373
- Bauer S (2006) Piezo-, pyro- and ferroelectrets: soft transducer materials for electromechanical energy conversion. *IEEE Trans Dielectr Electr Insul* 5:953–962
- Bauer S, Gerhard-Mulhaupt R et al (2004) Ferroelectrets: soft electroactive foams for transducers. *Phys Today* 57(2):37–43
- Bauer-Gogonea S, Bauer S (2001) Polymer electrets for electronics, sensors, and photonics. In: Nalwa HS (ed) *Handbook of advanced electronic and photonic materials and devices*. Academic, Burlington, pp 185–231

- Broadhurst MG, Davis GT et al (1978) Piezoelectricity and pyroelectricity in PVDF a model. *J Appl Phys* 49(10):4992–4997
- Brodribb JD, O'Colmain D et al (1975) The theory of photon-stimulated current spectroscopy. *J Phys D* 8:856–862
- Curie J, Curie P (1880) Développement par compression de l'electricité polaire dans les cristaux hémiedres a faces inclinées. *Bull Soc Mineral Fr* 3:90–93
- Eguchi M (1925) On the permanent electret. *Philos Mag* 49:178–192
- Farona MF (1996) Benzocyclobutenes in polymer chemistry. *Prog Polym Sci* 21(3):505–555
- Gray S (1732) A letter concerning the electricity of water, from Mr. Stephen Gray to Cromwell Mortimer, MD Secr. RS. *Philos Trans R Soc Lond Ser A* 37:285
- Graz I, Kaltenbrunner M et al (2006) Flexible ferroelectret field-effect transistor for large-area sensor skins and microphones. *Appl Phys Lett* 89:073501
- Gutmann F (1948) The electret. *Rev Mod Phys* 20:457
- Harris S, Mellinger A (2014) Towards a better understanding of dielectric barrier discharges in ferroelectrets: Paschen breakdown fields in micrometer sized voids. *J Appl Phys* 115:163302
- Hattori T, Takahashi T et al (1996) Piezoelectric and ferroelectric properties of polyurea-5 thin films prepared by vapor deposition polymerization. *J Appl Phys* 79:1713
- Heaviside O (1885) Electromagnetic induction and its propagation, electrization and electrification. *Natural electrets. Electrician* :230–231
- Hu Z, von Seggern H (2006) Breakdown-induced polarization buildup in porous fluoropolymer sandwiches: a thermally stable piezoelectret. *J Appl Phys* 99:024102
- Huang C, West JE et al (2007) Organic field-effect transistors and unipolar logic gates on charged electrets from spin-on organosilsesquioxane resins. *Adv Funct Mater* 17:142–153
- Jean-Mistral C, Vu Cong T et al (2012) Advances for dielectric elastomer generators: replacement of high voltage supply by electret. *Appl Phys Lett* 101:162901
- Kawai H (1969) The piezoelectricity of poly (vinylidene fluoride). *Jpn J Appl Phys* 8:975–976
- Kennedy AP, Babb DA et al (1995) Perfluorocyclobutane aromatic ether polymers. II. Thermal/oxidative stability and decomposition of a thermoset polymer. *J Polym Sci A Polym Chem* 33(11):1859–1865
- Kirjavainen K (1986) Electromechanical film and procedure for manufacturing the same. *European Patent Application* 0,182,764
- Lindner M, Bauer-Gogonea S et al (2002) Dielectric barrier microdischarges: mechanism for the charging of cellular piezoelectric polymers. *J Appl Phys* 91:5283
- Lovinger AJ (1983) Ferroelectric polymers. *Science* 220:1115
- Małecki JA (1999) Linear decay of charge in electrets. *Phys Rev B* 59:9954–9960
- McFee JH, Bergman JR Jr et al (1972) Pyroelectric and nonlinear optical properties of poled polyvinylidene fluoride films. *Ferroelectrics* 3(1):305–313
- Mellinger A, Camacho González F et al (2003) Ultraviolet-induced discharge currents and reduction of the piezoelectric coefficient in cellular polypropylene films. *Appl Phys Lett* 82:254–256
- Mellinger A, Camacho González F et al (2004) Photostimulated discharge in electret polymers: an alternative approach for investigating deep traps. *IEEE Trans Dielectr Electr Insul* 11:218–226
- Meunier M, Quirke N et al (2001) Molecular modeling of electron traps in polymer insulators: chemical defects and impurities. *J Chem Phys* 115:276–288
- Mopsik FI, Broadhurst MG (1975) Molecular dipole electrets. *J Appl Phys* 46(10):4204
- Neuschwandtner GS, Schwoedlauer R et al (2001) Piezo- and pyroelectricity of a polymer-foam space-charge electret. *J Appl Phys* 89:4503–4511
- Norwood RA, Findakly T et al (1992) Optical polymers and multifunctional materials. In: Hornak LA (ed) *Polymers for lightwave and integrated optics*. Marcel Dekker, New York, pp 287–320
- Qiu X (2010) Patterned piezo-, pyro-, and ferroelectricity of poled polymer electrets. *J Appl Phys* 108:011101

- Qiu X, Mellinger A et al (2007) Barrier discharges in cellular polypropylene ferroelectrets: how do they influence the electromechanical properties? *J Appl Phys* 101:104112
- Qiu X, Holländer L et al (2013) Patterned piezo-, pyro-, and ferroelectricity of poled polymer electrets. *J Appl Phys* 89:4503
- Riande E, Saiz E (1992) Dipole moments and birefringence of polymers. Prentice Hall, Englewood Cliffs
- Rollik D, Bauer S et al (1999) Separate contributions to the pyroelectricity in poly (vinylidene fluoride) from the amorphous and crystalline phases, as well as from their interface. *J Appl Phys* 85:3282–3288
- Savolainen A, Kirjavainen K et al (1989) Electrothermomechanical film: part 1. Design and characteristics. *J Macromol Sci A* 26(2–3):583–591
- Sessler GM (ed) (1987) *Electrets*, 2nd edn. Springer, Berlin
- Sessler GM, Hillenbrand J (1999) Electromechanical response of cellular electret films. *Appl Phys Lett* 75:3405–3407
- Sessler GM, West JE (1962) Self-biased condenser microphone with high capacitance. *J Acoust Soc Am* 34(11):1787–1788
- Sessler GM, Das-Gupta DK et al (1992) Piezo and pyroelectricity in electrets caused by charges, dipoles or both? *IEEE Trans Electr Insul* 27:872–897
- Sessler GM, Yang GM et al (1997) Electret properties of cycloolefin copolymers. In: Annual report, conference on electrical insulation and dielectric phenomena, IEEE service center, Piscataway, pp 467–470
- Singer KD, Sohn JE et al (1986) Second harmonic generation in poled polymer films. *Appl Phys Lett* 49(5):248–250
- Stockmayer WH (1967) Dielectric dispersion in solutions of flexible polymers. *Pure Appl Chem* 15 (3–4):539–554
- Teysseire G, Laurent C et al (2001) Deep trapping centers in crosslinked polyethylene investigated by molecular modeling and luminescence techniques. *IEEE Trans Dielectr Electr Insul* 8:744–752
- Van Turnhout J (1975) Use of polymers for electrets. *J Electrostat* 1(2):147–163
- Van Turnhout J (1999) Thermally stimulated discharge of electrets. In: Sessler GM (ed) *Electrets*, vol 1, 3. Laplacian Press, Morgan Hill, pp 81–215
- Vasudevan P, Nalwa HS et al (1979) Pyroelectricity in thiourea formaldehyde polymer. *J Appl Phys* 50:4324
- Wang S, Lin ZH et al (2013) Motion charged battery as sustainable flexible-power-unit. *ACS Nano* 7(12):11263–11271
- Wegener M, Bauer S (2005) Microstorms in cellular polymers: a route to soft piezoelectric transducer materials with engineered macroscopic dipoles. *ChemPhysChem* 6(6):1014–1025
- Xia Z, Gerhard-Multhaupt R (1999) High surface-charge stability of porous polytetrafluoroethylene electret films at room and elevated temperatures. *J Phys D Appl Phys* 32:L83–L85
- Xia Z, Wedel A et al (2003) Charge Storage and its dynamics in porous polytetrafluoroethylene (PTFE) film electrets. *IEEE Trans Dielectr Electr Insul* 10:102–108
- Xu HS, Cheng ZY et al (2001) Ferroelectric and electromechanical properties of poly(vinylidene fluoride-trifluoroethylene-chlorotrifluoroethylene) terpolymer. *Appl Phys Lett* 78:2360–2362
- Yue L, Wang X et al (2013) Study on evolution of deep charge traps in polyimide irradiated by low-energy protons using photo-stimulated discharge technique. *J Phys D Appl Phys* 46:145502
- Zhang X, Hillenbrand J et al (2006) Thermally stable fluorocarbon ferroelectrets with high piezoelectric coefficient. *Appl Phys A* 84:139–142
- Zhang X, Hillenbrand J et al (2007) Ferroelectrets with improved thermal stability made from fused fluorocarbon layers. *J Appl Phys* 101:054114-1
- Zhang X, Zhang X et al (2014) Low-cost, large-area, stretchable piezoelectric films based on irradiation-crosslinked poly (propylene). *Macromol Mater Eng* 299:290–295

Xunlin Qiu

Contents

1	Polymer Electrets	562
1.1	Modified Conventional Polymer Electret Materials with Improved Electret Properties	563
1.2	High-Performance Polymer Electrets	566
2	Ferroelectrets	570
2.1	Polyolefin Ferroelectret	572
2.2	Polyester Ferroelectret	575
2.3	Cyclo-Olefin Polymer (COP) and Copolymer (COC) Ferroelectret	578
2.4	Polycarbonate Ferroelectret	579
2.5	Fluoropolymer Ferroelectret	580
3	Summary	584
	References	585

Abstract

Recent progress relating to polymer electret and ferroelectret materials is reviewed. As for polymer electret materials, the development is described in two aspects: (i) Modified conventional polymer electret materials with improved electret properties. The improvement of the electret properties is achieved by incorporating suitable additives, by blending different polymer compounds, or by modifying with certain chemicals. Sometimes, the properties can be further enhanced by physical aging. (ii) Newly introduced high-performance polymer electrets. Parylene HT[®] and CYTOP are two examples. They can not only retain high surface charge densities but also show exceptional high temperature stability. Moreover, they are compatible with MEMS technology and therefore are particularly attractive for applications in micro power electret generators.

X. Qiu (✉)

Department of Physics and Astronomy, University of Potsdam, Potsdam-Golm, Germany
e-mail: xunlin.qiu@uni-potsdam.de

The research of ferroelectret, as a relatively new branch in the field of electret, has been advanced significantly in recent years. A considerable number of cellular polymer foams and polymer film systems containing internal cavities have been developed and identified as ferroelectrets. Following the early example of cellular polypropylene (PP) ferroelectret, cellular foam ferroelectrets have been developed from polyesters (polyethylene terephthalate PETP and poly(ethylene naphthalate) PENP), cyclo-olefin copolymer (COC), and fluoroethylene-propylene (FEP). The cellular structures, formed by techniques such as stretching filler-loaded polymer melt and foaming with supercritical CO₂, can be adjusted and optimized with gas-diffusion expansion process. Besides, the number of ferroelectrets of polymer film systems with internal cavities is rapidly increasing. These are layer structures, composed of hard (solid) and soft (highly porous) polymer layers, and polymer film systems containing regular cavities. Polytetrafluoroethylene (PTFE) (solid or porous) and polycarbonate (PC) are also added to the list of candidate materials for making this type of ferroelectrets. These exciting developments significantly enlarge the range of functional space-charge polymer electrets and bring forth numerous novel applications.

Keywords

Electrets • Ferroelectrets • Chemical modification • Physical aging • High performance polymers • Polymer foams • Polymer films

1 Polymer Electrets

The research and application of electrets very much rely on the availability of suitable materials. Conventional polymer electrets are discussed in previous books, book chapters, and review articles (Hilczer and Malecki 1986; Sessler 1999, 2001; Gerhard-Multhaupt 1999; Kressmann et al. 1999). In this section, the recent development in polymer electret materials is discussed.

Significant progress has been made in bettering the performance of conventional polymer electrets. This is achieved through, for example, incorporating suitable additives or blending different compounds. Physical aging brings further enhancement. For polymer electrets produced by means of corona charging (a charging method that is widely used in the electret industry), the deposited charges are normally trapped on or near the polymer surface. Therefore, surface modification of polymer electrets will directly affect charge trapping, charge detrapping, and charge transport. Modification can be done by using either reactive gases or chemical solvents. In view of their superior performance, the treated polymer electrets can be considered as “novel” electret materials.

Also, new polymer electret materials have been added to the family of electrets, i.e., parylene HT[®] (referred to as “polymer AF-4”) and the amorphous perfluorinated polymer CYTOP. The development of such high-performance electrets is mainly motivated by the application in micro electret power generators (Suzuki 2011; Yang

et al. 2012). High-performance electrets are required in such applications, in order to have generators with large output and long-standing performance. Fluoropolymer electrets such as polytetrafluoroethylene (PTFE) and fluorinated ethylene propylene (FEP) can provide good long-term and thermal stability. However, PTFE and FEP are not compatible with MEMS fabrication technology, since they are insoluble in solvents. Moreover, their surface charge density is insufficient for generators with high output. Parylene HT[®] and CYTOP are two types of high-performance polymer electrets which to a large extent fulfill the requirements.

1.1 Modified Conventional Polymer Electret Materials with Improved Electret Properties

1.1.1 Polymer Electrets with Physical Treatment

In recent years, colleagues at the University of Bayreuth have carried out comprehensive studies on the improvement of the properties of conventional polymer electrets, sometimes in collaboration with the Darmstadt University of Technology. Their works are reviewed in Erhard et al. (2010a) and therefore will be only briefly introduced here. The interested reader may refer to the previous review for details.

The materials under investigation are commodity polymers including polypropylene (PP), poly(phenylene ether) (PPE) and polystyrene (PS), and high-performance thermoplastic polyetherimide (PEI). It is demonstrated that the electret properties of PP and PEI can be significantly enhanced by incorporating suitable additives. Certain substituted 1,3,5-benzene based trisamides and bisamides are effective additives for PP electret. The additives create supramolecular charge traps via self-assembly. In order to optimize this effect, the additive concentration has to be low. In the case of PEI, phosphorus-based antioxidants are efficient additives. Pure PEI exhibits very poor charge storage capability. The surface potential decays almost completely in 24 h at 90 °C. By adding 0.5 wt% of organophosphonites Irgafos[®] P-EPQ and Irgafos[®] 126, the surface potential remains at 79 and 86 % of the initial value after being stored at 90 °C for a period of longer than 1400 h, respectively. It is also found that increasing the cooling rate during film process and physical aging prior to charging (Erhard et al. 2010b) lead to further improvement of the electret properties of additive-incorporated PP and PEI, respectively. In another study from the same group, polycarbonate (PC) electrets were improved by incorporating bisimide additives combined with physical aging (Erhard et al. 2010c).

PPE and PS are totally miscible over the entire composition range. Compared with neat PPE and PS, PPE/PS (composition ratio 75/25) blend films exhibit excellent charge stability, even at temperatures up to 120 °C. The superior charge stability of the blend is attributed to (1) increased packing density, which limits segmental motions below T_g and thus hinders the charge drift, and (2) nanoscale phase boundaries, which might act as charge traps. Physical aging can further reduce the free volume of the blend films, bringing forth beneficial effect on the electrets

properties. Incorporation of charging trapping sites by compounding the blend with the third component, i.e., triblockcopolymer poly(styrene-*b*-isobutylene-*b*-styrene) (SIBS), also leads to an improvement of the electret properties.

In the study of Ko et al., 2-(6-mercaptohexyl) was used as additive to improve the performance of COC polymers. By adding a concentration of 3497 mg/kg, the surface potential increases by 71 %, compared with that of a pure COC film (Ko et al. 2010).

1.1.2 Chemically Modified Polymer Electrets

An and colleagues treated low density polyethylene (LLDPE) with fluorine gas (which is diluted with nitrogen) (An et al. 2009a). The direct fluorination of the material deepens the traps in the surface layer. It is found the charges trapped in the deep traps block the injection of charge into the bulk of the material. The same group also reported oxyfluorination treatment on LDPE using gas mixture of F₂/N₂/O₂ (1:78:1) (An et al. 2009b). Such treatment leads to the formation of various polar groups in the surface layer. It turns out that the oxyfluorinated LDPE is less influenced by the by-products in the semicon electrode. Thus, the oxyfluorinated surface has deeper traps as compared with the virgin film. Because of the resultant high permittivity and the deeper traps of the surface layer, oxyfluorination significantly suppresses space charge injection into the bulk of LLDE. These results are particularly interesting for the application of LDPE as DC high voltage cables. In this application, the injection and accumulation of space charges is a main factor for the degradation of the material and therefore needs to be suppressed.

Rychkov et al. studied the effect of modification of PE, PTFE, and FEP with various chemical solvents on their electret properties (Rychkov et al. 2011a, b, 2012a, b, c, 2013). The chemicals for modification were used either in gas-phase state as vapors or in liquid state.

Modifications of PE with phosphorus trichloride (PCl₃) and titanium tetrachloride (TiCl₄) vapors as well as orthophosphoric acid (H₃PO₄) all result in significantly enhanced charge stability. Figure 1 shows thermally stimulated surface potential decay (charge TSD) of positively charged PE with and without PCl₃ modification (Rychkov et al. 2011a). It can be seen that modified PE films exhibit much better charge stability. For instance, the half-value temperature (i.e., the temperature at which the surface potential decays to half of its initial value) is shifted to higher temperature by 55 °C. The modification also eliminates the so-called crossover phenomenon that is often observed with virgin PE electrets (curves 1 and 2 in the figure). Thus, the PCl₃ modification on PE not only improves the charge stability but also increases the magnitude of the stabilized charges. Similar effects were observed for modification of PE with TiCl₄ (Rychkov et al. 2011b, 2012a).

Modification of PE with H₃PO₄ also leads to significant improvement of the charge stability. As shown in Fig. 2, the thermal stability of both positively and negatively charged PE samples was enhanced by about 60 °C with the modification using H₃PO₄ (Rychkov et al. 2012b).

Modifications of PTFE and FEP with TiCl₄ vapor yield remarkable improvement of the charge stability as well. For PTFE, the charge TSD curve for positive charge is

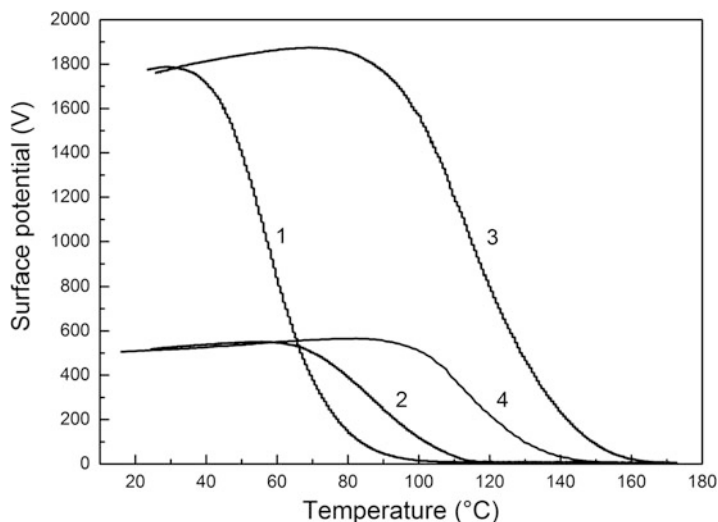


Fig. 1 Charge TSD in positively charged LDPE films. *1* and *2* virgin samples, *3* and *4* treated with PCl_3 vapors

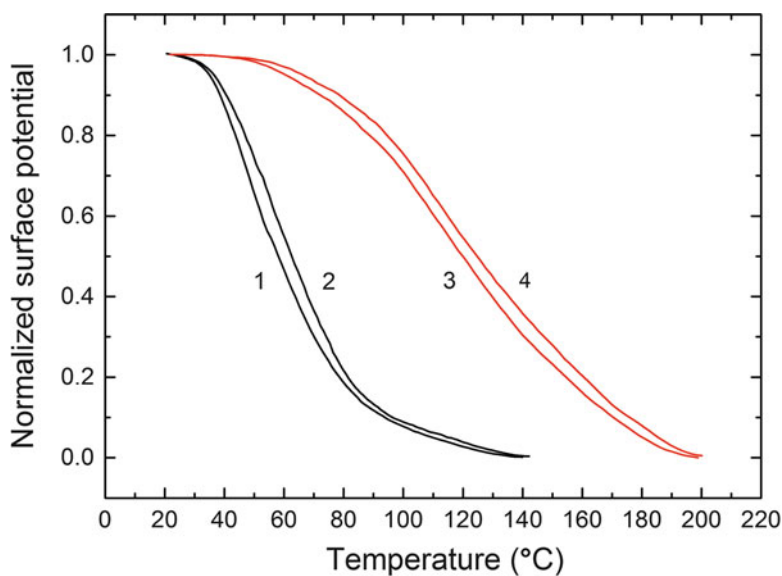


Fig. 2 Charge TSD in positively (*1* and *3*) and negatively (*2* and *4*) charged LDPE films without (*1* and *2*) and with (*3* and *4*) modification using H_3PO_4 (Rychkov et al. 2012b)

shifted to higher temperature by more than 100 °C (Rychkov and Gerhard 2011). For FEP, the thermal stability of positive charge is improved by more than 120 °C (Rychkov et al. 2013). Unlike PTFE for which the modification almost does not

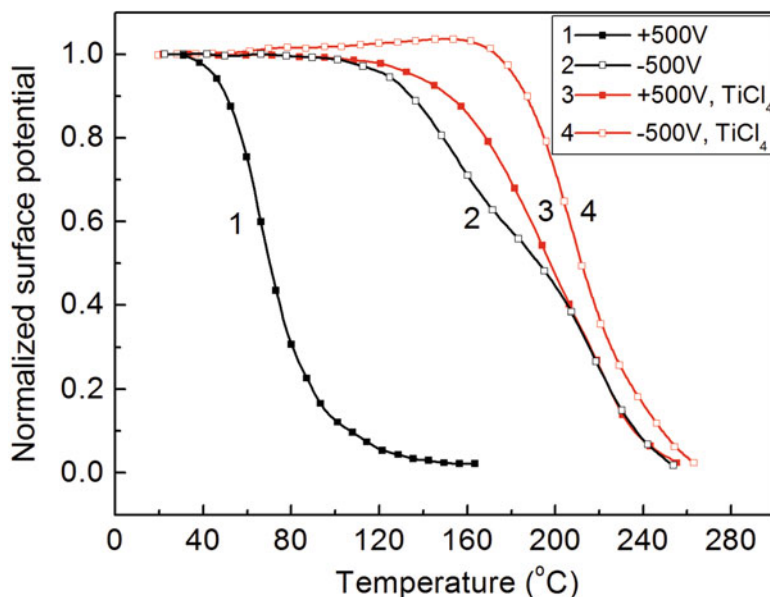


Fig. 3 Charge TSD of FEP films charged to ± 500 V. 1 and 2 without treatment, 3 and 4 treated with TiCl_4 vapor (Rychkov et al. 2013)

influence the negative charge stability, the thermal stability of negative charge in treated FEP is enhanced by about 20°C . As a result, the asymmetry in the charge stability of both polarities is largely reduced (Fig. 3).

The charge stabilization by the chemical modifications is attributed to the formation of new energetically deep traps on the modified surface. Element analysis reveals that titanium and oxygen are built into the surface after the modification with TiCl_4 vapor (Rychkov and Gerhard 2011). The scanning electron microscope (SEM) images show that for modification with H_3PO_4 , nanoislands, which have chemical compositions different from the polymer substrate, are formed on the polymer surface (Fig. 4) (Rychkov et al. 2012b). This might be the structural origin for the deeper traps formed during the modification. The attachment of new chemical structures to the surface molecules also decreases the molecular mobility, another possible reason for the overall enhancement of the charge stability.

1.2 High-Performance Polymer Electrets

1.2.1 Parylene

Parylene is the trade name for a number of chemical vapor deposited poly (p-xylylene) polymers. Due to its chemical inertness, conformal coating, and excellent barrier properties, parylene has been used in a wide range of applications, particularly as protective coatings for biomedical devices and microelectronics.

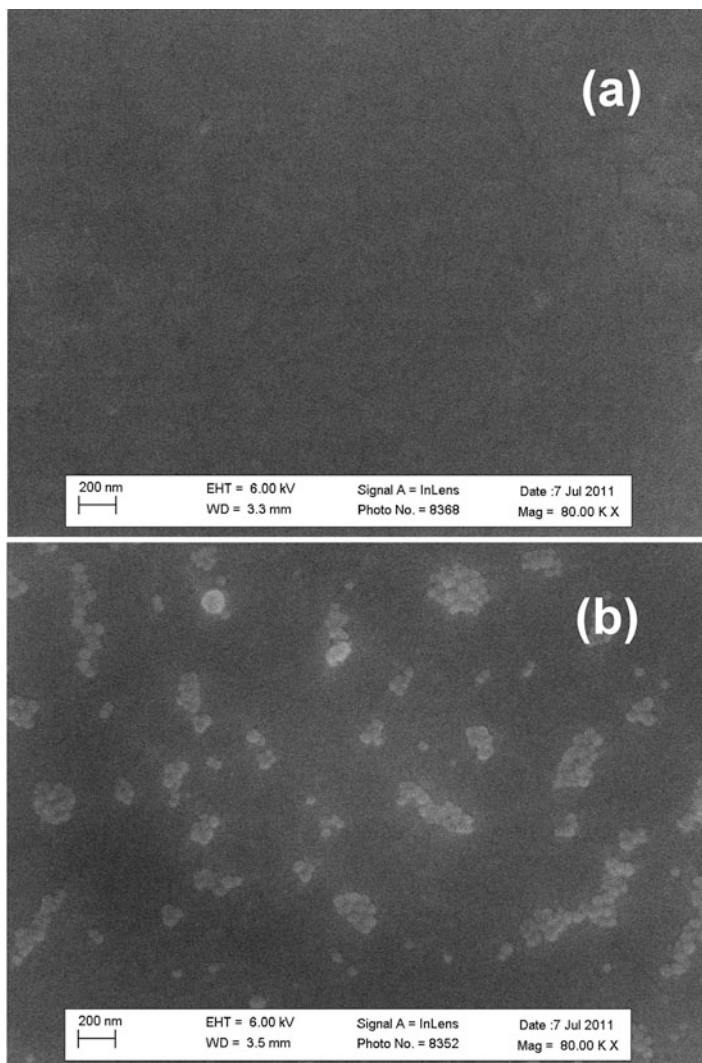


Fig. 4 SEM images of the surface of LDPE films without (a) and with (b) H_3PO_4 treatment (Rychkov et al. 2012b)

Commonly available parylene variants include parylene C, N, and D. Among them, parylene C is the most popular due to its combination of barrier properties, cost, and other processing advantages. Parylene HT[®] from Specialty Coating System (Indianapolis, IN, USA) is a recent development. Chemical compositions of these parylenes are shown in Fig. 5. Parylene HT[®] has the repeat unit $-CF_2-$ (the repeat unit of Teflon PTFE) in its aliphatic chemistry, and hence it has superior oxidative and UV stability.

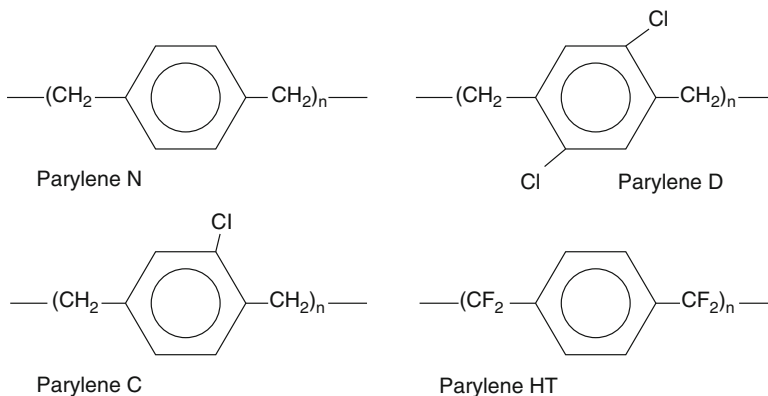


Fig. 5 Molecular compositions of typical commercially available parylene variants

In 1980, Raschke and Nowlin reported the first study on the electret properties of parylenes (Raschke and Nowlin 1980). They found that parylenes retain surface charge densities greater than or equal to Teflon electrets. In particular, parylene D and parylene HT[®] (referred to as “polymer AF-4”) show exceptional high temperature stability, remarkably better than Teflon electrets. Lo and Tai reported more comprehensive investigations on parylene HT[®] as an electret material (Lo and Tai 2008). The maximum surface potential they obtained is 204.58 V/ μm , corresponding to a surface charge density of 3.69 mC/m². Being stored in ambient conditions of room temperature and 60 % RH, the as-deposited parylene HT[®] shows a relatively large initial drop of the surface potential. However, it maintains a stable value of about 70 % of the initial surface potential after 330 days. It was also found that proper aging treatment can significantly improve the charge stability. When the parylene HT[®] sample is annealed at 400 °C for 1 h before charging, it retains 91 % of the initial surface potential after 330-day storage in ambient conditions.

The thermal stability of parylene HT[®] electrets was studied by means of thermally stimulated discharge measurements. Figure 6 illustrates the TSD surface potential and current of the as-deposited and annealed parylene HT[®] samples. The peak temperatures of the TSD current spectra occur at about 160 °C and 230 °C for the as-deposited and the annealed sample, respectively, higher than those of the TSD spectra of Teflon.

1.2.2 CYTOP

CYTOP is a type of perfluorinated polymer. Figure 7 shows the molecular compositions for three types of commercial grade CYTOP (Asahi Glass Co., Ltd). They have different end groups, i.e., trifluoromethyl (CTL-S), carboxyl (CTL-A), and amidosilyl (CTL-M). CYTOP is soluble in perfluorinated solvents and therefore is compatible with MEMS fabrication process. Thick films can be obtained by multiple spin coating. In addition, coated films can be patterned easily with conventional photolithography and O₂ plasma etching.

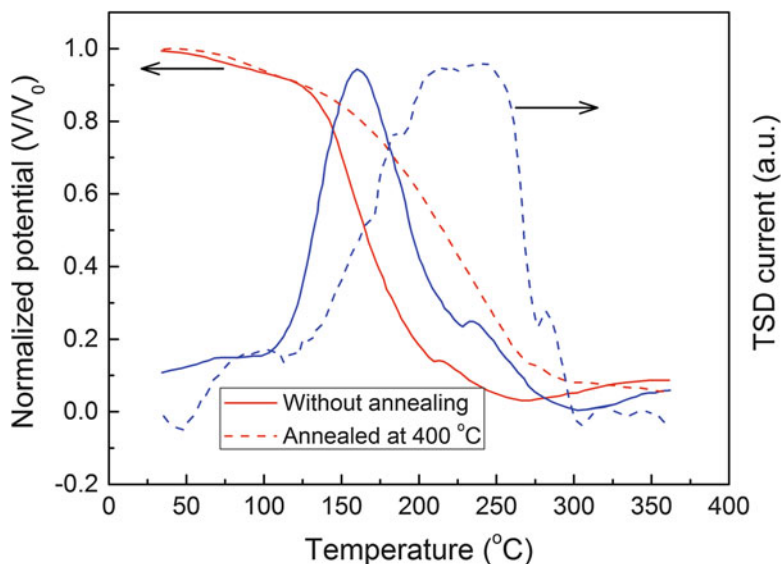


Fig. 6 Charge TSD and TSD current spectra of parylene HT[®] samples without annealing (*solid*) and annealed at 400 °C for 1 h before charging (*dashed*). The surface potentials are normalized to the initial values, and the TSD current is shown in an arbitrary unit (Lo and Tai 2008)

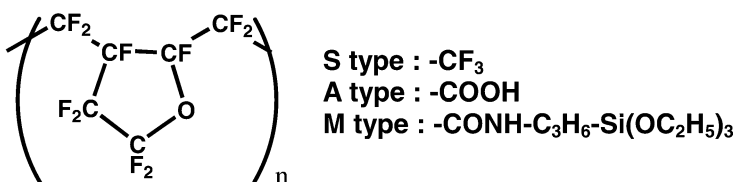


Fig. 7 Molecular composition and end groups of CYTOP

Suzuki and colleagues studied the electret properties of CYTOP (Arakawa et al. 2004; Tsutsumino et al. 2005, 2006; Sakane et al. 2008; Kashiwagi et al. 2011). It was found that the end groups have strong influence on the electret properties of CYTOP. CTL-A and CTL-M can not only retain high surface charge density but also exhibit good stability. As shown in Fig. 8, the initial surface charge density of CTL-M is as high as 1.3 mC/m^2 and is stable over a storage time longer than 4000 h. The initial surface charge density of CTL-A is about 0.8 mC/m^2 also stable over the same period of storage time. In comparison, CTL-S and Teflon AF have much lower surface charge density (Sakane et al. 2008).

The results indicate that the amidosilyl end group plays a critical role in the electret properties of CYTOP. Doping only 0.6–3.0 % of aminosilane into CTL-A can double the surface charge density and improve the thermal stability. CTL-A doped with 3.0 % of aminosilane shows a surface charge density of up to 1.5 mC/m^2 , higher than that of CTL-M (Fig. 8). By optimizing the charging voltage and the film

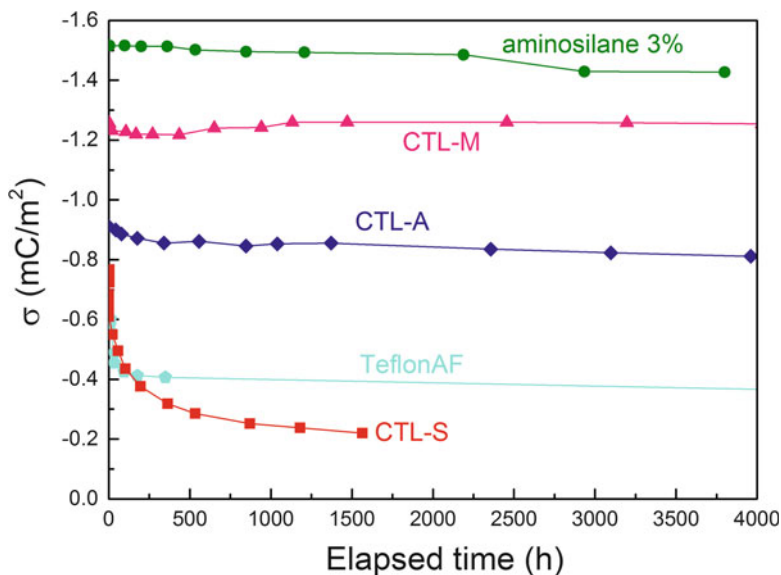


Fig. 8 Surface charge density as a function of storage time in ambient conditions (Suzuki 2011)

thickness, a surface charge density as high as that of parylene HT[®] (3.7 mC/m^2) is attainable with an aminosilane-doped CYTOP electret.

2 Ferroelectrets

Extensive studies on ferroelectrets were initiated around 1990 by colleagues from Finland using cellular polypropylene (PP). Afterward, cellular PP has become the workhorse of ferroelectret research and technology due mainly to its ease of processing and its high piezoelectricity. However, efforts have been continuously devoted to seeking ferroelectrets from different materials by means of a variety of preparation methods. This is driven mainly by the following two reasons: (i) the piezoelectricity of cellular PP ferroelectrets is stable only up to 60°C , which limits their application and (ii) the cavities in cellular PP foams always have a rather wide and not so well-controlled size and shape distribution so that only some of the cavities are optimal for charging and for transducer operation. For industrial applications, films with well-controlled distributions or even uniform values of cavity size and cavity shape are very desirable. Such films may be easily produced on a large scale with good reproducibility. As will be demonstrated in this section, a considerable number of cellular polymer films and cavity-containing polymer film systems have been developed as ferroelectrets in recent years. Some of the typical material parameters of polymer ferroelectrets that have been reported so far are given in Table 1.

Table 1 Material parameters of polymer ferroelectrets, i.e., film thickness t , resonance frequency f_p , elastic modulus c_{33} , piezoelectric d_{33} coefficient, and continuous service temperature (CST)

Ferroelectrets	t , μm	f_p , kHz	c_{33} , MPa	d_{33} , pC/N	CST, $^{\circ}\text{C}$	Reference	
Polyolefin	Cellular PP	37 ~ 130	0.9 ~ 10	140 ~ 500	50	Zhang et al. 2004; Wegener et al. 2004	
	Cellular PE	30	6 ~ 15	200 ~ 400	–	Tajitsu 2011	
Polyester	Cellular PETP	80 ~ 130	0.3 ~ 3.8	~476	–	Wirges et al. 2007	
	Cellular PENP	~130	1.4	60 ~ 140	80	Fang et al. 2007, 2008, 2010	
COC	Cellular COC	70 ~ 100	–	15	110	Saarniäki et al. 2006	
	COC assembly	~550	0.3 ~ 270	~1000	110	Li and Zeng 2013	
Polycarbonate	220	–	–	30	100	Sborikas et al. 2014	
Fluoro-polymer	FEP/cPTFE/FEP sandwich	85 ~ 250	0.3	~500	–	Zhukov et al. 2011; von Seggern et al. 2011	
	Cellular AF	9 ~ 60	0.15	600	120	Mellinger et al. 2001	
	Cellular FEP	270	–	50	–	Veronina et al. 2008	
	Fluoropolymer system (Fusion bonded + patterned)	60 ~ 500	20 ~ 100	0.3 ~ 0.55	160 ~ 500	120	Altafim et al. 2009; Zhang et al. 2014a
	Laser-bonded FEP	~170	31 ~ 53	0.3 ~ 0.8	160 ~ 350	120	Fang et al. 2011
AF + PDMS structure (microfabricated)	300	18	0.3	1000	–	Wang et al. 2012; Wang et al. 2013	

2.1 Polyolefin Ferroelectret

2.1.1 Polypropylene Ferroelectret

Pioneer work on ferroelectrets was done by colleagues from Finland using cellular polypropylene (PP) (Kirjavainen 1987; Savolainen and Kirjavainen 1989; Raukola 1998; Lekkala and Paajanen 1999). Various procedures were adopted in order to produce polymer foams. The traditional way is to use chemical and/or physical nucleating agents in molten polymer. The pressure in extruder, where plastic material is melted, compressed, and mixed, is sufficiently high to keep the melt nonfoamed. Immediately after the pressure drop in the head of the extruder or die foam, bubbles appear and grow, introducing a cellular structure in the polymer. Another widely used method is stretching filler-loaded polymers under suitable conditions (Raukola et al. 2002). Tiny mineral particles are often employed as fillers that serve as stress concentrators for microcracks during stretching of the film. Simultaneous or sequential stretching in two perpendicular directions results in films with lens-like cavities.

Usually, the foamed film is sealed with a thin nonvoided layer on each surface. Thus, the produced polymer foam has an ABA layered structure, where the few microns thick surface layers are smooth and homogeneous, and the thicker midlayer is full of lens-like cavities.

Very often, cavities formed by stretching filler-loaded polymers are too flat for efficient charging by means of microplasma discharges, because the plasma electrons cannot be accelerated sufficiently to ionize the gas molecules. Also, flat cavities give rather stiff films with reduced electromechanical response. With a pressure and temperature treatment, so-called gas-diffusion expansion (GDE) process, the size of the cavities can be adjusted (Paajanen et al. 2002; Zhang et al. 2004; Wegener et al. 2004). The external gas pressure is raised and kept at a high value for a certain period of time so that the gases diffuse into the cavities until the internal pressure of the cavities equalizes the external pressure. The polymer foam is inflated by a subsequent sudden release of the external gas pressure. The thickness expansion of the foam is stabilized by heat treatment at elevated temperatures during or right after the pressure treatment. Figure 9 shows the SEM images for a typical cellular PP foam that is produced by stretching filler-loaded polymer melt before (top) and after (bottom) GDE treatment. It should be noted that the film becomes stiffer again when over expanded, because the cavities are now turned into more stable spherical shapes. Therefore, a medium GDE is required for optimal electromechanical properties.

The cavities in cellular PP are highly compressible in the thickness direction due to the large anisotropy, whereas in the transverse directions the materials are much stiffer. Thus, cellular PP ferroelectrets show very large piezoelectric d_{33} coefficient. Values of hundreds of pC/N are often achieved, more than one order of magnitude greater than those found in conventional ferroelectric polymers. The transverse piezoelectric coefficient (d_{31} and d_{32}) is typically around 2 pC/N, two orders of magnitude lower than the d_{33} coefficient. This feature renders cellular PP ferroelectrets ideal candidates for flexible piezoelectric sensors, since they are essentially insensitive to the bending during operation. The pyroelectric coefficient

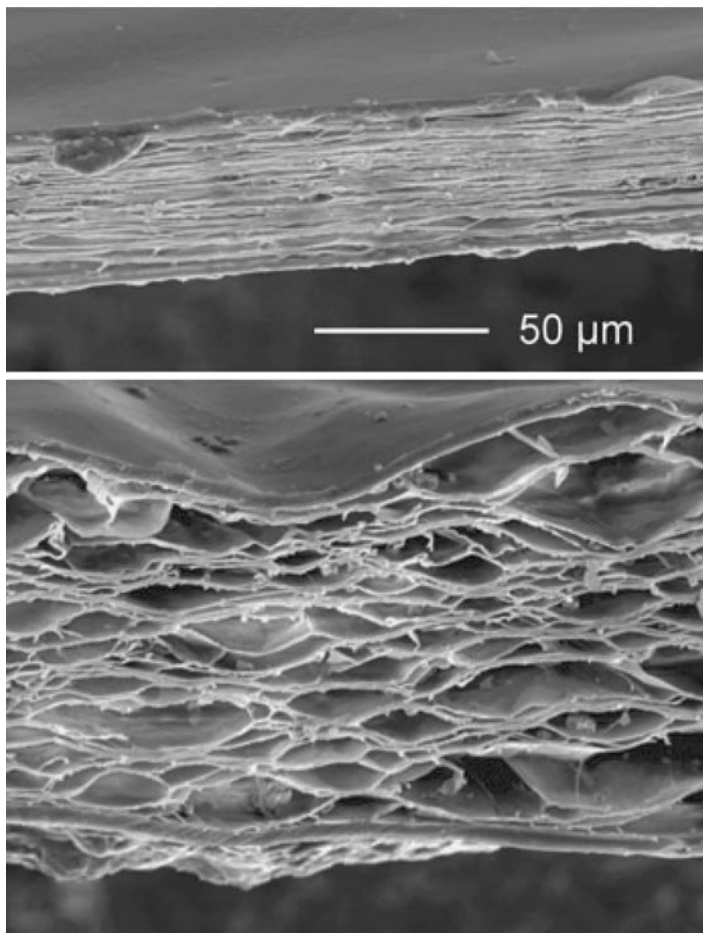


Fig. 9 SEM of the cross sections of cellular PP films. Top: not expanded. Bottom: expanded at a pressure of 5 MPa with a subsequent heat treatment at 100 °C. The length scale is the same for both micrographs. (Wegener et al. 2004)

of cellular PP ferroelectrets ($\sim 0.25 \mu\text{C}/\text{m}^2\text{K}$) is much smaller than that of polar polymers such as PVDF ($\sim 27 \mu\text{C}/\text{m}^2\text{K}$) (Neugschwandtner et al. 2001). For this reason, there have been so far only very few investigations of pyroelectricity in ferroelectrets.

2.1.2 Polyethylene Ferroelectret

Tajitsu and colleagues studied porous polyethylene as ferroelectret (Nakayama et al. 2009; Tajitsu 2011). The porous PE films prepared in their study have a thickness of 30 μm and a porosity ranging from 58 % to 85 %. Pores with a diameter of about 0.3 μm are evenly distributed throughout the sample. In spite of the rather

small pore size, the authors argued that they could charge the samples with corona poling and obtain a piezoelectric d_{33} coefficient up to 200 pC/N.

It should be noted that the cavities must be internally charged via a series of dielectric barrier discharges (DBDs) in order to render polymer foams ferroelectrets (Qiu et al. 2011). According to Paschen's law, the breakdown voltage of gas in a uniform electric field is a function of gas pressure p and electrode spacing d (which in the context of ferroelectret is equal to the cavity height). For air at atmospheric pressure, the breakdown voltage decreases with decreasing d and reaches its minimum at a spacing of about 8 μm and then increases sharply as d decreases further. Cavities with a height smaller than 3 or 4 μm require extremely high breakdown voltage and therefore are very difficult to charge with DBDs.

2.1.3 Chemically Modified Polyolefin Ferroelectret

From an application point of view, both the sensitivity and the thermal stability of electromechanical transducer materials are critical factors. As for ferroelectrets, the stability of the piezoelectricity is determined by two aspects: stability of the mechanically nonuniform structure and stability of the internally trapped charge. Obviously, the nonuniform structure will collapse at temperatures higher than the melting point T_m of the material. However, T_m is usually much higher than the temperature for charge detrapping. Thus, the charge stability usually determines the temperature range for the application of ferroelectrets. For cellular PP ferroelectrets, a significant loss in the piezoelectric sensitivity appears already at 60 °C, resulting from the low long-term thermal stability of the charges stored on the inner surfaces of the cavities (Mellinger et al. 2006). For this reason, the use of cellular PP is restricted in many applications that require thermal stabilities in excess of 60 °C (for example, in the automotive industry). The thermal stability of the piezoelectricity in PE ferroelectrets was not studied in the works of Tajitsu et al. Since PE is inferior to PP in terms of charge storage, a less stable piezoelectricity is to be expected for PE ferroelectrets as compared with cellular PP.

Since space charges are trapped on the surface of the electret material in a ferroelectret (inner surfaces of cavities or interfaces between different material phases), a surface modification can be a promising solution to improve the charge stability and in turn the thermal stability of the piezoelectricity. An et al. modified cellular PP with fluorine gas. It is found the direct fluorination leads not only to higher piezoelectricity but also better thermal stability of the sensitivity (An et al. 2009c). The improvement is more pronounced if the samples were fluorinated under high pressure and were posttreated by nitrous oxide and isothermal crystallization. As shown in Fig. 10, the piezoelectric d_{33} coefficient of the fluorinated and posttreated sample remains 58 % and 45 % of its initial value after being store at 70 °C for 151 h and at 90 °C for 224 h, respectively. The corresponding value for virgin samples is only 29 and 15 % (An et al. 2012).

In the study of Rychkov et al., ferroelectrets of low-density polyethylene (LDPE) were prepared by means of a template-based lamination technique (Rychkov

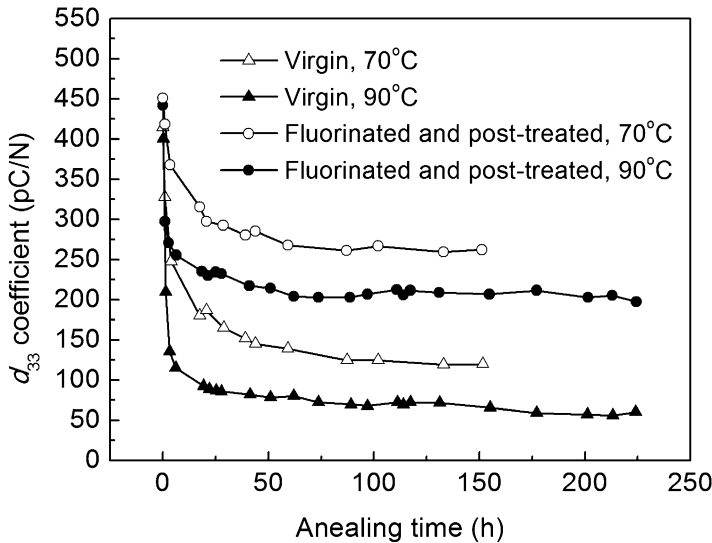


Fig. 10 d_{33} decay in fluorinated (*solid circles*) and virgin (*open circles*) cellular PP ferroelectrets (An et al. 2012)

et al. 2012b). The as-prepared PE ferroelectrets have low thermal stability of the piezoelectricity, owing to the poor electret properties of PE. A treatment of the samples with orthophosphoric acid results in significantly improved thermal stability of the charges. Consequently, the d_{33} -decay curves shift to higher temperature by 40 °C (Fig. 11).

Polyolefins have two obvious advantages, i.e., low price and ease processibility. However, the range of application of polyolefin ferroelectrets is limited by their quite low continuous service temperatures (CST). To overcome this limitation, ferroelectrets made from other polymers with higher CST are desired.

2.2 Polyester Ferroelectret

The concept and knowledge of ferroelectret, established with cellular PP ferroelectrets, is successfully applied to polyester polymers. At first, polyethylene terephthalate (PETP) foams produced in the industry were studied (Wegener et al. 2005a). It is found that the as-received PET foams are expanded too much and are too stiff to have noticeable piezoelectricity. Annealing at elevated temperatures reduces the thickness of the PET foams substantially. However, the cellular structure is kept as long as the annealing temperature is below 160 °C. By optimizing the annealing parameters, a maximum d_{33} coefficient of 23 pC/N is obtained. The corresponding elastic modulus of the PET ferroelectret is around 7 MPa.

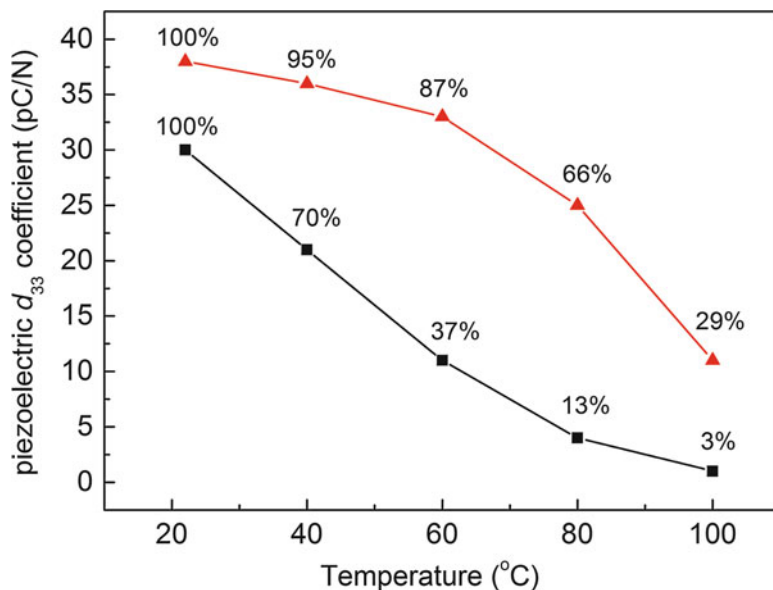


Fig. 11 Temperature dependence of d_{33} coefficients in laminated LDPE ferroelectrets (*black squares* – virgin samples; *red triangles* – modified with orthophosphoric acid) (Rychkov et al. 2012b)

Later, the same group reported cellular polyester films, including PETP (Wegener et al. 2005b; Wirges et al. 2007) and poly(ethylene naphthalate) (PENP) (Fang et al. 2007, 2008, 2010), fabricated through physical foaming of nonvoided films with supercritical carbon dioxide (scCO_2). Sample preparation consists of a sequence of steps as schematically shown in Fig. 12. A nonvoided commercial film is first exposed to pressurized CO_2 at room temperature. At certain high pressures, the CO_2 gas turns into supercritical phase. With storage time, scCO_2 penetrates into the bulk of the polymer film and eventually saturates. Parameters such as the gas pressure and the gas temperature need to be optimized since they strongly affect the penetration of gas molecules. Then the pressure is quickly released (Fig. 12a). This is followed by a thermal treatment on the film filled with scCO_2 at elevated temperature. As a result, the scCO_2 inside the film undergoes a phase change into gas and foams the film (Fig. 12b). The foamed structure can be further optimized by means of well-controlled biaxial stretching and sometimes subsequent gas-diffusion expansion. Figure 13 shows a SEM image of the cross-section of a PEN sample that was foamed, stretched, and expanded.

The optimized PETP and PENP ferroelectrets exhibit high piezoelectric d_{33} coefficient of 500 and 140 pC/N, respectively. The piezoelectric sensitivity of polyester ferroelectrets is stable at least up to 80 °C, slightly higher than that of cellular PP ferroelectrets. In particular, PENP ferroelectrets are still piezoelectrically active even after storage at 100 °C for 5 days.

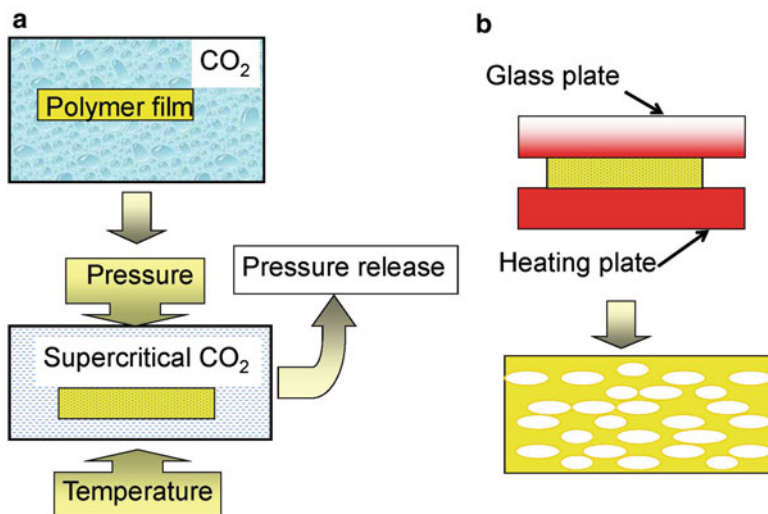


Fig. 12 Preparation of polymer foams using supercritical CO₂. (a) Penetration of scCO₂ into the polymer matrix. (b) Foaming of the polymer resulted from the phase change of the scCO₂

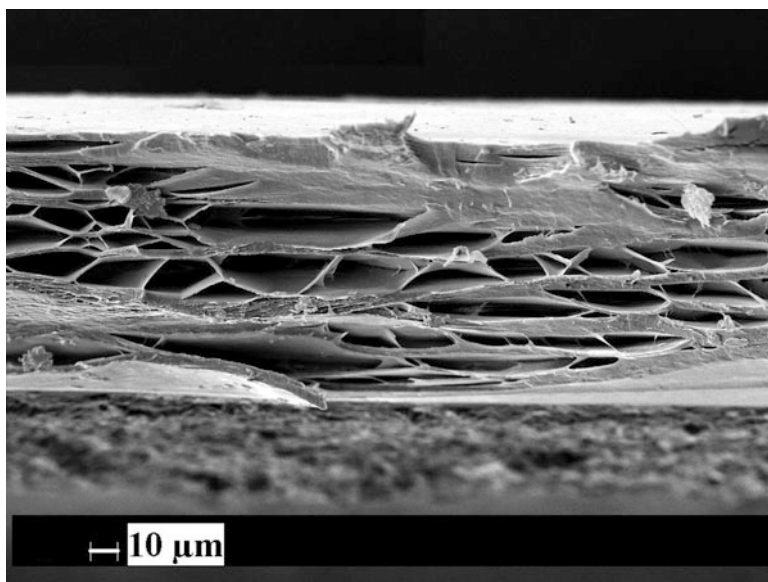


Fig. 13 SEM image of the cross section of a cellular PEN film. The sample is foamed with scCO₂, and the foam structure is further optimized by biaxial stretching and gas-diffusion expansion (Fang et al. 2007)

2.3 Cyclo-Olefin Polymer (COP) and Copolymer (COC) Ferroelectret

Cyclo-olefin based polymers show good electret properties with outstanding charge stability (Sessler et al. 1997) and therefore are promising candidate materials for ferroelectrets. In the works of Wegener et al. and Savijärvi et al., cyclo-olefin polymers were blended with different olefin polymers with lower glass transition temperature in order to improve the elastic properties (and thus the processability) of the materials (Wegener et al. 2005c; Savijärvi et al. 2005; Saarimäki et al. 2005, 2006). Cellular film structures were formed by stretching filler-loaded polymer compounds. The processing temperature window was very narrow compared with cellular PP foams. Gas diffusion expansion (GDE) procedures were carried out to optimize the cavity dimension. Piezoelectric d_{33} coefficients about 15 pC/N were obtained with the cellular cyclo-olefin ferroelectrets. The d_{33} coefficient is relatively small in comparison with that of cellular PP ferroelectrets. Nevertheless, the piezoelectric sensitivity of cyclo-olefin copolymer ferroelectrets exhibits good thermal stability up to 110 °C, markedly better than cellular PP and polyester ferroelectrets.

Recently, a scCO₂-assisted assembly approach has been proposed for producing COC film systems with regular cavity structure (Li and Zeng 2013). When a COC film is exposed to scCO₂, the surface glass transition temperature becomes significantly lower than that of the bulk due to strong COC-CO₂ interaction. As a result, the polymer chains near the surface are much more mobile and diffusive. Sample preparation is schematically shown in Fig. 14. Five-layer COC film stacks were employed. Two of the five films contained regular rectangular openings that were cut with a CO₂ laser. The openings had the same length and width and the same spacing between adjacent openings. Three COC films were separated by the two with

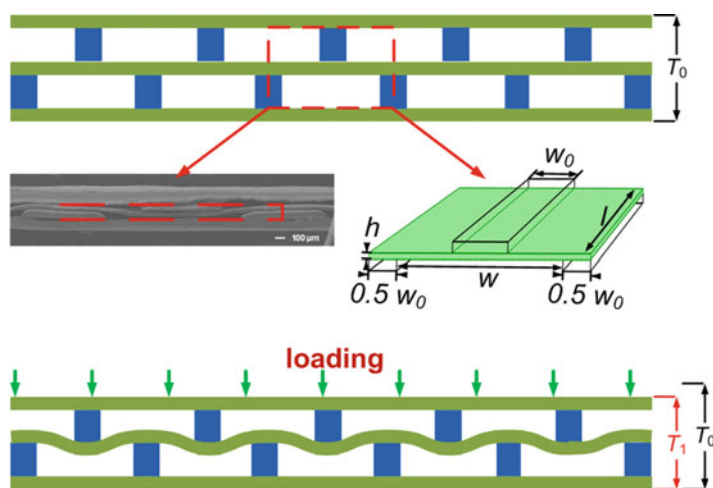


Fig. 14 Schematic view of the preparation process for COC film systems that contain regular cavity structure. Also shown is a SEM image of a COC ferroelectret sample (LiMCP 2013)

openings, the patterns being shifted by half of the total width of the opening and the spacing. The stack was then treated for 12 h in 10 MPa CO₂ at a temperature of 120 °C (60 °C lower than the glass transition temperature of COC). A good bonding between the interfaces was achieved. In this method, the bulk deformation is prevented since the temperature is much lower than the bulk T_g . This is a big advantage as compared with techniques using fusion bonding where deformation of the structure and thermal degradation of the material are big concerns.

As shown in Fig. 14, the compression of the sample is realized by the bending of the “unit cell.” Such COC ferroelectrets show significant piezoelectricity. Piezoelectric d_{33} coefficient of hundreds to 1000 pC/N was reported. Investigations of the thermal stability show that the piezoelectricity is stable at least up to 110 °C.

2.4 Polycarbonate Ferroelectret

Polycarbonate (PC) is a durable thermoplastic with high toughness and a large creep modulus, with good heat resistance, high dimensional stability, and good electrical insulation properties. Due to these particular features, PC is widely used in electronic applications, e.g., as dielectric in capacitors with high stability. It was also reported that PC films with additives exhibit excellent charge stability after thermal treatment (Erhard et al. 2010c). Cellular PC foams were successfully prepared by means of foaming with scCO₂ and also by stretching films containing low-molecular-weight components that can be subsequently removed through phase extraction (Bhrendt 2010). The PC foams were charged in a point-to-plate corona with a needle voltage of +32 kV. Unfortunately, the PC foams cannot be rendered piezoelectric in this way, probably because the foam sheets are too thick for efficient charging and/or the films are too stiff for sufficient deformation under mechanical or electrical stress.

New strategies have been proposed for making PC ferroelectrets. One strategy is rather easy to implement. A grid of double-sided adhesive tape with desired opening pattern was prepared by means of a computer-controlled laser cutting. Two polycarbonate (PC) films, which were metalized on one surface, were joined by the grid via their nonmetalized surfaces (Qiu et al. 2010). Thus, well-defined cavities are formed around the openings of the grid. After contact charging with 2 kV, the PC ferroelectrets show a piezoelectric d_{33} coefficient up to 30 pC/N.

In another strategy, PC ferroelectrets were prepared through the use of screen printing (Sborikas et al. 2014). Screen printing is often employed to deposit inks onto substrates ranging from ceramics to plastic materials, fabrics, and papers. For sample preparation, suitable ink materials are screen printed with desired pattern onto a piece of PC film. Then, the second PC film is placed on top of the ink pattern. With thermal treatment, two PC films are tightly bonded to each other by the polymer ink pattern, leading to a polymer system with well-defined cavities. Silver paste electrodes were screen printed onto both outer surfaces of the samples. After charging, the PC ferroelectrets exhibit d_{33} coefficient of about 30 pC/N, which is stable up to 100 °C.

2.5 Fluoropolymer Ferroelectret

Fluoropolymers, such as several kinds of Teflon (polytetrafluoroethylene [PTFE], fluoroethylenepropylene [FEP], tetrafluoroethylene-per-fluoromethoxyethylene copolymer [PFA], and amorphous Teflon [AF]), are very important electrets due to their excellent charge storage properties. When ferroelectrets are made from fluoropolymers, a good thermal stability of the piezoelectricity is to be expected. However, how to make cellular fluoropolymers is a big challenge because of their poor mechanical properties and severe creep behavior. Initially, porous PTFE was produced by means of unidirectional stretching at high temperature. Such films have open pore structures which is detrimental for the piezoelectricity. Cellular fluoropolymer foams were produced by solvent evaporation technique and foaming with scCO_2 . These techniques require relatively complex processing and lack good reproducibility. More recently, a number of other strategies have been proposed, including fusion bonding combined with patterning, laser bonding, as well as microfabrication.

2.5.1 Porous PTFE

Porous PTFE films were prepared from commercial nonporous PTFE plates by means of unidirectional stretching at high temperature. The porous films exhibit open structure of the pores. This is quite different from other types of polymer foams, such as cellular PP, which have closed-cavity structure. Porous PTFE shows excellent surface-charge storage stability, even at elevated temperature (Xia et al. 1999). Because of its open-pore structure, porous PTFE itself is not a promising piezoelectric material. During metallization of electrodes that are necessary for electrical contact for measuring the signal, the metallic particles go into the interfaces between the pores and the dielectric. As a result, the deposited charges are lost and the piezoelectricity of the film becomes extremely low. Nevertheless, porous PTFE is very suitable for preparing sandwich-structure ferroelectrets due to its high softness and excellent electret properties. Shortly after, layer stacks of porous and nonporous PTFE films as ferroelectrets were studied (Künstler et al. 2000; Gerhard-Multhaupt et al. 2000).

Von Seggern and colleagues prepared ferroelectrets by sandwiching a highly porous PTFE consisting of 91 % air and 9 % fibrous PTFE, so-called expanded PTFE (ePTFE), between two solid FEP layers (Hu and von Seggern 2005, 2006; Zhukov and von Seggern 2007a, b; von Seggern et al. 2010, 2011; Zhukov et al. 2011). In order to eliminate any excess air between adjacent layers, samples were subject to an initial evacuation step followed by a slow exposure to lab conditions. Figure 15 shows the cross section of such a fluoropolymer sandwich.

In such sandwiches, the FEP layers form structurally and electrically dense layers, sealing the open porous structure of the ePTFE layer. Upon corona charging, breakdown occurs within the pores when the electric field strength exceeds the Paschen-breakdown threshold value of air inside. Charges of both polarities are separated, and some of them are trapped on the inner surfaces of the top and bottom

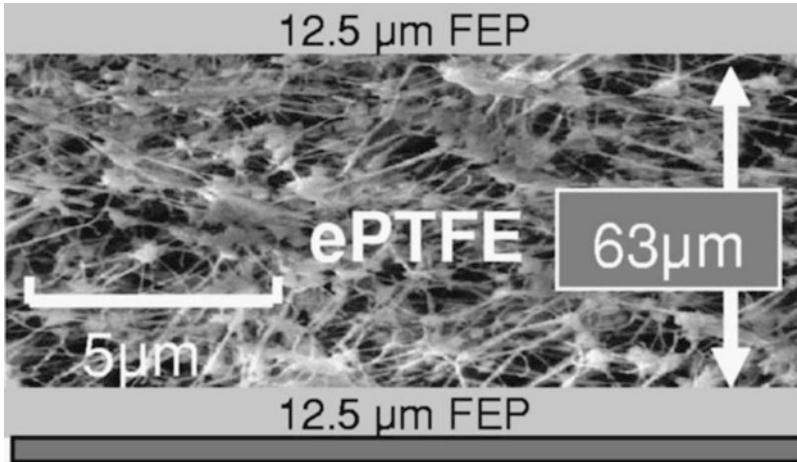


Fig. 15 FEP/ePTFE/FEP/metal layer system (Zhukov and von Seggern 2007a)

FEP layers. After charging, the FEP layers, separated by the ePTFE layer, form macroscopic dipoles, leading to strong piezoelectricity of the sample. The piezoelectric d_{33} coefficient is thermally stable if the sample is charged at elevated temperatures. However, the d_{33} decays from 800 to 400 pC/N under atmospheric pressures within 6 days, and repeated mechanical loading leads to a similar loss of piezoelectricity, apparently related to mechanical fatigue in the highly porous ePTFE.

2.5.2 Cellular Fluoropolymer Ferroelectret

Teflon AF is easier to process than other fluoropolymers. It can be dissolved in selected perfluorocarbon solvents, which allows the production of AF films by conventional techniques such as drop casting and spin coating. In the work of Mellinger et al., porous Teflon AF films with a thickness of 3–10 μm was obtained by boiling the solvent (Fluorinert FC-77 from 3 M) (Mellinger et al. 2001). Several layers were drop casted on top of each other in order to have the desired overall thickness. The porous film with open pores was sealed with nonporous AF films made by drop casting at room temperature. After corona charging, the Teflon AF ferroelectrets exhibit strong piezoelectricity with a d_{33} coefficient up to 600 pC/N. The piezoelectric sensitivity is stable at temperatures of at least 120 $^{\circ}\text{C}$.

Unlike the homopolymer PTFE, FEP is a meltprocessable thermoplastic copolymer. The above described technique of foaming with scCO_2 was also adopted to make cellular FEP foams (Veronina et al. 2008). The procedures for foaming of the material are similar to the case of polyester polymers. Usually, only one big void across the film thickness is generated in the FEP foams. After charging and electrode evaporation, the cellular FEP ferroelectrets show d_{33} coefficients up to 50 pC/N.

2.5.3 Cavity-Containing Fluoropolymer Film Systems Prepared by Fusion Bonding

Fluoropolymer film systems containing internal cavities have been prepared by several groups through fusion bonding technique. Altafim et al. developed FEP film systems with uniform cavities by thermal fusion combined with vacuum evacuation (Altafim et al. 2005, 2006). In their study, a stack of two FEP films was placed between two cylindrical metal plates which can be independently heated. The top plate is completely solid, while the bottom one has tiny holes that are connected to a vacuum pump. The bottom plate was separated from the stack of FEP films by a metal grid. Most of the air was removed through the holes of the bottom plate by means of the vacuum pump and the adjacent FEP film was sucked into the openings of the metal grid. By heating and pressing the top plate onto the stack, air cavities with the same diameter as the grid openings were created.

Later, ferroelectrets with well-controlled and uniform cavities were developed by a straightforward lamination process (Altafim et al. 2009). In this process, two polymer electret films are laminated around a template between them. The template, which can be made of metal foils or of polymers with a melting temperature higher than that of the electret films, contains regular openings through which the electret films can be fused with each other. Lamination is implemented at a temperature substantially higher than the melting temperature of the electret films yet lower than that of the template. After the outer layers have been fused, the template is removed, resulting in a polymer-film system with cavities of the designed pattern. Figure 16a schematically shows the preparation for tubular-channel FEP ferroelectrets. The template, made of an 100 μm

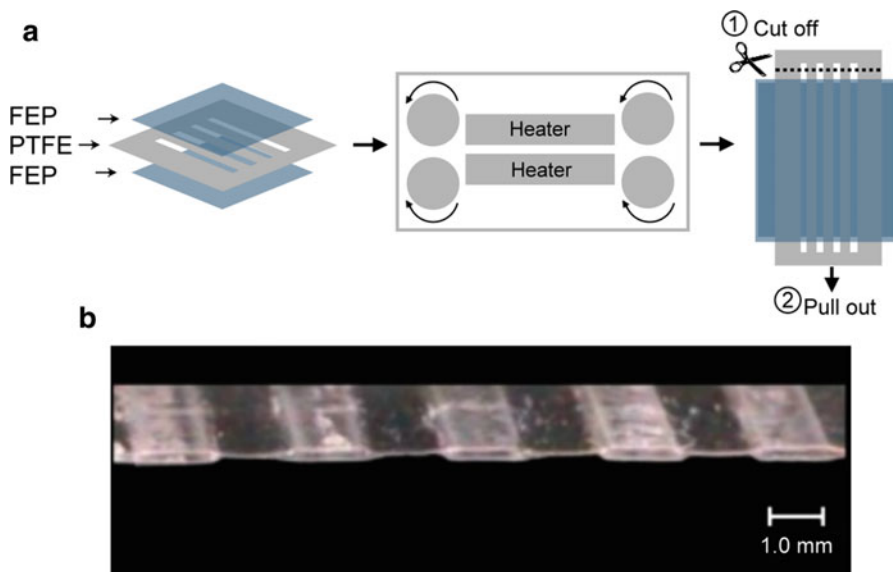


Fig. 16 (a) Schematic view of the preparation process for tubular-channel ferroelectrets. (b) Optical micrograph of the cross section of an FEP ferroelectret sample (Altafim et al. 2009)

thick PTFE by means of laser cutting, consists of several well-cut stripes with clearly defined and evenly distributed openings between them. The two solid FEP films have a thickness of 50 μm each. After being laminated at 300 $^{\circ}\text{C}$, the stack is naturally cooled down under laboratory conditions. The two FEP films are permanently fused with each other through the openings of the template. An FEP film system with open tubular cavities is obtained after removal of the PTFE template. Figure 16b shows an optical image of the cross section of such an FEP film system.

For stacks of very thin FEP and PTFE films, void-containing film systems can be obtained by directly pressing a metal mesh with (sub) millimeter spacing (Zhang et al. 2006, 2007). With a thermal treatment at 280 $^{\circ}\text{C}$, the polymer layers were fused underneath the wires of the metal mesh and cavities were formed between the fused areas because of the thermally expanding trapped air and the thermal softening of the fluoropolymer films. In several other works, rigid templates were used to bring forth the desired pattern in the fusion-bonded fluoropolymer film systems (Zhang et al. 2010, 2012, 2014a; Sun et al. 2011). When porous PTFE film is employed as the middle layer, the step of patterning can be skipped (Huang et al. 2008; Zhang et al. 2009, 2014b). For multilayer system consisting of FEP and porous PTFE, the film systems were bonded at a temperature between the melting point of FEP and that of PTFE. For porous and nonporous PTFE film systems, the film stacks were bonded by means of sintering.

2.5.4 FEP Ferroelectret Prepared by Laser Bonding

In the laser bonding technique, film stacks are locally fused by means of a laser beam (Fang et al. 2011). Commercial Teflon FEP films were used for the sample preparation. Regular square holes are cut into an FEP film separated by FEP stripes. The patterned film was sandwiched with two uniform FEP films. By applying a laser beam at selected points along the FEP stripes, the FEP melted locally and finally fused after the laser is moved away.

2.5.5 Teflon AF Ferroelectret by Microfabrication

Using microfabrication process, Wang et al. produced Teflon AF ferroelectrets built on cellular polydimethylsiloxane (PDMS) structures with micrometer-sized cavities (Wang et al. 2012, 2013). The sample fabrication consists of multilayer PDMS casting and stacking processes (Fig. 17). A photoresist mold is prepared on a silicon wafer. The cellular microstructure is duplicated to a thin PDMS layer that is casted on top of the mold. By bonding the patterned PDMS film to a blank thin PDMS layer, a PDMS foam with closed cavities is obtained. Multilayer structures can be constructed by repeating the casting and bonding processes. The cavities were filled with a solution of Teflon AF. Once the solvent evaporates, a thin layer of AF film deposits which assures good charge storage after internal charging of the cavities. During the processing, chemical or corona treatment is carried out in order to have easy peeling off or good bonding, respectively. Figure 18 shows the SEM image of the cross section of a sample. After electrode deposition and charging, the microfabricated ferroelectrets exhibit a piezoelectric d_{33} coefficient larger than 1000 pC/N.

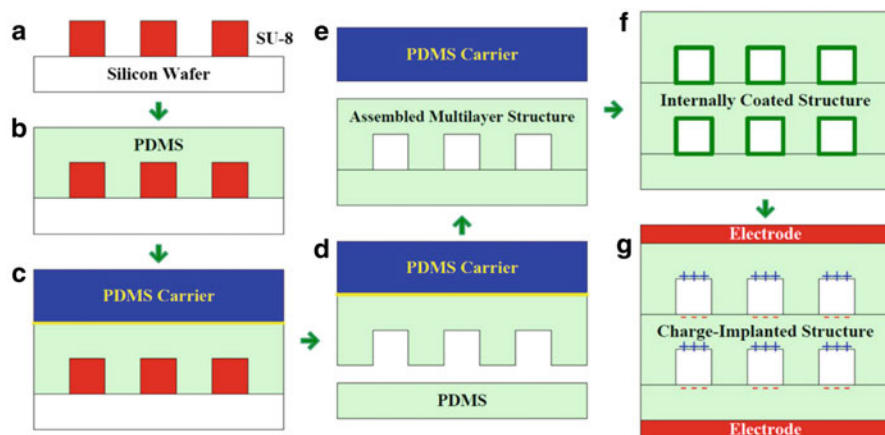


Fig. 17 Schematic illustration of the microfabrication of PDMS ferroelectrets (Wang et al. 2012)

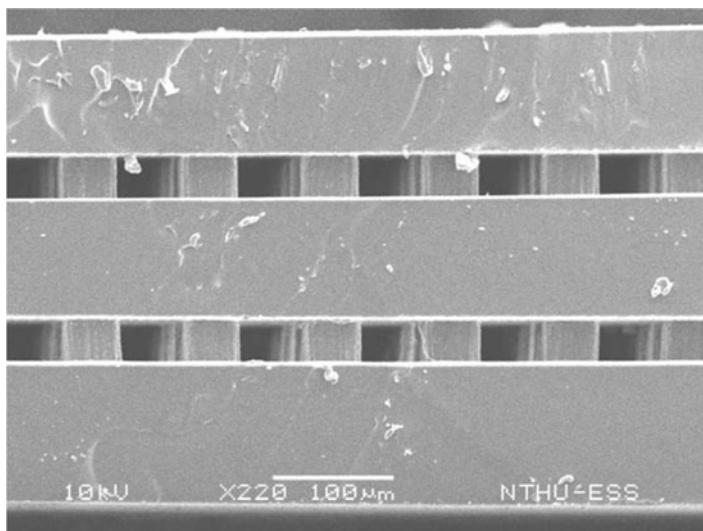


Fig. 18 Microfabricated cellular PDMS (Wang et al. 2013)

3 Summary

The development with respect to polymer electret materials has been active over the past years. A number of modified conventional polymer electret materials with superior electret properties have been reported. The improvement of electret properties were achieved by incorporating proper additives, by blending different polymer compounds, by physical aging, and by modifying with certain chemicals.

Besides, high-performance polymer electrets, such as Parylene HT[®] and certain types of CYTOP, were introduced to the family of electret materials. They exhibit not only excellent electret properties (high surface charge density with exceptional long-term and thermal stability) but also good compatibility with MEMS fabrication process.

As was also discussed in this chapter, very significant progress has been made in the development of ferroelectrets. A large number of polymer electrets, including polyolefins (PP and PE), polyesters (PETP and PENP), COC, PC, and fluoropolymers, were adopted to prepare ferroelectrets using a variety of techniques. By now, ferroelectrets with excellent electromechanical properties and with well-controlled cavity structures are becoming available.

The development of polymer electret and ferroelectret materials will certainly continue, and numerous novel applications using these new electret materials can be expected in the foreseeable future.

References

- Altafim RAC, Basso HC, Gonçalves Neto L, Lima L, Altafim RAP, de Aquino CV (2005) Piezoelectricity in multi-air voids electrets. In: Proceedings of conference electrical insulation dielectric phenomena, IEEE Service Center, Piscataway, pp 669–672
- Altafim RAC, Basso HC, Altafim RAP, Lima L, de Aquino CV, Gonçalves Neto L, Gerhard-Multhaupt R (2006) Piezoelectrets from thermo-formed bubble structures of fluoropolymer-electret films. *IEEE Trans Dielectr Electr Insul* 13(5):979–985
- Altafim RAP, Qiu X, Wirges W, Gerhard R, Altafim RAC, Basso HC, Jenninger W, Wagner J (2009) Template-based fluoroethylenepropylene piezoelectrets with tubular channels for transducer applications. *J Appl Phys* 106:014106
- An Z, Yang Q, Xie C, Jiang Y, Zheng F, Zhang Y (2009a) Suppression effect of surface fluorination on charge injection into linear low density polyethylene. *J Appl Phys* 105:064102
- An Z, Xie C, Jiang Y, Zheng F, Zhang Y (2009b) Significant suppression of space charge injection into linear low density polyethylene by surface oxyfluorination. *J Appl Phys* 106:104112
- An Z, Zhao M, Yao J, Zhang Y, Xia Z (2009c) Influence of fluorination on piezoelectric properties of cellular polypropylene ferroelectrets. *J Phys D Appl Phys* 42:015418
- An Z, Mao M, Cang J, Zhang Y, Zheng F (2012) Significantly improved piezoelectric thermal stability of cellular polypropylene films by high pressure fluorination and post-treatments. *J Appl Phys* 111:024111
- Arakawa Y, Suzuki Y, Kasagi N (2004) Micro seismic power generator using electret polymer film. In: Proceedings of powerMEMS 2004, Kyoto, pp 187–190
- Bhrendt N (2010) Tailored processing methods for cellular polycarbonate and polyetherimide films – new potentials for electret and piezoelectric applications. *IEEE Trans Dielectr Electr Insul* 17(4):1113
- Erhard DP, Deliani L, von Salis-Soglio C, Giesa R, Alstädt V, Schmidt HW (2010a) Recent advances in the improvement of polymer electret films. In: Müller AHE, Schmidt HW (eds) *Complex macromolecular systems II*, vol 228, Book series: advances in polymer science. Springer, Berlin, pp 155–207
- Erhard DP, Lovera D, Giesa R, Alstädt V, Schmidt HW (2010b) Influence of physical aging on the performance of corona-charged amorphous polymer electrets. *J Polym Sci B Polym Phys* 48:990–997
- Erhard DP, Lovera D, Jenninger W, Wagner J, Alstädt V, Schmidt H (2010c) Tailored additives to improve the electret performance of polycarbonates. *Macromol Chem Phys* 211:2179

- Fang P, Wegener M, Wirges W, Gerhard R (2007) Cellular polyethylene-naphthalate ferroelectrets: foaming in supercritical carbon dioxide, structural and electrical preparation, and resulting piezoelectricity. *Appl Phys Lett* 90:192908
- Fang P, Wirges W, Wegener M, Zirkel L, Gerhard R (2008) Cellular polyethylene-naphthalate films for ferroelectret applications: foaming, inflation and stretching, assessment of electromechanically relevant structural features. *E-Polymers* 8(1):487–495
- Fang P, Qiu X, Wirges W, Gerhard R, Zirkel L (2010) Polyethylene-naphthalate (PEN) ferroelectrets: cellular structure, piezoelectricity and thermal stability. *IEEE Trans Dielectr Electr Insul* 17(4):1079–1087
- Fang P, Wang F, Wirges W, Gerhard R, Basso HC (2011) Three-layer piezoelectrets from fluorinated ethylene-propylene (FEP) copolymer films. *Appl Phys A Mater Sci Process* 103:455–461
- Gerhard-Multhaupt R (ed) (1999) *Electrets*, vol 2, 3rd edn. Laplacian Press, Morgan Hill
- Gerhard-Multhaupt R, Küstler W, Goerne T, Pucher A, Weinhold T, Seiβ M, Xia Z, Wedel A, Danz R (2000) Porous PTFE space-charge electrets for piezoelectric applications. *IEEE Trans Dielectr Electr Insul* 7(4):480–488
- Hilczner B, Malecki J (1986) *Electrets*. Elsevier, Amsterdam
- Hu Z, von Seggern H (2005) Air-breakdown charging mechanism of fibrous polytetrafluoroethylene films. *J Appl Phys* 98:014108
- Hu Z, von Seggern H (2006) Breakdown-induced polarization buildup in porous fluoropolymer sandwiches: a thermally stable piezoelectret. *J Appl Phys* 99:024102
- Huang J, Zhang X, Xia Z, Wang X (2008) Piezoelectrets from laminated sandwiches of porous polytetrafluoroethylene films and nonporous fluoroethylenepropylene films. *J Appl Phys* 103:084111
- Kashiwagi K, Okano K, Miyajima T, Sera Y, Tanabe N, Morizawa Y, Suzuki Y (2011) Nano-cluster-enhanced high-performance perfluoro-polymer electrets for energy harvesting. *J Micromech Microeng* 21:125016
- Kirjavainen K (1987) Electromechanical film and procedure for manufacturing same. US Patent 4,654,546
- Ko WC, Tseng CK, Leu IY, Wu WJ, Lee AS, Lee CK (2010) Use of 2-(6-mercaptohexyl) malonic acid to adjust the morphology and electret properties of cyclic olefin copolymer and its application to flexible loudspeakers. *Smart Mater Struct* 19:055007
- Kressmann R, Sessler GM, Günther P (1999) Chapter 9: Space-charge electrets. In: Gerhard-Multhaupt R (ed) *Electrets*, vol 2, 3rd edn. Laplacian Press, Morgan Hill, pp 1–40
- Küstler W, Xia Z, Weinhold T, Pucher A, Gerhard-Multhaupt R (2000) Piezoelectricity of porous polytetrafluoroethylene single- and multiple-film electrets containing high charge densities of both polarities. *Appl Phys A Mater Sci Process* 70(1):5–8
- Lekkala J, Paajanen M (1999) EMFi-new electrets material for sensors and actuators. In: Proceedings of 10th international symposium electrets, Delphi, pp 743–746
- Li Y, Zeng C (2013) Low-temperature CO₂-assisted assembly of cyclic olefin copolymer ferroelectrets of high piezoelectricity and thermal stability. *Macromol Chem Phys* 214:2733–2738
- Lo HW, Tai YC (2008) Parylene-based electrets power generators. *J Micromech Microeng* 18:104006
- Mellinger A, Wegener M, Wirges W, Gerhard-Multhaupt R (2001) Thermally stable dynamic piezoelectricity in sandwich films of porous and non-porous amorphous fluoropolymer. *Appl Phys Lett* 79:1852–1854
- Mellinger A, Wegener M, Wirges W, Mallepally RR, Gerhard-Multhaupt R (2006) Thermal and temporal stability of ferroelectret films made from cellular polypropylene/air composites. *Ferroelectrics* 331:189–199
- Nakayama M, Uenaka Y, Kataoka S, Oda Y, Yamamoto K, Tajitsu Y (2009) Piezoelectricity of ferroelectret porous polyethylene thin film. *Jpn J Appl Phys* 48:09KE05
- Neuschwandtner GS, Schwödiauer R, Bauer-Gogonea S, Bauer S, Paajanen M, Lekkala J (2001) Piezo- and pyroelectricity of a polymer-foam space-charge electret. *J Appl Phys* 89:4503

- Paajanen M, Minkkinen H, Raukola J (2002) Gas diffusion expansion-increased thickness and enhanced electromechanical response of cellular polymer electret films. In: Proceedings of 11th international symposium electrets, Melbourne, pp 191–194
- Qiu X, Holländer L, Suárez RF, Wirges W, Gerhard R (2010) Polarization from dielectric-barrier discharges (DBDs) in ferroelectrets: mapping of the electric-field profiles by means of thermal-pulse-tomography (TPT). *Appl Phys Lett* 97:072905
- Qiu X, Gerhard R, Mellinger A (2011) Turning polymer foams or polymer-film systems into ferroelectrets: dielectric barrier discharges in voids. *IEEE Trans Dielectr Electr Insul* 18(1):34–42
- Raschke CR, Nowlin TE (1980) Polyparaxylylene electrets usable at high temperatures. *J Appl Polym Sci* 25:1639–1644
- Raukola J (1998) A new technology to manufacture polypropylene foam sheet and biaxially oriented foam film. Ph.D. thesis, Technical Research Centre of Finland. VTT Publication 361, Espoo
- Raukola J, Kuusinen N, Paajanen M (2002) Cellular electrets – from polymer granules to electro-mechanically active films. In: Proceedings of 11th international symposium electrets, Melbourne, pp 195–198
- Rychkov D, Gerhard R (2011) Stabilization of positive charge on polytetrafluoroethylene films treated with titanium-tetrachloride vapor. *Appl Phys Lett* 98:122901
- Rychkov D, Kuznetsov A, Rychkov A (2011a) Electret properties of polyethylene and polytetrafluoroethylene films with chemically modified surface. *IEEE Trans Dielectr Electr Insul* 18:8–14
- Rychkov D, Kuznetsov A, Rychkov A, Goldade V (2011b) Electret properties of polyethylene films modified with titanium tetrachloride vapor. In: Proceedings of 14th international symposium electrets, Montpellier, pp 111–112
- Rychkov D, Gerhard R, Ivanov V, Rychkov A (2012a) Enhanced electret charge stability on polyethylene films treated with titanium-tetrachloride vapor. *IEEE Trans Dielectr Electr Insul* 19(4):1305–1311
- Rychkov D, Altafim RAP, Qiu X, Gerhard R (2012b) Treatment with orthophosphoric acid enhances the thermal stability of the piezoelectricity in low-density polyethylene ferroelectrets. *J Appl Phys* 111:124105
- Rychkov D, Yablokov M, Rychkov A (2012c) Chemical and physical surface modification of PTFE films – an approach to produce stable electrets. *Appl Phys A Mater Sci Process* 107(3):589–596
- Rychkov D, Rychkov A, Efimov N, Malygin A, Gerhard R (2013) Higher stabilities of positive and negative charge on tetrafluoroethylene–hexafluoropropylene copolymer (FEP) electrets treated with titanium-tetrachloride vapor. *Appl Phys A* 112:283–287
- Saarimäki E, Paajanen M, Savijärvi AM, Minkkinen H (2005) Novel heat durable electromechanical film processing: preparations for electromechanical and electret applications. In: Proceedings of 12th international symposium electrets (ISE 12), IEEE Service Center, Piscataway, pp 220–223
- Saarimäki E, Paajanen M, Savijärvi AM, Minkkinen H, Wegener M, Voronina O, Schulze R, Wirges W, Gerhard-Mulhaupt R (2006) Novel heat durable electromechanical film processing: preparations for electromechanical and electret applications. *IEEE Trans Dielectr Electr Insul* 13(5):963–972
- Sakane Y, Suzuki Y, Kasagi N (2008) The development of a high-performance perfluorinated polymer electret and its application to micro power generation. *J Micromech Microeng* 18:104011
- Savijärvi AM, Paajanen M, Saarimäki E, Minkkinen H (2005) Novel heat durable electromechanical films: cellular film making from cyclic olefin polymers. In: Proceedings of 12th international symposium electrets (ISE 12), IEEE Service Center, Piscataway, pp 75–78
- Savolainen A, Kirjavainen K (1989) Electrothermomechanical film: Part I. Design and characteristics. *J Macromol Sci A Chem* 26(2&3):583–591
- Sborikas M, Qiu X, Wirges W, Gerhard R, Jenninger W, Lovera D (2014) Screen printing for producing ferroelectret systems with polymer-electret films and well-defined cavities. *Appl Phys A Mater Sci Process* 114:515–520

- Sessler GM (ed) (1999) *Electrets*, vol 1, 3rd edn. Laplacian Press, Morgan Hill
- Sessler GM (2001) *Electrets: recent developments*. *J Electrostat* 51–52:137–145
- Sessler GM, Yang GM, Hatke W (1997) *Electret properties of cycloolefin copolymers*. *Electrical insulation and dielectric phenomena*. In: Annual report conference on electrical insulation dielectric phenomena, IEEE Service Center, Piscataway, pp 467–470
- Sun Z, Zhang X, Xia Z, Qiu X, Wirges W, Gerhard R, Zeng C, Zhang C, Wang B (2011) *Polarization and piezoelectricity in polymer films with artificial void structure*. *Appl Phys A Mater Sci Process* 105:197–205
- Suzuki Y (2011) *Recent progress in MEMS electret generator for energy harvesting*. *IEEJ Trans Electr Electron Eng* 6:101–111
- Tajitsu Y (2011) *Piezoelectric properties of ferroelectret*. *Ferroelectrics* 415:57–66
- Tsutsumino T, Suzuki Y, Kasagi N, Tsurumi Y (2005) *High-performance polymer electret for micro seismic generator*. In: *Proceedings of powerMEMS 2005*, Tokyo, pp 9–12
- Tsutsumino T, Suzuki Y, Kasagi N, Sakane Y (2006) *Seismic power generator using high-performance polymer electret*. In: *Proceedings of international conference MEMS'06*, Istanbul, pp 98–101
- Veronina O, Wegener M, Wirges W, Gerhard R, Zirkel L, Münstedt H (2008) *Physical foaming of fluorinated ethylene-propylene (FEP) copolymers in supercritical carbon dioxide: single-film fluoropolymer piezoelectrets*. *Appl Phys A Mater Sci Process* 90:615–618
- von Seggern H, Zhukov S, Fedosov S (2010) *Poling dynamics and thermal stability of FEP/ePTFE/FEP sandwiches*. *IEEE Trans Dielectr Electr Insul* 17(4):1056–1065
- von Seggern H, Zhukov S, Fedosov S (2011) *Importance of geometry and breakdown field on the piezoelectric d_{33} coefficient of corona charged ferroelectret sandwiches*. *IEEE Trans Dielectr Electr Insul* 18(1):49–56
- Wang J, Hsu T, Yeh C, Tsai J, Su Y (2012) *Piezoelectric polydimethylsiloxane films for MEMS transducers*. *J Micromech Microeng* 22:015013
- Wang J, Tsai J, Su Y (2013) *Piezoelectric rubber films for highly sensitive impact measurement*. *J Micromech Microeng* 23:075009
- Wegener M, Wirges W, Fohlmeister J, Tiersch B, Gerhard-Multhaupt R (2004) *Two-step inflation of cellular polypropylene films: void-thickness increase and enhanced electromechanical properties*. *J Phys D Appl Phys* 37(4):623–627
- Wegener M, Wirges W, Gerhard-Multhaupt R (2005a) *Piezoelectric polyethylene terephthalate (PETP) foams – specifically designed and prepared ferroelectret films*. *Adv Eng Mater* 7:1128–1131
- Wegener M, Wirges W, Dietrich JP, Gerhard-Multhaupt R (2005b) *Polyethylene terephthalate (PETP) foams as ferroelectrets*. In: *Proceedings of 12th international symposium electrets (ISE 12)*, IEEE Service Center, Piscataway, pp 28–30
- Wegener M, Paajanen M, Voronina O, Schulze R, Wirges W, Gerhard-Multhaupt R (2005c) *Voided cyclo-olefin polymer films: ferroelectrets with high thermal stability*. In: *Proceedings of 12th international symposium electrets*, IEEE Service Center, Piscataway, pp 47–50
- Wirges W, Wegener M, Voronina O, Zirkel L, Gerhard-Multhaupt R (2007) *Optimized preparation of elastically soft, highly piezoelectric cellular ferroelectrets from nonvoided poly(ethylene terephthalate) films*. *Adv Funct Mater* 17:324–329
- Xia Z, Gerhard-Multhaupt R, Künstler W, Wedel A, Dan R (1999) *High surface-charge stability of porous polytetrafluoroethylene electret films at room and elevated temperatures*. *J Phys D Appl Phys* 32:L83
- Yang ZH, Wang J, Zhang JW (2012) *Research and development of micro electret power generators*. *SCIENCE CHINA Technol Sci* 55(3):581–587
- Zhang X, Hillenbrand J, Sessler GM (2004) *Piezoelectric d_{33} coefficient of cellular polypropylene subjected to expansion by pressure treatment*. *Appl Phys Lett* 85:1226–1228
- Zhang X, Hillenbrand J, Sessler GM (2006) *Thermally stable fluorocarbon ferroelectrets with high piezoelectric coefficient*. *Appl Phys A Mater Sci Process* 84:139–142

- Zhang X, Hillenbrand J, Sessler GM (2007) Ferroelectrets with improved thermal stability made from fused fluorocarbon layers. *J Appl Phys* 101:054114
- Zhang X, Wang X, Cao G, Pan D, Xia Z (2009) Polytetrafluoroethylene piezoelectrets prepared by sintering process. *Appl Phys A Mater Sci Process* 97:859–862
- Zhang X, Cao G, Sun Z, Xia Z (2010) Fabrication of fluoropolymer piezoelectrets by using rigid template: structure and thermal stability. *J Appl Phys* 108:064113
- Zhang X, Hillenbrand J, Sessler GM, Haberzettl S, Lou K (2012) Fluoroethylenepropylene ferroelectrets with patterned microstructure and high, thermally stable piezoelectricity. *Appl Phys A Mater Sci Process* 107:621–629
- Zhang X, Sessler GM, Wang Y (2014a) Fluoroethylenepropylene ferroelectret films with cross-tunnel structure for piezoelectric transducers and micro energy harvesters. *J Appl Phys* 116:074109
- Zhang X, Zhang X, Sessler GM, Gong X (2014b) Quasi-static and dynamic piezoelectric responses of layered polytetrafluoroethylene ferroelectrets. *J Phys D Appl Phys* 47:015501
- Zhukov S, von Seggern H (2007a) Breakdown-induced light emission and poling dynamics of porous fluoropolymers. *J Appl Phys* 101:084106
- Zhukov S, von Seggern H (2007b) Polarization hysteresis and piezoelectricity in open-porous fluoropolymer sandwiches. *J Appl Phys* 102:044109
- Zhukov S, Fedosov S, von Seggern H (2011) Piezoelectrets from sandwiched porous polytetrafluoroethylene (ePTFE) films: influence of porosity and geometry on charging properties. *J Phys D Appl Phys* 44(10):105501

Michael Wübbenhorst, Xiaoqing Zhang, and Tristan Putzeys

Contents

1	Introduction	592
2	Mechanical Characterization	593
2.1	Stress–Strain Curves (Without/With Electrodes)	594
3	Linear and Nonlinear Dielectric Measurements	597
3.1	Low-Field Dielectric Spectroscopy	597
3.2	Nonlinear Dielectric Spectroscopy at High AC Fields	599
3.3	Hysteresis Curves (Current and Voltage Modes)	601
3.4	Electrical Breakdown Measurements	603
4	Electromechanical Characterization	604
4.1	Measurements by Means of Direct Piezoelectric Effect	604
4.2	Measurements by Means of Inverse Piezoelectric Effect	606
4.3	Dielectric Resonance Spectroscopy: An All-Electrical Method	608
4.4	Thermal Stability of Piezoelectricity in Ferroelectrets	610
4.5	Applied Pressure Dependence of Piezoelectric d_{33} Coefficient	610
4.6	Frequency Dependence of Piezoelectric d_{33} Coefficient	611
5	One-, Two-, and Three-Dimensional Probing of Charge and Dipole Profiles	611
5.1	Thermal Methods for Probing 1D Charge and Polarization Distributions	612
5.2	Depth Profiling (1D) of Charge and Polarization Using Acoustical Waves	615
5.3	Piezo- and Pyroelectric Microscopy	617
6	Conclusion	619
	References	621

M. Wübbenhorst (✉) • T. Putzeys

Department of Physics and Astronomy, Soft Matter and Biophysics Section, KU Leuven, Leuven, Belgium

e-mail: wubbenhorst@fys.kuleuven.be; tristan.putzeys@fys.kuleuven.be

X. Zhang

School of Physics Science and Engineering, Tongji University, Shanghai, China

e-mail: x.zhang@tongji.edu.cn

Abstract

The successful development and optimization of EAPs requires quick, reliable, and precise characterization techniques for all relevant materials and device properties. This chapter gives a concise overview about specific techniques for the characterization of mechanical, electrical, and electromechanical properties of polymeric electrets with some emphasis on ferroelectrets.

Keywords

Bias-induced reverse piezoelectric response • Broadband dielectric spectroscopy (BDS) • Dielectric permittivity spectrum • Dielectric resonance spectroscopy • Elastic modulus • Ferroelectrets • Electrical breakdown • Acoustic method • Characterization • Dynamic coefficient • Interferometric method • Pressure and frequency dependence of piezoelectric coefficient • Profilometer • Quasistatic piezoelectric coefficient • Stress–strain curves • Thermal stability of piezoelectricity • Ferroelectric hysteresis • Impedance spectroscopy • Laser-induced pressure pulse • Layer-structure model of ferroelectret • Low-field dielectric spectroscopy • Nonlinear dielectric spectroscopy • Piezoelectrically generated pressure step technique (PPS) • Pyroelectric current spectrum • Pyroelectric microscopy • Pyroelectricity • Quasistatic method • Scale transform method • Scanning pyroelectric microscopy (SPEM) • Thermal step technique • Thermal wave technique • Thermal-pulse method • Weibull distribution

1 Introduction

The importance of polymer electrets for their application as EAPs generally relies on their piezoelectric properties, which originate from the existence of a permanent polarization. Traditionally, polymer electrets have been classified according to the molecular origin of this polarization, which might be *homocharges*, i.e., deeply trapped positive or negative “real” charges, or virtual charges as the result of a spontaneous dipolar polarization, also called *heterocharges* (Sessler 1987). While homocharge electrets are prepared by suitable charge injection procedures (corona poling, electron beam poling, etc.), heterocharge electrets rely on the spontaneous (ferroelectrics) or electrical field-induced formation of a polar arrangement of molecular dipoles.

In this context, *ferroelectrets* actually represent a third class of piezoelectric polymers in the sense that these cellular materials share features of charge electrets (real charges) with those of ferroelectric polymers (hysteresis-type *ED* characteristics) (Bauer et al. 2004; Lekkala et al. 1996). Moreover, ferroelectrets are characterized by extremely high piezoelectric d_{33} coefficients as well as an extreme anisotropy in their mechanical and electromechanical properties, which partially require specific characterization techniques (Dansachmüller et al. 2005).

This chapter tries to give a concise overview about representative techniques for the characterization of mechanical, electrical, and electromechanical properties of

polymeric electrets with emphasis on ferroelectric polymers and cellular electrets (*ferroelectrets*).

2 Mechanical Characterization

Figure 1 shows the schematic illustration of the formation of the ferroelectret from polymer foam and the scanning electron micrograph of the cross section of a cellular polypropylene (PP) ferroelectret film (Neugschwandtner et al. 2000). Since the typical shape of voids in ferroelectrets is flat (e.g., cellular PP ferroelectrets have lateral dimensions 10–100 μm and vertical dimensions of a few microns as shown in Fig. 1b), the Young's modulus in thickness direction is much smaller (~ 1 MPa) than that in lateral direction (~ 1 GPa). Due to the highly anisotropic nature of the microstructure and the properties of the ferroelectrets, the characterization of their mechanical and electromechanical properties requires specific techniques compared

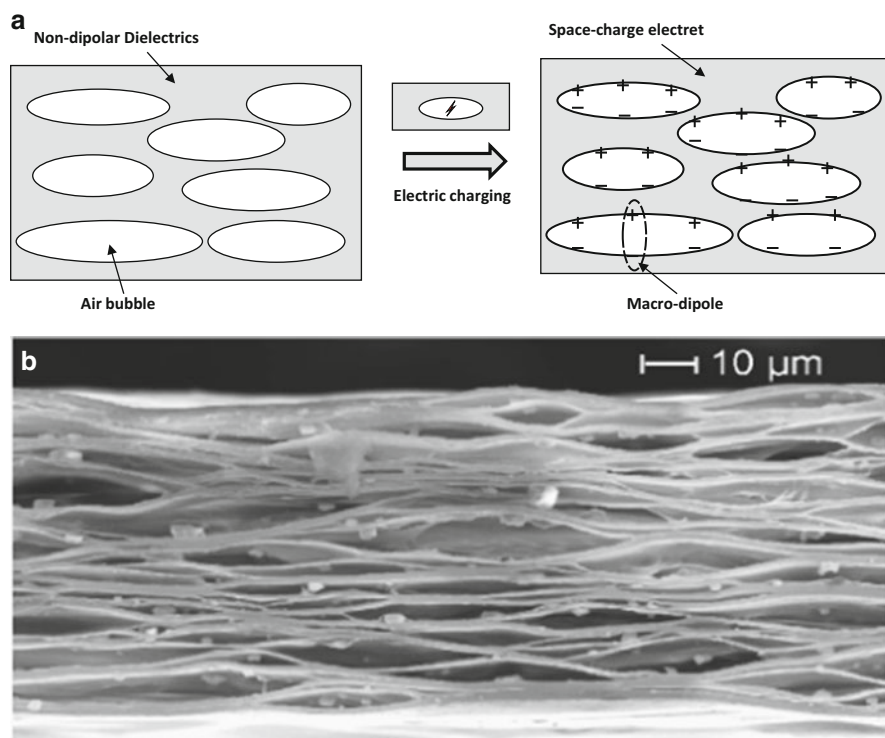
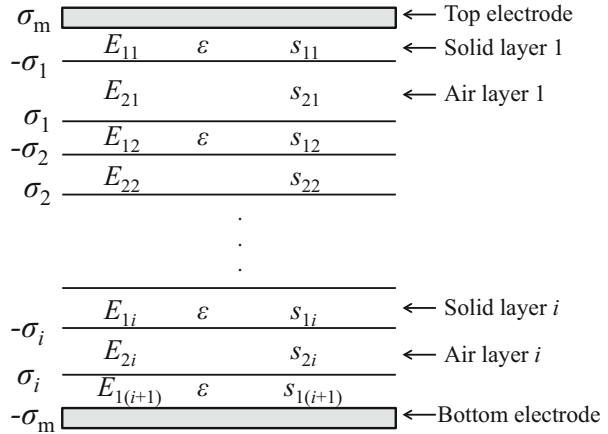


Fig. 1 (a) Schematic formation of ferroelectrets; (b) scanning electron micrograph of the cross section of a charged piezoelectric polymer foam (Reprinted from Neugschwandtner et al. (2000) with permission)

Fig. 2 Simplified model of ferroelectrets (Reprinted from Hillenbrand and Sessler (2000) with permission)



to other, e.g., ferroelectric polymer electrets. We will thus focus on the mechanical properties of cellular electrets, while the mechanical and electromechanical characterization of polymer electrets will be discussed in Sect. 4. Owing to their extreme mechanical anisotropy, the piezoelectric activity of ferroelectrets is normally characterized by the piezoelectric d_{33} coefficient. According to the layer-structure model of ferroelectret (Fig. 2), the piezoelectric d_{33} coefficient is given by (Paajanen et al. 2000; Sessler and Hillenbrand 1999):

$$d_{33} = \frac{\epsilon_1 s}{Y_3} \frac{s_1 \sum_i s_{2i} \sigma_i}{s_2 (s_1 + \epsilon_1 s_2)^2} \quad (1)$$

where ϵ_1 is relative permittivity of the solid dielectric material; s_1 , s_2 , and $s = s_1 + s_2$ are the solid dielectric layer, gap layer, and total thickness of the film, respectively; s_{2i} is the thickness of the i th air gap layer and $\sum s_{2i} = s_2$; σ_i is the surface charge density of i th layer; and Y_3 is the compressive modulus of the film in the thickness direction.

This theoretical model indicates that charge storage capability, corresponding to σ_i and its thermal stability, is of importance to the piezoelectric activity and thermal stability of the ferroelectrets. Hence, for obtaining thermally stable ferroelectrets, thermally stable space charges in the materials are necessary, while the compressive modulus Y_3 is inversely proportional to the d_{33} value. Therefore, an effective approach to enhance the piezoelectric effect in ferroelectrets is to enhance the charge density σ_i while reducing the Young's modulus Y_3 .

2.1 Stress–Strain Curves (Without/With Electrodes)

As ferroelectrets are a specific type of (voided) polymer material, they can show all the features of a glassy, brittle solid or an elastic rubber depending on the

temperature and time scale of measurement. Ferroelectrets can be described as viscoelastic materials, a generic term which emphasizes their intermediate position between viscous liquid and elastic solids. At low temperatures or high frequencies of measurement, ferroelectrets may be glass-like, while at high temperatures or low frequencies, the same material may be rubberlike. The mechanical properties in ferroelectrets may be characterized by stress–strain curves. However, because ferroelectrets are usually presented film-like with a typical thickness in the range from 40 to 500 μm and the deflection of thickness is very small, the stress–strain curves in the thickness direction for ferroelectrets are difficult to be obtained by using the generally utilized techniques, such as universal testing machine and dynamic mechanical analyzer (DMA), but measured in an indirect way using specific technique as described in the following section (Dansachmüller et al. 2005).

2.1.1 Stress–Strain Curve in Lateral Direction

The stress–strain diagram is used to find the modulus of elasticity in the lateral direction in ferroelectret films. The modulus of elasticity is determined as the slope of the initial portion of the curves. Since the modulus of elasticity depends on the strain, it is customarily found for strains not exceeding 0.5 %. Figure 3 shows the stress–strain curves of laminated fluorocarbon ferroelectret films in lateral direction at various temperatures measured by a DMA instrument (TA Instruments DMA Q800) (Sun et al. 2011).

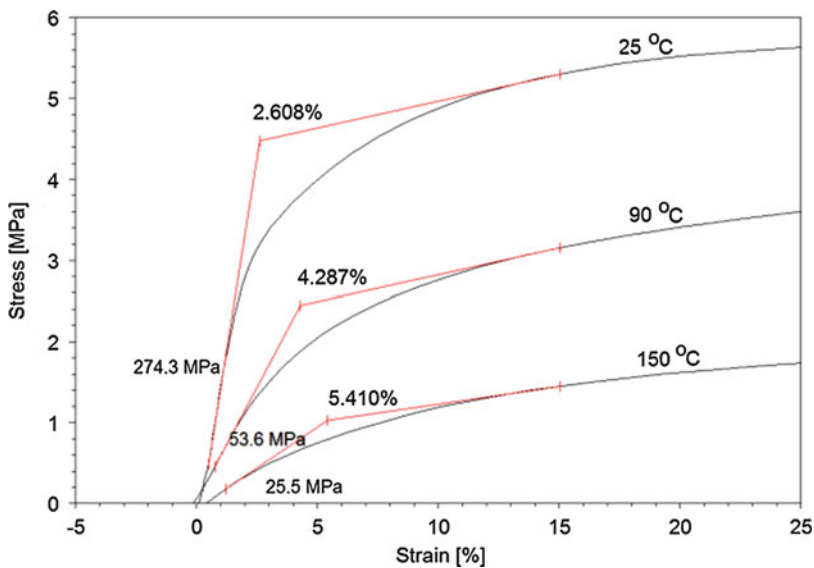


Fig. 3 Stress–strain relations of laminated film systems at various temperatures (Reprinted from Sun et al. (2011) with permission)

2.1.2 Stress–Strain Curve in Longitudinal Direction

During compression of polymeric foams, three characteristic stages of deformation are commonly observed. At low deformations, the polymer foam is in the linear elastic response regime, i.e., the stress increases linearly with deformation and the strain is recoverable. The second phase is characterized by continued deformation at relatively constant stress, known as the stress collapse plateau. And the final phase of deformation is densification where the foam begins to respond as a compacted solid. At this point the cellular structure within the material is collapsed, and further deformation requires compression of the solid foam material (Ouellet et al. 2006). As mentioned above, a specific technique is required to obtain stress–strain curves of ferroelectrets in thickness direction because the thickness in ferroelectrets is normally very thin, corresponding to very small deflections. Dansachmüller et al. developed an experimental technique that allows obtaining the stress–strain curves in ferroelectret films (Dansachmüller et al. 2005). This method may also be used to obtain the stress–strain curve for a polymer foam film without oriented “macro-dipoles.” The schematic of the experimental setup is shown in Fig. 4.

In this technique, the strain of the sample is determined by an indirect way. The stress-dependent capacitance of the sample is measured with an LCR meter. The foam sample is a simple capacitor with guard ring electrodes, and the foam is represented by a series connection of polymer layers with a total thickness s_1 and by an air gap with thickness s_2 . The capacitance of the sample is given by

$$\frac{1}{C(T)} = \frac{s_1}{\epsilon_0 \epsilon A} + \frac{s_2(T)}{\epsilon_0 A}, \quad (2)$$

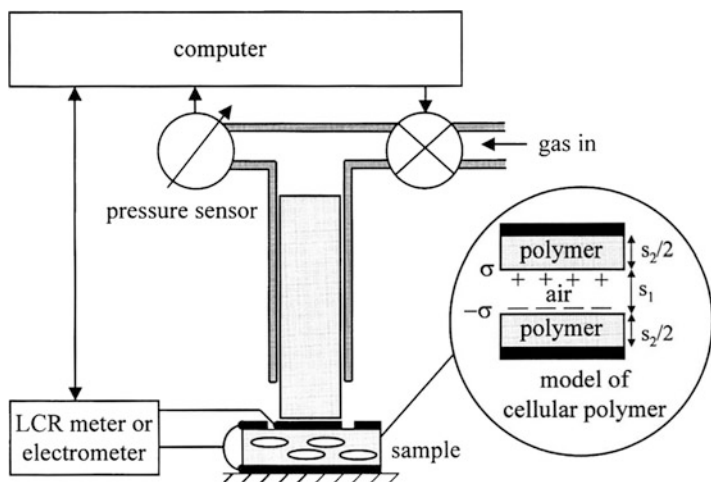


Fig. 4 Experimental setup for measuring the elastic modulus Y and the longitudinal transducer coefficient d_{33} of cellular ferroelectrets with a simple model for the ferroelectret (*inset*) (Reprinted from Dansachmüller et al. (2005) with permission)

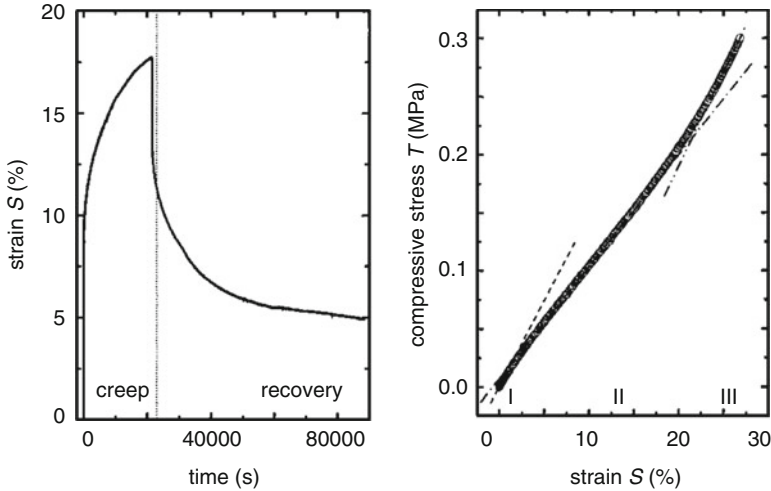


Fig. 5 (a) Time-dependent creep and recovery of cellular polypropylene with a density of 330 kg/m^3 ; (b) strain versus stress for cellular polypropylene with three characteristic nonlinearity regions (Reprinted from Dansachmüller et al. (2005) with permission)

where ε_0 is the permittivity of vacuum and ε the dielectric constant of the polymer and A the electrode area under mechanical stress. In Eq. 2 it is assumed that the applied compressive stress T solely results in a reduction of the void size. This assumption is self-consistent as the foam is much softer than bulk polymer, and the voids are more easily compressed than the surrounding polymer. Under this assumption, the strain $\Delta S = \frac{s_2\{T\} - s_2\{T=0\}}{s}$ of the polymer is calculated from the stress-dependent capacitance according to

$$\Delta S = \frac{\varepsilon_0 A}{s} \left\{ \frac{1}{C(T)} - \frac{1}{C(T=0)} \right\}, \quad (3)$$

where $s = s_1 + s_2$ is the initial thickness of the foam.

Figure 5 shows stress–strain curve of a cellular PP film determined by the method mentioned above. The strain of the foam displays a quasi-instantaneous elastic response with a strain $\sim 5\%$ (Dansachmüller et al. 2005).

3 Linear and Nonlinear Dielectric Measurements

3.1 Low-Field Dielectric Spectroscopy

Piezoelectric and electrostrictive polymers are generally good insulators, the electrical properties of which can be described by the dielectric permittivity ε_r . Owing to structural relaxation processes and eventually electrical conduction, the permittivity

might be time/frequency dependent and is hence described as a complex function of the angular frequency ω :

$$\varepsilon_r^*(\omega) = \varepsilon_r'(\omega) - j\varepsilon_r''(\omega) \quad (4)$$

Here, the real part is directly related to the electrical energy density w_e that can be stored reversibly in a capacitor according to

$$w_e = \varepsilon_0 \varepsilon_r E^2 / 2 \quad (5)$$

with E being the electrical field strength.

In contrast, the imaginary part ε_r'' accounts for the amount of dissipated electrical energy in the dielectric either due to (Ohmic) conduction or “molecular friction” related to molecular or charge relaxation processes. Dielectric losses thus lead to Joule’s heating and are undesired phenomena for EAP applications.

Dielectric properties can be measured by any instrument that provides the frequency-dependent impedance Z^* or complex capacitance C^* in the relevant frequency range. *Broadband dielectric spectroscopy* (BDS) is nowadays able to cover a frequency range from 10^{-5} Hz up to 10^{10} Hz with affordable instrumentation, typically combining frequency response analyzers (FRA), bridges, and network analyzers at the radio frequencies. A comprehensive overview about dielectric techniques, instrumentation, and modeling is given in Kremer and Schönhals (2002).

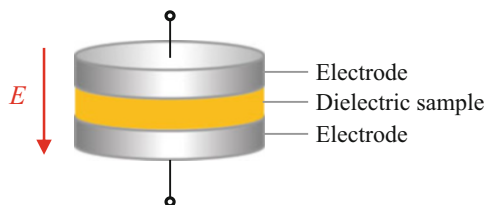
At low and medium frequencies ($f < 1\text{GHz}$), dielectric spectra are commonly taken in the parallel-plate geometry (cf. Fig. 6) that consists of two flat electrodes of the area A that sandwich a sheet or film of the material under investigation with thickness d . From the complex capacitance, the dielectric permittivity spectrum can then be derived by

$$C^*(\omega) = \varepsilon_0 \frac{\varepsilon^*(\omega)A}{d} \quad (6)$$

A typical example for the frequency- and temperature-dependent dielectric properties of a piezoelectric polymer is given in Fig. 7 that displays the α -relaxation, related the dynamic glass transition, of a polyvinylidene fluoride (PVDF) film along with an upswing of the dielectric loss at low frequencies due to electrical conduction.

For the analysis of dielectric spectra, various strategies are available, which yield quantitative parameters like the electrical conductivity σ , the strength $\Delta\varepsilon$ and relaxation time τ of possible relaxation processes, the high frequency permittivity ε_∞ , etc.

Fig. 6 Schematic sample arrangement in parallel-plate geometry for measurements of the dielectric spectrum



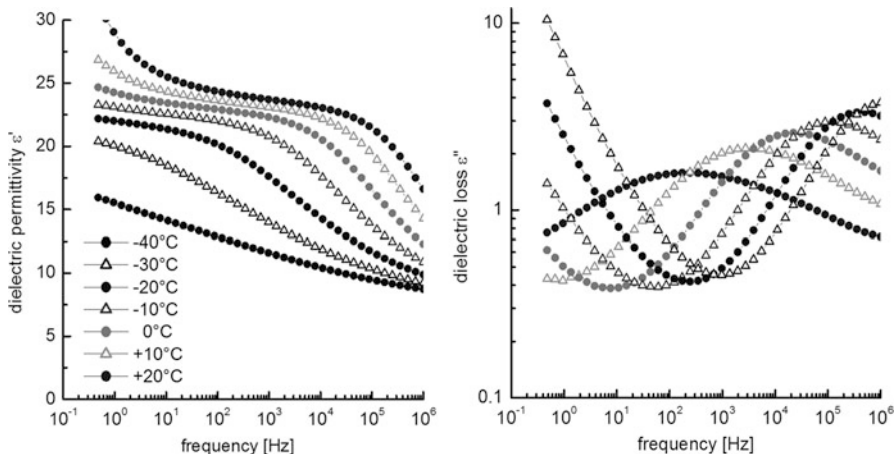


Fig. 7 Dielectric permittivity spectrum $\epsilon'(\omega)$ and dielectric loss spectra $\epsilon''(\omega)$ of a 1 μm thick film of PVDF at selected temperatures

A common approach to model the dielectric response, typically used for *impedance spectroscopy*, is based on equivalent circuits consisting of a number of resistors, capacitors, constant phase elements, and others. Alternatively, the dielectric response can be modeled by a set of model relaxation functions like the Debye function or more generalized (semiempirical) Cole–Cole, Cole–Davidson, or Dissado–Hill equation (Kremer and Schönhalz 2002).

For molecular relaxations like the primary (α)-relaxation in amorphous polymers, which exhibit an asymmetric broadening, i.e., an asymmetric underlying distribution in relaxation times, the most versatile Havriliak–Negami (HN) (Havriliak and Negami 1967) function is typically applied. A set of (additive) HN functions together with a term accounting for electrical conductivity (cf. Eq. 7) is the typical choice to fit feature-rich dielectric loss spectra $\epsilon''(\omega)$ like the example given in Fig. 7:

$$\epsilon'' = - \sum_{k=1}^n \text{Im} \left\{ \frac{\Delta\epsilon_k}{(1 + (i\omega\tau_k)^{a_k})^{b_k}} \right\} + \frac{\sigma}{\epsilon_0\omega} \quad (7)$$

This procedure yields quantitative relaxation parameters including the mean relaxation time τ and relaxation strength $\Delta\epsilon$. Other parameters in Eq. 7 are the vacuum permittivity, ϵ_0 , and the dc conductivity σ , while a and b describe the symmetric and asymmetric broadening of the relaxation time distribution function.

3.2 Nonlinear Dielectric Spectroscopy at High AC Fields

Common dielectric spectroscopy assumes linear response between the applied, time-dependent electric field $E(\omega t)$ and the resulting electrical displacement $D(\omega t + \delta)$, a condition that is fulfilled for weak fields, typically far below 1 V/ μm . At

substantially higher field strengths, nonlinear dielectric effects might occur for different reasons:

- (a) Saturation effects in the orientation polarizability when the argument of the Langevin function $\mu E/kT$ is no longer far below unity.
- (b) Collective switching of dipoles in case of ferroelectric polymers.
- (c) Nonlinear charge transport such as space-charge-limited currents or internal breakdown effects (ferroelectrets).
- (d) Field-induced changes of the permittivity (electrostriction) and capacity changes due to electromechanical effects like inverse piezoelectricity. Though field-induced dimensional changes not necessarily affect the (intrinsic) permittivity, they contribute to a nonlinear current response.

For a nonlinear dielectric, D can be expanded in powers of E ,

$$D = P_s + \varepsilon_0 \varepsilon_1 E + \varepsilon_0 \varepsilon_2 E^2 + \varepsilon_0 \varepsilon_3 E^3 + \dots \quad (8)$$

with P_s being the zero-field (spontaneous) polarization and ε_1 denoting the linear dielectric constant. Applying a sinusoidal excitation field

$$E(t) = E_0 \cos \omega t \quad (9)$$

with the amplitude E_0 , a general dielectric response containing components of the fundamental frequency together with higher harmonics is observed

$$D(t) = D_0 + D_1 \cos \omega t + D_2 \cos 2\omega t + D_3 \cos 3\omega t + \dots, \quad (10)$$

which can be measured through a periodical, non-sinusoidal current

$$j(t) = \frac{d}{dt} D(t) = \sum_{l=0}^{\infty} (j_l' \cos l\omega t + j_l'' \sin l\omega t). \quad (11)$$

The nonlinear permittivities ε_n can then be computed from a sum of Fourier coefficients; however, ε_n can also be obtained using the approximation

$$\varepsilon_0 \varepsilon_n \approx \frac{-1}{\omega_0} \frac{2^{n-1}}{n E_0^n} j_n'' \quad (12)$$

provided an appropriate excitation amplitude is chosen (Heiler and Ploss 1994).

The above technique has successfully been applied to the ferroelectric copolymer P(VDF-TrFE) by Heiler and Ploss (1994), who studied the linear permittivity ε_1 along with the second- and third-order permittivities ε_2 and ε_3 for poled and unpoled samples (cf. Fig. 8). While ε_1 reveals the ferroelectric to paraelectric transition including the typical Curie–Weiss behavior for $T > T_C$, the second-order permittivity appears to be sensitive to the state of poling. Combining ε_1 and ε_3 gives even

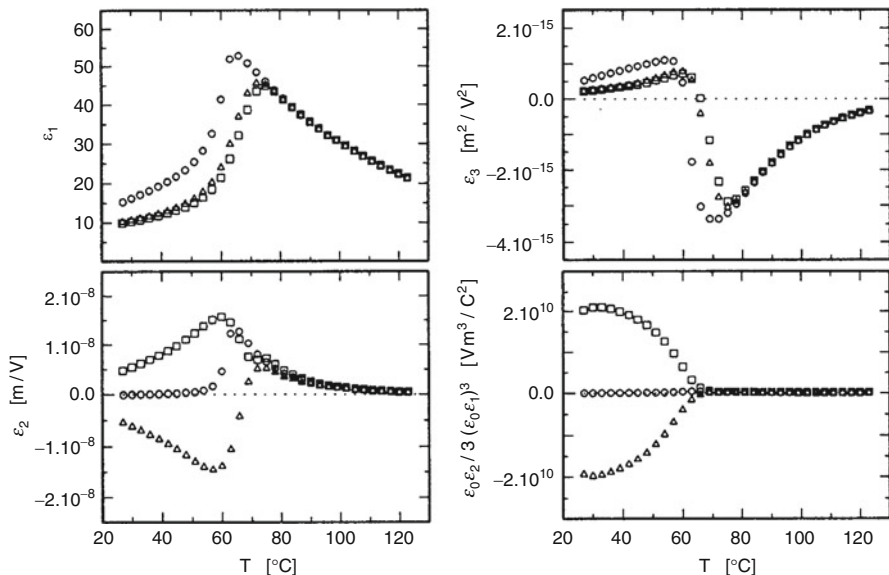


Fig. 8 First-, second-, and third-order permittivity of 56/44 mol-% P(VDF-TrFE) as a function of temperature. The nonlinearities were measured after poling the sample with $E_{pol} = 130 \text{ V}/\mu\text{m}$ (\square), after thermal depolarization (\circ), and after poling with $E_{pol} = -130 \text{ V}/\text{mm}$ (Δ). *Bottom right*: the remnant polarization reconstructed from the first- and second-order permittivity (Reprinted with permission from Heiler and Ploss (1994))

access to the remnant polarization according to Eq. 13 with γ being a Landau parameter:

$$\epsilon_0 \epsilon_2 / 3 (\epsilon_0 \epsilon_1)^3 \approx -\gamma P_r. \tag{13}$$

3.3 Hysteresis Curves (Current and Voltage Modes)

Apart from nonlinearities in their $D(E)$ characteristics, the dielectric displacement D of ferroelectric materials also depends on the electric field history, a phenomenon known as ferroelectric hysteresis. The common approach to measure $D(E)$ or $P(E)$ hysteresis curves utilizes the Sawyer–Tower circuit (Sawyer and Tower 1930) (cf. Fig. 9a) that operates in the voltage–voltage mode.

Here, the capacity C_x is the ferroelectric sample under investigation, and C_1 is a reference capacitor of a known capacity that is constant and independent of the applied voltage. The circuit is supplied with a periodical voltage U_{ac} , which might be sinusoidal, triangular (Furukawa et al. 1980), or of other shape. To display the $D(E)$ curves at the oscilloscope, the driving voltage ($\sim E$) is fed to the x-channel, while the reference capacitor builds up a voltage that is proportional to the dielectric displacement D with $D \approx P$ for materials with a high spontaneous polarization. An example

Fig. 9 (a) Principle of a Sawyer–Tower circuit in voltage–voltage mode. (b) Sample arrangement for current–voltage hysteresis measurements (Reprinted from Qiu et al. (2013) with permission)

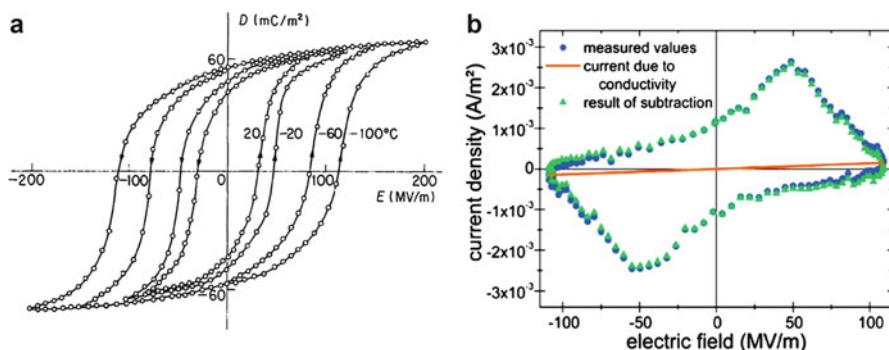
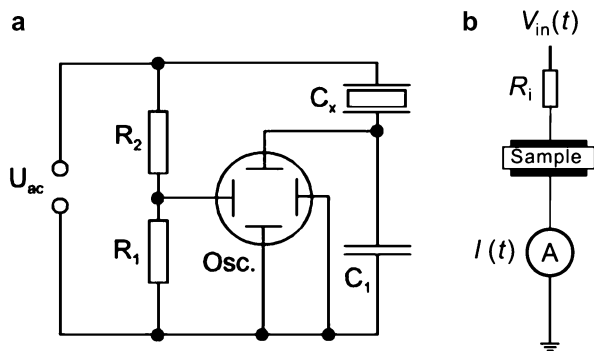


Fig. 10 (a) D versus E hysteresis loops for an as-prepared VDF-TrFE(55:45) copolymer at different temperatures measured under a 1/300 Hz triangular electric field (Reprinted from (Furukawa et al. 1980) with permission). (b) Measured and calculated current density–electric field dependence on PVDF during application of a bipolar electric field. For details see Wegener (2008) (Reprinted with permission)

is displayed in Fig. 10a showing the $D(E)$ curve for P(VDF-TrFE) (Takeo Furukawa et al. 1980).

Alternatively, hysteresis measurements can be performed in current–voltage mode (see Fig. 9b), which yield a current that might be separated into the following three components: (Qiu et al. 2013)

$$i = i_{cap} + i_p + i_{cond} = C_s \frac{dV_s}{dt} + A_s \frac{dP_s}{dt} + \frac{V_s}{R_s} \quad (14)$$

Here, A_s , R_s , and C_s denote the area, the electrical resistance, and the capacitance of the sample. By considering the capacitive component and, in case of highly conductive samples, the conduction current, the polarization current can be isolated to construct the true $i_p(E)$ curve. A representative example showing the current–voltage hysteresis curve obtained for PVDF is displayed in Fig. 10b.

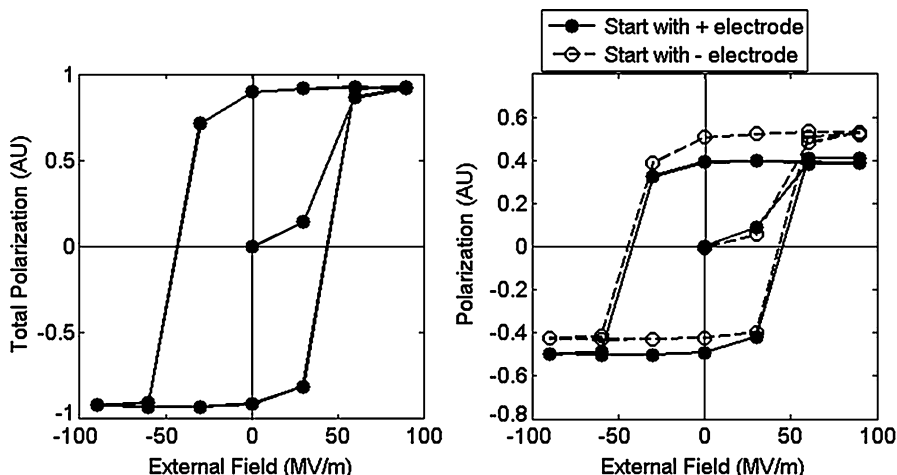


Fig. 11 Spatially resolved ferroelectric hysteresis curves on a thin film of P(VDF-TrFE) obtained by averaging over the partial or complete polarization distribution in thickness direction, measured via the pyroelectric effect using LIMM (cf. Sect. 5.1). Integration over the total sample thickness (*left*) results in the symmetric hysteresis curve, while the integration limited to half the sample thickness reveals an asymmetry (Reprinted from Putzeys and Wübbenhorst (2015a))

Finally, it should be mentioned that hysteresis curves $P(E)$ might also be deduced from polarization-related quantities such as the second harmonic activity, piezoelectric coefficients, and the pyroelectric activity. Figure 11 shows an example for a hysteresis curve obtained via spatially resolved pyroelectric experiments (Putzeys and Wübbenhorst 2015a).

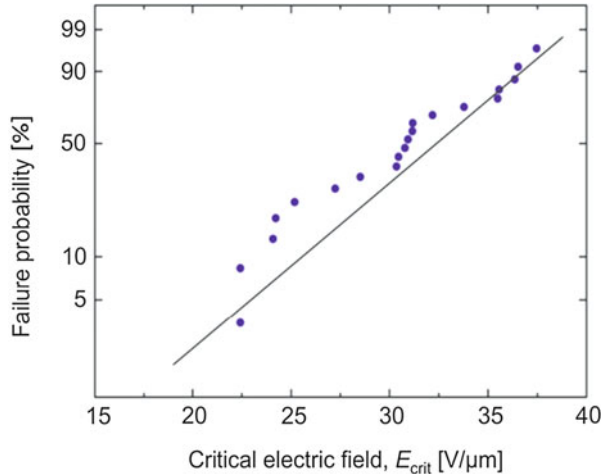
3.4 Electrical Breakdown Measurements

The application of high fields to charge or polarize polymer electrets inherently involves the risk of sample damage due to electrical breakdown. While local air breakdown in voids is part of the poling process, energy-rich discharges over large areas of ferroelectric polymers will lead to sample failure.

The probability for electrical breakdown depends on the dielectric strength E_{crit} , which in the first place depends on the specific material and reaches values between 10 and 170 MV/m for polymer insulators. The actual value might also depend on the sample thickness, the purity and homogeneity of the material, and the limiting current used for testing/poling.

To measure the dielectric strength, a flat specimen is exposed to an increasing electrical field till a progressive current increase indicates when the critical field strength has been reached. Since electrical breakdown is a statistical event, multiple experiments must be performed and evaluated, typically using the Weibull distribution (Weibull 1951). Figure 12 presents an example.

Fig. 12 Example data analysis using a Weibull plot (Reprinted from Carpi et al. (2015) with permission)



For a description of dielectric breakdown measurements and interpretation, although for soft elastomers, we refer to the work by Carpi et al. (2015).

4 Electromechanical Characterization

Because of the highly anisotropic nature of the microstructure and oriented “macro-dipoles” along the thickness direction in films, the piezoelectric d_{33} coefficient in ferroelectrets is normally two orders of magnitude larger than other piezoelectric coefficients, such as d_{31} and d_{32} . Therefore, d_{33} value is the most important parameter for characterization of piezoelectric effect in ferroelectrets. Table 1 lists some commonly used techniques in literature for measuring piezoelectric d_{33} coefficients in ferroelectrets. The d_{33} value is given by

$$d_{33} = \frac{\Delta\sigma}{\Delta P} = \frac{\Delta S}{\Delta E}, \quad (15)$$

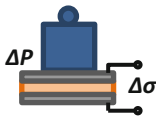
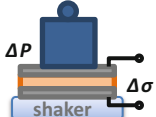
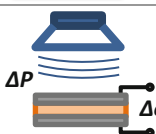
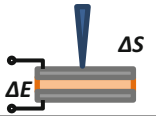
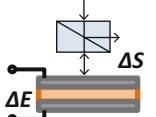
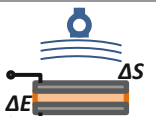
where $\Delta\sigma$ is the charge density, ΔP the applied stress, ΔS the strain, and ΔE the applied electric field.

4.1 Measurements by Means of Direct Piezoelectric Effect

4.1.1 Quasistatic Piezoelectric d_{33} Coefficient

Quasistatic piezoelectric d_{33} coefficient in ferroelectrets may be determined by using the direct piezoelectric effect. In this technique, a weight is manually or mechanically applied to or removed from the sample with electrodes, and the generated charge on the electrodes is measured with a charge amplifier or an electrometer (Sessler and Hillenbrand 1999; Gerhard-Multhaupt et al. 2000; Hillenbrand and

Table 1 Measuring methods for piezoelectric d_{33} coefficient in ferroelectrets

	Method	Schematic
Direct effect $d_{33} = \frac{\Delta\sigma}{\Delta P}$	Quasistatic method	
	Dynamic method (shaker excitation)	
	Acoustic and ultrasonic method (acoustic and ultrasonic excitation)	
Inverse effect $d_{33} = \frac{\Delta S}{\Delta E}$	Profilometer microscopy	
	Interferometer	
	Acoustic method (acoustic and ultrasonic wave generation)	

Sessler 2000; Kressmann 2001a; Künstler et al. 2000). The ratio of generated charge density to applied pressure is the quasistatic direct piezoelectric d_{33} coefficient. In order to eliminate contributions from the bending of the sample, a static (bias) force may be useful during the measurement. Since the removal of the weight from the sample is normally better controlled than its application in the manual mode, the weight is firstly applied to the sample for a relatively long time, and then the force is released and the amount of generated charge is measured (Zhang et al. 2010). The application of pressure to the sample during quasistatic measurement can also be achieved by means of pressurized air (Dansachmüller et al. 2005).

4.1.2 Dynamic d_{33} Coefficients Using Shaker

For the determination of dynamic d_{33} coefficient by direct piezoelectric effect, the sample and a mass m placed on it are accelerated sinusoidally by a shaker (Hillenbrand and Sessler 2004; Kressmann 2001a). Thus, the sample is loaded with two pressures, namely, the static force mg and the dynamic force ma , where g is the acceleration due to the gravity of the earth and a the dynamic acceleration. The dynamic acceleration can be measured with an accelerometer, which allows one

to determine the dynamic forces. In addition, as the charge generated by the piezoelectric film is measured, the d_{33} coefficient may be determined. By controlling the frequency and amplitude of the input signal of the shaker and varying the mass and the area of the sample or adaptor, the d_{33} value can be measured in a wide frequency (e.g., 10 Hz to a few kHz (Hillenbrand and Sessler 2004)) and pressure range.

4.1.3 Acoustic Method

The acoustic method, which also utilizes the direct piezoelectric effect, is a more indirect procedure for determining the d_{33} coefficient. It is based on a measurement of the sensitivity of a microphone built with the ferroelectret film in a free field (Kressmann 2001b; Xiaoqing Zhang et al. 2014; Zhang et al. 2012). An active dynamic loudspeaker is used as sound source and generates sound pressure in a broadband frequency range. If an ultrasonic sound source is used, the piezoelectric d_{33} coefficient in ultrasonic frequency range can also be determined. In response to the sound field generated by the loudspeaker, the microphone produces an output voltage V , which is recorded by an audio analyzer. To determine the reference free-field sound pressure p_{ff} at the location of the ferroelectret microphone, this microphone may be replaced by a calibrated microphone. Thus, it is possible to determine the free-field sensitivity $M_{ff} = V/p_{ff}$ of the ferroelectret microphone.

To calculate the dynamic piezoelectric d_{33} coefficient from the microphone sensitivity, the pressure sensitivity of the ferroelectret microphones is required. This sensitivity is defined as $M_p = V/p$, where p is the actual sound pressure p in front of the microphone after it is positioned in the sound field. This sound pressure differs at higher frequencies from the free-field value p_{ff} , due to diffraction effects. The value of p can be determined from p_{ff} by means of the free-field correction factor (Xiaoqing Zhang et al. 2014; Zhang et al. 2012). From such evaluations M_p was obtained, and the dynamic piezoelectric d_{33} coefficient of the ferroelectret is obtained by means of (Zhang et al. 2007)

$$d_{33} = M_p \cdot C_F / A_F \quad (16)$$

where C_F is the capacitance and A_F the area of the ferroelectret sample.

Since measurements are made such that the same sound pressure acts on all exposed points of the ferroelectret film, this evaluation of d_{33} yields an average value over the microphone area.

4.2 Measurements by Means of Inverse Piezoelectric Effect

4.2.1 Profilometer Microscopy

At low frequencies, for example, 10–30 Hz, a profilometer can be used to detect the surface vibration of the ferroelectret sample excited by a sinusoidal voltage

(Hillenbrand and Sessler 2000). Profile scans may be made electromechanically by moving the sample beneath a diamond-tipped stylus with rides over the surface of the sample. The relevant quantity, i.e., the amplitude of the periodic thickness change as function of the surface position, is obtained by applying a digital band-pass filter to the raw data. The ratio of thickness change to applied voltage yields the inverse piezoelectric d_{33} coefficient. A locally varying piezoelectric d_{33} coefficient in ferroelectrets can be detected by this method.

4.2.2 Interferometric Method

In this method, the sample is excited by applying an ac-voltage to its electrodes, the thickness variation is measured interferometrically over a relatively small area, and thus d_{33} can be calculated (Hillenbrand and Sessler 2000). Typically, the diameter of the laser spot is smaller than 100 μm . The value of d_{33} so determined thus corresponds to this area and one can determine local variations of d_{33} . The frequency range of these measurements can extend from 1 Hz to 400 kHz.

4.2.3 Acoustic Method

By means of the inverse piezoelectric effect, the ferroelectret samples can also be used as sound sources. Measurement of the sound pressure on axis in the far field yields the inverse d_{33} coefficient. In this method, the ferroelectret sample, driven sinusoidally with an AC voltage, is used as sound sources and can be modeled as a circular piston mounted in an infinite baffle (Kressmann 2001b; Sessler and Hillenbrand 2013). The on-axis sound pressure $p(r)$ generated by a circular piston with radius R and area πR^2 , mounted in an infinite baffle, at a distance r is given by

$$p(r) = \frac{1}{2r} \rho_0 R^2 \omega^2 d_{33} V, \quad (17)$$

where ρ_0 is the density of the medium, ω the angular frequency, and V the applied AC voltage. Therefore, the inverse piezoelectric d_{33} coefficient in audio and ultrasonic frequency range can be obtained.

Owing to the specific cavity microstructure and relatively rough surface of ferroelectrets, the piezoelectric d_{33} coefficients are locally dependent and the methods mentioned above are expected to measure different d_{33} coefficients. Therefore, one should be careful to compare the d_{33} values obtained in different methods. The quasistatic method primarily measures the d_{33} values of the surface protrusions. Therefore, quasistatic method yields the largest values as the protrusions are the most piezoelectric sensitive areas of the sample (e.g., fluoroethylenepropylene (FEP) films in Zhang et al. (2012)), but the smallest values in the opposite case (e.g., FEP/porous polytetrafluoroethylene (PTFE) films in Lou et al. (2012)). The profilometer and interferometric methods measure the d_{33} values at discrete spots with the capability of resolving d_{33} over the film surface. And the acoustic method provides an average value over the entire sample area (Zhang et al. 2007).

4.3 Dielectric Resonance Spectroscopy: An All-Electrical Method

The above experimental methods were devoted to the study of the piezoelectric d_{33} coefficient as this one is the relevant parameter of ferroelectrets. Ferroelectric polymers like PVDF and its copolymers show transversal and longitudinal piezoelectric activity depending on the degree and type of stretching (uniaxial vs. biaxial) causing molecular orientation.

In this section, we will outline a versatile approach—*dielectric resonance spectroscopy*—that allows the reveal of several electrical, mechanical, and electromechanical material parameters from a single experiment. This method, first applied by Neugschwandtner et al. (2000) to ferroelectrets and extensively described by Mellinger (2003), solely relies on the nowadays widespread availability of dielectric spectrometers with a frequency range up to the several hundred megahertz (see Sect. 3.1). By virtue of coupling of the electric field excitation with mechanical resonances via the piezoelectric coefficients, mechanical resonances show up in the dielectric spectrum and can be measured with high precision. Depending on the sample geometry, a length extension (LE) and a thickness extension (TE) are usually observed, optionally a width extension (WE) mode for rectangular sample sheets. An example spectrum of a 110 mm P(VDF-TrFE) film showing the fundamental and third harmonics of the TE mode is given in Fig. 13.

Let's consider the dielectric spectrum in Fig. 13 in the vicinity of the TE mode antiresonance frequency. Here the complex capacitance $C^*(\omega)$ is given by Mellinger (2003):

$$C^*(\omega) = \frac{\epsilon_r^S \epsilon_0 A}{h} \frac{1}{1 - k_{33}^2 \frac{\tan(\omega/4f_p)}{\omega/4f_p}} - iC_{\text{loss}} \quad (18)$$

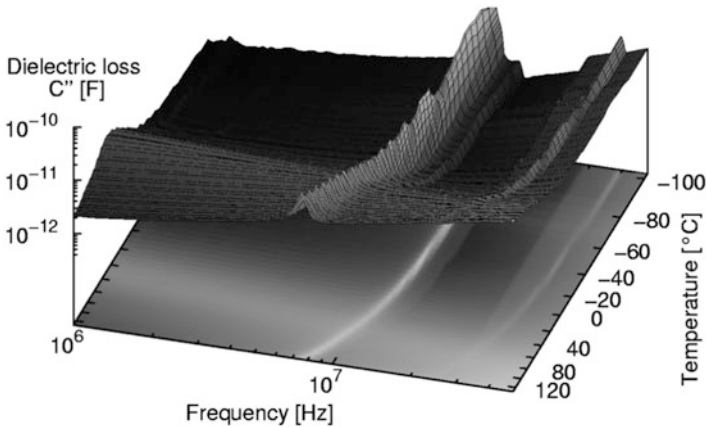


Fig. 13 Imaginary part of the complex capacitance C'' of a 110 mm P(VDF-TrFE) film (Piezotech SA) versus frequency and inverse temperature. Maxima correspond to the fundamental and the third harmonics of the thickness extension mode (Reprinted from Mellinger (2002) with permission)

where ϵ_r^S is the relative permittivity at constant strain, while A and h denote the effective sample area and thickness, respectively. Other quantities in Eq. 18 are k_{33} , the electromechanical coupling factor, and the complex antiresonance frequency of the TE mode f_p . In case of an unconstrained sample, f_p is depending on the complex elastic stiffness c_{33}^D under constant D and the sample density ρ according to

$$f_p = \frac{1}{2h} \sqrt{\frac{c_{33}^D}{\rho}} \quad (19)$$

The electromechanical coupling factor is then given by

$$k_{33}^2 = e_{33}^2 / (\epsilon_r^S \epsilon_0 c_{33}^D), \quad (20)$$

where the piezoelectric stress coefficient e can be obtained from the piezoelectric strain coefficient via the relation $e/c = d$. The term $-iC_{\text{loss}}$ in Eq. 18 relates to intrinsic dielectric losses of the sample, e.g., due to relaxation processes. Fitting the dielectric spectrum to Eq. 18 (cf. Fig. 14) yields the parameters k_{33} and f_p , which subsequently allow the evaluation of c_{33}^D and d_{33} using Eqs. 19 and 20.

Other piezoelectric coefficients, elastic constants, and coupling factors than the one discussed above can be evaluated in an analogue way by considering the corresponding LE and WE resonances. A comprehensive overview is given (Mellinger 2003).

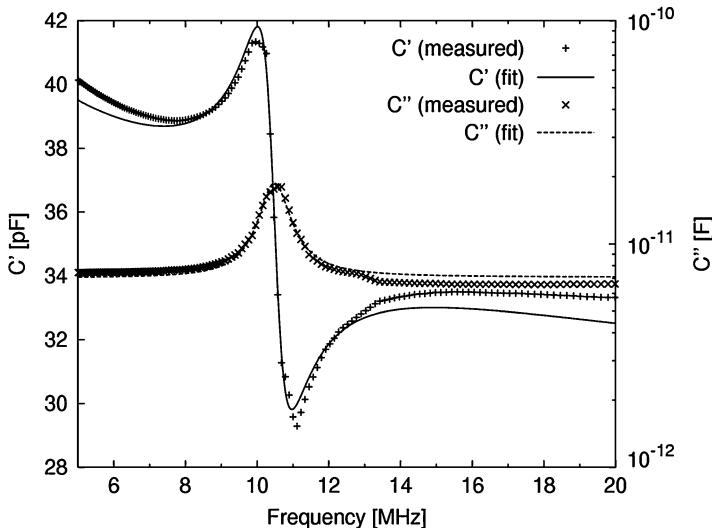


Fig. 14 Thickness-extension resonance of a 110 μm P(VDF-TrFE) film at 40 $^{\circ}\text{C}$. The lines represent the best fit of the experimental data to Eq. 18 (Reprinted from Mellinger (2002) with permission)

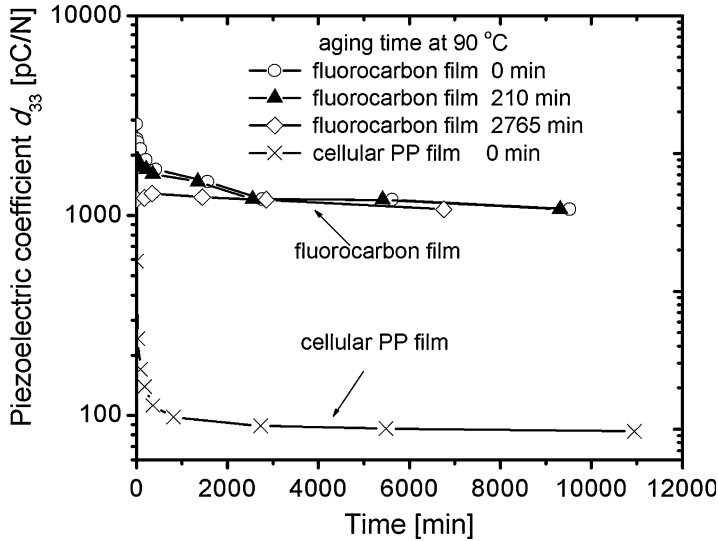


Fig. 15 Isothermal decay of quasistatic d_{33} coefficient for fluorocarbon polymer films, made from compact PTFE and FEP layers by using a mesh-controlled fusion bonding process, and PP films as a function of time at 90 °C (Reprinted from Zhang et al. (2007) with permission)

4.4 Thermal Stability of Piezoelectricity in Ferroelectrets

Thermal stability of piezoelectric d_{33} coefficients in ferroelectrets is of high importance in applications of such materials. Since the piezoelectricity in ferroelectrets originates from oriented “macro-dipoles” consisting of dipolar space charges in polymer matrix and specific void structure in the materials, both the thermal stability of space charges and mechanical properties of the polymer foam influence the thermal stability of piezoelectricity in ferroelectrets. The most common method for characterizing this thermal stability is measuring the isothermal decay of piezoelectric d_{33} coefficient at a given elevated temperature. In this method, the samples are annealed at given temperatures for a well-defined time prior to taking measurements of d_{33} at room temperature. By performing several such experiments, isothermal decay curves that characterize the thermal stability of the samples can be obtained. Figure 15 shows the isothermal decay of d_{33} coefficients for the fluorocarbon and PP ferroelectret films at the annealing temperature of 90 °C (Zhang et al. 2014).

4.5 Applied Pressure Dependence of Piezoelectric d_{33} Coefficient

The pressure dependence of the d_{33} coefficient is significant since it not only reveals the linearity of the piezoelectric effect in the material but also allows one to draw conclusions about the structure of the ferroelectrets (Hillenbrand and Sessler 2004;

Zhang et al. 2007). For the ferroelectrets with an open void, the linearity of d_{33} coefficient is in a small range of applied pressure. An extreme case is described in Hillenbrand and Sessler (2004), where a very large dynamic d_{33} coefficient up to 6000 pC/N was obtained as a conventional film electret microphone, using a permanently charged polyethylene terephthalate film parallel to an air gap, and was looked as a ferroelectret with an open void structure. The d_{33} value is independent of pressure for pressures up to 100 Pa. However, the d_{33} coefficients are generally decreasing proportional to the inverse of the applied pressure at static pressures in excess of a few hundred Pa, assuming that full deflection is already reached at such pressures. For the most extensively studied cellular PP ferroelectrets with closed void structure, the d_{33} coefficient shows a complex behavior of applied pressure dependence because of the nonlinear mechanical properties generated by flat voids and polymer matrix (Dansachmüller et al. 2005; Hillenbrand and Sessler 2004; Kressmann 2001a).

4.6 Frequency Dependence of Piezoelectric d_{33} Coefficient

The frequency dependence of d_{33} over a frequency range of more than eight decades can be obtained by utilizing two methods, namely, a step-response and an interferometric technique (Zhang et al. 2004). The step-response measurement is based on the quasistatic method utilizing the direct piezoelectric effect and employs, for data evaluation, a Fourier analysis of the temporal electrical response to the application of a pressure step. This method yields useful data in the frequency range from 10^{-3} Hz to several Hz. For frequencies from 1 Hz to 300 kHz, an interferometer can be utilized. In addition, acoustic method can also be used to obtain the frequency dependence of d_{33} in audio and ultrasonic ranges.

Figure 16 shows the data obtained from two expanded PP samples and a commercial PP sample, indicating a steady decrease of the d_{33} coefficient with increasing frequency up to the vicinity of the resonance at about 200–300 kHz, where a sharp peak appears. Above resonance, the coefficient drops steeply, as expected. The steady decrease from low frequencies up to the resonance region is mainly due to an increase of Young's modulus (Zhang et al. 2004).

5 One-, Two-, and Three-Dimensional Probing of Charge and Dipole Profiles

Although measurements of spontaneous or thermally stimulated currents or charges in electrets are well established for more than 50 years (Sessler 1997), methods for the nondestructive measurement of charge and polarization distributions in dielectrics are available for only the past 25–30 years. The majority of these high-resolution techniques can be classified by their principle of the generation of an electrical signal: *Thermal techniques* utilize inhomogeneous temperature profiles to induce a temporary distortion of the charge distribution, which results in a *pyroelectric* response of the dielectric sample. Alternatively, *acoustic techniques* are based on

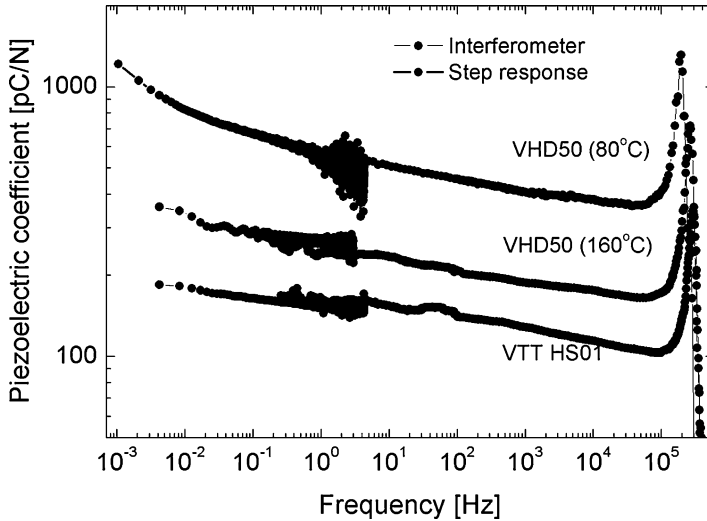


Fig. 16 Piezoelectric d_{33} coefficient determined by step response and interferometrically for two PP (Type VHD50) samples expanded at 80 °C and 160 °C, respectively, and for a commercial cellular PP ferroelectret (Type HS01, VTT) sample (Reprinted from Zhang et al. (2004) with permission)

the propagation of a pressure discontinuity which generates a piezoelectric response. A comprehensive review about thermal and acoustic methods is given by Sessler (Sessler 1997).

5.1 Thermal Methods for Probing 1D Charge and Polarization Distributions

Thermal techniques generally utilize instationary temperature profiles $T(x, t)$ that propagate through the sample by heat diffusion, the characteristic parameter of which is the thermal diffusivity $K = k/c\rho$. Depending on the type and time dependence of the excitation signal, we can distinguish three individual techniques, which are schematically shown in Fig. 17:

The *thermal wave technique*, also called LIMM (Lang and Das-Gupta 1981; Lang 1991), uses a sinusoidally modulated laser providing a periodical heat flux $H(\omega t)$ which hits the surface of an opaque, metalized sample. This periodical excitation with the angular frequency ω results in a specific temperature profile $T(x, \omega t)$ which has the properties of a highly damped and phase-shifted *thermal wave* with the thermal diffusion length $\mu_{th} = (2K/\omega)^{1/2}$ as the characteristic quantity (Figs. 18 and 19).

In contrast to the thermal wave technique, which operates in the frequency domain, the *thermal-pulse method* represents a transient technique operating in the time domain. This method was first described in 1975 (Collins 1975) and uses short light pulses of 10–100 μ s duration as excitation signal.

Fig. 17 Three common thermal excitation schemes $H(t)$ or $T(t)$ used in thermal wave techniques for the profiling of space charges: (a) thermal wave method (LIMM), (b) heat pulse method, and (c) thermal step technique

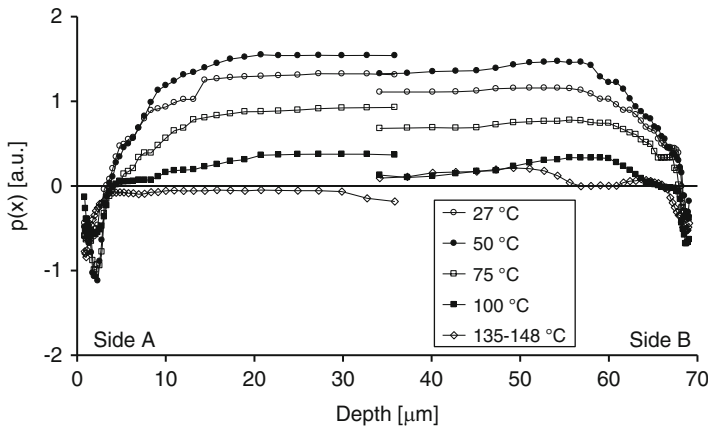
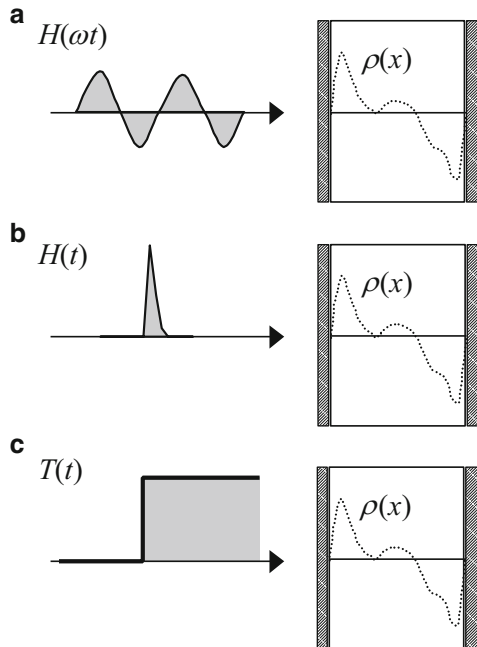


Fig. 18 Distribution of pyroelectric coefficient across a HS01 film at different temperatures obtained by thermal wave experiments on the two sides of the film (Reprinted from van Turnhout et al. (1999) with permission)

The third, *thermal step technique*, utilizes a steplike change of the surface temperature at one side of a dielectric sample, while the opposite side is kept at its initial temperature. In this experiment, the applied temperature step $\Delta T(t)$, initially restricted to the surface near region, propagates and gradually changes toward a

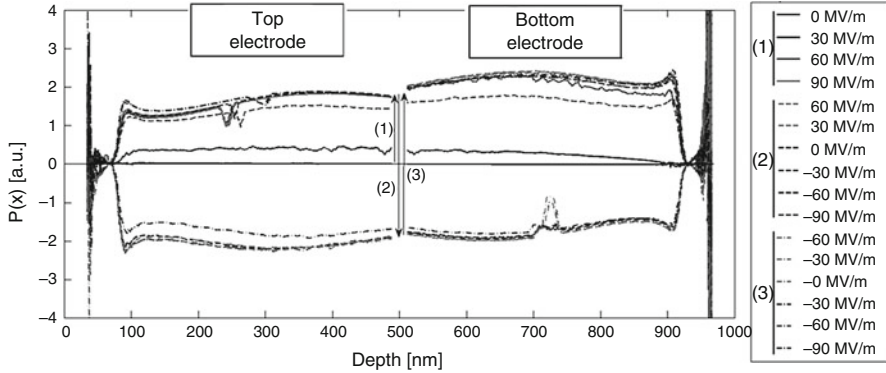


Fig. 19 Distribution of the pyroelectric coefficient across a 1 μm thin film of PVDF-TrFE (76:24), capped by vacuum deposited aluminum electrodes, at different external fields. Thermal waves were applied from both the *top* and *bottom* electrode (van Turnhout et al. 1999) (Reprinted from Putzeys and Wübbenhorst (2015a))

linear temperature gradient for $t > \infty$ (Tourelle et al. 1998). Although also being a time-domain technique, the thermal step method uses isothermal boundary conditions rather than a quasi-adiabatic situation as present in the methods (a) and (b).

For a two-side metalized, short-circuited sample, the current response is given by the integral equation (1), containing a generalized distribution function $G(x)$ and the particular temperature profile $T(x, t)$; L is the sample thickness:

$$J(t) = \frac{1}{L} \int_0^L G(x) \frac{\partial T(x, t)}{\partial t} dx \quad (21)$$

In case of only real charges, $G(x)$ has the simple form

$$G(x) = (\alpha_e - \alpha_x) \int_0^x \rho(x') dx' \quad (22)$$

and can be identified as being proportional to the internal field distribution $E(x) \propto G(x)$.

From Eq. 21, it is clear that the determination of the distribution function $G(x)$ requires the deconvolution of the integral equation knowing both the current response $I(t)$ or $I(\omega)$ (thermal wave technique) and the time derivative of the temperature profile $T(x, t)$. Various approaches to solve the deconvolution problem have been discussed (Sessler 1997).

A time-efficient and direct means of obtaining the depth profile from the pyroelectric response spectrum is the scale transform method, as described by Ploss and Bianzani (1994). The local pyroelectric response P at a depth z is proportional to the difference between the real and imaginary pyroelectric current, at a frequency where the thermal diffusion length μ_{th} is equal to the depth z .

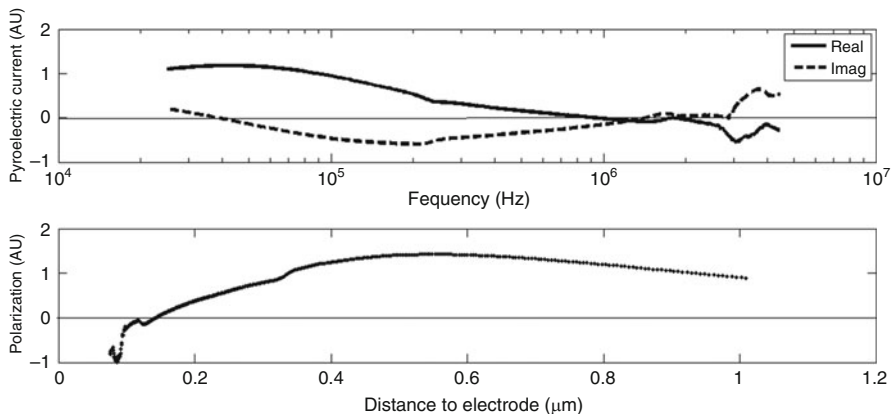


Fig. 20 (Top) A pyroelectric current spectrum of PVDF-TrFE (76:24). (Bottom) Result of the scale transform method. A high modulation frequency corresponds to a region close to the electrode, while lower modulation frequency provides information on the local polarization further from the electrode

$$P(z) \propto [\Re(I_p(\omega)) - \Im(I_p(\omega))] \quad (23)$$

$$z = \sqrt{\frac{2K}{\omega}}$$

An example of the ST method is given in Fig. 20.

5.2 Depth Profiling (1D) of Charge and Polarization Using Acoustical Waves

Instead of temperature fields, one can use pressure discontinuities in order to probe charge or polarization distributions in dielectrics. According to the pressure excitation method, one can distinguish three basic configurations: (a) the LIPP (*laser-induced pressure pulse*, Fig. 21) (Sessler et al. 1981) or PWP (pressure wave propagation) technique (Alquie et al. 1981), (b) the *piezoelectrically generated pressure step* technique (PPS, cf. Fig. 22) (Eisenmenger and Haardt 1982), and (c) the *pulsed electroacoustic method* (PEA, cf. Fig. 23) (Takada et al. 1987).

All acoustic techniques have in common that they probe the unknown charge or polarization distribution function by a local deformation (pressure inhomogeneity), which travels with sound velocity c through the sample and causes a local displacement of the distribution $H(x)$ at the position $x = ct$ resulting in a temporary modified distribution $H'(x, t)$. Consequently, image charges at the electrodes have to be redistributed to compensate the external field to zero and give rise to a current response. Owing to the high sound velocity of polymers of typically $c = 2000$ m/s,

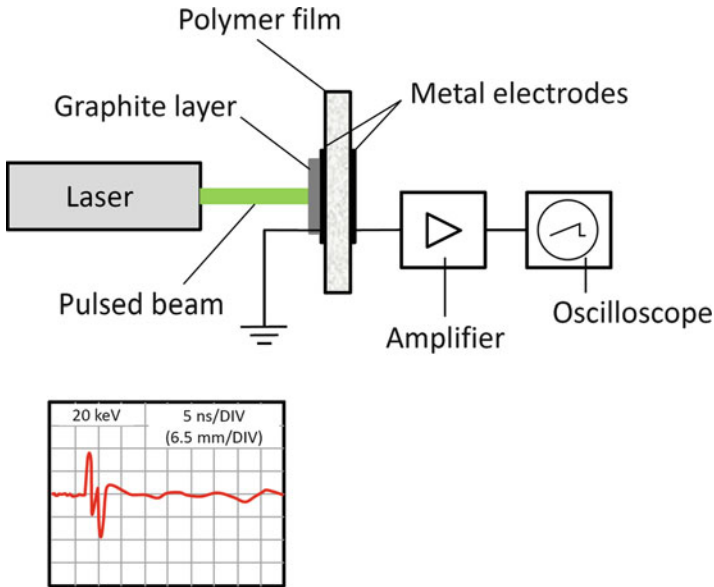


Fig. 21 Experimental setup for the simultaneous measurement of charge distributions and external currents (After Sessler et al. (1981))

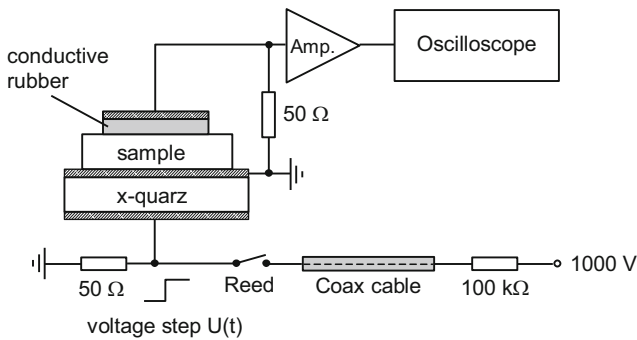


Fig. 22 Schematic setup of the PPS technique (After Eisenmenger and Haardt (1982))

one recognizes that very short pressure pulses or rise times (~ 1 ns) and high bandwidth electronics (~ 1 GHz) are prerequisites to achieve a high spatial resolution for charge/polarization inhomogeneities.

For example, the current response of a short-circuited sample to a pressure pulse (LIPP, PWP) of amplitude p and duration τ is given by (Ferreira and Gerhard-Multhaupt 1990)

$$J(t) = \frac{p\tau}{\rho_0 L} [H(x)]_{x=ct} \tag{24}$$

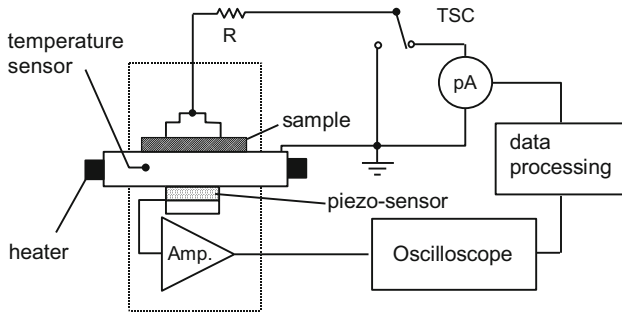


Fig. 23 Schema of the PEA setup (After Takada et al. (1987))

with

$$H(x) = (\gamma + 1)\rho(x) - \frac{de(x)}{dx} \quad (25)$$

Here the symbols ρ_0 , L , γ , and $e(x)$ denote the density, the sample thickness, the electrostriction coefficient, and the piezoelectric strain coefficient. From Eqs. 24 and 25, one sees that from the current response $J(t)$ of the pressure pulse experiment, the direct image of the space-charge distribution $\rho(x)$ or the gradient of the piezoelectric coefficient can be deduced by using the simple transformation $x = ct$.

Alternatively, the use of a pressure step (PPS-technique) results in a current response which maps, in case of only real charges, the internal field distribution $E(x)$ (Eisenmenger and Haardt 1982):

$$J(t) = \frac{p\tau}{\rho_0 cL} \left[\int_0^x H(x') dx' \right]_{x=ct} \quad (26)$$

It should be emphasized that a separation of a complex distributions $H(x)$, when representing a superimposed charge $\rho(x)$ and a polarization distribution (here linked to $e(x)$) according to Eq. 25, is not possible unless additional information about the distributions is available from other experiments.

5.3 Piezo- and Pyroelectric Microscopy

The controlled deformation of the EAPs is greatly dependent on the distribution of its piezoelectric and ferroelectric properties. The lateral homogeneity of these properties is of particular high importance. Visualization of these lateral distributions is possible via imaging of the local piezoelectric and pyroelectric activity.

5.3.1 Reverse Piezoelectric Response Imaging

Imaging of the lateral piezoelectric activity can be obtained by reverse piezoelectric response. One example is profilometer microscopy, as discussed earlier in Sect. 5.2,

where a stylus is translated across the electret's surface to detect the surface vibration when excited by a sinusoidal voltage. A different technique is piezoresponse force microscopy (PFM), where the conducting tip of an atomic force microscope (AFM) applies an AC voltage to the sample's surface. The bias-induced reverse piezoelectric response causes a local deformation, measurable via deflection of the tip. The first harmonic of the signal is a measure for the polarization distribution, while the phase of the signal can reveal the absolute orientation of the domain. The resolution is in the order of a few nanometers (Batagiannis et al. 2010).

5.3.2 Pyroelectric Microscopy

Pyroelectric microscopy is similar to the LImm, heat pulse, and thermal step techniques discussed earlier. The main difference is that rather than changing the temperature of the metal electrodes, in pyroelectric microscopy the temperature change is induced directly in the sample under investigation. The pyroelectric response is measured by nearby electrodes in the form of surface charge fluctuations (Quintel et al. 1998). In scanning pyroelectric microscopy (SPEM), which operates in the frequency domain, a harmonically modulated laser beam is translated across the sample's surface, yielding a pyroelectric response image (Quintel et al. 1998). Figure 24 shows the schematic and a photograph of a SPEM setup. The spatial resolution is in the order of one micrometer (Putzeys and Wübbenhorst 2015b).

An increase of the modulation frequency results in a local response closer to the sample's surface, similar to the LImm measurements (Sect. 5.1). In Fig. 25, a ferroelectret is measured at different frequencies. At high frequency, the subsurface cellular structure becomes visible.

SPEM has also been used to reveal the lateral polarization distribution in the biopolymer chitin, as found in insect wings. Revealing a pyroelectric and possible piezoelectric response from both membrane and supporting veins (Fig. 26; Putzeys and Wübbenhorst 2015b).

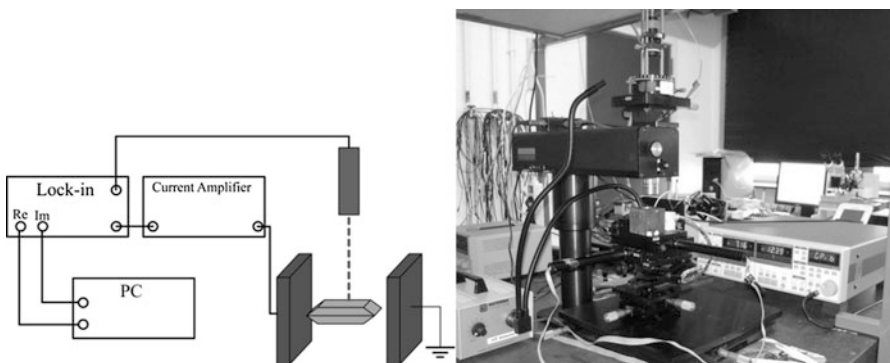


Fig. 24 Schematic of the SPEM setup alongside a photograph of the experimental setup. A lock-in amplifier modulates the output of a laser diode; the pyroelectric current is amplified by a transimpedance amplifier. The lock-in amplifier correlates the signal from the current amplifier output, and the data are stored on a computer

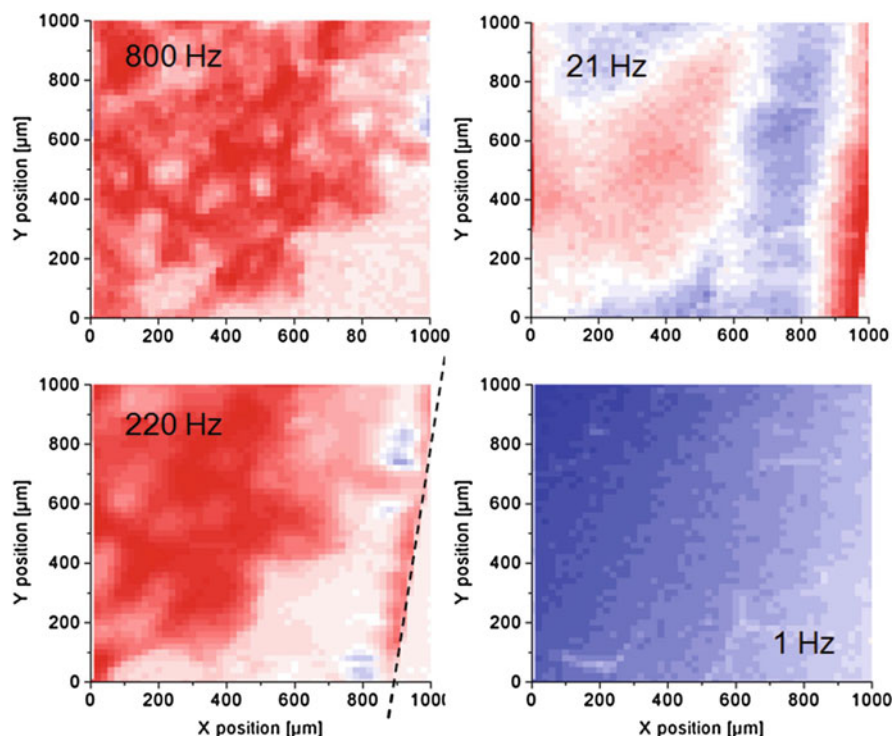


Fig. 25 Pyroelectric image of a ferroelectret measured at different frequencies. At high frequencies, the cellular structure underneath the surface is revealed

An example of pyroelectric scanning in the time domain is the thermal-pulse tomography (TPT) method (Suárez et al. 2006). A focused, pulsed laser heats a circular spot. While the thermal pulse diffuses through the sample, the response current is recorded. From this transient current, the distribution of space charges and electric dipoles can be reconstructed using thermal deconvolution tools, such as the scale transform method discussed earlier (Mellinger et al. 2005). Thermal-pulse tomography produces three-dimensional images with a lateral resolution of about $30\ \mu\text{m}$ and a depth resolution better than $0.5\ \mu\text{m}$ by scanning the laser spot across the ferroelectric's surface (Mellinger et al. 2008).

6 Conclusion

The present chapter provided, on an introductory level, a representative description of experimental methods for the characterization of the mechanical, electrical, and electromechanical properties of polymeric electrets. For obvious reasons, not all experimental approaches could be addressed. A couple of “standard” techniques for measuring electret properties such as thermally stimulated discharge (TSD)

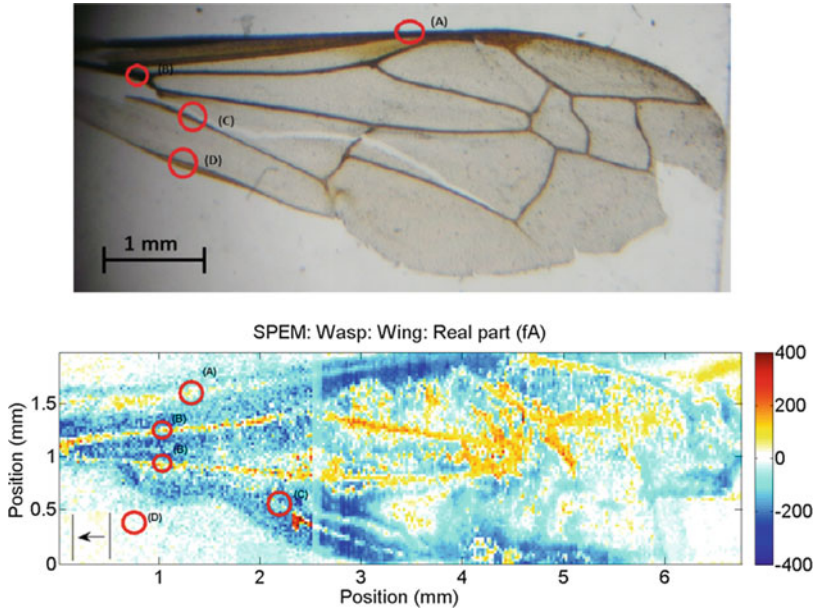


Fig. 26 (Top) Photograph and (Bottom) pyroelectric response map of a wasp's wing (Reprinted from Putzeys and Wübbenhorst (2015b) with permission)

experiments or generic test methods was only be touched briefly; for more insights, the reader could refer to specialized books, such as Sessler (1987).

The particular choice of the authors was rather to put emphasis on experimental techniques that are either *specifically relevant* or *powerful* with respect to ferroelectric polymers and ferroelectrets or represent *recent* experimental developments and trends. In this sense, room was given to nonlinear dielectric properties that can be probed by nonlinear dielectric spectroscopy and various types of hysteresis experiments. Besides a systematic description of piezoelectric and inverse piezoelectric techniques, we have added dielectric resonance spectroscopy as an “all-round” approach yielding elastic, piezoelectric, and dielectric properties of polymer electrets in a single dielectric measurement.

A key feature of any piezoelectric polymer is its underlying polarization and/or charge distribution, which can vary substantially as the result of the poling process, surface phenomena, or even material heterogeneities. Spatial variations in the piezoelectric properties might reduce the performance of EAP-based devices and give rise to complex electromechanical responses including bending deformations. On the other hand, a full control over the spatial piezoelectric activity is a prerequisite to design sophisticated transducers based on patterned piezoelectric structures in one, two, or three dimensions. To account for this demand, the last section of this chapter was exclusively devoted to space-charge/polarization profiling techniques that cover resolutions from tens of μm down to the nanometer scale.

Acknowledgments Two of the authors (TP, MW) acknowledge financial support from the Research Council of the KU Leuven, project OT/11/065.

References

- Alquie C, Dreyfus G, Lewiner J (1981) Stress-wave probing of electric field distributions in dielectrics. *Phys Rev Lett* 47:1483–1487
- Batagiannis A, Wübbenhorst M, Hulliger J (2010) Piezo- and pyroelectric microscopy. *Curr Opin Solid State Mater Sci* 14:9
- Bauer S, Gerhard-Multhaupt R, Sessler GM (2004) Ferroelectrets: soft electroactive foams for transducers. *Phys Today* 57:37–43
- Carpi F, Anderson I, Bauer S, Frediani G, Gallone G, Gei M, Graaf C, Jean-Mistral C, Kaal W, Kofod G, Kolloche M, Kornbluh R, Lassen B, Matysek M, Michel S, Nowak S, Benjamin OB, Pei Q, Pelrine R, Rechenbach B, Rosset S, Shea H (2015) Standards for dielectric elastomer transducers. *Smart Mater Struct* 24:105025
- Collins RE (1975) Distribution of charge in electrets. *Appl Phys Lett* 26:675–677
- Dansachmüller M, Schwödiauer R, Bauer-Gogonea S, Bauer S, Paajanen M, Raukola J (2005) Elastic and electromechanical properties of polypropylene foam ferroelectrets. *Appl Phys Lett* 86:031910
- Eisenmenger W, Haardt M (1982) Observation of charge compensated polarization zones in polyvinylidene fluoride (PVDF) films by piezoelectric acoustic step-wave response. *Solid State Commun* 41:917–920
- Ferreira GFL, Gerhard-Multhaupt R (1990) Derivation of response equations for the nondestructive probing of charge and polarization profiles. *Phys Rev B* 42:7317–7321
- Furukawa T, Date M, Fukada E, Tajit Y, Akio C (1980) Ferroelectric behavior in the copolymer of vinylidene fluoride and trifluoroethylene. *Jpn J Appl Phys* 19:L109
- Gerhard-Multhaupt R, Kunstler W, Gome T, Pucher A, Weinhold T, Seiss M, Xia Z, Wedel A, Danz R (2000) Porous PTFE space-charge electrets for piezoelectric applications. *Dielectr Electr Insul IEEE Trans* 7:480–488
- Havriliak S, Negami S (1967) A complex plane representation of dielectric and mechanical relaxation processes in some polymers. *Polymer* 8:161–210
- Heiler B, Ploss B (1994) Dielectric nonlinearities of P(VDF-TrFE). In: *Electrets*, (ISE 8), 8th international symposium on, pp. 662–667, DOI:10.1109/ISE.1994.514848
- Hillenbrand J, Sessler GM (2000) Piezoelectricity in cellular electret films. *Dielectr Electr Insul IEEE Trans* 7:537–542
- Hillenbrand J, Sessler GM (2004) Quasistatic and dynamic piezoelectric coefficients of polymer foams and polymer film systems. *Dielectr Electr Insul IEEE Trans* 11:72–79
- Kremer F, Schönhals A (2002) *Broadband dielectric spectroscopy*. Springer, Berlin
- Kressmann R (2001a) Linear and nonlinear piezoelectric response of charged cellular polypropylene. *J Appl Phys* 90:3489–3496
- Kressmann R (2001b) New piezoelectric polymer for air-borne and water-borne sound transducers. *J Acoust Soc Am* 109:1412–1416
- Künstler W, Xia Z, Weinhold T, Pucher A, Gerhard-Multhaupt R (2000) Piezoelectricity of porous polytetrafluoroethylene single- and multiple-film electrets containing high charge densities of both polarities. *Appl Phys A* 70:5–8
- Lang SB (1991) Laser intensity modulation method (LIMM): experimental techniques, theory and solution of the integral equation. *Ferroelectrics* 118:343–361
- Lang SB, Das-Gupta DK (1981) A technique for determining the polarization distribution in thin polymer electrets using periodic heating. *Ferroelectrics* 39:1249–1252
- Lekkala J, Poramo R, Nyholm K (1996) EMF force sensor-a flexible and sensitive electret film for physiological applications. *Med Biol Eng Comput* 34:67–69

- Lou K, Zhang X, Xia Z (2012) Piezoelectric performance of fluor polymer sandwiches with different void structures. *Appl Phys A* 107:613–620
- Mellinger A (2002) Piezoelectric resonances in the dielectric spectrum of polymer films. *Dielectr Newsl Novocontrol* 16, Issue April:1–8
- Mellinger A (2003) Dielectric resonance spectroscopy: a versatile tool in the quest for better piezoelectric polymers. *IEEE Trans Dielectr Electr Insul* 10:842–861
- Mellinger A, Singh R, Wegener M, Wirges W, Suarez RF, Lang SB, Santos LF, Gerhard-Multhaupt R (2005) High-resolution three-dimensional space-charge and polarization mapping with thermal pulses. In: *Electrets*, 2005. ISE-12. 12th international symposium on, pp. 212–215, DOI: 10.1109/ISE.2005.1612358
- Mellinger A, Flores-Suárez R, Singh R, Wegener M, Wirges W, Gerhard R, Lang S (2008) Thermal-pulse tomography of space-charge and polarization distributions in electret polymers. *Int J Thermophys* 29:2046–2054
- Neuschwandtner GS, Schwödäuer R, Vieytes M, Bauer-Gogonea S, Bauer S, Hillenbrand J, Kressmann R, Sessler GM, Paajanen M, Lekkala J (2000) Large and broadband piezoelectricity in smart polymer-foam space-charge electrets. *Appl Phys Lett* 77:3827–3829
- Ouellet S, Cronin D, Worswick M (2006) Compressive response of polymeric foams under quasi-static, medium and high strain rate conditions. *Polym Test* 25:731–743
- Paajanen M, Välimäki H, Lekkala J (2000) Modeling the electromechanical film (EMFi). *J Electrostat* 48:193
- Ploss B, Bianzani O (1994) Polarization profiling of the surface region of PVDF and P(VDF-TrFE). In: *Electrets*, (ISE 8), 8th international symposium on, pp. 206–211, DOI:10.1109/ISE.1994.514769
- Putzeys T, Wübberhorst M (2015a) Asymmetric polarization and hysteresis behaviour in ferroelectric P(VDF-TrFE) (76:24) copolymer thin films spatially resolved via LIMM. *Phys Chem Chem Phys* 17:7767–7774
- Putzeys T, Wübberhorst M (2015b) Polarization domain information on insect wing chitin using the Scanning PyroElectric Microscope (SPEM). *IEEE Trans Dielectr Electr Insul* 22:1394–1400
- Qiu X, Hollander L, Wirges W, Gerhard R, Cury Basso H (2013) Direct hysteresis measurements on ferroelectret films by means of a modified Sawyer-Tower circuit. *J Appl Phys* 113:224106
- Quintel A, Hulliger J, Wübberhorst M (1998) Analysis of the polarization distribution in a polar perhydrotriphenylene inclusion compound by scanning pyroelectric microscopy. *J Phys Chem B* 102:4277–4283
- Sawyer CB, Tower CH (1930) Rochelle salt as a dielectric. *Phys Rev* 35:269–273
- Sessler GM (1987) *Electrets*. Springer, Berlin/Heidelberg
- Sessler GM (1997) Charge distribution and transport in polymers. *Dielectr Electr Insul IEEE Trans* 4:614–628
- Sessler GM, Hillenbrand J (1999) Electromechanical response of cellular electrets films. *Appl Phys Lett* 75:3405–3407
- Sessler GM, Hillenbrand J (2013) Figure of merit of piezoelectret transducers for pulse-echo or transmit-receive systems for airborne ultrasound. *Appl Phys Lett* 103:122904
- Sessler GM, West JE, Gerhard R (1981) Measurement of charge distribution in polymer electrets by a new pressure-pulse method. *Polym Bull* 6:109–111
- Suárez RF, Mellinger A, Wegener M, Wirges W, Gerhard-Multhaupt R, Rajeev S (2006) Thermal-pulse tomography of polarization distributions in a cylindrical geometry. *Dielectr Electr Insul IEEE Trans* 13:1030–1035
- Sun Z, Zhang X, Xia Z, Qiu X, Wirges W, Gerhard R, Zeng C, Zhang C, Wang B (2011) Polarization and piezoelectricity in polymer films with artificial void structure. *Appl Phys A* 105:197–205
- Takada T, Maeno T, Kushibe H (1987) An electric stress-pulse technique for the measurement of charges in a plastic plate irradiated by an electron beam. *Electr Insul IEEE Trans EI-22:497–501*

- Tourelle A, Notingher P, Vella N, Malrieu S, Castellon J, Agnel S (1998) The thermal step technique: an advanced method for studying the properties and testing the quality of polymers. *Polym Int* 46:81–92
- van Turnhout J, Staal RE, Wübbenhorst M, de Haan P (1999) Distribution and stability of charges in porous polypropylene films. In: 10th international symposium on electrets (ISE 10). European Cultural Center of Delphi, 22–24 Sept 1999, IEEE Service Center, Piscataway
- Wegener M (2008) Polarization-electric field hysteresis of ferroelectric PVDF films: comparison of different measurement regimes. *Rev Sci Instrum* 79:106103
- Weibull W (1951) A statistical distribution function of wide applicability. *J Appl Mech* 18:293–297
- Zhang X, Hillenbrand J, Sessler GM (2004) Piezoelectric d_{33} coefficient of cellular polypropylene subjected to expansion by pressure treatment. *Appl Phys Lett* 85:1226–1228
- Zhang X, Hillenbrand J, Sessler GM (2007) Ferroelectrets with improved thermal stability made from fused fluorocarbon layers. *J Appl Phys* 101:054114
- Zhang X, Cao G, Sun Z, Xia Z (2010) Fabrication of fluoropolymer piezoelectrets by using rigid template: structure and thermal stability. *J Appl Phys* 108:064113
- Zhang X, Hillenbrand J, Sessler GM, Haberzettl S, Lou K (2012) Fluoroethylenepropylene ferroelectrets with patterned microstructure and high, thermally stable piezoelectricity. *Appl Phys A* 107:621–629
- Zhang X, Zhang XW, Sessler GM, Gong X (2014) Quasi-static and dynamic piezoelectric responses of layered polytetrafluoroethylene ferroelectrets. *J Phys D Appl Phys* 47:015501

Yuji Suzuki and Yoshinobu Yasuno

Contents

1	Introduction	626
2	Acoustic Applications of Electrets/Ferroelectrets	626
2.1	Microphone	626
2.2	Earphone/Loudspeaker	631
2.3	Acoustic Applications of Cellular Polymer	633
3	Motor, Power Generator, and Energy Harvester	634
3.1	Motor and Rotational Power Generator	634
3.2	Vibration Energy Harvester	637
4	Summary	642
	References	642

Abstract

Polymer electret and ferroelectrets have unique characteristics such as electrostatic transduction without external voltage, light weight, flexibility, and so on. Their most successful applications are microphones and air filters, but various other types of devices have also been proposed. In this chapter, after giving overview of their applications, developments of acoustic devices and power generators/energy harvesters are discussed.

Keywords

Microphone • Loudspeaker • Power generator • Energy harvester

Y. Suzuki (✉)

The University of Tokyo, Tokyo, Japan

e-mail: ysuzuki@mesl.t.u-tokyo.ac.jp

Y. Yasuno

Kobayashi Institute of Physical Research, Tokyo, Japan

e-mail: yasuno@kobayashi-riken.or.jp

1 Introduction

The first application of electret is the thin-film microphone proposed by Sessler and West (1962). After that, electret has been applied to various acoustic applications such as microphones and loud speakers. In addition, as electromechanical transducers, electrophotography (e.g., Schaffert 1975), phonograph cartridges (e.g., Kawakami 1969), touch or key transducers (e.g., Sessler et al. 1973), display devices (Bruneel and Micheron 1977), switch (Sato and Takamatsu 1986) and relays (e.g., Ichiya et al. 1995) have been proposed. Electret transducers that are directly driven by a digital signal were also proposed for direct analog-to-digital conversion (Yasuno and Riko 1999). Electret-based dosimeter was proposed for detection of gamma rays (e.g., Ikeya and Miki 1980; Son and Babak 2006). Air filter is another large application area of electrets (van Turnhout et al. 1980; Thakur et al. 2013). As described below, electret-based power generation attracted much attention in the last decade (Suzuki 2011).

Applications of electrets are extensively described in Sessler and West (1973, 1987). In the following sections, two main application areas of electret and ferroelectret, i.e., acoustic devices and power generators/energy harvesters will be discussed.

2 Acoustic Applications of Electrets/Ferroelectrets

In this section, acoustic applications of electrets such as microphones, earphones, loudspeakers, underwater acoustic transducers, and other electromechanical transducers are discussed. Since electret condenser microphones (ECMs) were introduced by G. M. Sessler and J. E. West in 1962, ECMs have been applied in various fields. For instance, ECMs were widely used in built-in cassette tape recorders. In 2000, its quantity was much increased for mobile phone applications. As the technology has been extended to fields such as communications, vehicles, medicines, and security, new features including vibration noise-resistance, small size, power saving, and resistance to high-frequency noise have been developed. ECMs are now necessary acoustic parts in small mobile devices (Fig. 1).

2.1 Microphone

ECMs are a form of electrostatic transducer. An electric field generated by the electret charge is used as an alternative to the external bias system of conventional electrostatic transducers. The element technologies of an omnidirectional ECM are compatible with other ECMs such as directive ECMs in the common basic technology. This section describes the basics of omnidirectional ECM and derives a general formula for its sensitivity and frequency characteristics.

Figure 2 illustrates the fundamental configuration of the acoustic and electrical systems of an ECM. The omnidirectional condenser microphone forms a capacitor

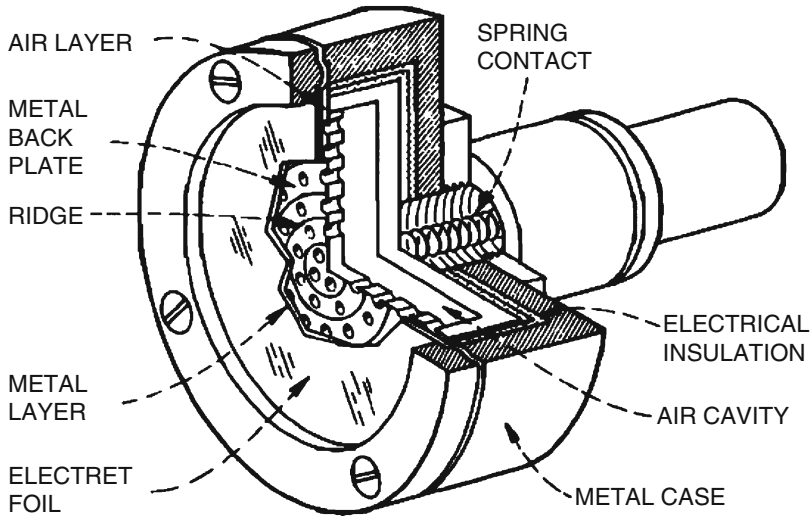


Fig. 1 Foil electret microphone (Sessler and West 1973) (Reproduced with permission from AIP)

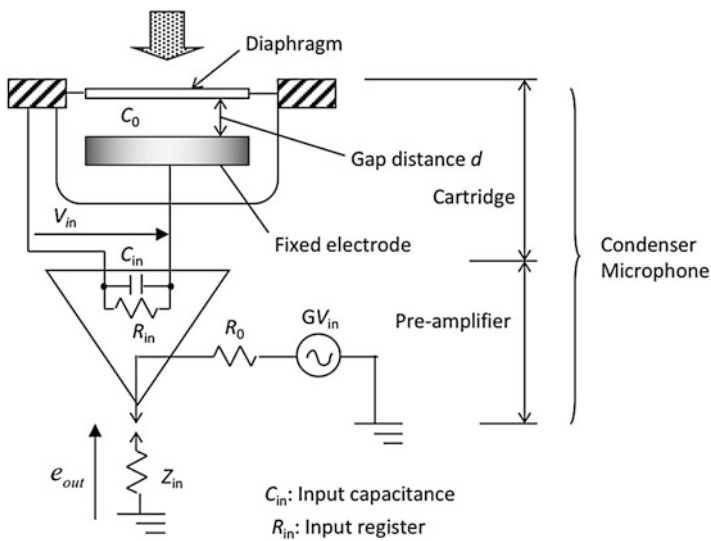


Fig. 2 Fundamental configuration of ECM

between the diaphragm and a fixed electrode. The amount of charge Q which is stored therein is

$$Q = C_0 V_b = \text{const.} \tag{1}$$

Here, the static capacitance is $C_0 = \epsilon_0 S/d$, where S is the electrode area, ϵ_0 is the vacuum permittivity, and V_b is the externally applied voltage.

When an external force changes the capacitance C_0 by ΔC , and the RC time constant $R_{in}(C_{in} + C_0)$ is sufficiently large that no current flows in normal operating conditions, then the voltage becomes

$$V' = \frac{Q}{C_0 + \Delta C} = \frac{1}{1 + \Delta C/C_0} V_b \tag{2}$$

If $\Delta C/C_0 \ll 1$,

$$V' = (1 - \Delta C/C_0)V_b \tag{3}$$

The variation e_0 is then

$$e_0 = -\Delta C/C_0 V_b \tag{4}$$

Because the capacitance change ΔC is due to the small change in the gap from d to $(d - \Delta d)$ by the sound pressure, Eq. 4 leads to

$$e_0 = -\Delta d/d V_b \tag{5}$$

Thus, the output of the omnidirectional condenser microphone depends on the minute displacement Δd of the diaphragm area of S by the sound pressure P_0 . The diaphragm displacement can be obtained by an equivalent circuit analysis in a lumped-parameter system as follows.

Figure 3 presents the equivalent circuit of an omnidirectional ECM. The sound inlet and the volume of the front chamber are represented by the equivalent mass m_1 , the equivalent resistance r_1 , and the equivalent stiffness S_1 . The diaphragm is represented by the equivalent mass m_0 , the equivalent resistance r_0 , and equivalent stiffness S_0 .

On the other hand, m_2 , r_2 , and S_2 of the back chamber represent a thin fluid layer between the diaphragm and the fixed electrode. The equivalent stiffness S_b

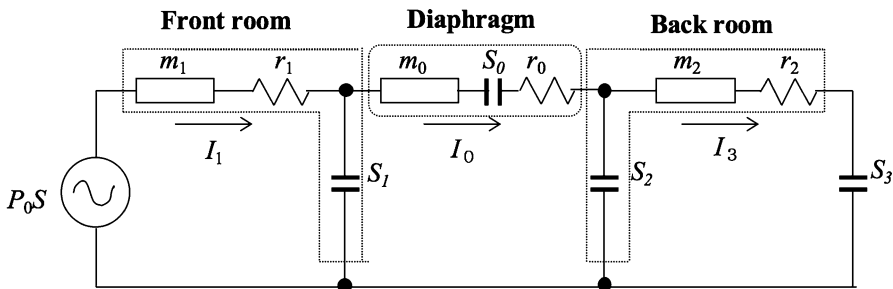


Fig. 3 Equivalent circuit of an omnidirectional ECM

corresponds to the actual volume of the back chamber. Current I_d corresponds to the vibration speed of the diaphragm, obtained from the vibration displacement by time integration of the vibration velocity.

The effect of the front chamber in the equivalent circuit of Fig. 3, which determines the cut-off frequency for the high-frequency range, is not considered in the basic design of the frequency sensitivity, so that $m_1 = 0$, $r_1 = 0$, and $S_1 = \infty$.

Microphone output e_0 is calculated as follows:

$$e_0 = -\frac{V_b S}{d} \cdot \frac{1}{\{S_0 + S_b - \omega^2 m_0\} + j\omega r_0} P_0 \quad (6)$$

The overall sensitivity is determined from the output of microphone e_0 and the transmission loss of the amplifier used for the impedance conversion.

In the mobile device, a built-in ECM is required to withstand the vibration noise from instruments. The vibration sensitivity is proportional to the area density of the diaphragm, with a smaller area density being better. Therefore, it is necessary to separate the electret material in order to improve the vibration resistance by using a lightweight diaphragm. The vibration-proof ECM has a structure that forms an electret on a fixed electrode with light, thin materials used for the diaphragm, as shown in Fig. 4. This is because mobile instruments require an antivibration device, and the fixed-electrode electret method is the main technique for this.

For professional use, microphones with a push-pull electret structure are also employed. Unidirectional ECMs that deliver a faithful response at high sound-pressure levels over a wide dynamic range have also been developed. Structure of the push-pull electret microphone (Sakamoto et al. 1979) is depicted in Fig. 5.

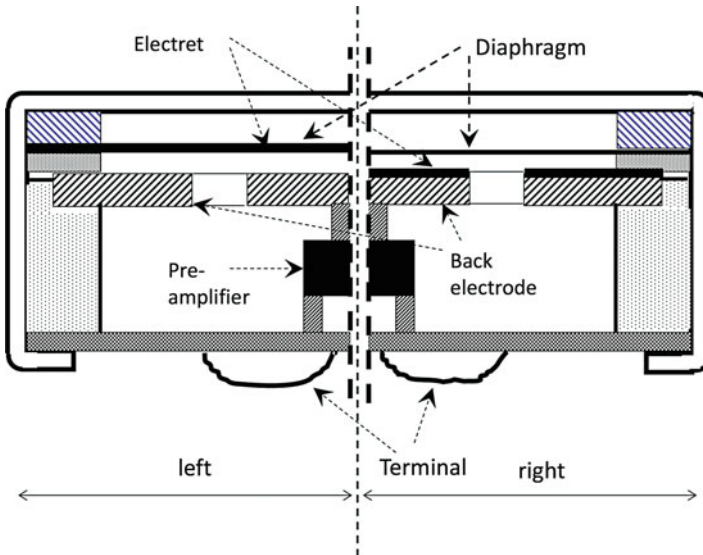


Fig. 4 Antivibration structure (*right*) and conventional structure (*left*)

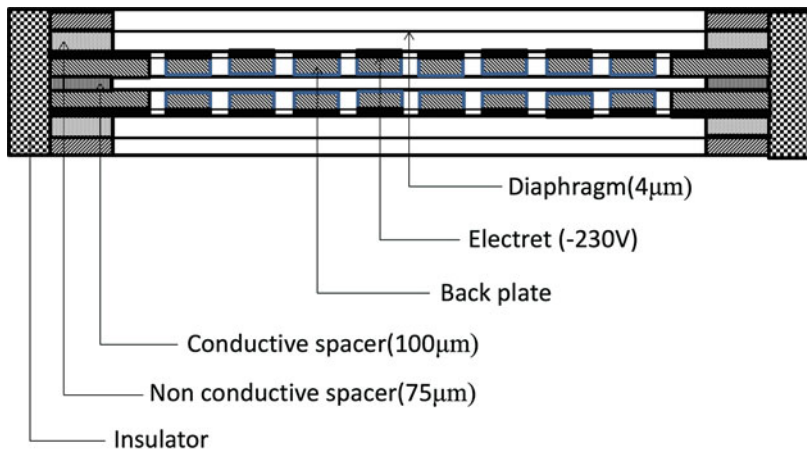


Fig. 5 Cross-section view of a push-pull electret transducer (Sakamoto et al. 1979)

Nonlinear distortion of the microphone cartridge and preamplifier has been improved with the push-pull structure.

The directivity of the microphone should be controlled depending on its intended use. A structure in which the sound incidence comes only from the front sound inlet of the electrostatic unit, sensing the pressure equally in all directions, is an omnidirectional one. On the other hand, a bidirectional response has been obtained using a symmetrical structure with a rear acoustic equivalent circuit the same as the front acoustic equivalent circuit of the diaphragm. Further, to obtain a unidirectional response, the phase circuit controls both the bidirectional and the omnidirectional components.

When audio equipment is used in a noisy environment, it is necessary to use a close-talking electret microphone to suppress the surrounding noises. Generally, close-talking ECMs apply a pressure gradient between the pressure entering the front sound inlet and that entering the rear sound inlet to the diaphragm. The ratio of the pressure gradient of the plane waves P_f to that of spherical waves P_s is as follows.

$$\frac{P_s}{P_f} = \sqrt{1 - \frac{2d}{L} + \left(\frac{c}{2\pi fL}\right)^2} \quad (7)$$

where d is the distance between the acoustic terminals (the acoustic separation between the front and rear inlets), L is the distance from the sound source, c is the speed of sound, and f is the frequency.

The pressure gradient tends to be larger with spherical waves than with plane waves in the low-frequency region. Thus, with low-amplitude sound sources or under close-talking conditions such as when users place the microphone close to their mouths, the waves entering the microphone are similar to spherical waves and the sensitivity intensifies in the low frequencies. This is the close-talking effect.

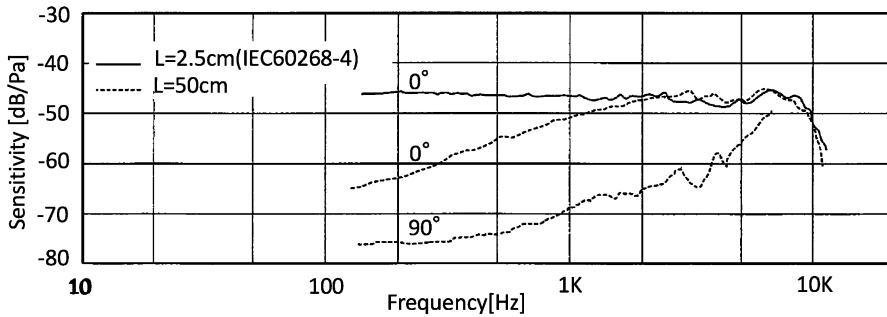


Fig. 6 Close-talking characteristics of the ECM (Panasonic WM-55D)

In contrast, because the source of the surrounding noise is relatively far from the ECM, the sound of this noise enters the microphone in the form of plane waves. As a result, the pressure gradient does not rise in the low-frequency region, and the microphone output drops substantially. This mechanism causes a considerable increase in the S/N ratio for the surrounding noise. The close-talking ECM produces flat frequency characteristics in the low-frequency region, 25 mm from the lip ring of an artificial mouth as shown in Fig. 6. At 90 degrees to the front and rear directions, the attenuation reaches more than 20 dB.

Hsieh et al. (1997) employed microelectromechanical system (MEMS) technologies to develop a miniature ECM using polymer electret as shown in Fig. 7. The diaphragm is 0.91 μm LPCVD silicon nitride fabricated through backside anisotropic wet etching of $\langle 100 \rangle$ silicon substrate. Teflon AF is spun on with the thickness of 1.2 μm over the nitride membrane and is used as the electret layer. After charging, the silicon chip with the diaphragm is bonded to the other silicon chip with a photoresist spacer.

More recently, MEMS microphones based on a single wafer are proposed (Hagiwara et al. 2010). With the aid of a soft-X-ray charging method, $\text{SiO}_2/\text{Si}_3\text{N}_4$ thin-film electret inside the silicon structure is successfully charged. The practical use of the ultrasmall silicon electret microphone has also been studied (Goto et al. 2011).

2.2 Earphone/Loudspeaker

Electrostatic speaker and earphone did not become popular because they need special driving circuits for the capacitive load. The equivalent circuits for the electret-based device and the device with external bias are the same, but the electromechanical force factor is different. For the electret speakers, the induced charge becomes unstable for a large gap as can be seen in microphones. Based on optimization studies of the acoustic parameters from an equivalent-circuit analysis, nonlinear distortion in a push-pull structure derived from a single-ended structure

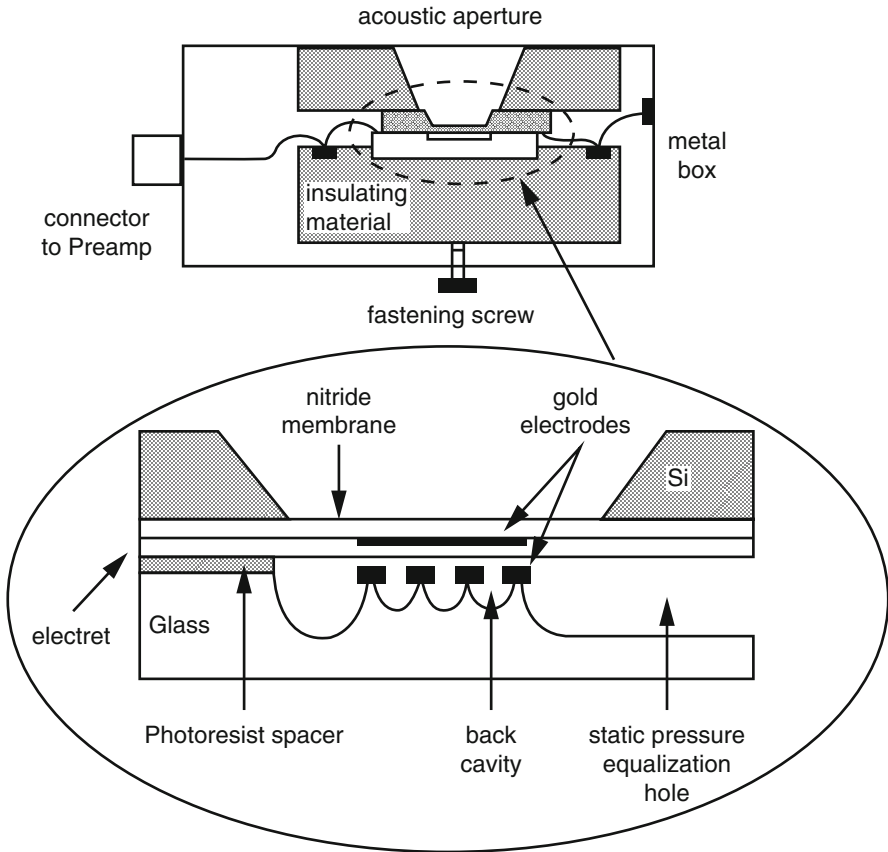


Fig. 7 MEMS microphone using polymer electret (Hsieh et al. 1997) (Reproduced with permission from IEEE)

was reduced in previous studies. Recently, Chen et al. (2012) proposed a practical model of the cell type for further developments.

Structure of electrostatic speakers is identical to that of microphone, and a single-ended push-pull method is generally used (Mellow and Karkkainen 2008). In the basic patented push-pull structure, the transducer generally consists of a combination of two electrets metallized on one side and touching each other with their metal layers, sandwiched between two perforated metal electrodes. By properly applying the AC signal to the two electrodes, the electrical distortion can be completely eliminated (Sessler and West 1962), which is effective in push-pull electret earphone applications. Atoji and Aoi (1974) proposed a method for reducing distortion by applying the AC signal on one side of a push-pull configuration. Sakamoto et al. (1975) proposed a device with a thin-metal diaphragm and with electret set on both sides of the electrodes. Baja et al. (2010) proposed an optimization method for the push-pull structure.

2.3 Acoustic Applications of Cellular Polymer

Recently, electrets made with cellular structured polymers have received attention as new piezoelectric materials with a high piezoelectric d_{33} coefficient exceeding 100 pC/N. In particular, research on cellular polypropylene (PP) film has been conducted to improve both its physical characteristics and its applications (Neugschwandtner et al. 2000; Hillenbrand and Sessler 2000; Paajanen et al. 1998, 2001; Zhang et al. 2007).

Cellular PP is biaxially stretched PP and has porous voids inside as shown in Fig. 8. It becomes electret through dielectric barrier discharging in the micro voids and exhibits ferroelectric-like behavior such as polarization-voltage hysteresis. This is due to the electrical dipole and may also be expressed as ferroelectrets or piezoelectrets distinct from piezoelectric materials.

Ferroelectret is a flexible, sheet-like static transducer with a simple structure. Its applications will expand by improving the electromechanical conversion coefficient and stability of the temperature resistance (Yasuno et al. 2010; Kodama et al. 2009). The working temperature of the cellular PP should be below 60 °C, but porous PTFE (Cao et al. 1998) and FEP nanoporous material (Chiang et al. 2005) can be used at higher temperatures.

The sensitivity M based on the simplified electromechanical model is as follows:

$$M = d_{33} \frac{S_1 + \varepsilon S_2}{\varepsilon \varepsilon_0} \quad (8)$$

where S_1 is the total thickness of the polymer solid layers, S_2 is the total thickness of the polymer gaseous layers, and ε_0 and ε are the vacuum and relative permittivity.

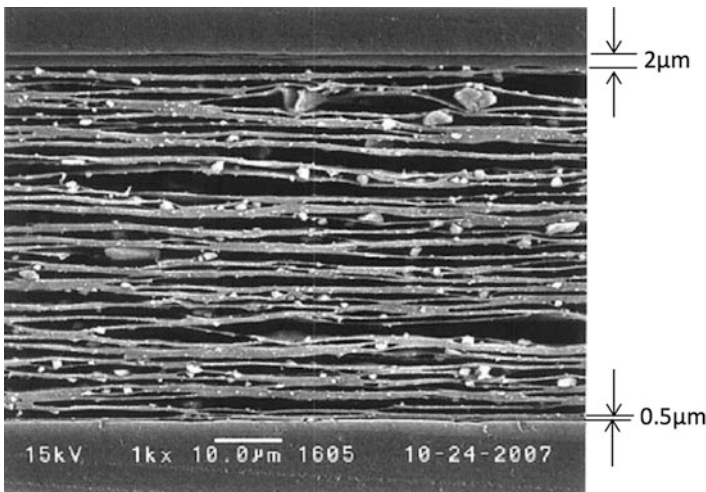


Fig. 8 A cross-sectional SEM image of the cellular PP

Broadband microphones (from the audible range to ultrasound), which can be achieved in a converter using the piezoelectric properties d_{33} in the thickness direction, have already been applied as transducer elements in an airborne ultrasound transducer (Yasuno et al. 2010). Application to ultrasonic probes for medical use is also expected.

Lekkala and Paayanen (1999) proposed metalized porous PP as ElectroMechanical Film (EMFi). By utilizing the EMFi material, Reinhard et al. (2007) reported that the transmitter emitted a sound pressure level up to 90 dB at a distance of 1 m, and the ultrasonic receiver had a sensitivity of 500 $\mu\text{V}/\text{Pa}$. The sensitivity of an ultrasonic receiving transducer without an FET reached -226 dB re 1 $\text{V}/\mu\text{Pa}$, which exceeds that of a PVDF-based MHz-range hydrophone (Horino et al. 2012).

3 Motor, Power Generator, and Energy Harvester

3.1 Motor and Rotational Power Generator

Jefimenko and Walker (1971) gave a review of early studies on electrostatic motor. Electret motor using “slot effect” (Fig. 9) is also described. They prototyped a 5 inch diameter motor and realized 1500 rpm rotation with 8 kV driving voltage. Tada (1993) also developed a 2-pole electret motor using Teflon FEP as electret, which has a 60 mm diameter rotor, and obtained 1260 rpm rotation with 1.4 kV driving voltage.

Jefimenko and Walker (1978) developed a 6 inch diameter 2-pole generator and obtained 25 mW at 6000 rpm, which is similar with the eletret motor. Tada (1992) developed a complete model of rotational electret generators and obtained 1 mW at 5000 rpm with a 90 mm diameter 4-pole generator. More recently, Boland et al. (2003) derived a simple analytical formula for the output power by neglecting the parasitic capacitance and obtained 25 μW with an 8 mm diameter 4-pole generator fabricated with MEMS technologies.

For a rotational generator with n poles and total area A_0 running at a rotational frequency of f , in which the rate of change in the overlapping area between the electret and the counter electrode dA/dt is constant, the output power can be written as

$$P = \frac{\sigma^2 d^2 R}{\left\{ \varepsilon_2 \varepsilon_0 R + \frac{1}{n A_0 f} (\varepsilon_2 g + \varepsilon_1 d) \right\}^2}, \quad (9)$$

where σ , ε_1 , ε_2 , d , and g are the surface charge density of the electret, the relative permittivities of the air gap and the electret, the thickness of the electret, and the gap

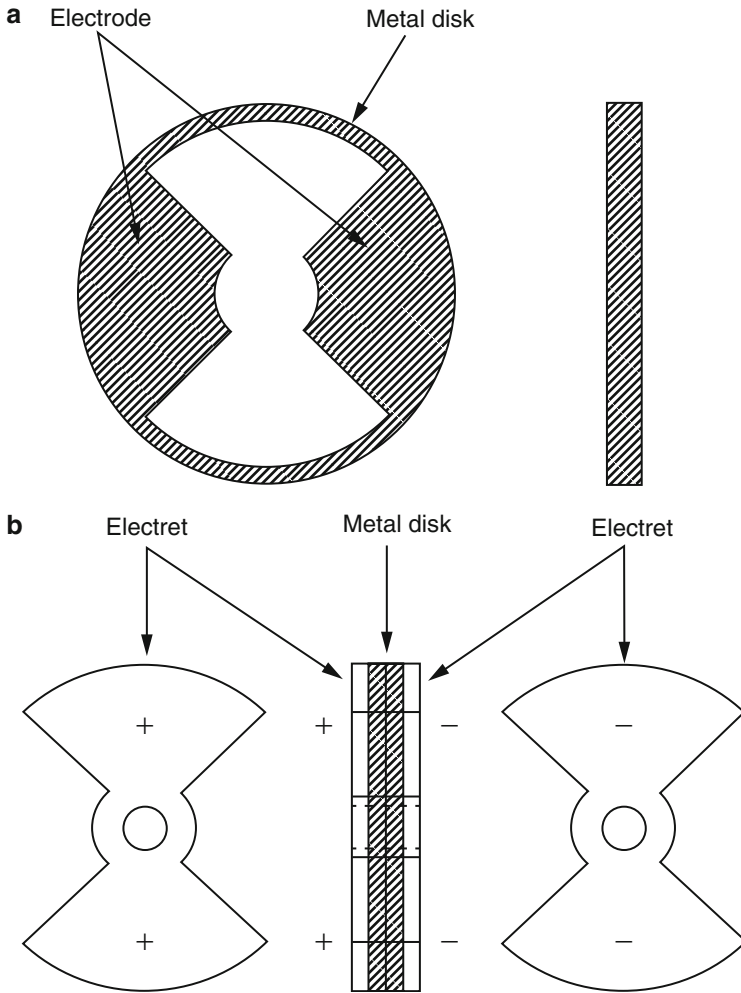


Fig. 9 Electret motor using the slot effect. (a) One of two disks of a 2-pole stator, (b) complex structure rotor of which pole number 2 (Tada 1993) (Reproduced with permission from IEEE)

distance between the electret and the counter electrode, respectively. The optimum load R_i is

$$R_i = \frac{1}{\epsilon_0 n A_0 f} \left(\frac{g}{\epsilon_1} + \frac{d}{\epsilon_2} \right), \quad (10)$$

and the output voltage and the maximum power at the matched impedance are

$$P_{\max} = \frac{\sigma^2 \cdot nA_0 f}{4 \frac{\varepsilon_2 \varepsilon_0}{d} \left(\frac{\varepsilon_2 g}{\varepsilon_1 d} + 1 \right)} = \frac{\varepsilon_0 V_s^2 \cdot nA_0 f}{4 \left(\frac{g}{\varepsilon_1} + \frac{d}{\varepsilon_2} \right)}, \quad (11)$$

$$V_{\max} = \frac{\sigma d}{2\varepsilon\varepsilon_0} = \frac{V_s}{2}, \quad (12)$$

where V_s is the surface potential of electret. It can be seen in Eq. 11 that the output power is proportional to the frequency f and the area A_0 . On the other hand, in electromagnetic generators, the output power is proportional to $(A_0 f)^2$. Therefore, electret generators are superior to electromagnetic counterparts for small area and low operation frequency. In addition, as shown in Eq. 12, the output voltage is independent on f or A_0 , showing high output voltage of electret generators, which is another advantage of electret generators (Fig. 10).

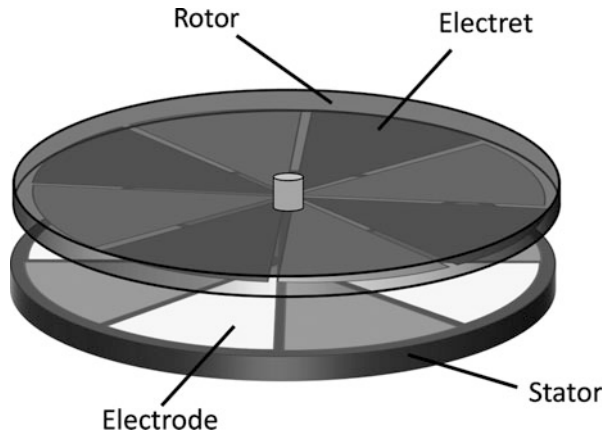
In Eq. 11, since the output power is proportional to V_s^2 , development of electret materials with high surface potential is crucial for larger output power. Note that Eq. 11 overestimates the output power P_{\max} when the parasitic capacitance C_p has a finite value. In addition, R_i given by Eq. 10 overestimates the matched impedance.

Bartsch et al. (2009) incorporated the effect of the parasitic capacitance for rotational generators and derived an analytical formula for the output power:

$$P = \frac{d^2 \sigma^2 R}{\varepsilon_2^2 \varepsilon_0^2 (R + R_i)^3} \left\{ R + R_i - 4C_p n f R R_i \tanh \left(\frac{R + R_i}{4C_p n f R R_i} \right) \right\}, \quad (13)$$

They demonstrated that Eq. 13 can mimic the response of generators for different values of C_p . Equation 11 is recovered by setting $C_p = 0$ in Eq. 13. Note that both Eqs. 11 and 13 can only be applied to rotational generators, in which the rate of change in the overlapping area is constant.

Fig. 10 Rotational electret generator



3.2 Vibration Energy Harvester

Energy harvesting is a method to capture energy naturally present in the environment for the purpose of powering low-power electronics such as wireless sensors and wearable devices (Roundy et al. 2003; Beeby et al. 2006; Mitcheson et al. 2008; Vullers et al. 2009). Body heat, human motion, mechanical/structural vibration, radio frequency, and ambient light can be the energy source. Among them, vibration is believed to be the most widely distributed in the environment. Since the vibration frequency range existing in the environment is below 100 Hz, electret power generators should have higher output power than electromagnetic generators.

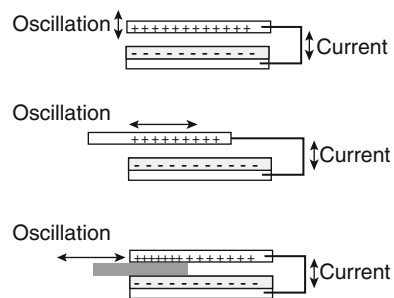
Figure 11 shows different configurations of electret generator. In the gap-closing type, the capacitance between the electret and the electrode is a nonlinear function of the amplitude, and the output power becomes large when the minimum gap during vibration is small. On the other hand, the output power diminishes when the amplitude is much smaller than the initial gap.

In the overlapping-area-change type, the capacitance change is a linear function of the amplitude. In this approach, large electrostatic attractive force acts between the substrates due to high surface potential of the electret. Thus, the gap control is crucial, since the stiction should be avoided while keeping the gap on the order of 10 μm . In the permittivity change type, material with high permittivity is inserted in between the electrode and the electret.

Chiu and Lee (2013) and Takahashi (2013) separately developed an out-of-plane electret generator having a similar structure of Fig. 11a. Figure 12 shows the device developed by Takahashi (2013), in which amorphous fluorinated polymer CYTOP (Asahi Glass) is used as the electret. Up to 50 μW at 29 Hz and 1.6 G (G: gravity acceleration) is obtained. Boisseau et al. (2011) prototyped a cantilever-shaped out-of-plane generator with a mass and an electrode on the cantilever tip. Advantage of this type of generators is that a plain electret layer can be used, by which charging issues for patterned electrets could be avoided. However, to suppress permanent stiction and to obtain higher output power with larger oscillation amplitude, device thickness is usually much larger than in-plane generators.

Lo and Tai (2008) developed an electret generator without tethers. The rotor can slide freely relative to the stator, and then induced charges on the electrodes vary with the position of the rotor. With a rotor coated with parylene

Fig. 11 Different configurations of electret generator. (a) Gap closing, (b) Overlapping-area change, (c) Permittivity change



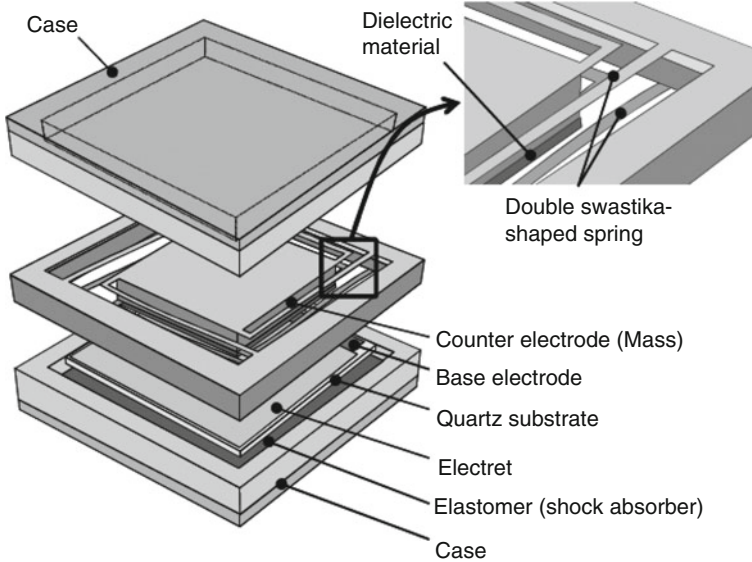


Fig. 12 Gap-closing electret generator with out-of-plane vibration (Takahashi 2013) (Reproduced with permission from IEEE)

HT electrets ($5 \text{ mm} \times 6 \text{ mm} \times 9 \text{ mm}$), a maximum output power of $18 \text{ }\mu\text{W}$ was obtained at 50 Hz vibration.

Masaki (2011) developed an in-plane electret generator ($20 \text{ mm} \times 20 \text{ mm} \times 4 \text{ mm}$) as shown in Fig. 13. They employed CYTOP EGG electret (Sakane et al. 2008; Kashiwagi et al. 2011), which enables high surface charge density of 2 mC/m^2 at the film thickness of $15 \text{ }\mu\text{m}$. Glass plates with patterned electrodes and electrets are fabricated with MEMS technologies, and the other parts are made with precision machining. The total weight of the generator is only 3.7 g. They employ a low-friction mechanical support to keep the gap. They also devised a trench between the stripe-shaped electrodes to reduce the parasitic capacitance and obtained output power as large as $100 \text{ }\mu\text{W}$ at 30 Hz and 0.15 G acceleration.

Suzuki et al. (2010) and Matsumoto et al. (2011) developed a MEMS electret generator as shown in Fig. 14. The top substrate consists of a Si proof mass ($11.6 \text{ mm} \times 10.2 \text{ mm}$) supported by the $20\text{-}\mu\text{m}$ -wide parylene high-aspect-ratio springs (Suzuki and Tai 2006) for low resonant frequency. A nonlinear hardening spring enables large amplitude in the wide frequency range. Patterned electrets and electrodes in a dual-phase arrangement are formed on both the Si mass and the bottom substrate. Electrostatic repulsive force using the patterned electret is used to keep the gap at around $35 \text{ }\mu\text{m}$. The width of the patterned electret and electrode is $480 \text{ }\mu\text{m}$. Up to output power of $6 \text{ }\mu\text{W}$ is obtained at 40 Hz and 1.4 G acceleration. They also demonstrated intermittent RF transmission using the output power of this generator.

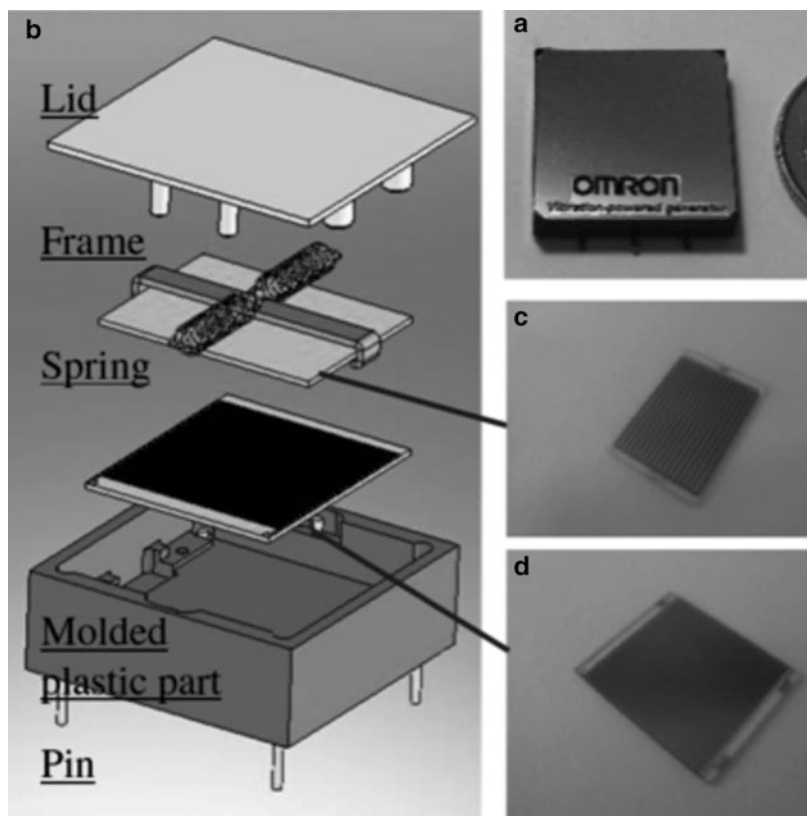


Fig. 13 In-plane electret generator fabricated with precision machining (Masaki 2011) (Courtesy of Dr. T. Seki)

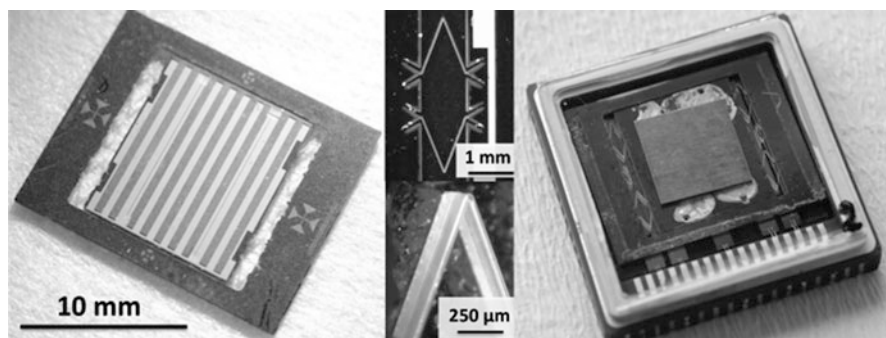


Fig. 14 In-plane energy harvester with CYTOP electret and parylene high-aspect-ratio spring (Suzuki et al. 2010)

Naruse et al. (2009) used a micro-ball bearing to realize large amplitude oscillation in their electret generator. They employ SiO₂-based electrets with an air gap of 38–57 μm. By using an in-plane amplitude as large as 15 mm, they obtained an output power of 40 μW at a very-low-frequency vibration of 2 Hz at 0.4 G acceleration.

Sonoda et al. (2015) developed an electret generator with a Si spring. They employed a plain CYTOP film on interdigital electrodes as the electret, made slits in between the fixed electrodes, and used the slits as the grid for the corona charging after assembling. By applying appropriate voltage to each side of the electrode, they can make selective corona charging for positive and negative charge stripes on the CYTOP film. A maximum output power of 9.8 μW has been obtained at 352 Hz and 7 G acceleration.

Renaud et al. (2013) developed a high-frequency electret generator with a Si spring. They first etch a Si substrate to form 250-μm-wide striped-shaped recesses with a depth of 100 μm and oxidized the substrate to form a corrugated surface with a SiO₂-Si₃N₄ electret layer. The air gap and the maximum amplitude are 10 μm and 100 μm, respectively. They obtained output power up to 160 μW at 728 Hz and 2.9 G acceleration.

Although comb drives are often used for electrostatic generators, corona charging cannot be applied, since the possible charge accumulation near the gap opening suppresses penetration of corona ions into the gap. Sterken et al. (2003) employed electret for priming charge to the comb-drive capacitors, but the possible stiction due to electrostatic attractive force impedes this approach.

Suzuki et al. (2012) used a bias-temperature method for drifting potassium ions in potassium-rich SiO₂ electret at 700 K. They obtained up to 90 V surface potential on the comb finger. They also prototyped in-plane overlapping-area-change electret generator using this charging technology.

Fu and Suzuki (2014) used the soft-X-ray charging method (Hagiwara et al. 2012) for in-plane comb-drive electret generator with a 7-μm-wide gap. They confirmed that up to ±60 V surface potential is obtained with the bias voltage of 130 V through the surface potential measurement using Kelvin force microscopy. Figure 15 shows their prototype using the SOI process. They obtained up to 1.6 μW at 266 Hz and 2 G acceleration. The conversion efficiency is as high as 57 %.

Piezoelectrets/ferroelectrets are also employed for vibration energy harvesting.

Pondrom et al. (2015) prototyped an out-of-plane vibration energy harvester using PP-based piezoelectret films. They employed a 40 g mass and obtained 18 μW at 140 Hz and 1 G with a single layer of the piezoelectret film of 25 mm².

Luo et al. (2015) employed a stacked EMFi films up to 80 layers and made a power generator for insole. With the stack of 60 mm × 70 mm, 100 μJ/step has been obtained, enabling one 8-bit wireless data transmission every 3–4 steps with a ZigBee transmitter.

Figure 16 shows (Feng et al. 2012) MEMS piezoelectret energy harvester using cellular parylene structure. Using trench-filling parylene technology, high-aspect-ratio (HAR) cellular parylene spring ($t_p = 15 \mu\text{m}$, $t_g = 25 \mu\text{m}$, height of the

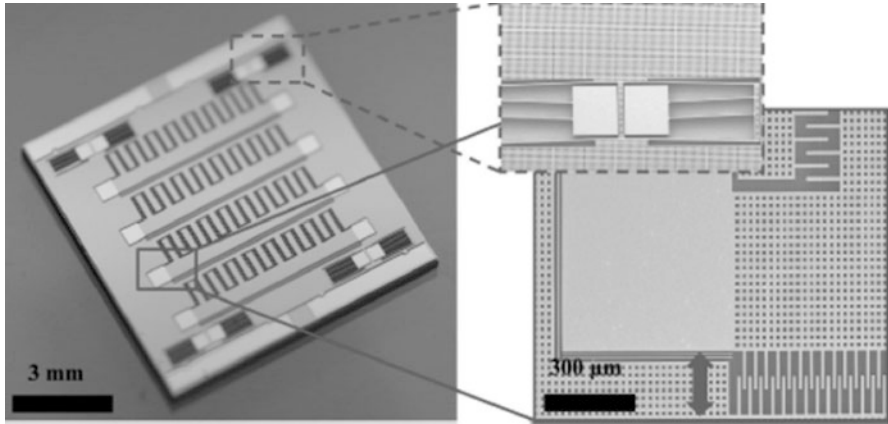


Fig. 15 Soft-X-ray-charged in-plane comb-drive electret generator (Fu and Suzuki 2014)

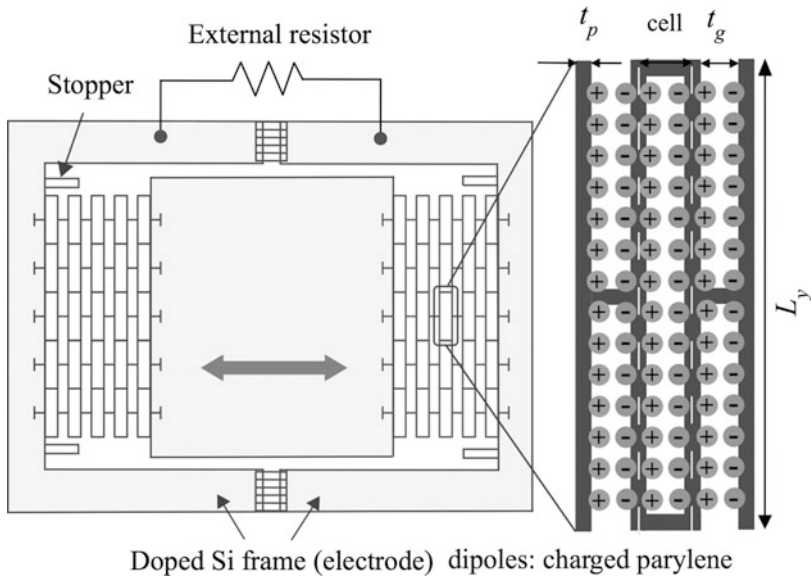


Fig. 16 MEMS piezoelectret energy harvester using cellular parylene structure. $t_p = 15 \mu\text{m}$, $t_g = 25 \mu\text{m}$, and $L_y = 8.2 \text{ mm}$ (Feng et al. 2012)

honeycomb = $350 \mu\text{m}$, and $L_y = 8.2 \text{ mm}$) is obtained for in-plane low-frequency piezoelectret transducers. The sidewalls of the cellular parylene structure are charged using soft-X-ray irradiation (Hagiwara et al. 2012), and high piezoelectric sensitivity up to 960 V/N at its resonant frequency of 149 Hz has been obtained. Output power of the similar early prototype (Feng and Suzuki 2014) is 53 nW at 205 Hz and 2 G .

4 Summary

For conventional applications such as microphones or air filter, surface potential on the order of 10 V is sufficient. Therefore, the main research focus was on development of low-cost electret material using hydrocarbon polymer. However, for energy harvesting, high surface potential is necessary. This triggers recent developments of higher performance electret materials as well as various prototype energy harvesters, which can make a significant contribution toward further expansion of electret applications.

References

- Atoji N, Aoi T (1974) Electrostatic acoustic transducer. US Patent No 3,833,770
- Baia MR et al (2010) Experimental modeling and design optimization of push-pull electret loudspeakers. *J Acoust Soc Am* 127:2274–2281
- Bartsch U et al (2009) Influence of parasitic capacitances on the power output of electret-based energy harvesting generators. In: 9th international workshop micro and nanotechnology for power generation and energy conversion applications (PowerMEMS 2009), Washington, DC, pp 332–335
- Beeby SP et al (2006) Energy harvesting vibration sources for micro systems applications. *Meas Sci Technol* 17:175–195
- Boisseau S et al (2011) Cantilever-based electret energy harvester. *Smart Mater Struct* 20(10):105013
- Boland J et al (2003) Micro electret power generator. In: 16th IEEE international conference micro electro mechanical systems (MEMS'03), Kyoto, pp 538–541
- Bruneel JL, Micheron F (1977) Optical display device using bistable electrets. *Appl Phys Lett* 30(8):382–383
- Cao Y et al (1998) Study of porous dielectrics as electret materials. *IEEE Trans Dielectr Electr Insul* 5(1):58–62
- Chen YC et al (2012) Tailoring the performance of flexible electret loudspeakers by varying cell actuator formation. *IEEE Trans Dielectr Electr Insul* 19(4):1094–1100
- Chiang DM et al (2005) PALS and SPM/EFM investigation of charge nano-porous electret films. *Chem Phys Lett* 412(1–3):50–54
- Chiu Y, Lee YC (2013) Flat and robust out-of-plane vibrational electret energy harvester. *J Micromech Microeng* 23(1):015012
- Feng Y et al (2012) Trench-filled cellular parylene electret for piezoelectric transducer. *Appl Phys Lett* 100(26):262901
- Feng Y, Suzuki Y (2014) All-polymer piezoelectret energy harvester with embedded PEDOT electrode. In: 27th IEEE international conference micro electro mechanical systems (MEMS'14), San Francisco, pp 374–377
- Fu Q, Suzuki Y (2014) MEMS vibration electret energy harvester with combined electrodes. In: 27th IEEE international conference micro electro mechanical systems (MEMS'14), San Francisco, pp 409–412
- Goto M et al (2011) Development of silicon electret condenser microphone with SiO₂/Si₃N₄ electret. In: Proceedings of the 37th international conference micro and nano engineering (MNE 2011), O-MEMS-29, Berlin, p 417
- Hagiwara K et al (2010) Soft X-ray charging method for a silicon electret condenser microphone. *Appl Phys Exp* 3(9):091502
- Hagiwara K et al (2012) Electret charging method based on soft X ray photoionization for MEMS transducers. *IEEE Trans Dielectr Electr Insul* 19(4):1291–1298

- Hillenbrand J, Sessler GM (2000) Piezoelectricity in cellular electret films. *IEEE Trans Dielectr Electr Insul* 7(4):537–542
- Horino T et al (2012) Application of cellular polypropylene to ultrasonic transducers in water. *Proc Symp Ultrasonic Electr* 33:525–526
- Hsieh WH et al (1997) A micromachined thin-film Teflon electret microphone. *Int Conf Solid-State Sensors Actuators* 1:425–428
- Ichiya M et al (1995) Electrostatic actuator with electret. *IEICE Trans Electron* E78-C(2):128–131
- Ikeya M, Miki T (1980) Electret dosimeter utilizing as multiplication. *Health Phys* 39(5):797–799
- Jefimenko O, Walker DK (1971) Electrostatic motors. *Phys Teach* 9(3):121–128
- Jefimenko O, Walker DK (1978) Electrostatic current generator having a disk electret as an active element. *IEEE Trans Ind Appl IA-14*(6):537–540
- Kashiwagi K et al (2011) Nano-cluster-enhanced high-performance perfluoro-polymer electrets for micro power generation. *J Micromech Microeng* 21(12):125016
- Kawakami H (1969) An electrostatic condenser type phonograph pickup cartridge. *Audio Eng Soc* 693:B-3
- Kodama H et al. (2009) A study of time stability of piezoelectricity in porous polypropylene electrets. In: *Proceedings of IEEE international ultrasonics symposium, Roma*, pp 1730–1733
- Lekkala J, Paayanan M (1999) EMFi – new electret material for sensor and actuators. In: *Proceedings of the 10th international symposium on electrets, Athens*, pp 743–746
- Luo Z et al (2015) Multilayer ferroelectret-based energy harvesting insole. *J Phys Conf Ser* 660:012118
- Lo HW, Tai YC (2008) Parylene-based electret power generators. *J Micromech Microeng* 18(10):104006
- Masaki T (2011) Power output enhancement of a vibration-driven electret generator for wireless sensor applications. *J Micromech Microeng* 21(10):104004
- Matsumoto K et al (2011) Vibration-powered battery-less sensor node using electret generator. In: *11th international workshop on micro and nanotechnology for power generation and energy conversion applications (PowerMEMS 2011)*, Seoul, pp 134–137
- Mellow T, Karkkainen L (2008) On the forces in single-ended and push-pull electret transducers. *J Acoust Soc Am* 124(3):1497–1504
- Mitcheson EM et al (2008) Energy harvesting from human and machine motion for wireless electronic devices. *Proc IEEE* 96:1457–1486
- Naruse Y et al (2009) Electrostatic micro power generator from low frequency vibration such as human motion. *J Micromech Microeng* 19(9):094002
- Neugschwandtner GS et al (2000) Large and broadband piezoelectricity in smart polymer-foam space-charge electrets. *Appl Phys Lett* 77(23):3827–3829
- Paajanen M et al (1998) Electro-mechanical film EMFi—a new multipurpose electret material. *Sensors Actuators A* 84(1–2):95–102
- Paajanen M et al (2001) Electro-mechanical modeling and properties of the electret film EMFi. *IEEE Trans Dielectr Electr Insul* 8(4):629–636
- Pondrom P et al (2015) Energy harvesting with single-layer and stacked piezoelectret films. *IEEE Trans Dielectr Electr Insul* 22(3):1470–1476
- Roundy S et al (2003) A study of low level vibrations as a power source for wireless sensor nodes. *Comput Commun* 26(11):1131–1144
- Reinhard L et al (2007) Broadband ultrasonic transducer. In: *19th international congress on acoustics, Madrid*
- Renaud M et al (2013) High performance electrostatic MEMS vibration energy harvester with corrugated inorganic $\text{SiO}_2\text{-Si}_3\text{N}_4$ electret. In: *17th international conference solid-state sensors, actuators, and microsystems (transducers' 13)*, Barcelona, pp 693–696
- Sakamoto N et al (1975) Frequency response of an electrostatic horn-tweeter with electret. In: *52th audio engineering society convention*, p 1064, Audio Engineering Society, New York
- Sakamoto N et al (1979) Design of low distortion condenser microphone using push-pull electret transducer. In: *64th audio engineering society convention*, New York, p 1517

- Sakane Y et al (2008) Development of high-performance perfluorinated polymer electret film and its application to micro power generation. *J Micromech Microeng* 18(10):104011
- Sato R, Takamatsu T (1986) An electret switch. *IEEE Trans Electr Insul* 32(3):449–455
- Schaffert RM (1975) *Electrophotography*. Wiley, New York
- Sessler GM, West JE (1962) US Patent 3,118,022
- Sessler GM et al (1973) New touch actuator based on the foil-electret principle. *IEEE Trans Com* 21(1):61–65
- Sessler GM, West JE (1973) Electret transducers: a review. *J Acoust Soc Am* 53(6):1589–1600
- Sessler GM, West JE (1987) Applications. In: Sessler GM (ed) *Electret*, vol 33, Topics in applied physics. Springer, Berlin, pp 347–381
- Son C, Babak Z (2006) A micromachined electret-based transponder for in-situ radiation measurement. *IEEE Electr Dev Lett* 27(11):884–886
- Sonoda K et al (2015) Improvement of power generation in low acceleration for electrostatic energy harvester by using bipolar charging method. *IEEJ Trans Sens Micromach* 135(9):372–377
- Sterken T et al (2003) An electret-based electrostatic μ -generator. In: 12nd international conference solid-state sensors, actuators and microsystems (transducers '03), Boston, pp 1291–1294
- Suzuki Y, Tai YC (2006) Micromachined high-aspect-ratio parylene spring and its application to low-frequency accelerometers. *J Microelectromech Syst* 15(5):1364–1370
- Suzuki Y et al (2010) A MEMS electret generator with electrostatic levitation for vibration-driven energy harvesting applications. *J Micromech Microeng* 20(10):104002
- Suzuki Y (2011) Recent progress in MEMS electret generator for energy harvesting. *IEEJ Trans Electr Electr Eng* 6(2):101–111
- Suzuki M et al (2012) Electrostatic micro power generator using potassium ion electret forming on a comb-drive actuator. In: 12nd Int. Workshop micro and nanotechnology for power generation and energy conversion applications (PowerMEMS 2012), Atlanta, pp. 247–250
- Tada Y (1992) Experimental characteristics of electret generator using polymer film electrets. *Jpn J Appl Phys* 31(3):846–851
- Tada Y (1993) Improvement of conventional electret motors. *IEEE Trans Electr Insul* 23(3):402–410
- Takahashi T (2013) A miniature harvester of vertical vibratory capacitive type achieving several tens microwatt for broad frequency of 20–40 Hz. In: 17th international conference solid-state sensors, actuators, and microsystems (transducers' 13), Barcelona, pp 1340–1343
- Thakur R, Das D, Das A (2013) Electret air filters. *Sep Purif Rev* 42(2):87–129
- van Turnhout J et al (1980) Electret filters for high-efficiency air cleaning. *J Electrostat* 8(4):369–379
- Vullers R et al (2009) Micropower energy harvesting. *Solid-State Electron* 53:684–693
- Yasuno Y, Riko Y (1999) An approach to integrated electret electroacoustic transducer -Experimental digital microphone. In: Proceedings of the 10th international symposium on electret (ISE10), Athens, pp 727–730
- Yasuno Y et al (2010) Electro-acoustic transducers with cellular polymer electrets. In: 20th international congress on acoustics, Sydney
- Zhang X et al (2007) Improvement of piezoelectric coefficient of cellular polypropylene films by repeated expansions. *J Electrostatics* 62:94–100

Dmitry Rychkov and Ruy Alberto Pisani Altafim

Contents

1 Models of Charge Decay in Polymer Electrets	646
2 Ferroelectret: Electret Microphone Model	654
3 Conclusion	657
References	657

Abstract

Ferroelectrets are a new class of electroactive polymers. These materials are highly heterogeneous and represent, in essence, a composite made of nonpolar polymer and air. The surfaces of inner cavities obtained via foaming, inflation, or templating can be charged with dielectric barrier discharges, thus creating large macroscopic dipoles with high piezoelectric response. The stability of the piezoelectricity is determined by how well the polymer material can retain these charges, i.e., by its electret properties. Thus, thermal and temporal stability of the ferroelectret is governed by processes of charge transport and storage in the polymer it is made of. In this chapter we will discuss several alternative models of charge decay in polymers as well as a simple model for piezoelectric coefficient, based on electret microphone principle.

Keywords

Electrets • Ferroelectrets • Charge storage • Charge transport • Charge decay models

D. Rychkov (✉)

Institute of Physics and Astronomy, University of Potsdam, Potsdam, Germany
e-mail: rychkov@uni-potsdam.de

R.A.P. Altafim

Departamento de Sistemas de Computação, Federal University of Paraíba, João Pessoa, PB, Brazil
e-mail: altafim@gmail.com

1 Models of Charge Decay in Polymer Electrets

Most of the modern theories (Berlepsch 1985, 1991; Chen 2010; Chudleigh 1977; Kanazawa et al. 1972; Kiess and Rehwald 1980; Kressman et al. 1999; Le Roy et al. 2004; Remke and Seggern 1983; Rychkov et al. 1992; Seggern 1979; Sessler 1999; Tang et al. 2007; Toomer and Lewis 1980; Watson 1990; Watson et al. 1991; Wintle 1971; Xu et al. 2007) attribute the electret state relaxation in nonpolar polymers to the process of charge transport in its own electric field. At the same time, the intrinsic ohmic conductivity of the polymer is considered to be so small as to have no influence on the charge transport.

For nonpolar fluoropolymers these considerations have a solid experimental basis. For example, the charge transport through the sample in the direction of the electrode surface is confirmed by direct charge profiling methods (Chen et al. 2007; Dang et al. 2006; Kressman et al. 1999; Künstler and Gerhard-Multhaupt 1997; Montanari et al. 2001; Rychkov and Gerhard 2011; Sessler 1999; Sessler et al. 1992; Teysseire et al. 2001) as well as some additional experiments (Boitzov et al. 1990; Seggern et al. 1984).

Most of the electrets are in fact heterogeneous structures containing at least one polymer-metal interface. Such heterogeneous nature is typically not taken into account, and electret state is assumed to be solely a bulk phenomenon. Besides, most of the models postulate that charge transport is controlled by monoenergetic traps. Obviously, such simplifications lead to discrepancies between model predictions and experimentally obtained data. However, charge decay in nonpolar polymer-metal structures is usually modeled based on the following assumptions:

- There is no interaction with the environment.
- There is no charge injection from the electrode.
- Diffusion component of the current can be neglected.
- There is no dipolar polarization.
- Electret decay is due to the charge drifting in its own electric field and ohmic current tending to compensate the excess charge.

As a result the net current can be represented as a sum of the displacement current and conduction current:

$$j(t) = \varepsilon\varepsilon_0 \frac{\partial F(x, t)}{\partial t} + j_c(x, t), \quad (1)$$

where the conduction current density is given by

$$j_c(x, t) = [\gamma + \mu\rho(x, t)] \cdot F(x, t) \quad (2)$$

In Eq. 2 $\gamma = q(n^+ \mu^+ + n^- \mu^-)$ is the uniform conductivity and $\mu\rho(x, t)F(x, t)$ is the component of the excess charge current ($F(x, t)$, internal electric field of the electret). For the non-shortcd sample, $j(t) = 0$, and thus,

$$\varepsilon\varepsilon_0 \frac{\partial F(x, t)}{\partial t} + [\gamma + \mu\rho(x, t)] \cdot F(x, t) = 0 \quad (3)$$

The above formula is valid when there is no trapping, as well as when the retrapping is fast. In the latter case, μ should be considered as trap-modulated mobility (Anta et al. 2002; Kiess and Rehwald 1980; Montanari et al. 2001). Using Poisson equation and taking into account that the surface potential V is the integral of $F(x, t)$, Eq. 3 can be integrated and solved with respect to V to obtain the following:

$$\tau_\gamma \frac{dV(t)}{dt} + \frac{1}{2}\mu\tau_\gamma F^2(L, t) + V(t) = 0, \quad (4)$$

where $\tau_\gamma = \varepsilon\varepsilon_0\gamma^{-1}$ is the Maxwell's relaxation time. Equation 4 can be analyzed using the notion of charge carrier's time of flight, which at zero conductivity equals

$$t_T = L^2[\mu V_0]^{-1} \quad (5)$$

Generally, if $\gamma \neq 0$ the time of flight is given by (Kanazawa et al. 1972)

$$t_{T\gamma} = \tau_\gamma \cdot \ln\left(\frac{\tau_\gamma}{\tau_\gamma - t_T}\right) \quad (6)$$

If $t \leq t_{T\gamma}$, then the homocharge has not yet reached the metal electrodes and

$$F(L, t) = F(L, 0)\exp(-t/\tau_\gamma). \quad (7)$$

If $t > t_{T\gamma}$, then the sample will have a homogenous charge density distribution $\rho(x)$, and

$$V(t) = 0, 5F(L, t)L \quad (8)$$

As a result, the surface potential decay in both cases can be described as follows:

$$\frac{V(t)}{V_0} = \exp\left(-\frac{t}{\tau_\gamma}\right) \left[1 - \frac{1}{2}\left(\frac{\tau_\gamma}{t_T}\right) \left(1 - \exp\left(-\frac{t}{\tau_\gamma}\right)\right)\right], \quad t \leq t_{T\gamma} \quad (9)$$

$$\frac{V(t)}{V_0} = \frac{1}{2} \cdot \frac{t_T}{\tau_\gamma} - \exp\left(-\frac{t}{\tau_\gamma}\right) \left[1 - \exp\left(-\frac{t}{\tau_\gamma}\right)\right]^{-1}, \quad t > t_{T\gamma} \quad (10)$$

If the conductivity is negligible, then according to the model by Batra (Batra et al. 1970),

$$\frac{V(t)}{V_0} = 1 - \frac{1}{2} \cdot \frac{t}{t_T}, \quad t < t_T \quad (11)$$

$$\frac{V(t)}{V_0} = \frac{1}{2} \cdot \frac{t_T}{t}, \quad t \geq t_T \quad (12)$$

Homocharge transport has also been considered in models that allow for deep trapping in the bulk of the film. For example, in the model by Wintle (1971), quasi-free carriers drift through the dielectric with conductivity $\gamma = 0$ and fill the deep traps of one sort where they are trapped interminably. As a result, the surface potential decay is described via the following equations:

$$\frac{V(t)}{V_0} = 1 - \frac{1}{2} \cdot \frac{\tau_n}{t_{Tn}} \left[1 - \exp\left(-\frac{t}{\tau_n}\right) \right], \quad t < t_{Tn} \quad (13)$$

$$\frac{V(t)}{V_0} = \frac{1}{2} \cdot \frac{t_{Tn}}{\tau_n} \left[1 - \exp\left(-\frac{t}{\tau_n}\right) \right]^{-1}, \quad t \geq t_{Tn} \quad (14)$$

where $\tau_n = \varepsilon\varepsilon_0(\mu_C q N_t)^{-1}$ is the relaxation time, μ_C is the free carrier mobility, N_t is the concentration of deep traps, and t_{Tn} is the time of flight given by Eq. 6 where τ_γ is replaced with τ_n .

From Equation 14 it is obvious that the electret will never discharge completely in Wintle's model. If a charge lifetime in the trap is finite, then the surface potential of the electret structure should, in time, reduce to zero. Homocharge relaxation in this case is determined by the three following parameters: the mobility of the quasi-free charge carriers μ , the mean free time of a carrier between traps τ_F , and the mean capture time in a deep trap τ_T . The presence of volume densities of the quasi-free and trapped charge carriers in the sample (ρ_F and ρ_T) modifies somewhat the system of equations governing the homocharge transport (Chudleigh 1977):

$$\varepsilon\varepsilon_0 \frac{\partial F(x,t)}{\partial t} + \mu \rho_F(x,t) \cdot F(x,t) = 0 \quad (15)$$

$$\frac{\partial F(x,t)}{\partial x} + \frac{1}{\varepsilon\varepsilon_0} (\rho_F(x,t) + \rho_T(x,t)) \quad (16)$$

$$\frac{\partial \rho_T(x,t)}{\partial t} = \frac{\rho_F(x,t)}{\tau_F} - \frac{\rho_T(x,t)}{\tau_T} \quad (17)$$

This system of equations can be numerically solved with a suitable choice of initial and boundary conditions. Thus, in the model by Chadleigh (1977), the homocharge at $t = 0$ is immediately injected into the bulk and the boundary condition for the electric field on the surface is

$$F(0,t) = 0 \quad (18)$$

The calculations indicate that, in this case, at $t < t_T$ surface potential decay kinetics is practically identical with that predicted by Batra's model (11). At the final stages, however, the decay proceeds slower than in the models that do not take into account

deep trapping. Recently the above models were further developed (Barybin and Shapovalov 2008; Barybin et al. 2012) to include more complex discharge mechanisms that consider drift, deep trapping, finite conductivity, as well as surface-localized states. As a result, the solution contains, at least, three to four fitting parameters.

Polymers as highly disordered materials are characterized by a very broad spectrum of localized states. That is why homocharge transport in polymers occurs under conditions of continuous and repeated trapping in energy-distributed localized states. In the above models, this was addressed by assuming a simplified two discrete levels trap distribution – shallow and deep traps. A rigorous consideration was carried out by Arkhipov and Rudenko (Arkhipov et al. 1987; Rudenko and Arkhipov 1978). In their works the process of charge localization and delocalization is described within the following equations:

$$n(x, t) = n_c(x, t) + \int_0^{\infty} \rho(x, t, E) dE \quad (19)$$

$$\frac{\partial \rho(x, t, E)}{\partial t} = \frac{1}{\tau_0} \left[\frac{N(E)}{N_l} \right] \cdot n_c(x, t) - \frac{1}{\tau_0} \left[\frac{N_c}{N_l} \right] \cdot \exp\left(-\frac{E}{kT}\right) \cdot \rho(x, t, E) \quad (20)$$

where n is the net density of charge carriers, n_c is the density of delocalized carriers, NdE is the density of the localized state in the interval from E to $E + \Delta E$, ρdE is the population density of the localized states, τ_0 is the lifetime of delocalized carriers, and N_l and N_c are the densities of localized and delocalized states, respectively.

In open-circuit conditions, Eqs. 19 and 20 are, as usual, supplemented with net current and Poisson equations:

$$q\mu_c n_c(x, t) \cdot F(x, t) + \varepsilon \varepsilon_0 \frac{\partial F(x, t)}{\partial t} = 0 \quad (21)$$

$$\frac{\partial F(x, t)}{\partial x} = \frac{q}{\varepsilon \varepsilon_0} n(x, t) \quad (22)$$

with initial and boundary conditions as follows:

$$F(x, 0) = V_0/L = F_0 \quad (23)$$

$$F(0, t) = F_0(1 - p), \quad 0 < p \leq 1 \quad (24)$$

where p is the parameter that determines the level of injection.

The general solution obtained by Arkhipov and Rudenko for the arbitrary energy distribution of localized states is rather difficult for the analysis and determination of the distribution function ($N(E)$) based only on experimental $V(t)$ curves. If, however, the type of the distribution function is known, then the parameters of the energy spectrum can be easily obtained from experimental curves. For example, for the exponential distribution of the type,

$$N(E) = \frac{N_t}{E_0} \exp\left(-\frac{E}{E_0}\right) \quad (25)$$

it has been shown that the time dependence of the surface potential relaxation rate can be described with the following set of equations:

$$\frac{dV(t)}{dt} \sim t^{-(1-\alpha)}, \quad t \leq t_T^* \quad (26)$$

$$\frac{dV(t)}{dt} \sim t^{-(1+\alpha)}, \quad t > t_T^* \quad (27)$$

where t_T^* is the characteristic time which sometimes is described as a charge packet time of flight; and

$$\alpha = KT[\Delta E_0]^{-1} \quad (28)$$

is the dispersion parameter (ΔE_0 , trap energy spectrum dispersion).

Equations of this type (Eqs. 26 and 27) describe reasonably well the discharge in the range of corona electrets – in particular in polyethylene (Berlepsch 1991). This model, however, disagrees considerably with experimental data obtained for non-polar fluoropolymers, notably those charged in positive corona. In this case the model does not take into account homocharge trapping in surface and near-metal layers.

The necessity to allow for the deep trapping in the surface layer has been acknowledged for a long time already (Batra et al. 1970; Lewis 1990; Rychkov et al. 1992; Seggern 1979). Thus, in Batra's model the influence of the surface traps is taken into account via the notion of "instant injection" of the surface homocharge. In this model at $t = 0$, only a part p of the initial homocharge is instantly transferred into the bulk, while the rest of the charge $(1-p)\sigma_0$ remains trapped in the deep surface traps. This results in the following equations for $V(t)$:

$$\frac{V(t)}{V_0} = 1 - \frac{1}{2}p(2-p)\frac{t}{t_T}, \quad 0 \leq t \leq t_T \quad (29)$$

$$\frac{V(t)}{V_0} = \frac{1}{2} \left[\frac{t_T}{t} + (1-p)^2 \frac{t}{t_T} \right], \quad t_T \leq t \leq t_F \quad (30)$$

$$\frac{V(t)}{V_0} = 1 - p, \quad t > t_F \quad (31)$$

where $t_F = t_T(1-p)^{-1}$ is the time of flight of the rear front of charge carriers.

In publication by Berlepsch (1985), Batra's model was further developed taking into account the charge trapping in shallow and deep traps in the bulk. For the time values that are less than the time of flight, the following equation has been obtained:

$$\frac{V(t)}{V_0} = 1 - \frac{1}{2}\mu V_0 L^{-2} \left[1 - (1-p)^2 \right] \frac{1}{R} \left[r_r t + \frac{r_t}{R} (1 - e^{-Rt}) \right] \quad (32)$$

where $R = r_r + r_t$, while r_r and r_t are the time constants for release and trapping in the deep traps, respectively. μ is the shallow-trap-controlled mobility. With carefully selected parameters, Eq. 32 could reasonably well describe the discharge of polyethylene electrets. However, it must be noted that the same experimental data were described by the author with Eqs. 26 and 27 equally well. This example shows that formal similarity between experimental and simulated curves is not enough to validate a model or to claim anything definite about the mechanisms of charge relaxation in polymer electrets.

The notion of “instant injection” gives an overly simplified picture of the homocharge transport from the surface layer into the bulk, as it does not allow for the activation nature of the charge release from the surface traps. This was remedied to a point by Sonnonstine and Perlman (1975) in a model where the boundary condition for the electric field on the surface is as follows:

$$F(0, t) = \frac{V_0}{L} \exp\left(-\frac{t}{\tau_s}\right) \quad (33)$$

where $\tau_s = \omega_s^{-1} \exp(E_s/kT)$ is the homocharge lifetime on the surface. The model was also extended for the case when the mobility is field dependent. As a result the obtained equations for $V(t)$ could very well qualitatively describe even the “cross-over” phenomenon observed in certain electret structures. The phenomenon manifests itself as $V(t)$ curves obtained at higher initial values of surface potential V_0 crossing those obtained for samples with lower V_0 (Chen 2010; Rychkov et al. 2011).

The idea of thermally activated charge transfer from the surface layer into the bulk is also employed in the model by Seggern (1979). In this model the system of Equations (15, 16, and 17) is considered with a boundary condition (33). The solutions for $V(t)$ are obtained numerically.

Toomer and Lewis (1980) while trying to account for the complexity of surface trap energy spectrum have assumed that the homocharge is held in the surface-localized states from which it has to be released prior to the transport through the bulk of the polymer. That is why in their model, the electric field on the surface is given by

$$F(0, t) = \frac{V_0}{L} \sum_n G_n \exp\left(-\frac{t}{\tau_{sn}}\right) \quad (34)$$

where G_n is the fraction of the charge on the surface with a lifetime of τ_{sn} . By limiting the times to be less than the time of flight and with some simplifying assumptions, the authors derived Equation (35) with which they later fitted experimental curves for polyethylene electrets. It has been found that the transfer of charge into the bulk of polyethylene film occurs as a result of activation from two to three different groups of surface traps:

$$V(t) = V_0 - \frac{\mu_C}{2R} \left(\frac{V_0}{L} \right)^2 \cdot \int_0^t \left(r_r + r_t \exp(-Rt) \cdot \left[1 - \left(\sum_n G_n \exp\left(-\frac{t}{\tau_{sn}}\right) \right)^2 \right] \right) dt \quad (35)$$

The common feature of the models discussed so far is the main mechanism of electret discharge – namely, the homocharge drift. Other mechanisms only modify to certain extent this fundamental process. In the literature, however, other models are quite widely spread (Kieß and Rehwald 1980; Watson 1990; Watson et al. 1991), where the main limiting mechanism for the electret discharge is the process of mobile charge carrier generation and not the drift. These models describe so-called emission-limited discharge, whereas the drift models describe the alternative case – “space-charge-limited discharge.”

In “emission-limited discharge” models during the whole discharge process, the drifting space charge is small and does not influence the electric charge distribution within the sample. The electric field is determined by the charges still not involved in the transport, instead. Thus, the electric field relaxes while retaining the initial spatial distribution. As a result, the surface potential decay of an electret is determined by the surface trap depletion rate or by the rate of emission of the compensation charge from the electrode. That is why surface potential relaxation in these models happens concurrently with the change in the surface charge density:

$$\frac{dV(t)}{dt} = \frac{1}{C} \cdot \frac{d\sigma(t)}{dt} \quad (36)$$

where C is the effective specific capacitance of the electret.

Known models describing “emission-limited discharge” differ in mechanisms responsible for the charge transfer from the surface into the bulk. Most often these mechanisms include Schottky emission, tunneling, and thermal activation from discrete traps (Abkowitz et al. 1995; Kressman et al. 1999; Sessler 1999). Publications that allow for the continuous spectrum of surface traps are relatively few in number (Watson 1990; Watson et al. 1991), although the need for such an approach is obvious due to the highly disordered nature of the polymer surface.

In nonpolar fluoropolymers relaxation of positive electret charge can be very well described based on the above assumption about the role of the surface traps and their non-discrete energy spectrum. In this case charges are thermally activated from the deep surface traps having quasi-continuous energy distribution. In the bulk, the homocharge drifts through the sample in the quasi-free state interacting with the shallow bulk traps (lifetime in the bulk trap is much smaller than that on the surface). The final discharge of the electret is possible only when the homocharge is released from the surface traps and recombined with the compensation charge. Based on the

theory by Simmons (Simmons and Tam 1973), the isothermal surface potential decay can be described as follows:

$$\frac{V(t)}{V_0} = 1 - kT \int_0^t \frac{1}{t} f_0^*(E_S) N^*(E_S) dt \quad (37)$$

where

$$E_S = kT \ln(\omega_S t) \quad (38)$$

In Eqs. 37 and 38, $f_0^*(E_S)N^*(E_S)$ is the arbitrary distribution function of the activation energy E_S for the occupied surface traps and ω_S is their frequency factor. It has been shown experimentally that the distribution function can be recovered from the isothermal surface potential decay data obtained at several different temperatures and plotted as $t \cdot (dV/dt)$ versus $\lg t$.

In case of thermally stimulated surface potential decay (Simmons et al. 1973), the temperature of the electret is being increased with a constant heating rate β and the decay itself is described by the following equations:

$$\frac{V(T)}{V_0} = 1 - \frac{1}{\beta} \int_{T_0}^T D f_0^*(E_S) N^*(E_S) dT \quad (39)$$

$$E_S = T \cdot \left(\lg \frac{\omega_S}{\beta} + a \right) b - c \quad (40)$$

If E_S units are eV and T , ω_S , and β have SI units, then coefficients in Eq. 40 have the following values: $a = 1.66$, $b = 1.92 \cdot 10^{-4}$, and $c = 0.015$. In Eq. 39 D is the weakly temperature-dependent coefficient equal to $T^{-1}(1.2 \cdot \beta \cdot E_S)$.

Thus, the model can be used to determine the energy spectrum of the surface traps in nonpolar polymers. For example, in Boitzov et al. (1990), Rychkov and Boitsov (1999), and Rychkov et al. (1992), it has been shown that in fluoropolymers, the surface traps have a continuous energy distribution between 0.9 and 1.4 eV with a frequency factor of 10^{13} Hz.

In nonpolar fluoropolymers charged negatively, the electret decay is governed by considerably more complex mechanisms (Seggern 1979, 1981b). Here the deep bulk traps play the main role in the charge transport. As a result, charge decay is highly asymmetrical with respect to the sign of the homocharge.

The list of the models presented here is by no means exhaustive and new models are being developed and presented in the literature regularly. However, charge trapping still holds the central position when different mechanisms for electret decay and charge transport are considered. As ferroelectrets ultimately rely on

charge retention on the inner surfaces of their internal cavities, most of the modern models for electret decay can be directly applied to study the stability of piezoelectricity in such materials.

2 Ferroelectret: Electret Microphone Model

As reported, ferroelectrets are thin polymer films with open or closed cavities, such as a foamed material although they differ from those due to the trapped electrical charges on the inner void surfaces. These characteristics allow the material to exhibit high d_{33} piezoelectric coefficients. In this section we describe the most accepted model, which explains this electromechanical behavior.

In order to develop the model, a first approximation of the multi-voided complex structure of the foamed film is defined as presented in a cross-section view in Fig. 1a. This simplified design was rearranged in a multilayer system composed by solid polymer films spaced by air layers as shown in Fig. 1b. From this, a further simplification of the structure can be performed by grouping all of the solid layers and the air layers into a three-layer system as shown in Fig. 2a.

After reducing the complex voided structure to a simplified three-layer system, the electret microphone theory can be applied. To demonstrate the relation between this theory and the ferroelectret model, the electric charged layered system, as shown in Fig. 2b, was considered. The charged model represents the charges trapped on the inner void surfaces and the charges induced on the proximity of the electrodes, after the structure has been submitted to an external high electric field and dielectric barrier discharges had occurred inside the air cavities.

Regarding this trapped charge model, the electrical representation can then be further expressed as shown in Fig. 3, where σ_0 and σ_1 are charge densities induced on the electrodes and on the inner surface of the cavities, respectively; ϵ and ϵ_0 are the respective polymer and the air permittivities; E_{11} , E_{12} , and E_2 are the internal electric fields; d_{11} and d_{12} are the polymer layer thicknesses; and d_2 is the total air layer thickness.

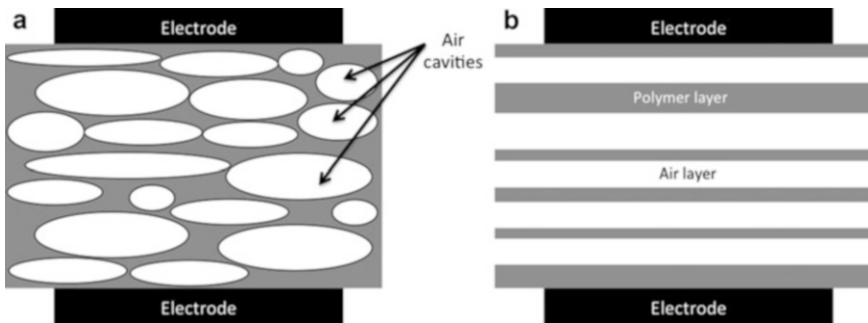


Fig. 1 (a) Cross-section representation of a polypropylene voided film and (b) the simplified structure of the voided film with multiple layers of solid films and air

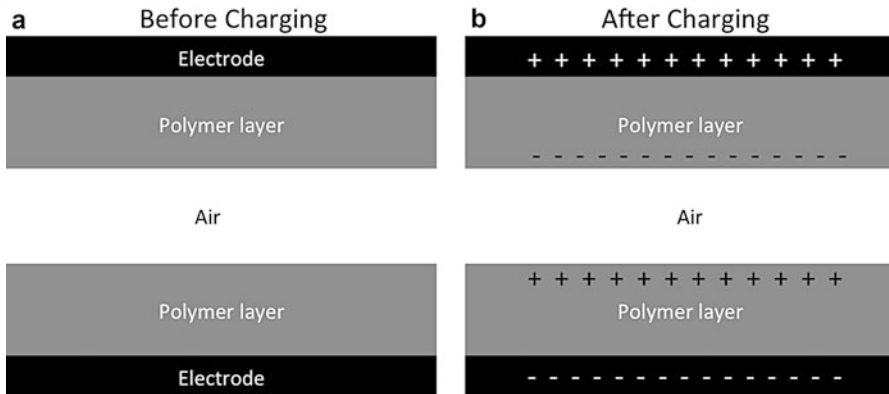


Fig. 2 (a) Three-layer system representing the foamed piezoelectric structure and (b) the same structure after it has been electrically charged

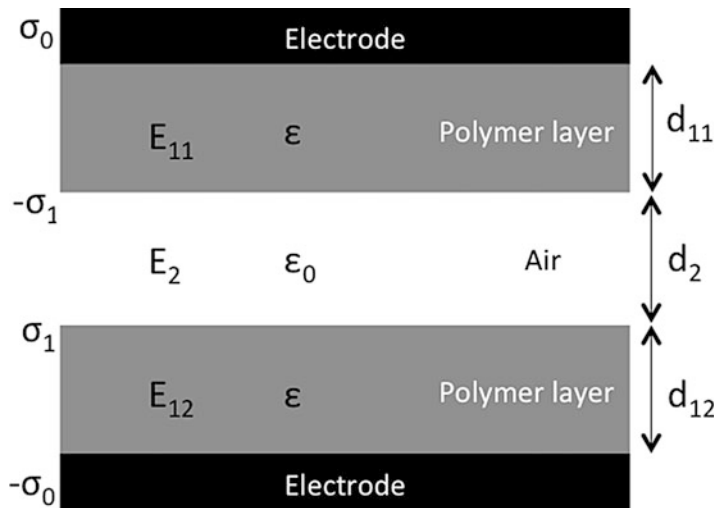


Fig. 3 Electrical model considering the electric fields, the charges densities, and the involved material permittivity, i.e., polymer and air

The electric fields can then be expressed as

$$E_{11} = \frac{\sigma_0}{\epsilon\epsilon_0} \quad E_2 = -\left(\frac{\sigma_1}{\epsilon_0} - \frac{\sigma_0}{\epsilon_0}\right) \quad E_{12} = \frac{\sigma_0}{\epsilon\epsilon_0} \quad (41)$$

Assuming a potential difference (ΔV) between the upper and the lower electrodes equals to zero, the sum between the product of the electric fields and its respective thickness can be written as

$$\frac{\sigma_0 d_{11}}{\varepsilon \varepsilon_0} - \left(\frac{\sigma_1}{\varepsilon_0} - \frac{\sigma_0}{\varepsilon_0} \right) d_2 + \frac{\sigma_0 d_{12}}{\varepsilon \varepsilon_0} = 0 \quad (42)$$

If one assumes the distances d_{11} and d_{12} are equal, then the polymer layer thickness can be represented as being d_1 , and d_{11} and d_{12} can be replaced by $d_1/2$, leading to a charge density on the electrodes recalculated from Eq. 42 as

$$\begin{aligned} \Rightarrow \frac{\sigma_0 d_1}{\varepsilon} - (\sigma_1 - \sigma_0) d_2 &= 0 \\ \Rightarrow \sigma_0 \left(\frac{d_1}{\varepsilon} + d_2 \right) - \sigma_1 d_2 &= 0 \\ \Rightarrow \sigma_0 &= \left(\frac{\sigma_1 d_2 \varepsilon}{d_1 + \varepsilon d_2} \right) \end{aligned} \quad (43)$$

In order to obtain the piezoelectric response, an external force perpendicular to the ferroelectret must be applied. This force induces a mechanical deformation in the multilayer structure in the thickness direction, which in the ferroelectrets is mainly due to the compression or expansion of the air layers. Therefore, the thickness variation in the structure (δ) can be represented by Eq. 44, where Δ_p is the applied pressure variation, Y is the multilayer elastic modulus, and d the ferroelectret total thickness, i.e., $(d_1 + d_2)$:

$$\delta = \frac{\Delta_p}{Y} d \quad (44)$$

After the ferroelectret is mechanically deformed, the equilibrium of the induced electrical charge on the electrodes immediately changes. Suppose upper and bottom electrodes are physically connected to a resistive load. In such a case, electrical charges will flow from one electrode to another to restore the equilibrium. The amount of compensating charges is defined as ΔQ and can be expressed as in Eq. 45, where A is the electrode area:

$$\Delta Q = A[\sigma_0(d_2 - \delta) - \sigma_0(d_2)] \quad (45)$$

Regarding small deformations, the term $\sigma_0(d_2 - \delta) - \sigma_0(d_2)$ in Eq. 45 can be approximated to the first term in Taylor series in relation to δ . Therefore, the charge variation (ΔQ) can now be redefined as follows:

$$\Delta Q = A \sigma_1 \varepsilon \left(\frac{d_1}{d_1 + \varepsilon d_2} \right) \delta \quad (46)$$

And since charge variation ΔQ divided by the electrode area (A) is equal to a variation in the charge density ($\Delta \sigma$), and the thickness deformation δ in Eq. 46 can be replaced by Eq. 44, Eq 46 can now be simplified to the following equation, which represents the piezoelectric coefficient of the ferroelectret (Hillenbrand et al. 2005):

$$\frac{\Delta\sigma}{\Delta p} = \frac{\varepsilon d}{Y} \frac{d_1 \sigma_1}{(d_1 + \varepsilon d_2)^2} \quad (47)$$

Thus, this simple model highlights the influence of the ferroelectret's mechanical and electrical properties on the obtainable values of piezoelectric coefficients.

3 Conclusion

In this chapter we have tried to give an overview of models that describe the processes determining the piezoelectricity in ferroelectrets. Being polymer materials with cavities inside, ferroelectrets can be treated as polymer electrets both in terms of charge stability and the origin of piezoelectricity. Thus, in the first part of the chapter, several models describing charge storage and decay in nonpolar polymers are considered. Even though the models employ different approaches to charge transport in polymers, the most important feature among all of them is the role of localized states or traps. In electrets in ferroelectrets alike, charge traps control temporal and thermal stability as well as the poling characteristics. In the second part of the chapter, a simple model based on the electret microphone principle relates piezoelectric coefficients in ferroelectric to their mechanical and dielectric properties.

References

- Abkowitz M, Mizes H, Facci J (1995) Emission limited injection by thermally assisted tunneling into a trap-free transport polymer. *J Appl Phys* 66(10):1288–1290
- Anta J, Marcelli G, Meunier M, Quirke N (2002) Models of electron trapping and transport in polyethylene: current-voltage characteristics. *J Appl Phys* 92(2):1002–1008
- Arkhipov V, Iovu M, Rudenko A, Shutov S (1987) Multiple trapping model: approximate and exact solutions. *Solid State Commun* 62(5):339–340
- Barybin A, Shapovalov V (2008) Charge relaxation in conducting dielectric films with shallow and deep traps. *Phys Solid State* 50(5):815–827
- Barybin A, Zav'yalov A, Shapovalov V (2012) Effect of surface traps on relaxation of injected charge in dielectric films. *Phys Solid State* 54(1):53–61
- Batra I, Kanazawa K, Seki H (1970) Discharge characteristics of photoconducting insulators. *J Appl Phys* 41:3416–3422
- Berlepsch H (1985) Interpretation of surface potential kinetics in HDPE by a trapping model. *J Phys D Appl Phys* 18:1155–1170
- Berlepsch H (1991) Xerographic depletion discharge versus injection for modeling the surface potential decay in insulators. In: *Proceedings of the 7th international symposium electrets (ISE-7)*, Berlin, pp 78–83
- Boitzov V, Rychkov A, Rozkov I (1990) Charge storage and relaxation control techniques in electrets. *Mater Sci* 16(1–3):225–230
- Chen G (2010) A new model for surface potential decay of corona-charged polymers. *J Phys D Appl Phys* 43:1–7
- Chen G, Xu Z, Zhang L (2007) Measurement of the surface potential decay of corona-charged polymer films using the pulsed electroacoustic method. *Meas Sci Technol* 18:1453–1458

- Chudleigh P (1977) Charge transport through a polymer foil. *J Appl Phys* 44(11):4591–4596
- Dang W, Tahara M, Tajima J, Tanaka Y, Watanabe R, Takada T (2006) Observation of charge distribution in electron beam irradiated polymers using pulsed electro-acoustic method. In: Annual report, IEEE conference on electrical insulation and dielectric phenomena, Kansas City, pp 138–141
- Hillenbrand J, Sessler G, Zhang X (2005) Verification of a model for the piezoelectric d_{33} coefficient of cellular electret films. *J Appl Phys* 98:0641051
- Kanazawa K, Batra I, Wintle H (1972) Decay of surface potential in insulators. *J Appl Phys* 43(2):719–720
- Kiess H, Rehwald W (1980) Electric conduction in amorphous polymers. *Colloid Polym Sci* 258(3):241–251
- Kressman R, Sessler G, Gunter P (1999) Space-charge electrets. In: Gerhard-Mulhaupt R (ed) *Electrets*, vol 2, 3rd edn. Laplacian Press, Morgan Hill, pp 1–40
- Künstler W, Gerhard-Mulhaupt R (1997) Space-charge profiles with high densities in uniform and nonuniform polymer dielectrics. In: Annual report, IEEE conference on electrical insulation and dielectric phenomena, Minneapolis, pp 72–75
- Le Roy S, Segur P, Peyssedre G, Laurent C (2004) Description of dipolar charge transport in polyethylene using a fluid model with a constant mobility: model prediction. *J Phys D Appl Phys* 37:298–305
- Lewis T (1990) Charge transport, charge injection and breakdown in polymeric insulators. *J Phys D Appl Phys* 23:1469–1478
- Montanari G, Mazzanti G, Palmieri F, Motori A, Perego G, Serra S (2001) Space-charge trapping and conduction in LDPE, HDPE and XLPE. *J Phys D Appl Phys* 34:2902–2911
- Remke R, Seggern H (1983) Modeling of thermally stimulated currents in polytetrafluoroethylene. *J Appl Phys* 54(9):5262–5266
- Rudenko A, Arkhipov V (1978) Trap-controlled transient current injection in amorphous materials. *J Non-Cryst Solids* 20(2):163–189
- Rychkov A, Boitsov V (1999) Charge relaxation in PTFE-AL structures having interfacial region modified by the glow discharge. In: Proceedings of the 10th international symposium electrets (ISE-10), Delphi, pp 91–94
- Rychkov D, Gerhard R (2011) Stabilization of positive charge on polytetrafluoroethylene films treated with titanium-tetrachloride vapor. *Appl Phys Lett* 98(12):122901
- Rychkov A, Cross G, Gonchar H (1992) Charge relaxation in structures containing non-polar polymer-metal interfaces. *J Phys D Appl Phys* 25:986–991
- Rychkov D, Kuznetsov A, Rychkov A (2011) Electret properties of polyethylene and polytetrafluoroethylene films with chemically modified surface. *IEEE Trans Dielectr Electr Insul* 18(1):8–14
- Seggern H (1979) A new model of isothermal charge transport for negatively corona-charged Teflon. *J Appl Phys* 50:7039–7043
- Seggern H (1981b) Detection of surface and bulk traps. *J Appl Phys* 52:4086–4089
- Seggern H, West J, Kubli R (1984) Determination of charge centroids in two-side metallized electrets. *Rev Sci Instr* 55(6):964–967
- Sessler G (1999) Distribution and transport of charge in polymers. In: Gerhard-Mulhaupt R (ed) *Electrets*, vol 2, 3rd edn. Laplacian Press, Morgan Hill, pp 41–80
- Sessler G, Alguie C, Lewiner J (1992) Charge distribution in Teflon FEP (fluoroethylenepropylene) negatively corona-charged to high potentials. *J Appl Phys* 71:2280–2284
- Simmons J, Tam M (1973) Theory of isothermal currents and direct determination of trap parameters in semiconductors and insulators containing arbitrary trap distributions. *Phys Rev B* 7(8):3706–3713
- Simmons J, Taylor G, Tam MC (1973) Thermally stimulated currents in semiconductors and insulators having arbitrary trap distributions. *Phys Rev B* 7(8):3714–3719
- Sonnontsine T, Perlman M (1975) Surface-potential decay in insulators with field-dependent mobility and injection efficiency. *J Appl Phys* 46:3975–3981

- Tang M, An Z, Xia Z, Zhang X (2007) Electret properties and chemical modification of cellular polypropylene films. *J Electrostat* 65:203–208
- Teyssedre G, Laurent C, Montanari G, Palmieri F, See A, Dissado L, Fothergill J (2001) Charge distribution and electroluminescence in cross-linked polyethylene under DC field. *J Phys D Appl Phys* 34:2830–2844
- Toomer R, Lewis T (1980) Charge trapping in corona-charged polyethylene films. *J Phys D Appl Phys* 13:1343–1356
- Watson P (1990) The energy distribution of localized states in polystyrene, based on isothermal discharge measurements. *J Phys D Appl Phys* 23:1479–1484
- Watson P, Schmidlin F, La Donna R (1991) The trapping of electrons in polystyrene. In: Proceedings of the 7th international symposium electrets, Berlin, pp 3–10
- Wintle H (1971) Decay of excess charge in dielectrics having shorted electrodes. *J Appl Phys* 42:4724–4730
- Xu Z, Zhang L, Chen G (2007) Decay of electric charge on corona charged polyethylene. *J Phys D Appl Phys* 40:7085–7089

Polymer Electrets and Ferroelectrets as EAPs: How to Start Experimenting with Them

29

Simona Bauer-Gogonea, Siegfried Bauer, Richard Baumgartner, Alexander Kogler, Markus Krause, and Reinhard Schwödiauer

Contents

1	Introduction	662
2	Equivalent Circuits and Measurement Signals	663
3	Ferroelectret Force Sensors	665
4	Playing with the Ferroelectret Sensors	666
5	Summary	667
	References	667

Abstract

Ferroelectrets are used in capacitive piezoelectric sensors. When a force is applied to such a sensor, an electrical signal is generated. We first describe the equivalent circuit representation of a ferroelectret sensor element and proceed with the coupling of the sensor element to a measurement device. Based on the governing equations for the measurement signal following a given time-dependent force, we show that the sensors measure either force or force rate. We illustrate the use of ferroelectrets by proposing a reaction game using ferroelectret sensor elements. Several sensor elements are coupled to a measurement instrument, such as an oscilloscope, while forces are applied by the gamers as fast as possible with their hands. The sensor element is easily prepared by students within a few minutes, immediately enabling playing with the elements, followed by a fundamental understanding of ferroelectret force sensing.

S. Bauer-Gogonea (✉) • S. Bauer • R. Baumgartner • A. Kogler • M. Krause • R. Schwödiauer
Soft Matter Physics, Johannes Kepler University Linz, Linz, Austria
e-mail: simona.bauer-gogonea@jku.at; sbauer@jku.at; richard.baumgartner@jku.at;
alexander.kogler@jku.at; markus.krause@jku.at; reinhard.schwodiauer@jku.at

Keywords

Cellular ferroelectret foil • Equivalent circuit of ferroelectret film sensor • Ferroelectret force sensor • Force rate measurements • Oscilloscope

1 Introduction

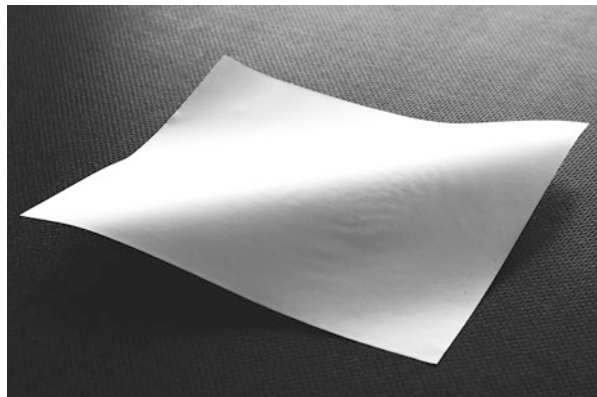
Ferroelectrets are internally charged cellular polymers displaying large longitudinal piezoelectricity, combined with negligible transverse piezoelectricity (Sessler and Hillenbrand 1999; Paajanen et al. 2000; Neugschwandtner et al. 2000; Neugschwandtner et al. 2001; Gerhard-Multhaupt 2002; Bauer et al. 2004; Bauer 2006). The longitudinal piezoelectric d_{33} coefficient is typically around 100 pC/N, while the transverse piezoelectric d_{31} and d_{32} coefficients are usually 1–2 pC/N only. Ferroelectrets are best used in the thickness mode, with negligible responses upon bending. They are thus ideal sensor materials for force sensing, for example, in keypads and in bed sensors for sleep monitoring (EMFIT 2015).

How to best start experimenting with them? The easiest way is the use of small sheets for research use offered by a manufacturer of ferroelectrets (EMFIT 2015). Such a sheet has a size of $600 \times 990 \text{ mm}^2$, enabling the fabrication of a large number of sensor elements with a typical size of $1 \times 1 \text{ cm}^2$ (Fig. 1).

The ferroelectret foil is internally charged and can be used after depositing electrodes on both film surfaces. Here, electrically conductive inks provide a simple means to prepare differently shaped electrodes.

In this chapter, we will first develop the equivalent circuit description of a ferroelectret sensor and the coupling of a sensor to measurement circuits. The governing equation for the measurement signal, following a given time-dependent force, is discussed to derive a guideline under which conditions the sensor measures force or force rate and illustrates the use of such sensors in a simple reaction game experiment. The sensors are easily prepared by students and enable them learning the fundamentals of ferroelectret force sensing by playing with the sensors.

Fig. 1 Photo of a cellular ferroelectret foil. The non-metallized foils are internally charged and ready to use after preparing electrodes on both surfaces of the film



2 Equivalent Circuits and Measurement Signals

The commercially available ferroelectret film is based on polyolefin foam manufactured in a continuous biaxial orientation process, followed by an expansion process to adjust the mechanical and the piezoelectric properties (Fig. 2 left). The equivalent circuit of a ferroelectret film sensor consists of a current source in parallel to the sensor capacitance (Fig. 2 right). The sensor capacitance C_P follows from $C_P = \epsilon_0 \epsilon A / s$, where ϵ_0 is the permittivity of vacuum, ϵ is the dielectric constant of the ferroelectret foam, A is the electrode area, and s is the thickness of the film. With a typical thickness of $s = 70 \mu\text{m}$ and a dielectric constant of $\epsilon = 1.5$, the sensor capacitance is 19 pF/cm^2 , a small capacitance in comparison to other piezoelectric sensor elements. The ferroelectret sensor element produces a current $i(t)$ when a force $F(t)$ is applied to the sensor element, according to $i(t) = d_{33} \dot{F}(t)$, where the dot represents the time derivative $dF(t)/dt$. In the following we will set $d_{33} = d$, as the transverse piezoelectric coefficients are negligible in ferroelectrets.

In order to derive the governing equations of a ferroelectret sensor, we need to consider the coupling of the sensor to a measurement circuit (Sirohi and Chopra 2000). The simplest equivalent circuit of a measurement unit consists of an input capacitance C_A and an input resistance R_A (Fig. 3).

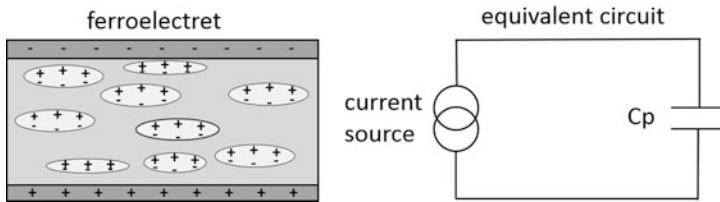


Fig. 2 Schematic cross section of the ferroelectret foil shown in Fig. 1 (left). Ferroelectrets are cellular polymers, with oppositely charged voids. Equivalent circuit representation of the cellular ferroelectret foil (right). The ferroelectret is represented by a current source and by a capacitor. Current is generated when electrical forces are applied to the ferroelectret. The capacitance of a ferroelectret foil is small, typically around 20 pF for a capacitor with an area of 1 cm^2

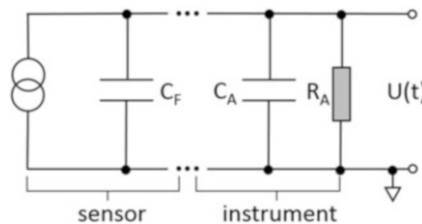


Fig. 3 Equivalent circuit for the coupling of a ferroelectret sensor to a measuring device. The device is represented by its input capacitance C_A and by its input resistance R_A . The measurement signal is the voltage across the capacitors and the resistance

Typical values for an oscilloscope are $C_A = 25$ pF, and $R_A = 1$ M Ω . The signal measured is the voltage across the capacitors C_F of the ferroelectret and the capacity C_A and resistance R_A of the measurement device. Based on the equivalent circuit model, it is now possible to derive the governing equations for the measurement signal following a prescribed force signal $F(t)$.

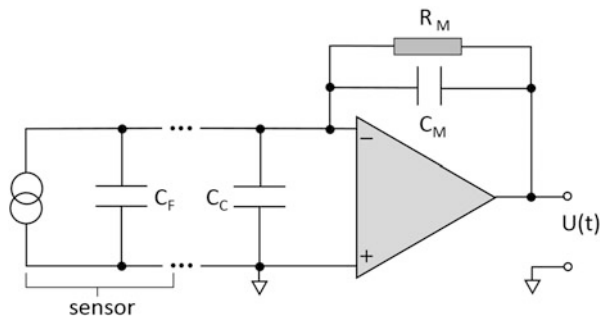
The current delivered by the piezoelectric sensor element charges the capacitor $C = C_A + C_F$ and feeds the resistor $R = R_A$. Employing Kirchhoff's law, we obtain the governing equation of the piezoelectric ferroelectret sensor element (Sirohi and Chopra 2000):

$$\frac{i(t)}{C} = \frac{d\dot{F}(t)}{C} = \dot{U}(t) + \frac{U(t)}{\tau} \quad (1)$$

with the time constant $\tau = RC$. Equation 1 shows under which conditions the sensor element measures the applied force $F(t)$ or the force rate $\dot{F}(t)$. When the force signal $F(t)$ shows small variations within one time constant, the derivative $\dot{U}(t)$ becomes negligible in comparison to $U(t)$; under these conditions, the sensor measures the force rate $U(t)/R = d\dot{F}(t)$. On the other hand, when the sensor signal varies significantly within one time constant, the sensor directly measures the force $U(t) = dF(t)/C$. Usually, force rate measurements occur when the sensor is directly coupled to an oscilloscope. With an input capacitance of 25 pF, an input resistance of 1 M Ω , and a sensor capacitance of 19 pF (for a 1 cm² sensor element), a time constant of 44 μ s is obtained. For forces applied with a human finger or hand, the time scale for force variations is on the order of a few ms or larger, significantly exceeding the time constant.

Often it is desirable to control the time constant, independent of sensor, cable, and input capacitances. In such a case it is recommended to use a charge amplifier (Fig. 4). The current delivered by the piezoelectric element is directly transferred to the capacitor C_M and the resistor R_M , irrespective of the sensor and cable capacitances C_F and C_C . Under these conditions, the time constant is easily adjusted to allow for low-frequency measurements, where the sensor signal now follows the time-dependent force $dF(t)/C_M$.

Fig. 4 Connection of a ferroelectret sensor with a charge amplifier. The charges generated by the ferroelectret sensor are the same as those on the measurement capacitance C_M



3 Ferroelectret Force Sensors

Having derived the governing equations for the measurement signal, we can now proceed with the fabrication of the ferroelectret sensor elements. The suggested preparation method is simple and can be accomplished by any student. Cut a piece of the ferroelectret sensor film and paste an electrode with an area around 1 cm^2 on the top surface with conductive ink (Fig. 5).

After drying, paste the counter electrode on the bottom surface of the sensor foil. With two wires attached to the conductive ink electrodes, the sensor is ready for use. To illustrate how the sensor measures force or force rate, we have applied a mechanical force to the sensor element, with a pressurized polytetrafluoroethylene (Teflon) bar (Fig. 6; Dansachmüller et al. 2005).

When connected to a charge amplifier, the measured signal directly represents the rectangular varying compressive mechanical force from the Teflon bar (Fig. 7 top).

Fig. 5 Preparation of the ferroelectret sensor element by pasting conductive ink on the surface, to form the capacitor electrodes

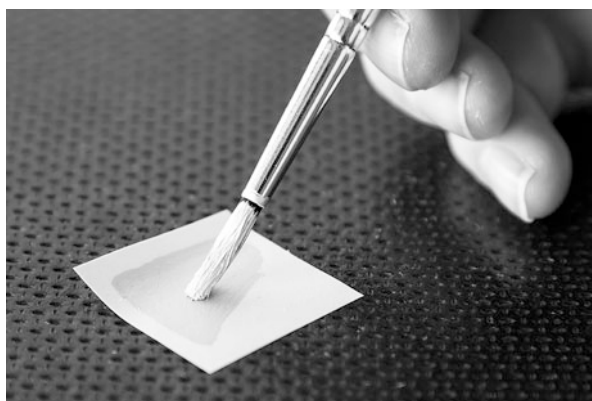


Fig. 6 Experimental setup for testing ferroelectret sensors. The arrangement allows for measurements of the elastic modulus (when the LCR meter is applied) or for the characterization of the piezoelectric d_{33} coefficient (when the electrometer is employed). Force is applied to the sensor by a Teflon bar; the force magnitude is adjusted by pressurized air (Redrawn with permission from (Dansachmüller et al. 2005))

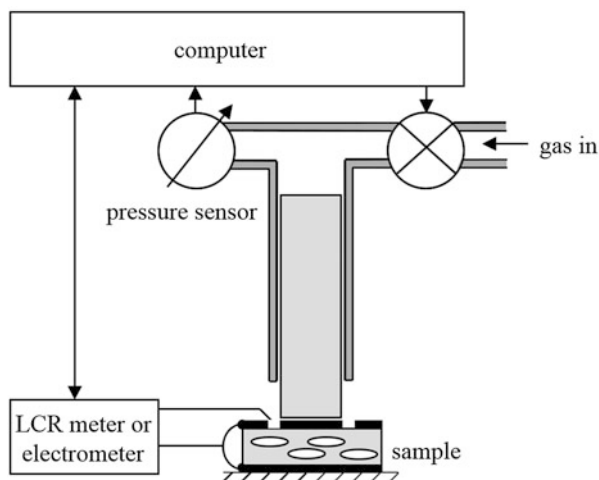
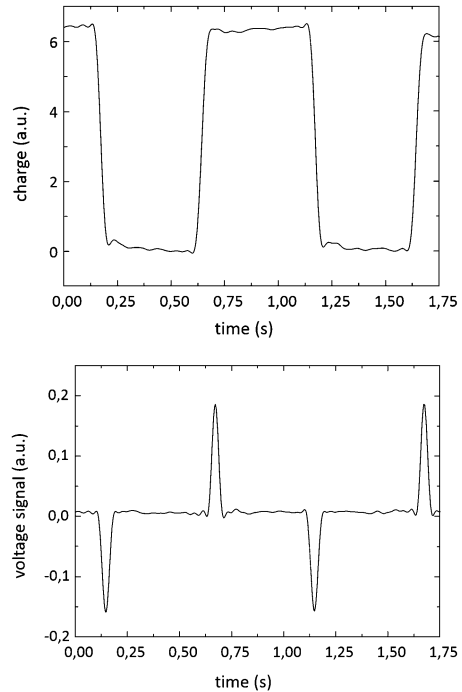


Fig. 7 Force measurement with a ferroelectret sensor coupled to a charge amplifier (*top*). A rectangular varying compressive force is applied to the sample. Force rate measurement, when the ferroelectret sensor is connected to a digital oscilloscope (*bottom*). Measurement signals can be calibrated to determine the piezoelectric coefficient of the ferroelectret foam sensor



By connecting the sensor element to a digital oscilloscope, the force rate is measured (Fig. 7 bottom).

4 Playing with the Ferroelectret Sensors

Playing is the highest form of research, as Einstein quoted. Having fun in science education is an element that easily allows getting the attention of students. A simple reaction game with the prepared sensors enables students understanding measurements with ferroelectrets. We have employed four of the sensors and connected them to a four-channel digital oscilloscope, to allow playing by four students. The oscilloscope is triggered by the voltage signal of a mobile phone random timer alarm. The one applying a force as fast as possible to the sensor by a clap with the hand is winning. Force is applied to the sensor elements across 3d printed pads, which protect the sensor element (Fig. 8).

The traces on the oscilloscope in the photo of Fig. 8 depict four typical measurement signals; from the curves, it is obvious that the sensors measure the force rate. The winner is immediately obvious from the signal traces. The game is also useful to teach students the generation and interpretation of signals from ferroelectret sensors. The proposed approach to start experimenting with ferroelectrets enables students to not only fabricate a simple ferroelectret force sensor but also to play with the sensor

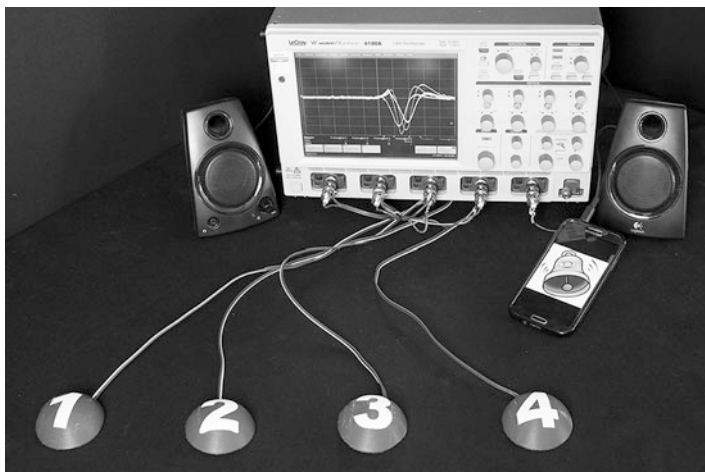


Fig. 8 Four sensor elements connected to a four-channel digital oscilloscope. Force is applied to the sensor elements via 3d printed pads, which are also used to protect the sensor elements. Ready to play, who will be the winner?

elements and to gain a deep understanding of force and/or force rate measurements with ferroelectrets.

5 Summary

To start experimenting with ferroelectrets, a simple sensor design is proposed. The sensor is easily prepared within a few minutes and can be directly used to measure transient forces or force rates. Combined in a reaction game, students will immediately see that their prepared sensors nicely work, and by analyzing the signals, they gain a deep understanding of force and force rate measurements with ferroelectrets. By calibrating the sensor signals, even quantitative force measurements are easily possible. With this simple experiment in mind, students can then proceed to more complex research questions, using ferroelectret sensors as microphones or ultrasound generators and detectors.

Acknowledgments Work partially supported by the Austrian Science Funds and by the European Research Council (Advanced Investigators Grant SoftMap).

References

- Bauer S (2006) Pyro-, piezo- and ferroelectrets: soft transducer materials for electromechanical energy conversion. *IEEE Trans Dielectr Electr Insul* 13:953–962
- Bauer S, Gerhard-Multhaupt R, Sessler GM (2004) Ferroelectrets: soft electroactive foams for transducers. *Phys Today* 57:37–43

- Dansachmüller M, Schwödiauer R, Bauer-Gogonea S, Bauer S, Paajanen M, Raukola J (2005) Elastic and electromechanical properties of polypropylene foam ferroelectrets. *Appl Phys Lett* 86:031910
- EMFIT Homepage (manufacturer of ferroelectret foils and sensors) (2015) <http://shop-eu.emfit.com/collections/sensors-ferroelectret-films>. Accessed on 26 Nov 2015
- Gerhard-Mulhaupt R (2002) Less can be more: holes in polymers lead to a new paradigm of piezoelectric materials for electret transducers. *IEEE Trans Dielectr Electr Insul* 9:850–859
- Neuschwandtner GS, Schwödiauer R, Bauer-Gogonea S, Bauer S, Paajanen M, Lekkala J (2001) Piezo- and pyroelectricity of a polymer-foam space-charge electret. *J Appl Phys* 89:4503–4511
- Neuschwandtner GS, Schwödiauer R, Vieytes M, Bauer-Gogonea S, Bauer S, Hillenbrand J, Kressmann R, Sessler GM, Paajanen M, Lekkala J (2000) Large and broadband piezoelectricity in smart polymer-foam space-charge electrets. *Appl Phys Lett* 77:3827–3829
- Paajanen M, Lekkala J, Kirjavainen K (2000) ElectroMechanical Film EMFi – a new multipurpose electret material. *Sensors Actuators* 84:95–102
- Sessler GM, Hillenbrand J (1999) Electromechanical response of cellular electret films. *Appl Phys Lett* 75:3405–3407
- Sirohi J, Chopra I (2000) Fundamental understanding of piezoelectric strain sensors. *J Intell Mater Syst Struct* 11:246–256

Section VII
Dielectric Elastomers

Ron Pelrine and Roy Kornbluh

Contents

1	Introduction	672
2	Principle of Operation of Dielectric Elastomer Transducers	673
3	General Considerations for Dielectric Elastomer Transducers and Common Failure Modes	677
4	Configurations of Dielectric Elastomer Transducers	679
5	Summary and Discussion	684
	References	686

Abstract

Dielectric elastomer transducers are a class of electroactive polymers that operate based on the interaction of quasi-static electric charges with deformable dielectric and electrode materials. The basic functional element of a dielectric elastomer transducer is a thin dielectric film sandwiched between electrodes. When a dielectric elastomer transducer is used as an actuator, voltage applied across the film causes unlike charges on opposite electrodes to attract and like charges on each electrode to repel. The net result is compressive stress in the thickness direction and tensile stresses in the planar directions. When a dielectric elastomer transducer is used as a generator or sensor, stretching the film will vary the voltage and energy state of applied charges (i.e., the functional element is a stretchable capacitor). Analysis of a simplified model derives an expression for the effective total strain that is twice that for a rigid plate capacitor. The performance of dielectric elastomer transducers is limited by lifetime issues associated

R. Pelrine • R. Kornbluh (✉)
SRI International, Menlo Park, CA, USA
e-mail: ron.pelrine@sri.com; roy.kornbluh@sri.com

with dielectric breakdown and mechanical failure of the film or electrodes. The basic functional element can be incorporated into practical transducers in a wide range of configurations. The particular configuration chosen depends on many factors, including the magnitude of the desired strain or force, the available space or desired form factor, and the required bandwidth (speed of response).

Keywords

Actuator • Artificial muscle • Dielectric elastomer • Electroactive polymer • Generator • Sensor • Transducer

1 Introduction

Dielectric elastomer technology is an electrostatic transducer technology based on old scientific phenomena – the attraction of opposite electric charges and the repulsion of like charges.

To begin understanding how dielectric elastomer technology works (and the derivation of the name), consider the structure shown in Fig. 1. Electrically, this structure is a capacitor consisting of two plates of conductive material sandwiching an insulating, dielectric material with the electric field exerting forces and stresses. The electric field pressure generated by opposite charges pulls the plates together. While this effect is fairly well known, perhaps less commonly appreciated is that the like charges within a plate generate a stress that tends to stretch the plates in the plane of the insulating film. In most capacitors, the dielectric and the plates are rigid on the scale of electric forces, so the strains are negligible.

Figure 2 shows what happens to this physical situation when the stiffness of the different materials changes. If the stiffness of either the electrode materials or the insulating film is much greater than the electric field stress, the structure won't deform much; consequently, very little electric energy can be converted to mechanical energy (or vice versa, in a generator). On the other hand, if the electric field pressure is a substantial fraction of the static strength of the electrode-dielectric

Fig. 1 Arrows indicate electric stresses in a capacitor configuration, edge view

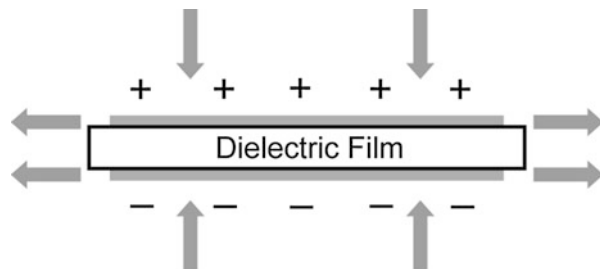
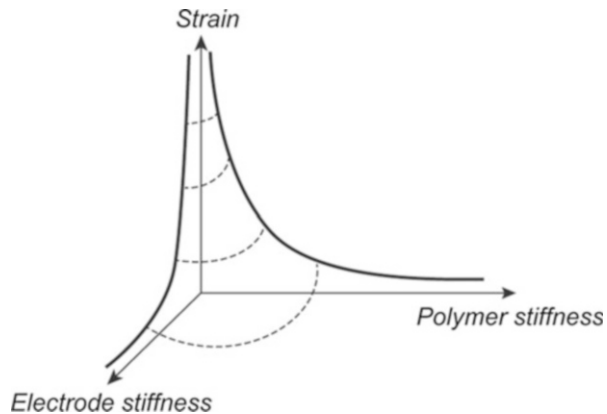


Fig. 2 Qualitative capacitor behavior when materials have fixed electric properties, but different stiffness qualities



structure, the structure can deform significantly and convert a greater amount of electrical energy to mechanical energy.

The best conversion of electrical to mechanical energy and the highest strains occur when the electrodes and the dielectric are soft and compliant. Because many insulating materials can withstand electric fields generating approximately 0.1–1.0 MPa stress, dielectric materials with elastic moduli less than 10 MPa can couple or deform well to this level of applied electric field stress, reaching high strain levels and electrical-to-mechanical energy conversion. Materials that can deform to high strains and elastically recover with moduli of 10 MPa or less generally fall into the category of elastomer and gel materials. Thus, the name *dielectric elastomer* is used to describe this type of electroactive polymer technology.

Although elastomers are the most common and well-known class of materials used for dielectric elastomer technology, the basic electrostatic phenomena extends to stiffer polymers and even non-polymer materials. For example, a hypothetical polymer with a modulus of 100 MPa and maximum elastic strain of 5 % is generally not considered an elastomer, but if it can support substantial electric fields and actuated strains of approximately 1 %, it could be a useful dielectric for some applications that do not require a highly efficient coupling to the electric field. Electrostatic squeezing and stretching of any material due to free charges is often referred to as *Maxwell stress*, so low-strain applications can use materials that are not elastomers in the usual sense.

2 Principle of Operation of Dielectric Elastomer Transducers

Real materials, particularly polymers, exhibit complex phenomena, such as hysteresis, electrical leakage, crack growth, and others. Later chapters in this section will explore the detailed characterization and modeling of realistic dielectric elastomer

materials. This chapter uses a simplified material model to explain the basic physics of dielectric elastomer transduction, specifically assuming:

- Isotropic polymer and electrode material
- Infinitely conductive electrodes
- Constant moduli of elasticity for the dielectric
- Zero modulus of elasticity for the electrode material (highly compliant material, such as powder or conductive grease)
- Negligible electrical leakage
- Negligible hysteresis and viscoelasticity (perfect elasticity)
- Incompressible materials (infinite bulk modulus)

Although no real material completely satisfies all these conditions, many materials can approximate these assumptions over a range of transducer operating conditions.

The last assumption in the list above, incompressible materials, can be written mathematically for the dielectric as

$$(1 + s_{xx})(1 + s_{yy})(1 + s_{zz}) = 1 \quad (1)$$

where s_{xx} , s_{yy} , and s_{zz} are the strains in orthogonal directions. This is generally a very good assumption, as bulk moduli are typically orders of magnitude larger than elastic moduli. For example, silicone elastomer is a common dielectric elastomer material and often has an elastic modulus in the range 0.1–10 MPa, whereas its bulk modulus is typically 1.5–2.0 GPa, roughly three orders of magnitude higher. For most purposes, deformation of an elastomer is a constant volume deformation; that is, if a material stretches in one direction, it contracts in another direction to maintain a

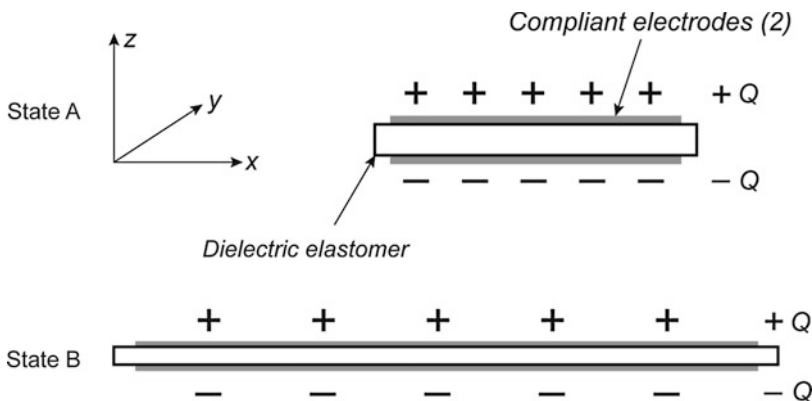


Fig. 3 Dielectric elastomer configuration in two arbitrary strained states with constant charge Q

fixed volume. For small strains, this condition is also sometimes expressed as a Poisson ratio $\nu = 0.5$, with real materials such as silicone in the range $\nu = 0.47\text{--}0.49$.

As with other electromechanical technologies, the behavior of dielectric elastomer transducers depends both mechanically and electrically on the boundary conditions. To illustrate, Fig. 3 shows a dielectric elastomer transducer with a constant charge Q in strain State A and the same charge Q in strain State B.

In Fig. 3, x , y , and z are Cartesian coordinates with x and y in the plane of the film and z in the thickness direction.

The basic electrical energy equations for a capacitor are

$$C = \epsilon_o \epsilon A / z \quad (2)$$

$$E_e = 0.5 Q^2 / C \quad (3)$$

where C is the capacitance, ϵ_o is the permittivity of free space (8.85×10^{-12} F/m), ϵ is the relative dielectric constant of the material, A is the area sandwiched between electrodes, and z is the dielectric thickness.

Noting that

$$A = x_o y_o (1 + s_{xx})(1 + s_{yy}) \quad (4)$$

$$z = z_o (1 + s_{zz}) \quad (5)$$

where x_o , y_o , and z_o are the original, unstrained dimensions, Eq. 1 can be used to write this relationship as

$$A z = x_o y_o z_o = v_o \quad (6)$$

where v_o is the constant volume of the dielectric.

Using Eq. 6 in Eqs. 2 and 3 yields the simplified forms:

$$C = \epsilon_o \epsilon v_o / z^2 \quad (7)$$

$$E_e = 0.5 Q^2 / C = 0.5 Q^2 z^2 / \epsilon_o \epsilon v_o \quad (8)$$

Equation 8 shows that the electrical energy of the dielectric elastomer capacitor changes as the material is stretched or contracted. Since this discussion assumes perfect conductivity of the electrodes and no electrical leakage, the change in electrical energy must be equal in magnitude and opposite in sign to the change in mechanical energy (E_m) of the system (elastomer plus any coupled parasitic or intentional load).

For simplicity, the change between State A and State B is a small or differential change caused by a differential change in thickness, dz . Hence, to equate mechanical and electrical energy changes to first order:

$$dE_m = -dE_e = -Q^2 z dz / \epsilon_0 \epsilon v_o \quad (9)$$

The change of mechanical energy as an effective pressure or stress, P_{eff} , squeezing the film over area A can be expressed as

$$dE_m = -P_{eff} A dz = -P_{eff} (v_o/z) dz \quad (10)$$

Combining Eqs. 9 and 10 results in

$$\begin{aligned} -P_{eff} (v_o/z) dz &= -Q^2 z dz / \epsilon_0 \epsilon v_o \\ P_{eff} &= Q^2 z^2 / \epsilon_0 \epsilon v_o^2 = (Q/C)^2 \epsilon_0 \epsilon / z^2 \end{aligned} \quad (11)$$

where Eq. 7 is substituted for C in the last equality. Expressing the voltage, V , on the capacitive element as $V = Q/C$, the effective pressure becomes

$$P_{eff} = \epsilon_0 \epsilon V^2 / z^2 \quad (12)$$

Readers familiar with stresses in air gap capacitors will note that the effective pressure P_{eff} is twice the normal stress calculated for a rigid plate capacitor. In a rigid plate capacitor with an air gap, the device cannot stretch, so it converts electrical to mechanical energy at half the rate for a given thickness change.

That the stretching mode also converts electrical to mechanical energy can be seen from the basic Eqs. 2 and 3, where holding thickness z is fixed and changing the area A still changes the electrical energy. In practice with an elastomer, however, the area stretching and the thickness contraction are directly coupled through the constant volume condition of Eq. 1, so effective pressure is a useful simplifying concept in a film with constant volume. If the constant volume condition in Eq. 1 is invalid, as is often the case for non-elastomer materials, the physics is more complicated, and both A and z must be carried as variables rather than be reduced to one variable.

The effective electric field pressure in Eq. 12 causes the dielectric material to deform according to its elasticity. The amount of deformation depends on the film's boundary conditions. For free boundary conditions (zero external force on the film's boundaries), the deformation or strain in z can be written as

$$s_{zz} = -P_{eff} / Y = -\epsilon_0 \epsilon V^2 / (Y z^2) \quad (13)$$

where Y is the modulus of elasticity. For small s_{zz} , z can be approximated as z_o on the right-hand side of Eq. 13. Large strains require the substitution, $z = z_o (1 + s_{zz})$. The resulting cubic equation in s_{zz} can be solved exactly (Pelrine et al. 1998), albeit with a considerable increase in expression complexity.

Isotropic materials with free boundary conditions also have $s_{yy} = s_{xx}$. Using Eq. 1 requires first order $s_{zz} + 2 s_{xx} = 0$, or

$$s_{xx} = -0.5s_{zz} \quad (\text{isotropic, free boundary, small } s_{zz}) \quad (14)$$

Equation 14 (or the more exact but more complicated derivation from Eq. 1) is a useful formula when s_{zz} is difficult to measure directly.

The derivation of the transduction energy in the above analysis is valid for both actuation (electrical-to-mechanical energy) and generation (mechanical-to-electric energy) modes. It is also valid for mixed actuation and generation modes, which can be used for variable stiffness and active damping. The direction of the energy conversion depends on the parameter P_{eff} relative to both the dielectric's elastic restoring stress and any external loading.

Considering just elastic restoring stress, the material is in equilibrium when the elastic restoring stress balances the effective pressure P_{eff} . If P_{eff} is greater than the elastic restoring stress, the dielectric will actuate by contracting in thickness, z , and converting electrical energy to mechanical energy. On the other hand, if P_{eff} is less than the elastic restoring forces, the elastomer will expand in thickness and convert mechanical energy to electrical energy in a generator mode.

3 General Considerations for Dielectric Elastomer Transducers and Common Failure Modes

Although dielectric elastomers can transduce electrical and mechanical energy in either direction, different types of devices tend to emphasize different properties. At a basic level, devices can be either high-field dielectric devices, like actuators and generators, or low-field dielectric elastomer devices, like sensors.

Low fields and relatively low voltages are easier to generate and control electronically. More importantly, low fields do not usually have the catastrophic failure modes sometimes seen with high fields exerting high stresses. Thus, low-field applications are typically focused on performance, stability, and patterning rather than on device reliability. An example of a low-field application is a sensor that measures DC position by measuring the dielectric elastomer's variable capacitance when it is stretched (Pelrine et al. 2001). Dielectric elastomers are particularly attractive for such applications because they can be patterned into complex sensor arrays.

High-field applications like actuators and generators always pose trade-offs between device drive levels (e.g., field or voltage) and device lifetime. Dielectric elastomer actuators and generators are not unique in this regard, as most existing actuation technologies have similar tradeoffs. However, dielectric elastomer EAP devices are still relatively new (thus, less characterized) technologies compared to electromagnetics and piezoelectricity. Also, the wide range of potential polymer and electrode materials and configurations makes trade-offs in lifetime vs. performance less well known and characterized.

Preventing failure modes at ever higher levels of performance and longer lifetimes is an active area of dielectric elastomer research. The following information describes several of the more common failure modes and remedies for high-field dielectric elastomers.

Direct Dielectric Breakdown. All insulating materials, including dielectric elastomers, present trade-offs between maximum applied field strength and application lifetime. In a dielectric transducer, electric field breakdown will occur as the field across the dielectric elastomer is increased. Material choices and geometry can also influence electric breakdown phenomena. For example, sharp metal edges can cause higher electric field concentrations and exacerbate electric breakdown. However, in dielectric elastomers, electric breakdown is often a symptom of some other type of failure rather than the cause.

Electromechanical Instability. As noted earlier, if the effective field pressure P_{eff} is higher than the restoring stresses (typically the elastic stresses, but also loads, viscoelasticity, and other factors that resist the electric stress), the thickness of the dielectric elastomer film will contract. For some materials, the contraction increases the restoring stresses enough to reach equilibrium and stop the contraction. For other dielectric elastomer materials, most notably some of the commercially available acrylic adhesive films, the restoring stress increases more slowly than P_{eff} increases as the film gets thinner; see Eq. 12. P_{eff} increases as approximately z^{-2} , holding V constant. In this case, the film becomes unstable and continues to contract in thickness, often locally, until breakdown occurs. The symptom in this case is dielectric breakdown, but the actual cause of the failure is a mismatch between field pressures and mechanical restoring stresses.

Crack Initiation and Growth. Dielectric elastomer transducers can fail by cracking, particularly after many cycles of fatigue cracking and growth to failure. Even without actuation, cracks can grow slowly if the elastomer is prestrained. As with electromechanical instabilities, cracks first occurring in the active area can manifest as electric breakdown even when electric forces did not cause the failure. Edges tend to be more vulnerable to cracking, so securing the dielectric film at the edges with a compatible adhesive or other methods is critical for extending the life cycle of many dielectric elastomer transducers.

Humidity. The electric breakdown strength (and leakage) of dielectric elastomer transducers is often affected by humidity. Lower humidity can dramatically raise the breakdown strength of many dielectric elastomer materials. Humidity can be artificially lowered by using, for example, desiccants. Packaging is an issue for low-humidity operation; however, most designs operate at atmospheric conditions.

Grain Migration. Many compliant electrode materials are composed of particulate materials, such as graphite powder. In some cases, after repeated actuation, the particles can migrate to form partially or completely electrically isolated islands, which do not give full actuation. The symptom of grain migration is gradually decreasing performance.

4 Configurations of Dielectric Elastomer Transducers

At the level of the fundamental functional element, dielectric elastomers are composed of a thin film with compliant electrodes. However, in a practical dielectric elastomer transducer, the pressures generated in the film must be coupled to produce a desired output, or the dielectric elastomer must be deformed by an output, as for a generator or sensor. For simplicity, much of our discussion is in the context of actuation, but most of the information also applies to generators or sensors.

The basic thin film can be configured into a practical device in several ways, based on the type of load coupling or on the actuator shape or structure. Since there are just a few types of loading (distributed, uniaxial, multiaxial), the following material includes both load coupling and structure. The configuration categories are:

- Free-standing planar
- Rigid framed planar
- Flexible framed planar
- Bending
- Tubular and rolled
- Diaphragms (pressure loaded)
- Thickness mode

Other configurations may be possible, but most devices fit into these categories. Figures 4, 5, 6, 7, 8, 9, and 10 illustrate these configurations and provide specific examples.

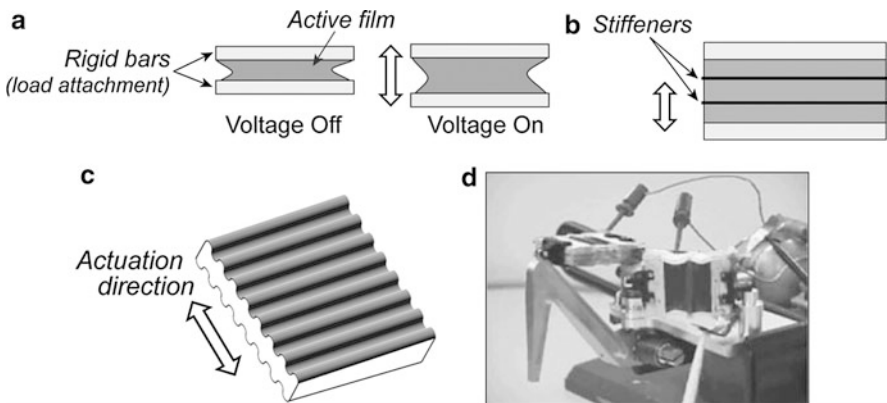


Fig. 4 Free-standing planar actuators. (a) Trench actuators. Wide shapes with rigid edges on the long sides allow the film to deform primarily in the short direction. (b) Directional compliance with stiffeners. Stiffeners can constrain the motion to one direction while allowing greater stroke. (c) Directional compliance with corrugated flexible, but inextensible, electrodes. Flexible electrodes (e.g., thin metal) can also provide directional compliance. (The thickness direction is exaggerated for illustration purposes.) (d) Stacked planar actuators each with a single stiffener. Actuators are used to move an insect-like robot leg

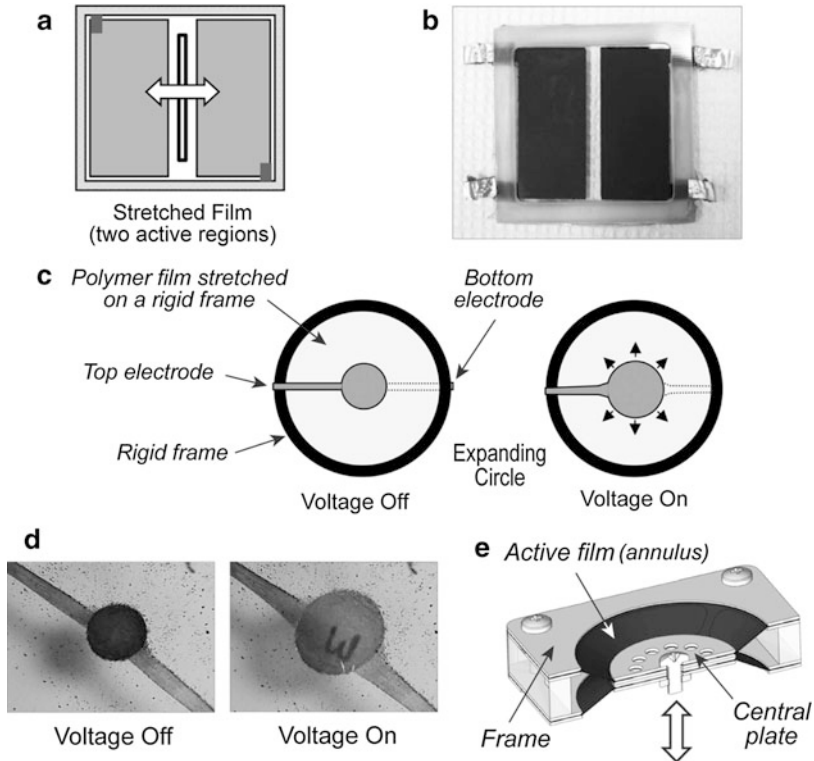


Fig. 5 Rigid framed actuators. (a) Framed stretched-film (prestrained) actuator with two active regions. The output coupling bar is at the center. (b) Example of framed stretched-film (prestrained) actuator with two active regions. (c) Circular framed stretched-film actuator. The *circle* expands uniformly when a voltage is applied. (d) The active region of a circular framed stretched-film actuator. Although there is no force coupling to a load, the expansion of the film can produce effects, such as modulation of light, by changing the optical density of the coated film. (e) Cross-sectional model of a framed actuator. Motion and load coupling is in the out-of-plane direction. This particular actuator, developed by Artificial Muscle, Inc., consists of two-mirror image stacked actuators connected to a single load (*central plate*) (Photo source: Artificial Muscle, Inc.)

In some cases, the configurations for dielectric elastomer transducers are similar to those used for piezoelectric (or other field effects) ceramics and polymers. In other cases, owing to the large strain capabilities of elastomers, the configurations are more novel.

For simplicity, the examples include only single-layer versions of the configurations. In nearly all cases, individual layers can be stacked to produce greater forces. Similarly, many of the actuators can be concatenated end to end to achieve

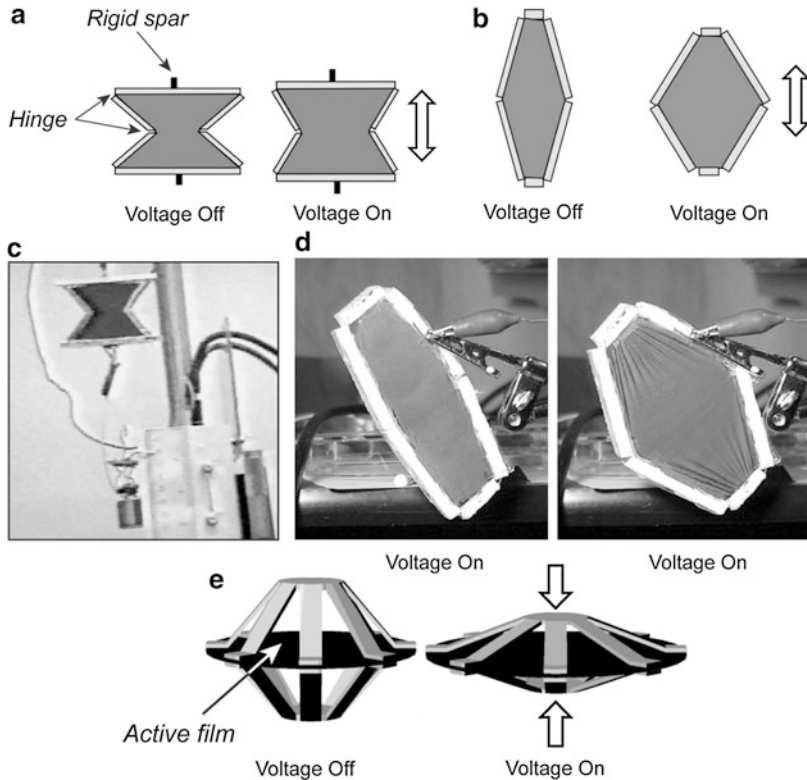


Fig. 6 Flexible framed actuators. (a) The bowtie configuration uses a linkage formed by rigid spars around the perimeter of the active area to couple biaxial expansion to uniaxial output. (b) In the bow configuration, the frame couples and balances the elastic forces from the polymer resulting in greater motions and energy output for a given input. (c) A bowtie actuator holding a 100 g mass. (d) A bow actuator undergoing actuation. (e) The spider configuration uses a radially symmetric mechanism attached to the edges of a circular active area. The frame of the spider actuator flexes in an out-of-plane direction

greater strokes. The individual actuators can also be arrayed in a matrix (or any desired pattern) on a monolithic substrate. Figures 4, 5, 6, 7, 8, 9, and 10 provide examples of all of these approaches to increasing the stroke, forces, or spatial control.

The specific geometry is also important. Geometry can either desirably or undesirably constrain motion. For example, a stacked actuator that is short in the direction of motion and attached to rigid end plates that constrain deformation will have a smaller stroke in response to an applied voltage than an actuator with a greater aspect ratio (thinner in the direction transverse to the motion), even if the overall length is the same. In contrast, free-standing film actuators (as well as tubes,

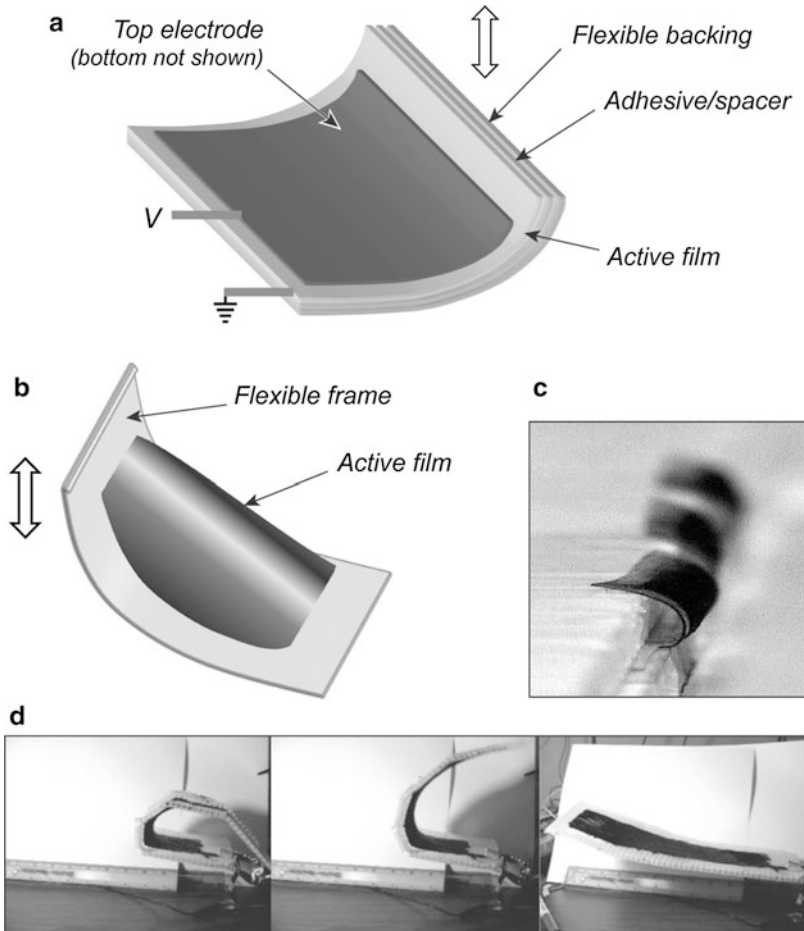


Fig. 7 Bending actuators. **(a)** Unimorph bending beam actuator. Mirroring this structure on the opposite side of the flexible backing creates a bimorph bending actuator. **(b)** Saddle actuator. Stretched film with a bent flexible or articulated frame forms a saddle shape. Elongation causes the frame to flatten. The bending forces in a saddle actuator are greater than a bending beam actuator due to out-of-plane leverage. **(c)** Linear array of bending beam actuators. The large strain capabilities of dielectric elastomers allows for large bending angles. In some cases, the actuators can curl into a scroll configuration (or uncurl from a scroll). **(d)** A saddle actuator with an articulated frame unbending from the application of a voltage

rolls, and rigid framed actuators) couple forces more efficiently to the output if they have a very low aspect ratio (short in the direction of the desired output). More detailed information on actuator geometry is included in subsequent chapters on modeling.

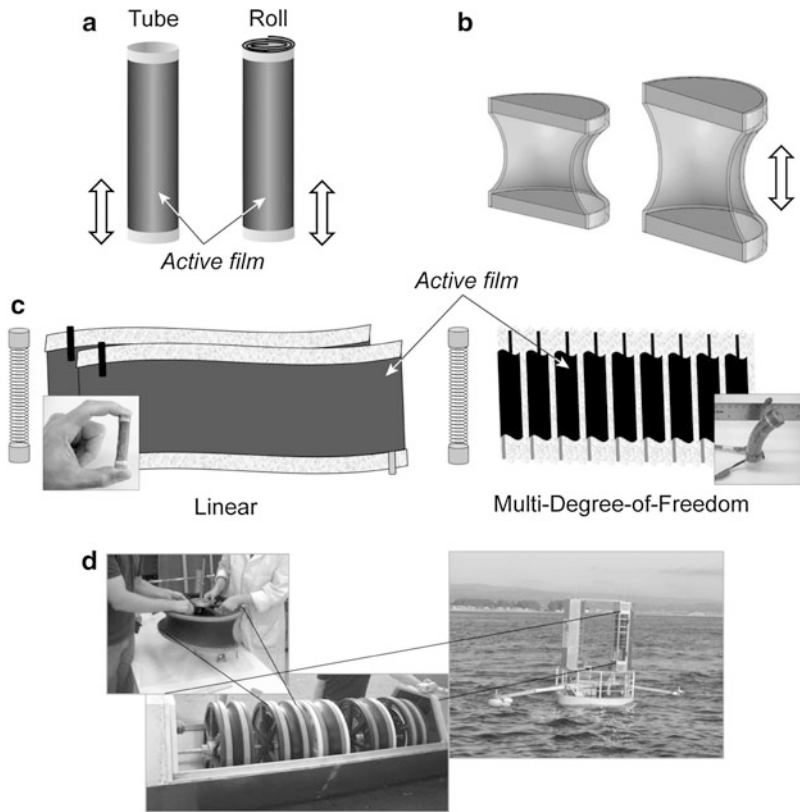


Fig. 8 Tubular and rolled actuators. (a) Free-standing tubular and rolled actuators. Tubes or rolls of active material provide linear actuation in the axial direction (or produce a volume change for pumping resulting from both axial and circumferential deformation). (b) Cross section of a draped tubular actuator. Prestrained film can be stretched between end caps to make draped rolls or tubes. (c) Spring rolls. Double layers of film can be wrapped around a compressed spring. Application of a voltage elongates the spring. Single actuation area (*left*) provides axial motion. Patterned actuation areas (*right*) can provide bending in one or two directions and axial motion. Spring rolls do not have to be circular in cross section. (d) Concatenated and nested (four concentric single-layer rolls) draped rolls used for experiments on harvesting ocean wave energy. Outriggers on the buoy (*right*) stretch and contract the rolls as waves pass

The particular configuration chosen depends on the magnitude of the desired strain or force (or pressure), the available space or desired form factor, the bandwidth (speed of response), and other factors.

Figure 4 illustrates four types of free-standing actuators.

Figure 5 provides diagrams and examples of rigid framed actuators.

Figure 6 provides diagrams and examples of flexible framed actuators.

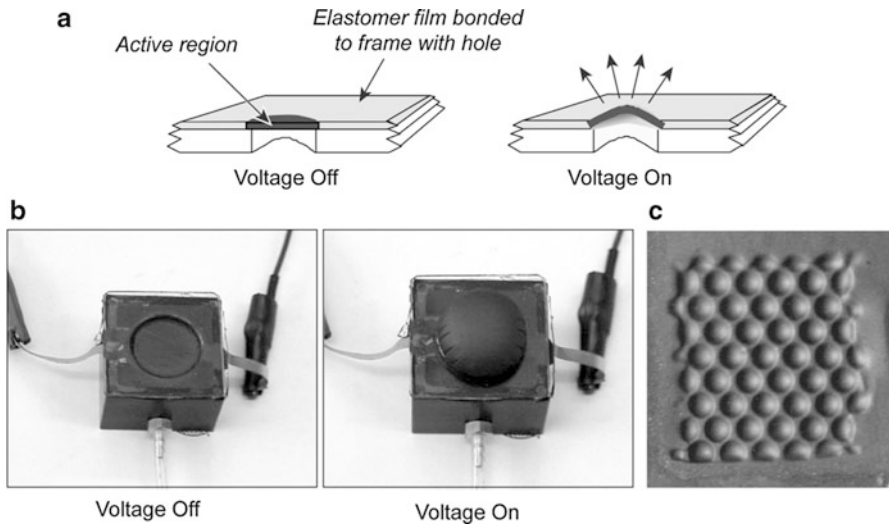


Fig. 9 Pressure-loaded diaphragm actuators. (a) Planar diaphragm. Positive pressure causes bulge in active region. Foam can replace fluid pressure. (b) Diaphragm actuator showing large out-of-plane motion in response to an applied voltage. Diaphragm actuators can be used for loudspeakers or pumps. (c) Array of diaphragm actuators (each 5.5 mm in diameter) made from a single elastomer film on a matrix of circular holes

Figure 7 provides diagrams and examples of bending actuators.

Figure 8 provides diagrams and examples of tubular and rolled actuators.

Figure 9 provides diagrams and examples of pressure-loaded diaphragm actuators.

Figure 10 provides diagrams and examples of thickness-mode actuators.

5 Summary and Discussion

This chapter describes how a simple electrostatic phenomenon provides the foundation for an important class of electroactive polymer transducers and presents the basic principles of operation, modeling, failure modes, and configurations for dielectric elastomers.

Dielectric elastomers occupy an important niche in transducer technology. As-field-activated materials, they are fast acting and efficient, and, unlike most field-activated materials, they are capable of extremely large strains. Actuation strains of more than 100 % have been produced (Pelrine et al. 2000). Because a wide variety of elastomer and electrode materials may be used, dielectric elastomer technology can be considered for a wide range of applications, including uses in

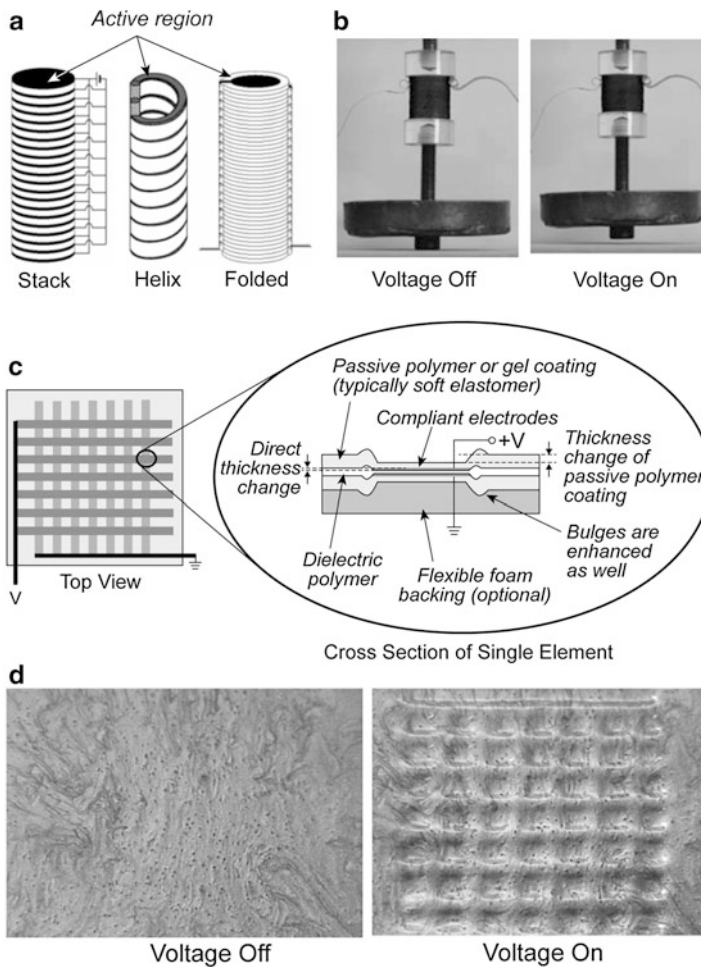


Fig. 10 Thickness-mode actuators. **(a)** Stack actuators. Multiple film layers can produce large motions in the thickness direction. Helices and folding can also produce stacking (Source: F. Carpi, University of Pisa). **(b)** A stack actuator (2 cm high) contracting from the application of a voltage (Source: G. Kovacs, EMPA). **(c)** Enhanced thickness-mode actuator. A thick, soft gel layer effectively increases the thickness of a thickness-mode actuator without requiring higher voltages or additional layers. Enhanced thickness-mode actuators (and stacks in general) are well suited for use in arrays; the patterns can include individually addressable “taxels” for programmable surface features. **(d)** An array of enhanced-thickness-mode “taxels” undergoing actuation

extreme environments or in many-device arrays, when low-cost production is a requirement.

We hope that this discussion of fundamentals will enable the reader to better understand the more detailed discussions on materials, modeling, and applications in the remaining chapters of this section.

References

- Pelrine R, Kornbluh R, Joseph J (1998) Electrostriction of polymer dielectrics with compliant electrodes as a means of actuation. *Sensors Actuators A Phys* 64(1):74–85
- Pelrine R, Kornbluh R, Pei Q, Joseph J (2000) High-speed electrically actuated elastomers with over 100 % strain. *Science* 287(5454):836–839
- Pelrine R, Kornbluh R, Eckerle J, et al (2001) Dielectric elastomers: generator mode fundamentals and applications. In: *Proceedings of SPIE 4329, smart structures and materials 2001: electroactive polymer actuators and devices*, Newport Beach, pp 148–156. doi: 10.1117/12.432640

Anne L. Skov, Qibing Pei, Dorina Opris, Richard J. Spontak, Giuseppe Gallone, Herbert Shea, and Mohammed Y. Benslimane

Contents

1	Elastomers	688
1.1	Silicone-Based Materials as Dielectric Elastomers	688
1.2	Dielectric Elastomers Based on Acrylate Copolymers	692
1.3	Dielectric Elastomers Based on Polyurethanes	696
1.4	Physically Networked Block Copolymer Systems as Dielectric Elastomers	700

A.L. Skov (✉)

Technical University of Denmark (DTU), Lyngby, Denmark

e-mail: al@kt.dtu.dk

Q. Pei

Henry Samueli School of Engineering and Applied Science, University of California – Los Angeles, Los Angeles, CA, USA

e-mail: qpei@seas.ucla.edu

D. Opris

Functional Polymers Laboratory, EMPA, Swiss Federal Laboratories for Materials Science and Technology, Dübendorf, Switzerland

e-mail: Dorina.Opris@empa.ch

R.J. Spontak

Department of Chemical and Biomolecular Engineering, North Carolina State University, Raleigh, NC, USA

e-mail: rich_spontak@ncsu.edu

G. Gallone

Department of Civil and Industrial Engineering, University of Pisa, Pisa, Italy

e-mail: g.gallone@ing.unipi.it

H. Shea

LMTS: Microsystems For Space Technologies Lab, EPFL, Neuchatel, Switzerland

e-mail: herbert.shea@epfl.ch

M.Y. Benslimane

Danfoss PolyPower A/S, Nordborg, Denmark

e-mail: benslimane@danfoss.dk

2	Compliant Electrode Materials	704
2.1	Carbon-Based Electrodes	706
2.2	Metallic Thin-Film Electrodes	707
2.3	Novel Electrodes	708
3	Summary and Discussion	709
	References	710

Abstract

Dielectric elastomer actuators (DEAs) consist of a thin elastomer with even thinner compliant electrodes, both of equal importance for obtaining actuation. In this chapter, materials for both elastomers and electrodes will be discussed.

Keywords

Dielectric elastomers • Silicone • Polyurethane • Acrylics

1 Elastomers

Requirements for elastomers used as dielectric elastomers (DEs) are many and are currently not all met by one single elastomer. For dielectric elastomers, several good candidates exist, each with their particular strength. In the following sections, the four major types of elastomers are discussed in more detail, namely, silicones, acrylates, polyurethanes, and thermoplastic elastomer (TPE) copolymers.

1.1 Silicone-Based Materials as Dielectric Elastomers

Polysiloxanes, or silicones as they are commonly called, are semi-inorganic polymers that are composed of a siloxane (Si-O) backbone and carry two organic hydrocarbon substituents. The most important polysiloxane is polydimethylsiloxane (PDMS), where the organic substituents are methyl groups. Silicones possess a very low glass transition temperature (T_g), as low as $-120\text{ }^\circ\text{C}$, and they are usually stable to temperatures higher than $300\text{ }^\circ\text{C}$ (Madsen et al. 2013). They have good oxidation and UV resistance, high gas permeability, excellent electrical and mechanical properties, and high electrical breakdown values and are biocompatible. It is therefore not surprising that such materials caught the attention of the dielectric elastomer actuator community both in academia and industry. The first DEA products were fabricated from this material (Biggs et al. 2013; Brochu and Pei 2010).

This subchapter will describe how to prepare thin silicone elastomeric films for DEAs and includes a brief survey of present cross-linking strategies, how backbones can be modified with substituents other than methyl, and which composites have been developed to improve material performance. Cross-linking is required to obtain attractive elastic properties, while modification with polar substituents and the creation of composites aim at increasing the permittivity and therefore serve to increase the response of the material to an external electrical stimulus.

1.1.1 Cross-Linking Strategies

We first describe how to efficiently cross-link silicones and restrict the discussion for simplicity to PDMS. As mentioned before, PDMS is liquid and must be cross-linked to ensure elastomeric properties. Therefore, an end-functionalized PDMS of a certain M_w is reacted with cross-linkers that have at least three reactive groups to form an elastomeric matrix. The cross-linking is performed either at room or elevated temperatures or in the presence of UV light. Figure 1 shows the most common reactions used for cross-linking silicones, for which appropriate precursors are commercially available. The equations, though standard chemistry, deserve a few comments. The most frequently used reaction to produce silicone elastomer films is the vinyl addition cure between a silyl hydride and a vinyl group catalyzed by a platinum complex (reaction (a) in Fig. 1) (Bejenariu et al. 2012; Stoyanov et al. 2013). This cross-linking allows formation of elastomers with a high level of network control. Additionally, no by-products are formed during cross-linking, and low-viscosity formulations that allow solvent-free film formations are available. Typical commercial formulations contain two components that are mixed together shortly before use. Once mixed, the cross-linking reaction commences and usually

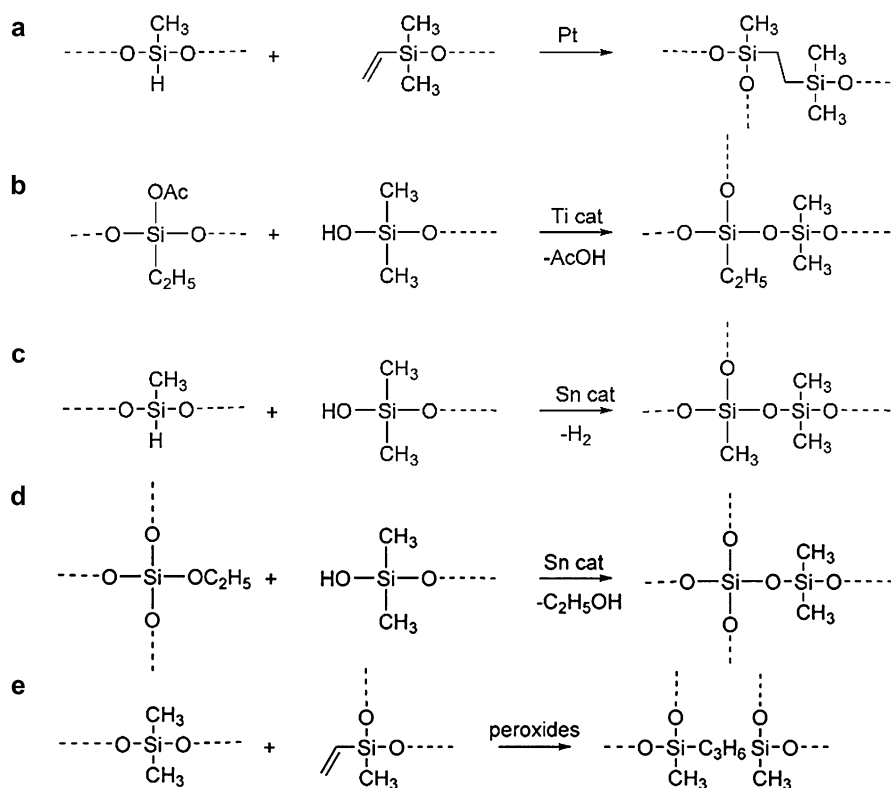


Fig. 1 Cross-linking reactions used for the formation of silicone elastomers

limits the amount of time left for processing. This reaction is, however, very sensitive to impurities that can poison the catalyst (e.g., sulfur- or amine-containing substances). Hydroxyl end-functionalized silicones can be cured at room temperature by a condensation reaction (b) between the hydroxyl groups and ethyltriacetoxysilane cross-linker (Opris et al. 2011). This reaction proceeds very fast after the titanium 2-ethylhexoxide catalyst is added, leaving limited time for film formation. Such silicones might be attractive when very fast film formation at room temperature is required. The reactions presented in equations (c) and (d) differ from (a) in that they are insensitive to additives, but they require long reaction times. It is noteworthy that the rather toxic dibutyltin dilaurate catalyst used might hinder the applicability of such materials in some DEA products. So far, reaction (e) has been less explored for the production of DEA materials. It proceeds at elevated temperatures in the presence of peroxides, and high- M_w PDMS is required to ensure good elastic properties. The advantage of this system is that little to no change in the mechanical properties of the resulting film is expected over time. The photo-cross-linking of acrylates in the presence of UV light to generate silicone elastomers is also known. Typical commercial formulations consist of only one component, which is stored in dark vessels. Other chemical reactions have also been used, but appropriate chain functionalization is required (Rambarran et al. 2012; Riffle et al. 1983).

The mechanical properties of the resulting elastomers depend strongly on network density. While a low- M_w PDMS allows for formation of highly cross-linked, stiff materials, high- M_w PDMS provides access to lightly cross-linked and therefore soft materials. Soft silicones can be actuated at a lower voltage as compared to stiffer ones, but they have reduced mechanical robustness. Unfortunately, high- M_w PDMS liquids tend to possess very high viscosity, which is detrimental for the processing of thin films prior to cross-linking. To decrease the viscosity, solvents are used and cast films are subsequently formed by letting the solvent evaporate. The viscosity problem can also be overcome by using low-viscosity formulations wherein PDMS chain extension and cross-linking are conducted in a single step. To increase the tear strength of silicones, surface-treated silica nanoparticles are often used. Typical concentrations range from 5 to 30 vol%, whereby stiffer materials are obtained at higher filler loading. When ethyltetraethoxy silane is used, as is the case for reaction (d) in Fig. 1, silica is generated in situ. Alternatively, high tear strength silicones are also prepared when an “elastic cross-linker” is used. This enables preparation of soft elastomers that can reinforce at large strain (Bejenariu et al. 2012).

1.1.2 Composites

In the following section, preparation of silicone composites and films thereof is discussed. A highly homogenous solution of PDMS precursor and cross-linker is first formed. To adjust the viscosity of the mixture, solvents such as toluene, heptane, or cyclohexane can be used. Fillers including surface-treated silica can also be added. When particles are used, it is recommended that they be dispersed using a tip sonicator or a SpeedMixer. After a homogenous dispersion is formed, the catalyst is added. To remove the air bubbles (if a SpeedMixer is not used), further sonication

for about 5 min in a sonicator bath may be needed. Films can then be cast in a Teflon Petri dish or on Teflon foil and allowed to cross-link. Since the cross-linking reaction for the condensation curing of PDMS is rather difficult to quench, sufficient time should be allotted for aging. Special care is required regarding the stability of the components as they carry reactive groups that might be sensitive to moisture.

Now that the cross-linking aspect and thin-film formation have been explained, the next important aspect addresses how to make silicone-based materials with as high as possible permittivity. As indicated above, there are two strategies being pursued: the introduction of polar groups to the backbone (instead of methyl) and the blending of silicone matrix materials with highly polarizable ceramic and conductive fillers. Ceramic fillers such as TiO_2 (Skov et al. 2013), lead magnesium niobate–lead titanate (Gallone et al. 2007), BaTiO_3 (Carpi and De Rossi 2005; Lotz et al. 2008; Szabo et al. 2003; Zhang et al. 2008), and $\text{CaCu}_3\text{Ti}_4\text{O}_{12}$ (Romasanta et al. 2012) have all been previously investigated for this purpose. Although an increase in the permittivity was observed at all frequencies, this increase was mostly accompanied by increases in the elastic moduli and the dielectric loss, as well as a decrease in the electrical breakdown. Whenever conductive fillers are used, special care must be exercised to avoid agglomeration of the filler, which could result in percolation and consequently an electrical breakdown even at very low filler concentrations (Carpi et al. 2008). It is therefore essential that the conductive filler is encapsulated in an insulating shell prior to blending (Molberg et al. 2010). While silicones with increased permittivity and good elastomeric properties have been prepared by this approach, the electrical breakdown did not change significantly (Opris et al. 2011).

1.1.3 Functionalization

It is known that polar groups can increase the permittivity of a polymer and this approach was also explored recently for silicone materials. For such chemical functionalization, silicones containing Si-H groups were used as anchor points to attach polar groups by a post-polymerization chemical modification (hydrosilylation) (Fig. 2). Polar groups such as trifluoropropyl (Böse et al. 2012), *p*-nitroaniline (Kussmaul et al. 2011), or cyanopropyl (Risse et al. 2012) have been employed. Although an increase in permittivity was observed by increasing the concentration of polar groups, the increase was limited to values below 7 at high frequencies. Commercial access to silicones containing Si-H groups is limited to

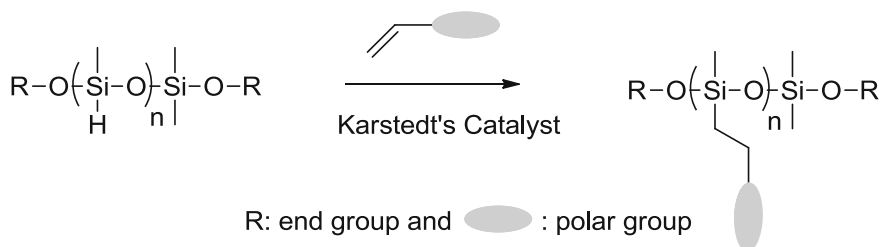


Fig. 2 Functionalization of polysiloxane chain with polar side groups via hydrosilylation

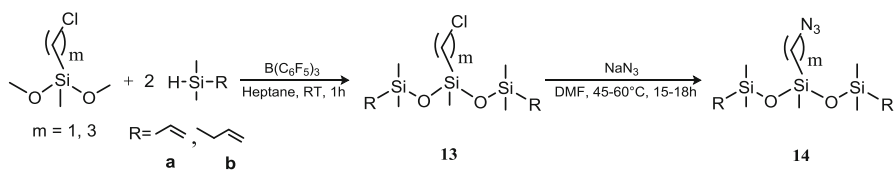


Fig. 3 Synthetic route to azido-functional chain extender (Madsen et al. 2014)

polymers typically with $M_w < 20,000$ g/mol. After dipole functionalization and cross-linking, the materials formed show insufficient mechanical properties, and therefore, they can only be used as fillers in silicone matrix materials with improved mechanical properties. As a consequence, however, these blended silicone materials become nonhomogeneous. Nonhomogeneity leads to the formation of interfaces and defects and, therefore, a higher probability of material failure.

Therefore, it would be interesting to have telechelic high- M_w polysiloxanes that carry anchor groups in their chains. While a high- M_w polymer will ensure good elastic properties, the anchor groups would permit polar side group functionalization, and the end groups would allow for controlled cross-linking. This approach, however, requires tedious synthesis steps, but would yield homogenous materials in contrast to the commonly applied blending of higher permittivity phases into a silicone matrix. First attempts to achieve this were recently reported (Madsen et al. 2013).

Madsen et al. (2014) recently developed a toolbox for obtaining homogeneously functionalized silicone elastomers by the use of a clickable chain extender (Fig. 3), which greatly facilitates the targeted formulation of silicone elastomers in modular fashion, as illustrated in Fig. 4. The chloro-functional intermediate in scheme X furthermore was shown to simultaneously increase the dielectric permittivity and decrease the dielectric loss of the resulting silicone elastomers. These initial results indicate that a sensitive balance of certain properties such as elastic moduli, permittivity, dielectric loss, conductivity, and electrical breakdown is required to optimize the electromechanical response for DEAs. However, with the recent developments reported for silicone elastomers, an increasing number of DEA-targeted properties can be more fully developed.

1.2 Dielectric Elastomers Based on Acrylate Copolymers

Acrylate copolymers are among the most intensively investigated dielectric elastomers. These elastomers exhibit extremely large actuation strain, pressure, and specific energy density when a high driving voltage is applied across the thin polymer films. In the meantime, most of such polymers are viscoelastic, leading to slow response speed. Synthetic effort to improve material performance has focused on suppressing electromechanical instability, increasing response speed or broadening application temperature range, and adding high dielectric fillers to increase the dielectric constant.

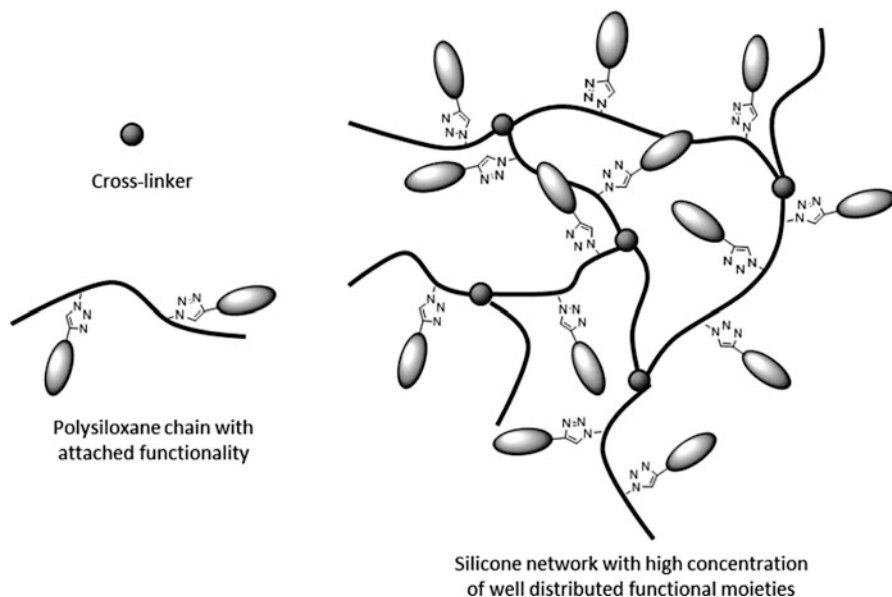


Fig. 4 Schematic illustration of functional polysiloxanes used in elastomer synthesis

1.2.1 Suppressing Electromechanical Instability

The acrylate copolymer that was first studied as a high-strain dielectric elastomer was the VHB 4910 adhesive film produced by 3M. The commercial film is 1 mm thick and had to be stretched to about 100 μm thick so that it could be actuated at a few kV. Quickly, it was found that the prestretching was actually key to achieving high actuation strains and high energy densities and worked on most other dielectric elastomers as well (Pelrine et al. 2000b). Careful analysis showed that electromechanical instability, a pull-in effect, was responsible for the dielectric breakdown of unprestrained films with low modulus and a slow upturn on the stress-strain response (Kornbluh et al. 1999; Plante and Dubowsky 2006; Zhao and Suo 2007). As seen in Fig. 5, prestrain increases the stiffness at low strains and moves the rapid upturn of stress to lower strains to effectively deter pull-in (Brochu and Pei 2010).

Prestrain can cause several practical problems including mechanical instability at interfaces between the soft elastomer and the rigid prestrain-supporting structure, as well as stress relaxation and actuator fabrication complexity. To reduce or eliminate mechanical prestrain while retaining its performance benefits, interpenetrating polymer networks (IPNs) were investigated as a new dielectric elastomer (Ha et al. 2006). In one approach, the VHB adhesive film was used as the initial elastomeric network. Cross-linkable liquid acrylate monomers were introduced into highly prestrained acrylic films and cured to form the second elastomeric network (Fig. 6). When the interpenetrating elastomeric network films were allowed to relax to zero external stress, the acrylic network would contract, compressing the additive network. In the resulting free-standing films, the two networks were in balance, one in high tension

Fig. 5 Characteristic stress of a dielectric elastomer film as a function of mechanical strain or electric field (constant voltage condition). The charts with origin at O are for a non-prestrained film and at O' for the prestrained film. The cross (X) indicates dielectric breakdown and the circles indicate maximum stable actuation

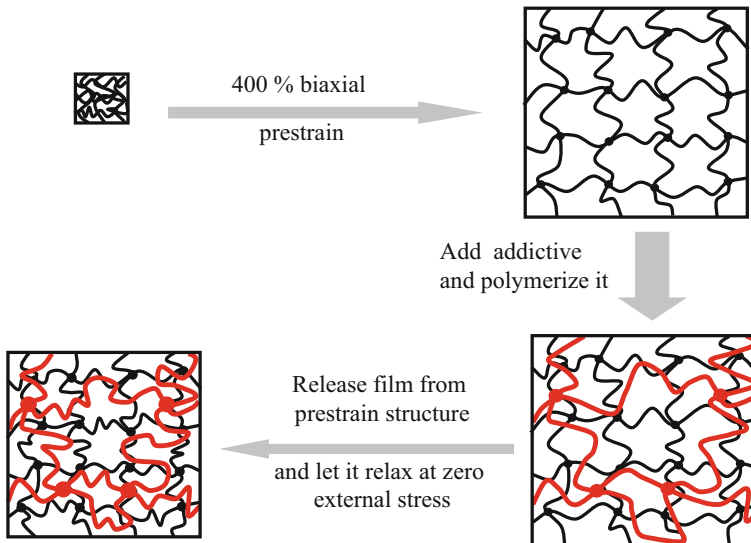
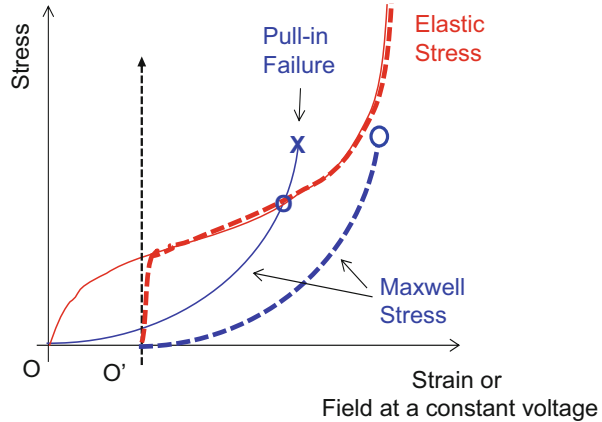


Fig. 6 Illustration of the fabrication of an IPN film comprising two internally balanced tension and compression networks

and the other in high compression. The preserved prestrain of the VHB networks can be varied over a wide range depending on the concentration of functional monomers. Free-standing IPN films were shown to exhibit electrically induced strains up to 300 %, comparable to highly prestrained acrylic films.

Acrylate-based dielectric elastomers could also be synthesized from commercial commodity monomers. Thus, dielectric elastomer precursor solutions were formulated containing a prepolymer (oligomer), reactive diluents, photoinitiators, and other additives (Niu et al. 2013). The oligomer, or a blend of a few oligomers, was selected as the framework responsible for the basic mechanical properties of the

material system. Reactive diluents, including monofunctional and/or multifunctional acrylates, were used to adjust rheology, provide cross-linking, and precisely tune the mechanical properties of the material. Photoinitiators were used to initialize the polymerization by UV light. The liquid precursor could be cast into thin films and UV cured to form dielectric elastomer films. Varying the amount of cross-linker comonomer in the precursor allowed tuning the stress–strain relationship and suppressing electromechanical instability while maintaining high-strain performance. The resulting dielectric elastomers were capable of high actuation strain (>100 %), high energy density (>1 J/g), and good temperature and frequency response without requiring prestretching. The material could be fabricated using conventional coating techniques, and the process could allow for high-volume throughput of stacked dielectric elastomer actuators.

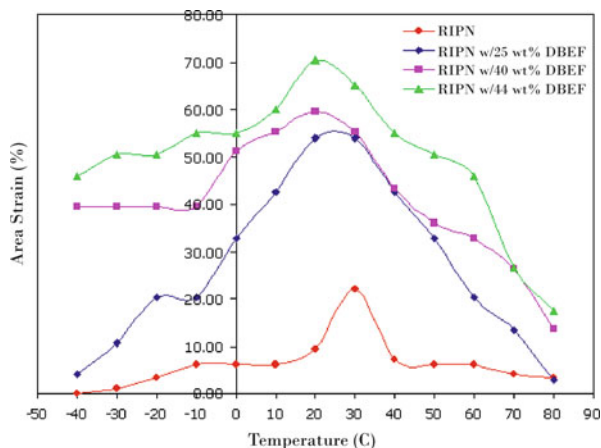
1.2.2 Increasing Response Speed

Conventional acrylate-based and their IPN elastomers exhibit exceedingly small strain at low temperatures. At 0 °C and below, as the temperature approaches the T_g of the acrylate polymers, the polymer chains begin to “freeze” and can hardly move around within the polymer matrix. At room temperature (which is not much higher than T_g), viscoelastic responses are rather high and impede the actuation speed. Plasticizers are known for their ability to modify the mechanical behavior of polymers. Among commonly used plasticizers, dibutoxyethoxyethyl formal (DBEF) and bis(2-ethylhexyl) phthalate (DOP) were found capable of greatly improving the acrylate polymer properties (Zhang et al. 2010). Resulting IPN films treated with these plasticizers become softer and possess a lower elastic modulus and reduced T_g . At ambient temperature, strains in areal expansion of the films are higher than the unplasticized films due to a reduction in the elastic modulus. At temperatures below 0 °C, DBEF-treated IPN films still had significant deformation (as large as 215 % areal strain) with a sample containing 40 wt% DBEF tested at –40 °C, unlike unplasticized (referred to as relaxed IPN, RIPN) films that showed little response to an electric field at –30 °C and –40 °C (Fig. 7). Above room temperature, the areal strains of all samples, both plasticized and unplasticized, decrease with increasing temperature. The treated films can be actuated at room temperature to 100 % strain at frequencies as high as 100 Hz while the magnitude of strain does not show significant degradation from 1 to 100 Hz.

1.2.3 High Dielectric Acrylate Elastomers

The actuation voltage of dielectric elastomer actuators is typically on the order of a few kV. Various high dielectric constant filler materials have been investigated to increase the dielectric constants and improve the actuation strains, force outputs, and energy densities of the compliant polymer actuators and generators. Aluminum nanoparticles had been used to effectively increase the dielectric constant of an acrylate copolymer. The surfaces of the nanoparticles were functionalized with methacrylate groups so that the nanoparticles were copolymerized with the acrylate comonomers during bulk polymerization to form uniform nanocomposites. In this approach, the nanoparticle loading could be as high as 4.0 vol% (15 wt%) to raise the

Fig. 7 *Left:* Strain behavior of relaxed IPN (RIPN) films plasticized with 25, 40, and 44 wt% DBEF (see figure legend) at temperatures ranging from $-40\text{ }^{\circ}\text{C}$ to $80\text{ }^{\circ}\text{C}$. *Right:* Applied voltage is 5 kV. Large deformation (215 % areal strain) of an RIPN film plasticized with 40 wt% DBEF and actuated at $-40\text{ }^{\circ}\text{C}$ (From Zhang et al. 2010. Copyright © 2010 Society of Chemical Industry)



dielectric constant to 8.4 without significantly increasing the leakage current. The dielectric strength was 140 MV/m, which is on par with most high-performing dielectric elastomers without high dielectric fillers. The nanocomposite exhibited a maximum actuation strain of 56 % and a significantly higher actuation force output than the neat acrylate copolymer.

1.3 Dielectric Elastomers Based on Polyurethanes

In addition to the above discussed families of silicones and acrylates, another family of polymers that can be exploited for DEA applications includes polyurethanes. Studies of polyurethane-based DEAs have reported promising results for this class of materials, which specifically exhibit great potential for use as artificial muscles. The first commercial polyurethane, with the characteristic carbamate group $-(\text{NH})(\text{CO})\text{O}-$ backbone (Fig. 8), was realized in 1937 by Bayer (1947). The simplest and most common reaction scheme, although not the only one possible, to synthesize the urethane linkage is to combine polydiisocyanate with a polydiol by a polyaddition reaction, as displayed in Fig. 8.

By appropriate choice of the R_1 and R_2 groups (Fig. 8), it is possible to customize the characteristics of the final product through a large spectrum of mechanical properties. Furthermore, either by using polyol or polyisocyanate components with

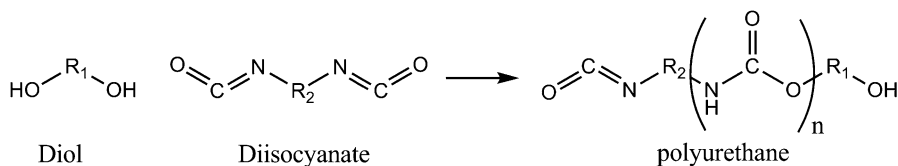


Fig. 8 Simple reaction scheme between a diol and a diisocyanate to form a polyurethane

more than two reactive functions or by introducing unsaturated segments in the polymer backbone, it is also possible to make the final polymer a cross-linkable elastomer. As a matter of fact, polyurethanes represent in general one of the most versatile families of polymers that exist. Due to the high tunability of their mechanical properties, which can range from stiff plastics to very soft elastomers and ultralight foams, polyurethane elastomers (PUEs) may outperform many other materials in flexibility, elasticity, tear resistance, adhesive strength, and durability. Despite such promising characteristics and the ability of polyurethanes elastomers to actuate under high electric fields, this class of elastomers has not enjoyed the same widespread attention of the other two most popular polymer classes (i.e., silicones and acrylates) in the field of DEAs, and the number of related studies available in the literature remains rather limited.

One of the first efforts that studied the behavior of a polyurethane as a DEA dates back to 1997, when the actuation response of a polyurethane elastomer prepared from polyester glycol, p-phenylene diisocyanate, and a mixture of 1,2-propanediol and 1,1,1-tris(hydroxymethyl)propane as a chain extender was reported (Ueda et al. 1997). In the same year, Zhang and co-workers (1997) studied the electromechanical responses of a polyurethane elastomer. Pelrine et al. (2000a) later compared the strain response to applied electric fields for a variety of elastomers, demonstrating that silicone polymers provided the best combination of high strain and energy density, making them preferable over polyurethanes. This last finding might have contributed in driving the interest of researchers toward preferring silicones and acrylates with respect to polyurethanes in subsequent years.

In any case, polyurethane dielectric elastomers have continued to be studied in the last decade, particularly with regard to the possibility of increasing their actuation performance. It is well known that both dielectric and mechanical properties are key parameters governing the electromechanical response of any dielectric elastomer, which can be in principle improved by an increase of the dielectric constant and by a decrease of the elastic modulus. In order to increase the dielectric permittivity of a polymer elastomeric matrix, various methods are available (Carpi et al. 2008), such as making composites or blends with highly polarizable phases. Table 1 constitutes a non-exhaustive list of works from the literature, mostly relying on such methods for improving the performance of polyurethane dielectric elastomers. The studies are classified in terms of system complexity and component materials.

Some significant results from the studies included in Table 1 are summarized in Table 2.

Table 1 Some examples of modified polyurethane-based dielectric elastomers selected from the literature

System	Filler/blend component	References
Simple matrix	–	(Fukuda et al. 2012a)
Random composites	Cu-coated phospholipids	(Chiou et al. 2003)
	CB	(Cameron et al. 2004)
	CB (nanoparticles)	(Guiffard et al. 2006)
		(Roussel et al. 2014)
	BaTiO ₃ or TiO ₂ or PMN-PT	(Gallone et al. 2010)
	BaTiO ₃	(Fukuda et al. 2012b)
	PolyCuPc/PANI	(Huang et al. 2004)
	CuPc (nanoparticles)	(Wang et al. 2014)
	PANI	(Chwang et al. 2004)
	f-CNT	(Galantini et al. 2013)
Air pores + coronal charging	(Galantini et al. 2012)	
Polymer blending	PDMS	(Chiou et al. 2003)
	PDMS	(Gallone et al. 2010)
	PDMS	(Kussmaul et al. 2013)

Notes: *f-CNT* functionalized carbon nanotubes, *CuPc* copper phthalocyanine, *CB* carbon black, *PANI* polyaniline

Table 2 Summary of the main results achieved by several of the studies reported in Table 1

System	Strain (%)	Electric field (V/μm)	References
PU/CB	–7.4 (l)	17.4	(Guiffard et al. 2006)
PU/PolyCuPc/PANI	–9.0 (l)	20.0	(Huang et al. 2004)
PU/CuPc	–17.7 (l)	10.0	(Wang et al. 2014)
PU/CB	0.035 (t)	0.7	(Cameron et al. 2004)
PU/f-CNT	1.1 (t)	5.5	(Galantini et al. 2013)
PU/PDMS	3.0 (t)	5.5	(Gallone et al. 2010)

Note: The strain of the actuator may be transverse (*t*) or longitudinal (*l*)

Apart from the studies based on various self-made polyurethane molecules, there are also reports focused on the use of a commercial polyurethane as a DEA (Galantini et al. 2012, 2013; Gallone et al. 2010). As an example of such commercial elastomer, Poly 74-20 from Polytek Development Corp. (USA) is supplied by the manufacturer in the form of two pre-synthesized liquid components, one containing a diol mixture and the other one containing a diisocyanate solution. The method of preparing this product is very user-friendly, since it simply requires mixing the two solutions in the right ratios and letting the resultant mixture react quiescently at room temperature for several hours. Thus, it becomes very easy to approach the technology of dielectric elastomers with the desired formulation by dispersing proper additives prior to the reaction.

A very attractive feature of PUEs that makes this class of elastomers unique in the panorama of DEAs is their ability to exhibit intrinsic bending behavior. The

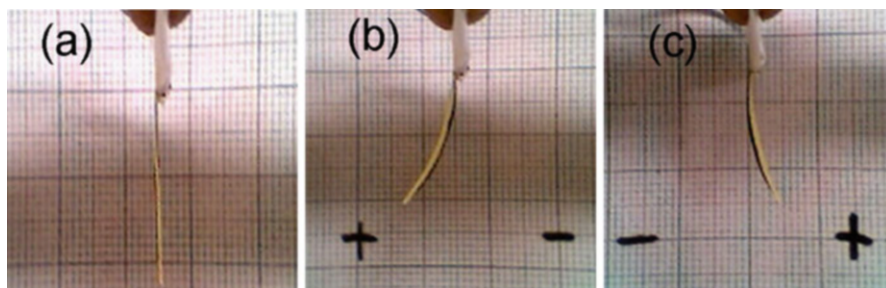


Fig. 9 Pictures of the bender actuator: at rest, in (a), and during stimulation by a voltage of 3 kV at two opposite polarities, in (b) and (c)

spontaneous tendency of PUE actuators to bend becomes particularly evident when they are left free, that is, when no prestretch is applied to them, as shown in Fig. 9. In 1999, Kurita and co-workers (1999) obtained a patent for exploiting the possibilities afforded by the bending behavior of polyurethane elastomers. In the same year, Kyokane et al. (1999) reported a polyurethane elastomer behaving as a unimorph bender actuator, with its deflection increasing with increasing applied voltage. They also doped the polyurethane elastomer by adding C_{60} derivatives to the matrix and found that doped samples were able to operate at lower voltages. Interestingly, they demonstrated the operation of a pincer-type actuator, fabricated by coupling two strips of unimorph actuators, which could smoothly pick up a sponge in the same manner as two opposing fingers.

The presence of hysteresis in the bending response of films composed of segmented polyester polyurethanes was reported by Watanabe et al. (2001). The hysteresis was related to the absorption current during stimulation, and its origin was attributed to ionic polarization, due to ionic impurities in the polyurethane, lasting after the removal of the electric field. Such hysteresis implies that prior application of an electric field not only significantly improves the bending speed in successive applications but also controls the bending direction in the case of subsequent application of an electric field of opposite polarity. Tartarisco et al. (2009) confirmed both the bending feature and the hysteresis in the commercial polyurethane compound Poly 74-20 and demonstrated that it is possible to fabricate polyurethane-based miniature actuators by using a pressure-assisted microsyringe (PAM) system. The achieved bender displayed opposite bending during the positive and negative periods of stimulation, with a maximum bending greater than 30° . A possible explanation for the bending phenomenon was formulated by supposing the presence, inside the bender, of positive- and negative-charged particles or segmental bodies with different diameters, masses, and mobilities, one or both being capable of displacement upon exposure to an external electric field. The voltage applied to the bender would thus generate selective charge migration toward the electrodes, which would result in a gradient of elastic modulus between the bender surfaces. Such a gradient, in response to the Maxwell stress temporarily acting on the dielectric elastomer, would finally cause it to flex by a mechanism similar to that acting in

bimorph benders. In this kind of system, the differences in the rigidity of the opposite surfaces are not fixed a priori, as in usual bimorph benders. Rather, they are induced by the same driving field and are thus dependent on its polarity as well. Nevertheless, when the voltage polarity is switched, the response of such a device shows a transient which should account for the mechanical relaxation that the system must undergo, presumably involving different time scales for different charge types. Only when a complete redistribution of charges has taken place the bender can start to bend coherently with the new inverted voltage polarity. Instead, during the transient, the system maintains a sort of “fading memory” of its nonuniform elastic modulus distribution, so that any Maxwell stress applied to the device, whatever the driving tension polarity, would cause bending in the previously memorized direction, thus producing hysteresis.

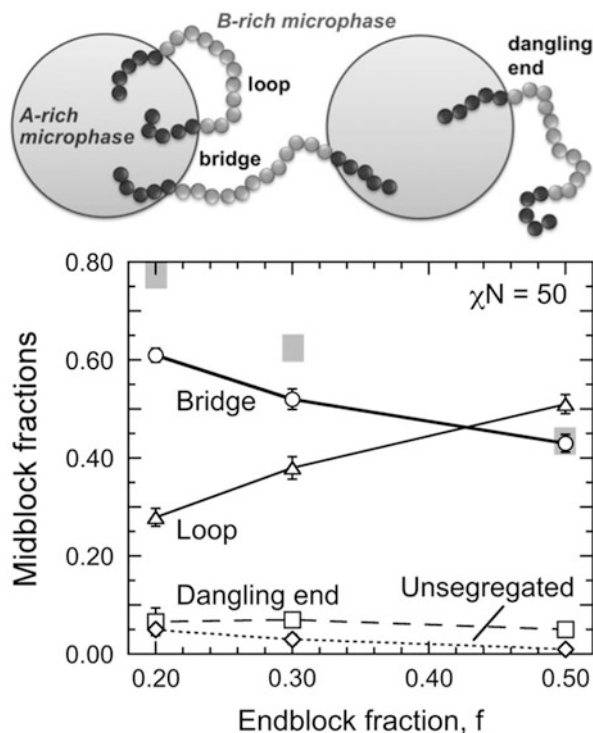
1.4 Physically Networked Block Copolymer Systems as Dielectric Elastomers

Triblock copolymers are capable of forming physical networks that can, depending on the chemical constitution of the blocks, permit the materials to behave as elastomers. Upon addition of a midblock-selective oligomeric liquid, these network systems exhibit highly tunable thermodynamic and (electro)mechanical properties. In the case of relatively nonpolar systems, electroactuation is largely governed by a low modulus and high elasticity. As physically cross-linked dielectric elastomers, these materials are capable of achieving remarkable area actuation strains ($\approx 300\%$) and very high electromechanical coupling efficiencies ($>90\%$) at relatively low electric fields. Besides being recyclable, they tend to exhibit low hysteresis upon strain cycling, and they have been successfully used to *i*) explore the underlying physics of the electromechanical modulus and *ii*) decouple the roles of mechanical prestrain and specimen thickness during electroactuation. Changing the viscosity of the midblock-selective liquid can greatly improve the blocking stress and energy density of these unique materials, while permitting mechanical impedance matching, as well as control over shape-recovery kinetics. Dielectric elastomers composed of more highly polar copolymer systems are capable of actuating beyond 100% without the need for any mechanical prestrain or chemical alteration. Selective solvation of triblock copolymer networks represents an effective means by which to tailor the function and properties of electroactive polymers through systematic manipulation of copolymer and solvent attributes.

1.4.1 Phase Behavior of Block Copolymer Systems

Block copolymers are macromolecules that consist of two or more long, contiguous sequences (“blocks”) of repeat units. Under favorable thermodynamic conditions, the blocks in a bicomponent copolymer undergo self-assembly and organize into well-defined, periodic nanostructures that depend on several material factors (Bates and Fredrickson 1999; Hamley 1998), such as copolymer incompatibility (χN , where χ is the Flory–Huggins interaction parameter and N is the number of statistical units

Fig. 10 Copolymer conformations (*top*) and corresponding midblock fractions from simulations (*bottom*)



along the backbone) and molecular composition (f). While most studies of molecular self-assembly and surface templating have focused on the AB diblock archetype, the ABA triblock design is capable of not only organizing into the same nanostructures as AB diblock copolymers but also developing a physically cross-linked molecular network (Tallury et al. 2014). Upon self-assembly, the B-midblock of ABA molecules can adopt three conformations: a bridge (each endblock resides in a different microdomain), a loop (both endblocks locate in the same microdomain), and a dangling end (one endblock lies in an A-rich microdomain, while the other remains mixed with B). These scenarios, along with results from dissipative particle dynamics (DPD) simulations, are presented in Fig. 10. In the event that the endblocks are glassy or semicrystalline and the midblock is rubbery, these copolymers behave as thermoplastic elastomers (TPEs) (Holden et al. 2004) and are used in a diverse range of contemporary technologies ranging from flexible electronics (Zhu et al. 2013) and microfluidics (Sudarsan et al. 2005) to fuel cells (Elabd and Hickner 2011) and sensors (Kofod et al. 2011). Addition of a midblock-selective liquid to a TPE can serve to either swell the existing copolymer nanostructure or alter the interfacial curvature, thereby inducing a morphological transformation, while retaining a molecular network (Krishnan et al. 2012). In fact, as a macromolecular surfactant, the copolymer can likewise self-assemble into soft nanostructures upon incorporation of two block-selective species, as evidenced by the ternary phase

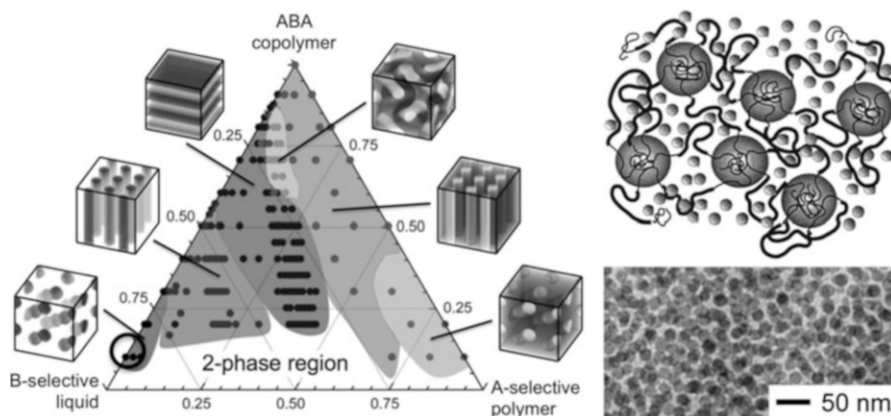


Fig. 11 Ternary TPE/liquid/polymer phase diagram (*left*) and schematic diagram and transmission electron micrograph (*top and bottom right*, respectively) of the blend that behaves as a DEA (*circled* on the phase diagram)

diagram displayed in Fig. 11. To simplify matters, we only consider the spherical (micellar) morphology along the copolymer/liquid axis in the design of DEAs, since the simulations and complementary theoretical predictions (shaded regions; Matsen and Thompson (1999)) provided in Fig. 10 indicate that the spherical morphology formed by ABA triblock copolymers possesses the highest bridging fraction. An electron microscopy image of the nanostructure, as well as a graphical depiction, is included in Fig. 11.

1.4.2 Electroactuation of Nonpolar TPE Systems

Nonpolar TPE systems of interest here consist of styrenic (S) endblocks and a hydrogenated rubbery midblock (ethylene-*co*-butylene, EB, or ethylene-*co*-propylene, EP) and are commonly referred to as SEBS or SEPS copolymers, respectively. Midblock-selective oligomeric liquids must be chosen to avoid dissolution in, and plasticization of, the glassy endblocks, which serve to stabilize the copolymer network. For this reason, long-chain aliphatic liquids such as mineral oil (MO) and squalane are typically used to fabricate midblock-solvated TPE blends. The liquids can be incorporated into the copolymer via melt blending or co-dissolution in a relatively neutral solvent, such as toluene. As seen in Fig. 12, copolymer characteristics, such as N and f , and blend composition (w_{BC}) are adjustable material properties that regulate the (electro)mechanical properties of TPE/MO blends. Since the area actuation strain can be expressed in terms of the transverse strain through the use of constitutive relationships and the electric field is related to the Maxwell stress for an ideal DEA, actuation results such as those provided in Fig. 12a for TPE/MO blends can be recast into stress–strain curves from which values of the electromechanical moduli can be extracted. Such moduli are presented as a function of the TPE concentration in the blend (C) at two levels of mechanical prestrain in Fig. 13a. These results (Krishnan et al. 2011) show that *i*) the scaling relationship (modulus \sim

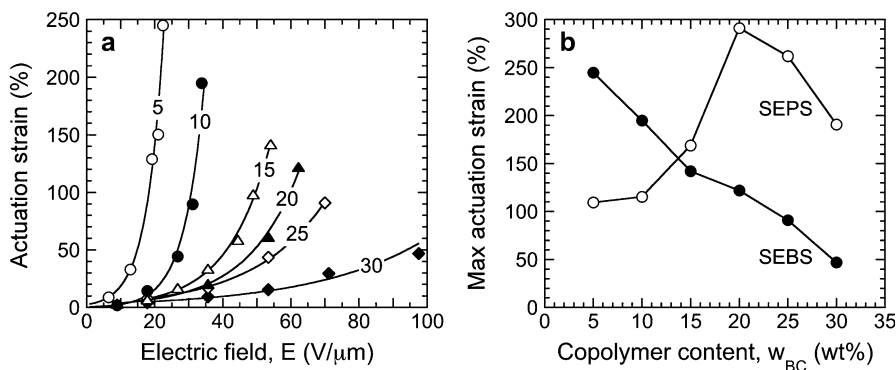


Fig. 12 (a) Actuation strain as a function of electric field for TPE/MO blends differing in w_{BC} (labeled) and (b) maximum actuation strain as a function of w_{BC} for two different types of TPEs (labeled) at varying specimen thicknesses

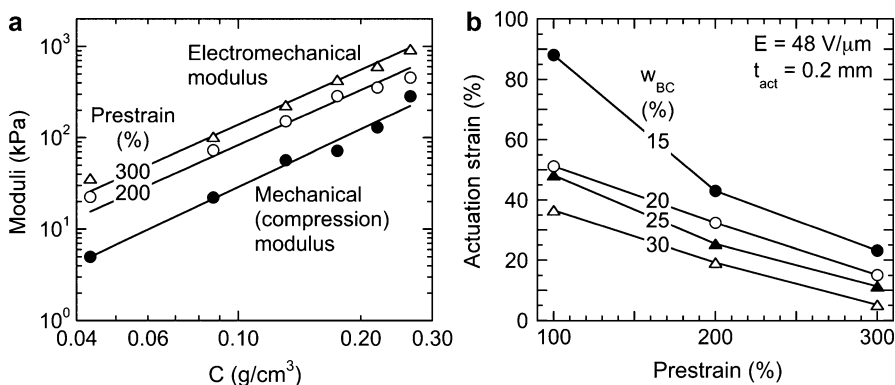


Fig. 13 (a) Moduli extracted from mechanical and electromechanical tests, the latter at different prestrain levels (labeled), as a function of TPE concentration, and (b) actuation strain as a function of prestrain for blends with the *same* pre-actuation thickness

C^n , where $n \approx 2$) observed for purely mechanical compression is retained for electroactuated systems, which has important theoretical implications (Vega et al. 2001), and (ii) an increase in mechanical prestrain promotes an increase in modulus due to pre-actuation chain stretching. Due to their physical tunability, these TPE/MO blends can also be designed to test the widely held belief that mechanical prestrain (applied to reduce specimen thickness and thus lower the applied potential required to achieve a desired electric field) does not strongly affect actuation performance. Electroactuation strains are displayed in Fig. 13b for TPE/MO blends differing in concentration wherein the actuation thickness (t_{act}) is held constant, but the coupled pre-actuation thickness/mechanical prestrain values are varied. These results confirm that mechanical prestrain can significantly influence actuation performance (even under isofield conditions). Another means by which to modify the

electroactuation response of TPE/MO blends is through physical incorporation of a chemically matched diblock copolymer. By doing so, the fraction of midblock bridges is affected, and the electric field required to induce actuation is lowered. Lastly, while most dielectric elastomers respond quickly to an applied field, substitution of a relatively high-viscosity midblock-selective additive (e.g., a hydrogenated tackifying agent) for MO in TPE blends can slow down actuation kinetics while improving metrics such as the energy density (Vargantwar et al. 2011). Blends containing both additives, which must be fully miscible, can be used to finely tune the actuation response.

1.4.3 Electroactuation of Moderately Polar TPE Systems

The TPE/oil design paradigm discussed thus far is fully extendable to other, non-styrenic copolymers, such as wholly acrylic TPEs. In this case, the endblocks must be composed of a glassy material such as poly(methyl methacrylate), whereas the midblock is based on a “soft” acrylic, such as *n*-butyl acrylate. Although midblock-selective liquids with higher dielectric constants (e.g., dioctyl phthalate) can be used to improve electroactuation (since the Maxwell stress depends proportionately on the dielectric constant of an ideal dielectric elastomer), the intrinsically low interblock incompatibility is responsible for plasticizing the glassy cross-links and reducing the stability of the TPE network at high strains. With this limitation notwithstanding, a distinguishing benefit of these materials is that they undergo substantial actuation (>100 % strain with up to 78 % efficiency) without any mechanical prestrain (Vargantwar et al. 2012).

2 Compliant Electrode Materials

DEAs have electrodes on both sides of the elastomer membrane to transfer in and out the electrical charges needed for electrostatic actuation. Electrodes play a major, but often overlooked, role in DEA performance: displacement, speed, lifetime, and manufacturability are all tightly coupled to the electrodes. A comprehensive review is given by Rosset and Shea (2013). Strictly speaking, electrodes are not required for the function of DEAs. One can spray electrical charges by coronal discharge directly on a dielectric, as shown by Röntgen in 1880 and as demonstrated with today’s materials by Keplinger et al. (2010). Operating without electrodes has a number of tantalizing advantages, but the drawbacks are such that no devices are now realized without compliant electrodes.

What requirements must electrodes for DEAs meet? They must be sufficiently conductive to transfer charges quickly on the elastomer, remain conductive at strains in excess of 100 %, and not deteriorate even after many millions of cycles. To avoid reducing the actuation strain, they must also not add significant stiffness to the dielectric membrane, a major challenge given the soft elastomers used for DEAs. It must be possible to pattern the electrodes and to make reliable electrical contact to them. They must not dry or otherwise densify, and they must be robust with regard to mechanical wear. Ideally, electrodes also enable self-sensing and even self-switching

and thus have a well-defined change in resistance with strain. For any application other than a proof of concept, the electrodes must be manufacturable, i.e., produced reliably at high volume and at reasonable cost.

Given all these requirements, operating without electrodes seems like the best way to fabricate DEAs: no stiffening, no limit on strain before conduction is lost, and the ability to operate in charge rather than in voltage mode, thus avoiding electro-mechanical instabilities inherent to DEAs. However, spraying charge on and off a membrane requires equipment and an experimental setup far more complex than driving charge on/off electrodes. In contrast, applying a voltage to bring charges to an electrode is straightforward. Electrodes can be patterned to define exactly where charge will be present and hence where actuation will occur. This is very important for many devices, where independent electrodes are positioned on a single DEA membrane, as nicely illustrated by the vibrotactile display from TU Darmstadt (Matysek et al. 2010) or the rotary motor from the University of Auckland (Anderson et al. 2010).

Electrodes are therefore an unavoidable component of DEAs and must be explicitly considered from the design stage and included in modeling if one wishes to obtain accurate performance models. In a recent review, Rosset and Shea (2013) have categorized electrodes for DEAs as (a) carbonaceous, (b) metallic thin film, or (c) novel. For details, we refer the reader to that review and the references provided therein. We follow this classification here, with an overview given in Fig. 14. When comparing electrodes, in addition to intrinsic electrical and mechanical properties, one must also consider the ease by which the electrodes can be applied and patterned, as well as their lifetime. Different applications require different electrodes.

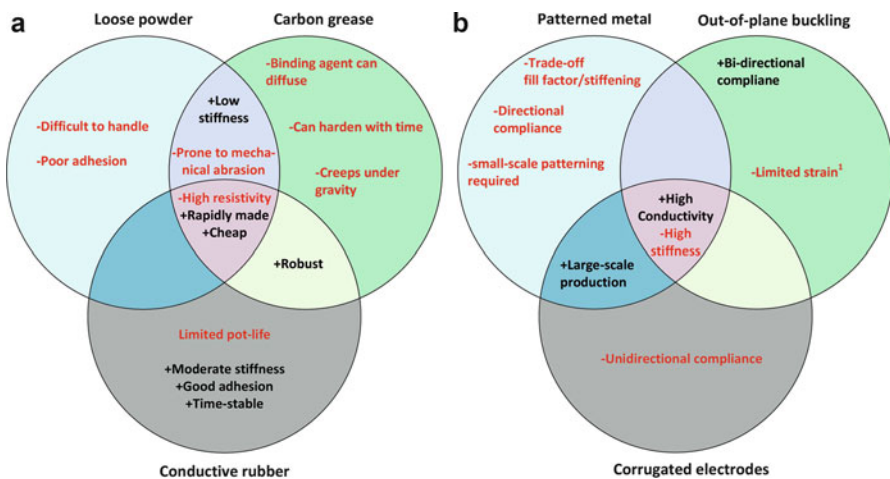


Fig. 14 Main characteristics of (a) carbon-based electrodes and (b) metallic thin-film electrodes for DEAs (Rosset and Shea 2013)

2.1 Carbon-Based Electrodes

Carbon-based electrodes can be made from *i*) carbon powder, *ii*) carbon grease, or *iii*) a carbon–elastomer composite. For quick experiments, carbon powder and carbon grease are very appealing options and were the electrodes used for nearly all early papers. Since the acrylic elastomer VHB is an adhesive, simply sprinkling carbon powder (e.g., carbon black such as Ketjenblack EC-300 J from AkzoNobel or graphite) can make an acceptable electrode, adding negligible stiffness and requiring very little effort. Challenges with carbon powder are handling (static electricity makes for a messy process!), conductivity at large strains is difficult to maintain, and the lifetime is very limited since any contact with the electrode can lead to the removal of the carbon powder. Carbon greases, such as Nyogel 755G from Nye Lubricants, are carbon powder embedded in a viscous binder and are therefore much easier to handle than bare carbon powder. They are often patterned with a paintbrush or a color shaper, allowing features down to a few mm to be defined if sufficient care is taken. To quickly try a new concept, carbon grease is very efficient. It is however not very robust as it simply smears off if one inadvertently touches it. It also dries out over time, and the grease can interact with (or diffuse into) some elastomers. The viscous nature of the grease makes it unsuitable for any application where speed or the absence of a viscous response is needed.

If one wishes to make a DEA device that is more robust or that is to be commercialized, one must look for alternatives to carbon powder or carbon grease. An increasingly used technique is to mix carbon powder with an elastomer (typically a soft silicone) to make stretchable composite electrodes, which is only cross-linked after having been transferred onto the DEA membrane, as recently illustrated (Araromi et al. 2014). Such electrodes are mechanically robust, as the conductive powder is encapsulated in an elastomer matrix. A downside is that carbon–silicone composite electrodes can add stiffness to the DEA, thereby reducing the actuation strain. The more highly carbon loaded the composite is, the greater its stiffness will be. Since the powder must be well dispersed in the matrix, carbon powder is generally preferred over metal particles. Exfoliated graphite has also been used with success (Kujawski et al. 2010). Making the electrode as thin as possible reduces the stiffening impact.

Patterning carbon-based electrodes can be achieved by a number of means. One might prefer a noncontact technique not to damage the thin DEA membrane. Shadow masking can be used with powders if the powder is airbrushed or applied as an aerosol from solution, as in the highly automated multilayer process developed by TU Darmstadt (Schlaak et al. 2005) for which each layer of graphite electrode is then covered with a subsequent silicone layer. Stamping, and similar transfer techniques such as pad-printing, can allow the transfer of very fine features and of thin (few μm) layers with high throughput. Aschwanden and Stemmer have achieved 50 μm features by stamping carbon powder on VHB (Aschwanden and Stemmer 2007), whereas Araromi et al. used a commercial pad-printer (Teca-Print TPM101) to transfer conductive ink consisting of carbon black in a soft uncured PDMS to a variety of silicone membranes (Araromi et al. 2014). The carbon ink is typically

diluted prior to printing to obtain a viscosity suitable for transfer by the selected stamping process.

2.2 Metallic Thin-Film Electrodes

When one thinks of electrodes, metals are generally the first material one considers, as they are excellent conductors and are routinely patterned on the nanometer scale. Metals are however roughly five orders of magnitude stiffer than elastomers and fracture at strains of only a few percent. Thus simply evaporating metal on a thin polymer membrane will not yield a DEA with desired properties, since the electrodes will greatly stiffen the DEA and break at 2–3 % actuation strain. Two classes of solutions have been developed to make metal electrodes for DEAs: patterned electrodes and thin-film electrodes on corrugated membranes. Patterning electrodes in horseshoe or meander or zigzag shapes can allow for many tens of percent strain in one or two directions with no damage to the electrode (Pimpin et al. 2007). This technique, while widely used for interconnects in flexible electronics, is not particularly well suited for DEAs as the area covered by the electrodes is smaller than the area of the actuator. Shadow masking, liftoff, and etching following photolithography are techniques that allow patterned metal electrodes. Lithography on soft elastomers requires special techniques, as previously described (Guo and Deweerth 2010).

Thin metallic electrodes deposited onto corrugated surfaces of elastomer films have been successfully demonstrated for the first time in 2002 by Benslimane et al. (2002). This type of electrode is intentionally designed to be anisotropic, allowing for unidirectional elongation without the need for any mechanical prestrain or supporting frame. The groundbreaking corrugated electrode designed had a topology that favored up to 33 % strain in the direction of compliance with a corrugation depth-to-period ratio close to 0.4–0.5 (4–5 μm depth and 10 μm period). Large-scale manufacturing of elastomer material with this type of electrode has been established and made possible by Danfoss PolyPower A/S by combining roll-to-roll coating and vacuum deposition techniques (Kiil and Benslimane 2009). In 2010, a new configuration of the compliant electrode based on the same principle but increasing the corrugation depth-to-period ratio to nearly 1 (7 μm depth and 7 μm period) has been successfully demonstrated and commercially manufactured (Benslimane et al. 2010a, b). The electrode consists of silver and its nominal thickness is 110 nm. With this new electrode configuration, strains of up to 80 % without any substantial electrode damage are made possible. Furthermore, this new configuration results in electrodes that are mechanically more compliant than the very first one introduced in 2002, thereby allowing for more transducer strain as a consequence of lower equivalent elastic moduli.

When designing such electrodes, it is important to optimize not only the corrugation topology as discussed previously but also the shape using curved profiles to avoid the appearance of mechanically weak sections that in the long term will result in fatigue and electrode damage, reducing electrode lifetime. Another important aspect to

consider when designing such electrodes is the optimization of the corrugation depth with respect to the elastomer film thickness. Distortions and nonuniformities of the electric field distribution across the film thickness can occur if the corrugation height is of comparable size to the film thickness as can be easily shown by electrostatic calculations or FEA simulations. It is typically recommended to maintain the ratio between corrugation depth and film thickness below 0.15. When considering much thinner elastomer films (less than 20 μm), it is important to subsequently reduce the corrugation depth and period on the one hand and the electrode thickness on the other hand, as these parameters affect the electrode stiffness and subsequently the overall transducer stiffness in the direction of compliance.

2.3 Novel Electrodes

A wide range of techniques have been explored to make compliant electrodes for DEAs, often aiming at adding specific functionality such as optical transparency or the ability to recover from a short circuit by self-clearing. These varied techniques have produced electrodes with excellent properties, but are still at an exploratory stage. For example, ionic conductors (electrolytes) can conduct up to tens of kHz and have been used in soft hydrogels as transparent and highly compliant electrodes for DEAs as loudspeakers (Keplinger et al. 2013) and strain sensors (Chen et al. 2014). These electrodes were 98.9 % transparent for visible light. Single-wall carbon nanotubes (SWCNTs) and silver nanowires have been used to make 91 % transparent electrodes for DEAs with 190 % area actuation (Shian et al. 2012). Stretchable partially transparent metal electrodes have been realized by implanting metallic nanoclusters up to 100 nm below the surface of the elastomer by either ion implantation (Niklaus and Shea 2011) or supersonic cluster beam implantation (Corbelli et al. 2011). Other techniques include photopatternable electrodes (Urdaneta et al. 2007) and “crumpled” metal films, obtained by metalizing highly prestretched elastomer membranes (Low and Lau 2013).

Since DEAs are often operated near the electric field at which they fail and since breakdown through the dielectric is initiated at a single point, having electrodes that act as a fuse and cease to conduct when a given current density is exceeded can greatly extend the lifetime of DEAs. This fuse action is referred as “self-clearing,” as the electrodes vaporize or burn up only very near the point where the short circuit will occur, protecting the DEA from further damage and allowing continued operation.

Conductive polyaniline (PANI) nanofibers, poly(3-decyloxythiophene), and carbon nanotube thin films are capable of forming highly compliant electrodes with fault-tolerant behavior (Yuan et al. 2007). Ultrathin PANI and SWCNT films are both capable of “self-clearing” (Lam et al. 2008; Yuan et al. 2008). Nanowires and tubes are of particular interest since they are capable of maintaining a percolation network at large strains, thus reducing the required electrode thickness while still allowing for maximum strain performance. For instance, PANI nanofiber films provided good actuation characteristics, provided fault tolerance, and had a

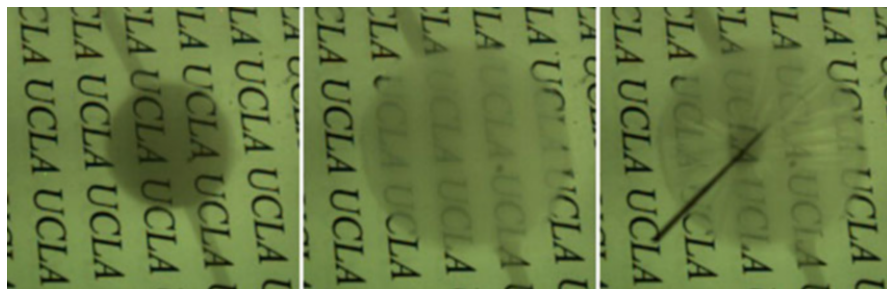


Fig. 15 Fault tolerance of SWCNT electrodes. The dielectric elastomer actuator is able to withstand puncture and maintain a high level of strain due to self-clearing of SWCNTs around puncture. From left to right: prestrained VHB acrylic actuator with SWCNT electrodes; actuated; actuated with a cactus pin through the active area

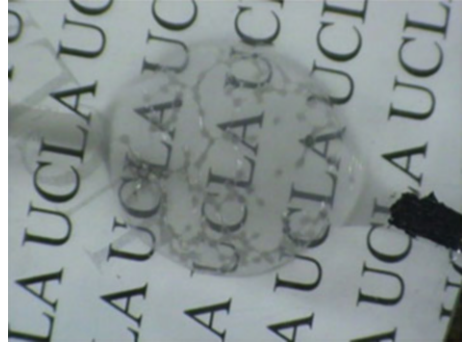
negligible influence on the mechanical properties of the film but lost conductivity over time (Lam et al. 2008). When tested on VHB 4905 films, the electrodes provided a maximum area strain of 97 % at 3 kV and demonstrated self-clearing with a preserved strain of 91 % after the first clearing event. Carbon nanotubes were much more promising for obtaining fault tolerance (Yuan et al. 2008). In this case, SWCNTs provided excellent actuation characteristics (on par with carbon grease), had a negligible influence on mechanical properties of the film, and remained stable over longer periods of time.

Dielectric failure is one of the leading causes for premature device failure of dielectric elastomers. The fault tolerance of devices with SWCNT electrodes is demonstrated in Fig. 15. In this test, a prestrained circular VHB acrylic actuator was punctured with a cactus pin and maintained at very high actuation strains. In separate tests, the actuators were driven at a high field until the occurrence of a localized breakdown, at which point the actuators “self-cleared” and recovered well from the local failures and retained high actuation strains. The SWCNTs in the region surrounding the short were burned off. The addition of self-clearing introduces fault tolerance to DEAs and can dramatically increase device lifetime. During constant voltage actuation, a SWCNT-coated dielectric elastomer could be actuated for a long duration of time, surviving a number of localized dielectric failure and self-clearing occurrences while the actuator remained functional (Yuan et al. 2009). The constant actuation lifetime could be increased by two orders of magnitude over carbon grease electrode-based devices (Fig. 16).

3 Summary and Discussion

Dielectric elastomers occupy an important niche in transducer technology. As field-activated materials, they are fast-acting and efficient, and, unlike most field-activated materials, they are capable of extremely large strains. Actuation strains of more than 100 % have been produced (Pelrine et al. 2000b). Because a wide variety of

Fig. 16 A dielectric elastomer actuator based on self-clearable SWCNT compliant electrode. The actuation survived dozens of localized dielectric breakdowns, each leaving behind a darker dot in the image as a result of SWCNT self-clearing



elastomer and electrode materials may be used, dielectric elastomer technology can be considered for a wide range of applications, including uses in extreme environments or in many-device arrays, when low-cost production is a requirement.

We hope that this discussion of materials will enable the reader to better understand the fundamental properties of dielectric elastomers and how the different classes of elastomers perform with respect to some of the important parameters for dielectric elastomer uses as well as how to design suitable electrode systems.

References

- Anderson IA, Hale T, Gisby T et al (2010) A thin membrane artificial muscle rotary motor. *Appl Phys Mater Sci Process* 98:75–83
- Araromi OA, Gavrilovich I, Shintake J et al (2014) Rollable multisegment dielectric elastomer minimum energy structures for a deployable microsatellite gripper. *IEEE/ASME Trans Mechatron* 20:438–446
- Aschwanden M, Stemmer A (2007) Low voltage, highly tunable diffraction grating based on dielectric elastomer actuators. *Proc SPIE* 6524:65241N
- Bates FS, Fredrickson GH (1999) Block copolymers – designer soft materials. *Phys Today* 52:32–38
- Bayer O (1947) Das Di-isocyanat-polyadditionsverfahren; (polyurethane). *Angew Chem* 59:257–288
- Bejenariu AG, Yu L, Skov AL (2012) Low moduli elastomers with low viscous dissipation. *Soft Matter* 8:3917–3923
- Benslimane M, Gravesen P, Group MT et al (2002) Mechanical properties of dielectric elastomer actuators with smart metallic compliant electrodes. *Proc SPIE* 4695:150–157
- Benslimane M, Kiil H-E, Tryson MJ (2010a) Electro-mechanical properties of novel large strain PolyPower film and laminate components for DEAP actuator and sensor applications. *Proc SPIE* 7642:764231
- Benslimane MY, Kiil H, Tryson MJ (2010b) Dielectric electro-active polymer push actuators: performance and challenges. *Polym Int* 59:415–421
- Biggs J, Danielmeier K, Hitzbleck J et al (2013) Electroactive polymers: developments of and perspectives for dielectric elastomers. *Angew Chem Int Ed* 52:9409–9421
- Böse H, Uhl D, Rabindranath R et al (2012) Novel DEA with organically modified silicone elastomer for permittivity enhancement. *Proc SPIE* 8340:83402E
- Brochu P, Pei Q (2010) Advances in dielectric elastomers for actuators and artificial muscles. *Macromol Rapid Commun* 31:10–36

- Cameron CG, Underhill RS, Rawji M et al (2004) Conductive filler – elastomer composite for Maxwell stress actuator applications. *Proc SPIE* 5385:51–59
- Carpi F, De Rossi D (2005) Improvement of electromechanical actuating performances of a silicone dielectric elastomer by dispersion of titanium dioxide powder. *IEEE Trans Dielectr Electr Insul* 12:835–843
- Carpi F, Gallone G, Galantini F, et al (2008) Enhancing the dielectric permittivity of elastomers. In: Carpi F, De Rossi D, Kornbluh R, Pelrine RE, Sommer-Larsen P (eds) *Dielectric elastomers as electromechanical transducers: fundamentals, materials, devices, models & applications of an emerging elect, Dielectric elastomers as electromechanical transducers*. pp 51–68
- Chen B, Lu JJ, Yang CH et al (2014) Highly stretchable and transparent ionogels as nonvolatile conductors for dielectric elastomer transducers. *ACS Appl Mater Interfaces* 6:7840–7845
- Chiou BS, Lankford AR, Schoen PE (2003) Modifying tubule distribution in tubule-filled composites by using polyurethane-polydimethylsiloxane interpenetrating polymer networks. *J Appl Polym Sci* 89:1032–1038
- Chwang CP, Liu CD, Huang SW et al (2004) Synthesis and characterization of high dielectric constant polyaniline/polyurethane blends. *Synth Met* 142:275–281
- Corbelli G, Ghisleri C, Marelli M et al (2011) Highly deformable nanostructured elastomeric electrodes with improving conductivity upon cyclical stretching. *Adv Mater* 23:4504–4508
- Elabd YA, Hickner MA (2011) Block copolymers for fuel cells. *Macromolecules* 44:1–11
- Fukuda T, Luo ZW, Ito A (2012a) Development of dielectric elastomer actuators – Part I: performance of polyurethane film actuators with dangling chains and network structures. *Adv Mater Res* 557–559:1852–1856
- Fukuda T, Luo ZW, Ito A (2012b) Development of dielectric elastomer actuators – Part II: preparation of the high dielectric constant film actuators containing BaTiO₃ particles. *Adv Mater Res* 557–559:1869–1874
- Galantini F, Gallone G, Carpi F (2012) Effects of corona treatment on electrical and mechanical properties of a porous dielectric elastomer. *IEEE Trans Dielectr Electr Insul* 19:1203–1207
- Galantini F, Bianchi S, Castelvetro V et al (2013) Functionalized carbon nanotubes as a filler for dielectric elastomer composites with improved actuation performance. *Smart Mater Struct* 22:055025
- Gallone G, Carpi F, De Rossi D et al (2007) Dielectric constant enhancement in a silicone elastomer filled with lead magnesium niobate-lead titanate. *Mater Sci Eng C* 27:110–116
- Gallone G, Galantini F, Carpi F (2010) Perspectives for new dielectric elastomers with improved electromechanical actuation performance: composites versus blends. *Polym Int* 59:400–406
- Guiffard B, Seveyrat L, Sebald G et al (2006) Enhanced electric field-induced strain in non-percolative carbon nanopowder/polyurethane composites. *J Phys D Appl Phys* 39:3053–3057
- Guo L, Deweerth SP (2010) An effective lift-off method for patterning high-density gold interconnects on an elastomeric substrate. *Small* 6:2847–2852
- Ha SM, Yuan W, Pei Q et al (2006) Interpenetrating polymer networks for high-performance electroelastomer artificial muscles. *Adv Mater* 18:887–891
- Hamley IW (1998) *The physics of block copolymers*. Oxford University Press, New York/Oxford
- Holden G, Legge NR, Quirk RP (2004) *Thermoplastic elastomers*, 3rd edn. Hanser, Munich
- Huang C, Zhang QM, DeBotton G et al (2004) All-organic dielectric percolative three-component composite materials with high electromechanical response. *Appl Phys Lett* 84:4391–4393
- Keplinger C, Kaltenbrunner M, Arnold N et al (2010) Rontgen’s electrode-free elastomer actuators without electromechanical pull-in instability. *Proc Natl Acad Sci U S A* 107:4505–4510
- Keplinger C, Sun J, Foo CC et al (2013) Stretchable, transparent, ionic conductors. *Science* 341:984–987
- Kiil H-E, Benslimane M (2009) Scalable industrial manufacturing of DEAP. *Proc SPIE* 7287:72870R
- Kofod G, Risse S, Stoyanov H et al (2011) Broad-spectrum enhancement of polymer composite dielectric constant at ultra-low doping caused by silica-supported copper nanoparticles. *Composites* 5:1623–1629

- Kornbluh RD, Pelrine R, Joseph J et al (1999) High-field electrostriction of elastomeric polymer dielectrics for actuation. *Proc SPIE* 3669:149–161
- Krishnan AS, Vargantwar PH, Ghosh TK et al (2011) Electroactuation of solvated triblock copolymer dielectric elastomers: decoupling the roles of mechanical prestrain and specimen thickness. *J Polym Sci B Polym Phys* 49:1569–1582
- Krishnan AS, Smith SD, Spontak RJ (2012) Ternary phase behavior of a triblock copolymer in the presence of an endblock-selective homopolymer and a midblock-selective oil. *Macromolecules* 45:6056–6067
- Kujawski M, Pearse JD and Smela E (2010) Elastomers filled with exfoliated graphite as compliant electrodes. *Carbon Elsevier Ltd* 48:2409–2417
- Kurita Y, Ueda T and Kasazaki T (1999) Polyurethane elastomer actuator. U.S. Patent N. 5,977,685
- Kusssmaul B, Risse S, Kofod G et al (2011) Enhancement of dielectric permittivity and electromechanical response in silicone elastomers: molecular grafting of organic dipoles to the macromolecular network. *Adv Funct Mater* 21:4589–4594
- Kusssmaul B, Risse S, Wegener M et al (2013) New DEA materials by organic modification of silicone and polyurethane networks. *Proc SPIE* 8687:86872S
- Kyokane J, Ishimoto H, Yugen H et al (1999) Electro-contraction effect of polyurethane elastomer (PUE) and its application to actuators. *Synth Met* 103:2366–2367
- Lam T, Tran H, Yuan W et al (2008) Polyaniline nanofibers as a novel electrode material for fault-tolerant dielectric elastomer actuators. *Proc SPIE* 6927:692700
- Lotz P, Matysek M, Lechner P et al (2008) Dielectric elastomer actuators using improved thin film processing and nanosized particles. *Proc SPIE* 6927:692723
- Low S-H, Lau G-K (2013) The effect of folds in thin metal film electrodes used in dielectric elastomer actuators. *Proc SPIE* 8687:86872P
- Madsen FB, Dimitrov I, Dagaard AE et al (2013) Novel cross-linkers for PDMS networks for controlled and well distributed grafting of functionalities by click chemistry. *Polym Chem* 4:1700–1707
- Madsen FB, Javakhishvili I, Jensen RE et al (2014) Synthesis of telechelic vinyl/allyl functional siloxane copolymers with structural control. *Polym Chem R Soc Chem* 5:7054–7061
- Matsen MW, Thompson RB (1999) Equilibrium behavior of asymmetric ABA triblock copolymer melts. *J Chem Phys* 111:7139–7146
- Matysek M, Lotz P, Flittner K et al (2010) Vibrotactile display for mobile applications based on dielectric elastomer stack actuators. *Proc SPIE* 7642:76420D
- Molberg M, Crespy D, Rupper P et al (2010) High breakdown field dielectric elastomer actuators using encapsulated polyaniline as high dielectric constant filler. *Adv Funct Mater* 20:3280–3291
- Niklaus M, Shea HR (2011) Electrical conductivity and Young's modulus of flexible nanocomposites made by metal-ion implantation of polydimethylsiloxane: the relationship between nanostructure and macroscopic properties. *Acta Mater* 59:830–840
- Niu X, Stoyanov H, Hu W et al (2013) Synthesizing a new dielectric elastomer exhibiting large actuation strain and suppressed electromechanical instability without prestretching. *J Polym Sci B Polym Phys* 51:197–206
- Opris DM, Molberg M, Walder C et al (2011) New silicone composites for dielectric elastomer actuator applications in competition with acrylic foil. *Adv Funct Mater* 21:3531–3539
- Pelrine R, Kornbluh R, Joseph J et al (2000a) High-field deformation of elastomeric dielectrics for actuators. *Mater Sci Eng C* 11:89–100
- Pelrine R, Kornbluh R, Pei Q et al (2000b) High-speed electrically actuated elastomers with strain greater than 100%. *Science* 287:836–839
- Pimpin A, Suzuki Y, Kasagi N (2007) Microelectrostrictive actuator with large out-of-plane deformation for flow-control application. *J Microelectromech Syst* 16:753–764
- Plante J, Dubowsky S (2006) On the nature of dielectric elastomer actuators and its implications for their design. *Proc SPIE* 6168:61681J
- Rambarran T, Gonzaga F, Brook MA (2012) Generic, metal-free cross-linking and modification of silicone elastomers using click ligation. *Macromolecules* 45:2276–2285

- Riffle JS, Yilgor I, Tran C et al (1983) Elastomeric polysiloxane modifiers for epoxy network – synthesis of functional oligomers and network formation studies. *ACS Symp Ser* 221:21–54
- Risse S, Kussmaul B, Krüger H et al (2012) Synergistic improvement of actuation properties with compatibilized high permittivity filler. *Adv Funct Mater* 22:3958–3962
- Romasanta LJ, Leret P, Casaban L et al (2012) Towards materials with enhanced electro-mechanical response: $\text{CaCu}_3\text{Ti}_4\text{O}_{12}$ -polydimethylsiloxane composites. *J Mater Chem* 22:24705–24712
- Rosset S, Shea HR (2013) Flexible and stretchable electrodes for dielectric elastomer actuators. *Appl Phys A Mater Sci Process* 110:281–307
- Roussel M, Malhaire C, Deman A-L et al (2014) Electromechanical study of polyurethane films with carbon black nanoparticles for MEMS actuators. *J Micromech Microeng* 24:055011
- Schlaak HF, Jungmann M, Matysek M et al (2005) Novel multilayer electrostatic solid-state actuators with elastic dielectric. *Proc SPIE* 5759:121–133
- Shian S, Diebold RM, McNamara A et al (2012) Highly compliant transparent electrodes. *Appl Phys Lett* 101:061101
- Skov AL, Vudayagiri S, Benslimane M (2013) Novel silicone elastomer formulations for DEAPs. *Proc SPIE* 8687:868711
- Stoyanov H, Brochu P, Niu X et al (2013) Long lifetime, fault-tolerant freestanding actuators based on a silicone dielectric elastomer and self-clearing carbon nanotube compliant electrodes. *RSC Adv* 3:2272–2278
- Sudarso AP, Wang J, Ugaz VM (2005) Thermoplastic elastomer gels: an advanced substrate for microfluidic chemical analysis systems. *Anal Chem* 77:5167–5173
- Szabo JP, Hiltz JA, Cameron CG et al (2003) Elastomeric composites with high dielectric constant for use in Maxwell stress actuators. *Proc SPIE* 5051:180–190
- Tallury SS, Spontak RJ, Pasquinelli MA (2014) Dissipative particle dynamics of triblock copolymer melts: a midblock conformational study at moderate segregation. *J Chem Phys* 141:047448
- Tartarisco G, Gallone G, Carpi F, et al (2009) Polyurethane unimorph bender microfabricated with pressure assisted microsyringe (PAM) for biomedical applications. *Mater Sci Eng C Elsevier B.V.* 29:1835–1841
- Ueda T, Kasazaki T, Kunitake N et al (1997) Polyurethane elastomer actuator. *Synth Met* 85:1415–1416
- Urdaneta MG, Delille R, Smela E (2007) Stretchable electrodes with high conductivity and photo-patternability. *Adv Mater* 19:2629–2633
- Vargantwar PH, Shankar R, Krishnan AS et al (2011) Exceptional versatility of solvated block copolymer/ionomer networks as electroactive polymers. *Soft Matter* 7:1651–1655
- Vargantwar PH, Özçam AE, Ghosh TK et al (2012) Prestrain-free dielectric elastomers based on acrylic thermoplastic elastomer gels: a morphological and (electro)mechanical property study. *Adv Funct Mater* 22:2100–2113
- Vega DA, Sebastian JM, Loo YL et al (2001) Phase behavior and viscoelastic properties of entangled block copolymer gels. *J Polym Sci B Polym Phys* 39:2183–2197
- Wang J, Wu C, Liu R et al (2014) Enhanced dielectric behavior in nanocomposites of polyurethane bonded with copper phthalocyanine oligomers. *Polym J* 46:285–292
- Watanabe M, Suzuki M, Hirako Y et al (2001) Hysteresis in bending electrostriction of polyurethane films. *J Appl Polym Sci* 79:1121–1126
- Yuan W, Lam T, Biggs J et al (2007) New electrode materials for dielectric elastomer actuators. *Proc SPIE* 6524:65240N
- Yuan W, Hu L, Yu Z et al (2008) Fault-tolerant dielectric elastomer actuators using single-walled carbon nanotube electrodes. *Adv Mater* 20:621–625
- Yuan W, Brochu P, Ha SM et al (2009) Dielectric oil coated single-walled carbon nanotube electrodes for stable, large-strain actuation with dielectric elastomers. *Sensors Actuators A Phys* 155:278–284
- Zhang QM, Su J, Kim CH et al (1997) An experimental investigation of electromechanical response in a dielectric acrylic elastomer. *J Appl Phys* 81:2770–2776

-
- Zhang Z, Liu L, Fan J et al (2008) New silicone dielectric elastomer with a high dielectric constant. Proc SPIE 6926:692610
- Zhang H, Düring L, Kovacs G et al (2010) Interpenetrating polymer networks based on acrylic elastomers and plasticizers with improved actuation temperature range. Polym Int 59:384–390
- Zhao X, Suo Z (2007) Method to analyze electromechanical stability of dielectric elastomers. Appl Phys Lett 91:061921
- Zhu S, So JH, Mays R et al (2013) Ultrastretchable fibers with metallic conductivity using a liquid metal alloy core. Adv Funct Mater 23:2308–2314

Helmut F. Schlaak, Massimiliano Gei, Eliana Bortot, Henry Haus,
and Holger Mößinger

Contents

1	Introduction and Definition	716
2	Theoretical and Fundamental Modeling of Dielectric Elastomers	716
2.1	Nonlinear Mechanical Behavior of Soft Elastomers	716
2.2	Electroelastic Constitutive Equations of Dielectric Elastomers	718
2.3	Actuation Laws of a Planar Soft Dielectric Device	724
3	Modeling of Dielectric Elastomers Using Lumped Parameters	726
3.1	Electrical Model	727
3.2	Mechanical Model	730
3.3	Combined Electrical and Mechanical Model	735
4	Conclusion	737
	References	737

Abstract

The effective use of dielectric elastomers (DE) in actual transducers requires the definition of reliable design tools which correctly predict their electromechanical behavior. In this chapter, we present two different approaches for modeling DE. The first approach is focussed on describing the electroelastic behavior of DEs in the framework of finite-strain electromechanics. The second approach,

H.F. Schlaak (✉) • H. Haus • H. Mößinger
Institute of Electromechanical Design, Technische Universität Darmstadt, Darmstadt, Germany
e-mail: schlaak@emk.tu-darmstadt.de; h.haus@emk.tu-darmstadt.de;
h.moessinger@emk.tu-darmstadt.de

M. Gei
School of Engineering, Cardiff University, Cardiff, UK
e-mail: geim@cardiff.ac.uk

E. Bortot
Faculty of Mechanical Engineering, Technion - Israel Institute of Technology, Haifa, Israel
e-mail: eliana.b@tx.technion.ac.il

based on lumped parameters, is motivated by the desire to provide a simple and adequate description of the behavior of DE actuators under the influence of an electrical voltage applied to the electrodes.

Keywords

Dielectric elastomers • Models • Dynamic • Nonlinear • Lumped parameters • Electroelasticity

1 Introduction and Definition

Dielectric elastomers are the fundamental components of soft transducers which rely on the coupling between the mechanical and the electrical behavior of the material. To ensure that this technology is suitable for a specific application and that a DE is able to meet particular specifications, a fundamental knowledge about the electro-mechanical characteristics of DEs is essential. Depending on the application, static and dynamic responses must be predictable to design the transducer itself and also the whole device which is integrating the DE.

Different models describing DEs are derived and verified in this chapter to address the required mathematical description of the transducers behavior. Two inherently different methods based on the finite-strain electromechanics on the one hand and on lumped parameters on the other hand are presented in the following sections.

2 Theoretical and Fundamental Modeling of Dielectric Elastomers

2.1 Nonlinear Mechanical Behavior of Soft Elastomers

Soft elastomers are compliant materials capable of undergoing large strains when subjected to balanced external forces. All these materials display viscoelastic and/or damaging behaviors (more or less evident depending on loading rates and properties of the material); however, the main hypotheses assumed in their modeling is that they are conservative (or hyperelastic) and isotropic, with a strain-energy density per unit initial volume depending on the principal stretches λ_i ($i = x, y, z$), namely, $W(\lambda_x, \lambda_y, \lambda_z)$. Often these materials are volume preserving (incompressible), then $J = \lambda_x \lambda_y \lambda_z = 1$. The Cauchy (true) stress σ_{ij} governs the equilibrium of the elastomer: at the boundary of the body, $\sigma_{ij}n_j$ matches the external applied traction t_i^m (n_i is the outward unit normal) and, in the absence of body forces, σ_{ij} is divergence free.

As typical strains for soft elastomers are large, the current, deformed configuration is different from the natural, undeformed one. For this reason, the concept of nominal stress, defined in general as the force per unit reference area, becomes important, especially when dealing with the formulation of constitutive equations.

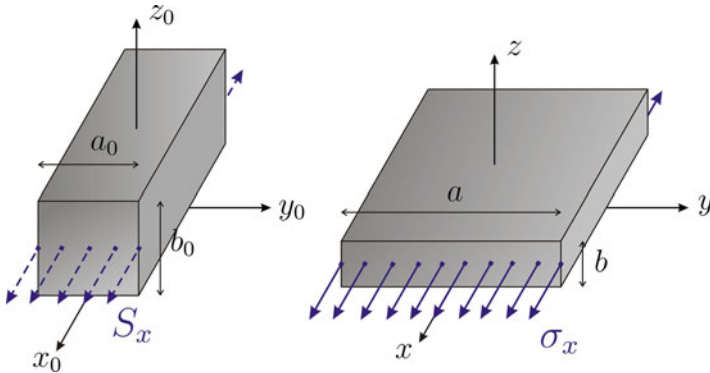


Fig. 1 Reference (*left*) and current (*right*) configurations of a rubber band pulled uniaxially

The nominal stress, denoted by S_{ij} , carries the same information provided by the Cauchy stress in terms of current equilibrium but taking area elements of the undeformed configuration. To clarify the concept, let us consider a rubber band pulled uniaxially (Fig. 1). The current cross-section has the area $a b$ and is subjected to the uniform stress σ_x , whereas in the natural configuration the cross-section area is $a_0 \cdot b_0$. The only nonvanishing component S_x of the nominal stress is such that $S_x a_0 b_0 = \sigma_x a b$. As the current and the initial edge lengths are linked by the stretch along their common direction, namely, $a = \lambda_y a_0$ and $b = \lambda_z b_0$, the relationship $J \sigma_x = \lambda_x S_x$ can be established and generalized in terms of principal stresses as

$$J \sigma_i = \lambda_i S_i \quad (i = x, y, z; \text{ index } i \text{ not summed}). \quad (1)$$

The theory of nonlinear, isotropic, hyperelasticity shows (Ogden 1997) that the principal nominal stresses are given, respectively for compressible and incompressible solids, by

$$S_i = \frac{\partial W}{\partial \lambda_i} \quad (J \neq 1), \quad S_i = \frac{\partial W}{\partial \lambda_i} - p \frac{1}{\lambda_i} \quad (J = 1), \quad (2)$$

where, again, $i = x, y, z$, and p is a hydrostatic pressure to be determined imposing boundary conditions.

We close this brief summary by listing two of the main strain-energy densities employed for modeling elastomeric materials:

- Neo-Hookean model,

$$W(\lambda_x, \lambda_y, \lambda_z) = \frac{\mu}{2} (\lambda_x^2 + \lambda_y^2 + \lambda_z^2 - 3); \quad (3)$$

- Gent model,

$$W(\lambda_x, \lambda_y, \lambda_z) = -\frac{\mu}{2} J_m \ln [1 - (\lambda_x^2 + \lambda_y^2 + \lambda_z^2 - 3)/J_m], \quad (4)$$

where μ is the initial shear modulus and J_m , not to be confused with J , is a parameter governing the maximum stretchability of the material. For an incompressible solid, $\mu = Y/3$, where Y is the Young's modulus. We refer to Carpi and Gei (2013) for an overview of all main hyperelastic models employed in the mechanics of elastomers.

2.2 Electroelastic Constitutive Equations of Dielectric Elastomers

In an electroelastic boundary-value problem (BVP), the stress state at a point of the dielectric depends on the mechanical and the electrostatic variables. Similarly to the elastic problem, we can think of a true stress σ_{ij} which is in equilibrium with the external (volume and surface) mechanical forces that are applied to the elastomer (Dorfmann and Ogden 2005; McMeeking and Landis 2005; Suo et al. 2008). This quantity is often referred to as the total (true) stress to which a *total* nominal stress can be associated employing again Eq. 1. The adjective “total” refers to the properties for which the two stresses contain both mechanical and electrical information (often in a coupled way) at each point of the deformed elastomer, defined via constitutive equations.

It is important to point out that as the electrostatic problem must be solved in all space \mathbb{R}^3 , whenever an electric field exists outside the dielectric an associated Maxwell stress can be defined (see next Section). Therefore, equilibrium at the external boundary of the elastomer must be understood in terms of the jump between the stresses at the two sides (Bertoldi and Gei 2011).

In the planar actuator of Fig. 2a, for instance, any mechanical external force is applied to the elastomer and the electric field outside the body is assumed negligible, so both total true and nominal stresses vanish identically throughout the actuator ($\sigma_{ij} = S_{ij} = 0$). For an isotropic material, this is expressed as

$$\sigma_i = S_i = 0 \quad (i = x, y, z). \quad (5)$$

2.2.1 Maxwell Stress Associated with an Electric Field in Vacuum

Consider now a simple, ideal, charged, parallel-plate capacitor whose electrodes, infinite in extension, are maintained in equilibrium by a continuous distribution of thin threads (Fig. 2b). This problem can be easily solved recalling that the diffuse constraint on each plate counteracts the attraction pressure between the conductors (an issue addressed in all books of electrostatics), then threads are pulled by a pressure equal to $\epsilon_0 E^2/2$, where E is the intensity of the electric field. Alternatively, this relevant result can be achieved thinking that in the space between the plates,

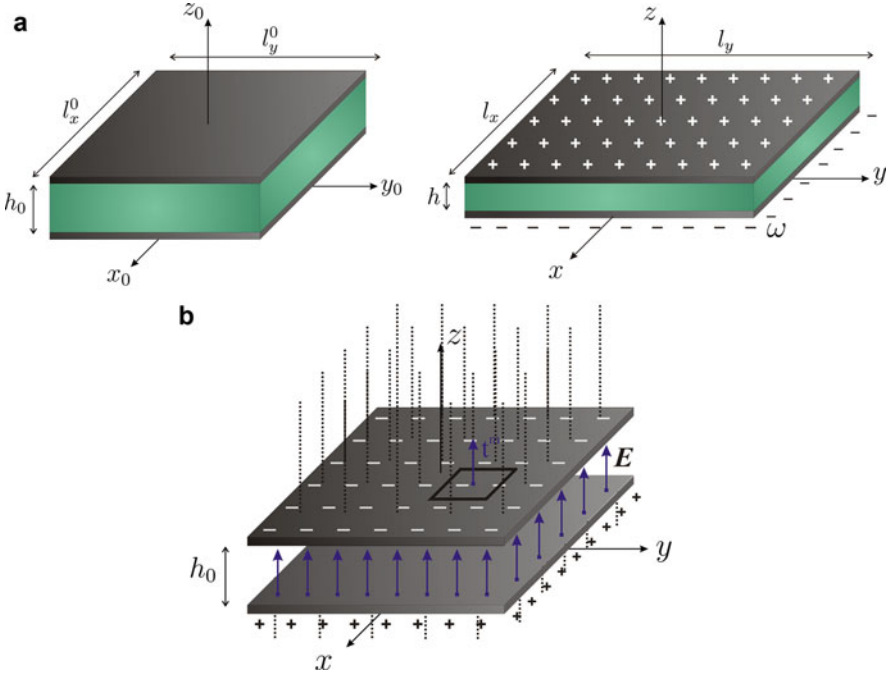


Fig. 2 (a) Reference (*left*) and current (*right*) configurations of a planar soft dielectric actuator. Symbol ω represents the current charge density; (b) parallel-plate capacitor in vacuum

where the electric field is nonvanishing, the Maxwell stress is present. For a generic electric field E_i its components are

$$\sigma_{ij}^* = \epsilon_0 \left(E_i E_j - \frac{1}{2} E_k E_k \delta_{ij} \right), \tag{6}$$

where δ_{ij} represents the Kronecker delta. In the coordinate system and for the problem sketched in Fig. 2b, the Maxwell stress takes the diagonal form $\sigma_{ij}^* = \text{diag} [-\epsilon_0 E^2/2, -\epsilon_0 E^2/2, \epsilon_0 E^2/2]$.

Now, as anticipated, the Maxwell stress plays exactly the same role as the total stress for the dielectric. Then, it is in equilibrium with the external mechanical traction t_i^m required to maintain the plates at rest. Assuming, for the top plate, the outward normal $n_i = [0, 0, 1]$, it turns out that

$$t_i^m = \sigma_{ij}^* n_j = \epsilon_0 E^2/2 [0, 0, 1], \tag{7}$$

which coincides with the previous result. The upper plate is subjected to an outward mechanical pressure which balances the electric pressure. In passing, we note that the Maxwell stress ideally induces a compressive pressure to infinitesimal surface elements with its normal orthogonal to axis z .

2.2.2 Nominal Electrical Quantities

Voltage V and charge q in a capacitor are closely related to the notion of electric field (E_i) and electric displacement field (D_i), respectively. In particular, the general relationship $E_i = -(\text{grad } V)_i$ is specialized to $E = E_z = V/h$ for the actuator displayed in Fig. 2a. Moreover, as outside the actuator the electric field is vanishing, the normal component of the electric displacement field matches the charge density, i.e., $D_z = D = q/l_x l_y = \omega$. Similarly to stress, nominal electrical quantities can be also defined. The nominal electric field is $E^0 = V/h^0$, while the nominal electric displacement is defined as $D^0 = q/l_x^0 l_y^0 = \omega^0$. Recalling the definition of stretch, the following useful identities between current and nominal fields can be pinpointed:

$$E^0 = \lambda_z E, D^0 = J \frac{1}{\lambda_z} D. \quad (8)$$

We close this section reminding that an ideal dielectric is such that vectors $D_i = \varepsilon E_i$ are aligned with constant of proportionality ε , the dielectric permittivity, independent of strains.

2.2.3 Constitutive Equations for Compressible Soft Dielectrics

Most soft elastomers are nearly incompressible and the adoption of the hypothesis of incompressibility in the constitutive equations allows for some simplifications in the analytical calculations. However, this choice has some shortcomings: (i) the constraint $J = 1$ poses difficulties in the convergence of computational algorithms when numerical solutions are sought and (ii) the structure of the constitutive electroelastic equations are not completely revealed because of the presence of the hydrostatic pressure. Therefore, aiming at elucidating the latter item, we prefer to formulate the constitutive equations and solve a relevant boundary-value problem, for a soft dielectric beginning from the compressible case.

To this end, we consider an ideal dielectric membrane which is homogeneous, isotropic, hyperelastic, compressible ($J \neq 1$), and not electrostrictive (then the permittivity does not depend on strain). The body is subjected only to an electric field generated by an electric potential V between the stretchable electrodes coating the two extended opposite surfaces of the membrane (Fig. 2a). Neglecting fringing effects, the deformation undergone by the film is homogeneous, represented by a set of constant principal stretches $\lambda_x, \lambda_y, \lambda_z$ taken along the three directions x, y , and z , respectively. Outside the device the electric field vanishes and inside the membrane it is uniform and aligned along axis z . The specimen is mechanically unloaded, then true and nominal total stresses vanish (Eq. 5).

As a preparatory calculation for the formulation of constitutive equations, we take note of the term $q\delta V/(l_x^0 l_y^0 h^0)$ which corresponds to the change in electrostatic energy per unit initial volume brought about by a small perturbation of the voltage V at constant charge. This quantity can be rephrased as a function of D^0 and E^0 as $-D^0 \delta E^0$, where the minus is justified by the circumstance that the

electric field is the negative gradient of the electrostatic potential (see Sect. 2.2.2 in this chapter).

By perturbing independently the three stretches, the work done on the initial unit volume of the elastomers by each stress component is accounted. Summing up all contributions, the total change of energy stored in the material is equal to

$$\delta W = S_x \delta \lambda_x + S_y \delta \lambda_y + S_z \delta \lambda_z - D^0 \delta E^0. \quad (9)$$

Assuming a strain-energy density $W(\lambda_x, \lambda_y, \lambda_z, E^0)$, we can observe that the same change can be mathematically formally written as

$$\delta W = \frac{\partial W}{\partial \lambda_x} \delta \lambda_x + \frac{\partial W}{\partial \lambda_y} \delta \lambda_y + \frac{\partial W}{\partial \lambda_z} \delta \lambda_z + \frac{\partial W}{\partial E^0} \delta E^0, \quad (10)$$

so that the comparison between the two expressions yields the constitutive equations for a compressible, isotropic soft dielectric, namely,

$$S_i = \frac{\partial W}{\partial \lambda_i} \quad (i = x, y, z), \quad D^0 = -\frac{\partial W}{\partial E^0}. \quad (11)$$

Total true stress and current electric displacement can be easily determined by Eq. 1 and the second part of of Eq. 8.

We aim at solving the BVP associated with Fig. 2a assuming an ideal dielectric behavior of the elastomer. With this additional assumption, the most general form of a strain-energy function corresponds to

$$W(\lambda_x, \lambda_y, \lambda_z, E^0) = W_{mech}(\lambda_x, \lambda_y, \lambda_z) - \frac{\varepsilon}{2} \lambda_x \lambda_y \lambda_z \left(\frac{E^0}{\lambda_z} \right)^2, \quad (12)$$

where W_{mech} is the mechanical part of the energy function, depending only on the principal stretches (see Sect. 2.1).

It is not difficult to show that upon application of Eq. 11, the ideal electric relationship is recovered. Indeed,

$$D^0 = -\frac{\partial W}{\partial E^0} = \varepsilon \lambda_x \lambda_y \lambda_z \frac{E^0}{\lambda_z^2}, \quad (13)$$

and $D = \varepsilon E$ follows from Eq. 8. Other expressions of the term where E^0 appears in W imply the presence of the stretches in the equation between D and E . In this case the dielectric is no longer ideal and the permittivity depends on the strain.

Equation 11₁ provides the components of the nominal true stress, i.e.,

$$S_k = S_k^{mech} - \frac{\varepsilon}{2} \frac{J}{\lambda_k} \left(\frac{E^0}{\lambda_z} \right)^2 = S_k^{mech} - \frac{\varepsilon}{2} \frac{\lambda_x \lambda_y \lambda_z}{\lambda_k} E^2 \quad (k = x, y), \quad (14)$$

$$S_z = S_z^{mech} + \frac{\varepsilon}{2} \frac{J}{\lambda_z} \left(\frac{E^0}{\lambda_z} \right)^2 = S_z^{mech} + \frac{\varepsilon}{2} \lambda_x \lambda_y E^2, \quad (15)$$

where we have introduced the mechanical contribution of the stress

$$S_i^{mech}(\lambda_x, \lambda_y, \lambda_z) = \frac{\partial W_{mech}}{\partial \lambda_i}. \quad (16)$$

Equation 1 leads to the total true stress components as

$$\sigma_k = \sigma_k^{mech} - \frac{\varepsilon}{2} E^2 \quad (k = x, y), \quad \sigma_z = \sigma_z^{mech} + \frac{\varepsilon}{2} E^2, \quad (17)$$

where formally $\sigma_i^{mech}(\lambda_x, \lambda_y, \lambda_z)$. Note that the three components just derived are the specialization, to principal directions and to an electric field aligned along one of these directions, of the general relationship

$$\sigma_{ij} = \sigma_{ij}^{mech} + \varepsilon \left(E_i E_j - \frac{1}{2} E_k E_k \delta_{ij} \right), \quad (18)$$

where the second term of the right-hand side has the structure of a Maxwell stress but with ε_0 replaced by ε (see Sect. 2.2.1).

2.2.4 Constitutive Equations for Incompressible Soft Dielectrics

For an incompressible material ($J = \lambda_x \lambda_y \lambda_z = 1$), superimposing an arbitrary hydrostatic pressure p will not change the stored energy. Therefore, the change studied in Eq. 10 becomes

$$\begin{aligned} \delta W = S_x \delta \lambda_x + S_y \delta \lambda_y + S_z \delta \lambda_z - D^0 \delta E^0 \\ + p (\lambda_y \lambda_z \delta \lambda_x + \lambda_x \lambda_z \delta \lambda_y + \lambda_x \lambda_y \delta \lambda_z). \end{aligned} \quad (19)$$

A procedure analogous to that leading to Eq. 11 yields the set of sought constitutive equations

$$S_i = \frac{\partial W}{\partial \lambda_i} - p \frac{1}{\lambda_i}, \quad D^0 = -\frac{\partial W}{\partial E^0}. \quad (20)$$

Adopting the strain energy Eq. 12, but now with $J = \lambda_x \lambda_y \lambda_z = 1$,

$$W(\lambda_x, \lambda_y, \lambda_z, E^0) = W_{mech}(\lambda_x, \lambda_y, \lambda_z) - \frac{\varepsilon}{2} \left(\frac{E^0}{\lambda_z} \right)^2, \quad (21)$$

It turns out that in this case the nominal electric displacement is given by

$$D^0 = -\frac{\partial W}{\partial E^0} = \varepsilon \frac{E^0}{\lambda_z^2}, \tag{22}$$

whereas in the stress state the hydrostatic pressure p , which can be determined by imposing the boundary conditions, appears, i.e.,

$$\sigma_k = \sigma_k^{mech} - \frac{\varepsilon}{2} E^2 - p \quad (k = x, y), \quad \sigma_z = \sigma_z^{mech} + \frac{\varepsilon}{2} E^2 - p, \tag{23}$$

where the mechanical contribution of stress associated with the elastic response of the elastomer has been introduced again.

With the constitutive equations at hand, imposing the boundary conditions the actuation laws $\lambda_i = f(E)$ or $\lambda_i = f(V)$ can be computed (Sect. 2.3).

2.2.5 The Pelrine’s Model

In one of the first papers dealing with dielectric elastomers, Pelrine et al. (1998) proposed a widely used model to analyze stresses and strains in a thin elastomeric membrane subjected to a transverse electric field. The notion of Maxwell’s pressure $p_{el} = \varepsilon E^2$ is well known among the EAP research community. How does this concept match with the theory developed here? This can be easily explained recalling that the stress measure adopted by Pelrine et al. (1998) corresponds to our σ_{ij}^{mech} , and their model is valid only for incompressible materials.

Consider first a compressible material (Fig. 3a). The boundary condition 5 applied to Eq. 17 yields

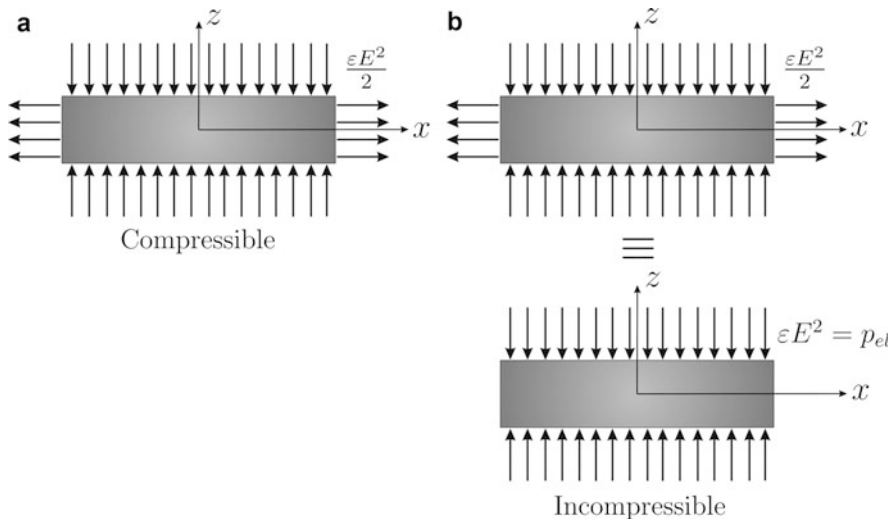


Fig. 3 Maxwell pressure of the Pelrine’s model for: (a) compressible and (b) incompressible actuators. In all sketches the section along the plane xz is reported

$$\sigma_x^{mech} = \sigma_y^{mech} = +\frac{\varepsilon}{2}E^2, \quad \sigma_z^{mech} = -\frac{\varepsilon}{2}E^2, \quad (24)$$

Hence the actual in-plane mechanical stress is equal and opposite to the mechanical stress along the transverse direction.

For an incompressible solid, superimposing an arbitrary hydrostatic pressure will not change the response of the material. Then only the stress difference $\sigma_z - \sigma_x$ (or $\sigma_z - \sigma_y$) counts. Transforming Eq. 23, it turns out that boundary conditions 5 provide the stress differences

$$\sigma_z^{mech} - \sigma_x^{mech} = \sigma_z^{mech} - \sigma_y^{mech} = -\varepsilon E^2. \quad (25)$$

Setting arbitrarily $\sigma_x^{mech} = \sigma_y^{mech} = 0$, both equations boil down to

$$\sigma_z^{mech} = -\varepsilon E^2 = -p_{el}. \quad (26)$$

The strain is obtained considering the material linear elastic.

2.3 Actuation Laws of a Planar Soft Dielectric Device

The electromechanical response of a soft dielectric actuator is well represented by two dimensionless diagrams: voltage versus in-plane stretch and voltage versus charge. We provide here such diagrams for the planar actuator represented in Fig. 2a for the boundary conditions 5 and for two incompressible ideal soft dielectrics, both following the strain energy Eq. 21, but with different functions \mathcal{W}_{mech} : one is modeled as a neo-Hookean material, the other as a Gent nonlinear solid (Sect. 2.1).

The plots are sketched in terms of dimensionless variables: voltage and charge density per unit reference area are defined as

$$\bar{V} = (V/h^0)\sqrt{\varepsilon/\mu} = E^0\sqrt{\varepsilon/\mu}, \quad \bar{\omega}^0 = \omega^0/\sqrt{\varepsilon\mu}, \quad (27)$$

respectively, with the permittivity ε and the initial shear modulus μ . For the Gent material, $J_m=100$.

The expression of the dimensionless voltage as a function of the in-plane stretch ($\lambda = \lambda_x = \lambda_y$) can be written explicitly for the two different mechanical models, namely,

$$\bar{V} = \frac{\sqrt{\lambda^6 - 1}}{\lambda^4}, \quad \bar{V} = \frac{\sqrt{J_m(\lambda^6 - 1)}}{\lambda^2\sqrt{J_m\lambda^4 - 2\lambda^6 - 1}}, \quad (28)$$

for the neo-Hookean and the Gent material, respectively. These are represented in Fig. 4a. We observe that the maximum \bar{V} at low stretches (point A) is reached at $\lambda \cong 1.26$ for both models, but the peak value of the Gent material ($\bar{V} = 0.70$) is

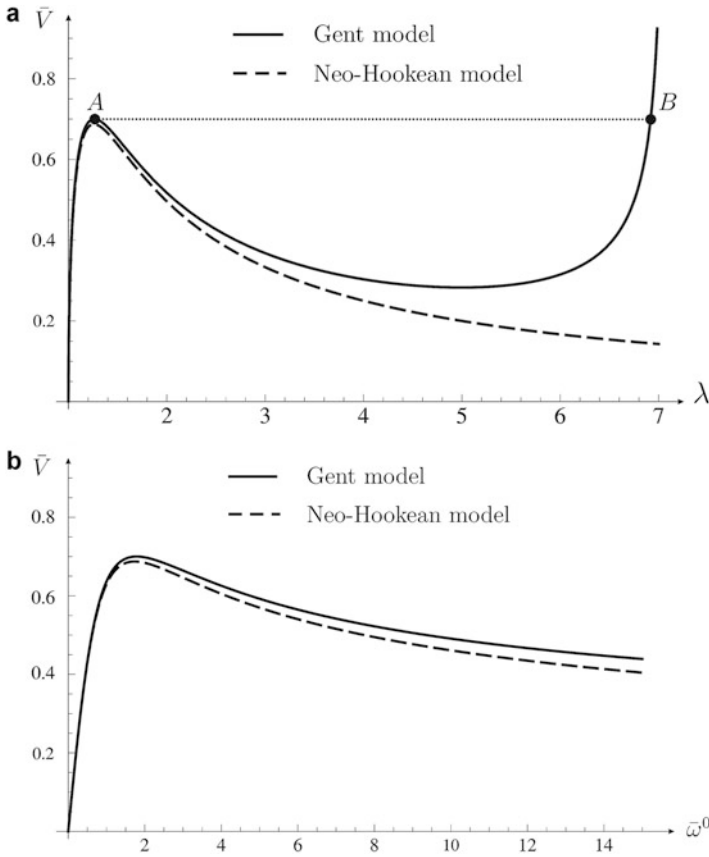


Fig. 4 Actuation diagrams of the planar device represented in Fig. 2a for two elastic material model: **(a)** voltage versus in-plane stretch. **(b)** voltage versus charge

slightly higher than that of the neo-Hookean solid, for which $\bar{V}_{\max} = 0.68$. When the point A is reached, electromechanical instability occurs, and in the case of the Gent model it coincides with a snap-through instability that moves the system towards a new equilibrium configuration at point B on the stiffening branch of the solution. For the neo-Hookean material, any equilibrium configuration is predicted for a dimensionless voltage $\bar{V} > \bar{V}_{\max}$: The elastomer is not able to sustain the attractive force between the electrodes beyond this threshold.

The voltage-charge diagram represents the equilibrium path in terms of electrical quantities. For the neo-Hookean material the law can be written analytically as

$$\bar{V} = \frac{\bar{\omega}^0}{(1 + \bar{\omega}^{02})^{2/3}}, \tag{29}$$

for which, at $\bar{V}_{\max} = 0.68$ the dimensionless charge is equal to $\bar{w}^0 = 1.73$. Similarly to the previous plot, neo-Hookean and Gent models share a similar behavior until the peak point, and then they diverge. In the current diagram, the stiffening effect of the latter model is visible for \bar{w}^0 on the order of one thousand (out of bounds of Fig. 4b).

3 Modeling of Dielectric Elastomers Using Lumped Parameters

As described above, dielectric elastomers consist of two compliant electrodes which embed an elastic dielectric. When the electrodes are supplied with a voltage V , the electrical field will cause the electrical charges on the electrodes to attract one another. In fact, the electrodes squeeze the dielectric, resulting in an electrostatic pressure p_{el} . Since the dielectric is incompressible, the elastomer film contracts in thickness and expands in area as shown in Fig. 5.

To effectuate the reverse actuator deformation, the voltage has to be decreased. Charge will be removed from the electrodes, and the actuator will return to its initial state, due to the elastic nature of the elastomeric dielectric.

In the following sections, this behavior is described by electrical and mechanical models separately and finally combined to an electromechanical model consisting of lumped parameters.

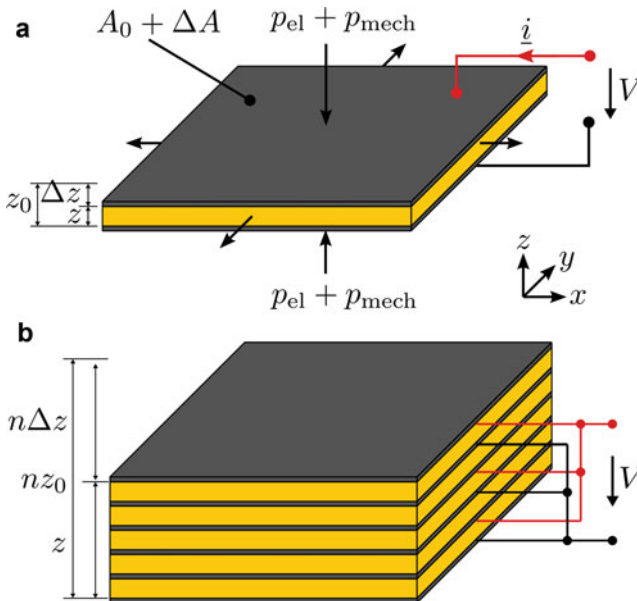


Fig. 5 Schematic principle of DE for (a) single layer DE actuator and (b) multilayer DE stack actuator (DESA) providing n times the deflection of a single layer DE

3.1 Electrical Model

The DE structure given in Fig. 5a can be seen as a plate capacitor setup. From this setup, we can derive a simplified electrical equivalent circuit consisting of the actuator capacitance C_a in series to the feeding line resistance R_s . This model can be seen in Fig. 6a.

To model the leakage of charges through the dielectric material a resistance R_p parallel to C_a can be added, resulting in the layout depicted in Fig. 6b.

The electrical models in Fig. 6 are usually a good description of the electrical behavior of the actuator, as long as the length to width ratio (x_0 to y_0) of the active area is between 1/3 and 3 (Haus et al. 2013). For most applications, the model in Fig. 6a is sufficient, as the leakage current through the dielectric is typically negligible, as R_p is typically in the range above 10 G Ω (Haus et al. 2013). For low frequencies (\ll 0.1 Hz) or energy harvesting applications, the influence of R_p may still have to be considered.

The models above are not only valid for single layer DE but also for multilayer stacked DE, consisting of n layers, as depicted in Fig. 5b (Haus et al. 2013).

The value of the capacitance C_a can be derived from Eq. 30, with ϵ_0 the vacuum permittivity and ϵ_r the relative permittivity of the dielectric material. In case of a single layer actuator the number of layers n is 1.

$$C_a = n \cdot C_{a, \text{single}} = n \cdot \epsilon_0 \epsilon_r \frac{A_0}{z_0} \quad (30)$$

The value of the series resistance R_s can be derived from the electrode geometry and the sheet resistance R_{\square} of the electrode material. The relation is given in Eq. 31 for single layer DE and in Eq. 32 for multilayer DE with a higher number of layers, so that the influence of the outer layers is negligible (Haus et al. 2013).

$$R_s = 2(R_e + R_c + R_w) = 2 \left(\frac{l}{w} R + R_c + R_w \right) \quad (31)$$

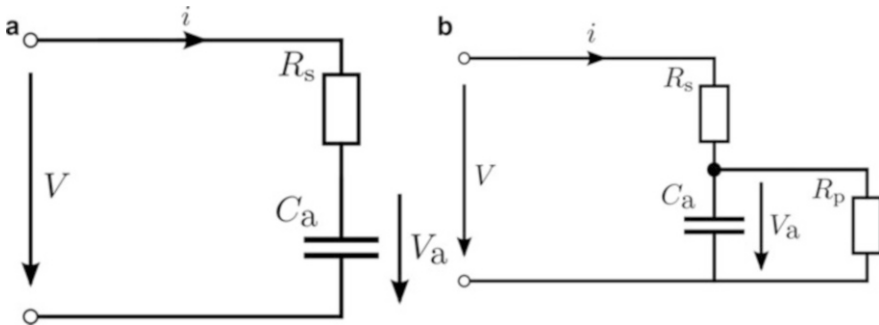


Fig. 6 Simple equivalent circuit (a) without leakage and (b) with leakage modeled by R_p

$$R_s = \frac{4(R_e + R_c)}{n} + 2R_w = \frac{4\left(\frac{l}{w}R + R_c\right)}{n} + 2R_w \quad (32)$$

The parameters l and w describe the length and width of the electrode area. The value of the sheet resistance R_{\square} can be obtained by four-point measurement (van der Pauw 1958). The value of the contact resistance R_c is to be obtained by measurements. A measurement setup is described in Haus et al. (2013). The resistance of the feed line wire R_w is usually small compared to the other values and thus may be neglected.

To verify the model parameters or obtain the parameter values for an existing actuator, a frequency sweep to measure the DE's electrical impedance can be done.

The impedance $Z(\omega)$ for above models are given in Eq. 33 including R_p and in Eq. 34 neglecting R_p . Complex variables in the frequency domain are used to examine the frequency-dependent behavior.

$$Z_1(\omega) = \frac{V(\omega)}{i(\omega)} = R_s + \frac{R_p}{1 + j\omega C_a R_p}, \quad \omega = 2\pi f \quad (33)$$

$$Z_2(\omega) = \frac{V(\omega)}{i(\omega)} = R_s + \frac{1}{j\omega C_a} \quad (34)$$

Figure 7a shows the schematic plot of the magnitude of the impedance $Z_1(\omega)$. Figure 7b shows the measured impedance of a real DE with 20 active layers, a single layer thickness of 50 μm , and an initial electrode area of 100 mm^2 . In comparison to Fig. 7a, the first plateau of $R_p + R_s$ is not reached in the measurement. The frequency $\omega_1 = \frac{1}{C_a R_p}$ is way outside the measured frequency range, therefore using the simplified model from Fig. 6a is suitable.

Fitting the impedance curve for the DE in Fig. 7b to the model, e.g., by using the Levenberg-Marquardt algorithm (Moré and Jorge 1978), results in R_s of 79.9 k Ω and C_a of 1.28 nF.

Using the model parameters, one can now calculate the transfer functions for the models, Eqs. 35 and 36 respectively, to derive the voltage across the actuator capacitance (Eq. 37).

$$H_1(\omega) = \frac{1}{1 + \frac{R_s}{R_p}} \frac{1}{1 + j\omega R_s C_a} \quad (35)$$

$$H_2(\omega) = \frac{1}{1 + j\omega R_s C_a} \quad (36)$$

$$V_a(\omega) = H(\omega) V(\omega) \quad (37)$$

The voltage $V_a(\omega)$ across the actuator capacitance can now be used to calculate the electromechanical pressure p_{el} acting on the DE using Eq. 38.

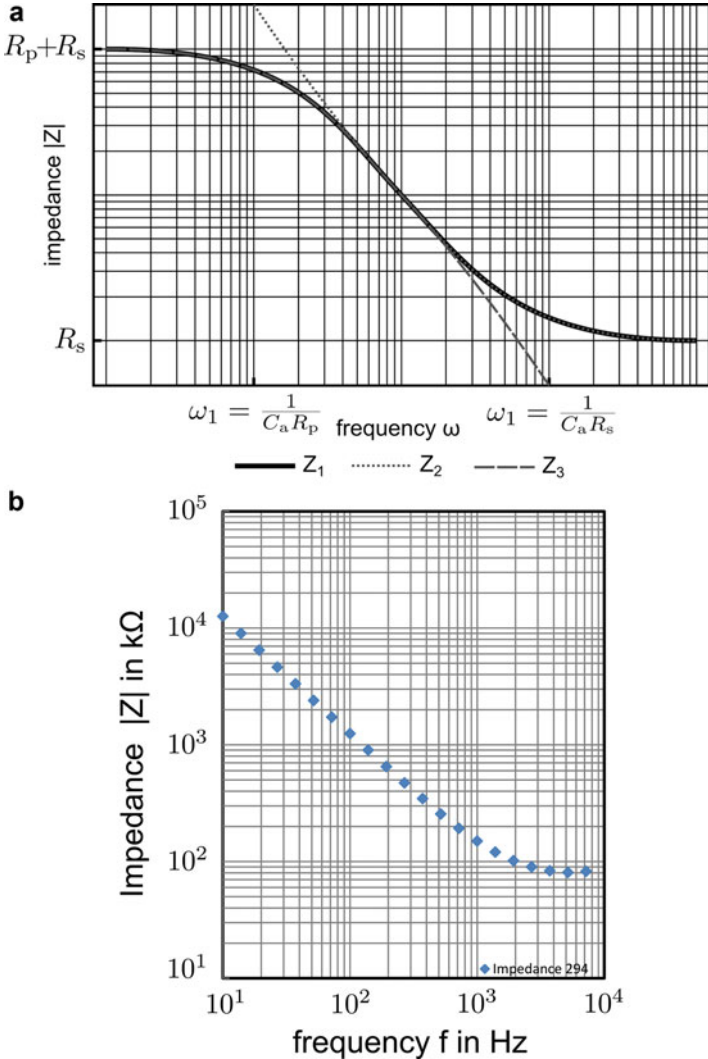


Fig. 7 (a) Schematic plot of the frequency-dependent impedance of the DE. (b) Measurement results of a DE frequency sweep. The parameter fit results in $R_s = 79,9 \text{ k}\Omega$, $C_a = 1,28 \text{ nF}$

$$p_{el}(\omega) = \epsilon_0 \epsilon_r \frac{V_a^2(\omega)}{z_0^2} \tag{38}$$

While Eq. 38 ignores the change of the actuator capacitance caused by the deflection of the actuator, Eq. 39 takes the thickness change into account. Equation 40 even considers the change in area which has to occur, as the dielectric material is assumed incompressible ($J = 1$) (Lotz 2009; Matysek 2010; Mößinger 2010).

$$p_{el}(\omega) = \epsilon_0 \epsilon_r \frac{V_a^2(\omega)}{(z_0 - \Delta z)^2} \quad (39)$$

$$p_{el}(\omega) = \epsilon_0 \epsilon_r \frac{V_a^2(\omega) z_0}{(z_0 - \Delta z)^3} \quad (40)$$

The use of Eq. 38 provides the advantage of requiring no feedback of the mechanical actuation, thus simplifying calculations. However, for larger deflections (see Sect. 3.2.1) the relation from Eqs. 39 and 40 is better suited to describe the behavior of the DE.

The pressure $p_{el}(\omega)$, multiplied by the initial area A_0 , or the actual area A , of the DE results in the actuation force $F(\omega)$ (Eq. 41).

$$F(\omega) = A_{(0)} p_{el}(\omega) \quad (41)$$

This force is used as input for the mechanical model described in the next section.

3.2 Mechanical Model

The mechanical behavior of DEs depends on the type of stimulation. For static stimuli the final deformation will be reached depending on the compliance of the elastomer. In case of dynamic stimulation, transient effects leading to more complex models have to be considered.

All DEs used in the experiments described in Sect. 3 of this chapter are multilayer stack actuators fabricated according to Schlaak et al. (2005) and Lotz et al. (2011) and consist of dielectric layers spin coated from the PDMS Wacker P7670 and graphite powder electrodes.

3.2.1 Static Stimulation

In compliance with their intrinsic elastomeric behavior the mechanical characteristics of DEs correspond to a mechanical spring. The electrically field-induced contraction of the elastomer between the electrodes causes a material movement in lateral direction due to its incompressibility. Obviously the actuator dimensions (electrode area, total height), the deformation ratio, and the boundary conditions (passive surroundings, contact area, and clamps) define the resulting compliance. According to the required conditions we measure the deformation dependent force.

The uniaxial compressive modulus Y_c describes the passive counter pressure acting against the electrical field and can be derived using the actuator's geometry. The ratio of actuation pressure p_{el} and counteracting modulus determines the resulting deformation ratio:

$$\frac{\Delta z}{z_0} = \frac{1}{Y_c} p_{el}(\omega). \quad (42)$$

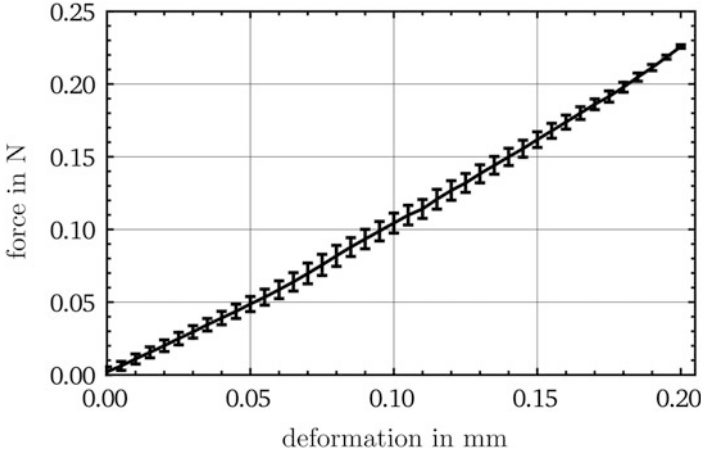


Fig. 8 Stress–strain characteristic of passive DE (30 dielectric layers; each 30 μm , circular electrode; diameter = 15 mm)

Measuring the increasing force for a given deformation by an external load with the measurement setup described in Haus et al. (2013) leads to the force–deflection graph shown in Fig. 8. As the strain corresponds to the planned actuating state, the uniaxial compressive modulus can be interpolated using the area of the probe head and the height of the actuator. The calculated modulus for the characterized DE is 210 kPa.

To model the mechanical characteristic of the DE, the modulus Y_c has to be determined as described above. The actual thickness of the DE is measured by two optical displacement sensors from top and bottom to avoid any adulteration due to the effects of gravity. More details about the used setup to measure the change of thickness of the actuator can be found in Matysek et al. (2008).

To calculate the deformation, we compare two different equations: Eq. 43 using the initial electrical field and Eq. 44 where the change in thickness and area caused by the actuation corresponding to Eq. 40 is taken into account.

$$\frac{\Delta z}{z_0} = \varepsilon_0 \varepsilon_r \frac{V^2}{(z_0)^2} \frac{1}{Y_c} \quad (43)$$

$$\frac{\Delta z}{z_0} = \varepsilon_0 \varepsilon_r z_0 \frac{V^2}{(z_0 - \Delta z)^3} \frac{1}{Y_c} \quad (44)$$

Figure 9 shows the measured static deflection in comparison to the two calculated deformation curves according to Eqs. 43 and 44. The DE consists of 30 active dielectric layers each 10 μm in height and has an active electrode area of 25 mm^2 . The determined uniaxial compressive modulus Y_c is 500 kPa.

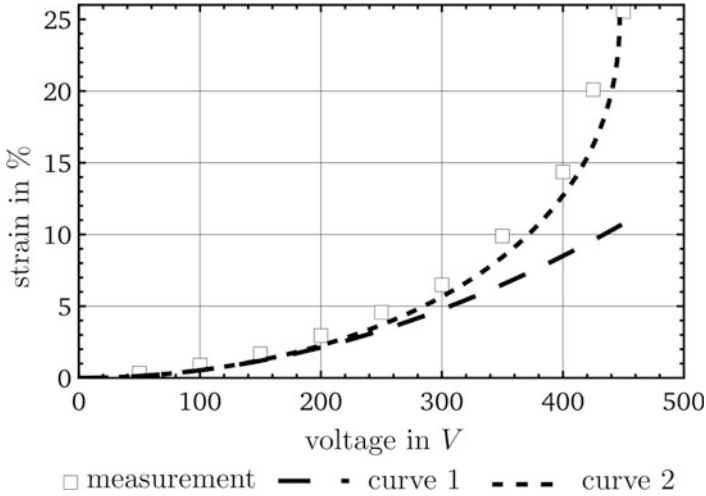


Fig. 9 Measured and calculated mechanical impedance. Curve 1 is calculated by using Eq. 43, curve 2 calculated by Eq. 44

The results show that Eq. 43 can obviously only be used for small deformation ratios up to 5 %. For higher strains the change of thickness needs to be considered according to Eq. 44.

3.2.2 Dynamic Stimulation

The mechanical behavior of elastomers corresponds to a combination of elastic and viscous characteristics. The resulting mechanical equivalent network to describe the so-called viscoelastic effects consists of a spring and a damper, respectively.

According to the literature the effects of relaxation and creep can be described by the mechanical Maxwell and Voigt model, respectively (Gent 1992). The corresponding mechanical equivalent circuits the related force-deformation characteristic and the equations describing the motion of the network, and the transient effect are shown in Table 1.


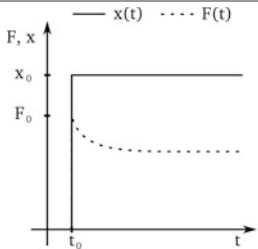
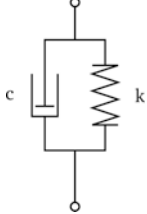
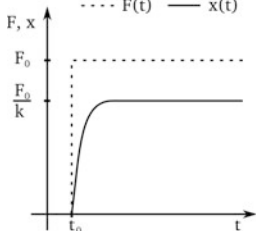
Both transient effects are described by exponential functions. The ratio of force F to velocity v is defined as the mechanical impedance

$$Z_{\text{mech}} = \frac{F}{v}. \quad (45)$$

The mechanical impedance of a spring with the spring constant k is defined as $Z_{\text{spring}} = k/j\omega$ and for a damper with the damping coefficient c as $Z_{\text{damper}} = c$.

The models mentioned above are based on phenomenological quality and are able to describe either relaxation or creeping. To describe both effects the models can be combined to the standard linear solid (SLS) model as shown in Fig. 10a. Consequently, the mechanical impedance of the SLS model Z_{SLS} results from serial and parallel connection of the single elements and is given by

Table 1 Summary of mechanical Maxwell and Voigt model

Mech. model	Equivalent circuit	Force-deformation characteristic	Equations
Maxwell			$\frac{dx}{dt} = \frac{1}{k} \left(\frac{dF}{dt} \right) + \frac{F}{c}$ $\frac{dF}{dt} = 0: F = F_0 e^{-t/\tau}$
Voigt			$F = kx + c \left(\frac{dx}{dt} \right)$ $\frac{dF}{dt} = 0:$ $x = \frac{F_0}{k} (1 - e^{-t/\tau})$

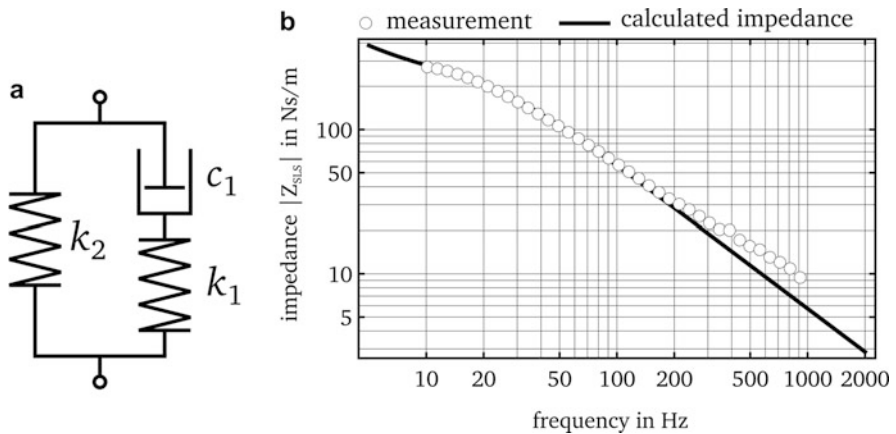


Fig. 10 SLS model. (a) Mechanical equivalent circuit. (b) Comparison of measurement and calculated mechanical impedance

$$Z_{SLS} = \frac{k_2}{j\omega} + \frac{1}{\frac{j\omega}{k_1} + \frac{1}{c_1}} \tag{46}$$

Figure 10b compares the measured mechanical impedance of a DE with 30 dielectric layers each 40 μm in height to the curve fitted impedance according to the SLS model.

Table 2 SLS model parameters

Parameter	Unit	Value
No. of layers n	1	30
Single layer thickness z_0	μm	40
Total thickness d_0	μm	1240
Active area A	mm^2	25
Spring constant k_1	kN/m	27,1
Spring constant k_2	kN/m	8,88
Damping coefficient c_1	Ns/m	210

The mechanical impedance is measured for several frequencies up to a maximum of 1 kHz limited by the equipment with the setup described in Haus et al. (2013). An electrodynamic oscillator excites the test sample with constant force amplitude. The acquired acceleration is integrated to derive the velocity and hence to calculate the mechanical impedance according to Eq. 45. The geometric parameters of the DE and the calculated parameters for the SLS model are summarized in Table 2.

However, the SLS model shows a limited compliance with the measured results especially in the frequency range above 200 Hz. To model the actuator for larger frequency ranges the number of Maxwell and Voigt models has to be increased. Consequently, dynamic transient behavior is no longer represented by a single exponential equation, but by an exponential series, the so-called Prony method (Gent 1992). While this method allows us to match the mechanical impedance to a higher bandwidth, the number of parameters is strongly increased and calculation becomes much more complex. Especially without a good set of starting parameters, calculation is hardly possible: Weak parameters typically cause oscillation of variables, and hence matching criteria cannot reach convergence (Schmidt and Gaul 2001).

The use of fractional derivatives for the constitutive equation allows us to define a more general, rheological element (Bagley 1989). A high bandwidth fit is possible using fewer variables than Prony's method. The relation of stress T and strain S for the fractional element is defined as

$$T = p \frac{d^\vartheta}{dt^\vartheta} S, \quad (47)$$

where the stress is defined as

$$T = F/A \quad (48)$$

and the strain as

$$S = \Delta z/z_0. \quad (49)$$

In literature the use of the fractional element is sometimes referred to by the term spring-pot, as it behaves between a spring ($\vartheta = 0$) and a damper ($\vartheta = 1$). It is visualized by a rhombus and defined by the proportional factor p and the fractional

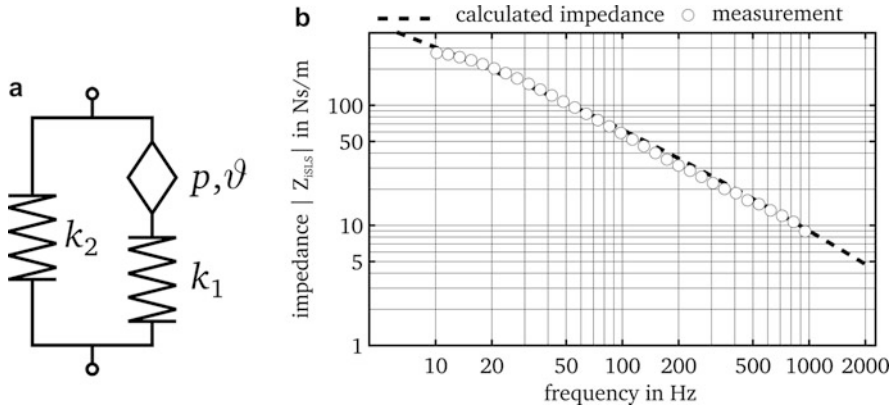


Fig. 11 Improved model with fractional element. (a) Mechanical equivalent circuit. (b) Comparison of measurement and calculated mechanical impedance

Table 3 Improved model parameters

Parameter	Unit	Value
Spring constant k_1	kN/m	7,24
Spring constant k_2	kN/m	5,03
Proportional factor p	Ns ^θ /m	210
Fractional degree	1	0,5

degree ϑ (Koeller 1984). The mechanical impedance of the fractional element is defined as $Z_{frac} = p/(j\omega)^\vartheta$. Using the fractional element by replacing mechanical dampers leads to the new mechanical equivalent network as shown in Fig. 11a and the mechanical impedance

$$Z_{iSLS} = \frac{k_2}{j\omega} + \frac{1}{\frac{j\omega}{k_1} + \frac{(j\omega)^\vartheta}{p}} \tag{50}$$

The calculated impedance for the improved model is compared to the measured impedance in Fig. 11b. The DE used is the same as compared to the SLS model before. The improved model using the fractional element fits quite well in the complete analyzable frequency range. The analysis of the applicability of the fractional model for a larger bandwidth will be a focus of future work. The calculated parameters for the improved model are summarized in Table 3.

3.3 Combined Electrical and Mechanical Model

Merging the electrical and mechanical characterizations we get the combined model shown in Fig. 12.

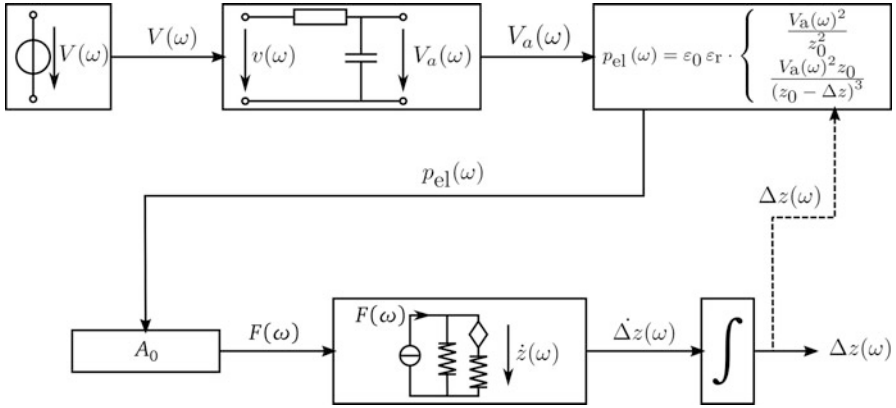


Fig. 12 Combined electrical and mechanical lumped parameter model showing the full signal transduction from electrical stimuli to mechanical output. Calculation method for $p_{el}(\omega)$ may be chosen from Eqs. 38 or 40, according to Sect. 3.2.1 in this chapter

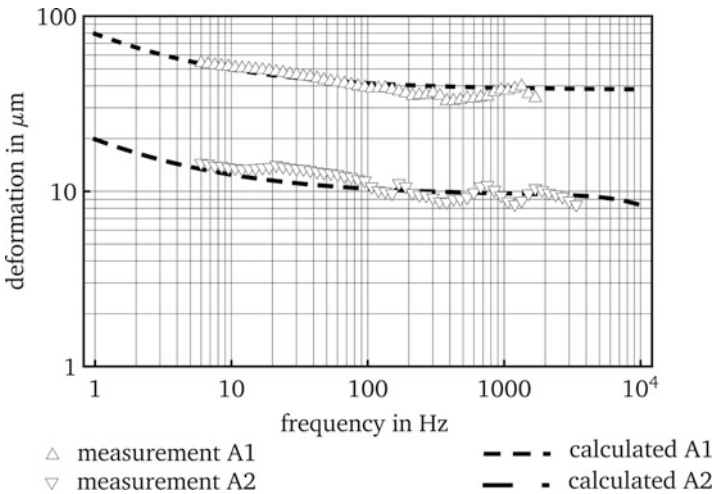


Fig. 13 Comparison between the predictive model and the measurements taken from the two real actuators from Table 4 for the model given in Fig. 12 by using Eq. 20

Depending on which equation is used for calculation of the electrical pressure (Eqs. 38, 39, and 40), the deflection Δz is reinserted into the calculation or not, depicted by the dashed line in Fig. 12.

Figure 13 shows the comparison of the model, using Eq. 38, and the measurements for two different actuators. The geometric details of these two actuators are found in Table 4.

The results show that the described lumped parameter model describes the behavior of a real DE very well over a wide frequency range.

Table 4 Actuator parameters

Actuator	C_a (pF)	R_s (k Ω)	No. of layers n	Film thickness (μm)	Driving voltage (V)
A1	460	10	30	50	1400
A2	490	100	30	30	700

4 Conclusion

In this chapter, we presented two different approaches for modeling DE. The first approach is focussed on describing the behavior of DE under electrical and mechanical stresses using the fundamental laws of electromechanics. The resulting model allows a correct representation of the actual forces and deformations appearing in a DE. This makes the model well suited for the description of complex geometries and FEM simulation of the DE behavior.

The second phenomenological approach using lumped parameters is motivated by the desire to provide a simple and adequate description of the behavior of existing DE actuators under the influence of an electrical voltage applied to the electrodes using network theory. The model parameters are determined directly from the actuator geometry or by performing simple measurements. The final lumped parameter model describes the response of the DE quite well over a large frequency range.

References

- Bagley RL (1989) Power law and fractional calculus model of viscoelasticity. *AIAA J* 27:1412–1417
- Bertoldi K, Gei M (2011) Instabilities in multilayered soft dielectrics. *J Mech Phys Solids* 59:18–42
- Carpí F, Gei M (2013) Predictive stress–stretch models of elastomers up to the characteristic flex. *Smart Mater Struct* 22(10):104011
- Dorfmann A, Ogden RW (2005) Nonlinear electroelasticity. *Acta Mech* 174:167–183
- Gent AN (1992) *Engineering with rubber: how to design rubber components*. Hanser Verlag, Munich
- Haus H, Matysek M, Mößinger H et al (2013) Modelling and characterization of dielectric elastomer stack actuators. *Smart Mater Struct* 22:104009 (12pp)
- Koeller RC (1984) Applications of fractional calculus to the theory of viscoelasticity. *J Appl Mech* 51:299–307
- Lotz P (2009) Dielektrische Elastomerstapelaktoren für ein peristaltisches Fluidfördersystem. Dissertation Technische Universität Darmstadt, Darmstadt
- Lotz P, Matysek M, Schlaak HF (2011) Fabrication and application of miniaturized dielectric elastomer stack actuators. *IEEE/ASME Trans Mechatron* 16:58–66
- Moré JJ (1978) The Levenberg-Marquardt algorithm: Implementation and theory, in numerical analysis, Bd. 630, G. A. Watson, Hrsg. Springer Berlin Heidelberg, S. 105–116
- Matysek M (2010) Dielektrische Elastomeraktoren in Multilayer-Technologie für taktile Displays. Dissertation Technische Universität Darmstadt, Darmstadt
- Matysek M, Lotz P, Flittner K et al (2008) High-precision characterization of dielectric elastomer stack actuators and their material parameters. *Smart Struct Mater: Proc SPIE* 6927:692722

- McMeeking RM, Landis CM (2005) Electrostatic forces and stored energy for deformable dielectric materials. *J Appl Mech* 72:581–590
- Mößinger H (2010) Demonstrating the application of dielectric polymer actuators for tactile feedback in a mobile consumer device. Master thesis technische Universität Darmstadt, Darmstadt
- Ogden RW (1997) *Nonlinear elastic deformations*. Dover, New York
- Pelrine RE, Kornbluh RD, Joseph JP (1998) Electrostriction of polymer dielectrics with compliant electrodes as a means of actuation. *Sensors Actuators* 64:77–85
- Schlaak HF, Jungmann M, Matysek M et al (2005) Novel multilayer electrostatic solid state actuators with elastic dielectric. *Smart Struct Mater: Proc. SPIE* 5759:121–133
- Schmidt A, Gaul L (2001) Bestimmung des komplexen Elastizitätsmoduls eines Polymers zur Identifikation eines viskoelastischen Stoffgesetzes mit fraktionalen Zeitableitungen. In: *Proceedings of Deutsche Gesellschaft für Zerstörungsfreie Prüfung Jahrestagung 75*, Berlin
- Suo Z, Zhao X, Green WH (2008) A nonlinear field theory of deformable dielectrics. *J Mech Phys Solids* 56(2):467–486
- van der Pauw LJ (1958) A method of measuring the resistivity and hall coefficient on lamellae of arbitrary shape. *Philips Tech Rev* 20:220–224

Qibing Pei, Wei Hu, David McCoul, Silmon James Biggs,
David Stadler, and Federico Carpi

Contents

1	Introduction	740
2	Biologically Inspired Robotics	740
2.1	Walking Robots	741
2.2	Flapping-Wing Vehicles	742
2.3	A Fish-Like Airship	742
2.4	DEMES Grippers	744
3	Tactile Feedback and Displays	744
3.1	Tactile Displays Based on Thickness-Mode Actuators	744
3.2	Tactile Displays Based on Stacked Actuators	745
3.3	Tactile Displays Based on Shear-Transmission Actuators	746
3.4	Tactile Displays Based on Hydrostatically Coupled Actuators	746
3.5	Tactile Displays Based on Buckling Diaphragms	747
3.6	Tactile Displays Made of Tubular Actuators	748
4	Tunable Optics	749
4.1	Laser Speckle Reducers	749
4.2	Tunable Lenses	749
5	Fluid Control and Microfluidics	752

Q. Pei (✉) • W. Hu • D. McCoul
Henry Samueli School of Engineering and Applied Science, University of California – Los Angeles, Los Angeles, CA, USA
e-mail: qpei@seas.ucla.edu; wei.hu.ucla@gmail.com; david.mccoul@epfl.ch

S.J. Biggs
Parker Hannifin Inc., Sunnyvale, CA, USA
e-mail: james@artificialmuscle.com

D. Stadler
Optotune AG, Dietikon, Switzerland
e-mail: david.stadler@optotune.com

F. Carpi
School of Engineering and Materials Science, Queen Mary University of London, London, UK
e-mail: f.carpi@qmul.ac.uk

6	Capacitive Sensors	756
6.1	The Basic of Capacitive Sensors	756
6.2	Actuators as Sensors	756
6.3	Sensing While Actuating	757
6.4	A Compression Sensing Mat	758
7	Energy Harvesting	759
7.1	Operation Modes of a DEG	760
7.2	A Heel-Strike Generator	761
7.3	A Buoy Energy Generator	761
8	Other Important Applications	761
8.1	A Dielectric Elastomer Switch	761
8.2	A Cell Stretcher	762
9	Conclusion and Remarks	763
	References	763

Abstract

The unique advantages of dielectric elastomers have stimulated a great number of applications which can be categorized into actuators, energy harvesters, and sensors. This chapter presents multiple electromechanical transduction systems including biologically inspired robotics, tactile feedback and displays, tunable optics, fluid control and microfluidics, capacitive sensors, and energy harvesters.

Keywords

Actuators • Dielectric elastomers • Energy generators • Sensors

1 Introduction

Among all the EAPs, dielectric elastomers (DEs) exhibit a unique combination of properties, including large strain, fast response, high energy density, quiet operation, mechanical compliancy, lightweight, solid state, and low cost, which have stimulated the imagination of numerous researchers and application engineers (Brochu and Pei 2010; Anderson et al. 2012). The actuation, generation, and sensing functions of DEs have been utilized in various electromechanical transduction systems such as robotics, fluidic control, energy generation, biomedical devices, haptic feedback, and so on. This chapter surveys several important applications of DE materials, including device structures, prototypes, and commercial products.

2 Biologically Inspired Robotics

Animals have offered good examples of motions and movements. Comparing with conventional electroactive materials and systems, DEs share more similarities with natural muscles such as soft and lightweight. Multiple types of robot prototypes, which can walk, fly, or grip, made of DEs have been investigated and demonstrated.

These robots are potentially useful for transportation and surveillance, thanks to the materials' high energy density and quiet operation.

2.1 Walking Robots

SRI International pioneered the DE-based walking robots. They have presented four generations of hexapod walking robots as shown in Fig. 1 since 2001.

FLEX 1 was the first walking robot using DE actuators (Eckerle et al. 2001). This robot implemented the characters of a cockroach, with six legs, a tripod gait, and a lightweight but rigid body. Each leg was powered by a Bowtie actuator and had two degrees of freedom, up/down, as well as forward/back rotation. Although it was a milestone in the history of walking robots, the speed of **FLEX 1** was too slow to be practical, and the reliability of the bowtie actuators was another issue.

All the other three robots developed in SRI International used spring roll actuators instead of Bowtie actuators. A spring roll actuator contained a compressed spring wrapped with a DE film with pasted electrodes. Depending on the electrode pattern and the actuated portion of the DE film, the spring roll actuator was able to show multiple actuation modes. This device had a higher actuation power and better reliability than a Bowtie actuator did.

FLEX 2 was an improved version of **FLEX 1**, with two more powerful spring roll actuators taking over one bowtie actuator on each leg. The onboard battery was removed to reduce the total weight (Pelrine et al. 2002). As improved from **FLEX 2**,

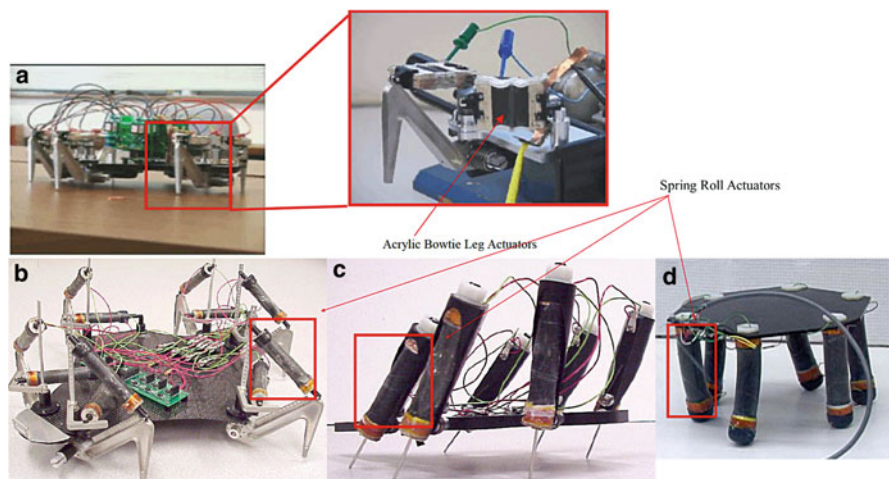


Fig. 1 Four generations of walking robots using DE technology developed in SRI International: (a) FLEX 1, (b) FLEX 2, (c) Skitter, and (d) MERobot ((a) and (b) Reproduced with permission from Pelrine et al. 2002)

Table 1 Comparison of four walking robots developed in SRI International (Eckerle et al. 2001; Pelrine et al. 2002; Pei et al. 2002, 2004)

Walking robot	FLEX 1	FLEX 2	Skitter	MERobot
Dimension (cm)	36	–	20 × 15	18 × 18 × 18
Weight (g)	670	–	220	292
Battery	On board	Off board	–	–
Speed	~ cm/h	3.5 cm/s	7 cm/s	14 cm/s

Skitter (Pei et al. 2002) and **MERobot** (Pei et al. 2004) both used spring roll actuators not only as the motion power but also the structural components. In other words, these actuators were essentially the legs of these robots. This would help further reduce the total weights of the robots.

The characteristics of these four walking robots are summarized in Table 1.

Recently, Nguyen presented a quadruped robot driven by multi-stacked DE actuators (Nguyen et al. 2014). The multi-stacked DE actuators were fabricated using DE films without pre-stretching, which would further improve the reliability of the robots as the potential stress relaxation issue in spring roll actuators was solved.

2.2 Flapping-Wing Vehicles

Researchers also integrated DEs into flapping-wing vehicles. The robot developed by SRI International (Fig. 2a) was inspired by flying insects whose wings are driven indirectly by muscles located in their thoraxes. Multi-staked actuators were driving the wings. Moreover, this device also exploited resonance to increase the energy output of the DE actuator and the efficiency of the mechanism, the same as insects and hummingbirds (Pelrine et al. 2002). Figure 2b shows another flapping bird device using a spring roll actuator as the core to power the wings. Although both devices achieved large flapping motions but neither of them were able to fly like real birds. Limitations include the heavy weight of the structure and the low operation frequency of the employed DEs (Lau et al. 2014).

2.3 A Fish-Like Airship

Jordi et al. presented an airship mimicking a fish in water. The airship was propelled by undulating its hull and a caudal fin like a rainbow trout. As shown in Fig. 3, the propelling was realized through actuation of selected parts in the fish. The DE was stretched unsymmetrically, confined by reinforcing carbon rods and polyamide string, and then produced linear actuation. The actuators worked together to create

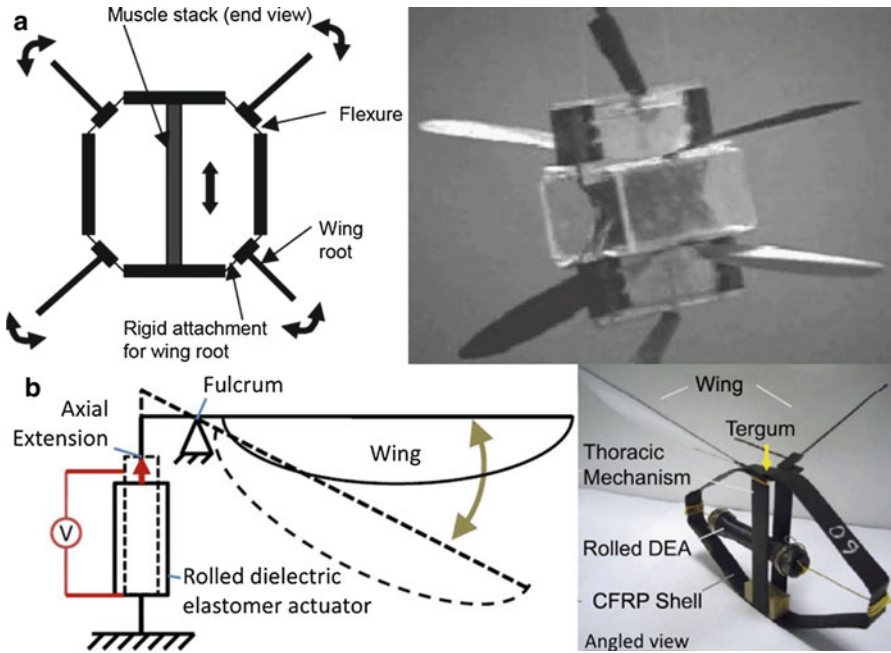


Fig. 2 Two flapping-wing vehicle prototypes ((a) Reproduced with permission from Pelrine et al. 2002; (b) Figure courtesy from Dr. Gih Keong Lau, NTU, Singapore)

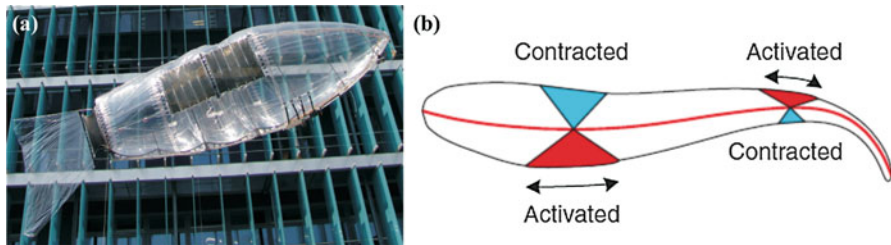


Fig. 3 (a) A photo of the 8 m long air fish; (b) the working principle of the airship (Reproduced with permission from Jordi et al. 2010)

bending on the whole fish. The fish was controlled by a ground station through a commercial WLAN module.

The maximum speed of this air fish was 0.45 m/s at an operation frequency of 0.25 Hz. Although the speed was low compared with its large size, this airship could be operated quietly and suitable for applications like animal observation, surveillance, and filming at a concert (Jordi et al. 2010).

2.4 DEMES Grippers

A gripper can be integrated with several bending actuators. Recently, DE minimum energy structures (DEMESs) were used to fabricate grippers. DEMESs refer to structures with a stretched DE film on a flexible frame, which would transformed into other configuration to minimize the systems' energy. These structures can unfold on the application of electric fields due to actuation of stretched DE film (Kofod et al. 2006). Araromi et al. utilized this DEMES technology and developed deployable gripper (Araromi et al. 2015). This gripper could wrap objects of various shapes and sizes. This device was less than 0.65 g but was able to produce a gripping force of 2.2 mN (0.22 g) and a maximum change in tip angle of $\sim 60^\circ$.

3 Tactile Feedback and Displays

Tactile displays apply forces to the skin to stimulate the sense of touch. The applications of tactile displays range from a one-note linear resonant actuator to refreshable Braille displays (Biggs and Srinivasan 2002a,b). Most commercial products use electromagnetic and piezoceramic mechanisms. However, there is an increasing interest in using the DE technology.

There are several representative types of tactile displays made of DEs: they are separately described below.

3.1 Tactile Displays Based on Thickness-Mode Actuators

A display developed at SRI International (Fig. 4) has inspired many subsequent efforts. A soft flat polymer surface (Fig. 4a) was dimpled by depressions (Fig. 4b) when the dielectric elastomer actuators bonded to the bottom surface were actuated (Prahlad et al. 2005). Key elements of this design included:

1. The soft layer of polymer overlying the actuators provided electrical insulation considering DE actuators typically worked at high voltages.

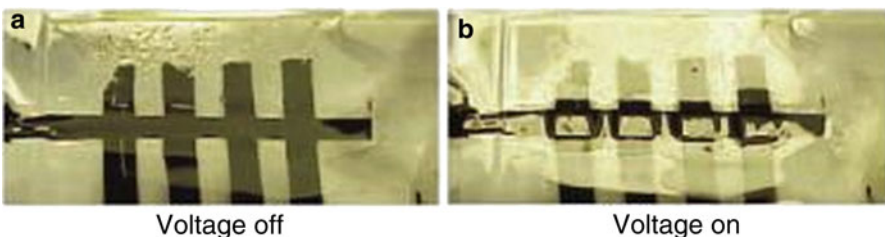
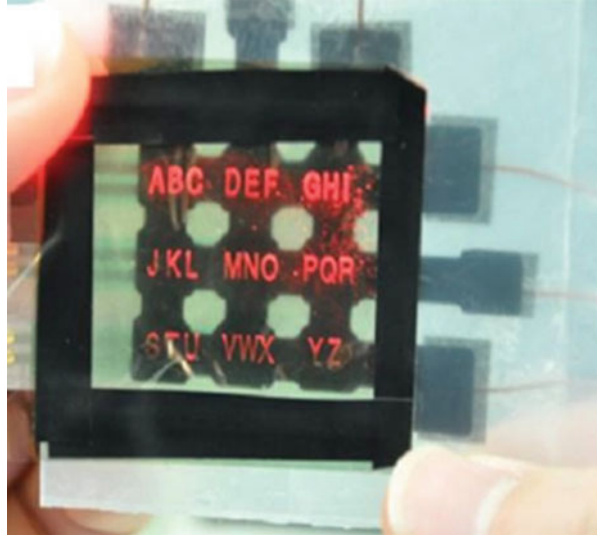


Fig. 4 A “thickness-mode” actuator array: (a) voltage off and (b) voltage on (Reproduced with permission from Prahlad et al. 2005)

Fig. 5 A thickness-mode actuator behind an edge-illuminated flexible visual display enables localized key-press confirmation (Photo courtesy from Dr. Sungryul Yun, ETRI, Korea)



2. The insulation layer acted as a displacement-amplifying mechanical transmission as well.
3. The row-and-column arrangement of the actuators in the image suggested drive electronics with matrix addressing.

From this basic design, several variations have followed over the years. Covering an array of thickness-mode actuators (Fig. 4) with a flexible visual display (Fig. 5) allows for localized touch feedback (Yun et al. 2014). Turning on a given actuator mainly moves the portion of screen overlying it. This construction was demonstrated recently with an edge-illuminated light guide. The recent development of highly transparent and stable ionogel electrodes (Chen et al. 2014) may enable designs in which the tactile display overlies the visual display.

3.2 Tactile Displays Based on Stacked Actuators

In most of the display thickness is passive material; the actuator may not generate enough force to deform the skin. In principle, the additional force can be provided by operating a thicker layer of dielectric at higher voltage, but in practice it is more common to stack multiple actuator layers, to keep down the operating voltage. Matysek et al. demonstrated this concept by stacking 80 μm -thick silicone actuators, as shown in Fig. 6 (Matysek et al. 2009). Mößinger et al. also developed a tactile display comprised of 40 silicone layers, each 40 μm thick. This device can provide satisfactory tactile sensation when operated at 1 kV and can conform to the biaxial curvature of a computer mouse (Mößinger et al. 2014).

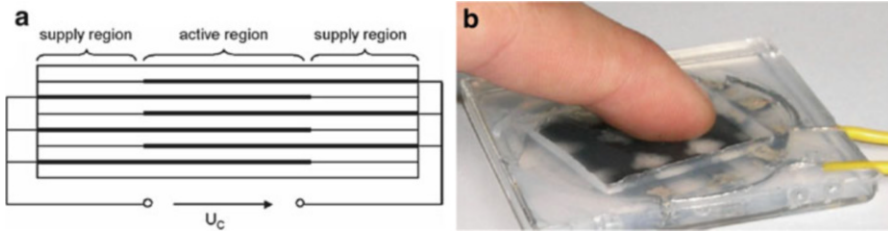
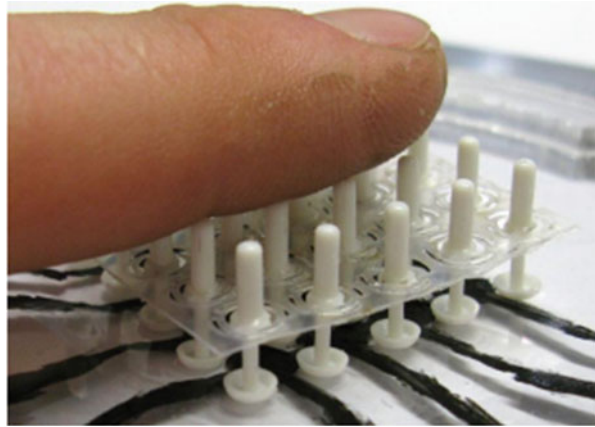


Fig. 6 (a) Schematic cross section of an actuator stack; (b) A 3 by 3 matrix tactile display with DEAs. Actuator size: 5 by 5 mm² (Reproduced with permission from Matysek et al. 2009)

Fig. 7 A shear array (Reproduced with permission from Knoop and Rossiter 2014)



3.3 Tactile Displays Based on Shear-Transmission Actuators

An alternative to the thickness-mode and stack actuators has recently been demonstrated (Fig. 7). An array of pivoting pins provides electrical isolation between the skin and a matrix of polymer actuators (Fig. 7, black traces at bottom). The actuators don't lower the pins, but instead, shift the bases of the pins laterally. The transmission ratio can be adjusted to match skin stiffness by varying the pin lengths above and below the gimbal. Although the skin is stiffer in shear than indentation, smaller displacements suffice to create the same sensation level (Knoop and Rossiter 2014).

3.4 Tactile Displays Based on Hydrostatically Coupled Actuators

Some designs for DEA tactile displays are based on the hydrostatically coupled configuration (Carpi et al. 2010). As illustrated in Fig. 8, a circular patch of DE film is constrained by a rigid frame. Actuation that thins and expands the film makes it

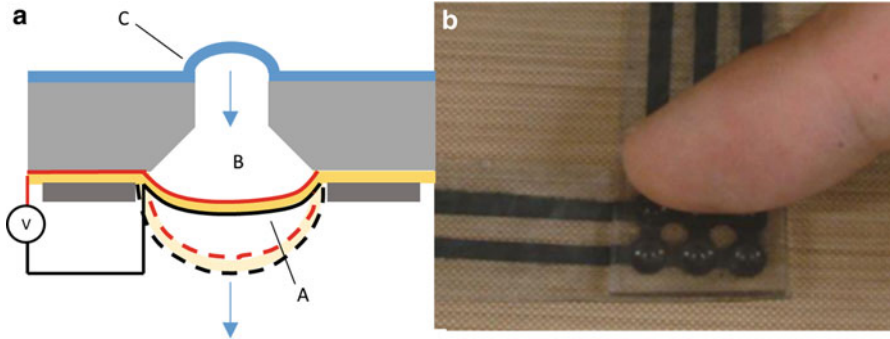


Fig. 8 (a) Schematic illustration of a hydrostatically coupled actuator: a DEA membrane (*A*) is coupled to a chamber containing a fluid (*B*) which provides electrical insulation and hydraulic transmission for driving a tactile surface (*C*); (b) example of a prototype display ((b) Reproduced with permission from Lee et al. 2014)

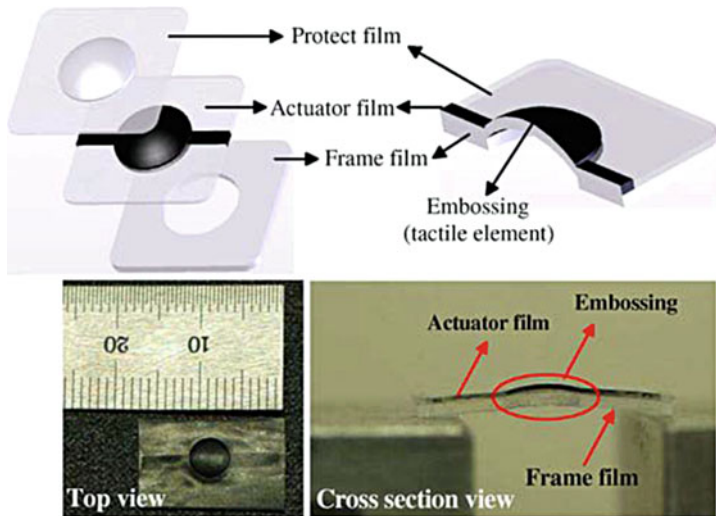


Fig. 9 An embossed silicone taxel Figure courtesy from Dr. Hyouk Ryeol Choi, SKKU, Korea)

buckle out of plane. The displacement of the buckled diaphragm is coupled to a flexible skin-contact layer by means of a fluid (Carpi et al. 2010, 2011a; Lee et al. 2014).

3.5 Tactile Displays Based on Buckling Diaphragms

Other designs for DEA tactile displays are based on buckling diaphragms. An example is shown in Fig. 9, where one or more actuator layers are biased upward

either by embossing them (Koo et al. 2008) or backing them with a layer of bumps (Choi et al. 2009). Actuation arches the active layers upward. The arch is relatively thick compared to the span. This allows it to support the compressive load required to raise a Braille pin or indent the skin.

A Braille cell (Fig. 10) has been developed that uses a bistable electroactive polymer with a glass transition temperature slightly above room temperature (Yu et al. 2009). The poly-(tert-butyl-acrylate) dielectric layer was heated with alternating current. The diaphragms were selectively actuated and then allowed to cool and stiffen in the actuated position. This latched the diaphragm in the raised state with voltage off. In this design, battery life was a challenge due to the resistive heating. Another issue was the cost of transistors that can gate the high voltage, which was common in all displays based on DEs.

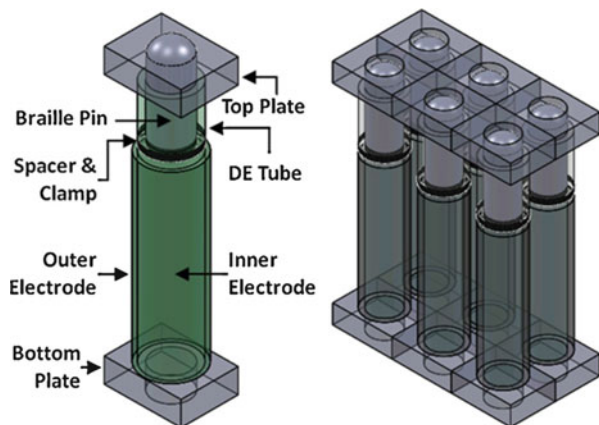
3.6 Tactile Displays Made of Tubular Actuators

Another refreshable Braille display based on tubular DEA was demonstrated by Chakraborti et al. As demonstrated in Fig. 11, each Braille pin is attached to a tubular actuator with a spacer and a clamp. While voltage is applied to the tubular actuator, the Braille pin will move up driven by the displacement of the actuator.



Fig. 10 A bistable electroactive polymer Braille cell, developed by Pei's group, spells out UCLA (Maffi et al. 2013b)

Fig. 11 An illustration of a Braille cell based on tubular DA actuators: *Left*: a single actuator; *right*: assembly of actuators in a Braille cell (Reproduced with permission from Chakraborti et al. 2012)



To obtain enough z direction actuation movement using the tubular actuator, optimal prestrain, which is 90 % circumferentially and 43 % axially in this case, was applied. With 120 kV/mm electric field, the cells can produce more than 1 mm displacement.

4 Tunable Optics

DEA can be integrated into tunable optical devices including laser speckle reducers and lenses, as described below.

4.1 Laser Speckle Reducers

Laser projection systems have both a broader color spectrum and a higher lifetime compared to conventional illumination systems. However, lasers have the inherent problem of speckle: on rough optical surfaces (e.g., a wall or a cinema screen), local interferences cause a grainy pattern of spots observable with a camera or naked eye. This effect causes noise in projected images but also reduces the resolution of measurement systems.

To reduce this problem, the company Optotune AG has developed and commercializes a DEA-based “Laser Speckle Reducer” (LSR) (Optotune 2015). The device functions in a similar way to a rotating diffuser, although it is more compact and economical. A diffuser is mounted on an elastic membrane and set into circular motion using four planar DEAs (actuating sectors), as illustrated in Fig. 12.

Figure 13 shows the commercial device. The actuators are based on a carbon-based electrode material deposited on a 10 μm -thick elastomer film (proprietary information). With proper timing of the actuating sectors’ activation, a planar circular oscillation of the diffuser can be generated. Using the resonance frequency of the mechanical structure, the diffuser can laterally deflect between 300 and 500 μm at frequencies of about 300 Hz.

An example of speckle reduction enabled by this device is presented in Fig. 14. Optimal reduction is realized with high rotation speed, large oscillation amplitudes, high-resolution diffuser patterns, and long observer integration times.

The advantages of this DEA-based approach are represented by compact design, the absence of mechanics, silent operation, wide temperature range, and low power consumption (about 10 mW). The actuation of this LSR requires 300 V. So, battery-operated devices must include voltage conversion electronics, e.g., a flyback converter, which takes up around 40 mm^2 of PCB space with Optotune’s solution shown above.

4.2 Tunable Lenses

Electrical control of optical focusing is important in several fields, such as consumer electronics, medical diagnostics, and optical communications. Tunable lenses are

Fig. 12 Working principle of the laser speckle reducer: (a) no voltage is applied and the diffuser is centered; (b) the upper actuating sector is active, translating the diffuser downward; (c) two sectors are active which results in a translation of the diffuser to the bottom right corner; (d) the left sector is active giving a translation to the right. Alternation of the activation of the sectors results into a circular motion of the diffuser

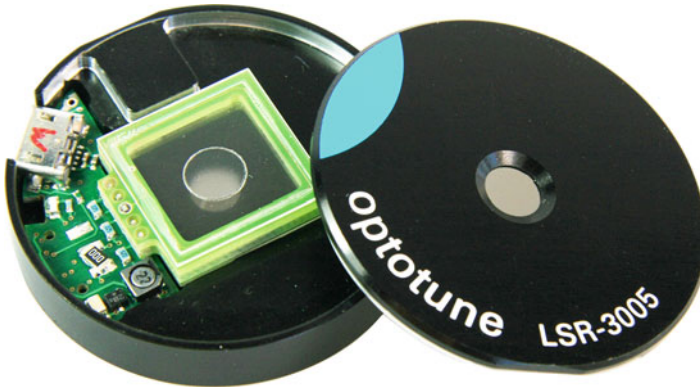
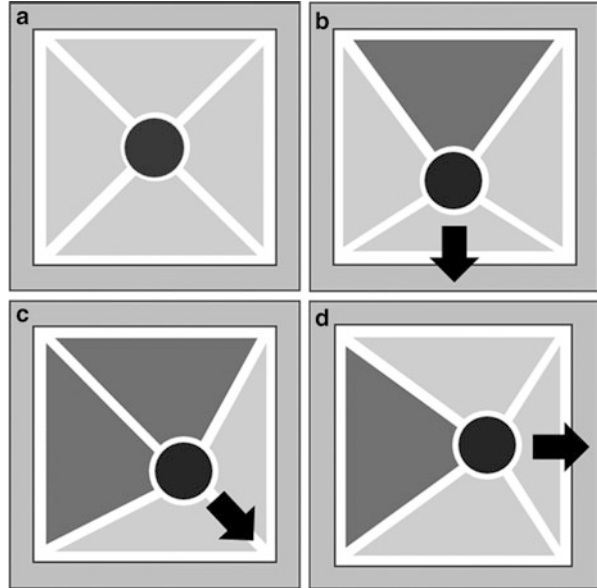


Fig. 13 Optotune's laser speckle reducer LSR-3000 with an aperture of 5 mm. Attached to the side of the rectangular structure the necessary electronics to drive the LSR is visible

studied as possible alternatives to complex, bulky, and expensive state-of-the-art approaches based on shifting constant-focus lenses. Among the actuation mechanisms investigated to possibly control the shape of liquid-based lenses, DEAs offer promising features in terms of focal length variation and stability, fast and silent operation, compact size, low weight, shock tolerance, low power consumption, and no overheating (Carpi et al. 2011b; Maffi et al. 2015).

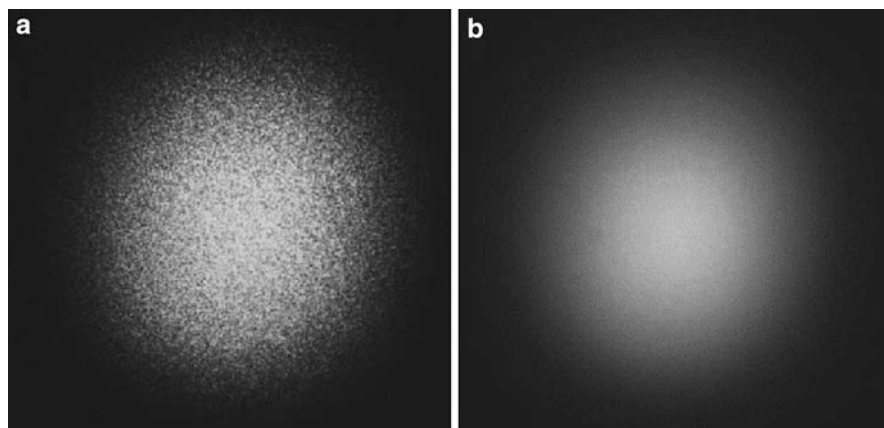


Fig. 14 Experimental demonstration of the speckle reduction: (a) speckle pattern; (b) the active LSR significantly reduces the speckle effect

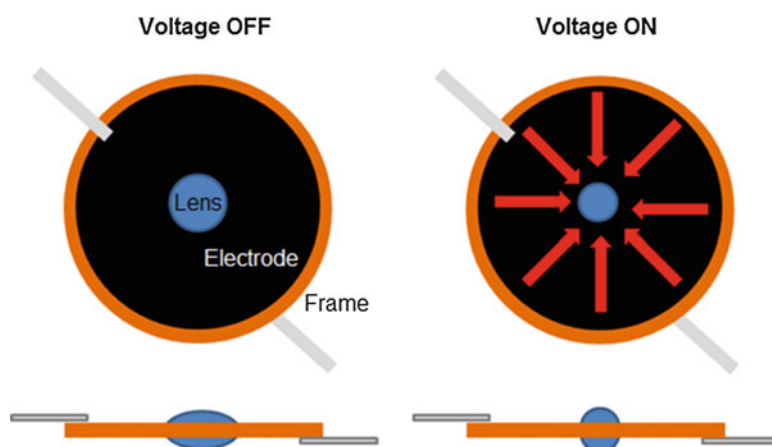
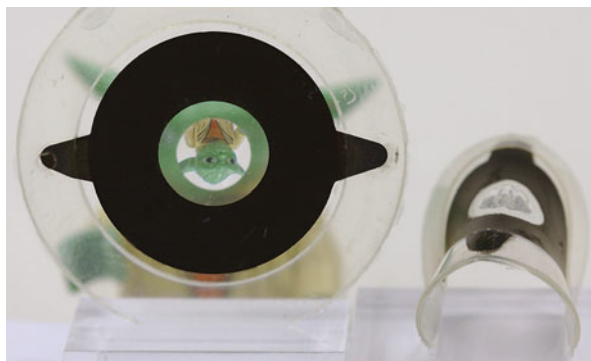


Fig. 15 Structure and working principle a DEA tunable lens

One type of DEA-based tunable lens is schematically represented in Fig. 15. It consists of a liquid-based lens surrounded by an annular DEA. The latter consists of a DE membrane sandwiched between two annular compliant electrodes. An external circular rigid frame maintains a radial pre-stretch of the membrane, which increases actuation performance by preventing snap-through electromechanical instability. By applying a voltage between the electrodes, the DE membrane is squeezed in thickness and it tends to expand radially to preserve its volume constant. The membrane can only expand toward the inner region. This leads to a reduction of the diameter of

Fig. 16 Example of a DEA tunable lens obtained as described in Maffli et al. (2015) (Photo courtesy of Dr Samuel Rosset, EPFL, Switzerland)



the electrode-free central area that hosts the lens. As a result of this, the lens reduces its curvature and, therefore, also its focal length.

This type of tunable lens was first described in 2011, using the 3 M VHB 4905 acrylic elastomer film (Carpi et al. 2011b). Recently, a much improved version was obtained with a silicone elastomer, demonstrating the world's fastest and thinnest tunable optical lens (Fig. 16) made of electro-responsive smart materials (Maffli et al. 2015).

Other types of demonstrated DEA-based tunable lenses include systems where a liquid is pumped back and forth from the lens region by means of hydrostatically coupled DEA membranes (Niklaus et al. 2010; Wei et al. 2014; Liang et al. 2014) or where transparent compact structures have been obtained by coating with conductive-polymer-based transparent electrodes either liquid-based lenses (Shian et al. 2013) or single buckling membranes (Son et al. 2012).

5 Fluid Control and Microfluidics

Over the past several decades, the field of microfluidics has blossomed into a highly interdisciplinary field. Electroactive polymers are currently a growing field in microfluidics.

In perhaps one of the first attempts to integrate EAPs in a microfluidic device, Price and Culbertson created a sample injection microfluidic chip combining a dielectric elastomer with electroosmotic actuation (Price and Culbertson 2009). In this electroosmotic injection-mode actuation, standard DE actuation is combined with an electrophoretic microchip, depicted in Fig. 17. First, a constant electric field was applied across the microchannels of the PDMS chip by applying a voltage to sample reservoir 1 and buffer reservoir 2 and grounding the waste reservoirs 3 and 4. The same voltage applied to reservoirs 1 and 2 was also applied to the patterned electrode. To actuate the DE, the voltage applied to the patterned electrode was switched to zero, creating a potential difference between the patterned electrode and charged microchannel and compressing the EAP layer. Finally, an injection was

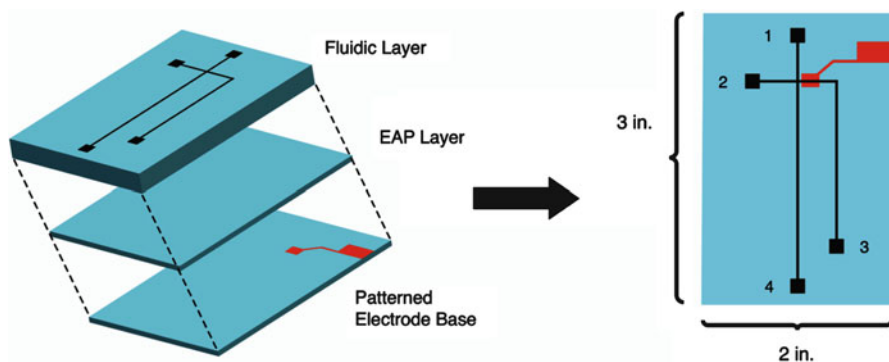


Fig. 17 The pictured EAM device consists of an electrophoretic PDMS microchannel system bonded to a ~ 40 μm -thick PDMS dielectric elastomer (EAP) layer. This layer is in turn bonded to a glass substrate with a lithographically patterned electrode (Reproduced with permission from Price and Culbertson 2009)

performed by returning the patterned electrode voltage to its original nonzero value. Doing so switches off the DE, causing the EAP layer to quickly relax and pump fluid. These injections are faster than 200 ms, and the injection volume can be modified by altering the electric field across the EAP layer prior to discharging (Price and Culbertson 2009).

Figure 18 demonstrated an electroactive microfluid system developed in the Pei and Di Carlo groups, using DEs with low modulus, large actuation strain as the active channel walls. The cross-sectional geometry of the microchannel could be actively and reversibly altered with the actuation of channel walls such that the channel blockage could be cleared (Murray et al. 2013; McCoul et al. 2013). McCoul and Murray et al. designed and tested PDMS microfluidic systems paired with dielectric elastomer stack actuators of anisotropically prestrained 3MTM VHBTM 4910 adhesive films and single-walled carbon nanotubes (SWCNTs), pictured in Fig. 18a–c. These electroactive microfluidic (EAM) devices demonstrated active increases in microchannel width when 3 and 4 kV voltages were applied (Fig. 18d). Fluorescence microscopy also indicated an accompanying increase in channel depth with actuation, which could be seen by the increasing channel brightness in the micrograph of Fig. 18d. The cross-sectional area strains at 3 and 4 kV were approximately 2.9 % and 7.4 %, respectively. The EAM was then interfaced with a syringe pump, and the pressure was measured upstream. Linear pressure-flow plots were developed, which showed decreasing fluidic resistance with actuation, from 0.192 psi/($\mu\text{L}/\text{min}$) at 0 kV to 0.160 and 0.157 psi/($\mu\text{L}/\text{min}$) at 3 and 4 kV, respectively. Active de-clogging was tested in situ with the EAM devices by introducing ~ 50 μm diameter PDMS microbeads and other smaller particulate debris into the system. After a channel blockage was confirmed, three actuation attempts successfully cleared the blockage, as detailed in Fig. 18e. Further tests indicated that the EAM devices were biocompatible with HeLa cells at 3 kV (Murray et al. 2013; McCoul et al. 2013).

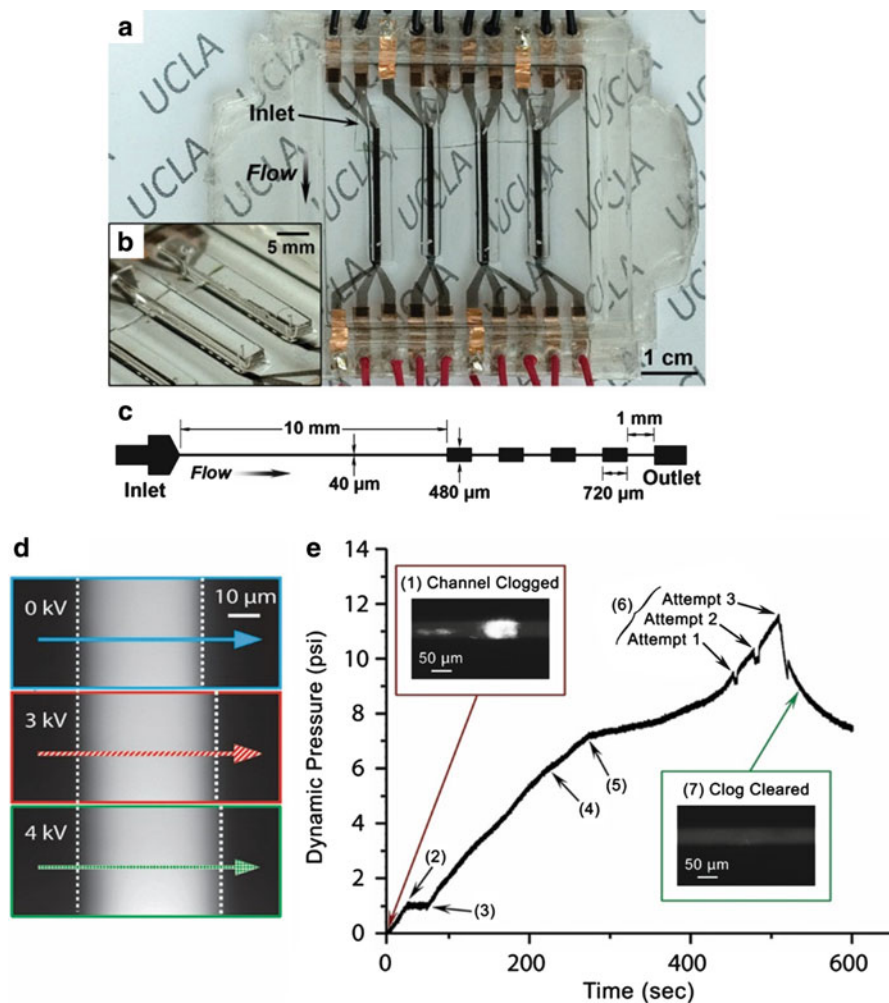


Fig. 18 (a) Photograph of the chip with four independent EAM devices. (b) Profile view of some of the EAM devices. The microchannel wells are visible to the naked eye, seen above the black SWCNT electrode strips. (c) Schematic of the 40 μm -wide, 50 μm -deep microchannel, with a series of wells downstream that could eventually serve as actively configurable cell sorting and trapping nodes. (d) Micrograph of the microchannel, demonstrating active channel deformation under applied actuation voltage. The arrows indicate a displacement in the width direction. There was also an increase in channel depth with increasing voltage, and these changes in cross-sectional area lowered the fluidic resistance of the system. (e) Demonstration of channel de-clogging. *Primary events:* (1) channel clogged, (6) channel actuated, (7) clog cleared. *Secondary events:* (2) flow is stopped to confirm a blockage, (3) flow is resumed, (4) blockage passively dislodged, (5) blockage re-lodges. Brief dynamic drops in intersystem pressure are visible at actuation attempts 1 and 2

The Shea group has recently demonstrated a “zipping”-mode microfluidic device useful for pumping fluid (Maffli et al. 2012; Gebbers et al. 2012; Maffli et al. 2013a,b). In standard “parallel-plate” DE actuation mode, a planar dielectric membrane is coated on opposing sides with flexible electrodes, and the dielectric is compressed by the Maxwell pressure generated between the compliant electrodes. However, in the zipping actuation mode, a dielectric membrane is coated on only one side by a flexible electrode, which is sequentially attracted to a rigid electrode on the uncoated side, such as aluminum (Fig. 19a; Maffli et al. 2013a). Zipping-mode actuation is also possible with a rigid dielectric (Fig. 19b), in which a dielectric membrane is coated on its inner face with a flexible electrode, and a rigid dielectric coats a rigid electrode (Gebbers et al. 2012). A peristaltic pump can be constructed by placing several such DE zipping actuators in series, illustrated in Fig. 19c. In this

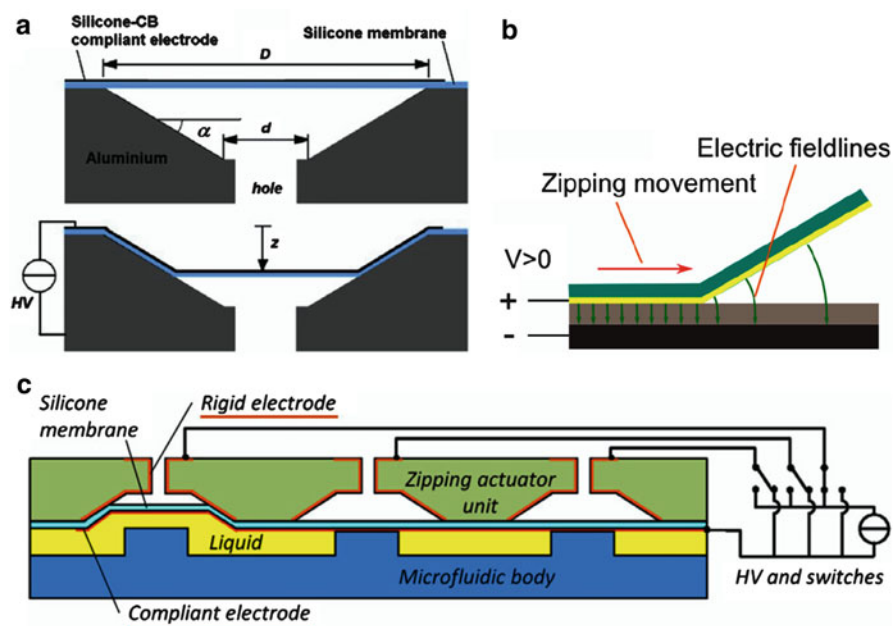


Fig. 19 (a) Cross-section of a conical zipping actuator consisting of a silicone elastomer coated on the outer surface with a silicone-bound carbon black compliant electrode and a rigid electrode of aluminum, which also serves as a structural component. Zipping-mode actuation draws the silicone toward the aluminum, and a hole allows air to displace. (b) Zipping actuation is also possible with a rigid dielectric. Pictured is a (green) silicone membrane coated on its inner surface with a (yellow) compliant electrode, which is drawn toward a (dark gray) rigid electrode coated with a (light gray) rigid dielectric. (c) A microfluidic peristaltic pump concept with a series of zipping actuators ((a) (c) Reproduced with permission from Maffli et al. 2013b; (b) Reproduced with permission from Gebbers et al. 2012)

configuration, fluid is drawn upward above the pillar when the first actuator in the series zips. Next, the first actuator zips down while the second zips up, both sealing the fluid from backflow and drawing the fluid forward. The process can then repeat for the desired length of linear pumping (Maffli et al. 2013b). Although the compliant electrode side of the silicone membrane comes into contact with the liquid in the microchannel, the cured silicone-bound carbon black is unlikely to detach into the fluid. Also, the electric field is restricted to the region between the compliant and rigid electrodes, which does not intersect the microfluidic channel, allowing zipping microfluidic devices to be potentially biocompatible.

6 Capacitive Sensors

6.1 The Basic of Capacitive Sensors

The basic mechanism of a capacitive sensor is to detect the signal of capacitance change. As the capacitance is directly related to the geometry of the capacitor, there are basically two operation modes: thickness changing and area changing as shown in Fig. 20 (Rosenthal et al. 2007).

A dielectric elastomer film, when coated with compliant electrodes on both sides, is essentially a soft capacitor, in which large deformation is achievable. Moreover, with proper circuit configuration, DEs could be functioning both like an actuator and a sensor simultaneously, like neutral muscle in which no extra sensing units are necessary. This brings in the several advantages including lightweight and low cost.

6.2 Actuators as Sensors

As mentioned in Sect. 2, Pei et al. invented spring roll actuators which were then used as legs for MERobots. The authors also used the actuators as strain sensors. Figure 21 displays the capacitance change of one actuator upon axial tension and

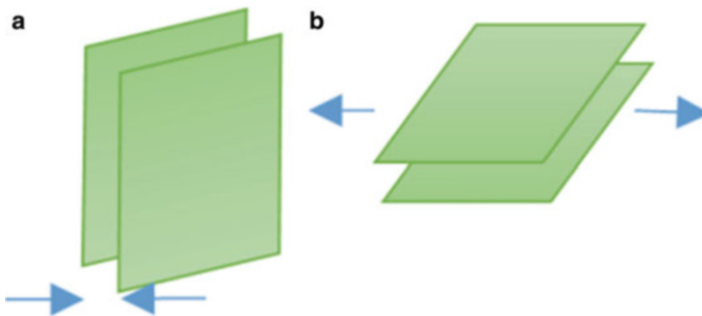


Fig. 20 (a) A thickness-changing capacitor and (b) an area-changing capacitor

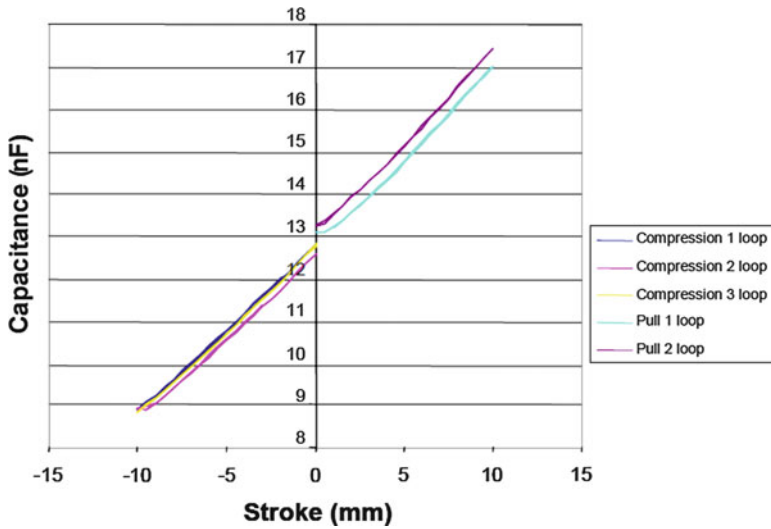


Fig. 21 Capacitance change of a spring roll actuator with tension and compression

compression. The capacitance increased linearly with the length of the spring roll. However, there was some creep of the stretched elastomer such that there was an offset near-zero stroke (Pei et al. 2002).

Son et al. studied the dynamic sensing properties of tubular DE actuators with dynamic pressure input. The dynamic sensing response greatly depended on the viscoelastic properties of the DE materials. The maximum capacitance value of the 3M™ VHB™ sensor at 2.0 Hz decayed during repeated charging and discharging. In comparison, silicone elastomer had a better performance, showing a non-decaying response up to 4.7 Hz (Son and Goulbourne 2010).

Carbon-based electrodes have been widely used in DE actuators whose resistance is in the scale of kOhm/sq. The resistance may even increase at large strain. Benslimane et al. proposed a silver-based electrode to address this problem. This silver electrode was formed through depositing Ag on a corrugated surface. The strain could reach up to 33 % linearly without much loss of conductivity. In the sensing test, the capacitance changed linearly with elongation and showed good reversibility as well (Benslimane et al. 2002).

6.3 Sensing While Actuating

To better mimic natural muscle, actuators and sensors should function at the same time. This creates challenges in the sensing circuit design. Gisby et al. developed a system which can detect not only capacitance of the actuated DE but also the series resistance of the electrode and the leakage current through the soft capacitor (Gisby

et al. 2011). The capacitive measurement was enabled by a pulse width modulation (PWM) which simultaneously generated a high voltage for actuation and an oscillation to sense the capacitance. As displayed in Fig. 22, the sensed actuation data matched well with that captured by a camera.

6.4 A Compression Sensing Mat

To increase the sensitivity of compression load, Böse and Fuß recently proposed a novel sensing mat structure (Böse and Fuß 2014). As schematically illustrated in Fig. 23, this sensor contains a wave profile made of thick elastomer film and a thin elastomer film sandwiched between compliant electrodes. When this structure is compressed, the thin elastomer film will be stretched by the profile, providing a change in the capacitance. Compared with conventional compression

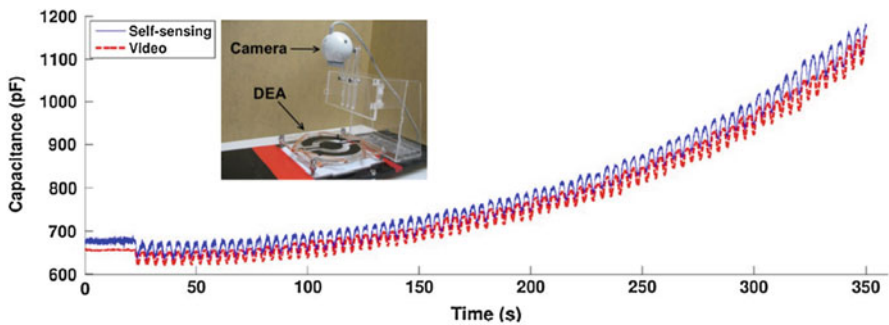


Fig. 22 The capacitance of a DEA as estimated by the self-sensing process and as estimated using video extensometry (Reproduced with permission from Gisby et al. 2011)

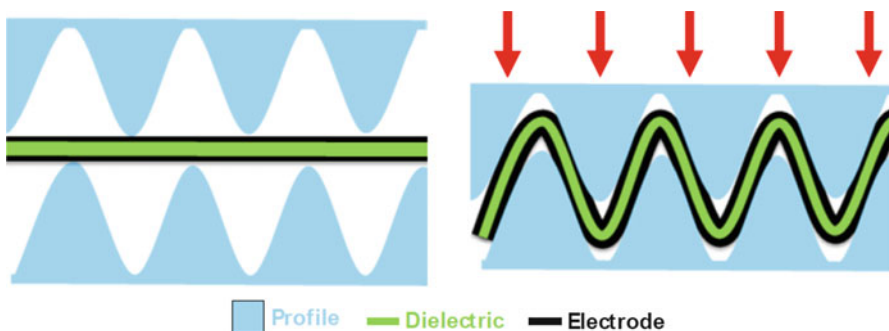


Fig. 23 Basic principle of the compression sensing mat. With a compression load, the dielectric elastomer film (*green*) is stretched by the profile (*blue*), giving a change in the capacitance (Figure courtesy from Dr. Holger Böse, ISC Fraunhofer, Germany)

sensors, the strain of the soft capacitor is enlarged thus a better sensitivity is achieved.

7 Energy Harvesting

A DE energy harvester or generator (DEG) works essentially in the reverse way of a DEA. In an operation cycle, a DEG is stretched in the in plane and charged. As the elastomer film is relaxed, the same charges will come closer while the opposite charges will be separated farther away (Fig. 24). Therefore, the electric energy in the system is increased and could be harvested (Brochu 2012).

Table 2 compares the characters of different electricity generation technologies, including two smart materials, DE, and piezoelectric ceramic and conventional electromagnetic generators. DEGs demonstrate great advantages in terms of mechanical compliancy, specific energy density, conversion efficiency, and cost. Additionally, DEGs are good for large linear motion compared to rotary motion

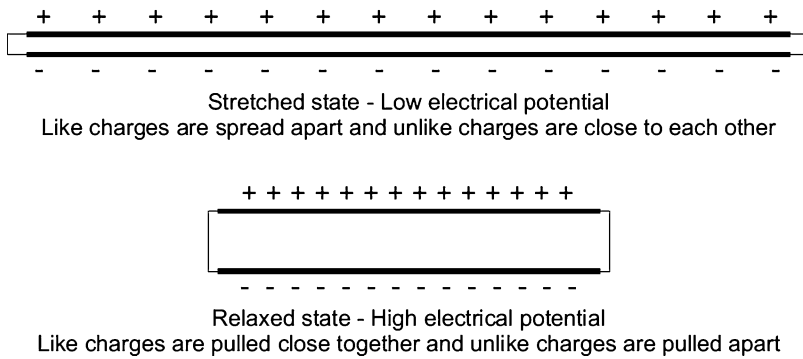


Fig. 24 Working principle of a DEG

Table 2 Comparison of generator technologies (Kornbluh et al. 2011, 2012)

Technology	DE	Piezoelectric ceramic	Electromagnetic
Stiffness	0.1–10 MPa	50–100 GPa	N/A
Specific energy density (J/g)	0.4 (0.05 for long lifetime operation)	0.01	0.004
Frequency range	0.1–100 Hz	10 Hz–1 kHz	100 Hz–10 kHz
Maximum efficiency	>50 %	>50 %	<20 %
Cost	Low	High	High
Device complexity	Low	Low	High
Reliability	Low	High	High

and low-frequency application in the range from 0.1 to 100 Hz, which are the typical motion frequencies in human and nature.

7.1 Operation Modes of a DEG

A DEG can be operated in three different modes: constant charge, constant voltage, and constant electric field as shown in Fig. 25.

In all the three modes, there are four steps in one operation cycle: (1) the DE film (**State 1**) is stretched mechanically with zero charge on it (to **State 2**); (2) charges are injected onto the film (to **State 3**); (3) the film is allowed to relax and either the charge amount, voltage, or electric field is kept constant (to **State 4**); and (4) charges are removed and the film is returned to zero charge and zero stretch states.

In a *Constant Charge* generation cycle, the charges are introduced after the film is stretched and kept constant. The electrical energy at any time after charging is given by the equation:

$$e = \frac{1}{2}CV^2 = \frac{1}{2}\frac{Q^2}{C} = \frac{1}{2}QV = \frac{1}{2}\frac{Q^2P}{\epsilon_r\epsilon_0A^2}$$

where Q is the charge amount on the electrodes, and P is the volume of the elastomer film, which equals $A \times z$ (area times thickness). The electrical energy produced per cycle (e_{gen}) is the difference between the electrical energies of the unstretched (mechanical relaxed) (e_u) and stretched (initially charged) (e_s) states:

$$e_{gen} = e_u - e_s = \frac{1}{2}\frac{Q^2P}{\epsilon_r\epsilon_0}\left(\frac{1}{A_u^2} - \frac{1}{A_s^2}\right) = \frac{1}{2}C_sV_b\left(\frac{C_s}{C_u} - 1\right)$$

where V_b is the bias voltage applied to the film in the stretched state. In a constant charge cycle, the energy output is strongly depending on the change in between the stretched and relaxed states and the bias voltage.

From the calculation, it is concluded that, in a constant charge mode, energy is generated through the increase in electrical potential of charges on film. We can also

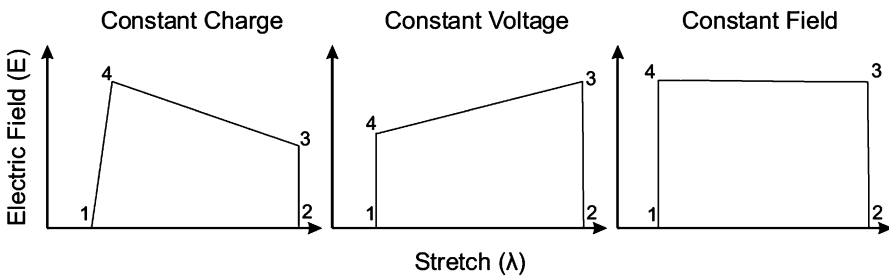


Fig. 25 Three operation modes of a DEG

conclude through similar calculation that energy is generated through the flow of charge onto and off the film in a constant voltage cycle, while in a constant electric field cycle, energy is generated by both the flow of charge onto and off the film and the increase in electrical potential of charges on the film.

7.2 A Heel-Strike Generator

Human's walking motion is a good source of energy for DEGs since it has low frequency and is naturally linear. A heel-strike generator would not add any physical burden to the wearer but provide energy which could charge small portable devices. Kornbluh et al. created a proof-of-principle generator using dielectric elastomers.

This device used a diaphragm structure with multilayer polymer elastomer as the active material. A displacement of 2–6 mm in one strike was enough to deform the elastomer films to more than 50 % area strain. This device produced an electrical energy output of 0.8 J/step or about 1 W. The output specific energy density of this device was 0.4 J/g (Kornbluh et al. 2012; Pelrine et al. 2001).

7.3 A Buoy Energy Generator

Another attractive application is buoy generators which use wave motion with low frequency and large amplitude as the mechanical energy to stretch DE films. Chiba et al. carried out ocean experiment using DEGs installed on a buoy in Tampa Bay, 1.6 km off the coast, a water depth of ~5 m.

The DEG was able to generate a peak power of 1.2 W and average power of 2.5 W at 10 cm wave height (Chiba et al. 2008, 2011). Other DEGs to utilize the energy of wave motion are being developed by SBM Offshore in Monaco (Czech et al. 2010) and PolyWEC in Spain (Moretti et al. 2014).

8 Other Important Applications

8.1 A Dielectric Elastomer Switch

Although dielectric elastomers function as different soft devices, the need of electronics brings non-compliance into the system. O'Brien et al. proposed a dielectric elastomer switch to address this problem. This switch took advantage of electrode piezoresistivity and underwent orders of magnitude changes in resistance when stretched. As shown in Fig. 26, the switch was combined with a DE actuator. When either DE element was activated, but not both, the strain applied to the switch was low, but the strain will increase when both the actuators were actuated. This caused the switch to conduct only when both actuators are active. When this switch was configured into a voltage divider circuit, it had the function of a NAND gate (O'Brien et al. 2010).

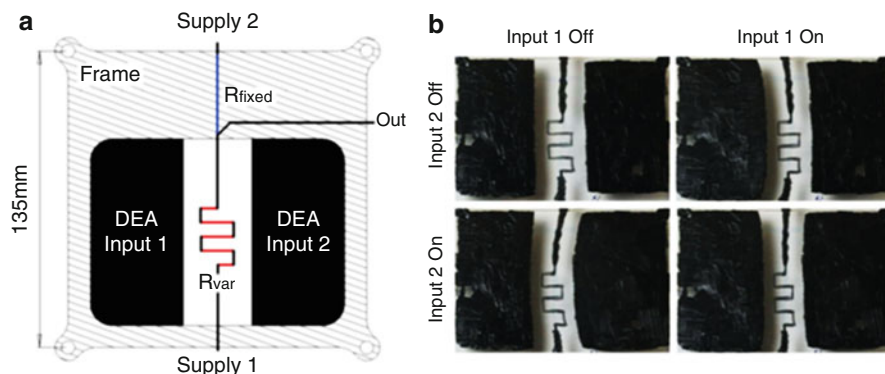


Fig. 26 (a) NAND gate design: the resistance of R_{var} will only drop below R_{fixed} when both inputs are charged. (b) DE NAND gate in action (Reproduced with permission from O'Brien et al. 2010)

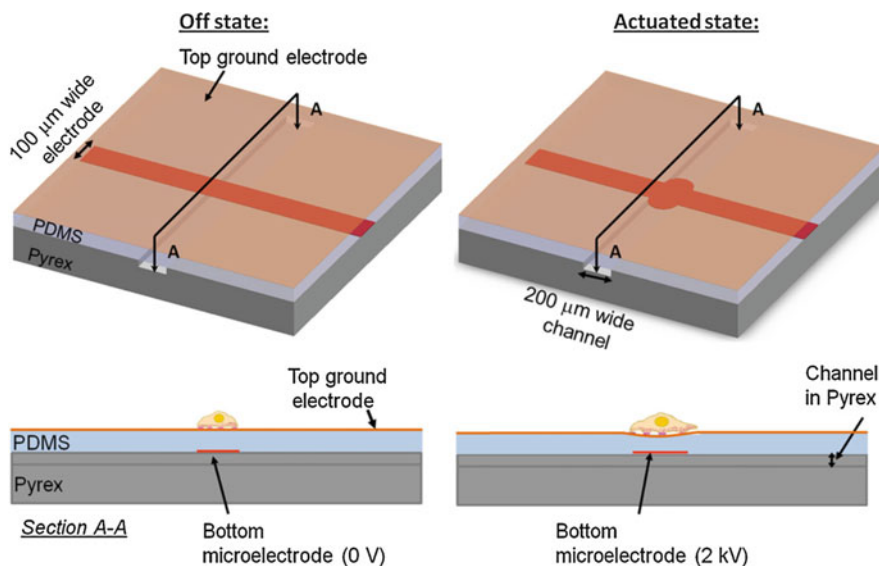


Fig. 27 Schematic of on cell stretcher (Reproduced with permission from Akbari and Shea 2012)

8.2 A Cell Stretcher

Cells' behaviors under mechanical strains have been of great interest, but conventional mechano-transduction is too large to monitor single cells. Akbari et al. fabricated DE into arrays of $100\ \mu\text{m}$ by $200\ \mu\text{m}$ sized actuators. These actuators will stretch uniaxially when voltages are applied and provide the stretching to cells (Akbari and Shea 2012) (See Fig. 27).

9 Conclusion and Remarks

A variety of applications of DEs have been reviewed covering a wide range of fields, including robotics, tactile displays, fluid control, sensors, and generators. While new design and applications are continuously being introduced, some of these application concepts are gradually being transitioned into commercial products. Examples include capacitive sensors for human motion measurement produced by the company StretchSense, laser speckle reducers produced by the company Optotune, and headphones being developed by the company Artificial Muscle Inc.

Whether many of the application ideas could end up in consumers' hands with mass production still hinges on key materials' issues, especially reliability, as fatigue during repeated large-strain deformation and stress concentration remains challenging in this field. Other challenges include high voltage circuit design, device integration, and safety concern. In a word, multidisciplinary collaboration is essential to push DE technology to a new stage.

References

- Akbari S, Shea H (2012) Microfabrication and characterization of an array of dielectric elastomer actuators generating uniaxial strain to stretch individual cells. *J Micromech Microeng* 22 (4):045020
- Anderson I, Gisby T, McKay T et al (2012) Multi-functional dielectric elastomer artificial muscles for soft and smart machines. *J Appl Phys* 112(4):041101
- Araromi O, Gavrillovich I, Shintake J et al (2015) Rollable multisegment dielectric elastomer minimum energy structures for a deployable microsatellite gripper. *IEEE/ASME Trans Mechatron* 20(1):438–446
- Benslimane M, Gravensen P, Sommer-Larsen P (2002) Mechanical properties of dielectric elastomer actuators with smart metallic compliant electrodes. *Proc SPIE* 4695:150–157
- Biggs J, Srinivasan M (2002a) Haptic interfaces. In: Hale K, Stanney K (eds) *Handbook of virtual environments*. Lawrence Erlbaum Associates, London, pp 93–116
- Biggs J, Srinivasan M (2002b) Tangential versus normal displacements of skin: relative effectiveness for producing tactile sensations. In: *Proceedings of 10th symposium on haptic interfaces virtual environ teleoperator systems HAPTICS*, Orlando, pp 121–128
- Böse H, Fuß E (2014) Novel dielectric elastomer sensors for compression load detection. *Proc SPIE* 9056:905614
- Brochu P (2012) *Dielectric elastomers for actuation and energy harvesting*. University of California, Los Angeles
- Brochu P, Pei Q (2010) Advances in dielectric elastomers for actuators and artificial muscles. *Macromol Rapid Commun* 31(1):325–329
- Carpi F, Frediani G, De Rossi D (2010) Hydrostatically coupled dielectric elastomer actuators. *IEEE/ASME Trans Mechatron* 15(2):308–315
- Carpi F, Frediani G, De Rossi D (2011a) Opportunities of hydrostatically coupled dielectric elastomer actuators for haptic interfaces. *Proc SPIE* 7976:797618
- Carpi F, Frediani G, Turco S et al (2011b) Bioinspired tuneable lens with muscle like electroactive elastomers. *Adv Funct Mater* 21(21):4152–4158
- Chakraborti P, Toprakci H, Yang P et al (2012) A compact dielectric elastomer tubular actuator for refreshable Braille displays. *Sensors Actuators A Phys* 179:151–157
- Chen B, Lu J, Yang C et al (2014) Highly stretchable and transparent ionogels as nonvolatile conductors for dielectric elastomer transducers. *ACS Appl Mater Interfaces* 6(10):7840–7845

- Chiba S, Waki M, Kornbluh R et al (2008) Innovative power generators for energy harvesting using electroactive polymer artificial muscles. *Proc SPIE* 6927:692715
- Chiba S, Waki M, Kornbluh R et al (2011) Current status and future prospects of power generators using dielectric elastomers. *Smart Mater Struct* 20(12):124006
- Choi H, Kim D, Vuong N et al (2009) Development of integrated tactile display devices. *Proc SPIE* 7287:72871C
- Czech B, van Kessel R, Bauer P et al (2010) Energy harvesting using dielectric elastomers. In: *Proceedings of 14th international power electron motion control conference EPE-PEMC*, Ohrid, S4, pp 18–23
- Eckerle J, Stanford S, Marlow J et al (2001) A biologically inspired hexapedal robot using field-effect electroactive elastomer artificial muscles. *Proc SPIE* 4332:269–280
- Gebbers P, Grätzel C, Maffli L et al (2012) Zipping it up: DEAs independent of the elastomer's electric breakdown field. *Proc SPIE* 8340:83402P
- Gisby T, O'Brien B, Xie S et al (2011) Closed loop control of dielectric elastomer actuators. *Proc SPIE* 7976:797620
- Jordi C, Michel S, Fink E (2010) Fish-like propulsion of an airship with planar membrane dielectric elastomer actuators. *Bioinspir Biomim* 5(2):026007
- Knoop L, Rossiter J (2014) Towards shear tactile displays with DEAs. *Proc SPIE* 9056:905610
- Kofod G, Paajanen M, Bauer S (2006) Self-organized minimum-energy structures for dielectric elastomer actuators. *Appl Phys A* 85(2):141–143
- Koo I, Jung K, Koo J et al (2008) Development of soft-actuator-based wearable tactile display. *IEEE Trans Robot* 24(3):549–558
- Kornbluh R, Pelrine R, Prahlah H et al (2011) From boots to buoys: promises and challenges of dielectric elastomer energy harvesting. *Proc SPIE* 7976:797605
- Kornbluh R, Pelrine R, Prahlah H et al (2012) Dielectric elastomers: stretching the capabilities of energy harvesting. *MRS Bull* 37(03):246–253
- Lau G, Lim H, Teo J et al (2014) Lightweight mechanical amplifiers for rolled dielectric elastomer actuators and their integration with bio-inspired wing flappers. *Smart Mater Struct* 23(2):025021
- Lee H, Phung H, Lee D (2014) Design analysis and fabrication of arrayed tactile display based on dielectric elastomer actuator. *Sensors Actuators A Phys* 205:191–198
- Liang D, Lin Z-F, Huang C-C et al (2014) Tunable lens driven by dielectric elastomer actuator with ionic electrodes. *Micro Nano Lett* 9(12):869–873
- Maffli L, O'Brien B, Rosset S et al (2012) Pump it up. *Proc SPIE* 8340:83492G
- Maffli L, Rosset S, Shea H et al (2013a) Mm-size bistable zipping dielectric elastomer actuators for integrated microfluidics. *Proc SPIE* 8687:86872M
- Maffli L, Rosset S, Shea H (2013b) Zipping dielectric elastomer actuators: characterization, design and modeling. *Smart Mater Struct* 22(10):104013
- Maffli L, Rosset S, Ghilardi M, Carpi F, Shea H (2015) Ultrafast all polymer electrically tunable silicone lenses. *Adv Funct Mater* 25(11):1656–1665
- Matysek M, Lotz P, Winterstein T et al (2009) Dielectric elastomer actuators for tactile display. In: *IEEE EuroHaptics conference and symposium on haptic interfaces for virtual environment and teleoperator systems 3rd joint*. Salt Lake City, pp 290–295
- McCoul D, Murray C, Di Carlo D et al (2013) Dielectric elastomer actuators for active microfluidic control. *Proc SPIE* 8687:86872G
- Moretti G, Fontana M, Vertechy R (2014) Parallelogram-shaped dielectric elastomer generators: analytical model and experimental validation. *J Intell Mater Syst Struct* 26(6):740–751
- Möbinger H, Haus H, Kauer M et al (2014) Tactile feedback to the palm using arbitrarily shaped DEA. *Proc SPIE* 9056:90563C
- Murray C, McCoul D, Sollier E et al (2013) Electro-adaptive microfluidics for active tuning of channel geometry using polymer actuators. *Microfluid Nanofluid* 14(1–2):345–358
- Nguyen C, Phung H, Nguyen T et al (2014) A small biomimetic quadruped robot driven by multistacked dielectric elastomer actuators. *Smart Mater Struct* 23(6):065005

- Niklaus M, Rosset S, Shea H (2010) Array of lenses with individually tunable focal-length based on transparent ion-implanted EAPs. *Proc SPIE* 7642:76422K
- O'Brien B, Calius E, Inamura T et al (2010) Dielectric elastomer switches for smart artificial muscles. *Appl Phys A* 100(2):385–389
- Optotune AG (2015) Available on www.optotune.com. Accessed 25 May 2015
- Pei Q, Pelrine R, Stanford S et al (2002) Multifunctional electroelastomer rolls and their application for biomimetic walking robots. *Proc SPIE* 4698:246–253
- Pei Q, Rosenthal M, Stanford S et al (2004) Multiple-degrees-of-freedom electroelastomer roll actuators. *Smart Mater Struct* 13(5):N86–N92
- Pelrine R, Kornbluh R, Eckerle J et al (2001) Dielectric elastomers: generator mode fundamentals and applications. *Proc SPIE* 4329:148–156
- Pelrine R, Kornbluh R, Pei Q et al (2002) Dielectric elastomer artificial muscle actuators: toward biomimetic motion. *Proc SPIE* 4695:126–137
- Prahlad H, Pelrine R, Kornbluh R et al (2005) Programmable surface deformation: thickness-mode electroactive polymer actuators and their applications. *Proc SPIE* 5759:102–113
- Price A, Culbertson C (2009) Generation of nonbiased hydrodynamic injections on microfluidic devices using integrated dielectric elastomer actuators. *Anal Chem* 81(21):8942–8948
- Rosenthal M, Bonwit N, Duncheon C et al (2007) Applications of dielectric elastomer EPAM sensors. *Proc SPIE* 6524:65241F
- Shian S, Diebold R, Clarke D (2013) Tunable lenses using transparent dielectric elastomer actuators. *Opt Express* 21:8669–8676
- Son S, Goulbourne N (2010) Dynamic response of tubular dielectric elastomer transducers. *Int J Solids Struct* 47(20):2672–2679
- Son S, Pugal D, Hwang T et al (2012) Electromechanically driven variable-focus lens based on transparent dielectric elastomer. *Appl Opt* 51:2987–2996
- Wei K, Domicone N, Zhao Y (2014) Electroactive liquid lens driven by an annular membrane. *Opt Lett* 39:1318–1321
- Yu Z, Yuan W, Brochu P et al (2009) Large-strain, rigid-to-rigid deformation of bistable electroactive polymers. *Appl Phys Lett* 95(19):192904
- Yun S, Park S, Park B et al (2014) Polymer-based flexible visuo-haptic display. *IEEE/ASME Trans Mechatron* 19(4):1463–1469

Herbert Shea, Soo Jin Adrian Koh, Ingrid Graz, and Jun Shintake

Contents

1	Introduction	768
2	Membrane Materials	769
3	Actuators	770
3.1	Expanding Circle	771
3.2	Minimum Energy Structure	772
3.3	kV DEA Drive Circuit	773
4	Energy Harvesters	773
4.1	Principle of Operation	773
4.2	Cycle of Operation and Harvesting Circuit Design	777
4.3	Characterizing the Performance of DE Energy Harvesters	779
4.4	Collecting Data and Analysis of Results	782
4.5	Direct Demonstration of Energy Harvesting	784
	References	786

H. Shea (✉)

LMTS: Microsystems For Space Technologies Lab, EPFL, Neuchatel, Switzerland

e-mail: herbert.shea@epfl.ch

S.J.A. Koh

Department of Mechanical Engineering, National University of Singapore, Singapore, Singapore

e-mail: adrian_koh@nus.edu.sg

I. Graz

Soft Matter Physics, Johannes Kepler University Linz, Linz, Austria

e-mail: Ingrid.graz@jku.at

J. Shintake

LIS: Laboratory of Intelligent Systems, EPFL, Lausanne, Switzerland

e-mail: jun.shintake@epfl.ch

Abstract

As can be seen from the large number of videos of home-made dielectric elastomer actuators (DEAs) on YouTube, getting started making DEAs is straightforward and can be done at low cost. This chapter provides information on making two types of basic dielectric elastomer actuators, as well as detailed information on using DE for energy harvesting (converting mechanical energy into electrical energy).

A word of caution about high voltages: Voltages of several thousand volts are required to operate DEAs. The user must therefore exercise caution to avoid electrocution or electrical fires. In addition to taking steps to limit the current delivered by the power supply in the event of a short circuit or of accidental contact, one must also keep in mind that a DEA is a large capacitor capable of storing very large electrical charge, which means that even a “human-safe” current-limited power supply can expose the user to lethal shocks. Arcing in air can easily occur, and short-circuits through the thin membrane are common, linking the high-voltage side to the low-voltage side. Do not use high-voltage circuits unless you have appropriate safety training and experience, as they can be dangerous.

Keywords

Dielectric Elastomer Actuator (DEA) • Dielectric Elastomer Generator (DEG) • silicone membrane • Compliant electrodes • VHB • Dielectric Elastomer Minimum Energy Structure (DEMES)

1 Introduction

Simple dielectric elastomer actuators can readily be made in an afternoon with basic tools and from low-cost materials that can all easily be ordered online. Many examples of simple actuators with instructions can be found on YouTube (simply search for “dielectric elastomer actuator”). The “Soft Robotics Toolkit” website (<http://softroboticstoolkit.com/book/dielectric-elastomer-actuators>) provides detailed steps with clear images and complete list of all required items. For more detailed process based on silicone membranes, see Rosset et al. (2015).

Making a “high-performance” DEA requires more attention to design and materials, but the focus of this chapter is on allowing newcomers to the field to start fabricating and testing devices. The chapter covers basic fabrication of two types of DE actuators, as well as a detailed primer on using DE for energy harvesting. The reader can thus start exploiting different facets of dielectric elastomer transducers: actuations, energy harvesting, and sensing.

A basic actuator/harvester/sensor consists of at least electrical contacts, elastomer membrane, and stretchable electrodes. In addition, nearly all actuators also have a rigid frame to hold a prestretch.

2 Membrane Materials

Different dielectric elastomers used in DEAs have been described in a previous chapter of this book. By far, the most widespread dielectric material for simple experimentation is the acrylic elastomer VHB™ made by 3M, which is sold as industrial adhesive (it was not designed for DEAs but rather for fixing objects on walls). VHB™ allows for large actuation strain in DEA configuration and can be easily obtained. VHB™ tapes type 4905 and 4910 are 500 μm and 1 mm thick and can be ordered in many different widths (Fig. 1).

Silicone membranes allow for faster DEA devices with less viscous effects, but are not as widely available as thin membranes, and must rather be cast or spin coated. This allows greater control over thickness and materials but is much less convenient for quick experimentation. A method for casting silicone membranes is given by Araromi et al. (2015) and Maffi et al. (2013). For those wishing to use silicone without having to cast films, Wacker Chemie sells rolls of 5–50 μm thick silicone films under the trade name Elastosil 2030. Parker also commercializes a thin elastomer film for EAPs, available on Amazon. For energy harvesting applications, natural rubber can be an interesting material (Kaltseis et al. 2014) and can easily be purchased in long rolls (Fig. 2).

For a number of reasons presented in previous chapters of this book, the elastomer film is often prestretched, and a rigid frame is therefore needed to maintain the pretstretch. VHB™ is often highly prestretched (typically 9x to 25x increase in area), which can be done manually for simple devices, or with dedicated equipment for larger systems (see Schausberger et al. (2015) for an elegant and low-cost stretching tool). VHB has the practical advantage of being very sticky (since designed as an adhesive), which makes it very easy to attach to a frame simply by pressing it onto a smooth surface. It also makes it possible to use carbon powder as compliant electrodes as the powder adheres to the VHB.

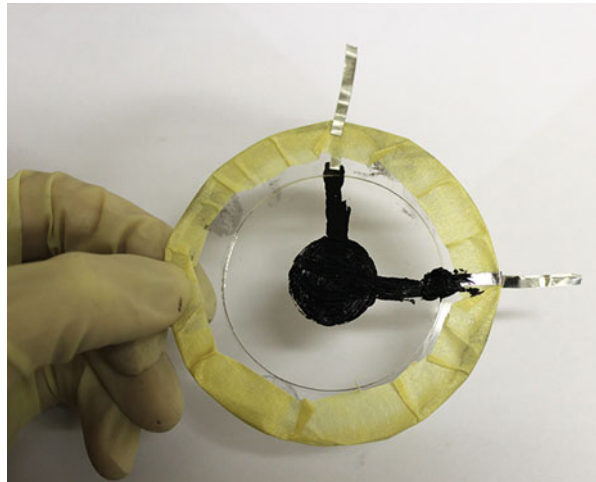
Fig. 1 3M VHB™ tape: a commonly used dielectric for DEAs (the tape is transparent, the backing is red)



Fig. 2 Oppo Band natural rubber



Fig. 3 Expanding circle actuator of carbon grease electrodes on VHB acrylic (Courtesy J. Shintake and B. Schubert)

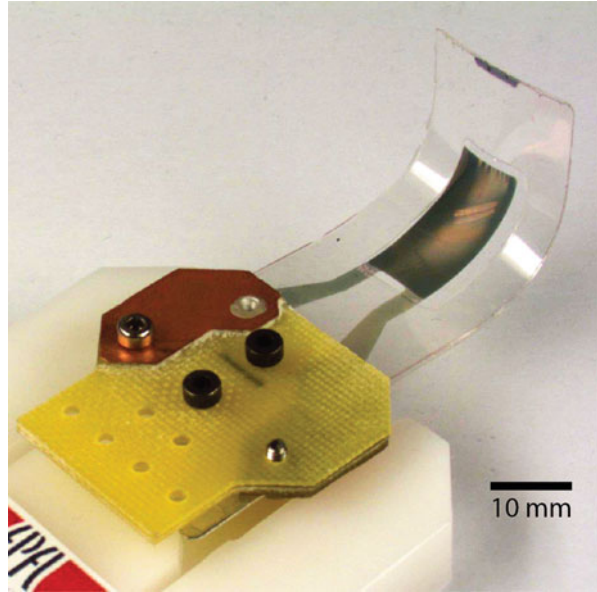


3 Actuators

We describe in this chapter two simple devices: (a) the expanding circle actuator and (b) a curling “minimum energy structure” (illustrated in Figs. 3 and 4).

The “classic” expanding circle device, as used in the landmark paper by Pelrine et al. (2000) and shown in Fig. 3, is one of the easiest devices to make and provides a

Fig. 4 DEMES devices, which uncurls when a voltage is applied. Details on process in Shintake et al. (2013) and in Araromi et al. (2015)



dramatic display of the large-area strain possible with DEAs. With minor geometrical variations, it can be used to drive in-plane motion, for instance, for tunable gratings (Rosset et al. 2013) or, when exciting out-of-plane modes, also loudspeakers (Keplinger et al. 2013).

3.1 Expanding Circle

The steps to make expanding circle DEA devices are well described in several websites including the informative and detailed Soft Robotics Toolkit site <http://softroboticstoolkit.com/book/dea-fabrication>. There are three key steps:

- Stretch the elastomer membrane on a frame
- Apply the compliant electrodes on both sides
- Make electrical contact with metal tape to the carbon electrodes

PMMA (plexiglass) is a convenient transparent frame material, but any smooth and easily machined holder will do. It is highly preferred to use an insulator for the frame, due to the high-voltage contacts to the electrodes that are supported by the frame.

Compliant electrodes for DEAs have been discussed in a previous chapter of this book. Carbon grease allows for the quickest experimentation. Commonly used conductive greases include MG Chemicals Carbon Conductive Grease 846-80G and Nyogel 755G from Nye Lubricants. Be careful to avoid damaging the membrane when applying with a paintbrush or color shaper. A stencil can make accurate

patterning easier. Compliant electrodes can also be made by mixing carbon black with silicones, as summarized by Rosset (Rosset and Shea 2012).

A difficult practical point is reliably electrically contacting the compliant electrodes. This is commonly done with strips of copper or aluminum tape that are glued to the frame and onto which the grease is painted. More elegant solution using printed circuit boards are preferred for longer-term operation.

Applying a voltage between the electrodes leads to an increase in area of the circle. The maximum field depends on the membrane material, prestretch, and defects but can be up to $200 \text{ V}/\mu\text{m}$ (i.e., up to of order 10 kV for a 0.5 mm thick VHB film prestretched 3x on both axis).

3.2 Minimum Energy Structure

Dielectric elastomer minimum energy structure (DEMES) was introduced by Kofod et al. (2007) and the principle is illustrated in Fig. 5. A prestretched DEA is attached to a flexible (but not stretchable!) flat frame, such as sheet of PET. When released, the assembly bends due to the partial contraction of the DEA. Applying a voltage causes the DEA to expand, relieving some of the strain, bringing the device closer to the initial flat shape of the frame. Complex shapes can be realized (Petralia and Wood 2010) and large bending motion achieved (Araromi et al. 2015).

The DEMES devices are slightly more complex to make than expanding circle devices, as there is the additional step of bonding a flexible frame to the DEA and then typically a cutting step to release the complete device.

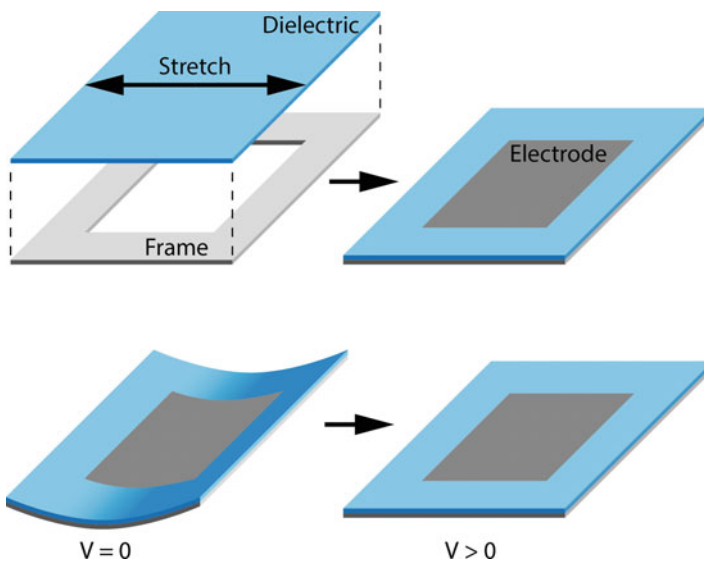


Fig. 5 DEMES principle of operation: a prestretched DEA is bonded to a flexible frame. The tension in the DEA leads to a curled-up shape, which can be uncurled by applying a drive voltage to the DEA

The steps to fabricate the DEMES device used student practical sessions at Johannes Kepler University in Linz are illustrated in Fig. 6. Two thicknesses of bending frame are used to define a “hinge” and a more solid region. The recommended elastomer is VHB4905, the thin PET is an overhead transparency sheet (100 μm thick), and the thick PET is 220 μm thick.

3.3 kV DEA Drive Circuit

To apply a DC voltage of several kV, the simplest but most expensive solution is to use a commercial high-voltage power supply, such as Stanford Research System PS350, which gives a very stable and computer-controlled output voltage with user-selectable compliance current. If AC actuation is desired (e.g., for a loudspeaker or for vibration damping), high-voltage amplifiers such as those made by Trek (http://www.trekinc.com/products/HV_Amp.asp) allow operation at several kV up to several kHz.

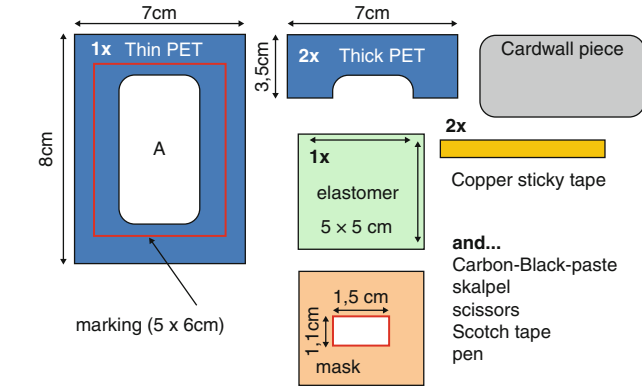
Since the DEAs require only a very low current, many labs fabricate their own high-voltage power supplies based on commercially available compact proportional DC–DC converters, such as those from EMCO High Voltage (www.emcohighvoltage.com) or from American High Voltage (www.ahv.com). They are available in many voltage and power levels. Lower power devices are cheaper and slightly safer but take longer to charge the DEA.

To determine the maximum output current needed (in practice one selects the power rating once the operating voltage is determined) from the DC–DC converter, one should consider the total charge Q that is to be placed on the electrodes. We know $Q = CV$, where $C = \epsilon\epsilon_0 \frac{A}{d}$ is the capacitance of the DEA device of area A and thickness d and V the operating voltage. But we also know that $Q = \int Idt \approx I(\Delta t)$, where I is the charging current and Δt the charging time. So $I = \epsilon\epsilon_0 \frac{AV}{d} \frac{1}{\Delta t}$ to a reasonable approximation (ignoring, for instance, the change in thickness during actuation and the RC time constant of the device due to the finite resistance of the electrodes). Typically charging currents of hundreds of μA are amply sufficient unless very fast motion is needed or if one is driving very large devices, so one can generally use the lowest-power DC–DC converter available (Fig. 7).

4 Energy Harvesters

4.1 Principle of Operation

A dielectric elastomer (DE) is stretchable. Mechanical stretch alters its capacitance. For a DE that is electrically charged, varying its mechanical state changes its corresponding electrical state. In this sense, the DE functions like a sensor. However, due to the ability of a DE to store a large amount of mechanical energy and electrical charge, changes in electrical state as a result of mechanical stimulus is capable of



Parts list for making DEMES

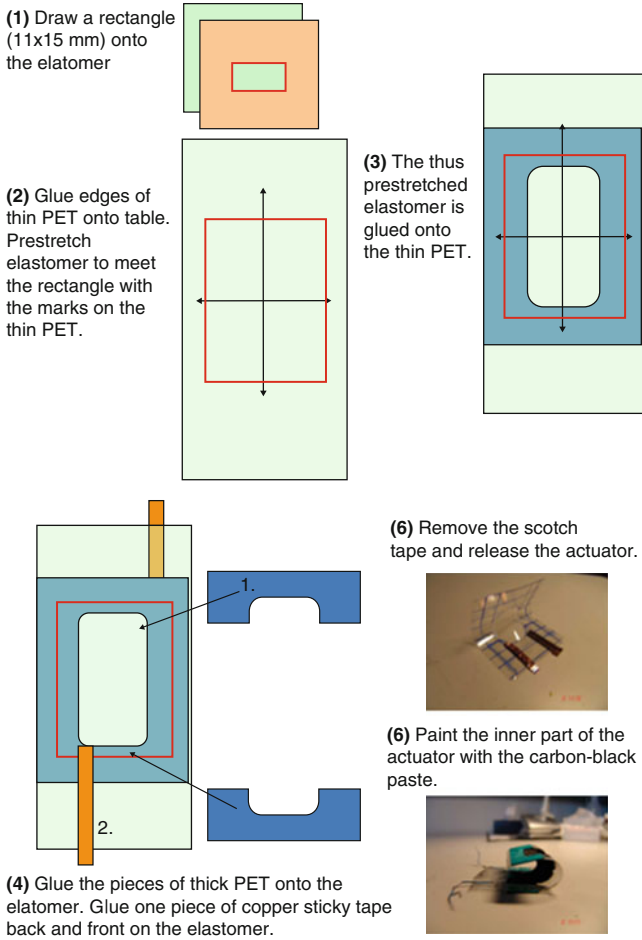


Fig. 6 DEMES fabrication steps (as used at the Johannes Kepler University)

Fig. 7 Two high-voltage DC-DC converters from EMCO High Voltage (Courtesy S. Schlatter)

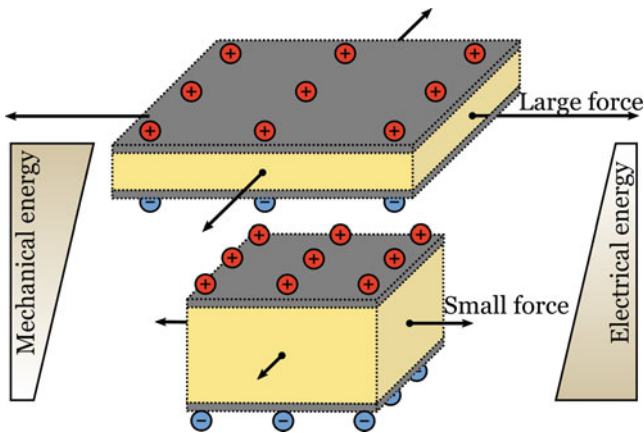
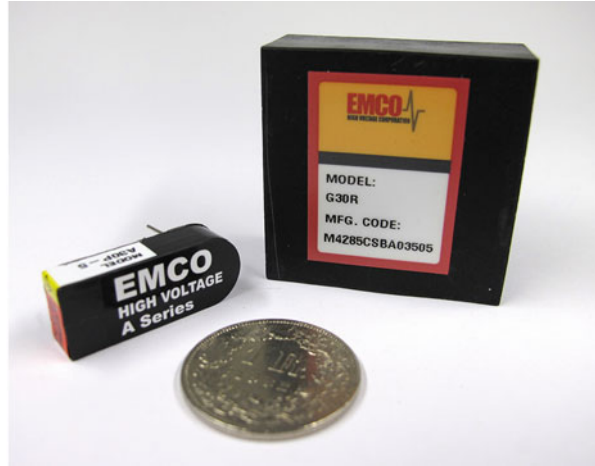


Fig. 8 Operating principle of a dielectric elastomer generator (Reproduced with permission from Kaltseis et al. (2014). Copyright 2014, RSC Publications)

delivering electrical output large enough to power small- to medium-sized electrical loads (Peltine et al. 2001). Hence, a DE also functions as a soft and stretchable generator.

Consider a rectangular DE membrane, with unstretched planar dimensions L_1 and L_2 and thickness H . H is small, compared with L_1 and L_2 . The DE may be stretched in its plane, increasing its planar dimensions. One may define the ratio between the stretched lengths (l_1, l_2) and the unstretched lengths (L_1, L_2) as $\lambda_1 = l_1/L_1$ and $\lambda_2 = l_2/L_2$. Assuming that the DE is incompressible, simple calculations will show that the capacitance change of a DE scales with the in-plane stretches λ_1 and λ_2 as $\lambda_1^2 \lambda_2^2$. Mechanical stretching hence increases the capacitance, thereby enabling the DE to store more electrical charges at its stretched state (Fig. 8, top schematic).

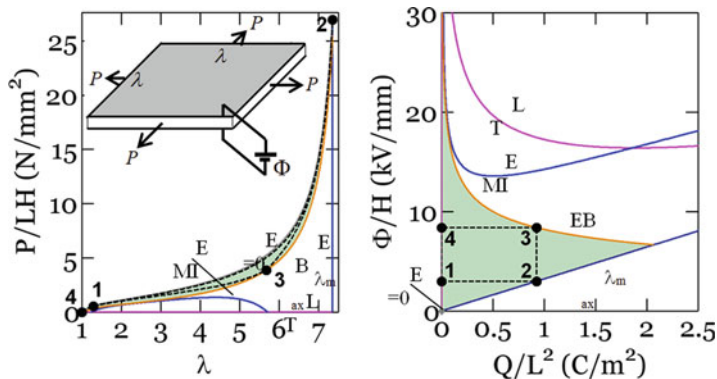


Fig. 9 Operating maps of allowable states and adaptation of a cycle on map

When the mechanical stretch is removed, for example, in an open-circuit condition, the voltage between the electrodes will increase (Fig. 8, bottom schematic). This higher voltage allows charges to be delivered to power an electrical load. In essence, a DE functions like a charge pump, transferring electrical charges from a low-electrical potential to a high-electrical potential, when it is mechanically stretched and relaxed (Kaltseis et al. 2014).

To design an operating cycle that gives a maximum possible output, we plot a map of allowable states that denotes the operating limits (Fig. 9) of a DE (Koh et al. 2009). These operating limits combine to give an operating cycle that delivers the maximum possible amount of energy (Shian et al. 2014). To construct these limits, we ask: How does a DE fail?

A DE may fail in various ways. One may draw these limits on work-conjugate planes, so as to facilitate direct calculation of energy. These limits also combine to create a map of allowable states of operation (Fig. 9). This map may then be used to design operating cycles that fit within the map of allowable states, and hence, optimize the output of the cycle (for example, cycle **1234** in Fig. 9). We illustrate the construction of such a map based on the following operating limits: mechanical rupture as denoted by the maximum stretch (λ_{max}), electrical breakdown (EB) of the dielectric, loss of tension (LT), electromechanical instability (EMI), and zero electric field ($E = 0$). The first two limits (λ_{max} and EB) denote structural failure of the DE, which renders the DE inoperable. The next two (LT and EMI) denote limits that may or may not lead to structural failure but to be avoided to retain optimal performance of the DE. Zero electric field ($E = 0$) is an essential condition for a nonpolar dielectric. For more details on the construction of operating maps, please refer to Koh et al. (2009, 2010).

Figure 9 illustrates an example of an operating map. The elastomer is modeled using the Gent material model (Gent 1996). It is assumed to be a linear dielectric and is an ideal dielectric with dielectric constant that is independent of stretch. The small-strain shear modulus is $\mu = 5.0$ MPa, limiting stretch parameter of $J_{lim} = 125$, dielectric breakdown strength $E_{EB} = 200$ MV/m, and dielectric constant of $\epsilon_r = 10$.

Work-conjugates plotted were force (P) versus stretch (λ), and voltage (Φ) versus charge (Q). The work-conjugate quantities of P , Φ , and Q were normalized with the undeformed elastomer dimensions of length (L) and thickness (H). The applied mechanical stretch is equally biaxial on the plane of the elastomer membrane.

4.2 Cycle of Operation and Harvesting Circuit Design

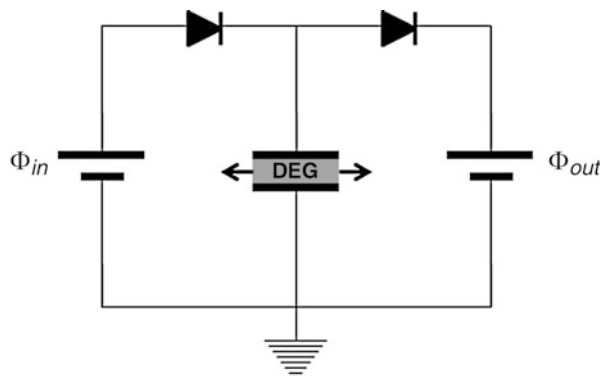
We fit a cycle of operation **1234** onto the map as shown in Fig. 9. This is a circuit that toggles between a constant input voltage (low voltage) along $1 \rightarrow 2$ and a constant output voltage (high voltage) along $3 \rightarrow 4$, while the DE membrane is cyclically stretched ($4 \rightarrow 1 \rightarrow 2$) and relaxed ($2 \rightarrow 3 \rightarrow 4$). This cycle circumscribes a rectangle on the voltage (Φ) versus charge (Q) work-conjugate plane, reminiscent to that of a thermodynamic Carnot cycle.

The basic components of a DE harvesting circuit for the above cycle consist of an input electric source (Φ_{in}), a dielectric elastomer generator (DEG), and an electrical load or storage device (Φ_{out}) to receive the output power (Fig. 10).

We present a circuit that consists of two capacitors with very large capacitances as input and output reservoirs, compared with the capacitance of the DE (Kaltseis et al. 2011; 2014). This circuit bears a complete resemblance with Fig. 10, except that Φ_{in} and Φ_{out} are capacitor reservoirs. This circuit allows the energy flows into and out of the DEG to be tracked, and thereby enabling the performance of the DEG to be quantified. The input and output capacitors are first charged to Φ_{in} (low voltage) and Φ_{out} (high voltage), respectively. The flow of current into and out of the DE is governed by the forward diodes and the relative potential differences between the DEG and the input/output reservoirs (Fig. 10).

This circuit works as follows: At the uncharged state, the DEG draws charges from capacitor Φ_{in} . This is because the voltage across the DEG is lower than that of Φ_{in} . However, no charges will be flowing from capacitor Φ_{out} into the DEG, due to the forward diode. Once the voltage of the DE equilibrates with Φ_{in} , the DEG is stretched. The change in capacitance of the DEG by mechanical stretch

Fig. 10 Basic components of a DE energy harvesting circuit



instantaneously lowers its voltage but is also instantaneously replenished by charges from Φ_{in} , keeping the voltage in quasi-static equilibrium between Φ_{in} and the DEG. When the DEG reaches its maximum stretch, relaxation of the DEG will lead to a boost in voltage across the DEG. This happens because at commencement of relaxation, the voltage across the DEG becomes larger than Φ_{in} ; no current will flow back to Φ_{in} due to the forward diode. Further, no current will flow to Φ_{out} , as the voltage at the start of relaxation is still lower than Φ_{out} . This makes the relaxation of the DEG to be in an “open-circuit” condition, which allows the DEG to boost its voltage with no charge inflow/outflow. This will continue until the voltage across the DEG reaches Φ_{out} . Once that happens, further relaxation will push charges to flow to Φ_{out} . Continual relaxation of the DE allows the voltage across the DEG to be held in quasi-static equilibrium with Φ_{out} . When the DEG reaches a prescribed minimum stretch, the cycle repeats.

One disadvantage of this circuit is the voltage across the input and output capacitor (Φ_{in} and Φ_{out}) cannot be directly measured. As the cycles progress, the input reservoir gets progressively discharged, while the output reservoir gets progressively charged. The rate of charge/discharge follows a time-scale determined by the resistive–capacitive (RC) time constant of the capacitors. The drift in voltage due to discharge/charge cannot be directly measured. Since the voltage across the DEG is inferred from Φ_{in} and Φ_{out} , the circuit may need to be recalibrated once the shift in Φ_{in} and Φ_{out} becomes too significant.

To ensure delivery of charges at stable voltages, one may consult an alternative proposed by Huang et al. (2013). A schematic of the circuit is shown in Fig. 11.

This circuit consists of two parts: the harvesting circuit (H) and the probing circuits (P). The harvesting circuit consists of the input power that primes the DEG (Φ_L), the DEG, and an output circuit that consists of a drain resistor (R_2), coupled with a reverse Zener diode (D_2) of rating Φ_H , which corresponds to the prescribed output voltage Φ_{out} . The probing circuits measure the charging current to the DEG

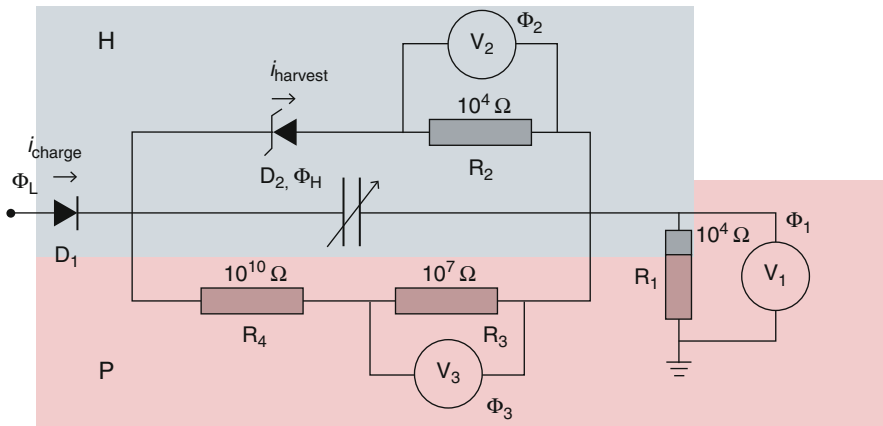


Fig. 11 Energy harvesting circuit that enables voltage across DEG to be tracked

(V_1 , R_1 , and Φ_1), and the voltage across the DEG (V_3 , R_3 and Φ_3), through the potential divider (R_3 and R_4). This circuit is relatively more complex than the two-capacitor circuit described above, but it enables delivery of charges at steady voltages and also allows the voltage across the DEG to be directly measured.

For this section on energy harvesting, we shall only describe an experiment conducted with the two-capacitor circuit. This circuit is simple enough for a beginner to perform a quick experiment. For readers keen to perform experiments using the latter circuit or others, please consult other existing literature (Huang et al. 2013; Graf and Maas 2011; McKay et al. 2010).

4.3 Characterizing the Performance of DE Energy Harvesters

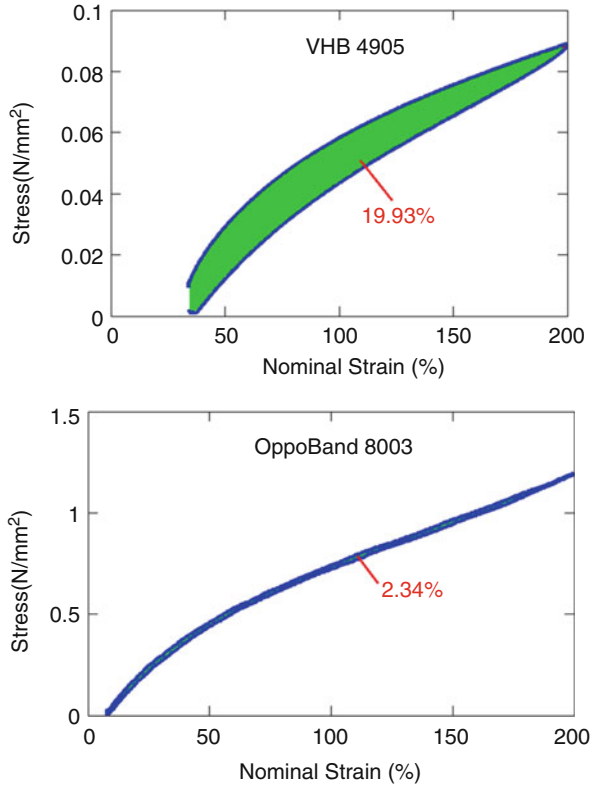
To conduct an energy harvesting experiment that characterizes the performance of a DEG, the following items are required:

- (a) Dielectric elastomer (DE)
- (b) Mechanical excitation source
- (c) Input electrical source
- (d) Output reservoir
- (e) Voltmeters and pressure/load sensors
- (f) Diodes and resistors
- (g) Data acquisition systems
- (h) Input and output display (may be optional)

Choices on the dielectric vary. As mentioned earlier in this chapter, commonly studied dielectrics include acrylic-based polymers (VHB), silicone rubber, and natural rubber. We propose a quick way to appraise the performance of a dielectric as an energy harvester, by means of a hysteresis test. As an example, we present an experiment conducted on two classes of dielectrics: acrylic VHB polymer and natural rubber. VHB acrylic-based polymer is known to be highly viscous. Natural rubber, on the other hand, is highly elastic over a range of mechanical strains beyond 400 %. We select an over-the-counter therapeutic medical band as an object of investigation (Fig. 2). This medical band is used for physiotherapy exercises, and hence, its mechanical durability is assured.

A hysteresis test subjects a sample to a cyclic, constant strain-rate stress–strain test. A sample is stretched and relaxed at constant strain rate, up to a prescribed maximum stretch. This maximum stretch is measured against the undeformed, initial length of the specimen, termed the nominal stretch/strain. In general, the stress–strain response during stretching is not perfectly coincident with that during relaxation. The resulting loop circumscribed by a cycle of stretching and relaxation gives the hysteresis loop. The area bounded by this loop quantifies the amount of mechanical energy dissipated as heat during a cycle of operation. This energy is irrecoverable and will not participate in the energy harvesting process. Hence, one may desire a material with a small hysteresis loop for energy harvesting.

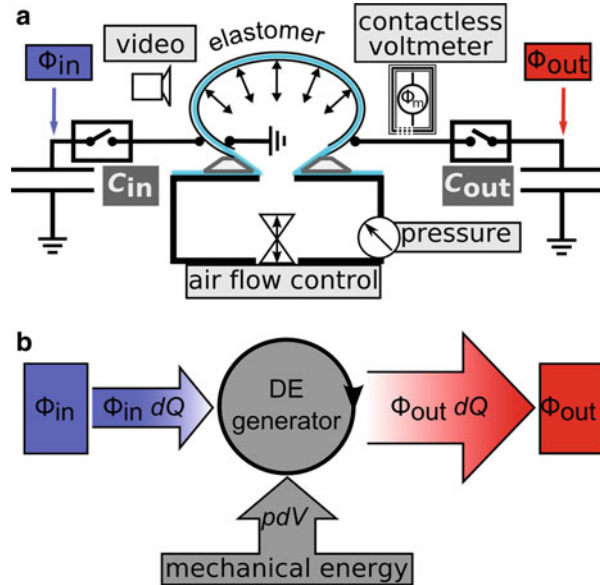
Fig. 12 Hysteresis test on a VHB acrylic elastomer and natural rubber



We perform the hysteresis test on a Zwick Universal Testing Machine (UTM). The elastomer underwent 100 cycles of testing, with a nominal strain amplitude of 200 % (maximum stretch = 3.0). The applied strain rate was 100 % per second. Figure 12 compares the hysteresis loops for acrylic-based VHB and natural rubber (Oppoband) at the 100th cycle of testing. The residual strain observed for VHB is a consequence of incomplete strain relaxation accumulated from previous test cycles, which reflects significant viscosity of this material. It was observed that the hysteresis loop of natural rubber is significantly smaller than VHB and that the accumulated residual strain is negligible. Hysteresis is quantified by the area bounded by the hysteresis loop, divided by the total energy stored during stretching, expressed in percentage. Physically, this value quantifies the percentage of energy lost by hysteresis for each stretch-relax cycle. From Fig. 12, natural rubber is a better material for energy harvesting, due to its good elasticity and low hysteresis. An additional advantage for natural rubber is its significantly lower cost as compared with the proprietary 3M VHB tape (Kaltseis et al. 2014).

In the energy harvesting experiment, the DE must be mechanically stretched. This must be done in a consistent, cyclic fashion. In principle, any arbitrary method may be used to prescribe time-varying stretch on the DE. We present the “inflating

Fig. 13 A DE membrane connected to a pressure chamber (Reproduced with permission from Kaltseis et al. (2011). Copyright 2011, AIP Publishing LLC)



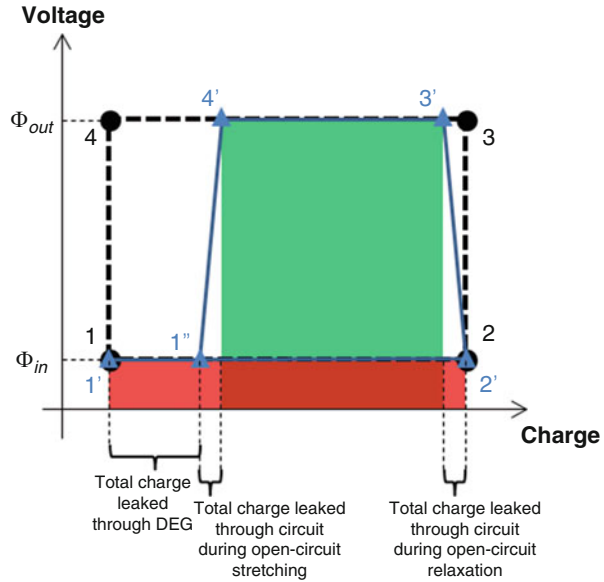
membrane” as an example (Fig. 13). The mechanical excitation source is a pressure chamber.

The DE is first wrapped and clamped on a circular-shaped outlet of a small pressure chamber. The DE is stretched by means of varying air pressure, inflating and deflating the membrane. The varying air pressure may be programmed using an Arduino[®] controller, with a feedback loop provided by a pressure sensor to maintain a consistent cycle of maximum pressure. For this experiment, the DE is approximately equal biaxially stretched in regions around its apex but under a state of “pure shear” at its clamped edges. This setup is shown in Fig. 13.

The mechanical assembly will then be hooked up to the harvesting circuit. The circuit design shown in Figs. 10 and 13 enables the energy harvesting cycle to be timed solely based on the mechanical input signal.

In reality, charges may be lost through the circuit and its components as heat or leak through the DE as leakage current (Gisby et al. 2010). Hence, the experimental cycle (1'2'3'4' on Fig. 14) and the ideal cycle (1234) may not be identical (Foo et al. 2012b). Circuit and leakage losses (Fig. 14) play a significant role in determining the energy conversion efficiency, in addition to the mechanical hysteric losses (Fig. 12). The magnitude of loss depends on rate of operation. For fast cycles, current loss per cycle is small, while hysteresis loop is large, due to insufficient time for viscous effects to fully dissipate. Conversely, for slow cycles, current loss per cycle is large, while hysteresis loop is small. The notion of *fast* and *slow* depends on the time-scale of the processes. Previous works have shown that the process time-scale for viscous relaxation of acrylic-based VHB elastomers is in the order of 10^2 s (Foo et al. 2012a), while that for current losses scales with the resistive–capacitive

Fig. 14 Ideal versus experimental harvesting cycle



(RC) time-constant, which is in the order of 10^3 s (Gisby et al. 2010; Foo et al. 2012a). Consequently, to minimize losses, one may choose to operate in the region of between 10^2 and 10^3 s for VHB elastomer to minimize losses, or select a nonviscous elastomer to operate at a very fast rate.

4.4 Collecting Data and Analysis of Results

Primarily, four sets of physical data must be captured: force, displacement, voltage, and charge. For a comprehensive analysis of energy flow, voltage and charge variations must be monitored in the input and output reservoirs (sources), together with the force, displacement, voltage, and charge on the dielectric elastomer.

All physical data may be captured and digitized using a data acquisition (DAQ) unit, for example, the National Instruments NI6356 DAQ. A DAQ converts analog signals into digital signals for ease of data processing and analysis. Analog signals from voltmeters and load cells are electronically captured by the DAQ. The DAQ then converts these signals into electrical pulses at a prescribed frequency, also known as sampling rate. All physical data are captured over time. Hence, one should ensure that all data capture is in sync. One should further note that the prescribed sampling rate must be sufficiently large to capture accurate profiles of all time-histories.

Figure 15a shows a sample of data captured from the inflating membrane experiment, for a natural rubber membrane as the dielectric (Kaltseis et al. 2014). The figure shows data capture for the sixth cycle of operation. The reason for discarding the first five cycles is to allow the Mullin's effect to elapse, so that the

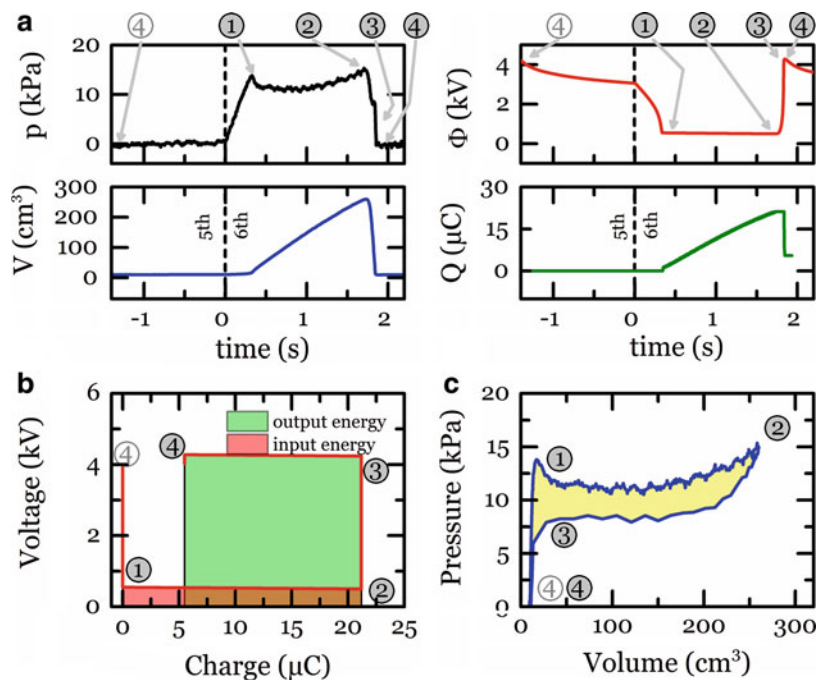


Fig. 15 Experimental data to characterize performance of a DEG (Reproduced with permission from Kaltseis et al. (2014). Copyright 2014, RSC Publications)

cyclical deformation of the rubber membrane attains a steady state of operation. In these plots, the pressure p and volume V of the inflating membrane was captured in place of force and displacement, respectively. Pressure p refers to the excess pressure in the pressure chamber to inflate the membrane, which was measured with a JUMOTM dTRANS p30 pressure sensor. The volume V of the membrane was determined by video capture, whereby image analysis was done to compute V . Charge Q on the DE was inferred from voltage measurement on the DE membrane (Φ_m), using a contactless Kelvin probe voltmeter (TREKTM model 341A), to minimize charge loss from the membrane to the measurement device.

Due to the charge drawn from the input reservoir, Φ_m will see a slight decrease during process 1→2. In order to infer the charge Q on the membrane, we assume that $\Phi_m = \Phi_{in}$ (voltage of the input reservoir). Hence, $\Delta Q_{in} = C_{in}\Delta\Phi_m$. We infer the charges transferred to the output reservoir in a similar manner. The time-history plots are then collated for all four quantities, which enable the work-conjugate plots for the experiment (Fig. 15b, c) to be constructed.

From the work-conjugate plots (Fig. 15b, c), the energy/power yield and the conversion efficiency may be computed.

One may choose to define the output yield as the *gross* output energy/power and/or the *net* output energy/power. The *gross* output energy (Y_g) refers to the total

Table 1 Performance parameters of natural rubber DEG

Gross energy yield	65.9 mJ
Net energy yield	55.3 mJ
Net power yield	30.7 mW
Conversion efficiency	7.2 %
Energy leak	23.1 mJ
Specific gross energy	444 mJ/g
Specific net energy	373 mJ/g
Specific net power	207 mW/g

amount of electrical energy produced by the DE to do work. Hence, $Y_g = \Phi_{out}(Q_3 - Q_4)$, where Φ_{out} refers to the output voltage, indicated by states **3**→**4**. The *net* output energy (Y_n) refers to the gross output energy *less* the input electrical energy that was used to prime the DE. Hence, $Y_n = Y_g - \Phi_{in}(Q_2 - Q_1)$, where Φ_{in} refers to the input voltage, indicated by states **1**→**2**. One may observe very small variations in voltage along **1**→**2** and **3**→**4** due to charge flows between the DE and the input/output reservoirs. However, as the reservoirs are assumed to be very large capacitors as compared with the DE, such variations in voltage may be neglected. The power yield per cycle is simply the energy yield divided by the duration of that cycle. The output yields may be further normalized by the active mass and material volume of the membrane, to arrive at the specific energy/power and the energy/power density, respectively.

We unambiguously define conversion efficiency to be the *net* output energy divided by the input mechanical energy, given as: $\eta = Y_n/Y_m$. Y_m is computed from the area bounded by the cycle contour, plotted on the mechanical work-conjugate plot (in this case, the pressure-volume plot).

Electrical energy may be lost through current leakage. Current may leak through the elastomer or through the circuit during open-circuit stretching or relaxation. The latter is due to imperfect diodes, resistors, and connectors. Consequently, on the electrical work-conjugate plot (Figs. 14 and 15b), **2**→**3** and **4**→**1** may not be perfectly vertical. On the two-capacitor circuit, the loss of charges during open-circuit stretching/relaxation cannot be directly measured. However, one may fairly assume that the process along **2**→**3** and **4**→**1** is fast enough so that the charge loss via circuit leakage is small. Nevertheless, the experiment will provide a measure of the total amount of electrical energy lost due to charge leakage, during a particular cycle of operation (Y_{leak}). In particular, it is defined as: $Y_{leak} = (Q_2 - Q_1)(\Phi_{34} - \Phi_{12}) - Y_n$.

For this experiment, we used a circular membrane of diameter 30 mm and thickness 0.21 mm, of natural rubber samples as shown in Fig. 2. The output parameters are shown in Table 1.

4.5 Direct Demonstration of Energy Harvesting

If one wishes to demonstrate energy harvesting without the need to track energy flows, the output source may be replaced with an electrical load, for instance, an LED panel. In this case, the voltage rating of the electrical load may not match Φ_{out} .

Fig. 16 Circuit for demonstration of energy harvesting

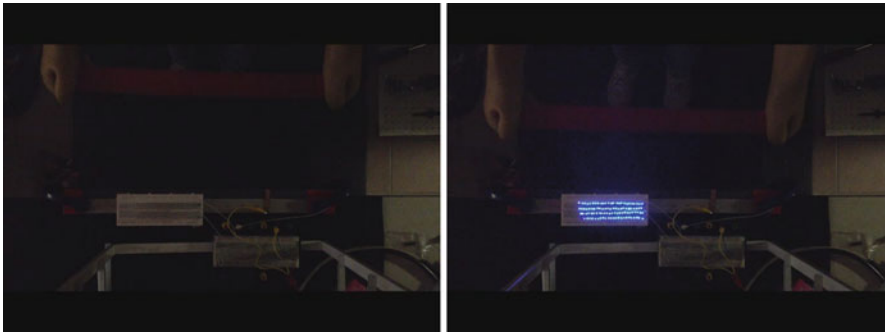
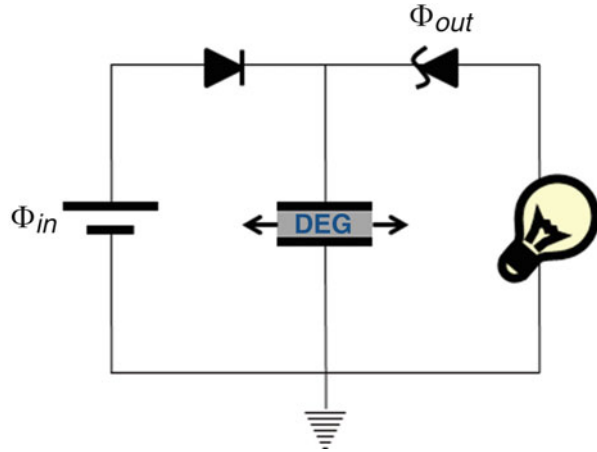


Fig. 17 Direct demonstration of DEG powering LEDs

Hence, a reverse Zener diode must be used. A Zener diode regulates current flow from the DEG to the electrical load. It acts as a current barrier, which only allows current to flow when the driving voltage is larger than the Zener diode rating. In this case, we design our Zener diode rating to match Φ_{out} . In our experiment, the Zener diodes were rated 100 V each (1N5271B, Microsemi Commercial Components Group). We connect 10 Zener diodes in series to establish a 1 kV Φ_{out} . A schematic of the circuit is shown in Fig. 16.

We set Φ_{in} to be 700 V and Φ_{out} as 1 kV. We are able to demonstrate, by manual stretching of the DEG in a uniaxial fashion, that a panel of 100 LEDs is powered (Fig. 17). Since the power rating of one LED is 4 mW, we therefore demonstrate that, by mechanically deforming the DEG, a power of at least 0.4 W was delivered.

In this section, we provided a recipe to characterize the performance of DEGs and demonstrate the operation of a DEG through powering of a LED panel. From here, more complex circuits may be designed to further maximize or optimize the performance of a DEG.

References

- Araromi OA, Gavrilovich I, Shintake J, Rosset S, Richard M, Gass V, Shea HR (2015) Rollable multisegment dielectric elastomer minimum energy structures for a deployable microsatellite gripper. *IEEE/ASME Trans Mechatron* 20(1):438–446. doi:10.1109/TMECH.2014.2329367
- Foo CC, Cai S, Koh SJA, Bauer S, Suo Z (2012a) Model of dissipative dielectric elastomers. *J Appl Phys* 111:034102. doi:10.1063/1.3680878
- Foo CC, Koh SJA, Keplinger C, Kaltseis R, Bauer S, Suo Z (2012b) Performance of dissipative dielectric elastomer generators. *J Appl Phys* 111:094107. doi:10.1063/1.4714557
- Gent AN (1996) A new constitutive relation for rubber. *Rubber Chem Tech* 69(1):59–61. doi:10.5254/1.3538357
- Gisby TA, Xie SQ, Calius EP, Anderson IA (2010) Leakage current as a predictor of failure in dielectric elastomer actuators. *Proc SPIE* 7642:764213. doi:10.1117/12.847835
- Graf C, Maas J (2011) Energy harvesting cycles based on electro active polymers. *Proc SPIE* 7642:764217. doi:10.1117/12.853597
- Huang J, Shian S, Suo Z, Clarke DR (2013) Maximizing the energy density of dielectric elastomer generators using equal-biaxial loading. *Adv Funct Mater* 23:5056–5061. doi:10.1002/adfm.201300402
- Kaltseis R, Keplinger C, Baumgartner R, Kaltenbrunner M, Li T, Mächler P, Schwödiauer R, Suo Z, Bauer S (2011) Method for measuring energy generation and efficiency of dielectric elastomer generators. *Appl Phys Lett* 99:162904. doi:10.1063/1.3653239
- Kaltseis R, Keplinger C, Koh SJA, Baumgartner R, Goh YF, Ng WH, Kogler A, Tröls A, Foo CC, Suo Z, Bauer S (2014) Natural rubber for sustainable high-power electrical energy generation. *RCS Adv* 4:27905–27913. doi:10.1039/c4ra03090g
- Keplinger C, Sun J-Y, Foo CC, Rothmund P, Whitesides GM, Suo Z (2013) Stretchable, transparent, ionic conductors. *Science* 341(6149):984–987. doi:10.1126/science.1240228
- Kofod G, Wirges W, Pajananen M, Bauer S (2007) Energy minimization for self-organized structure formation and actuation. *Appl Phys Lett* 90(8):081916. doi.org/10.1063/1.2695785
- Koh SJA, Zhao X, Suo Z (2009) Maximal energy that can be converted by a dielectric elastomer generator. *Appl Phys Lett* 94:262902. doi:10.1063/1.3167773
- Koh SJA, Keplinger C, Li T, Bauer S, Suo Z (2010) Dielectric elastomer generators: how much energy can be converted? *IEEE/ASME Trans Mech* 16(1):33–41. doi:10.1109/TMECH.2010.2089635
- Maffli L, Rosset S, Shea HR (2013) Zipping dielectric elastomer actuators: characterization, design and modeling. *Smart Mater Struct* 22(10):104013. doi:10.1088/0964-1726/22/10/104013
- McKay T, O'Brien B, Calius E, Anderson I (2010) Self-priming dielectric elastomer generators. *Smart Mater Struct* 19:055025. doi:10.1088/0964-1726/19/5/055025
- Pelrine R, Kornbluh RD, Pei Q, Joseph J (2000) High-speed electrically actuated elastomers with strain greater than 100 %. *Science* 287(5454):836–839. doi:10.1126/science.287.5454.836
- Pelrine R, Kornbluh RD, Eckerle J, Jeuck P, Oh S, Pei Q, Stanford S (2001) Dielectric elastomers: generator mode fundamentals and applications. In: *Proceedings of SPIE 4329, smart structures and materials 2001: electroactive polymer actuators and devices*, vol 148. doi:10.1117/12.432640
- Petralia MT, Wood RJ (2010) Fabrication and analysis of dielectric-elastomer minimum-energy structures for highly-deformable soft robotic systems. In: *Proceedings of 2010 IEEE/RSJ international conference on intelligent robots and systems*, Taipei, pp 2357–2363
- Rosset S, Shea HR (2012) Flexible and stretchable electrodes for dielectric elastomer actuators. *Appl Phys A* 110(2):281–307. doi:10.1007/s00339-012-7402-8
- Rosset S, O'Brien BM, Gisby T, Xu D, Shea HR, Anderson I a (2013) Self-sensing dielectric elastomer actuators in closed-loop operation. *Smart Mater Struct* 22(10):104018. doi:10.1088/0964-1726/22/10/104018
- Rosset S, Araromi OA, Schlatter S, Shea H (2015) Fabrication process of silicone-based dielectric elastomer actuators. *J Vis Exp* (108):e53423. doi:10.3791/53423

-
- Schausberger SE, Kaltseis R, Drack M, Cakmak UD, Major Z, Bauer S (2015) Cost-efficient open source desktop size radial stretching system with force sensor. *IEEE Access* 3:556
- Shian S, Huang J, Zhu S, Clarke DR (2014) Optimizing the electrical energy conversion cycle of dielectric elastomer generators. *Adv Mater* 26:6617–6621. doi:10.1002/adma.201402291
- Shintake J, Rosset S, Floreano D, Shea H (2013) Effect of mechanical parameters on dielectric elastomer minimum energy structures. In: *Proceedings of SPIE 8687, electroactive polymer actuators and devices (EAPAD)*. doi:10.1117/12.2009368

Index

- A**
- Acoustic applications of electrets/ferroelectrets
 - electrostatic speaker and earphone, 632
 - microphone, 626–631
 - Acrylate copolymers
 - DBEF, 695, 696
 - electromechanical instability, 693–695
 - high dielectric acrylate elastomers, 695–696
 - RIPN films, 695, 696
 - Active flexure, 272
 - Actuation metrics, conducting polymers, 343
 - speed, 347–348
 - volume change, 345–347
 - Actuation model, 182–183
 - Actuation principle, 294
 - Actuator materials, 5
 - Actuators, 28, 38, 41, 43
 - bilayer configuration, 261–263
 - devices and artificial muscles, 89
 - electrical characterization, 481
 - electromechanical characterization
 - (*see* Electromechanical characterization)
 - free-standing polymer, 260
 - linear stroke polymer, 263
 - mechanical characterization, 481–482
 - in microfluidics, 93–95
 - PPy–metal coil composite, 264
 - tri-layer configuration, 266–275
 - Affine deformation, 494, 496
 - Analog circuits, 96
 - Arduino[®] controller, 781
 - Atomic force microscopy (AFM), 338–339
 - Augmented system, 204
- B**
- Back relaxation effect, 228
 - Batra's model, 650
 - Bend, 500
 - Bending actuators, 684
 - characterisation techniques, 321–326
 - diaphragm pumps, 386–388
 - flexural-jointed gripper, 390
 - swimming devices, 389–390
 - Bending principle, 267
 - Bias-induced reverse piezoelectric response, 618
 - Bilayer actuators, 303–305
 - characterisation, 322
 - fabrication methods for, 304
 - Bilayer and trilayer actuators
 - characterizations of, 420–422
 - electrochemical cell, 419
 - experimental procedure, 417–419
 - materials, 416–417
 - Bilayer configuration, actuators, 261–263
 - Biomimetic robots, 196–202
 - Black box model, 77, 84, 189, 373, 376
 - conducting polymer actuators, 376–377
 - conducting polymer sensors, 373–374
 - Blocking force, 483
 - Boltzmann constant, 139
 - Braille cell, 401, 748
 - Broadband dielectric spectroscopy (BDS), 598
 - Broadband microphones, 634
- C**
- Capacitive sensors, 756–759
 - Carbide-derived carbons (CDCs), 156, 446–449
 - Carbon-based electrodes, 706–707
 - Carbon nanotubes (CNTs), 440, 444–446
 - CDC, 447
 - electrochemical CNT yarn, 468
 - hybrid yarns and coiled yarns, 457–460
 - nanogears, 444–446
 - and porous amorphous carbon, 450–451

- Carbon nanotubes (CNTs) (*cont.*)
 properties of, 456
 torsional actuation in, 456
 twisted neat CNT yarns, 466
 wax-filled CNT yarns, 463
- Cauchy stress, 716
- Cell clinic, 310, 395
- Cellular ferroelectret foil, 662
- Cellular polymers, acoustic applications of, 633–634
- Characterisation techniques
 atomic force microscopy, 338–339
 bending CP actuators, 321–326
 laser-scanning micrometry (LSM), 339–343
 linear actuators, 326–334
 profilometry, 334–338
- Charge density, 139, 175, 356
- Charge electrets, 553–554
- Charge injection model, 444
- Charge transport, 646
- Charge variation, 656
- Chemical creeping, 246
- Chemical plating method, 134
- Computer-controlled milling machine, 225
- Conducting materials, 86–88
- Conducting polymer actuators
 applications, 314
 bending structures, 359–361
 bilayer actuators, 303–305
 black box model, 376–377
 charge dependent modulus, 357
 charge–voltage relationship, 362–363
 chemical and physical vapour deposition, 299
 creep and stress relaxation, 357–359
 diffusion models, 366–368
 electromechanical coupling and efficiency, 368–369
 electronic and ionic conductivity, 363
 facilities and equipment, 295
 gray box model, 378–379
 inertial effects and rare limits, 361
 integration in complex devices, 308–312
 IPN, 303–305, 306
 oxidative coupling, 300
 patterning and subtractive techniques, 296–299
 performance, 314
 polymer anisotropy, 356
 rate limiting factors, 364–366
 specifications, 314
 spin coating, 302
 strain and charge, 355–356
 stress–strain relationship, 357
 trilayer actuators, 305–306
 vapour phase polymerization, 301
- Conducting polymer microactuators
 biocompatibility, 395
 cell biology, 395–398
 medical devices, 398–400
 microdevices, 391–393
 microfluidics and drug delivery, 393–395
- Conducting polymers (CPs)
 bending artificial muscles, 242–243
 creeping effects, 246
 electrochemical model, 245–246
 electrochemomechanical characterization, 246
 exchange of cations, reduction (n-doping), 241
 hysteresis, asymmetry, osmotic and electro-osmotic effects, 246
 irreversible parallel reactions, 246
 linear artificial muscles, 243
 liquid electrolyte, 416–422
 materials, 239
 mechanical and mathematical models, 244–245
 movement, reproducibility of, 246
 open air, 422–433
 operation principle, 239–240
 oxidation, 240–241
 sensing motors, 247–248
- Conducting polymer sensors
 black box model, 373–374
 mechanisms, 370–372
- Conduction current density, 646
- Constant charge generation cycle, 760
- Continuum model, 61, 78
- Cooperative diffusion coefficient, 16
- Coupled multi-field formulation, 60
- Crack initiation and growth, 678
- Creep, 330–332
- Cross-linking, 10
- Cyclic voltammetry (CV), 137, 144, 421
- CYTOP, 568–570
- D**
- Darcy's permeability, 140
- Data acquisition (DAQ), 782
- Deflecting/bending tubes, 269
- Degree-of-sulfonation (DOS), 166
- Degree of swelling, 107–108
- DE minimum energy structures (DEMESs), 744
- DE stack actuator (DESA), 726

- Dextran, 40
- Diaphragm pumps, 386–388
- Dibutoxyethoxyethyl formal (DBEF), 695, 696
- Dibutyltin dilaurate, 426
- Dielectric elastomer actuators (DEAs), 706
 - compliant electrodes for, 771
 - DEMES principle of operation, 772
 - kV DEA drive circuit, 773
 - metal electrodes for, 707
 - polyurethane, 696, 698
 - silicone membranes, 769
 - soft elastomers, 704
 - transparent electrodes for, 708
- Dielectric elastomer generator (DEG)
 - buoy energy generator, 761
 - direct demonstration of, 785
 - energy harvesting circuit, 778
 - heel strike generator, 761
 - natural rubber, performance parameters of, 784
 - “open-circuit” condition, 778
 - operating principle of, 775
 - operation modes of, 760–761
 - working principle of, 759
- Dielectric elastomer minimum energy structure (DEMES), 772–773
- Dielectric elastomers (DEs)
 - acrylate copolymers, 692–696
 - actuator parameters, 737
 - capacitive sensors, 756–759
 - carbon-based electrodes, 706–707
 - cell stretcher, 762
 - compressible soft dielectrics, constitutive equations for, 720–722
 - definition, 716
 - DEMES grippers, 744
 - dynamic stimulation, 732–735
 - electrical model, 727–730
 - energy harvesters (*see* Energy harvesters, dielectric elastomer)
 - fish-like airship, 742–743
 - flapping wing vehicles, 742
 - fluid control and microfluidics, 752–756
 - incompressible soft dielectrics, constitutive equations for, 722–723
 - kV DEA drive circuit, 773
 - Maxwell stress, electric field, 718–719
 - membrane materials, 769
 - metallic thin-film electrodes, 707–708
 - minimum energy structure, 772–773
 - nominal electrical quantities, 720
 - nonlinear mechanical behaviour, soft elastomers, 716–718
 - Pelrine’s model, 723–724
 - physically-networked block copolymer systems, 700–704
 - planar soft dielectric device, actuation laws of, 724–726
 - polyurethanes, 696–700
 - schematic principle of, 726
 - silicone-based materials, 688–692
 - static stimulation, 730–732
 - SWCNTs, 709, 753–754
 - switch, 761
 - tactile feedback and displays (*see* Tactile displays)
 - tunable optics (*see* Tunable optics)
 - VHB™, 769
 - walking robots, 741–742
- Dielectric elastomer transducers
 - configurations, 679
 - failure modes, 677–678
 - operation principles, 673–677
- Dielectric permittivity spectrum, 598
- Dielectric resonance spectroscopy, 608–609
- Dielectrostriction, 490, 501–504
- Diffusion models, 366–368
- Dimethyl sulfoxide (DMSO), 282, 283
- Dipole electrets
 - amorphous dipole electrets, 556–557
 - semicrystalline dipole electrets, 557
- Dipyrrole alkane, 330
- Direct assembly method, 134, 156
- Direct assembly process, 441
- Direct dielectric breakdown, 678
- Direct piezoelectricity, 490–494, 496, 497, 503
- Dirichlet boundary conditions, 177
- Discrete circuits, 95–96
- Dissipative particle dynamics (DPD), 701
- Donnan potential, 370
- 4D printing, 274
- Dry etching technique, 298
- Dynamic light scattering (DLS) technique, 111
- E**
- EAP transducers
 - actuators (*see* Actuators)
 - poly(3,4-ethylenedioxythiophene) poly(styrene sulfonate), 281–283
 - as sensors, 275–281
- Earphone, 631
- Elastic modulus, ferroelectrets, 596
- Electret generator
 - configurations of, 637
 - gap-closing, 638

- Electret generator (*cont.*)
 high-frequency, 640
 in-plane, 639
 MEMS, 84, 95, 268, 274, 631, 632, 638
 out-of-plane, 637
- Electret microphone model, 654–657
- Electret motor, 634
- Electrets
 charge stability in, 557–558
 history of, 552–553
 polymer electrets (*see* Polymer electrets)
- Electrical breakdown, 603–604
- Electrical conductivity, 137
- Electrical control, 475–480
- Electrical impedance model, 179–182
- Electric polarization, 493
- Electroactive microfluidic (EAM) devices,
 753, 754
- Electroactive polymer (EAP), IPMCs. *See* Ionic
 polymer-metal composites (IPMCs)
- Electroactive scaffold, 397
- Electroactuation
 moderately polar TPE systems, 704
 nonpolar TPE systems, 702–704
- Electrochemical impedance spectroscopy
 (EIS), 481
- Electrochemically-driven actuators
 electrode on, 474
 equivalent electrical circuit, 476
 modulation technique, 478–479
 operating voltage of, 474
 rectangular voltage, 477
 sinusoidal voltage, 477–478
 voltage vs. current control, 478
- Electrochemically-driven carbon based
 materials
 bending actuation, characterization of,
 442–443
 carbide-derived carbon, 446–449
 CNTs, 444–446
 device configuration, 441–442
 Faradaic charge transfer reactions, 443
 porous amorphous carbon, 450–451
 research motivation and application,
 440–441
- Electrochemical stability window (ESW), 480
- Electrochemical synthesis, 300
- Electrochemomechanical strain (ECMS), 330
- Electrode materials
 metallic electrode materials, 153–156
 non-metallic electrode materials, 156–158
- Electrode plating method, 218
- Electrodeposition, 260
- Electrokinetic effect, 370
- Electromechanical characterization
 blocking force, 483
 isotonic strain measurement, 484
 unobstructed, 'free' actuation, 482–483
- Electromechanical coupling, 368–369
- Electromechanical energy harvesting, 542–543
- Electromechanical instabilities, 678
- Electro-mechanical materials, 499
- Electron beam lithography, 117
- Electronic conducting polymers (ECPs),
 414, 415, 422, 429, 431
- Electronic conductivity, 366
- Electronic skins, 538
- Electro-responsive hydrogels, 41–44
- Electrospinning, 538
- Electrostriction, 490, 501–504
- Electrostrictive graft elastomers (G-elastomers),
 525–526
- Electrostrictive polymer and piezoelectric
 polymer. *See* Piezoelectric polymers
- Electrostrictive polymers
 electrostrictive graft elastomers, 525–526
 HEEI P(VDF-TrFE) copolymers, 524–525
 P(VDF-TrFE)-based terpolymers, 526–527
 PVDF-based copolymers, 527–528
- Electrothermally-driven actuators
 benefit, 473
 control for, 475–476
- Electrothermally-driven carbon based materials
 device configurations, 461–462
 hybrid yarns and coiled yarns, 457–460
 tensile actuation (*see* Tensile actuation)
 torsional actuation performance
 (*see* Torsional actuation)
- Emission-limited discharge model, 652
- Energy harvesters, dielectric elastomer
 cycle of operation and harvesting circuit
 design, 777–779
 data and analysis of results, 782–784
 direct demonstration of, 784–785
 hysteresis test, 779, 780
 ideal vs. experimental harvesting
 cycle, 782
 pressure chamber, 781
 principle of operation, 773–777
 VHB acrylic elastomer and natural
 rubber, 780
- Energy harvesting, 206
 biomimetic fish tail, undulations of, 207
 dielectric elastomer, 759–761
 torsional vibrations, 208
 wedge slamming impacts, 208–209

- Equivalent circuit of ferroelectret film
 sensor, 663
- Equivalent series resistance (ESR), 476
- Euler–Bernoulli beam, 199
- F**
- Fabrication techniques, 86
- Faraday’s laws, 239
- Fatigue, 332
- Ferroelectret force sensor, 665–667
- Ferroelectrets, 554–555
- acoustic method, 606, 607
 - characterisation, 592
 - chemically modified polyolefin, 564–566
 - cyclo-olefin polymer and copolymer, 578–579
 - dielectric resonance spectroscopy, 608–609
 - dynamic coefficient, 605
 - electrostatic speaker and earphone, 632
 - fluoropolymers (*see* Fluoropolymer ferroelectret)
 - formation of, 593
 - interferometric method, 607
 - layer-structure model, 594
 - material parameters, 571
 - microphone, 626–631
 - polycarbonate, 579
 - polyester, 575–576
 - polyethylene, 573–574
 - polypropylene, 572–573
 - pressure and frequency dependence of piezoelectric coefficient, 610–611
 - profilometer, 606
 - quasi-static piezoelectric coefficient, 604–605
 - stress–strain curves, 594–597
 - thermal stability of piezoelectricity, 610
- Ferroelectric and piezoelectric polymers.
 See Piezoelectric polymers
- Ferroelectric hysteresis, 601
- Finite element analysis (FEA), 195
- Fixed-electrode electret method, 629
- Flexible framed actuators, 683
- Flexible printed circuit boards (FPCB), 312, 313
- Flexoelectricity, 500–505
- Flexural-jointed gripper, 390
- Flory–Rehner parameter, 9
- Fluid micropump, 387
- Fluoropolymer ferroelectret
- cavities, 582–583
 - cellular, 581
 - laser bonding technique, 583
 - porous PTFE, 580
 - teflon AF ferroelectrets, 583
- Foil electret microphone, 627
- Force rate measurements, 664
- Free-standing actuators, 683
- Free-standing polymer actuator, 260
- Freeze-dried bacterial cellulose (FDBC), 163, 164
- G**
- Gas-diffusion expansion (GDE) process, 572
- Gent model, 718
- Gibbs free energy, 491
- Graphene-Nafion polymer actuator, 165
- Grey box models, 373
- conducting polymer actuators, 378–379
- Gross output energy, 783
- H**
- Hammerstein model, 186
- Heterodyne scattering, 111
- High-energy-electron irradiated (HEEI) P (VDF-TrFE) copolymers, 524–525
- High-performance polymer electrets
- CYTOP, 561–562, 568–570
 - parylene, 566–568
- Homocharge transport, 648
- Hooke’s law, 175
- Human-machine interface (HMI), 522
- Humidity, 678
- Humidity-sensitive linear actuators, 402–404
- Hydrogels
- actuator devices and artificial muscles, 89
 - actuators, 5
 - challenges, 21–22
 - characteristics, 103
 - characterization, 107–115
 - classification, 104
 - conducting materials, 86–88
 - fabrication techniques, 86
 - medical devices, 90
 - optical devices, 89–90
 - patterning, 115–118
 - physical properties, 5
 - preparation, 104–106
 - sensitivities, 20–21
 - swelling kinetics, 14–20
 - thermodynamics, 6–14
 - thermostats and chemostats, 90–92
- Hysteresis, 246

I

- Impedance spectroscopy, 599
- Impregnation-reduction method, 153
- Ink-jet printing, 118
- Integrated control technique, 313
- Integrated microchemomechanical systems, 93
- Interpenetrating polymer networks (IPNs), 306–308, 424–427, 693, 695
- Inverse piezoelectricity, 490–493
- Ionic charge, 355
- Ionic liquid/polyurethane (IL/PU) gels, 283
- Ionic liquids (ILs), 219, 475
- Ionic polymer gels, 59, 60
- Ionic polymer-metal composites (IPMCs), 178, 476
 - active micro-catheter, 192–194
 - actuation model, 182–183
 - advantages of, 135
 - biomedical and human affinity applications, 132
 - biopolymer membrane materials, 162–164
 - characterization of IPMC actuators, 136–137
 - complex deformations, 225–227
 - device configuration, 134–135
 - electrical impedance model, 179–182
 - electric current, 132
 - electrochemistry of, 143–144
 - electromechanical characterization of, 219–225
 - electromechanical modeling of, 138–142
 - electromechanical properties of, 158
 - fabrication of, 216–219
 - feedforward and feedback control, 227–230
 - fish-like robots, 197–198
 - human affinity tactile devices, 195–196
 - ionic current, polymer membrane, 172–175
 - mechanical properties of, 144–146
 - mechanical simulations, 184–189
 - metallic electrode materials, 153–156
 - micropump, 194–195
 - model reduction, 183–184
 - nanocarbon-composite membrane materials, 164–167
 - Navier equations, 176
 - Neumann boundary conditions, 177
 - non-metallic electrode materials, 156–158
 - sensor/actuator integrated (feedback) systems (*see* Sensor/actuator feedback systems)
 - solid mechanics physics, 175–176
 - sulfonated block copolymer membrane materials, 159–162

- sulfonated hydrocarbon backbone membranes, 159
 - swimming snake robot, 198–199
 - tubular IPMC actuator, 193
 - walking robots, 200–201
- Ion mobility, 363
- IPMC actuators. *See* Ionic polymer-metal composites (IPMCs)
- Isothermal surface potential decay, 653

J

- Joule heating, 282

K

- Kelvin–Voigt model, 358

L

- Labs-on-a chip, 92–96
- Lame's constants, 175
- Lamina emergent mechanism, 274, 280
- Laser bonding technique, 583
- Laser displacement sensor, 221, 330
- Laser induced pressure pulse, 615, 616
- Laser micrometry, 323
- Laser-scanning micrometry (LSM), 339–343
- Laser speckle reducer (LSR), 749
- Layer-structure model of ferroelectret, 594
- Light responsive hydrogels, 39–41
- Linear actuators
 - Braille cell, 401
 - characterisation techniques, 326–334
 - humidity-sensitive, 402–404
 - origami actuators, 405–406
- Linear elastic material model, 175
- Linear stroke polymer actuator, 263
- Linear time invariant (LTI) system, 188, 203
- Loudspeaker, 631
- Lower critical solution temperature (LCST), 6, 36
- Lower critical transition temperature (LCST) behaviour, 85
- Low-field dielectric spectroscopy, 597–599
- Lutamer[®], 326

M

- MATLAB, 230
- Maxwell and Voigt model, 733
- Maxwell model, 359

- Maxwell stress, 673, 718–719
Mechanical creeping, 246
Mechanochemoelectrical behavior, 276
Medical devices, 90
MEMS piezoelectret energy harvester, 640
Metallic thin-film electrodes, 707–708
Microactuators, 262
Microanastomosis connector, 398
Microcontact printing technique, 118
Microelectromechanical systems (MEMS), 84,
95, 268, 274, 631, 632, 638
Microfluidics, 92–96
Micro-gripping system, 325
Microhinges, 392
Micro linear positioner, 274
Microphone, 626–631
Microporous carbon, 444
Microprinting technology, 441
Micropump, 194–195
Modeling, 59, 61, 65, 76, 78
different scales, 61–62
Molding process, 226
Multiwalled nanotube (MWNT), 457, 459,
461, 465
- N**
NAND gate design, 762
Navier equations, 176, 177
NEMO, 271, 276, 390
Neo-Hookean model, 717
Nernst equation, 362
Nernst–Planck equation, 138, 174, 176
Net output energy, 784
Neumann boundary conditions, 177
Newton's second law, 176
Non-affine deformation, 495–496
Nonlinear dielectric spectroscopy,
599–601
Numerical simulation, 59, 60, 70
- O**
Odd-numbered nylons
annealing temperature, 516
molecular structures and ferroelectricity of,
515–516
Omnidirectional condenser microphone, 626
Onsager coefficients, 140
Optical devices, 89–90
Origami actuators, 405–406
Oscilloscope, 664
Overoxidization, 299
- Oxidation (p-doping)
exchange of anions, 240–241
exchange of cations, 241
Oxyfluorinated surface, 564
- P**
Padé approximation, 183
PANI nanofiber. *See* Polyaniline (PANI)
Parallel five-bar mechanism, 273
Parasitic capacitance for rotational
generators, 636
Particle image velocimetry (PIV) system, 209
Parylene, 566–568
Parylene HT[®], 562
Paschen's law, 574
PEDOT nanorods. *See* Poly
(3,4-ethylenedioxythiophene) (PEDOT)
Pelrine's model, 723–724
Pendent sulfonated chitosan (PSC), 166
Perfluorinated ionic polymers (PIPs), 217
Perfluorinated polymers, 134
Peristaltic motion, 268
Petal-shaped diaphragm, 268
Phase transition, 109–110
Photodegradable ortho-nitrobenzyl (o-NB)
groups, 40
Photolithography, 117
Photomasks, 296
Photoresponsive PAAm/PEG based
hydrogels, 40
Photostimulated discharge (PSD)
spectroscopy, 558
pH-responsive hydrogels, 38–39
pH sensitive hydrogels, 21
Physically-networked block copolymer systems
electroactuation, 702–704
phase behaviour of, 700–702
Physics-based model, 138, 172–177
Piezoelectrically generated pressure step
technique, 615, 616
Piezoelectricity
bending, 501
discovery, 490
principles of, 490–493
torsional, 501
Piezoelectric polymers
electromechanical energy harvesting,
542–543
electronic skins, 538
loudspeakers, tactile sensors and Braille
displays, 539–542
mechanisms, 511

- Piezoelectric polymers (*cont.*)
 printing of, 535–538
 properties, 519–520
 PVDF (*see* Polyvinylidene fluoride (PVDF))
 shear piezoelectric polymers, 520–523
- Plasma enhanced CVD (PECVD), 299
- Plurionics, 38
- PNIPAAm gels, 111
- PNIPAM, 6, 8–10, 20–21, 37, 85, 109–111
- Poisson–Nernst–Planck (PNP) model, 139, 175
- Poisson's equation, 139
- Poisson's ratio, 176
- Polarization–voltage hysteresis, 633
- Poloxamer, 38
- Poly(3,4-ethylenedioxythiophene) (PEDOT), 43, 414, 423, 426, 427
- Poly(*N,N*-diethylacrylamide) (PDEAAm), 38
- Poly(*N*-isopropylacrylamide) (PNIPAAm), 4, 85
- Poly(*N*-vinylcaprolactam) (PVCL), 37
- Polyacrylamide (PAAm), 38
- Polyacrylic acid (PAA), 38
- Polyaniline (PANI), 157, 162, 163, 708
- Polycarbonate ferroelectret, 579
- Polydimethylsiloxane (PDMS), 118, 688, 690, 706
- Polyelectrolyte gels, 58, 60, 78
- Polyester ferroelectret, 575–576
- Polyethylene ferroelectret, 573–574
- Poly-L-lactic acid (PLLA), 520
 origin of piezoelectricity, 521–522
 as practical sensing material, 522–523
- Polymer electrets
 charge electrets, 553–554
 chemically modified, 564–566
 dipole electrets, 556–557
 ferroelectrets, 554–555
 high-performance (*see* High-performance polymer electrets)
 with physical treatment, 563–564
- Poly(3,4-ethylenedioxythiophene) poly(styrene sulfonate) (PEDOT/PSS), 281–283
- Poly(acrylic acid)/poly(vinyl alcohol)-gel, 105
- Polypropylene ferroelectret, 572–573
- Polypyrrole (PPY)
 actuation mechanism of, 422
 electrogeneration of, 417
 electropolymerization of pyrrole monomer, 417
 oxidation and reduction reaction of, 414
- Polypyrrole creep, 331
- Polytetrafluoroethylene (PTFE), 553
- Polyurethane elastomers (PUEs), 697
- Polyurethanes, 696–700
- Polyvinylidene fluoride (PVDF), 422–424, 527–528, 534, 535, 538, 543
 Curie transition temperature, 514
 melting temperature, 514
 nylon 11–PVDF blends, 518–519
 odd-numbered polyamides (nylons), 514–517
 PVDF-nylon 11 bilaminates, 517–518
 structures of, 512–513
- PPy bulk microactuator, 309
- PPy–metal coil composite, 264
- PPy–zigzag metal composite actuator, 265
- Pressure-assisted microsyringe (PAM) system, 699
- Pressure-loaded diaphragm actuators, 684
- Printing techniques, 118
- Profilometer, 334–338, 606
- Prony method, 734
- Pulse width modulation (PWM), 478, 758
- Push-pull electret transducer, 630
- P(VDF-TrFE)-based terpolymers, 526–527
- PVDF-based copolymers, 527–528
- PWM control signal. *See* Pulse width modulation (PWM)
- Pyroelectric current spectrum, 615
- Pyroelectricity, 603
- Pyroelectric microscopy, 618
- PYZOFLEX[®] technology, 535
- Q**
- Quasi-irreversible swelling, 337
- Quasi-static method, 607
- Quasi-static piezoelectric coefficient, 604–605
- R**
- Radial basis function (RBF), 186
- Rectangular voltage, 477
- Relaxed IPN (RIPN) films, 695, 696
- Relaxor ferroelectric polymers, 541
- Resistive-capacitive (RC), 778
- Resonance frequency, 361
- Reversible expansion vs. strain, 347
- Rigid-framed actuators, 680
- Rotational electret generator, 634–636
- S**
- Sacrificial layer technique, 303–305
- Scale transform method, 614
- Scanning electron microscope (SEM), 137, 457, 458, 460

- Scanning pyroelectric microscopy (SPEM), 618
- Sensor/actuator feedback systems
- energy harvesting (*see* Energy harvesting)
 - estimation method, 203–204
 - feedback control, sensor signal, 204–206
 - sensor function of, 202–203
- Shape memory alloy (SMA) actuators, 403
- Silicone-based materials, dielectric elastomers
- composites, 690–691
 - cross-linking strategies, 689–690
 - functionalization, 691–692
- Single-walled carbon nanotubes (SWCNTs), 708, 709, 753, 754
- Sinusoidal voltage, 477–478
- Slot effect, eletret motor, 634, 635
- Smart hydrogels
- description, 4
 - electro-responsive hydrogels, 41–44
 - light responsive hydrogels, 39–41
 - pH-responsive hydrogels, 38–39
 - temperature-responsive hydrogels, 36–38
- Sodium acrylate, 106
- Soft lithography, 296
- Sol–gel content, 108
- Sol–gel transition, 110
- Solid polymer electrolyte (SPE), 306, 424
- Solid-state actuators, 266
- Solvent-sensitive hydrogels, 20
- SPE membrane. *See* Solid polymer electrolyte (SPE)
- Spin coating, 302
- Splay, 500
- Spray-painting, 441
- Spring model, 493–500
- Standard linear solid (SLS) model, 359, 732, 734
- Statistical theory, 59, 61–65
- Stiffening spring system, 279
- Stokes–Einstein law, 140
- Strain, 490–492, 503
- Strain rates, 284
- Stress, 490–492, 503
- Sulfonated hydrocarbon polymers, 135
- Sulfonated poly(amic acid) (SPAA), 160
- Sulfonated poly(styrene-ran-ethylene) (SPSE), 159
- Sulfonated polyimide (SPI), 160
- Surface potential relaxation rate, 650
- Swelling behavior, hydrogels, 30, 33, 35, 37, 42
- Swelling effect, 297
- Swelling process, 115
- Swelling theory, Doi, 17–19
- Swimming devices, 389
- T**
- Tactile displays
- buckling diaphragms, 747–748
 - hydrostatically-coupled actuators, 746–747
 - shear-transmission actuators, 746
 - stacked actuators, 745
 - thickness-mode actuators, 744–745
 - tubular actuators, 748–749
- Tanaka-Fillmore theory, 14–17
- Teflon AF, 581
- Temperature-responsive hydrogels, 36–38
- Temperature-sensitive hydrogels, 20
- Tensile actuation
- neat twisted yarns, 465–466
 - wax-filled twisted and coiled yarns, 466–468
- Tetronics, 38
- Thermal-pulse method, 612
- Thermal step technique, 613
- Thermal wave technique, 612
- Thermoplastic elastomers (TPEs), 701, 702
- moderately polar TPE systems, 704
 - nonpolar TPE systems, 702–704
- Thermostats and chemostats, 90–92
- Thickness mode actuators, 685
- Torsional actuation
- over-damped hybrid yarn muscles, 463–464
 - wax-filled single ply yarn muscles, 462–463
- Transmission line circuit (TLC) model, 144
- Trapped charge model, 654
- Trilayer actuators, 305–306
- and bilayers (*see* Bilayer and trilayer actuators)
 - force characterizations, 432
 - IPNs, 424–427
 - load curves and metrics, 433
 - PVDF membrane, 422–424
 - strain characterizations, 429–431
- Tube-in-tube actuator node (TITAN), 268, 270, 387
- Tubular and rolled actuators, 683
- Tunable optics
- laser speckle reducers, 749
 - tunable lenses, 749–752
- Twist, 500
- Two-domain Heckmann diagram, 492
- U**
- Upper critical solution temperature (UCST), 37

V

Van't Hoff factor, 240
Vapor grown carbon fibers (VGCFs), 448
Vapour phase polymerization (VPP)
 technique, 301
VHB acrylic elastomer and natural rubber, 780
Viscoelastic effects, 732
Volume change, 294
Volumetric capacitance, 362

W

WANDA, 272, 277, 390
Water content (W_C), 136

Weibull distribution, 603
Wet etching, 297
Wiechert model, 359
Wintle's model, 648

Y

Young's modulus, 176, 182, 285

Z

Zener diode, 785